ICMMPE 2022

Conference proceedings

INTERNATIONAL CONFERENCE ON MECHANICAL, MANUFACTURING AND PROCESS ENGINEERING

25-27 JUNE 2022

VENUE:
DUET, GAZIPUR

MODE:
HYBRID
(PHYSICAL AND VIRTUAL)

CONFERENCE PROCEEDINGS

International Conference on Mechanical, Manufacturing and Process Engineering (ICMMPE 2022)

25-27 June 2022
Faculty of Mechanical Engineering, DUET, Gazipur, Bangladesh
https://icmmpeduet.com/

Organized by

Faculty of Mechanical Engineering

Department of Mechanical Engineering
Department of Textile Engineering
Department of Industrial and Production Engineering
Department of Materials and Metallurgical Engineering
Department of Chemical and Food Engineering
Institute of Energy Engineering

Publication Partner

AIP Publishing

Indexed In

Scopus®

ELSEVIER

WEB OF SCIENCE™

Clarivate Analytics

Sponsors

KAI ALTECH
GROUP
Trusted Quality
Worldwide
Manufacturer of
ALUMINIUM
Profiles
KAI
ALUMINIUM
ALTECH
ALUMINIUM
EDF
ALUMINIUM
KAI BANGLADESH ALUMINIUM LTD.
ALTECH ALUMINIUM INDUSTRIES LIMITED
Plot #1, Road # 5, Block #J, Baridhara, Dhaka-1212.
Telephone: +88 02 222280018, 02 8834313

অগ্রণী ব্যাংক লিমিটেড
Agrani Bank Limited
দেশ ও জাতির সেবায় প্রতিশ্রুতিবদ্ধ
Committed to Serve the Nation
www.allbankbd.com

CONFERENCE PROCEEDINGS

International Conference On
Mechanical, Manufacturing and Process Engineering
25-27 June 2022

All rights reserved. No part of this publication may be reproduced, stored, retrieved system, or transmitted, in any form or by any means, without the written permission of the publisher, nor be otherwise circulated in any form of binding or cover.

The individual contributions in this publication/abstracts and any liabilities arising from them remain the responsibility of the authors.

The publisher is not responsible for possible damages, which could be a result of content derived from this publication/abstracts.

CONFERENCE COMMITTEE

Chief Patron

Prof. Dr. Md. Habibur Rahman
Vice-Chancellor, DUET, Gazipur

Patron

Prof. Dr. Mohammad Abdur Rashid
Pro-Vice Chancellor, DUET, Gazipur

Conference Chair

Prof. Dr. Himangshu Bhowmik,
Dean, Faculty of Mechanical Engineering, DUET, Gazipur

Conference Secretary

Prof. Dr. Mohammad Washim Dewan,
Dept. of ME, DUET, Gazipur

ORGANIZING COMMITTEE

Chair:
Prof. Dr. Md. Kamruzzaman, Head, Dept. of ME, DUET, Gazipur

Co-Chair:
Prof. Dr. Hasan Mohammad Mostofa Afroz, Head, Dept. of CFE, DUET, Gazipur
Prof. Dr. Md. Arefin Kowser, Head, Dept. of MME, DUET, Gazipur
Prof. Dr. Md. Anowar Hossain, Head, Dept. of IPE, DUET, Gazipur
Prof. Dr. Nayeem Md. Lutful Huq, Director, Institute of EE, DUET, Gazipur

Secretary:
Prof. Dr. Shahjalal Khandaker, Head, Dept. of TE, DUET, Gazipur

TECHNICAL COMMITTEE

Chair:
Prof. Dr. Mohammad Asaduzzaman Chowdhury, Dept. of ME, DUET, Gazipur

Co-Chair:
Prof. Dr. Mohammad Zoynal Abedin, Dept. of ME, DUET, Gazipur
Prof. Dr. Md. Anowar Hossain, Dept. ME, DUET, Gazipur
Prof. Dr. Md. Abdus Shahid, Dept. of TE, DUET, Gazipur
Prof. Dr. Md. Mostaqur Rahman, Dept. of ME, DUET, Gazipur
Dr. Md. Abdullahil Kafi, Associate Professor, Dept. of TE, DUET, Gazipur
Dr. Mohammad Zakaria, Associate Professor, Dept. of TE, DUET, Gazipur
Mr. Prithbey Raj Dey, Assistant Professor, Dept. of IPE, DUET, Gazipur
Dr. Biplov Kumar Roy, Assistant Professor, Dept. of ME, DUET, Gazipur
Dr. Shafiqul Islam, Assistant Professor, Dept. of TE, DUET, Gazipur
Md. Shovon Zahid, Assistant Professor, Dept. of IPE, DUET, Gazipur
Mr. Md. Abdul Aziz, Assistant Professor, Institute of EE, DUET, Gazipur
Dr. Md. Shofiul Azam, Assistant Professor, Dept. of CFE, DUET, Gazipur

Secretary:

Dr. Forkan Sarker, Associate Professor, Dept. of TE, DUET, Gazipur

PUBLICATION AND EDITORIAL COMMITTEE

Editor:
Prof. Dr. A. N. M. Mominul Islam Mukut, Dept. of ME, Gazipur

Editorial Member:
Prof. Dr. Khurshida Sharmin, Dept. of ME, DUET, Gazipur
Mr. Mohammed Moinul Islam, Associate Professor, Dept. of ME, DUET, Gazipur
Dr. Abdur Rahman, Associate Professor, Dept. of TE, DUET, Gazipur
Dr. Md. Mostafizur Rahman, Associate Professor, Dept. of ME, DUET, Gazipur
Dr. Biplov Kumar Roy, Assistant Professor, Dept. of ME, DUET, Gazipur

Associate Editor:

Dr. Md. Shahin Mia, Assistant Professor, Dept. of ME, DUET, Gazipur

Welcome to ICMMPE 2022

On behalf of the organizing committee, we are delighted to invite you to the 1st International Conference on Mechanical, Manufacturing and Process Engineering (ICMMPE 2022) at Dhaka University of Engineering & Technology (DUET), Gazipur, Bangladesh organized by the Faculty of Mechanical Engineering. This year ICMMPE is going to be a 3-day long event organized in both physical and online mode, wherein the focus areas are: advanced materials, applied mechanics, nano technology, refrigeration and air-conditioning, thermos-fluid, Tribology.

ICMMPE 2022 provides an ideal platform for researchers from both academic and industry to present their latest research results, technologies and exchange new ideas. The scholarly research articles will be published in AIP Conference Proceedings, indexed by SCOPUS (Elsevier), Web of Science and Scimago. This conference creates adequate space for discussion for trendy topics in mechanical, material and process engineering with eight (8) keynote speeches from world renowned researchers from academia and industry.

We warmly welcome you to this academic ceremony of ICMMPE 2022 and hope this will broaden and edify your world of knowledge and information.

KEYNOTE SPEAKERS

Professor Dr. Bhaba R. Sarker, PhD, PE

Elton G. Yates Distinguished Professor of Industrial Engineering,
Department of Mechanical and Industrial Engineering,
Louisiana State University, Baton Rouge, LA 70803

Professor Dr. Ashim Datta

Department of Biological and Environmental Engineering,
Cornell University, Ithaca, New York

Professor Dr. T M Indra Mahlia

University of Technology Sydney, Australia

Professor Dr. Akio MIYARA

Department of Mechanical Engineering,
Saga University, Saga, Japan

KEYNOTE SPEAKERS

Professor Dr. Bidyut Baran Saha
Principal Investigator,
International Institute for Carbon-Neutral Energy Research, Kyushu University, Japan

Professor Dato' Ts Dr. Kamaruzzaman Bin Sopian
Director,
Solar Energy Research Institute, Universiti Kebangsaan Malaysia, 43600 Bangi Selangor, Malaysia

Professor Dato' Ts Dr. Ahmad Mujahid Ahmad Zaidi FCILT PTech
Deputy Vice-Chancellor (Academic and International),
National Defense University of Malaysia

Professor Dr. Josua P Meyer

Department of Mechanical and Aeronautical Engineering,
University of Pretoria, South Africa

Contents

Paper ID	Paper Title	Page No.
0299	Effect of Silica Aerogel on Mechanical and Thermal Properties of the Natural Fiber Reinforced Epoxy-Resin Composites and Hybrid Composites	1
0661	Design, Development and Performance Analysis of a Two Degree of Freedom Solar Tracking System	9
1007	Modeling and Simulation of Battery Driven Three-wheeler Vehicle in Bangladesh by Using MATLAB-SIMULINK	14
1141	A Comparative Scenario from Bangladeshi Industries on Engineering Parameters of Utility Machines	21
1200	GIS-AHP Approach for Wind Farm Site Selection in Bangladesh	27
1276	The Assessment of Non-COVID Patients' Hospital Visitation in a Upazilla Health Complex in Bangladesh During the COVID-19 Pandemic Situation	32
1536	Laminar Flame Speed and Markstein Length of premixed flames for the mixture of N-Dodecane and Methyl Decanoate	40
1647	A Low-Cost Intelligent Automated Door Security System Based on Fingerprints Using Microcontroller	47
1777	Numerical Analysis of Displacement and Stress Field on a Femur Bone Made of Ti-6Al-4V and SS316L	53
2504	Analyzing Failure Modes of Turbochargers for Engine-based Power Plants by Combined SWARA-FMEA Approach	61
2689	Prediction of Heart Disease Using Different Machine Learning Algorithms and Their Performance Assessment	67
2706	Ergonomics Analysis of Working Posture of Sawmill Worker Using Digital Human Modeling (DHM)	75
2884	Development of Low-Cost Single Degree Rectilinear Spring Mass Damper Open Loop System	86
2962	Experimental Study of Flow Field on Upper Surface of NACA 0015 & NACA 2418 at Different Angle of Attack	93
3019	Friction Stir Spot Welding: A novel approach to weld Polyvinyl Chloride	98
3165	Production and Mechanical Characterization of Biofiber/Glass/epoxy Hybrid Composites	103
3597	Effect of Grooved Depth Ratio on Flow Friction and Heat Transfer in Enclosure Using D2Q9 Lattice Boltzmann Method	109
3673	Numerical Investigation on Thermal Performance of Vertical U-tube Ground Heat Exchanger	117
4142	A General Method to Develop Mathematical Model for Estimating Ship Repairing Man-Hour	123
4377	Electrical Risk Domains in Ready-Made Garments Industries of Bangladesh: Applying Entropy Method to Prioritize	129
4564	Design, Fabrication, and Performance Analysis of An Eco-friendly Gutter Cleaner	135
4664	Numerical Simulation of Aerodynamic Performance of Biconvex Supersonic Airfoil	142
4855	Fracture Analysis of Adhesively Bonded Joints as a Function of Temperature	148
4986	Prioritizing Fire Risk Criteria in Ready-Made Garments Factories of Bangladesh by Applying CRITIC Method	154
5056	Modeling of 3D Printable Electrical Machineries Ferromagnetic Parts	160
5152	Numerical Investigation of Stress Field Near the Vertex of a 3D Three Layer Piezoelectric Bonded Joint	167

5552	Horizontal Axis Solar Tracking System to Enhance Efficiency with Accuracy Test by Machine Learning	172
5600	Investigation of Structural and Optical Properties of Pure and Cr-doped ZrO2 Thin Film, synthesized by Spray Pyrolysis	178
5710	Investigation of Arc Welding Joining Effects on Tensile Behavior of Marine Grade-A Mild Steel	182
6076	Adsorptive Removal of Congo Red by using Rice Husk	189
6171	Experimental Investigation on the Microstructure and Hardness of Over-aged Cast Aluminum-7 Silicon-0.3 Magnesium Alloy	195
6336	Determination of Polycyclic Aromatic Hydrocarbons in smoked meat products from Sylhet region of Bangladesh by Gas Chromatography-Mass Spectrometry (GC-MS)	200
6533	Experiment on the influence of particle size & carrier gas on exhaust characteristics during the combustion of pulverized bituminous coal.	207
6607	Supplier Selection and Evaluation using Genetic Algorithm: A Case Study in an Apparel Manufacturing Organization	214
6636	Colorometric Analysis and Fastness Properties of Mulberry Filament Silk Fabric Dyed with Azadirachta Indica Extraction	220
6643	Enhancing the Efficiency of Photovoltaic Panels by Cleaning and Cooling Techniques	227
6901	Ergonomic Assessment of Helmet for Young Adults in Bangladesh	233
7145	Analysis of Mechanical Properties of Biocompatible Materials Magnesium Alloy for Male Femoral Bone Fracture	240
7156	Effect of Shapes and Cooling Media on the Performance of Flexible Photovoltaic Panels under the Climatic Conditions of Khulna	246
7161	Performance Evaluation of Composite Polymer Electrolytes Based On Li+ Concentration In Lithium Metal Electrode	253
7195	Key Factors for Automation in the Tanning Industry in Bangladesh	265
7228	Performance Comparison Between Flat Fin Mini Channel Heat Exchanger and Wire on Tube Heat Exchanger	272
7278	Fatigue Failure Analysis of Elevator Rope Under Vibration	278
7522	Effect of Rice Husk Ash (RHA) on the Mechanical Properties of Aluminum-Cu Alloy based Metal Matrix Composites	284
7536	Study of Nanoscale Plasticity in Al - Ti Alloy Nanocube by Molecular Dynamics Simulation	290
8009	Selection of Air Compressor for Pharmaceuticals: An Approach with TOPSIS	296
8137	Analytical Solution of Vibration of Simply Supported Beam under Eccentric Axial Compressive Loading	301
8238	Trigonella Foenum-Graecum Seeds Extract as a Natural Inhibitor for Mild Steel in HCl Solution	307
8304	Microstructural Investigation of Seven-layered Aluminium-Aluminium Oxide Graded Composite Material Prepared Through Pressureless Sintering	312
8372	A Study on Design of Micro-Hydropower Power Plant for Run-off Water Sources in Bangladesh	318
8462	Evaluation of mechanical properties of SG295 steel at elevated temperatures in LPG cylinder with heat treatment	326
8472	Enhanced Mechanical Properties and Stimulation of hMSC Responses to HAp Particles Layered Porous Collagen Composite Scaffolds under 2-Phase Condition for Bone Regeneration	330
8506	Development and Control of a Hydraulic Actuator System for Industrial Applications	338
9131	Energy Consumption Behavior Analysis and Investigation of Submersible Pumping System Efficiency in Different Bore well at Barind tract of Bangladesh	344
9230	Experimental Study of Granular Materials Mixing in A Slowly Rotating Drum by Image Analysis	349
9253	Modeling and Numerical Analysis of Spiral Tube Ground Heat Exchanger to Enhance the Performance	355
9363	A Universal Battery Charging System for Ultra-Low Power Energy Harvester Applications in IoT Devices	361

9411	Energy, Exergy and Performance Analysis of High Temperature Heat Pump Cycle Using Low GWP Refrigerants	366
9435	Effective Removal of Lead from Wastewater Using Functionalized Magnesium/Aluminium-Layered Double Hydroxide	374
9447	MCDM framework of stock market using AHP, GRA, and ANP incorporated with TOPSIS followed by a SWOT analysis	379
9771	The Use of Portable Electricity Generators in Edo State, Nigeria	390
9812	An Environment Friendly Combined Method of Axial Hydro Floating and Kinetic River Turbine Based on Water Depth	394

Paper ID: 0299

International Conference on Mechanical, Manufacturing and Process Engineering (ICMMPE – 2022)

Organizer: Faculty of Mechanical Engineering, Dhaka University of Engineering & Technology (DUET), Gazipur, Bangladesh

Website: https://icmmpeduet.com/

Effect of Silica Aerogel on Mechanical and Thermal Properties of the Natural Fiber Reinforced Epoxy-Resin Composites and Hybrid Composites

Adib Bin Rashid, Subrina Akhi, Farjana Akter, Noosrat Zabin Huda

Industrial and Production Engineering Department
Military Institute of Science and Technology (MIST), Dhaka, Bangladesh

E-mail: adib8809@gmail.com

ABSTRACT

Natural fiber reinforced hybrid composites are one of the widely used materials in different engineering sectors. Composite materials played an important role in the reduction of weight, so they were used for both structural applications and components of automobiles, spacecraft, and aircraft. Various industrial and infrastructural appliances like doors, walls, fixtures, panels, window frames, roofs, vanity sinks, shower stalls, and even swimming pools are among the items that can be made with natural fiber-reinforced composites. These composites should have noble thermal and fire-retardant properties, low wettability along with good mechanical properties. Hence, the main aim of this work is to manufacture a hybrid composite of different percentages of shredded fibers (banana, pineapple, jute, and Nano silica aerogel mixed glass fiber) reinforced with epoxy resin with the help of the compression molding method. Here, Fibers will provide the strength and stiffness of the composite, and epoxy resin will work as the matrix. On the other hand, aerogel will be used as the filler material which can improve not only the mechanical properties but also the fire retardancy and hydrophobicity of the composites. To characterize the composite materials tensile, flexural, hardness, flammability, and water absorption tests were done and found that mixing aerogel with the composite may significantly reduce the flammability and increases the mechanical and hydrophobic properties.

Keywords: Hybrid Composite; Jute Fiber; Banana Fiber; Pineapple Fiber; Glass fiber; Silica Aerogel.

1. INTRODUCTION

Natural fibers are easy to handle, light to carry, and also durable, strong, and properly functional which adds great properties to be used in the hybrid composite. In some cases, natural fiber works also as an alternative to synthetic fiber. Pineapple fiber has been proved as an alternative to synthetic fiber [1] and so did banana and jute fiber [2]. Totally or partially recyclable, biodegradable natural fiber-reinforced polymer composite materials are quickly expanding their usage in terms of industrial applications and fundamental research [3]. Natural Fiber composites are more eco-friendly and have applications in transportation (automobiles, trains,marine vehicles, aerospace and aeroplane), building and construction (ceiling paneling, partition boards), packaging, and consumer products [3].

Natural fiber composite has great potential in the market and day by day new research is going on but the flammability of natural fiber reinforced polymer composite remained an untouched topic, nowadays a lot of research and further investigation are going on. A restricted measure of writing has been distributed on the fire-resistant strategies and combustibility variable of regular fibers-based polymer lattice composites [4]. Fiber-reinforced composite materials have higher strength-to-weight ratios and excellent structural and mechanical properties, along with corrosion, chemical, fire and wear resistance, including being cost-effective to produce [5]. While there have been many studies, it's found that short-length fiber and shredded fiber in composite make difference. For maximum tensile(10 percent fiber weight. i.e 17.73 MPa) strength the short fiber (186 J/m) showed up and for maximum impact strength, the short powder fiber works best whereas for flexural strength, both short and shredded fiber is comparable [6]. There should be an optimum amount of flame retardant percentage for good mechanical properties [7]. Two different additives of flame retardants are compounded with the composites. The loading of flame retardants is limited to 20 wt% in order to leave a space for natural fibers as well as the polymer and to keep the overall composite mechanical properties. The flame retardants are added in the ratio of 1:1 [8], [9]

Polypropylene (PP), sodium bicarbonate (FR1) and monoammonium phosphate (FR2) are flame retardant materials with that mango seed and zea mays were mixed and made of six samples and went through some tests. The flame retardants which were added in the ratio 1:1 and in FR ratio it gave different results. And the flame resistance observed at 36.3% for PP/MSF/FR1/FR2 and had a good

result than other composites [10]. K.Muthukumar et al. [11] used six different combinations of pineapple, banana and jute fiber to find the best thermal insulator for insulation purposes. It was found that thermal conductivity is inversely proportional to the thickness of the composite.

Aerogels being the lightest solids with high pore volume and high surface area offers enormous potential in a wide range of applications along with heat resistivity. Aerogels are now utilized for thermal insulation, but they can also be employed for electrochemistry (supercapacitors), carrier of catalysts and other active agents, filler materials, and tissue engineering [12]. Having effective strength, good toughness, and appreciable resilience, epoxy resin also possess good resistance to moisture and chemical attack. It is also a good electrical insulator [13]. In this work, epoxy resin was used as adhesive. Venkata Prasad et al. [14] analysed the effect of mechanical and thermal properties of Sisal/PLA Nanocomposites with adding various amounts of silica aerogel particles which showed Silica aerogel has significant impact on sisal fiber composite. With the increasing content of silica aerogel thermal stability and tensile, flexural strength increases. Kucharek et al. [15] produced aerogel particle-filled resin and analyzed effect of resin viscosity on pore infiltration and density in the composites. The results depict that adding silica aerogel particles into resin can significantly reduce (40%) resin density and heat conductivity.

Zhi Li et al. [18] fabricated Aramid fiber reinforced silica aerogel composites for thermal insulation and studied the mechanical and thermal properties of the composite. Their findings showed, the fiber worked as a skeleton and the conductivity of the composites increased with fiber percentages. Whereas, in case of density the opposite property was shown. It was also found that for the composites thermal stability depended completely on silica aerogel. Hence, banana, pineapple, and jute fiber with aerogel can be explored.

It is also evident that treated fiber shows better mechanical performance[14], [16]. Although, there are some negative impacts of the chemical treatment on the mechanical properties for jute fiber too [17,18]. So, we experimented with treated pineapple fiber, banana fiber and untreated jute fiber.

Here in this work, composite fabrication out of treated banana fiber, treated pineapple fiber, and untreated jute fiber is done; mixing with epoxy resin and aerogel insulation mat powder with different percentages. To understand the thermal and mechanical properties, the fabricated composites did undergo by tensile,flexural, impact test, hardness, flammability, and water absorption tests.

2. MATERIALS AND METHOD

Initially, untreated banana, pineapple and jute fiber were collected from the local market whose properties are shown in Table 1. Nano Silica Aerogel mixed fiberglass insulation mat is used as the reinforment material to improve the thermal and hydrophobic property of the composite whose ts specifications are given in Table 2.

Table 1: Properties of Natural Fiber

Fiber	Jute Fiber	Banana Fiber	Pineapple Fiber
Tensile strength (MPa) (%)	200-450	550	413-1627
Tensile modulus (GPa)	20-55	3.5	3.5
Elongation at break (%)	1.16-1.5	2.9-4.3	6-Feb
Diameter of the fiber (microns)	120-180	80-250	20-80
Density (g/cm^3)	1.45	1.35	1.07
Cellulose Content (%)	61-71	63-64	81
Hemi cellulose (%)	14-20	19	18.8
Lignin (%)	13-Dec	5	12.7
Moisture (%)	9	11	11.8

Table 2: Properties of Nano Silica Aerogel mixed with Fiberglass

Property	Value
Material	Fiberglass + Nano Silica Aerogel
Color	White
Density	180-220kg/m3
Applicable Temperature	-200℃ ~ +1000℃
Hydrophobicity	Absolute Hydrophobicity (Below 350℃)
Thermal Conductivity	0.012 - 0.018w/m·k (At 25℃)
Low-Temperature Bending	≤99%
Breaking Elongation	65%
Bending Strength	45KP
Compressive Strength	32N

2.1 Fiber Preparation

Natural Fiber, collected from the market and later was treated with chemical. As untreated fibers absorb moisture naturally, which leads to delamination between the fiber and matrix. As a result, it compromises the composite's material strength. All the fiber was chemically treated with 6% NaOH

and it was immersed in the solution of NaOH for 2 hours. After that wet fiber was dried with the help of sunlight for 8 hours and later it was dried in the drier for 5-6 hours at 60°C. Then the treated fibers were shredded with the help of a shredder as shown in the figure1.

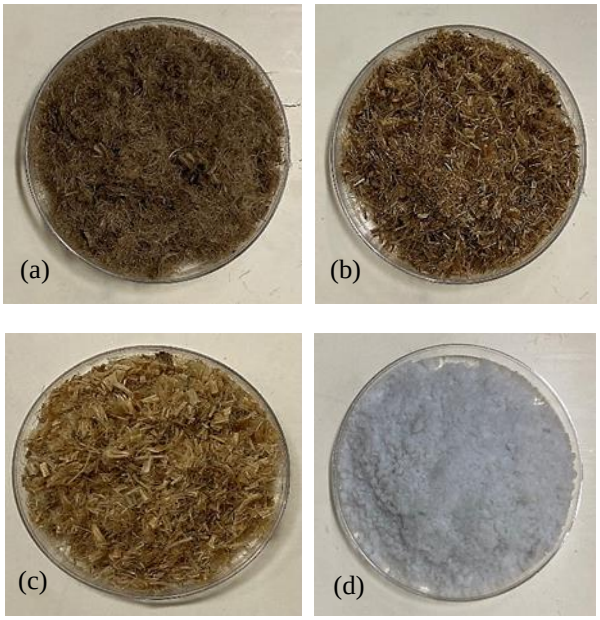

Fig. 1: Shredded (a) Jute Fiber (b) Banana Fiber (c) Pineapple (d) Nano Silica Aerogel mixed Fiberglass

Table 3: Mixing ratios of fiber, aerogel, and epoxy resin reinforcement

Specimen No (Annotation)	Fiber type	Fiber quantity	Aerogel	Epoxy Resin + Hardener
S1 (J50)	Jute Fiber	50%	Null	50%
S2 (J30A20)	Jute Fiber	30%	20%	50%
S3 (J25A25)	Jute Fiber	25%	25%	50%
S4 (B50)	Banana Fiber	50%	Null	50%
S5 (B30A20)	Banana Fiber	30%	20%	50%
S6 (B25A25)	Banana Fiber	25%	25%	50%
S7 (P50)	Pineapple Fiber	50%	Null	50%
S8 (P30A20)	Pineapple Fiber	30%	20%	50%
S9 (P25A25)	Pineapple Fiber	25%	25%	50%
S10 (A50)	Null	Null	50%	50%

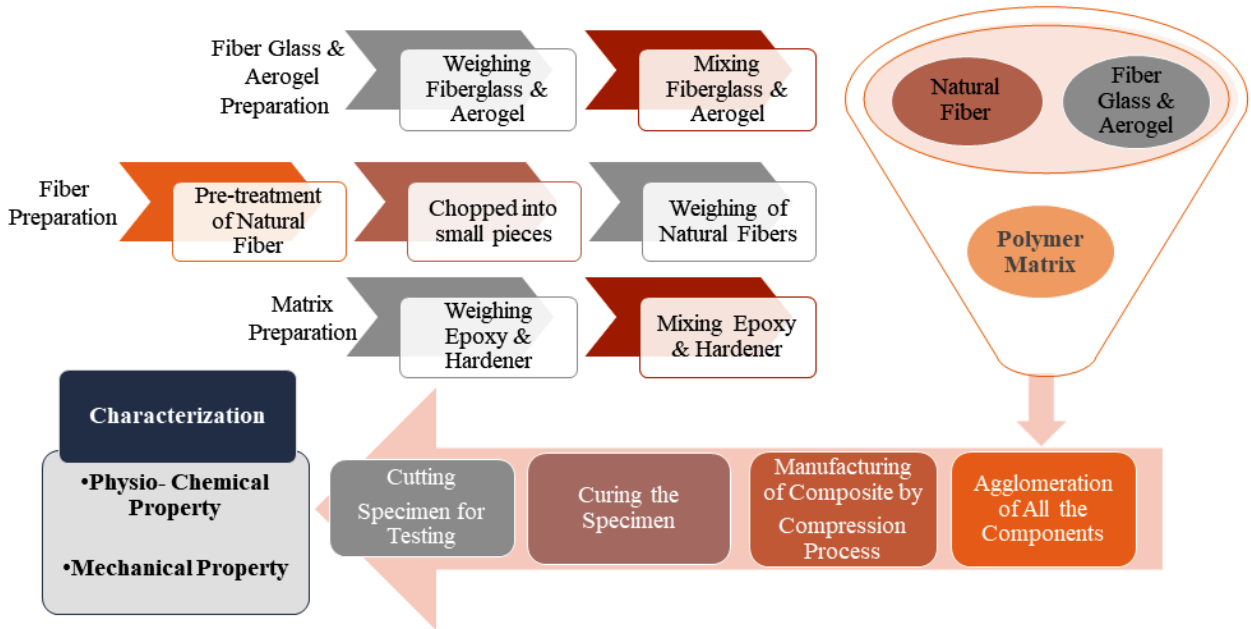

Fig. 2: Flowchart of the fabrication procedure

2.2 Fabrication of Composite

Flowchart of fabrication procedure of composite is shown in the figure no 2 and fabricated fiber reinforced composites are shown in the figure 3. In some research, it showed that shredded fibers have better mechanical characteristics and properties and it is almost enhanced to a greater extent. So shredded fiber greatly influenced the final result of the composites because of different tensions or compression behavior of the reinforcements. Due to the deviation of mechanical properties between shredded fiber, aerogel and adhesive the produced composite in this study is expected to react differently to the relative ratio and wt% of fiber, aerogel and fiber. To evaluate the effect of different wt% of fiber, aerogel and epoxy resin on the mechanical properties, ten different samples were fabricated by keeping the epoxy resin and hardener constant and by changing the wt% of fiber and aerogel. Each fiber have total three samples with three different weight percentages and ratio as shown in table 3.

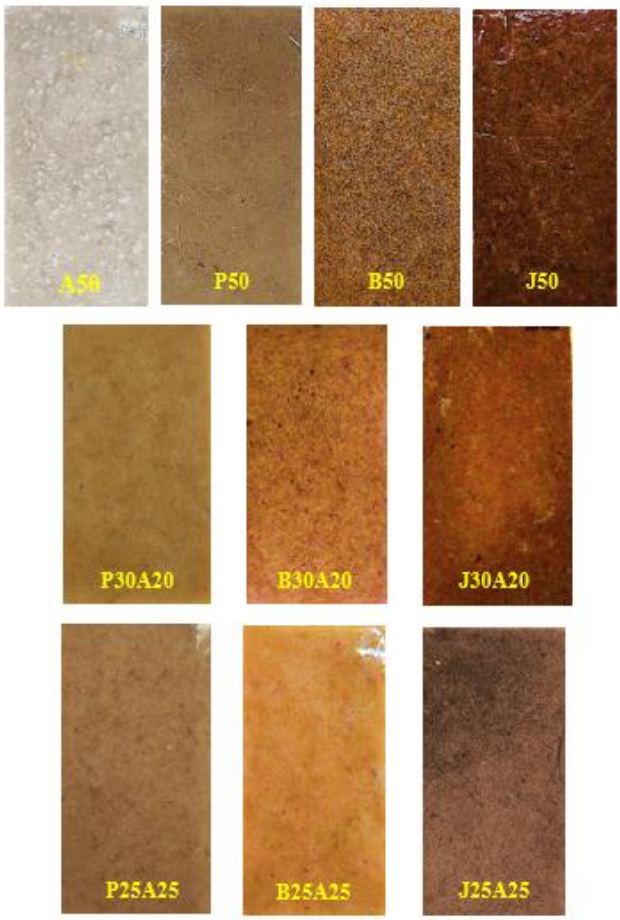

Fig. 3: Fabricated Composites

At first shredded silicon aerogel mixed glass fiber and nutaral fiber was mixed in a plastic beaker according to their ratio and weight. In another Plastic Beaker epoxy resin and hardener was mixed with a ratio of 2:1. After mixing the adhesive the fiber and aerogel was mixed with it carefully. That's how ten different samples of composites were made according to the samples presents on figure 3 and table 3. The mixture of the reinforcement was later poured into the mold and distributed uniformly. The mold (Fig.4) was fabricated using plastic wood having 1.2cm depth, 10 cm width and 18cm length. To avoid any types of shrinkage, void, in the mold a laminated paper was clipped with it and then Hydraulic Hot plate is used for the compression process.

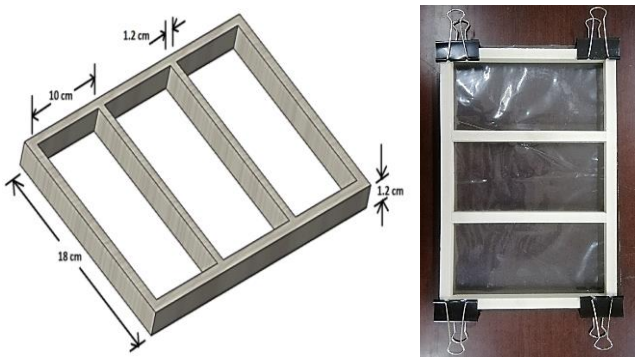

(a) (b)

Fig. 4: (a) 3D design of Mold ; (b) Mold fabricated with plastic wood

3.0 RESULTS AND DISCUSSION

3.1 Tensile test

The tensile has been carried out according to the ASTM D5868. The test was done with the Universal Testing Machine. The length and width of the sample was kept 20.45mm and 7.6mm respectively. Maximum 100 KN load was given and the speed of the test was 1.3mm/min. The sample was kept in the grips of the tensile machine and pulled at 1.3mm/min until failure.

Fig 5 shows that tensile strength increases with the addition of aerogel for banana and pineapple and jute fiber. It is found that the composites of 25% Pinaple fiber and 25 %aerogel give the maximum strength which is 26.33 MPa.

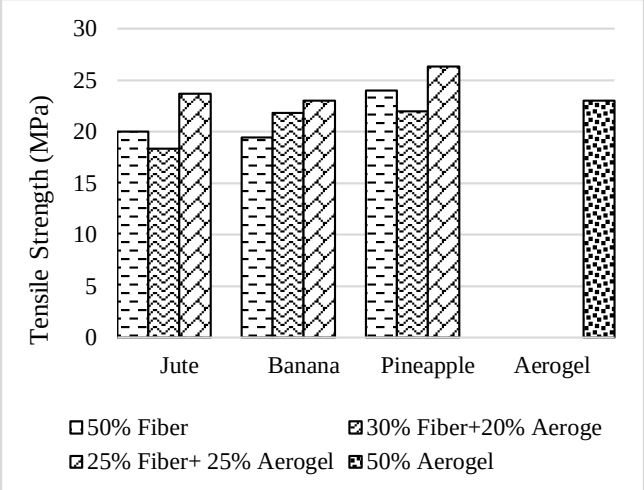

Fig. 5: Tensile Strength Graph for all specimens

3.2 Flexural Test

The flexural test has been done according to the ASTM Standard D-790. The length and width of the sample was kept at 20.45mm and 7.6mm respectively. The test speed has been set up to 2mm/min and the span of the test was taken at 100mm.

Fig 6 shows that The highest flexural strength has been seen achieved in specimens S3, S6, and S9 respectively where it is with 25 wt% of fiber and aerogel. Pinapple fiber showed the highest flexural strength in 25 wt% aerogel and 25wt% fiber.

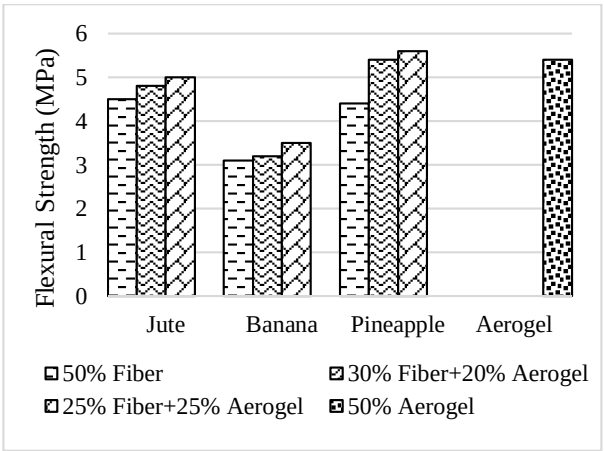

Fig. 6: Flexural Strength Graph for all specimen

3.3 Impact Test

Charpy impact test was done on all the specimens with QPI-IC-21J UNIVERSAL CHARPY/Izod Analog Impact Tester. It shows how much energy is required to break typical test specimens. The machine shows an initial angle of 149° without impact. Our first job was to determine the angles of every specimen after impact and then document it. From the data of the angles, the required energy to break each specimen was found with the help of software.

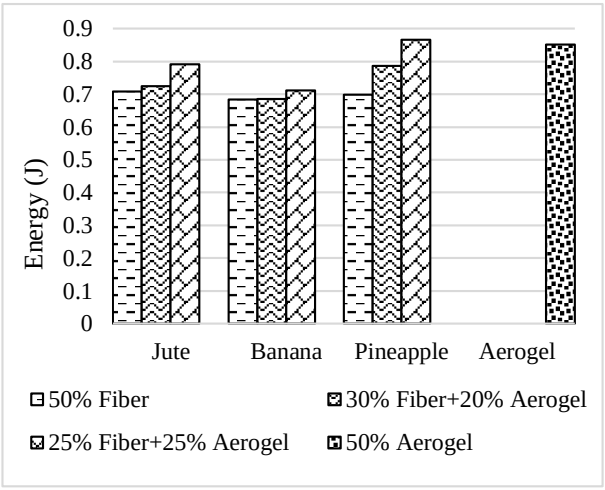

Fig. 7: Impact test graph for all specimen

From the fig 7, it is seen that, 25% Aerogel and 25% Fiber combination gives the highest result for impact test for all of the 3 different fibers (0.792, 0.692, 0.866). Amongst them, the pineapple fiber (25% Jute+25% Aerogel) showed the highest value of energy absorbed. As the percentage of aerogel increases, the capability of the composites to absorb energy also increases for each type of fiber-reinforced composites except for jute.

3.4 Shore D Hardness

Shore hardness is a measurement of a material's resistance to needle penetration when subjected to a specified spring tension. The test was done with the help of 'Digital Shore Durometer Hardness Tester Meter.

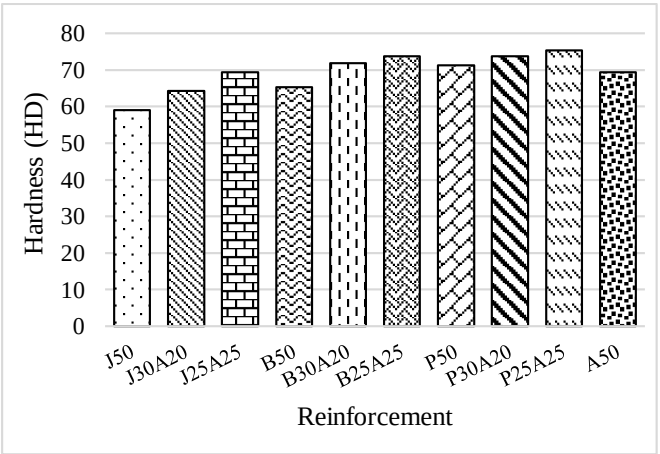

Fig. 8: Shore D Hardness graph for all specimens

By analyzing fig 8 it can be concluded that as the aerogel percentage increases up-to 20% with jute and banana fiber, the hardness increases. But after that as the aerogel weight percentage increases, the hardness decreases a bit. For pineapple, no change showed when 20 wt% aerogel is added. It increased the hardness when 25 wt% aerogel is added.

3.5 Flammability Test

Flammability testing determines how soon a material or finished product may ignite or burn when exposed to or used near fire or heat. A experimental setup (Fig 9). for testing flammability was prepared to test the specimens. The setup consists of a gas burner, specimen holder, and IR camera. By the aid of this setup, burning time to reach max temperature for each specimen with the help of a stopwatch could be measured.

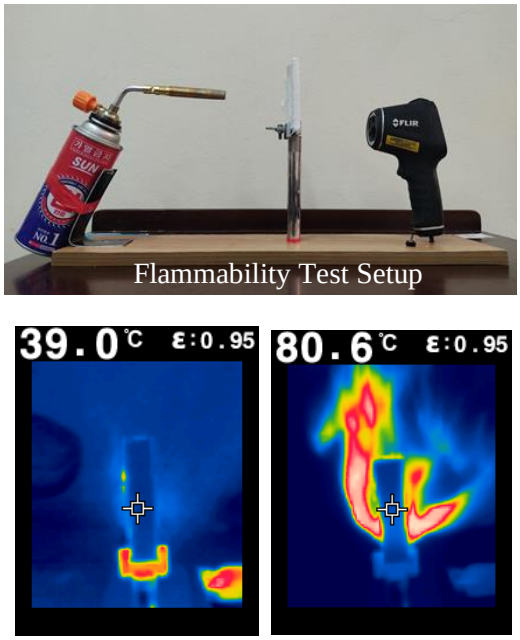

Fig. 9: Flammability test

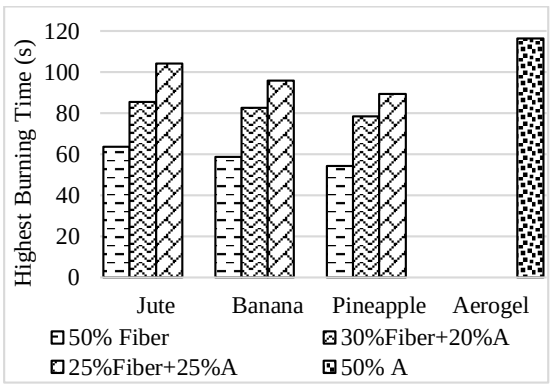

Fig. 10: Flammability test result

From the first Fig 10, It is found that among these composites which contain more percentages of aerogel it takes much more time to raise the temperature compared to other composite combinations. Hence, sample S10 (A50) takes highest time to burn.

25% fiber with 25% aerogel could withstand the highest temperature. Hence, Fig 10 depicts that 25% jute fiber with 25% aerogel burned for the highest time in seconds.

3.6 Water Absorption Test

Water absorption analysis was done by immersing the test samples into the normal surface water. All the composites specimens was immersed in the water (Fig.11) for a week at room temperature. The specimens were withdrawn from the water and wiped dry to remove the surface water before the weight measurements.

Fig. 11: Specimens before (Left) and after submerging in water (Right)

With the help of the data obtained from the test, the difference in the weight of the composites can easily be determined. Fig 12, 13, and 14 shows the changes in weight for jute fiber, banana fiber and pineapple fiber respectively.

It has been identified from the figures that each composite absorbs water very promptly at the initial stage, then slows down and finally reaches a saturation stage.

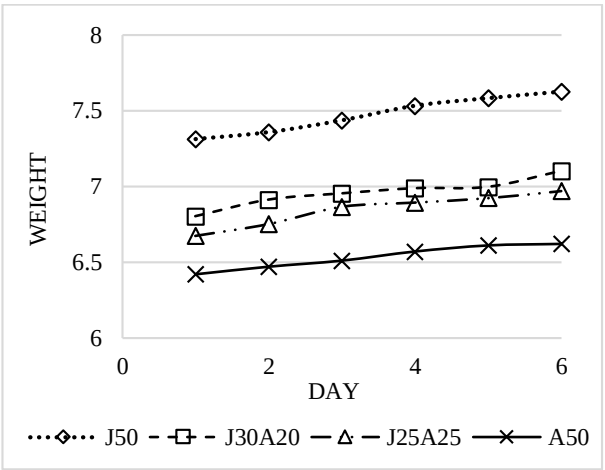

Fig. 12: Weight of the specimen for 5 days (Jute Fiber)

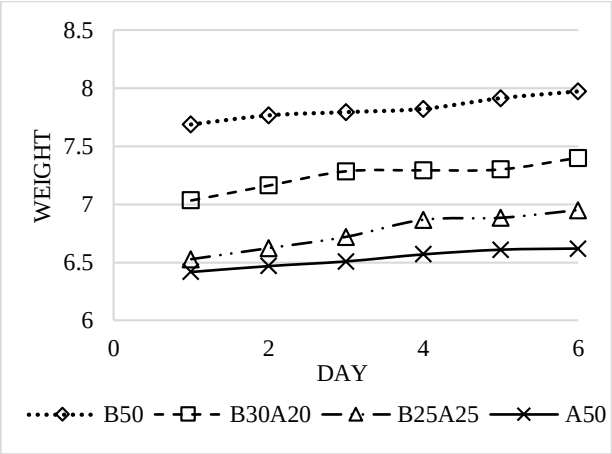

Fig. 13: Weight of the specimen for 5 days (Banana Fiber)

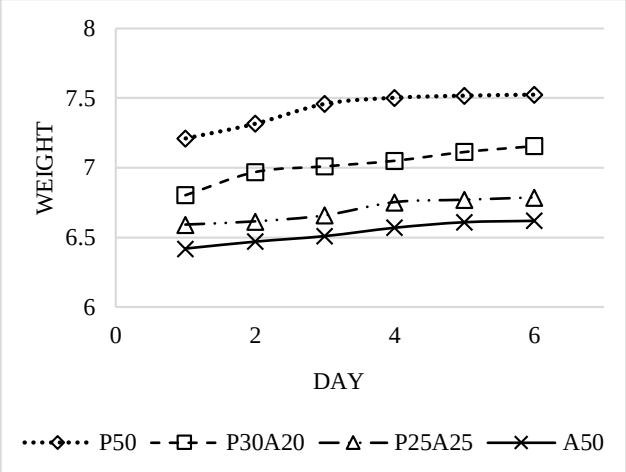

Fig. 14: Weight of the specimen for 5 days (Pineapple Fiber)

From the graphs, it can be concluded that the composites absorb little water over a long time. Significantly, S1 with Jute 50% shows the highest difference (0.709g) of weight which indicates it absorbs more water than other specimens. On the other hand, S2 having 30% Jute with 20% aerogel shows the least difference (0.222g). Also, there was not much change in weight in the case of aerogel composite.

4. CONCLUSION

This project investigated the properties of natural fiber reinforced aerogel-filled epoxy resin composites.10 different specimens were composed with different percentages of fibers and aerogel. As adherent, pineapple fiber, banana fiber, jute fiber, and super light silica aerogel mixed glass fiber was used for the fabrication of composites. AW 106 IN Epoxy Resin and Epoxy Hardener HV 953 U were incorporated to fabricate the composite. Firstly, shredded fibers and aerogel were mixed with epoxy resin. A plastic mold was used to compose the composites. After successfully composing the specimensns, the specimens went through different tests to find their properties under different conditions.

From the test results of the composites, the following conclusion can be drawn:

I. From the comparative analysis of the tensile test, it has been found that S9 comprised of 25% pineapple and 25% aerogel shows the maximum tensile strength which is 26.33 MPa.

II. From the comparative analysis of the flexural test, it has been found that S9 shows the maximum Flexural strength which is 5.6 MPa.

III. Charpy impact test determines the toughness of a material. From the values we got from the test, it has been found that S9 shows the greatest hardness and the energy absorbed by it was 0.886 J.

IV. Sample no. 9 comprised of 25% pineapple and 25% aerogel gives the maximum value of Shore D hardness which is 75.33 HD.

V. Flammability test shows that, as the percentage of aerogel increases, the composites need more time to raise the temperature.

VI. Water absorption test helped to determine whether the composites would absorb moisture. The test was conducted for 5 days to determine the changes in weight or size. It was found that all of the composites absorbed water as the days went by. It is also evident that the addition of Aerogel can significantly reduce the water absorption property.

ACKNOWLEDGMENT

The authors acknowledge and thank the Bangladesh Council of Scientific and Industrial Research (BCSIR), Bangladesh (www.bcsir.gov.bd) for providing facilities to undertake the Impact Test experiments.

REFERENCES

[1] S. H. Sheikh Md Fadzullah and Z. Mustafa, “Fabrication and processing of Pineapple leaf fiber reinforced composites,” in *Green Approaches to Biocomposite Materials Science and Engineering*, IGI Global, 2016, pp. 125–147. doi: 10.4018/978-1-5225-0424-5.ch006.

[2] M. Akhtarul Islam, “Chemical Sensor Developmen View project Development of electrochemical sensors View project Natural Fiber as a substitute to Synthetic Fiber in Polymer

Composites: A Review," 2013. [Online]. Available: https://www.researchgate.net/publication/284223539

[3] K. Rohit and S. Dixit, "A review - future aspect of natural fiber reinforced composite," *Polymers from Renewable Resources*, vol. 7, no. 2, pp. 43–60, May 2016, doi: 10.1177/204124791600700202.

[4] M. N. Prabhakar, A. U. R. Shah, and J.-I. Song, "A Review on the Flammability and Flame Retardant Properties of Natural Fibers and Polymer Matrix Based Composites," *Composites Research*, vol. 28, no. 2, pp. 29–39, Apr. 2015, doi: 10.7234/composres.2015.28.2.029.

[5] D. K. Rajak, D. D. Pagar, P. L. Menezes, and E. Linul, "Fiber-reinforced polymer composites: Manufacturing, properties, and applications," *Polymers*, vol. 11, no. 10. MDPI AG, Oct. 01, 2019. doi: 10.3390/polym11101667.

[6] N. Nayak, H. N. Reddappa, V. Bhat, and M. Ravikumar, "Comparative study of effect of sisal fibres in powder and short form on the mechanical properties of polypropylene," in *AIP Conference Proceedings*, Oct. 2020, vol. 2274. doi: 10.1063/5.0022594.

[7] A. Elsabbagh, L. Steuernagel, and J. Ring, "Natural Fibre/PA6 composites with flame retardance properties: Extrusion and characterisation," *Composites Part B: Engineering*, vol. 108, pp. 325–333, Jan. 2017, doi: 10.1016/j.compositesb.2016.10.012.

[8] K. N. Bharath and S. Basavarajappa, "Flammability Characteristics of Chemical Treated Woven Natural Fabric Reinforced Phenol Formaldehyde Composites," *Procedia Materials Science*, vol. 5, pp. 1880–1886, 2014, doi: 10.1016/j.mspro.2014.07.507.

[9] M. A. Kumar, G. Ramachandra Reddy, K. R. Vishnu Mahesh, K. V. P. Chakradhar, and Y. V. M. Reddy, "Performance of Zea mays fiber reinforced epoxy composites," 2011. [Online]. Available: http://www.urpjournals.com

[10] B. Ksj, S. A. Anurag Sai, and S. Mohan VNRT, "Article ID: IJMET_08_07_021 Cite this Article: Fabrication and Performance Analysis of Flame Retardant and Natural Fibers Reinforced Composites," *International Journal of Mechanical Engineering and Technology (IJMET)*, vol. 8, no. 7, pp. 172–180, 2017,[Online].Available: http://iaeme.com/Home/issue/IJMET?Volume=8&Issue=7http://iaeme.com

[11] K. Muthukumar, R. v. Sabariraj, S. Dinesh Kumar, and T. Sathish, "Investigation of thermal conductivity and thermal resistance analysis on different combination of natural fiber composites of Banana, Pineapple and Jute," in *Materials Today: Proceedings*, 2020, vol. 21, pp. 976–980. doi: 10.1016/j.matpr.2019.09.140.

[12] I. Smirnova and P. Gurikov, "Aerogel production: Current status, research directions, and future opportunities," *Journal of Supercritical Fluids*, vol. 134, pp. 228–233, Apr. 2018, doi: 10.1016/j.supflu.2017.12.037.

[13] V. Mittal, R. Saini, and S. Sinha, "Natural fiber-mediated epoxy composites - A review," *Composites Part B: Engineering*, vol. 99, pp. 425–435, Aug. 2016, doi: 10.1016/j.compositesb.2016.06.051.

[14] C. Venkata Prasad, P. Sudhakara, M. N. Prabhakar, A. Ur Rehman Shah, and J. il Song, "An Investigation on the Effect of Silica Aerogel Content on Thermal and Mechanical Properties of Sisal/PLA Nano Composites," *Polymer Composites*, vol. 39, no. 3, pp. 835–840, Mar. 2018, doi: 10.1002/pc.24005.

[15] M. Kucharek, W. MacRae, and L. Yang, "Investigation of the effects of silica aerogel particles on thermal and mechanical properties of epoxy composites," *Composites Part A: Applied Science and Manufacturing*, vol. 139, Dec. 2020, doi: 10.1016/j.compositesa.2020.106108.

[16] K. B. Prakash *et al.*, "Influence of Fiber Volume and Fiber Length on Thermal and Flexural Properties of a Hybrid Natural Polymer Composite Prepared with Banana Stem, Pineapple Leaf, and S-Glass," *Advances in Materials Science and Engineering*, vol. 2021, 2021, doi: 10.1155/2021/6329400.

[17] J. I. P. Singh, S. Singh, and V. Dhawan, "Effect of alkali treatment on mechanical properties of jute fiber-reinforced partially biodegradable green composites using epoxy resin matrix," *Polymers and Polymer Composites*, vol. 28, no. 6, pp. 388–397, Jul. 2020, doi: 10.1177/0967391119880046.

[18] Aranno, T.M., Mia, S., Khan, M.S.U., Hasan, M.M., Supto, N.S., Sujon, A.S., Rashid, A.B. and Ferdous, M.S., 2019, September. Fabrication, experimental investigation of jute fiber reinforced epoxy composites and hybrid composites. In IOP Conference Series: Materials Science and Engineering (Vol. 628, No. 1, p. 012011). IOP Publishing.

[19[Z. Li, X. Cheng, S. He, X. Shi, L. Gong, and H. Zhang, "Aramid fibers reinforced silica aerogel composites with low thermal conductivity and improved mechanical performance," *Composites Part A: Applied Science and Manufacturing*, vol. 84, pp. 316–325, May 2016, doi: 10.1016/j.compositesa.2016.02.014.

Paper ID: 0661

International Conference on Mechanical, Manufacturing and Process Engineering (ICMMPE – 2022)

Organizer: Faculty of Mechanical Engineering, Dhaka University of Engineering & Technology (DUET), Gazipur, Bangladesh

Website: https://icmmpeduet.com/

Design, Development and Performance Analysis of a Two Degree of Freedom Solar Tracking System

Mohammad Harun-Or-Rashid[1], Afsana Hossain Asha[2], Himadry Shekhar Roy[2]

[1,2] Department of Mechanical and Production Engineering
Ahsanullah University of Science and Technology
Dhaka-1208, Bangladesh

E-mail: harun_edu@yahoo.com, harun.mpe@aust.edu

ABSTRACT

Design, construction as well as performance analysis of a two degree of freedom solar tracking system are explained in this paper. In static position, solar panel cannot produce electricity up to its full potential. That's why, nowadays, tacking systems are being applied to increase the output of solar panels. Various types of tracking and controlling systems are available for solar tracking. In the present study, a test unit was developed and experiment was conducted. In the experiment, sun path diagram is used for properly tracking the sun throughout the year. For controlling the setup Arduino-Uno and as rotating mechanism two sets of spur gears are used. The setup is rotated in two axes by two sets of spur gears which are powered by two stepper motors. The main concern of this paper is to design a solar tracking mechanism that can rotate in two axes and analyze the power output of solar panel in static position and the solar panel with tracking system. Finally, power outputs of different conditions are compared. After comparing the power outputs, it can be seen that the dual-axis sun tracking system generated 11.393% more power (watts) than the static one.

Keywords: Dual axis solar tracking system, Fixed angled solar tracking system, Solar panel.

1. INTRODUCTION

In this modern era, electrical energy has become an essential and basic part of daily life. The role of electricity in building up this modern civilization cannot be determined in scale. Fossil energy has played a vital role in fulfilling the energy requirement. Generally, hydrocarbon resources or fossil fuels are used for electricity production. But fossil assets are not unlimited and overuse of these sources for the last two decades has been increased significantly [1]. A study shows that, globally, there will be 36% increase in fossil fuels usage between the year 2011 and 2030 for energy production, if the annual consumption rate is 1.6% [2]. In fact, in power sector there is 13.5% increase in fossil fuel-based power generation. This overuse has cause degradation in the reserve of fossil fuels worldwide. Regarding current storage and utilization rate of fossil fuels the world will only manage 122 years for coal, 60 years for natural gas and 42 years for oil [3]. Besides, now the world is facing serious consequences of climate change which is the result of global warming and CO_2 emission because of the excess use of fossil fuels [4]. To fight climate change, environmental pollution and global warming; maintain the current reserve of fossil fuels and to meet the present energy demand it has become a necessity to find an alternative source that leads to the solution of renewable energy [5].

Solar energy is being used in numerous ways by people all around the world for daily uses from ancient times, but solar energy was not harnessed for electricity generation until French scientist Alexandre-Edmond Becquerel first discovered the photovoltaic (PV) effect that allows the conversion of sunlight into electricity in 1839 [6, 7]. It took a long time to make the PV cells available for consumers until Bell Laboratories started production of PV cells in 1950s [8]. After that numerous researches have been done on PV cells and solar tracking mechanism to increase the electricity generation. To improve the efficiency level of solar PV cells tracking system was first introduced by Array Technologies Inc. (ATI) in 1989 using dual-axis single-pole tracking system. For the last 31 years, ATI has continuously evolved tracking systems, optimizing to reduce component requirements by minimizing motors, controllers and sensors. Present study focuses on solar tracking mechanism using sun path throughout the year with gear system.

Normally static solar panels are used for electricity generation for households which are fixed at a tilt angle according to their specific latitude while facing north or south [9]. As the sun's position can vary up to 30°s zenithally throughout the year in southern or western sky

respectively for the western or southern hemisphere, therefore, the solar panels cannot be utilized to their full potential. Consequently, to improve electricity production tracker systems can be applied. Basically, there are two types of tracking system: single axis solar tracker [10, 11, 12, 13, 14] and dual axis solar tracker [15]. Single axis trackers rotate about one axis, azimuthally from east to west. Dual axis trackers rotate both azimuthally and zenithally or vertically according to the global position in southern or northern hemisphere.Since there is lack of work in Dual axis tracking system therefore this topic is selected.

After studying different research papers on solar harnessing system, it was found that all the solar tracking systems include sensors like- light dependent resistor (LDR) sensors, voltage sensors or sun path diagram to track the sun in the sky and as rotating mechanism actuators are being used. In this study, it was decided to use gears as a rotating mechanism to operate the solar tracking setup with the help of Arduino-Uno and sun path diagram was used to pinpoint the sun's location throughout the year accurately. With the help of SolidWorks, the design of the dual axis solar tracking system was completed. In the setup, two sets of spur gears are used that are powered by two stepper motors. Stepper motors are used to control the angle variation that is needed to rotate the solar panel in desired angle with more precision. The dual axis solar tracking system is shown in Fig. 1.

The main objective of this research were to develop a dual axis solar tracking system, get the power output from a fixed angle panel and sun path tracker panel, then compare those power output readings so that the better one can be obtained.

2. EXPERIMENTAL SETUP

Before development of the experimental setup it is necessay to know the several important terms like sun path diagram, elevation angle, declination and azimuth angle. Sun path refers to the apparent significant seasonal and hourly positional changes of the Sun, as the Earth rotates and orbit around the sun. The relative position of the sun is a major factor in the performance of solar energy systems. The diagram that helps to find out the Sun's relative position in the sky throughout the year is Sun path diagram. Observing the sun from earth, the solar hour angle (ω) is an expression of time, expressed in angular measurement, usually degrees, from solar noon. One hour corresponds to an angle of 15°. On the other hand, the elevation angle (α) is the angular height of the sun in the sky measured from the horizontal. The elevation angle is 0° at sunrise and 90° when the sun is directly overhead. Fig. 2 shows the elevation angle and its mathematical formula is presented in Eq. 1.

$$\alpha = sin^{-1}[sin\delta cos\emptyset + cos\delta\ cos\psi\ cos\omega] \quad (1)$$

Here, ϕ and ψ are represent the latitude of the location and azimuth angle respectively. On the other hand, the declination angle (δ) is between the equator and a line drawn from the center of the Earth to the center of the sun. Declination varies seasonally as earth rotates about a tilted angle of 23.45° on its axis while rotating around the sun. Eq. (2) represents the declination angle.

$$\delta = 23.45\ sin\left[\frac{2\pi(284+n)}{365}\right] \quad (2)$$

Here, n is the number of days. Fig. 3 shows the azimuth angle.

(a) (b)

Fig. 1: (a) Side view of dual axis solar tracking setup, (b) Complete setup of dual axis solar tracking system

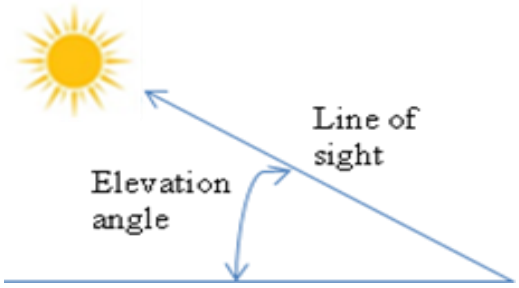

Fig. 2: Elevation angle

A solar cell or photovoltaic cell is an electrical device which, through the photovoltaic effect, converts the energy of light directly into electrical energy. The solar panel used in this experiment is a polycrystalline silicon solar panel, manufactured by TOKO BP SOLAR, Germany. A solar panel is shown in Fig. 4 and its specifications are presented in Table 1.

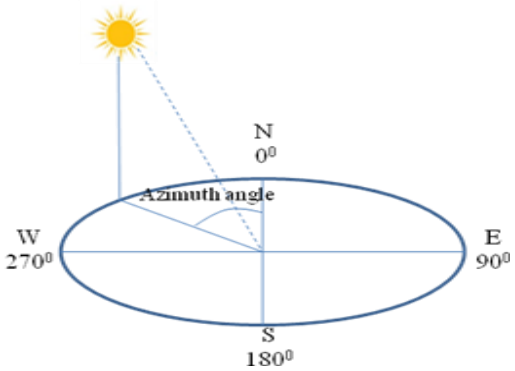

Fig. 3: Azimuth angle

Fig. 4: Solar panel

Table 1. Specifications of the solar panel

Technical criteria	Value
Peak power	15 W
Short circuit current	0.92 A
Open circuit voltage	21.8 V
Maximum power current	0.83 A
Maximum power voltage	18 V

Fig. 5: Stepper motor

Stepper motor is a motor that moves in discrete steps, one step at a time. It is generally used in a variety of applications where precise position control is desirable such as 3D printer, laser cutter and pick and place machine. In this study, two 17HS4401 bipolar stepper motors are used. This stepper motor has 1.8° step angle (200 steps /revolution) with 0.4N-m holding torque. A stepper motor is shown in Fig. 5. Motor specifications are presented in Table 2.

Motor driver acts as an interface between the motor and the control circuit. Motor requires high amount of current whereas the controller circuit works on low current signals. Hence, the function of motor driver is to take a low-current control signal and then turn it into a higher-current signal that can drive the motor.

For controlling the stepper motors Arduino Uno microcontroller board is used. It is selected due to its low cost, vast library, support many sensors and much easier language for programming. An Arduino Uno is shown in Fig. 6.

Table 2. Physical and technical specifications of the stepper motor

Technical specifications	**Values**
Motor type	17HS4401 bipolar stepper motor
Step size	1.8 degrees
Rated Current/Phase	1.7A
Holding torque	0.46 Nm
Physical specification	
Body length	40mm
Frame size	42 x 42mm
Shaft diameter	5mm
Number of wire leads	4
Wire length	400mm
Weight	280g
Temperature rise	80^0C Max

Fig. 6: Arduino Uno

A charge controller is needed to maintain the electrical parameters of a solar panel. A better charge controller can increase the longevity of a solar panel and reduce the chance of system failure. There are different types of charge

(a) (b)

Fig. 7: (a) Lipo battery for power supply, (b) Lead acid battery for store energy

controllers available in the local market. Among them DY-002 charge controller was selected because it has a digital display to monitor parameters. Furthermore, there are two 5V USB 2.0 ports in the charge controller as a result microcontroller and the data logger can be directly powered through the USB port.

Battery is one of the vital components in this experiment. There are two types of battery needed in this experiment, one for power supply to the servo motor and Arduino Uno, and the other one for storing the produced direct current. Due to better efficiency, Lipo battery is being used as power source in this experiment. The Lipo battery is a rechargeable lithium-ion battery that uses a polymer electrolyte rather than a liquid electrolyte. From this electrolyte, high conductivity semisolid (gel) polymers are found. These batteries provide higher specific energy than other lithium battery and are used in applications where weight is a critical feature. On the other hand, a lead acid rechargeable battery is used for store electric energy produced by the solar panel. Two batteries are presented in Fig. 7.

The stand and mounting frame are constructed from square shaped Iron and Aluminium bar. The frames were preciously cut according to the dimensions provided from SolidWorks design.

The optimum tilt angle was set by using a ruler and a protractor. A ruler was set onto the frame and then the ruler was aligned with the protractor into 23 degrees. This is a simple way to get the optimum tilt angle. The tilt angle is checked on regular basis to make sure that the panel frame stayed at the tilt angle.

The data acquisition system includes the charge controller, battery and a DC load. Due to some issues regarding the charge controller, voltage and current readings were taken using a multi-meter. The data acquired from the data acquisition system were voltage and current. All the data were collected and organized according to their date and time. Then the output power was calculated by multiplying voltage and current [Eq. (3)].

$$\text{Power} = \text{Voltage} \times \text{Current} \quad (3)$$

The efficiency was calculated on the basis of the rated voltage of 18V of the solar panel. It was calculated by using Eq. (4).

$$\text{Efficiency} = (\text{Output voltage} \div \text{Rated Voltage}) \times 100\% \quad (4)$$

3. RESULTS AND DISCUSSION

Voltage and current readings for fixed angled solar panel were taken from 3rd January to 8th January from 9am to 4pm. On the other hand, voltage and current readings for dual axis solar tracking system were taken from 10th January to 15th January from 9am to 4pm.

Average voltage at different time is shown in Fig. 8. Here, the graph states that the average peak point was at 1:00 pm and the average lowest point was at 9:00 am. Average maximum voltage of dual axis and fixed axis was measured 20.43V and 20.133V at 1:00 pm and average minimum voltage was measured 16.333V for dual axis and 14.367V for fixed axis at 9:00 am. Here it is seen that voltage reading is higher at dual axis compare to fixed axis. This is because, dual axis solar panel can acquire more energy from sunlinght. Due to the Sun's position in the sky the graph change gradually.

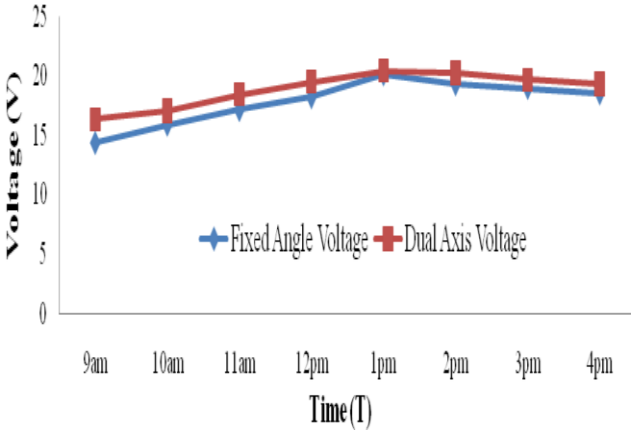

Fig. 8: Average voltage versus time graph

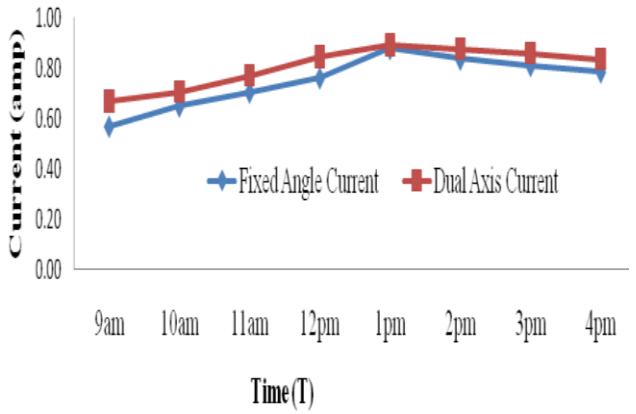

Fig. 9: Average current versus time graph

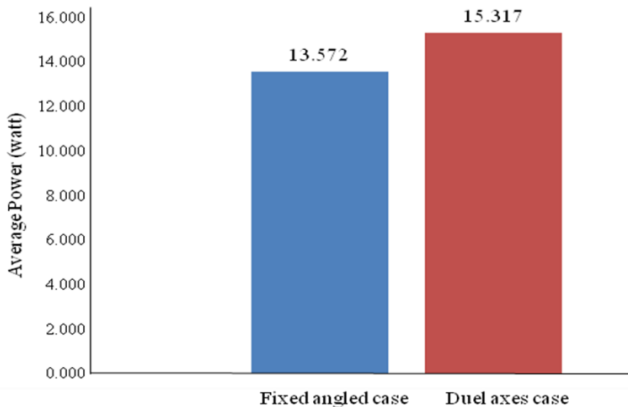

Fig. 10: Output power comparison between dual axis and fixed angled solar panel

Average current at different time is shown in Fig. 9. Here, the graph states that the average peak point was at 1:00 pm and the average lowest point was at 9:00 am. Average maximum current of dual axis and fixed axis was measured 0.893A and 0.877A and average minimum current was measured 0.677A for dual axis and 0.570A for fixed axis. Here it is found that, current reading is higher at dual axis compare to fixed axis. Since dual axis solar tracking system is facing the Sun more than the fixed axis system therefore, more current is produced.

Daily average power output of dual axis solar tracker system and fixed angled panel system are presented in Fig. 10. From experimental data it is seen that the daily output power of dual axis solar tracker system is 11.393% higher than the fixed angled panel system.

4. CONCLUSION

The main objective of this research was to estimate the solar energy at fixed angle and different angle of a solar panel. To do so a solar tracking system was developed and experiment was conducted. The result shows that after implementing tracking mechanism, the power output has increased by a fair margin of 11.393%. All the data were taken for a few days in winter. If more data could have been taken for a larger period of time in winter as well as in summer then it might have shown more accurate results. Finally, since power output of dual axis solar tracking system is higher than at fixed angle therefore it is suggested to use dual axis solar tracking mechanism rather than fixed angle mechanism.

ACKNOWLEDGEMENT

We are grateful to Ahsanullah University of Science and Technology, Tejgaon Industrial Area, Dhaka 1208, Bangladesh for all kind of facilitates.

REFERENCES

1. International Energy Agency (IEA) report, “Resources to Reserves 2013,” June 2013.
2. M. T. Islam, S. A. Shahir, T. M. I. Uddin, and A. Z. Saifullah, “Current energy scenario and future prospect of renewable energy in Bangladesh,” *Renew. Sustain. Energy Rev.*, vol. 39, pp. 1074–1088, 2014.
3. N. Lior, “Energy resources and use: The present (2008) situation and possible sustainable paths to the future,” *Energy*, vol. 35, no. 6, pp. 2631–2638, 2010.
4. International Energy Agency (IEA) report, “CO2 Emissions From Fuel Combustion Highlights,” 2015.
5. F. Ahmed, A. Q. Al Amin, M. Hasanuzzaman, and R. Saidur, “Alternative energy resources in Bangladesh and future prospect,” *Renew. Sustain. Energy Rev.*, vol. 25, pp. 698–707, 2013.
6. J. L. D. S. Silva, H. S. Moreira, D. D. B. Mesquita, and M. G. Villalva, “A review and analysis of technologies applied in PV modules,” 2019 IEEE PES Innovative Smart Grid Technologies Conference - Latin America (ISGT Latin America), pp. 4–5, Nov. 2019.
7. H. J. Moller, “SEMICONDUCTORS FOR SOLAR APPLICATIONS,” Middle East, Vol. 35, pp. 205–418, 1991.
8. L. Szab´o, “The history of using solar energy,” Proceedings – 2017 International Conference on Modern Power Systems, MPS 2017, June 2017.
9. J. Kern, I. Harris, “On the optimum tilt of a solar collector”, Solarlar Energy, DOI: 10.1016/0038-092X(75)90064-X, Vol. 17, No. 2, pp. 97-102, May 1975.
10. R. Bayindir, E. Kabalci, H. I. Bülbül, and C. Can, “Optimization of Operating Conditions of Photovoltaic Systems: A Case Study”, 1st International Conference on Renewable Energy Research and Applications, Nagasaki, pp. 1-4, 11-14 Nov. 2012.
11. A. Ponniran, A. Hashim, and H. Ali Munir, “A Design of Single Axis Sun Tracking System”, 5th International Power Engineering and Optimization Conference, pp. 107-110, June 2011.
12. S. Ghabusnejad, A. Majdi, and S. A. Davari, “Using P&O Based Sensorless Method In Single Axis Solar Tracker”, International Journal of Renewable Energy Research, Vol. 9, no 1, pp.532-541, March,2019.
13. J. Hu, and T. Yachi, “Photovoltaic Systems with Solar Tracking Mirrors”, 2nd International Conference on Renewable Energy Research and Applications, pp. 201-204, 20-23 October 2013.
14. A. Al-Ghasem, G. Tashtoush, and M. Aladeemy, “Experimental Study of tracking 2-D Compound Parabolic Concentrator (CPC) with flat plate absorber”, 2nd International Conference on Renewable Energy Research and Applications, pp. 779-782, 20-23 October 2013.
15. J. Beltrán A., J. L. González Rubio S., and C. D. Garcia-Beltran, “Design, Manufacturing and Performance Test of a Solar Tracker Made by a Embedded Control”, Electronics, Robotics and Automotive Mechanics Conference, pp. 129-134, 25-28 Sep. 2007.
16. C. Sanna, M. Garonska, and A. Damiano, “Energy Performance of Concentrator and Flat Plate Photovoltaics in the Mediterranean Area”, 4th International Conference on Renewable Energy Research and Applications, pp. 760-765, 22-25 Nov.2015.
17. N. AL-Rousan, M. AL-Rousan, A. Shareiah, and H. AL-Najjar, “Choosing the Efficient Tracking Method for Real Time Tracking System in Jordan and it's neighbors to Get Maximum Gained Power Based on Experimental Data”, 1st International Conference on Renewable Energy Research and Applications, Nagasaki, pp. 1-6, 11-14 Nov. 2012.

Paper ID: 1007

International Conference on Mechanical, Manufacturing and Process Engineering (ICMMPE – 2022)

Organizer: Faculty of Mechanical Engineering, Dhaka University of Engineering & Technology (DUET), Gazipur, Bangladesh

Website: https://icmmpeduet.com/

Title: Modeling of a Battery Driven Three-wheeler Electric Vehicle in Bangladesh by Using MATLAB-SIMULINK

Nafisa Tasnim [1], Md. Asadouzzaman [2] and Md. Abdul Aziz Bhuiyan [3]

[1]Department of Mechanical and Production Engineering, Islamic University of Technology (IUT), Gazipur-1704, Bangladesh.
[2]Department of Electrical Engineering, Dhaka University of Engineering and Technology (DUET), Gazipur-1707, Bangladesh.
[3]Department of Mechanical and Production Engineering, Islamic University of Technology (IUT), Gazipur-1704, Bangladesh.

E-mail: nafisatasnim@iut-dhaka.edu asadouzzaman@duet.ac.bd abdulazizbhuiyan@iut-dhaka.edu

ABSTRACT

Because of rising air pollution, the depletion of fossil fuels, and the current fuel price increase, there is widespread interest in electric vehicles (EVs). The modeling and simulation of EVs have grown in popularity in order to better understand their performance and produce a more efficient model. In recent years, electric vehicles also have gained popularity in Bangladesh. For more than a decade, three-wheeled battery-powered electric vehicles known as "Easybikes" have been used to transport passengers in Bangladesh, and the number is growing by the day. The MATLAB-Simulink tool was used in this study to create a system-level model of a three-wheeled battery-powered Electric Vehicle. The vehicle's performance, such as speed, torque, power, and energy, were measured over time using various parameters. The system-level block simulation revealed that the vehicle power consumption was 2~2.5 kwh with the new European Driving Cycle (NEDC) (Cycle time-3.5 hrs.) and 0.9~1.2 kwh with the New York City Cycle (NYCC) (Cycle time-3.5 hrs.) depending on load. After 3.5 hours of runtime with various total vehicle weights and the vehicle's State of Charge (SoC) is 48.7V~23.3V with NEDC and 56.3V~55.1V with NYCC. This study aims to lay the groundwork for future research and development of battery-powered three-wheeler EVs.

Keywords: Three-wheeled Battery driven EV, MATLAB-Simulink, System-level model, Drive cycles-NEDC, NYCC, Energy consumptions.

1. INTRODUCTION

In the twentieth century, gas emissions from burning fuel increased global tension regarding the environmental impact and its effect on human health and ecology. Among all the emissions of Carbon dioxide, around 25% of this is contributed by the transport sector [1]. The burning fuel in transportation dissipated a good amount of Carbon dioxide, Hydro-Carbon gas, oxides of Nitrogen and Sulphur, and different harmful pollutants [2]–[4]. Due to a large number of pollution, limited fossil fuel sources, and the present price hike of fuel, Battery driven Electric vehicles (BEVs) can be a good alternative to Internal Combustion Engine (ICE) vehicles which associate to mitigate the carbon footprint in the transportation sector [5]. In the past, from 1918 Electric Vehicles (EVs) were available [6] but because of the availability of the excess amount of fossil fuel and the ability to obtain high speed the Internal Combustion Engines (ICE) vehicle rapidly developed and spread worldwide. At present time with technical innovation EVs make our life simpler, and safer, and with the consumption of energy, they also generate and store electricity. In terms of global gas emissions, energy conservation, fuel supply security, and other factors, battery-powered electric cars outperform traditional fuel vehicles, attracting the attention of a wide variety of automotive manufacturers and governments. This vehicle received its power from batteries as electrical energy and then utilizes this energy through motor drive and converts its electrical energy into mechanical rotational energy and drives the vehicle. [7]–[9].

The functional principle of battery-driven EVs is quite similar to basic combustion engine vehicles, instead of a combustion engine, it is operated by an electric motor along with a motor controller by utilizing batteries as the power source of this vehicle rather than fuel and to regain the power batteries need to recharge by connecting electricity [10]–[12]. The EVs get their tractional force from the electric motor and use the electrochemical energy conversion linkage system between the vehicle energy source and the powertrain of the vehicle.

EVs can benefit from design ideas such as a lighter body structure, lower rolling resistance, and more aerodynamic body design. EV architecture is simpler than that of conventional internal combustion engine-driven vehicles because it is powered by batteries. There is no complex engine setup, no clutch, and no need for a manual the transmission system, or exhaust pipe [13]–[15].

To examine the operation of electric drive trains, several simulation and modeling packages have been developed. Previous academics have put a lot of effort into modeling an electric vehicle. [16]–[18]. The study of Husain & Islam [16] displayed the best use of computer tools in the initial design stage of an EV to demonstrate the functional model, energy consumption of the vehicle, and modified model for the efficient performance of the EV. Their main focus was on the electric propulsion unit and the drive evaluation to meet performance desires using a switched reluctance motor (SRM). Bambang [17] study the power flow calculation and design of a model by MATLAB/Simulink software and find the power flow response following the energy system of a small electric vehicle. A model of BEV was developed with MATLAB/Simulink by O. Vatan, whose battery capacity is 30 kWh and the vehicle consumes 0.58 kWh/100km inside and 0.44 kWh/100km outside the city [18]. Mathematical modeling, analysis, simulation, and dynamic model of the series-parallel hybrid electric vehicle have also been developed with Xmath and Matlab/Simulink (Mathworks) [19]. Based on efficiency, cost, safety, and weight, X. D. Xue, tried to determine the suitable electric motor for EVs and found that a permanent magnet synchronous motor performs better [20].

To perform these mathematical modeling, simulation, and dynamic model several computer programs like-Simple EV simulation (SIMPLEV) [21], MARVEL [22], CarSim [23], ADVISOR [24], MATLAB-Simulink [25], and others [26] are used. MATLAB is a computer programming software that helps to design and analyze the products and Simulink is a MATLAB-based tool that helps to do modeling, simulate, and analyze systems as a primary interface graphical block diagram. To estimate and optimize the energy consumption of Electric Vehicles, we need to have a good model of EV to prevent the wrong conclusions.

In terms of performance and servicing, electric vehicles outperform internal combustion engines. The adoption of limited-speed Electric Vehicles (EVs) such as e-bicycles and e-three-wheelers is expanding day by day due to their simple driving mode, low vehicle purchase price, easy maintenance, and low transportation costs. LEVs are used for short-distance travel and tourist sightseeing in metropolitan areas for passenger transportation and transporting products, and in many touristic places such as Bangkok, Pattaya, and Cox's Bazar, LEVs are used for short-distance travel and tourist sightseeing [27]. Currently, the Bangladesh government also emphasize battery-driven and hybrid Electric vehicles (EVs) rather than conventional combustion engine vehicle. Different policies were made to encourage the manufacturer and importer to focus on EVs. Despite sufficient electric production back in the early 21st century, imported battery-driven Electric vehicles named “Easybike” were introduced in the local market for short-range transportation as limited speed vehicles. After that because of its low cost and easy-to-drive model, it becomes widely popular all over the country. Presently, it got so popular that it can be found in 64 districts and the approximate number of these vehicles could be 1.5million to 2 million. In the socio-economic and energy conservation concept, this vehicle has a great impact on this country. Though with the advancement of technology in motors and the availability of efficient batteries, the technical and functional structure remain the same over the last two decades. In this study, a system-level mathematical model is used for the components of the EV such as the Battery, Motor and Controller, Vehicle body, and driver to simulate the performance of the EV. The MATLAB-SIMULINK tool was used to simulate the system. The simulation was run with two different drive cycles, named NEDC and NYCC with varying model parameters such as the total weight of the vehicle including driver and passenger.

2. METHODOLOGY

To perform a system-level simulation of Battery driven Electric Vehicle, the model was created using system-level design blocks of the components. Then the parameter was set according to a selected vehicle model. The blocks were integrated using MATLAB-Simulink. Then the system was simulated in two different drive cycles to analyze the performance, energy consumption, and state of charge of the Battery driven EV. Furthermore, for verification, MATLAB-Simulink was utilized to simulate the integrated Simulink model with e-Rickshaw Driving Cycle (ERDC) and it was observed in Figure 1 that the system-level blocks of Battery driven Electric Vehicle shows a similar speed-time graph with ERDC. E-Rickshaw Driving Cycle (ERDC) is a three-wheeled auto rickshaw driving cycle with a limited speed in an urban area in India[28].

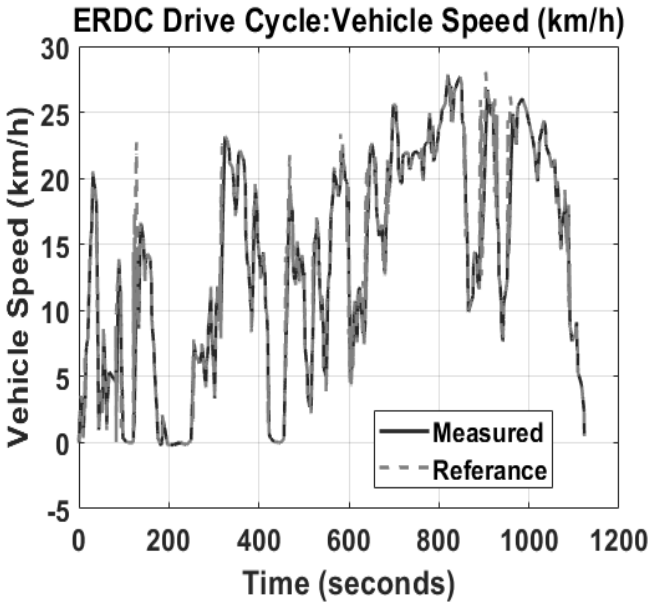

Fig. 1: Validate our model with ERDC drive cycle.

3. ELECTRICAL VEHICLE (EV) MODELING AND ITS COMPONENTS

The schematic block diagram of a three-wheeler single motor model of an Electric vehicle is developed. A rear axle act as a linkage between the two rear wheels and the electric motor. The battery system worked as energy storage and supply power to the system power as Electrical energy. Then, the motor transferred the Electrical energy into rotational energy through the rear wheel axle and this helps to drive the vehicle. This phenomenon is represented as a schematic diagram in Figure 2(a).

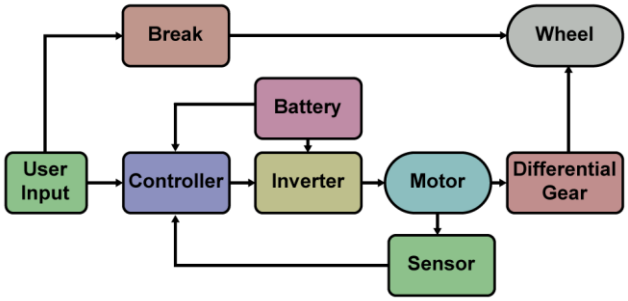

(a)

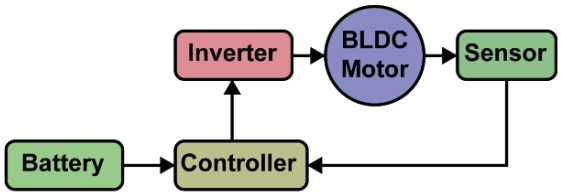

(b)

Fig. 2: (a) The schematic block diagram of Electric Vehicle and (b) energy flow.

3.1 Longitudinal Vehicle dynamics:

To evaluate the vehicle dynamics, during driving some resistance forces act on the vehicle. These resistance forces are rolling resistance, aerodynamic drag, and inertia resistance.

Aerodynamic resistance force (Fa) is the force that acts on objects moving in a fluid opposite to their motions. The aerodynamic resistance mainly depends on the frontal area and drag coefficient.

The rolling resistance force (Fr) is associated with energy loss due to frictional force on the tire contact area. Because of their elastic structure, a resistance force against the rotational movement of the tire develops in front of the wheel contact center, creating a rolling resistance force. The rolling resistance is varied with the rolling coefficient and vehicle mass. According to Newton's law of motion, an inertial force is generated in the opposing direction of motion as an object accelerates and decelerates. Inertia resistance force (Fi) is the force that the vehicle encounters during positive and negative acceleration. Equations 1,2,3 represent the formula of the aerodynamic resistance force, rolling resistance force Fr, and inertia resistance force

$$F_a = \frac{1}{2}\rho v^2 C_D A \quad (1)$$

$$F_r = mgC_r\cos\alpha \quad (2)$$

$$F_i = ma \quad (3)$$

v=speed of the vehicle
ρ= air density
A= Vehicle frontal area
C_D=drag coefficients

3.2 Electric Motor

In EVs, four different kinds of electric motors- Direct current motor, Asynchronous Motor, Permanent Magnet Synchronous motor, and Switched reluctance motor are used. As a result of evaluation [29], better efficiency and excellent controllability Permanent Magnet Synchronous motor (PMSM) is more suitable for this model.

3.3 Driving cycle

A driving cycle is a sequence of vehicle speed values as a function of time that includes a unique test drive that simulates a human starting the automobile and driving a short interstate journey, as though going to work. In this study, the Battery-driven EV was tested by the New European Driving Cycle (NEDC), which replicates low-speed city driving with numerous motor stops. Then it's also tested with the NYCC drive cycle to evaluate the vehicle's performance. The New York City Cycle (NYCC) is designed for low-speed vehicles in cities with frequent stops.

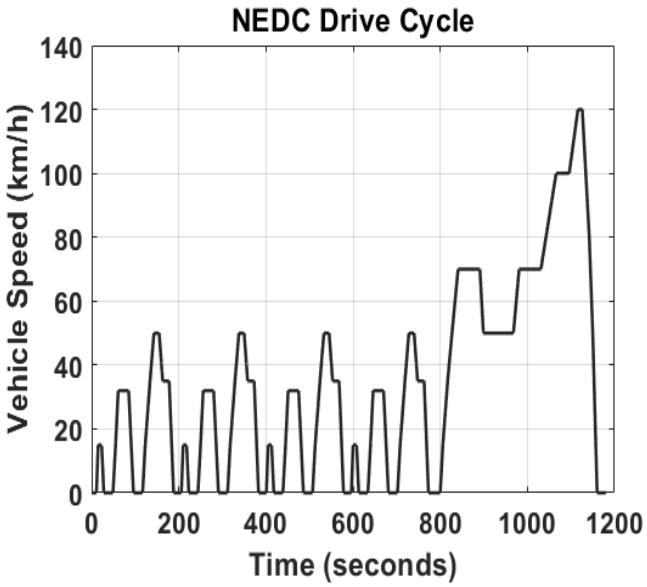

Fig. 3: NEDC Drive cycle data. [30]

3.4 Battery

In the battery-driven Electric vehicle battery is the only source of energy that provided power to the motor to drive the vehicle. The three-wheeler EVs mainly contains a simple battery pack based on a Lead-acid battery. But due to its less energy conversion efficiency worldwide Lithium-ion battery used.

3.5 Driver Model

This model is dependent on reference and real velocities in the forward MATLAB/Simulink simulation model (generally via a PI controller) [29]. The block generates braking and acceleration instructions by modulating 0 through 1 to represent a driver's dynamic reaction and monitor the current drive cycle. A feedback open-loop system was built to provide precise monitoring of continuous or signal-based steering, accelerating, braking, and gear command input. The throttle instruction from the driver model is converted into torque produced by the electric motor and sent to the transmission model.

4. PHYSICAL PARAMETER

The physical parameter of this battery-driven EV is divided into three parts, Vehicle parameters, Electrical parameters, and Environmental parameters. The parameter used to design the simulation model of a three-wheeler Electric Vehicle are specified in TABLE 1 & 2.

Table 1: Layout of manuscript

Vehicle parameters	Parameter value
Vehicle weight m (kg)	400
Air resistance coefficient Cd	0.2
Rolling resistance coefficient	0.0136
Frontal area A (m2)	2.3
Wheel rolling radius r (m)	0.3

Table 2: Physical Electrical parameter of EV.

Electrical parameters	Parameter value
Voltage	60
Capacity	100 AH
Motor	PMSM

5. SIMULATION MODEL OF EV

To model this EV, the block diagram of each component is linked up depending on their functional order. The driving cycle, vehicle, Permanent Magnet Synchronous motor (PMSM) model, transmission model, battery model, and vehicle dynamics are all included in the model depicted in Figure 4 (a). Each block is connected according to its functional design. Based on the mathematical equations and parameters applied to each component of the EV model, simulations are conducted in MATLAB/Simulink to testify the vehicle-designed parameters for performance under different conditions. Each block is connected according to its functional design.

The motor and controller block here is a system-level design of a PMSM, which means it simulates a motor by mathematical equation according to some parameter input such as maximum torque, power, and efficiency of the motor. In this simulation, a 12.5 N-m, 1500w, and 90% efficient motor is considered.

The vehicle body block is a longitudinal model of a vehicle. This block is modeled considering vehicle dynamics such as Vehicle Mass, Tire Radius, Rolling Resistance, Air Drag, and Road Gradient. A break port and axel port are exposed to control the vehicle using a rotating shaft and break signal.

The driver block is a proportional controller which commands the motor to accelerate or a brake. The difference in expected speed and measured speed is taken as input and the drive and brake signal is produced proportional to it.

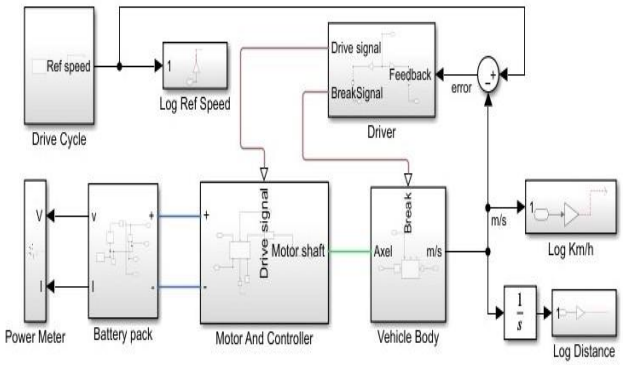

(a)

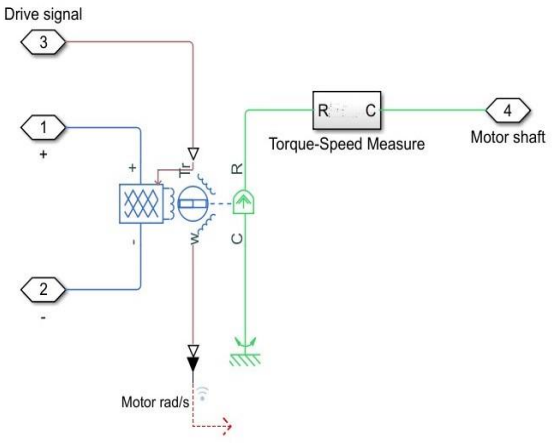

(b)

Fig. 4: (a) The Simulink model of integrated Electric vehicle and (b) System-level Motor controller subsystem.

6. RESULT AND DISCUSSION

The performance of different aspects of the vehicle was observed using system-level simulation with NEDC drive Cycle. Figure 5(a) shows the speed achieved by the vehicle at different times of the drive cycle. The comparison of the measured speed with the expected reference drive cycle speed was displayed as a function of time. It shows that the vehicle system-level model was not able to follow the peak reference speed of the drive cycle as it is designed as a low-speed vehicle.

The measured torque during the drive cycle was displayed in Figure 5(b). Due to its low weight and small frontal area, the torque required in this model is not so large. With the moment of acceleration, the corresponding torque is high and at deacceleration time the corresponding torque becomes negative. And Figure 5(c) represents the power consumption during the cycle. It is observed that during breaking the power consumption is negative, this represents the regeneration action of the motor.

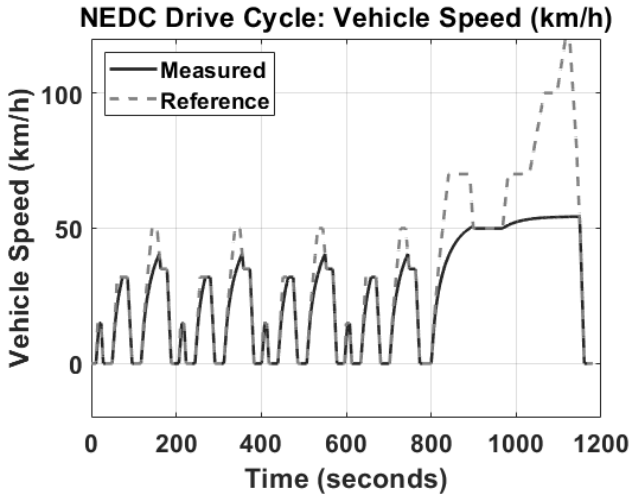

(a)

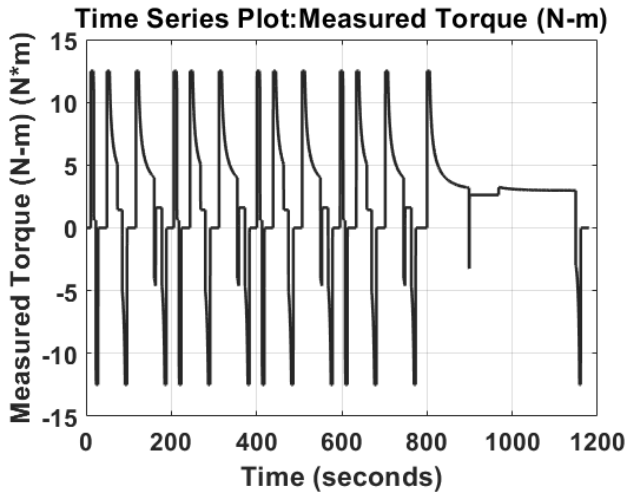

(b)

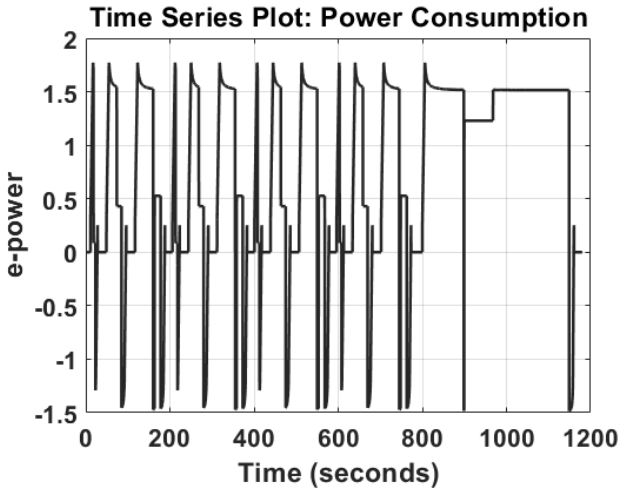

(c)

Fig. 5: Power, Vehicle speed, and Measured torque as a function of time in 1180 seconds.

NYCC drive cycle was also used to test the performance of the vehicle. NYCC is a standard drive cycle developed for dynamometer testing of low-speed vehicles in cities with frequent stops. Performance in this drive cycle is shown in Figure 6

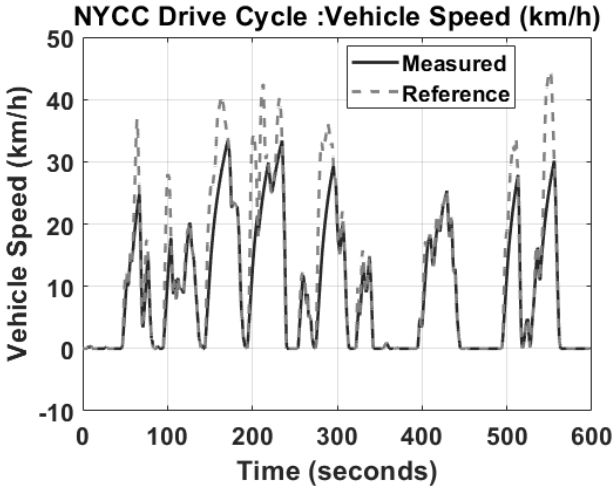

Fig. 6: Simulation on NYCC drive cycle.

The simulation results from the system model such as power conservation (kwh), distance traveled (km), and the State of Charge (SoC) (v) for two different drive cycles NEDC AND NYCC with a run time of 3.5 hrs. are displayed at Table 2 & Table 3.

Table 3: Power consumption and Distance traveled in 3.5 hrs. run time with different total vehicle weights.

Total weight	NEDC		NYCC	
	Power Consump-tion (kwh)	Distance Traveled (Km)	Power Consump-tion (kwh)	Distance Traveled (Km)
460	2	94.1	0.9	35.6
580	2.3	90.7	1.1	33.8
700	2.5	86.7	1.2	32.3

Both NEDC and NYCC simulation above was run for 3.5 hours. It is observed from the data that, power consumption increases and distance traveled decreases with the increase of the total vehicle weight. Here total vehicle weight means the total weight of the vehicle with one driver-460kg, with Tow Pssangers-580kg, and with Four Passengers-700kg. Despite the same runtime distance traveled during the NYCC cycle is less because the vehicle was running at a slower speed.

Table 4: SoC after 3.5 hrs. of run time with different total vehicle weights.

Total weight	NEDC	NYCC
	SoC (V)	SoC (V)
460	48.7	56.3
580	42.4	56.2
700	23.3	55.1

As vehicle weight increases, the state of charge falls rapidly. State of charge of the battery after 3.5 hrs. of runtime with different "Total vehicle weight" as shown in Figure 5.

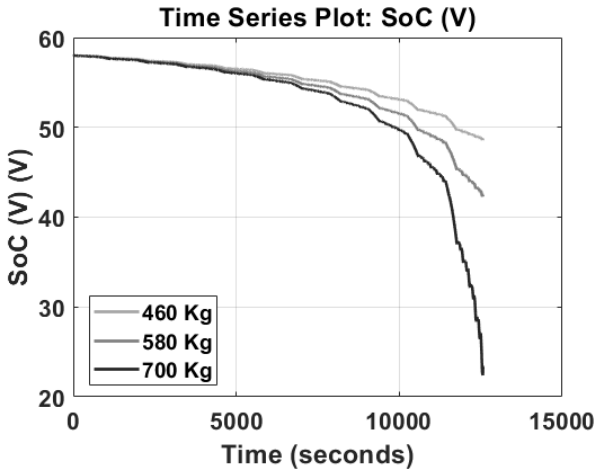

Fig. 7: Compare SoC under different load conditions.

7. CONCLUSION

In this research, we look at one of Bangladesh's most popular three-wheeler electric vehicles. By using MATLAB-Simulink, the components of a battery-powered EV were simulated to assess the existing model setup power output, compare reference speed and vehicle speed for a specific driving cycle, and measure energy consumption. This compact three-wheeler EV with minimal battery storage and regenerative braking technology might be quite beneficial in urban areas for short-distance travel due to its reduced weight and speed. There are still many opportunities for developing a better battery-powered EV model that will serve as the foundation for future research. The use of electricity, modeling, and simulation are highly essential for automobile designers to identify the ideal voltage, current, capacity, battery charge status, and correct size of the item, to get better aerodynamic and electrical efficiency.

REFERENCES

.[1] L. Chapman, "Transport and climate change: a review," *J. Transp. Geogr.*, vol. 15, no. 5, pp. 354–367, Sep. 2007, doi: 10.1016/j.jtrangeo.2006.11.008.

[2] Y. Wu *et al.*, "On-road vehicle emissions and their control in China: A review and outlook," *Sci. Total Environ.*, vol. 574, pp. 332–349, Jan. 2017, doi: 10.1016/j.scitotenv.2016.09.040.

[3] A. Faiz, B. Bahadur Ale, and R. K. Nagarkoti, "The role of inspection and maintenance in controlling vehicular emissions in Kathmandu valley, Nepal," *Atmos. Environ.*, vol. 40, no. 31, pp. 5967–5975, Oct. 2006, doi: 10.1016/j.atmosenv.2005.11.064.

[4] J. P. A. Neeft, M. Makkee, and J. A. Moulijn, "Diesel particulate emission control," 1996.

[5] P. Ahmadi, "Environmental impacts and behavioral drivers of deep decarbonization for transportation through electric vehicles," *J. Clean. Prod.*, vol. 225, pp. 1209–1219, Jul. 2019, doi: 10.1016/j.jclepro.2019.03.334.

[6] M. Bertoluzzo, G. Buja, V. Cossalter, A. Doria, and D. Mazzaro, "Getting around in electric vehicles," *IEEE Ind. Electron. Mag.*, vol. 2, no. 3, pp. 10–18, 2008, doi: 10.1109/MIE.2008.928606.

[7] H. Shareef, M. M. Islam, and A. Mohamed, "A review of the stage-of-the-art charging technologies, placement methodologies, and impacts of electric vehicles," *Renewable and Sustainable Energy Reviews*, vol. 64. Elsevier Ltd, pp. 403–420, Oct. 01, 2016. doi: 10.1016/j.rser.2016.06.033.

[8] S. Arora, W. Shen, and A. Kapoor, "Review of mechanical design and strategic placement technique of a robust battery pack for electric vehicles," *Renewable and Sustainable Energy Reviews*, vol. 60. Elsevier Ltd, pp. 1319–1331, Jul. 01, 2016. doi: 10.1016/j.rser.2016.03.013.

[9] G. O. Isobe, F, Itakura, Y, Osumi, Y, Li, *One Motor Type Electric Vehicle Drive System*. 2020.

[10] S. F. Tie and C. W. Tan, "A review of energy sources and energy management system in electric vehicles," *Renewable and Sustainable Energy Reviews*, vol. 20. pp. 82–102, 2013. doi: 10.1016/j.rser.2012.11.077.

[11] S. Phuyal, D. Bista, and R. Bista, "Challenges, Opportunities and Future Directions of Smart Manufacturing: A State of Art Review," *Sustainable Futures*, vol. 2. Elsevier Ltd, Jan. 01, 2020. doi: 10.1016/j.sftr.2020.100023.

[12] "Internet of Things in Power Industry: Current Scenario of Nepal." [Online]. Available: http://www.iaras.org/iaras/journals/ijitws

[13] M. Ehsani, Y. Gao, and S. Longo, *Modern Electric, Hybrid Electric, and Fuel Cell Vehicles*. 2018.

[14] C. Anderson and E. P. Aerovironment, "The Effects of APU Characteristics on the Design of Hybrid Control Strategies for Hybrid Electric Vehicles Reprinted from: Design Innovations in Electric and Hybrid Electric Vehicles (SP-1089)-* =For Advancing Mobility Jr(lC and Sea ~ i r and Spacem International Congress and Exposition Detroit, Michigan."

[15] L. Zhang, L. Li, B. Qi, and J. Song, "Configuration Analysis and Performance Comparison of Drive Systems for Pure Electric Vehicle," in *SAE Technical Papers*, Apr. 2015, vol. 2015-April, no. April. doi: 10.4271/2015-01-1165.

[16] Husain I and I. MS., "Design, modeling and simulation of an electric vehicle system." 1999. [Online]. Available: https://www.jstor.org/stable/44733867

[17] B. Sri Kaloko, mr. Soebagio, and M. Hery Purnomo, "Design and Development of Small Electric Vehicle using MATLAB/Simulink," *Int. J. Comput. Appl.*, vol. 24, no. 6, pp. 19–23, 2011, doi: 10.5120/2960-3940.

[18] oral Vatan, "Modelling and Simulation of Longitudinal Dynamics of Electric Vehicles," no. February, 2011.

[19] V. F. Dr. Vladimir, "Dynamic Modeling and Control of Hybrid Electric Vehicle Powertrain Syatems," *Gastron. ecuatoriana y Tur. local.*, vol. 1, no. 69, pp. 5–24, 1967.

[20] X. . Xue, K. W. E. Cheng, and N. . Cheung, "Selection of electric motor drives for electric vehicles. In Power Engineering Conference," 2008, [Online]. Available: https://ieeexplore.ieee.org/abstract/document/4813059

[21] G. Cole, *Simple electric vehicle simulation (SIMPLEV)* ,.

[22] W. W. Marr and W. J. Walsh, "LIFE-CYCLE COST EVALUATIONS OF ELECTRIC/HYBRID VEHICLES," 1992.

[23] J. Bumby, P. Clarke, and I. Forster, "Computer modelling of the automotive energy requirements for internal combustion engine and battery electric-powered vehicles," 1985.

[24] K. B. Wipke and M. R. Cuddy, "Using an advanced vehicle simulator (ADVISOR) to guide hybrid vehicle propulsion system development", [Online]. Available: http://www.hev.doe.gov/

[25] "Matlab/simulink." The Mathworks Inc., Natick, MA.

[26] K. L. Butler, M. Ehsani, and P. Kamath, "A Matlab-Based Modeling and Simulation Package for Electric and Hybrid Electric Vehicle Design," 1999.

[27] A. M. Saleque, S. H. Khan, A. M. A. Khan, and S. Hoque, "Drivetrain design and feasibility analysis of electric three-wheeler powered by renewable energy sources," *4th Int. Conf. Adv. Electr. Eng. ICAEE 2017*, vol. 2018-Janua, pp. 432–438, 2017, doi: 10.1109/ICAEE.2017.8255395.

[28] R. Lairenlakpam, G. D. Thakre, P. Gupta, Y. Singh, and P. Kumar, "Effect of different drive modes on energy consumption of an electric auto rickshaw," *2017 IEEE Transp. Electrif. Conf. ITEC-India 2017*, vol. 2018-Janua, pp. 1–5, 2018, doi: 10.1109/ITEC-India.2017.8333832.

[29] T. Markel *et al.*, "ADVISOR: A systems analysis tool for advanced vehicle modeling," *J. Power Sources*, vol. 110, no. 2, pp. 255–266, 2002, doi: 10.1016/S0378-7753(02)00189-1.

[30] V. Schwarzer and R. Ghorbani, "Drive cycle generation for design optimization of electric vehicles," *IEEE Trans. Veh. Technol.*, vol. 62, no. 1, pp. 89–97, 2013, doi: 10.1109/TVT.2012.2219889.

Paper ID: 1141

International Conference on Mechanical, Manufacturing and Process Engineering (ICMMPE – 2022)

Organizer: Faculty of Mechanical Engineering, Dhaka University of Engineering & Technology (DUET), Gazipur, Bangladesh

Website: https://icmmpeduet.com/

A Comparative Scenario from Bangladeshi Industries on Engineering Parameters of Utility Machines

Md. Saiful Islam[1], Md. Ismail Tushar[2], M. Mahbubur Rahman[3], Md. Tanvir Siraj[4], Asif Kabir[5], and Johirol Islam[6]

[1,5,6]Department of Mechanical Engineering, BUET, Dhaka, Bangladesh
[2]Department of Pharmaceutical Sciences, North South University, Bashundhara, Dhaka, Bangladesh
[3]Department of Mechanical Engineering, DUET, Gazipur, Bangladesh
[4]Department of Industrial and Production Engineering, BUET, Dhaka, Bangladesh

E-mail: saifulmebuet@gmail.com[1], mmrahman@duet.ac.bd[3], asifkabir121@gmail.com[5]

ABSTRACT

A company's active operation depends on its engineering department. One of the departments in this area is maintenance, which is responsible for keeping the machinery functioning smoothly. Maintenance work includes both the upkeep of manufacturing machines and utility maintenance. Utility services are an essential feature of every industry's engineering department's maintenance sector. Substations, generators, pumps, ETP (Effluent Treatment Plant), water treatment plants, compressors, and other utility services equipment are often used. Chemical, RMG (Ready-Made Garment), pharmaceutical, and other industries have different utility services. These companies provide utilities to the entire industry as well as install, maintain, and repair machinery. For this study, data were acquired from the engineering departments of various Bangladeshi industries' utility services. We can wrap things up with a basic chunk. In terms of boilers, the chemical industry has employed larger capacity boilers than the clothing and pharmaceutical industries. The size of the industry and the rate of production are the most important factors. The bulk of compressors used in Bangladesh, according to surveys, are made in Germany and the United States. The great majority of generators used in Bangladesh are also built in the United States. According to estimates, the bulk of water treatment plant equipment used in Bangladesh is made in India or the United States.

Keywords: Utility Service; Maintenance Equipment; Boiler; Pump; Generator; Compressor.

1. INTRODUCTION

Since the Industrial Revolution, maintaining engineering equipment in the field has been a challenge. Despite significant improvements in effectively maintaining equipment in the field, due to considerations such as size, cost, complexity, and competitiveness, equipment maintenance remains a difficulty. Needless to say, today's maintenance procedures, particularly in the manufacturing and process industries, service providers, and so on, are market-driven. An event could have an immediate impact on the environment, performance, or safety. As a result, there is a clear requirement for comprehensive asset management and maintenance methods that will have a beneficial impact on crucial success variables including safety, product quality, innovation speed, price, profitability, and on-time delivery. Maintenance activities are defined as those that employ resources to physically carry out actions and duties related to the equipment maintenance function, such as testing, servicing, repair, calibration, overhaul, and modification.

There are elements of uncertainty and the possibility of error in all of the factors that influence the performance of equipment and plant, including physical data inaccuracy, basic behavior correlations such as pipe friction or gas-liquid distribution or tray efficiency, as well as essential design estimates and calculations, not entirely known behavior of construction materials, the uncertainty of future market demands, and changes in operating performance w The project's viability, the operators, public's safety, and the design engineer's reputation and career are all on the line.

From the preparation of raw materials to the finishing phase, the fabric or garment manufacturing process is energy-intensive. All of the primary activities engaged here include steam generation in the boiler and distribution system. As a result, the goal of this research is to evaluate the overall performance of the steam system employed in Bangladesh's textile and garment industries. At both the steam generation and distribution units, the amount of heat lost through various sources was calculated. The amount of heat energy consumed in the process was also calculated.

The heating and cooling thermal loads of buildings are influenced by many design elements. Building envelope characteristics such as building shape and orientation, wall and roof constructions, window kinds and sizes, and HVAC system characteristics such as type, efficiency, and operating

settings are among these parameters. The interaction reliance of these elements on total building energy usage can make determining the ideal combination of design features that can reduce energy consumption and cost while maintaining desirable indoor thermal comfort conditions more difficult for building designers.

When choosing cost-effective pump materials, all of the aspects must be considered. Phillips and Francis used examples from the oil and gas industry to highlight key themes, but the same ideas may be applied to the selection of materials for wastewater treatment. The most crucial component is to obtain as much information as possible about the likely composition of the effluent, as well as the likely variations over the system's lifetime. In practice, this is often difficult, so it's best to estimate the worst-case scenario because if a pump fails unexpectedly, you'll lose all of your working time.

A generator is a machine that combines the electrical starting and generating operations required by combustion engines into a single unit. This necessitates both low-speed high-torque and high-speed constant-power operation, two incompatible criteria. This study evaluates various machine types for usage as an S/G and then picks and optimizes many PM machines, stressing the trade-offs to be made between the various operating modes and how this impacts the machine's weight.

The selection and design of clever and cost-effective compressors are discussed as a critical necessity for a successful grass-roots or retrofit project.; inherent operating characteristics of the two basic types of compressors, namely, positive-displacement or centrifugal machines; features and design constraints of different types of compressors that are particularly relevant to the Consumer Price Index (CPI), namely, screw, reciprocating, and integrally geared centrifugal compressors.

The main objective of this research is to show the real scenario of Bangladeshi industries on engineering parameters of utility machines and compared the data of the industry's engineering department's maintenance sector. Substations, generators, pumps, ETP (Effluent Treatment Plant), water treatment plants, compressors, and other utility services equipment.

2. LITERATURE REVIEW

Maintenance activities are defined by Dhillon, B. S et al [1] as those that employ resources to physically conduct actions and duties associated with the equipment maintenance function, such as testing, servicing, repair, calibration, overhaul, and modification. Job planning is a critical component of good maintenance management. Successful maintenance companies monitor their performance regularly using a variety of methods.

Over the years, a substantial body of standards has evolved to assure the safe and cost-effective design, manufacture, and testing of equipment, structures, and materials explained by Couper, J. R. et al [2]. A particularly useful use of preliminary design is that it might show a lack of specific data required for the final design. The highest heat loss was discovered to occur during steam production via the dry flue gas explained by S. Saha et al [3].

Youssef Bichiou et al [4] develop and presents a complete energy modeling environment for effectively selecting both building envelope characteristics and heating and air conditioning system design and operating parameters. Some recent research validates the previous statement for both experimental [5] and numerical methods [6]. Similarly by using third-party software researchers can propose better air conditioning design solutions [7].

Material selection of wastewater after pumps is a complicated activity that necessitates knowledge of materials, corrosion, and the interaction of chemicals in the specific fluid which is explained in the paper of Roger Francis et al [8]. Furthermore, it is critical to understand if Modular Integrated Construction (MIC) is feasible since this can dramatically restrict the operating limitations of particular materials. Some recent experiment has been conducted by selecting a specific pump in an evaporative cooling system using different local low-cost materials as cooling pads [9].

A generator is a mechanism that combines the electrical starting and generating operations required by combustion engines into a single machine. This necessitates both low-speed high-torque and high-speed constant-power operation, both of which are incompatible needs. Martin van der et al [10] study that beginning times for aerospace gas turbines are in the region of 10-30 seconds, and to avoid overheating, the starting performance of the electrical machine becomes as crucial as the generator performance.

Compressors are used to boost a fluid's pressure. The most popular compressors are reciprocating and centrifugal. Barnett, J. M. et al [11] study that engineers should aim to reduce the entire life-cycle cost of compression while maintaining dependability when selecting a compressor type and writing specifications for it. Considerable compressor dependability has always come at a high price. However, one of the main points of this article is that sufficient dependability may frequently be achieved with lower-cost equipment by focusing on the basics of the compressor's design and application in the process. Following are a few instances.

The equipment specifications for demineralization systems included criteria that represented this application, Endpoint Detection and Response (EDR) are intrinsic process advantages, based on EDR's capacity to run at higher recovery without the need for constant chemical addition for scale control (based on side-by-side pilot testing with reverse osmosis) which is studied by James C. Lozier et al [12]. Each train will have two hydraulic stages that will remove roughly 75% of the total dissolved solids (TDS).

All utility equipment has its research criteria. When industry needs to select all of these utility services, they need to follow some criteria to select the optimal one for that type of industry.

3. DATA COLLECTION AND ILLUSTRATIONS

The engineering department of any industrial sector is critical to the industry's active operation. All of the engineering department where we collected our data is efficient in their industry. They provide utility assistance to the whole industry, including machine installation, maintenance, and troubleshooting. In this paper, we have various data from various types of industries.

There are different kinds of industries in Bangladesh We focus on that kind of industry where the utility services in the Engineering department have a boiler, compressor, pump, water treatment plant, HVAC, etc. After visiting different types of industries like pharmaceutical, multinational companies, garments sector, and chemical factories we have collected our data and compressed it so that we can compare our collected data and illustrate it in different types of graphs to show the present scenario of the Engineering department of different industries in Bangladesh.

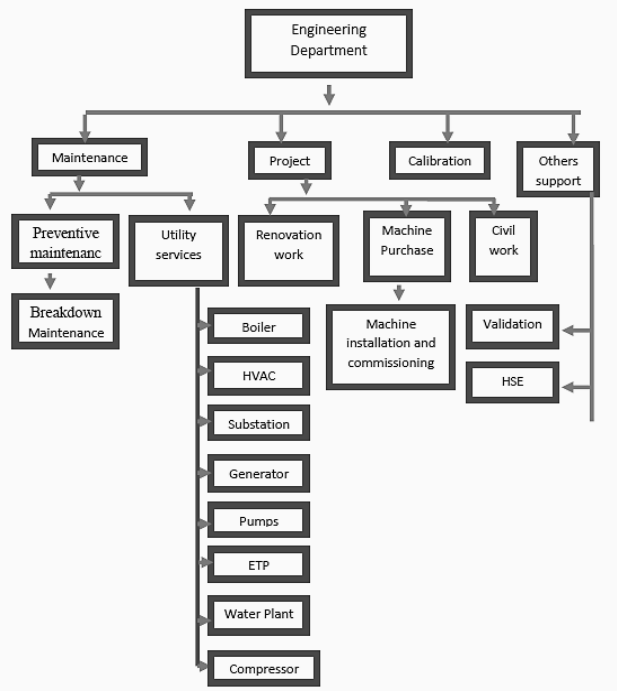

Fig. 1: Engineering department chart

3.1 Boiler

A boiler is a closed vessel that heats a fluid (usually water). Industry cannot be imagined without boilers. Their capacity is generally represented as (kg per hour). Large capacity boilers have been used in the Chemical industry than in the garments and pharmaceutical industry. It is mostly determined by the scale of the industry and the rate of production. The pharmaceutical sector needs smaller boilers than other industries.

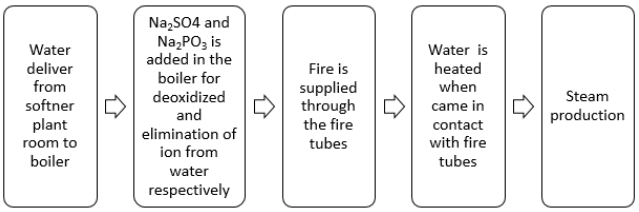

Fig. 2: Working process of boiler

Table 1: Data collection of boilers in different industries

SI No	Model	Brand Name & Origin	MC Capacity (Kg/hr)
1	Horizontal fire tube ZFR	BOSCH, Germany	31751
2	Steam Fire Tube	Cochran, UK	12000
3	Thermo-Boiler H 4000 LV	In-plan, Germany	8313
4	Thermo-Boiler S/TH-50 BE	Ascentec, Germany	8313
5	Steam Fire Tube	Cochran, UK	7710
6	Thermo boiler Hoko-RA-1500	SKI, Italy	3117
7	Steam Fire Tube	Byworth Boiler, UK	2721
8	EGB Water Tube	Clayton, USA	2200
9	Fire Tube GWB Boiler	Power Master, UK	1814
10	Thermo-Boiler H 4000 LV	Daelim, Germany	831

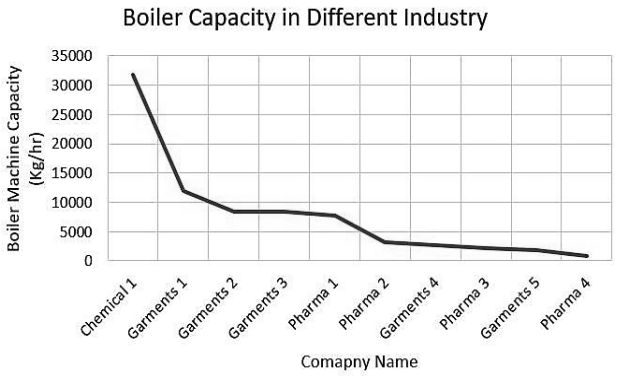

Fig. 3: Boiler machine capacity in Kg/hr for different types of industry (chemical, RMG, pharmaceutical)

From the above curve, it has been easily seen that the chemical industry which needs more water to be heated needs more capacity. Similarly, pharmaceutical industries need fewer capacity-based boilers. And RMG sector needs an average size boiler.

3.2 Compressor

A compressor is a mechanical device that decreases the volume of gas to enhance the pressure of the gas. A gas compressor that is used to compress air is known as an air compressor. Compressors and pumps are similar in that they both increase fluid pressure and may move it through a pipe.

Table 2: Compressor Data in different industries

SI No	Model	Brand Name & Origin	MC Capacity (m^3/min)
1	L75RS-10A	Comp-Air, Germany	13.99
2	L75RS-13A	Comp-Air, Germany	13.99
3	L75RS-13A	Comp-Air, Germany	13.99
4	Air Compressor	SULLAIR160, USA	13.50
5	L75-10A	Comp-Air, Germany	12.44
6	L75-10A	Comp-Air, Germany	12.44
7	L75-10A	Comp-Air, Germany	12.44
8	Air Compressor	SULLAIR160, USA	6.50
9	Air Compressor	SULLAIR160, USA	6.50
10	Air Compressor	SULLAIR160, USA	6.50

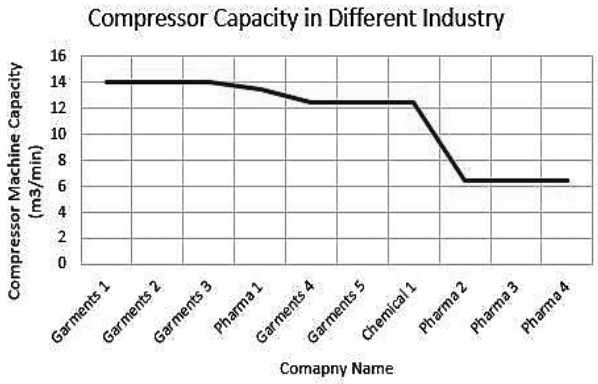

Fig. 4: Compressor machine capacity in m^3/min for different types of industry (chemical, RMG, pharmaceutical)

The capacity of the compressor is generally represented as (m^3/Min). According to the studies, the majority of compressors used in Bangladesh are manufactured in Germany and the USA. Two types of data have been found from data collection. The lower portion is used in pharmaceutical industries whereas the upper capacity compressor is used in garment industries.

This study discusses the most important selection criteria for an air compressor to be used in different types of industries. Because often these things create a decision-making challenge when selecting an air compressor for these types of factories like RMG, pharmaceutical, chemical, etc.

3.3 Pump

A pump does not create pressure, but it does move or flow liquid. It generates the flow needed to create pressure, which is a function of the system's fluid flow resistance.

Table 3: Data collection of the pump in different industries

SI No	Name of M/C	Brand Name & Origin	MC Capacity (M^3/hr)
1	Centrifugal Type centrifugal pump	KSB, China	3000
2	Submersible Type Deep Pump	Pannelli, Italy	300
3	Submersible Type Deep Pump	KSB, Germany	175
4	Submersible Type Deep Pump	Pannelli, Italy	150
5	Submersible Type Deep Pump	KSB, Germany	145
6	Submersible Type Deep Pump	Pannelli, Italy	96
7	Vertical Type Boosting Pump	KSB, Germany	90
8	Vertical Type Boosting Pump	Regent, Australia	90
9	Submersible Type Deep Pump	KSB, Germany	65
10	Vertical Type Boosting Pump	Grundfos, Denmark	30

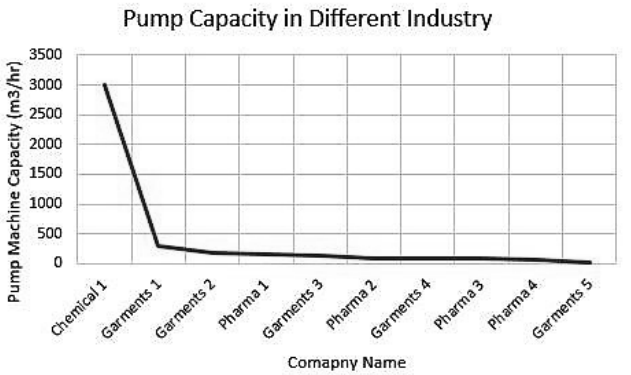

Fig. 5: Pump machine capacity in m^3/hr for different types of industry (chemical, RMG, pharmaceutical)

Pump machine capacity in m^3/hr. The largest capacity pump is used in the chemical and RMG sectors. Pumps are imported from several countries for use in the Bangladeshi industry. The price of Chinese pumps is low than others. Only the chemical industry needs higher capacity pumps rather than the others.

3.4 Generator

A generator is a device that converts mechanical to electrical energy. When you're not linked to the power grid, it powers your electronics and appliances. Generators are essential safety equipment in the event of natural catastrophes such as hurricanes and snowstorms, as well as any other power outage. Many data have been collected from different types of industries to see that real-life scenario. Most of cases there are two types of them. Either the gas one or the diesel one has been used.

Table 4: Data collection of generators in different industries

SI No	Name of M/C and Model	Model, Brand Name & Origin	MC Capacity (KW)
1	Gas Generator	G-3512H, Caterpillar, USA	2557
2	Gas Generator	G-3520C, Caterpillar, USA	2000
3	Diesel Generator	D-3516B, Caterpillar, USA	1950
4	Diesel Generator	D-3516B, Caterpillar, USA	1600
5	Gas Generator	G-3512H, Caterpillar, USA	1500
6	Gas Generator	G-3512E, Caterpillar, USA	1500
7	Diesel Generator	D 125, Caterpillar, USA	1056
8	Gas Generator	G-3516H, Caterpillar, USA	1000
9	Diesel Generator	D 616 DS, Caterpillar, USA	640
10	Diesel Generator	D 616 DS, GE, Austria	400

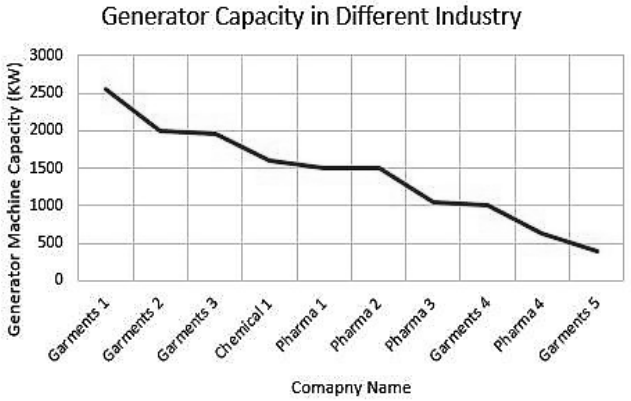

Fig. 6: Generator machine capacity in KW for different types of industry (chemical, RMG, pharmaceutical)

According to assessments, the vast majority of generators used in Bangladesh are made in the USA. Generator machine capacity calculated by KW.

3.5 Water Treatment Plant

The four basic unit processes are chemical coagulation, flocculation, sedimentation, filtration, and disinfection. As the water passes through the various treatment procedures, chemicals are added to it.

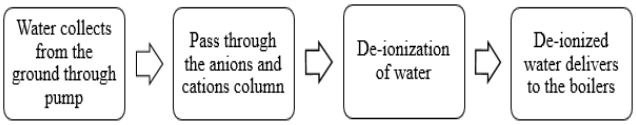

Fig. 7: Working process of the water treatment plant

Table 5: Data collection of WTP in different industries

SI No	M/C Name	Brand Name & Origin	MC Capacity (M^3/hr)
1	WTP	Ion Exchange, India	150
2	WTP	Ion Exchange, India	150
3	WTP	Ion Exchange, India	115
4	WTP	Pharma-lab, India	75
5	WTP	Stilmas, Italy	72
6	WTP	Alfa laval, USA	60
7	WTP	Alfa laval, USA	55
8	WTP	USF, USA	50
9	WTP	Alfa laval, USA	50
10	WTP	Alfa laval, USA	50

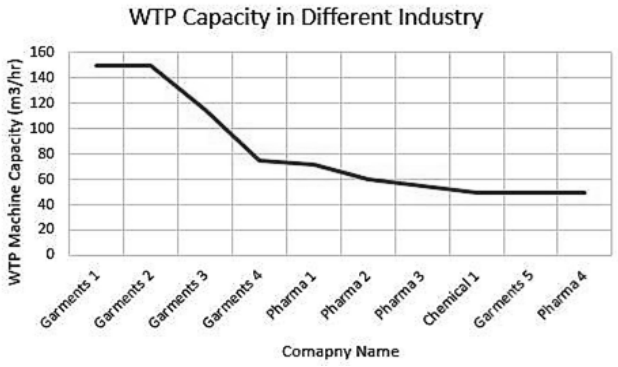

Fig. 8: Water treatment plant machine capacity in m^3/hr for different types of industry (chemical, RMG, pharmaceutical)

According to estimates, the great majority of water treatment plant equipment utilized in Bangladesh is manufactured in INDIA and the USA.

4. RESULT AND DISCUSSION

Maintenance is the field and profession of using engineering principles to improve the maintainability, dependability, and availability of equipment by optimizing technology, methods, and division budgets. This here shows that the Chemical, RMG, and Pharmaceutical industries used various types of engineering equipment of different sizes, capacities, and utility services.

The largest capacity boilers about 32000 kg/hr have been used in chemical industries and the RMG sector. In the pharmaceutical sector used in a small capacity about 831 kg/hr boilers are used. In this scenario of German technology, the boiler is widely used in the industrial sector of Bangladesh. In the chemical industry, the maintenance of the boiler has to be done quickly and carefully.

In Bangladesh, the major portion of compressors is made in Germany and the United States. The pharmaceutical industry uses (6.50 m^3/min) the small capacity compressor, while the Garment industry uses the larger capacity compressor of about 14 m^3/min.

Chemical and RMG industries use the biggest capacity pump. Pumps are imported for usage in the Bangladeshi industry from a variety of countries. Chinese pumps are less expensive than others. Only the chemical industry used more powerful pumps about 3000 m^3/hr.

The great majority of generators used in Bangladesh, according to estimates, are manufactured in the United States. The capacity of a generator is calculated in KW. In the garments sector largest generator used in Bangladesh is about 2600KW. In other industries pharmaceutical and chemical industries small capacity generators are used more than in the RMG sector.

A large proportion of water treatment plant equipment used in Bangladesh is made in INDIA and the United States. In the RMG sector largest WTP about 150 m3/hr used in Bangladesh. Other industries also used various types of WTP within the capacity of the plant.

5. CONCLUSION

This research represents many criteria for the utility services of the engineering department's maintenance section. So the conclusions are,

- It is required to maintain standard quality as well as the engineering parameters of the selected utility machinery. For example, the pharmaceutical industry is highly sensitive to the hygiene issue.
- This study has considered some engineering parameters of the machinery, at the same time taking some real-life parameters as the selection criteria for this industrial machinery.
- Industrial managers of any factories can be benefitted from the above-presented data of machinery selection, thus overcoming the challenge of balancing the engineering parameters and the standard quality.

In future studies, criteria weights can be determined. Some other criteria that have been discussed but not utilized in this study can also be utilized in the future work of machinery selection. This study only utilized the measurable criteria. However, non-measurable criteria like brand reliability, performance, and service providing, were not included in the decision-making framework. In the future, these criteria can also be included to be evaluated by the subjective judgment of the decision-makers.

REFERENCES

[1] Dhillon, B. S. (2002). Engineering maintenance: A Modern Approach, CRC press.

[2] Couper, J. R., Penney, W. R., Fair, J. R., & Walas, S. M. (2005). Chemical process equipment: selection and design. Gulf professional publishing, Elsevier: Amsterdam, Boston.

[3] Saha, S., Sayem, N. A., Khan, M. M. A., & Biswas, P. K. (2021). Overall performance of steam system used in garment industries in Bangladesh: a case study–based approach. Energy Efficiency, 14(2), 1-18.

[4] Bichiou, Y., & Krarti, M. (2011). Optimization of envelope and HVAC systems selection for residential buildings. Energy and Buildings, 43(12), 3373-3382.

[5] Islam, M., Kabir, A., Arka, A. M., & Rahman, M. A. (2019, Aug). A Numerical Study on the Performance and Energy Efficiency Improvement Opportunity of Transport Refrigeration Vehicles in Bangladesh. Dhaka, 5th World Congress on Mechanical, Chemical, and Material Engineering At Lisbon, Portugal.

[6] Islam, M., Kabir, A., Arka, A. M., & Rahman, M. A. (2019, July). Assessment of the transport refrigeration system in Bangladesh and numerical simulation of the refrigeration performance. In AIP Conference Proceedings (Vol. 2121, No. 1, p. 030013). AIP Publishing LLC.

[7] Imtiaz, F., Bhuiyan, M. S. A., & Rahman, M. A. (2020). Assessment of thermal performance of transport refrigeration vehicles by modifications in the compartment design and storage pattern. In IEICES, Vol. 6, 284-291.

[8] Francis, R. (2018, May). The Selection of Pump Materials for Handling Waste Waters, CEOCOR, RF Materials Ltd, Stratford-upon-Avon, Warwickshire, UK.

[9] Alam, M. F., Sazidy, A. S., Kabir, A., Mridha, G., Litu, N. A., & Rahman, M. A. (2017, June). An experimental study on the design, performance, and suitability of evaporative cooling system using different indigenous materials. In AIP Conference Proceedings (Vol. 1851, No. 1, p. 020075). AIP Publishing LLC.

[10] Van der Geest, M., Polinder, H., Ferreira, J. A., & Zeilstra, D. (2013, May). Machine selection and initial design of an aerospace starter/generator. In International Electric Machines & Drives Conference, IEEE, 196-203.

[11] Barnett, J. M., & Schramke, T. M. (2000). Cost-effective compressor selection and specification. Chemical Engineering, 107(10), 70-70.

[12] Lozier, J., Smith, G., Chapman, J., & Gattis, D. (1992). Selection, design, and procurement of a demineralization system for a surface water treatment plant. Desalination, 88(1-3), 3-31.

Paper ID: 1200
International Conference on Mechanical, Manufacturing and Process Engineering (ICMMPE – 2022)
Organizer: Faculty of Mechanical Engineering, Dhaka University of Engineering & Technology (DUET), Gazipur, Bangladesh
Website: https://icmmpeduet.com/

GIS-AHP Approach for Wind Farm Site Selection in Bangladesh

Md. Rakibul Islam, Md. Rabiul Islam*, H. M. Imran

Institute of Water and Environment, Dhaka University of Engineering & Technology, Gazipur
Gazipur-1707, Bangladesh

E-mail: mriceduet@gmail.com, rakibulceduet@gmail.com

ABSTRACT

One of the most enticing alternative energy sources is wind energy because of its low operating, maintenance, and production costs, as well as its low environmental impact. Identifying the best locations for wind power plants (WPPs) is a significant difficulty in wind energy development, requiring extensive and comprehensive evaluations of a number of factors. This study presents a high-resolution wind farm suitability map on the basis of Geographic Information System (GIS) and Analytical Hierarchy Process (AHP) approaches that take into consideration social, environmental, technological, and geographical challenges, encompassing eight unique criteria. Wind speed, slope, and elevation were found to have the most weighting criteria, with 32 %, 27 %, and 12 %, respectively. However, the final suitability map revealed that 11.27 % and 2.52 % of the country's land, respectively, are of high and very high potential for the installation of wind farms, which are deemed capable of fulfilling a substantial portion of the nation's electricity needs.

Keywords: Wind Farm; GIS; AHP; Bangladesh.

1. INTRODUCTION

The electricity sector in Bangladesh is primarily reliant on fossil fuels, with natural gas and coal acting as the country's principal power generating sources. Natural gas generates 62.9% of Bangladesh's electricity, with diesel accounting for 10%, coal for 5%, heavy oil for 3%, and renewables accounting for 3.3 %.[1]. Renewable energy sources like solar, biomass, wind, and hydropower are now being evaluated as potential climate change mitigation alternatives [2]. Wind energy is one of the most important and fastest-growing renewable energy sources due to its cleaner, renewability, and low impact on people and the environment. Wind turbines (WTs) are also simple to install and operate, with cheap operating and maintenance expenses. [3].

Many factors that influence the result of wind energy projects must be considered during their implementation. One of the most critical components is locating an acceptable investment site for a wind power plant (WPP) while taking into account the implementation requirements in terms of economics, technology, the environment, and land use. Other key factors to consider when determining where to develop a wind farm are the detrimental effects of WTs on Birds and fauna, shadow flashes, scenic aspects, and harmonic distortion [4]. As a result, the windiest areas aren't always the greatest; instead, to identify the best sites, a trade-off should always be established in between sets of financial, environmental, and ecological issues [5]. Multi-criteria decision-making (MCDM) techniques are used to find ideal sites for wind farms. Some MCDM strategies that can be used in conjunction with a GIS environment are the rating method, AHP, ranking method, weighted sum method (WSM), Weighted Linear Combination (WLC), trade-off analysis method, analytic network process (ANP), Boolean overlay operation, trade-off analysis method, Order Weighted Average (OWA), concordance analysis, and Elimination Et Choice Translating Reality (ELECT) [6]. The AHP is the most extensively used MCDM tool in research when examining green energy sites because it is basic, easy, and can check the coherence of the decision. It has the advantage of simplifying decision-making difficulties that require a high level of consistency and flexibility. This research focuses on merging AHP and GIS for the most optimal wind farm site selection in various areas over Bangladesh.

2. MATERIALS AND METHODS

2.1 Study Area

The study area, Bangladesh, is spatially extended from 20°34′ N and 88°01′ E to 26°38′ N and 92°41′ E in South Asia and is surrounded by India on three sides (i.e., west, north, and northeast). Its southeast border is Myanmar while the southern side embraces the Bay of Bengal with a distributed coastal area (Fig. 1)

2.2 Land Suitability Evaluation Factors

Eight assessment factors, such as wind speed, slope, proximity to a city, elevation, distance between power grid and transmission system, airport distance, major highways and railways, and lightning strike flash rates, were established and used as input to ArcMap 10.8 to do a geographic study and choose the optimum WT installation

Fig. 1: Study area map of Bangladesh.

locations in Bangladesh. In this study, locations with average wind speeds ranging from 3 to 20 ms-1 were considered for wind farm siting [7].And, suitability map, here, excludes areas with slopes of higher than 15%[8]. In the case of residential areas, locations beyond 1.0 km are regarded as ideal sites for wind farm installation [9]. WTs are, however, typically positioned on elevated ground to catch higher wind speeds [10]. The highest altitude reached here is 1250 meters, while the lowest was 0 meters. To limit the effect of electromagnetic fields created by TLs, which may harm human health, a minimum safe distance of 0.5 km is regarded between power TLs and the power grid [8][11]. The least distance from major airports is considered 3 kilometers [12]. The minimal distance from major roads and trains for this project is 0.5 km [13]. To protect wind turbine from thunder disruption, regions with a flash rate greater than 80 fl.km^{-2}yr^{-1} are designated as prohibited zones [14].

2.3 AHP based Multi-Criteria Decision-Making

AHP technique is solved using a hierarchical model that includes objectives, criteria, sub-criteria, and options[15]. The hierarchy is calculated after the problem is set on formation [16]. To compare the criteria in one hierarchy level to the criteria in the next hierarchy level, a pairwise comparison matrix is built using the preference scale[17].
The pairwise comparison matrix is normalized to derive weights or priority. The weights are in the 0–1.0 range, and their total is 1.0. The consistency ratio established by Saaty (1980) is used to quantify the consistency of pairwise comparison judgments[17]. Equation (1) is used to calculate CR, where CI is the consistency index, m is the primary eigenvalue of the comparison matrix, and RI is the random index, which is dependent on the matrix size (n),which can be found in [15].

$$CR = \frac{CI}{RI}, \; CI = \frac{\lambda_m - n}{n-1} \tag{1}$$

2.4 GIS Processing

This seems to be Bangladesh's first geospatial suitability analysis evidence based on a combined AHP-GIS technique regarding wind farm allocation. The suitability map was prepared employing ArcMap 10.8, and the geo-information data was obtained from open sources. To determine the inappropriate and ideal locations for wind farms, this study uses eleven limitations that represent eight evaluation parameters. All sets of factors included in the geographical analysis model were determined using expert evaluations, research area features, and scholarly reviews.

2.5 Generating the Wind Farm Suitability Map

The suitability map was created using GIS software to create a categorized map for each criterion. The maps that result indicate the criteria that were evaluated as well as their rankings. All maps were gererated in a raster format with the cell size 30 m× 30 m, then sorted into a relative class. The wind speed map was created by applying the reclassifying process. The slope map is created using digital elevation model (DEM) of the study area. The elevation map has also been categorized according to the elevation criteria rank. In addition, for the LIS/OTD Total Flash Density Map, a distribution map of different lightning strike levels in Bangladesh was created using the reclassifying tool. The map is resampled to a resolution of 30m, and the reclassification process is carried out accordingly. Furthermore, a classified map of distance from urban areas was created using a vector map of the city, and the "Euclidean distance" tool was used to calculate the various distances. Using the digitized maps, the Euclidean distance tool was also used to calculate the distance from the road network and the distance from power transmission lines. Then, using the Map Algebra spatial analyst tool, reclassification suitability maps of assessment factors were created. The final step was to do weighted overlay analysis. Using the "Weighted Overlay" technique, each suitability evaluation map was given a specific weight based on AHP results, and multiple reclassified geographic raster data layers were blended to generate the study's final suitability score. Suitability is divided into five categories: very high, high, medium, low, and very low.

3. RESULTS AND DISCUSSION

The findings of a geographic analysis of wind energy system sites in Bangladesh using AHP-GIS are presented and discussed in detail. This includes the quantitative data for the

best weighting of the assessment parameters as well as the ultimate land suitability map.

3.1 AHP Results

The optimised weights of the eight criteria influencing factors (C1: wind speed; C2: slope; C3: elevation; C4: proximity to TLs; C5: proximity to cities; C6: distance from roads and railways; C7: proximity to airports; C8: lightning strike flash rate) are determined in this study using the AHP-based MCDM process. When identifying the optimal locations for WT construction in the study area, the criteria factor C1 was found to have the greatest priority weight (32%). C2 through C8 are the remaining criteria factors, and their priority weight is diminishing. In this analysis consistency ratio was found, CR = 0.075 that is less than 0.10.

3.2 Out Come of Land Suitability Evaluation Factors

According to the spatial distribution of the wind speed, approximately 64.42 % of the land is found appropriate for wind farm development. 0.01 % of the land area has a very high wind speed, 0.59 % has a high wind speed, and 40.85 % has a moderate wind speed (4 to 5 ms^{-1}).

The land slope is also considered an important factor since it can accelerate the wind speed through the venturi effect. In terms of slope, it is recognized that 46.44% of the land in Bangladesh is an ideal location for wind farm development. According to the proximity to TLs map, the majority of the land area (58.31%) is located near the national grid. Furthermore, the distance from significant cities or metropolitan areas reveals that 2.84 % of the land area is (1–5 km) away, while 5.88% is (5–10 km) away, demonstrating that these are the prime locations for wind farms. However, 15.49% of the area is located between 10 and 20 kilometers from major cities, making it a potential wind energy investment location. Furthermore, more than half of the area is located more than 30 kilometers far from urban regions.

Proximity to roads and railways: approximately 29.42 % of the land area is separated (0.5–5 km) from the land transportation network, i.e., roads and railways, which is a possible location for wind farms. Furthermore, about 25.40 % of the land area is located 5 to 20 km away from roads and railways, making it acceptable for wind energy investments, whereas 24.15 % is deemed less favorable or unsuitable for wind farm establishment.

A point's perpendicular height above the mean sea level known as land elevation or land form, has a considerable influence on wind farm installation. In this study, it is found that more than 99 % of the land area is appropriate for developing wind farms as its elevation is less than 0.5 km. Hill tracts having a height of more than 1km are considered undesirable for wind farm installations.

3.3 Wind Farm Suitability Category

According to the suitability of wind farm installation, the study area is split into six categories: very high, high, moderate, low, very low, and inappropriate (Fig. 2 & Table 1). Wind farm suitability map reveals that 2.52 % (3718.76 km^2) of the investigated land has very high suitability, 11.27 % (16631.14 km^2) has high suitability, 35.54 % (53922.08 km^2) has moderate suitability, 25.36 % (37423.75 km^2) has low suitability, 1.57 % (841.15 km^2) has very low suitability, and 23.74 % (35033.12 km^2) is unsuitable for wind farm placement. The elevated and appropriate sites, which account for 13.79 % of the land, would be considered candidate locations for wind energy projects, prompting investments and plans for approval in these areas.

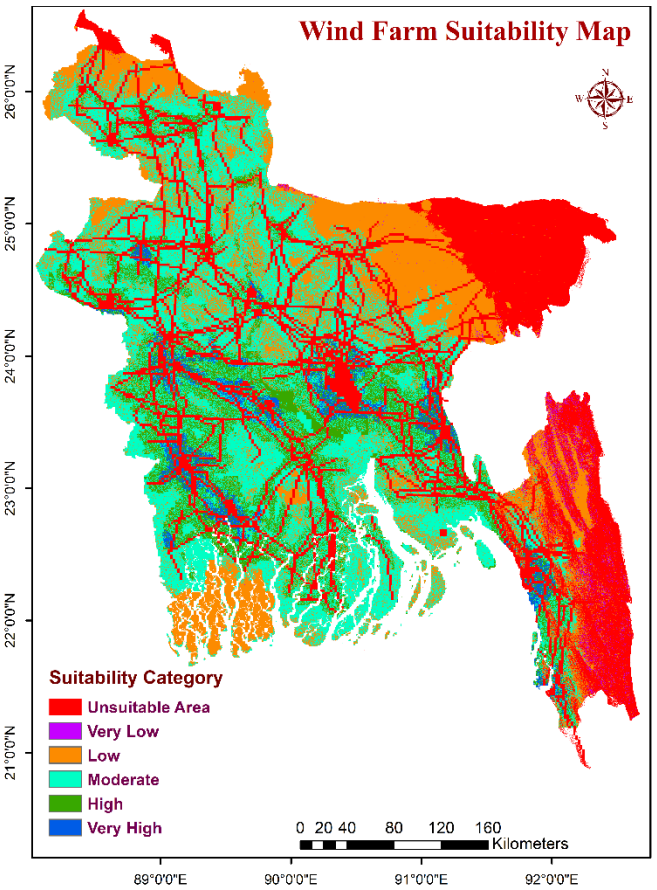

Fig. 2: Suitability map of wind farms' locations.

The most favorable zones are found in the western and southern middle parts of Bangladesh, according to the suitability map. Furthermore, coastal areas are thought to be ideal for the construction of wind farms. These locations are particularly well-suited because they share a number of characteristics that make wind farms feasible, including excellent land slope and elevation, strong wind activity, proximity to grid TLs and airports, proximity from urban and rural communities, as well as least lightning awareness.

Table 1: The regions of each suitability class, as well as their proportions in the study area.

SN	Suitability Categories	Map Color	Area (km^2)	Coverage (%)
1	Unsuitable	Red	35033.12	23.74
2	Very low	Purple	841.15	1.57
3	Low	Orange	37423.75	25.36
4	Moderate	Cyan	53922.08	35.54
5	High	Green	16631.14	11.27
6	Very high	Blue	3718.76	2.52

4. CONCLUSION

The primary goal of this study is to locate viable wind farm sites in Bangladesh, where no prior studies have been published to fill this research gap. In order to achieve this aim, the AHP evaluation as well as the GIS platform were integrated. Eight criteria were used to find the optimal places for wind farms, which included environmental, social, financial, and technological concerns. Despite the fact that lightning flash frequency has a strong influence on WT safety and functioning, it was included in the criteria selection. The research looked at wind speed, slopes, proximity of power lines and power stations, distances between urban areas, distances from airport, elevation, distances from major highways and railways, and flashover flashing rate, among several other factors. The study offered a complete analysis of wind farm site appropriateness based on the criteria prioritizing. As per the spatial analysis, 23.74 % is inappropriate for wind farm development. Due to low wind resource potential and challenging topographical limitations, most of these sites are located in the country's eastern region and are unsuitable. On the other hand, wind farms were found to be feasible in 76.26 % of the country's land area (1.57 % is very low, 25.36 % is low, 35.54 % is moderate, 11.27 % is high, and 2.52 % is very high suitable). The findings are intended to minimize the amount of money spent, the time it takes to build, and the resources needed to design and implement wind energy projects in Bangladesh. One of the study's shortcomings is the use of publicly available online data, some of which is low resolution and can even be validated due to a lack of field observations, which is costly. Similarly, a variety of criteria, namely the financial feasibility study and its impact on the selection of best sites, must be explored. This study is designed to provide a preliminary analysis of the location of renewable energy projects with the aim of assisting decision-makers in developing an action plan for urban expansion and renewable energy projects. Such studies can provide accurate design for the installation of wind turbine systems on a relatively small scale, such as in local government districts and cities.

REFERENCES

[1] M. Taheruzzaman and P. Janik, “Electric Energy Access in Bangladesh,” *Trans. Environ. Electr. Eng.*, vol. 1, no. 2, 2016, doi: 10.22149/teee.v1i2.13.

[2] S. D. Pohekar and M. Ramachandran, “Application of multi-criteria decision making to sustainable energy planning - A review,” *Renew. Sustain. Energy Rev.*, vol. 8, no. 4, pp. 365–381, 2004, doi: 10.1016/j.rser.2003.12.007.

[3] M. T. Islam, S. A. Shahir, T. M. I. Uddin, and A. Z. A. Saifullah, “Current energy scenario and future prospect of renewable energy in Bangladesh,” *Renew. Sustain. Energy Rev.*, vol. 39, pp. 1074–1088, 2014, doi: 10.1016/j.rser.2014.07.149.

[4] A. S. Zalhaf *et al.*, “A high-resolution wind farms suitability mapping using gis and fuzzy ahp approach: A national-level case study in Sudan,” *Sustain.*, vol. 14, no. 1, pp. 1–21, 2022, doi: 10.3390/su14010358.

[5] “(PDF) Site Suitability Analysis for Developing Wind Farms in Pakistan: A GIS-Based Multi-Criteria Modeling Approach.” https://www.researchgate.net/publication/330015520_Site_Suitability_Analysis_for_Developing_Wind_Farms_in_Pakistan_A_GIS-Based_Multi-Criteria_Modeling_Approach (accessed Mar. 26, 2022).

[6] M. Elkadeem, A. Younes, S. Sharshir, P. C.-A. Energy, and undefined 2021, “Sustainable siting and design optimization of hybrid renewable energy system: A geospatial multi-criteria analysis,” *Elsevier*, Accessed: Mar. 26, 2022. [Online]. Available: https://www.sciencedirect.com/science/article/pii/S0306261921005250

[7] D. Pamučar, L. Gigović, Z. Bajić, M. J.- Sustainability, and undefined 2017, “Location selection for wind farms using GIS multi-criteria hybrid model: An approach based on fuzzy and rough numbers,” *mdpi.com*, Accessed: Mar. 26, 2022. [Online]. Available: https://www.mdpi.com/212172

[8] Y. Xu *et al.*, “Site selection of wind farms using GIS and multi-criteria decision making method in Wafangdian, China,” *Elsevier*, Accessed: Mar. 26, 2022. [Online]. Available: https://www.sciencedirect.com/science/article/pii/S0360544220313293

[9] E. T.-S. E. T. and Assessments and undefined 2021, “Land suitability assessment for wind farms through best-worst method and GIS in Balıkesir province of Turkey,” *Elsevier*, Accessed: Mar. 26, 2022. [Online]. Available: https://www.sciencedirect.com/science/article/pii/S2213138821005026

[10] A. Zalhaf, … M. A.-S.-I. R., and undefined 2019, “Assessment of wind turbine transient overvoltages when struck by lightning: experimental and analytical study,” *ieeexplore.ieee.org*, Accessed: Mar. 26, 2022. [Online]. Available: https://ieeexplore.ieee.org/iel7/4159946/8732273/08732279.pdf

[11] K. Kotb, M. Elkadeem, A. Khalil, … S. I.-E. C. and, and undefined 2021, “A fuzzy decision-making model for optimal design of solar, wind, diesel-based RO desalination integrating flow-battery and pumped-hydro storage: Case,” *Elsevier*, Accessed: Mar. 26, 2022. [Online]. Available: https://www.sciencedirect.com/science/article/pii/S0196890421001382

[12] L. Gigović, D. Pamučar, D. Božanić, S. L.-R. energy, and

undefined 2017, “Application of the GIS-DANP-MABAC multi-criteria model for selecting the location of wind farms: A case study of Vojvodina, Serbia,” *Elsevier*, Accessed: Mar. 26, 2022. [Online]. Available: https://www.sciencedirect.com/science/article/pii/S0960148116310412

[13] Z. Ullah, M. Elkadeem, K. Kotb, I. Taha, S. W.-R. Energy, and undefined 2021, “Multi-criteria decision-making model for optimal planning of on/off grid hybrid solar, wind, hydro, biomass clean electricity supply,” *Elsevier*, Accessed: Mar. 26, 2022. [Online]. Available: https://www.sciencedirect.com/science/article/pii/S0960148121010673

[14] R. Said, M. M.-24th international lightning detection, and undefined 2016, “GLD360 upgrade: Performance analysis and applications,” *training.weather.gov*, Accessed: Mar. 26, 2022. [Online]. Available: https://training.weather.gov/wdtd/courses/woc/severe/data-fusion/lightning/gb-ltg-prod/story_content/external_files/Said_Murphy_2016.pdf

[15] T. L. Saaty, “An Exposition of the AHP in Reply to the Paper ‘Remarks on the Analytic Hierarchy Process,’” *Manage. Sci.*, vol. 36, no. 3, pp. 259–268, Mar. 1990, doi: 10.1287/MNSC.36.3.259.

[16] “Konumsal karar problemlerinde analitik hiyerarşi... - Google Scholar.” https://scholar.google.com/scholar?hl=en&as_sdt=0%2C5&q=Konumsal+karar+problemlerinde+analitik+hiyerarşi+yönteminin+kullanılması&btnG= (accessed Mar. 30, 2022).

[17] “The Analytic Hierarchy Process: Planning, Priority... - Google Scholar.” https://scholar.google.com/scholar?hl=en&as_sdt=0%2C5&q=The+Analytic+Hierarchy+Process%3A+Planning%2C+Priority+Setting%2C+Resource+Allocation%2C+and+%282001%29&btnG= (accessed Mar. 30, 2022).

Paper ID: 1276

International Conference on Mechanical, Manufacturing and Process Engineering (ICMMPE – 2022)

Organizer: Faculty of Mechanical Engineering, Dhaka University of Engineering & Technology (DUET), Gazipur, Bangladesh

Website: https://icmmpeduet.com/

The Assessment of Non-COVID Patients' Hospital Visitation in a Upazilla Health Complex in Bangladesh During the COVID-19 Pandemic Situation

Md. Foysal Uddin[1,*], Md. Arafat Rahman[1] and Md. Sazol Ahmmed[1]

[1]Department of Industrial & Production Engineering, Rajshahi University of Engineering & Technology, Rajshahi, Bangladesh.

E-mail: 1605020@student.ruet.ac.bd

ABSTRACT

Non-COVID patients have been treated with almost no interest when the COVID-19 pandemic started to get bigger in every country. But keeping them at a distance only fueled the situation by straining on the hospital resources and pressurizing on the hospital staff. To mitigate this situation, no attempt has been made to understand their visitation behavior in this pandemic situation. Since a country's daily new cases can be a powerful indicator of the country's coronavirus situation and non-COVID patients' attitude towards hospital visitation during the pandemic situation, this study investigates the underlying relationship between them. It assesses whether the visitation of non-COVID patient decreases with the increase of new COVID cases in Bangladesh during different lockdown phases. Pearson correlation analysis has been adopted to do the intended analysis and it is done in various sections of the lockdown phase. Segmentation of the timeline of the pandemic works as an excuse to observe the effect of lockdown. From the government to hospital management and the general public, everyone wants a stable, if not minimal, visitation to the hospital because it is one of the most dangerous places for disease spread and to avoid wasting hospital resources. With the initial stages of development of the disease, the population has shown a negative tendency for hospital visitation. But to a surprise, the negative attitude has not been present throughout the pandemic situation as one might hope, which is evident by correlation analysis and its p-value. Rather, the visitation assessment reveals that it was more affected by lockdown rules over the course.

Keywords: Non-COVID; Lockdown; Hospital Visitation; Public Health.

1. INTRODUCTION

When the world was faced with a new pandemic, most countries in the world were hit with the hard truth of their health care system. This pandemic was the result of a respiratory disease caused by the novel coronavirus infection, which is also known as SARS-CoV-2 or severe acute respiratory syndrome coronavirus 2 [1]. If social distancing policies are not implemented and the number of COVID-19 patients is not reduced, hospitals around the world will be overcrowded, staff will be exhausted, and hospital resources will be stretched. Saturated hospitals mean the reduction of normal health care systems and the death of patients with an acute condition. So, people all over the world tried to flatten the curve also to reduce the number of patients admitted to the hospital so that they can provide adequate health care to all patients.

As of November 1, 2020, the total number of cases of COVID-19 patients is almost 50 million and total deaths is almost 1.20 million [2]. Although most countries have almost coped with the spread of viruses through NPI (Non-Pharmaceutical –Intervention) [3], the number of new cases is still rising. So, countries which have loosened their suppression and mitigation policies to contain the virus may have to rethink their policies which are clearly needed for reducing new infection through human contact [4]. Moreover, according to the World Health Organization, the second wave is still yet to hit in most countries, whereas some countries are still recovering from the first wave, such as Bangladesh. Now we can understand that the pandemic is far from over and there may be some significant changes in the future.

Bangladesh, a densely populated South Asian country, has seen some fruitful results of adapting NPI policies after the first three cases of COVID-19 on March 8, 2020 [2]. The number of total infected patients is 410,988 and total deaths of 5,966 by November 2, 2020. Due to insufficient testing facilities, a lack of contact tracing, and apathy in the general population, the number of daily new cases is already being called into question. According to a news article, the first wave of COVID-19 is still yet to over as the percentage of daily infection did not go under 10% [1]. After the initial hit, hospitals in the capital changed their health care policy dramatically overnight, which resulted in a lot of confusion, a stop to the routine checkup, and serious problems with patients with an acute condition. No patients were allowed in

the hospital without proper clarification of the patient's disease and to add distress, all non-COVID patients were to produce a certificate to clarify they did not contain the virus. This is a major issue when people need to go to the emergency room or when a routine checkup could result in serious problems, such as in the case of dialysis, diabetics, and newborn babies. As a result, the number of non-COVID patients has dropped significantly.

One study found that patients with myocardial infections and strokes even with acute conditions were denied admission, leading up to a 60% decrease in these patients. Another research, [5] raises the question if the mortality rate of acute coronary syndrome (ACS) in northern Italy has seen a rise due to COVID-19. This further emphasizes the lack of attention to non-COVID patients during this pandemic. With a huge decrease in admission of patients, many fears that in future it could adversely affect already saturated hospitals. This may come as an increase in readmission, length of stay, and number of emergency cases, thus resulting in a huge spike in the number of infected patients [6].

With frequent surges of new COVID patients, attention should be paid to non-COVID patient health care as well, and appropriate steps should be taken to manage the situation in most hospitals in Bangladesh, primarily districts or Upazilla Health Complexes. This article tries to investigate any correlation between the number of non-COVID patients' daily visits and the number of new cases daily found in Bangladesh. This will give an understanding of whether hospitals should increase their resources to cope with increased visitation..

2. LITERATURE REVIEW

Correlation has been widely adopted by many researchers to investigate the underlying relation between two continuous variables. One study [7] states that correlation gives a sense of strength and direction of that relationship. It also explains linear regression as an analysis of the relative impact of the predictor or independent variable on outcome variable or dependent variable. According to another [8], the variables do not require statistical evidence to be evaluated, and much of the choice of variables is based on intuition. Correlation and regression analysis are said to be the analysis of association. Correlation and regression analysis have always been useful in the medical and health care systems for scientifically proving various assumptions and hypotheses. Recently [9] it has been found that increasing HbA1c or Glycated Hemoglobin level was strongly correlated with Coronary Artery disease severity of Non-diabetic Patients through a correlation study. One researcher [10] has found that organizational commitment is positively related to organizational climate with a regression analysis in public hospitals in North Cyrus. While identifying the underlying factors influencing nurses missing care in private hospitals [11] used a descriptive and correlational study. To add another important research, [12] to forecast hospital visits using linear regression with correlating between patients and patients. So, it is clear that correlation and simple linear regression analysis can be adopted

to analyze the relation between hospital staff and patients' underlying behavior. Now, recent studies that have been done to improve the condition of the health care system mainly include how the virus is spread, the number of affected people, trend in the infected population and an attempt to forecast the affected people to prepare the hospitals in terms of resources such as hospital beds, respiratory systems et. The pandemic models which are used to predict how a disease will evolve in a population, the SEIR model is the most popular and accepted one and a variation of which is the SEIRD model [13]. One research [14] done by Columbia University on the population of a metropolitan area forecasts the number of affected people with some assumptions made related to social distancing policies. A group of researchers have [15] developed a mechanistic model which was used to forecast the hospital pressure throughout the United States whose parameter was based on demographic data. A fill compartmental SEIRD model was developed by [16] to explain the hospital dynamics and sub-compartments to describe the length of stay of residents. Here, the residents' rate was proposed as Erlang Distribution to forecast hospital demand. Finally, one of the few researchers who used an incremental approach and extended their model to grid search approach to include parameter estimation and later implemented time dependent SEIRD model is a study [13].Someone [17] also considered the trend analysis in India to explain the spread of the disease in different states. One research from Bangladesh [18] tried to analyze the pandemic by modifying the SEIR model into a SEIIsR epidemic model by considering infected people in the hospital isolation compartment before they started to spread the disease. They did not consider the asymptomatic spread in their analysis. Surprisingly, only one study has used a time series forecasting method such as ARIMA to predict the number of people who may be affected. During the past, most research concerning the pandemic and Bangladesh has always focused on the socio-economic perspective [19], mental health [20], public perception [21] and suicide rate [22] during the lockdown. All of them fail to address the health care treatment of non-COVID patients despite having multiple reports of serious mistreatment. One exception is [23], which looks into the health of non-COVID patients in Dhaka's slums.

3. METHODOLOGY

3.1 Hypothesis Formulation

The data set for this case study has been divided into several parts and each part was tested for the correlation

analysis. The main factor of classifying data was the lockdown situation. First the whole data set was parted as (a) Lockdown Course and (b) Post Lockdown Course. Then the first part was broken down into further two groups. For the lockdown course of-
(i) Strict Lockdown Phase: Duration of this time period was only for the month of April.
(ii) Moderate Lockdown Phase: This phase was for the time duration when the lockdown phase was kind of phasing out in all over Bangladesh. Duration of this time period lasted from May to June.

For these three classifications three pairs of hypotheses were created to carry out the analysis. These hypotheses were based on the fact that as the number of daily new cases rises the hospital visitation of non-covid patients should be increasing. In other words, these two variables should not have a positive correlation in any phase.

- Hypothesis for strict lockdown phase

H_0: There exists no significant negative correlation between non-covid patients' visitation and daily new cases during the month of April.
H_1: There exists a significant negative correlation between non-covid patients' visitation and daily new cases during the month of April.

- Hypothesis for moderate lockdown phase

H_0: There exists no significant negative correlation between non-covid patients' visitation and daily new cases during the months of May and June.
H_1: There exists a significant negative correlation between non-covid patients' visitation and daily new cases during the months of May and June.

- Hypothesis for entire lockdown phase.

H_0: There exists no significant negative correlation between non-covid patients' visitation and daily new cases during the months of April and October.
H_1: There exists a significant negative correlation between non-covid patients' visitation and daily new cases during the months of April and October.

3.2 Software

For this analysis 'IBM SPSS Statistics 26' was used. This software is specifically used for statistical analysis and widely used for its easy to understand interface and the ability to carry out most of the statistical analysis.

4. RESULT AND DISCUSSION

4.1 Data Collection

Data was collected from an Upazilla Health Complex with 50 beds. During the lockdown period part of this hospital was turned into an isolation compartment which is perfect for analyzing effect of new cases non-covid visitation behavior. The data was collected from March 1, 2020 to October 31, 2020. Because before March, the general population did not feel any effect of COVID-19 and government lockdown was started at 23rd march. So, this collecting data from March will give us a really good idea about hospital visitation.

4.2 Data Transformation

Every government hospital in Bangladesh remains closed on weekend i.e. Friday. This created a problem from obtaining a smooth curve and analysis. So, every Friday was filled with the average between last and the next day visitation. This process fills out the missing values and creates a perfect dataset for analysis. For this process the data was first loaded into Microsoft Excel and all the averages were done manually. The entire data set has been divided into several groups and each group is tested for examining the underlying relationship between two continuous variables.

4.3 Trend Analysis

First, a linear graph is produced to get a sense of the data.

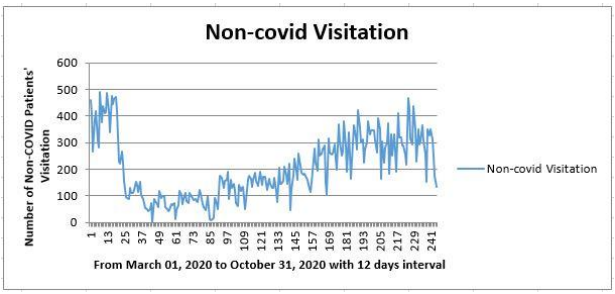

Figure 4.1: Visual graph of non-COVID patient visitation from March till October.

This graph takes the total eight months from March 1, 2020 to October 31, 2020 and transforms it into days and graphs the number of non-COVID patients' visitation during this time. From figure 1 it is clearly apparent that after the initial lockdown the number of visitations has been the lowest. Throughout this time period there was a strict lockdown in the area. This lockdown situation was changed after some time in accordance with the government law. After that there is a gradual upward trend indicating the increase in visitation. Almost reaches as the same range as before lockdown near the month of October. Now we take a look at the graph of daily new cases of covid 19-

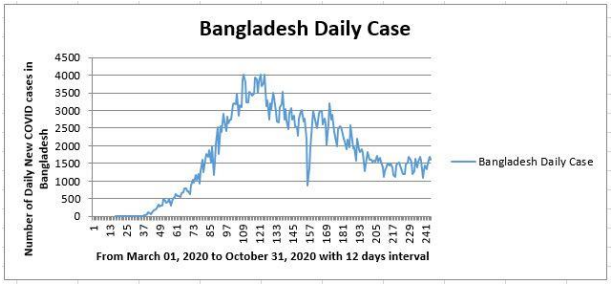

Figure 4.2: Number daily new COVID-19 cases in Bangladesh.

This graph is also produced by transforming the montys into days and plottong the rise and fall of daily new COVID cases in Bangladesh. After seeing an exponential increase, the number of daily new cases has been reduced thanks to government policies of social distancing and general awareness among people. Though the trend of new cases has not been totally downward, it has been stable for the month of October.

4.3 Test of Normality

One of the assumptions of bivariate correlation is the sample distribution is normal. Though it is not strictly followed, this case examined the normality for the whole sample of two variables to find out if these two variables follow the normal distribution. The following analysis shows the normality test of the whole data set.

Variable: non-covid patients' visitation

With the SPSS software the entire sample of non-covid patients' visitation from April to October was evaluated. Tests of normality and histogram can give us a concrete idea about sample distribution. First checking the histogram reveals that the sample is not normally distributed.

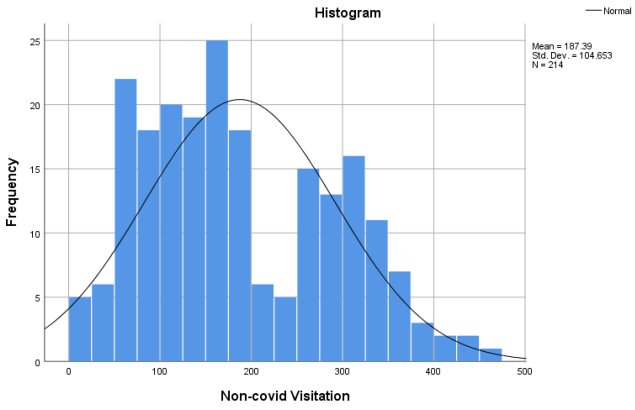

Figure 4.3: Histogram of Non-Covid Patient's Visitation.

Table 4.1: Tests of Normality for Non-Covid Patient's Visitation.

Tests of Normality						
	Kolmogorov-Smirnov[a]			Shapiro-Wilk		
	Statistic	df	Sig.	Statistic	df	Sig.
Non-covid Visitation	.099	214	.000	.958	214	.000
a. Lilliefors Significance Correction						

It is seen from the normality table that both of significance of Kolmogorov-Smirnov and Shapiro-Wilk test is less than .05. This concludes that the variable non-covid patients' visitation is not normally distributed. In order to gain the normalcy first the sample was ranked and the inverse normal distribution was done on the ranked variable. Ultimately the following results are obtained

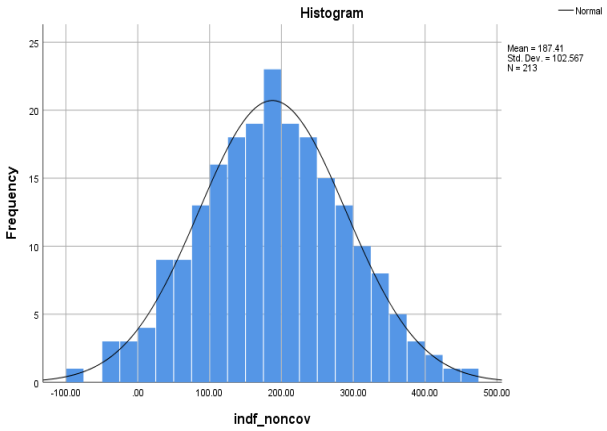

Figure 4.4: Histogram of Transformed Non-Covid Patient's Visitation.

Table 4.2: Tests of Normality Transformed Non-Covid Patient's Visitation

Tests of Normality						
	Kolmogorov-Smirnov[a]			Shapiro-Wilk		
	Statistic	Df	Sig.	Statistic	df	Sig.
indf_noncov	.011	213	.200*	.998	213	.999
*. This is a lower bound of the true significance.						
a. Lilliefors Significance Correction						

Histogram clearly shows a normal distribution. Now the significance of Kolmogorov-Smirnov is .200≻ 0.05 and the significance of Shapiro-Wilk is .999 > .05. Both these indicate that the sample is now normally distributed.

Variable: Bangladesh daily new cases

The explorative descriptive statistics analysis of this variable unveils its distribution nature and conclusions can be easily drawn from histogram and tests of normality.

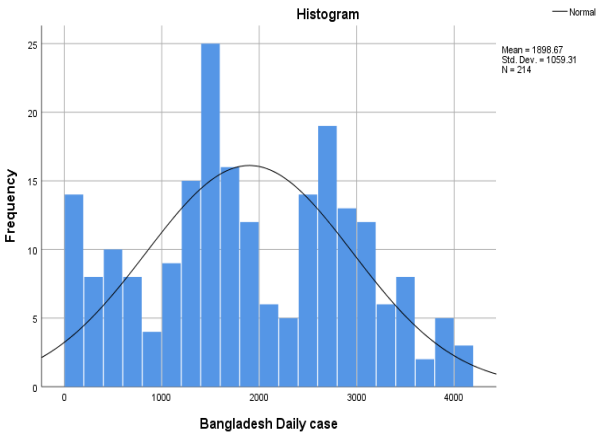

Figure 4.5: Histogram of Bangladesh Daily Cases.

Table 4.3: Tests of Normality for Bangladesh Daily Cases.

Tests of Normality						
	Kolmogorov-Smirnov[a]			Shapiro-Wilk		
	Statistic	df	Sig.	Statistic	df	Sig.
Bangladesh Daily case	.076	214	.004	.972	214	.000
a. Lilliefors Significance Correction						

A glance at the histogram makes it clear that the sample is not normally distributed. Furthermore, tests of significance of Kolmogorov-Smirnov and Shapiro-Wilk are .004<.05 and .000<.05 respectively.

To transform this sample, the previous procedure was applied. The inverse normal distribution finally gives the following results of a normal distribution. This conclusion was drawn because Kolmogorov-Smirnov significance is 0.200>.05 and Shapiro-Wilk significance .999>.05.

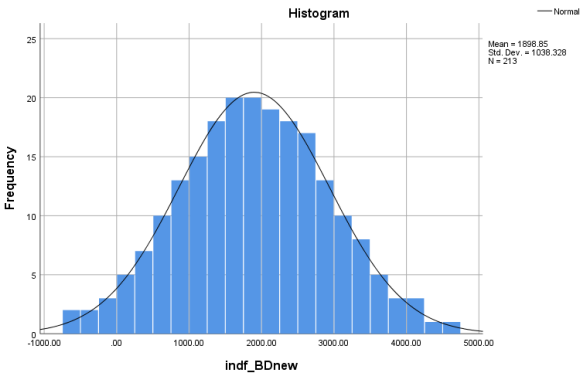

Figure 4.6: Histogram of Transformed Bangladesh Daily Cases.

Table 4.4: Tests of Normality Transformed Bangladesh Daily Cases.

Tests of Normality						
	Kolmogorov-Smirnov[a]			Shapiro-Wilk		
	Statistic	Df	Sig.	Statistic	df	Sig.
indf_BDnew	.008	213	.200*	.998	213	.999
*. This is a lower bound of the true significance.						
a. Lilliefors Significance Correction						

4.4 Correlation Analysis

The analysis is started with the first month of lockdown. First both variables were put through a normality test then, the correlation analysis began. The bivariate analysis was chosen under the correlation tab from analysis bar. Non-covid patients' visitation was chosen as dependent variable and daily new cases was chosen as independent variable. After that both of them was selected for the analysis. The following table has been produced as the output.

Table 4.5: Correlation Analysis for April between Bangladesh Daily Case and Non-COVID Patient.

Correlations (April)			
		Bangladesh Daily case	Non-COVID Visitation
Bangladesh Daily case	Pearson Correlation	1	-.500**
	Sig. (2-tailed)		.005
	N	30	30
Non-covid Visitation	Pearson Correlation	-.500**	1
	Sig. (2-tailed)	.005	
	N	30	30
**. Correlation is significant at the 0.01 level (2-tailed).			

As the data suggests, there is a strong negative correlation between Bangladesh daily new cases and non-covid patient visitation in the hospital. The Pearson correlation coefficient is -0.500. The negative sign indicates that the relationship that exists between these variables is negative and the magnitude suggests that correlation is strong. Now if we look at the p-value or the significant value, it is seen that correlation is significant as .005<.01. In conclusion the null hypothesis for this part of the data set is rejected i.e. there is a statistically significant linear relationship.

Now the focus is shifted to the second part of the lockdown course when the implementation was moderate. The sample data is put into the software and necessary analysis was done to create the output of May-June time period.

Table 4.6: Correlation Analysis for May to June between Bangladesh Daily Case and Non-covid Patient.

Correlations (May-June)			
		Non-COVID Visitation	Bangladesh Daily case
Non-covid Visitation	Pearson Correlation	1	.499**
	Sig. (2-tailed)		.000
	N	61	61
Bangladesh Daily case	Pearson Correlation	.499**	1
	Sig. (2-tailed)	.000	
	N	61	61
**. Correlation is significant at the 0.01 level (2-tailed).			

The value of r = 0.499 indicates that there is a strong positive relationship and p-value = .000 < .01, indicating that the linear relationship is statistically significant. These results can be interpreted as the number of non-covid patient increases with the daily new cases. The reality of the situation forces us to reject alternative hypothesis and a failure to reject the null hypothesis. There is no significant negative relationship between non-covid patients' visitation and new affected covid patient in Bangladesh.
Now the overall data have been tested for correlation. This will shed some light whether people really decreased their visitation in the entire lockdown period.

Table 4.7: Correlation Analysis for April to October between Bangladesh Daily Case and Non-COVID Patient.

Correlations (April-October)			
		Non-COVID Visitation	Bangladesh Daily case
Non-covid Visitation	Pearson Correlation	1	.135*
	Sig. (2-tailed)		.048
	N	214	214
Bangladesh Daily case	Pearson Correlation	.135*	1
	Sig. (2-tailed)	.048	
	N	214	214
*. Correlation is significant at the 0.05 level (2-tailed).			

This result also shows a positive correlation with an r-value of 0.135. With a significance level of 0.048<.05. So, with this statistically significant correlation, we fail to reject the null hypothesis. In the entire time period, there is no statistically significant negative correlation between non-covid patient's visitation with daily new cases of Covid-19. With a large data sample, the level of significance changes. As with this data sample the number of sample points are 214 and degree of freedom becomes (214-2) or 212. Degree of freedom determines the level of significance. Normally with 200 sample points the critical value of correlation coefficient becomes ±0.130. The r value being outside of the critical value is actually an indicator of statistical significance. This is further solidified by p-value.

4.5 Discussion

The goal of this study was to discover how the visitation behavior of non-COVID patients changed during the pandemic situation and assess this phenomenon with some other factors related to their visitation. This study kept a focus on two things. The daily new cases in Bangladesh are mentioned explicitly, and the lockdown situation in that Upazilla is mentioned implicitly. Rather than considering the entire timeline, this study focuses on the specific situation of the lockdown and then compares it to the daily new COVID cases. It answers some questions, like if hospital visitation really decreases as the pandemic grows bigger in the country or if people feel less concerned with daily cases and more with the lockdown situation in the area.

When the newly found coronavirus threatened the entire population, the whole country went into strict lockdown. The number of daily new cases increased while visitation decreased. The correlation analysis clearly showed a string negative correlation with a Pearson value of-.500 and a p-value of .005. Next, the analysis took on the time period when the lockdown was moderate in the area. With the lift of lockdown there has shown a positive correlation with the daily new cases. This conclusion came from the fact that r-value is .499 and p-value .000. This means two things; the daily new cases had an impact initially, but as time passed and with the lift of the lockdown situation, the correlation became from strong negative to strong positive. The hypothesis test with the correlation analysis was done to find out whether the increasing number of daily new cases has an overall negative relation with hospital visitation. But with a sad act, this study has not been able to find any evidence to support the hypothesis. Moreover, the results bitterly show a positive relationship with a p-value .048.

This study's real-world application is that people in the outlying areas of town only respond to the strict phase of a lockdown situation. The increase in visitation only proves the preceding point. Managerial implication from this study could be that hospital management should distribute hospital resources and schedule focusing on the lockdown phase rather than the increased number of daily new cases in the country. Governments, if they consider that the hospital can be a place for spreading infectious diseases, can minimize visitation by implementing strict, not moderate, lockdown. That means no marketplace, no grocery store, no open educational institution, minimum movement and last but least, only critical and emergency patients are allowed in the hospital.

4. CONCLUSION

This study can be considered as a cautionary analysis for the hospital environment during the initial part of the pandemic. They manage, distribute resources and schedule staff shifts or at least be prepared for what might happen if the strict portion of the lockdown is over. As evident from this analysis, it clearly indicates that general people's concern is mainly motivated by government implemented rules and restrictions rather than the national growing concern or news about an infectious disease. The overall arc of this phenomenon can be easily explained by those correlation analyses. Management must take action in order to avoid any strain on the hospital resources so that patients in critical condition must have the opportunity of getting the necessary attention they need in that situation. Moreover, they can implore the government to make the strict lockdown last longer. This will make best use of hospital resources in time of a pandemic situation. This study will be beneficial to the broader population by adopting it throughout the country in hospitals and medical institutes. It can manage to reduce the total infected population at a low rate. In addition, the scarce resources in the medical field can be properly distributed in time of a pandemic among the large population. This allows hospital administration to focus on the most critical patients, both COVID and non-COVID. By assessing the behavior of the local population, hospital management will always be in an advantageous position. Hospitals can then decide whether or not to expand their compartment to accommodate COVID patients. This method can also be adopted in any pandemic situation where people have to maintain social distancing and the government has to lower public movement by imposing lockdown rules.

As the adopted approach in the study was to compare and figure out the underlying relationship between only two variables in the pandemic time, the first constraint is found by not considering other factors that also influence the patients' behavior. Another limitation is the small sample data. This study only looked at the country's single upazilla hospital. It may be a bit of a stretch to infer any conclusion about the whole country. Future research could focus on the entire country or on any region-specific behavior will also benefit because more future research can be done if they can more accurately assess the behavior of the population by considering two or more new variables and their effect on human nature. Moreover, more people might be influenced to do research on non-COVID patients to manage hospital resources or keep the infected rate low.

.

ACKNOWLEDGMENT

We are also thankful to our course teacher for giving us the opportunity to do this case study and for giving us the appropriate guidance throughout the process. Then we would like to extend our gratitude to our supervisor, Md. Sazol Ahmed, Lecturer Dept. of IPE, RUET. This study could not have been completed if he hadn't provided us with necessary direction, important facts and data and finally his encouragement, without which we would be at a loss. We would also like to mention all the teachers of our department who were also helpful. Finally, our peers also deserved a token of our gratitude as they have been supportive in this case study.

REFERENCES

[1] World Health Organization, "Covid-19 Situation Report," *World Heal. Organ.*, vol. 31, no. 2, pp. 61–66, 2020.

[2] "COVID-19 cases worldwide by day | Statista." https://www.statista.com/statistics/1103040/cumulative-coronavirus-covid19-cases-number-worldwide-by-day/ (accessed Apr. 01, 2021).

[3] S. Lai *et al.*, "Effect of non-pharmaceutical interventions to contain COVID-19 in China," *Nature*, vol. 585, no. 7825, pp. 410–413, 2020, doi: 10.1038/s41586-020-2293-x.

[4] M. McKee and D. Stuckler, "If the world fails to protect the economy, COVID-19 will damage health not just now but also in the future," *Nat. Med.*, vol. 26, no. 5, pp. 640–642, 2020, doi: 10.1038/s41591-020-0863-y.

[5] S. Period, C. Periods, S. Year, and P. Year, "C or r e sp ondence Reduced Rate of Hospital Admissions for ACS during Covid-19 Outbreak in Northern Italy," pp. 1–3, 2020.

[6] "How Hospitals Can Meet the Needs of Non-Covid Patients During the Pandemic." https://hbr.org/2020/07/how-hospitals-can-meet-the-needs-of-non-covid-patients-during-the-pandemic (accessed Apr. 01, 2021).

[7] S. Il Pak and T. H. Oh, "Correlation and simple linear regression," *J. Vet. Clin.*, vol. 27, no. 4, pp. 427–434, 2010, doi: 10.1007/978-3-319-89993-0_6.

[8] R. Norouzian, "The Palgrave Handbook of Applied Linguistics Research Methodology," *Palgrave Handb. Appl. Linguist. Res. Methodol.*, 2018, doi: 10.1057/978-1-137-59900-1.

[9] B. Dutta, M. Neginhal, and F. Iqbal, "Glycated hemoglobin (HBA1C) correlation with severity of coronary artery disease in non-diabetic patients - A hospital based study from North-Eastern India," *J. Clin. Diagnostic Res.*, vol. 10, no. 9, pp. OC20–OC23, 2016, doi: 10.7860/JCDR/2016/22378.8525.

[10] A. Berberoglu, "Impact of organizational climate on organizational commitment and perceived organizational

performance: Empirical evidence from public hospitals," *BMC Health Serv. Res.*, vol. 18, no. 1, pp. 1–9, 2018, doi: 10.1186/s12913-018-3149-z.

[11] R. Hernández-Cruz, M. G. Moreno-Monsiváis, S. Cheverría-Rivera, and A. Díaz-Oviedo, "Factores que influyen en el cuidado de enfermería perdido en pacientes de un hospital privado," *Rev. Lat. Am. Enfermagem*, vol. 25, 2017, doi: 10.1590/1518-8345.1227.2877.

[12] W. M. Baihaqi, M. Dianingrum, K. A. N. Ramadhan, and T. Hariguna, "Linear regression method to model and forecast the number of patient visits in the hospital," *Proc. - 2018 3rd Int. Conf. Inf. Technol. Inf. Syst. Electr. Eng. ICITISEE 2018*, pp. 247–252, 2018, doi: 10.1109/ICITISEE.2018.8720979.

[13] T. Rapolu, B. Nutakki, T. S. Rani, and S. D. Bhavani, "A time-dependent SEIRD model for forecasting the COVID-19 transmission dynamics," *medRxiv*, pp. 1–20, 2020, doi: 10.1101/2020.05.29.20113571.

[14] T. Yamana, S. Pei, S. Kandula, and J. Shaman, "Projection of COVID-19 cases and deaths in the US as individual states re-open May 4, 2020," *medRxiv*, 2020, doi: 10.1101/2020.05.04.20090670.

[15] S. M. Moghadas *et al.*, "Projecting hospital utilization during the COVID-19 outbreaks in the United States," *Proc. Natl. Acad. Sci. U. S. A.*, vol. 117, no. 16, pp. 9122–9126, 2020, doi: 10.1073/pnas.2004064117.

[16] M. A. Capistrán, A. Capella, and J. A. Christen, "Forecasting hospital demand during COVID-19 pandemic outbreaks," *arXiv*, pp. 1–30, 2020.

[17] R. Gupta and S. K. Pal, "Trend Analysis and Forecasting of COVID-19 outbreak in India," *medRxiv*, pp. 1–19, 2020, doi: 10.1101/2020.03.26.20044511.

[18] A. mukid Md. Mukaddas, M. Sannyal, Q. Ali, and M. Tanbir Kuhel, "Transmission Dynamics of COVID-19 in Bangladesh- A Compartmental Modeling Approach," pp. 8–15, 2020, [Online]. Available: https://papers.ssrn.com/sol3/papers.cfm?abstract_id=3644855.

[19] R. K. Biswas, S. Huq, and A. Afiaz, "Relaxed lockdown in Bangladesh during COVID-19: Should economy outweigh health?," *Int. J. Heal. Policy Manag.*, vol. 9, no. 11, pp. 488–490, 2020, doi: 10.34172/ijhpm.2020.98.

[20] S. M. D. U. Islam, M. Bodrud-Doza, R. M. Khan, M. A. Haque, and M. A. Mamun, "Exploring COVID-19 stress and its factors in Bangladesh: A perception-based study," *Heliyon*, vol. 6, no. 7, pp. 1–10, 2020, doi: 10.1016/j.heliyon.2020.e04399.

[21] M. Shammi, M. Bodrud-Doza, A. R. M. T. Islam, and M. M. Rahman, *Strategic assessment of COVID-19 pandemic in Bangladesh: comparative lockdown scenario analysis, public perception, and management for sustainability*, no. 0123456789. 2020.

[22] M. D. Mamun, M. A. , Griffithsc, "First COVID-19 suicide case in Bangladesh due to fear of COVID-19 and xenophobia: Possible suicide prevention strategies," no. January, 2020.

[23] S. A. K. S. Ahmed *et al.*, "Impact of the societal response to COVID-19 on access to healthcare for non-COVID-19 health issues in slum communities of Bangladesh, Kenya, Nigeria and Pakistan: results of pre-COVID and COVID-19 lockdown stakeholder engagements," *BMJ Glob. Heal.*, vol. 5, no. 8, p. e003042, 2020, doi: 10.1136/bmjgh-2020-003042.

[24] M. M. Jeffery *et al.*, "Trends in Emergency Department Visits and Hospital Admissions in Health Care Systems in 5 States in the First Months of the COVID-19 Pandemic in the US," *JAMA Intern. Med.*, vol. 180, no. 10, pp. 1328–1333, 2020, doi: 10.1001/jamainternmed.2020.3288.

[25] J. J. Baugh *et al.*, "The cases not seen: Patterns of emergency department visits and procedures in the era of COVID-19," *Am. J. Emerg. Med.*, 2020, doi: 10.1016/j.ajem.2020.10.081.

[26] R. (Roanoke C. E. Walpole, R. (Virginia T. H. Myers, Sh. (Radford U. L. Myers, and K. (University o T. at S. A. Ye, *Probability & Statistics for Engineers & Scientists*, NINTH EDIT. Pearson, 2012

Paper ID: 1536
International Conference on Mechanical, Manufacturing and Process Engineering (ICMMPE – 2022)
Organizer: Faculty of Mechanical Engineering, Dhaka University of Engineering & Technology (DUET), Gazipur, Bangladesh
Website: https://icmmpeduet.com/

Laminar Flame Speed and Markstein Length of premixed flames for the mixture of N-Dodecane and Methyl Decanoate

Faihim Ahmed[1] and Ki Yong Lee[2]

[1]Department of Mechanical Engineering, Khulna University of Engineering & Technology, Khulna, 9203, Bangladesh
[2]Department of Mechanical Engineering, Andong National University, Andong, 36729, South Korea
E-mail: ahmedfaihim.kuet@gmail.com

ABSTRACT

This research has experimentally determined the laminar flame speed and Markstein length of the mixtures of n-dodecane(DD) and methyl decanoate(MD), which are measured at different elevated pressures(P=2, 4 & 6atm) and temperature(473K) with respect to equivalence ratio. Schlieren technique is used for outwardly propagating spherical flames developed inside a constant volume combustion chamber. Experimental results are compared with the measured laminar flame speed and the Markstein length of n-dodecane and methyl decanoate. For each pressure, the laminar flame speed is the highest for all mixtures at an equivalence ratio of around 1.1. The flame speeds of the mixture of n-dodecane and methyl decanoate are between the flame speeds of 100% n-dodecane and 100% methyl decanoate. As the amount of methyl decanoate added to the mixture is increased, the flame speeds of the mixture are decreased. The measured Markstein length of the mixture is highest at low pressure and has decreased with the increase of pressure and equivalence ratio. The tendency of the Markstein length of the mixture has well followed that of hydrocarbon.

Keywords: Laminar Flame Speed; Markstein Length; Methyl Decanoate; N- Dodecane; Schlieren Technique.

1. INTRODUCTION

To respond to the demand of the current world's energy and to find the best solution for the energy crisis, researchers are doing their ceaseless task. As a result, various modes of energy harvesting have already been discovered, while some are still in the invention process. Among them, the leading share of global primary energy consumption has always been fossil fuels, as well as conventional fuels[1]. Due to the high usage of conventional fuel oil, researchers felt to find another potential candidate which is nothing but biodiesel[2]. Between these two kinds of fuel oil, the dominant species is hydrocarbon[3,4]. Most of the researchers agreed that hydrocarbon would serve as a potential future generation surrogate fuel[3-5]. Due to the high appearance of hydrocarbons, it attracts researchers to deal with it.

Too much research has already been performed for alcohol and diesel or gasoline surrogate fuel[6-8]. The laminar flame speed measurements of larger molecular weight fuels such as diesel and single or multi-component surrogate fuels have made significant progress in recent years[9-15]. Also, pure gasoline surrogate components like n-heptane, iso-octane, and their mixtures were extensively explored[16-20]. In recent years, n-decane and n-dodecane have been extensively studied and are the most representing components of diesel fuel[9,12,21-22].

Firstly, Kumar and Sung[26] provided the data of n-dodecane at atmospheric pressure for two different temperatures. Later, other researchers[14,27-29] performed their research for n-dodecane based on data provided by Kumar and Sung[26]. Richter et al.[29] measured the laminar burning speed of several neat fuel components, including n-dodecane, which assessed using the cone-angle method at a preheat temperature of 473K and at ambient and elevated pressures to generate new data for the development of new surrogate models for Jet A-1.

Recently, biodiesel comes forward with its versatile properties. Non-toxicity, biodegradability and usability in as both pure and blended with other fuels draw the interest of the researchers. The main source of synthesized biodiesel fuel is animal fat, vegetable oils, etc. [23]. Due to non-toxicity, biodegradability, low carbon emission, fewer pollutants, and easily manageability[23], biodiesel gains its popularity among the researchers to deal with it. Though not too much research is done yet with methyl esters, methyl decanoate(MD) has fulfilled the flame speed trend of hydrocarbons better than other methyl esters[24,25]. These results make interest in researching with a mixture of fuel, which is nothing but a mixture of n-dodecane(DD) and methyl decanoate.

Detailed chemical kinetic mechanism of methyl decanoate (MD) has created by Herbinet et al.[30]. They concluded that their methyl decanoate mechanism is very effective in reproducing the oxidation effect in the main constituents of biodiesels, which is methyl esters. They further claimed that methyl decanoate imitated much closer characteristics to actual biodiesels. Gail et al. [31] had previously studied comparing the kinetic characteristics of diesel to their 16-18 carbon atom chains. Most of the biodiesel surrogate has a double chemical bond without the oxygenated bond in their chemical structure. But this

double bond is missing in MD[32]. This double bond is the precursor of soot and makes the structure of biodiesel unsaturated. Zhang et al.[33] showed that the appearance of a double bond decreased the reactivity of the fuel/air mixture in comparison to the saturated C_9 ester.

Talukder and Lee[34] measured laminar flame speed and Markstein length of methyl decanoate at elevated pressures and different temperatures. They validated their experimental results with a numerical scheme. The experimentally provided data are in well-match with the numerical trend. At high-pressure P = 6atm, they were unable to collect data in the fuel-rich condition because the flame gets the cellular structure too early after combustion.

From the literature[14,23,25,26,29,34], it observed that both n-dodecane and methyl decanoate fulfill the pattern of flame speed. Until now, there are no data found of flame speed about the mixture of n-dodecane and methyl decanoate. The objective of this experimental research is to provide the experimental viable data on the flame speed of the mixture of n-dodecane and methyl decanoate at temperature 473K and pressure 2, 4, and 6 atm over a variety of equivalence ratios(ϕ = 0.8–1.4). Besides, Markstein length has been provided for the mixture of fuel.

2. Experimental Setup & Methodology

2.1 Experimental Setup

Tahtouh et al.[35] proposed a setup that was properly Matched with the experimental set up used in this experiment. For monitoring flame front propagation, the Schlieren technique is used. A combustion chamber with constant volume, air heating system, temperature, pressure monitoring system, and optical access & data recovery system are the primary consisting arrangements, as shown in Fig. 1.

The internal combustion chamber is cylindrical, whose specification is ID=70mm, Length=70mm, and total interior volume=302.155cm3. The combustion chamber can withstand the pressure up to 10atm at a temperature of around 520K. A decrease in pressure of less than 0.01atm within 300 seconds is regarded as the proper state for experimenting with any desired pressure and temperature. During the experiment, maximum ±2K is allowed to fluctuate. With the help of electric voltage, the inside chamber temperature is controlled.

From a 'fresh air, cylinder', the air with standard composition is fed into the 'air heating cylinder' and heated by electric conductors under the required initial pressure. The heated air cylinders have a temperature of 2 to 3 K higher than the combustion chamber temperature. For ensuring the system remains leakage-free throughout the experiment, all air transport tube points are frequently checked.

Thermocouples of the temperature measurement device(HEWLETT PACKARD 34970A data acquisition/switch unit) measure temperatures inside a chamber and different parts of the entire system. The

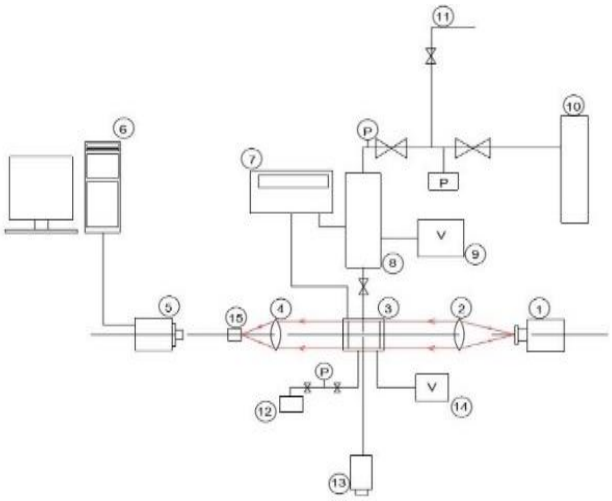

Fig. 1. Schematic diagram of the experimental setup
(1. Light source; 2 & 4. Lenses; 3. Combustion Chamber; 15. knife-edge; 5. Camera; 6. Data acquisition computer; 7. Temperature measuring unit; 8. Air heating cylinder; 9 & 14. Voltage controllers; 10. Pressurized air cylinder; 11. Pressure releasing pipes; 12. Vacuum pump; 13. Ignition trigger; P. Pressure gauges/sensors)

appropriate pressure sensor (AEP transducers; capacity up to 20 bars) is used to measure pressures in both the chamber and air heating cylinder.

The quartz windows on either end of the cylindrical chamber allow optical access to the interior of the chamber. An LED(15021) DDK(17J-15), designed by SPG(Anyang), is used as a light source. Light from the source passed through the two lenses and a combustion chamber placed between the two lenses. Light after passing the second lens then focused on the high-speed camera(Phantom Miro M310-6GB color camera; size: 640×480 at 10,000 fps). To acquire data, the camera is linked to a computer.

For creating a negative pressure within the chamber, the vacuum pump is fixed with the chamber. Also, it helps to ease fuel injection and cleans the chamber inside after combustion. The injection of fuel is facilitated by a plug valve mounted on the chamber. Within 240 seconds, the total combustion process is usually completed. So, it is necessary to confirm that the system is without leaking for at least 300 seconds at the time of the leak testing experiment. A vacuum pump is developed to produce a negative pressure within the chamber before the injection of the fuel to guarantee that the total fuel input is absorbed into the chamber. Since the inside temperature exceeds the boiling point of the fuel, injected liquid fuel is vaporized immediately inside the chamber. It is required for 90-120 seconds to ensure a homogeneous mixture after the injection of both fuel and air into the chamber.

2.2 Laminar Flame Speed Calculation Methodology

The image of the laminar flame front in the process of temporal propagations, which are taken from one of our experimental attempts, are presented in Fig. 2. After ignition initiates, the flame propagates spherically outward to the chamber wall (shown in Fig. 2). This flame configuration is known as a spherical boom.

The flame front is influenced by the stretching rate throughout the temporal evolution. Markstein [40] suggested that the local burning speed is linearly affected with the local stretch, including strain rate and curvature effects. The relation between flame propagation and the stretch rate is proposed by Clavin[36].

$$V_S = V_{S0} - L_b . K \quad (1)$$

V_S is the stretched flame propagation speed; it demonstrated as $V_s = \frac{dr_u}{dt}$; V_{S0} is the unstretched propagation flame speed, L_b is the Markstein length for the burned gas and $K = \frac{1}{A} \cdot \frac{dA}{dt}$, is the overall stretch of the flame, which represents the rate of change in time for a flame surface element of the region(A).

In this experimental situation, K can be described as a spherical expansion of the flame front

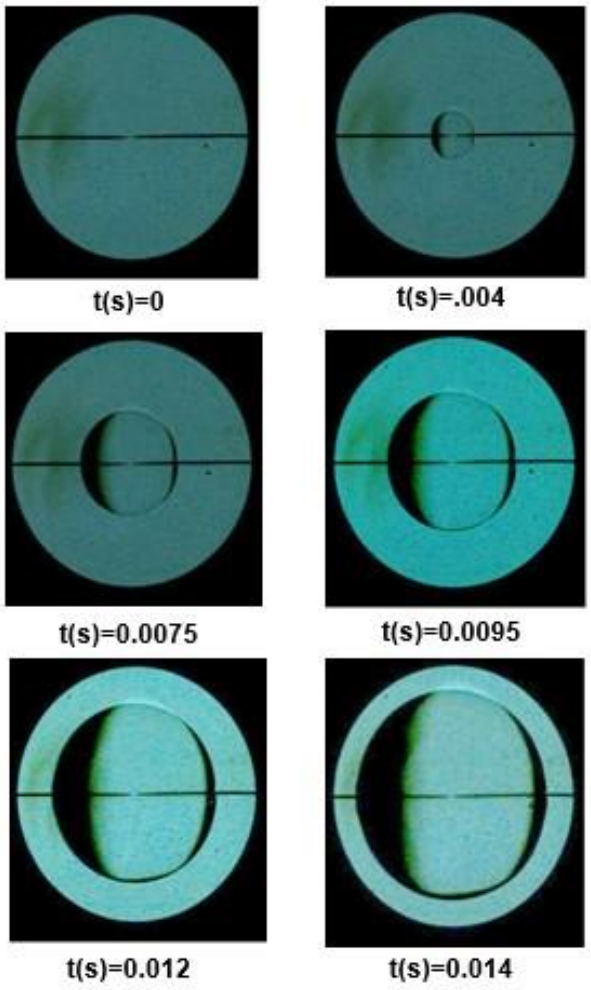

Fig. 2. The images of the flame front propagation of 50%DD & 50%MD/air mixture of ϕ = 0.8 at P = 4atm at T= 473K, t = time in seconds.

$$K = \frac{2}{r_u} . \frac{dr_u}{dt} \quad (2)$$

The unstretched speed of laminar flame propagation speed and the density ratio can be achieved as a result of constant-pressure flame propagation:

$$u_{l0} = \frac{\rho_b}{\rho_u} . V_{S0} \quad (3)$$

ρ_b, the burnt gas density and ρ_u, the unburnt gas density

Three distinct methods for extracting the laminar flame data are explored by Tahtouh et al. [35]. This present study employs the second methodology[37] among them, which uses the least mean square and needs only a temporal evolution of radius to obtain the laminar burning velocity. The following is the approach:

Eq.(2) is substituted into Eq.(1) followed by integration, which is given to Eq.(4):

$$r(t) - r(t_0) + 2.L_b . \ln\left(\frac{r(t)}{r(t_0)}\right) = V_{S0} . (t - t_0) \quad (4)$$

The Markstein length, L_b and the unstretched propagation speed, V_{S0} are considered constant. For every step of the time, Eq. (4) is necessary to verify. The issue is, therefore, to optimize the function of the least-squares,

$$\psi(L_b, V_{S0}) = \sum_{i=1}^{N} \left(t_i - t_0 - \frac{r_i - r_0}{V_{S0}} - 2.\frac{L_b}{V_{S0}} . \ln\left(\frac{r_i}{r_0}\right) \right)^2 \quad (5)$$

N is the number of time steps taken with unknowns L_b and V_{S0}. The L_b and V_{S0} values which minimize the previous equation, are the following system solutions:

$$\begin{cases} \frac{d\psi}{dL_b} = 0 \\ \frac{d\psi}{dV_{S0}} = 0 \end{cases}$$

The second condition is quantified to obtain the value of V_{S0} using MATLAB programs. The value u_{l0} is then measured.

3. Result & Discussion

3.1 Effect of MD addition on Flame Speed

The measured laminar flame speeds of the mixture of n-dodecane and methyl decanoate as a function of equivalence ratio are presented in Figs 3-5 for three different pressures, P = 2, 4, and 6 atm. A comparison with 100% n-dodecane[29] and 100% methyl decanoate[34] is shown in Figs 3-5 in order to verify the experimental data of the present work. Richer et al.[34] used the cone-angle method and a preheat temperature of 473K and pressures of 0.1, 0.3 and 0.6 MPa to measure the laminar flame speeds of 100% n-dodecane. The linear interpolation is done to expect the flame speeds at P = 2 and 4 atm, the results of which are presented in Figs 3-5. Talukder and Lee[34] measured the flame speeds of 100% methyl decanoate from

outwardly propagating spherical flames in the combustion chamber at a preheat temperature of 473K and pressures of 2, 4 and 6 atm. The flame speeds of 100% n-dodecane are higher than those of 100% methyl decanoate because of the difference in the heating value of both fuels.

In this experiment, n-dodecane is used as the main fuel and methyl decanoate as an additive. The flame speeds of the mixture of n-dodecane and methyl decanoate is between the flame speeds of 100% n-dodecane and 100% methyl decanoate, as shown in Figs 3-5.

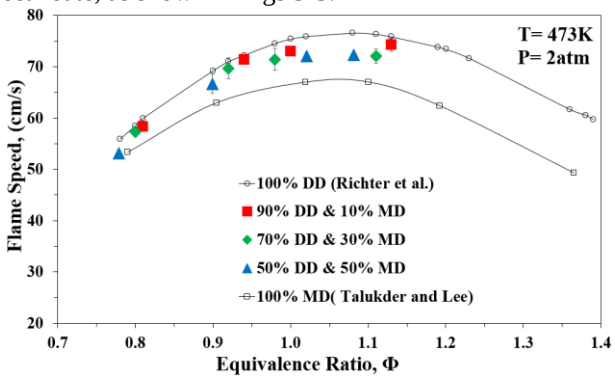

Fig. 3. Experimental result for the laminar flame speed of all mixture fuels, including validation fuels at T= 473K, P= 2atm

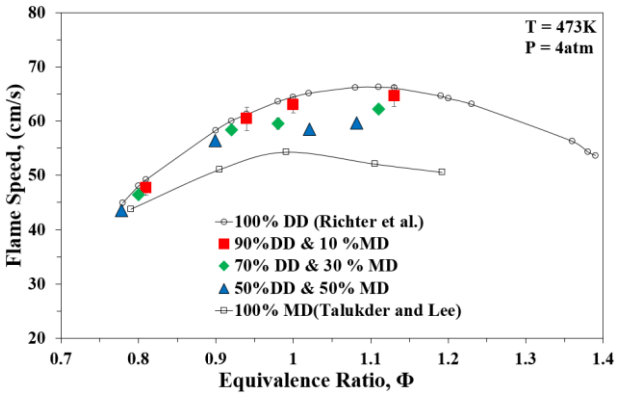

Fig. 4. Experimental result for the laminar flame speed of all mixture fuels, including validation fuels at T= 473K, P= 4atm

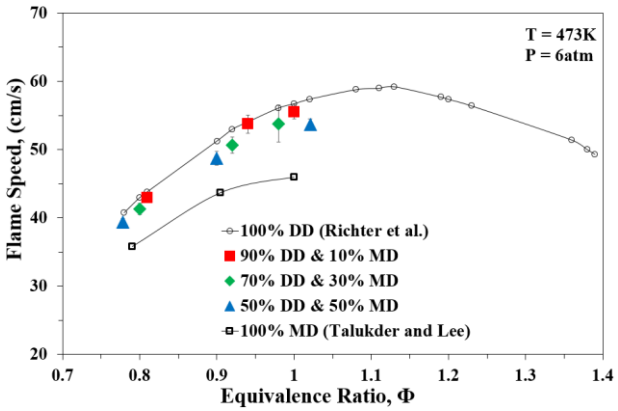

Fig. 5. Experimental result for the laminar flame speed of all mixture fuels, including validation fuels at T= 473K, P= 6atm

As the amount of methyl decanoate added in the mixture is increased the flame speeds of the mixture are decreased. The same trend is shown in the condition of a given pressure. The flame speeds in the fuel-rich condition are unable to be measured with outwardly propagating spherical flames in the combustion chamber unlike the cone-angle method. This is because the cellular structure on the spherical flame appears while the flame is spreading out as pressure is increased in the combustion chamber.

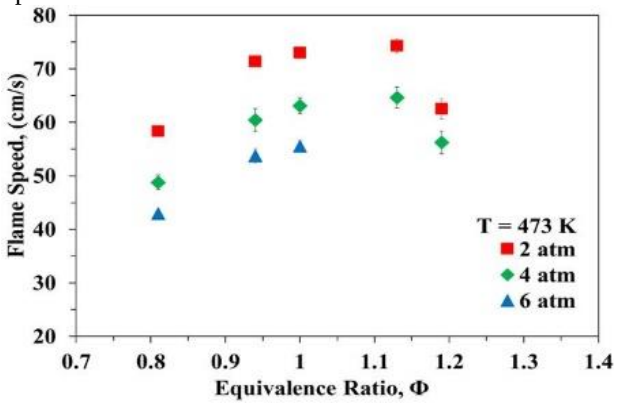

Fig. 6. Flame speed for 90%DD & 10%MD/air premixed flames at different elevated pressure and T= 473K.

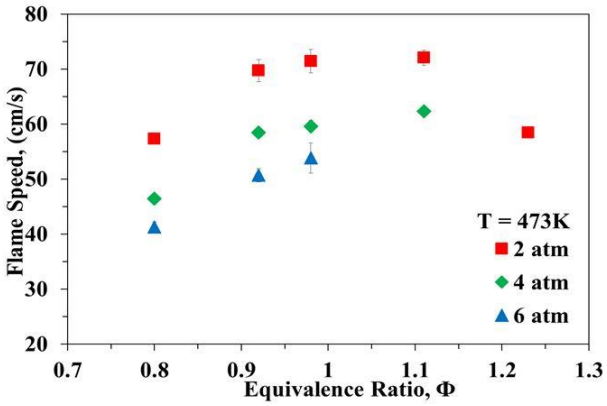

Fig. 7. Flame speed for 70%DD & 30%MD/air premixed flames at different elevated pressure and T= 473K.

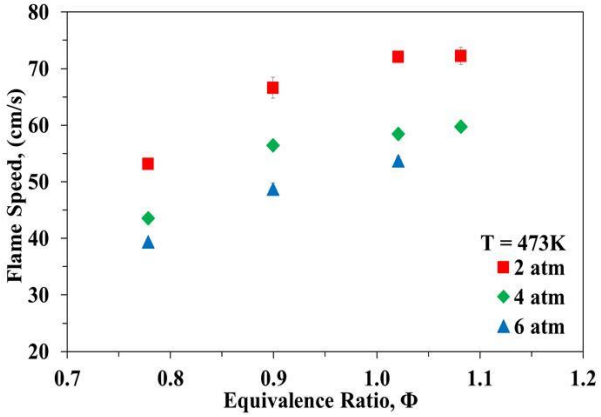

Fig. 8. Flame speed for 50%DD & 50%MD/air premixed flames at different elevated pressure and T= 473K

3.2 Effect of Pressure on Flame Speed

Figs 6-8 summarize the measured laminar flame speeds of the mixture of n-dodecane and methyl decanoate to investigate the effect of pressure at the conditions of the three mixtures. The effect of pressure on the flame speed is clearly shown for all three mixtures. Flame speed is decreased with the increase of pressure. Flame speed has the maximum value around the equivalence ratio of 1.1 and shows a decreasing trend toward the fuel-lean region. The distribution of flame speed with respect to the equivalence ratio follows the tendency of hydrocarbon fuels even when biofuel is added. Even with an increase in pressure, the addition of 50% biofuel to the hydrocarbon fuel does not significantly affect the characteristics of the hydrocarbon fuel.

3.3 Effect of Pressure on Markstein Length

The tendency of giving the information of Markstein length is quite crucial as the effect of pressure and equivalence ratio on Markstein length for the mixture of n-dodecane and methyl decanoate is clearly shown in Figs. 9-11. The measured Markstein lengths for the mixture of n-dodecane and methyl decanoate are downward with respect to equivalence ratio and their values are decreased as pressure is increased. The data trend of Markstein's length are found downward and stable. The tendency of methyl decanoate on Markstein length is downward with the increase of pressure and equivalence ratio[29]. Although there is no information about the trend of Markstein length of n-dodecane, it can be predicted from the data of Markstein length of decane[38,39] which has a similar structure. Since both n-dodecane and decane are from the alkane group and n-dodecane is decane with (CH2)2 added in the structure. It is estimated that the trend of Markstein length of n-dodecane will follow that of decane. So, the trend of Markstein length of n-dodecane will be downward with the increase of pressure and equivalence ratio, similar to higher alkanes molecules[40]. The present Markstein length data have well followed the trend of the data provided by other researchers [29,38,39].

4. Conclusion

An experimental investigation has been performed to measure the laminar flame speed and Markstein length of the mixtures of n-dodecane as the main fuel and methyl decanoate as an additive. Three mixture fuels are used such as 90%DD & 10%MD, 70%DD & 30%MD, and 50%DD & 50%MD. The laminar flame speed and Markstein's length have been measured for these three mixtures at an initial temperature of 473K and elevated pressures (P=2, 4, and 6 atm) over a wide range of equivalence ratios. The experimental result has been compared with the measured laminar flame speed and the Markstein length of 100% n-dodecane and 100% methyl decanoate. It is investigated that the laminar flame speed and Markstein length for the mixtures of n-dodecane and methyl decanoate have decreased with the addition of methyl decanoate into the mixture and with the increase of pressure. For three cases of the mixture and pressures given, the maximum laminar flame speed has been found at an equivalence ratio around ϕ = 1.1, like in the case of 100% hydrocarbon fuel. The trend of Markstein length of the mixture has been decreased with the increase of equivalence ratio. It has been known

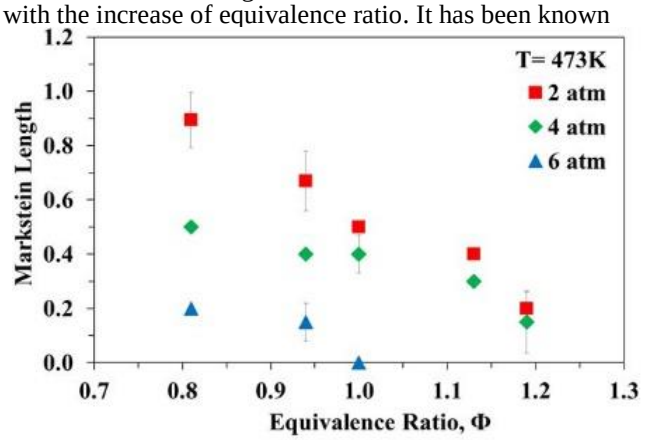

Fig. 9. Markstein Length for 90%DD & 10%MD/air premixed flames at different elevated pressure and T= 473K

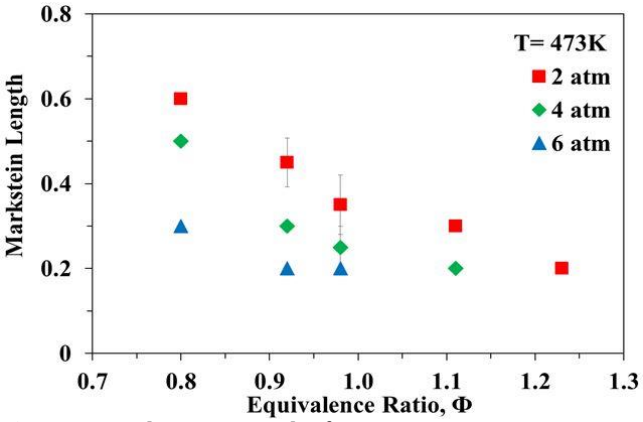

Fig. 10. Markstein Length for 70%DD & 30%MD/air premixed flames at different elevated pressure and T= 473K.

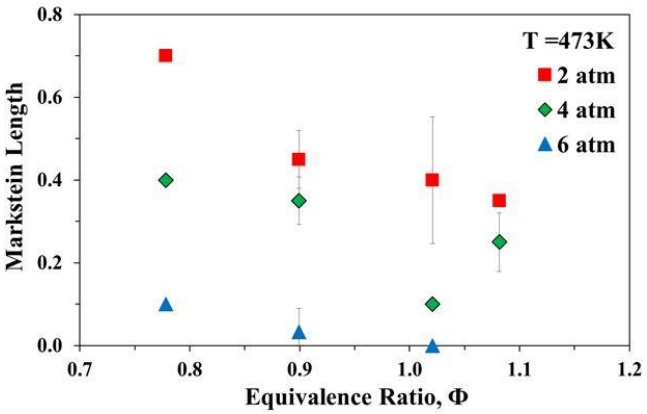

Fig. 11. Markstein Length for 50%DD & 50%MD/air premixed flames at different elevated pressure and T= 473K

that the flame speed and Markstein length are greatly affected by the addition of methyl decanoate, pressure, and equivalence ratio.

Nomenclature

DD : N-Dodecane
MD : Methyl Decanoate
P : Pressure
T : Temperature
t : Time
ϕ : Equivalence ratio
Sl : Flame speed
V_S : stretched propagation flame speed
V_{S0} : Unstretched propagation flame speed
L_b : Markstein Length for Burnt Gas
K : Total Stretch Acting on the flame
r_u : Flame front radius
ψ : Least-squares function
u_{l0} : Laminar flame Speed
ρ_b : The density of burned gases
ρ_u : The density of unburned gases

REFERENCES

[1] I. Yildiz, 1.12 Fossil Fuels, Comprehensive Energy Systems, Vol. 1, pp. 521-567, 2018.

[2] Z. Luo, M. Plomer, T. Lu, S. Som, D. E. Longman, S. M. Sarathy and W. J Pitz, A reduced mechanism for biodiesel surrogates for compression ignition engine applications, fuel, Vol. 99, pp. 143-153 , 2012.

[3] D. Kim and A. Violi, Hydrocarbons for the next generation of jet fuel surrogates, fuel, Vol. 228 (15), pp. 438-444, 2018.

[4] W. J Pitz and C. Mueller, Recent progress in the development of diesel surrogate fuels, Progress in Energy and Combustion Science, Vol. 37 (3), pp. 330-350, 2011.

[5] F. L. Dryer, Chemical kinetic and combustion characteristics of transportation fuels, Proceed. Combust. Inst., Vol. 35 (1), pp. 117-144, 2015.

[6] M. Karabektas and M. Hosoz, Performance and emission characteristics of a diesel engine using isobutanol-diesel fuel blends, Renewable Energy, Vol. 34, pp. 1554-1559, 2009.

[7] Y.Yacoub, R.Bata and M. Gautam, The performance and emission characteristics of C_1-C_5 alcohol-gasoline blends with matched oxygen content in a single-cylinder spark-ignition engine, Proc. Inst. Mech. Eng., Vol. 212, pp. 363-379, 1998.

[8] M. A. Quadis, O. Haddad and M. Quadaista, The effect of alcohol fumigation on diesel engine performance and emissions, Energy Convers. Manage., Vol. 41, pp.389-399, 2000.

[9] A. Comandini, T. Dubois and N. Chaumeix, Laminar flame speeds of n-decane, n-butylbenzene, and n-propyl cyclohexane mixtures, Proceed. Combust. Inst., Vol. 35 (1) , pp. 671-678, 2015.

[10] D. Darcy, H. Nakamura, C. J. Tobin, M. Mehl, W.K. Metcalfe, W. J. Pitz, C. K. Westbrook and H. J. Curran, An experimental and modeling study of surrogate mixtures of n-propyl- and n-butylbenzene in n-heptane to simulate n-decyl benzene ignition", Combust. Flame, Vol. 161(6), pp. 1460-1473, 2014.

[11] B. Galmiche, F. Halter and F. Foucher, Effects of high pressure, high temperature and dilution on laminar burning velocities and Markstein lengths of iso-octane/air mixtures, Combust. Flame, Vol. 159 (11), , pp. 3286-3299, 2012.

[12] X. Hui, C. Zhang, M. Xia and C. J. Sung, Effects of hydrogen addition on combustion characteristics of n-decane/air mixtures, Combust. Flame, Vol. 161 (9), pp. 2252-2262, 2014.

[13] M. Zeng, W. Yuan, Y. Wang, W. Zhou, L. Zhang, F. Qi and Y. Li, Experimental and kinetic modeling study of pyrolysis and oxidation of n-decane, Combust. Flame, Vol. 161, pp. 1701-1715, 2014.

[14] X. Hui and C.J. Sung, Laminar flame speeds of transportation-relevant hydrocarbons and jet fuels at elevated temperatures and pressures, fuel, Vol. 109, pp.191-200, 2013.

[15] A. Holley, Y. Dong, M. Andac, F. Egolfopoulos and T. Edwards, Ignition and extinction of nonpremixed flames of single-component liquid hydrocarbons, jet fuels, and their surrogates, Proceed. Combust. Inst., Vol. 31 (1), pp. 205-1213, 2007.

[16] E. Varea, V. Modica, B. Renou and A. M. Boukhalfa, Pressure effects on laminar burning velocities and Markstein lengths for Isooctane/Ethanol/Air mixtures, Proceed. Combust. Inst., Vol. 34 (1), pp. 735-744, 2013.

[17] J. Beeckmann, L. Cai and H. Pitsch, Experimental investigation of the laminar burning velocities of methanol, ethanol, n-propanol, and n-butanol at high pressure, fuel, Vol. 117 (A) , pp. 340-350, 2014.

[18] P. Dirrenberger, P. Glaude, R. Bounaceur, H. L. Gall, A. P. da Cruz, A. Konnov and F. B. Leclerc, Laminar burning velocity of gasoline with addition of ethanol, fuel, Vol. 115, pp. 162-169, 2014.

[19] E. Varea, V. Modica, A. Vandel and B. Renou, Measurement of laminar burning velocity and Markstein length relative to fresh gases using a new postprocessing procedure: Application to laminar spherical flames for methane, ethanol and iso-octane/air mixtures, Combust. Flame, Vol. 159 (2), pp. 577-590, 2012.

[20] J. V. Lipzig, E. Nilsson, L. D. Goey and A. Konnov, Laminar burning velocities of n-heptane, iso-octane, ethanol and their binary and tertiary mixtures, Fuel, Vol. 90(8), pp. 2773-2781, 2011.

[21] D. Singh, T. Nishiie and Q. Li, Experimental and Kinetic Modeling Study of the Combustion of Decane, Jet-A, and S-8 in Laminar Premixed Flames, Combust. Science. Tech., Vol. 183 (10), pp. 1002-1026, 2011.

[22] D. Kim, J. Martz and A. Violi, A surrogate for emulating the physical and chemical properties of conventional jet fuel, Combust. Flame, Vol. 161 (6), pp. 1489-1498, 2014.

[23] J. V Gerpen, Biodiesel processing and production, Fuel Process. Tech., Vol. 86 (10), pp. 1097–1107, 2005.

[24] O. Herbinet, W. J. Pitz and C.K. Westbrook. Detailed chemical

kinetic oxidation mechanism for a biodiesel surrogate, Combust. Flame, Vol. 154, pp. 507-528, 2008.

[25] Y. L. Wang, Q. Feng, F. N. Egolfopoulos and T. T. Tsotsis, Studies of C_4 and C_{10} methyl ester flames, Combust. Flame, Vol. 158, pp. 1507-1519, 2011.

[26] K. Kumar and C. J. Sung, Laminar flame speeds and extinction limits of preheated n-decane/O2/N2 and n-dodecane/O2/N2 mixtures, Combust. Flame, Vol. 151, pp. 1701-1715, 2014.

[27] C. Ji, E. Dames, Y. L.Wang, H. Wang and F. N. Egolfopoulos, Propagation and extinction of premixed C_5–C_{12} *n*-alkane flames, Combust. Flame, Vol. 157 (2), pp. 277-287, 2010.

[28] C. V. Naik, K. V. Puduppakkam, A. Modak, E. Meeks, Y. L. Wang, Q. Feng and T. T. Tsotsis, Detailed chemical kinetic mechanism for surrogates of alternative jet fuels, Combust. Flame, Vol. 158 (3), pp. 434-445, 2011.

[29] S. Richter, M. B. Raida, C. Naumann and U. Riedel, Measurement of the Laminar Burning Velocity of Neat Jet Fuel Components, Proceed. World Congress. Moment. Heat.Mass Transfer (MHMT'16), Prague, Czech Republic – April 4 – 5, Paper No. CSP 115, 2016.

[30] O. Herbinet, W.J. Pitz and C. K. Westbrook, Detailed chemical kinetic oxidation mechanism for a biodiesel surrogate, Combust. Flame, Vol. 154, pp. 507–528, 2008.

[31] S.Gail, M.J. Thomson, S.M. Sarathy, S. A. Syed, P.Dagaut, P. Dievar, A.J. Marchese and F.L Dryer, A wide-ranging kinetic modeling study of methyl butanoate combustion, Proceed. Combust. Inst., Vol. 31, pp. 305-311, 2007.

[32] O. Herbinet, W. J. Pitz and C. K. Westbrook, Detailed chemical kinetic mechanism for the oxidation of biodiesel fuels, Combust. Flame, Vol. 157, pp. 893-908 , 2010.

[33] Y. Zhang, Y. Yang and A. L. Boehman, Premixed ignition behavior of C_9 fatty acid esters: A motored engine study, Combust. Flame, Vol. 156, pp. 1202-1213, 2009.

[34] N. Talukder and K. Y. Lee, Laminar flame speeds and Markstein lengths of methyl decanoate-air premixed flames at elevated pressures and temperatures, fuel, Vol. 234, pp. 1346-1353, 2018.

[35] T. Tahtouh, F. Halter and C. Mounalam-Rousselle, Measurement of laminar burning speeds and Markstein lengths using a novel methodology, Combust. Flame, Vol. 156, pp. 1735-1753, 2009.

[36] P. Clavin, Dynamic behavior of premixed flame fronts in laminar and turbulent flows, progress. Energy and Combust. Science., Vol. 11, pp. 1-59, 1985.

[37] A. A. Burluka, M. Fairweather, M. B. Ormsby, C. G. W. Sheppard and R. Wooley, The laminar burning properties of premixed methane-hydrogen flames determined using a novel analysis method, Third European Combustion Meeting, 2007.

[38] D. Singh, T. Nishiie and L. Qiao, Laminar Burning Speeds and Markstein Lengths of n-Decane/Air, n-Decane/O2/He, Jet-A/Air and S-8/Air Flames,48th AIAA Aerospace Sciences Meeting Including the New Horizons Forum and Aerospace Exposition, Orlando, Florida, 4 - 7 January, AIAA 2010-951, 2010.

[39] R. L. Dortz, M. Bellenoue, L. Bonneau, E. Mazanchenko, J. Sotton and C. Strozzi, Laminar Burning Velocities and Markstein Lengths of Jet Fuel Surrogate/Air Mixtures in a Spherical Chamber, 8th European combust. Meeting, Dubrovink, Croatia, Apr, 2017.

[40] J.K. Bechtold and M. Matalon, The dependence of the Markstein Length on stoichiometry, Combustion and Flame, Vol. 127 (1-2), pp. 1906-1913, 2001.

.

Paper ID: 1647
International Conference on Mechanical, Manufacturing and Process Engineering (ICMMPE – 2022)
Organizer: Faculty of Mechanical Engineering, Dhaka University of Engineering & Technology (DUET), Gazipur, Bangladesh
Website: https://icmmpeduet.com/

A Low-Cost Intelligent Automated Door Security System Based on Fingerprints Using Microcontroller

Md. Saiful Islam[1], Md. Monir Hossain[2], Md. Nazmul Hasan[3], Asif Kabir[4], Md. Soriful Islam[5] and Amit Sutradhar[6]

[1,4]Department of Mechanical Engineering, BUET, Dhaka-1000, Bangladesh
[2,3,5,6] Department of Mechanical Engineering, DUET, Gazipur-1707, Bangladesh

E-mail: saifulmebuet@gmail.com[1], miraz17me27@gmail.com[2]

ABSTRACT

In many countries, security has played a crucial role in maintaining secrecy so that no one else has access to them. Security systems are now required at all times to secure critical data and even money. This paper discusses a low-cost, secure fingerprint-based door-opening system that can be employed in a range of institutions and organizations. Other authentication techniques exist, such as passwords and RFID, but this is the most secure and cost-effective. In this project, biometrics are being employed to guarantee absolute security while also making the task easier. The creation of a security system that stores the credentials of one or more valid user fingerprints prevents unauthorized access. A fingerprint is detected and validated for authentication by a sensor. The door will open automatically if the fingerprints match; else, a buzzer connected to an audio amplifier will play, warning anyone around. A microcontroller-based biometric storage framework with a brief informing framework (SMS-based) can also be built to protect the security of an individual's private and classified belongings.

Keywords: Automation; Biometric; Fingerprint; Microcontroller; Sensor; Security System.

1. INTRODUCTION

Security is a primary concern, and in today's hectic, competitive world, humans cannot find ways to manually secure their confidential belongings. Instead, he discovers an alternative that can provide full-fledged security while also being atomized. In today's ubiquitous network society, where people can easily access their information at any time and from any location, there is also the risk that others can easily access the same information at any time.

Unique identifying technologies that really can differentiate between registered legal users and imposters have been developed in response to this risk. Numbers and combinations can be recalled or guesses.

As an answer to these issues, biometric verification innovation, which distinguishes individuals because of their special organic data, is acquiring ubiquity. The ID and acknowledgment of an individual because of conduct or physiological qualities are alluded to as biometrics. An account holder's body behaviors (habits) or characteristics are recorded in a database during biometric authentication the attempt is then compared to others who may attempt to access the account to determine whether it is legitimate. Many companies have analyzed and developed biometric authentication technology, with a focus on fingerprints, faces, and voiceprints. Fingerprint, face, iris, voice, signature, and hand geometry recognition and verification are common biometrics studies.

Many more modalities are still in the early stages of research and evaluation. Fingerprinting is one of the best biometric features accessible, offering a high mismatch ratio, and high accuracy in terms of security, and reliability. Currently, the only way to run a bank locker is to use locks with keys. This does not imply that we will provide adequate security for our lockers. We are using two separate technologies, embedded systems and biometrics, to guarantee flawless security and make our work easier. A multi-agent system and computer system developed for specific control functions within a larger system, frequently with real-time computing restrictions, is referred to as an embedded system. Various efforts are made to provide security for all residences. To date, no complete security has been discovered. There are various kinds of security systems.

Fig. 1: Module and fingerprint recognition with various features [1]

They are as follows: lock and Key System, Digital Code Lock, Padlocks, Deadbolts, Password Authentication, Identification Number, RFID Card Authentication, Biometrics, Voice Recognition, Face Recognition, Iris Scan, Fingerprint Technology (Fig. 1), Signature Identification, Door Phones, Monitored System, Unmonitored System, Wireless Alarm Systems, Electric Current Home Alarm, Electromagnetic Lock, Electronic Strikes, Electronic Deadbolts, and Latches.

Sometimes finger-based security system has to face the problem of poor image matching performance of the image recognition method. But there is some recently proposed method where the authors showed that the performance of restoration and reconstruction has been improved. [2] [3]

The main purpose of this study is to design and develop a fingerprint biometric security system, to use software to create and simulate a circuit, to achieve high-security accuracy, to use the microcontroller system, to produce the hardware for the system, to use fingerprints of the index and thumb fingers, to preserve this information in a database, and to use fingerprints to access the secured system. A buzzer will sound to alert the user to the software programming language C if an unrecognized fingerprint is identified.

2. LITERATURE REVIEW

To address the issue of the image recognition method's poor image matching performance, a fingerprint image recognition method based on a convolution neural network was developed by Tian et al. [3]. Smoothing, convergence, equalization, background foreground segmentation, and distortion correction are used to pre-process the defaced fingerprint image in this method, and By integrating the neighborhood judgment approach, the feature points of the defaced fingerprint picture are retrieved, and the information pseudo feature points are deleted by fusing the feature points, the center points are extracted from the defaced fingerprint image, and the center blob is removed.

Lourde et al. [4] deal with the problem of selecting an optimal algorithm for fingerprint matching to design a system that meets the required performance and accuracy specifications. MATLAB simulations were used to compare two competing algorithms against a common database.

In this paper, Nagaty et al. [5] introduce a new resource fingerprint identification technique that integrates the minutiae information in a fingerprint with information from neighboring ridges. The essential thought behind this framework is to partition the unique finger impression matching issue into a few little sub-issues that utilize picture energy minimization and are addressed iteratively.

Zhu et al. [6] According to research, traditional automobile identifying systems include key systems, door-controlling systems, Ultra High Frequency (UHF) sending/receiving systems, alarm systems, and so on. If the key is lost or stolen, those who do not have ownership can use it to open the car door. This limitation can be overcome by biometric recognition technologies.

While some of the Delaunay triangle-based structure's pleasant qualities have been used in numerous fingerprint authentication systems with positive results, Yang et al. [7] observed that the bulk of these systems run without template protection. Furthermore, these systems' feature sets and similarity measurements are incompatible with current template protection approaches.

In 1980 the MCU series named Intel MCS-51 or 8051 was made by Intel for use in the introduced structures [8]. In the early 1990s and 1980s, Intel's actual versions were utilized, and upgraded binary compatible equivalents are still commonly used today. It's an example of a complicated instruction set computer with separate memory areas for program instructions and data (with certain RISC design elements like a big register set and register windows). Furthermore, multiple studies have been conducted in which researchers have created robotic hands using various types of microcontrollers [9].

Kamble et al. [10] introduced that ATM (Automatic Teller Machine) security components require unique mark checks, utilizing biometrics and hybridization in this review. The unique mark include was picked due to its accessibility, constancy, and high precision. A unique mark-based biometric framework might be promptly introduced to get the ATM. How these ATMs work in this framework is that when a client puts their unique finger impression on the finger impression module and gets to the ATM to pull out cash, the machine needs to examine the finger impression of the client who is utilizing the machine.

Verma et al. [11] concentrated on the plan and execution of an advanced security framework that can be sent to a safe zone where just genuine individuals can enter. We introduced a security framework with an entryway locking framework that utilized aloof RFID to initiate, check, and approve the client as well as open the entryway progressively for secure access.

The benefit of using passive RFID is that it does not require a battery, and passive tags are lighter and less expensive than active tags. investigated the design and implementation of a digital security system that can be deployed in a secure zone where only authorized individuals can enter We put in place a security system that included a door locking system that used passive RFID to activate, authenticate, and validate the user while also unlocking the door in real-time. Passive RFID has the advantage of not requiring passive tags and a battery, are lighter and less expensive than active tags.

3. METHODOLOGY

In this study, a developmental method was used, which involved the systematic use of the concepts of an existing device to develop a new system. The system's working model was also assembled using the prototyping technique.

The study included hardware development, in which the system was built using market-available components, and

software development, in which programs were written using available programming languages.

A 9-12 biometric locker system will provide access to the system. The ATNEGA 644 microcontroller on the Arduino board will be utilized to connect the input and output hardware components.

The fingerprint sensor for biometric recognition is one of the input devices. When someone who isn't supposed to unlock the locker tries to do so, the LCDs are the operation of the locker. The Arduino integrated development environment will be used to program the microcontroller.

To do anything useful, a microcontroller must be programmed. If you want to start simple, Arduino programming is a little easier. When the fingerprint module is connected to the microcontroller, it enters user mode. In this mode, stored images are compared to scanned images.

When a user accesses our application, the images of their fingerprints that are authorized to open the locker door are saved in the module with a unique ID. To demonstrate that the individuals are authorized to open the locker door, their fingerprint images must be scanned. The scanner is connected to an 8051 microcontroller, which will control the scanning process. After the scanning is finished, the user must enter his password into a keypad to open his locker. The locker will be opened immediately. The locker door will close if the key is pressed again with the help of the keypad once the work is completed. A buzzer will play if someone tries to detect his/her fingerprint image without his permission that is interfaced with the controller, and if the user enters the wrong password, another detection will be alarmed by the buzzer. Instead of him/her, the current user can create a new user as the user of the same locker through a new registration process, and the old user's fingerprint image will be deleted. There is also the option to change the password.

3.1 Experimental Result

Step 1: When the board is powered up, the initial displays on the LCD are as shown below.
Step 2: When the fingerprints do not match.
Step 3: Display on LCD when a person's fingerprint matches.
Step 4: We must enter a valid password.
Step 5: When an invalid password is entered, an error message is displayed on the LCD.
Step 6: When the password is matched, two options are displayed.
Step 7: When option 1 is selected, the display appears on the LCD.
Step 8: After we finish our work, we must close the locker door by pressing key 3 and returning to step 1.
Step 9: When option 2 is selected after step 5, it displays four options. Select the required option; for example, if option 4 (cancel) is selected, the process returns to step 1.

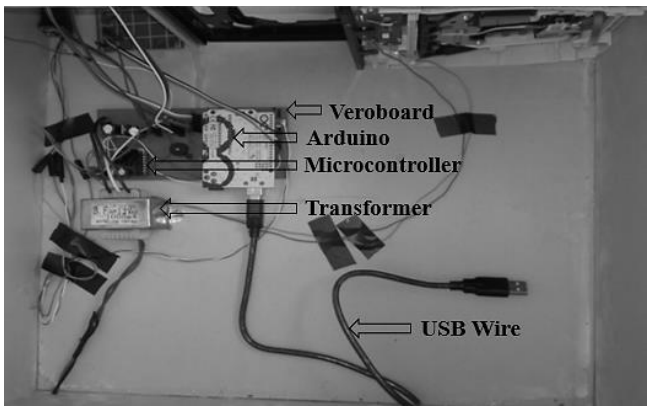

Fig. 2: Hardware of the part

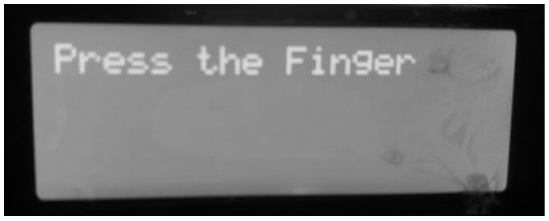

Fig. 3: Indication to scan the finger

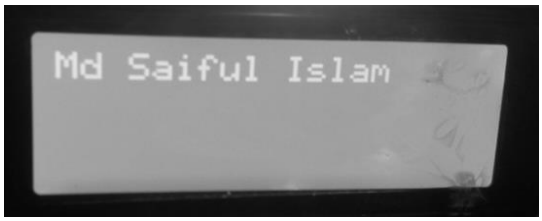

Fig. 4: Recognized person presses the finger

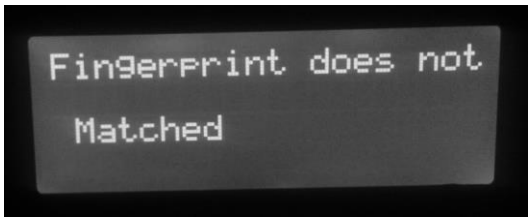

Fig. 5: Unrecognized person press the finger

Fig. 6: Front side of the project

3.2. System Description

To run this project, we must first run it in "Settings mode" or "Admin mode." In this mode, we must enter data into the database of the fingerprint sensor, which requires us to take fingerprint impressions of the person to whom we wish to grant access to our security system. This can be done only once, or whenever a new entry is required in the system. The project must then be used in "Normal mode or Search mode." The device matches the fingerprint input at its optical plate to the fingerprint previously saved in its flash memory in this mode. It delivers an OK signal along with the person's identifying number if the entry matches the memory. However, if the entry does not match the memory, an error signal is generated. The microcontroller receives the fingerprint sensor's output. The result information is then analyzed by the microcontroller. A microcontroller can turn on a suitable gadget in light of the information got. At the point when the unique finger impression module conveys an OK message, the microcontroller actuates a hand-off and an engine. Assuming the blunder yield is gotten, the Buzzer is enacted.

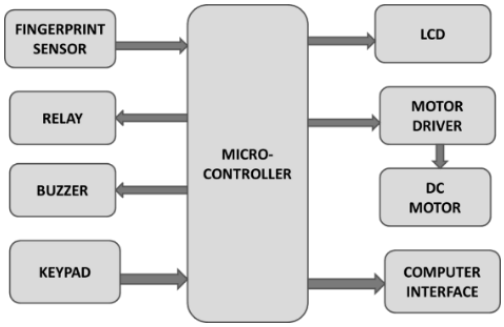

Fig. 7: Block diagram of the system

The R305 is outfitted with an optical biometric finger impression peruse which is a unique mark sensor. It. Our task's CPU (focal handling unit) is a microcontroller. We'll utilize a microcontroller from the 8051 families. For this situation, a 162 alphanumeric Liquid Crystal Display (LCD) was utilized, and that implies it can show letter sets as well as numbers on two lines of 16 characters each. The invalid access to open the door is indicated by a buzzer. Using the keypad, the user will enter various commands. The following are the keypad's various keys: I. Create a fingerprint entry II. Search for a fingerprint III. Delete the fingerprint module's database.

There are two other data acquisition algorithms, in addition to the optical sensor algorithm, which are the capacitive sensor utilization method and ultrasound technology-based sensors. In our project, we attempted to use the first method, optical sensors. As a result, we have not discussed the other two methods.

3.3 Image pre-Processing

The pre-processing steps attempt to compensate for lighting, contrast, and other inconsistencies introduced by the sensor during the acquisition process. There are numerous processes, but the following are the most well-known at the moment: Gaussian Blur: A convolution operation applied to the original fingerprint image to reduce image noise introduced by the sensor during data acquisition. Sliding window contrast adjustment is used to compensate for any illumination abnormalities within a fingerprint as well as to achieve uniformity in the contrast between various fingerprints. Adjusting the intensity level of the ridges and valleys using a histogram: This is the final step in enhancing the ridges and valleys.

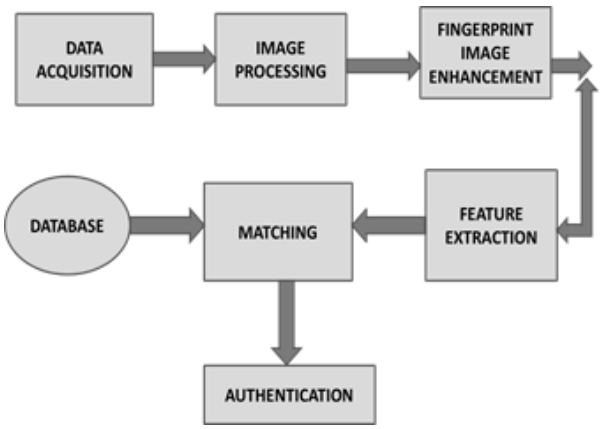

Fig. 8: Fingerprint matching algorithm architecture

4. DESIGN AND SIMULATION

The model-based plan approach is great for Embedded System Design. This project makes use of the Proteus tool. The Proteus tool also includes virtual instruments such as an oscilloscope and a logic analyzer for monitoring the system's signals. To build the microcontroller framework, Proteus permits get-together code to be collected and downloaded on virtual 8051 microcontrollers employing a bit-by-bit plan cycle of LED, LCD, Serial Communication, connecting switch, and Fingerprint Module. A compiler is used to code in the C language. The system is set up and executed using the generated hex code.

The fingerprint technology security door lock was designed around a Micro-Controller Unit (MCU), PIC16F628A, which reads in fingerprints from a fingerprint scanner and only pre-registered fingerprints have access to a secure compartment. This embedded security system's main input is the fingerprint scanner. The read fingerprints are compared to those in the microcontroller's memory that have been pre-programmed. At the point when a match is found, the microcontroller produces a HIGH sign, which enacts the semiconductor transfer exchanging stage, which controls the opening and shutting of the demonstrated mechanized entryway. The status of this embedded security system is displayed on an alphanumeric LCD in this configuration. It

displays a welcome message by default, prompting the user to submit their fingerprint.

Table 1: Problem while taking finger

Problem	Fingerprint Snapshot
Finger Misplacement	
Dirty Finger	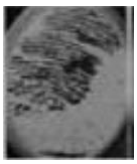
Orientation	
Skin Problem	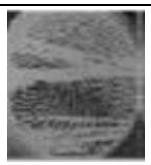
Wet Finger	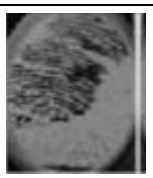

When a match is found, the message "ACCESS GRANTED" is displayed; otherwise, the message "ACCESS DENIED" is displayed. The SN-FPR-UART was used to implement the fingerprint input stage. It is a tiny fingerprint reader module that is specifically developed for the project development due to its robustness.

4.1 The Door Movement Mechanism

The motor drive mechanism for the modeled automated door is based on a 5V DC motor that can be controlled in both directions (clockwise and anti-clockwise). The polarity of a DC motor is switched to make it run in both directions. Because the Microcontroller's outputs have not produced enough current for driving the motor directly, transistor relay switch stages are required. When a fingerprint matches one of the pre-stored fingerprints, the Microcontroller sends a high (digital 1) output pin to drive the motor clockwise, allowing the automated door to open. The high output has a ten-second length, while output A2 is kept short (digital 0). After a ten-second high on A1, the microcontroller yields a high on A2 and a low on A1 for five seconds to move the motor in the counterclockwise heading, shutting the entryway. Flipping the A1 and A2 as per the table beneath controls the whole engine heading control.

Table 2: A truth table from the output to motor response

Outputs		**Motor response**
A1	**A2**	
0	0	Off
0	1	Anti-clockwise
1	0	Clockwise

Flat plywood sheets were used to construct the door. The wooden sheets were joined together with adhesive gum to form the body of the door system. This depicts the data flow between the various segments of the security door system, as shown below:

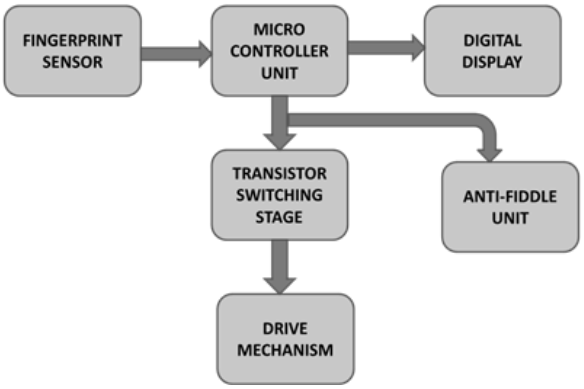

Fig. 9: Data flow diagram

4.2 Construction

The project's physical realization is critical. The paperwork is converted into finished hardware here. Following completion of all paper designs and analysis, the project was implemented, constructed, and tested to ensure its functionality. This project's construction was completed in three stages. First, in C language, write the code (driver) that controls the microcontroller. The entire project is then created on an experiment board that is solder-less. Following that, the Vero-boards circuits were soldered, and the entire project was attached to the casing.

4.3 Implementation and Simulation

The breadboard was used to create this project. The power supply was initially inspired by a bench power supply in the electronics laboratory. Before welding the power supply stage, the circuits were tried for usefulness. The breadboard execution of the undertaking was effective, and it met the ideal plan objectives, with each stage proceeding as planned. Before beginning soldering work, the entire electrical portion of the project was simulated on the PROTEUS simulation platform to ensure that everything worked properly.

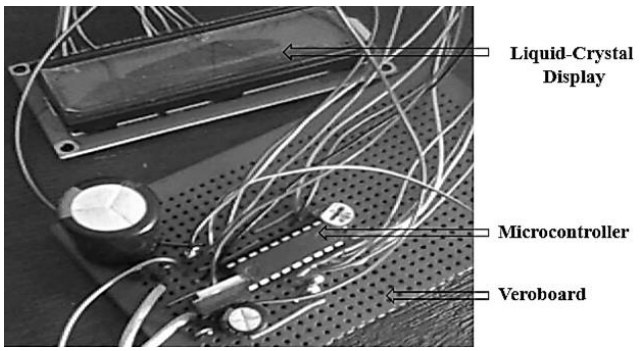

Fig. 10: Components layout on Vero-board

Before soldering the circuit on the Vero board, it was tested stage by stage according to the block representation on the breadboard. During the testing and implementation procedure, the following test and measuring equipment was employed.

During the breadboard test before installing the project's power source, this was utilized to supply voltage to the various stages of the circuit. The power supply was also utilized to test several stages before they were finally soldered during the project.

The oscilloscope was used to inspect the power supply waveform for ripples and to ensure that all waveforms and frequencies were correct. To ensure proper oscillation at 4MHz, the waveform of the oscillation of the crystal oscillator used was monitored.

Voltage, resistance, continuity, current, frequency, temperature, and transistor h are all measured by a digital multi-meter. The process of implementing the design on the board necessitated the measurement of parameters such as voltage, continuity, current, and resistance values of the components, as well as frequency measurement in some cases. The output of the voltage regulators used in this project was checked using a digital millimeter.

5. CONCLUSION AND RECOMMENDATION

This project successfully demonstrated a functional, low-cost, and simple microcontroller-based door access control system. A real-life equivalent of the prototype can be developed with minimal development costs and relatively low operational costs for environments requiring high levels of security, such as banks, military research facilities, and large private investment firms.

The plan is achieved by interacting an SN-FPR-UART Finger peruser with the PIC16F648A Microcontroller, which fills in as the mind box for the whole gotten entryway framework. To show the framework's working status, an LCD status show is utilized. The SN-FPR-UART is used to execute a unique mark input stage, and an entryway development component is utilized to permit the robotized entryway framework to move in both clockwise and hostile to clockwise headings. It is a tiny fingerprint reader module that is specifically developed for the project development due to its robustness and the following exceptional qualities. The development ensures security against the illegal entry of any entity into the room; the mechanism can be implemented in a broader sense on a door with restricted access.

As a component of the exploration, a microcontroller-based biometric storage framework with a short informing framework (SMS) can be created to safeguard the security of an individual's private and classified belongings. In the review, a formative exploration strategy comprising equipment and programming advancement was utilized. The framework would have the option to filter a finger, match it to a formerly saved design, and open the storage. The Global System for Mobile (GSM) module will want to send an instant message giving the storage's auto-produced password assuming an unnoticed unique finger impression is found.

REFERENCES

[1] Yadav, D. K., Singh, S., Pujari, S., & Mishra, P. (2015). Fingerprint-based attendance system using microcontroller and LabView. International Journal of Advanced Research in Electrical, Electronics and Instrumentation Engineering, 4(6), 5111-5121.

[2] Tian, Y., Yeo, B. T., Cropley, V., & Zalesky, A. (2021). High-resolution connectomic fingerprints: Mapping neural identity and behavior. NeuroImage, 229, 117695.

[3] Tian, L., Xu, H., & Zheng, X. (2021). Research on fingerprint image recognition based on convolution neural network. International Journal of Biometrics, 13(1), 64-79.

[4] Lourde, M., & Khosla, D. (2010). Fingerprint identification in biometric security systems. International Journal of Computer and Electrical Engineering, 2(5), 852.

[5] Nagaty, K. A. (2004, January). An energy-based fingerprint matching system. In First IEEE Consumer Communications and Networking Conference, 2004. CCNC 2004. (pp. 706-709). IEEE.

[6] Zhu, Z., & Chen, F. (2011, October). Fingerprint recognition-based access controlling system for automobiles. In 2011 4th International Congress on Image and Signal Processing (Vol. 4, pp. 1899-1902). IEEE.

[7] Yang, W., Hu, J., & Wang, S. (2014). A Delaunay quadrangle-based fingerprint authentication system with template protection using topology code for local registration and security enhancement. IEEE transactions on Information Forensics and Security, 9(7), 1179-1192.

[8] Wharton, J. (1980). An introduction to the intel-mcs-51 single-chip microcomputer family. Intel Corporation.

[9] Kabir, A. (2014, April). SCARA: Selective Compliance Assembly Robotic Arm. Asif Kabir. https://doi.org/10.13140/RG.2.2.36504.55044

[10] Kamble, P. D., & Gawali, B. W. (2012). Fingerprint Verification of ATM Security System by Using Biometric and Hybridization. International Journal of Scientific and Research Publications, 2(11).

[11] Verma, G. K., & Tripathi, P. (2010). A digital security system with a door lock system using RFID technology. International Journal of Computer Applications, 5(11), 6-8.

Paper ID: 1777
International Conference on Mechanical, Manufacturing and Process Engineering (ICMMPE – 2022)
Organizer: Faculty of Mechanical Engineering, Dhaka University of Engineering & Technology (DUET), Gazipur, Bangladesh
Website: https://icmmpeduet.com/

Numerical Analysis of Displacement and Stress Field on a Femur Bone Made of Ti-6Al-4V and SS316L

Md. Sakib Shahriar[1], Dr. Nasrin Akhter[2], Dr. Md. Shahidul Islam[3]
[1,3] Department of Mechanical Engineering, Khulna University of Engineering & Technology, Bangladesh
[2] Department of Biomedical Engineering, Khulna University of Engineering & Technology, Bangladesh

E-mail:sakibshawon3@gmail.com

ABSTRACT

Biomechanics is an important term in the engineering and medical sector. The femur bone is the longest and the strongest bone in the human skeleton system that buttresses the human body during walking and standing. Displacement and stress develop on femur bone that varies at different working positions. In this study, three-dimensional models of the human femur bone and hip contact forces are utilized for investing femur bone and prosthetic bone during walking and standing activities. The prosthetic design of the femur is an important part of the total femoral replacement (TFR) field. Total femur replacement is used as an alternative to lower limb amputation when femur bone faces cancer. Normal stresses and total displacement are acquired from femur bone and prosthetics bone (Ti-6Al-4V, SS316L) by using finite element software (ANSYS 16.2). In the femur neck-shaft angle and femoral head, the maximum normal stress and maximum total deformation developed. Ti-6Al-4V material developed greater maximum normal stress and maximum total deformation of femur bone than SS316L material. The results of the studies are useful for the orthopedic specialist to understand the biomechanical behavior of the femur bone and femur bone prosthesis.

Keywords: Total femur replacement; Prosthetic femur bone; Biomechanics; Stress developed on femur bone; Femur simulation

1. INTRODUCTION

Biomechanics is the applied mechanical principles of living systems that are considered as the study of structure, function and biological motion systems with mechanical aspects. Biomechanics play a crucial role in the prosthetic design of any body part of humans and outline the proper function of the body during human activity. Biomechanical function and biological structures can be simulated and investigated using biophysics concepts and laws [1]. The finite element method (FEM) is a useful tool for biomechanics modeling. The irregular shape of the biomechanical object, intricate tissue microstructure of the biological system, and loading circumstances are all concerns that arise when using the FE approach to simulate biomechanics models [2]. Time differences between two consecutive occurrences of cyclic events of walking or other activities constitute a gait cycle. When one foot first makes contact with the ground gait cycle begins and when that same foot makes contact with the ground again, the gait cycle ends [3]. The component of an external force acting on the head of the femoral which are a transient load. In dynamic and static activities, Hip joint loads have been studied in several studies [4] [5].

Amputation of the lower limb is substituted by total femoral replacement when femur bone faces malignant and sarcoma. The prosthetic design of the total femur is play an important role for fix the issue of limb amputation [6]

Cortical bone and Trabecular bone are essential elements of the femur bone. The property of cortical bone is compact, rigid and denser whereas trabecular bone more flexible, adaptable and less dense for incorporating spongy structure. In human skeleton system, the longest and largest femur bone remains strongest in compressive load. To create the human knee joint the distal portion of femur bone meshes with tibia bone at the proximal end part. To create the hip joint, femur bone articulated with the acetabulum at the proximal end of femur. The largest weight percentage of human body contains femur bone and also support to human body during walking, standing [8].

For oncologic and non-oncologic indications, lower limb amputation is substituted by salvage arthroplasty procedure that is known as total femoral replacement (TFR). Femur bone is one of the common bone to affected by primary and secondary malignancies and also affected by Ewing's sarcoma, osteosarcoma, pleomorphic undifferentiated sarcoma, chondrosarcoma and bony metastases. In modern prosthetics surgery, hip joint, knee joint and total femur bone replacement are extreme limb preservation surgery examples. To reconstruct femoral integrity and proper function of femur used as total femur replacement. [6]

From 1993 to 2007, nine patients had been going through total femur reconstruction and resection surgery called total femur replacement surgery. In nine patients, four of them were affected by primary malignant femur

bone tumor, another four of them affected by primary malignant type soft tissue tumor and one of them affected by metastatic. After 51 months follow up of nine patients, four patients of them still alive and other five of them patients died of femur bone malignant disease [7].
After extensive femur resection, endoprosthetic femur replacement are used to restore mechanical and functional behavior.

The stress analysis of femur bone is needed for understanding of the behavior of stress field with gait cycle. So far numerous research studies have been carried out to investigate femur stress field. A.E. Yousif , M.Y. Aziz analyzed normal stress in femur bone during walking and standing position. Femur bone model extracted from computer tomography (CT) data image. Mechanical behavior data of femur bone collected by simulation of femur bone in finite element method. In this study, three dimensional human femur bone mode has been developed and the force component data of hip contact forces used to analysis mechanical behavior of femur bone during walking and standing up activity [9]. R. Nareliya and V. Kumar investigated stress and deformation in femur bone. They are extract geometrical model of femur from CT scan data [1]. Pradosh Pritam Dash and Kaushal Kishor analyzed peak stress value and normal stress pattern of human femur during walking, standing, stair climbing and knee bending activities [10]. Ajay Dhanopia and D.Manish Bhargava analyzed fracture of femur bone with different material of prosthetic plate and also analyzed deformation and stress in femur bone [11]. Nithin Kumar and T. Tandon analyzed normal stress pattern of human femur during walking, standing, jumping and running activities [12]. E. Isaza and L. Garcia investigated isotropic and anisotropic model shows the difference between the stress distributions on the femur head and also investigated fracture risk for low density bone [8]. A.V. Javir and Dr. M. S. Kirkire analyzed 3D white light scanning is used to get the true shape of femur bone and also analyzed resultant force acting at different frontal and transverse angles to optimize prosthesis [13]. G. Bergmanna and G. Deuretzbacher investigated force component of hip contact forces and unit of gait patterns from routine activities. This forces are time dependen [4]. Sachin G. Ghalme and Ankush Mankar analyzed biomaterials in hip joint replacement and summarize the evolution of the biomaterial from early days of metals [14]. Xishi Wang and Tian Ying Wang analyzed stress level and peak stress at the human hip joint during routine activities which determine the hip degeneracy [15]. Georg Bergmann and Alwina Bender analyzed force and moment at the human hip joint during routine activities [5]. Liang Peng, Jing Bai analyzed the comparison of isotropic and orthotropic material property on femur and also analyzed the relationship between CT numbers, Hounsfield Unit (*HU*), and bone material properties [16]. J. Koerber and S. Eberle analyzed to develop and validate patient-specific finite element analysis (FEA) generated from CT data for the evaluation of fracture stability. Finite element analysis from CT scans may be a useful tool to predict mechanical stiffness and local deformation of a bone-implant interface with a reasonable level of accuracy and this could be a useful tool to evaluate osteosynthesis options for a particular fracture scenario [17]. Deepak Ramanathan et.al. analyzed the current surgical technique used in total femoral replacement and also analyzed functional outcomes and complications of total femoral replacement [6]. Total femoral replacement is able to reconstruct femoral integrity and function for this reason prosthetic material play important role in this investigation.

2. MATERIAL AND METHODS

2.1 Biomaterial of Total Femoral Replacement

In the treatment of fractures, metal implants used for treatment which properties are non-magnetic and high density. For compatible X-ray imaging and magnetic resonance imaging (MRI) techniques material property is more important for selecting material which material implant will be used for TFR. Static, dynamic and repetitive load are subjected to artificial implants. Proper combination of strength and ductility are required in artificial metal implants. Excellent combination of rigidity, elasticity, strength, toughness and corrosion resistance are required in orthopedic implants for fracture resistance. Wear resistance metals are required for avoided from friction debris formation.

In this study, stainless steel 316L (SS316L) and titanium alloy (Ti-6Al-4V) material are used for total femoral replacement because of these materials have high density, strength and wear resistance properties. Stainless steel 316L and Ti-6Al-4V alloy material are used in bone fracture fixation treatment. Stainless steel 316L (SS316L) composed of chromium 16-18.5%, molybdenum 2-3%, nickel 10-14%, manganese less than 2%, silicon less than 1%, carbon less than 0.003% and balanced iron. Ti-6Al-4V composed of aluminum 5.5-6.75%, vanadium 3.5-4.5%, carbon 0.08%, oxygen 0.2% and balanced titanium [18].

2.2 Methodology

Firstly, three dimensional left femur bone model was developed for analysis purposes in finite element. The methodology to acquire the solid geometry model starts with a 40 years old male patient's femur sample, which has been scanned using a 3D Laser Scanner [8]. The scanned model is a (.stl) format 3D model. In early studies density of human femur bone was analyzed by DICOM (Digital Imaging and Communications in Medicine) image format which is obtained data from the application of CT scan. Binary data element sets are contained in Digital Imaging and Communications in Medicine DICOM. Gray scaled two dimensional images of a human is made from binary data of CT scan in the DICOM form. Bone material

properties obtained from gray scaled images data values which are averaged and converted from each element analysis by the Hounsfield unit. CT scans radio density used for relative quantitative estimation of Hounsfield unit (*HU*), where its value is also termed CT number. Tissue's linear X-ray attenuation coefficient considers as pixel map that is converted to CT scan image. In the Hounsfield scale, pixel map values are scaled and air linear X-ray attenuation coefficient considers -1024 and also consider for water is 0 [1]. This bone was investigated through finite element method by preparing mesh where bone material and prosthetic material used and boundary conditions defined then results of simulation extracted.

2.3 Material Definition

For stress analysis of human femur bone model, material properties of femur bone are treated as important parameters and assigned the value of parameter according to different literature. The density of femur bone is important parameter to analysis the bone model and the density data of femur bone has been taken from mathematical relation which correlates the Hounsfield unit (*HU*) unit

$$\rho = 4.64\times10^{-4} HU + 1 \quad (1)$$

where, ρ = bone density (g/cm^3)

The Hounsfield unit (*HU*) is taken 800 for trabecular bone and 2200 for cortical bone. The range of for bone is from +700 for trabecular (cancellous) to +3000 for cortical [7]. These *HU* values are substituted to equation (1) to get the density for trabecular and cortical bones.

The values of the modulus of elasticity for the human femur bone model which assumed as orthotropic and homogeneous property have been taken from empirical relationships that relates the density of the femur bone (cortical and trabecular) with the modulus of elasticity [7] [17].

$$E_{1c} = E_{2c} = 2314\times\rho^{1.57} \quad (2)$$

$$E_{3c} = 2065\times\rho^{3.09} \quad (3)$$

$$E_{1t} = E_{2t} = 1157\times\rho^{1.79} \quad (4)$$

$$E_{3t} = 1904\times\rho^{1.64} \quad (5)$$

, $$\nu_{12} = 0.4,\ \nu_{23} = \nu_{31} = 0.25 \quad (6)$$

Where, indexes c and t represent cortical and trabecular, Indexes 1,2,3 represents accordingly radial, circumferential and longitudinal direction of bone,

E = Modulus of Elasticity (MPa), ν = Poisson ratio.

Isotropic materials have two independent constants and orthotropic materials have nine independent variable. The below Table 1 and 2 represents the parameter that are assigned for femur bone model used as mechanical properties.

Table 1: Isotropic material properties of femur bone and prosthetic bone [11]

Parameter	Femur bone	SS316L	Ti-6Al-4V
Density (g/cm^3)	1.75	7.75	4.5
Young's modulus *E* (GPa)	16.7	193	120
Poisson's ratio,*v*	0.3	0.31	0.32
Ultimate Tensile Strength (MPa)	43.44 ± 3.62	485	993
Ultimate Compressive Strength (MPa)	115.29 ± 12.94	570	1086

Table 2: Orthotropic material properties of human femur bone [9]

Parameter	Cortical Bone	Trabecular Bone
Hounsfield unit (*HU*)	2200	800
Density (g/cm^3)	2.0208	1.3712
Modulus of Elasticity (MPa)	$E_1 = 6982.9$	$E_1 = 2029.4$
	$E_2 = 6982.9$	$E_2 = 2029.4$
	$E_3 = 18155$	$E_3 = 3195.3$
Poisson's ratio	$v_{12} = 0.4$	$v_{12} = 0.4$
	$v_{23} = 0.25$	$v_{23} = 0.25$
	$v_{31} = 0.25$	$v_{31} = 0.25$
Shear Modulus (GPa)	$G_{12} = 4.69$	$G_{12} = 4.69$
	$G_{23} = 5.61$	$G_{23} = 5.61$
	$G_{31} = 7.68$	$G_{31} = 7.68$

2.4 Boundary condition

Boundary condition of femur bone model is required for the finite element analysis. In the distal end of femur bone has been applied fixed boundary condition for FE analysis and hip contact forces has been applied on the head of the femur bone for analysis the deformation and normal stress during daily human activity. The hip contact force is time depended or transient. Length of femur bone is 0.43m. Neck shaft angle is located in the proximal side of bone and formed by femoral neck shaft axis and femoral shaft axis.

2.5 Mesh Preparation

Mesh generation is a very important and vital step of femur bone model for analysis in finite element and generated mesh using ANSYS Workbench 16.2. Mesh is

generated using sizing functions of 5mm per element. Tetrahedral element number used for femur bone model are 2821117 and the node number is 398592. For obtaining the result accurately, face size of 3mm is used on the femur and also used inflation function to refine the mesh

2.6 Loading Condition

The dynamic response of a structure under the action of any general time-dependent loads is determined by the transient structural analysis [19]. In Transient analysis, the hip contact load that applied on the femoral head during a complete gait cycle activity is need to measure the values and simulated that are time dependent values. Table 3 represents the description of walking and standing activity.

Table 3: Description of daily routine activities [10]

Activity	Description
Normal Walking	Normal speed walking on level ground, average speed is 3.9 km/h or 1.1 m/s
Standing Up	Standing up when chair height is 50 cm, arms hold at the chest height

These hip contact forces have been plotted with respect to the gait cycle for routine activity as shown in following, **Fig. 1**.

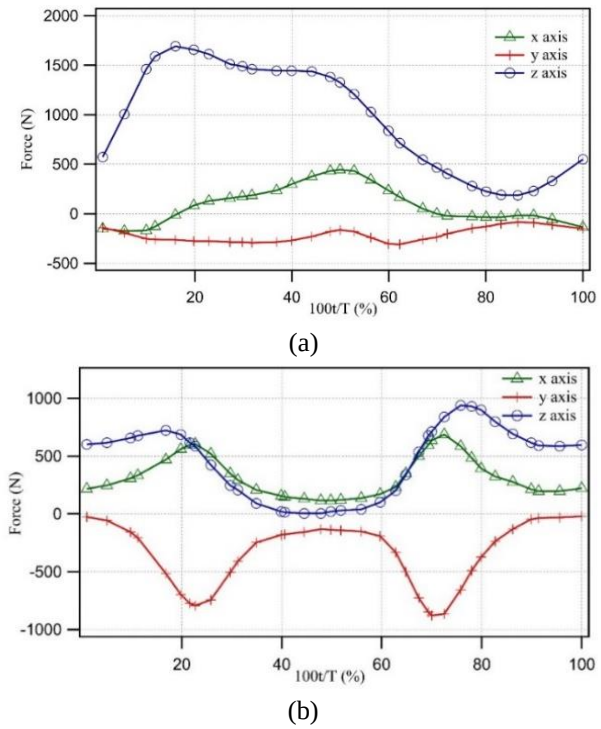

Fig. 1: Hip Contact Load during (a) Normal Walking, (b) Standing Up condition

Hip contact force during routine activity are found from different literature [10]. This force has been applied on the head of the femur in different activity.

3. RESULT AND DISCUSSION

The normal stress distributions and total displacement obtained from transient analysis of loads on femoral head during normal walking, standing up activities have been shown in Fig. 2-9. The normal stresses in bone by taking the isotropic and orthotropic types of bone material during daily activities (normal walking, standing up) are computed using the present developed 3D model that generated from CT data. Failure stress for femur bone material is 113.23 MPa for bone fracture [20].In addition to that the normal stresses in bone by taking the bone prosthetic material (Ti-6Al-4V and SS316L) during daily activities (normal walking, standing up) are also computed. In this research work, FEM is used for finding solutions of equations in physical problems under boundary conditions. The normal stress and total deformation of femur bone with bone material (Isotropic and Orthotropic) and prosthetic material (Ti-6Al-4V and SS316L) is plotted against time.

3.1 Normal Walking

The normal stress distribution Fig. 2 and total deformation Fig. 3 of femur bone material (isotropic and orthotropic) and prosthetic material (Ti-6Al-4V and SS316L) during normal walking position is shown with time variable as a gait cycle.

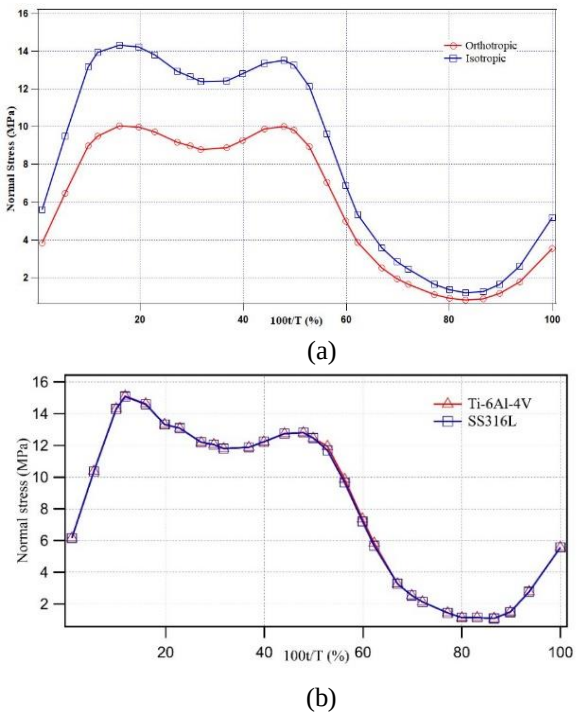

Fig. 2: Normal stress distribution during normal walking for (a) Bone Material, (b) Prosthetic material

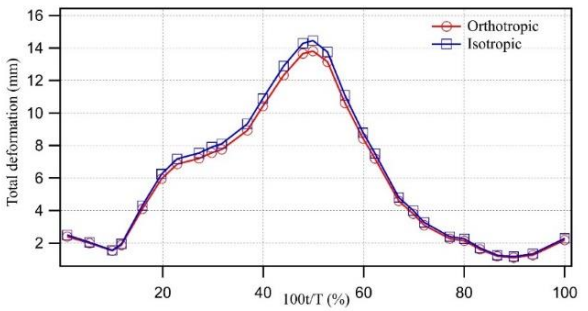

(a)

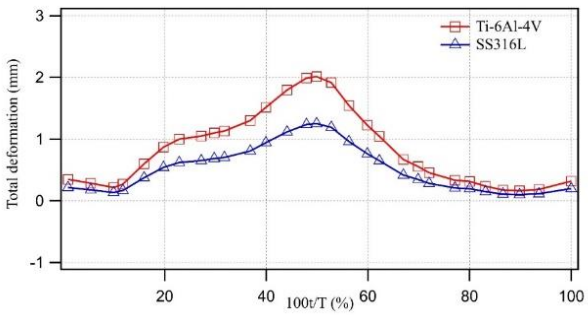

(b)

Fig. 3: Total deformation during normal walking for (a) Bone Material, (b) Prosthetic material

In this analysis, maximum stress for bone orthotropic material and isotropic material is found 10.052 MPa and 14.313 MPa. Also, maximum stress for Ti-6Al-4V material and SS316L material is found 15.113 MPa and 15.085 MPa. In normal walking condition, stress developed in Ti-6Al-4V material's bone is greater than SS316L material but the stress developed nature have similarity. From contour Fig. 4, maximum stress is always found in femoral neck shaft angle during walking gait cycle.

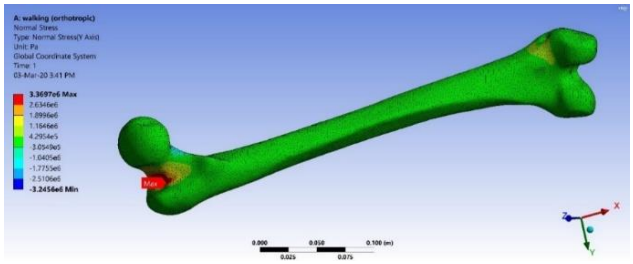

(a)

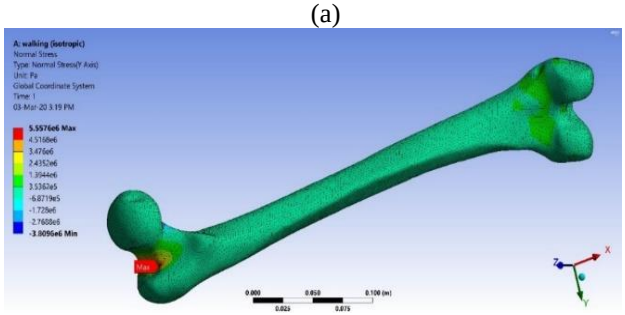

(b)

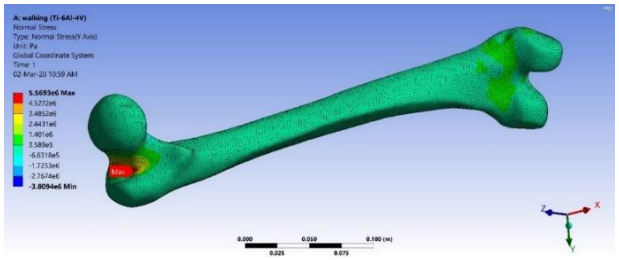

(c)

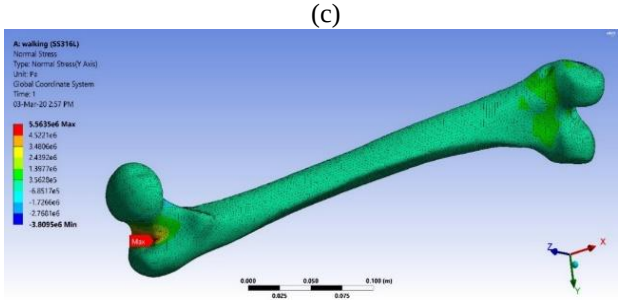

(d)

Fig. 4: Normal stress distribution during normal walking for (a) Bone orthotropic material, (b) Bone isotropic material, (c) Ti-6Al-4V material, (d) SS316L material

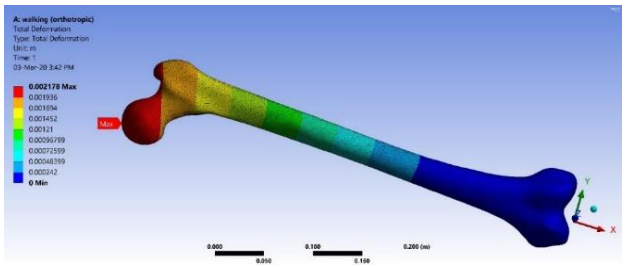

(a)

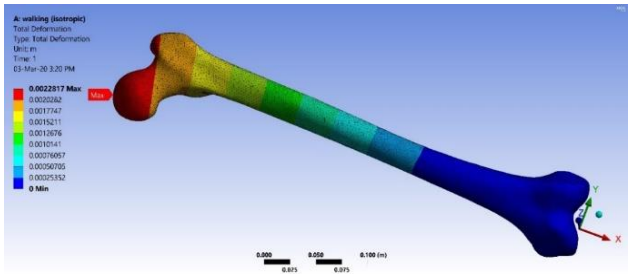

(b)

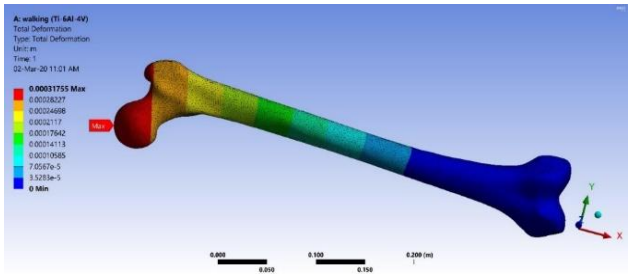

(c)

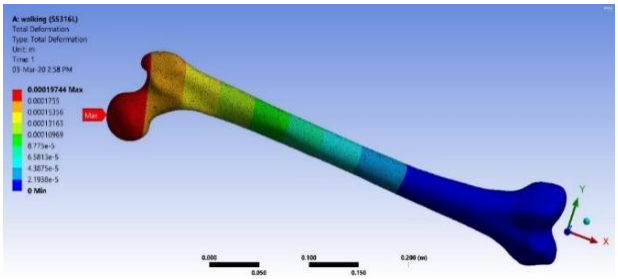

(d)

Fig. 5: Total deformation during normal walking for (a) bone orthotropic material, (b) bone isotropic material, (c) Ti-6Al-4V material, (d) SS316L material

In this analysis, maximum deformation for bone orthotropic material and isotropic material is found 13.811mm and 14.45 mm. In this analysis, maximum deformation for Ti-6Al-4V material and SS316L material is found 2.0118mm and 1.2506mm. In normal walking condition, deformation in Ti-6Al-4V material's bone is greater than SS316L material but the deformation developed nature have similarity. From contour Fig. 5, maximum deformation is always found in femoral head during normal walking gait cycle

In normal walking condition, maximum stress and maximum deformation of femur bone material (orthotropic and isotropic bone material, Ti-6Al-4V and SS316L) is shown in following Table 4. This neck shaft angle is formed by femoral neck shaft axis and femoral shaft axis.

Table 4: Maximum stress distribution and maximum deformation of femur bone during normal walking

Activity	Material	Maximum stress (MPa)	Maximum deformation (mm)
Normal walking	Bone orthotropic	10.052	13.811
	Bone isotropic	14.313	14.45
	Ti-6Al-4V	15.113	2.0118
	SS316L	15.085	1.2506

3.2 Standing Up

The normal stress distribution Fig. 6 and total deformation Fig. 7 of femur with bone material (Isotropic and Orthotropic) and prosthetic material (Ti-6Al-4V and SS316L) during standing up position is shown with time variable as a gait cycle.

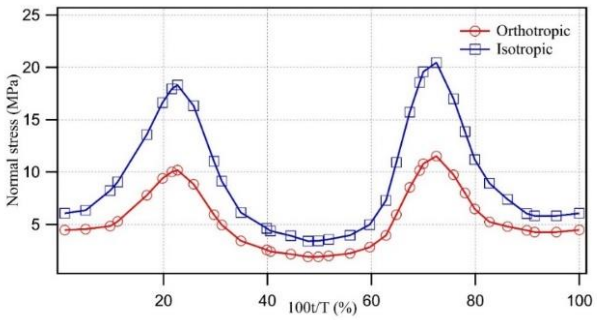

(a)

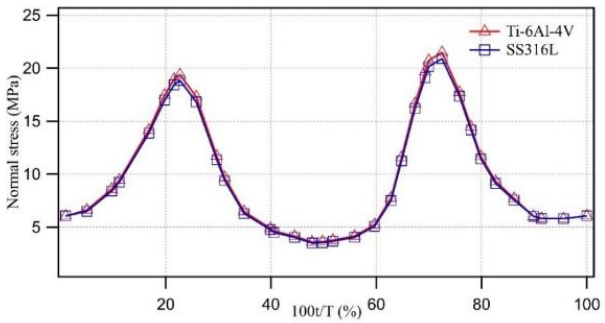

(b)

Fig. 6: Normal stress distribution during standing up condition for (a) Bone material, (b)Prosthetic material

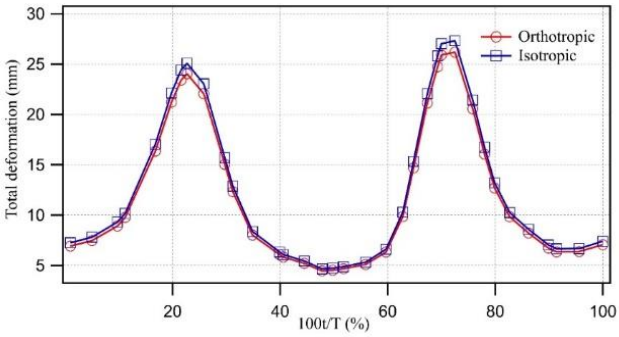

(a)

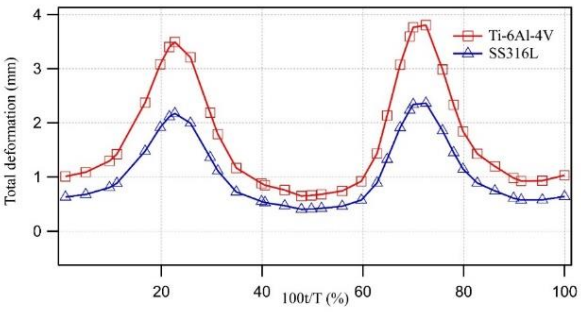

(b)

Fig. 7: Total deformation during standing up condition for (a) Bone material, (b)Prosthetic material

In this analysis, maximum stress for bone orthotropic material and isotropic material is found 11.525 MPa and 20.425 MPa. In this analysis, maximum stress for Ti-6Al-4V material and SS316L material is found 21.45 MPa and 20.897 MPa. In standing up condition, stress developed in Ti-6Al-4V material's bone is greater than SS316L material but the stress developed nature have similarity. From contour Fig. 8, maximum stress is always found in femoral neck shaft angle during standing up gait cycle.

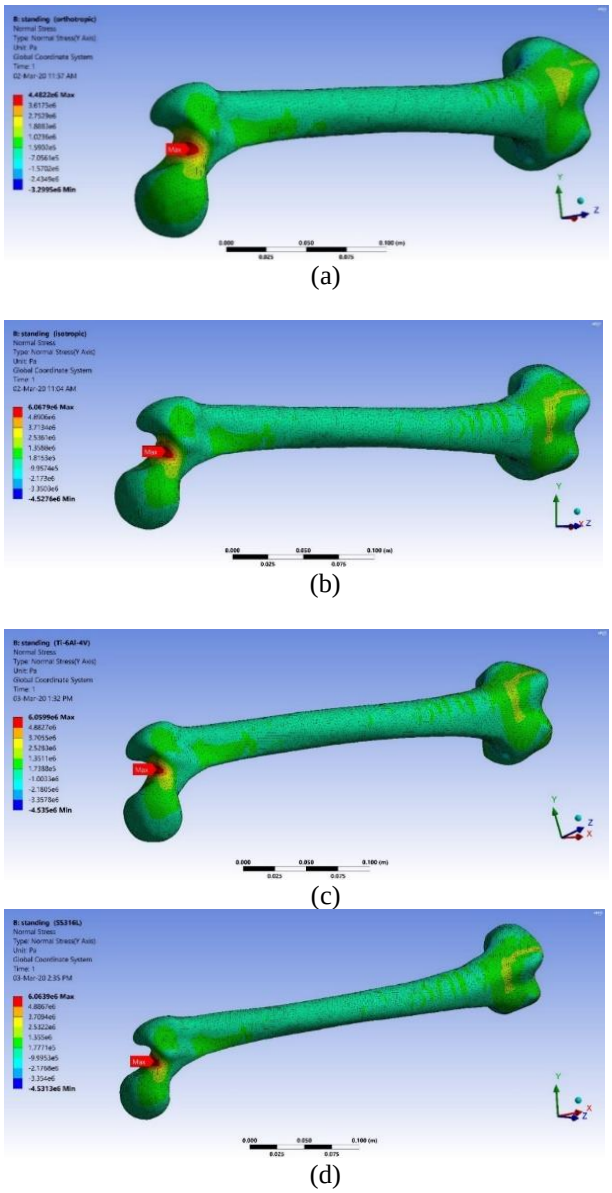

(a) (b) (c) (d)

Fig. 8: Normal stress distribution during standing up condition for (a) Bone orthotropic material,(b) Bone isotropic material, (c) Ti-6Al-4V material, (d) SS316L material

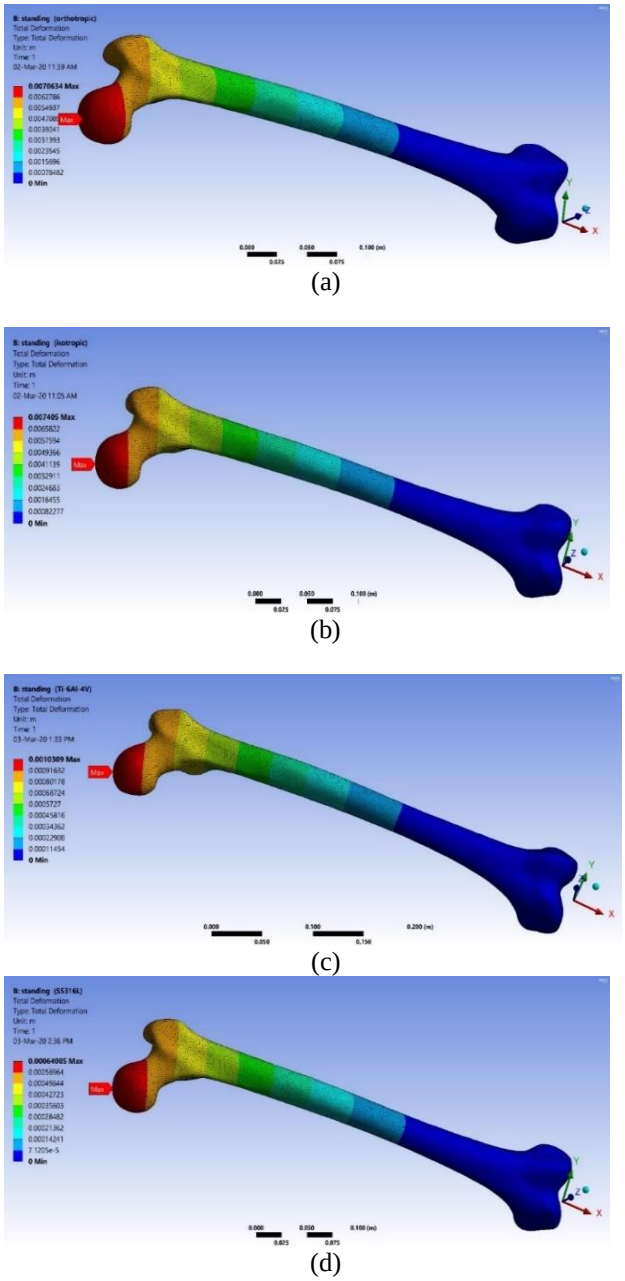

(a) (b) (c) (d)

Fig. 9: Total deformation during standing up condition for (a) Bone orthotropic material, (b) Bone isotropic material, (c) Ti-6Al-4V material, (d) SS316L material

In this analysis, maximum deformation for bone orthotropic material and isotropic material is found 26.184mm and 27.317 mm. In this analysis, maximum deformation for Ti-6Al-4V material and SS316L material is found 3.8027mm and 2.364mm. In standing up condition, deformation in Ti-6Al-4V material's bone is greater than SS316L material but the deformation developed nature have similarity. From contour Fig. 9, maximum deformation is always found in femoral head during standing up gait cycle

In standing up condition, maximum stress and total deformation of femur bone material (orthotropic and

isotropic bone material, Ti-6Al-4V and SS316L) is shown in following Table 5.

Table 5: Maximum stress distribution and maximum deformation of femur bone during standing up

Activity	Material	Maximum stress (MPa)	Maximum deformation (mm)
Standing up	Bone orthotropic	11.525	26.184
	Bone isotropic	20.425	27.317
	Ti-6Al-4V	21.45	3.8027
	SS316L	20.897	2.364

4. CONCLUSION

In this research work, the behavior of human femur bone is analyzed in different loading condition. Normal stress distribution and total deformation for walking and standing activities are calculated in this study. Graphs are plotted for stress distribution and total deformation respect to time variable as gait cycle.

Normal stress and total deformation developed nature have similarities. Normal stress of bone for bone material (orthotropic and isotropic) are found lower than fracture stress. Maximum normal stress and maximum total deformation developed in neck-shaft angle and femoral head. So, the probability of femur neck fracture is high. Maximum normal stress and maximum total deformation of femur bone for Ti-6Al-4V material is higher than SS316L material. So, SS316L material is better for prosthetic femur bone design.

The methods used in this paper can be used to generate prosthetic designs for different bones, which will help in bone replacement.

ACKNOWLEDGMENT

The completion of this research could not have been possible without Femur bone which was provided by Luis Enrique Isaza Velasquez, Department of Mechanical Engineering, Universidad Tecnologica de Pereira, Colombia.

REFERENCES

[1] R. Nareliya and V. Kumar, “Biomechanical Analysis of Human Femur Bone,” International Journal of Engineering Science and Technology (IJEST), vol. 3, no. 4, pp. 3090-3094, 2011.

[2] Lengsfeld and Kaminsky, “Sensitivity of Femoral Strain Pattern Analyses to Resultant and Muscle Forces at the Hip Joint,” Journal of Medical Engineering Physics, vol. 18, no. 1, pp. 70-78.

[3] J. Perry and J. M. Burnfield, “Gait Analysis, Normal and Pathological Function,” Journal of Sports Science & Medicine, vol. 9, no. 2, 2010.

[4] G. Bergmanna and G. Deuretzbacher, “Hip contact forces and gait patterns from routine activities,” Journal of Biomechanics, p. 859–871, 2001.

[5] G. Bergmann and A. Bender, “Standardized Loads Acting in Hip Implants,” PLOS ONE, May 19, 2016.

[6] D. Ramanathan and M. B. Siqueira, “Current concepts in total femoral replacement,” World Journal of Orthopedics, vol. 5, pp. 919-926, 2015.

[7] A. R. Ahmed, “Total femur replacement,” Archives of Orthopaedic and Trauma Surgery, 2009.

[8] E. Isaza and L. Garcia, “Determination of Mechanic Resistance of Osseous Element through Finite Element Modeling,” in COMSOL Conference, Boston, 2013.

[9] A. Yousif and M.Y. Aziz, “Biomechanical Analysis of the human femur bone during normal walking and standing up,” IOSR Journal of Engineering (IOSRJEN), vol. 2, no. 8, pp. 13-19, 2012.

[10] P. P. Dash, K. Kishor and S. K. Panda, “Biomechanical Stressanalysis of Human Femur Bone,” in International Conference on Computer Aided Engineering, December 2013.

[11] A. Dhanopia and D.Manish, “Finite Element Analysis of Human Fracture Femur Bone Implantation with PMMA Thermoplastic Prosthetic Plate,” 11th International Symposium on Plasticity and Impact Mechanics, Implast 2016, pp. 1658-1665, 2017.

[12] N. K. KC and T. Tandon, “Biomechanical stress analysis of a Human Femur bone using ANSYS,” 4th International Conference on Materials Processing and Characterization, p. 2115 – 2120, 2015

[13] A. Javir and D. M. S. Kirkire, “Finite element analysis of Femur prosthesis,” in International Conference on Nascent Technologies in the Engineering Field (ICNTE-2017), January 2017.

[14] S. G. Ghalme and Ankush Mankar, “Biomaterials in Hip Joint Replacement,” International Journal of Materials Science and Engineering, vol. 4, no. 2, June 2016.

[15] X. Wang and T. Y. Wang, “The hip stress level analysis for human routine activities,” Biomedical Engineering Applications Basis and Communications, vol. 17, no. 3, pp. 153-158, 2005

[15] X. Wang and T. Y. Wang, The hip stress level analysis for human routine activities, Biomedical Engineering Applications Basis and Communications, vol. 17, no. 3, pp. 153-158, 2005

[16] L. Peng and J. Bai, “Comparison of isotropic and orthotropic material property assignments on femoral finite element models under two loading conditions,” Medical Engineering & Physics, vol. 28, no. 3, p. 227–233, April 2006.

[17] J. Koerber and S. Eberle, “Evaluation of Osteosynthesis Options and Fracture Healing Progress from Computed Tomography Based Finite Element Analysis,” International Federation for Medical and Biological Engineering (IFMBE), vol. 25, January 2010.

[18] H. Hermawan, D. Ramdan and J. R. P. Djuansjah, “Metals for Biomedical Applications,” IntechOpen, 2011.

[19] A. Inc., ANSYS Workbench User Guide, November 2009.

[20] K. V. Arun and K. K. Jadhav, “Behaviour of Human Femur Bone Under Bending and Impact Loads,” European Journal of Clinical and Biomedical Sciences, vol. 2, no. 3, pp. 6-13,2016

Paper ID: 2504

International Conference on Mechanical, Manufacturing and Process Engineering (ICMMPE – 2022)

Organizer: Faculty of Mechanical Engineering, Dhaka University of Engineering & Technology (DUET), Gazipur, Bangladesh

Website: https://icmmpeduet.com/

Analyzing Failure Modes of Turbochargers for Engine-based Power Plants by Combined SWARA-FMEA Approach

Ahmed Farhan[1], Md. Tanvir Siraj[2], Aklima Ahmed Nishi[3], Sheikh Navid Shadab Jamil[4], Rafsan Ahmed[5], Asif Kabir[6], Saddam Hossen[7]

[1,2,3]Department of Industrial and Production Engineering, BUET, Dhaka-1000, Bangladesh
[4,5,6]Department of Mechanical Engineering, BUET, Dhaka-1000, Bangladesh
[7]Department of Mechanical Engineering, DUET, Gazipur-1707, Bangladesh

E-mail: ahmed.farhan.04.05@gmail.com[1], tanvir25392@gmail.com[2]

ABSTRACT

A turbocharger is an essential mounting installed with the Internal Combustion (IC) engine of an engine-based power plant. Analyzing various failure modes of a turbocharger and their effects on operational safety and the performance of the engine is a crucial task for the managers of power plants. However, most of the existing scholarly articles on turbochargers' failure modes focused only on automobile turbochargers. Therefore, this study is conducted to determine some of the critical failure modes of industrial turbochargers mounted with large diesel engines of power plants through a relevant literature review. Then a Stepwise Weight Assessment Ratio Analysis (SWARA) and a Failure Mode and Effects Analysis (FMEA) are carried on with a combined approach to find the Risk Priority Number (RPN) of the failure modes. In this study, three criteria of the classic FMEA method- severity, probability, and detectability are weighted by the SWARA method. Then the weights are utilized in the FMEA to find the RPN values based on the weights of the criteria. Experienced maintenance managers of power plants have participated in a simple questionnaire-based evaluation process to opine in various steps of this study. In this study, surging of the turbocharger, rubbing of rotating parts, and increase in speed are detected as the top three failure modes with the highest RPN. The result achieved from this study is expected to help the managers of power plants to be more careful with the prioritized failure modes of the turbochargers for early detection and avoiding unnecessary failures.

Keywords: Turbocharger; Failure Mode and Effects Analysis; Stepwise Weight Assessment Ratio Analysis; Risk Priority Number

1. INTRODUCTION

Power plants need to run continuously to be synchronized with grid operations. Unscheduled downtime caused by any equipment failure can hamper productivity and decrease the reliability factor of a plant [1]. The engine-based power plants utilize the IC engines as the prime mover to generate electricity. The turbocharger installed with the engine of a power plant is an essential element of the scavenge air system, which influences the power output, efficiency of the engine, and exhaust gas emission [2]. The turbocharger and engine need to run simultaneously. Therefore, any unwanted failure of the turbocharger causes downtime of the engine, thus hindering continuous electricity generation. Precautionary failure analysis of turbochargers can help the operation and maintenance personnel of the power plants to detect and avoid unnecessary failures [1].

Several studies have depicted various mechanisms, improvisations, and analyses of turbocharger technology. For example, Pakale and Patel [3] concluded that turbochargers enhance the output of an IC engine without increasing the cylinder capacity; Panting et al. [4] showed that turbocharging of IC engines increases both power density and the cycle efficiency relative to naturally aspirated engines; Naser and Bashkim [5] presented simulated outcomes of temperature and pressure in engine cylinders for intercooler of the turbocharger, and also pressure and temperature change in intake and exhaust manifold of the engine; Galindo et al. [6] presented an analytical study of thermal energy transfer for a two-stage turbocharging with inter and aftercooler; Watel et al. [7] presented an orientation of low and high-pressure turbochargers in a series to overcome the effects of reduced exhaust pressure occurred at low speed of the engine, and so on. There are also several studies in the literature that have presented various techniques of failure analysis of turbochargers. For instance, Xu et al. [8] divided the turbocharger components into different clusters to sort out the failure modes and then analyzed them with an expert opinion-based fuzzy inferencing method; Liu [9] described that traditional FMEA has a shortcoming of obtaining similar RPN for different failure modes; Emovon [10] depicted a case study of hybrid multi-criteria decision making (MCDM) based FMEA framework for turbocharger; Knežević [2] presented a fault tree analysis method to diagnose turbocharger failures, and so on. However, no study has yet been conducted with the SWARA-FMEA combination to analyze the failure modes of the turbochargers used in power plant operations. Therefore, this study aims to present a SWARA-FMEA hybridized framework to find a weighted

RPN-based prioritization of the failure modes of turbochargers.

SWARA is a popular MCDM method that was introduced by Keršuliene et al. to determine the subjective weights of criteria [11]. The mathematical operation of this technique is comparatively simpler, and the obtained result is more consistent than Analytic Hierarchy Process (AHP) or pair-wise comparison-based other techniques. The SWARA method has been utilized to find criteria weights in land selection problems [12], supplier selection problems [13], performance evaluation [14], supply chain barriers determining [15], project risk prioritizing [16], and so on.

The novelty of this study is to mitigate the research gap in analyzing failure modes of turbochargers mounted in the large diesel engines of power plants. This study is going to perform a methodological approach by fulfilling the following objectives:

a) To determine failure criteria weights by SWARA.
b) To analyze the failure modes of the turbocharger.
c) To utilize the obtained weights of criteria in FMEA to determine the weighted RPN of the failures.
d) To depict a prioritization of the failure modes.

The rest of the paper is organized as: Section 2 is for discussing different components of turbochargers, Section 3 is for describing the methodology and calculation of the study, Section 4 is for results and discussions, and Section 5 is for a conclusion of the paper. Table 1 is showing a list of nomenclature used in this paper.

Table 1: List of Nomenclature

Nomenclature	Referred to
MCDM	Multi-Criteria Decision Making
FMEA	Failure Mode and Effects Analysis
IC	Internal Combustion
RPN	Risk Priority Number
SWARA	Stepwise Weight Assessment Ratio Analysis
WPM	Weighted Product Model

2. COMPONENTS OF TURBOCHARGER

A turbocharger is a specially designed mechanical device with a turbine and compressor working together on the same axis of rotation (see Fig. 1).

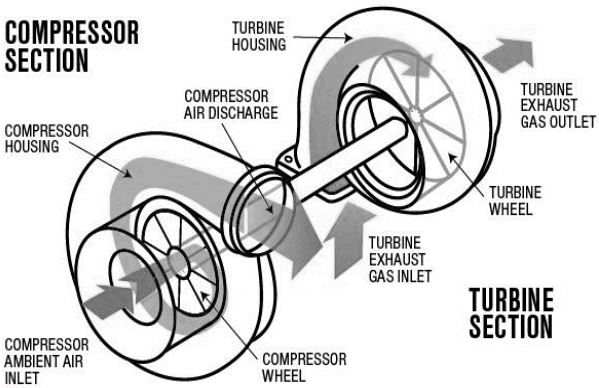

Fig. 1: Operating principle of a turbocharger [17]

The turbine gets energy from the exhaust gas of the IC engine, and the compressor gets energy from the turbine to force compressed air into the combustion chamber (see Fig. 2). This mechanism brings more charge air into the engine cylinder, thus increasing the combustion and power output of the engine [2], [3].

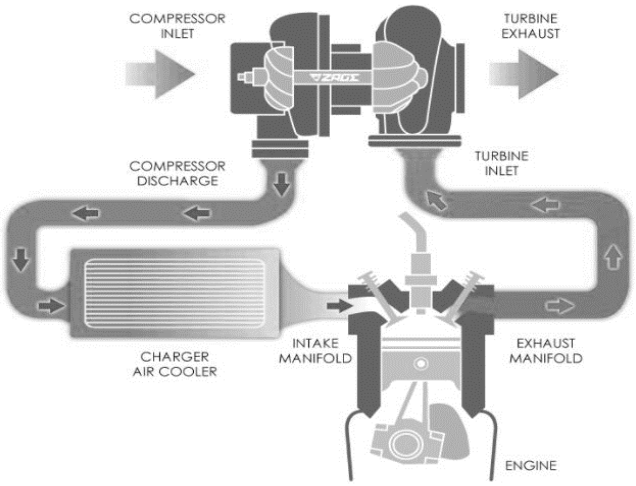

Fig. 2: Schematic diagram of turbocharging system [17]

There are different types of turbochargers like axial flow type, radial flow type, single, twin, twin-scroll, etc. [17]. Failure modes of a turbocharger largely depend on the system components. As a rotating machine, bearings and shafts are very important components of the turbocharger [2]. Besides these, some other fundamental components of a turbocharger are an air diffuser, filter silencer, compressor casing, turbine casing, compressor wheel, turbine wheel, nozzle ring, etc. A schematic diagram of the turbocharging system for an engine can be found in Fig. 2.

3. METHODOLOGY

This study has been designed and conducted with a methodological approach described below:

Step 1. Form a panel of experienced maintenance personnel from engine-based power generation plants.

Step 2. Enlist some basic failure modes of turbochargers based on the literature review, and experts' opinions and analyze regular maintenance data of the power plants.

Step 3. Take responses from the experts with a questionnaire-based survey to determine the weights of the criteria by applying the SWARA method and determine the risk values of failure modes.

Step 4. Utilize the obtained weights of the criteria and the risk values of the failure modes to determine the weighted RPN in the FMEA method.

Step 5. Prioritize the failure modes based on the descending values of the weighted RPN of the failure modes.

For this study purpose, 5 experienced maintenance managers of power plants have been interviewed to take responses at different stages of the study. All the experts have more than 10 years of working experience in engine-based power plant maintenance. Along with the literature

review, plant maintenance records from 3 engine-based power plants have been analyzed and reviewed by a panel of experts to enlist the basic failure modes of the turbochargers (see Table 2). Besides the failure modes, probable causes of failures have also been enlisted.

3.1 SWARA method

The basic technique of the SWARA method is based on the determination of the difference in the decimal preference values of the criteria. Experts have evaluated the importance of the criteria with a 5-points Likert scale, where 1 is very low and 5 is very high.

Table 2: Determined critical failure modes of a turbocharger with probable causes from existing literature

Failure period	Failure Modes (with relevant sources)	Probable Causes
Malfunction when starting	Delayed start-up (F1) [18]	Damaged bearing
		The rotor got rubbed with the outer casing
		Penetration of unwanted foreign object
	Abnormal vibrations (F2) [2], [19], [20]	Bearing damaged
		Unbalanced rotor
		Damaged turbine shaft
		Damaged compressor wheel
	Rubbing of rotating parts (F3) [20], [21]	Clearance is less than tolerance
Malfunction during operation	Lubricating Oil Pressure low (F4) [2]	Heavily contaminated oil filter
		Defective lube oil pump
		Faulty manometer display
		Excessive axial clearance of the rotor
	Drop-in speed (F5) [18], [22]	Malfunctioned pulse charging in engine cylinders
		Contaminated turbine shaft
		Contaminated nozzle ring
		Damaged rotor components
		Damaged Bearing
		Leaked exhaust lines of the engine
		Leaked charge air ducts of the engine
	Reduced compressor efficiency (F6) [2]	Exhaust gas temperature too high
		The malfunctioned injection system of the engine cylinder
		Blocked filter silencer of the turbocharger by dirt
		Contaminated compressor wheel
		Contaminated/damaged turbine shaft
		Sensor fault
		Contaminated charge air cooler
		Insufficient ventilation in the charge air cooler
		Unsealed air receiver of the engine
		Mistimed fuel injection in the engine cylinder
		Misadjusted valve controller of the engine
	Charge Air pressure too low (F7) [2]	Faulty manometer display
		Pressure dropped by filter silencer contamination
		Contaminated/damaged compressor wheel
		Contaminated/damaged turbine shaft
		High exhaust gas backpressure
	Charge air pressure too high (F8) [18]	The malfunctioned injection system of the engine cylinder
		Mistimed fuel injection in the engine cylinder
	Increase in speed (F9) [2], [8]	Contaminated compressor components
		Increased blade vibration of the compressor wheel
		Damaged blade of the compressor wheel
	Surging of the turbocharger (F10) [2], [20]	Contaminated/damaged protective grating
		Contaminated filter silencer
		Contaminated air diffuser
		Blocked charge air duct
Malfunction when stopping	Runout Noises (F11) [19]	Damaged bearing
		The rotor got rubbed with the outer casing
		Penetration of unwanted foreign object
	Runout time too short (F12) [21]	Damaged bearing
		The rotor got rubbed with the outer casing
		Penetration of unwanted foreign object
	Speed measuring system failure (F13) [19]	Sensor fault

Later the evaluations have been aggregated with geometric mean and then converted to decimal values by simple linear arithmetical operation. Thus, the score values (p_j) of the criteria are obtained. Further details procedure of the SWARA [11] method can be found below:

Step 1. Order the criteria according to the preferences of the experts.

Step 2. Find the comparative significance (s_j), starting from the second preferred criterion following Equation (1).

$$s_{j-1} = p_j - p_{j-1} \qquad (1)$$

Step 3. Compute the comparative coefficient (k_j) by applying Equation (2).

$$k_j = \begin{cases} 1, & j = 1 \\ s_j + 1, & j > 1 \end{cases} \qquad (2)$$

Step 4. Determine the recalculated weight (q_j), by using Equation (3)

$$q_j = \begin{cases} 1, & j = 1 \\ \frac{k_{j-1}}{k_j}, & j > 1 \end{cases} \quad (3)$$

Step 5. Calculate the weights of the criteria (w_j) by using Equation (4)

$$w_j = \frac{q_j}{\sum_{j=1}^{n} q_j} \quad (4)$$

3.2 FMEA method

The basic principle of the FMEA method is to assign the severity (S), probability (P), and detectability (D) values for each of the failure modes and then multiplied together to find the RPN [9]. A questionnaire-based evaluation can be used to gather experts' feedback for failure modes. The evaluation scores are placed on a 10-point scale. For severity, 1 is very minor, and 10 is extremely severe. For probability, 1 is nearly impossible, and 10 is almost certain. For detectability, 1 is very easy to detect and 10 is extremely difficult to detect. The mathematical expression for the FMEA method can be found in Equation (5)

$$RPN = Severity \times Probability \times Detectability \quad (5)$$

This study has utilized a modified application for the FMEA in which the basic principle is similar to the traditional method. 5 experts have evaluated the failure modes. Then, the evaluation scores are aggregated with a geometric mean. Finally, the concept of the Weighted Product Model (WPM) has been applied to determine the RPN of the failure modes. In that concept, weights of the criteria are used as the power of the evaluation scores before multiplying the values [23], as shown in Equation (6)

$$A_i^{WPM} = \prod_{j=1}^{n} X_{ij}^{w_i} \quad (6)$$

3.3 Calculations

Calculated weights of the criteria by the SWARA method can be found in Table 3 and Fig. 3.

Table 3: Calculated weights of the criteria

Preference order	Criteria	Pj	Sj	Kj	qj	wj
1	S	0.875		1.000	1.000	0.390
2	D	0.673	0.202	1.202	0.832	0.324
3	P	0.540	0.133	1.133	0.735	0.286

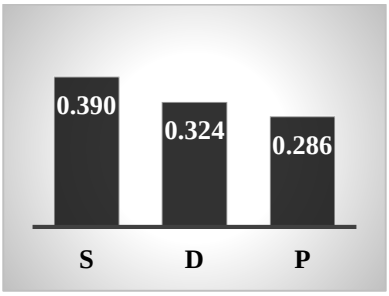

Fig. 3: Criteria weights

Computed aggregated evaluation scores of the failure modes of the turbocharger can be found in Table 4.

Table 4: Aggregated evaluations of the failure modes

	S	P	D
F1	3.178	5.933	3.817
F2	6.787	5.578	5.785
F3	6.188	7.384	7.789
F4	6.382	5.578	4.573
F5	3.565	6.382	5.378
F6	7.584	6.382	6.581
F7	3.776	6.188	6.787
F8	5.578	5.785	6.581
F9	6.581	5.578	8.790
F10	8.191	7.384	7.789
F11	4.782	6.188	6.188
F12	5.186	6.188	4.782
F13	3.776	6.787	8.790

Calculated weighted aggregated scores, RPN of the failure modes, and ranking can be found in Table 5.

Table 5: Weighted RPN and ranking of failure modes

	S	P	D	RPN	Ranking
F1	1.569	1.665	1.544	4.032	**13**
F2	2.109	1.636	1.767	6.093	**5**
F3	2.034	1.772	1.946	7.013	**2**
F4	2.059	1.636	1.637	5.512	**9**
F5	1.641	1.700	1.725	4.812	**12**
F6	2.202	1.700	1.842	6.894	**4**
F7	1.678	1.685	1.861	5.260	**11**
F8	1.953	1.653	1.842	5.947	**6**
F9	2.083	1.636	2.023	6.895	**3**
F10	2.269	1.772	1.946	7.823	**1**
F11	1.840	1.685	1.806	5.597	**8**
F12	1.899	1.685	1.661	5.313	**10**
F13	1.678	1.730	2.023	5.874	**7**

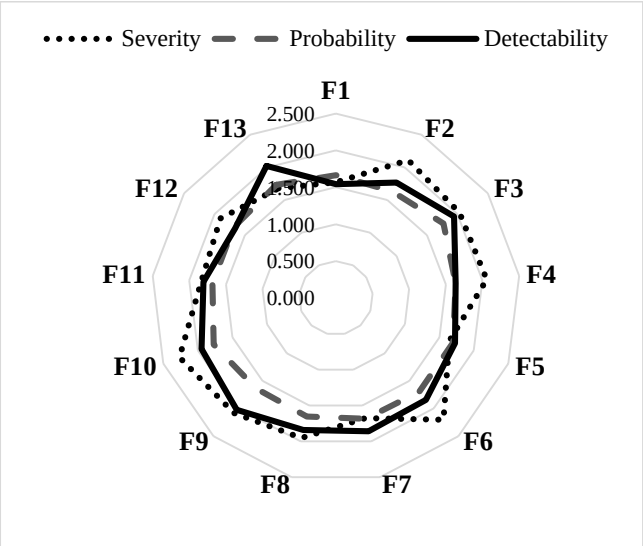

Fig. 4: Comparison of the obtained scores with Radar-chart

Here, Fig. 4 is depicting a Radar chart of the comparison of the obtained scores of the failure modes in each criterion.

It shows that obtaining the optimum score in all criteria rather than obtaining an outlier score in any one criterion makes a failure mode more prioritized over another. Fig. 5 is for showing the prioritization of the failure modes based on their obtained RPN from the final calculation.

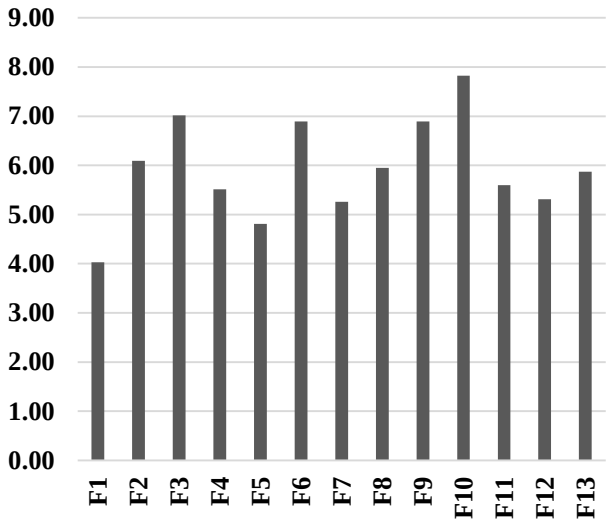

Fig. 5: Obtained result of the study

4. RESULTS AND DISCUSSIONS

This study finds the weights of the FMEA criteria with the SWARA method as Severity (0.390)> Detectability (0.324)> Probability (0.286). Experienced maintenance managers of power plants have weighted the criterion severity the most. This criterion is directly related to the life safety issues during operation. Besides this, severity also detects the impact of a failure mode on the overall operational failure [7]. Then, the experts decided that criterion detectability carries more weight than criterion probability. If a failure mode cannot be detected before the incident occurs, the severity of the failure becomes higher. There are many failures of a turbocharger that are very difficult to be detected. Those often misguide the maintenance personnel thus causing elongation of downtime of the plant. The probability of a failure mode can be described as a prediction of a failure based on previous incidents. Making some critical decisions about a failure only considering the probability is not effective most of the time. In a critical and technical operational condition of an IC engine and turbocharger, managers do not rely on the probability of a failure for major decision-making. Therefore, probability obtains fewer weights among the three criteria of the FMEA method.

This study has determined RPNs of the failure modes of the turbocharger used for power plant engines are as F10> F3> F9> F6> F2> F8> F13> F11> F4> F12> F7> F5> F1. From the obtained result, the top 5 failure modes can be discussed in this section.

'Surging of the turbocharger' obtains the highest weighted RPN among all the failure modes. Surging is a high pitch of vibration and creates a highly audible noise [24]. It impacts directly the performance of a turbocharger and becomes the reason for efficiency reduction. Diesel engines used in power plants are of low or medium speed. Surging phenomena are common for turbochargers in such engines. Whenever the gas flows with comparatively higher oscillation in the turbocharger, a reverse flow of scavenging air through the diffuser and impeller blades causes surging [20]. The bearing condition of the turbocharger shaft and proper lubricating oil should always be maintained, removing all blockage from the charge air duct is necessary to minimize this surging phenomenon.

In this study, the 'rubbing of rotating parts' is determined as the failure mode with the second-highest RPN. This is very hazardous for the physical condition and lifetime of the turbocharger. A turbocharger is a device with a very high speed. Rubbing the rotting parts like turbine or compressors blades can cause serious wearing and energy loss. This can also be the reason for the major breakdown of turbochargers which can be very severe in operational conditions [25]. Rubbing is sometimes overlooked due to the toughness of detectability in a high-speed machine. Unbalance shafts, improper bearings, uneven clearance with the casing, etc. are the causes of this type of failure mode.

'Increase in speed' of the turbocharger is another important failure mode to look after. Sudden speed up can be caused by an increase in exhaust temperature or pressure. The temperature and pressure of exhaust gas can increase due to air filter fault [2], or overloading of the engine. In this type of situation, the emergency shutdown of engines may require. Therefore, it is a very serious issue for power plant operations. However, sometimes sensor fault of the speed measuring system can mislead the speed increase of turbochargers. So, detecting the real cause of this phenomenon is comparatively more difficult than other failures.

'Reduced compressor efficiency' is another important failure mode to be noticed. The failures already described earlier in this section like, surging and rubbing of rotating parts are the main reasons for decreasing compressor efficiency. Some other causes can be detected for this failure (see Table 1). If the efficiency of the compressor reduces, the amount of intake air will be less in the combustion chamber. This will cause the efficiency loss of the engine as well. Therefore, to increase engine efficiency, the performance of the turbocharger's compressor should be monitored carefully.

'Abnormal vibrations' during the startup of the engine is another major failure mode of the turbocharger. At the starting time, the engine itself vibrates a lot. If there is any pre-existing abnormality in the bearings, rotors, and wheels of the turbocharger, the vibration can lead to major hazardous situations at starting of an engine. Therefore, regular monitoring is required to avoid such failure.

The top prioritized failure modes determined in this study were also described as the most critical failure modes of the industrial turbocharger in some of the previous studies

in the literature [2], [8], [20]. This comparability shows the relevance of the result obtained from this study.

5. CONCLUSION

This study has discussed some critical failure modes of the industrial turbocharger to determine the prioritization with a hybrid SWARA-FMEA approach.

Key results of the study: A prioritization or ranking of the critical failure modes of the industrial turbocharger is the main outcome of this study. The hybridized framework and the obtained result from this study can aid the managers to think of preventive maintenance and servicing schedule in a specific order based on the prioritization of the failure modes.

Contribution to the literature: The traditional FMEA often gives the same RPN for multiple failure modes, thus creating confusion for the industrial managers while taking critical decisions. The weighted RPN method of this study can minimize that drawback. Fulfilling the research gap in the case of analyzing the failure modes for industrial turbochargers is another important contribution of this work.

Some future study scope: More experienced industrial and academic experts can be involved in the evaluation procedure in future studies of FMEA for turbochargers. Some other combinations of the MCDM approach to design another hybridization framework can also be a prospective scope of the study. More characteristics and aspects of the failure modes can be discussed as well.

REFERENCES

[1] Kolawole, A., Agboola, O.O., Ikubanni, P.P., Raji, O.G. and Okechukwu Osueke, C., Reliability, and power loss analysis: A case study of a power plant in Nigeria. Cogent Engineering, 6(1), p.1579426, 2019.

[2] Knežević, V., Orović, J., Stazić, L. and Čulin, J., Fault tree analysis and failure diagnosis of marine diesel engine turbocharger system. Journal of Marine Science and Engineering, 8(12), p.1004, 2020.

[3] Pakale, P.N., and Patel, S.U., Performance analysis of IC engine using supercharger and turbocharger-A review. IJRET: International Journal of Research in Engineering and Technology, 4(2), pp.17-22, 2015.

[4] Panting, J., Pullen, K.R. and Martinez-Botas, R.F., Turbocharger motor-generator for improvement of transient performance in an internal combustion engine. Proceedings of the Institution of Mechanical Engineers, Part D: Journal of Automobile Engineering, 215(3), pp.369-383, 2001.

[5] Naser, B.L. and Bashkim, I.B., Effect of Intercooler on Turbocharged Diesel Engine Performance, 2009.

[6] Galindo, J., Serrano, J.R., Climent, H. and Varnier, O., Impact of two-stage turbocharging architectures on pumping losses of automotive engines based on an analytical model. Energy Conversion and Management, 51(10), pp.1958-1969, 2010.

[7] Watel, E., Pagot, A., Pacaud, P. and Schmitt, J.C., Matching and evaluating methods for Euro 6 and efficient two-stage turbocharging diesel engine. In SAE 2010 World Congress & Exhibition (No. 2010-01-1229), 2009.

[8] Xu, K., Zhu, M., Fan, Z. and Gao, J., FMEA of turbocharged diesel engine system using fuzzy inferencing. SAE transactions, pp.529-535, 2000.

[9] Liu, H.C., You, J.X., Ding, X.F. and Su, Q., Improving risk evaluation in FMEA with a hybrid multiple criteria decision-making method. International Journal of Quality & Reliability Management, 2015.

[10] Emovon, I., Improving risk analysis capability of FMEA using evaluation based on distance from average solution (EDAS): a case study of turbocharger system. Journal of mechanical and energy engineering, 2, 2018.

[11] Keršuliene, V., Zavadskas, E. K., and Turskis, Z., Selection of rational dispute resolution method by applying new stepwise weight assessment ratio analysis (SWARA). Journal of business economics and management, 11 (2), 243–258, 2010.

[12] Majeed, R. A., and Breesam, H. K., Application of SWARA technique to find criteria weights for selecting landfill site in Baghdad governorate. In IOP conference series: Materials science and engineering (Vol. 1090, p. 012045), 2021.

[13] Singh, R. K., and Modgil, S., Supplier selection using SWARA and WASPAS–a case study of Indian cement industry. Measuring Business Excellence, 2020.

[14] Ulutaş, A., and Karaköy, Ç., An analysis of the logistics performance index of EU countries with an integrated MCDM model. Economics and Business Review, 5 (4), 49–69, 2019.

[15] Agarwal, S., Kant, R., and Shankar, R., Evaluating solutions to overcome humanitarian supply chain management barriers: a hybrid fuzzy SWARA–fuzzy WASPAS approach. International Journal of Disaster Risk Reduction, 51, 101838., 2020.

[16] Valipour, A., Sarvari, H., and Tamošaitiene, J., Risk assessment in PPP projects by applying different MCDM methods and comparative results analysis. Administrative Sciences, 8 (4), 80., 2018.

[17] Automotriz, M. I. Y., Turbocharger: components, working principles, and types. Ingeniería y mecánica automotriz. https://www.ingenieriaymecanicaautomotriz.com/turbocharger-components-working-principles-and-types/, 2019.

[18] Linsel, J., and Wanner, S., Two-stage Supercharging with a Scroll-type Supercharger and an Exhaust Gas Turbocharger. MTZ worldwide, 76(11), 18-23, 2015.

[19] Kirk, R. G., Alsaeed, A., Liptrap, J., Lindsey, C., Sutherland, D., Dillon, B., ... and Sterling, J., Experimental test results for vibration of a high speed diesel engine turbocharger. Tribology Transactions, 51(4), 422-427, 2008.

[20] Aretakis, N., Mathioudakis, K., Kefalakis, M. and Papailiou, K., Turbocharger unstable operation diagnosis using vibroacoustic measurements. J. Eng. Gas Turbines Power, 126(4), pp.840-847, 2004.

[21] Zhang, J., Sun, H., Hu, L., and He, H., Fault diagnosis and failure prediction by thrust load analysis for a turbocharger thrust bearing. In Turbo Expo: Power for Land, Sea, and Air (Vol. 44014, pp. 491-498), 2010.

[22] Vanhaelst, R., Kheir, A., and Czajka, J., A systematic analysis of the friction losses on bearings of modern turbocharger. Combustion Engines, 55(1), 22-31, 2016.

[23] Tofallis, C., Add or multiply? a tutorial on ranking and choosing with multiple criteria. INFORMS Transactions on education, 14 (3), 109–119, 2014.

[24] Kaushik, M., What is Turbocharger Surging? Marine Insight. https://www.marineinsight.com/main-engine/what-is-turbocharger-surging/, 2021.

[25] Bari, A. M., Siraj, M. T., Paul, S. K., & Khan, S. A., A hybrid multi-criteria decision-making approach for analyzing operational hazards in Heavy Fuel Oil-based power plants. Decision Analytics Journal, 100069, 2022.

Paper ID: 2689
International Conference on Mechanical, Manufacturing and Process Engineering (ICMMPE – 2022)
Organizer: Faculty of Mechanical Engineering, Dhaka University of Engineering & Technology (DUET), Gazipur, Bangladesh
Website: https://icmmpeduet.com/

Prediction of Heart Disease Using Different Machine Learning Algorithms And Their Performance Assessment

Ar-Rafi Hriday[1], Md. Limon Mia[1] and Md. Sazol Ahmmed [2]

[1] Department of Industrial & Production Engineering, Rajshahi University of Engineering & Technology, Rajshahi, Bangladesh-6204

[2] Assistant Professor, Department of Industrial & Production Engineering, Rajshahi University of Engineering & Technology, Bangladesh-6204

E-mail: arrafihriday@gmail.com

ABSTRACT

Disease diagnosis is the most important activity in the healthcare sector. Many lives can be saved if a disease is detected early. Machine learning classification techniques can greatly benefit the medical field by allowing for more precise and timely disease diagnosis. As a result, both doctors and patients can save time. Heart disease is the world's leading cause of death today, making it one of the most challenging diseases to diagnose. We present a survey of machine learning classification methods that have been proposed to assist healthcare professionals in diagnosing heart disease in this paper. There have been used two datasets. The UCI-heart-disease dataset and another Heart Disease Dataset are publicly available on the Kaggle website and used in our experiment. Both datasets contain 14 features of patient information. By applying different machine learning techniques such as Support vector machine (SVM), K-nearest neighbors (KNN), Decision Tree, and Tensor Flow (TF), we have achieved the highest 96.42% accuracy at KNN. We also show a comparison of the result of different techniques and datasets. Lastly, the more extensive dataset has provided more accuracy.

Keywords: Heart Disease; Prediction; Machine Learning; Data preprocessing; Visualization.

1. INTRODUCTION

The heart is considered one of the essential organs of the body. The heart functions as a pump that circulates blood across the body. That beats an average of 70 times in one minute [1]. The heart's ability to act efficiently is critical to human life. If the heart's capacity is inadequate, it can have an effect on various parts of the human body, including the cerebrum, kidneys, and so on. If the dissemination of blood by the body is wasteful, organs such as the heart and mind will suffer. Blood capture is often referred to as a stroke in the cerebrum, which is considered a heart attack. There are various forms of heart disease that affect different parts of the body [2].

1. Coronary artery disease (CAD)
2. Cardiomyopathy (heart disease)
3. Cardiovascular heart disease
4. Ischemic heart disease (IHD) is a form of ischemic heart disease
5. Hypertension (high blood pressure)
6. Congestive heart failure
7. Cardiomyopathy (inflammation of the heat)
8. Heart disease caused by Volvulus

Several factors increase the risk of heart disease. There are many factors that establish the risk of heart disease, such as a family history of cardiovascular disease, smoking, bad technique of feeding, fast pulse, cholesterol, high blood cholesterol, obesity, physical inertia, obesity, high blood pressure, stress or hypertension, chest pain, drug use, etc. [3]. For decades, heart disease (also known as cardiovascular disease) has been the leading cause of death worldwide. As per the most recent data published in 2017 by the WHO, In Bangladesh, deaths from heart disease accounted for 14.31 percent of total deaths and each year 17.9 million people die because of cardiovascular disease, 31 percent of the global deaths [4]. Between 1986 and 2006, a new study in rural Bangladesh found a dramatic increase in heart disease. Male mortality rates for age-standardized heart disease increased 30-fold (from 16 to 483 deaths per 100,000) and female mortality rates increased 47-fold (from 7 to 330 deaths per 100,000). In non-communicable diseases, there was a nine-fold increase (NCDs) [5].

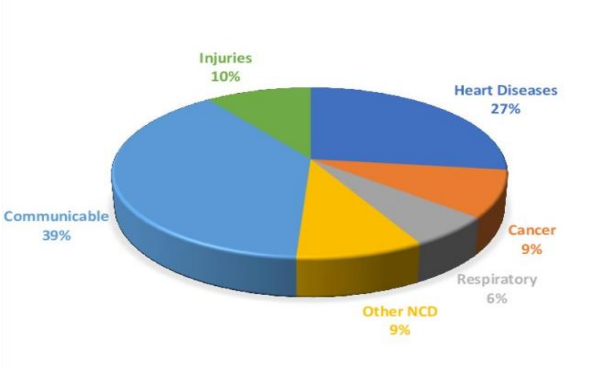

Fig. 1: Different Causes of Death in Bangladesh.

Generally, patients don't get enough to prepare for heart attack, but he got some symptoms that presume the probability of heart disease. There must be big data in the health care sector for infections, especially heart-related problems. This data can be used for the recognition of a similar patient early. Its need to analyze and categorize but not easy to do that work. Online data provide 76 attributes and not easy to handle them [6]. Here machine learning paves the way. Different types of algorithm are used to classify data some of them are clustering analysis, classification techniques, deep learning. Data can be trained and test here then have the model to get the probability of occurrence prediction which is most recent vogue. ML algorithm takes few times and provide better finding thus has been reduced cost and time.Generally, KNN, SVM, Deep Learning, Decision tree are used and these provide 67 to 92% accuracy [7]. Most of the researchers have used these techniques and so on. They also used hybrid algorithm. Some of them have used secondary data from online (UCI) and hardly of them used primary data.

Our objective is to predict whether a new patient has heart disease or not and find the maximum accuracy of two datasets and compare the result. Except for some private hospitals, most of the govt. Facilities are ancient. They were Struggling to handle an excessive patient with limited facilities. No planning has been made to resolve the issue. A lot of data is available but not in use which could have been helpful. Intern doctors need much time to become experts due to a lack of data analysis. Proper prediction is necessary to give the best service, but it is required early and precisely, which is impossible yet. Disease trends change time adequate analysis of data make concern. A lot of people are dying, struggling with a lot of diseases. Heart disease is one of the most critical issue, but we yet to see advanced technical implementation to brake the misery of the poor people.

We will analyze and categorize data according to similar characteristics and easily compare new data with them. Implementation of machine learning algorithms can play a significant role here. With the help of K-Nearest Neighbor (KNN), Support Vector Machine (SMV), Decision Tree, and Tensor Flow (TF) machine learning techniques, the prediction will be carried out. After collecting data, it will be preprocessed and visualized. Then processed data will be used to train and test every model. Then models will predict possessing the possibility of heart disease with its learning. Finally, a comparison of the effectiveness of these models will be shown.

.

2. LITERATURE REVIEW

There has been great related work like this paper; handling a large amount of data is quite tricky where the technical process application pares the way to be fast and effective. For this reason, machine learning is famous and has been used for decades. Different data analysis techniques are used in some areas of clustering type, classification-based, layer-based, and neural network type. Hence comes the performance comparison and effectiveness accuracy and precision. Most of the paper has used different algorithm and shows their result. Some of them have been compared among them. Mohan et.al has shown a comparison among different model and shown accuracy with using UCI dataset. Have been used 13 attributes and found best accuracy at HRFLM (88.4%) and SMV (86.1%) [7]. Different machine learning calculations were carried out by Dinesh et al. For example, Logistic regression, Random forest, Naïve Bayes, Gradient boosting and SMV. They have also collected database from UCI machine learning respiratory. Their better result come out at Logistic regression (86%) and Naïve Bayes (84%). Support Vector Machine (SMV) provided (79%) [8]. In this study, the paper has depicted diverse method such as classifications (decision tree), (clustering, KNN), and (deep learning), (logistic regression). They have shown that random forest got 91.2% accuracy and logistic regression 92.76% [9]. Amin Ul Haq and Memon et.al proposed a hybrid intelligent machine learning based predictive system for diagnosis of heart disease. They used Cleveland heart disease dataset. They have shown different accuracy at different proposed model, Such as logistic regression 84% accuracy, KNN 76% accuracy and also artificial neural network 76%, Naïve Bayes 83% accuracy [10]. After executing studying over the paper, we have seen of using several classification machine learning algorithms, such as, Naïve Bayes (86.41%), ANN (89.01%), Decision tree (76%), KNN (94%), SMV (61.86%), Hybrid use (86.55%) where hybrid model much better result as well [11]. Koushik and Arup et.al used seven classifiers such as Navie Bayes, Bayes Net and SMO etc. They have collected only 116 sample and used 11 attributes and got overall 67 to 70% accuracy on seven classify [12]. Andreeva and his colleague executed several method foe diagnosis heart diseases using different data mining techniques where naïve

Bayes showed 78.563%, decision tree showed 75.723%, Neural network showed 82.773% accuracy [13]. VV Ramalingam have used SMV, KNN, and ANN and got accuracy of 82 to 94%. Dataset was from UCI which is very common as well [14]. Rajesh did not mention the accuracy rate, talked just about what he got. Have found more accurate result and mention the use of combination of Naïve Bayes and K-mean [15]. My Chau Tu, Dongil Shin, and DongKyoo Shin attempted a Bagging Approach to Effective Diagnosis of Heart Disease. They have shown bagging (81.41%) is more accurate than decision tree (78.91%) but the generated knowledge or combined models are difficult to analyze [16]. An Optimized Stacked Support Vector Machines Based Expert System for the Effective Prediction of Heart Failure was attempted by Liaqat Ali et al. The aim of this paper is to make it easier to diagnose heart failure. The SVM model was used to filter out irrelevant functions, while the second model served as a predictive model. A hybrid grid search algorithm was used to optimize both models. The proposed approach outperformed ten well-known existing approaches in the literature as well as other cutting-edge machine learning models. It was also discovered that the proposed model increases the traditional SVM model's power by 3.3 percent. [17]. Performance evaluation of various machine learning techniques for prediction of heart disease was attempted by Ashok Kumar Dwivedi. In this paper, SMV, ANN, Logistic regression, Naive Bayes, tree classification, and KNN are used, with Logistic regression (85%) providing the most reliable results [18]. Ebenezer O. Olaniyi tried to diagnose heart disease using a neural network. They found that KNN (45.67 percent), Decision Tree (84.35 percent), Nave Bayes (82.31 percent), WAC (84 percent), and BPNN were all accurate (85 percent) [19]. Heart Disease Prediction and Classification Using Machine Learning Algorithms Optimized by Particle Swarm Optimization and Ant Colony Optimization was attempted by Youness Khourdifi. The models that are most likely to function in the data set are Nearest Neighbor KNN, Random Forest RF, and Artificial Neural Network MLP. FCBF, PSO, and ACO's proposed optimized model has a KNN accuracy score of 99.65 percent and an RF accuracy score of 99.6 percent [20]. Mythili T., Dev Mukherji et al. attempted to develop a heart disease prediction model using SVM, Decision Trees and Logistic Regression (SDL). This paper proposed a method for predicting heart disease using a combination of support vector machines, logistic regression, and decision trees, but no neural network or ensemble algorithms were used [21]. They have considered 13 attributes and introduced four separate algorithms for precision analysis. They found that Gaussian Naive Bayes and Random Forest are giving the highest degree of accuracy in dataset, which is 91.21 per cent and Decision Tree, is performing the lowest degree of accuracy of 84.62 percent [22]. They have used Multi Layers Perception (MLP) in the proposed framework due to its performance and precision. Also, the algorithms produce the consistent an output nearby, dependent on the feedback given by the user [23]. Kelwade and Salanker suggested the RBFN, which operates on both linear and nonlinear heart disease datasets. The network has a 95.9% accuracy rate [24]. For the Cleveland dataset, Karayilan and Kiliç proposed an ANN predictive model using the back propagation algorithm, which achieved accuracy of nearly 95% [25]. Uyar and Ilhan used a genetic algorithm (GA) combined with a recurrent fuzzy neural network to diagnose heart disease with a 97.78 percent accuracy [26].

After executing a lot of surveys, it has been found that the prediction accuracy rate didn't very much. Some researchers get higher results in SMV; others may get in KNN or Logistic Regression, ANN, Deep Learning, and Hybrid models, but the variation is not remarkable. Hybrid models get almost the same percentage of result in every survey, 84 to 87 percent, and a new type of application have been used. Every paper was much close to each other that it didn't need to get a complete overview of models and algorithm studying a lot. Everyone uses 3 to 7 methods on average. Most researchers have used limited attributes and less data, but we have used two datasets and more test & train data, which gives more precise results. Also, compare the impact of datasets no one researcher may not see.

3. THEORETICAL BACKGROUND

3.1 K Nearest Neighbor (KNN)

It is a clustering-based algorithm for absolute value. Data from the data are plotted in XY plane to find similarities or dissimilarities forming many groups. In a group they possess the closest characteristics. And group member quantity refers K (nearest neighbor). It has seen 4 from the figure we have shown. K-Nearest Neighbor is a classification algorithm that uses a collection of labeled points to teach it how to mark new ones.

The algorithm categorizes cases based on how close they are to each other. Data points near each other in the KNN are referred to as neighbors. Cases with the same class marks are clustered together. The distance between two instances measures dissimilarity. This disparity can be assessed in a variety of ways. It was achieved using Euclidean distance in this case. Each data point (x, y) is plotted in the XY plane. Choose a K worth. Calculate the Euclidean distance (D) between the cases in the data set and the new issue.

We have trained the model with 70% data and tested the model with the rest of the data. Using the formula given bellow the Euclidean distance was measured. The distance value have been used to makes some clusters, specially neigbour cluster. K means members inside the clusters.Arbitarily a value was taken for K and similarity was observed.After repeating the process, increasing or decreasing the value of K the most suitable value was

found. Compared values ,presented in Fig 2.1 .KNN model scored highest when it took 5 neighbours.

The formula for calculating this distance:

$$D = \sqrt{\sum_{i=1}^{n} (X_i - Y_i)^2} \quad (1)$$

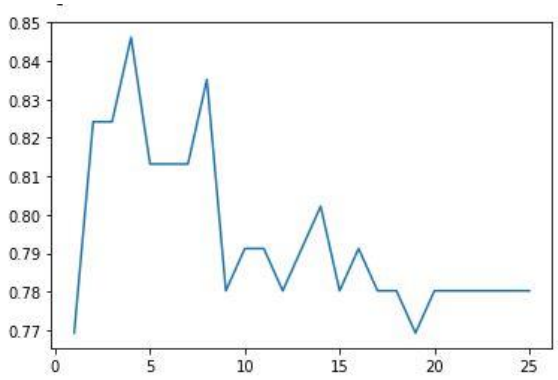

Fig. 2: Finding K Nearest Neighbor's Value.

3.2 Support Vector Machine

Support Vector Machine (SVM) are supervised learning models which analyze data for classification. One the model has been trained, it can be used to predict a new or unknown case with high accuracy. It classifies cases by finding a separator. Here SMV worked by first mapping data to a high dimensional feature space to be categorized and then a separator wass estimated. The separator have been drawn as a hyperplane not linear. Data points fell into two categories with a curve. Then mapped data to three-dimensional space and the separator is shown as the plane. This plane has been used to classify new or unknown causes.

3.3 Decision Tree

Is to create a model that might be useful for another patient with the same illness in the future. The dataset's feature set includes age, chest pain, cholesterol, and other factors, and the target is heart disease, which is classified as (1) or (0) using a binary classifier. Decision trees are constructed by dividing the training set into two or more nodes, single nodes are also split into sub-nodes. Each sub-node contained same categories of data. Each attribute considered individually to build a decision tree. First, selection of a feature from the dataset and calculated the attribute's significance in the data splitting. Splited the data based on the best attribute's value, then went to each branch and repeated the process for the remaining features. Following the construction of these trees, estimation was done of the class of unknown events. The method divided the training records into segments by minimizing impurity at each level using recursive partitioning. The entropy of data in a node was used to measure its impurity. The sum of information disorder or randomness in the data was measured by entropy. The entropy in a node is measured for each node and was determined by how much random data it contains. It has been searching for trees with the smallest entropy in their nodes in decision trees. The homogeneity of the samples in that node was also calculated using the entropy. The entropy of a model is zero if the samples are homogeneous and one if the pieces are evenly divided. Node's entropy was easily measure using the attribute's frequency table and the entropy formula, where P stands for the proportion or ratio of a group. Then tested various features to see which one was the most efficient, resulting in two more pure branches. knowledge gain was such information that could raise the degree of certainty. It was a tree's entropy before the split minus the weighted entropy after the attribute split. Entropy is opposites to information gain .As entropy or randomness decreases, the knowledge gain, or degree of certainty, rises and vice versa. So, identifying attributes that return the most knowledge benefit was the key to building a decision tree.

3.4 Tensor Flow

Tensor Flow is an open-source artificial intelligence library. A vector or matrix of n Dimension representing all the operations conducted inside graph. The graph was a set of computations that took place successively. It allowed to the development of data flow graphical structures that described how data moves through a graph or a series of processing nodes. Each node in the graph represented a mathematical operation and each connection or edge between nodes was a multidimensional array. It was used to create a large-scale neural network with many layers(Input layer, hidden layers,output layers). The mathematical model actually functioned in hidden layers.

4. METHODOLOGY

There have been a collection of two datasets, one is more significant, and another is relatively smaller. Then both the data sets were preprocessed and visualized. After that, machine learning methods were applied. A large portion of the data was used to train (70%) and others to test. For this purpose, four-fold clustering was used. With the help of KNN, SMV, Decision Tree, and Tensor Flow techniques, the prediction was made. Lastly, it was found

out which machine learning model gave the best result and accuracy in predicting heart disease.

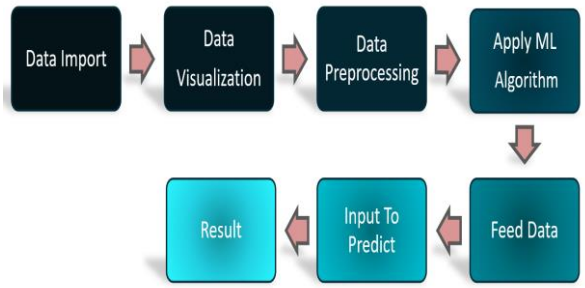

Fig. 3: Working flow diagram of proposed model.

5. DATA COLLECTION & RESULT ANALYSIS

5.1 Data collection

We have collected 2 datasets from Kaggle. The first one is from UCI heart disease dataset [27]. And the second one is Heart disease dataset of David Lapp [28]. Basically, they are secondary data where first data set contain 303 patient's record and the other 1025. Each data set makes a matrix. Every patient's record represents a row and number of attributes represent column.70% of the data was trained and 30% was used for test. This figure1 just gives a recorded view in the model. It ensures the data are exactly ready to processing.

	age	sex	cp	trestbps	chol	fbs	restecg	thalach	exang	oldpeak	slope	ca	thal	target
0	63	1	3	145	233	1	0	150	0	2.3	0	0	1	1
1	37	1	2	130	250	0	1	187	0	3.5	0	0	2	1
2	41	0	1	130	204	0	0	172	0	1.4	2	0	2	1
3	56	1	1	120	236	0	1	178	0	0.8	2	0	2	1
4	57	0	0	120	354	0	1	163	1	0.6	2	0	2	1
...	...	...	...	...	...	...	...	...	...	...	...	...	...	...
298	57	0	0	140	241	0	1	123	1	0.2	1	0	3	0
299	45	1	3	110	264	0	1	132	0	1.2	1	0	3	0
300	68	1	0	144	193	1	1	141	0	3.4	1	2	3	0
301	57	1	0	130	131	0	1	115	1	1.2	1	1	3	0
302	57	0	1	130	236	0	0	174	0	0.0	1	1	2	0

303 rows × 14 columns

Fig. 4: Brief of Frist Data Set Attributes.

	age	sex	cp	trestbps	chol	fbs	restecg	thalach	exang	oldpeak	slope	ca	thal	target
0	52	1	0	125	212	0	1	168	0	1.0	2	2	3	0
1	53	1	0	140	203	1	0	155	1	3.1	0	0	3	0
2	70	1	0	145	174	0	1	125	1	2.6	0	0	3	0
3	61	1	0	148	203	0	1	161	0	0.0	2	1	3	0
4	62	0	0	138	294	1	1	106	0	1.9	1	3	2	0
...	...	...	...	...	...	...	...	...	...	...	...	...	...	...
1020	59	1	1	140	221	0	1	164	1	0.0	2	0	2	1
1021	60	1	0	125	258	0	0	141	1	2.8	1	1	3	0
1022	47	1	0	110	275	0	0	118	1	1.0	1	1	2	0
1023	50	0	0	110	254	0	0	159	0	0.0	2	0	2	1
1024	54	1	0	120	188	0	1	113	0	1.4	1	1	3	0

1025 rows × 14 columns

Fig. 5: Brief of Second Data Set Attributes.

5.2 Attribute Analysis

Age is an essential factor closely related; the more aging, the higher the tendency to reveal heart disease. Usually, females are less intended to heart disease relative to males. Chest pain can help to measure the level or symptoms of heart disease. Higher and lower blood pressure are detrimental to the heart. Excessive of them can harm. Cholesterol is one of the crucial factors to cause heart functioning. The higher cholesterol the higher chance to heart blockage. FBS (Blood sugar level on fasting) it's important because sugar level maintenance causes dysfunction in later times. As well, resting thatch, old peak is also the essential factor. SAS (stress, altitude, sleep) are considered an important factor of the attribute as a person's capability to maintain pressure and stress impact the heart. Longtime stress and excessive pressure cause heart problems. The patient should be proper statement on this.

Table 1: Descriptions of Attributes.

Attribute	Description of Attributes	Type
1. Age	Patient's age in years	Numeric
2. Sex	Represent Male (1), Female (0)	Nominal
3. Chest Pain	The type of Chest pain (categorized in 3 values)	Nominal
4.Testbps	Level of blood pressure at resting mood(mm/Hg)	Nominal
5.Cholesterol	Serum cholesterol in mg/dl	Numeric
6.Fbs	Blood sugar levels on fasting >120 mg/dl;(1-True,0-False)	Nominal

7.Resting	Result of electrocardiogram (Binary value)	Numeric
8.Thalach	The performance of the optimum heart rate	Numeric
9.Exang	Angina induced by exercise (yes -1, No- 0)	Numeric
10.Old Peak	Exercise-induce ST depression in comparison with the state of rest	Nominal
11.Slope	Three values for the ST section calculated in terms of the slope during peak exercise.	Numeric
12.Ca	Stress, attitude, and proper sleep (0 to 3 value)	Nominal
13.Thal	The condition of the heart is represented by clearly numbered values. (1 to 3)	Numeric
14.Target	Heart Disease found (1), Not found (0)	Nominal

5.3 Corelation Analysis

Figure 6 describe the correlation between each attribute. Relation weight varies 0 to 1. Strong relation means near to 1. Here link has shown for 6 attributes. How they are dependent to each other. For example, age and trestbps have higher weighted relation (0.27) where age and thalach negative connection means period hardly relates to thalach.

`

Fig. 6: Attribute Correlation Heatmap.

5.4 Result Analysis

We have found our accuracy 82.31%,85.42% at Tensor Flow, 85.71%,96.42% accuracy at K Nearest Neighbor, SMV gave 81.31%, 94.48% accuracy, and Decision Tree has found 74.42%,95.2% as well. Results have been shown from two datasets. The model was trained with 50 to 70% of the data, and the rest was used to test it. Models will take 13 attributes of a new patient and provide 0 or 1 value of prediction. Patients who have heart disease will be recognized by 1 and 0 have no heart disease.

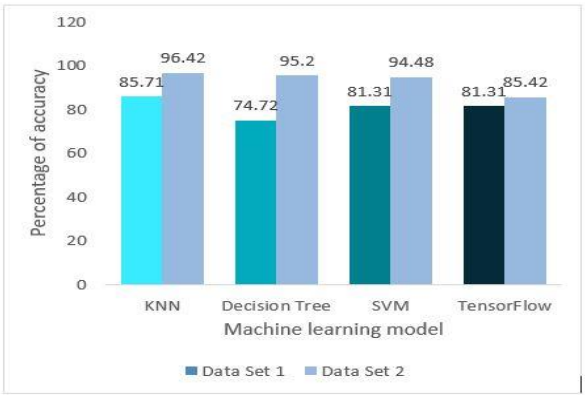

Fig. 7: Comparison of Accuracy among Two Datasets.

6. CONCLUSION & FUTURE WORK

In this work, Several algorithms such as KNN, Decision Tree, SVM, and Tensor Flow are applied to the heart disease dataset. Then, each classification algorithm's outcome is used to determine the better classifiers among them. More data give the highest accuracy of the result. In this experiment, KNN gives the highest performance at 96.42% for dataset 2.

However, there are several limitations to this approach. There are several missing attributes in the gathered heart disease data that are updated.. As a result, we are limited in our reach. This effort produced good results. In the future, we will use the most recent heart disease information to achieve more accurate results from contemporary learning strategies such as Artificial Neural networks, Deep learning, and advanced machine learning techniques.

REFERENCES

[1] M. S. ISLAM and M. J. AHMMED, "HEART DISEASE RISK PREDICTION USING MACHINE LEARNING TECHNIQUES," *Africa's potential Ecol. Intensif. Agric.*, vol. 53, no. 9, pp. 1689–1699, 2013.

[2] M. A. jabbar, B. L. Deekshatulu, and P. Chandra, "Classification of Heart Disease Using K- Nearest Neighbor and Genetic Algorithm," *Procedia Technol.*, vol. 10, pp. 85–94, 2013.

[3] Y. Xing, J. Wang, Z. Zhao, and A. Gao, "Combination Data Mining Methods with New Medical Data to Predicting Outcome of Coronary Heart Disease," *2007 Int. Conf. Converg. Inf. Technol. Comb.*, pp. 868–872, 2008.

[4] "Cardiovascular diseases." [Online]. Available: https://www.who.int/health-topics/cardiovascular-diseases/#tab=tab_1. [Accessed: 17-Apr-2021].

[5] "Bangladesh | Cadi." [Online]. Available: https://cadiresearch.org/topic/asian-indian-heart-disease/cadi-bangladesh. [Accessed: 29-Apr-2021].

[6] "UCI Machine Learning Repository: Heart Disease Data Set." [Online]. Available: https://archive.ics.uci.edu/ml/datasets/Heart+Disease. [Accessed: 30-Apr-2021].

[7] S. Mohan, C. Thirumalai, and G. Srivastava, "Effective heart disease prediction using hybrid machine learning techniques," *IEEE Access*, vol. 7, pp. 81542–81554, 2019.

[8] M. Balakrishnan, A. B. Arockia Christopher, P. Ramprakash, and A. Logeswari, "Prediction of Cardiovascular Disease using Machine Learning," *J. Phys. Conf. Ser.*, vol. 1767, no. 1, pp. 1–7, 2021.

[9] S. M. M. Hasan, M. A. Mamun, M. P. Uddin, and M. A. Hossain, "Comparative Analysis of Classification Approaches for Heart Disease Prediction," *Int. Conf. Comput. Commun. Chem. Mater. Electron. Eng. IC4ME2 2018*, pp. 1–4, 2018.

[10] A. U. Haq, J. P. Li, M. H. Memon, S. Nazir, R. Sun, and I. Garciá-Magarinõ, "A hybrid intelligent system framework for the prediction of heart disease using machine learning algorithms," *Mob. Inf. Syst.*, vol. 2018, 2018.

[11] M. Aljanabi, M. Qutqut, and M. Hijjawi, "Machine Learning Classification Techniques for Heart Disease Prediction: A Review," *Int. J. Eng. Technol.*, vol. 7, no. October, pp. 5373–5379, 2018.

[12] K. C. Howlader, "Performance Analysis of Different Classification Algorithms that Predict Heart Disease Severity in Bangladesh," *Int. J. Comput. Sci. Inf. Secur.*, vol. 15, no. 5, pp. 332–340, 2017.

[13] P. Andreeva, "Data Modelling and Specific Rule Generation via Data Mining Techniques. International Conference on Computer Systems and Technologies - CompSysTech.," *Int. Conf. Comput. Syst. Technol. - CompSysTech' 2006*, pp. 1–6, 2006.

[14] V. V. Ramalingam, A. Dandapath, and M. Karthik Raja, "Heart disease prediction using machine learning techniques: A survey," *Int. J. Eng. Technol.*, vol. 7, no. 2.8 Special Issue 8, pp. 684–687, 2018.

[15] N. Rajesh, T. Maneesha, S. Hafeez, and H. Krishna, "Prediction of heart disease using machine learning algorithms," *Int. J. Eng. Technol.*, vol. 7, no. 2.32 Special Issue 32, pp. 363–366, 2018.

[16] M. C. Tu, D. Shin, and D. K. Shin, "Effective diagnosis of heart disease through bagging approach," *Proc. 2009 2nd Int. Conf. Biomed. Eng. Informatics, BMEI 2009*, 2009.

[17] L. Ali *et al.*, "An Optimized Stacked Support Vector Machines Based Expert System for the Effective Prediction of Heart Failure," *IEEE Access*, vol. 7, pp. 54007–54014, 2019.

[18] A. K. Dwivedi, "Performance evaluation of different machine learning techniques for prediction of heart disease," *Neural Comput. Appl.*, vol. 29, no. 10, pp. 685–693, 2018.

[19] E. O. Olaniyi, O. K. Oyedotun, A. Helwan, and K. Adnan, "Neural network diagnosis of heart disease," *2015 Int. Conf. Adv. Biomed. Eng. ICABME 2015*, pp. 21–24, 2015.

[20] Y. Khourdifi and M. Bahaj, "Heart disease prediction and classification using machine learning algorithms optimized by particle swarm optimization and ant colony optimization," *Int. J. Intell. Eng. Syst.*, vol. 12, no. 1, pp. 242–252, 2019.

[21] M. T., D. Mukherji, N. Padalia, and A. Naidu, "A Heart Disease Prediction Model using SVM-Decision Trees-Logistic Regression (SDL)," *Int. J. Comput. Appl.*, vol. 68, no. 16, pp. 11–15, 2013.

[22] M. Praveen Kumar Reddy, T. Sunil Kumar Reddy, S. Balakrishnan, S. M. Basha, and R. K. Poluru, "Heart disease prediction using machine learning algorithm," *Int. J. Innov. Technol. Explor. Eng.*, vol. 8, no. 10, pp. 2603–2606, 2019.

[23] G. Choudhary and S. Narayan Singh, "Prediction of heart disease using machine learning algorithms," *Proc. Int. Conf. Smart Technol. Comput. Electr. Electron. ICSTCEE 2020*, no. Iceca, pp. 197–202, 2020.

[24] J. P. Kelwade and S. S. Salankar, "Comparative study of neural networks for prediction of cardiac arrhythmias," *Int. Conf. Autom. Control Dyn. Optim. Tech. ICACDOT 2016*, pp. 1062–1066, 2017.

[25] T. Karayilan and Ö. Kiliç, "Prediction of Heart disease using neural network," *2nd Int. Conf. Comput. Sci. Eng. UBMK 2017*, pp. 719–723, 2017.

[26] K. Uyar and A. Ilhan, "Diagnosis of heart disease using genetic algorithm based trained recurrent fuzzy neural networks," *Procedia Comput. Sci.*, vol. 120, pp. 588–593, 2017.

[27] "Heart Disease UCI | Kaggle." [Online]. Available: https://www.kaggle.com/ronitf/heart-disease-uci. [Accessed: 29-Apr-2021].

[28] "Heart Disease Dataset | Kaggle." [Online]. Available: https://www.kaggle.com/johnsmith88/heart-disease-dataset. [Accessed: 29-Apr-2021].

APPENDIX:

```
import sklearn
import numpy as np
import pandas as pd
import plotly as plot
import plotly.express as px
import plotly.graph_objs as go

import cufflinks as cf
import matplotlib.pyplot as plt
import seaborn as sns
import os
from sklearn.metrics import accuracy_score,mean_squared_error
import plotly.offline as pyo
from plotly.offline import init_notebook_mode,plot,iplot

pyo.init_notebook_mode(connected=True)
cf.go_offline()
heart=pd.read_csv('heart.csv')
info = ["age","1: male, 0: female","chest pain type, 1: typical angina, 2: aty
pical angina, 3: non-
anginal pain, 4: asymptomatic","resting blood pressure"," serum cholestora
l in mg/dl","fasting blood sugar > 120 mg/dl","resting electrocardiographic
 results (values 0,1,2)"," maximum heart rate achieved","exercise induced
angina","oldpeak = ST depression induced by exercise relative to rest","the
 slope of the peak exercise ST segment","number of major vessels (0-
3) colored by flourosopy","thal: 3 = normal; 6 = fixed defect; 7 = reversabl
e defect"]
for i in range(len(info)):
    print(heart.columns[i]+":\t\t\t"+info[i])
heart['target']

heart.groupby('target').size()
heart.groupby('target').sum()
heart.info()
heart['target'].unique()
heart.hist(figsize=(14,14))
plt.show()
plt.bar(x=heart['sex'],height=heart['age'])
plt.show()
sns.barplot(x=heart['sex'],y=heart['age'],hue=heart['target'])
sns.barplot(heart["cp"],heart['target'])
sns.barplot(heart["sex"],heart['target'])
px.bar(heart,heart['sex'],heart['target'])
sns.distplot(heart["thal"])
sns.pairplot(heart,hue='target')
numeric_columns=['trestbps','chol','thalach','age','oldpeak']
sns.pairplot(heart[numeric_columns])
y = heart["target"]

sns.countplot(y)

target_temp = heart.target.value_counts()

print(target_temp)
# create a correlation heatmap
sns.heatmap(heart[numeric_columns].corr(),annot=True, cmap='terrain', li
newidths=0.1)
fig=plt.gcf()
fig.set_size_inches(8,6)
plt.show()
# create four distplots
plt.figure(figsize=(12,10))
plt.subplot(221)
sns.distplot(heart[heart['target']==0].age)
plt.title('Age of patients without heart disease')
plt.subplot(222)
sns.distplot(heart[heart['target']==1].age)
plt.title('Age of patients with heart disease')
plt.subplot(223)
sns.distplot(heart[heart['target']==0].thalach )
plt.title('Max heart rate of patients without heart disease')
plt.subplot(224)
sns.distplot(heart[heart['target']==1].thalach )
plt.title('Max heart rate of patients with heart disease')
plt.show()
plt.figure(figsize=(13,6))
plt.subplot(121)
sns.violinplot(x="target", y="thalach", data=heart, inner=None)
sns.swarmplot(x="target", y="thalach", data=heart, color='w', alpha=0.5)


plt.subplot(122)
sns.swarmplot(x="target", y="thalach", data=heart)
plt.show()
heart
# create pairplot and two barplots
plt.figure(figsize=(16,6))
plt.subplot(131)
sns.pointplot(x="sex", y="target", hue='cp', data=heart)
plt.legend(['male = 1', 'female = 0'])
plt.subplot(132)
sns.barplot(x="exang", y="target", data=heart)
plt.legend(['yes = 1', 'no = 0'])
plt.subplot(133)
sns.countplot(x="slope", hue='target', data=heart)
plt.show()
heart['target'].value_counts()
heart['target'].sum()
heart['target'].unique()
heart.isnull().sum()
X,y=heart,heart.target
X.drop('target',axis=1,inplace=True)
X.shape
y.shape
from sklearn.model_selection import train_test_split
from sklearn.preprocessing import StandardScaler
sc = StandardScaler()
X = sc.fit_transform(X)
X_train,X_test,y_train,y_test=train_test_split(X,y,random_state=10,test_si
ze=0.3,shuffle=True)
X_test
y_test
print ("train_set_x shape: " + str(X_train.shape))
print ("train_set_y shape: " + str(y_train.shape))
print ("test_set_x shape: " + str(X_test.shape))
print ("test_set_y shape: " + str(y_test.shape))
# Decision Tree Classifier
scores_dict = {}
from sklearn.tree import DecisionTreeClassifier
dt=DecisionTreeClassifier()
dt.fit(X_train,y_train)
prediction=dt.predict(X_test)
accuracy_dt=accuracy_score(y_test,prediction)*100
print("Accuracy on training set: {:.3f}".format(dt.score(X_train, y_train)))
print("Accuracy on test set: {:.3f}".format(dt.score(X_test, y_test)))
prediction
X_DT=np.array([[63 ,1, 3,145,233,1,0,150,0,2.3,0,0,1]])
X_DT_prediction=dt.predict(X_DT)
X_DT_prediction[0]
```

Paper ID: 2706
International Conference on Mechanical, Manufacturing and Process Engineering (ICMMPE – 2022)
Organizer: Faculty of Mechanical Engineering, Dhaka University of Engineering & Technology (DUET), Gazipur, Bangladesh
Website: https://icmmpeduet.com/

Ergonomics Analysis of Working Posture of Sawmill Worker Using Digital Human Modeling (DHM)

Md. Sumon Rahman[1,a)], Md. Masum Billah[1,b)], Md. Mahafuj Anam Murad[1,c)], Rakesh Roy[1,d)]

[1]*Department of Industrial and Production Engineering*
Jashore University of Science and Technology, Jashor7408, Bangladesh

[a)]Corresponding author: sumon.just16@gmail.com
[b)]md.masumbillah1675@gmail.com
[c)]mahafujmurad.info@gmail.com
[d)]rakeshroy996@gmail.com

Abstract: Manual material handling workers in sawmills are often exposed to physical discomfort or pain while performing the task. This health problem can have a long-term impact on productivity and worker efficiency. The primary goals of this study are to determine the prevalence of physical discomfort and examine the working postures of manual sawmill workers. One hundred fifty sawmill workers from Jashore, Bangladesh participate voluntarily in this study. Prevalence of body pain is assessed using structured questionnaires and discussions. In the Digital Human Model (CATIA V5R21), the working posture was reconstructed and developed, and then RULA (Rapid Upper Limb Assessment) assessment was performed. Results indicate that a top portion (78%) of the workers suffered from pain in different body parts. Whereas the most affected body region was the trunk (71%), and high levels of discomfort were in the neck (51%), trunk (45%), leg (39%), and wrist (20%). In addition, it has been found that the selected workers were working in awkward postures involving heavy manual lifting, carrying, pulling, and pushing the wood. From the RULA analysis, all postures indicated high-risk scores of 6 and 7, indicating necessary action to be taken immediately. Ergonomic solutions were suggested, and the improved postures were assessed using RULA, with a score of 3 indicating a low-risk posture. A new workstation design is proposed to decrease the fatigue induced by the original method. The findings show that awkward working posture risks may even be reduced by using effective ergonomic measures.

Keywords: Physical discomfort, working postures, RULA, Digital Human Modeling

1. INTRODUCTION

Ergonomics is a field of science that involves the interaction of humans and the factors that influence their performance [1]. Several ergonomics factors play an essential role in maintaining workers' health, safety, comfort, and productivity. Some important ergonomics factors are high work repetition, forceful exertions, and sustained/repetitive awkward working postures. Without proper ergonomics implementation in the workplace can result from various injuries and dangers, including muscle strains, joint sprains, and musculoskeletal disorders

(MSDs). When workers are exposed to frequent and repetitive activities with awkward or abnormal postures (bending, twisting, stretching, vibration), leading to physical discomfort and pain. Manual material handling tasks (pushing, pulling, carrying, lifting, lowering, and moving) involve transporting or supporting a load. Due to heavy workload and exertion cause awkward body postures. These are considered ergonomics hazards and may reduce working capacity and increase occupational illness, staff turnover, compensation cost, and sick leave [2]. As a result of this disadvantage, it is essential to protect the workers' health, and their working posture is one of the aspects that should be investigated when performing specific jobs.

Many comprehensive studies have been conducted to analyze risks in awkward postures by ergonomic assessment tools such as RULA, REBA, QEC, NIOSH lifting equation, etc.. [3]. Among these, the RULA risk levels may have been more intimately correlated to postural loading conditions such as pains, MHTs, and stress at the trunk, as well as MSDs. Researchers [4,5,6] used the ergonomic assessment tools RULA and REBA on workers in the sawmill Polypropylene yarn industry and agricultural sector. They found a relationship exists between the working posture and the development of physical discomfort. The authors also suggested ergonomic interventions for reducing the risk of MSDs.

The literature shows that it is very essential to assess the working postures, physiological, cognitive, and biomechanical demand, and man-machine productivity analyses. The Digital Human Model (DHM) is a helpful tool for studying, designing, analyzing, and visualizing movements and awkward postures in a three-dimensional context. When this technology is combined with computer-aided software, it becomes even more efficient. The functions of DHM are many, including the ability to move human manikin in predefined motion, postural analysis, reach analysis, carrying analysis, push/pull analysis, RULA analysis, and the provision to scale 3D manikin by available anthropometry data. Designers or ergonomics can include ergonomic aspects on human subjects using the Digital Human Model without taking precise observations at the beginning of the design phase [7]. Different versions of Digital Human Model (DHM) software have been designed for different applications and design aspects, such as RAMSIS software for vehicle ergonomics modeling and analysis [8]. SANTOS was also built to serve various industries, including aviation, armed services, and healthcare ergonomics [9]. For logistic purposes, the 3Dimensional static strength prediction program (3DSSPP) application has been made [10]. Rapid Upper Limb Assessment (RULA) is built on the research of McAtamne et al.[11]. Moreover, it has incorporated with CATIA V5 software in the DHM module. The upper region of the human body is the focus of this form of comfort assessment. This makes the process of designing and developing various human postures or activities easier, better realistic, more precise, and less minute [12].

As for this study, the workers have been selected from several sawmills as their work characteristics (bending, lifting, carrying, pulling, and pushing the wood) are frequently associated with physical discomfort. For the RULA postural assessment tool, the Computer-Aided Three-dimensional Interactive Application (CATIA) program was chosen to examine the working posture of the selected participants. Thus, the objectives of this study are to find the physical discomfort of the workers and analyze the working posture through digital human modeling.

2. METHODOLOGY

2.1. Subject of the study and the data gathered

To conduct this study, one hundred fifty sawmill workers were randomly selected from 15 sawmills in Jashore, Bangladesh. A participant with at least one year of working experience and a minimum age of 18 years old was chosen. A baseline survey was conducted using questionnaires and discussions to determine the physical discomfort and awkward body position. The workers were asked to identify the six body parts to feel discomfort or not. They were also asked to rate their level of discomfort with each body area (Low, Medium, or High). While conducting his regular task, a video camera was used to record his working cycle positions. The snapshots of significant body postures were taken to further analysis.

2.2. Digital Human modeling in CATIA

Digital Human Modeling software (CATIA V5R21) was used to model the selected working postures in this research. The postures analysis tool RULA has been incorporated with CATIA. The Computer-Aided Three-dimensional Interactive Application (CATIA) produces a replica of the postures as manikin to perform the RULA. The RULA analysis was then performed on the manikin to determine the postural discomfort the workers experienced [13].

2.3. Postural analysis

Postural analysis was deemed a powerful technique for evaluating associations between body postures and physical discomfort [14]. Various postural analysis techniques have been used to identify the stress of different work stages [6]. The Rapid Upper Limb Assessment (RULA) method was applied within this study to assess the selected postures for each work activity. Because most upper body parts are used for performing the sawmill activities. The RULA is a valuable and effective method for assessing body postural analysis and correcting awkward work postures. It examines the severity of the postural risk factors and provides a final score that varies between 1 to 7. According to the RULA, body parts are divided into two body sections: A and B. Section A includes the upper arm, lower arm, and wrists. Section B included the neck, trunk, and legs. In CATIA, a number and color code display the RULA total scores.

The final scores achieved the color changes from green for a level of "negligible danger" to red for a level of "severe risk." If the color is green, it indicates good posture (final score of 1 and 2) and is not repeated for lengthy periods. The final scores of 3 and 4 (yellow color) indicate that more inquiry is needed, and those future improvements in posture are inevitable. The orange color (final score 5 and 6) indicates that more research is needed and that the posture should be modified as soon as possible. The ultimate score of 7 (red color) indicates that further inquiry is required and that the posture must be changed immediately. Table 1 shows the score range and associated color code of RULA.

Table 1: RULA color code in CATIA Software

Segment	Score Range	Color associated to the score					
		1	2	3	4	5	6
Upper arm	1 to 6						
Forearm	1 to 3						
Wrist	1 to 4						
Wrist twist	1 to 2						
Neck	1 to 6						
Trunk	1 to 6						

3. RESULTS AND DISCUSSION

3.1. Participant's response

The average age of the participants was 35.36 (SD ± 12.59) years, as shown in Table 2. The worker was selected with at least one year of working experience. Mean BMI indicates that maximum workers are in normal health.

Table 2: General information of the selected workers (N=150)

Variables	Minimum	Maximum	Mean	Standard Deviation (SD)
Age (Years)	18	61	35.36	± 12.59
Working Experience (Years)	1	36	12.7	± 10.12
Working time (Hours)	6	12	9	± 1.92
Weight (Kg)	43	81	55.35	±7.94
Height (meters)	1.4	1.9	1.59	±0.049
Body Mass Index (BMI)	15	32	20.15	± 2.15

The Prevalence of participant's body discomfort is shown in Figure 1. Results indicate that 78% of the total participants suffered from at least one body part pain. Among the six body segments, the maximum portion of the workers felt pain in the trunk (71%). In contrast, the least portion was suffered from wrist pain.

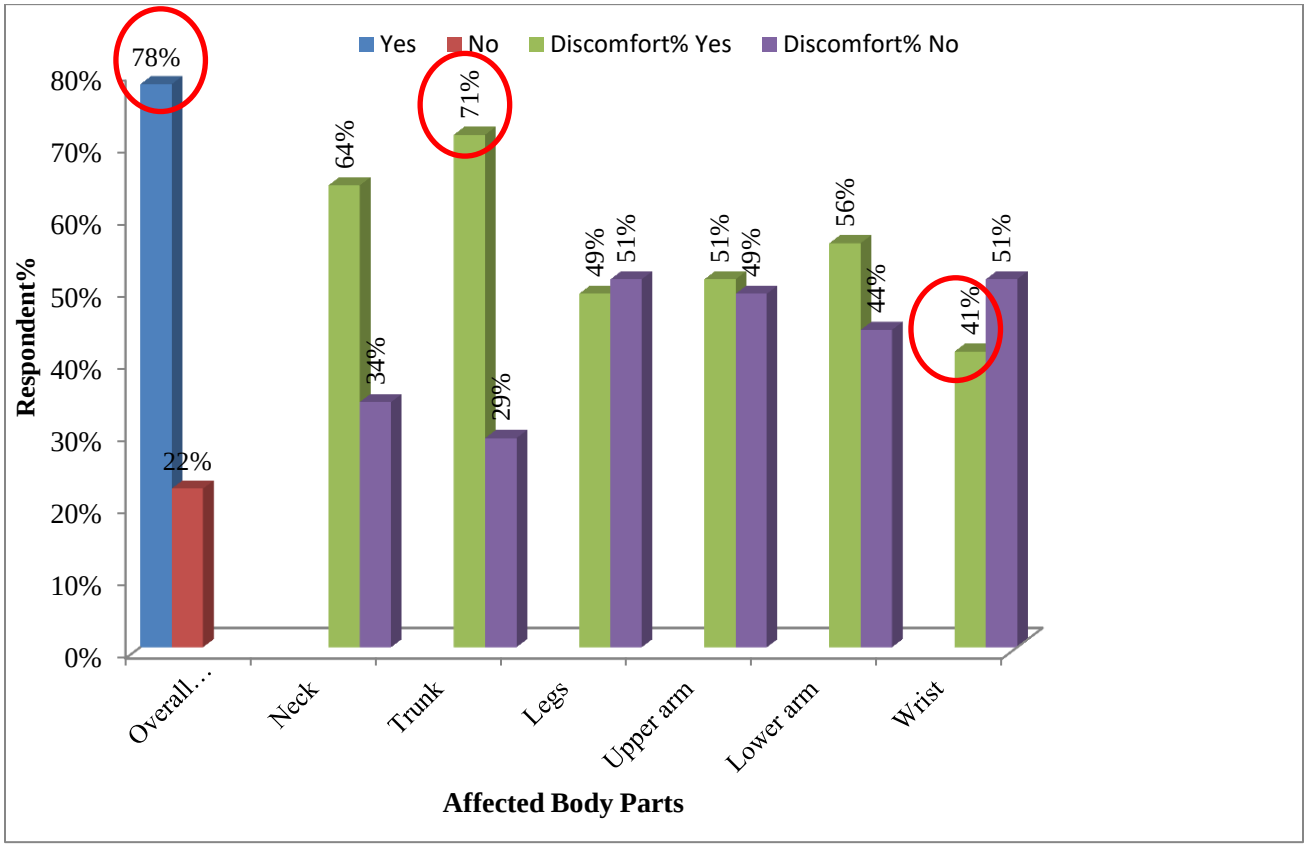

Figure 1: Prevalence of participant's body discomfort

Table 3 represents the severity level of worker body discomfort. The neck was the highest (51%) severity body segment among the six body parts. At the same time, the upper arm was the lowest (12%) severity body segment. On the other hand, interviewed workers felt medium (6%) and low level (3%) discomfort for legs and wrist.

Table 3: Workers complains about ergonomics aspects in the level of physical discomfort

Body Parts	Discomfort Level		
	Low	Medium	High
Neck	5%	8%	51%
Trunk	6%	20%	45%
Legs	4%	6%	39%
Upper arm	20%	19%%	12%
Lower arm	15%	12%	29%
Wrist	3%	18%	20%

3.2. Postures analysis

3.2.1. Postures analysis of lifting task

Figure 2(a) consists of lifting wood from the ground on the sawmill's table.

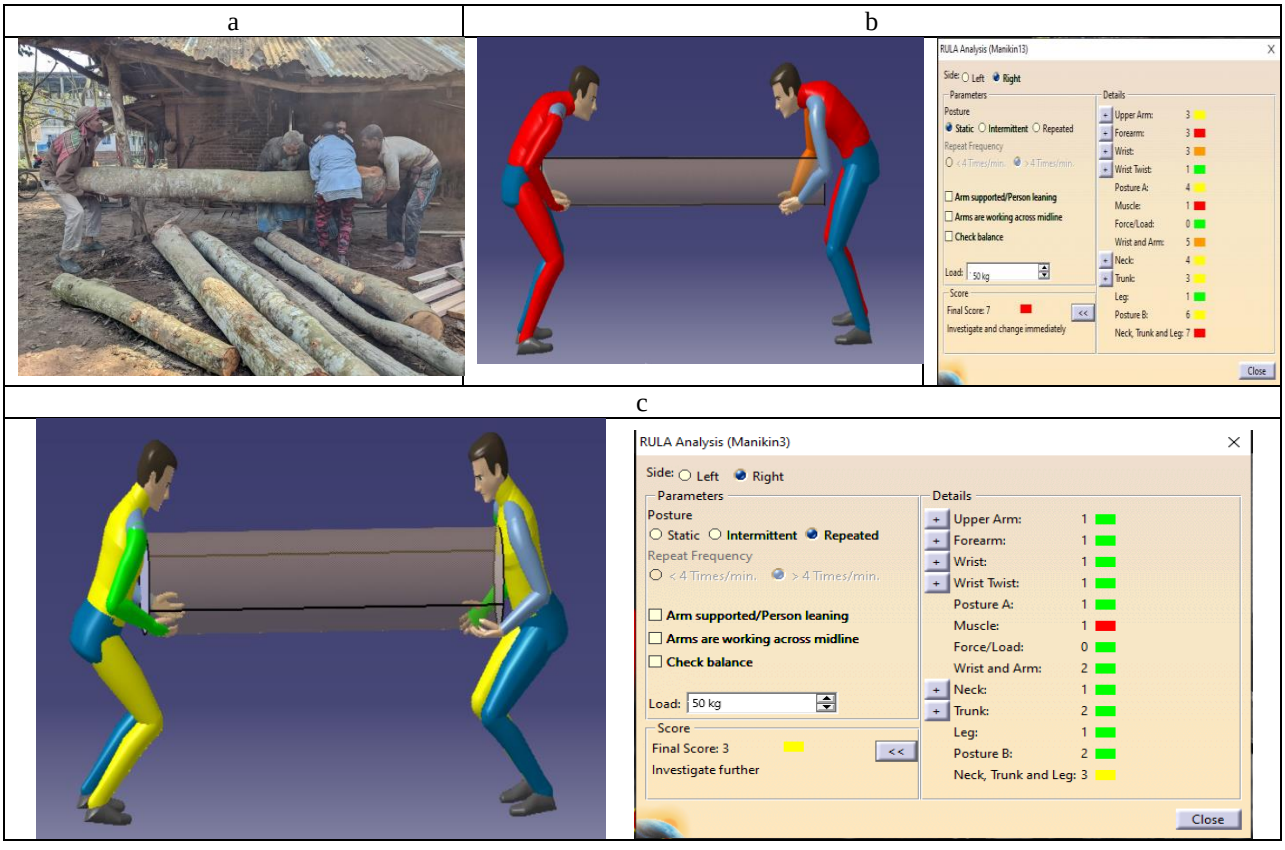

Figure 2: Current working postures (a) and Digital Human Modeling in CATIA and RULA scores (b) of wood lifting after ergonomic intervention (c).

The poorest working posture of the workers while doing the lifting jobs in the sawmill is selected as shown in Figure 2(a). For Rapid Upper Limb Analysis (RULA), the workers' actual pictures are transformed using CATIA software V5R21. Physical discomfort is conceivable with the chosen postures. This position has a RULA score of 6, suggesting that the worker is at high risk. The new posture was developed modeled in CATIA, as shown in Figure 2(c), and it is analyzed using RULA. This improved posture obtains a final score of 3, suggesting a medium risk category.

3.2.2. Postures analysis of carrying task

The carrying activity in the sawmill involves carrying the woodblock to the saw point (Fig. 3(a)). The RULA score is 6 in the digital model (Fig. 3(b)), which is outside acceptable ranges and requires immediate intervention. The simulation body postures and related body RULA score 3 are shown in Figure 3(c). This score indicates that the modified body posture is a medium risk zone**.**

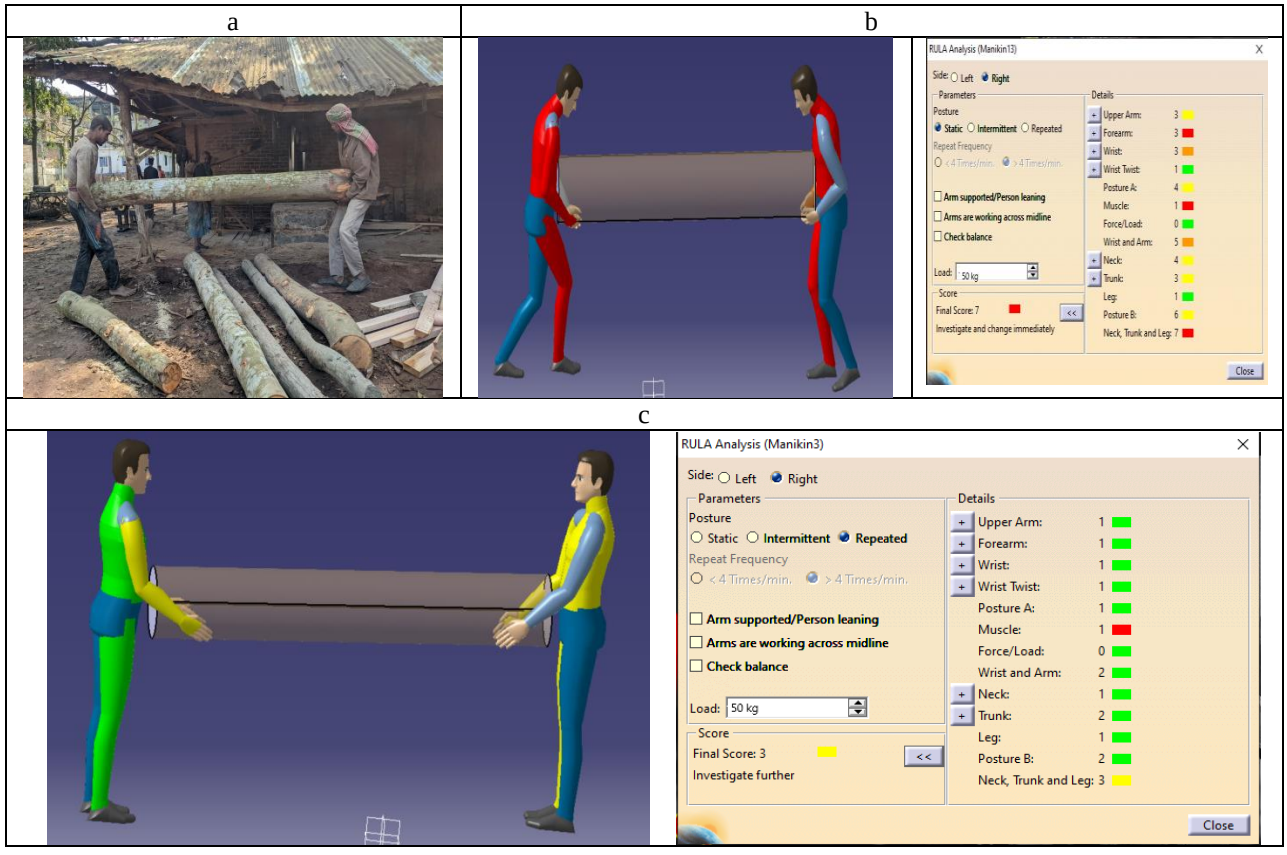

Figure 3: Current working postures (a) and Digital Human Modeling in CATIA and RULA scores (b) of wood carrying after ergonomic modification (c).

3.2.3. Postures analysis of pulling task

Figures 4 (a) and (b) illustrate the workers' actual working postures when pulling wood off the working table. To perform Rapid Upper Limb Analysis, the actual pictures of the workers are converted in CATIA V5 software. Workers are forced to awkward posture, as shown in the Figure 4(a), and the picked postures are prone to causing physical pain.

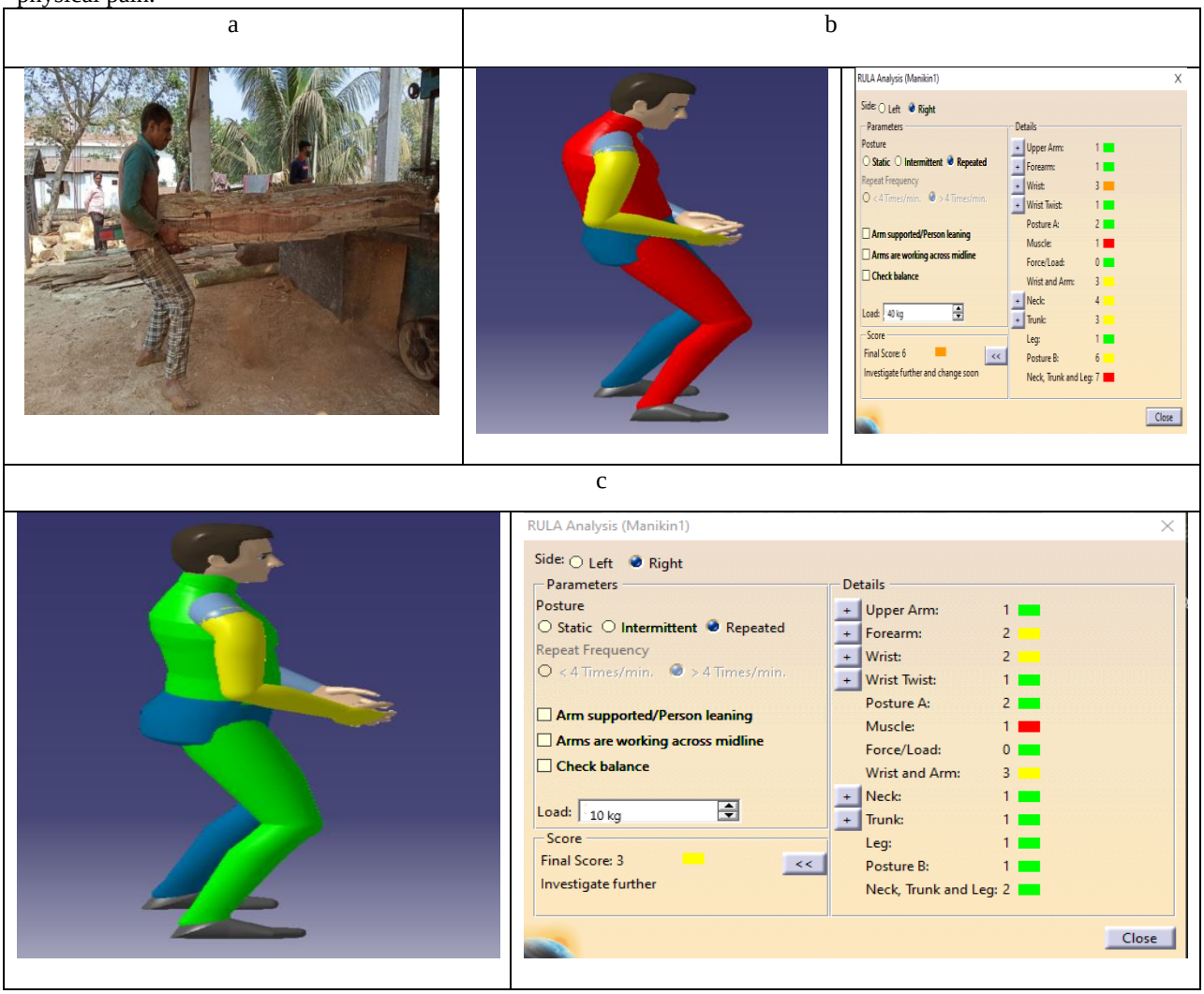

Figure 4: Real working postures (a) and Digital Human Modeling in CATIA and RULA scores (b) after ergonomic intervention (c) for pulling wood**.**

In Figure 4 (a), the work involves pulling the wood to cut the desired shape of the raw wood. This posture has a RULA score of 6, indicating that the worker is at high risk and that a change in posture is required right once to avoid future difficulties. The most affected body parts are muscle, neck, and trunk. Researchers used the same

procedure and found a similar result for the workers in the steel industry [15]. A human manikin with the appropriate body measurements is built and modeled in CATIA to resolve these problems (Fig. 4(c)). RULA method is used to analyze the modeled human manikin. It provides a final score of 3, which indicates that the risk is low, as shown in Figure 4(c). Ergonomic interventions and workplace improvements such as adding a rolling ring to the table (Fig. 6(b)) have been demonstrated to minimize the risk of physical illnesses.

3.2.4. Postures analysis of pushing task

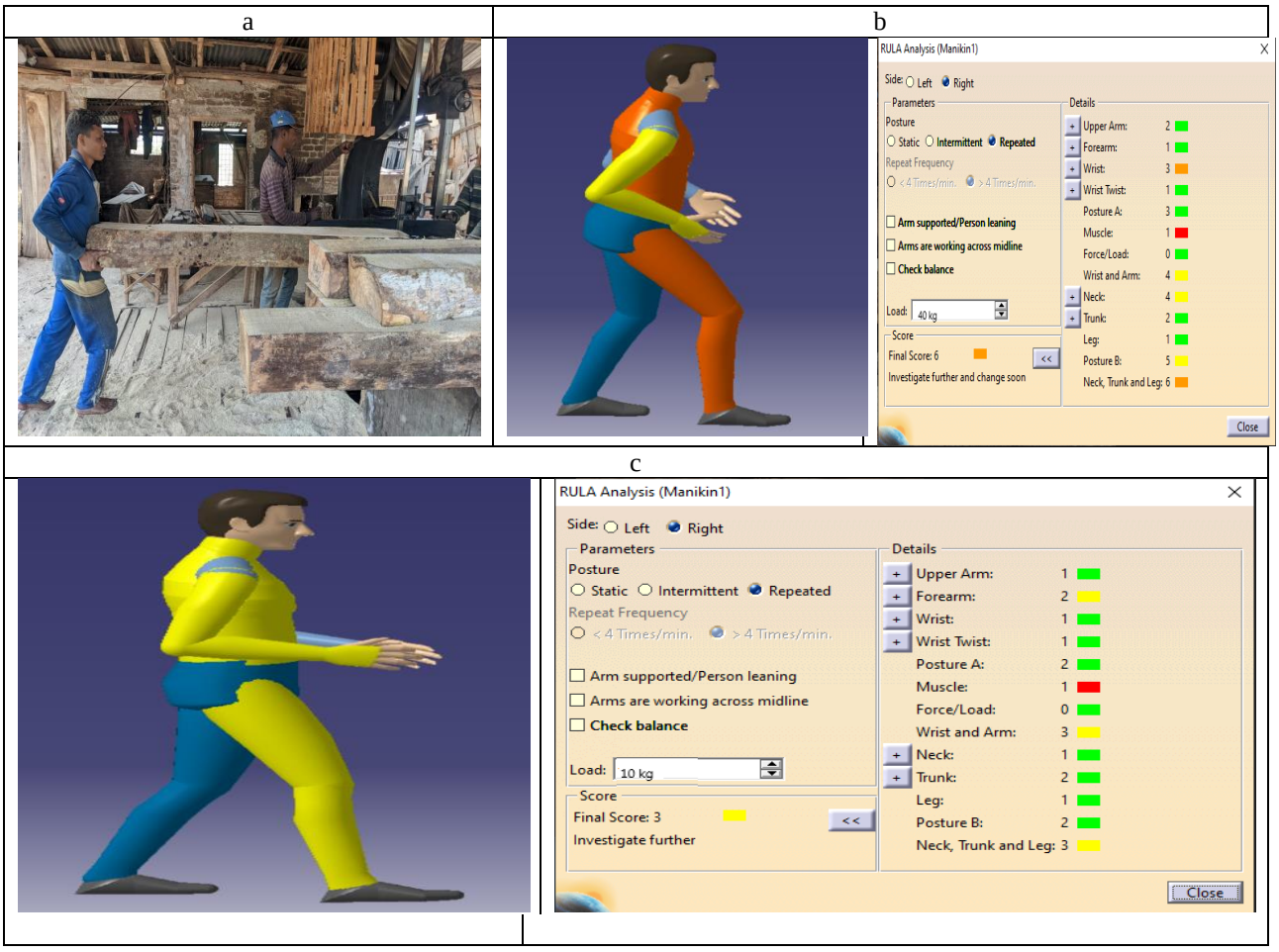

Figure 5: Current working postures (a) and Digital Human Modeling in CATIA and RULA scores (b) after ergonomic intervention (c) of pushing wood.

Figures 5 (a) and (b) represent the workers' actual working postures while pushing wood on the working table. The actual pictures of the workers are converted in CATIA V5R21 software to perform Rapid Upper Limb Analysis. Workers are subjected to awkward posture, as shown in the Figure 5(a), and the picked postures are prone to causing physical pain. The process in Figure 5(a) involves pushing the wood in order to slice the raw wood into the

appropriate shape. The RULA score for this position is 6, indicating that the worker is at high risk. Hussain et al. [16] revealed that the workers perform in the small-scale industry with abnormal postures. A change in posture and immediate investigation are required to obtain correct solutions. Low-cost ergonomics interventions can reduce postural risks in similar postures, as illustrated in Figures 5(a) and 5(b). The suggested change is modeled in CATIA, as shown in Figure 5(c). The RULA score is reduced to 6 to 3, indicating medium risk.

3.3. Design of new workstation

Figures 6(a) and 6(b) show the old and improved workstations. In the old workstation, there had no mechanical conveyer as results workers lift wood manually. In addition, a rolling platform has been added to the new worktable. This improvement has the potential to mitigate the subject's discomfort.

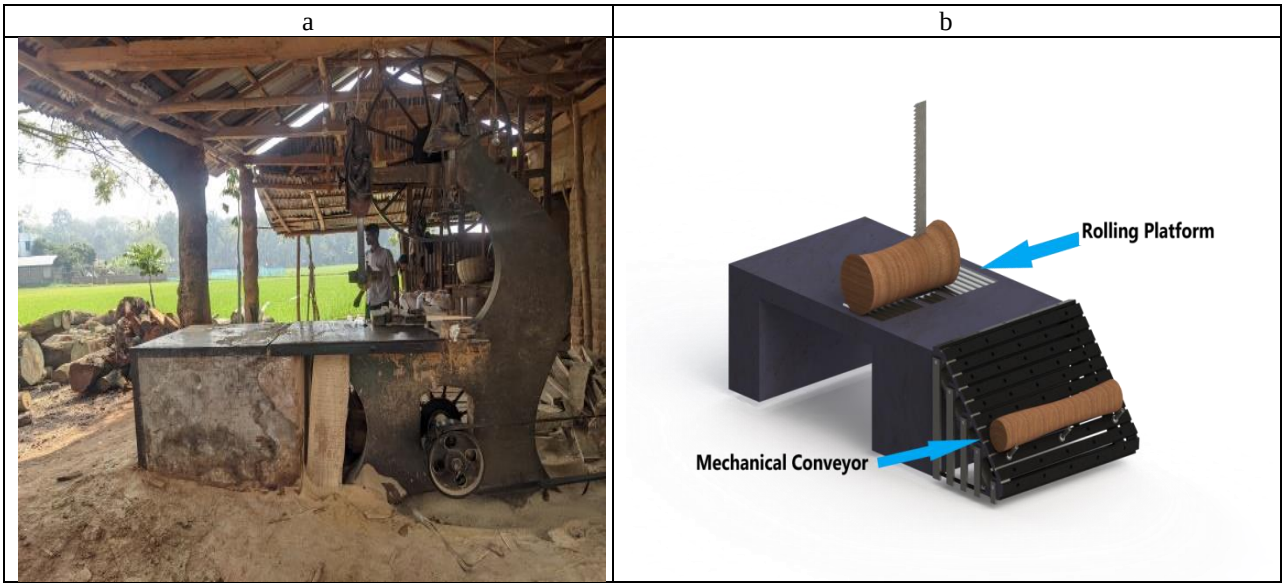

Figure 6: Existing (a) and new proposed (b) workstation

CONCLUSIONS

It can be concluded that the manual material handling workers in sawmills are frequently exposed to physical discomfort or pain, especially in the upper parts of their body while doing their tasks. The high severity of body regions was in their trunk (51%) and neck (45%). The participants in this study were performing tasks by adopting poor postures, which are very risky and unsafe. The Rapid Upper Limb Assessment scores of the selected postures were 6 to 7, which is very high and requires detailed investigation and immediate change in the postures. The selected working postures were modeled and simulated using CATIA V5R21 software to indicate the postural risk level and corrected postures were suggested based on simulation results. The simulated working postures obtained final RULA scores of three, suggesting a medium risk category. Ergonomic modifications in workplace design are suggested, as they will significantly reduce postural stress. Changing the saw table utilized by the rolling platform

and the mechanical conveyer for lifting the wood on the working table is also one of the immediate remedies that can reduce the number of complaints associated with physical discomfort. Further studies about the noise level, dust, and biomechanics analysis of the working posture can be conducted, which will help to mitigate the workers' discomfort.

REFERENCES

1. Licht, D. M., Polzella, D. J., & Boff, K. (1989). Human Factors, Ergonomics, and Human Factors Engineering: An Analysis of Definitions. CSERIAC-89-01. Wright Patterson AFB, Dayton, OH: CSERIAC
2. Vink, P., Koningsveld, E. A., & Molenbroek, J. F. (2006). Positive outcomes of participatory ergonomics in terms of greater comfort and higher productivity. Applied ergonomics, 37(4), 537-546.
3. Kee, D. (2022). Systematic Comparison of OWAS, RULA, and REBA Based on a Literature Review. International journal of environmental research and public health, 19(1), 595.
4. Qutubuddin, S. M., Hebbal, S. S., & Kumar, A. C. S. (2013). An ergonomic study of work related musculoskeletal disorder risks in Indian Saw Mills. Journal of Mechanical and Civil Engineering, 7(5), 7-13.
5. Kabilmiharbi, N., & Selamat, F. E. (2016). Rula analysis of work-related musculoskeletal disorder among polypropylene fibrillated yarn industry worker using Digital Human Modelling (DHM). Malaysian Journal of Public Health Medicine, 2016 (Specialissue), 53-60.
6. Gangopadhyay, S., & Dev, S. (2014). Design and evaluation of ergonomic interventions for the prevention of musculoskeletal disorders in India. Annals of occupational and environmental medicine, 26(1), 1-6.
7. De Magistris, G., Micaelli, A., Evrard, P., Andriot, C., Savin, J., Gaudez, C., & Marsot, J.(2013). Dynamic control of DHM for ergonomic assessments. International Journal of Industrial Ergonomics, 43(2), 170–180.
8. Bubb, H. (2002). Computer aided tools of ergonomics and system design. Human Factors and Ergonomics in Manufacturing & Service Industries, 12(3), 249-265.
9. Abdel-Malek, K., Yang, J., Marler, T., Beck, S., Mathai, A., Zhou, X., ... & Arora, J. (2006). Towards a new generation of virtual humans. International Journal of Human Factors Modelling and Simulation, 1(1), 2-39.
10. Chaffin, D. B. (1997). Development of computerized human static strength simulation model for job design. Human Factors and Ergonomics in Manufacturing & Service Industries, 7(4), 305-322.
11. McAtamney, L., and Corlett, E. N. (1993). RULA: a survey method for the investigation of work-related upper limb disorders. Applied ergonomics, 24(2), 91-99.
12. Fritzsche L (2010) Ergonomics risk assessment with digital human models in car assembly: simulation versus real life. Human Factors and Ergonomics in Manufacturing & Service Industries, 20(4):287–299
13. Deros, B. M., Daruis, D. D., Ismail, A. R., Sawal, N. A., & Ghani, J. A. (2010). Work-related musculoskeletal disorders among workers' performing manual material handling work in an automotive manufacturing company. American Journal of applied sciences, 7(8), 1087.
14. Kee, D., and Karwowski, W., (2007). A comparison of three observational techniques for assessing postural loads in industry. International Journal of Occupational Safety and Ergonomics, 13(1), 3-14,
15. Mohammed, A. R., Mohamed, M. O., Alhubaishy, Y. A., Nasser, K. A., & Fahim, I. S. (2020). Ergonomic analysis of a working posture in steel industry in Egypt using digital human modeling. SN Applied Sciences, 2(12), 1-8.

16. Hussain, M. M., Qutubuddin, S. M., Kumar, K. P. R., & Reddy, C. K. (2019). Digital human modeling in ergonomic risk assessment of working postures using RULA. In Proceedings of the International Conference on Industrial Engineering and Operations Management Bangkok, Thailand.

Paper ID: 2884

International Conference on Mechanical, Manufacturing and Process Engineering (ICMMPE – 2022)

Organizer: Faculty of Mechanical Engineering, Dhaka University of Engineering & Technology (DUET), Gazipur, Bangladesh

Website: https://icmmpeduet.com/

Development of Low-Cost Single Degree Rectilinear Spring Mass Damper Open Loop System

Karthikeyan[1], Mohaimen Siddique[2], Sayed Al Rafid[3], Tanzim Hassan Jim[4], Sadman Sadid[5], Rezaul Karim Nayeem[6], Mir Sadia Islam[7], Nishat Sal Sabila[8]

Aeronautical Engineering Department, Military Institute of Science & Technology, Mirpur -1216, Dhaka, Bangladesh

karthik.af@gmail.com[1], mohaimensiddique1@gmail.com[2], sayed.rafid@gmail.com[3], zimhassan9515@gmail.com[4], sadmansadid420@gmail.com[5], rknayeem77@gmail.com[6], mirkashpia07@gmail.com[7], nishatsalsabila7@gmail.com[8]

ABSTRACT

A second-order system is fundamental to understanding the characteristics of the dynamics of a physical system. The higher-order equations can also be formed as an equivalent second-order to appreciate the behavior using defining parameters. In this work, an effort was made to develop a single-degree second-order Spring Mass Damper (SMD) using commonly available low-cost resources. The hardware allows the variations of parameters including mass, spring constant and damper. The integrated software with the hardware allows recording of the instrumented data and processing it to conclude on the dynamic characteristics. The hardware work was preceded by the design of the whole setup in Solidworks matching the dimensions of Commercial Off-The-Shelf (COTS) items. This was followed by designing individual components to suit the functionality, dimensions and adaptability of an experiment. The actuator was designed to function with a DC motor. This actuator was used to hit the mass and simulate an impulse force to the system. Two Linear Variable Differential Transformers (LVDTs) were utilized as position sensors for instrumentation. The LVDT gave the evolution of the position of mass over time. The interface between the hardware and software was made through an NI DAQ 6009. The software, in Labview, front end enabled controlling and capturing of data on the screen for further processing into dynamics parameters. The interface screen provided instruction and logic of computations for dynamics parameters.

Keywords: Spring, Mass, Damper, Second Order System

1. INTRODUCTION

A physical system can be modeled using a spring mass and damper system (SMD). This ability to formulate any causal physical system into SMD or LCR (Inductor Capacitor & Resistor) enables the prediction of the response of the system to varied inputs. Therefore, it is often the first step in design to model the system into an equivalent SMD or LCR circuit to predict stability and control the output as desired. Even in cases of higher order systems they are reduced to equivalent second order systems with similar defining parameters. An effort was made to develop a system to capture a single degree SMD characteristics for the academic environment as a stepping stone to understanding the factors affecting it [1].

There are many good models available in the market that provide the ability to change the variables and get different transfer functions. The Model ECP 210 is one such comprehensive model to understand the SMD characteristics. The components utilized in the setup are sturdy and have an aesthetic value which also makes it high in price. This work is inspired by the Model ECP 210. The work tries to replicate a similar product using low-cost items and features including changing variables. However, the device developed envisaged only an open loop system and a single degree of freedom. The cost incurred in developing the product was nearly one-fifteenth of the original cost of the device.

The device allows to change the variables including mass through modules of mass, air damper value through exit hole openings using screws and spring constant by replacing them. The Linear Variable Differential Transformer (LVDT) sensor attached to the mass captures the position evolution over time. The software made on a LabVIEW platform allows for converting the acquired position data into natural frequency and damping coefficients and thereby figuring out the characteristic equation of the transfer function [2].

The paper would discuss the work carried out to develop in terms of hardware and software. The covers the simple methods employed to get the hardware to suit the requirements and challenges to integrate as a system. It also covers the logic included in the software to control the experiment. Efforts of using commonly available low-cost items and modifying them to meet the requirements have been the central idea. In the following paragraphs, the work is enumerated as per the elements being used. The improvisation, if any, on any item taken off the shelf has been elaborated. Finally, the experiment was conducted for varied components value and observed for its output. The output was compared with the physical governing laws to verify the validity of the system. The same has been

discussed using graphical results and was found to be in agreement with expected outcomes.

2. FABRICATION

2.1 Solidworks model

The pre-fabrication work is an important step toward getting a complete idea of the size of the components. Initially, the list of COTS items like the DC motor, LVDT sensor and springs dimensions were identified. Using these dimensions, a model was prepared in Solidworks to get an overview of raw materials and proportionate dimensions that would be required for fabrication. The model prepared with placements of components is shown in the Fig. 1. The physical placement was thereafter planned accordingly to cater to the overall design.

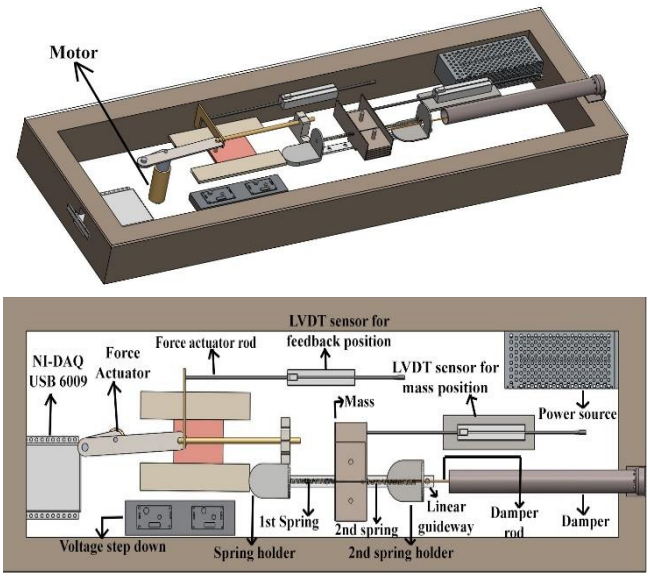

Fig. 1: Solidworks Model for the Setup

2.2 Position Sensor

Two LVDT position sensors, KTR11, of 100 mm were utilized for this project. Since the LVDT functions on the principle of the transformer, there will not be any friction that would act as a damper and affect motion. The sensor has total length coverage of 10 cm and therefore allowed 5 cm on either side of the center. The sensor [4] required a reference DC voltage for operation. One sensor was interlinked to the mass to measure the evolution of position and the other sensor was interlinked to the actuator. The actuator at the start needs to be farthest from the mass to cause maximum impact to initiate oscillation. The second sensor enabled monitoring of the actuator position.

2.3 DC Motor and Electrical Setup

For the purpose of generating the impact to the mass, an actuator was designed which was driven by a DC motor. The DC motor operated with 12 V DC. The NI DAQ was able to provide an output voltage in the range of 0-5V. This mandated the use of a DC motor driver as an interface between the two. As an interface L298N a dual H-bridge, shown in Fig. 2, was utilized for providing the required voltage of 12 volts at the motor terminal. It supports the simultaneous operation of two motors. The change of direction and variable voltage input functionality was not utilized as the stepper motor was not used. Also, the same was not supported by the NI DAQ 6009. The motor driver [3] consumed 2V DC, which was compensated through an input voltage of 14 V DC.

The operation of the DC motor was controlled by a software in LabVIEW through the NI DAQ 6009 USB card [6]. The NI card was selected due to its ease of integrating with LabVIEW and an adequate number of analog input and output ports. In order to reduce the cost significantly, the usage of the Arduino card could have also been explored. In spite of using the NI DAQ card, the total cost was less than a fifteenth of Model ECP 210 cost to serve meaningful utility. The overall implemented electrical schematic setup is shown in Fig. 3.

2.4 Mass Cart

The mass envisages for the project were to be modular for easy replacement and handling. Therefore instead of a mass, it was decided to have a cart in which modular masses would be fixed. The modular masses were designed in the form of coins each weighing 50 gm which could be placed in a cart with the help of two attachment points. The force was applied to the cart instead of the mass. The cart was made of aluminum weighing 60.74 gm. The mass cart is shown in the Fig. 4.

The mass cart owing to the weight would have significant motion friction when moved over the surface. In order to reduce the friction due to motion, a rail was utilized which had a ball bearing to take the load. The surface area being lesser with the ball bearing reduce the friction. The mass rail is shown in the Fig. 5.

2.5 Spring

Most commonly available springs were either tensile or compressive. The problem faced with spring was that springs with the available order of spring constant were having good recoil and settled to final value without overshoots. In order to demonstrate a second order system with low damping, it was essential to have an overshoot above the final value. This was accomplished by using two tensile springs on either side

of the mass cart as shown in the Fig 4. The spring was connected at the reference node firmly fixed over the mass rail. The springs were positioned to ensure nil tensile force during the non-operative period and thereby maintain an equilibrium position.

2.6 Damper

The simulation work was carried out prior to preparing the components with suitable value. In the case of damper, COTS was not available and therefore were left either the option designing by self. The damper was prepared using a PVC cylindrical pipe with one of the far ends closed completely, as shown in the Fig 6. The other open end was connected with a plastic disc of diameter nearly equal to the pipe. The edges of the disc were covered with rubber material and were oiled to reduce friction and have a smooth movement of the disc. The disc was connected to the mass cart using a piston rod of low mass. The requirement of variable damper value for different experiments was achieved through multiple holes in the far closed end of the cylinder. For higher damping values the holes were closed using screws and for lower values were kept open.

2.7 Force Actuator

There is a requirement for a force actuator to exert onto the mass cart. The force will have to be similar to an impulse function to observe the characteristics of a homogeneous system. This was accomplished by fabricating two arm actuator fitted onto the DC motor shaft, as shown in the Fig 7. The rotary motion of the DC motor shaft was converted into reciprocating motion which gave the necessary momentum to the mass by hitting. During the design stage, care was taken to have the length of the arm not to interfere with the oscillation of the mass post impacting the mass.

2.8 Hardware Setup

The hardware was assembled as per the Solidworks design. Adequate caution was exercised to avoid misalignment of height and length. The misalignment would result in non-rectilinear motion and thereby incorrect modeling of the system. A common Power Supply unit was utilized to connect to the commercial power supply and provide different outputs to consumers, including the motor driver and LVDTs. The whole of the setup was installed on the Perspex sheet of 6mm thickness and was supported at the perimeter with light weight aluminum sheet metal. The complete assembled setup for the experiment is shown in the Fig. 8.

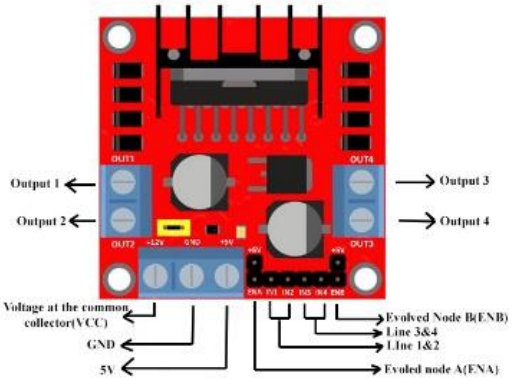

Fig. 2: L298N Double H- Bridge Motor Driver

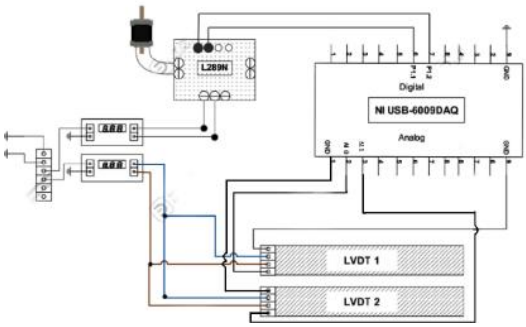

Fig. 3: Electrical Circuit Diagram

Fig. 4: Mass Cart Setup

Fig. 5: Mass Rail

Fig. 6: Variable Damper

Fig. 7: Force Actuator

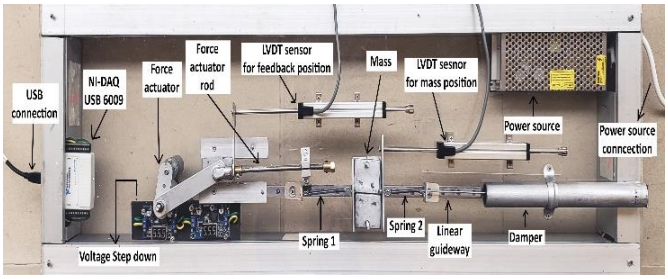

Fig. 8: Complete Setup

3. SOFTWARE DEVELOPMENT

The goal was to acquire accurate data and correctly interpret or compute physical phenomena and from these recorded phenomena deduce calculations for Damping ratio, Natural Frequency, etc. These were achieved through a software in Labview with the following capability in sequential order:

a) Identifying the actuator's position
b) Operating the actuator
c) Data acquisition and
d) Assess the SMD system's characteristics.

3.1 Identifying Actuator's Position

The actuator needs to be away from the mass cart to ensure maximum hitting force. In order to ensure this the position of the actuator needs to be ascertained. LVDT2 was utilized to determine the position of the actuator. This information was used in the software to caution the user with "Do not start actuator" while the actuator was close to the mass. This was accompanied by a red light until the actuator reached the farthest distance from the mass, as shown in the Fig. 10. On this caution, the user is expected to move the actuator away from the mass cart which would be akin to the initialization of the experiment. When it reached the furthest point, the white light "Start actuator" appeared. Essentially, the logic of this system is based on comparing the electrical voltage signal from LVDT2 to the voltage signal from the farthest point from the mass position. When the actuator reached its maximum distance, "Start actuator" appeared with white light, indicating that users are in the correct state to start the actuator at that moment. The flowchart for actuator decision making is shown in the Fig. 9.

3.2 Operating Actuator

The actuator was driven by a DC motor with an rpm of 400 and powered by a 12-volt battery. Due to the open-loop nature of our system, we required just one hit from a single spin of the DC motor. Thus, a while loop with a timer was used to regulate the DC motor for a single rotation. It took 60/400 = 0.15 seconds, which translates into 150 milliseconds However, after testing and iteration, it was determined that 250 milliseconds was appropriate for a flawless strike on the mass. The actuator was then controlled by a 250 ms timer with a while loop. As a caution, the operation of the actuator was disabled by a logic till the actuator has moved back to the farthest point from the mass.

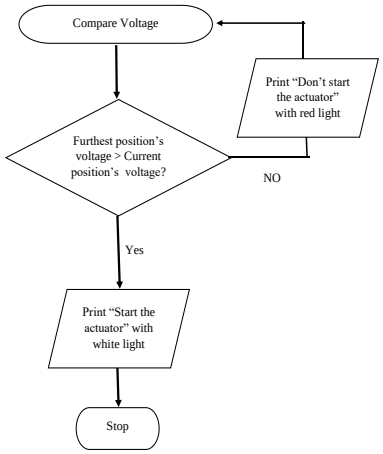

Fig. 9: Flowchart for Actuator Operation

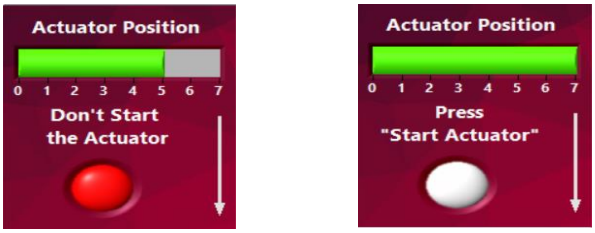

Fig.10: Screenshot for Actuator position logic

3.3 Data Acquisition

LVDT1 continuously monitors the mass position and generates equivalent electrical signals. A program was built to collect these electrical signals for further analysis of SMD system parameters. The screenshot of acquired data is placed in the Fig. 11. The system could be operated with the following variables:

a) Varying mass
b) Varying spring constant
c) Varying damper

3.4 Assess the SMD System's Characteristics

The data were analyzed to ascertain the system characteristics and validate the functionality. The acquired data was processed to be converted into defining parameters. The evolution of defining parameters with varying mass/damping values was checked for the laws of physics.

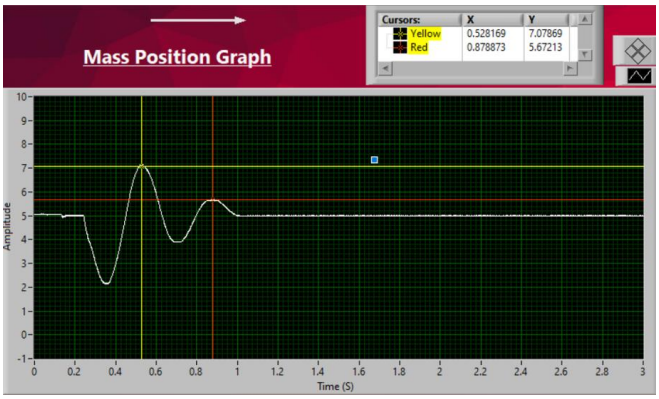

Fig. 11: Acquired Data

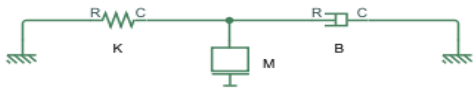

Fig. 12: Spring Mass Damper System

The differential equation for the general Spring Mass Damper system, Fig. 12, is given by

$$M\frac{d^2y}{dt^2} + B\frac{dy}{dt} + Ky = 0 \quad (3.1)$$

$$\text{Or, } \frac{d^2y}{dt^2} + \frac{B}{M}\frac{dy}{dt} + \frac{K}{M}y = 0$$

$$\text{Or, } \frac{d^2y}{dt^2} + 2\,\zeta\,\omega_n\,\frac{dy}{dt} + \omega_n\,y = 0$$

By replacing through transfer function "s", the characteristics equation is and the roots are

$$\text{Or, } s^2 + 2\,\zeta\,w_n s + w_n^2 = 0$$

$$\text{Or, } s = \frac{-2\zeta\,w_n \pm \sqrt{4\,\zeta^2 w_n^2 - 4\,w_n^2}}{2}$$

$$\text{Or, } s = -\zeta\omega_n \pm \omega_n\sqrt{1-\zeta^2}$$

$$\text{Or, } s = -\sigma \pm +j\,\omega_d \quad (3.2)$$

[Where, $\sigma = \zeta\omega_n$ & Damped Natural Frequency, $\omega_d = \omega_n\sqrt{1-\zeta^2}$]

Therefore, the complete solution of the general differential equation is $y = e^{-\sigma t}(C_1 \sin\omega_d t + C_2 \cos\omega_d t)$ (3.3)
This solution is oscillatory, but the amplitude steadily decreases due to the negative exponential component.

Value of σ:

By choosing any 2 peak's/Valley's amplitude,

$$\frac{y(t_1)}{y(t_2)} = \frac{Ae^{-\sigma t_1}\cos(\omega_d t_1 - \sigma)}{Ae^{-\sigma t_2}\cos(\omega_d t_2 - \sigma)}$$

$$\text{Or, } \ln\frac{y(t_1)}{y(t_2)} = -\sigma t_1 + \sigma t_2 = \sigma(t_2 - t_1)$$

$$\sigma = \frac{1}{T}\times\ln\frac{y(t_1)}{y(t_2)} \quad (3.4)$$

Where,

$y(t_1)$ = Amplitude at the time "t_1"
$y(t_2)$ = Amplitude at the time "t_2"
T = Time Period $= \frac{t_2 - t_1}{n}$
n = Difference between peak /valley number

Damped Frequency (f_d): $f_d = \frac{1}{T}$ (3.5)

Natural Frequency (f_n): $f_n = \frac{f_d}{\sqrt{1-\zeta^2}}$ (3.6)

$\omega_n = 2\,\pi\,f_n$ (3.7)

The equations from 3.4 to 3.7, were absorbed in software to determine and assess the properties of the SMD system.

4. DATA ANALYSIS FOR VALIDATION

After being hit by the actuator, the LVDT1 continuously generates equivalent electrical signals corresponding to the mechanical motion of mass. The motion was captured and could be exported for offline usage as well. The screenshot of the software front end is shown in the Fig. 13. For the open loop system designed, we observed underdamped oscillation of peaks and valleys in two scenarios

a) Varying Mass
b) Varying damper

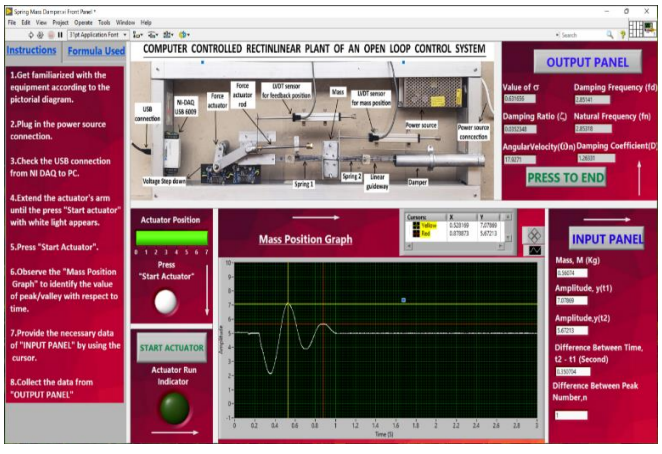

Fig. 13: Software Front End Screenshot

4.1 Data Analysis with varying Mass for Validation

The mass of housing is 0.06074 Kg. Every coin of the mass bar weighs 0.050 kg. Post the actuator hit the mass cart, data was collected through the given input and subsequently after each experiment an additional mass coin was added for the next experiment. Tables 1 and 2 summarize the data collection for system behavior for varying masses with a peak difference of one.

Table 1: Input panel Data with varying mass

Sigma, σ	Damp Ratio, ẟ	Damp Freq. fd	Natural Freq. fn	Angular Vel. ωn	Damp Coeffi. D
1.36	0.04	5.50	5.51	34.60	2.73
1.15	0.04	5.04	5.04	31.66	2.31
0.76	0.03	4.64	4.64	29.17	1.52
0.95	0.04	4.23	4.23	26.57	1.91
0.88	0.04	3.94	3.95	24.80	1.77
0.88	0.04	3.64	3.64	22.89	1.75
0.86	0.04	3.43	3.43	21.57	1.71
0.77	0.04	3.24	3.24	20.38	1.54
0.75	0.04	3.11	3.12	19.58	1.51
0.73	0.04	3.00	3.00	18.84	1.47
0.61	0.03	2.92	2.92	18.37	1.22

We know, $\omega_n = 2\pi f_n = \sqrt{\frac{k}{M}}$. So, $f_n \propto \sqrt{\frac{1}{M}}$. So, It is evident from the graph shown in Fig. 14 & 15 that with the change in mass of the cart the natural frequency and the damping coefficient varied as expected from the laws of physics.

Table 2: Output Panel Data for Varying Mass

Mass of Bar (Kg)	Total Mass (Kg)	y_t1	y_t2	t_1	t_2	Time Period
0	0.06	6.89	5.38	0.27	0.45	0.18
0.05	0.11	6.86	5.45	0.40	0.60	0.20
0.1	0.16	8.59	7.29	0.49	0.71	0.22
0.15	0.21	6.97	5.56	0.31	0.55	0.24
0.2	0.26	7.01	5.60	0.33	0.59	0.25
0.25	0.31	7.08	5.56	0.43	0.71	0.27
0.3	0.36	7.19	5.60	0.40	0.69	0.29
0.35	0.41	7.15	5.64	0.37	0.68	0.31
0.4	0.46	7.22	5.67	0.59	0.91	0.32
0.45	0.51	7.30	5.71	0.41	0.74	0.33
0.5	0.56	6.68	5.42	0.39	0.73	0.34

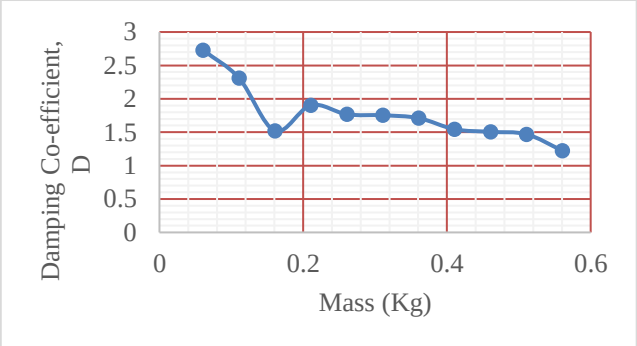

Fig. 14: Effect on damping coefficient with increasing mass

4.2 Data Analysis with varying Damper for Validation

There were 4 holes in the damper. Firstly, the actuator hit constant mass, data was collected without closing any holes through given input and further for each hit by the actuator, every time, 1 hole of the damper was closed and taken the data after actuator hit and observed the effect of closing holes of the damper. Table 3 summarizes the data collection and indicates which values were provided as input and which values were obtained as output as a result of the varying damper.

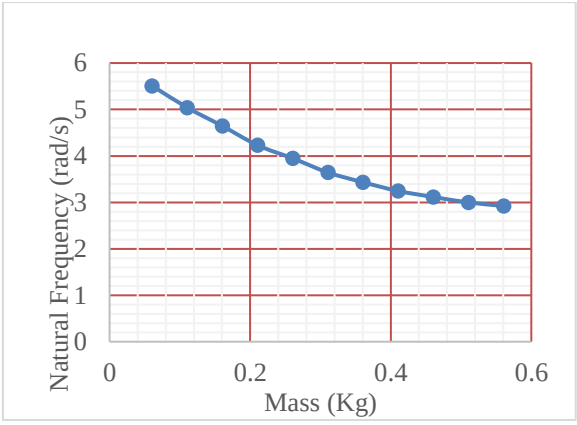

Fig. 15: Effect on the natural frequency with increasing mass

Table 3: Output Data with Varying Damper

Damping Hole Closed	σ	ẟ	fd	fn	ωn
1	0.98	0.03	5.50	5.51	34.60
2	1.05	0.03	5.38	5.38	33.81
3	1.17	0.03	5.38	5.38	33.82

From Equation 3.8, $D = 2\,\zeta\,\omega_n$. Again, $\sigma = \zeta\omega_n$. The graph shown in the Fig 16 and 17, shows the variation of sigma and natural frequency with variation in Damping value. The natural frequency is remaining almost unchanged while the sigma increased as per the physics. The laws of physics thereby are validated.

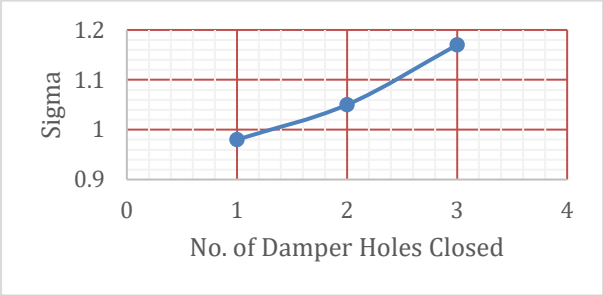

Fig 16: Effect on Sigma, $\boldsymbol{\sigma}$ with varying damper

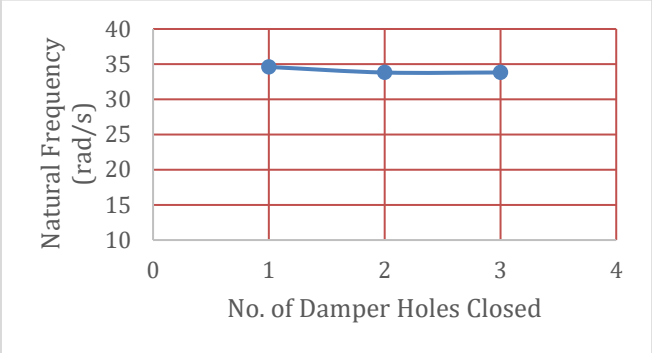

Fig. 17: Effect on the angular velocity with varying damper

5. CONCLUSION

The project achieved all the objectives set for demonstrating the open loop spring mass damper system. We envisage the next step in this project would be to approach a closed loop system. An attempt towards that would require a stepper motor and a suitable DAQ card. This project could have been accomplished with a low cost DAQ card as well but for the long life of the equipment, the NI card was chosen.

REFERENCES

[1] H. L. Harrison and H. G. Bollinger, "Orientation to Automatic Controls," in Introduction to Automatic Controls, 2nd ed., E. F. Obert, Ed., Scranton, Pennsylvania: Internation Textbook Company, 1969, p. 460.

[2] Chandrasekara, C. & Davari, A. (2004) Experiments for the undergraduate control laboratory. Proceedings of the Annual Southeastern Symposium on System Theory. 36, 488–491. doi:10.1109/ssst.2004.1295705.

[3] Farag, A. & Werner, H. (2002) Robust H2 controller design and tuning for the ACC benchmark problem and a real-time application. IFAC. doi:10.3182/20020721-6-es-1901.00348.

[4] George, A., Sunny, A., Cyriac, J. & Francis, M. (2016) Signal processing in LVDT for automatic calibration. International Conference on Electrical, Electronics, and Optimization Techniques, ICEEOT 2016. 1114–1118. doi:10.1109/ICEEOT.2016.7754858.

[5] Bogdan, M. (2009) Measurement experiment, using NI USB-6008 data acquisition. Journal of Electrical and Electronics Engineering. 2 (1), 117–120.

[6] Abou-Hanna, J., Abuzaid, W., Fakheri, A. & Okamura, K. (2006) Flexible Labview based experiments modules for teaching engineering fundamentals. Proceedings of 2006

Paper ID: 2962
International Conference on Mechanical, Manufacturing and Process Engineering (ICMMPE – 2022)
Organizer: Faculty of Mechanical Engineering, Dhaka University of Engineering & Technology (DUET), Gazipur, Bangladesh
Website: https://icmmpeduet.com/

Experimental Study of Flow Field on Upper Surface of NACA 0015 & NACA 2418 at Different Angle of Attack

Towsibur Rahman[1], Ariful Islam Shubho[2], Md Sakib[3] and Noman Safa[4]

[1,2,4]Department of Aeronautical Engineering, Military Institute of Science & Technology(MIST), Dhaka, Bangladesh
[3]Department of Petroleum and Mining Engineering, Military Institute of Science & Technology(MIST), Dhaka, Bangladesh
E-mail: towsibur.aero08@gmail.com

ABSTRACT

The study of flow field over the upper surface of an airfoil has extensively been considered a topic of interest in aerodynamic science. In this study, the flow field over the upper surface of a symmetric airfoil and an asymmetric airfoil has been observed. NACA 0015 has been utilized for the symmetric airfoil, and NACA 2418 has been employed for the asymmetric airfoil. The method is completely usual, but here we apply it to the conventional airfoils vertical to the wind. The study has been carried out at Reynolds Number, Re=2*105. For this Reynolds number, the comparative analysis between the flow field of symmetric and asymmetric airfoils has been done here. The main focus of this study is to determine the characteristics of the flow field created over a symmetric and an asymmetric airfoil and find out the variation of this effect at distinct angles of attack. This study differentiates among the performances and sets up characteristic graphs that help comprehend the flow fields of two polar opposite objects more readily. The slightest variation in the angle of attack leads to a certain amount of impact, which, if studied, can be helpful for various aerodynamic problems. So an attempt has been made to find this divergence using a closed-loop wind tunnel and two small-scale airfoil models.

Keywords: Flow characteristics; Airfoi; angle of attack; laminar flow; turbulent flow.

1. INTRODUCTION

Experimental studies on the airfoils have been conducted throughout many years to distinguish between flow patterns across the top surfaces of the symmetric and asymmetric airfoil [1]. It has been done to provide enough information to help solve aerodynamic problems in the future [2]. Initially, it was decided to carry out only experimental studies, but further decisions on flow direction patterns were investigated along with the results in order to better analyze the results. Studies of airfoil flows have been uplifted mostly by actions to avoid or lessen unwanted effects such as flutter, vibrations, buffeting, gust response and dynamic stall [3-4]. The prospective scope of the project is to simulate the dynamic stall phenomenon of any airfoil [5]. The study was based on the boundary layer concept of flow pattern change over airfoils.

In the experiment, it was the fact that the Wind Tunnel functioned at low velocity, resulting in variation of flow pattern from the actual theoretical concept, which encouraged us to make two new symmetric and asymmetric airfoils and execute the study on those rather than the existing ones [6]. Flow over symmetric airfoil; laminar flow pattern changes very slowly with the angle of attack with a normal shift in velocity and pressure [7]. There is a more inferior chance of any wake region being formed. However, if the angle of attack is raised, the wake region will commensurately increase [8]. Whereas flow over asymmetric airfoil should be laminar in ideal condition, with the angle of attack, the flow turns into turbulent from laminar drastically [9-10]. And in this case, velocity becomes negative due to turbulence. The negative rate refers to a transformation in velocity direction for adverse pressure [11]. Due to adverse pressure and change in velocity direction, there is always a possibility of a wake region being created in the asymmetric airfoil [12-13]. For similar rises of the angle of attack, the wake region will be greater in the asymmetric airfoil condition than the symmetric airfoil [14].

2. EXPERIMENTAL SETUP

2.1 Test Section

The test section was the most vital part of modifying the experimental setup. The test models were set in the test section with the help of the mounting system. Eventually, the top wall of the test section was modified so that pressure, velocity, and flow direction could be found over each point of the test model and upstream and downstream of the test model. The material used was a plexi-glass sheet of 5 mm thickness.

2.2 Top Wall and Slider

The top wall was modified for accommodating the traverse mechanism at an upstream position at 60 mm from the front of the test section, and a hole was formed for the static port, which is about 36 mm from the front of the test section. A group of 7 mm breadth and 170 mm length was created at 196 mm from the semblance of the test section. For the yield of this group, the yaw meter can be hauled all over the test model and also upstream and downstream of the airfoil. On the top wall, a slider was used at which three holes were created at 90 mm, 70 mm, 30 mm, respectively, from the front of the slider for fitting the yaw meter. The yaw meter is fitted on the slider with the help of the traverse mechanism. The slider allows the yaw meter to move over the airfoil surface in the x-direction and also upstream and downstream of the airfoil. The diameter of the holes for accommodating the yaw meter is 7 mm.

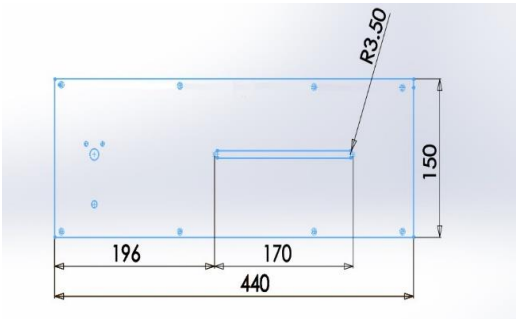

(a)

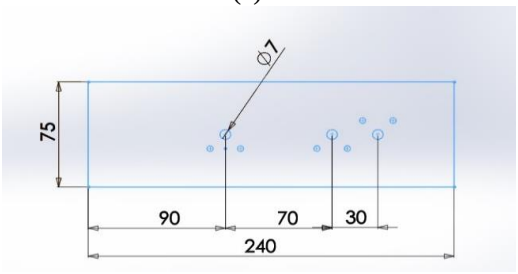

(b)

Fig. 1: (a) Top wall; (b) Slider.

2.3 NACA Airfoil Setup

NACA 2418 was first mounted at 0° AOA for the experiment, and total and static pressure was measured. Then traverse mechanisms were accommodated at different positions of the slider separately, and pressures at three tubes of yaw meter were measured at various points over the airfoil and upstream of the airfoil. The same process was repeated for different y-position, which means at different heights over the airfoil. And the whole above process was done for the Reynolds Number $2*10^5$. The AOA of the airfoil was gradually changed from 0° to different angles varied as 5, 10 and 15°. The same procedure was followed for the set-up of the NACA 0015 airfoil.

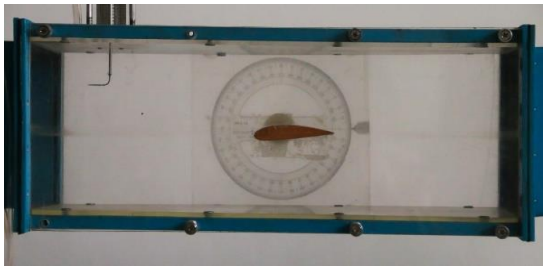

(a)

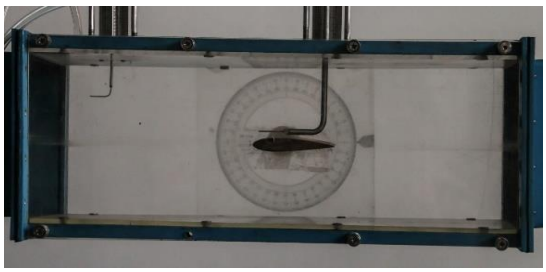

(b)

Fig. 2: (a) NACA 2418 airfoil set-up; (b) NACA 0015 airfoil set-up.

2.4 Yaw Meter Calibration

Yaw meter was calibrated in a swirling flow field within engineering tolerance to determine the value of m and c from the equation stated below-

$$\tan\theta = m\Psi + c \quad [15\text{-}16]$$

Table 1: Yaw Meter Calibration.

α	tanα	P1	P2	P3	Ψ = tanα
0	0	14.2	9	0.34	0.34
5	0.088	11.75	10.5	0.08	0.6
10	0.176	9.25	12.25	-0.185	0.87
15	0.268	6.5	14.5	-0.5	1.1825
20	0.364	3	16.75	-0.89	1.57
25	0.466	0.75	18.5	-1.43	2.11
30	0.577	-0.25	19.5	-2.11	2.79

The values from the table were used to plot the $\tan\theta$ vs Ψ

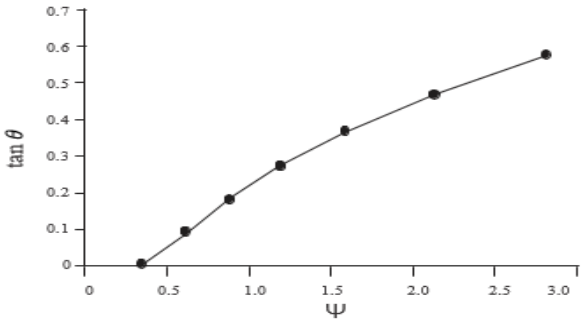

Fig. 3: Calibration of Yaw meter.

3. EXPERIMENTAL RESULTS AND DISCUSSION

The horizontal axis velocity profile is presented, and yaw meter height is shown on the vertical axis. A different angle of attack is used to apprehend the flow velocity profile over the airfoil. Overall, the velocity profile range from approximately 0.097 m/s to about 1.13 m/s. Yaw meter height is from 0 cm to 0.35 cm. As the flow is not influenced in the upper portion of the airfoil, flow velocity remains steady in the upper part of the test section. However, in the origin or middle portion, the flow velocity is greatly deflected by the presence of the substance. As flow contacts across the leading edge to the trailing edge in the airfoil, the flow turns laminar into turbulent.

In Figure 4, flow is steady in the upper portion of the airfoil, while in the lower part, it significantly changes. When x/c is 0, flow strikes the origin of the airfoil while flow velocity remains constant in the upper part. It is generally known as the stagnation point, where flow pressure is maximum, but flow velocity is minimum (approximately 0 m/s). Then, flow velocity increases with x/c (horizontal distance) increment. When x/c is equivalent to 1, the flow velocity is more than 0.7 m/s but less than 0.8 m/s which is the lowest velocity of the 0º angle of attack position of the airfoil. At first, flow in the airfoil's upper surface is laminar, but then it alters into turbulence with the succession of the leading edge to the trailing edge.

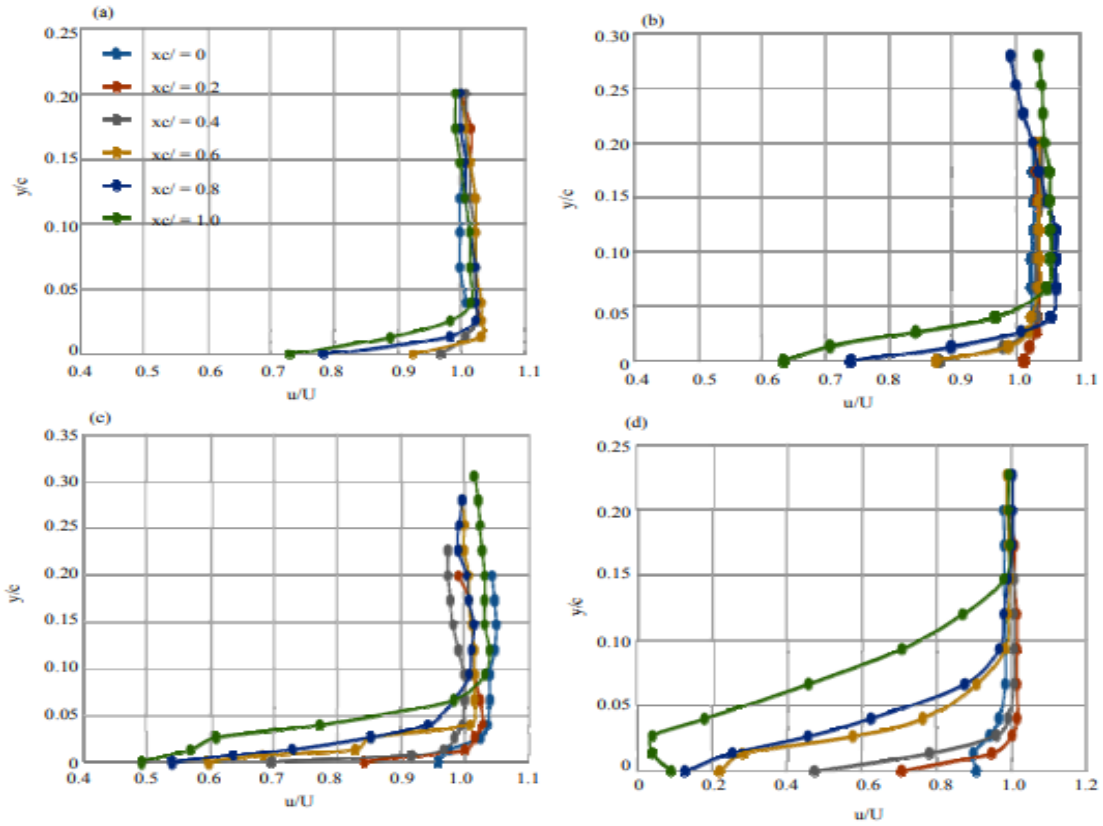

Fig. 4: Velocity profile over upper surface of NACA 0015 airfoil at Re = $2*10^5$, (a) AOA 0º, (b) AOA 5º, (c) AOA 10º, (d) AOA 15º.

NACA 2418 is fabricated and employed to determine the velocity alongside flow characteristics over the airfoil's upper surface. Rate greatly altered for the generation of the huge wake in the trailing edge. It shifts into turbulence for the adverse pressure gradient. Overall, the flow velocity is steady across the upper portion of the test section because there is no influence on any object.

In figure 5(a), where x/c equals zero, flow is constant in the upper region. Yet, the flow does not have any mark for the airfoil. It has not any influence for x/c=0.2, 0.4 as well. At x/c=0.6, on the surface of the cylinder, the flow velocity is around 1.009 m/s. As the yaw meter moved ahead, the speed again decreased (x/c=0.8). When x/c is 1, flow speed subsides most. There, velocity is greater than 0.75 m/s but less than eight m/s. At 0º, AOA flow generation from

laminar to turbulent is quite slower than other AOA positions of the airfoil. The angle of attack is 5^{o} in figure 5(b), where flow transforms laminar to turbulent quickly At the end of the airfoil section (x/c=1), the flow speed becomes approximately 0.65 m/s. Figure 5(c) and 5(d) flow again subside. The lowest rate for AOA 10º is about 0.3 m/s, and for AOA 15º is around 0 m/s. AOA 15º, flow heavily affected by the turbulence. The adverse pressure gradient flow converts laminar to turbulent quicker than any other AOA position.

than 0º angle of attack. With the distance reduction by 0.2, flow velocity greatly reduces than previously.

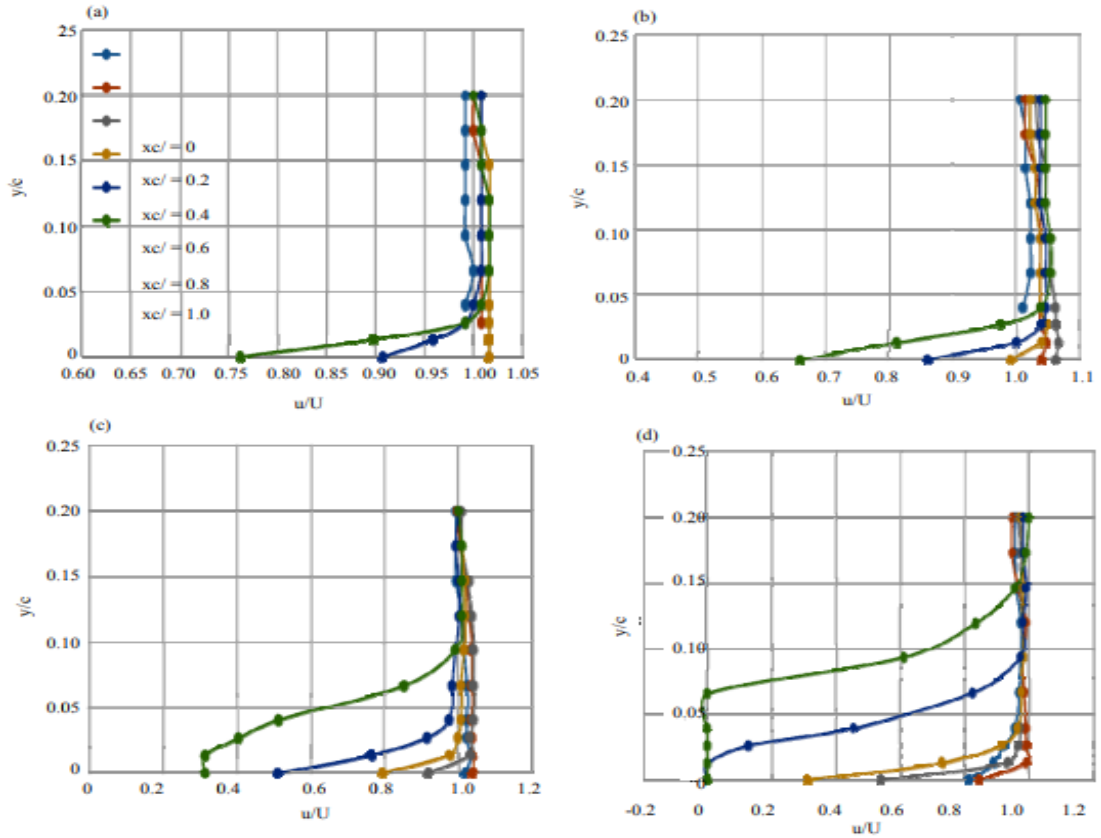

Fig. 5: Velocity profile over upper surface of NACA 2418 airfoil at Re = $2*10^{5}$, (a) AOA 0º, (b) AOA 5º, (c) AOA 10º, (d) AOA 15º.

At 0º AOA, laminar airflow characteristic has been seen over the upstream of the symmetric airfoil, and this corresponds to the actual phenomenon already established. As with the increment of AOA and airflow occurring upstream of the airfoil, there is a transition from laminar to turbulent flow. At 10º and 15º, most change happening is seen and could observe turbulent region characteristics. Values are taken in the x-direction at only 6 points, which has assisted the results of our observation. This helps pinpoint the exact location in the x-direction at which the transition occurs. There has been an observation of a similar phenomenon of laminar flow changing into the turbulent flow as per the increase in AOA and the change in x/c position near the trailing edge. Taking values after the trailing edge area would have provided extended observation on wake characteristics.

By observing the flow characteristics of the symmetric airfoil, airflow transition from laminar to turbulent is encountered, with the increase in AOA and x/c position movement towards the trailing edge. Now, if we try to compare both the airfoils, we need to consider their change in airflow with change in AOA and change of x/c position. For the asymmetric airfoil at 0º AOA, it was seen that laminar flow is occurring almost everywhere from the leading edge to the trailing edge of the airfoil. But there was a sudden change as we changed the AOA from 5º to 10º, which was not too significant for the symmetric airfoil. And at 15º, we could observe the utmost turbulent region, and almost wake characteristics were achieved as few values near the trailing edge came in negative.

4. CONCLUSION

The difference in flow characteristics over a symmetric and asymmetric airfoil is carried out to experience and compare with the actual phenomena. NACA 0015 is used as the symmetric airfoil, and NACA 2418 has applied as the asymmetric airfoil. Small scale airfoil model is employed, and a two-dimensional flow per unit width is developed over the model to measure airfoil properties instead of a finite wing. Bernoulli's equation is applied to illustrate the relation between velocity, manometric height and three-tube probe equation to determine the flow velocity and direction over the airfoils. In the experiment, flow property only at Reynolds number $2*10^5$ is evaluated. More accurate flow characteristics can be found at a lower Reynolds number. Velocities over the airfoil have been measured at 1.5 cm intervals in the x-direction and at various positions in y-direction for each of the points to plot the velocity profile graphs. Results came similar to the actual phenomena. By modifying the test section and using advanced pressure sensors, flow characteristics beneath the airfoil can be achieved.

ACKNOWLEDGEMENT

We are grateful to Dr. M. A. Taher Ali, Professor of the Aeronautical Engineering Department, who allowed us to do the research at the Military Institute of Science and Technology Applied Aerodynamics Laboratory. Thanks to the staff at the laboratory and also the staff of the Machine lab for helping us directly and indirectly.

REFERENCES

[1] W. J. McCroskey, "Unsteady Airfoils," Annual Review of Fluid Mechanics, 14, 285-311 (1982).

[2] M. Lin and H. Sarlak, "A comparative study on the flow over an airfoil using transitional turbulence models," AIP Conference Proceedings. Vol. 1738. No. 1. AIP Publishing LLC, 2016.

[3] M. S. Genç, I. Karasu and H. H. Açıkel, "An experimental study on aerodynamics of NACA2415 aerofoil at low Re numbers," Experimental Thermal and Fluid Science, Vol. 39, pp. 252-264, 2012.

[4] A. Garcia-Sagrado and T. Hynes, "Wall pressure sources near an airfoil trailing edge under turbulent boundary layers," Vol. 51, pp. 1057-1071, 2011.

[5] P. F. Melani, F. Balduzzi, G. Ferrara and A. Bianchini, "An annotated database of Reynolds aerodynamic coefficients for the NACA0018 airfoil," AIP Conference proceedings, pp. 020110, 2019.

[6] H. Sogukpinar and I. Bozkurt, "Implement of different turbulence model to find proper model to estimate aerodynamic properties of airfoils," AIP Conference Proceedings, pp. 020003, 2018.

[7] M. M. Saad, S. B. Mohd, M. F. Zulkafli and W. M. E. Shibani, "A TomoPIV Flow Field Study of NACA 63-215 Hydrofoil With CFD Comparison," Fluids Engineering Division Summer Meeting, Vol. 59070. American Society of Mechanical Engineers, 2019.

[8] H. Sogukpinar, "Implementation of different turbulence model to find proper model to estimate aerodynamic properties of airfoils," AIP conference proceedings, Vol. 1935. No. 1. AIP Publishing LLC, 2018.

[9] W. L. Siauw, J. P. Bonnet, J. Tensi, L. Cordier, B. R. Noack and L. Cattafesta, "Transient dynamics of the flow around a NACA 0015 airfoil using fluidic vortex generators," International Journal of Heat and Fluid Flow. Vol. 31, No. 3, pp. 450-459, 2010.

[10] Md. T. Islam, A. M. E. Arefin, M. H. Masud and M. Mourshed, "The effect of Reynolds number on the performance of a modified NACA 2412 airfoil," AIP conference proceedings, Vol. 1980, No. 1. AIP Publishing LLC, 2018.

[11] A. Colidiuc, B. Suatean and S. Galetuse, "Aerodynamic characteristics of wing profiles wind generators," AIP Conference Proceedings, pp. 1494, 2011.

[12] Md. I. Khar, K. Ahasan and Md. Ali, "Numerical investigation of drug reduction using moving surface boundary layer control (MSBC) on NACA 0012 airfoil," AIP Conference Proceedings, pp. 040011, 2018.

[13] Md. S. Islam, S. M. Hakim, Md. Ali and Md. Q. Islam, "Numerical investigation on boundary layer control through moving surface in NACA 0012 airfoil," AIP Conference Proceedings, Vol. 1851. No. 1. AIP Publishing LLC, 2017.

[14] M. Goszewski, A. Moyer, Z. Bazan and D. J. Wagner, "Exploring student difficulties with pressure in a fluid," AIP Conference Proceedings, pp. 154, 2013.

[15] P.A. Blackmore, " A static pressure probe for use in turbulent three-dimentional flows," Vol. 25, pp. 207-218, 1987.

[16] T. Rahman and A. I. Shubho, "Experimental study to observe the change of flow characteristics on a stationary cylinder and a rotary cylinder with two different rotational speeds," Journal of Mechanical Engineering, Automation and Control Systems, Vol. 2, No. 1, pp. 19-35, 2021.

Paper ID: 3019
International Conference on Mechanical, Manufacturing and Process Engineering (ICMMPE – 2022)
Organizer: Faculty of Mechanical Engineering, Dhaka University of Engineering & Technology (DUET), Gazipur, Bangladesh
Website: https://icmmpeduet.com/

Friction Stir Spot Welding: A novel approach to weld Polyvinyl Chloride

Kanta Sarma[1] Manash J Borah[1] and Niharendu Saha [2]

[1]Department of Mechanical Engineering, Assam Down Town University
[2] Department Of Mechanical Engineering, Assam Engineering College
E-mail: sarmakanta44@gmail.com

ABSTRACT

Unlike mechanical fasteners, joining thermoplastics with friction welding has huge advantages. It has not been many days that welding has been considered as a conventional method for joining plastic materials. Friction stir spot welding is a branch of friction stir welding. A lot of research has been going on using materials like thermoplastics and their joining processes. Polyvinyl chloride also known as PVC, is a vastly used thermoplastic. Polyvinyl chloride has numerous applications like packaging, constructions etc. In this study, Friction stir spot welding experiment was carried out in commercial PVC sheets. The experiments were conducted with different tools having different shapes of pin (triangular, square, circular). The temperature of the heat-affected zone was recorded followed by the cooling curve. Considering tool geometry the triangular probe showed highest joining efficiency as well as the highest peek temperature was recorded with the same tool. Friction stir spot welding can add a different dimension in terms of joining polyvinyl chloride and various plastic materials if applied into manufacturing industries.

Keywords: Friction stir welding; Friction stir spot welding; Polyvinyl Chloride.

1. INTRODUCTION

In recent years, the manufacturing companies have been focusing on engineering thermoplastics and composite materials. the fact that they have gave gained so much popularity among the manufacturing industries, their lightweightness has played an important role which causes to increase the overall efficiency[1]. Other parameters such as variation in design, low costing, high specific strength, lesser weight etc. played a part too for its huge acceptance rate[2]. Another main aim of this booming industry is to minimize pollution caused by fuel consumption and to increase the energy efficiency. These aims can be obtained by innovating and manufacturing materials like composite materials and light weight alloys [3]. Researchers have been experimenting to achieve desired weld quality for thermoplastic materials with techniques such as; extrusion, hot plate, hot gas etc. [4]. The efficiency of the joint materials found to be quite poor followed by poor microstructure and mechanical properties. Apart from solid state processes like ultrasonic welding, the base material of the weld samples present very poor thermal properties with conventional joining methods. Other processes like adhesive bonding and mechanical fastening had been practiced for long time but these processes have limitations too. Also, adhesive bonds are well known for their high sensitivity to environmental agents like temperature, moisture etc. [5][6]. Moreover, Such bonding processes requires surface preparation which causes to compromise the quality and efficiency of the base metal. Conventional fusion methods can not be implemented on the thermoplastics since they have a very low melting point. there is mechanical fastening process which might be used but such fastening processes comes with rivets, nuts and bolts that tends to increase the weight of the base material incredibly high and makes it inconvenient to work with. To achieve a better-quality welding and as a joining process of such materials like thermoplastics and different alloys, friction welding is suitable since it does not change the features of the base material as well as doesn't end up melting it [5].

Friction stir welding was first developed at 1991 at TWI. it is nothing but a solid-state joining process[7]. FSSW is a variant of FSW with slight differences. Such as; tool translation is absent in FSSW. So, it is usually used for lap joining for materials with smaller thickness whereas FSW is usually performed on materials that requires butt joints forming a line of contact [8]. FSSW was first developed as a commercial purpose to weld materials with low melting point like aluminium in the automobile industry to replace resistance stir welding (RSW)[9]. The FSSW process requires a tool and the tool is usually accompanied by a pin and shoulder having a diameter bigger than the pin. The typical FSSW process consists three phases; plunging, stirring and retracting. The weld material is caused to be expelled from due to the plunging of the tool. And then the upper and lower base material starts to melt and mix due to pressure and heat generated from the rotating tool. Hence, the joint is formed due to the fording pressure created by the tool [10].

Due to the high demand of the thermoplastics and polymers, the application of the friction welding in such materials have increased too. But Friction welding have some weld defects too which leads to poor tensile strength

of the welded materials [11]. Friction welding has been considered a feasible way to weld polymers and dissimilar materials. Researchers also found that weld strength often varies on the process parameters [10][12]. Even the number of weld spots or welding style (double spot, zigzag style) comes into consideration in strength analysis [13]. Hence, in this study selection of the process parameters has been taken into consideration. Along with the welding parameters, such as tool rotational speed, the effect of the tool geometry has been investigated with three different tool profiles (circular, triangular, square). Finally, for the evaluation the welded joints ; temperature distribution profile, cooling curve, tensile tests along with efficiency have been investigated in this study.

2. EXPERIMENTAL PROCEDURES

2.1 Material properties

In this study polyvinyl chloride also known as PVC has been taken as base material. PVC is in high demand these days due its availability and cheaper costing. The thickness of the plates were 5mm each. The spot welding was conducted using lap joint formation. The table below shows the physical properties of the base material obtained from the experiment.

Table 1: Material Properties Of Base Material

Base material	Melting temperature ℃	Glass temperature ℃	Tensile strength (MPa)	Young's modulus GPa
PVC	212	87	18	2.8

2.2 Tool Design

℃

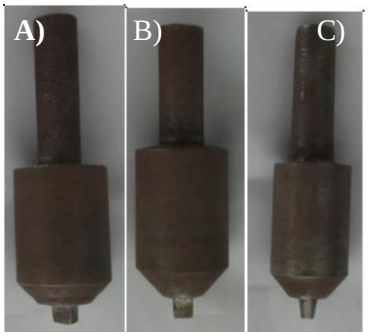

Fig 1: Types of tools : A) Trinangular probe, B) Square probe, C) Circular probe

To investigate the effect of tool geometry on the base material three different shapes of tools have been considered. Tools with square triangular and circular pin were used for performing the experiment. All the tools were prepared and fabricated in the university workshop using mild steel and the probe or the pin of all the three tools (square,triangular,circular) had a length of 6.4mm. Mild steel has high thermal conductivity with a melting point of 1350-1550°C which provides the tool shoulders to generate enough heat to melt down the base material and formring the joints. The images of the tools have been shown in fig 1.

2.3 Welding procedure

The experimental procedures were performed in PVC sheets which had a thickness of 5mm each. Commercial PVC samples (polyvinyl chloride) from the same sheet has been taken to avoid any sorts of effects of materials change. Before starting the welding procedures, the samples were clamped tightly (as shown in the fig 3) using two straps of mild steel plates with the help of nuts and bolts. It is essential to make sure that the samples were fixed properly and not movable during the welding.

Fig 2: Radial Drilling Machine

Fig 3: Experimental Set up

A radial drilling machine was used to perform this experiment. The tool was attached on the spindle of the drilling machine. Firstly, the tool was placed and plunged between the clamped straps. All the three samples of the PVC plates were welded at a single pass with a specific tool rotational speed. Formation of plasticized zone would be visible around the pin of the tool. Friction between the plates and the rotational tool causes to generate adequate amount of heat that increases the temperature of the advancing side as well as it causes to mix the materials. After the completion of the welding, the tool is moved back

to it's original position. By doing so, the welded materials cool down and ends up solidifying by joining together. A keyhole which is a common defect in FSSW process; is visible in the upper plate. Thermoplastics are well known for their bad heat conduction. For this reason, the the lower plate is not effected by this keyhole defect as shown in fig 4.

3. RESULTS & DISCUSSION

After a few trial and error method the ideal rpm for all the three samples were selected as 720 rpm. As this this spot welding there was no transverse speed other than tool rotational speed. The depth of peneteration of the tool was near about 80% of the total thickness, i.e around 8mm. All the final experiments were run at a tool rotational speed of 720 rpm. Using a laser temperature gun (as shown in fig 3) the maximum temperatre for all the three samples were recorded. Also, to establish a cooling curve, the temperature was recorded at a time interval of 5s. the rotational speed of the tool was kept constant for all the samples. The effect of tool geometry (square, trinangular, circular) were discussed here. Moreover, how the tool geometry effects the tensile strength of the welded samples are compared in terms of efficiency.

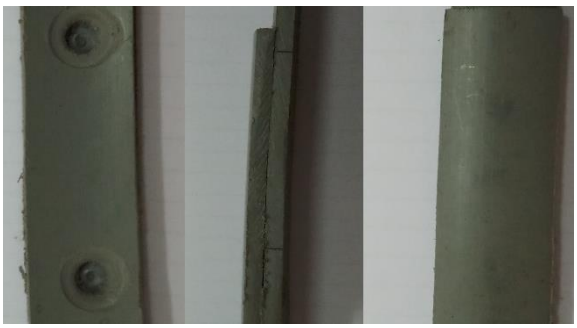

Fig 4: Double spot friction stir welding lap joint

3.1 Temperature Analysis

The temperature of the welded samples were recorded considering the nugget zone of the samples. Three temperature Vs time graphs has been presented for three different shapes of tool. It took 70 seconds for the weld samples to obtain room temperature. the tool variation has negligible effect on PVC samples.

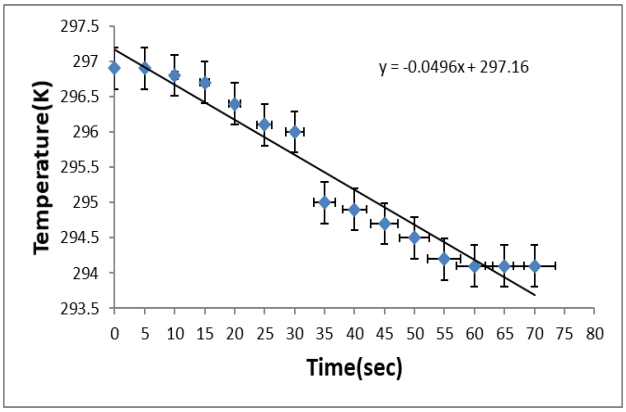

Fig 5: Cooling Curve of FSSW sample carried out by Triangular Probe Tool

The highest temperature was recorded as 296.9K with triangular probe. The maximum temperature was obtained as 296.7K with square probe and the circular probe showed a maximum temperature of 296.1K. The cooling curves with maximum temperature has been shown below (fig 5,6 and 7)

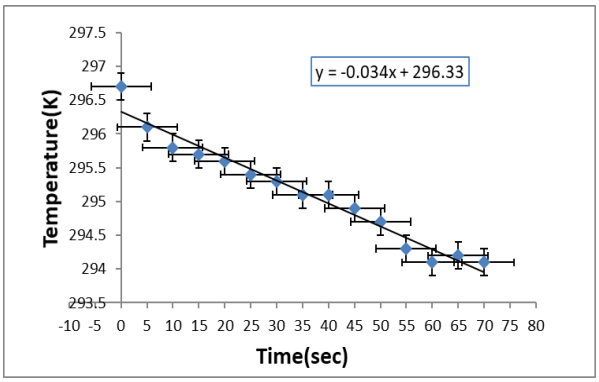

Fig 6: Cooling Curve of FSSW sample carried out by Square Probe Tool

.

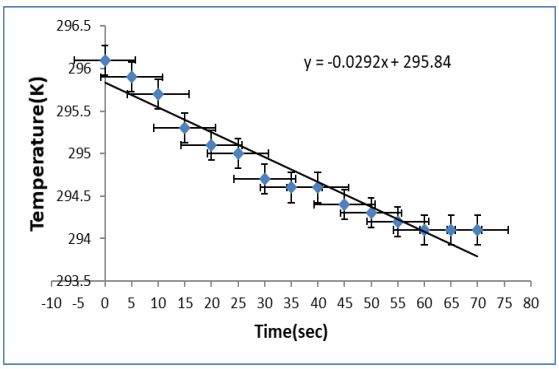

Fig 7: Cooling Curve of FSSW sample carried out by Circular Probe Tool

For clear understanding of the effect of different tools on the weld samples, a bar chart has been shown. It's evident from the figure that the triangular pin caused the highest maximum temperature on the welded samples. It's because of the low edged angles of the tool. The triangualar pin has sharper edges than the circular and the square shaped pin. The sharp edges cause more material to expel from the workpiece material, hence the highest maximum temperature is achieved. With the increasing angle of the edges of the tool, the sharpness decreases. Thus, it causes less material to expel. Although this difference between the variation in temperature is less than the alloys since PVC is a bad heat conductor.

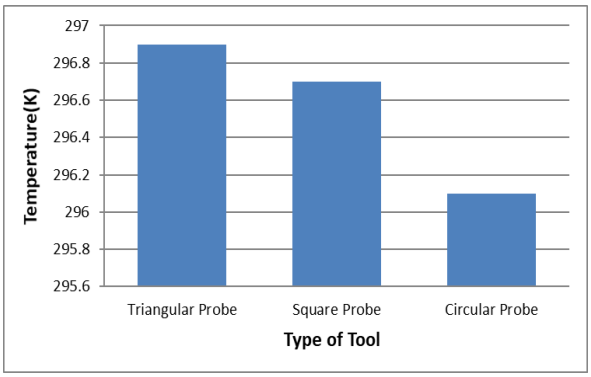

Fig 8: Temperature-tool geometry graph

3.2 Strength analysis

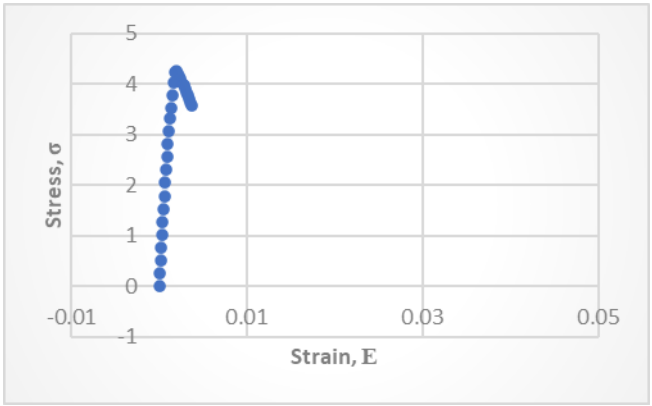

Fig 9: Stress-Strain curve for PVC

Using UTM the strength of the base material and the welded samples were recorded. The base material showed strength of 18 MPa. Then the strength of the welded samples were recorded. The joining efficiency of the weld samples has been figured out using following formula:

$$\text{Joining efficiency} = \frac{strength\ of\ the\ material}{strength\ of\ the\ base\ material} \quad (1)$$

Table 2: Ultimate strength

Type of tool	Ultimate Strength of weld samples (MPa)	Joining efficiency η٪
Triangular probe tool	4.26	23.6
Square probe tool	2.61	14.5
Circular probe tool	0.9	5

The strength of the welded samples are less than the base material due to the material flow and expelled material from the weld joint. The highest weld strength was achieved with the sample which was welded by the triangular shaped tool pin. The highest weld strength of the weld samples was recorded as 4.26 MPa. Then the second highest was achieved by the square shaped tool and the lowest was recorded with the circular shaped tool pin. Joining efficiency has been determined for all three samples. Similarly, the highest joining efficiency was obtained as 23.6% for the sample which was welded with triangular shaped tool. A graph has been demonstrated that shows the effect of tool geometry in terms of joining efficiency.

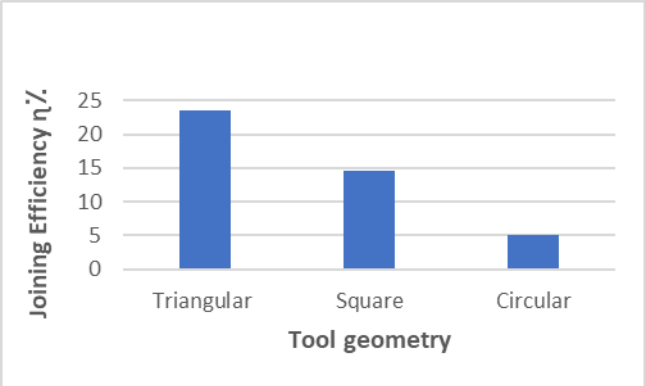

Fig 10: Strength of different FSSW samples welded by different tool

4. CONCLUSION

From the above experiment and results it can be concluded that conducting FSSW on thermoplastic material like PVC is possible in a radial drilling machine with certain RPM. Eventhough thermoplastics or engineering plastics are bad heat conductor, using a perfect tool material which is capable of generating enough heat (in this case mild steel) can solve that issue. Not only the tool material, but also the tool geometry plays an important role while joining PVC with FSSW process. It is evident from this experiment that tools with sharp edges (triangular) provide the highest

maximum temperature and highest weld strength. As with the triangular shaped pin; due to their geometrical structure the intermixing spaces between the two plates are more, hence the produced weld strength is much higher. Only by changing the tool geometry; choosing tools with sharper edges can increase the joining efficiency by 8% to 18%. Also, by increasing the number of weld spots, the strength of the welded PVC sheets can be improved.

ACKNOWLEDGMENT

This work is supported by the technicians of the workshop from Mechanical Department of Assam Downtown University, Guwahati, Assam.

REFERENCES

[1] S. T. Amancio-Filho and J. F. dos Santos, "Joining of polymers and polymer-metal hybrid structures: Recent developments and trends," *Polymer Engineering and Science*, vol. 49, no. 8, pp. 1461–1476, Aug. 2009.

[2] P. Kah, H. Väst, C. Magnus, R. Suoranta, and J. Martikainen, "Techniques for joining dissimilar materials: Metals and polymers Tribological behaviour of TiC-SiC composite View project Improved material properties in lithium-ion battery joints (EMPIRE) View project TECHNIQUES FOR JOINING DISSIMILAR MATERIALS: METALS AND POLYMERS." [Online]. Available: https://www.researchgate.net/publication/266672380

[3] A. B. Abibe, S. T. Amancio-Filho, J. F. dos Santos, and E. Hage, "Mechanical and failure behaviour of hybrid polymer-metal staked joints," *Materials and Design*, vol. 46, pp. 338–347, Apr. 2013.

[4] Electrical Manufacturing & Coil Winding Association., Institute of Electrical and Electronics Engineers., National Electrical Manufacturers Association., and Ind.) Electrical Manufacturing & Coil Winding Conference (26th : 2003 : Indianapolis, *Proceedings, Electrical Insulation Conference and Electrical Manufacturing & Coil Winding Technology Conference : Indiana Convention Cnter, Indianapolis, Indiana, September 23-25, 2003*. IEEE, 2003.

[5] S. K. Sahu, K. Pal, and S. Das, "Parametric study on joint quality in friction stir welding of polycarbonate," in *Materials Today: Proceedings*, 2020, vol. 39, pp. 1275–1280.

[6] J. H. Kweon, J. W. Jung, T. H. Kim, J. H. Choi, and D. H. Kim, "Failure of carbon composite-to-aluminum joints with combined mechanical fastening and adhesive bonding," *Composite Structures*, vol. 75, no. 1–4, pp. 192–198, Sep. 2006.

[7] W. M. Thomas, "Friction stir welding and related friction process characteristics," 1998. [Online]. Available: https://www.researchgate.net/publication/273122758

[8] A. Arici and Ş. Mert, "Friction stir spot welding of polypropylene," *Journal of Reinforced Plastics and Composites*, vol. 27, no. 18, pp. 2001–2004, Dec. 2008.

[9] M. K. Bilici and A. I. Yükler, "Influence of tool geometry and process parameters on macrostructure and static strength in friction stir spot welded polyethylene sheets," *Materials and Design*, vol. 33, no. 1, pp. 145–152, Jan. 2012.

[10] S. H. Dashatan, T. Azdast, S. R. Ahmadi, and A. Bagheri, "Friction stir spot welding of dissimilar polymethyl methacrylate and acrylonitrile butadiene styrene sheets," *Materials and Design*, vol. 45, pp. 135–141, 2013.

[11] V. Jaiganesh, B. Maruthu, and E. Gopinath, "Optimization of process parameters on friction stir welding of high density polypropylene plate," in *Procedia Engineering*, 2014, vol. 97, pp. 1957–1965.

[12] M. Rezaee Hajideh, M. Farahani, S. A. D. Alavi, and N. Molla Ramezani, "Investigation on the effects of tool geometry on the microstructure and the mechanical properties of dissimilar friction stir welded polyethylene and polypropylene sheets," *Journal of Manufacturing Processes*, vol. 26, pp. 269–279, Apr. 2017.

[13] Mr. Manash Jyoti Borah, Dr Niharendu Saha, "System and Method for Double spot Zigzag Friction Welding," Indian Patent No. 201831045232, Date of Patent 15.01.2021.

Paper ID: 3165
International Conference on Mechanical, Manufacturing and Process Engineering (ICMMPE – 2022)
Organizer: Faculty of Mechanical Engineering, Dhaka University of Engineering & Technology (DUET), Gazipur, Bangladesh
Website: https://icmmpeduet.com/

Production and Mechanical Characterization of Biofiber/Glass/epoxy Hybrid Composites

A Razzaq , M S Rabbi*, Sababa Irfan Moma and Snigdha Das

Department of Mechanical Engineering, Chittagong University of Engineering & Technology

*E-mail: rabbi@cuet.ac.bd

ABSTRACT

Hybrid composites combine multiple types of fibers in the same matrix to increase the effect of fiber characteristics on the overall qualities of the composite. Because of their practical benefits like low cost, low density, biodegradability, renewable, and environment friendly and comparable mechanical properties with synthetic fibre composites, nowadays, interest in hybridization is increasing in a revolutionary way both in research and application. This experimental study deals with developing and investigating a partially eco-friendly banana-jute-glass fibre reinforced epoxy hybrid composite. Samples of 500 mm × 500 mm × 7 mm were fabricated using the Hand layup method having different stacking sequence. The fiber surface were modified by alkalisation and acetylation treatment. The ASTM standard specimens were investigated to measure tensile, flexural, impact strength, and water absorption properties. GJBJG sample exhibited preferable tensile and flexural properties, while JBGBJ sample had the best impact property. Water absorption was found maximum for JBGBJ specimen.

Keywords: Hybrid composites; Hand Layup; Surface treatment; Mechanical Characterization.

1. INTRODUCTION

With the advancement of technology and industrial establishment, the necessity for eco- friendly and sustainable materials from the bio-mass or industrial by-products is a matter of great concern now a days. On account of this concern, the use of natural fiber has increased significantly in composite world from the last few decades. Natural fiber-based composites offer superior characters such as low cost, low density, good damping properties, recyclability, renewability, high availability, biodegradability, less abrasive damage to equipment etc [1-2]. However, most natural fibre-based composites lack mechanical properties compared to synthetic fibre ones, as their mechanical characteristics are far inferior to those of synthetic fibers. They also have a high vulnerability to water absorption, low dimensional stability, variable characteristics, poor thermal resistance, and incompatibility with polymeric matrices, all of which result in poor fibre/matrix interface adhesion.. On the other hand, although synthetic fibers have excellent mechanical, electrical, thermal properties as well as high specific properties, high strength to weight ratio, corrosion resistant and high fatigue etc. it has many disadvantages mainly to the environment and health as well as high cost of processing, non-recyclability etc [3].

An effective solution to these conflicting natures of synthetic (Carbon, glass, and aramid) and natural fiber (jute, sisal, banana, bamboo, kenaf, coir etc.) is to create a superior but cost-effective composite by integrating natural and synthetic fibers in the same matrix material and maximizing the qualities of both fibers [4]. The goal of hybridization is to achieve a synergistic impact between the constituents on the overall characteristics of composites. A combination of high-performance fibre with low-performance fibre provides versatility in the performance of the product. Additional benefits of hybrid composites include weight savings, less cost, lower notch sensitivity, increased fracture toughness, thermal stability, extended fatigue life, and excellent impact resistance.[5-9]

Although much research has been done on a variety of hybrid composites, there has been very little on the hybridization of three types of fiber to get the desired composite properties. The mechanical properties of synthetic and natural fiber reinforced hybrid composites have been the subject of several studies. However, The idea that coupling two types of natural fibers with glass fiber in a polymer could produce a synergy in terms of better performance has yet to be thoroughly addressed. This study intends to develop a hybrid composite using both jute and banana fibre incorporation with glass, which is expected to have better mechanical characteristics than conventional two fibre-based hybrid composites.

2. EXPERIMENTAL

2.1 Materials:

The composites in this research were prepared using banana (Musa sapientum) fiber, jute (Corchorus capsularis) fibre, and glass fiber reinforcement whereas epoxy resin was used as the matrix. Banana fibre (B) has been collected from Sirajganj, Bangladesh, while the jute fibres (J) mats were obtained from local markets. The commercial-grade epoxy resin and the hardener has been collected from the

local supplier. Dry woven E-Glass fabric (WR600) (G) roving of with a weight of 600 gm is chosen as the synthetic fibre to fabricate the specimen. Cheimcal composition and the physical properties are listed in Table 1 and Table 2, respectively.

Table 1: Chemical composition of Jute and Banana fibers [10]

Property	Banana fiber	Jute fiber
Cellulose (%)	63	60
Hemicellulose (%)	22	12
Lignin (%)	5	14
Moisture (%)	10	-

Table 2:Physical condition of the materials [11]

Property	Banana fiber	Jute fiber	E-glass fiber
Density (g/cm^3)	1.35	1.4	2.62
Tensile strength (MPa)	529	393	3450
Tensile modulus (GPa)	8.2	11.5	70
% elongation	2.1	1.6	2.4

Jute woven fabrics and banana fibers were cut according to the length of the specimen and were cleaned up with pressurized water to carry away undesirable organic materials present on the surface. The fibres were then set to dried under direct sunlight for 8 h for removing moisture present in it. Figure 1 and 2 depicted the collected jute fibre and banana fibre, respectively.

The collected natural fibres were treated with alkali and acetic anhydride, and the later process of neutralization was done by treating the fibre with the acetic acid solution. Chemicals such as acetic acid, acetic anhydride and sulphuric acid , sodium hydroxide have been collected from a local chemical supplier.

2.2 Chemical Treatment:

In alkalization, the jute and banana fibres were soaked in a 5 % (w/v) aqueous alkaline (NaOH) solution separately at room temperature, maintaining fibres: solution ratio of 1:15 (w/w) for 2 hours with intermittent stirring for proper de-polymerization of cellulose, hemicellulose, pectin and lignin. Alkali treatment inflates the amorphous regions of the fibres and causes the removal of approximately 41% of the hemicellulose cementing material in the fibre. Upon soaking, the fibres were rinsed multiple times with distilled water before being soaked in distilled water containing acetic acid (1%) to eliminate any remaining NaOH. The neutrality of the fibres was confirmed using a pH paper followed by rinsing with distilled water until they were alkali free. The final pH maintained was 7. Finally, The fibres were treated for hours in the open air/sun and then for 24 hours in a 600°C oven.

The alkaline-treated dry fibres were immersed in glacial acetic acid for 1 h at room temperature. It was transferred to acetic anhydride with one drop of concentrated H_2SO_4 and continue the modification process for 5 more minutes. Subsequently, the fibre was taken out from the mixture and washed with distilled water until all unreacted chemicals were removed, then dried the materials at room temperature for 1 day followed by drying using woven for 12 hours at 60°C.

Fig.1 : Untreated and Treated Jute Fibre Mat

Fig. 2 : Untreated and Treated Banana Fibres

2.3 Composite Fabrication:

A wooden mold in dimension 500 mm × 500 mm × 25 mm was used in this study to prepare the samples. On the upper and bottom sides of the wooden mold, a mold release sheet and PVA (polyvinyl alcohol) spray were applied for quick and easy removal of the sample.

The mixing ratio of epoxy resin and hardener was maintained (10:1). Typically, a fiber to resin ratio of 60% fiber to 40% resin is appropriate. The method used for fabricating the specimen is the hand layup, where all the operations were done manually. During preparation of specimen, room temperature and 65% average relative humidity was maintained.

Release gel was sprayed on the inner surface of the top mould plate, which was then retained on the stacked layers, after the plastic sheet was laid down. The final composite was fastened at all feasible ends with wooden reapers. Finally, for a perfect setup, a rectangular concrete bar with the same cross-section weighing 25 kg was placed on the aforesaid arrangement for 24 hours. For an epoxy-based system, at room temperature, the average curing time is 24 - 48 hours. After curing, the specimen was collected and processed farther. To remove the moisture percentage, the sample was kept for several hours in sunlight after fabrication. Figure 3 illustrates the entire hand lay-up process for composite fabrication.

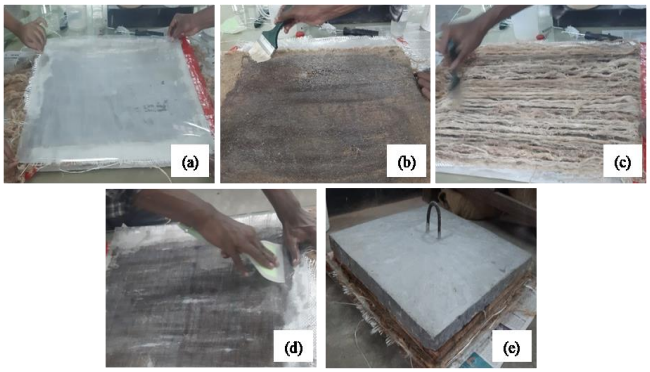

Fig. 3 : Placing (a) glass, (b) jute, (c) banana fibre, (d) squeezing out excess resin by a plastic spreader, (e) weight for compressing the specimen

The composite sample consisted of 5 layers, and three different combinations were fabricated, varied with stacking sequence of glass, banana, and jute (GBJBG, GJBJG, and JBGJB) while maintaining the constant weight proportion of each fibre. The total weight proportion of fibres (glass, jute, and banana) was 35%, while the epoxy polymer was 65%.

Following the curing procedure, the composite specimens were cut into the required ASTM dimensions for investigation. For gathering each test data, three samples were investigated.

3. RESULTS AND DISCUSSION

3.1 Tensile Properties:

Using universal testing machine, tensile properties of the specimens were investigated. Displacement, elongation at break and tensile properties for the various specimens are depicted in Figure 4 and 5, respectively.

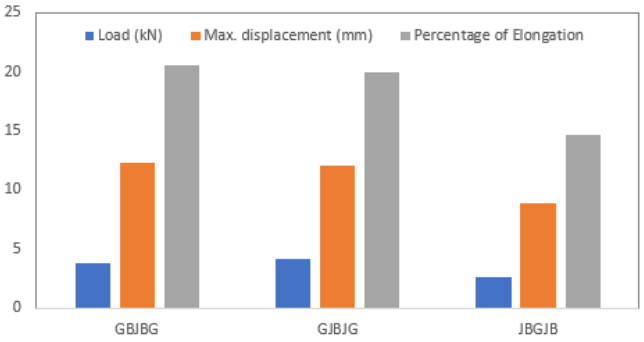

Fig. 4: Break Load, Maximum Displacement and Percentage of elongation for various samples

.

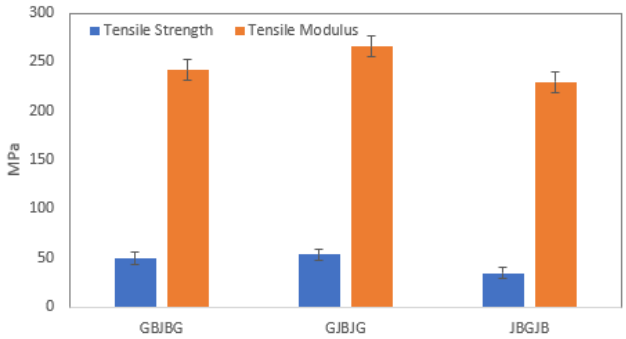

Fig.5 : Tensile properties of composites

Figure 4 compares the break load, maximum displacement, and percentage elongation of several composites. It demonstrates that the GBJBG composite has a lower percentage elongation than the hybrid GJBJG composite, indicating that the hybrid GBJBG composite can sustain greater strain before failure than the GJBJG composite. The tensile strength was lowest for the JBGJB specimen. The GJBJG composite exhibits the maximum Break Load, tensile strength and tensile modulus value of 4.17kN, 53.19 MPa and 265.95, respectively. The stacking sequence JBGJB has the lowest value for all the tensile properties.

Several studies [12-14] have shown that the stacking order has a substantial impact on the composite's mechanical characteristics. All of the research shows that using high-strength fiber as the skin increases the mechanical properties of the sandwich composite, which is also evident here. Both the top and bottom of the GBJBG and GJBJG composites are laminated with glass fiber, which improves the surface polish and increases strength. The high strength and modulus woven jute fibre at the top and bottom layers of the GJBJB, on the other hand, enabled it bear the imposed stress, while the core banana fibres absorbed and distributed the loads uniformly.

The tensile characteristics of the composites are greatly influenced by the alignment of the banana and jute fibres. The natural woven jute mat at the outer portion of the banana fibres has a high tensile strength, which

withstands tensile stress, while the banana core bears the stresses and distributes them evenly. When excessive strength material is employed as an exterior layer, which is the principal load-bearing component in tensile strength calculations, the tensile strength is increased. The advantages of the mat woven jute fibre structure have been noticed in prior studies [15]. The extent of fibre pull out and fracture determines tensile failure.In the case of JBGJB, strong glass fibre lamination was absent at the composite's outer layers, which made them have poor tensile properties.

According to previous studies, the stacking sequence is one of the most important variables in increasing the mechanical properties of a natural hybrid composite. Fibers are spread out in varied fiber orientations in this experiment so that the area of contact between Jute and banana fibers increased composite tensile strength. The tensile modulus is a rigidity and stiffness measurement.

It is investigated that the GJBJG sequence in hybrid composites had the best tensile characteristics when compared to the GBJBG hybrid. The GJBJG epoxy hybrid composite is telling when compared to other types of composites combinations, according to the tensile test results.

3.2 Flexural Properties:

It is found that in flexure test also similar trend has been followed. Layered composite of GJBJG exhibits higher flexural strength and modulus as 297.1 MPa and 5.31 GPa respectively.

Figure 6 and 7 shows the flexural properties and associated information for various specimens.

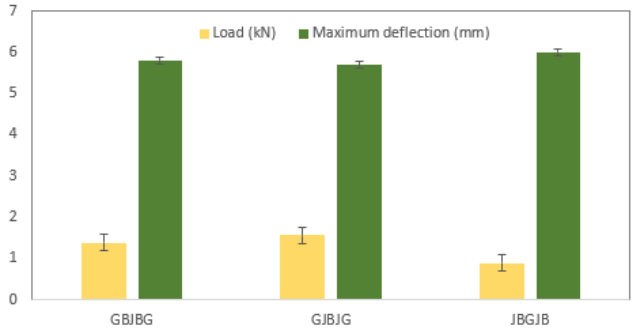

Fig.6: Different Flexural Properties of the Fabricated Composite Specimens.

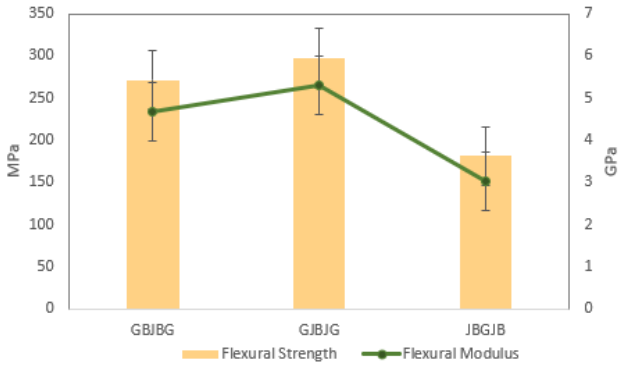

Fig.7: Flexural strength of the fabricated composite specimens.

Under bending force, the upper layer is compressed, the bottom layer is tensioned, and the mid layer is sheared, according to the fundamental bending theory. According to this hypothesis, the predominant load carrying elements in sandwich composites are the exterior layers, hence external layers should be built of high strength fibres to withstand large loads and so improve the composite's qualities. The use of glass fiber as a skin layer improves the composites' strength and stiffness. The outer layer of both GBJBG and GJBJG composites is made up of strong glass fiber. Because of the woven jute mat, the composite constructed of JBJ has a higher flexural strength and modulus than BJB. Woven fabrics are tightly bound and show less damage at the break due to increased fibre-matrix interlocking. As a result, the jute fibre mat is stronger than individual unidirectional banana fibres. Jute mat at the external side and banana as the inner layer enhances the flexural properties of the composites.

Flexural strength and modulus of natural fiber-reinforced polymer composites are influenced by a variety of elements. The results suggest that the strength of the stacking layers of reinforcing composites had an impact on flexural strength and modulus.

The GJBJG configurations were shown to have a better interfacial bonding characteristic than the GBJBG sample, resulting in improved flexural performance. It also demonstrates that, while hybridization improves the composite's properties, the layering sequence has a significantly greater impact on the composite's flexural capabilities.

3.3 Impact properties:

The impact test is used to determine the material's ability to withstand impact force and the amount of energy absorbed. The Charpy impact test machine is used to determine the impact properties. Figure 8 shows a comparison of the impact test results of various composites. The stacking sequence of the fibres has been discovered to be more essential than composition in determining impact toughness. The impact-resistant qualities of the composite

are mostly influenced by resin toughness rather than fiber strength and stiffness. [16].

When compared to the other specimens, the JBGJB sequence has a very high impact strength, as shown by the analysis. 6.8 J of energy is absorbed by the JBGJB composite. The lack of glass fibre in the outer layer accounts for the high strength. When crack propagates, it travels through the matrix and the natural fibres of the composite. It goes to the next layer of fibres existing in a different direction when it hits the end of a fibre in one direction. By increasing the surface area of fracture, this change in layers absorbs more energy than a composite that is simply oriented in direction.

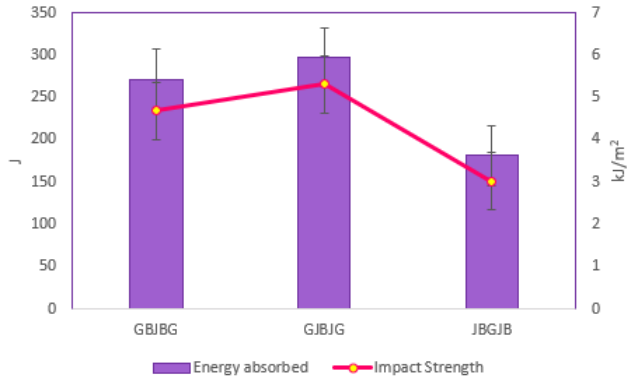

Fig.8: Energy absorbed and impact strength of the fabricated composite specimens

3.4 Hardness properties:

Hardness of a material can be defined as its resistance to deformation caused by a compressive force applied by a sharp object. The hardness values of the composites are compared in Fig. 9. It is found that the presence of glass fibre in the specimens along with its location in the stacking sequence is responsible for the its resistance to penetration.

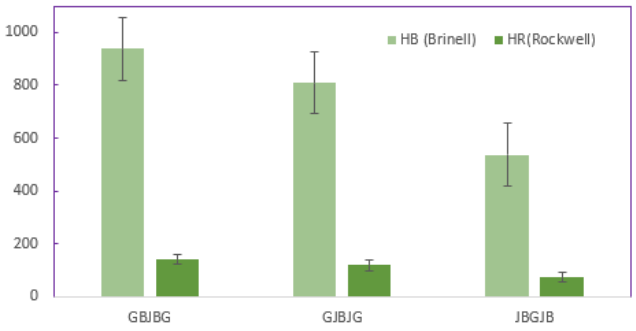

Fig. 9: Brinell and Rockwell hardness of the fabricated composite specimens.

3.5 Water Absorption Properties:

The difference between the specimen's dry and wet weight was used to estimate the moisture absorption % of the hybrid fibre reinforced epoxy composites. The weight growth percentage as a function of time for hybrid fibre reinforced epoxy composite samples (GBJBG, GJBJG, JBGJB) immersed in distilled water at room temperature at 24 hour intervals is shown in Fig. 10. Because of the affinity of jute fibres for moisture, the JBGJB composite has the highest percentage of moisture absorption of all the composites evaluated. Jute fiber has higher absorption, diffusion, and permeability coefficients than banana fiber, allowing the composite of JBJ sequence to absorb more moisture. The moisture absorption percentage of the GBJBG composite is 18.18. The characteristics of lignocellulosic fibres play a big role in water uptake. Natural fibres have hydrophilic characteristics more than synthetic fibres. The presence of glass fibre on the GBJBG and GJBJG composite surface resulted in less water absorption than the JBGJB composite, which has hydrophilic jute fibre mats on the surface. Figure 10 depicts the moisture absorption results of the samples.

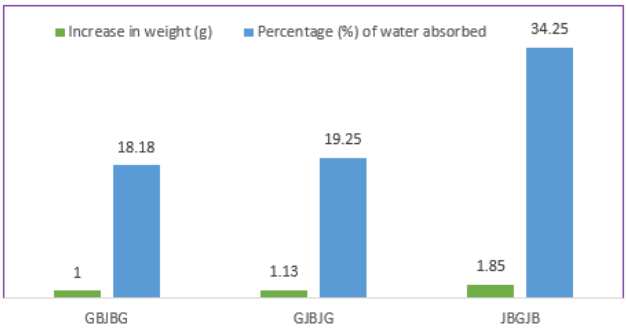

Fig.10: Moisture absorption properties of the fabricated composite specimens

4. CONCLUSIONS

In today's climate, researchers are in search of developing new eco-friendly alternatives for conventional materials, and as a result, extensive studies are taking position in the hybrid composites field. Hybrid composites can be produced using several production techniques. In the composite fabrication hand layup technique was commonly used till now.

A new type of fibre composite is experimentally investigated in this work. The hand layup method is used to successfully construct chemically treated jute and banana fibre reinforced epoxy composites with the highest fibre weight fraction of 0.40. Based on the values obtained from the various tests, the mechanical properties of the chemically treated hybrid composite materials were evaluated and analyzed in detail. The results of the experimental study can be summarized as follows:

1. The orientation in which fibres are layered has a considerable impact on tensile and flexural strength.

2. The hybrid laminate has optimal strength and modulus, as well as two outer glass plies on either side of the natural fibre.
3. The tensile properties of the GJBJG composite are relatively better than the GBJBG composite, and It has a value of 53.19 Mpa tensile strength and 265.95 MPa tensile modulus.
4. The GJBJG composite has the maximum flexural strength because its strength grows as interfacial adhesion increases. The GJBJG composite also has the highest flexural modulus..
5. The JBGBJ composite has an impact strength of 8.9 J, which is higher than the other two sequences.
6. The GBJBG has a maximum hardness value among all the sequences.
7. The water absorption results showed that the developed hybrid composite JBGBJ absorb 34.25% water, which is maximum compared to the other developed composites.

A study of all of the laminates' parameters found that the hybrid laminate GJBJG provides an excellent mix of properties and cost. Banana and jute fibers are abundant in agricultural resources, and they are less expensive than synthetic fibers. Furthermore, as previously mentioned, they have high mechanical qualities, therefore the hybrid of these natural fibres can be employed for a variety of purposes. Chemically treated Jute-banana-glass fibre hybrid composites are suggested for usage in polymer composites instead of synthetic fibres.

REFERENCES

[1] Mahir FI, Keya KN, Sarker B, et al. A brief review on natural fiber used as a replacement of synthetic fiber in polymer composites. Materials Engineering Research, 2019, 1(2): 86-97.
[2] Li M, Pu Y, Thomas VM, Yoo CG, Ozcan S, Deng Y, Nelson K, Ragauskas AJ, “Recent Advancements of Plant-Based Natural Fiber–Reinforced Composites and Their Applications”, *Composites Part B*,2020
[3] P. Noorunnisa Khanam, H. P. S. Abdul Khalil, M. Jawaid, G. Ramachandra Reddy, C. Surya Narayana, S. Venkata Naidu, “Sisal/Carbon Fibre Reinforced Hybrid Composites: Tensile, Flexural and Chemical Resistance Properties” J Polym Environ (2010) 18:727–733
[4] Shahzad A, Choudhry RS, “Design and Manufacturing of Natural Fiber/Synthetic Fiber Reinforced Polymer Hybrid Composites”. Handbook Composites Renew. Mater, 2017, 2: 411-447.
[5] Haneefa A, Bindu P, Aravind I, Thomas S, “Studies on tensile and flexural properties of short banana/glass hybrid fibre reinforced polystyrene composites”, J Compos Mater, 2008 42(15):1471–1489
[6] Reddy GV, Khanam PN, Shobha Rani T, Chowdoji Rao K, Venkata Naidu S, “Chemical resistance studies of kapok/ glass and kapok/sisal fabrics reinforced unsaturated polyester hybrid composites”, Bull Pure Appl Sci, 2007, 26 C(1):17–25
[7] Indicula M, Malhotra SK, Joseph K, Thomas S, “Dynamic mechanical analysis of randomly oriented intimately mixed short banana/sisal hybrid fibre reinforced polyester composites”, Compos Sci Technol, 2005, 65:1077–1087
[8] Pothan LA, Ptschke P, Habler R, Thomas S, “The static and dynamic mechanical properties of banana and glass fibre woven fabric-reinforced polyester composite”. J Compos Mater, 2005, 39(11):1007–1025
[9] Abu Bakar Hariharan A, Abdul Khalil HPS, “Lignocellulose-based hybrid bilayer laminate composite: part 1–studies on tensile and impact behavior of oil palm fiber-glass fiber-reinforced epoxy resin”. J Compos Mater, 2005, 39(8):663–684
[10] Devireddy, Siva Bhaskara Rao, and Sandhyarani Biswas. "Physical and mechanical behavior of unidirectional banana/jute fiber reinforced epoxy based hybrid composites", Polymer composites 38.7 2017, 1396-1403
[11] Singh, Jashanpreet, et al. "Properties of glass-fiber hybrid composites: a review." Polymer-Plastics Technology and Engineering 56.5 (2017): 455-469.
12. Pani, Preeti Ranjan, et al. "Flexural and specific wear rate of seawater aged bamboo, jute and glass fiber reinforced polymer hybrid composites." Materials Today: Proceedings 18 (2019): 3409-3414.
13. Bhoopathi, R., M. Ramesh, and C. Deepa. "Fabrication and property evaluation of banana-hemp-glass fiber reinforced composites." Procedia Engineering 97 (2014): 2032-2041.
14. Bhoopathi, R., et al. "Experimental investigation on mechanical properties of hemp-banana-glass fiber reinforced composites." Applied Mechanics and Materials. Vol. 766. Trans Tech Publications Ltd, 2015
15. Jawaid, M., HPS Abdul Khalil, and A. Abu Bakar. "Mechanical performance of oil palm empty fruit bunches/jute fibres reinforced epoxy hybrid composites." Materials Science and Engineering: A 527.29-30 (2010): 7944-7949.
16. Priya, S. Padma, and S. K. Rai. "Mechanical performance of biofiber/glass-reinforced epoxy hybrid composites." Journal of industrial textiles 35.3 (2006): 217-226.

Paper ID: 3597
International Conference on Mechanical, Manufacturing and Process Engineering (ICMMPE – 2022)
Organizer: Faculty of Mechanical Engineering, Dhaka University of Engineering & Technology (DUET), Gazipur, Bangladesh
Website: https://icmmpeduet.com/

Title: Effect of Grooved Depth Ratio on Flow Friction and Heat Transfer in Enclosure Using D2Q9 Lattice Boltzmann Method

R. Biswas[1], A. Khanom[2], M. M. R. Litan[2] and M.A.Taher[3]

[1]Ph. D Student, Dhaka University of Engineering & Technology and
Assistant Professor, Open School, Bangladesh Open University, Gazipur
[2]MS Student, Dhaka University of Engineering & Technology
[3]Professor, Department of Mathematics, Dhaka University of Engineering & Technology

Corresponding _author: tahermath@duet.ac.bd

ABSTRACT

In the present study, a two-dimensional (2D) Lattice Boltzmann Method (LBM) is applied for numerical simulation on the natural convective flow and heat transfer in a grooved enclosure. The boundaries conditions are (a) the top wall is fixed and heated (b) the inclined walls are cold and (c) two side walls are adiabatic. The main focus of the present paper is to investigate the effects of velocity and temperature for different Grashof number (Gr) with different Grooved Depth Ratio (GDR). The results are presented as velocity, temperature contours, stream function, Average Nusselt Numbers (ANU) for different GDR and Grashof Numbers (Gr). The result depicts that much of the area of the enclosure is affected by the hot temperature of the top wall for higher frequencies according to increasing GDR but the area of the enclosure is exaggerate d in terms of increasing Gr and showing lower frequencies. The overall heat transfer rate is increasing for increasing GDR with different Gr. The present simulations found small inconsistencies in the calculated values of the Nusselt numbers. Because of variation of heat transfer, it can happen at these Grashof numbers.

Keywords: Flow Friction; Heat Transfer; Grooved Depth Ratio (GDR); Grooved Enclosure;

1. INTRODUCTION

Fluid flows and heat transfers in closed enclosures have received great attention from researchers for many years due to their prime importance in lubrication technologies, electronics cooling, solar collectors, food processing. Thereby, an extensive number of papers about natural convection flow and heat transfer in enclosure containing different boundary conditions are studied [1]-[5]. The results give the high temperature at the top and low temperature at the bottom region of the enclosure. The Prandtl number has a minimal effect on the overall rate of heat transfer. The Rayleigh number is grown, the buoyancy force is enhanced and consequently the convective transport is increased. Nusselt numbers are varied according to the Rayleigh numbers, the streamlines and isotherms achieved a maximum for the distribution of partial heater and also increasing Rayleigh number. A review of the heat transfer process by mixed convection of lid-driven cavity with various shapes of geometries was reported by Mustafa et al. [7]. They have discussed the heat transfer enhancement techniques with different velocity and thermal boundary conditions in many geometries of the cavity such as triangle, square, circle, rectangle and wavy with lid-driven. Saha et al. [8] carried out a numerical study of transverse mixed convection inside a vented enclosure with different inlet and outlet locations. They have revealed that the temperature distribution in the flow fields significantly depends on inlet and outlet positions. Using the finite element method, the problem of natural convection heat transfer and fluid flow in a triangular enclosure with uniform and non-uniform bottom heating has been reported by Roy et al. [9]. The effects of various types of cavity shapes on thermal and fluid behaviors are described in the lid-driven cavity flow with different methods [10-13]. In recent years, the Lattice Boltzmann Method (LBM), based on the Boltzmann equation (BE), has been used by many authors as an alternative to the traditional approach for solving the Navier–Stokes (N–S) equations numerically [14-15]. In conventional CFD, the macroscopic N-S approach to simulate fluid flows while the LBM uses a mesoscopic simulation model instead of directly solving the macroscopic fluid quantities (velocity, pressure and temperature), the movement of the fluid particles is considered with some other approximations. Mansouri at al [16] studied that the MRT-LBM simulation of natural convection in a Rayleigh-Benard cavity with linearly varying temperatures on the sides are applied to a micro polar fluid. They discovered that velocity will increase with higher Ra and Nu of radiation has almost constant values along the horizontal wall.

The main purpose of this study is to find out the effect of grooved depth ratio on flow friction and heat transfer when the top plate is heated and fixed of the enclosure and inclined walls are cold. Quantitative data are presented in terms of streamlines, isotherms and heat transfer characteristics. The simulation results are compared with

other numerical values and a very good agreement is found. As far as we know, no one researchers have considered said problem yet. The computations for the present simulation were carried out with a code developed by the authors and written in FORTRAN language.

2. MATHEMATICAL MODEL AND SIMULATION METHODOLOGY

2.1 Physical Properties of the problem

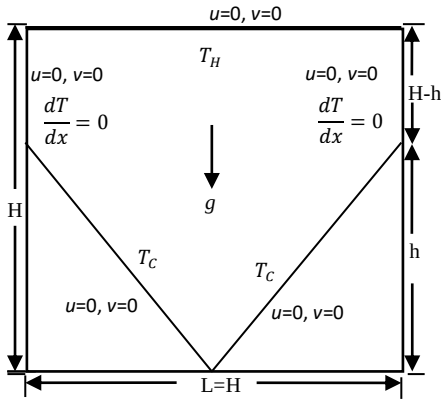

Fig. 1: Schematic diagram of the grooved cavity with boundary conditions.

The geometry and boundary conditions of the present problem is displayed in **Fig. 1** The mentioned problem is two dimensional fixed upper plate of the square grooved cavity with a side length *H*. The grooved depth ratio (GDR) is defined as h/H, where h is grooved depth. If GDR=0, it becomes a square and if GDR=1.0, it becomes a triangle. So, for 0 < GDR <1, it represents a pentagon. Therefore, the shape of the cavity depends on GDR. In the present study, GDR=0.0, 0.25, 0.50, 0.75 and 1.0 are considered, where the upper portion of the cavity is maintained at a uniform higher temperature T_H. When GDR=0.0, the lower wall maintained at a lower temperature T_C whereas the left and right walls are assumed to be adiabatic. When 0 <GDR <1, in that case, it represents a pentagon, whose two sides inclined walls are at a lower temperature T_C whereas the left and right vertical walls (*H-h*) are adiabatic. However, if GDR=1.0, the cavity becomes a triangle, in this case, the two inclined walls maintained a lower temperature T_C, whereas the upper one is fixed with higher temperature. The working fluid is taken to be incompressible, Newtonian with air properties such as Pr=0.713.

2.2 Mathematical Formulation

The general form of the Lattice Boltzmann equations for flow and temperature fields with external forces can be written as the following form. For this model, it is important to consider the Bhatnagar, Gross and Krook (BGK) approximations, first proposed by in 1954. It is based on the notation of a local equilibrium which corresponds to a Maxwell-Boltzmann distribution evaluated at each point in space for the local value of density, velocity and temperature.

$$M_k(x + e_k\Delta t, t + \Delta t) - M_k(x,t) = -\frac{1}{\tau_m}\left[\left[M_k(x,t) - M_k^{eq}(x,t)\right] + \Delta t e_k F\right] \quad (1)$$

$$E_k(x + e_k\Delta t, t + \Delta t) - E_k(x,t) = -\frac{1}{\tau_T}\left[\left[E(x,t) - E_k^{eq}(x,t)\right]\right] \quad (2)$$

Here, M_k and E_k are momentum and energy distribution functions respectively for finite set of discrete particle velocity vector e_k, k=0, 1, . . . 8. Δt denotes lattice time step, F is the external force in direction of lattice velocity, τ_m and τ_T represent the lattice relaxation time for the flow and temperature fields. The LBM has been built up on the D2Q9 model (two dimensional lattices with nine particle velocities), i.e. at each node of the lattice has three kinds of particles: a rest particle, the particles that move in the co-ordinate directions and the particles that move in the diagonal directions. Therefore, the equilibrium distribution functions for momentum and energy can be formulated as:

$$M_k^{eq} = \omega_k \rho\left[1 + \frac{e_k.u}{c_s^2} + \frac{1}{2}\frac{(e_k.u)^2}{c_s^4} - \frac{1}{2}\frac{u^2}{c_s^2}\right] \quad (3)$$

$$E_k^{eq} = \omega_k \varepsilon\left[1 + \frac{e_k.u}{c_s^2} + \frac{1}{2}\frac{(e_k.u)^2}{c_s^4} - \frac{1}{2}\frac{u^2}{c_s^2}\right] \quad (4)$$

where u and ρ are the macroscopic velocity and density respectively, ω_k is weighting factor. $c_s = c/\sqrt{3}$ is the lattice speed of sound, $c = \Delta x/\Delta t$ is Courant-Friedrichs- Lewy (CFL) number, Δx, and Δt are lattice space and lattice time steps respectively. The internal energy variable of the fluid particles is represented by $\varepsilon = \sum_k E_k(x,t)$. The kinetic viscosity υ and the thermal diffusivity α, are defined in terms of their respective relaxation times as

$\nu = c_s^2\Delta t\left(\tau_m - \frac{1}{2}\right)$ and $\alpha = c_s^2\Delta t\left(\tau_T - \frac{1}{2}\right)$

In order to introduce the force term in the model, the buoyancy force can be calculated in vertical direction as $F = 3\omega_k g_y \Delta T$. To ensure that the problem works in near incompressible regime, the characteristic velocity for both natural $U = \sqrt{g_y \beta \Delta T H}$ and force $U_w = \frac{Re\mu}{\rho H}$ regimes should be small compare with fluid speed of sound. U_w is the upper velocity, H is the height of the cavity. The ratio of the buoyancy force to the product of viscous force and heat diffusion rates defines the Rayleigh number as

$Ra = Pr.Gr = \frac{g\beta\Delta T H^3}{\alpha\nu}$, where $Gr = \frac{g\beta\Delta T H^3}{\nu^2}$ denotes the Grashof number, and $Pr = \upsilon/\alpha$ is called Prandtl number. For convection, the flow is driven by temperature or mass gradient, i.e., by the buoyancy force, where the momentum and energy equations are coupled. Hence, there is an extra force term that needs to be considered in solving the LB equations. The macroscopic variables of interest, such as density, velocity, temperature, pressure, etc. can easily be obtained from microscopic particle distribution functions for momentum and energy by solving Eqs. (2) - (4) with other LBM approaches

$$\rho = \sum_k M_k \ , \rho u = \sum_k e_k M_k \ \text{ and } T = \frac{\varepsilon}{\rho c_p} = \frac{\sum_k E_k(x,t)}{\rho c_p} \quad (5)$$

The solutions of velocity and temperature filed are used respectively to evaluate the heat transfer performance. To investigate the local heat transfer performance for the local Nusselt number, Nu_x is denoted by

$$Nu_x = \frac{h_x L}{k} = \frac{L}{T_H - T_C}\frac{\partial u}{\partial y} \quad (6)$$

Where, h_x is local heat transfer coefficient. Therefore, based on the result of local Nusselt number, the average Nusselt number can be evaluated by integration as:

$$Nu = \frac{1}{L}\int_0^L Nu_x \quad (7)$$

The average heat transfer rate for Nusselt number (ANU) is obtained from the above equation (7).

2.3 Code Validation

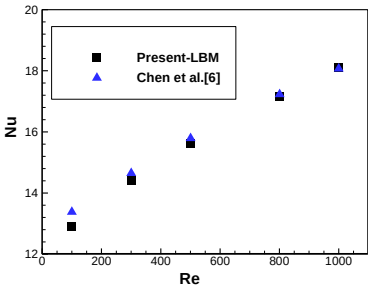

Fig. 2: The average heat transfer rate in terms of Nusselt number with Reynolds number.

To verify the code of this model, a comparison was made with results of Chen et al. [6]. Note that, Chen et al. [6] used a different approach (FEM) for solving the problem in contrast to the present LBM. The variation of Nusselt number, Nu, with Reynolds number, on the heated different shape cavities filled with air, Pr=0.71 is shown in **Fig. 2**. It is illustrated that the results of present LBM simulations are very good agreement with numerical results of Chen et al. [6].

3. RESULTS AND DISCUSSIONS

In the current study, numerical results of fluid flow and temperature profiles inside the grooved cavity for various cases are displayed here with isotherms and streamlines respectively.

3.1 Effect on Temprtature for different GDR with Gr

Figs. 3-6 the effect of natural convection paparameter are illustrated contour of temperature for various grooved depth ratios (GDR) with different Grashof (Gr) numbers.

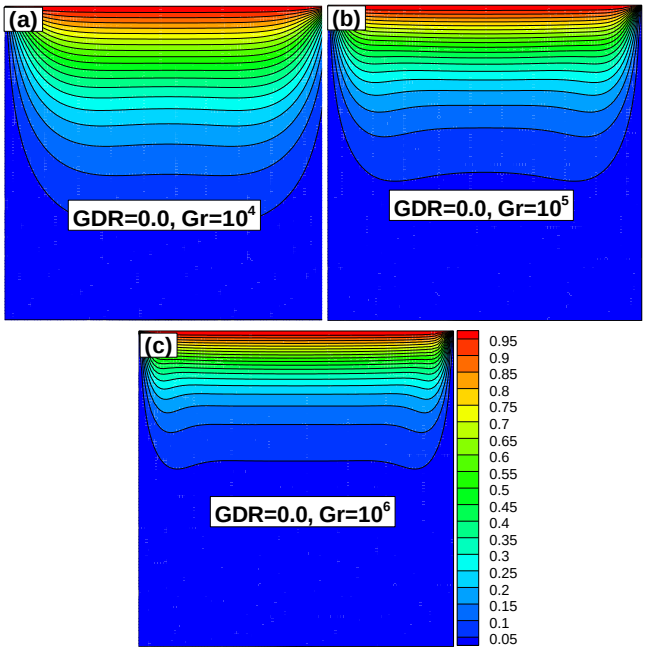

Fig. 3: Isotherms for GDR=0.0 with (a) $Gr=10^4$, (b) $Gr=10^5$ and (c) $Gr=10^6$

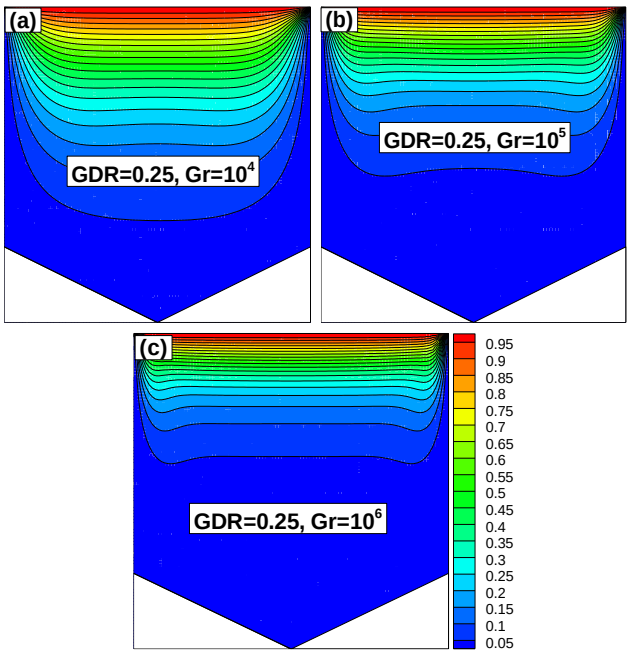

Fig. 4: Isotherms for GDR=0.25 with (a)$Gr=10^4$, (b)$Gr=10^5$ and (c) $Gr=10^6$

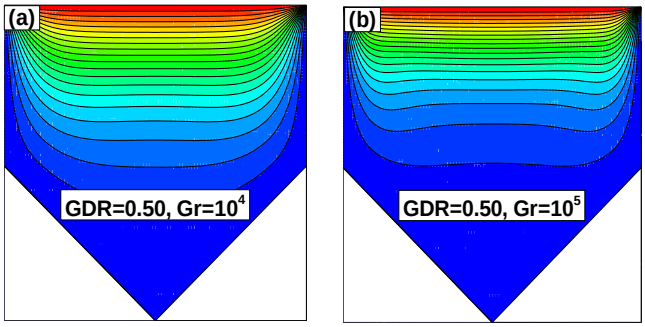

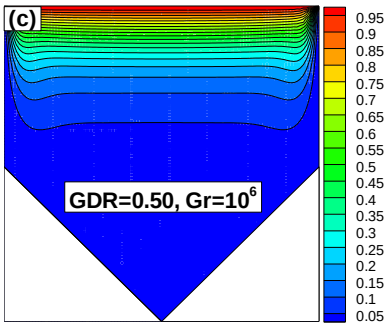

Fig. 5: Isotherms for GDR=0.50 with (a) Gr=10^4, (b) Gr=10^5 and (c) Gr=10^6

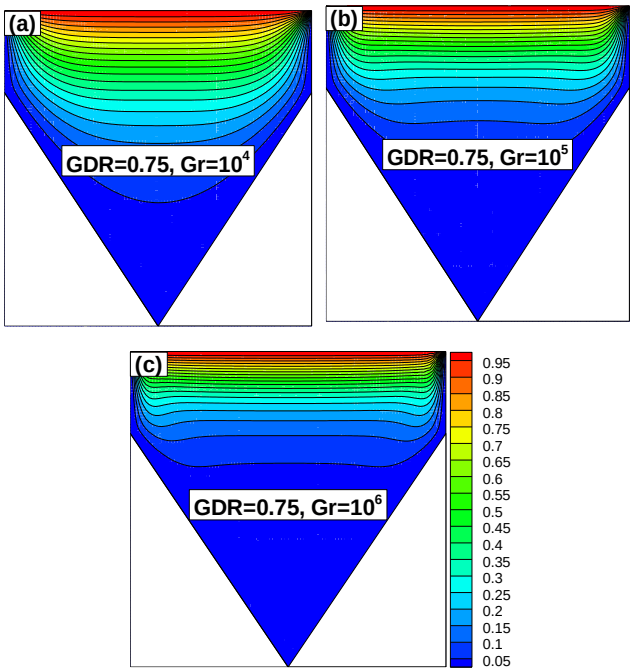

Fig. 6: Isotherms for GDR=0.75 with (a) Gr=10^4, (b) Gr=10^5 and (c) Gr=10^6

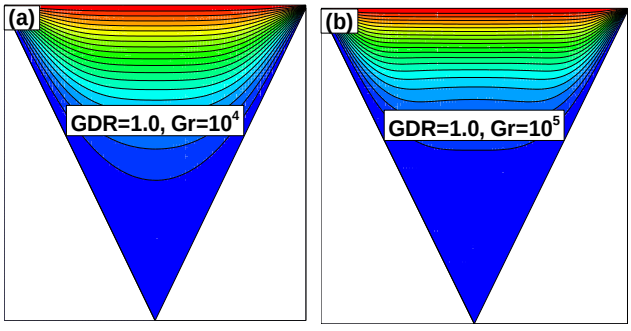

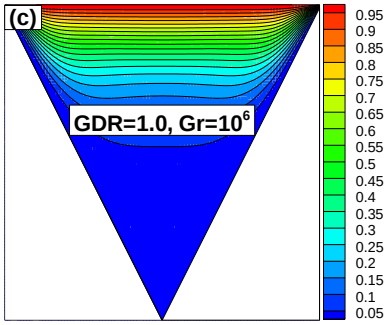

Fig. 7: Isotherms for GDR= 1.0 with (a) Gr=10^4, (b) Gr=10^5 and (c) Gr=10^6

Figs 3-7 are discussed for the natural convection; the greatest influence on isotherms is achieved. It is obvious that if the effect of buoyancy force decreases. With the increase of GDR and Gr, the natural convection becomes stronger and the forced convection becomes weaker respectively, so the change of isotherms is slight. This is because the two vertical walls (left and right) are adiabatic and the fluid has no heat exchange with those walls, though the inclined walls are maintained at a cold temperature where the top wall is hot but not moving. However, if the values of GDR increase from 0.0 to 1.0, a tiny effect on isotherms is observed. So the above figures depict that much of the area of the enclosure is affected by the hot temperature of the top wall for higher frequencies according to increasing GDR but the area of the enclosure is exaggerated in terms of increasing Gr and showing lower frequencies.

3.2 Effect on Streamlines in terms of different GDR and Gr

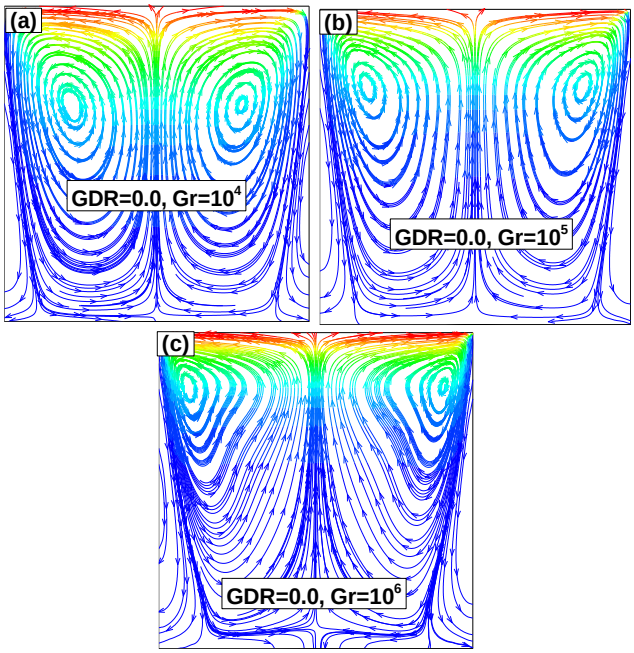

Fig. 8: Streamlines for GDR=0.0 with (a) Gr =10^4,(b)Gr =10^5 and (c)Gr=10^6

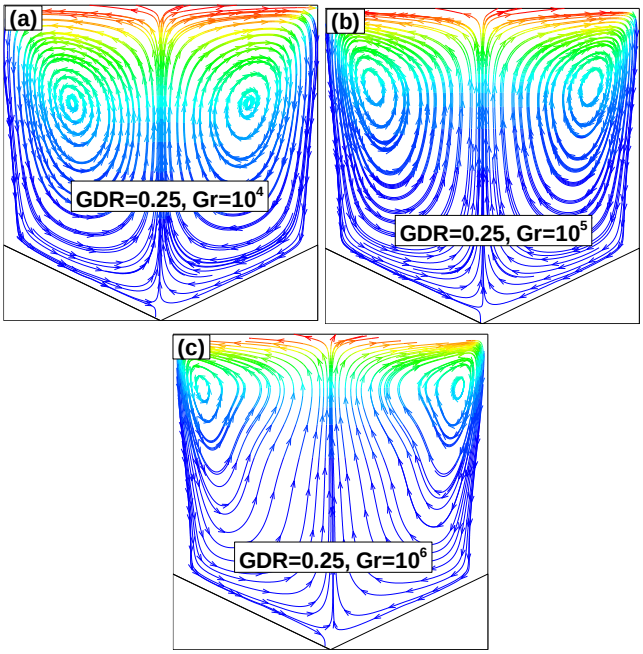

Fig. 9: Streamlines for GDR=0.25 with (a)Gr =10^4,(b)Gr =10^5 and (c) Gr=10^6

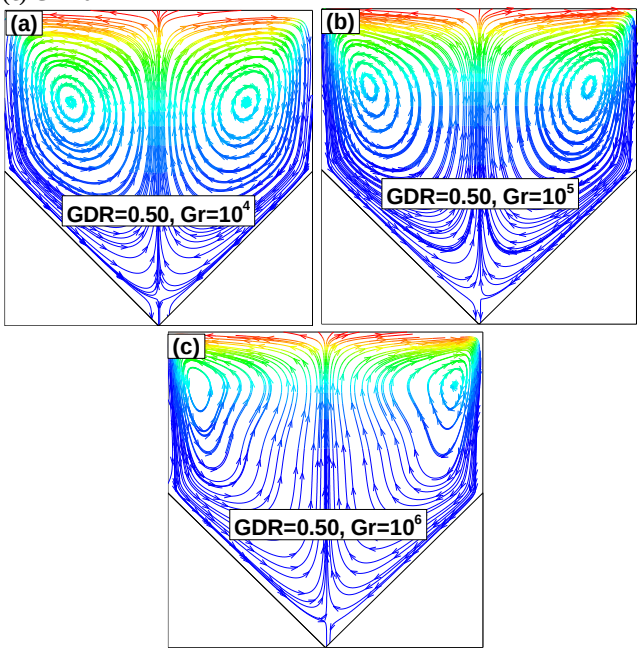

Fig. 10: Streamlines for GDR =0.50 with (a) Gr =10^4, (b)Gr =10^5 and (c)Gr =10^6

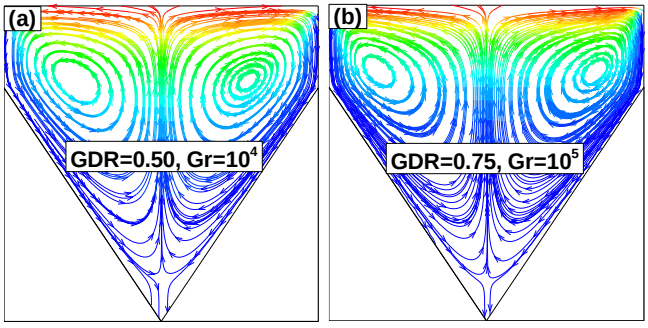

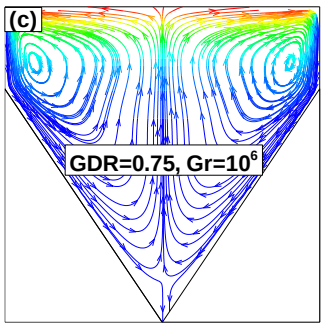

Fig. 11: Streamlines for GDR =0.75 with (a) Gr =10^4, (b) Gr =10^5 and (c) Gr=10^6

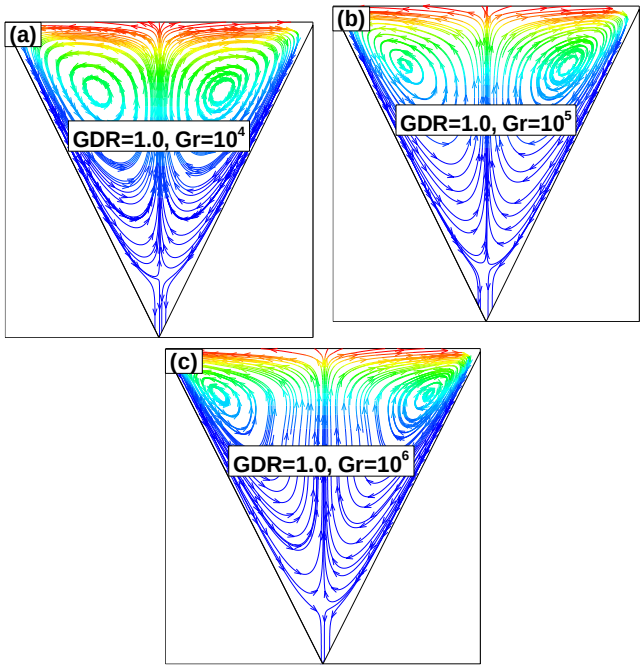

Fig. 12: Streamlines for GDR =1.0 with (a) Gr =10^4, (b) Gr =10^5 and (c) Gr=10^6

Figs. 8-12, when GR=0.0, it represents a square cavity. It is seen as a strong primary vortex or circulation throughout the cavity due to natural convection for the top wall is hot and the bottom wall is cold in terms of different Gr = 10^4, 10^5, 10^6. Besides this, weak secondary circulations are observed at the left and right of the cavity because the top wall is hot and besides two walls are adiabatic. Further increasing GDR, the weaker circulation becomes stronger. The same types of flow phenomenon are found for increasing GDR. The figure also depicts that the streamlines are separated into equally two parts.

3.3 Results on velocity against different Grashof numbers (Gr) with GDR

The profiles of the vertical velocity component at the mid-height of the cavity are plotted in Figures 13, 14, and 15 for different values of GRD =0.0, 0.25, 0.50, 0.75, 1.0, and Gr

=10^4, 10^5, 10^6. It can be seen from these figures that these profiles are well affected by the variation of GDR. The behavior changes drastically when increasing GDR.

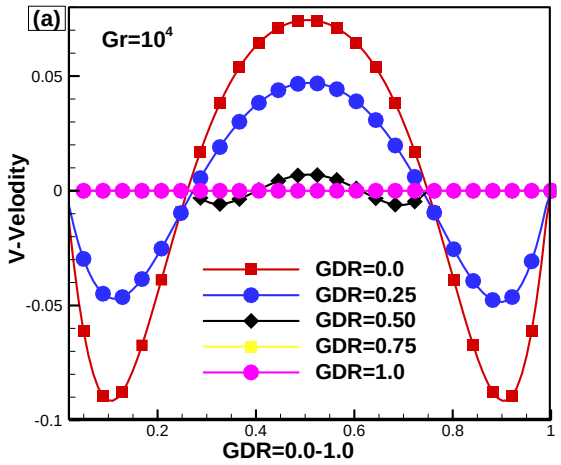

Fig. 13: Velocity for different GDR with Gr =10^4

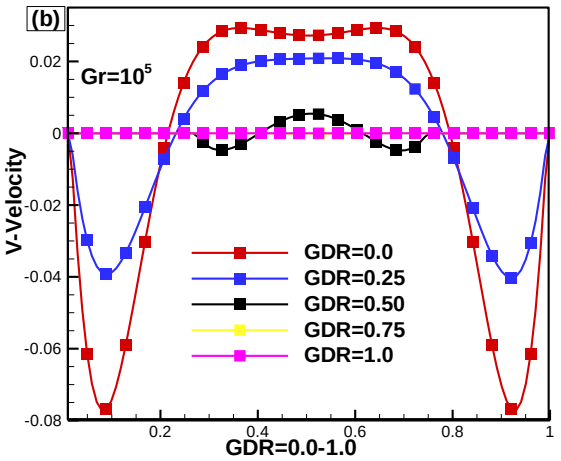

Fig. 14: Velocity for different GDR with Gr =10^5.

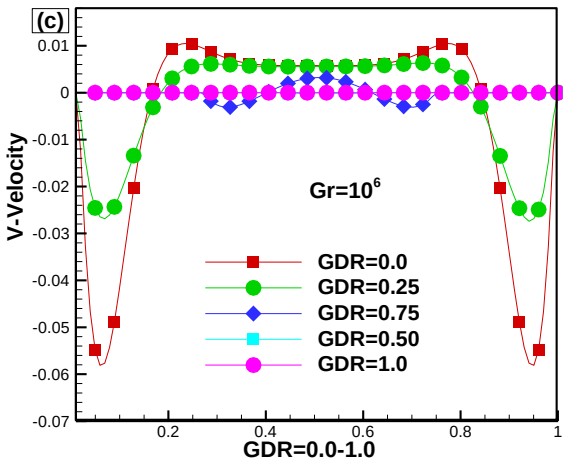

Fig. 15: Velocity for different GDR with Gr =10^6.

For the lowest value of GDR=0.0, the maximum velocity Vmax = 0.65 at x= 0.5 with Grashof number Gr=10^4 have been shown in the **Fig. 13**. **Fig. 14** depicts that the lowest velocity Vmin =-0.09 at X=0.1 and X=0.8 with Grashof number Gr=10^5. So, from **Figs. 13-15** we conclude that with the increase of Grashof number the velocity is decreasing in terms of different GDR and it also discovers that the velocity of the fluid is practically zero for GDR=1 with different Gr=10^4,10^5,10^6 and it becomes a straight line.

3.4. Outcomes on velocity for Gr=10^4,10^5,10^6 with different GDR

The following **Figs. 16-20 show** that the phenomenon is well affected by the variation of Gr with different GDR. The behavior changes radically when increasing Gr.

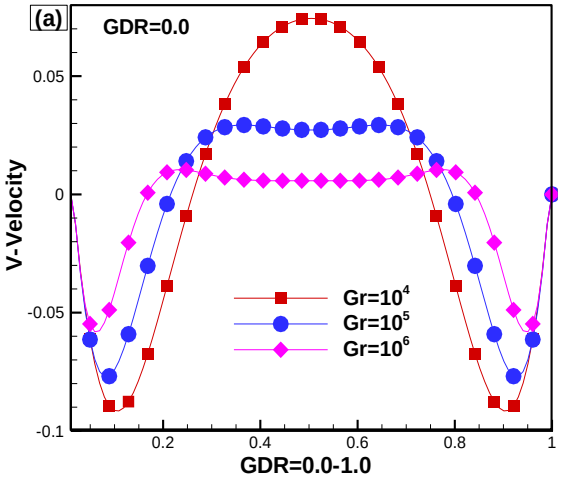

Fig. 16: Velocity for GDR=0.0 with different Gr=10^4, 10^5,10^6

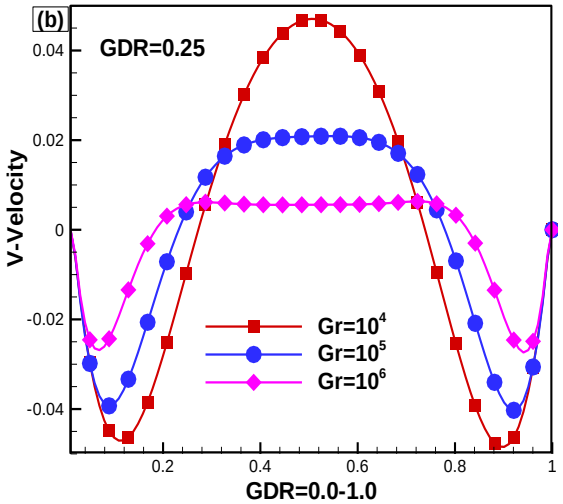

Fig. 17: Velocity for GDR=0.25 in terms of different Gr=10^4, 10^5,10^6

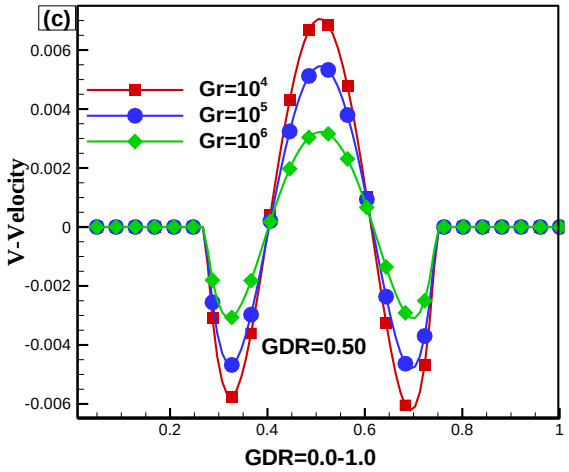

Fig. 18: Velocity for GDR=0.50 with different Gr=10^4, 10^5,10^6

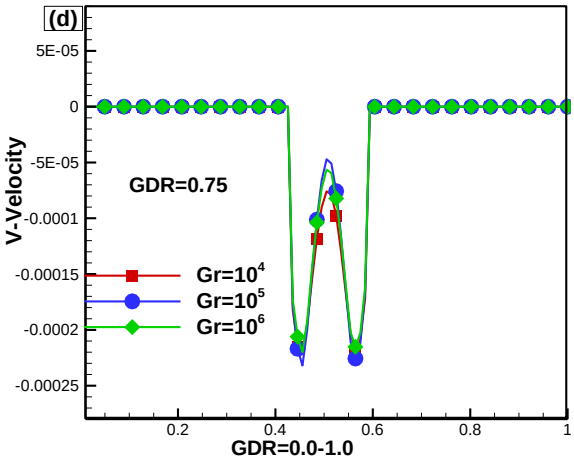

Fig. 19: Velocity for GDR=0.75 with different Gr=10^4, 10^5,10^6

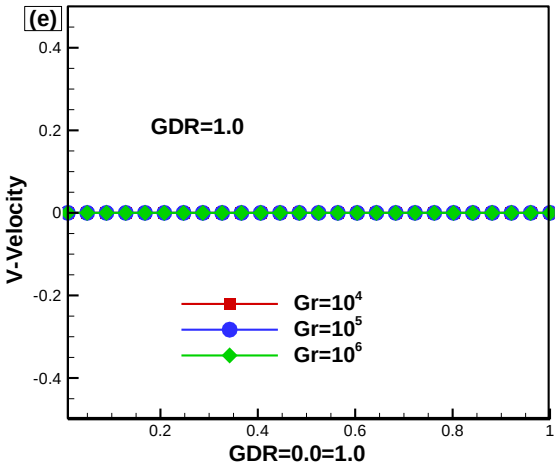

Fig. 20: Velocity for GDR=1.0 with different Gr =10^4, 10^5,10^6

Figs. 16-20 reveal that the velocity is the highest when the Gr is lowest. For the lowest value of Gr=10^4, the maximum velocity Vmax =0.57 at X= 0.5 with GDR=0.0 and the velocity gradually decreases according to the increasing the value of Gr=10^4, 10^5, 10^6. **Fig. 19** shows that the velocity is less than zero for GDR=0.75 in terms of Gr=10^4, 10^5,10^6. **Fig. 20** depicts that when the GDR is 1.0 there is no effect on velocity in terms of different Gr.

3.4. Results on average heat transfer in terms of Grashof numbers with different GDR

The effect on average Nusselt number (Nu) due to changing Gr with GDR is shown in **Figs. 21-22.** The investigation shows the effects of Grashof numbers on natural convection and heat transfer for different GDR.

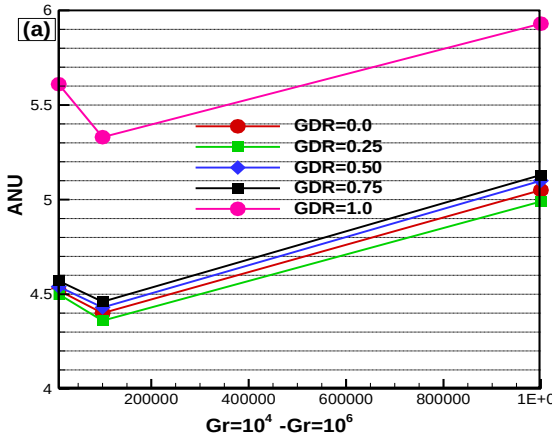

Fig. 21: Average heat transfer in terms of Grashof numbers with different GDR

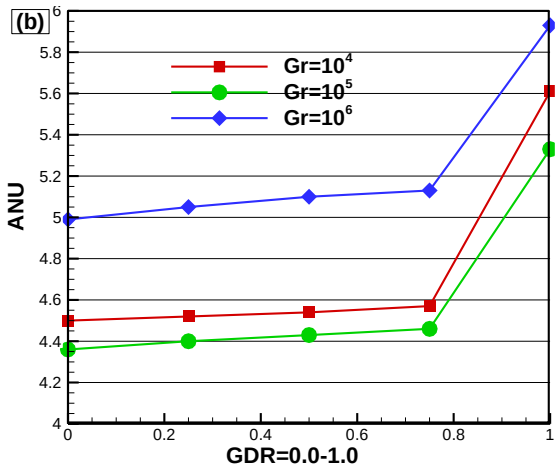

Fig. 22: The average Nusselt numbers against different GDR with Grashof numbers.

Fig. 21-22 show that **t**he average Nusselt numbers are increasing in terms of growing GDR. It also depicts that the ANU are decreasing for the rising of Gr. With increasing the Grashof numbers, for one value shows the flow and temperature fields break the symmetry. The present simulations found small discrepancies in the calculated values of the Nusselt numbers. This is most likely because of the variation of heat transfer at these Grashof numbers.

4. CONCLUSION

Two-dimensional numerical simulations using the LBM are carried out to understand the effect of fluid on the natural convective flow and heat transfer in a grooved enclosure with heated upper plate. The main focus of the present paper is to investigate the effects of heat transfer for Grashof number with different Grooved Depth Ratio (GDR), temperature distribution, streamlines, velocity, and average Nusselt number.

- The area of the enclosure is affected by the hot temperature of the top wall for higher frequencies according to increasing of GDR at the same time the area of the enclosure is exaggerated in terms of increasing Gr and showing lower frequencies.
- The main vortex is related to the hot fixed top wall whereas the secondary vortex is related to the buoyancy force mechanism.
- The results show that the streamlines are separated by equally two parts for the heated top wall and the cold bottom two walls.
- For the lowest value of GDR figures represent the maximum velocity.
- When the GDR is 1.0 there is no effect on velocity in terms of different Gr.
- The overall heat transfer rate is increasing for increasing GDR with different Gr.
- The present simulations found small inconsistencies in the calculated values of the Nusselt number. Because of variation of heat transfer, it can happen at these Grashof number.

REFERENCES

[1] Nasr A. Jabbar, Sarmad A. Abdul Hussein, Kadhim Al-Chlaihawi, Qusay S. Alanssari & Luay S. Al-Ansari, “CFD Analysis of Natural Convection in a Square Cavity with Two Thin Baffles of Different Lengths and Positions on the Vertical Opposite Walls,” Journal of Mechanical Engineering Research and Developments, Vol. 43, No. 3, pp. 174-185, 2020.

[2] Yanga, J., Wang, Y., Zhang, X., Pan, Y., “Effect of Rayleigh numbers on natural convection and heat transfer with thermal radiation in a cavity partially filled with porous medium,” 9th International Symposium on Heating, Ventilation and Air Conditioning (ISHVAC) and the 3rd International Conference on Building Energy and Environment (COBEE), No.121, pp. 1171 – 1178, 2015.

[3] Dixit, H. N. and Babu, V., “Simulation of high Rayleigh number natural convection in a square cavity using the lattice Boltzmann method,” International Journal of Heat and Mass Transfer, Vol. 49. No. 3-4, pp. 727-739, 2006.

[4] Surendar, R., Muthtamilselvan, M., Abdalla, B. A. and Al-Mdallal, Q., “Natural convection in a partially heated square cavity with an inner square block,” Proceedings of International Conference on Advances in Materials Research (ICAMR - 2019).

[5] Iyi, D, and Hasanb, R., “Natural Convection Flow and Heat Transfer in an Enclosure Containing Staggered Arrangement of Blockages,” 6th BSME International Conference on Thermal Engineering (ICTE), Vol. 105, pp.176-183, 2014.

[6] C-L Chen and C-H, Cheng. “Numerical study of flow and thermal behavior of lid-drievn flows in cavities of small aspect ratios”, Int. J. Num. Methods in Fluid, Vol.52, pp.785-799, 2006.

[7] M.A.S. Mustafa, H.M. Hussain, A. A. Abtan, and L.J. Habeeb, “Review on mixed convection heat transfer in different geometries of cavity with lid driven”, Journal of Mechanical Engineering Research and Developments”, vol.43, no.7, pp.12-25, 2020.

[8] S. Saha, M.T. Islam, M. Ali, M.A.H. Mamun, and M.Q. Islam, “ Effect of inlet and outlet locations on transverse mixed convection inside a vented enclosure”, Journal of Mechanical Engineering, Vol. ME36, pp.27-37,2006.

[9] S. Roy, T. Basak, Ch. Thirumalesh, Ch. M. Krishna, “Finite elements simulation on natural convection flow in a triangular enclosure due to uniform and non uniform bottom heating", Journal of Heat Transfer, Vol.130, pp. 032501-10, 2008.

[10] M. A. Taher, S. C. Saha, Y.W.Lee, and H. D. Kim.,"Numerical study of Lid-driven square cavity with heat generation using LBM", American J. Fluid Dynamics, Vol.03, no.02, pp.40-47,2013.

[11] M. A. Taher, H. D. Kim, and Y.W.Lee, “LBM simulation of friction factor and heat transfer on the moving lid of a triangular enclosure”, Heat Transfer Research, Vol.48, no.11, pp.1025-1045, 2017.

[12] A.A.R. Darzi, M.Farhadi, K.Sedighi, E. Fattahi, and H. Nemati, “Mixed convection simulation on inclined lid-driven cavity using lattice Boltzmann method”, IJST trans. Mech. Eng., Vo. l.35, pp.73-83, 2016.

[13] T. S. Cheng, “Characteristics of mixed convection heat Transfer in a lid-driven cavity with various Richardson and Prandtl number”, Int. J. Thermal Science, Vol.50,

[14] A. A. R. Darzi, M. Farhadi, K. Sedighi, E. Fattahi, and H. Nemati, “Mixed convection simulation on inclined lid-driven cavity using lattice Boltzmann method”, IJST trans. Mechanical Engineering., Vol.35,pp.73-83,2011.

[15] M. A. Taher, S. C. Saha, and Y.W.Lee, “Effects of aspect ratios on flow friction and thermal behavior inside a close domain using lattice Boltzmann method” American Journal of Applied Mathematics, Vol.3, no.3, pp.1-7,2015.

[16] Mansouri, A. E., Hasnaoui, M., Amahmid, A., Dahani, Y., Alouah, M., Hasnaoui, S., Khaoula, R., Ouahas, M., and Bennacer, R., “MRT-LBM Ssimulation of Natural Convection in a Rayleigh-Benard Cavity with Linearly Varying Temperatures on the sides: Application to a Micropolar fluid,” Frontiers in Heat and Mass Transfer (FHMT), Vol. 9, No. 28, pp. 1-14, 2017.

Paper ID: 3673

International Conference on Mechanical, Manufacturing and Process Engineering (ICMMPE – 2022)

Organizer: Faculty of Mechanical Engineering, Dhaka University of Engineering & Technology (DUET), Gazipur, Bangladesh

Website: https://icmmpeduet.com/

Numerical Investigation on Thermal Performance of Modified Vertical U-tube Ground Heat Exchanger

Nafisa Lubaba[1], Md. Hasan Ali[1], Nahid Hasan[1] and Nahyan Ahnaf Pratik[1]

[1]Department of Energy Science and Engineering, Khulna University of Engineering & Technology, Khulna-9203, Bangladesh

E-mail: hasan@ese.kuet.ac.bd

ABSTRACT

This paper presents the performance analysis of U-tube Ground Heat Exchanger (GHE). Numerical simulation was done by using ANSYS Fluent software. For the purpose of enhancement of the thermal performance of U-tube GHE, the traditional design was modified. For the modification, the total length and material volume of the U-tube GHEs are kept same as the conventional U-tube model. Then the U-tube was partitioned in a manner that there is an upper portion and a lower portion. Diameter of the upper part was reduced and of the lower part was increased. Furthermore, a different design in which one of the legs of the U-tube was maintained smaller in diameter and the other leg was maintained large in diameter. All the modified designs are simulated for 72 hours of operation and for a flow rate of 2 liter/minute. For the different modifications, the heat transfer rate per meter borehole is 28.69W/m, 22.53 W/m, 21.32 W/m, 26.33 W/m, 30.34 W/m, 24.61 W/m respectively, whereas, the heat transfer rate per meter borehole for the U-tube is 21.18 W/m. Among the modified configurations, all the configurations give a higher heat transfer rate than the conventional U-tube configuration. Since the material volume of modified U- tube GHE is same as the conventional U-tube design and those models are capable of giving better performance, hence the modified configurations are more attractive than the conventional U-tube design.

Keywords: Ground source heat pump, Heat exchange rate, Numerical simulation, U-tube ground heat exchanger.

1. INTRODUCTION

In recent years, geothermal energy has become an alternative energy source having a great environmental and economic benefits. For depths more than 5 m, ground temperatures are essentially constant throughout the year. Which is continued to 9 to 12 meters depth [1]. At a depth more than 5 m, the ground temperature is not affected by ambient temperature and solar radiation. Therefore, a stable ground temperature at this depth can be used to extract heat from (winter season) or reject (summer season) heat to the ground soil. In winter, the ground is warmer than the atmosphere and in summer the ground is cooler. Ground source heat pump (GSHP) system is used for cooling or heating purpose by rejecting heat to or extracting heat from ground [2]. Geothermal energy is used by GSHP for different purposes, like cooling, heating, generating electrical power etc. There are two types of GSHP system, which are open loop system and closed loop system. For the arrangement of the closed loop system there is needed a ground heat exchanger (GHE) [3].

GHE is used to extract heat from or reject heat to the ground soil and GHE is coupled to ground source heat pump (GSHP) system for building heating or cooling application [4]. For the operation of GHE, there is a working fluid which flows through the GHE, exchanges heat with the ground. During summer heat is rejected in the ground through the heat exchanging fluid and then the cooler fluid is used in domestic purposes or for space cooling. This procedure is reversed in winter. In winter heat is extracted from the ground.

GSHP system is a solution to the increasing environmental pollution. It uses a clean geothermal energy, and it is an environment friendly solution. The main limitations of GSHP system are installation cost is higher and sometimes it is also complex according to the design of the GHE. But after installation, it is really easy to maintain the system which is cost effective than other conventional air-conditioning systems. Again, GSHP system has lower power consumption than conventional Air Source Heat Pump (ASHP) systems. Consequently, the GSHP system is a helpful side for the environment [4]. The electricity which is needed for the pumping the working fluid through the GHE is also low, it about 25-50% less electricity than the traditional air conditioners and heaters [5].

There are different types of GHEs are available such as vertically and horizontally installed. The vertical GHE installed in a vertical borehole, whereas a horizontal GHE installed in a horizontal trench. Horizontal GHE needs more land space than the vertical GHE. As the vertical GHEs are buried in larger depths than horizontal GHE under the ground where more stable temperature exists, therefore, the

thermal performances are higher for vertical GHE. Chen et al. [6] worked on a vertical GSHE. They analyzed that how much the depth should be good for vertical heat exchanger. Vertical ground heat exchangers are now mostly used than horizontal ground heat exchangers.

There are different types of vertical GHEs based on their shape. Among them, the U-tube heat exchanger is the simplest one. A spiral GHE can give better thermal performance than U-tube GHE. The main disadvantages of spiral tube heat exchanger are the higher pressure drop than that of U-tube GHE [7]. On the other hand, in U-tube GHE, the thermal interference between inlet and outlet tube reduces the performance of U-tube GHE [8]. Li et al. [9] found a solution to overcome the thermal interference. That is insulating the outlet tube of U-tube GHE. As a result, the heat exchange between the two legs (inlet and outlet) is reduced, results a better thermal performance. Lee et al. [10] suggested a new technique for reducing thermal interference. The part between the two legs of U-tube is filled with air as insulating material. As a result, the heat exchange between the two legs of U-tube is reduced, and thus the thermal interference is reduced. Consequently, increases the thermal performance of U-GHE.

Chen et al. [11] analyzed the influence of different materials on the vertical U-tube GHE. They showed that the heat flux in the ground heat exchanger is directly proportional to the thermal conductivity coefficient of the grout materials. They also examined that the heat convection in the tube can be increased by increasing the velocity of inlet water. Zheng et al. [12] developed a mathematical model to analyze the soil and borehole temperature field around vertical U-tube GHE. Liao et al. [13] proposed correlations of effective pipe-to pipe, pipe-to borehole, borehole-to-borehole thermal resistance for vertical single U-tube GHE.

All the previous works on U-tube GHE are based on constant cross-sectional tube diameter. To improve the thermal performance of U-tube heat exchanger, some modifications of U-tube GHE were carried out in the present study. The modified configurations may help to utilize the ground temperature evenly and to reduce thermal interference. For the purpose of enhancement of the thermal performance of U-tube GHE, the traditional design was modified. For the modification, the total length and material volume of the U-tube GHEs are kept same as the conventional U-tube model. Then the U-tube was partitioned in a manner that there is an upper portion and a lower portion. Diameter of the upper part was reduced and of the lower part was increased. Furthermore, a different design in which one of the legs of the U-tube was maintained smaller in diameter and the other leg was maintained large in diameter. Then simulations were done to optimize the thermal performance of U-tube GHE.

2. DESCRIPTION OF PHYSICAL MODEL AND SIMULATION PROCEDURE

Jalaluddin and Miyara [7] worked on a vertical U-tube GHE to analyze its thermal performance and compared it with spiral GHE. The simulation work of this paper is done according to their used parameters. And the result will be compared to their result for validation.

In the first stage, the U-tube was designed according to the parameters and properties listed in table 1 and table 2. Then the traditional design of U-tube GHE was modified to enhance the performance. Traditional U-tube GHE is shown in Fig. 1 and all of the modifications are shown in Fig. 2. Description of the modified configurations are listed in table III. After designing, the U-tube (configuration-1) is simulated with applying the same boundary conditions of Jalaluddin and Miyara [7] and considering similar properties of materials. The simulation results of the configuration-1 (C-1) were validated with previous work done by Jalaluddin and Miyara [7]. Then simulation was conducted for all other modified configurations.

Fig. 1 shows the U-tube GHE surrounded by borehole, which has a total length of 20 m, an inlet tube and an outlet tube. The material for GHE is polyethylene. Clay is considered as ground soil and backfill material is silica sand.

Table 1: Properties and parameters of the ground heat exchanger material (polyethylene)

Parameters	Value	Units
Thermal conductivity	0.35	W/(m K)
Specific heat	2300	J/(kg K)
Density	920	kg/m^3
Outer diameter	0.033	m
Inner diameter	0.026	m
Leg spacing of U-tube	0.2	m
Length of the tube	20	m
Borehole diameter	0.25	m
Soil diameter	10	m
Depth of soil	25	m

Table 2: Properties of the silica sand (backfill material) and clay (soil)

	Parameters	Value	Units
Silica sand	Thermal conductivity	1.4	W/(m K)
	Specific heat	750	J/(kg K)
	Density	2210	kg/m^3
Clay	Thermal conductivity	1.2	W/(m K)
	Specific heat	1800	J/(kg K)
	Density	1700	kg/m^3

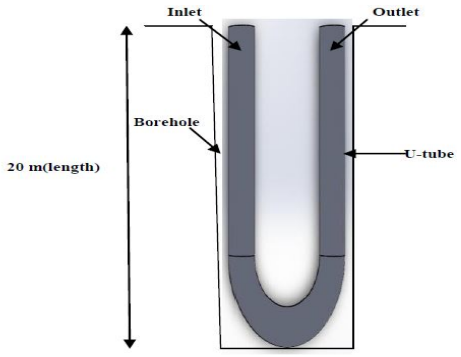

Fig. 1: Traditional U-tube GHE (Configuration 1).

In the modified U-tube designs, the tubes are divided in two portions. Upper portion with a smaller diameter and the lower portion which has larger diameter than the upper portion of the tube. As the upper part is small in diameter so the thermal interference will may decrease than the traditional design, which results in a better performance of the U-GHE. Fig. 2 shows the design model of the modified U-tube GHEs.

The diameter of the upper part and the lower part are altered to see the changes in the result. In configuration 1 (C-1), traditional U-GHE was considered. In configuration 2 (C-2), the length of the upper part and the lower part are kept equal, diameter was changed is shown in Fig. 2(a). Configuration 3 and 4 (C-3 and C-4) consist of the length of the upper part is kept larger than the lower part shown in Fig. 2(b). Configuration 5 and 6 (C-5 and C-6) consist of upper part length is kept smaller than the lower part shown in Fig. 2(c). Finally, in configuration 7 (C-7), whole of the inlet tube diameter was kept smaller than outlet tube is shown in Fig. 2(d). For the Configuration 7, diameter of the inlet tube is 21 mm and the outer tube diameter is 31 mm. In all of the modified configurations, total material volume of the GHE were same as traditional U-tube GHE (configuration 1). Dimensions of all modified design are summarized in table 3.

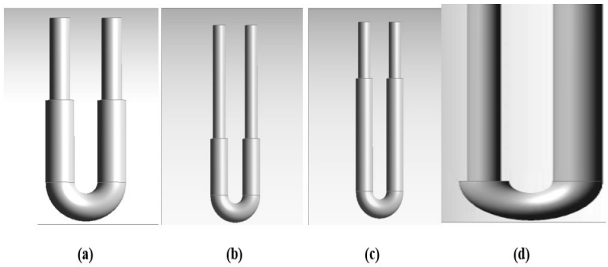

Fig. 2: Different configurations of U-tube model (a) U-tube heat exchanger with smaller diameter in the upper part and larger diameter in lower part, (b) Upper part is larger than the lower part, (c) Lower part is larger than the upper part, (d) Whole of the inlet tube has smaller diameter than the outlet tube.

Table 3: Description of the configurations in which "C" donates "Configuration"

Configuration	Upper part length (m)	Lower part length (m)	Upper part diameter (mm)	Lower part diameter (mm)
C-1	10	10	26	26
C-2	10	10	21	31
C-3	12	8	22	32
C-4	15	5	23	33
C-5	8	12	20	30
C-6	5	15	18	28
C-7	20 (inlet)	20 (outlet)	21 (inlet)	31 (outlet)

3. SIMULATION SETUP

In this present work, ANSYS Fluent software was used for the simulation purpose. Geometries of the GHE models, backfill material and surrounding ground are designed in ANSYS Design Modeler. After completing the geometry, meshing of the whole model is done. The mesh results are shown in Fig. 3.

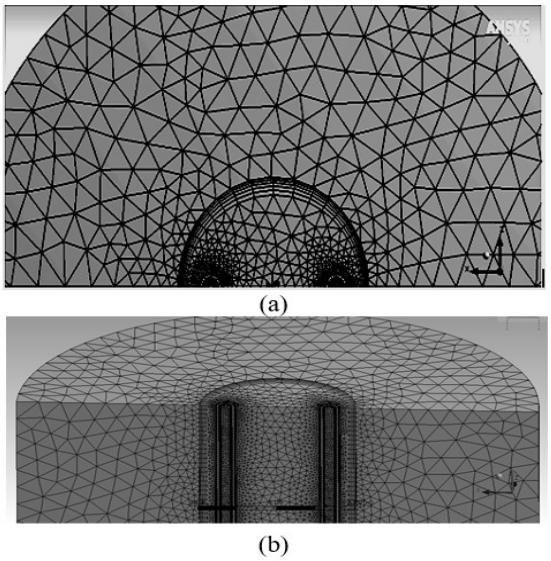

Fig. 3: Meshing of the model (a)Top view, (b)vertical section view.

All of the simulations were done for cooling purpose, continuous operation of 72 hours. In cooling mode of operation, the heat transfer fluid is pumped through the GHE and fluid release heat to the ground. As a result, the temperature of the fluid is decreased. The outlet temperature is observed to analyze the performance of the GHE.

4. MODEL VALIDATION

To justify the acceptance of present simulation work, validation of this work was done by comparing the result of traditional U-tube GHE with the previous work done by Jalaluddin and Miyara [7] considering similar conditions. This simulation is a transient, laminar flow, pressure based with a water flow rate of 2 liter/minute. The temperature of the water at the inlet kept to be constant at 300.15K. Even though the ground temperature is affected by atmospheric temperature up to 5 m depth, the main focus of the present paper is the modifications of U-tube GHE to improve the thermal performance. Therefore, the initial ground temperature was kept constant at 290.85 K, which is similar to the previous work of Jalaluddin and Miyara [7]. After that, validation and all other simulations were performed considering this constant ground temperature of 290.85 K.

Fig. 4 shows outlet temperature of water from present simulation work and previous work of Jalaluddin and Miyara [7]. It can be seen from Fig. 4 that, there are slightly difference in the temperatures of the outlet water of the simulated result and result from the paper. Also, heat transfer rate after 72 hours was calculated for present simulation. The heat transfer rate after 72 hours for present simulation and previous work [7] are 341.45 W and 342.13 W respectively. The results of the simulation are nearly equal to the values of the previous work. Therefore, the present simulation is a good acceptance with previous results.

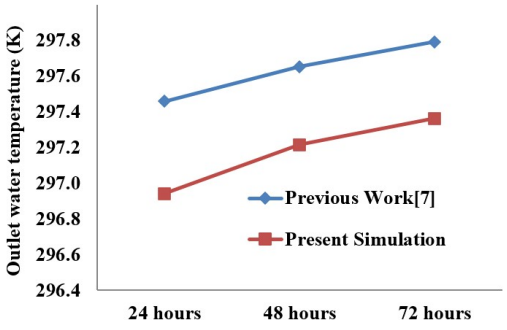

Fig. 4: Outlet water temperature of the paper and the simulation result after 24h, 48h and 72h.

5. RESULTS AND DISCUSSIONS

For the performance analysis of all the models, simulations were carried out considering similar properties of each model, the ground, borehole and tube. The flow rate is 2 liter/minute, inlet temperature is 300.15K. All the results of those configurations are compared to the result of C-1.

5.1 Outlet Water Temperature

For every configuration, the inlet water temperature was 300.15K and these simulations were done for cooling purpose. Hence it is expected that the outlet water temperature should be lower than 300.15K. For all the configurations, the outlet water temperature is shown in Fig. 5. It can be seen that for C-2 and C-6, the outlet water temperature is 296.82K and 296.02K after 72 hours of operation, which are low compared to other designs. This result indicates that these two configurations will give better cooling performances than the others.

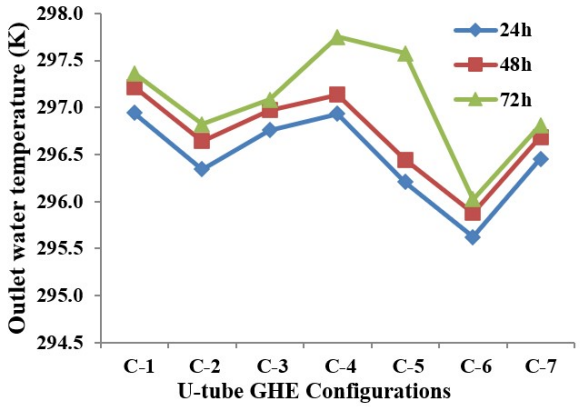

Fig. 5: Outlet water temperature for all the configurations after 24h, 48h and 72h operation.

5.2 Heat Transfer Rate

After the simulation, the heat transfer rate was calculated by using following equation:

$$Q = m \times c_p \times \Delta T \quad (1)$$

Where m stands for mass flow rate. Cp denotes specific heat and temperature difference of the inlet and outlet water is denoted by ΔT. After calculation of heat transfer rate, the average heat transfer rate was calculated for 72 hours of continuous operation and shown in Fig. 6. For C-2 and C-6, the heat transfer rate is higher than the other configurations. For all of the configurations, the total material volume is kept equal. Therefore, the cost of installation will be same for all configurations. If C-2 and C-6 are used then it will give higher heat transfer rate with the same cost. The average heat exchange rate is increased about 35.43% in case of C-2, and about 43.19% in case of C-6 than the average heat exchange rate of C-1.

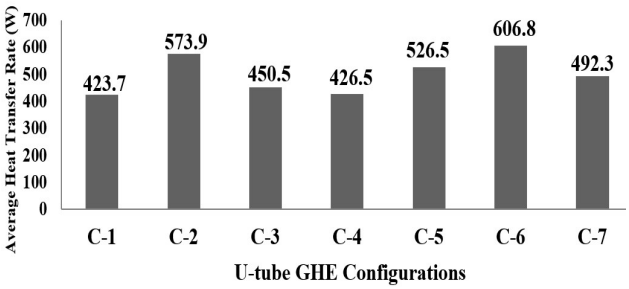

Fig. 6: Average heat transfer rate of the different types of U-tube heat exchanger.

5.3 Temperature Distribution

In Fig. 7 and Fig. 8, the temperature profile of C-2 and C-7 are shown for better understanding of heat transfer analysis. From these two figures, it is seen that the temperature distribution around the GHEs almost similar from top to bottom of the GHE. This happens because of as the soil becomes saturated equally around the GHE.

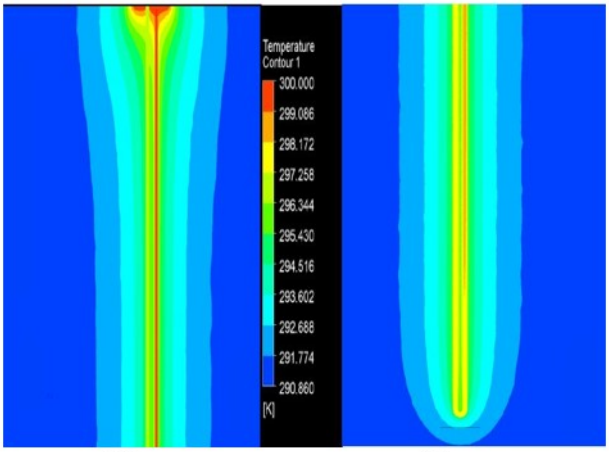

Fig. 7: Temperature contour of C-2 (a) upper part, (b) lower part.

5.3 Pressure Drop

The pressure drop for all the configurations from the simulation result are shown in Fig. 9. Pressure drop also can be calculated using following equations:

$$\Delta P = f_s \cdot \left(\frac{l_p}{d_i}\right) \cdot \left(\frac{\rho v^2}{2}\right) \quad (2)$$

Where, f_s is friction factor, l_p is the length of the straight tube, d_i is the diameter, ρ is the density, v is the velocity of the circulated water.

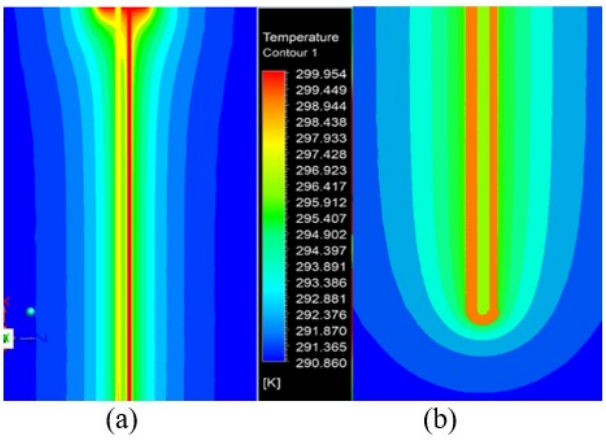

Fig. 8: Temperature contour of C-7 (a) upper part, (b) lower part.

For the straight tube and for laminar flow, the friction factor is,

$$f_s = \frac{64}{R_e} \quad (3)$$

There is a sudden expansion in the tube where the diameter of the tube suddenly increased. For this sudden expansion the pressure drop will be calculated by the following equation:

$$\Delta P_e = \frac{v_1^2}{2g}\left(1 - \frac{A_1}{A_2}\right)^2 \quad (4)$$

Here, v_1 is the velocity of entering water, A_1 and A_2 are the area of smaller part and larger part.

For the sudden contraction, the following equation is used.

$$\Delta p_c = \frac{\rho(v_0 - v_1)^2}{2} \quad (5)$$

For the curved part of the tube the following correlation was used [14]:

$$f_c = \frac{\frac{64}{R_e}}{\left(1 - \left[1 - \left(\frac{11.6}{D_e}\right)^{0.45}\right]^{\frac{1}{1.45}}\right)} \quad (6)$$

Where,

$$D_e = R_e \cdot \frac{d_i}{D}^{0.5} \quad (7)$$

For C-1 the pressure drop was calculated according to the following equation:

$$\Delta P_{total} = \Delta P_{inlet} + \Delta P_{outlet} + \Delta P_{curved} \quad (8)$$

For the other configurations, the pressure drop due to sudden contraction and sudden expansion terms were also added with the pressure drop through the GHE. For C-1, pressure drop from simulation and calculation are 114.4 Pa and 103.1 Pa respectively. Simulated pressure drop for other configurations are higher than that of C-1. Based on the heat transfer rate results shown in Fig. 6 and pressure drop shown in Fig. 9, the modification of U-tube GHE

helps to improve the thermal performance of U-tube GHE considering small increases of pressure drop.

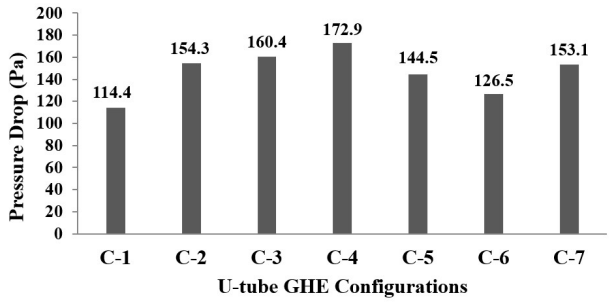

Fig. 9: Total pressure drop from the simulation results for all configuration.

6. CONCLUSION

Thermal performance based on outlet water temperature and heat exchange rate for different modified model of U-tube GHE were numerically examined and results were compared with traditional U-tube GHE. The modified designs give a better performance than the conventional U-tube design. The average heat exchange rate is increased about 35.43% in case of C-2, and about 43.19% in case of C-6 than the average heat exchange rate of C-1. Other modifications in this study can be adopted for better performance. Therefore, if the design is changed in the present modification ranges, then the results can improve, at the same time the installation cost, spaces and other parameters will be same, as the total material volume is kept equal. Again, from the simulation result it is seen that the modified configurations have slightly higher pressure drop than C-1. But for C-6 the difference in the pressure drop with C-1 is very small. Hence, it can be said that the installation of any modified configurations of the conventional U-tube GHE will be efficient in the way of economical as well as energy usage.

REFERENCES

[1] D. Inaudi, R. Belli, and D. Posenato, "Distributed sensing for damage localization," Bridg. Maintenance, Safety, Manag. Resil. Sustain. Proc. Sixth Int. Conf. Bridg. Maintenance, Saf. Manag., pp. 399–406, 2012.

[2] S. K. Shah, L. Aye, and B. Rismanchi, "Undisturbed ground temperature in Melbourne," AIP Conf. Proc., vol. 2121, no. July, 2019.

[3] I. David, C. Ștefănescu, and I. Vlad, "Efficiency assessment of ground-source heat pumps in comparison with classical heating syastem," Int. Multidiscip. Sci. GeoConference Surv. Geol. Min. Ecol. Manag. SGEM, vol. 1, no. 4, pp. 191–198, 2015.

[4] M. Hasan Ali, "Numerical Optimization of Double Tube GHE for Ground Source Heat Pump," Int. J. Sustain. Green Energy, vol. 6, no. 5, p. 64, 2017.

[5] M. H. Ali, K. Kariya, and A. Miyara, "Performance analysis of slinky horizontal ground heat exchangers for a ground source heat pump system," Resources, vol. 6, no. 4, pp. 1–18, 2017.

[6] J. Chen, L. Xia, B. Li, and D. Mmereki, "Simulation and experimental analysis of optimal buried depth of the vertical U-tube ground heat exchanger for a ground-coupled heat pump system," Renew. Energy, vol. 73, pp. 46–54, 2015.

[7] Jalaluddin and A. Miyara, "Thermal performance and pressure drop of spiral-tube ground heat exchangers for ground-source heat pump," Appl. Therm. Eng., vol. 90, pp. 630–637, 2015.

[8] N. K. Muraya, D. L. O'Neal, and W. M. Heffington, "Thermal interference of adjacent legs in a vertical U-tube heat exchanger for a ground-coupled heat pump," ASHRAE Trans., vol. 102, no. 2, pp. 12–21, 1996.

[9] X. Y. Li, T. Y. Li, Qu D. Q., & J. W. Yu. A new solution for thermal interference of vertical U-tube ground heat exchanger for cold area in China. Geothermics, 65, 72–80. 2017.

[10] LEE C., Gil H., Choi H., & Kang S. H. Numerical characterization of heat transfer in closed-loop vertical ground heat exchanger. Science China Technological Sciences, 53(1), 111–116, 2010.

[11] S. Chen, J. Mao, X. Han, C. Li, and L. Liu, "Numerical analysis of the factors influencing a vertical U-tube ground heat exchanger," Sustain., vol. 8, no. 9, 2016.

[12] Z. Zheng, W. Wang, and C. Ji, "A study on the thermal performance of vertical U-tube ground heat exchangers," Energy Procedia, vol. 12, no. December 2011, pp. 906–914, 2011.

[13] Q. Liao, C. Zhou, W. Cui, and T. C. Jen, "New Correlations for Thermal Resistances of Vertical Single U-Tube Ground Heat Exchanger," J. Therm. Sci. Eng. Appl., vol. 4, no. 3, 2012.

[14] C.M. White, Streamline flow through curved pipes, in: Proceedings of theRoyal Society of London, 1929.

Paper ID: 4142
International Conference on Mechanical, Manufacturing and Process Engineering (ICMMPE – 2022)
Organizer: Faculty of Mechanical Engineering, Dhaka University of Engineering & Technology (DUET), Gazipur, Bangladesh
Website: https://icmmpeduet.com/

A General Method to Develop Mathematical Model for Estimating Ship Repairing Man-Hour

Ahammad Abdullah[1], Hafizur Rahman [2], Md. Imran Uddin[3], and Md. Jobayer Mia[4]

[1]PhD student, Florida Atlantic University
[2]Bangladesh University of Engineering and Technology (BUET), Bangladesh
[3]Accident Research Institute (ARI), Bangladesh University of Engineering and Technology, Bangladesh
[4]Department of Naval Architecture and Offshore Engineering, BSMR Maritime University, Bangladesh

E-mail: naoe17002.jobayer@bsmrmu.edu.bd

ABSTRACT

In case of new shipbuilding or ship repair, most of the industries are labour-oriented, and their labour cost is comparatively higher than other industries. Limited skilled workers are available to work in this vast sector. Therefore, the demand for ship repair labour and its cost is always at its peak. In this sense, the labour cost is significant and crucial issue for the ship repair industry. For regular or routine repair works, labour expenditure carries a good portion of the repair bill. In some cases, the amount of labour expenditure caries 60-70 percent of the total bill. Lesser man-hour can be converted into a lower final bill. It increases the dockyard capacity which will ultimately keep the position high in the competitive market. In this study, a method has been developed to formulate the mathematical model which will be used in estimating the ship repair man-hour for different types of vessels. To summarize the method, an algorithm has been established where all the steps are shown step by step. Multiple linear regression theory along with the least-square method has been used in this method. For the proposed method, man-hour is considered as the dependent variable whereas ship's age, displacement, and repair works are the independent variables. In conclusion, the primary aim of this article is to show how to build a mathematical model for estimating ship repairing man-hours, which will help management give better service and support.

Keywords: Ship Repair; Man-Hour; Multiple Linear Regression; Mathematical Model.

NOMENCLATURE

SR_{LH}	Ship repairing labour hour (hour)
R_{GS}	quantity of different logistic (nos.)
R_{PW}	structural steel repair works (ton)
R_{HCP}	hull cleaning and painting works (m^2)
R_P	pipe repairing works (m)
R_{UWF}	underwater fittings (nos.)
SSR	Regression Sum of Square
SSE	Error Sum of Square
SST	Total Sum of Square
s	Standard error
R^2	Coefficient of multiple determination
R^2_{adj}	Adjusted R square
MSE	Mean Square Error
k	Number of variable
n	Number of sample
C_P	Mallow's Statistic
VIF	Variance Inflation Factor

1. INTRODUCTION

Ships and vessels are one of the most crucial factors in global trade and economy. About 70 % [1] of the world's commodities are transported through ships like container vessels, oil tankers, cargo vessels, etc. To keep such fleets fully operational, dry docks, slipways, and floating docks hold a very tight schedule throughout the year and earn a significant amount of revenue for themselves and the national economy. Besides, to keep the industries operational, many people are engaged and earn their livelihood. On the other hand, it is mentionable that ship repair industries are fully labor-oriented organizations and very few portions of these sectors are automated. Thus, the labor cost is very much high in the ship repairing sector compared to other industries. Another reason is that skilled laborers are not available, and the nature of the job is different. That's why the demand for skilled workers in the ship repair industry is always at its peak. Maintaining the schedule of repair and optimizing man-hour /labor hours are the two vital factors to survive in the competitive market. Consequently, this is the crucial part of yard management to

collect the pertinent information to calculate the repair expenditure, especially the labor cost estimation. Minimizing the labor hour and maximizing the output is the key to survive in the competitive field.

In the dry-docking yard or new shipbuilding yard, about 50-60% of the cost is contributed by man-hour, and the rest of the expenditure is done from raw material, consumable items, utility services, etc. Good planning of repair works and the estimation of optimized man-hour for a repair project at the beginning stage are significant parts for the yard authority. The management authority needs to gather severalinformation to prepare the ship owner's financial proposal. The berthing charge of the vessels and some tariff works can easily be estimated, but labor hour estimation before starting the work is very tough. Repair activities include plate works, pipe works, painting, hull cleaning, outfitting, engine overhaul, electrical equipment change, etc. From this point of view, the author, who has eight years of practical experience in ship repair and the new shipbuilding industry, got the inspiration to develop a method for calculating the ship repair labor hour before docking the ship.

First of all, it needs to identify the parameters (repair works) which are the most influential in dominating the ship repair labor hour. A relation is developed between dependent and independent variables by the multiple linear regression method after finalizing the repair works. In this method, repair works like sandblasting, painting works, steel structural repair, piping works, hull cleaning, etc., are considered independent variables, and ship repair labor hours are considered dependent variables. The least-square method is used to equate the regression coefficient. Finally, some statistical parameters are used to justify model validation, and residual analysis is performed to give the final confirmation of the mathematical model for the developed method. This paper aims to explore a universal method that can estimate the ship repair labor hour before docking a ship. On the other hand, this thesis identifies the influential parameters (scope of repair works) which control the ship repair labor hour/ man-hour.

The Later part of this paper is arranged as follows. Firstly, it discusses the brief literature review in this field. Secondly, it discusses the detailed methodology under the two subsections, like this study's theory and the mathematical model development steps with an algorithm. Thirdly, it explains the discussion on the developed method and its loophole. The final section concludes the whole thesis with recommendations and discusses the further scope of research in this field.

2. LITERATURE REVIEW

Ship building and repair work is a complex process of engineering and management. Budget estimation is one of the most crucial factor to build a new ship or repair existing one. Though budget estimation is crucial factor, most of the researches to estimate ship works' financial cost have been conducted on new building vessels. The work on repair work cost or repair hour estimation is comparatively limited. Several investigations have been conducted on ship repair with different methods and purposes. Some of those are discussed here.

Jose R. et al. (2009) [2] conducted an investigation on dry-docking survey where they used the Goal programming method/Multi-criteria decision method to estimate ship repair costs. This article proposed a system for balancing the time and cost of ship repairs.

Later in Apostolidis et al (2012) [3] estimated the relation between dry-docking cost and different parameters of the ship. These parameters included ship dimension, ship service life, and repair time needed (days). He had focused on ships repaired in Persian Gulf region. The author suggested future improvement of the model they developed by including other parameters namely steel works, pipe works, mechanical works, etc.

Recently (2016) [4] Kr Dev et al. also proposed a mathematical model regarding ship repair labour cost estimation. Firstly, the author has identified the parameters that have significant impact on repair time (labour- days) and then suggested a model based on their discussion and findings of the interrelationship among different variables.

In this research, the authors have attempted to construct a general methodology to estimate the ship repair labour hour using the multilinear regression analysis technique. The repair hour then can be converted to labour cost by considering per hour labour cost at the desire time or location. The main motivation is to develop a common methodology for all types of ships. In this regard, different parameters are considered as independent variables including hull-plate works, pipe works, underwater fittings, machinery works, etc. The process developed in the work can be used to develop full-scale mathematical model to estimate repair labour hours for any sort of vessel and ship.

3. METHODOLOGY

3.1 Theoretical Background

A methodology has been developed which can be used to estimate the ship repair labor hour. This section discusses the methodology and theory related to the developed model, as well as the statistical relationship between ship repairing labor and associated independent variables. The following function is chosen as a result of the fact that individual independent variables are linearly associated with the dependent variable as required by the linear regression model. [5]

$$SR_{LH} = f\,(R_{GS}, R_{PW}, R_{HCP,} R_P, R_{UWF}) \quad \text{.....(1)}$$

Where SR_{LH} = is ship repairing labour hour which is the dependent variable. R_{GS} is the quantity of different logistic supports like use of the dock crane unit, use of the fork and side lift unit. This unit is measured in terms of hours. The use

of any logistic support like dock crane, forklift, or side lift in an interval of thirty minutes then it is considered as one unit. R_{PW} is the quantity of structural steel repair works (ton). This is measured, in terms of weight (ton).To calculate the weight of the plate, length, breadth, thickness, etc. are considered. R_{HCP} is the quantity of hull cleaning and painting works (m^2). This is measured in terms of area. R_P is the quantity of pipe repairing works in different locations. This is measured, in terms of the running meter (m). R_{UWF} is the number of underwater fittings like zinc anode, echo sounder, etc., and measured in terms of number.

More than one independent variable is required in the regression model in most research problems where regression analysis is used. When the coefficients of this model are linear, it is referred to as a multiple linear regression model. This multiple linear regression method makes a relationship between dependent and independent variables in order to forecast the dependent variable against a set of independent variables.

The regression model used in this study is as follows:

$$y = f(x_1, x_2, x_3 \cdots, x_k) \text{.....(2)}$$

Here, y represents the dependent variable that repairs labour hour in this work and the remaining variables x_1, x_2, x_3….. etc. are independent variables that include hull plate works, painting, underwater fittings, etc. There can be *k* number of independent variables. A general understanding is that for *n* number of values of y there will be *n* *k number of data available for independent variables.

Equation 1 can be written as follows considering all the variables:

$$y_i = b_0 + b_1 x_{1i} + b_2 x_{2i} + \cdots + b_k x_{ki} \text{….....(3)}$$

Where, i = 1, 2, 3,…….,n and b_1, b_2, b_3, …, b_k are the regression coefficients that need to be determined to construct the multiple linear regression model.

The multiple linear regression model can be expressed with a residual term as [6] :

$$y_i = b_0 + b_1 x_{1i} + b_2 x_{2i} + \cdots + b_k x_{ki} + e_i \text{.....(4)}$$

Here, e_i provides the residual of the regression model that should have the lowest possible value. Hence, the sum of errors (SSE) should also be minimum. The expression for SSE is as follows:

$$SSE = \sum_{i=1}^{n} e_i^2 = \sum_{i=1}^{n} (y_i - b_0 - b_1 x_{1i} \cdots - b_k x_{ki})^2 \text{.....(5)}$$

Equation 4 is differentiated with respect to different coefficients b_0, b_1,…,b_k. The results are set to zero and the following equations are obtained. There are total k+1 number of equations available.

$$n * b_0 + b_1 \sum_{i=1}^{n} x_{1i} + b_2 \sum_{i=1}^{n} x_{2i} + \ldots + b_{ki} = \sum_{i=1}^{n} y_i \text{ ……..…..(6)}$$

$$b_0 \sum_{i=1}^{n} x_{1i} + b_1 \sum_{i=1}^{n} x_{1i}^2 + b_2 \sum_{i=1}^{n} x_{1i}\, x_{\cdot 2i} + \ldots + b_{ki} \sum_{i=1}^{n} x_{1i} x_{ki} = b_{ki} \sum_{i=1}^{n} x_{1i} y_i \text{ ……..…..(7)}$$

$$b_0 \sum_{i=1}^{n} x_{2i} + b_1 \sum_{i=1}^{n} x_{1i}\, x_{2i} + b_2 \sum_{i=1}^{n} x_{2i}^2 + \ldots\ldots\ldots + b_{ki} \sum_{i=1}^{n} x_{2i} x_{ki} = b_{ki} \sum_{i=1}^{n} x_{2i} y_i \text{ ……..(8)}$$

……

……

……

$$b_0 \sum_{i=1}^{n} x_{ki} + b_1 \sum_{i=1}^{n} x_{ki}\, x_{\cdot 1i} + b_2 \sum_{i=1}^{n} x_{ki}\, x_{\cdot 2i} + \ldots\ldots + b_{ki} \sum_{i=1}^{n} x_{ki}^2 = b_{ki} \sum_{i=1}^{n} x_{ki} y_i \text{ ……..(9)}$$

The values of required statistical parameters/notations can be estimated using the collected sets of data points. With those values, the preceding equations can be converted into concurrent equations. By solving the concurrent equation using any standard procedure, the values of the regression coefficients and the required predicted model's equation can be found. Several statistical parameters have been considered in order to demonstrate the mathematical model's adequacy. Considered criteria and statistical parameters are discussed in this thesis.

3.1.1 Coefficient of Determination (R^2)

For a linear regression model, the coefficient of determination or coefficient of multiple determination expresses the proportion of the discrepancy in the dependent variable (Y) described by the independent variables (X). The coefficient of multiple determination is expressed as follows by Levine et al. (1997). [7]

$$R^2 = \frac{SSR}{SST} \text{……(10)}$$

SSR denotes the regression sum of squares, and SST denotes the sum of SSR and SSE. SSR equals the sum of the squared deviations between the predicted and mean values of y. SSE, on the other hand, equals the sum of the squared differences between the observed and predicted values of y [7].

Along with R^2, another important statistical parameter in multiple linear regression is adjusted R^2, which helps to identify the pivotal variable to improve model accuracy. The

adjusted R-squared is a modified R-squared that accounts for the number of independent variables in the developed model. Only if the new variable improves the model more than would be expected by chance does the adjusted R-squared increase. It falls when a variable improves the model by less than what would be expected by chance [7, 8]. The adjusted R^2 equation is as follows:

$$R^2(adj) = 1 - \left[(1 - R^2)\frac{n-1}{n-k-1}\right] \dots\dots\dots\dots\dots\dots\dots (11)$$

Where,

R^2 = Coefficient of multiple determination
k = Number of variable
n = Number of sample

3.1.2 Mean square error (MSE)

The average squared deviation between independent data sets and predictions from the fitted equation for the related values of the independent variables is defined as the mean square error of prediction. The variance of prediction and the square of the bias of prediction are both included in the mean squared error of prediction [9]. MSE calculates how far the predicted values differ from the observed values. It is natural to anticipate that the distance will be short. As a result, the best regression model, according to the MSE criterion, is the one with the lowest MSE.

3.1.3 Mallow's C_P Statistic

C_P is a statistical parameter that is generally used to identify the best subset model where a number of independent variables or predictors are available for forecasting some output. Small C_P is effective for identifying the best subset among the so many combinations of independent variables. The C_p statistics are calculated from the following formula:

$$C_p = \frac{SS(RES)_p}{MSE_{all}} + 2(p+1) - n \dots\dots\dots\dots\dots\dots\dots\dots\dots (12)$$

Where p is the number of independent variables in a given regression model. The residual sum of squares from p variable subsets is denoted by $SS(Res)_p$. MSE_{all} is the mean square error that takes into account all independent variables. Finally, n represents the number of samples [9]. A large value of C_p not near p+1, suggests that some important predictors/independent variables have been missed from the analysis. In this case, it is suggested to use the smallest value of C_p near p+1.

3.1.4 Standard Error

Standard error of multiple regression analysis is also known as the standard error of the estimate, explains the mean distance that the observed values fall from the regression line. Theoretically, it tells the wrong estimation of the regression model is on average using the units of the independent variable. In this paper the theoretical formula for standard error is considered as follows:

$$s = \sqrt{\frac{SSE}{n-k-1}} \dots\dots\dots\dots\dots\dots\dots\dots\dots\dots\dots\dots\dots (13)$$

The symbols have the usual meaning as explained above.

3.1.5 F-Statistics

The F-statistic is the test statistic for F-tests. Theoretically, F-statistics is the ratio of two variances like variance between sample means and variance within the samples. Variance is a measure of dispersion that how the observed data are dispersed from the mean value. Large value indicates the grater dispersion from mean. For passing the model f must be greater than $f_{critical}$. In this thesis, the F-statistics is denoted by f and the theoretical formula of this parameter is as follows.

$$f = \frac{\frac{SSR}{k}}{\frac{SSE}{n-k-1}} = \frac{\frac{SSR}{k}}{s^2} \dots\dots\dots\dots\dots\dots\dots\dots\dots\dots\dots (14)$$

3.1.6 Variance Inflation Factor

Multicollinearity is a significant problem in selecting the best-suited mathematical model by using the multiple linear regression method. The multiple linear regression method depicts that there is no presence of multicollinearity among the independent variables. When independent variables are correlated with each other then the value of standard error increases and the variance of the predictor's coefficients is inflated. To identify the correlated variables, a tool is used named is variance inflation factor (VIF). VIF has estimated is as follows:

$$VIF = \frac{1}{1-R^2} \dots\dots\dots\dots\dots\dots\dots\dots\dots\dots\dots\dots\dots (15)$$

Where, R^2 is the coefficient of determination for a regression model mentioned earlier. If the value of VIF is 5 (five) or more then it is considered that the independent variables are highly correlated with each other and it should be rejected from the regression model [10].

3.2 Proposed Method

A method for estimating the ship repairing labor hour can be developed using the above stated multiple regression theory,

model selection parameters, and model validation statistical parameters. The initial stage in this method is to choose the independent variables, and the independent variables chosen are essential in predicting the final estimated labor hour. Checking for multicollinearity in independent variables entails identifying the influential variable that can more accurately forecast the labor hour and dominate the dependent variable (Ship Repair labor hour). Variation Inflation Factor (VIF) does this verification by checking the multicollinearity among the independent variables. The next step is to check the linearity of the independent variables, which is done using a scatter plot between the dependent and independent variables. Stepwise regression is then performed using the previously described model selection parameters (R-squared and f-statistics), and the best-suited models are selected using the parameters (R-squared, Adjusted R-squared, MSE, and C_p). After the selection of the best subsets, residual analysis is used to analyze the pattern of residuals against predicted variables and residual versus independent variables. If deviations are observed, the variables that do not match the residual analysis criteria are transformed. Finally, a mathematical model for predicting ship repair labor hours has been developed.

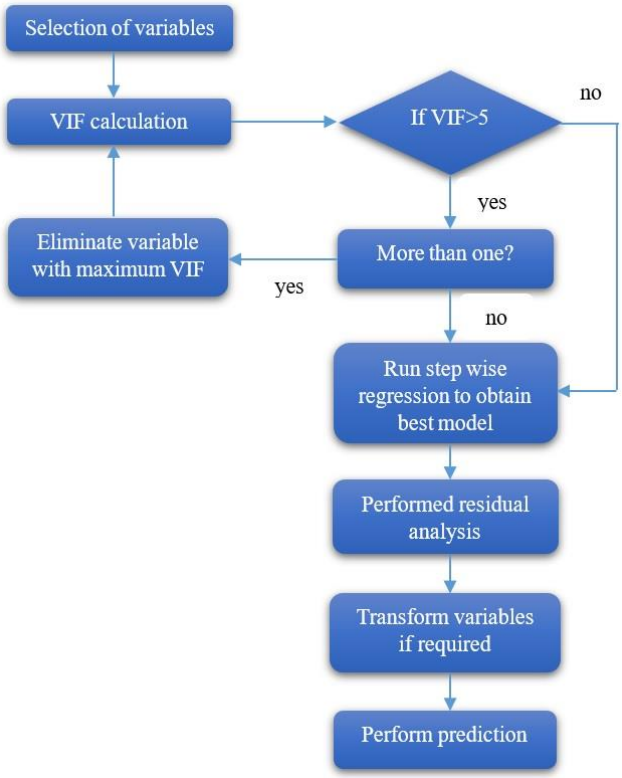

Fig. 1: Flow chart of the developed method for labour hour.

Now all the steps of this study can be summarized as follows with an algorithm/ flowchart (Figure-1).

The steps are as follows:

Step-1: Selection of independent variables

Step-2: Multicollinearity checking using VIF

Step-3: Linearity verification using scattered graphs

Step-4: Stepwise regression to choose the best subset of independent variables

Step-5: Selecting the best fit model that satisfies all the statistical parameters mentioned earlier section

Step-6: Conducting the final analysis (Residual Analysis)

Step-7: Transformation of variables if needed to handle any violations including linearity and other assumptions.

Step-8: Finalizing the model for prediction

4. DISCUSSION

The first step in developing a model in this study is to identify the influential independent variables that are not correlated. Because multicollinearity is a significant barrier to obtaining a good fit model. Multicollinearity reduces model accuracy while also increasing the standard error and VIF values. Furthermore, selecting the best subset is an important aspect of this research. During the stepwise regression stage, numerous combinations are formed. Theoretically, there are 2^n (n is the number of predictors) possible combinations. Finding the optimal subsets among these large combinations is tough, but using some of the factors stated before, it becomes easier. The coefficient of determination and the value of *f* statistics must be examined first in stepwise regression. Finally, the best subsets will be chosen based on a number of criteria, including a lower MSE value, a higher adjusted R-square, and a lower standard error value. The value of the R-square of best subsets represents the model accuracy as well as the model's error estimation. For example, if the value of R-square is 0.646, it means 64.6% of the variation in the dependent variable is contributed to the change in independent variables, and resting is called the erroneous estimation. The absence of one or more dominant independent variables that are responsible for the variation in the dependent variable leads to error estimation. This error estimation may occur for various reasons.

To begin, there is a wide range of repair work depending on the ship type, with the exception of some basic jobs such as sandblasting, painting, hull cleaning, structural steel repair, valves and pipelines, machinery equipment overhauling, and so on. Second, some repair jobs need the completion of two or more steps. The whole labor hour will be included in the mathematical model if every step of the repair operation is addressed. Furthermore, a low R-square value might occur if the sorted data is inconsistent, meaning some of the predictors have less significance.The valid reason for zero values is that some ships do not have any significant types of jobs, and it leads to a lower value of R-square. On the other hand, the value of less error estimation is dependent on the considered number of predictors. So, the value of the coefficient of multiple determination and the error estimation are closely related to each other, which means if the value of R-square is high, then the value of error estimation will be low and vice versa.

Finally, the proposed method will support dockyards and shipyards in estimating labor hours prior to docking a ship for routine maintenance. After calculating the labor hour against a set of projected repair works, the dockyard can estimate the labor cost of a project using the proposed method. At the conclusion of the project, the authority can compare the actual and expected labor hours to determine the hour deviation, which will act as a reference for the authority in the future.

5. CONCLUSION

This article explains a method for constructing a mathematical model that can be used to estimate ship repairing labor hours for any type of ship. Using this method (Figure-1), any shipyard or dockyard authority can design a mathematical model based on their own data for various ship types. These constructed models can be useful for comparing and estimating labor hours for ongoing and forthcoming projects. Furthermore, this study shows how to determine the influential parameters (independent variables) of ship repairing labor hour in order to have an effective mathematical model (tool), which is the most essential step in the proposed method. To summarize, this tool will assist management in surviving in a competitive market by forecasting the labor hour before to docking a ship. This is the author's first approach to estimating the labor-hour in various types of ship repairing works. Further research may include developing a methodology to estimate ship repair times, which will also be beneficial to shipyard authorities.

ACKNOWLEDGEMENT

The authors are grateful to Dr. Zobair Ibn Awal, Bangladesh University of Engineering and Technology, Bangladesh who has guided the authors to conduct this research with his knowledge and intellectual. Moreover, the authors are also thankful to Chittagong Dry-Dock limited, Bangladesh, for providing the data sample and other required information, which also assisted a lot to develop the above mentioned method (Figure-1).

REFERENCES

[1] T. M. Executive, 'The Maritime Executive,' https://www.maritime-executive.com/article/global-freight-demand-to-triple-by-2050, 2019.

[2] R. Jose and S. C., 'A goal programming model for vessel dry docking,' Journal of Ship Production, vol. 25, no. 2, p. 95–98, 2009.

[3] A. Apostolidis, J. Kokarakis and A. Merikas, 'Modeling the Dry-dock ing cost—the case of tankers,' Journal of Ship Production and Design, vol. 28, no. 3, p. 134–143, 2012.

[4] A. Kr Dev and M. Saha, 'Modeling and Analysis of Ship Repairing Time and Labour,' Journal of Ship Production and Design, 2016.

[5] J. Rawlings, S. Pantula and D. Dickey, 'Applied Regression Analysis: A Research Tool,' 1932.

[6] R. E. Walpole and R. H. Myers, 'Probability and Statistics for Engineers and Scientists 9th Ed.,' 1978.

[7] D. S. Levine, K. D.F and M. Berenson, 'Statistics for Managers Using Microsoft Exel, 5th Ed.,' Prentice Hall, 1997.

[8] W. Mendenhall, R. Beaver and B. Beaver, 'Introduction to Probability and Statistics. Cengage Learning,' 2013.

[9] J. Rawlings, S. Pantula and D. Dickey, 'Applied regression analysis: a research tool,' Springer Science & Business Media, 1998.

[10] J. I. Daoud, 'Multicollinearity and Regression Analysis,' Journal of Physics: Conf. Series 949, 2017.

Paper ID: 4377
International Conference on Mechanical, Manufacturing and Process Engineering (ICMMPE – 2022)
Organizer: Faculty of Mechanical Engineering, Dhaka University of Engineering & Technology (DUET), Gazipur, Bangladesh
Website: https://icmmpeduet.com/

Electrical Risk Domains in Ready-Made Garments Industries of Bangladesh: Applying Entropy Method to Prioritize

Md. Tanvir Siraj[1], Md. Mehedi Hasan[2], Md Faiaz Al Islam[3], Sheikh Navid Shadab Jamil[4], Asif kabir[5] and M Mahbubur Rahman[6]

[1]Department of Industrial and Production Engineering, BUET, Dhaka-1000, Bangladesh
[2]Department of Electrical and Electronic Engineering, KUET, Khulna-9203, Bangladesh
[3,4,5] Department of Mechanical Engineering, BUET, Dhaka-1000, Bangladesh
[6]Department of Mechanical Engineering, DUET, Gazipur-1707, Bangladesh

E-mail[1]: tanvir25392@gmail.com

ABSTRACT

Ready-Made Garments (RMG) sector of Bangladesh is one of the largest RMG exporting industries in the world. Several Severe electrical accidents at the RMG factories in the last few decades took many lives and destroy properties and reputations as well. A methodological approach to identifying and prioritizing the electrical risk factors can minimize this type of deadly electrical accident in RMG factories and create the most desired workplace safety and sustainability. This study proposes a Multi-Criteria Decision-Making (MCDM) method, the Entropy Method, to analyze the electrical risk factors of RMG factories in a quantitative approach to assist the decision-makers of this sector. In this study, electrical safety inspection reports from randomly selected 50 RMG factories have been analyzed to gather the most critical electrical risk factors in 6 different clusters or domains. These are- Cable and Cable Supports, Testing and Periodic Maintenance, Management and Documentation, Utility and Substation, Earthing systems, and Distribution Board. Then the Entropy method has been applied to find the objective weights of the 6 selected domains. For calculation, the percentage value of the observed number of risk factors in each of the domains for the 50 factories has been considered. The study finds Management and Documentation, Testing and Periodic Maintenance, and Utility and Substation as the most weighted domains for the electrical risk factors. The obtained result is expected to aid the industrial managers of RMG sector to be more focused on the specific risk domain to get a hierarchical solution in a complex decision-making environment.

Keywords: Ready-Made Garment; Electrical Risk Domains; Multi-Criteria Decision-Making; Entropy Method

1. INTRODUCTION

RMG sector of Bangladesh employs more than 4 million people in around 4500 factories [1], [2]. Maintaining a safe working environment for this large amount of people is always a critical issue for the industrial managers of this sector. RMG sector has faced several deadly electrical incidents in the last few decades [3]. The fire in Tazreen Fashions Ltd. in 2012 can be mentioned here. It was caused by an electrical short circuit and became the reason for more than 100 deaths and 300 injuries [4]. Besides this, electrocutions and electrical fire are the most frequently occurring accidents in RMG factories [5], [6], [7]. After initiating regular safety inspections in around 1700 RMG factories in 2013 by the Accord (Accord on Fire and Building Safety in Bangladesh), hazardous incidents have been minimized at a significant level [4], [8]. But in the rest of the RMG factories, which are not inspected or monitored properly, several electrical risk factors exist yet to be mitigated. A methodological study on electrical risk factors observed from the already inspected RMG factories can be effective in this regard.

Some works are existing in the literature for the assessment of electrical safety issues in the RMG sector of Bangladesh. For example, descriptive studies on electrical safety inspections in the RMG factories have been conducted [6], [9], [10], thermographic test results have been analyzed [11], and historical data on the deadly incidents have been presented statistically [3], prediction of electrical burns have been provided with a probabilistic model [7], an electrical risk index has been proposed for the RMG factories [5], and so on.

Electrical safety issues have been discussed in some other recent papers as well, which are not confined to RMG factories only [12], [13], [14], [15], [16]. However, no study has yet depicted the weights and prioritization of the domains in which most of the electrical risk factors exist to aid industrial managers. This gap in the literature is worthy to be filled.

Though each of the domains for electrical risk factors can be treated independently, they do not carry the same weight to the decision-makers of the industry. Industrial managers need to work in a complex environment with many constraints like resource limitation, cost minimization, maintaining production continuity, etc. For this, they need to prioritize the specific risk domains on which they need to give more focus than others. Therefore, a hierarchical order

can help them in this regard. Existing studies have been conducted by applying various qualitative and quantitative approaches to analyze electrical risk factors. However, none of the studies has prioritized the domains of the electrical risks to draw more attention to one over another to be mitigated hierarchically. Considering this research gap, this study aims to find the objective weights of the domains for electrical risk factors in RMG industries utilizing the Entropy method.

The Entropy method was introduced by Shanon in 1948 to be used in information theory which was derived from a concept of thermodynamics. At present, this is a very famous method among researchers to solve various MCDM problems where decision-makers prefer objective weights of a criterion over subjective weights. In this method, the higher the degree of dispersion among the objective values of the alternatives for a criterion, the higher the entropy value and the lower the weights that criterion will achieve [17], [18].

For this study, electrical safety inspection reports from randomly selected 50 RMG factories have been accumulated at first from the Accord's website (https://bangladeshaccord.org/factories). Next, 6 domains for the most frequently observed electrical risk factors have been extracted from the selected reports, and different existing literature. Later, based on the percent of risk factors in each domain in the existing reports, the objective weights of the domains have been determined by the Entropy method.

This research aims to address the following objectives:

a) To sort and enlist the domains of the electrical risk factors for RMG factories.

b) To find objective weights of the risk domains by the Entropy method.

c) To generate a prioritization of the risk domains.

The rest of the paper is divided into the following sections: Section 2 discusses the literature review. Section 3 depicts the research methodologies, and calculations. Section 4 discusses the obtained results. Section 5 describes the managerial implications of the study. Finally, Section 6 is for discussing the conclusion and some future research directions.

2. Literature Review

Structured and methodological electrical safety inspections at factories can minimize the damage to life and property [9]. The electrical risk factors can be identified, and the domains of the risk factors can be determined only by conducting properly standardized safety inspections. The scope of various safety inspections in RMG factories and some other aspects of the safety inspections have been depicted with various comparative and descriptive statistics and historical data in some of the existing studies [3], [6], [10], [19], [20]. Those studies discussed various correlations of safety inspection-related variables like causes, effects, inspection findings, inspection structures, etc. However, they did not attempt to prioritize the domains for electrical risk factors in RMG industries.

Islam et al. [5] computed the electrical risk index (ERI) to decide about some RMG factories. They assigned weights to the risk factors detected in electrical safety inspections. The weights and the frequencies of the risk factors were used to create three priority levels which are high, medium, and low. The main drawback of their method was to assign random weights to the risk factors. There was no methodological approach. This present study is going to overcome that drawback.

Haque et al. [7] predicted burn incidents by analyzing faulty electrical connections with probabilistic statistics. The prediction framework was established with empirical probability. But there was no prioritizing approach for the domains of electrical risk factors. Similarly, Islam et al. [11] experimented with the thermographic test to find the electrical load versus temperature correlation. Though the thermographic test is essential to detect hot spots in the electrical conductors, the objective of that study was different from this present work.

Besides studies on electrical safety issues in the RMG sector, there are some related works in recent literature. Some descriptive works among them are- Neitzel [16] discussed the importance of electrical safety training; Araneo et al. [15] discussed probable hazardous situations in research laboratories and preventive action plans; Reddy [14] described causes and mitigation techniques of some electrical accidents etc. The descriptive statistical approach has been utilized by some of the papers like electrical safety inspection findings from paper-manufacturing factories and animal food-manufacturing factories have been analyzed [13]; global electrical accident data from industry in the last 10 years have been presented, and so on. However, none of those works tried to prioritize the domains for electrical risk factors, which is the prime goal of this study.

This ongoing study has utilized an MCDM technique, the Entropy method. This objective weighting method has been used in various recent decision-making works where objective data are available to assist the decision-makers like Chen [21] utilized the Entropy method for building material supplier selection; Liu and Cui [22] applied the Entropy method to identify hazard source for building construction; Zhao et al. [18] evaluated national electric power development condition of some selected countries by the Entropy method; Guo [23] used the Entropy method with software simulation data to decide on road capacity for deciding on traffic system; and Ding et al., [17] evaluated sustainability of urban development based on statistical data analyzed with the Entropy method. However, no previous research utilized the Entropy method so far to prioritize any industrial risk factors or their observing domains, which justifies the novelty of the proposed study.

3. Methodology and Calculations

This study proposes a methodological approach to prioritize the observing domains of the most frequent

electrical risk factors from RMG factories. The methodology is designed with below explained 4 steps:

Step 1. Gather electrical safety inspection reports of randomly selected 50 RMG factories from the website of Accord (https://bangladeshaccord.org/factories).

Step 2. Sort out and enlist the risk domains of the most observed electrical risk factors from the inspection reports.

Step 3. Determine the objective weight of the risk domains by the Entropy method based on the percent of risk factors in each domain for 50 factories.

Step 4. Generate a prioritizing list of the risk domains.

3.1 Data Collection

Details of the selected risk domains to be prioritized in this study are shown in Table 1.

Table 1: Selected risk domains for electrical risk factors in RMG industries of Bangladesh

Risk Domain	Description	Source
Cable and Cable Supports (C)	Risk factors related to cable connections and supports and electrical wiring systems are listed in this domain. Such as buried power cable in the concrete floor, overloaded cable tray, improper support and protection for hanging cables, etc.	[7], [5], [20], [14]
Testing and Periodic Maintenance (T)	Risk factors related to different test results and maintenance irregularity are listed in this domain. Such as irregular resistance tests, irregular thermographic surveys, hot spot detection by thermal imaging, etc.	[9], [11], [13]
Management and Documentation (M)	Risk factors due to managerial negligence and improper documentation are listed in this domain. Such as no Lock-Out-Tag-Out (LOTO) policy, improper Personal Protective Equipment (PPE), improper electrical tools for maintenance personnel, no Lightning Protection System (LPS) for high-risk indexed structures, no electrical safety training program, etc.	[9], [12]
Utility and Substation (U)	Risk factors related to different utility machines and substations are listed in this domain. Such as inadequate maintenance clearance, oil levels low in the transformer conservator tank, heat sources near electrical installations, etc.	[7], [11], [13]
Earthing System (E)	Different earthing-related risk factors are listed in this domain. Such as LPS earthing merged with main electrical system earthing, non-segregated earth connections for different electrical installations, inadequate number of earth pits, etc.	[7], [14], [20], [24]
Distribution Board (D)	Electrical distribution boards and panel-related risk factors are listed in this domain. Such as congested bus bars, distribution board adjacent to a water source, unterminated live wire inside the panel, a discrepancy between installed circuit breakers size and load demand, connected cables to busbar terminal without cable lug, etc.	[7], [13], [20]

After analyzing electrical inspection reports of randomly selected 50 RMG factories (denoted as F1, F2, F3, …, F50), the percentage of risk factors has been computed concerning the total number of risk factors or the total number of inspection findings in each domain (see Table 2) Those reports have been generated and published by the Accord after conducting factory inspections by the trained electrical safety engineers [8].

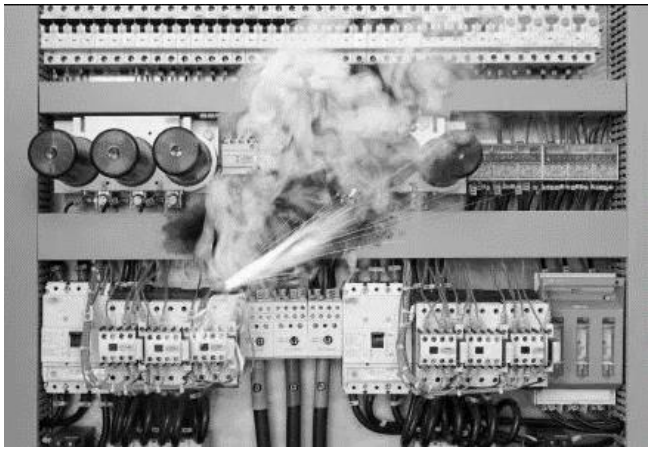

Fig. 1: Initiating fire from an electrical short circuit [25]

3.2 Entropy Method

For decision-making purposes, the Entropy method deals with practical observation or numerical data like

.

Table 2: Percentage of risk factors in each risk domain for randomly selected 50 RMG factories

	C	T	M	U	E	D
F1	17%	17%	6%	23%	6%	31%
F2	7%	7%	7%	13%	20%	47%
F3	19%	13%	11%	13%	7%	37%
F4	14%	9%	11%	16%	16%	34%
F5	17%	4%	22%	9%	17%	30%
F6	11%	6%	11%	6%	17%	50%
F7	15%	15%	8%	23%	15%	23%
F8	19%	15%	15%	12%	19%	19%
F9	10%	20%	10%	10%	10%	40%
F10	15%	10%	8%	17%	8%	42%
F11	14%	7%	21%	7%	7%	43%
F12	17%	3%	17%	14%	6%	44%
F13	28%	7%	17%	17%	7%	24%
F14	26%	5%	5%	11%	5%	47%
F15	9%	9%	9%	27%	18%	27%
F16	4%	13%	13%	4%	17%	48%
F17	25%	4%	7%	14%	14%	36%
F18	29%	14%	14%	14%	14%	14%
F19	14%	14%	14%	14%	14%	29%
F20	14%	3%	19%	36%	6%	22%
F21	19%	16%	10%	10%	10%	35%
F22	8%	8%	8%	25%	8%	42%
F23	16%	5%	5%	37%	16%	21%
F24	8%	8%	42%	8%	17%	17%
F25	13%	27%	7%	7%	13%	33%
F26	21%	5%	16%	11%	5%	42%
F27	25%	8%	25%	8%	8%	25%
F28	11%	11%	33%	11%	11%	22%
F29	17%	17%	17%	17%	17%	17%
F30	17%	17%	17%	17%	17%	17%
F31	6%	6%	12%	6%	12%	59%
F32	22%	9%	13%	4%	9%	43%
F33	23%	11%	9%	17%	13%	28%
F34	20%	10%	30%	10%	10%	20%
F35	13%	7%	7%	20%	7%	47%
F36	17%	7%	15%	20%	7%	34%
F37	23%	15%	23%	8%	23%	8%
F38	29%	5%	14%	5%	14%	33%
F39	10%	10%	30%	10%	20%	20%
F40	20%	20%	10%	10%	20%	20%
F41	11%	11%	22%	6%	6%	44%
F42	28%	3%	10%	17%	14%	28%
F43	25%	13%	25%	13%	13%	13%
F44	17%	8%	17%	17%	8%	33%
F45	14%	14%	29%	14%	14%	14%
F46	9%	9%	27%	9%	9%	36%
F47	17%	7%	10%	19%	7%	40%
F48	18%	18%	18%	9%	9%	27%
F49	11%	21%	16%	21%	5%	26%
F50	15%	13%	18%	13%	15%	28%

laboratory test results, statistics, simulation value, capacity, measurement, and so on [18].

This study aims to utilize the percent of electrical inspection findings or risk factors in each of the risk domains as a numerical input to calculate the entropy values and the weights of the risk domains. The details procedure of the Entropy method [21] can be found below:

Step 1. Generate the initial decision matrix for 50 RMG factories (See Table 2). The mathematical expression for the initial decision-matrix is as Equation (1)

$$D = \begin{array}{c|cccc} & C1 & C2 & \dots & Cn \\ F1 & d_{11} & d_{12} & \dots & d_{1n} \\ F2 & d_{21} & d_{22} & \dots & d_{2n} \\ \dots & \dots & \dots & \dots & \dots \\ \dots & \dots & \dots & \dots & \dots \\ Fm & d_{m1} & d_{m2} & \dots & d_{mn} \end{array} \qquad (1)$$

Step 2. Normalize the initial decision-matrix by using Equation (2)

$$r_{ij} = \frac{d_{ij}}{\sum_{i=1}^{m} d_{ij}} \qquad (2)$$

Step 3. Calculate the entropy value for each risk domain by using Equation (3)

$$e_j = -\frac{1}{\ln(m)} \sum_{i=1}^{m} r_{ij} ln(r_{ij}) \qquad (3)$$

Here, m= Number of Alternatives (In this study, m= 50, as 50 factories have been considered)

Step 4. Compute the weights of the risk domains by using Equation (4)

$$w_j = \frac{1 - e_j}{\sum_{j=1}^{n}(1 - e_j)} \qquad (4)$$

3.3 Calculations

After applying the normalization operation to the initial decision-matrix, obtained normalized decision-matrix can be found in Table 3.

Table 3: Normalized Decision-Matrix

	C	T	M	U	E	D
F1	0.021	0.032	0.007	0.033	0.010	0.020
F2	0.008	0.012	0.009	0.019	0.033	0.030
F3	0.022	0.024	0.014	0.019	0.012	0.024
F4	0.016	0.017	0.015	0.023	0.026	0.022
F5	0.021	0.008	0.028	0.012	0.029	0.019
---	---	---	---	---	---	---	---
---	---	---	---	---	---	---	---
F46	0.011	0.017	0.035	0.013	0.015	0.023
F47	0.020	0.013	0.012	0.027	0.012	0.026
F48	0.022	0.034	0.023	0.013	0.015	0.017
F49	0.013	0.039	0.020	0.030	0.009	0.017
F50	0.018	0.023	0.022	0.018	0.025	0.018

Entropy values and weights for the risk domains have been calculated from this normalized decision matrix. Those can be found in Table 4. A graphical presentation of the obtained weights can be found in Figure 2.

Table 4: Calculated entropy values, weights, and prioritization of the selected risk domains

	C	T	M	U	E	D
F1	-0.080	-0.110	-0.036	-0.112	-0.044	-0.079
F2	-0.039	-0.055	-0.041	-0.076	-0.113	-0.105
F3	-0.085	-0.090	-0.061	-0.074	-0.054	-0.089
F4	-0.068	-0.069	-0.062	-0.086	-0.096	-0.084
F5	-0.081	-0.039	-0.100	-0.055	-0.102	-0.077
---	---	---	---	---	---	---
---	---	---	---	---	---	---
F46	-0.050	-0.069	-0.117	-0.057	-0.063	-0.088
F47	-0.079	-0.058	-0.054	-0.098	-0.053	-0.095
F48	-0.084	-0.115	-0.088	-0.057	-0.063	-0.071
F49	-0.056	-0.127	-0.079	-0.106	-0.041	-0.069
F50	-0.073	-0.088	-0.085	-0.072	-0.092	-0.071
ej	0.9816	0.9688	0.9682	0.9689	0.9789	0.9821
1-ej	0.0183	0.0311	0.0317	0.0310	0.0211	0.0179
wj	**0.1214**	**0.2056**	**0.2098**	**0.2051**	**0.1395**	**0.1183**
Rank	**5**	**2**	**1**	**3**	**4**	**6**

4. Results and Discussion

This study determines the weights of the risk domains for electrical risk factors by the Entropy method (see Table 4 and Figure 2) Management and Documentation (0.20984)> Testing and Periodic Maintenance (0.20566)> Utility and Substation (0.20518)> Earthing System (0.13950)> Cable and Cable Supports (0.12145)> Distribution Board (0.11837). As the Entropy method is a measurement of dispersion among the objective values, larger dispersion creates larger entropy and smaller weight. Therefore, the obtained weights from this study indicate, that during electrical safety inspections at the RMG factories, 'Management and Documentation' related risk factors are very common observation from the inspectors, and the percentage of the lackings for the factories in this risk domain is comparatively consistent than the percentage of lackings in other risk domains. On the other hand, the percentage of the risk factors related to distribution boards is very high in some of the factories, while, in some of the factories the percentage is very low (see Table 2). Because of this dispersive pattern of the percentage of risk factors, the weight of the 'Distribution Board' risk domain is the minimum of all.

Proper management and documentation are reflections of the willingness and awareness of the top management of the factory [26]. The same applies to the scheduled testing of different installations and performing periodic maintenance. Hence, the top two highly weighted risk domains show that there is a lack of awareness about electrical safety among the top management of the RMG factories. The regulatory authority should be more focused on this issue to ensure a safe and sound workplace in the RMG sector. An interesting

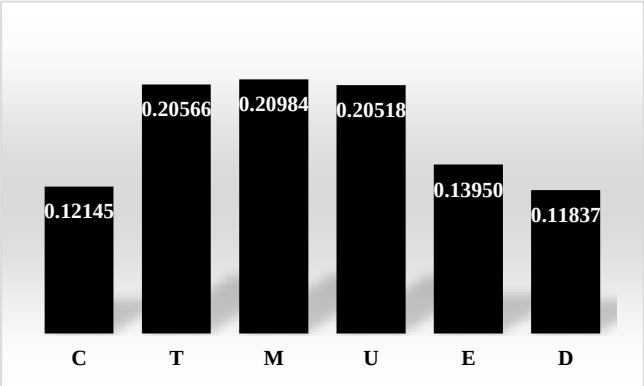

Fig. 2: Weights of the risk domains to be prioritized

observation from this result is that the weights of the top-ranked risk domains obtained by the Entropy method are not very significantly different from each other. That means the number of electrical risk factors from those risk domains is very consistent in the RMG factories. Decision-makers need to be more concerned to mitigate those risk factors under the top prioritized risk domains with extensive priority.

5. Managerial Implications

Obtained results have been shared with several industrial managers to gain a better understanding of the implications of this study. Industrial managers have to work within limitations and challenges like resource constraints, reaching productivity targets, minimizing maintenance time, etc. Therefore, looking after all the electrical risk domains at the same time is not practical. Managers need to be strategic to mitigate the risk factors by prioritizing their risk domains. In such situations, they can follow the prioritization of the risk domains achieved from this study to overcome the issues effectively. Industrial managers can follow this result to generate a hierarchical action plan for electrical risk mitigation, rather than go for a vague decision.

6. CONCLUSION

A novel approach to implementing the Entropy method has been depicted in this study. Generally, electrical safety inspections are conducted in RMG factories by trained electrical safety engineers of the Accord. Though their observations about the risk factors are structured, various human factors can influence generation reports during an inspection. This study has analyzed electrical inspection reports from randomly selected 50 RMG factories. Percent of risks in each domain has been considered for numerical input of the Entropy method. So, the interesting thing is that the objective weights of the risk domains for this study are basically obtained by the subjective judgment of the inspectors.

This study shows, that only the willingness and awareness of the management can reduce the electrical risk factors to a significant extent. Management of RMG factories should be more aware of proper documentation

of all the procedures including testing and periodic maintenance. Proper documentation develops accountabilities among the personnel, thus minimizing risk. In a developing country like Bangladesh, managers need to be calculative to utilize their limited resources. The study can assist them by showing the prioritization of the electrical risk domains to be focused on step by step.

In the future, some other experts' opinion-based MCDM techniques can be applied to get an extensive overview of the electrical safety of RMG factories. Determining a prioritization of the mitigation action plan can also be a new addition to this field of study. Showing interrelation among the risk domains based on the influence of one risk domain over another can also be considered a study scope.

REFERENCES

[1] Statista., Number of garment factories Bangladesh 2010-2019. Retrieved from https://www.statista.com/statistics/987697/bangladesh-number-garment-factories/, 2021.

[2] Fathi, N., Safety First: Bangladesh Garment Industry Rebounds. Retrieved from https://www.ifc.org/wps/wcm/connect/news_ext_content/ifc_external_corporate_site/news+and+events/news/insights/bangladesh-garment-industry, 2021.

[3] Hasan, M. M., Mahmud, A., and Islam, M. S., Deadly incidents in Bangladeshi apparel industry and illustrating the causes and effects of these incidents. Journal of Finance and Accounting, 5 (5), 193–199, 2017.

[4] Wiersma, J., Fire safety in the ready-made garment industry in Bangladesh, five years after Rana plaza. Safety in Garment Industry, 16, 2018.

[5] Islam, M. M., Ashraf, M. N., and Bhuiyan, M. I. H., A new electrical risk index for electrical safety assessment of RMG industries in Bangladesh. In Proceedings on international conference on disaster risk management, 2019.

[6] Moazzem, K. G., Halim, S. F. B., and Shafayat, M., Can a sustainable inspection system be developed? the case of RMG sector in Bangladesh. Centre for Policy Dialogue, 2018.

[7] Haque, F., Marma, H.-U.-M., and Chowdhury, A., Prediction of burn incidents due to faulty installations in RMG factories in Bangladesh. In *2017 international conference on electrical, computer and communication engineering (ecce)* (pp. 733–737), 2017.

[8] Accord., The Bangladesh Accord on Fire and Building Safety. Retrieved from https://bangladeshaccord.org/factories, 2021.

[9] Hossain, M. S., and Salam, K., Basic approach of an electrical safety assessment in RMG industries: Development of electrical hazards. *Journal of Modern Science and Technology*, *3*(1), 40–46, 2015.

[10] Bhuiyan, M., Majumder, S., Arafat, Y., Rahman, S., and Islam, M., On the guidelines for electrical safety audits in RMG industry of Bangladesh. Safety in Garment Industry, 26, 2018.

[11] Islam, S. R., Huque, M. M., Khan, L. A., and Hossain, M. I. An experimental thermographic safety audit focusing on temperature rise vs load in electrical installations in a Bangladesh garments factory. In 2017 4th international conference on advances in electrical engineering (ICAEE) (pp. 561–564), 2017.

[12] Anderson, R., McGaw, S., and Parra, G., Electrical safety in industrial construction: An analysis of 10 years of incidents in the global engineering, procurement, and construction industry. IEEE Industry Applications Magazine, 27 (3), 31–41, 2021.

[13] Charoenchit, S., and Thongchaisuratkrul, C., Safety inspection of electrical systems case study in paper and animal food factories. GMSARN International Journal 15, 331–339, 2021.

[14] Reddy, B. K., Safety in use of electrical appliances. International Journal for Research and Development, 7., 2019.

[15] Araneo, R., Dehghanian, P., and Mitolo, M., On electrical safety in academic laboratories. IEEE Transactions on Industry Applications, 55 (6), 5613–5620, 2019.

[16] Neitzel, D. K., Electrical safety training requirements for all personnel. In 2018 IEEE IAS pulp, paper and forest industries conference (PPFIC) (pp. 1–5), 2018.

[17] Ding, L., Shao, Z., Zhang, H., Xu, C., and Wu, D., A comprehensive evaluation of urban sustainable development in China based on the TOPSIS-Entropy method. Sustainability, 8 (8), 746., 2016.

[18] Zhao, D., Li, C., Wang, Q., and Yuan, J., Comprehensive evaluation of national electric power development based on cloud model and entropy method and TOPSIS: A case study in 11 countries. Journal of Cleaner Production, 277, 123190., 2020.

[19] James, P., Miles, L., Croucher, R., and Houssart, M., Regulating factory safety in the Bangladeshi garment industry. Regulation and Governance, 13 (3), 431–444, 2019.

[20] Hasan, S. M. T., Kaium, A., Ahmed, S., Mehmood, S., Kristensen, A., and Ahsan, D., Risk assessment and cost benefit analysis of occupational safety intervention for readymade garment factories: A case study of Bangladesh. In Safety and reliability-safe societies in a changing world: Proceedings of European safety and reliability conference (ESREL) (pp. 3917–3925), 2019.

[21] Chen, C.-H., A novel multi-criteria decision-making model for building material supplier selection based on Entropy-AHP weighted TOPSIS. Entropy, 22 (2), 259., 2020.

[22] Liu, Y., and Cui, J., Identification of hazard sources in prefabricated building construction by entropy weight method. In IOP conference series: Earth and environmental science (Vol. 560, p. 012073)., 2020.

[23] Guo, S., Application of entropy weight method in the evaluation of the road capacity of open area. In AIP conference proceedings (Vol. 1839, p. 020120), 2017.

[24] Drobyazko, O. N., Fundamentals of Electrical Safety Theory: Current State and Development Prospects. Russian Electrical Engineering, 89(12), 728-732, 2018.

[25] RMG Bangladesh, Electrical short circuit main reason of fire in RMG sector. https://rmgbd.net/2016/09/electrical-short-circuit-main-reason-of-fire-in-rmg-sector/, 2016.

[26] Bari, A. M., Siraj, M. T., Paul, S. K., & Khan, S. A., A hybrid multi-criteria decision-making approach for analyzing operational hazards in Heavy Fuel Oil-based power plants. Decision Analytics Journal, 100069, 2022.

Paper ID: 4564
International Conference on Mechanical, Manufacturing and Process Engineering (ICMMPE – 2022)
Organizer: Faculty of Mechanical Engineering, Dhaka University of Engineering & Technology (DUET), Gazipur, Bangladesh
Website: https://icmmpeduet.com/

Design, Fabrication, and Performance Analysis of An Eco-friendly Gutter Cleaner

Abu Saleh Md. Nakib Uddin[1], Fahima Akter Azrin[2], M. M. Aflatun Kawsar[3], Faria Akter Tonny[4], Md Minhazur Rahman Zehad[5], MD Ashfakul Karim Kaushik[6], Doulotuzzaman Xames[7], Adib Bin Rashid[8]

[1-8]Industrial and Production Engineering Department, Military Institute of Science and Technology (MIST), Dhaka, Bangladesh

E-mail: adib8809@gmail.com

ABSTRACT

The drainage cleaning system of Bangladesh is manual and quite harmful to the drain cleaner's health. In the country's traditional drainage cleaning system, the workers have to get down into the gutter and collect the garbage with their own hands. This act is very harmful to their health and quite inhumane too. Also, this manual process is very time-consuming, and proper cleaning is still not ensured. Under these circumstance, the typical drainage cleaning should be transformed into a new automated drainage cleaning system that saves time with less power consumption and so that a better and healthier cleaning system is ensured. Nowadays all the operations or working processes are preferable when it is automated or digital instead of manual. As Eco-friendly Gutter Cleaning System is for improving the existing cleaning system, its main features are safely cleaning, tackling gutter jamming, and cleaning gutter or drain with very low power consumption with fast cleaning. Our device ensures continuous cleaning process which do not allow to create any blockage in the gutter.

Keywords: Drainage Cleaning System; Automated; Eco-friendly; Gutter Cleaner.

1. INTRODUCTION

The drainage problem is one of the deadful problems that discourage the development of the country. The dumping of solid wastes in the drain is a very common scenario in the country. Indiscriminate dumping of solid wastes in drains is resulting in stagnation of water [1]. If those solids contain any sharp edge of glass or if steel or any poisonous chemical are present in the garbage and the workers clean the drain by hand, it may be very dangerous for their skin and health. So, it is time to make our drainage cleaning system automated.

The traditional gutter cleaning system is functioned by gutter cleaners which is not suitable for human life. Infact. it may put the workes at higher risk for serious diseases. P. D. Chaudhuri and G. S. Gajare showed that a drainage cleaner machine is a replacement for the manual drainage cleaning process which collects the solid wastes at the junction points of the drainage system. This machine has a continuous rotation of chain consisting of a lifter, which lifts the garbage and dumping into the collecting bin. When there is high velocity running water of drainage lines, the machine will work very effectively [2].

Generally, all the collected metallic and non-metallic materials are stored together in the bin. Releasing those collected wastes into the environment is very harmful as metallic is not biodegradable [3].

In this paper, we focus on designing and developing an automated and eco-friendly gutter cleaner that will help gutter cleaners to remain healthy instead of manual cleaning.

M. Halingali et al. proposed a robotic and stationary system to collect wastes without putting people at any risk. A lifter is connected with a chain and collects the garages. The chain rotates by a motor and put the garages in the collecting bin. The other parts of this machine are the shaft, bearing, sprocket, basement, etc. to run the whole system [4].

R. Sathiyakala et al. suggested the same methodology with a special bucket which is used an evaporate system to convert the sewage into dry matter. As a result, there remains no risk of any kind of affection of the bacteria. They modified their bucket with the ARM board (ARDUINO), named as E-bucket meaning electronic bucket [5].

After observing some previous models of gutter cleaning systems, it can be concluded that many specific empirical studies have been carried out and categories such as automatic drainage cleaning systems and their automation have been studied to a great depth. Our main point of interest will be making this traditional cleaning system more eco-friendly, additionally to make the odd work for the minors more healthy, harmless, and enjoyable that people give up on terming it as an odd job with the help

of automation and sensors; by making the equipment more cost and time-efficient.

2. METHODOLOGY

2.1 Scopes of Eco-friendly Gutter Cleaner

As the project is focused on making our existing gutter cleaning system more efficient, less harmful for human health, and more eco-friendly, it can add extra benefits to many aspects of our present life.

Society: Sanitation is in a very terrible condition in our society. Here, drainage systems are mostly cleared only once a year. There is lack of coordination among the authorities including 14 government agencies including the two Dhaka City Corporations and Dhaka WASA responsible for maintenance of the drainage systems [6]. So, here comes our first field to install an automated cleaning system to improve our drainage cleaning system one step forward and ensure all the roadside gutter or drain healthily and effectively.

Industry: Industrialization has rapidly progressed in Bangladesh. Industrialization brings significant structural changes to the economy. The major industries are cotton, textiles, jute, garments, pharmaceutical, tea processing, paper newsprint, cement, etc [7]. These industries release a large number of solid wastes into the environment. When industrial wastes come out in large drains, they can be the cause of massive blockage in the drain/ gutter. So, this machine can clean the solid wastes regularly. As a result, there will have little chance to build any blockage in the gutter and the environment of the industry will remain clean, healthy, and slightly at the same time.

2.2 Survey Findings

To find out the people's opinion on a typical drainage cleaning system, an online survey through Google forms was conducted. The survey shows a very clear picture that most of the people do not think the existing drainage cleaning system is suitable for our society and recommend the automated cleaning system.

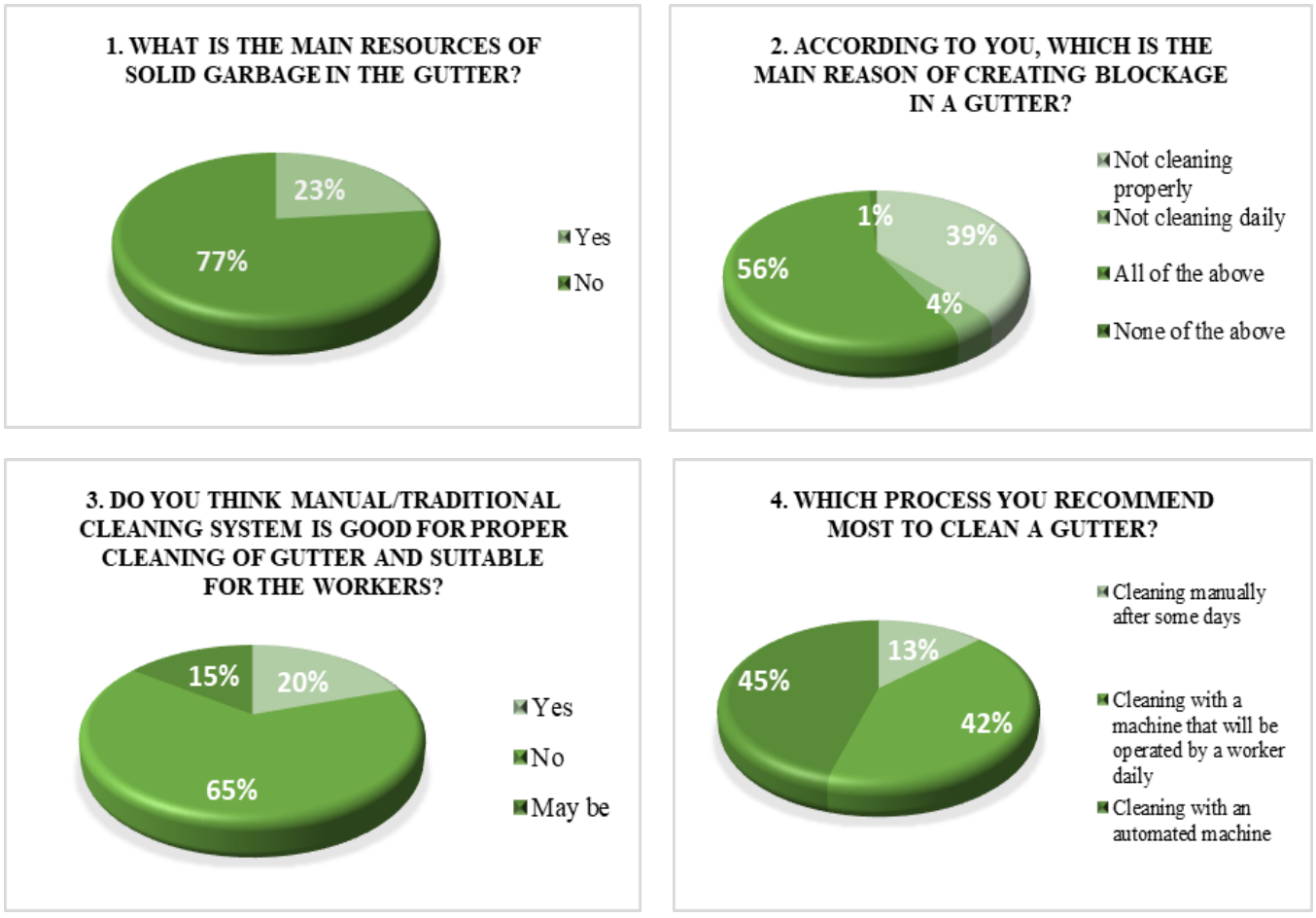

Fig. 1: Survey Findings

2.3 Quality Function Deployment

Quality Function Deployment (QFD) is a structured approach to defining customer needs and translating them into specific plans to produce a product. The understanding of people's opinions is summarized in a product planning matrix or "House of Quality". These matrices are used to translate higher-level "what's" or needs into lower-level "how's" – product requirements or technical characteristics to satisfy these needs. [8]

The House of Quality for Eco-friendly Gutter Cleaner is shown in Fig. 2.

Symbol	Relationship	Ratings
⊕	Strong	9
⊕	Moderate	3
⊖	Weak	1

Correlation	
Positive	+
Strongly Positive	+ +
Negative	-
Strongly Negative	- -
No Relation	

		Customer Ratings	% of Ratings	Flexibility	Material Used	Bin Volume	Availability	Solar system	Operational and fixed cost	Efficiency	Digital Segregation	Our Product
Customer Requirements	Daily servicing	4	9.8			⊕		⊕		⊖		5
	Ease of use	3	7.3	⊕	⊕			⊖				2
	Low Power Comsumption	4	9.8						⊕	⊕		4
	Longevity	5	12.2		⊕				⊕			4
	Waste Cleaning	4	9.8			⊕					⊕	5
	Eco-friendly	5	12.2		⊕			⊕		⊖		5
	Relaibility	4	9.8		⊕			⊕				4
	Digital Feature	4	9.8	⊕			⊕				⊕	3
	Automation	5	12.2	⊕						⊕	⊕	4
	Reasonable Price	3	7.3	⊕	⊕		⊕		⊕	⊕		3
	Our Importance Ratings			135	136	72	51	104	92	105	97	3
	% of Rating			17	17.2	9.1	6.4	13.1	11.6	13.3	12.2	

Fig. 2: House of Quality for Eco-friendly Gutter Cleaner

Here, some common needs related to the drainage cleaning system like daily servicing, ease of use, lower power consumption, etc. are being compared with some technical terms like flexibility, availability, and so on. Here, customer rating, percentage of rating, and our product performance rating are also shown which were figured out by group discussions. The relationships of some symbols have been defined: plus as strong, circular plus as moderate, and circular minus as weak and fix the ratings of Likert Scale of 9-3-1, respectively. In the diagram, daily servicing has a strong relationship with the bin volume and solar system, but weak relation with efficiency because daily servicing does not affect efficiency. In the same way, the relation between all the basic customer needs and technical requirements are established. Then, technical correlations are also shown with some symbols. For example, bin volume has a strong positive relation with operational and fixed costs, which means if bin volume is increased, the cost will also increase. Other correlations also can be explained in the same way.

2.4 Component Hierarchy

2.4.1 Main Body Parts

The main body parts of our automated machine are the Motor, Gear, Shaft, Bearing, Sprocket, Chain, Lifter, Basement, Collecting bin. The machine is placed across a gutter so that only water flows through the lower basement. Floating wastes like bottles, plastic, cans, covers, etc. are lifted by lifters that are connected to the chain. The chain revolves with the sprocket wheel which is driven by the shaft where the shaft is rotated from the motor and gear. The energy provided to the motor is electrical energy. When the motor runs, the chain starts to circulate and makes the lifter lift. The wastage material is lifted by lifter teeth and stored in storage or collecting bin. Once the collecting bin is full, the waste materials are removed from the bin.

2.4.2 Energy Conversion

Solar panels and batteries (as an alternate) require to provide electrical energy [9]. Further, it will run the motor by converting it into mechanical energy and rotate the gear. These gears will convert the mechanical rotational energy from the motor and rotate the shaft. We use a battery along with solar panel in case of cloudy or rainy days.

2.4.3 Working Principle

The main purpose of designing the gutter cleaner is to clean the gutters healthily and make our existing cleaning system more efficient and environmentally friendly. This machine will collect the garbage like metallic, and non-metallic from a gutter and store them in the bin separately. To operate these features, it require two mechanisms which are Pulley Belt Mechanism and Lifting Mechanism.When we give power to this machine, the motor starts functioning, which provides rotation to the shaft and through the help of the shaft. A-Pulley belt mechanism is required to rotate a shaft. The shaft is connected with a pulley belt and it is connected to the motor.A lifting mechanism is needed to collect garbage from the gutter and keep to the collecting bin. In this case, sprockets that are fixed to the shaft, also rotate. Due to the rotation of the sprocket, the chain connected to the sprocket rotates. As the chain turns, the two lifters, which are connected to the chain at half-length of the chain, start turning as well. When one lifter completes one round from down to upward direction, it takes all the garbage materials like waste bottles, plastic, tins, etc., on the grid and drops it in the collecting bin attached at the back. Since there are two lifters, the collection rate of garbage will be more. This is how this machine helps us clean sewage or any trash from the water. The devices are placed across drains so that only water flows through lower grids; waste like a bottle, etc. floating in the gutter are lifted by the teeth of lifters that are connected to the chain. A gear driven by a motor attaches this chain. When the motor runs, the chain starts to circulate with the lifter. The waste materials are raised by the lifter and stored in a waste storage tank.

The main body parts, mechanisms, and energy conversion are illustrated in one component hierarchy in Fig 3.

2.5 Used Materials and Processes

Table 1: Selected Materials for every part

Parts Name	Material
Basement, Body, Shaft (Upper), Lifter	Gray Cast Iron
Collecting Bin	Stainless Steel
Shaft (Lower)	Mild Steel

Table 2: Selected Processes for different manufacturing purposes

Purpose	Process
Permanent Joining	Arc Welding
Temporary Joining	Nut Bolt
Finishing	Non Precision Grinding
Coloring	Spray Paint

These materials and processes are selected from different options by using the weighted average method.

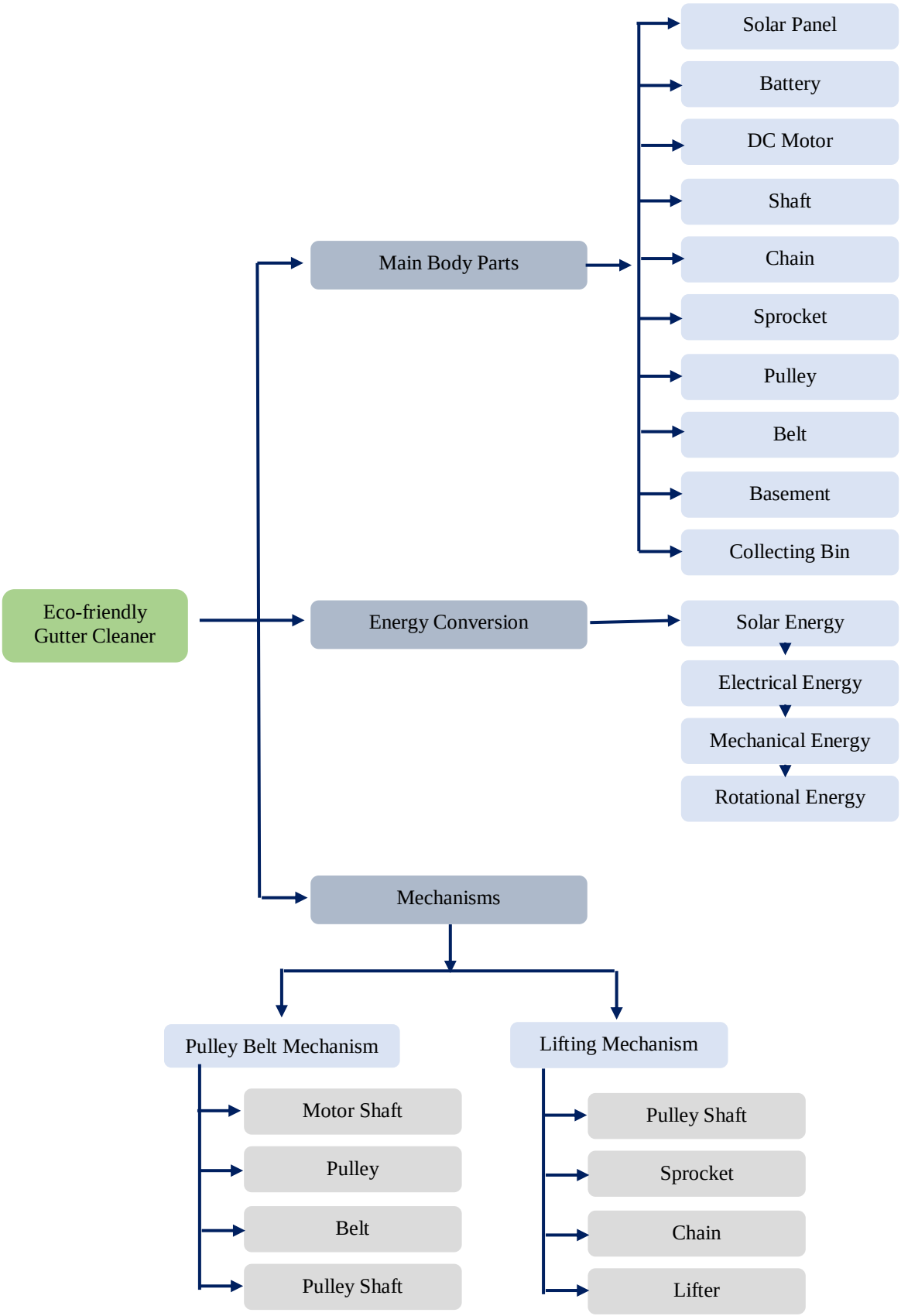

Fig. 3: Component Hierarchy of Eco-friendly Gutter Cleaner

2.6 Cluster Function Structure

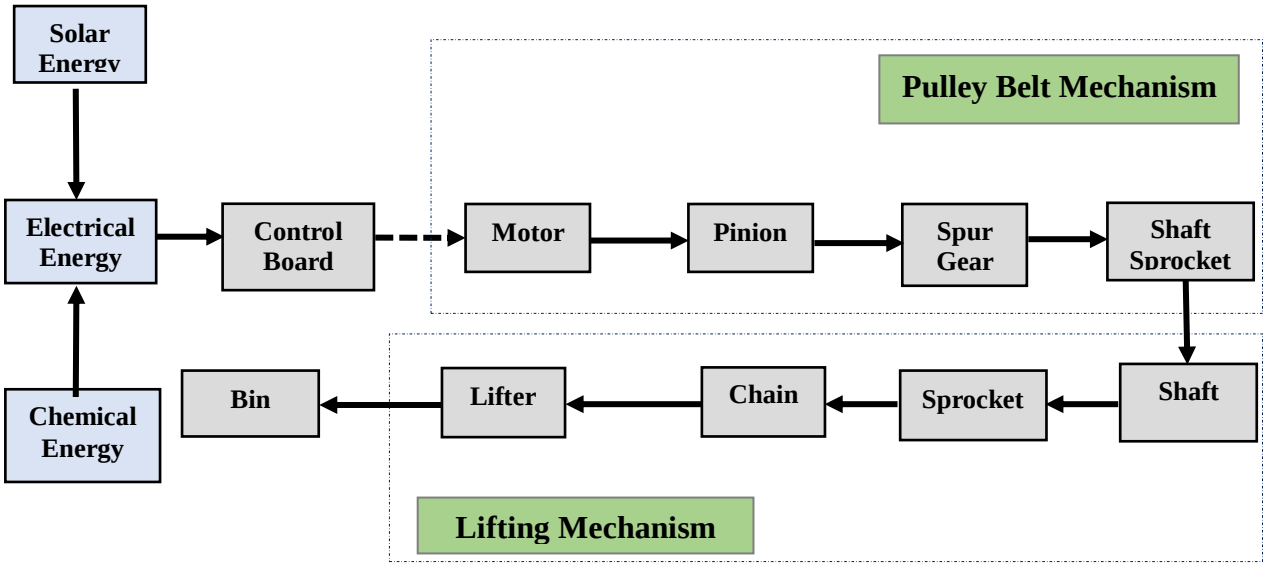

Fig. 4: Cluster Function Structure of Eco-friendly Gutter Cleaner

3. DESIGN ANALYSIS

Design analysis is a critical aspect before we fabricate the product. Furthermore, how a product will run and the way it works is determined through design analysis. We have designed our products in Solid works. Then, we were able to simulate our product in a three-dimensional shape and further did the analysis it improve this product.

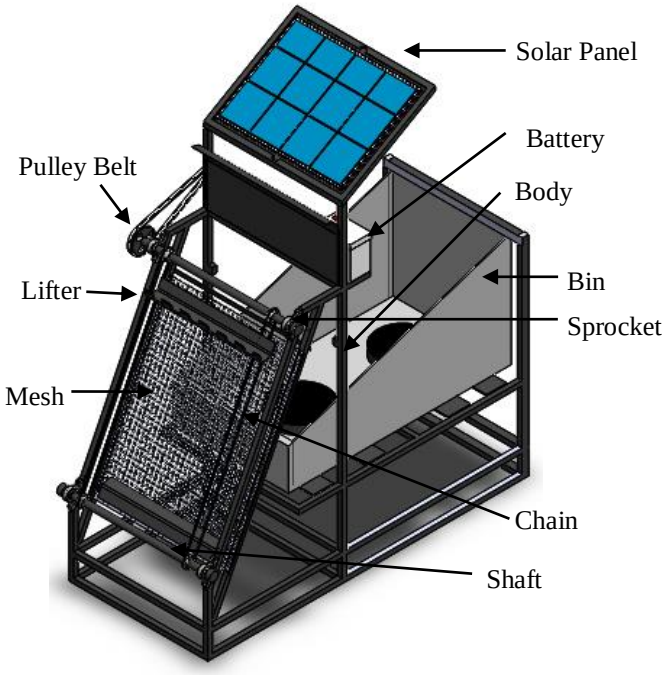

Fig. 5: Prototype of Eco-friendly Gutter Cleaner

By design analysis, we were able to simulate our product and it helped us to out the shortcomings[10]. After a lot of simulations and analysis, the product design was made ready to go for manufacturing.

4. RESULT & DISCUSSION

The outcome of the product after manufacturing is shown in Fig 6.

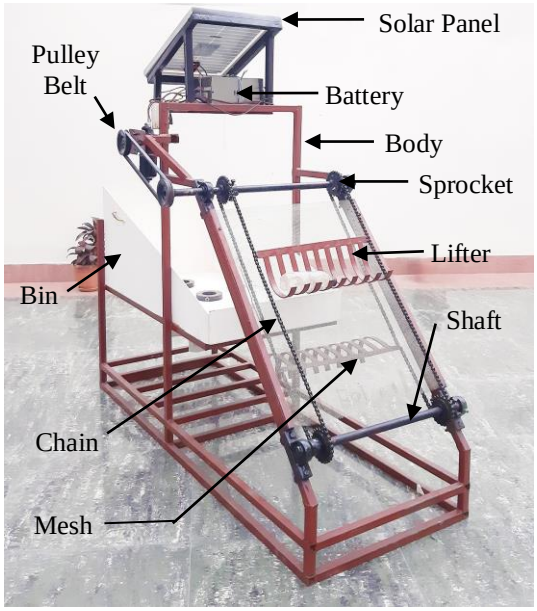

Fig. 6: Eco-friendly Gutter Cleaner

The machine is fabricated in order to use it for cleaning daily in a continuous process. In the gutter or drain, there are not so have very heavyweight garbage. After setting the cleaner at a drain, some observations were taken about its cleaning capacity.

Table 3: Observation of Per Minutes Lifting Capacity

Observation No	Number of Lifting	Average Weight Taken by Each Lifter (gm)	Amount of Garbage Collected in Bin per min (gm)
1	18	362	6516
2	18	356	6408
3	18	339	6102
4	18	387	6966
5	18	367	6606

From the observations, the average number of lifting per minute is 18 times and the machine can collect an average 6520 gm of garbage per minute.

The hourly collecting capacity of this machine =(6520×60) gm =391200 gm =39.12 kg

5. CONCLUSION

Our product is solar-based which is very much efficient as a power source. Moreover, it will be comforting for the end-users like the cleaner workers. Using it will make them feel better rather than feeling low and subjugated, and thinking of it as an odd job. These were the main aims and objectives of our project which are described in this paper and we find the satisfaction in accomplishing this task. The world is changing and to change this world already many remarkable innovations have been made by the researchers. To improve now the most useful basis is improvisation and modification. In this paper we have implemented our ideas to improve the gutter cleaning system. We belive that our device will come out useful and improve the quality of life.

REFERENCES

[1] P. R. Robinson, “Safety and the Environment,” in Springer Handbook of Petroleum Technology, Springer, 2017, pp. 85–147

[2] P. D. Chaudhuri and G. S. Gajare, "Design and Fabrication of Semi-Automated Drainage Cleaning System," International Journal of Engineering Research & Technology (IJERT), vol. 9, no. 2278-0181, April-2020.

[3] B. &. R. P. Bhaskaran, "DESIGN AND DEVELOPMENT AUTOMATIC SEWAGE CLEANING MACHINE," Huazhong Keji Daxue Xuebao (Ziran Kexue Ban)/Journal of Huazhong University of Science and Technology (Natural Science Edition), vol. 50, pp. 1-7, 2021.

[4] M. Halingali, M. Hosamani and M. Magdum, "AUTOMATED GUTTER CLEANING SYSTEM UNDER SWACHH," SHAIKH COLLEGE OF ENGINEERING AND TECHNOLOGY, India, 2018-2019.

[5] D. K. K. et.al., "“Automatic Sewage Cleaning Equipment”," in International Conference on Explorations and Innovations in Engineering and Technology, 2016.

[6] Rahman, Md & Islam, Md. Sahidul. (2019). Dhaka WASA: Governance Challenges and Way forward. 10.13140/RG.2.2.11501.95202.

[7] N.Adarsh, “MAPPING TRADE COMPLENTARITY OF INDIA, BANGLADESH, PAKISTAN AND SRI LANKA,” p. 42.

[8] K. T. Ulrich and S. D. Eppinger, *Product design and development*, 5th ed. New York: McGraw-Hill/Irwin, 2012.

[9] S. Nunoo, J. C. Attachie and C. K. Abraham, "Using solar power as an alternative source of electrical energy for street lighting in Ghana," 2010 IEEE Conference on Innovative Technologies for an Efficient and Reliable Electricity Supply, 2010, pp.467-471,doi:10.1109/CITRES.2010.5619814.

[10] Mourtzis, Dimitris. (2019). Simulation in the design and operation of manufacturing systems: state of the art and new trends. International Journal of Production Research. 58. 1-23. 10.1080/00207543.2019.1636321.

Paper ID: 4664
International Conference on Mechanical, Manufacturing and Process Engineering (ICMMPE – 2022)
Organizer: Faculty of Mechanical Engineering, Dhaka University of Engineering & Technology (DUET), Gazipur, Bangladesh
Website: https://icmmpeduet.com/

Numerical Simulation of Aerodynamic Performance of Biconvex Supersonic Airfoil

Md. Ashraful Islam[1*], Md. Zulkarna-En [2], Md. Abdul Hasib[3] and A.N.M. Mominul Islam Mukut[4]

[1, 2, 3] Department of Mechanical Engineering, Khulna University of Engineering & Technology, Khulna-9203, Bangladesh
[4]Department of Mechanical Engineering, Dhaka University of Engineering & Technology, Gazipur 1707, Bangladesh

E-mail: md.islam@me.kuet.ac.bd

ABSTRACT

A study of supersonic flow and the flow field around a biconvex airfoil has been evaluated in this work. The study includes aerodynamic characteristics such as lift, drag and pressure coefficient of the airfoil. The analysis was based on RANS numerical method, including an SST k-w viscous interaction. A series of simulations were carried out for Mach number ranging from 1.2 to 3.5, with the variation of the angle of attack (α) ranging from 0° to 20°. It is observed from this study that lift and drag coefficients both increase with angle of attack for a fixed Mach number and decreases with Mach number for a fixed angle of attack. The studied biconvex airfoil generates about 1% more lift at a higher Mach number. However, airfoil generates less drag compared to other supersonic airfoils.

Keywords: SST k-ω viscous modelling; Supersonic aerodynamics; Biconvex airfoil; Angle of attack; Mach number

1. INTRODUCTION

Pressure and shear stress are distributed across the airfoil when air flows around an airfoil. Lift and drag forces are created as a result of the resulting aerodynamic force. The component of aerodynamic force perpendicular to the relative wind is defined as "lift". "Drag" is defined as the component of aerodynamic force that is proportional to the relative wind speed. When there is a pressure difference between an airfoil's top and bottom surfaces, a lift is created. When an airfoil flows through a viscous fluid, it enters a flow regime known as the boundary layer, which forms a low-thickness, large velocity gradient around it. The interaction and contact of a solid body with a fluid produces drag, which is a mechanical force. When fluid flows over an airfoil, an airfoil drag is formed, owing to the component of pressure distribution around the airfoil in the flow direction and the presence of skin friction between the airfoil surface and the fluid. There is an extra drag component for supersonic airfoils known as "wave drag," which is caused by the development of various shock waves.

In supersonic flow past an airfoil, the total drag is the sum of pressure drag (also known as form drag), skin friction drag, and wave drag. The linearized theory (Ackeret's theory), higher-order theory (Busemann's theory), and shock expansion theory can be used to realize aerodynamic characteristics around a 2D thin airfoil in inviscid supersonic flows. A linearized perturbation potential equation is used in linearised theory, which forms a classical wave equation after some modifications $\lambda^2 \phi_{xx} - \phi_{yy} = 0$. According to this equation, the emergence of several waves characterizes supersonic flow fields. Second-order: Busemann's theory is similar to the linearized theory, but it takes into account the linearized theory's second term by extending it using Taylor's expansion. As a result, compared to linearized theory, it delivers more accurate pressure coefficient results. In actuality, supersonic flow through bodies necessitates the formation of compression and expansion changes to achieve flow rotation. The preceding two theories assumed that the compression and expansion changes in flow direction are modest enough that the inviscid flow is isentropic, with all waves being Mach waves. Lift, drag, and other factors can be computed by examining shock and expansion waves.

Supersonic flow over aerospace structures has a wide variety of applications in aeronautics. Biconvex airfoils are extensively employed in aerospace engineering, and researchers have done many works. The Supersonic aircraft uses biconvex wedge airfoils, but any analysis data for these two airfoils are not available easily [1]. Such bodies in the supersonic flow field create singularities in the flow, such as shock and expansion waves. The effect of these singularities when such airfoils are used in supersonic flight increases the undesirable drag. This additional component of drag other than form and skin drag is often referred to as wave drag, and it is found that this component of drag can be minimized if the shock is kept attached to the body in flight. This can be achieved by designing a thinner cross-section with sharp leading and trailing edges, unlike subsonic airfoils whose rounded leading edge produces a

detached shock [2], which causes greater drag than the attached shock. It is essential to know aerodynamic parameters to design wings.

The aerodynamic characteristic of biconvex airfoils can be analyzed using many ways; however, they are mainly classified into two types, (a) high-fidelity and (b) low-fidelity techniques. The first includes experimental measurements and numerical simulations, and the second includes the shock-expansion theory and the linearized theory [3]. The CFD method can be very helpful in analyzing and obtaining the results of the aerodynamic characteristics of a supersonic airfoil. The CFD package mainly works as Pre-processor, solver, and post-Pro-processor. In pre-processor geometry and meshing are included. In solver, solver solves the problem numerically using boundary conditions and various turbulence modelling. In the post-processor, the analysis of the results is done.

A biconvex airfoil with a slightly curved leading edge was studied by S. S. Benadict Bensiger and N. Prasanth [4]. They used asymmetric airfoil with a 6% thickness. They used Gambit software to design and mesh the airfoil and Ansys Fluent software to simulate it. Md. Abdul Hamid et al. [5] examined compressible flow characteristics around a biconvex arc airfoil in a channel. They did numerical computation for a 12 percent thick biconvex circular arc airfoil in a two-dimensional channel. They applied Reynolds averaged Navier-Stokes equations with two-equation k-ω shear stress transfer (SST) turbulence models for numerical study. Efe Kinaci [6] investigated supersonic flow over a double circular airfoil with varying radius. He created the airfoil in Gridgen V15, a mesh generation program, and simulated it in Star-CCM+. He demonstrated the location and magnitude of leading and trailing edge shocks. He also computed the lift and drag coefficients. Tejas Shivaji Tharkude and Dr. Zheng (Jeremy) Li RRR investigated Supersonic Natural Laminar Flow on a Biconvex Airfoil Wing. They studied the behavior of a thin airfoil at supersonic speeds using Supersonic Natural Laminar Flow, and the thin airfoil was used to design wings for a Supersonic Business Jet (SBJ). They concluded that, as a result of the iterative nature of flow simulation, the lift and drag coefficients and forces based on analytical and numerical calculations are nearly identical and satisfactory. In the present work, an attempt is made to analyze the aerodynamic characteristics at high Mach number and compressible flow of 2D biconvex aerofoils with varying the angle of attack.

2. METHODOLOGY

2.1 Airfoil

The geometry of the airfoil is generated using Space Claim (Shown in Fig. 1). Where, M∞ represents the Free Stream Mach Number, α is the Angle of Attack, C is the chord length, which is set equal to 1 meter, and δ is the half wedge angle, which is set equal to 5° and t represents the maximum thickness. The upper and lower surface of the biconvex airfoil is generated using two sets of equations, $\frac{y_u}{c} = 0.1\frac{x}{c}(1-\frac{x}{c})$ and $\frac{y_l}{c} = -0.1\frac{x}{c}(1-\frac{x}{c})$, respectively, Where C is 1 meter, which gives a unit chord 5% thick biconvex airfoil (Shown in Fig.1).

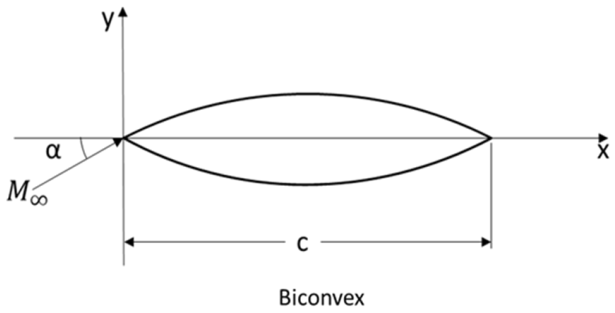

Fig. 1: Schematic of a biconvex supersonic airfoil

2.2 Computational Method

ANSYS Fluent software was used to run the simulations. The simulations were carried out with varying the angle of attack. As the flow is compressible, i.e., density is not constant, so density-based solver was selected. The energy equation was turned on. The fluid flow over the airfoil is also turbulent, so the RANS (Reynolds Average Navier-Stokes) equation was solved. The Reynolds Average Navier-Stokes (RANS) is a time-averaged equation and can be expressed as:

$$\frac{\partial(\rho u_i)}{\partial x_i} = 0 \qquad (1)$$

$$\frac{\partial(\rho u_i u_j)}{\partial x_i} = \frac{\partial p}{\partial x_i} + \frac{\partial}{\partial x_i}\left[\mu\left(\frac{\partial u_i}{\partial x_i} + \frac{\partial u_j}{\partial x_i} - \frac{2}{3}\delta_{ij}\frac{\partial u_l}{\partial x_l}\right)\right] + \frac{\partial}{\partial x_i}\left(-\rho\overline{u'_i u'_j}\right) \qquad (2)$$

here,

u = velocity of the fluid

ρ = density of the fluid

μ = dynamic viscosity of the fluid

The fluid element's mean momentum change to flow instability and convection by the mean flow is defined on the left side of this equation. The Reynolds stress $\left(-\rho\overline{u'_i u'_j}\right)$ regulates this adjustment, which is governed by the mean body force, isotropic stress due to the mean pressure field, viscous stresses, and visible stress due to the fluctuating velocity field. To solve the RANS equations, this nonlinear stress term necessitates additional modelling, which has resulted in a wide range of turbulence models [7].

2.3 Computational Domain and Boundary Conditions

A computation C-type domain was created to run the simulations around the biconvex airfoil. For the airfoil, a

cord length(C) of 1 meter is selected. The domain has been extended by 12.5C on upstream and by 20C downstream from the trailing edge to minimize the boundary effect [8], as shown in Fig. 2. For simulation, the airfoil surface is selected as a no-slip boundary condition. The whole outer domain ABCDEF is selected as a pressure-farfield boundary condition where the velocity was input as Mach number (M). Instead of rotating the airfoils, the angle of attack (α) was changed in the present simulations by changing the direction of flow, which had the same effect on the airfoils. The x and y component of the flow can be calculated by Mcos(α) and Msin(α), respectively, for different angle of attack (α).

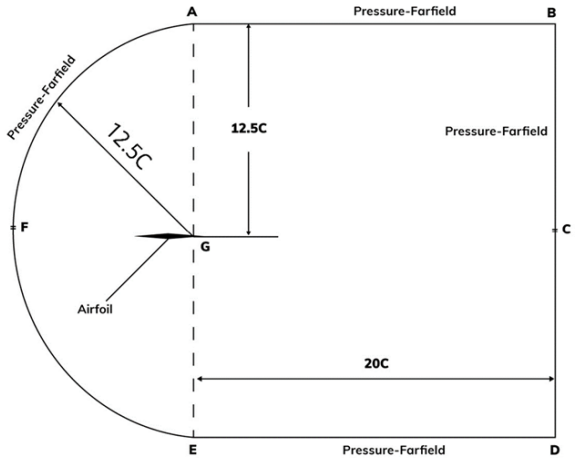

Fig. 2: Computational Domain and Boundary Conditions

2.4 Meshing

The meshing of the Biconvex airfoil was done by the commercial software ANSYS Meshing. The C-type structural mesh was developed to improve wall function and better convergence. The meshing with quadrilateral elements of biconvex airfoils for the whole domain and around the airfoils is shown in Fig. 3. Fig. 4 also shows the mesh sensitivity of the analysis.

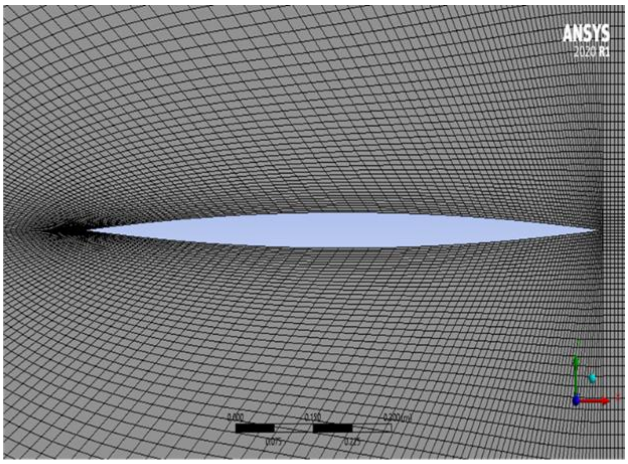

Mesh Around the airfoil

Fig. 3: Mesh of a biconvex airfoil

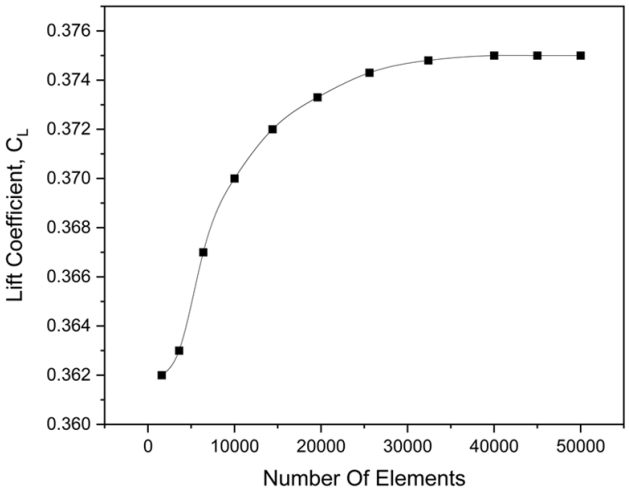

Fig. 4: Variation of Lift Coefficient with Number of Elements Biconvex Airfoil

3. RESULTS AND DISCUSSION

A series of simulations were done for five different Mach numbers (1.4, 2.0, 2.4, 3.0, 3.4) with varying the Angle of Attack (α) ranging from 0° to 20° for both airfoils. For every Mach number and Angle of Attack (α), lift coefficient (C_L), drag coefficient (C_d), pressure distribution over the surface of the airfoils is analyzed numerically. A RANS based solver is used for solving the turbulence model.

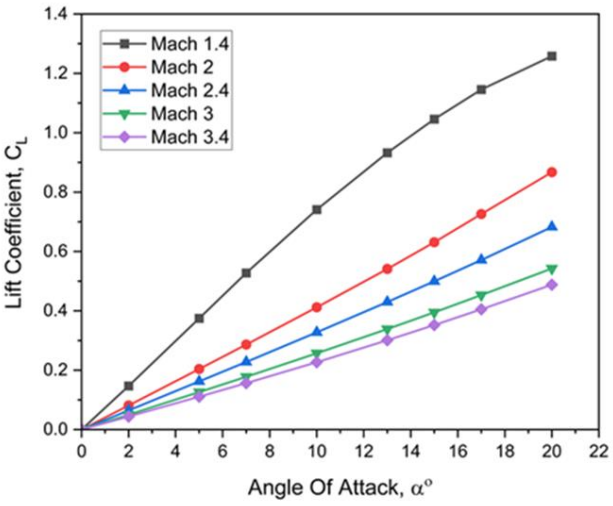

Fig. 5: Lift coefficient Vs Angle of Attack (α) at different Mach numbers of the Biconvex airfoil

The lift coefficient and drag coefficient variations for different angles of attack for five different Mach values are depicted in Fig. 5 and 6, respectively. In supersonic flow over the thin airfoil, the lift coefficient follows the equation $C_L = \frac{4\alpha}{\sqrt{M^2-1}}$, so with increasing the angle of attack (α), the lift coefficient increases for a fixed Mach number. As the

denominator of the aforementioned equation suggests for a fixed angle of attack, increasing the Mach number decreases the lift coefficient; for example, for a fixed 2° angle of attack, C_L = 0.146 at M=1.4 and C_L = .081 at M=2.0 for the biconvex airfoil.

So, for a fixed Mach number, increasing α will increase C_L, which can be observed in Fig. 5, where for every Mach number, the C_L Vs α graphs increase linearly for both airfoils. For Mach 1.4, the lift curve is linear before α = 10° for the biconvex airfoil. After that, with increasing α, a detached bow shock is created in front of the airfoil, reducing the lift.

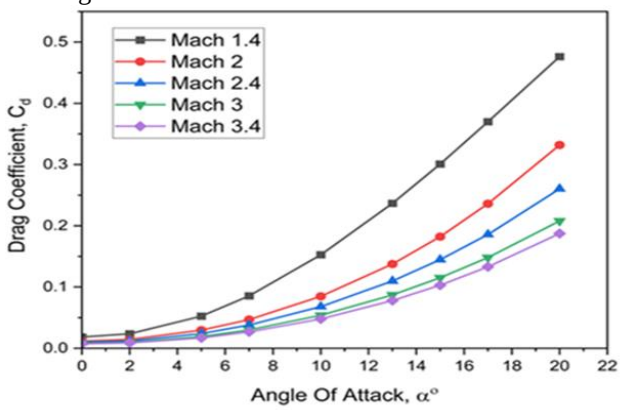

Fig. 6: Drag coefficient Vs Angle of Attack (α) at different Mach Number (a) Biconvex Airfoil

The drag coefficient increases with increasing the angle of attack (α) for a fixed Mach number and decrease with increasing the Mach number for a fixed angle of attack (α). For example, as shown in Fig. 6, for a fixed 2° angle of attack, C_d = 0.024 at M=1.4 and C_d = .014 at M=2.0. Due to the formation of a strong detached bow shock wave in front of the airfoils, as mentioned before, the drag increases significantly just after α=10°. From Fig. 7, the values of C_L/C_d increase with the angle of attack (α). Maximum C_L/C_d is at 3.46°, 3.72°, 3.89°, 3.99°, and 4.05° angle of attack (α) for Mach 1.4, 2.0, 2.4, 3.0, 3.4, respectively for the biconvex airfoil, shown in Fig. 7, (a), and the corresponding values of $(C_L/C_d)_{max}$ are 7.63, 7.18, 6.96, 6.77, 6.66 respectively. As can be observed from these data, the value of $(C_L/C_d)_{max}$ decreases with the increase in Mach number because lift coefficient increases and drag coefficient decreases with Mach number.

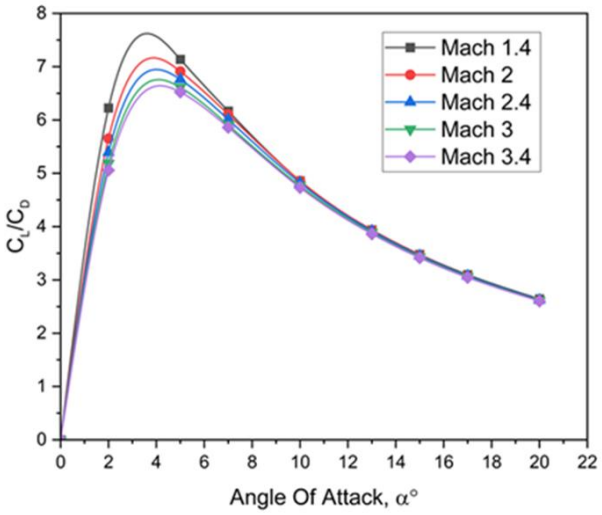

Fig. 7: Changes in lift-to-drag ratio Vs angle of attack (α) at different Mach numbers for Biconvex airfoil

The biconvex airfoil's Mach number and pressure contours are shown in Fig. 8 to Fig. 10. For fixed Mach 1.4, the Mach number contour of the biconvex airfoil is shown for the angle of attack, α= 2°, 5°, 10°, 15°, 20°, and it is observed that an attached oblique shock is created at the leading edge. After that, an expansion wave is created over the whole surface of the airfoil. For α=2° to α=5°, shown in Fig. 8, the leading-edge oblique shock is attached, and the downstream Mach number decreases after that region and increases gradually after the expansion wave till the trailing edge; where again, an oblique shock wave is created, and the Mach number is then decreased to finally the free stream value. At α=10°, it can be observed that the attached oblique shock is started to become a detached shock. At α=15° and α=20°, this detached shock is formed a strong bow shock in front of the leading edge, which reduces the Mach number to a minimum value of 0.02. The maximum value of Mach number 5.14 is observed at α=20° at the airfoil's upper surface, shown in Fig. 8 and Fig. 10, where the downstream flow accelerates after the expansion wave. The Mach number contours are shown in Fig. 9 and Fig. 10 for α=10° and α=15°, respectively. With increasing the Mach number from 1.4 to 3.4, it can be observed that the detached shock is created for Mach 1.4 at α=10° and α=15°, and has become attached at Mach 2.0. Further increasing the Mach number, the shock angle decreases, and at Mach 3.4, the shock is being curved at the lower surface of the airfoil.

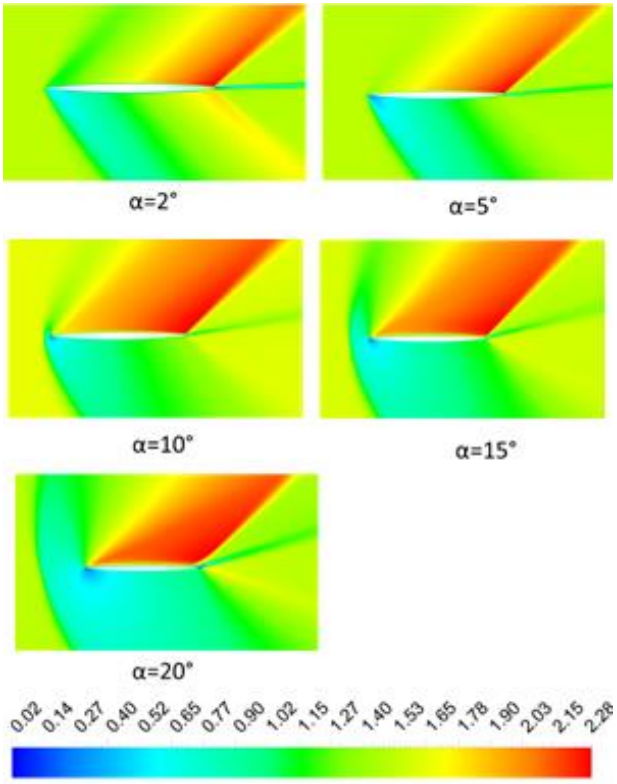

Fig. 8: Mach Number Contour of Mach 1.4 at Different Angle of Attack (α)

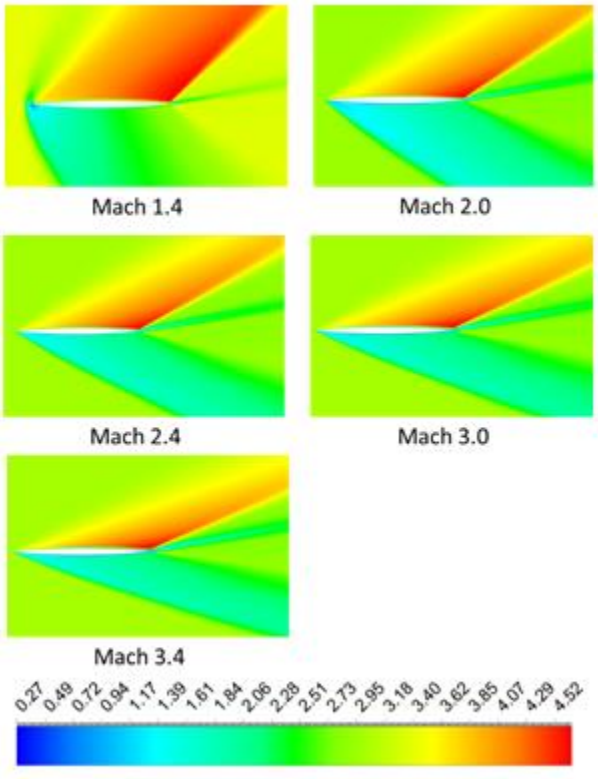

Fig. 9: Mach Number Contour at 10° Angle of Attack (α) at Different Mach Number

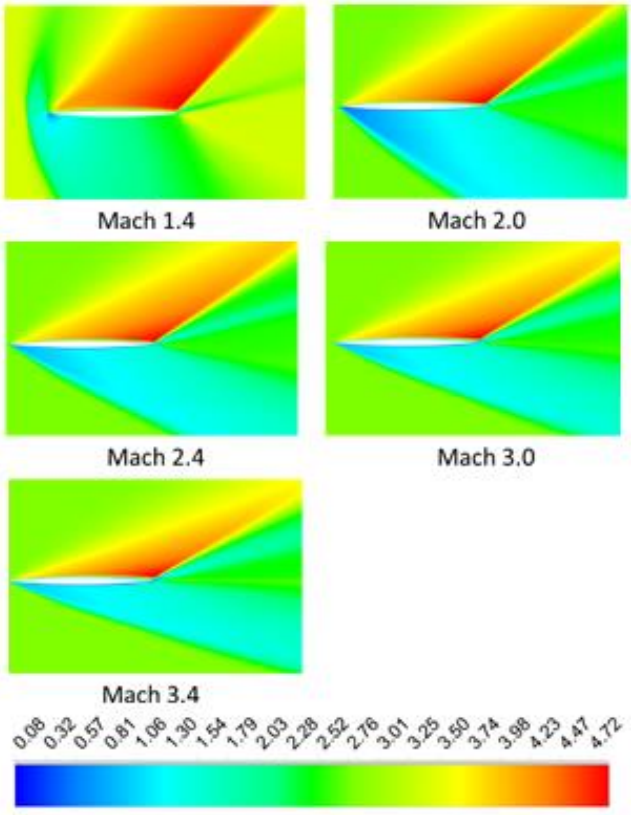

Fig. 10: Mach Number Contour at 15° Angle of Attack (α) at Different Mach Number

4. CONCLUSION

In this present study, a numerical simulation is performed to analyze the aerodynamic characteristics of the biconvex airfoil. The simulation is performed using ANSYS software. RANS based solver is used, and the SST k-ω model is used for viscous modelling. It is observed that at Mach 1.4, a detached bow shock wave is created in front of both airfoils at a higher angle of attack. Also, at higher Mach numbers, the detached shock wave in front of the airfoil becomes attached to the surface for every angle of attack. This simulation is done for the supersonic flow region, which can be expanded to the hypersonic region at higher Mach numbers. The temperature and aeroelastic effects can be further analyzed from this study. A supersonic Biplane with cross-sectional geometry from this study can be studied further, either numerically or experimentally, to compare the performance of this biconvex supersonic airfoil.

REFERENCES

1] D. Z. J. L. Tejas Shivaji Tharkude "Simulation Study of Supersonic Natural Laminar Flow on Wing with Biconvex Airfoil," INTERNATIONAL JOURNAL OF ENGINEERING RESEARCH & TECHNOLOGY (IJERT), vol. 07, no. 03, March 2018 March 2018.

[2] R. Nilifard and H. Ahmadikia, "Supersonic Flow over a Blunt Body using the Direct Simulation Monte Carlo Method and Navier-Stokes Equations," 2010.

[3] M. Y. Ahmed, "Surrogates for the Aerodynamic Coefficients of Supersonic Airfoils," in 53rd AIAA Aerospace Sciences Meeting, 2015, p. 0770.

[4] S. B. Bensiger and N. Prasanth, "Analysis of Bi-Convex Airfoil Using CFD Software at Supersonic and Hypersonic Speed," Elixir International Journal, vol. 53, pp. 11695-11698, 2012.

[5] M. A. Hamid, A. T. Hasan, S. Alimuzzaman, S. Matsuo, and T. Setoguchi, "Compressible flow characteristics around a biconvex arc airfoil in a channel," Propulsion and Power Research, vol. 3, no. 1, pp. 29-40, 2014.

[6] E. Kinaci, Supersonic flow over a double circular airfoil. 2015.

[7] B. E. Launder, "First steps in modelling turbulence and its origins: a commentary on Reynolds On the dynamical theory of incompressible viscous fluids and the determination of the criterion," vol. 373, no. 2039, p. 20140231, 2015.

[8] E. Hosseini, "CFD analysis of the aerodynamic characteristics of biconvex airfoil at compressible and high Mach numbers flow," SN Applied Sciences, vol. 1, no. 10, pp. 1-8, 2019.

Paper ID: 4855

International Conference on Mechanical, Manufacturing and Process Engineering (ICMMPE – 2022)

Organizer: Faculty of Mechanical Engineering, Dhaka University of Engineering & Technology (DUET), Gazipur, Bangladesh

Website: https://icmmpeduet.com/

Fracture Analysis of Adhesively Bonded Joints as a Function of Temperature

Golam Rabbi, Md. Abdul Hasib*, Arup Kumar Debnath, Md. Ashraful Islam

Department of Mechanical Engineering, Khulna University of Engineering & Technology, Khulna – 9203, Bangladesh.

E-mail: ahasib@me.kuet.ac.bd

ABSTRACT

In this study, adhesively bonded joints' fracture parameters have been investigated. Double Cantilever Beam (DCB) and End Notch Flexure (ENF) tests have been simulated using ABAQUS® simulation software to analyze the effect of low temperature on the epoxy adhesive Mode I and Mode II fracture toughness respectively. Varying material properties for different low temperatures have been used to simulate the tests at low-temperature conditions. The fracture load has been determined from the P-δ curve at various low temperatures. The stress intensity factor has been evaluated to get the strain energy release rate which has been used to describe the fracture toughness of the adhesive. The result showed that the fracture load and fracture toughness for Mode I slightly increases by the reduction in temperature. Whereas with the reduction of temperature fracture load and toughness for Mode II increases greatly. The fracture load has increased by 12.6% and 65.1% and the fracture toughness has increased by 36.5% and 84.3% with temperature reduced to -80°C from room temperature for Mode I and Mode II respectively.

Keywords: Double cantilever beam; End notch flexure; Stress intensity factor; Fracture toughness.

1. INTRODUCTION

Epoxy adhesives are excessively used in many industries, including aerospace, automotive, telecommunications, shipbuilding, etc. because of their fascinating characteristics. Most of the products from these industries have to perform under various environmental conditions. In aerospace structures, the high flight altitude contributes to a large temperature gradient for structures in addition to traditional mechanical loading. The normal temperature on a commercial aircraft's body is about -60°C, and the equivalent temperature of military aircraft used for flying at even higher altitudes is below -80°C. Spacecrafts and satellite carrier shuttles experience even lower temperatures [1]. Epoxy adhesive joints perform better under fatigue loads, allow different materials to be joined together and pose lower stress concentrations than alternative joining techniques. Accurate damage models must be available for the design of adhesively bonded joints to predict their fracture behavior. Therefore, it is important to have the material's fracture toughness to apply a fracture mechanics approach. The stiffness of the fractures varies with the type of load. The most important factors influencing the strength and rupture properties of the bonded joints across fluctuations in temperature include changes in the adhesive's mechanical properties and the disparity between the joined portion's thermal expansion coefficients [2]. In addition to the traditional mechanical stresses, the temperature-induced gradient stresses should be taken into consideration during the design phase, as the mechanical properties of the adhesives vary with temperature changes, creating a difference in the adhesive structure. One of the basic parameters which should be considered in the design process is the impact of temperature on the strength and fracture toughness of the adhesive joints. Different materials have different thermal expansion coefficients. When the adhesive joint is formed between different materials, due to the adhesive bond's motion constraint, the temperature change will cause thermal stresses in both arms.

Adhesive strength refers to an adhesive's ability to adhere to a surface and bond two surfaces together. Fracture toughness is a quantitative way to describe the resistance of a material to the propagation of cracks. Temperature dependence is usually shown by adhesive strength. Research that provides experimental data on adhesive joints with structural adhesives (especially epoxies) as a factor of temperature usually shows a reduction in toughness with rising and lowering temperatures [3-6]. This is due to the reduced strength of the adhesive at high temperatures, while the high thermal stresses and frailty of the adhesive are the cause of this behaviour at low temperatures [7].

It is also expected that fracture toughness will depend on temperature. Some researchers have experimented with fracture toughness in the tension or shearing of fine adhesive layers in adhesive bonds, but most of these studies are confined to research at room temperature. Melcher and Johnson [8] tested the fracture toughness of an adhesively bonded composite–composite joint in a cryogenic environment in Mode I. They found a significant decrease in the toughness of the fracture as opposed to room temperature (RT) at cryogenic temperature. Banea et al. [9] measured the Mode I fracture toughness of high-temperature RTV silicone adhesive joint throughout a large temperature range (from Room temperature to +260°C) indicating that fracture

toughness and traction separation laws depend on temperature. In an experimental study, Carlberger et al. [10] found that fracture toughness is not significantly affected by temperature, ranging from -40°C to +80°C (Tg of the epoxy adhesive tested in +90°C), and the maximum stress in the peel load decreases in monotony as the temperature rises in this range. Moreover, Cohesive Zone Models (CZM) have recently been used by researchers around the world to model crack initiation and development to predict the fracture behavior of the bonded joints accurately. Blackman et al. [11] used a CZM approach on Tapered Double Cantilever Beam (TDCB) and peel tests under Mode I loading, including two parameters Gc and σ_{max} to investigate the fracture of adhesively bonded joints. They observed that the compliance of the specimen and Gc relied on σ_{max} until a relatively high value. To assess the cohesive features of a ductile adhesive sheet used in a double cantilevered beam (DCB) experiment, Andersson and Stigh [12] used a reverse approach.

The relationship between stress and displacement can be split into three sections. Initially, the stress increases proportionally with the elongation (the adhesive layer's linear elastic behavior), till limit stress is reached. A region of the plateau is then observed which corresponds to the adhesive's plastic behavior. The curve ends with an adjustable parabolic component. Tvergaard and Hutchinson and Yang et al. used a similar constitutive principle on softening. Chai [13] studied the temperature effect on the energy of the fracture in the shear and found that the fracture energy in Mode II decreased in the range of $0.7 < T/Tg < 1.0$. For pure Mode II, only a few informations are available regarding the temperature dependency of fracture toughness. On the other hand, the control of crack duration in Mode II experiments is difficult, as propagation happens rapidly and without a consistent opening. Furthermore, it may be difficult to classify the crack tip due to micro-cracks in the significantly larger fracture phase zone (FPZ) [14]. Therefore, there is increasing interest in comparable or efficient crack methods which consist of using the experimental conformity and a beam theory-based relationship to measure the crack frequency. Banea et al. [7, 9] performed a double cantilever beam (CDM) and end notch flexure (ENF) test for analyzing the temperature dependency of the fracture toughness for Mode I and Mode II respectively. The result of their research exhibits temperature dependency of fracture strain, fracture toughness and fracture strength.

2. NUMERICAL MODELLING

In the FEM kit of ABAQUS®, a numerical study of the DCB joints and the ENF joints for Mode I and Mode II respectively, as a function of temperature was conducted to determine the feasibility of its CZM formulation. The numerical study was conducted using two-dimensional models taking into consideration of geometrical non-linearities for an accurate representation of the deformation behavior of the specimens, especially transverse deflection and arm rotation.

In this work, the Double Cantilever Beam (DCB) and End Notched Flexure (ENF) tests are simulated to establish the temperature effect of a low temperature (+22°C to -80°C) epoxy adhesive (Loctite EA-9466) on the adhesive model fracture toughness for Mode I and Mode II, respectively, using ABAQUS®. Its output i.e., the stress intensity factor was then converted to strain energy release rate. The fracture toughness was defined using the parameter strain energy release rate. The fracture load was determined from the P-δ curve obtained from the simulation.

2.1 Model Creation

The created parts which have been presented on Figure 1, 2 and 3 have been assembled using different constraints. Tie constraints have been used to tie the surfaces of the adhesive to the surface of the adherend surfaces. Interaction properties have been defined as hard contact for the lower surface of the upper arm and the upper surface of the lower arm to define their behavior during an interaction after the adhesive layer has failed.

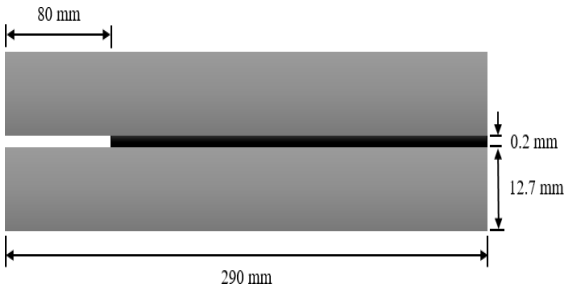

Fig. 1: Geometry for Mode I.

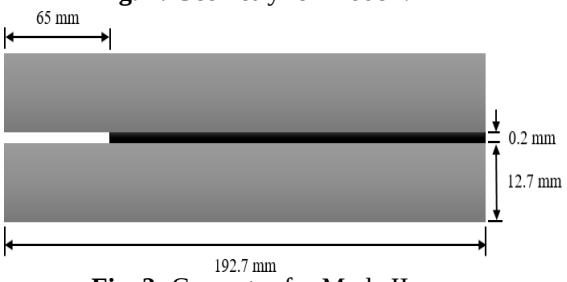

Fig. 2: Geometry for Mode II.

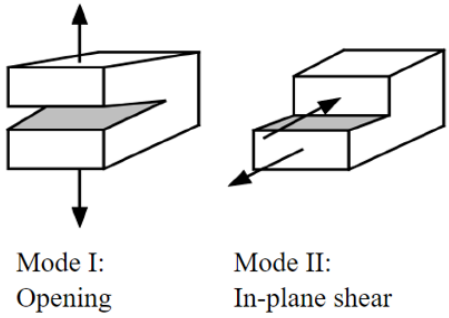

Fig 3: Mode I and II force distribution.

2.2 Material Properties

Banea et al. [7] experimented DCB test with the same material for adherend. The properties used in this work were taken from the mentioned author's research. The properties were provided by the supplier for their research which have been presented in Table 1.

Table 1: Mechanical and physical properties of steel

Tensile failure strength (MPa)	1000-1068
Yield stress (MPa)	861-930
Elongation (%)	14-17
Young's modulus, E (MPa)	205,000

A Rahmani [16] has performed experimental tests to analyze the properties of epoxy adhesive Loctite EA-9466 at varying low temperatures. The properties used in this work were taken from their research and presented in Table 2.

Table 2: Mechanical properties of the Loctite EA-9466

Temperature (°C) / Properties	22	-20	-60	-80
Elasticity Modulus (MPa)	1910	1957	2207	2524
Yield Strength (MPa)	41.33	67.73	79.66	93.87
Tensile Strength (MPa)	44.38	67.73	79.66	93.87
Poisson's Ratio	0.35	0.35	0.35	0.35
Elongation (%)	3.86	3.70	3.36	3.31

2.3 Boundary condition

From figure 4 for Mode I i.e., opening, as DCB specimen is used, the lower arm of the joint has been kept fixed. Two sets of boundary conditions are possible for keeping the arm fixed. One is to make the lower surface of the arm encastre i.e., fixed and the other is to make the right surface and lower left point of the lower arm encastre. In this work, the second method was used. Displacement was applied to the upper arm at the top left corner. For Mode II i.e., in-plane shear, as

Fig. 4: Boundary conditions for Mode I.

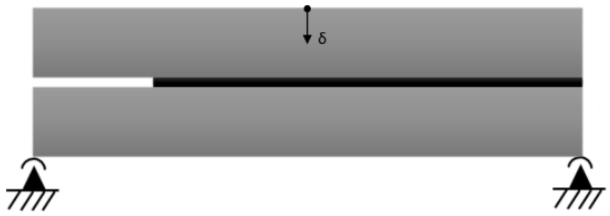

Fig. 5: Boundary conditions for Mode II.

ENF specimen is used the lower arm is given pinned boundary condition at the two ends of the lower surface. The load is applied downward at the midpoint of the upper arm's upper surface which has been showed in figure 5. For being Pinned the lower surface does not react in the *x*-direction. It's free to rotate about the *z*-axis.

2.4 Mesh Sensitivity

The mess sensitivity should be validated to ensure that the obtained result does not vary with the number of elements in the mesh.

The test arms were designed with plane strain 8- node quadrilateral solid finite elements (ABAQUS® CPE8) and the epoxy adhesive was modeled with cohesive 6- node elements, including the CZM bilinear mixed mode, consistent with the quadrilateral 8-node elements. For each neck, twelve solid finite elements have been used along the direction of thickness, with a finer mesh near the adhesive area [16,17]. The meshes were developed utilizing the automated meshing facilities of ABAQUS®, using a manual seeding method that involved biasing effects from the loading points to the crack tip in the horizontal direction, where strong stress gradients are necessary. A more precise mesh was used in the crack tip. From figure 6 it is visible that the value of GC stays the same for element sizes 27967 and 34164. Therefore, using 27967 elements reduce calculation and save time.

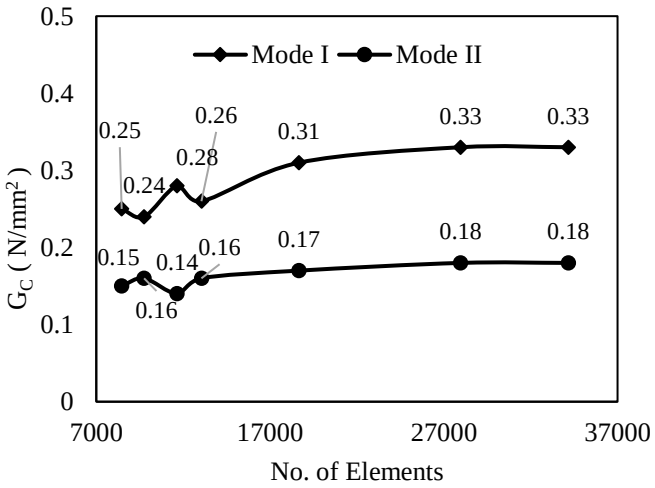

Fig. 6: Verifying mesh dependency.

3. RESULT AND DISCUSSION

3.1 Validation

In order to employ the present technique for further analysis, it is necessary to correlate the obtained results with published data. To validate the present model, the specimen was equipped and material properties are considered as same as of reference as A. Rahmani [16], F. Moroni and A. Pirondi [17]. Table 3 illustrates a comparative analysis of the strain energy release rate, i.e. the fracture toughness of the adhesive at room temperature by the present analysis and that of taking from literature. Values from different research shows that, G_{IC} is 0.31 J/mm^2 and 0.34 J/mm^2 whereas the obtained value of this study is about 0.33 J/mm^2 and the value of G_{IIC} is about 0.15 J/mm^2 whereas the obtained results of this study is 0.18 J/mm^2. So, it is observed that the present study maintains a very good agreement with the results from the literature.

Table 3: Validation of present work with previous work from literature.

Adherend-Adhesive	G_{IC} (J/mm^2)	G_{IIC} (J/mm^2)
Al-EA 9466 [16]	0.31	0.15
Al-EA 9466 [17]	0.34	-
St-EA 9466 [Present study]	0.33	0.18

3.2 P-δ Curve

Figure 7 displays the P-δ curve for Mode I at varying temperatures. The fracture load for Mode I respectively at 22°C, -20°C, -60°C, -80°C is 1.95 kN, 1.88 kN, 2.22 kN, 2.23 kN and the maximum displacement at fracture load is 0.5 mm, 0.32 mm, 0.25 mm, 0.25 mm. Figure 8 displays the P-δ curve for Mode II at different temperatures. The fracture load for Mode II respectively at 22°C, -20°C, -60°C, -80°C is 2.73 kN, 4.12 kN, 5.52 kN, 7.83 kN and the maximum displacement at fracture load is 2.05 mm, 2.07 mm, 2.07 mm, 2.16 mm. Figure 8 displays the P-δ curve for Mode II at different temperatures. The fracture load for Mode II respectively at 22°C, -20°C, -60°C, -80°C is 2.73 kN, 4.12 kN, 5.52 kN, 7.83 kN and the maximum displacement at fracture load is 2.05 mm, 2.07 mm, 2.07 mm, 2.16 mm.

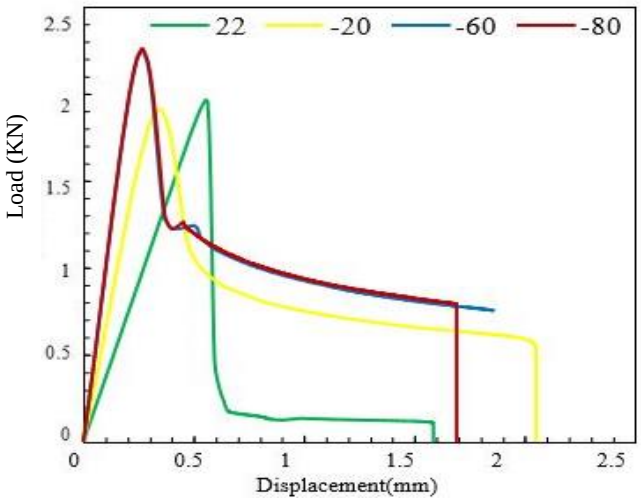

Fig. 7: P-δ curve for Mode I.

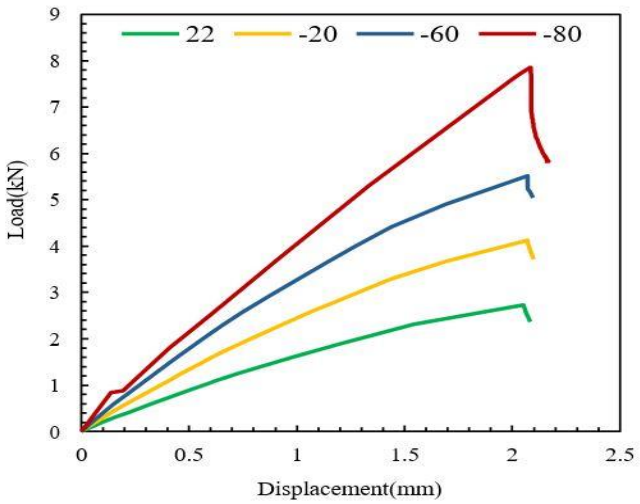

Fig. 8: P-δ curve for Mode II.

In the case of Mode I, the fracture load, displacement at the fracture point, and area under the curve have shown great change with reduced temperature. On the other hand, in the case of Mode II, fracture load, displacement at the fracture point, and the area under the curve show an increasing tendency with reduced temperature. These findings are concurrent with Cantwell [18] and Scott [19]. They also observed an increase in fracture loads with decreased temperature for polymer and epoxy adhesive. This is due to the added shear fracture loads. Displacement relates to molecular relaxation at low temperatures.

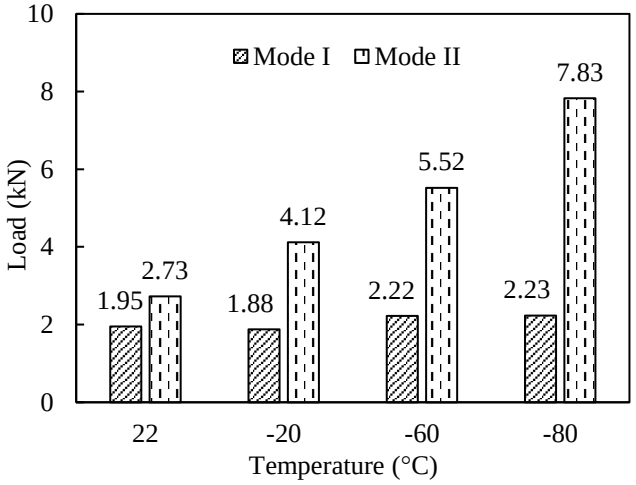

Fig. 9: Fracture loads at different temperatures for both Mode I and Mode II.

3.2 Fracture Load

Figure 9 describes the fracture loads of Mode I and Mode II at different temperatures. From the chart, it is clear that for Mode I, fracture load shows very little deviation with the decrease in temperature. On the contrary, for Mode II, fracture load increases with decreased temperature. By lowering the temperature from 22°C to -80°C, fracture load increased 12.6% and 65.1% for Mode I and Mode II respectively.

3.3 Fracture Toughness

Figure 10 shows fracture toughness for Mode I and Mode II at varying low temperatures. From the chart, it can be stated that fracture toughness increases slightly for Mode Iloading conditions but increases drastically with increasing temperature. By decreasing the temperature from 22°C to -80°C, fracture toughness increased 36.5% and 84.3% for Mode I and Mode II respectively.

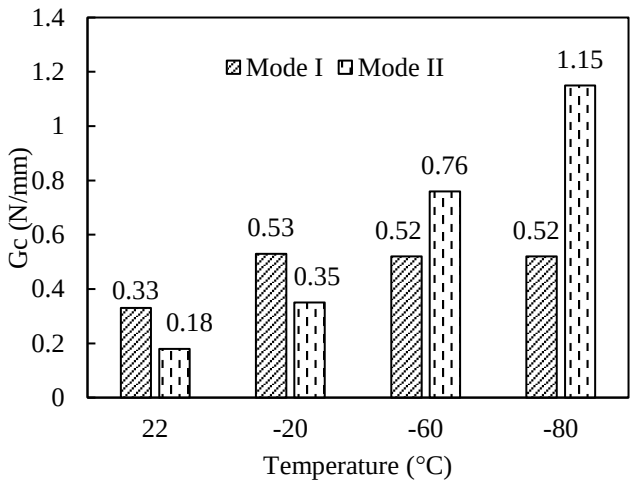

Fig. 10: Fracture toughness at different temperatures for Mode I and Mode II.

4. CONCLUSION

The goal of this research was to analyze how the fracture toughness of an epoxy adhesive Loctite EA- 9466 with steel as an adherend changes with the reduction in temperature in two different modes. DCB test and ENF tests were analyzed to create Mode I and Mode II loading conditions. The results at RT were verified by matching with results from similar works. Fracture load was found from the load-displacement curve. And the J-integral was evaluated to get the stress intensity factor which was converted to energy release rate describing the fracture toughness of the cohesive. The fracture load of the adhesive increased by 12.6% and 65.1% with temperature reduced to -80°C from RT for Mode I and Mode II respectively. The toughness of the adhesive increases by 36.5% and 84.3% by the reduction of temperature from RT to -80°C for Mode I and Mode II respectively. It was also found that the adhesive toughness increasing rate due to temperature fall is greater in pure Mode II than in pure Mode I.

REFERENCES

[1] Campbell FC. Manufacturing Technology for Aerospace Structural Materials. 2nd ed. Printed in Great Britain: Elsevier; ISBN-13: 978-1-85-617495-4, 2006.

[2] Na J, Mu W, Qin G, Tan W, Pu L. Effect of temperature on the mechanical properties of adhesively bonded basalt FRP-aluminum alloy joints in the automotive industry. Int. J. Adhes. 2018; 85: 138–148.

[3] Banea MD, da Silva LFM. The effect of temperature on the mechanical properties of adhesives for the automotive industry. In: Proceedings of the institution of mechanical engineers, Part L. Journal of Materials: Design and Applications, vol. 224, 2010 p. 51–62.

[4] Da Silva LFM, Adams RD. Measurement of the mechanical properties of structural adhesives in tension and shear over a wide range of temperatures. Journal of Adhesion Science and Technology 2005; 19:109–41.

[5] Adams RD, Mallick V. The effect of temperature on the strength of adhesively-bonded composite aluminum joints. Journal of Adhesion 1993; 43:17–33.

[6] Kang S-G, Kim M-G, Kim C-G. Evaluation of cryogenic performance of adhesives using composite-aluminum double-lap joints. Composite Structures 2007; 78:440–6.

[7] Banea, M. D., da Silva, L. F. M., and Campilho, R. D. S. G., Mode I fracture toughness of adhesively bonded joints as a function of temperature. Internet J. Adhesion and Adhesives 2011; 31(5), 273–279.

[8] Melcher RJ, Johnson WS. Mode I fracture toughness of an adhesively bonded composite–composite joint in a cryogenic environment. Composites Science and Technology2007; 67: 501–6.

[9] Banea MD, DaSilva LFM, Campilho RDSG. Temperature dependence of the fracture toughness of adhesively bonded joints. Journal of Adhesion Science and Technology 2010; 24:2 011–26.

[10] Carlberger T, Biel A, Stigh U. Influence of temperature and strain rate on cohesive properties of a structural epoxy adhesive. International Journal of Fracture 2009, 155:155–66.

[11] Blackman BRK, Hadavinia H, Kinloch AJ, Williams JG. The use of a cohesive zone model to study the fracture of fiber composites and adhesively bonded joints. Int. J. Fracture 2003; 119: 25–46.

[12] Andersson T, Stigh U. The stress-elongation relation for an adhesive layer loaded in peel using equilibrium of energetic forces. Int J Solids Struct. 2004; 41: 413-434.

[13] Chai, H., The effects of bond thickness, rate and temperature on the deformation and fracture of structural adhesives under shear loading. Internat. J. Fracture 2004; 130 (1): 497-515.

[14] O'Brien, T. K., Composite Interlaminar Shear Fracture Toughness, GIIc: Shear Measurement or Sheer Myth? ASTM STP 1998; 1330: 3–18.

[15] Blackman, B. R. K., Brunner, A. J., and Williams, Mode II fracture testing of composites: a new look at an old problem. J. G., Eng. Fract Mech 2006; 73 (16): 2443–2455.

[16] Rahmani A, Choupani N. Experimental and Numerical Analysis of Fracture Parameters of Adhesively Bonded Joints at Low Temperature. Engg. Fracture Mech. 2018.

[17] Moroni F, Musiari F, Romoli L and Pirondi A. Influence of laser treatment parameters on the mode I strain energy release rate of aluminum double cantilever beam joints. Int. J. Adhes. Adhes. 2018; 83: 15–23.

[18] Cantwell WJ. The interlaminar fracture behavior of carbon fiber reinforced plastics at low temperatures. Part G: Journal of Aerospace Engineering. 1996; 210: 1-7.

[19] Scott J. M., Wells G. M. and Phillips D. C. Low temperature crack propagation in epoxide resins. J Mater Sci. 1980; 15: 1436-1448.

Paper ID: 4986
International Conference on Mechanical, Manufacturing and Process Engineering (ICMMPE – 2022)
Organizer: Faculty of Mechanical Engineering, Dhaka University of Engineering & Technology (DUET), Gazipur, Bangladesh
Website: https://icmmpeduet.com/

Prioritizing Fire Risk Criteria in Ready-Made Garments Factories of Bangladesh by Applying CRITIC Method

Md. Tanvir Siraj[1], Md. Mehedi Hasan[2], Md. Saiful Islam[3], Asif Kabir[4], M. Mahbubur Rahman[5], S.M. Faysal Ahmed[6]

[1]Department of Industrial and Production Engineering, BUET, Dhaka-1000, Bangladesh
[2]Department of Electrical and Electronic Engineering, KUET, Khulna-9203, Bangladesh
[3,4,6]Department of Mechanical Engineering, BUET, Dhaka-1000, Bangladesh
[5]Department of Mechanical Engineering, DUET, Gazipur-1707, Bangladesh

E-mail: tanvir25392@gmail.com

ABSTRACT

The ready-made garments (RMG) industry of Bangladesh is one of the renowned export-oriented garment industries in the world. Several hazardous fire incidents at RMG factories in recent decades became a matter of concern for the national and international policymakers as well as stakeholders. Therefore, this study has been conducted to determine a prioritizing order of the fire risk factors of the RMG industry to assist decision-makers while implementing mitigation strategies. For this study, fire risk factors have been clustered into six criteria- causative factors, fire separation, egress obstruction, fire detection, fire protection, and egress lighting. Then the fire safety inspection reports of randomly selected 50 RMG factories have been analyzed with a Multi-Criteria Decision-making (MCDM) approach, the Criteria Importance Through Inter-Criteria Correlation (CRITIC) method, to determine the objective weights of the selected criteria. The number of risk factors observed in each criterion during fire safety inspections at the RMG factories has been considered as the numerical input for the CRITIC method. Prioritization has been obtained with the descending order of the computed weights for the risk criteria. This study finds that 'egress obstruction', 'causative factors', and 'fire separation' are the most three weighted risk criteria by applying the CRITIC method. This prioritization will be helpful for decision-makers when the hierarchical implementation of mitigation actions is necessary due to various managerial constraints. The result of this study is expected to aid the managers of RMG factories to be more specific and accurate in case of deciding in a challenging situation.

Keywords: Ready-Made Garment; Fire Risk Criteria; Multi Criteria Decision Making; Criteria Importance Through Inter-Criteria Correlation

1. INTRODUCTION

Bangladesh is one of the largest RMG manufacturing nations in the world exporting products to more than 150 countries [1]. There are around 4500 factories, and over 4 million people are working in the RMG sector [2], [3]. Ensuring a safe and sustainable workplace for such a huge industrial workforce is always a challenging issue for policymakers. In the last few decades, industrial fire-related hazardous incidents in RMG factories are the deadliest barriers to overcome by the managers of this sector [4]. The fire in Tazreen Fashion in 2012, which caused more than 100 deaths and 300 injuries, bring attention to the national and international community to find a sustainable solution against fire hazards [5]. In such a reality, the 'Accord' (Accord on fire and building safety in Bangladesh) was formed in 2013 as a safety monitoring organization for more than 1700 RMG factories and the fire safety scenario started to improve gradually [5], [6]. But there are a lot of scopes to improve yet in the remaining factories which are not under continuous monitoring by any regulatory authority. Fire safety inspections conducted with proper standardized structure at RMG factories can minimize the damage due to fire hazards [5], [6]. In this regard, analyzing the findings from the conducted fire safety inspections by the Accord can be insightful for the overall industry.

There are several studies on fire hazard issues in the RMG sector in recent literature. For instance, multiple works have been conducted to depict fire propagation characteristics, non-standard practices at factories, egress layout planning, evacuation scenarios, and so on [7], [8], [9]. Among those, Khan et al. [7] determined the negative effects of unsafe practices like egress obstruction, narrow escape, disturbance at fire door, etc. on the safe evacuation of the occupants during a fire incident; Nilufar and Choiti [8] tried to show a correlation between the spatial layout of the egress path and occupant's movement behavior in time of the fire; Khandoker et al. [9] depicted the fire propagation pattern in a multistoried RMG factory building and its impact on the evacuation. Those works were conducted with computer-based simulation with numerical input for different risk factors as variables. They suggested mitigating unsafe

practices and creating a safe evacuation environment during fire incidents. However, they did not attempt to prioritize the fire risk criteria to be mitigated one after another based on their priority.

Risky RMG factories have been sorted out by fire risk indexing (FRI) in some papers [10], [11]. For example, Islam and Roman [10] as well as Wadud and Huda [11] both divided the fire risk factors into two parameters- hard and soft. Hard parameters are for structural risk factors and soft parameters are for managerial risk factors. They tried to sort out the most vulnerable RMG factories based on the calculated FRI considering the hard and soft parameters of those factories. Barua et al. [12] showed a comparison between the existing and the standard fire evacuation practices in the RMG factories in a descriptive manner. Haque et al. [13] utilized the empirical statistical method to predict the number of burn incidents due to fire hazards from electrical faults. They took some electrical risk factors which are related to fire incidents as the computation variables. Some other recent works also focused on fire safety in the RMG sector. Those works discussed various aspects of fire risk factors, inspection regulation for fire safety, historical data on fire incidents, cause-effect analysis, and comparative analysis [4], [5], [14], [15], etc. However, no study has prioritized the fire risk criteria of the RMG sector to aid the industrial managers which can be identified as a research gap to be explored.

Besides those studies on the RMG sector, some other recent studies on urban and industrial fire risk factors can be mentioned here. For instance, Alkış et al. [16] determined a ranking of the surrounding structures based on their vulnerability during an industrial fire. For this, they utilized an MCDM technique, the Analytical Hierarchy Process (AHP). Dârmon [17] calculated the probability of various risky incidents related to fire hazards and predicted the consequences for industrial buildings. Omidvari et al. [18] determined the riskiest zone of a hospital during a fire incident. For this, they applied a combination of the failure mode effect analysis (FMEA) and MCDM techniques. Yilmaz et al. [19] analyzed the fire risk domains of the industrial area by applying an MCDM technique, the Fuzzy AHP. However, prioritizing the fire risk criteria by applying any of the objective criteria weighting methods for any industrial sector was not intended by the existing works in the literature. Therefore, this work is going to determine the prioritization of the fire risk criteria by applying an MCDM technique, the CRITIC method.

The CRITIC method is a popular MCDM method to find the objective weights of the criteria in such an environment where decision-makers are not confident to evaluate the criteria with their subjective judgment and there is a sufficient amount of numerical data of the alternatives for weighting the criteria [20] [21]. The CRITIC method deals with both the standard deviation within a data set and the correlation among the data sets for determining the objective weights of the criteria which makes it more accurate and consistent than other objective weighting methods [22], [23], [24]. There are several works in recent literature applying the CRITIC method to determine the objective criteria weights. For instance, by utilizing the CRITIC method, Wu et al. [21] evaluated the operational safety of urban rail transit, and Shi et al. [22] determined the weights for various power quality indicators by analyzing data from the power generation side and user side, Pan et al. [23] proposed a framework for the evaluation of a heavy traffic problem, and so on. However, fire risk criteria weighting based on the observation in fire safety inspections has not utilized the CRITIC method yet. This shows the novelty of this ongoing work.

In this study, fire safety inspection reports from randomly selected 50 RMG factories have been gathered from the website of the Accord at first (https://bangladeshaccord.org/factories). Then, the observed risk factors from the selected reports have been categorized into 6 different criteria with the help of existing literature and the fire safety inspection reports. Later, the number of risk factors in each criterion for the 50 sample factories have been sorted out to be utilized as the numerical input for the CRITIC method. Finally, the CRITIC method has been applied to determine the criteria weights that have been used to present the prioritization.

This study aims to fulfill the following objectives:

a) To categorize the fire risk factors into 6 criteria.
b) To sort out the number of risk factors observed in each of the criteria.
c) To determine the criteria weights by the CRITIC method.
d) To prioritize the fire risk criteria by the obtained weights.

The rest of the paper is arranged as: Section 2 is for describing the methodology and calculations, Section 3 is for discussing the obtained results, and Section 4 is for concluding the paper by discussing the managerial implications of the result and the future study scope briefly.

2. METHODOLOGY AND CALCULATIONS

The designed methodology for this study can be presented with the below explained 5 steps:

Step 1. Accumulate fire safety inspection reports of randomly selected 50 RMG factories from the website of Accord (https://bangladeshaccord.org/factories).

.

Step 2. Identify the fire risk criteria to categorize the fire risk factors.

Step 3. Determine the number of risk factors observed in each of the criteria by analyzing the fire safety inspection reports of the randomly selected 50 RMG factories.

Step 4. Apply the CRITIC method to obtain the objective criteria weights by utilizing the number of risk factors in each of the criteria for numerical computation.

Step 5. Prioritize the fire risk criteria based on their obtained weights.

2.1 Data Collection

Details of the selected fire risk criteria to be prioritized in this study are shown in Table 1.

Table 1: Selected fire risk criteria to categorize the fire risk factors for the RMG industry in Bangladesh

Risk Criteria	Description	Source
Causative Factors (CF)	Risk factors that can be indicated as the cause of the fire are categorized in this criterion. For example, non-standard electrical cable connections; unterminated live wire; congested cables and bus bars in the electrical distribution board; the presence of boiler and other heat sources on the production floor, etc.	[16], [17], [25]
Fire Separation (FS)	Risk factors related to the absence of fire-rated construction are categorized in this criterion. For example, no separation between boiler, generator, and transformer; openly stored combustible materials; Unsealed penetrations in the walls and ceiling; unseparated exit stairs with fire-rated walls; non-standard fire doors, etc.	[17], [25]
Egress Obstruction (EO)	Risk factors related to the obstruction of smooth egress are categorized in this criterion. For example, material storage in the egress paths; narrow or lengthy emergency egress paths; non-standard locking features in the egress doors; inadequate egress doors, etc.	[7], [8], [25]
Fire Detection (FD)	Risk factors related to the absence or non-standard feature of the fire/smoke detection system are categorized in this criterion. For example, the absence of an audible fire alarm; the absence of a fire detector in each corner of the floor; irregular inspection, testing, and maintenance (ITM) of the fire detector, etc.	[17], [18], [19]
Fire Protection (FP)	Risk factors related to the absence of non-standard features of the fire protection system are categorized in this criterion. For example, the absence of a sprinkler or standpipe; the capacity of a fire pump is less than the necessity; irregular ITM for the fire protection system, etc.	[25]
Egress Lighting (EL)	Risk factors related to the absence or non-standard feature of the lighting system in egress paths are categorized in this criterion. For example, inadequate lighting in the egress paths; absence of emergency lighting; absence of illuminated exit signs, etc.	[7], [19], [25]

After analyzing fire safety inspection reports generated by the Accord for 50 RMG factories (denoted as F1, F2, F3, …, F50), the number of risk factors in each of the criteria has been noted for further calculation. This can be found in the primary decision matrix shown in Table 2. Those reports have been published by the Accord after completing factory inspections by trained fire safety engineers [6].

2.2 CRITIC Method

For decision-making purposes, the CRITIC method can deal with numerical data or practical observations like simulation values, test results, statistics, various measurement parameters, and so on [20]. This study aims to utilize the number of fire safety inspection findings or fire risk factors in each of the risk categorizing criteria as a numerical input to compute the weights of the risk criteria by the CRITIC method. The details method ([20], [23]) can be found below:

Step 1. Generate the initial decision matrix for 50 RMG factories (See Table 2). The mathematical expression for the initial decision-matrix is as Equation (1)

$$D = \begin{array}{c} \\ F1 \\ F2 \\ \dots \\ \dots \\ Fm \end{array} \begin{array}{c} C1 \quad C2 \quad \dots \quad Cn \\ \begin{bmatrix} d_{11} & d_{12} & \dots & d_{1n} \\ d_{21} & d_{22} & \dots & d_{2n} \\ \dots & \dots & \dots & \dots \\ \dots & \dots & \dots & \dots \\ d_{m1} & d_{m2} & \dots & d_{mn} \end{bmatrix} \end{array} \quad (1)$$

Step 2. Normalize the initial decision-matrix by using Equation (2)

$$r_{ij} = \frac{d_{ij} - \min d_j}{\max d_j - \min d_j} \quad (2)$$

Step 3. Calculate the standard deviation for each of the risk criteria by using Equations (3) and (4)

Table 2: Number of risk factors in each risk criterion for randomly selected 50 RMG factories

	CF	FS	EO	FD	FP	EL
F1	1	1	4	2	2	2
F2	2	3	6	3	5	2
F3	5	4	10	4	5	4
F4	4	2	6	3	4	4
F5	1	1	2	3	1	1
F6	2	1	3	2	1	2
F7	7	4	13	10	6	8
F8	2	1	5	3	2	4
F9	2	1	4	2	2	3
F10	3	1	4	1	1	2
F11	2	2	7	2	3	3
F12	3	2	6	2	3	2
F13	9	6	8	6	8	8
F14	2	2	9	4	3	4
F15	1	0	4	4	1	5
F16	4	3	7	5	4	5
F17	3	1	4	2	2	3
F18	3	2	3	2	2	2
F19	4	1	4	4	2	2
F20	9	5	10	7	5	8
F21	4	2	7	4	2	2
F22	3	1	7	3	3	2
F23	3	1	11	3	2	4
F24	4	2	7	4	2	2
F25	3	4	6	2	5	4
F26	0	1	5	1	0	2
F27	1	1	2	1	3	1
F28	0	2	3	1	1	2
F29	1	3	8	3	2	3
F30	1	5	4	2	5	2
F31	0	3	2	2	4	4
F32	2	1	3	1	2	2
F33	6	2	10	3	4	3
F34	1	2	0	2	2	4
F35	2	2	3	1	2	0
F36	1	2	2	3	3	5
F37	6	4	4	2	5	4
F38	0	1	1	3	1	4
F39	4	1	4	1	2	3
F40	3	3	5	3	3	4
F41	2	3	6	4	4	6
F42	3	3	3	4	3	4
F43	4	4	14	4	5	5
F44	1	1	2	3	0	3
F45	1	2	9	4	1	5
F46	4	1	2	3	2	4
F47	7	5	8	7	7	10
F48	7	1	9	4	2	6
F49	4	2	3	2	3	3
F50	1	1	4	2	1	3

$$\bar{r_{ij}} = \frac{1}{m}\sum_{i=1}^{m} r_{ij} \qquad (3)$$

$$S_j = \sqrt{\frac{\sum_{i=1}^{m}(r_{ij}-\bar{r_{ij}})^2}{m-1}} \qquad (4)$$

Here, m= Number of Alternatives (In this study, 50 factories have been considered, so, m= 50); S_j= Standard Deviation

Step 4. Compute the linear correlation coefficient ($r_{j,j'}$) for each pair of criteria separately to form a symmetric matrix.

Step 5. Compute the conflicting character of the criteria by using Equation (5)

$$R_j = \sum_{j'=1}^{n}(1 - r_{j,j'}) \qquad (5)$$

Here, R_j is the correlation index of the j^{th} criterion and $r_{j,j'}$ is the linear correlation coefficient for j^{th} and j'^{th} criteria. The higher the value of R_j, the lower the conflict of that criterion with other criteria.

Step 6. Calculate the amount of information in each criterion by using Equation (6)

$$C_j = S_j \times R_j \qquad (6)$$

Here, S_j and R_j are obtained by using Equations (4) and (5) respectively.

Step 7. Calculate the weights of the criteria by using Equation (7)

$$W_j = \frac{C_j}{\sum_{j=1}^{n} C_j} \qquad (7)$$

Step 8. The final Prioritization of the criteria is done by descending order of the obtained weights.

2.3 Calculations

The calculated normalized matrix from the initial decision matrix can be found in Table 3. Standard deviation values (S_j) for the criteria have also been calculated.

Table 3: Normalized Decision-Matrix

	CF	FS	EO	FD	FP	EL
F1	0.111	0.167	0.286	0.111	0.250	0.200
F2	0.222	0.500	0.429	0.222	0.625	0.200
F3	0.556	0.667	0.714	0.333	0.625	0.400
F4	0.444	0.333	0.429	0.222	0.500	0.400
F5	0.111	0.167	0.143	0.222	0.125	0.100
---	---	---	---	---	---	---
---	---	---	---	---	---	---
F46	0.444	0.167	0.143	0.222	0.250	0.400
F47	0.778	0.833	0.571	0.667	0.875	1.000
F48	0.778	0.167	0.643	0.333	0.250	0.600
F49	0.444	0.333	0.214	0.111	0.375	0.300
F50	0.111	0.167	0.286	0.111	0.125	0.300
S_j	0.246	0.228	0.223	0.192	0.217	0.196

A symmetric matrix is formed with the linear correlation coefficient values which can be found in Table 4. Calculated R_j, C_j, and W_j Table 4 can be found in Table 5. The final prioritization of the criteria is also presented in Table 5 and Figure 1.

Table 4: Symmetric matrix with linear correlation coefficient values

	CF	FS	EO	FD	FP	EL
CF	1	0.536	0.572	0.640	0.651	0.604
FS	0.536	1	0.439	0.522	0.871	0.569
EO	0.572	0.439	1	0.621	0.486	0.484
FD	0.640	0.522	0.621	1	0.552	0.790
FP	0.651	0.871	0.486	0.552	1	0.605
EL	0.604	0.569	0.484	0.790	0.605	1

Table 5: R_j, C_j, W_j and prioritization of the criteria

	CF	FS	EO	FD	FP	EL	R_j	C_j	W_j	Rank
CF	0	0.464	0.428	0.360	0.349	0.396	1.997	0.491	0.186	**2**
FS	0.464	0	0.561	0.478	0.129	0.431	2.063	0.470	0.178	**3**
EO	0.428	0.561	0	0.379	0.514	0.516	2.397	0.535	0.203	**1**
FD	0.360	0.478	0.379	0	0.448	0.210	1.875	0.361	0.137	**6**
FP	0.349	0.129	0.514	0.448	0	0.395	1.836	0.399	0.151	**4**
EL	0.396	0.431	0.516	0.210	0.395	0	1.949	0.382	0.145	**5**

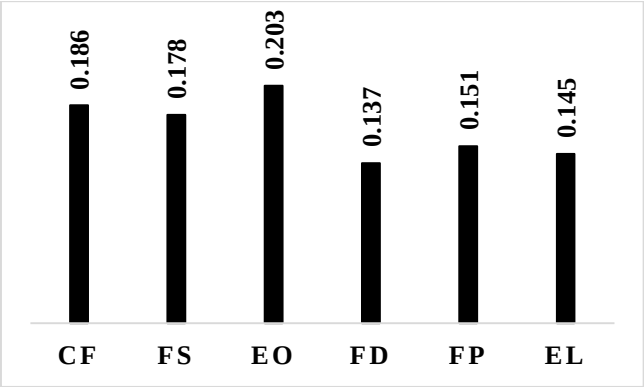

Fig. 1: Weights of the fire risk criteria for prioritization

3. RESULTS AND DISCUSSION

This study finds the weights of the fire risk criteria by the CRITIC method as (see Table 5 and Figure 1) Egress Obstruction (0.203)> Causative Factors (0.186)> Fire Separation (0.178)> Fire Protection (0.151)> Egress Lighting (0.145)> Fire Detection (0.137). The CRITIC method is a measurement considering both the deviation of the objective values for a criterion and the correlation of the objective values among the criteria. Therefore, the obtained weights from this study show, during fire safety inspections at the RMG factories, 'egress obstruction' related risk factors are the most prior observation from the inspectors, and the number of the risk factors for the factories in this risk criterion is comparatively more consistent than other risk criteria. On the other hand, the number of risk factors related to 'fire detection' for the selected factories is comparatively more dispersive in the pattern. Therefore, the weight for this criterion is the minimum.

Earlier studies show that egress obstruction is the main challenge for safe evacuation in the RMG factories [7], [8]. This criterion is directly related to life savings during a fire. Most of the RMG factories are designed with a very congested layout due to various constraints as well as managerial negligence. Thereby messy arrangements of the production floor, material storage, and machinery obstruct the egress paths which can be deadly during a fire evacuation. Moreover, unfeatured egress doors, locked doors, and the inadequacy of doors in comparison to the occupant load are some of the most frequently seen egress obstructions in RMG factories. The obtained result from this study prioritizes the egress obstruction-related risk factors most. That means while thinking of fire risk mitigation strategies, managers need to focus on removing all types of obstructions from the egress paths at first.

After assuring unobstructed egress, 'causative factors' for fire come next in the obtained result as the prioritized risk criteria. Fire from electrical faults like short circuits, or sparks has been identified as the most observed causative factor behind the major fire incidents in RMG factories [13]. Besides this, unprotected heat-producing instruments like boilers, generators, and transformers were also the reason for fire hazards [4], [26]. Fire incidents can be minimized by mitigating the causative factors following proper standards, thereby the result of this study, obtained from the fire safety inspection report analysis, emphasizes this criterion comparatively higher than the remaining criteria.

Fire separation helps to obstruct the propagation of fire which is the third prioritized risk criterion achieved in this study. Managers of the RMG factories often neglect the fundamental requirements of the fire separation because of their lack of awareness. The source of fire or the already affected area must be separated from the unaffected places to obstruct fire propagation [9]. Fire separation can be assured by various fire-rated construction like the fire-rated wall, fire doors, sealed penetration, etc.

After the top prioritized three fire risk criteria, mitigating the remaining three criteria- fire protection, egress lighting, and fire detection is part of maintaining the sustainability of the established fire safety practices in an RMG factory. The analyzed fire risk criteria in this study were also discussed and emphasized in many of the previous research works, which justifies the relevance of this work. So, managers may decide on the fire risk mitigation action plan focusing on the prioritized position of the risk criteria.

4. CONCLUSION

A novel approach to applying the CRITIC method has been depicted in this study. Generally, fire safety inspections are conducted in RMG factories by trained fire safety engineers of the Accord. Though their findings of the risk factors are structured, several human factors can affect the inspection reports. This study has considered fire safety inspection reports from 50 randomly selected RMG factories. The number of risk factors in each criterion for the selected factories has been taken as numerical input of the CRITIC method. Therefore, objective weights of the risk criteria obtained in this study are influenced by the subjective judgment of the fire safety inspectors.

In a developing country like Bangladesh, limited resources and managerial constraints always dominate the decision-making procedure of the industries. Mitigating all the risk factors at a time seems very impractical in this situation. The interesting finding from this study is to achieve a pattern for fire risk mitigation. First, make a safe evacuation environment; then, ensure removal of fire causative factors; next, install a fire separation structure; finally, ensure the sustainability of the established fire safety culture. The obtained result from this study can aid

managers to find a hierarchical mitigation strategy.

The size of a dataset is influential on the result obtained in the CRITIC method. In the future, various statistical sampling methods can be utilized to obtain an optimum dataset size and the fire safety inspection reports from more factories can be analyzed to compare the consistency of the result. Further, experts' opinion-based MCDM techniques can be applied to get an extensive overview of this study. Determining the influence of one risk criterion over another can also be considered an upcoming study scope.

REFERENCES

[1] BGMEA., BGMEA | About Garment Industry of Bangladesh. Retrieved from https://www.bgmea.com.bd/page/AboutGarmentsIndustry, 2021.

[2] Statista., Number of garment factories Bangladesh 2010-2019. Retrieved from https://www.statista.com/statistics/987697/bangladesh-number-garment-factories/, 2021.

[3] Fathi, N., Safety First: Bangladesh Garment Industry Rebounds. Retrieved from https://www.ifc.org/wps/wcm/connect/news_ext_content/ifc_external_corporate_site/news+and+events/news/insights/bangladesh-garment-industry, 2021.

[4] Hasan, M. M., Mahmud, A., and Islam, M. S., Deadly incidents in Bangladeshi apparel industry and illustrating the causes and effects of these incidents. Journal of Finance and Accounting, 5 (5), 193–199, 2017.

[5] Wiersma, J., Fire safety in the ready-made garment industry in Bangladesh, five years after Rana Plaza. Safety in Garment Industry, 16, 2018.

[6] Accord., The Bangladesh Accord on Fire and Building Safety. Retrieved from https://bangladeshaccord.org/factories, 2021.

[7] Khan, R. M., Bhuiyan, S. A. M., Haque, F. M., Wasi, M., and Rahman, M. A., Effects of unsafe workplace practices on the fire safety performance of ready-made garments (RMG) buildings. Safety Science, 144, 105470, 2021.

[8] Nilufar, F., and Choiti, S. S., Morphological properties of the spatial layout of factories–a key determinant in setting the emergency escape routes for evacuation. Proceedings of the 12th Space Syntax Symposium, 2019.

[9] Khandoker, M. A. R., Mou, R. J., Muntaha, M. A., and Rahman, M. A., Numerical simulation of fire in a multistoried ready-made garments factory using Pyrosim. In AIP conference proceedings (Vol. 1980, p. 050026), 2018.

[10] Islam, S., and Roman, R. I., Assessment of fire hazard on the readymade garment industry in Chittagong city, Bangladesh: A geo-spatial analysis of CEPZ and Baizid industrial hub. Indonesian Journal of Environmental Management and Sustainability, 3 (1), 20–28, 2019.

[11] Wadud, Z., and Huda, F. Y., Fire safety in the readymade garment sector in Bangladesh: Structural inadequacy versus management deficiency. Fire Technology, 53 (2), 793–814, 2017.

[12] Barua, U., Wiersma, J., Billah, M., and Ansary, M. A., Fire evacuation safety in Bangladesh readymade garment (RMG) factories: A comparison of standards and non-compliance issues of means of escape. Proceedings, Safety in The Garment Industry, Five Years After Rana Plaza, 78–88., 2018.

[13] Haque, F., Marma, H.-U.-M., and Chowdhury, A., Prediction of burn incidents due to faulty installations in RMG factories in Bangladesh. In 2017 international conference on electrical, computer and communication engineering (ecce) (pp. 733–737), 2017.

[14] James, P., Miles, L., Croucher, R., and Houssart, M., Regulating factory safety in the Bangladeshi garment industry. Regulation and Governance, 13 (3), 431–444, 2019.

[15] Moazzem, K. G., Halim, S. F. B., and Shafayat, M., Can a sustainable inspection system be developed? the case of RMG sector in Bangladesh. Centre for Policy Dialogue, 2018.

[16] Alkış, S., Aksoy, E., and Akpınar, K., Risk assessment of industrial fires for surrounding vulnerable facilities using a multi-criteria decision support approach and GIS. Fire, 4 (3), 53., 2021.

[17] Dârmon, R., Probabilistic methods to assess the fire risk of an industrial building. Procedia Manufacturing, 46, 543–548., 2020.

[18] Omidvari, F., Jahangiri, M., Mehryar, R., Alimohammadlou, M., and Kamalinia, M., Fire risk assessment in healthcare settings: Application of FMEA combined with multi-criteria decision-making methods. Mathematical Problems in Engineering, 2020.

[19] Yilmaz, F., Alp, S., Oz, B., and Alkoc, A., Analysis of the risks arising from fire installations in workplaces using the ranking method. Engineering, Technology and Applied Science Research, 10 (4), 5914–5920, 2020.

[20] Diakoulaki, D., Mavrotas, G., and Papayannakis, L., Determining objective weights in multiple criteria problems: The critic method. Computers & Operations Research, 22(7), 763-770, 1995.

[21] Wu, H. W., Zhen, J., and Zhang, J., Urban rail transit operation safety evaluation based on an improved CRITIC method and cloud model. Journal of Rail Transport Planning & Management, 16, 100206., 2020.

[22] Shi, H., Li, Y., Jiang, Z., and Yan, J., Comprehensive evaluation of power quality for microgrid based on CRITIC method. In 2020 IEEE 9th International Power Electronics and Motion Control Conference (IPEMC2020-ECCE Asia) (pp. 1667-1669). IEEE., 2020.

[23] Pan, B., Liu, S., Xie, Z., Shao, Y., Li, X., and Ge, R., Evaluating operational features of three unconventional intersections under heavy traffic based on CRITIC method. Sustainability, 13(8), 4098., 2021.

[24] Vujičić, M. D., Papić, M. Z., and Blagojević, M. D., Comparative analysis of objective techniques for criteria weighing in two MCDM methods on example of an air conditioner selection. Tehnika, 72(3), 422-429, 2017.

[25] Wang, Y., Hou, L., Li, M., and Zheng, R., A novel fire risk assessment approach for large-scale commercial and high-rise buildings based on fuzzy analytic hierarchy process (FAHP) and coupling revision. International journal of environmental research and public health, 18(13), 7187., 2021.

[26] Bari, A. M., Siraj, M. T., Paul, S. K., & Khan, S. A. (2022). A hybrid multi-criteria decision-making approach for analyzing operational hazards in Heavy Fuel Oil-based power plants. Decision Analytics Journal, 100069.

Paper ID: 5056
International Conference on Mechanical, Manufacturing and Process Engineering (ICMMPE – 2022)
Organizer: Faculty of Mechanical Engineering, Dhaka University of Engineering & Technology (DUET), Gazipur, Bangladesh
Website: https://icmmpeduet.com/

Modeling of 3D Printable Electrical Machineries Ferromagnetic Parts

Shinthia Binte Eskender[1], Anupam Saha[2] and Shaikh Ishtiaque Ahmed[3]

[1,2]Department of Materials Science and Engineering,
Khulna University of Engineering & Technology,
Khulna 9203, Bangladesh.
[3]Department of Industrial Engineering and Management,
Khulna University of Engineering & Technology,
Khulna 9203, Bangladesh.

E-mail: sinthiaoyshi@gmail.com

ABSTRACT

The electrical machinery core is formed with a ferromagnetic material that offers high magnetic properties. As ferromagnetic materials have high relative magnetic permeability, they are important in the formation of electromagnetic device cores. Conventional subtractive and powder metallurgy methods for fabrication electrical machineries offer significant core losses and reduce magnetic flux density and magnetic permeability. With the advancement of technology, the limitation of the traditional process can be overcome by using the additive manufacturing process. Hence, this paper proposes a 3D printable model of two types of single-phase transformers, referred to as E-I shape and U-I shape transformers respectively. Possibilities of designing the electrical machinery part which has a ferromagnetic core are investigated. The efficiency of the transformers is evaluated in terms of magnetic flux density distribution and volumetric loss density based on the results of a large number of Finite element simulation methods under various operating situations on COMSOL. The performance of various ferromagnetic materials such as Soft Iron (Fe) and Ferrite (Fe_2O_3) on the transformer core is evaluated. This analysis reveals that if U-I shaped transformer can be made from 3D printing, it will be the best feasible structure for higher operating frequency.

Keywords: 3D printing; Electrical machineries; Transformer; COMSOL.

1. INTRODUCTION

Energy is required in every aspect of our life and its demand is increasing day by day. So, the conversion of energy is needed to fulfill the energy demand.Electric machineries, such as electric motors, electric generators, transformers, and other machines that use electromagnetic forces, are widely used for energy conversion. The cores of electric machines are traditionally made using subtractive techniques and the powder metallurgy process. In the powder metallurgy process, fine metal powders are compacted in suitable dies, and sintering is used to create metal parts. Subtractive manufacturing procedures remove material from a roughly shaped initial part to create the final shape and dimensions. Magnetic cores of electric machines have been typically manufactured by stacking electric steel laminations using subtractive processes [1].

Laminations made with traditional methods for extremely efficient electric motors still have significant losses. Eddy current loss is generally proportional to the thickness of the lamination in general [2]. Thinner laminations can reduce core loss. These are significant obstacles in the classic subtractive printing approach for electrical machines. Powder metallurgy has an impact on magnetic, electrical, and mechanical properties, in addition to limiting design form and size flexibility [3]. The non-magnetic gap between each particle in insulated iron powders applied in soft magnetic composites has a detrimental impact on magnetic permeability, strength, and magnetic flux density. The binder added to the powder is difficult since it drops the magnetic permeability and supreme flux density [4].

Additive manufacturing (AM) or 3D printing technologies are considered a crucial component of the industry 4.0 revolution, due to their improved capabilities above traditional manufacturing techniques. Fully 3D printed objects have been found to have several advantages over conventionally based manufacturing, such as it can be used to print thin-walled hollow parts with high electrical resistivity, complicated core designs may be realized, it has strong core loss reduction potential, and it can considerably lower fabrication costs [3]. With this advancement in technology, the limitation of the traditional subtractive and powder metallurgy process can be overcome by using the additive manufacturing process.

Ferromagnetic materials are those whose dipoles align with each other in the presence of an external magnetic field. Ferromagnetic materials have high relative magnetic

permeability, which is crucial in the development of electromagnetic device cores that work with high magnetic flux for optimum performance.

In the previous study, Selective Laser melting (SLM), Binder jetting technology (BJT), Fused Deposition Modeling (FDM), and lamination object manufacturing (LOM) are the 3D printing technologies that have been used to build transformer, motor, and generator cores [2]–[6]. T. N. Lamichhane used FDM techniques for preparing ferromagnetic materials Machine Core [4], [7], [8]. In April 2021, [9] K. Onla worked on a 3D Multiphysics modeling of a three-phase transformer and proposed a three-dimensional Multiphysics model for temperature prediction of three types of three-phase transformers: Y-shape, three-columns, and five-columns transformers.

No researchers have shown the effect of 3D printable U-I and E-I shaped transformers on magnetic flux density and volumetric loss density based on FDM. In this study, U-I and E-I shaped transformer is designed by COMSOL Multiphysics. Then, the effect on magnetic flux density and volumetric loss density is simulated.

2. THEORIES OF ELECTRICAL MACHINERIES

An electrical machine converts mechanical energy into electrical energy or vice versa. Electric machineries, such as electric motors, electric generators, transformers, and other machines are widely used electric machineries in electrical engineering. Electrical motor application in the compression, drill machine, lathe machine, fans, refrigerator, crusher, pump, blower, and other machines. Radio, television, and telephone circuit used transformers, and for household purposes used distributed transformers [10]. Application of electrical generator-for Mining generator is used, a generator is used in RV camping, in construction site for power backup generator is used, and marine generator is used in boating. A transformer is a stationary device that converts alternating electricity from one voltage level to another (higher or lower), or from one voltage level to almost the same level, not changing its frequency. Mainly the motive of the transformer is to change the electrical voltage to a different value [1]. The transformer core's goal is to have a low-reluctance path whereby the greatest amount of flux of primary windings is transmitted through it and connected to the secondary winding. Transformers classified according to the lamination used core and shell-type are considered: U-I laminations, and E-I laminations. The shell-type transformer is a suitable decision for operating frequencies at the low level. The core type, on the other hand, is the best choice for greater operating frequency [5]. To increase the efficiency of the transformer it is high time to focus on the core materials property and structure of the transformer.

2.1 Geometry of U-I Shaped Lamination

The magnetic core of a core-type transformer is made up of laminations that form a rectangle-shaped frame. However, the entire amount of iron as well as the volume might be too enormous. Pooling a core enables decreasing the overall mass of iron. In such a balanced system, overall flow through all the core iron becomes zero as that's the composition from three balanced flows. A single-phase core type involves a larger magnetic core with two wound limbs(fig. 1).

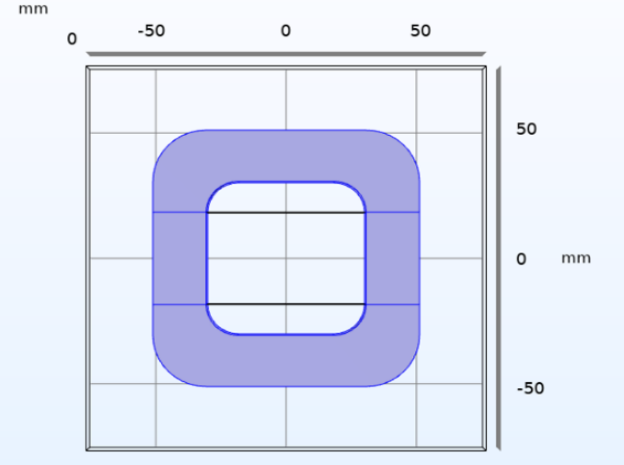

Fig. 1: Geometry of U-I shaped Core type transformer.

2.2 Geometry of E-I Shaped Lamination

A three-limb core is used to produce the core of a single-phase shell type transformer. This design improves the core's mechanical strength. It also improves the safety of windings against mechanical shocks from outside sources. In fig. 2 a single-phase shell type contains two magnetic E-cores which are coupled in a manner to construct a three-limb transformer, the center limb has been wound.

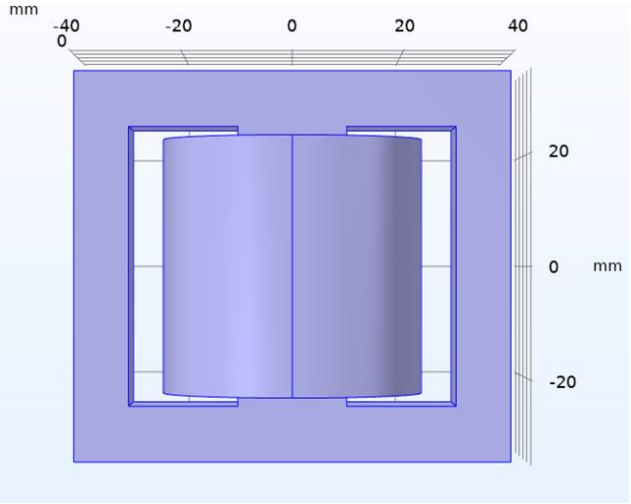

Fig. 2: Geometry of E-I shaped Shell type transformer.

3. MODELING AND SIMULATION PROCESS

3.1 Methodology

For modeling the transformer, the commercial finite element program COMSOL Multiphysics® Version 5.6 is used. In engineering and mathematics, the finite element method (FEM) seems to be an extensively accepted methodology for numerically solving differential equations. The FEM is indeed a basic numerical strategy for solving partial differential equations which take into account two or three spatial variables. This is completed by creating a mesh of the object: a numerical domain for the solution, with a finite number of points, that would be accomplished via a specific space finite difference method within spatial dimensions.

3.2 Input Materials

Materials utilized throughout this modeling would be those that help in a transformer; hence, we obtain three main materials i.e: Iron and Ferrite.

Soft Iron. The iron is being used as just a ferromagnetic material for simulating the transformer, whose primary function is to network magnetic flux. Table 1 shows the properties of iron.

Ferrite. The properties of Ferrite are shown in Table 1. Ferrite is a material having magnetic characteristics which may be used in a variety of electrical devices. Ferrite is also used to channel the magnetic flux in the transformer, used for modeling the ferromagnetic transformer core.

Table 1. Properties of Soft Iron and Ferrite.

Material property	Soft Iron	Ferrite
Relative permeability	2,00,000	4,000
Electrical Conductivity	1(S/m)	1(S/m)
Relative permittivity	1	1

3.3 Parameters and Variables

A parameter estimation study in COMSOL Multiphysics® can be used to estimate the values of inputs in a model. Parameter nodes are found under Global Definitions and can be used to create and define global parameters. There is always one parameter node accessible, and it cannot be moved or deleted. When arranging the parameters in numerous nodes, possibly with descriptive labeling, further parameter nodes can be added as needed.

Table 2. Parameters for U-I shaped laminated transformer.

Name	Description	Value
f	Frequency	60 Hz
Ns	Number of turns in secondary windings	100
Np	Number of turns in secondary windings	20

Table 3. Parameters for E-I shaped laminated transformer.

Name	Description	Value
Rp	Primary windings resistance	100 ohm
Ns	Number of turns in secondary windings	300
f	Frequency	50 Hz

To specify expressions as user-defined variables, use the Variables node. Global variables can be utilized in any context that takes variable expressions, including all Components and geometric entities, as long as their expressions are likewise global. Local variables, on the other hand, have a defined geometric domain. Such variables can only be utilized and assessed within a single Component, or on a limited number of domains, boundaries, edges, or points.

Table 4. Variables for U-I shaped laminated transformer.

Name	Description	Value
a	Steinmetz constant	50
b	Steinmetz constant	1.6
c	Steinmetz constant	1
PL	Power loss	a*(mf. normB) ^b*(f)^c
PL_total	Total power loss	intop1(PL)

Table 5. Variables for E-I shaped laminated transformer.

Name	Description	Value
Rs	Secondary side windings	10 ohm
Np	Number of turns in the primary winding	300
V	Supply voltage	25 V

3.3 Mesh

Any numerical solution to a problem, particularly one using finite elements, must begin with the design of a mesh depicting the field of inquiry. This stage is frequently delicate since the accuracy of finite element approximation is heavily dependent mostly on mesh structure.In the mesh analysis maximum element size is 5.25 mm and minimum element size is 0.225 mm from one node to another. Fig. 3 and Fig. 4 represents extremely fine meshing in U-I and E-I shaped transformer.

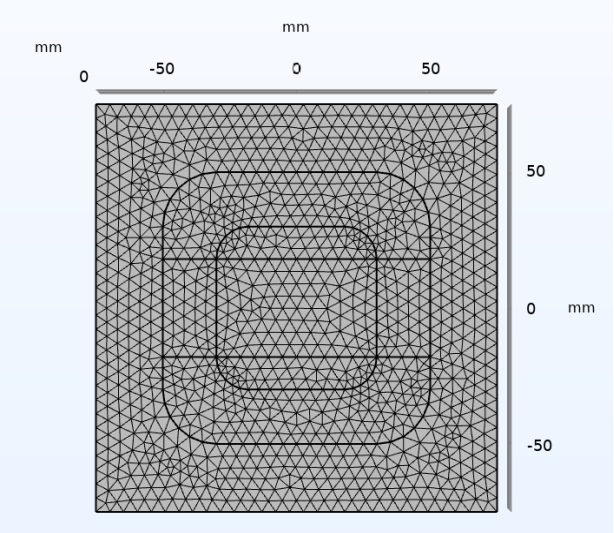

Fig. 3: Meshing of U-I shaped Shell type transformer.

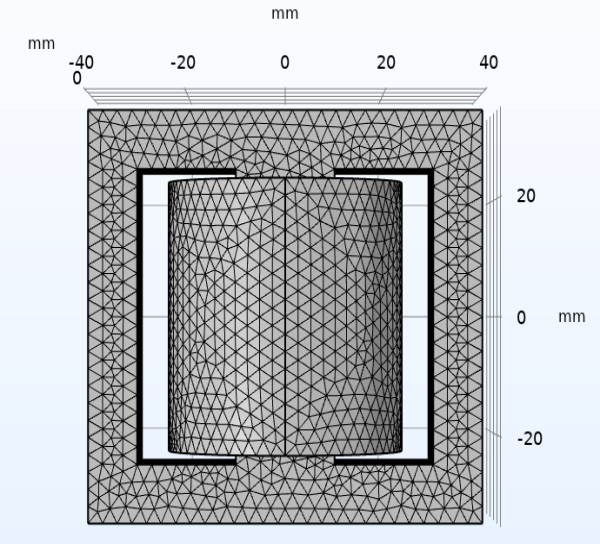

Fig. 4: Meshing of E-I shaped Shell type transformer.

4. SIMULATION RESULT

4.1 Magnetic Flux Density

Fig. 5 is the magnetic flux density profile of the E-I shaped transformer whose core part is formed by ferromagnetic soft iron. This profile is calculated by simulation software by studying the frequency domain step. Magnetic flux density(B) for ferromagnetic soft iron core's transformer has a quite uniform profile. Here, B is distributed in the core from 0.1 T to 0.6 T.

As E-I shaped laminated transformer has a lower air gap, it shows lower permeability(μ) which means a lower value of B than U-I shaped transformer. The reason behind this is the magnetic flux density is proportional to the permeability of the material. But shows a higher value of B than the core of the Ferrite as soft iron's value of μ is higher than the Ferrite.

In the Density of the magnetic flux profile, the magnetic field value is always at the saturation elbow. This could be owing to the presence of two additional flux return columns, which allow the magnetic field lines in the ferromagnetic circuit to travel freely.

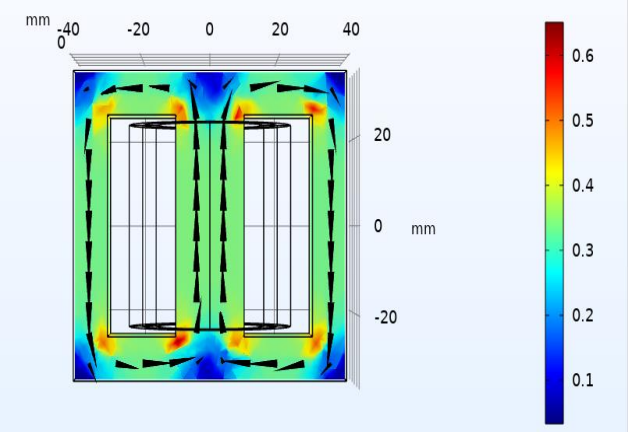

Fig. 5: Magnetic Flux Density of E-I shaped transformer (Soft Iron Core).

Fig. 6 illustrates the magnetic flux density profile of the E-I shaped transformer whose core part is formed by ferrite. Here, B is distributed in the core from 0.05 Tesla to 0.3 Tesla. However, When Ferrite is used in the E-I shaped transformer, B values are lower than the Soft Iron's core. As ferrite's μ is lower than the soft iron. Because B is proportional to the μ of the material, values of B of the ferrite core are lower than the soft Iron Core.

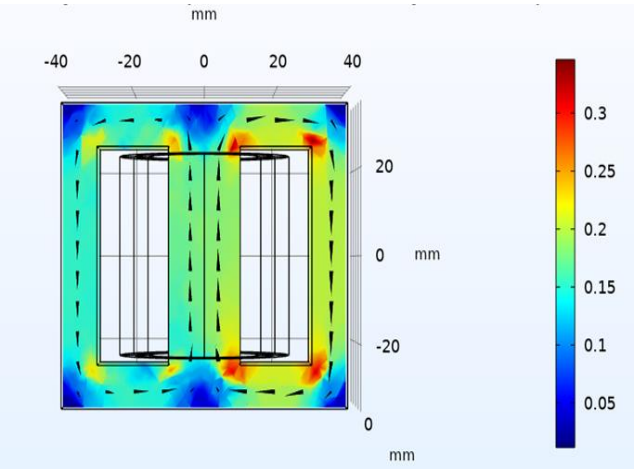

Fig. 6: Magnetic Flux Density of E-I shaped transformer (Ferrite Core).

Fig. 7 is the magnetic flux density profile of the U-I-shaped transformer whose core part is formed by ferromagnetic soft iron. This profile is calculated by simulation software by studying the frequency domain step. Here, B is distributed in the core from 7.08 $\times 10^{-8}$ T to 21.1 T. Number of windings of the secondary coil in this transformer is higher than the primary coil. As Number of secondary coils windings and primary coils windings is 100 and 20. B is proportional to the number of windings. From this profile, higher values of B were found near the secondary coils. As U-I shaped laminated transformer has a higher air gap, it shows higher values of μ which means a higher B value than E-I shaped laminated transformer. As soft iron has a higher value of μ than Ferrite. B value is higher in the soft iron core of the U-I laminated transformer than that of the Ferrite core because B is proportional to the material's μ.

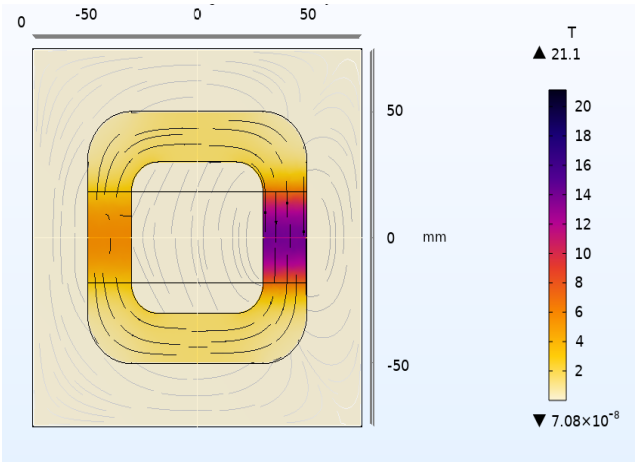

Fig. 7: Magnetic Flux Density of U-I shaped transformer (Soft Iron Core).

Fig. 8. is the magnetic flux density profile of the U-I shaped transformer whose core part is formed by ferrite. Here, B is distributed in the core from 7.4 $\times 10^{-8}$ T to 14.1 T. However, When Ferrite is used in the U-I shaped transformer, B values are lower than the Soft Iron's core. Because ferrite has a lesser μ than soft iron. B values of the ferrite core are lower than that of the soft iron core because B $\propto$ μ.

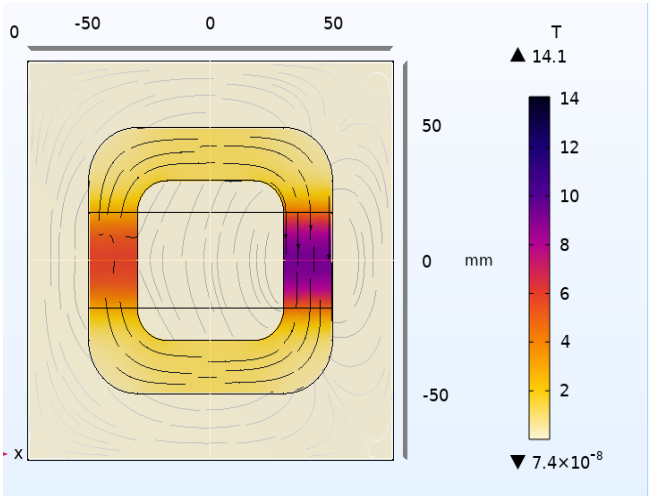

Fig. 8: Magnetic Flux Density of U-I shaped transformer (Ferrite Core).

4.2.Volumetric loss density

Fig. 9 is the volumetric loss density profile of the E-I shaped transformer whose core part is formed by ferromagnetic soft iron. Here, volumetric loss density is distributed in the core from 86.3 W/m^3 to 3.48×10^4 W/m^3. Volumetric loss density for ferromagnetic soft iron core's transformer has a quite uniform profile but values are moderately higher.

Multiplying the volumetric loss density by the effective core volume generates a total core loss. As the volumetric loss density rises, the total core loss rises with it. Core loss is more due to total flux through the entire core. When the air gap of the transformer is increased, reducing the slope of the B/H loop, reducing inductance and μ. The air gap also prevents core saturation. Less hysteresis loss is represented by a smaller hysteresis loop area (B/H loop). For lower air gap, the loss is higher comparatively in E-I shaped transformer than U-I shaped laminated transformer.

Because the core of a transformer is formed of soft iron magnetizing material, when a current passes through it, an alternating magnetic field is created, which causes a little current to flow through the core material again, increasing core losses.

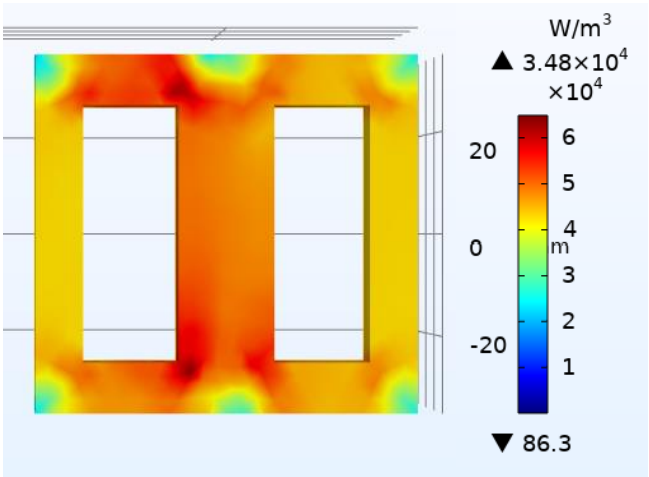

Fig. 9: Volumetric loss Density of E-I shaped transformer (Soft Iron Core).

Fig. 10 is the volumetric loss density profile of the E-I shaped transformer whose core part is formed by ferrite. Here, volumetric loss densities are distributed in the core from 63.2 W/m^3 to 3.26×10^4 W/m^3. Volumetric loss density for ferrite core's transformer has also quite uniform profile but values are moderately lower than soft iron's cored E-I transformer.

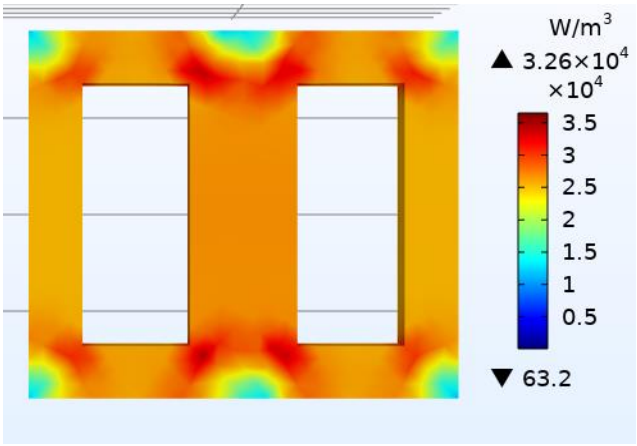

Fig. 10: Volumetric loss Density of E-I shaped transformer (Ferrite Core).

Fig. 11 is shown the Volumetric loss Density of U-I shaped transformer where Soft Iron is used as the Core material. Total core loss is attained by multiplying the volumetric loss density by the effective core volume. As, with increasing Volumetric loss density, total core loss is also increased. The secondary coil loss profile shows a higher volumetric loss density. Other parts of the core loss are in the range from 3.88 × 10^{-6} w/m^3 to 1 w/m^3.One reason for having core loss is lower in U-I lamination type transformer is using frequency above 5 kHz as the model's parameter. When the transformer's air gap is raised, the slope of the B/H loop is reduced, lowering permeability and inductance. The air gap also keeps the core from becoming saturated. A smaller hysteresis loop area (B/H loop) indicates less hysteresis loss. So, another reason, for larger air gap loss is less comparatively in U-I shaped transformers than E-I shaped laminated transformers. This is because only half of the total flux flows in the core because of having a large air gap.

As the transformer core of U-I lamination is made from soft iron magnetizing material, whenever a current flow around then an alternating magnetic field is produced that inures again small current to flow in the core material and increased the core losses than Ferrite transformer core.

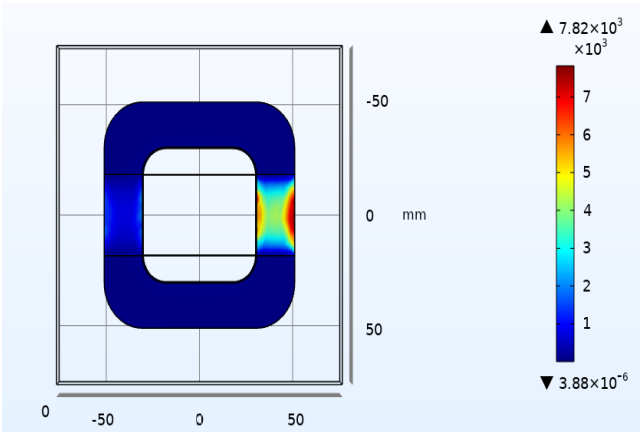

Fig. 11: Volumetric loss Density of U-I shaped transformer (Soft Iron Core).

From fig. 12 Volumetric loss Density has been found for U-I shaped transformers where Ferrite is used as Core material. The secondary coil loss profile shows a higher volumetric loss density. Other parts of the core loss are in the range from 1.41 × 10^{-7} w/m^3 to 1 w/m^3**.** However, When Ferrite is used in the U-I shaped transformer, Volumetric loss density values are lower than the Soft Iron's core.

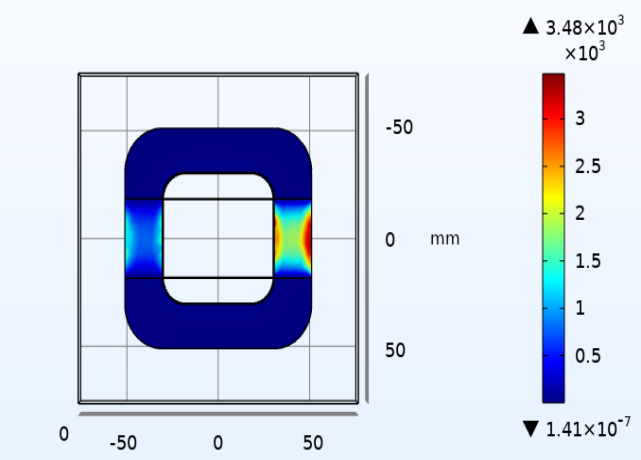

Fig. 12 : Volumetric loss Density of U-I shaped transformer (Ferrite Core).

4. CONCLUSION

In this research different structure transformers have been modeled through COMSOL Multiphysics simulation software and COMSOL-based FEM electromagnetic field and magnetic properties of them are analyzed. The findings of simulations have aided in determining the impact of various materials on those transformers. Magnetic flux density and volumetric loss density profile are plotted. The core material is varied and its impact on material properties is investigated. Supreme values of magnetic flux density are obtained in the Core Type (U-I laminated) transformer. Volumetric loss density is found higher in the shell type (E-I laminated) transformer. Magnetic flux density and volumetric loss density are both higher with using soft iron as core material than Ferrite core. Core type transformer is simulated at a higher operating frequency(60 Hz) than shall type transformer(50 Hz). The air gap should be higher for having less Volumetric loss in the transformer. Machine cores become easier to maintain as a result of fewer core loss of core type (U-I laminated) ferrite materials core. According to the magnetic flux density and volumetric loss density, the most significant and determining factors of the E-I shell type transformer is the excellent solution in the low range of operating frequency. The U-I core type, on the other hand, is the best choice for greater operating frequencies. U-I type transformer is most feasible for 3D printing.

In this analysis, only magnetic flux density and volumetric loss density properties were investigated only a limited range. In the future using other ferromagnetic material (Mu-metal,permalloy-78) hysteresis loss curve, current density distribution, heat transfer, the temperature distribution of L-L lamination, E-E lamination and other structured transformers can be analyzed. Transformer cores will be 3D printed in the future with FDM 3D printers. Property investigation of the 3d printed transformer will be continued with the practical investigation to verify the simulated result.

This is a notable fact that transformer topology is characterized by a significant amount of core loss, which may be a serious problem for some applications despite its strong potential for efficient magnetic density and volumetric loss density.

REFERENCES

[1] N. Kitaev, Ł. Kaiser, and A. Levskaya, "Reformer: The Efficient Transformer," pp. 1–12, 2020, [Online]. Available: http://arxiv.org/abs/2001.04451

[2] G. Bertotti, "Physical interpretation of eddy current losses in ferromagnetic materials. II. Analysis of experimental results," *J. Appl. Phys.*, vol. 57, no. 6, pp. 2118–2126, 1985, doi: 10.1063/1.334405.

[3] T. Q. Pham, T. T. Do, P. Kwon, and S. N. Foster, "Additive Manufacturing of High Performance Ferromagnetic Materials," *2018 IEEE Energy Convers. Congr. Expo. ECCE 2018*, no. January 2019, pp. 4303–4308, 2018, doi: 10.1109/ECCE.2018.8558245.

[4] K. Onla, C. Junior, K. Fankem, E. Duckler, D. T. Alix, and E. J. Yves, "3D Multiphysics Modelling of Three-Phase Transformer," vol. 10, no. 2, pp. 33–45, 2021.

[5] M. A. Bahmani, E. Agheb, T. Thiringer, H. K. Hoidalen, and Y. Serdyuk, "Core loss behavior in high frequency high power transformers-I: Effect of core topology," *J. Renew. Sustain. Energy*, vol. 4, no. 3, 2012, doi: 10.1063/1.4727910.

[6] F. Edition and C. April, "37, 311 (1951).," vol. 39, no. 1951, pp. 551–560, 1953.

[7] P. Pfwvdl *et al.*, "Characteristic Comparison of Transv versally Laminated Aniso otropic Synchronous Reluctance Motor Fabricatio on Based on 2D Lamin ation and 3D Printing," pp. 18–21.

[8] C. Ropoteanu, P. Svasta, and C. Ionescu, "Electro-thermal simulation study of different core shape planar transformer," *2016 IEEE 22nd Int. Symp. Des. Technol. Electron. Packag. SIITME 2016*, pp. 209–212, 2016, doi: 10.1109/SIITME.2016.7777279.

[9] K. S. Shinoy and B. Sebastian, "Modeling a Brushless DC Motor for an Advanced Actuation System Using COMSOL Multiphysics® Software," *Comsol.Jp*, [Online]. Available: https://www.comsol.jp/paper/download/367791/ks_abstract.pdf.

[10] G. Kron, "Generalized Theory of Electrical Machinery," *Trans. Am. Inst. Electr. Eng.*, vol. 49, no. 2, pp. 666–665, 1930, doi: 10.1109/T-AIEE.1930.5055554.

Paper ID: 5152
International Conference on Mechanical, Manufacturing and Process Engineering (ICMMPE – 2022)
Organizer: Faculty of Mechanical Engineering, Dhaka University of Engineering & Technology (DUET), Gazipur, Bangladesh
Website: https://icmmpeduet.com/

Numerical Investigation of Stress Field Near the Vertex of a 3D Three Layer Piezoelectric Bonded Joint

Rahul Sarker[1], Md. Shahidul Islam[2] and Somnath Somadder[3]

[1] Department of Mechanical Engineering, Khulna University of Engineering & Technology, Khulna-9203, BANGLADESH
[2] Department of Mechanical Engineering, Khulna University of Engineering & Technology, Khulna-9203, BANGLADESH
[3] Department of Mechanical Engineering, Khulna University of Engineering & Technology, Khulna-9203, BANGLADESH

E-mail: sarker1505076@stud.kuet.ac.bd

ABSTRACT

Stress singularity frequently occurs at a vertex in the interface of joints due to a discontinuity of material which finally causes debonding of material at the joint under mechanical or thermal loading. Consequently, it is one of the main factors to maintain the reliability of intelligent structures. In the present paper, different analyses of an isotropic piezoelectric joint in which two-layer of piezoelectric materials are bonded using a resin layer are performed. PZT 5A and PZT 8 are used as piezoelectric material and the analysis is done using ABAQUS 6.14 software. Firstly, the stress field at the vertex and along the interface edge of bonded joints are investigated numerically. Afterwards, the influence of interlayer thickness on the singular stress field at the interface of bonded joints was also determined by numerical analysis. Finally, the impact of interlayer thickness on the stress field is precisely examined. All the analyses are accomplished under constant mechanical and electrical loading. From these analyses, it is found that a significant amount of stress develops near the vertex and the interface edge which may further initiate fracture of the joint. It is also revealed that stress increments when the interlayer thickness goes up.

Keywords: Stress singularity; Piezoelectric Joint; Interlayer Thickness; Interface Edge.

1. INTRODUCTION

Piezoelectric materials are commonly used in mechatronic products designed for having special characteristics. Due to their high functionality, they are vastly used in intelligent structures for precise sensing and control purposes. Basically, there are two phenomena which permit the piezoelectric materials to be used as sensors and actuators in a control system. The first phenomenon is known as a direct piezoelectric effect which implies that the application of mechanical force or pressure to a piezoelectric material produces electrical charge/voltage. On the other hand, the application of electrical charge/voltage to the material is responded by induced strain/displacement, known as the converse piezoelectric effect [1]. The sensors are made of piezoelectric material attached to smart devices as a layered material system by means of adhesive bonding. When mechanical or electric loads are applied to the system failure frequently occurs at the edge of joints where the stress concentration rises due to the difference in mechanical properties and it is deleterious to fracture toughness and reliability of joints. Hence, it is essential to understand the effect of geometry and material parameter on the singular behaviour of the stress field near the vertex of multilayer piezoelectric stacks under combined mechanical and electrical loadings.

G.P. Zou et al. found the analytical solution of different metallic and composite bonded joints to evaluate stresses in different loading conditions. They have verified the results by FEM analysis also [2]. Fracture stress yield in the singular locations in adhesively bonded joints due to external load explained by Victor Weissberg et al. when investigating different analogous joints by linear elastic finite element analysis. In their work, crack-tip singularity and adhesive edge singularity both are investigated [3]. A. Baldan has studied a lot of factors which cause the environmental and mechanical performance and durability of the adhesively bonded joints. In his opinion environmental degradation at the interlayer of the bonding surface initiates most in-service failures [4]. Bin Chen et al. have worked on an axially tensile loaded adhesively bonded piezoelectric pipe-joint system. They have derived the computational formula for the stress transfer model to investigate the stress concentration. They precisely concluded that the smaller the thickness and the larger the shear modulus of the adhesive layer is, the greater the stress concentration will be [5]. Zunxu Liu et al. have applied an efficient analytical solution strategy to determine the adhesive stresses in balanced and unbalanced adhesively bonded joints with mixed force loading and/or displacement boundary conditions [6]. C. Lee et al. have investigated the various material characteristics, such as inelastic constitutive behaviour and debonding failure, of an adhesively bonded joint at cryogenic temperature using a

computational approach. They also have done a comparison of their model with another lap shear joint [7].

Therefore, it is indeed that plenty of research works have been done to uncover different sides of adhesively bonded joints. Due to extensive applications of adhesively bonded joints in modern technology further research is necessary to uncover more new perspectives on this demanding field. In this research work stress field near the vertex of a 3D three-layer piezoelectric bonded joint is numerically investigated using the finite element method.

2. MATERIALS AND METHODS

2.1 Governing Equations

Equation 1 shows the mechanical equilibrium:

$$\int_V \sigma : \delta\varepsilon dV = \int_S t.\delta u dS + \int_V f.\delta u dV \quad (1)$$

Where, δu is assumed as an arbitrary vector field and all the components of it are continuous. Again, $\delta\varepsilon^{def} = sym\frac{\partial \delta u}{\partial x}$

In equation 2, the electrical flux conservation equation is written as,

$$\int_V q.\delta E dV = \int_S q_S\, \delta\varphi dS + \int_V q_v \delta\varphi dV \quad (2)$$

Where, $\delta\varphi$ is an arbitrary scalar field which is considered to be continuous. Again $\delta E^{def} = sym\frac{\partial \delta\varphi}{\partial x}$

The constitutive equations which are used in Abaqus are given in equations 3 and 4:

$$\sigma_{ij} = D^E_{ijkl}\varepsilon_{kl} - e^{\varphi}_{mij}E_m \quad (3)$$

$$q_i = e^{\varphi}_{ijk}\varepsilon_{jkl} + D^{\varphi(\varepsilon)}_{ij}E_j \quad (4)$$

The material stiffness, piezoelectric constant and dielectric constant are denoted by D^E_{ijkl}, e^{φ}_{ijk} and D^{φ}_{ij} respectively.

The following solution is estimated from the finite element discretization:

$$u_c = N_u^T.u \quad (5)$$

$$V_c = N_V^T.V \quad (6)$$

where, the displacement shape functions are indicated by N_u and the electrical potential shape function is denoted by N_V .

For the strain and electric field, it can be written as,

$$S = B_u.u \quad (7)$$

$$E = B_V.V \quad (8)$$

Where,

$$B_u = \begin{bmatrix} \frac{\partial}{\partial x} & 0 & 0 & \frac{\partial}{\partial y} & 0 & \frac{\partial}{\partial z} \\ 0 & \frac{\partial}{\partial y} & 0 & \frac{\partial}{\partial x} & \frac{\partial}{\partial z} & 0 \\ 0 & 0 & \frac{\partial}{\partial z} & 0 & \frac{\partial}{\partial y} & \frac{\partial}{\partial x} \end{bmatrix}^T \quad (9)$$

$$B_V = \begin{bmatrix} \frac{\partial}{\partial x} & \frac{\partial}{\partial y} & \frac{\partial}{\partial z} \end{bmatrix}^T \quad (10)$$

The coupled finite element matrix equation is obtained by utilizing the variational principle and the finite element discretization,

$$\begin{bmatrix} M & 0 \\ 0 & 0 \end{bmatrix}\begin{bmatrix} \ddot{u} \\ \ddot{V} \end{bmatrix} + \begin{bmatrix} C & 0 \\ 0 & 0 \end{bmatrix}\begin{bmatrix} \dot{u} \\ \dot{V} \end{bmatrix} + \begin{bmatrix} K & K_z \\ K_z^T & K_d \end{bmatrix}\begin{bmatrix} u \\ V \end{bmatrix} = \begin{bmatrix} F \\ L \end{bmatrix} \quad (11)$$

Where,

$M = \int \rho N_u N_u^T dV$ denotes the structural Mass and the structural stiffness is indicated by $K = \int B_u^T C B_u dV$

The piezoelectric coupling matrix is expressed as follows $K_z = \int B_u^T e B_u dV$

Dielectric conductivity is denoted by $K_d = \int B_V^T \varepsilon B_V dV$

2.2 Material Property Table

Different properties such as Young's modulus, Poisson ratio, dielectric constant and piezoelectric constant of PZT-5A, PZT-8 and resin are given in the following table:

Table 1: Different properties of PZT-5A, PZT 8 and resin [8,9,10]

Material Constants	Materials		
	PZT-5A	Resin	PZT-8
Young's Modulus *GPa*	66	2	99
Poisson Ratio	0.31	0.39	0.31
Dielectric constants $\ln 10^{-9} F/m$	1.53	-	1.142
Piezoelectric constants $\ln 10^{-12} C/N$	585	0	330

2.3 Results and Discussion

The tri-material joint having three layers are shown in Fig. 1. The top and bottom sections are of piezoelectric materials named PZT-5A and PZT-8 respectively. And the middle section constitutes the adhesive. Here Resin is used as adhesive. Regarding boundary conditions, here an external load of 1 MPa and 1 C/m2 electrical load is applied on the top surface and electric displacement whose poling direction is parallel to the z-axis. The bottom surface is to be fixed. The electric potential on the bottom surface in the z-direction is also fixed.

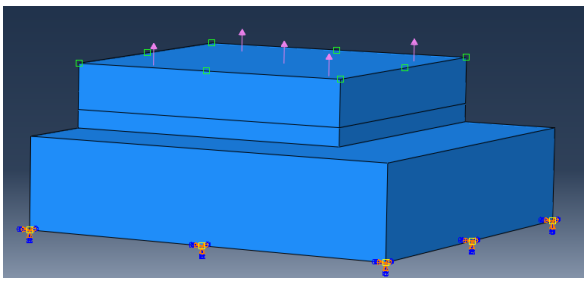

Fig. 1: Working model

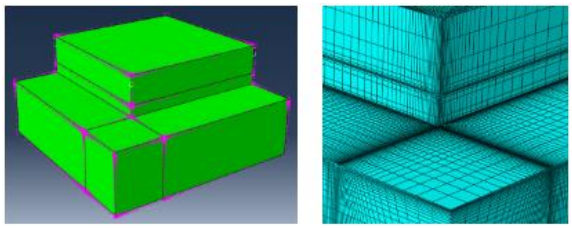

(a) (b)

Fig. 2: Meshing process (a) seed process (b) mesh pattern of vital point

In fig. 2, how the mesh of the model is generated is demonstrated. To reduce analysis time, number of elements are increased only at the edges which is shown in the seeding process in fig. 2 (a). In addition, the mesh pattern is manifested in fig. 2 (b) which is gotten after seeding. Before working on the model, a verification analysis has been done which is exposed in fig. 3. In this analysis, a research work [11] which is conducted using Boundary Element Method is verified by conducting a similar work using the finite element method. Comparing both works, a maximum error of 0.950082% is found.

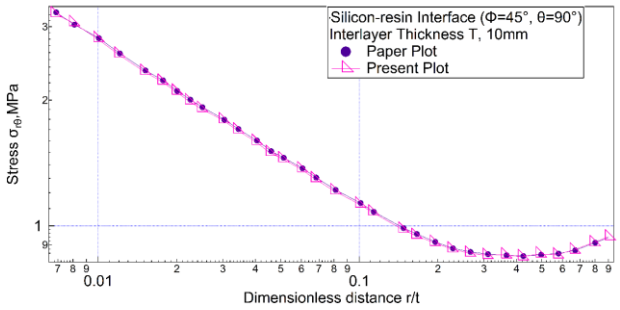

Fig. 3: Comparison of present work with reference paperwork for distribution of stress $\sigma_{\theta\theta}$ against dimensionless distance r/t

In fig. 4, a mesh dependency analysis is shown, which is carried out to find the proper mesh for what the final analysis result has been figured out.

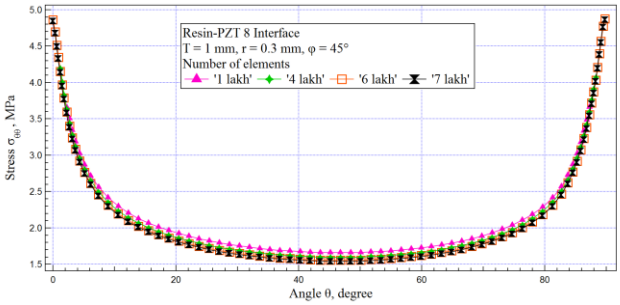

Fig. 4: Mesh dependency check for the working model

Mesh dependency is done for T=1 mm where 1 lakhs to 7 lakhs element number is tested. For creating the mesh, the C3D8E element type is applied. Ultimately, it is found that stress varies very little for element number of 6 lakhs or above. Thus, all the required results are obtained with approximately 6 lakhs of the element.

Results achieved are manifested here from fig. 5 to fig. 14.

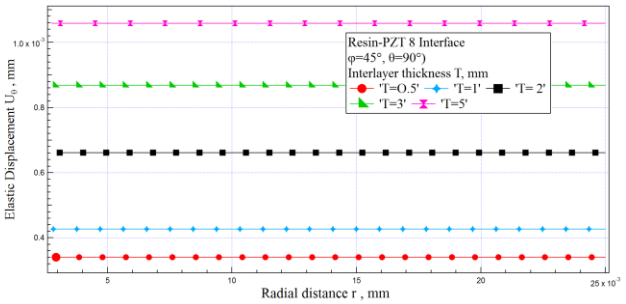

Fig. 5: Distribution of elastic displacement u_θ against radial distance r

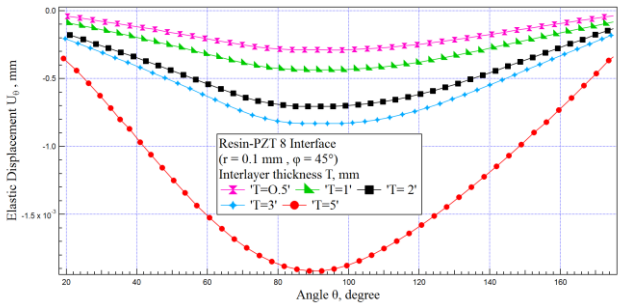

Fig. 6: Distribution of elastic displacement u_θ against the angle θ

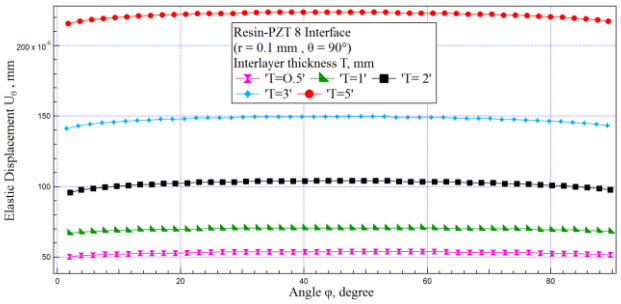

Fig. 7: Distribution of elastic displacement u_θ against the angle ϕ

In fig. 5 to fig. 7, elastic displacement U_θ is plotted against r, θ and ϕ respectively. It is disclosed that displacement is higher at the vertex and increases when interlayer thickness enhances. In addition, in fig. 6 displacement is symmetric at θ=90°, whereas, it is symmetric at ϕ=45°.

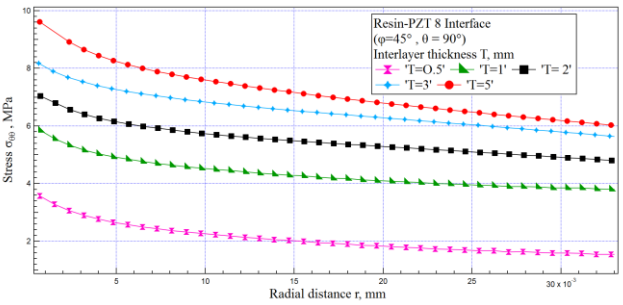

Fig. 8: Distribution of stress $\sigma_{\theta\theta}$ against radial distance r

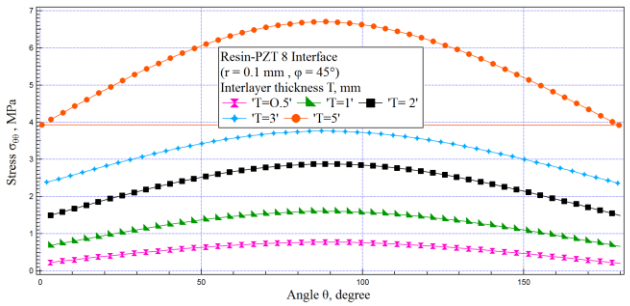

Fig. 9: Distribution of stress $\sigma_{\theta\theta}$ against the angle θ

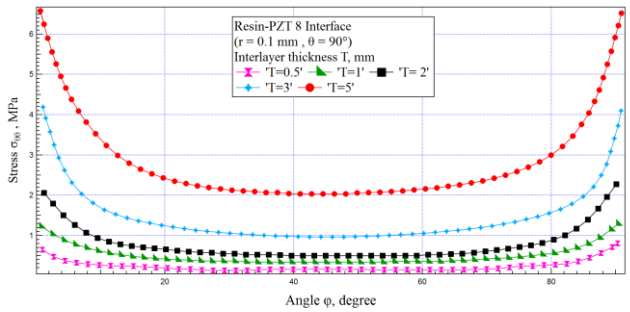

Fig. 10: Distribution of stress $\sigma_{\theta\theta}$ against the angle ϕ

In fig. 8, 9 and 10, stress $\sigma_{\theta\theta}$ is plotted against $r, \theta \; and \; \phi$. In fig. 8 stress is maximum at radial distance r=0 mm which is at the vertex. Similarly, in fig. 9, largest value of stress is witnessed at θ=0° and θ=180° which denotes the the interface edge. Finally, in fig. 10 maximum value of stress is found at ϕ=0° and ϕ=90°. Moreover, accumulated stress goes up with the increment of interlayer thickness.

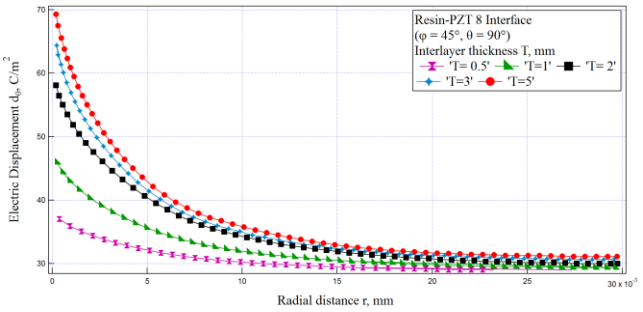

Fig. 11: Distribution of electric displacement d_θ against radial distance r

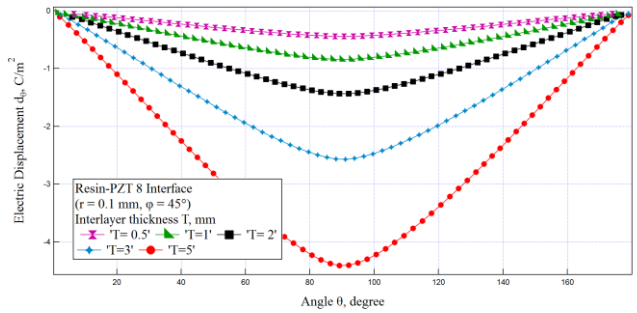

Fig. 12: Distribution of electric displacement d_θ against the angle θ

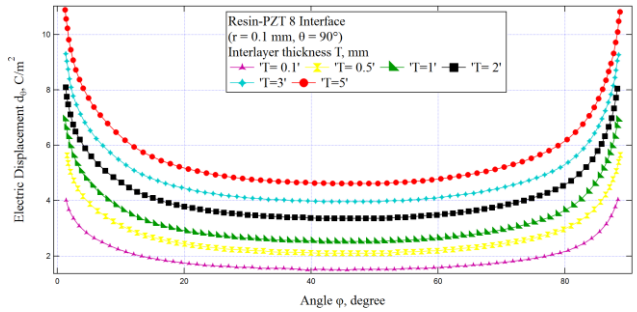

Fig. 13: Distribution of electric displacement d_θ against the angle ϕ

In fig. 11 to fig. 13 electric displacement is plotted against r, θ *and* ϕ. The characteristics of electric displacement are similar to elastic displacement.

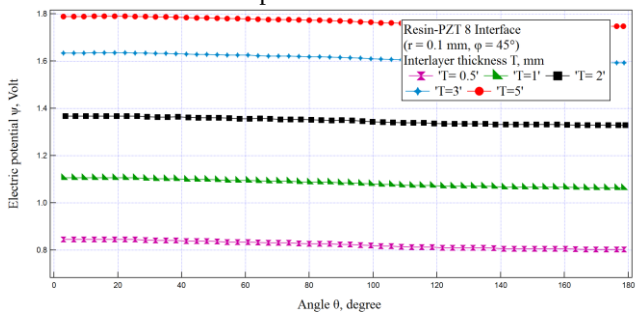

Fig. 14: Distribution of electric potential ψ against the angle θ

From fig. 14 it is observed that electric potential goes up with the enhancement of interlayer thickness.

4. CONCLUSION

In this research work, the angular function of displacement and stress within a three-layered adhesively bonded joint were analysed. The interlayer thickness was varied and its impact on the singular stress field was investigated. The highest value of stress and displacement is obtained close to the vertex and along with the interface, edge compared to other regions. Displacement and stress both increase with the increment of the interlayer thickness. As a result, it can be concluded that interlayer thickness should be as thin as possible to make the joint reliable.

REFERENCES

[1] M. Sunar, S.S. Rao, "Recent advances in sensing and control of flexible structures via piezoelectric materials technology," Applied Mechanics Reviews, pp. 1-16, 1999.

[2] G.P. Zou, K. Shahin, F. Taheri, "An analytical solution for the analysis of symmetric composite adhesively bonded joints," Composite Structure, pp. 499–510, 2004.

[3] V. Weissberg, M. Arcan, "Invariability of singular stress fields in adhesive bonded joints," International Journal of Fracture, pp. 75-83, 1992.

[4] A. Baldan, "Adhesively-bonded joints in metallic alloys, polymers and composite materials: Mechanical and environmental durability performance," Journal Of Materials Science, pp. 4729-4797, 2004.

[5] B. Chen, Q. Yuan, J. Luo, "Stress Concentration in Adhesive Layer of Adhesively Bonded Piezoelectric Pipe-Joint System," Journal of Superconductivity and Novel Magnetism, pp. 945-947, 2010.

[6] Z. Liu, Y. Huang, Z. Yin, S. Bennati, P.S. Valvo, "A general solution for the two-dimensional stress analysis of balanced and unbalanced adhesively bonded joints," International Journal of Adhesion & Adhesives, pp. 112-123, 2014.

[7] C. Lee, M. Chun, M. Kim, J. Lee, "Numerical evaluation for debonding failure phenomenon of adhesively bonded joints at cryogenic temperatures," Composites Science and Technology, pp. 1921–1929, 2011.

[8] Ceramic Materials (PZT) - Boston Piezo-Optics Inc. Available: https://bostonpiezooptics.com/ceramic-materials-pzt

[9] PZT 5A Properties, Available: https://www.efunda.com /materials/piezo/material_data/matdata_output.cfm?Material_ID=PZT-5A

[10] PZT 8 Properties, Available: https://www.efunda.com /materials/piezo/material_data/matdata_output.cfm?Material_ID=PZT-8

[11] H. Koguchi, M. Nakajima, "Influence of interlayer thickness on the intensity of singular stress filed in 3D three-layered joints under an external load," Journal of solid mechanics and materials Engineering, Vol. 4, pp. 7, 2010.

Paper ID: 5552
International Conference on Mechanical, Manufacturing and Process Engineering (ICMMPE – 2022)
Organizer: Faculty of Mechanical Engineering, Dhaka University of Engineering & Technology (DUET), Gazipur, Bangladesh
Website: https://icmmpeduet.com/

Horizontal Axis Solar Tracking System to Enhance Efficiency with Accuracy Test by Machine Learning

Jyothy Mondal[1], Nibir Mondol[2]

[1,2]Department of Energy Science and Engineering, Khulna University of Engineering & Technology, Khulna-9203, Bangladesh

E-mail: mondal1713024@stud.kuet.ac.bd
nibir@ese.kuet.ac.bd

ABSTRACT

As conventional energy resources are depleting day by day; renewable energy is the only hope to cope with the future energy crises. Our earth has numerous renewable energy resources and solar energy is the cleanest energy source. Moreover, solar energy refers to a type of sustainable energy source which can be used to generate electricity. Electricity production rate mainly depends on a few factors like solar cell temperature, solar cell raw materials, solar intensity and many more. In a fixed system, solar photovoltaic panels can't get topmost intensity as the sun's position is changing all day long in the sky. That is why an automated tracking system is required to improve the efficiency of a fixed state. In this paper, a horizontal axis solar tracking system using Arduino UNO and servo motor is built to analyze and implement the solar tracking system. The objectives of this paper are to track the sun and get topmost intensity from the sun and to compare the intensity between a horizontal axis solar tracking system and a static system to get better performance. For getting most energy from the sun, the solar photovoltaic panel is tracked using Arduino UNO, a servo motor which is used to rotate the solar panel, two light dependent resistors which are used to sense the light coming from the source, and solar panel. After collecting all the data of a sunny day in several days at several time intervals, analysis has been done and compared with a fixed solar panel system. Efficiency has been increased by tracking and data accuracy has been tested through machine learning which is a part of artificial intelligence and developed on the concept focusing on creating predictions using desktop computer or laptop. WEKA, which has built-in machine learning algorithms and using those algorithms, the system is tested whether it is running smoothly or not.

Keywords: Renewable Energy; Solar Tracking; Arduino UNO; Servo motor; Solar photovoltaic panel; Machine Learning.

1. INTRODUCTION

Now-a-days energy crisis is the main concern as the world's demand increases on natural energy resources. For this, people are looking for new alternative energy resources. Besides looking for new energy resources, scientists have concluded that, though renewable energy comes from natural resources, it can replace fossil fuels as well as it can power the whole world. All these things can be possible if we convert it from one form to another. For example, among renewable energy resources such as geothermal energy, wind energy, tidal energy, biogas energy, biomass energy and hydro energy, energy coming from the sun is environment-friendly and cost free as it is an unlimited source of energy. If we harness it properly, we can reduce the extra use of conventional sources of energy. Solar system can consume a huge amount of ray of light and thus produce electrical energy when it is placed at a perfect angle [1]. The countryside people of Bangladesh have initiated to use solar power for the generation of the electricity and for irrigation purposes. As Bangladesh is in the northern hemisphere, a steady solar system can soak up sunlight endlessly all day by confronting it in the south along a disposition of 23.45°. This paper has been designed to keep this in mind to make solar energy more efficient. For this solar panel with a tracking system has been built. Several tracking systems based on a single axis have been proposed by the researchers. Their proposed tracking system includes horizontal aligned single axis tracker (HSAT), vertical aligned single axis tracker (VSAT), horizontal wih tilted modules single axis tracker (HTSAT), polar aligned single axis tracker (PSAT) and tilted single axis tracker (TSAT). Single axis tracking is less complex [2]. Moreover, it needs less maintenance in comparison with double axis tracking. Tracking system refers to following the sun during the entire day which can maximize the energy output. The horizontal axis solar tracking system generates 25% more energy than a conventional system on a sunny day [3].

In this paper, the solar tracking system which is based on a single axis is introduced because it is the simplest tracker with the usage of less energy and also has minor complications than a multi axis system [4].

Numerous works had been carried out on analysis and implementation of the tracking systems. Some authors used a Fuzzy Logic Controller to implement the sunlight

tracking system. Not only the design but also the coding is complex. For this reason, a microcontroller based processor, named Arduino UNO is used which offers simple coding [5] and machine learning has been applied to the data which are collected from the system for detecting the systems working ability. Krishanu Das et al described their project as the scheme of a low priced solar tracker system where LDRs had been used to capture light intensity and servo motor had been utilized for the movement of the solar panel sensing light by LDRs. The performance of the solar tracking system had been investigated and differentiated the result from static one [3]. Siti Amley Jumaat et al discussed the development of horizontal single axis solar tracker using Arduino UNO because it had reasonable price, less complexity and could achieve the needed efficiency. For the advancement of their project, five LDRs had been used for detecting the sunlight to capture topmost light intensity and servo motor had been utilized to move solar panel to the topmost light source. The efficiency of the solar tracker using Arduino had been examined and then compared with the conventional solar cell [6]. Ei Ei Aung discussed the analysis and execution of a solar tracking system in his research paper where he used Arduino UNO, LDR sensors, and stepper motor to track the path of the sun. Moreover, a battery had been utilized to reserve the energy from the solar panel. The aim of his project was to fulfill the demand on electricity in rural areas. For this data analysis had been carried out and compared to sunny day and cloudy day data on hour to hour [7]. Rakshitha Rao et al demonstrated the arrangement of a solar tracking system using Arduino in their research paper. For conducting their research, light ward resistors had been used to measure the daylight falling on them, servo motors had been utilized to pivot the sunlight based board toward the extreme light source and sunlight based board retained the beams coming from the sun. Moreover, a code which was composed utilizing C programming had been used [8].

2. METHODOLOGY

This section is used for center of attention on the methods which are used to advance a horizontal axis solar tracking system using Arduino UNO and servo motor. This section is split up into three stages, one is machine learning and other two options are hardware development and software implementation. In the hardware development stage, two light dependent resistors (LDR) and servo motor have been used. LDRs have been used for collecting light coming from the sun and a servo motor has been used to rotate the solar cell at topmost position sensing light coming from the sun by LDRs [3]. In the software implementation stage, algorithms and flowchart of this system are introduced. It also describes the control of the circuit for the solar tracking system which is based on Arduino UNO where the program has been input to detect the sunlight through LDRs [7] and comparing the output of the LDRs, the servo motor will rotate in the direction of clockwise or anti clockwise. After collecting data, machine learning has been applied and accuracy has been tested through a software called, WEKA.

2.1 Machine Learning

WEKA is used in this system as a medium for machine learning. It is a user-friendly software to learn machine learning. WEKA, which is a collection of machine learning algorithms, applies machine learning straightforwardly to the data-sets. There are different types of machine learning algorithms such as NaïveBayes, Logistic, ClassificationViaRegression and many more. These are built-in classifiers which help in predicting glitch and other precarious circumstances based on the input data. The WEKA system mainly takes input in the form of an attribute relation file which indicates ARFF format. It is a standard way of representing data-sets.

2.2 Hardware Development

In this section, the components that are used for this system are described where solar cell, Arduino UNO, servo motor and LDRs have been used.

2.2.1 Solar cell

Solar cell is basically an electronic device which turns the energy of light directly into electricity by a physical and chemical phenomenon, named photovoltaic effect. The electric-powered characteristics such as voltage, current, resistance of a solar cell varies when sunlight hits the solar cell [2]. The polycrystalline solar cell that has been used in this system is shown on Fig. 1 and the specifications of the solar cell are presented in Table 2.

Fig. 1: Solar cell

Table 1: Specifications of solar cell

Type	1W 6V Solar Panel
Solar Cell	Polycrystalline Solar Cell
Maximum Power	1W
Voltage at Max Power	6V
Current at Max Power	167mA
Dimension	89.5x59.5mm

2.2.2 Light dependent resistor

Light Dependent Resistor (LDR) is also known as photoresistor or photo-conductive cell. It is an electronic component that can only receive energy. The resistance of a light dependent resistor changes due to the occurrence of light potency. When the occurrence of the light potency increases, the resistance of a photoresistor decreases. On the other hand, the resistance of a photoresistor increases with the decrease of the incident light intensity.

2.2.3 Servo motor

Servo motor is basically a rotary as well as linear actuator that are used in different appliances because it permits pinpoint control. Though they are tiny in size, they are effective. That is why they are utilized to run remote-controlled or radio-controlled systems. Servo motors are mainly conducted by dispatching electrical pulses of varying width, or pulse width modulation (PWM), through the medium of control wire. There is lowest pulse, highest pulse and recurrence rate. A servo motor generally can turn 90° only in either direction for a complete 180° variation in movement. The motor's impartial arrangement is determined by the site, where the servo motor has the consistent amount of revolving in the both clockwise or anti clockwise direction [2].

2.2.4 Arduino UNO

Arduino UNO is mainly known as a microcontroller board which is based on the ATmega328. It has mainly 14 input and output pins which are digital (among them 6 pins can be utilized as PWM outputs), 6 analog inputs, 16 MHz ceramic resonator, a USB connection, power jack, ICSP header, and reset button. It consists of every single thing that is essential to hold up the microcontroller. It can be straightforwardly connected to an electronic device which can be a desktop computer or laptop in association with USB cable. It can be also electrically powered with an AC-to-DC adapter or a battery to get it started. Programming languages like C, C++ is used in Arduino UNO. The Integrated Development Environment (IDE) is an application which is utilized to write down and upload programs to Arduino boards.

2.2.5 Block diagram

In this tracking system, Arduino Uno is used and the other components are LDR sensors, solar panel and servo motor. The block diagram for this tracking system is given in Fig. 2.

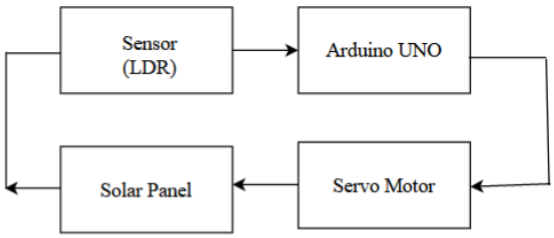

Fig. 2: Block diagram of a horizontal axis solar tracking system

Here, LDR sensors sense the light coming from the sun. After data collection from sunlight, it sends data to the Arduino UNO. Then Arduino takes the output of the LDRs as input and compares the results. Then Arduino UNO controls the servo motor by giving instructions to the servo motor whether to move the solar panel clockwise or anti clockwise direction. Therefore, the servo motor revolves the solar panel at maximum position.

2.3 Software Implementation

To compile the tracking system, Arduino IDE software is used.

2.3.1 Algorithm

The algorithm of this system are:

- Step 1. Analog data read from the analog channels
- Step 2. When the value of LDR1>the value of LDR2, then the servo motor will rotate clockwise
- Step 3. When the value of LDR2>the value of LDR1, the servo motor will rotate anti clockwise
- Step 4. When the value of LDR1=the value of LDR2, then the servo motor will be in the same position [3]

2.3.2 Flowchart

The flowchart of this system is presented in Fig. 3.

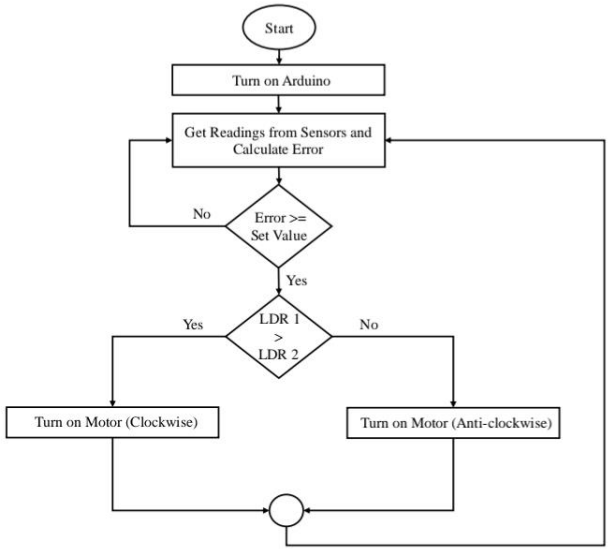

Fig. 3: Flowchart of horizontal axis solar tracking system

2.3.3 Experimental setup

The experimental setup for this system is shown in Fig. 4 where different types of components are also included. To get a better comparison, the tracking system and fixed system are kept together and the values of open circuit voltage, V_{oc} and short circuit current, I_{sc} are collected for both systems.

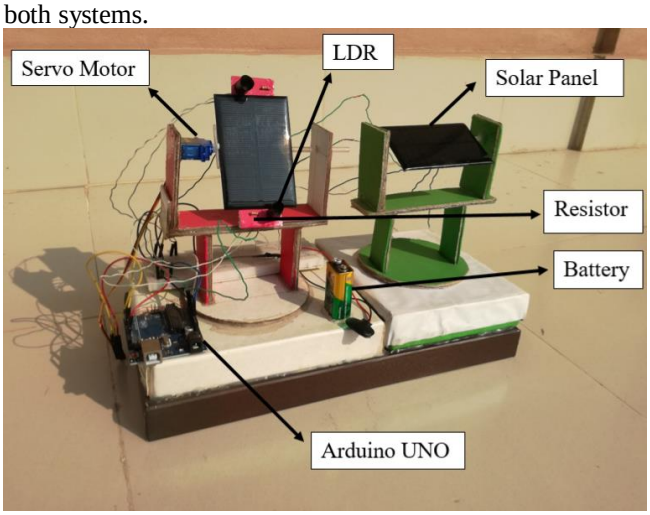

Fig. 4: Experimental setup for single axis solar tracking system with fixed system

3. RESULT AND DISCUSSION

The output data from the solar panel for both conventional and tracking systems are collected, when no load is connected. Moreover, all the data is gathered between 9AM to 4PM for a sunny day in several days at several time intervals. Among several days data, one set of data has shown in Table 2. From Table 2, it can be seen that, at 12:00 PM the solar intensity is high and due to high solar intensity, V_{oc} and I_{sc} are also high for both conventional and tracking systems. Moreover the value of V_{oc} and I_{sc} are nearly almost close to each other for both systems. On the other hand, the lowest values of V_{oc} and I_{sc} are found, when the intensity of the light decreases.

Table 2: Comparison of V_{oc} and I_{sc} between solar tracking system and without solar tracking system on a sunny day

Time	Intensity (w/m^2)	With Tracking		Without Tracking	
		V_{oc} (V)	I_{sc} (mA)	V_{oc} (V)	I_{sc} (mA)
9:00 AM	595	2.18	0.02	1.9	0.01
9:30 AM	645	2.75	0.05	2.68	0.04
10:00 AM	688	3.48	0.08	3.39	0.06
10:30 AM	738	3.98	0.1	3.87	0.09
11:00 AM	768	4.23	0.12	4.15	0.11
11:30 AM	796	4.3	0.15	4.23	0.14
12:00 PM	813	4.45	0.16	4.42	0.158
12:30 PM	779	4.25	0.14	4.2	0.13
1:00 PM	745	4.18	0.12	4.1	0.11
1:30 PM	722	3.88	0.095	3.75	0.09
2:00 PM	689	3.52	0.08	3.45	0.07
2:30 PM	659	3.24	0.06	3.1	0.05
3:00 PM	632	2.67	0.04	2.52	0.03
3:30 PM	595	2.18	0.02	1.9	0.01
4:00 PM	556	1.65	0	1.51	0

For better understanding the comparison of V_{oc} and I_{sc} between solar tracking system and without solar tracking system is shown in Fig. 5 and Fig. 6. For this line chart has been used which has one horizontal axis with two vertical axis.

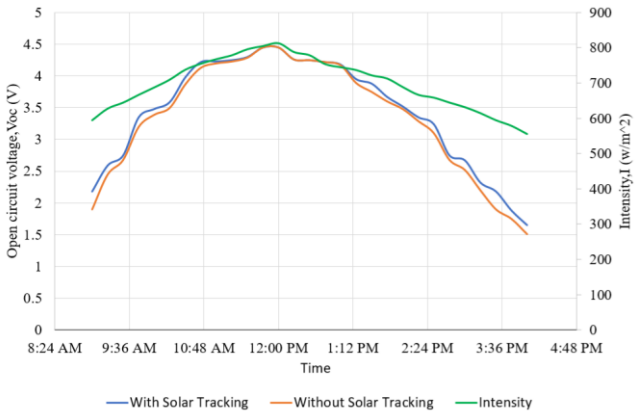

Fig. 5: Comparison of open circuit voltage between solar tracking system and without solar tracking system on a sunny day

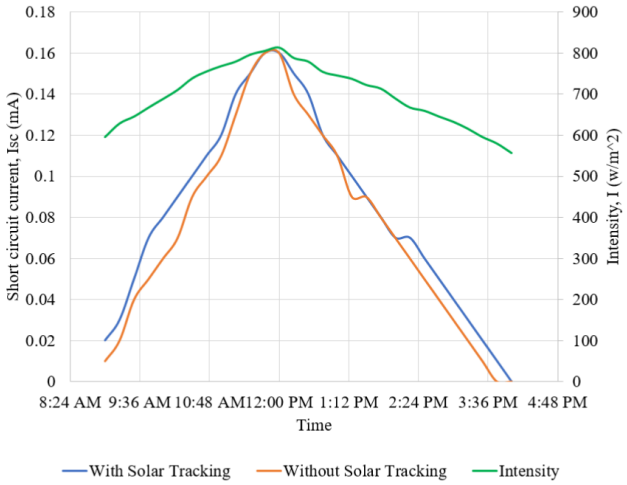

Fig. 6: Comparison of short circuit current between solar tracking system and without solar tracking system on a sunny day

After comparing and analyzing, from Fig. 5 and 6, it can be seen that the V_{oc} and I_{sc} are higher on a sunny day for a solar tracking system than a fixed system.

Table 3: Summary of the related works

Reviewed Paper	Data Taken for Sunny Day	Data Compared with Static Panel	Machine Learning
[3]	No	No	No
[6]	Yes	Yes	No
[7]	Yes	Yes	No
[8]	No	No	No

Table 3 shows that all the literature which had been reviewed does not cover the machine learning in tracking system, which gives inspiration to do this research.

3.1 Accuracy Testing

3.1.1 Accuracy of V_{oc} With solar tracking system

Various types of popular algorithms such as J48, AttributeSelectedClassifier, ClassificationViaRegression have been applied to observe the greatest accuracy for the given data. In J48 and AttributeSelectedClassifier, the prognostication of exactness is 72.4138%. In ClassificationViaRegression, the result is 93.103%.

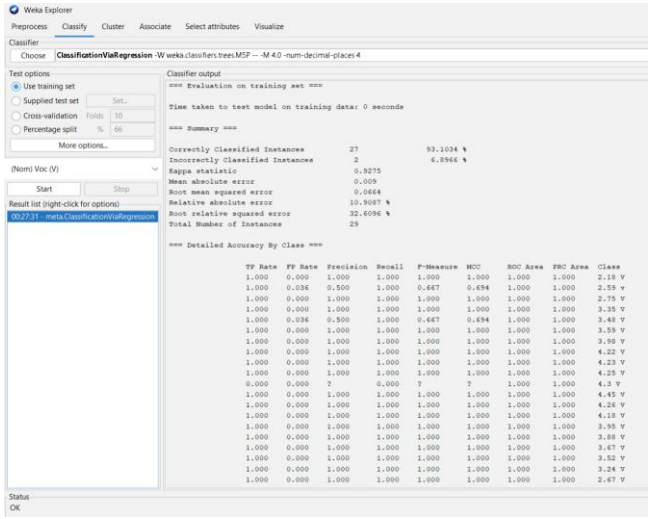

Fig. 7: Output of ClassificationViaRegression Algorithm for V_{oc} (with solar tracking system)

3.1.2 Accuracy of V_{oc} Without solar tracking system

Among different types of algorithms, in Logistic, the prognostication of exactness is 96.5517% and in AttributeSelectedClassifier, the accuracy result is 68.9655%.

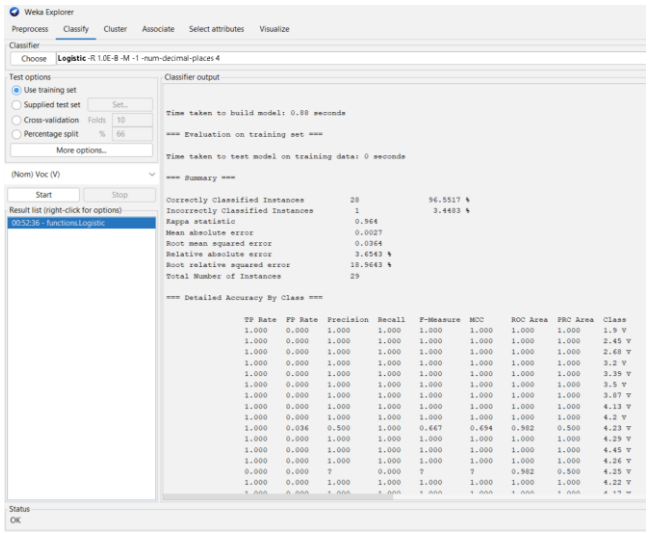

Fig. 8: Output of Logistic Algorithm for V_{oc} (without solar tracking system)

3.1.3 Accuracy of I_{sc} With solar tracking system

In J48 and AttributeSelectedClassifier, the prognostication of exactness is 96.5517%.

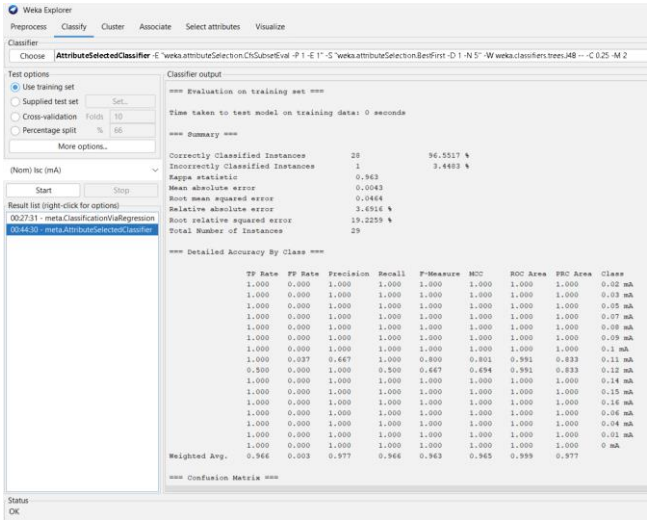

Fig. 9: Output of AttributeSelectedClassifier Algorithm for I_{sc} (with solar tracking system)

3.1.4 Accuracy of I_{sc} Without solar tracking system

In NaiveBayes the prognostication of exactness is 96.5517%.

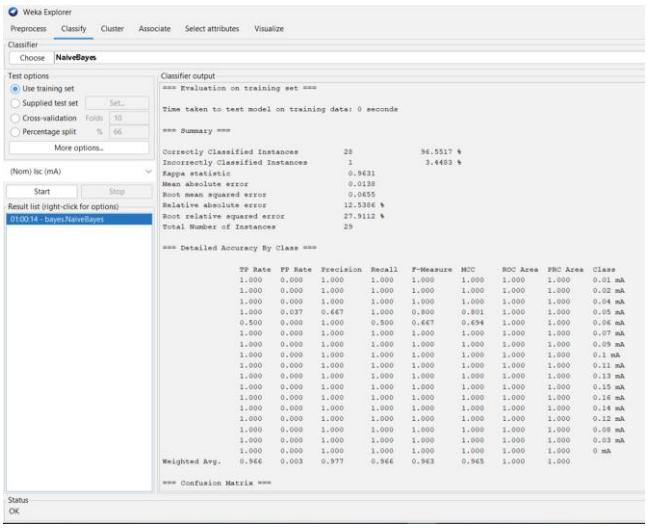

Fig. 10: Output of NaiveBayes Algorithm for I_{sc} (without solar tracking system)

3.1.5 Accuracy Classification

From the data, it can be said that, for V_{oc} and I_{sc}, the best prediction is found by using Classification Via Regression and Attribute Selected Classifier algorithm (93.103% and 96.5517%; with solar tracking system) and by using Logistic and NaiveBayes algorithm (96.5517%; without solar tracking system) which implies that the system offers indefectible and authentic output. Hence, the system is working correctly.

4. CONCLUSION

Horizontal axis solar tracking system has been fabricated to control the movement of the panel according to light intensity coming from the sun. After data collecting and comparing, it can be said that a tracking system produces more output than a conventional system during the hours on a sunny day. So, it has been proven through this paper that a horizontal axis solar tracking system is more efficient than a fixed solar panel system and by combining a few solar cells can be able to generate more power which can be used as power supply to a village. Moreover, testing this system through machine learning also indicates the validation and perfect working potentiality.

ACKNOWLEDGMENT

Authors would like to thank family members and partners who have contributed to develop this paper.

REFERENCES

[1] Shail Patel, “Review on Solar Tracker and Comparison on Single Axis Solar Tracker, Dual Axis Solar Tracker with Fixed Solar PV System”, International Journal of Innovation Research in Electrical, Electronics, Instrumentation and Control Engineering, Vol. 9, Issue 6, ISSN (Online) 2321-2004, 2021.

[2] Anshul Awasthi, Akash Kumar Shukla, Murali Manohar S.R., Chandrakant Dondariya, K.N. Shukla, Deepak Porwal, Geetam Richhariya, “Review on sun tracking technology in solar PV system”, Energy Reports, Volume 6, Pages 392-405, ISSN 2352-4847, 2020.

[3] Krishanu Das, Hridi Ghosh, Maitrayee Sengupta “Single axis solar tracking system using Microcontroller (ATmega328) and Servo Motor” in 2016, International Journal of Scientific and Research Publications, Volume 6, Issue 6, ISSN 2250-3153.J. Clerk Maxwell, A Treatise on Electricity and Magnetism, 3rd ed., vol. 2. Oxford: Clarendon, 1892, pp.68–73.

[4] M. Salaheldin Elsherbiny, Dr. Wagdy R. Anis, Dr. Ismail M. Hafez and Dr. AdelR. Mikhail “Design of single-axis and dual-axis solar tracking systems protected against high wind speeds” International Journal of Scientific & Technology Research, Vol.6, Issue 9, pp 85-89, 2017.

[5] Md. Nasim Reza, Md. Sanwar Hossain, Nibir Mondol, Md. Alamgir Kabir. "Design and Implementation of an Automatic Single Axis Solar Tracking System to Enhance the Performance of a Solar Photovoltaic Panel", International Conference on Science & Contemporary Technologies (ICSCT), 2021.

[6] Siti Amely Jumaat et al, “Horizontal Single Axis Solar Tracker Using Arduino Approach” Indonesian Journal of Electrical Engineering and Computer Science, Volume 12, ISSN 2502-4752, pp. 489b~496, 2018.

[7] Ei Ei Aung, “Single Axis Solar Tracking System”, International Journal of Science and Engineering Applications, Volume 8, Issue 08, ISSN 2319-7560, pp. 283-286, 2019.

[8] Rakshita Rao, Rashmi Rao, Sreecharan B R and Sumanth N S, “Solar Tracking Using Arduino”, International Journal of Research and Scientific Innovation (IJRSI) Volume 5, Issue 4, ISSN 2321-2705, 2018.

Paper ID: 5600
International Conference on Mechanical, Manufacturing and Process Engineering (ICMMPE – 2022)
Organizer: Faculty of Mechanical Engineering, Dhaka University of Engineering & Technology (DUET), Gazipur, Bangladesh
Website: https://icmmpeduet.com/

Investigation of Structural and Optical Properties of Pure and Cr-doped ZrO_2 Thin Film, synthesized by Spray Pyrolysis

Syed Muhammad Al Amin[1], Sanzida Rahman[2] Jiban Podder[3] and Fahmida Gulshan[2]

[1]Department of Materials and Metallurgical Engineering, Dhaka University of Engineering & Technology (DUET), Gazipur, Dhaka, Bangladesh
[2]Department of Materials and Metallurgical Engineering, Bangladesh University of Engineering and Technology (BUET), Dhaka, Bangladesh
[3]Department of Physics, Bangladesh University of Engineering and Technology (BUET), Dhaka, Bangladesh.
E-mail: syedalamin@duet.ac.bd

ABSTRACT

Nano-structured Zirconium oxide (ZrO_2) thin film has been subjected to research for its versatile use in gas sensors, fuel cells, nuclear reactors, and MOSFET gate dielectrics. In the present study, Spray Pyrolysis technique was used to successfully deposit pure and 2%, 4%, 6%, 8% Cr doped ZrO_2 thin films at 400°C. As deposited films are annealed in the air for one hour at 500°C. The structural and optical properties are investigated by using X-ray Diffraction and UV-VIS spectroscopy. XRD results show that all the films are polycrystalline with cubic crystal structure and have orientation preferably at (111). The lattice constant of pure ZrO_2 thin films is found to be 5.107 Å which varies slightly in Cr doped films. The crystallite size increases to 42 nm then decreases to 25 nm with Cr doping. Pure ZrO_2 thin films show about 75% transparency in the visible region and Cr doped films show a reduced transmittance with a maximum of about 45% transparency. Pure ZrO_2 thin films show a bandgap of 3.96 eV which changes in the range of 3.91-3.98 eV with doping percentage.

Keywords: ZrO2 thin film; Spray pyrolysis; Nanostructured thin film; Polycrystalline; Bandgap.

1. INTRODUCTION

Transition metal oxide thin film has recently piqued researchers' interest as a potential topic because of its applications in Light-emitting diodes(LEDs), supercapacitors, gas sensors, antireflective coating, and optoelectronic devices. Among many metals oxide, Zirconium oxide (ZrO_2) is one of the fascinating transition-metal oxide because of its unique physical, chemical, electrical, optical properties. Zirconium oxide has wide bandgap energy, high refractive index, high transparency in the visible region, low electrical conductivity, good thermal and chemical stability in contact with silicon [1]. ZrO_2 has three polymorphs: cubic, tetragonal, and monoclinic phases. The monoclinic phase is thermodynamically stable at room temperature, but at higher temperatures, the monoclinic phase become unstable and transformed into tetragonal and then cubic phases [2], [3]. The monoclinic phase transformed into tetragonal phase at 1205°C (1478 K) and transition from tetragonal to cubic phase occur at 2377°C (2650 K) [4]. ZrO_2 has application in fuel cells, thermal barrier coatings, and radiative protection. Furthermore, zirconium oxide used in dental restorations and biomedical hip implants [5]. Zirconia has recently been used as a replacement for SiO_2 in MOSFET gate dielectrics in the semiconductor industry.

Due to its wide range of practical applications, ZrO_2 thin films has been synthesized on different substrates by using a variety of deposition techniques. The ZrO_2 thin films have been synthesized by using numerous techniques such as spin coating method, pulse laser deposition, atomic layer deposition, RF magnetron sputtering, solution combustion method , dip coating method, chemical spray pyrolysis and ultrasonic spray pyrolysis method [6]–[9].

Only a few works have been done with Cr doped ZrO_2 thin films using the spray pyrolysis technique. The Spray Pyrolysis Technique (SPT) is widely used because of its simplicity and affordability. It is much more economical compared to other deposition techniques (such as sol-gel and chemical vapor deposition) which require several steps or a vacuum for deposition. In addition, spray pyrolysis offers a wide range of possibilities to prepare advanced ceramic powders and deposit films due to its wide chemical flexibility. For this reason, spray pyrolysis is used to deposit Pure and Cr doping ZrO_2 thin films and the effects of Cr doping on the structural, optical properties ZrO_2 thin film is investigated.

This paper consists of a total four sections. In the introduction, literature review of ZrO_2 thin films has been represented. The next section shows the detailed methodology of this study. In the results and discussion, the obtained data in this study are presented with comprehensive discussions. In the conclusion, summarized concluding remarks have been highlighted.

2. METHODOLOGY

Zirconium oxychloride ($ZrOCl_2.8H_2O$) used as mother solution and Chromium oxide (CrO_3) used as Cr source. 0.1M 100ml solutions were prepared using distilled water and adding calculated amount of reagents. It was magnetically stirred for 1 hour. So that the reagents completely dissolves. Then the solution was filtered using filter paper.

Fig 1: Powder of $ZrOCl_2.8H_2O$(left) and CrO_3 (right)

Glass substrates were firstly washed with detergent. Then they were washed with distilled water. Finally, they were washed with acetone and dried in hot air. Mild steel mask was used to cover the glass substrate. It allows condensation of the evaporated solution only in the exposed substrate areas.

The substrates were preheated to 450°C on hot plate. The solution was sprayed on the substrate at a constant rate while maintaining the substrate temperature ~400 °C for 10 minutes. Then film was kept on the hot plate for additional 6 minutes for homogenization. The samples were annealed for 1 hour at 500°C to enhance stability & crystallinity.

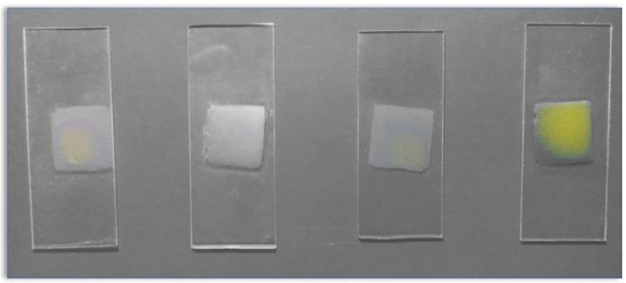

Fig. 2: Cr Doped ZrO_2 thin film on glass substrate

3. RESULTS & DISCUSSION

X-ray Diffraction and UV-VIS spectroscopy is used to investigate the structural and optical properties of undoped and doped ZrO_2 thin films

3.1 Structural Properties

The X-ray diffraction pattern of Pure and 2%, 4%, 6% 8% Cr doped ZrO_2 thin films deposited on glass substrate at 400°C are shown in Fig.3. All the prepared films are polycrystalline in nature & consist of cubic zirconium oxide phase. All the peaks in the patterns are indexed using the ICDD database by matching with samples having reference code 00-007-0337. The formation of cubic phase in pure ZrO_2 is attributed to crystal-size effects [10]. In case of Cr doped films, no additional peaks are found which indicate that no other phase other than cubic ZrO_2 is present in thin films. Doping of Cr results in a shifting of 2θ value of main peak (111).

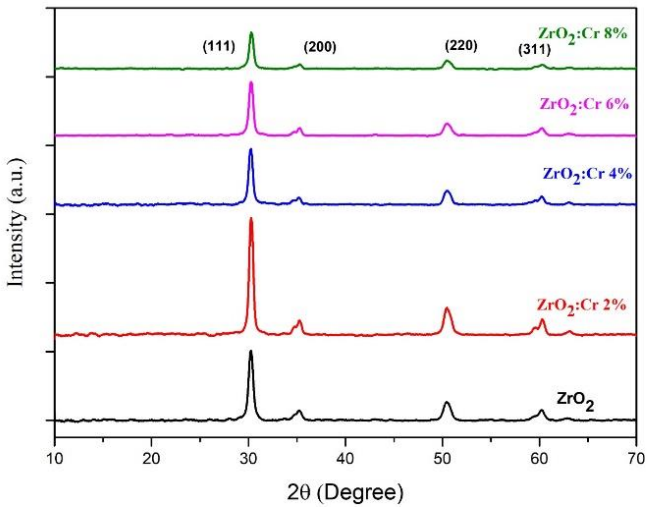

Fig. 3: XRD pattern of undoped and Cr doped ZrO_2 thin films

Lattice parameters are listed in Table 1. Both pure and Cr doped ZrO_2 films have lattice parameters close to 5.10 Å which are comparable to the standard values for ZrO_2 [11]. Cr doping sightly affect lattice parameters of the cubic crystal of ZrO_2. Possible reason may be smaller size of Cr^{3+} ion compared to Zr^{4+}. The Ionic radius of Zr^{4+} and Cr^{3+} are respectively 79 nm and 50 nm. As Cr^{3+} is smaller in size, when it substitutes Zr^{4+} ion, a little distortion occurs inside the crystal [9].

Table 1: Lattice Parameters of Pure and Cr-doped ZrO2 thin films

Sample	Lattice Parameter Å
Standard	5.11
ZrO_2	5.107
2% Cr doped ZrO_2	5.103
4% Cr doped ZrO_2	5.107
6% Cr doped ZrO_2	5.106
8% Cr doped ZrO_2	5.094

The Crystallite size of the Pure and doped ZrO_2 thin films are calculated using Debye–Scherrer equation

$$D = \frac{0.9\lambda}{\beta cos\theta} \quad (1)$$

Change in crystallite size with % doping is presented in Fig.4. All samples are nanocrystalline (<100nm). Crystallite

size increase to 45 nm due to Cr^{3+} substituting Zr^{4+} & then decrease to 25 nm due to formation of stress & segregation of dopants in GB.

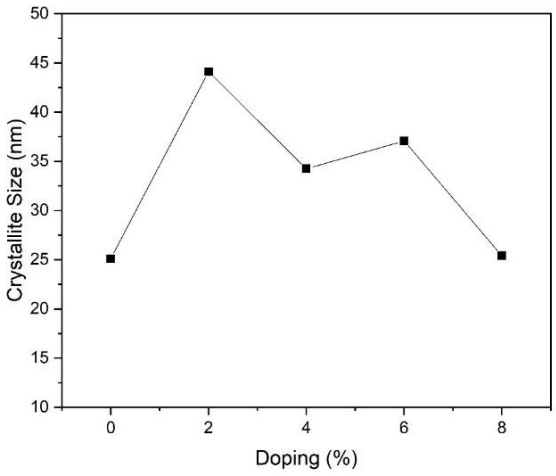

Fig.4: Variation of Crystallite size with Cr doping concentration

3.2 Optical Properties

Optical Transmission spectrum of Pure and Cr doped ZrO_2 films are presented in the wavelength region of 300-800 nm in Fig. 5. Pure, 4%, 8% Cr doped ZrO_2 film high transparency (~75%) in the visible region. 2% ,6% Cr doped ZrO_2 film show reduced transmittance (~45%). The decrease of transmittance can be attributed to light scattering by O_2 vacancies & scattering in grain boundaries [12].

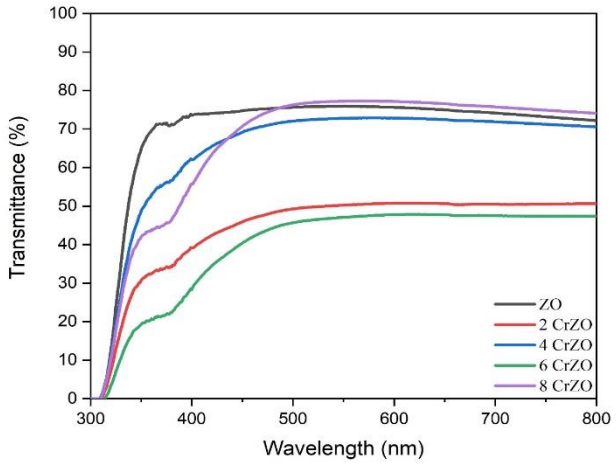

Fig. 5: Variation of transmittance with wavelength for ZO_2 and Cr doped ZO_2 thin films.

The optical bandgap was calculated based on spectral absorption using Tauc's relation equation mentioned in equation (2). The linear regions of the $(\alpha hv)^2$ versus hv plots are extrapolated on the energy axis showed in Fig. 6.

$$\alpha hv = B\,(hv - E_g)^2 \qquad (2)$$

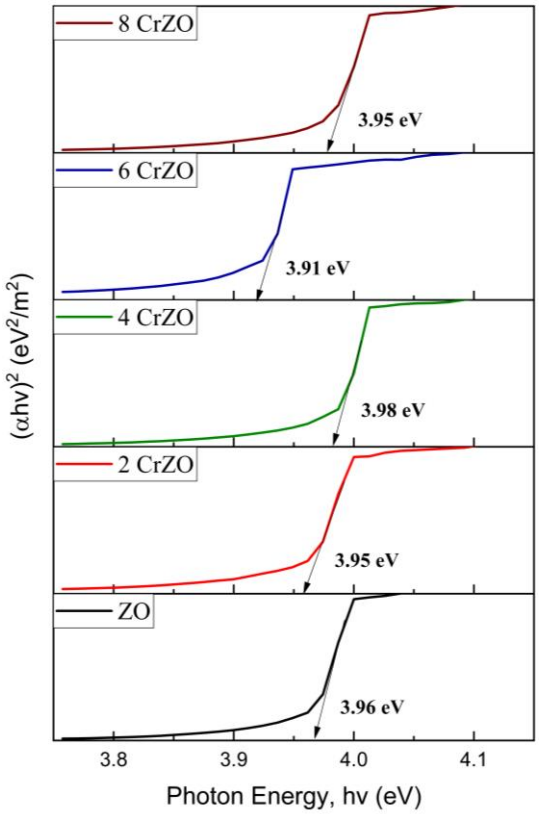

Fig. 6: Bandgap of ZO_2 and Cr doped ZO_2 thin films

Pure ZrO_2 shows a bandgap of 3.96 eV. The band gap energy of Cr doped ZrO_2 films is in the range of 3.91-3.98 eV. Emerging of the impurity level formed by Cr ions & Moss–Burstein effect simultaneously effect and create variation in bandgap of Cr doped thin films [13].

4. CONCLUSION

In this study, Pure and Cr doped ZrO_2 thin films with dopants concentrations of 2%, 4%, 6%, 8% are synthesized onto glass substrates at 400°C and then annealed at 500°C for one hour. The influence Cr doping concentration on structural and optical properties of ZrO_2 films are studied elaborately. All synthesized thin films are polycrystalline in nature and has cubic ZrO_2 phase. All films are nanocrystalline with in between 25nm to 44nm crystallite size. Lattice parameters of Cr doped ZrO_2 films remain close to Pure ZrO2 films due to smaller size of Cr ions. Pure ZrO_2 film shows high transparency (75%) in the visible region. Transmittance decreases by Cr-doping. The bandgap of Pure ZrO_2 film found to be 3.94 eV. With the addition of Cr, bandgap varies slightly. It can be inferred that Pure, Cr-doped ZrO_2 thin films synthesized by spray pyrolysis technique have good crystalline quality, high transparency in the visible region. The produced high quality Pure, Cr doped ZrO_2 thin films can be suitable for optoelectronic applications such as optical

filters, memory devices, capacitors in dynamic random-access memories.

REFERENCES

[1] A. Hojabri, "Structural and optical characterization of ZrO2 thin films grown on silicon and quartz substrates," *J. Theor. Appl. Phys.*, vol. 10, no. 3, pp. 219–224, Sep. 2016, doi: 10.1007/s40094-016-0218-8.

[2] X. Zhao and D. Vanderbilt, "Phonons and lattice dielectric properties of zirconia," *Phys. Rev. B*, vol. 65, no. 7, p. 075105, Jan. 2002, doi: 10.1103/PhysRevB.65.075105.

[3] G. Stapper, M. Bernasconi, N. Nicoloso, and M. Parrinello, "***Ab initio*** study of structural and electronic properties of yttria-stabilized cubic zirconia," *Phys. Rev. B*, vol. 59, no. 2, pp. 797–810, Jan. 1999, doi: 10.1103/PhysRevB.59.797.

[4] A. Kuwabara, T. Tohei, T. Yamamoto, and I. Tanaka, "*Ab initio* lattice dynamics and phase transformations of Zr O 2," *Phys. Rev. B*, vol. 71, no. 6, p. 064301, Feb. 2005, doi: 10.1103/PhysRevB.71.064301.

[5] A. Chroneos, B. Yildiz, A. Tarancón, D. Parfitt, and J. A. Kilner, "Oxygen diffusion in solid oxide fuel cell cathode and electrolyte materials: mechanistic insights from atomistic simulations," *Energy Environ. Sci.*, vol. 4, no. 8, p. 2774, 2011, doi: 10.1039/c0ee00717j.

[6] M. T. Soo *et al.*, "Elaboration and characterization of sol–gel derived ZrO2 thin films treated with hot water," *Appl. Surf. Sci.*, vol. 258, no. 13, pp. 5250–5258, Apr. 2012, doi: 10.1016/j.apsusc.2012.02.008.

[7] S. Salari and F. E. Ghodsi, "A significant enhancement in the photoluminescence emission of the Mg doped ZrO2 thin films by tailoring the effect of oxygen vacancy," *J. Lumin.*, vol. 182, pp. 289–299, Feb. 2017, doi: 10.1016/j.jlumin.2016.10.035.

[8] K. Kukli *et al.*, "Atomic layer deposition and properties of mixed Ta 2 O 5 and ZrO 2 films," *AIP Adv.*, vol. 7, no. 2, p. 025001, Feb. 2017, doi: 10.1063/1.4975928.

[9] A. H. O. Alkhayatt, S. A. Hussain, and E. A. Mahdi, "An investigation in to the impact of Ti doping on the structural, optical and sensing properties of spray deposited nanocrystalline ZrO2 thin films," *Optik*, vol. 159, pp. 305–314, Apr. 2018, doi: 10.1016/j.ijleo.2018.01.078.

[10] M. Tsuchiya, A. M. Minor, and S. Ramanathan, "Size-dependent phase transformations in nanoscale pure and Y-doped zirconia thin films," *Philos. Mag.*, vol. 87, no. 36, pp. 5673–5684, Dec. 2007, doi: 10.1080/14786430701708349.

[11] R. A. Ploc, "The lattice parameter of cubic ZrO2 formed on zirconium," *J. Nucl. Mater.*, vol. 99, no. 1, pp. 124–128, Jul. 1981, doi: 10.1016/0022-3115(81)90146-X.

[12] N.-Q. Yao, Z.-C. Liu, G.-R. Gu, and B.-J. Wu, "Structural, optical, and electrical properties of Cu-doped ZrO 2 films prepared by magnetron co-sputtering," *Chin. Phys. B*, vol. 26, no. 10, p. 106801, Sep. 2017, doi: 10.1088/1674-1056/26/10/106801.

[13] K. Joy, "Microstructure and optical properties of Ag-doped ZrO2 thin films prepared by sol gel method," J. Sol-Gel Sci. Technol., vol. 66, no. 2, pp. 293–300, May 2013, doi: 10.1007/s10971-013-3007-8.

Paper ID: 5710
International Conference on Mechanical, Manufacturing and Process Engineering (ICMMPE – 2022)
Organizer: Faculty of Mechanical Engineering, Dhaka University of Engineering & Technology (DUET), Gazipur, Bangladesh
Website: https://icmmpeduet.com/

Investigation of Arc Welding Joining Effects on Tensile Behavior of Marine Grade-A Mild Steel

M Muzibur Rahman[1], Maher Niger Prova[1], M Abdul Halim[1], S Reaz Ahmed[2]

[1]Department of Naval Architecture & Marine Engineering, Military Institute of Science and Technology (MIST), Dhaka
[2]Department of Mechanical Engineering, Bangladesh University of Engineering and Technology (BUET), Dhaka

E-mail: muzib1061@gmail.com

ABSTRACT

Welding is contributing the shipbuilding industries to produce perfectly watertight and oil-tight arrangements in ships with reasonable strength. However, welding line is a concern for failure under wave stress on ship at sea especially at rough weather. Therefore, it is very important to assess the mechanical strength of the weld joint for the sustainability of the vessel. But many aspects on this issue are yet to be addressed, and as such, the present paper is an attempt to evaluate the tensile behavior of a welding joint of marine grade mild steel. So, marine mild steel plates were collected and welding joints were developed by international class certified welder to make specimens and a series of experiments were carried out to observe the tensile behavior. The results of the investigations indicate that there is a significant decrease in tensile strength as well as fracture elongation of the samples at the joints developed by welding. Elastic modulus values are also being reduced as a consequence of welding joint. SEM images indicate the brittle fracture failure mode of welded marine grade mild steel whereas at seamless condition it has been found as ductile in nature. The toughness based on tensile behavior was also found decreased after welding by about 15% indicating the vulnerability level of welded joints. As a whole, the results obtained through the present work provides ingredients to the ship-builders as well as ship-owners for planning the schedule of periodical docking and maintenance of vessels.

Keywords: Marine grade; Mild steel; Arc welding; Tensile behavior.

1. INTRODUCTION

Welding is a process that is used in a wide variety of industries, be it aerospace, automotive, railroad, or any production industry. Most importantly, the shipbuilding industry relies heavily on the perfection of welding processes. Welding has become vital in the shipbuilding process since it can create joints that are water and oil-tight. To maintain the integrity of the ship, a strong weld joint is essential and the methods include shielded metal arc welding (SMAW), gas metal arc welding (GMAW), submerged arc welding (SAW), gas tungsten arc welding (GTAW), resistance welding (RW), etc. Amongst them, SMAW is the most popular for joining steel plates in shipbuilding and large diameter pipes manufacturing [1],[2]. Usually, SMAW is making hundreds of joints with several kilometers of welding lines to construct a ship. These welding lines on mild steel plates are more vulnerable than the plate itself due to number of reasons including lamellar tearing arising in joints especially in which the fusion boundary of the weld is parallel to the plate surface [3], [4].

In addition, the weld seam is left with residual stresses that lie around the yield strength of the material. Welding may also change in the microstructure and bonding energy distribution especially in the heat-affected zone (HAZ). So, one of the critical issues with welds is typically catastrophic failure of joints in machine parts or hull and in turn it affects the service life of the ship [2], [5]. A good number of research works are found in the literature survey dealing with welding process, welding defects, welding parameters, etc. For instance, Kumar and Kumar (2014) worked on the effect of input parameters on the mechanical properties during the metal inert gas welding (MIG) of mild steel [6]. Mohanta and Senapati (2018) investigated the effect of welding parameters on depth of penetration and heat input [7]. Samir (2015) investigated the effect of welding current on welding speed and hardness of heat effected zone and weld metal of mild steel material [8]. Yadav et al (2014) analyzed the HAZ of mild steel specimen for MIG welding for hardness and tensile strength [9]. Few more works can also be found in [10]-[16], however, there is a research gap yet to be carried out with respect to steel welding, especially, for marine grade mild steel (MS). It may be mentioned that marine grade steel has

slightly more alloying elements such as manganese, chromium, etc. compared to their ASTM grade counterparts, which helps to achieve higher strength and more corrosion resistance for shipbuilding applications. Therefore, this paper is an attempt to investigate the tensile behavior of marine grade MS prior and after arc welding experimentally and compare the results with finite element analysis.

2. MATERIALS AND METHODS

2.1 Sample Materials

Marine Grade-A mild steel has little higher alloying elements especially chromium to suite the structural requirements of ships and offshore installations in aggressive environments at sea. As such, the grade of this mild steel is approved by an International Association of Classicification Societies (IACS) authorised member classification society, such as, American Bureau of Shipping (ABS) of USA, Lloyd's Register (LR) of UK, Nippon Kaiji Kyokai (NKK) of Japan, etc. and the marine grade mild steel has no exact equivalency of ASTM grade. To carry out the present study, marine grade-A mild steel plates of size 6000 × 2000 × 5 mm were collected from a local shipyard of Bangladesh and cut into pieces of 300 × 300 × 5 mm.

To prepare welded samples few pieces of plates were butt-welded together. The welding parameters followed by the welders were 415 V and 155 A Current and single pass on both sides of the plate. The base metal parts were tack welded near two outer edges before welding to ensure proper joint between them. The welding was carried out by Classification Society qualified welders having enough experiences in 6G welding to ensure high standard quality requirements of shipbuilding industries. Moreover, the integrity of welding lines was inspected using Electro Magnetic Yolk.

The filler metal used in the process is coated MS electrodes (NAVANA Bond Marine Electrode E6013) of 3.2 mm diameter. These electrodes are specially designed for the use in multiple positions, i.e., down hand, horizontal, vertical upward and overhead welding positions for the construction of ships.

Test specimens were then made from both welded and non-welded plates as of dog bone shape with size 200 × 20 × 5 mm having gauge length (GL) of 50 mm following ASTM E-8. All the samples were sized using Computerized Numerical Control (CNC) plasma cutting machine so that dimensional accuracy could be maintained. After developing welded and seamless specimens, the chemical compositions both welded and seamless materials were examined using spectrometer test and the results found are shown in table 1.

Table 1: Chemical composition of sample materials (mass fraction %)

Elements	Marine Grade Seamless Mild Steel	Marine Grade Welded Mild Steel
Carbon	0.18	0.10
Silicon	0.11	0.16
Manganese	0.28	0.27
Chromium	0.12	0.06
Molybdenum	0.16	0.17
Cobalt	0.61	0.96
Niobium	0.14	0.15
Cerium	0.60	0.17
Tantalum	0.14	0.12
Iron	97.66	97.84

2.2 Experimental Investigations

A series of tensile experiments using the prepared specimens from both welded and non-welded (seamless) marine grade-A plates were carried out. Each experiment was repeated using similar samples to have data reliability for both seamless as well as welded plates. Hydraulic type universal testing machine (UTM) of Model No.1000HDX-G-G7CB was employed to perform the tensile tests for both group samples, i.e., seamless and welded materials. The UTM was operated at its preset default cross head speed, i.e., 5 mm/min in elastic strain range and 10 mm/min in plastic strain range.

Microstructures were examined using optical electronic microscope (OEM) of model BW-S500 having computer interfacing arrangement. In addition, the surface morphologies before and after tensile failure of sample materials were investigated using a field emission scanning electron microscope (FE-SEM) of model JEOL JSM-7600F with the magnification of ×500, ×1000, ×2000 and ×30000. EDX spectra of samples were also recorded by an electron dispersive spectrometer of model JEOL EX-37001 associated with the FE-SEM set up.

2.3 Finite Element Analysis

For finite element analysis (FEA), ANSYS Workbench was utilized, and FE model of the tensile test specimen was generated using SPACECLAIM 2021 R2 following ASTM Standard as to the experimental tensile test specimen. Since

there was no default engineering data for marine grade mild steel in ANSYS, a new material was created and the properties were given input for the created seamless material. Similarly, mechanical properties for welded Mild Steel were also given input as a new material. Accordingly, the properties for welded and seamless mild steel were assigned to the generated model before starting the analysis. Meshing was done with optimum element size with the application of 5 mm for tensile test of the FE model. During the execution of ANSYS program, one end of specimen model was applied with fixed support and the other was applied with an amount of displacement only in the longitudinal direction of the model. In this analysis, the model was given a displacement at which it reaches its fracture point and break down. Thereafter, the post processing is done which involves evaluating the solution after the solver tool is commanded. Specifying result items for this analysis are total deformation, directional deformation, equivalent stress, maximum principal stress, equivalent elastic strain and equivalent plastic strain.

3. RESULTS AND DISCUSSION

3.1 Tensile Behavior Obtained by UTM Tests

Load deflection data obtained through the tensile tests carried out using UTM have provided the stress-strain curves of usual patterns for both seamless and welded sample materials. The stress-strain results of five samples from each group are illustrated in fig. 1(a) and 1(b), respectively. Fig. 1(a) indicates that all five seamless samples are of ductile in nature with good tensile strength and high strain values to reach at the fracture point. Fig. 1(b) indicates similar stress-strain relations of welded samples up to some extent but the strain failed to reach the values of seamless material. Ultimate Tensile Strength (UTS) of seamless samples obtained on average from number tests is 551.14 MPa and the same for welded sample is 512.5 MPa. Comparing these two values with the reference to UTS of commercial MS, which is usually observed to be 440 MPa or so, they indicate strong behavior of marine grade quality. But, UTS has decreased from the base metal strength by 7% as a consequence of arc welding. It is because of microstructural change in the thermal effect in welding process. The properties of heat affected zone (HAZ) are different from that of base metal. As a result, the other parameters of tensile properties such as yield strength, maximum elongation, elastic modulus, etc. are also found different from their base metal. Thus, the welded sample has shown yield strength of 372 MPa and maximum elongation of 23% without demonstrating the notching period, where the seamless samples have shown their yield strength of 382 MPa and fracture elongation (maximum elongation) of 49%. It is also noticeable that few welded samples have failed even much earlier with significantly less strain values. The elastic modulus of welded sample is observed to be 13 GPa and that of the seamless samples is 12 GPa. Therefore, the stress-strain curves of welded samples shown in fig. 1(b) are steeper at the yield zone than those of fig. 1(a) indicating higher elastic modulus after welding for all observed cases.

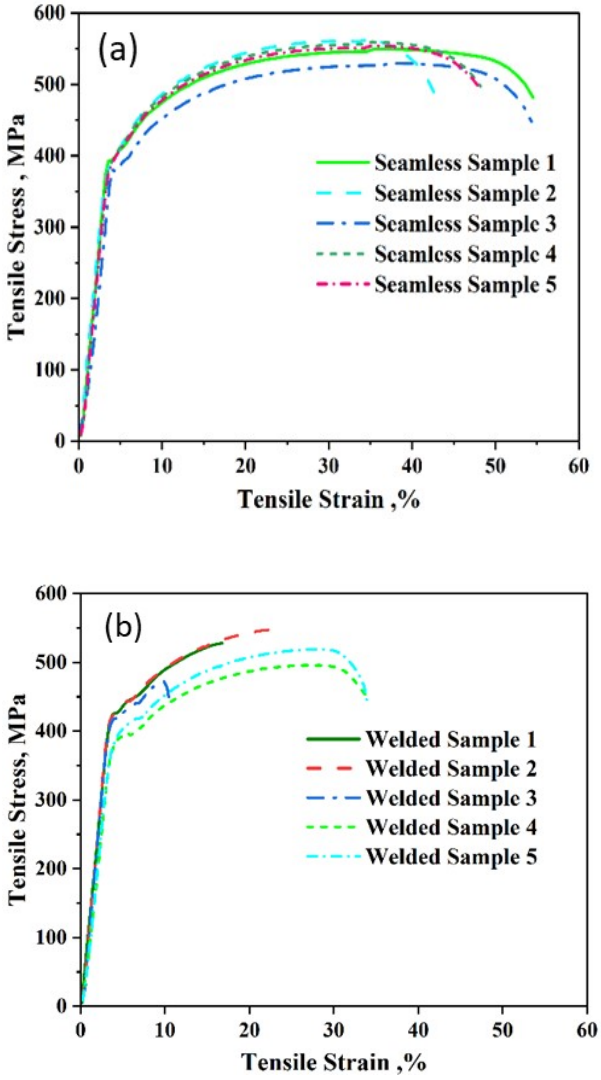

Fig. 1: Stress-strain curves of marine grade MS samples obtained by UTM tests: (a) seamless, (b) welded.

The stress-strain relations on average values of seamless and welded samples are shown in fig 2, which give clear indication of significant reduction in fracture strain level for welding. This reduction of strain has the consequence on the plastic region which in turn has reduced the toughness by about 38% compared to that of seamless MS.

Atcually, none of the samples has failed directly on the welding line, rather, the failure locations of welded samples are in between weld joint and base metal, i.e., very adjacent to the welding line. Therefore, it can be deduced that the base metal adjacent to welding line gets affected differentially than that of bulk material. As a whole, the welded marine grade plate is more prone to crack and failure than the seamless one due to thermal effect that occurred during welding process.

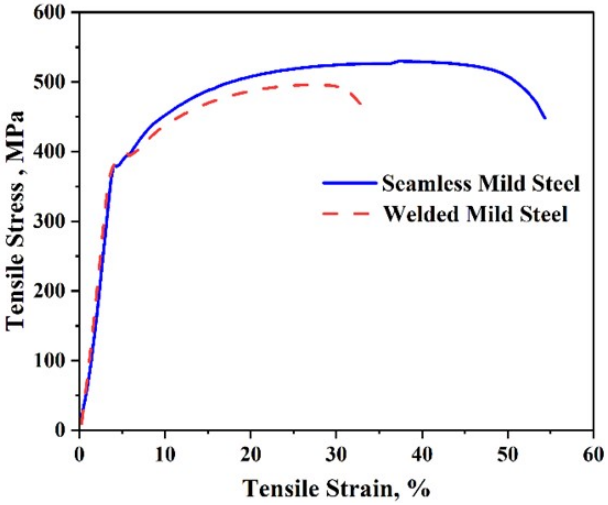

Fig. 2: Comparison of stress-strain behavioral pattern of marine grade MS with and without welding on average values obtained by UTM tests.

3.2 Tensile Behavior Obtained by FE Analysis

The finite element (FE) load-deflection analysis of marine grade mild steel with and without welding for tensile failure as done using ANSYS Workbench are presented in fig. 3 and fig. 4. These two figures indicate the stress concentration in different locations of the specimen, i.e, seamless material on the longer part of the fractured specimen where necking took place during tensile loading, and welded material on the shorter part at the edge of welding line.

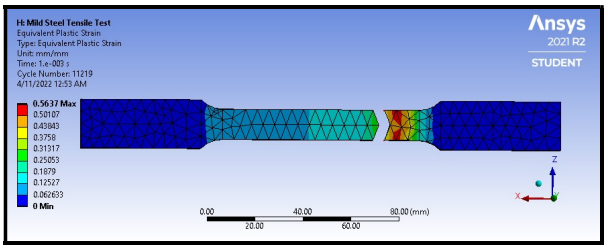

Fig. 3: Finite element analysis of sample for tensile failure obtained using ANSYS Mechanical for seamless marine grade mild steel.

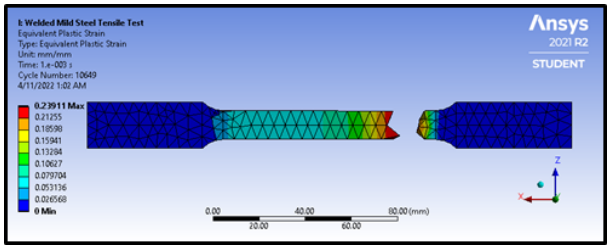

Fig. 4: Finite element analysis of sample for tensile failure obtained using ANSYS Mechanical for welded marine grade mild steel .

The stress-strain behaviors obtained through finite element simulation of both seamless and welded marine grade mild steel are presented in fig.5. The tensile parameters such as ultimate tensile strength and yield strength have been observed to be decreased by an average 7.2% and 2.9% respectively due to welding effect. Moreover, the average fracture strain is seen to be decreased remarkably, i.e., 53% after welding from the average value of seamless samples. The elastic modulus modulus values have also been found decreased as a result of welding.

Fig.5 clearly shows that the slope of stress-strain curve in the yield zone for welded material is higher than that of seamless material. It indicates the gaining of higher elastic modulus but sacrificing the strength. The seamless samples have displayed more ductile behavior with considerable ultimate strain values (about 55%) before tensile failure. On the other hand, welded samples have failed much earlier, i.e., at about 25% strain value. So, marine grade mild steel on the welding lines is harder and also more brittle than base plates of the ship.

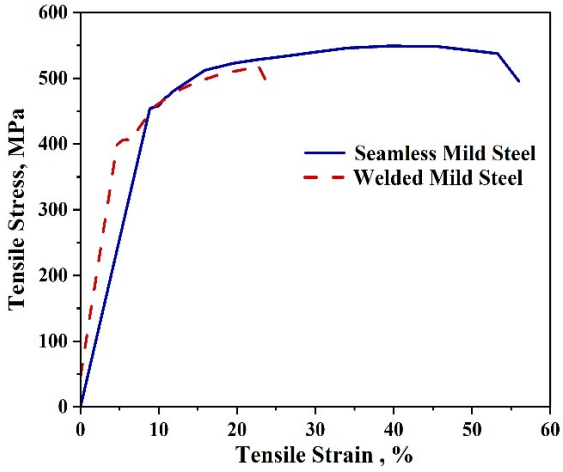

Fig. 5: Stress-strain curves of marine grade MS with and without welding obtained by FE simulation.

3.3 Comparison of FE Analysis and Experimental Results

If the stress-strain curves obtained from UTM tests is compared with the FE simulation results, a good agreement is observed. Fig. 6 and 7 are showing the comparative trends of stress-srain curves obtained through numerical methods and experimental works for seamless and welded mild steel specimens, respectively.

The UTS and elastic modulus calculated based on experimental results is approximately close to the values obtained using ANSYS although the yield strength seems higher in ANSYS result than that of the experimental results. This represents the specimen should have shown more elasticity but due to environmental and thermal effect it shows less elasticity in tensile test.

The graphs obtained by FE analysis are of similar pattern of stress-strain behavior obtained in the experimental results. Both means of investigations depict that the welding joints on marine grade mild steel plates have resulted in higher brittleness and lower strength than that of seamless plates.

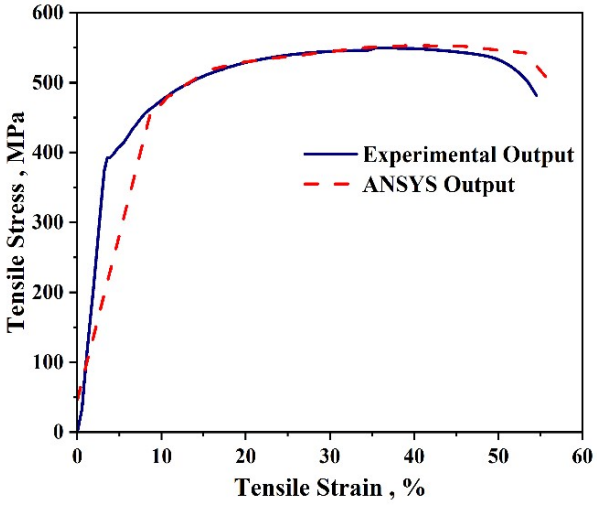

Fig. 6: Comparison of experimental stress-strain curve with FE simulation curve of seamless marine grade MS.

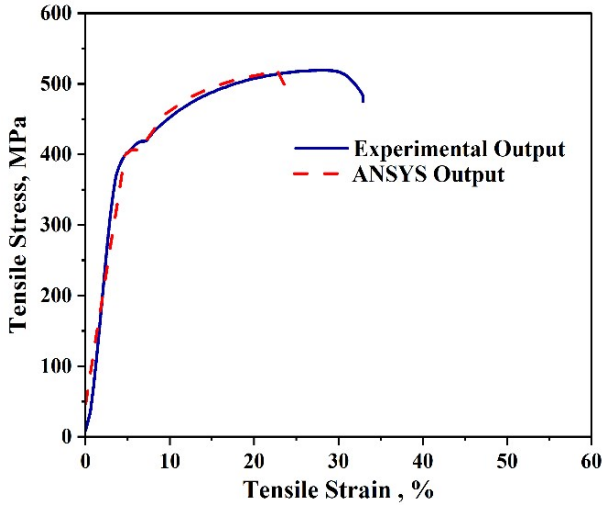

Fig. 7: Comparison of experimental stress-strain curve with FE simulation curve of welded marine grade MS.

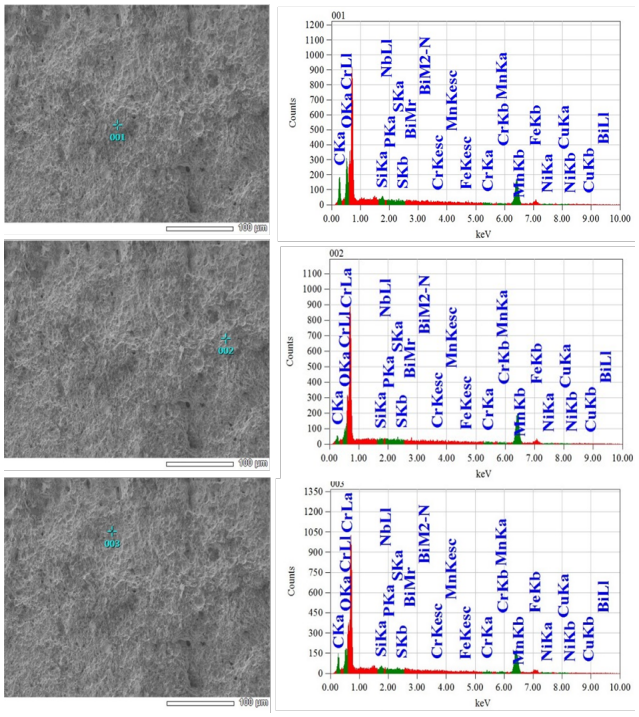

Fig. 8: SEM images and corresponding EDX spectra taken at different points on the fractured surface of seamless marine grade MS sample.

3.4 Microstructure of Tensile Fracture

The fractured surfaces of both seamless and welded samples were investigated after tensile tests and the differentiable FE-SEM images have been observed at number of locations of the samples. The FE-SEM images of seamless marine grade mild steel are presented in fig. 8 which depicts the more or less ductile nature failure with plastic collapses as similar to the observations in [17]-[19].

On the other hand, fig. 9 presents the FE-SEM images of failure surfaces of welded marine grade MS indicating little difference in tensile failure than that of seamless MS. It has occurred due to phase changes and crystallographic changes during thermal treatments in the welding process with grain size deformation and their coarsening. Here, the FE-SEM images are indicating the ductile nature of tensile failure along with the presence of partial shear of brittle mode failure mechanism [20],[21].

The FE-SEM correspding EDX results provide the indication of carbide formation in welded specimen. This can also be considered as a cause of higher elastic modulus and presence of brittle mode in tensile failure of welded specimen.

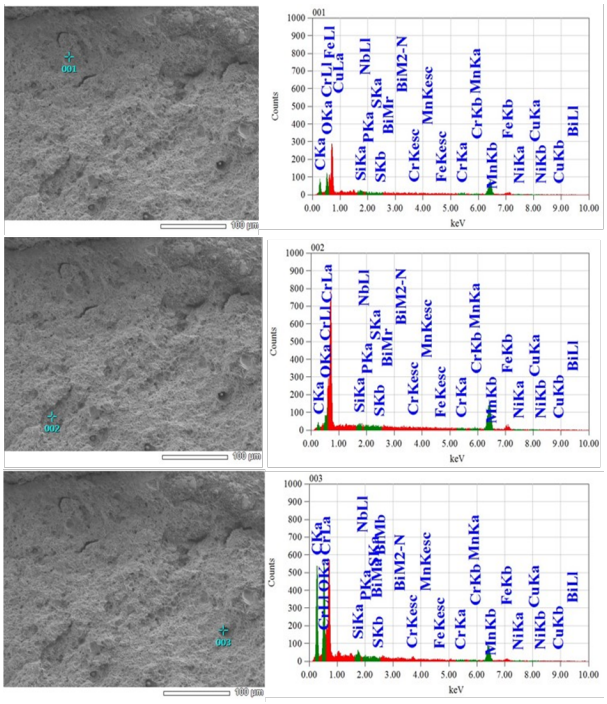

Fig. 9: SEM images and corresponding EDX spectra taken at different points on the fractured surface of welded marine grade MS sample.

4. CONCLUSION

The investigations carried out with the sample materials of mild steel marine grade-A with and without welding joint to compare the tensile behavior have brought the following findings in summarized form:

i. The tensile parameters observed from UTM tests, such as, ultimate tensile strength and yield strength have been observed to be decreased by an average 7% and 2.86% respectively due to welding effect. Moreover, the average fracture strain is seen to be decreased remarkably, i.e., 53% after welding from the average value of seamless samples.

ii. FE analysis has also shown similar behavioral changes in tensile parameters as the consequence of welding on marine grade mild steel.

iii. The FE-SEM images of tensile fracture surfaces provide the difference in failure pattern of seamless and welded sample. It is observed that the seamless mild steel has ductile inception while the welded ones have more of a brittle failure.

ACKNOWLEDGMENT

The authors are grateful to Dockyard & Engineering Works (DEW) Narayanganj for providing marine grade mild steel plates, Bangladesh University of Engineering & Technology (BUET) and Military Institute of Science & Technology (MIST) for providing laboratory facilities to carry out the research experiments.

REFERENCES

[1] N.R. Mandal, Ship construction and welding. Springer Series on Naval Architecture, Marine Engineering, Shipbuilding and Shipping Vol 2, 152 Beach Road, Gateway East, Singapore, 2017.

[2] P.L. Moore, The importance of welding quality in ship construction, in: G.G. Soares, P.K. Das, Analysis and Design of Marine Structures, Taylor & Francis, England, 2009.

[3] B. Norman (1994). Weldability of Ferritic Steels. Abington Publishing, Cambridge, England, 102-117.

[4] G. Vukelić, G. Vizentin, Common Case Studies of Marine Structural Failures, in: A. Ali, Failure Analysis and Prevention, IntechOpen, London, UK, 2017.

[5] S. Mamat, N.A. Sidek, N.A.A.M. Afandi, R.A.E. Roslan, T.P. Ter, T. Yuji, S. Tashiro, M. Tanaka, Observation of Microstructure and Mechanical Properties in Heat Affected Zone of As-Welded Carbon Steel by Using Plasma MIG Welding Process. *Metals* (2022) 12(2):315. doi.org/10.3390/met12020315

[6] R. Kumar, S. Kumar, Study of mechanical properties in mild steel using metal inert gas welding. IJRET (2014), 3(4), 751-756.

[7] G.K. Mohanta, A.K. Senapati, The effect of Welding Parameters on Mild Steel by MMAW. In IOP Conf. Series: Materials Science and Engineering, 410 (2018), 012015. doi:10.1088/1757-899X/410/1/012015

[8] Y. Samir, Investigation on effect of welding current on welding speed and hardness of HAZ and weld metal of mild steel. Int. J. Res. Eng. & Tech., 4(3), (2015), 44-48.

[9] P.K. Yadav, M. Abbas, S. Patel, Analysis of heat affected zone of mild steel specimen developed due to MIG welding, Int. J. Mech. Eng. & Rob. Res. 3(3), (2014), 399-404.

[10] B.K. Khamari, P.K. Sahu, B. B. Biswal, Microstructure Analysis of Arc Welded Mild Steel Plates, IOP Conf. Series: Materials Science and Engineering 377 (2018) 012049. doi:10.1088/1757-899X/377/1/012049

[11] Z. Boumerzoug, C. Derfouf, T. Baudin, Effect of welding on microstructure and mechanical properties of an industrial low carbon steel, Engineering, 2(7), (2010), 502.

[12] T. Tadavi, B. Jogi, S. Dhende, S. Banait, P. Wagh, Microscopic analysis of heat affected zone (HAZ) of submerged arc welding (SAW) joint for 1018 mild steel sheet, Int. Conf. on Comm. and Sig. Pro. (2016), 194-199. doi.org/10.2991/iccasp-16.2017.32

[13] O.B. Owolabi, S.C. Aduloju, S. C. Metu, C. E. Chukwunyelu, E.C. Okwuego, Evaluation of the effects of welding current on mechanical properties of welded joints between mild steel and low carbon steel. Am. J. Mater. Sci. Appl, 4(1), (2016) 1.

[14] D. Sumardiyanto, S. E. Susilowati, Effect of Welding Parameters on Mechanical Properties of Low Carbon Steel API 5L Shielded Metal Arc Welds, American J. of Materials Science, 9 (1), (2019), 15-21. doi: 10.5923/j.materials.20190901.03.

[15] S.F. Haider, M.M. Quazi, J. Bhatti, M.N. Bashir, I. Ali, Effect of Shielded Metal Arc Welding (SMAW) parameters on mechanical properties of low-carbon, mild and stainless-steel welded joints: A review, J. of Adv. in Tech. & Eng. Res., 5(5), (2019), 191-198. doi: 10.20474/jater-5.5.1

[16] S.I.A. Talabi, O.B.B. Owolabi, J.A.A. Adebisi, T. A. Yahaya, Effect of welding variables on mechanical properties of low carbon steel welded joint. Advances in Production Engineering & Management, 9(4), (2014), 181-186. http://dx.doi.org/10.14743/apem2014.4.186.

[17] B. C. Cerik, J. Choung, Ductile Fracture Behavior of Mild and High-Tensile Strength Shipbuilding Steels, *Appl. Sci.* 2020, *10*, 7034; doi:10.3390/app10207034

[18] Krasovskii, A. Y., Stepanenko, V. A., & Voinitskii, A. G. (1971). The mechanical properties and failure of mild steel in tension. Strength of Materials, 3(3), 298–303. doi:10.1007/bf01527442

[19] E.A. Alhassan, D.A. Olasehinde, A. Musonda1, O.M. Odeniyi, Tensile and flexural behaviour of steel materials used in the construction of crop processing machines, IOP Conf. Series: Earth and Environmental Science 445 (2020) 012044. doi:10.1088/1755-1315/445/1/012044

[20] T.R. Mahmood, Q.M. Doos, A.M. Al-Mukhtar, Failure Mechanisms and Modeling of Spot Welded Joints in Low, Structural Integrity Procedia 00 (2016) 000–0. doi: 10.1016/j.prostr.2018.06.013

[21] M. Kang, I.H. Jeon, H.N. Han, C. Kim, Tensile–Shear Fracture Behavior Prediction of HighStrength Steel Laser Overlap Welds, *Metals (*2018), *8*, 365. doi:10.3390/met8050365

Paper ID: 6076

International Conference on Mechanical, Manufacturing and Process Engineering (ICMMPE – 2022)

Organizer: Faculty of Mechanical Engineering, Dhaka University of Engineering & Technology (DUET), Gazipur, Bangladesh

Website: https://icmmpeduet.com/

Adsorptive Removal of Congo Red by using Rice Husk

S.M Sharif Iqbal Zaman, Md. Mahbub Hasan, Rajesh Chanda, Biplob Kumar Biswas*

Department of Chemical Engineering, Jashore University of Science and Technology, Jashore-7408, Bangladesh

E-mail: bk.biswas@just.edu.bd (corresponding author)

ABSTRACT

Congo red (shortly CR) is one of the most toxic anionic dyes, which causes severe health problems to human. Along with many other industries, textile industries used to discharge a considerable amount of wastewater which contains congo red and other colorful dyes, which are considered as pollutants. The removal of such type of dyes from industrial effluents and other wastewaters is a major challenge now-a-days. Adsorption is the most promising method for remediation to water pollution. In this study, rice husk (RH) was chemically modified (by using citric acid) to prepare a low-cost bio-adsorbent for removal of congo red from synthetic wastewater. Batch-wise adsorption was conducted by varying solid-to-liquid ratio (i.e. adsorbent dose), pH, time, and congo red concentration of the solution to find the effect of those factors. The physical properties of the modified rice husk adsorbent were examined FE-SEM, moisture content and bulk density. The maximum adsorption efficiency of modified rice husk was found to be 92% at pH 3 and at a dosage of 3.5 g/L. The optimum reaction time was 120 min at a shaking speed of 200 rpm and at room temperature. The result showed that a locally available and cheap biowaste material (rice husk) can be considered as a useful precursor for preparing an efficient adsorbent for congo red removal (through adsorptive removal) from aqueous solution.

Keywords: Adsorption; Kinetics; Congo red; Rice husk; Isotherm.

1. INTRODUCTION

Textile and dye industries discharge a considerable amount wastewater that contains various contaminants such as toxic compounds, acidic or basic compounds, dyes etc. in different concentration. The discharge of untreated effluent from the industries into the aquatic stream not only pollutes water but also threatens the ecosystem. Congo red (disodium salt of 3,3'-(1E,1'E)-biphenyl-4,4'-diylbis(diazene-2,1-diyl)bis(4-aminonaphthalene-1-sulfonate)) is an organic compund and a diazo dye, which is carcinogenic, mutagenic and non-biodegradable [1]. Although it is banned in many countries, congo red is still used in several countries. Therefore, finding an efficient method for congo red removal from wastewater is inevitable.

Dye-containing water and wastewater can be treated by different biological as well as physico-chemical treatement methods, which include but not limited to ion exchange, coagulation-floculation-precipitation, reverse osmosis, filtration, and adsorption. Most of these processes are either expensive or energy intensive [2,3]. Apart from that the biological treatment process is somewhat inefficient because of the non-biodegradabiliy of different dyes [4]. On the other hand dye removal using adsorption has been demonstrated to be an efficient method because of its simple design, low-cost, and high selectivity.

A numbers of easily available and low-cost agricultural by-products (bioadsorbents) has been developed in recent years, which includes wheat straw, peanut husk, orange peel, cashew nut shell, rice husk, date stones and so many [5]. Rice husk (RH) is an agricultural by-product and can be abundantly obtained from rice mills. It has been estimated that about 190 million tons of rice husk was produced in 2016 throughout the world [6]. A report revealed that the annual productin of rice husk was about 9 million tons [7]. So, the utilization of this readily available agro-based biowaste material would be beneficial. Furthermore, rice husk consists of cellulose (32%), which makes this a very good candidate for considering it as a potential adsorbent.

The aim of this study was to modify the RH through a simple chemical modification process and to find the influences of various parameters or factors, which include solution pH, adsorbent dose (solid-to-liquid ratio), adsorbate concentration, and time on the adsorption of congo red by using the prepared bioadsorbent. Thus the characterization of adsorbent was performed and at the same time kinetics as well as equilibrium experiments were conducted to elucidate the adsorption mechanisms.

2. MATERIALS AND METHODS

2.1. Chemicals

Precursor (rice husk) was collected from a local rice mill located in Barinagar Bazar in Jashore district of Bangladesh. Chemicals such as HCl, NaCl, NaOH, congo red ($C_{32}H_{22}N_6Na_2O_6S_2$), citric acid

($HOC(CO_2H)(CH_2CO_2H)_2$) were purchased from local market. All chemicals and reagents (Merck, Germany) used in the present research were of reagent grade with high purity. Congo red stock solution (1000 ppm) was prepared by dissolving it in deionized water. Stock solution was diluted (as required) to make working solution for conducting batch adsorption experiments.

2.2. Adsorbent preparation

Rice husk was first thoroughly washed with water to make sure removal of water soluble dust and dirt. It was then filtered and dried in oven. A measured amount of sample was soaked in 0.5 M citric acid for 2 h. After that time, the suspension was washed with deionized water repeatedly until the suspension attains a neutral pH. The suspension was then filtered and dried in oven. The dried sample was ground to make the particle size smaller.

2.3. Characterization

The adsorbent was characterized by determining its bulk density, moisture content, and surface charge. Moisture content was determined by direct method that involves in measuring weight loss of a specified amount of adsorbent before and after complete drying (at 105°C for 24 h) of the adsorbent in a dryer. On the other hand, the bulk density of the adsorbent is the mass of the adsorbent including its intergranular air space in unit volume. Moreover, scanning electron microscopy (SEM) was conducted by using a field emission-scanning electron microscope (Gemini SEM 500 FE-SEM, Zeiss, USA) to analytically observe the surface morphologis (shape, size, texture, porosity etc.) of the modified RH adsorbent.

2.4. Adsorption experiments

Bach-wise adsorption tests for congo red removal were carried out by maintaining 20 mg/ml of adsorbent-to-adsorbate ratio. Measured amount of adsorbent (rice husk) was taken in Erlenmeyer flasks in which certain amount of adsorbate (congo red solution) was poured so that the adsorbent-to-adsorbate ratio remain same. A constant shaking speed (200 rpm) was maintained for all adsorption experiments. For determining the effect of pH, the pH was varied from 1 to 9 while for determining the effect of time the solution pH was kept constant and shaking time was varied. On the other hand for determining isotherm, the initial concentration of congo red solution (adsorbate) was varied and all other parameters were kept constant. After a stipulated time, the whole suspension was filtered completely using filter paper and the filtrate concentration was determined with the help of UV-Vis spectroscopy (UV-1900i, Shimadzu, Japan). To adjust the initial pH at desired value, 0.1M HCl and 0.1M NaOH were used. The initial and final pH of the solutions were measured using a portable pH meter. The adsorption tests were conducted at room temperature. Each experiment was performed thrice and the average value was taken to plot graphs.

The percent of CR adsorption was calculated by using Eq. 1.

$$\%\,Adsorption = \{(C_{in} - C_{eq})/C_{in}\} \times 100 \quad (1)$$

where, C_{in} be the initial concentration (mg/L) and C_{eq} be the equilibrium concentration (mg/L) of congo red. Similarly the adsorption capacity (q) was calculated as follows:

$$q = \{(C_{in} - C_{eq}) \times V\}/M \quad (2)$$

where, q symbolizes the quantity of congo red adsorbed (mg/g) onto the modified rice husk adsorbent, V represents the volume of the adsorbate (L), and M denotes the amount of the modified RH in gram.

3. RESULT AND DISCUSSION

3.1.1. General characterization

Moisture content and density are two important characteristics of any adsorbent. The bulk density of the modified rice husk adsorbent was determined as 0.66 g/cm^3 while the moisture content was calculated to be 8.5%.

3.1.2. Point of zero charge (pH_{pzc}) determination

The isoelectric point or the point of zero charge (pH_{pzc}) is an essential physicochemical parameter for a specified surface in a specified aqueous solution. The pH_{pzc} defines the pH of the solution at which the net charge of entire adsorbent's surface is equal to zero when it comes in contact with water. In the present study the pH_{pzc} was determined as 4.5. Therefore, the total surface charge of the modified RH adsorbent is positive at pH < pH_{pzc} and negative at pH > pH_{pzc}. Since congo red is an anionic dye, it is estimated that CR will be adsorbed at pH lower than pH_{pzc} [8].

3.1.3. Scanning electron microscopy (SEM)

Scanning electron microscopy (SEM) is a significant characterizing parameter for adsorbent material because it provides tangible ideas about shape and porosity of the material. The morphology (shape, size, texture) of the surface of the adsorbent material (modified RH) was investigated using SEM. Figure 1 shows the SEM images of rice husk before and after the adsorption of congo red. From the figure, it is revealed that rice husk consists of considerable number of micropores and mesopores with several micrometer in size. Such porosity of the material favours the performance of adsorption from the aqueous solution. A large number of crystals of different shape were found at the surface of the adsorbent. This is because after treatment of rice husk with citric acid, functional groups were generated and attached on the surface [9]. On the

other hand, the pores are deemed to be occupied with congo red after the adsorption process. That is why no pores are observed, rather the surface seems to be homogeneous.

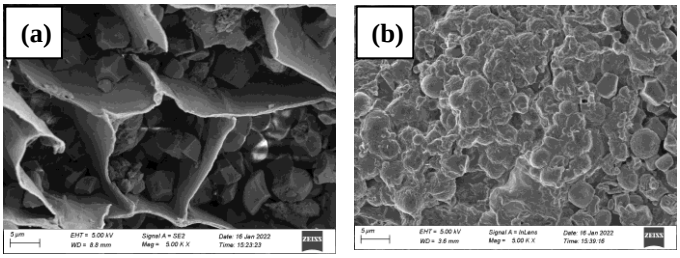

Fig. 1. SEM image of modified RH adsorbent (a) before and (b) after congo red adsorption.

3.2. Effect of adsorbent dose

Adsorbent dose is an essential parameter in adsorption process because it not only determines the amount of removal but also decides the economy of the process. Batchwise sorption experiments of congo red by chemically modified rice husk were conducted at room temperature. The amount of adsorbent was varied from 10 to 125 mg while pH (3.0) and shaking speed (200 rpm) were kept constant throughout the experiment. Experimental results in Fig. 2 shows that with the increase in adsorbent dose, the percentage removal of congo red rises (from 60% to 88%) at low dosage. At higher dosage, the active binding sites of adsorbent increases. So, active sites are readily available for congo red adsorption. Therefore the percentage removal of congo red from the solution increases with the increase in adsorbent dose. About 90.6% removal of congo red occurred at a dose of 3.5 g/L, where after no significant change in percentage removal observed. Therefore, the dosage of 3.5 g/L was set as an optimum, which was economically justified as well.

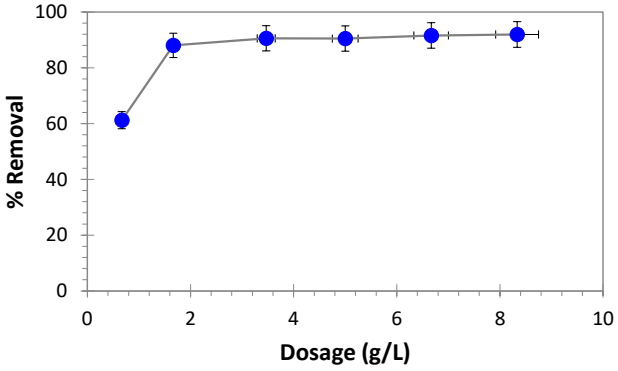

Fig. 2. Effect of the adsorbent dosage on adsorption of CR by modified RH.

3.3. Effect of pH on congo red adsorption

Generally the solution pH is considered as a significant parameter in adsorption process because it influences the solution chemistry and thus affects the adsorption quite a lot. In this investigation, the pH was varied in a range from 1 to 9. The removal was found to be 75% - 90% (as shown in Fig. 3). The maximum adsorption was observed to occur at pH 3 and after this pH the removal decreased. At lower pH (e.g. pH 3) the surface is positively charged, which facilitates to adsorb the anionic dye (CR) due to the electrostatic attractive force between negative sulfonic group (-R-SO_3^-) of congo red and the positively charged surface of the adsorbent.

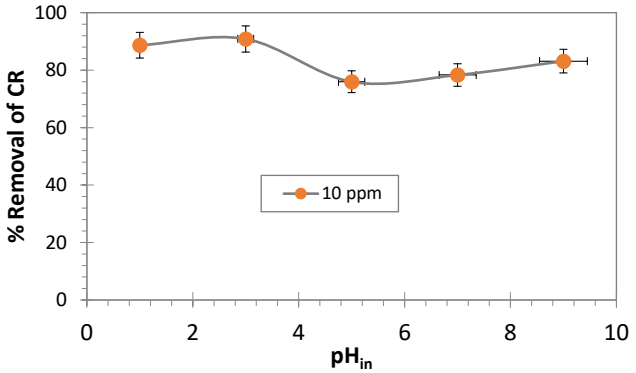

Fig. 3. Effect of the pH on adsorption of CR adsorbate by modified RH.

3.4. Effect of contact time and kinetic studies

To find the impact of contact time on congo red adsorption, experiments (batch-wise) were carried out at a varying reaction time keeping the adsorbate concentration constant. The results of the experiments are portrayed in Fig. 4 where it is apparent that at the initial stage (before 60 min) dye removal takes palce very rapidly and later on (after 60 min) the removal becomes slow and a plateau is formed. However, for the sake of completion of the reaction and to attain equilibrium, 120 min was allowed for running the adsorption reactions.

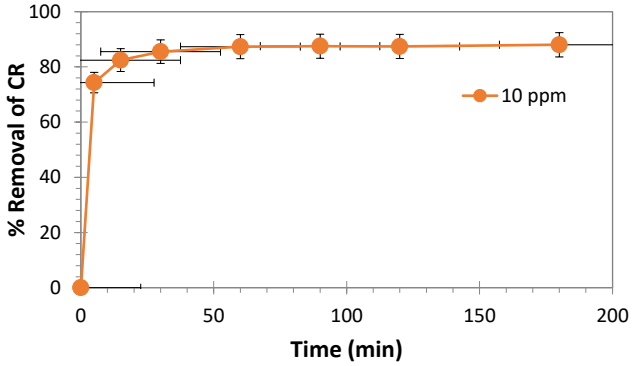

Fig. 4. Effect of contact time for congo red adsorption by modified rice husk.

In this research the kinetic studies for adsorption were investigated by using two well-known kinetic models, which were Lagergren's pseudo-first-order model and

pseudo-second-order model. Mathematical expressions of the kinetic models are mentioned below as Eq. 3 and Eq. 4.

$$\ln(q_e - q_t) = \ln q_e - k_1 t \quad (3)$$

$$\frac{t}{q_t} = \frac{1}{k_2 q_e^2} + \frac{t}{q_e} \quad (4)$$

where, q_e (mg/g) and q_t (mg/g) are denoted as sorption capcity at the equilibrium and that at time t (min), respectively, while k_1 and k_2 are symbolized as reaction rate constants respectively of pseudo-first-order adsorption and pseudo-second order adsorption. The kinetic models are depicted in Fig. 5(a) and 5(b). Considering the best fit linear model in terms of correlation coefficient values (R^2), it was clear that pseudo-second-order kinetic model yieled the best match within the experimentally obtained data. The rate constant (k_2) was calculated from the intercept of the plot Fig. 5(b) and found to be 3.11 g/(mg.min).

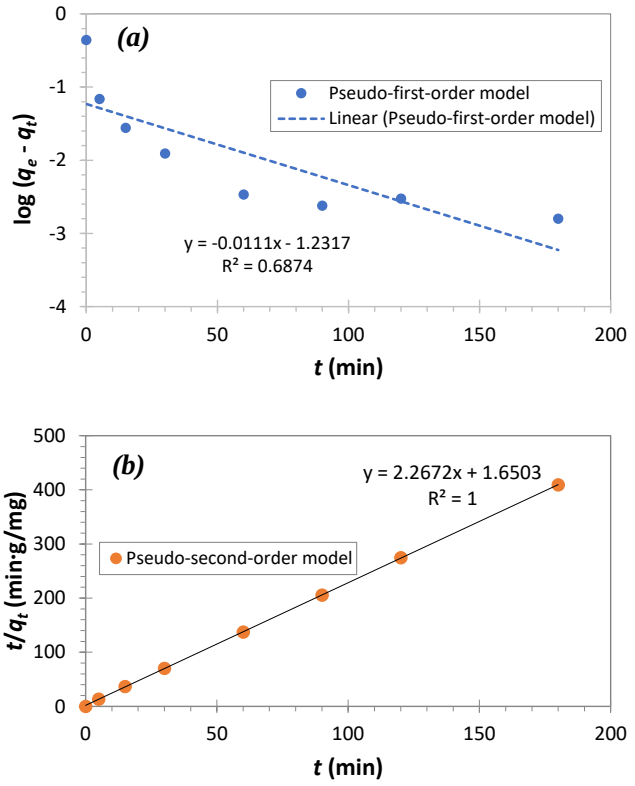

Fig. 5. Plot of (a) pseudo-first-order and (b) pseudo-second-order kinetic model for the adsorption of CR by modified RH.

3.5. Mechanism of transportation of congo red molecule

To comprehend the mechanism of adsorption of congo red by rice husk adsorbent, it is required to examine the data with intraparticle diffusion (ID) model. Usually in batchwise adsorption process, adsorbate is transported from the bulk solution to the surface of the adsorbent where external adsorption occurs. Finally the adsorbate moved through the the pores of the adsorbent. This phenomenon can be well-described by the Weber-Morris intraparticle diffusion model (Eq. 5).

$$q_t = k_{id} t^{1/2} + C \quad (5)$$

where, q_t (mg/g), k_{id} (mg/(g·min$^{1/2}$)), and C are denoted as adsorption capacity at time t (min), ID rate constant, and boundary layer thickness, respectively. ID rate constant (k_{id}) can be calculated from the slope of a plot of linear q_t vs $t^{1/2}$, which is shown in Fig. 6.

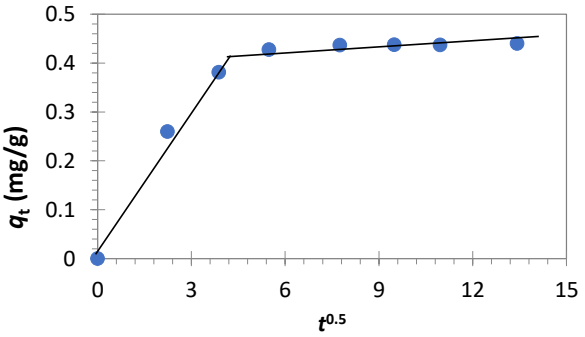

Fig. 6. Weber-Morris linear plot for CR adsorption by modified RH.

It is obvious from Fig. 6 that there are two different linear parts with different slope, which indicates a multistage adsorption of congo red by modied rice husk. The first linear region signifies an external surface adsorption or instantaneous adsorption resulting a faster mass transfer where as the second linear region implies pore diffusion or intraparticle diffusion that results slow diffusion inside the particles. The rate constants were determined as 0.0995 mg/(g·min$^{1/2}$) and 0.0014 mg/(g·min$^{1/2}$) for first linear region and second linear region, respectively.

3.6. Adsorption isotherms studies

Adsorption isotherm or equilibrium isotherm determines the maximum extent of adsorption on to the adsorbent under specific conditions. Fig. 7(a) shows the plot of experimental data with respect to equilibrium concentration of adsorbate (congo red). The figure depicts that at low concentration region, the sorption capacity rises with the increase in equilibrium concentration of congo red and at high concentration region, the curve gets eventually flat forming a plateau. This phenomenon suggests that the adsorption occurs according to the Langmuir isotherm model.

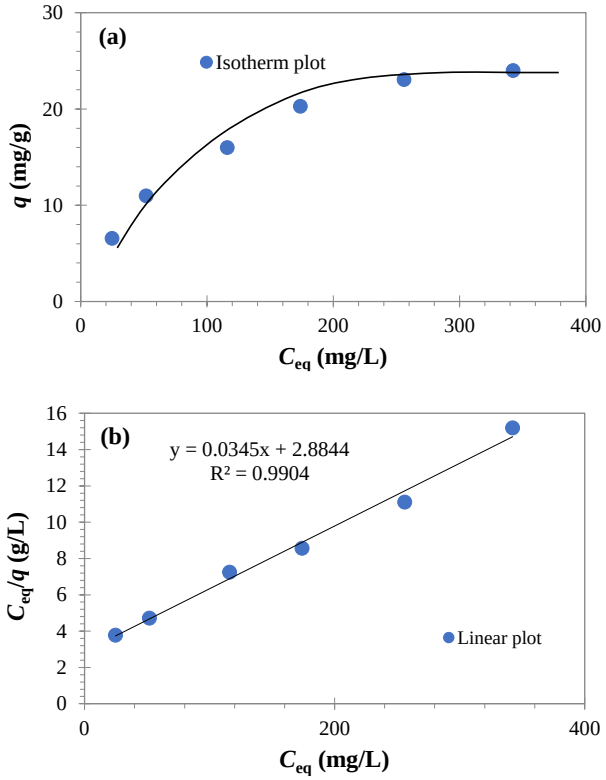

Fig. 7. Adsorption isotherm (a) and corresponding Langmuir isotherm plot (b) for CR adsorption.

The experimental data were further discussed by using a widely used isotherm model namely, Langmuir model. The Langmuir isotherm defines a gradual increase in surface occupancy until the entire adsorbent's surface area is occupied with a single layer of molecules and thereafter no further adsorption can occur. It relates to the surface area of the modified RH adsorbent covered by the congo red adsorbate molecules as a function of CR concentration at a fixed temperature (in this case room temperature). The Langmuir model is equated as follows (Eq. 6):

$$\frac{C_{eq}}{q_e} = \frac{1}{bq_m} + \frac{C_{eq}}{q_m} \qquad (6)$$

where, C_{eq} (mg/L), q_e (mg/g), q_m (mg/g) and b (L/mg) indicate equilibrium adsorbate concentration, equilibrium sorption capacity, adsorbent's maximum sorption capcity and Langmuir constant, respectively. By using the above-mentioned equation, $\frac{C_{eq}}{q_e}$ versus C_{eq} was plotted, which has been shown in Fig. 7(b). The maximum adsorption capacity (q_m) and the Langmuir constant (b) were determined from the slope and the intercept of the straight line, respectively. From this plot, q_m was calculated as 28 mg/g whereas b was determined to be 11.96 L/mg.

An alternative analysis of the equilibrium isotherm data was conducted to define a dimensionless constant (known as separation factor or essential factor), which defines the isotherm type. It designates the favorability of the isotherm [10]. The separation factor (R_L) can be equated as follows:

$$R_L = \frac{1}{1 + bC_{in}} \qquad (7)$$

where, b (L/mg) and C_{in} (mg/L) are termed as the Langmuir constant and the initial congo red (CR) concentration, respectively. It is to be noted that, if the extent of R_L stands between 0 and 1 (i.e. $0 < R_L < 1$), the adsorption type is favourable, whereas if R_L is greater than 1 (i.e. $R_L > 1$), the adsorption type is unfavorable. Moreover, $R_L = 1$ denotes a linear type of adsorption while $R_L = 0$ indicates an irreversible type sorption process [11]. Figure 8 displays a plot of R_L vs C_{in}, which evidently shows that the R_L values, calculated for all concentrations, remain between 0.068 and 0.653. Hence, the adsorption of CR by modified RH was supposed to be a favorable isotherm type at the studied conditions.

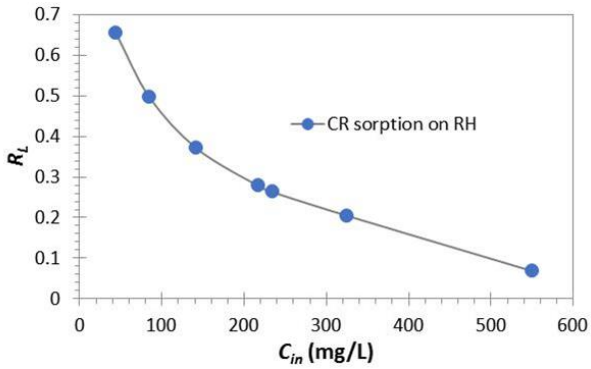

Fig. 8. Plot of separation factor for CR adsorption by modified RH.

4. CONCLUSION

Rice husk, an agricultural biowaste material, can be effectively utilized as an alternative, available and cost-effective bioadsorbent for congo red removal from aqueous solution. The adsorption of congo red from aqueous solution was studied under different experimental conditions in batch mode. Batch-wise adsorption was influenced by adsorbent dosage, solution pH, contact time and initial congo red concentration. The optimum adsorbent dose was 3.5 g/L. The extent of maximum adsorption was achieved at pH 3 and the maximum sorption capacity of the chemically modified rice husk adsorbent was 28 mg/g. Fitting of the adsorption equilibrium isotherm data exhibited that the Langmuir isotherm model was better suited for describing the adsorption process. This model also confirms a monolayer adsorption on the modified RH surface with a fixed number of localized active sites. The kinetic studies demonstrated that the adsorption process

meticulously followed the pseudo-second-order kinetic model. The intraparticle diffusion model exhibited that the congo red adsorption by modified rice husk adsorbent involved two adsorption steps: (i) the surface adsorption, and (ii) the intraparticle diffusion. The low-cost and locally available agrobiowaste material (rice husk) can thus be used as a prospective sorbent for congo red removal from aqueous solution through adsorption process.

REFERENCES

[1] Website of Phys.org, https://phys.org/news/2008-05-congo-red.html, website last visited on 10 March 2022.

[2] B.C. Oei, S. Ibrahim, S. Wang, H.M. Ang, "Surfactant modified barley straw for removal of acid and reactive dyes from aqueous solution" Bioresour. Technol. 100, 4292-4295, 2009.

[3] B.E. Tastan, S. Ertugrul, G. Donmez, "Effective bioremoval of reactive dye and heavy metals by Aspergillous versicolor" Bioresour. Technol. 101, 870-876, 2010.

[4] G. Ciardelli, N. Ranieri, "The treatment and reuse of wastewater in the textile industry by means of ozonization and electroflocculation" Water Res. 35, 567-572, 2001.

[5] J.O. Quansah, T. Hlaing, F.N. Lyonga, P.P. Kyi, S-H. Hong, C-G. Lee, S-J. Park, "Nascent rice husk as an adsorbent for removing cationic dyes from textile wastewater" Appl. Sci. 10, 3437, 2020.

[6] K.T. Tong, R. Vinai, M.N. Soutsos, "Use of Vietnamese rice husk ash for the production of sodium silicate as the activator for alkali-activated binders" J. Clean Prod. 201, 272-286, 2018.

[7] A.K.M.S. Islam, M. Ahiduzzaman, "Green electricity from rice husk: a model for Bangladesh" Book Chapter of Thermal Power Plant, Edited by M. Rasul, 2013.

[8] S. Parvin, M.M. Hussain, F. Akter, B.K. Biswas, "Removal of congo red by silver carp (*Hypophthalmichthys molitrix*) fish bone powder: kinetics, equilibrium, and thermodynamic study" J. Chemistry, Vol. 2021, Aticle ID 9535644.

[9] X. Li, Y. Li, "Adsorptive removal of dyes from aqueous solution by KMnO4-modified rice husk and rice straw" J. Chemisty, Vol. 2019, Article ID 8359491.

[10] T.W. Weber, R.K. Chakravorti, "Pore and solid diffusion models for fixed bed adsorbers" AIChE J. 1974.

[11] M. Arami, N.Y. Limaee, N.M. Mahmoodi, "Investigation on the adsorption capability of egg shell membrane towards model textile dyes" Chemosphere, 65(11), 1999-2008, 2006.

Paper ID: 6171

International Conference on Mechanical, Manufacturing and Process Engineering (ICMMPE – 2022)

Organizer: Faculty of Mechanical Engineering, Dhaka University of Engineering & Technology (DUET), Gazipur, Bangladesh

Website: https://icmmpeduet.com/

Experimental Investigation on the Microstructure and Hardness of Over-aged Cast Aluminium-7 Silicon-0.3 Magnesium Alloy

R Islam[1], M Akter[2], S M Al-Amin[3] and A K M B Rashid[4]

[1,3]Department of Materials and Metallurgical Engineering, Dhaka University of Engineering & Technology (DUET), Gazipur, Bangladesh

[2]Directorate of Project Planning, Bangladesh Power Development Board, Dhaka, Bangladesh

[4]Department of Materials and Metallurgical Engineering, Bangladesh University of Engineering & Technology (BUET), Dhaka-1000, Bangladesh

E-mail: mridul@duet.ac.bd

ABSTRACT

A great number of cast products in the automotive industry are mostly cast from Al–7Si–0.3 Mg (A356) alloy for its cast-ability, good fuel efficiency, high strength ratio, good weldability, and good corrosion resistance. The alloy in vehicle parts is used for an indefinite period of time at a moderate temperature environment, thus subjected to over-aging indirectly. The over-aged properties of this alloy are unknown. In this paper, the aging response to the microstructure and hardness of the cast Al–7Si–0.3 Mg alloy was investigated. As-cast, solution treated, and aged specimens of this material were tested. The microstructural observations of the alloy revealed the primary Al matrix with long acicular Si particles in the as-cast condition which is undesired since acicular particular causes stress concentration. Upon solution treatment, fragmentation of Si occurred and dendrites of π-FeAlMgS emerged. When aging at 170°C, with increasing aging time Si started to become spheroids, and the precipitates of Mg_2Si started to coarsen decreasing the dendrites. Brinell results showed that the maximum hardness is achieved when aging at 170°C between 1 and 5 hours. Exposed to excessive aging, it reduced the hardness slightly from the maximum values, whilst maintaining a higher value than the casting conditions, which is consistent regardless of aging. The increase in the hardness at the peak hardening zone is due to the dispersion of silicon throughout the microstructure.

Keywords: A356 alloy; Heat Treatment; Ovar-aging; Microstructure; Hardness.

1. INTRODUCTION

Among the lightweight alloys, aluminium alloys are dominated over other alloys due to their low density, high strength, excellent corrosion resistance, and low cost. Casting is one of the important routes of aluminium production and plays a significant role in the advancement of Al industries. Al-7Si-0.3Mg is one of the highly used commercial Al castings and has good stability, high specific strength, corrosion resistance, and excellent tensile and fatigue properties. Al-7Si-0.3Mg cast alloys have demand in the automobile, aerospace, and defense sector, and a demand for improved and more uniform mechanical properties increase continuously [1].

Several alloying elements such as Silicon, Magnesium, Copper, Iron, Zinc, and Manganese are added in cast Al alloy to improve the mechanical and morphological properties of alloys. Among them, aluminium-silicon alloy has good mechanical properties when the heat treatment process is applied to refine the grain size of alunimium, modifies the eutectic phase of silicon, and reduces the inter-dendritic arm spacing. The microstructure of silicon phase depends on the temperature difference and interface velocities. In most commercial eutectic alloys, the silicon eutectic is found a flaky irregular form. The morphology can be modified through the addition of impurity elements and changing solidification rates. Si particles act as crack initiators when cooling is done under the normal cooling condition. As a result, the mechanical properties of the alloy are reduced [2]. A coarse angular plate and needle morphology of eutectic silicon can be transformed into very fined closely branched plates with rounded edges by controlling cooling and solidification rates [3]. Aluminium-silicon alloys with magnesium show a good response to heat treatments [3], [4].

The mechanical properties of heat-treatable aluminium alloys can be improved by designing a specific heat-treatment process. Heat treatment is performed at an elevated temperature to allow soluble elements such as Mg

and Cu to become supersaturated in a solid solution, then, it is cooled fast enough so that solute can precipitate. The aim of the thermal treatment of the solution is to put the maximum quantity of curing solutes such as Cu and Mg into a solid solution in the Aluminium matrix.

Aluminium-silicon-magnesium alloys used in automotive engines must withstand a remarkable time period that changes the quantity and size of the different phases in the alloy microstructure [5], [6]. Therefore, their mechanical properties at that temperature and during that period are impacted accordingly. While the effect of aging develops mechanical properties, excessive aging has an adverse effect on this alloy [7]. Therefore, it is very beneficial to have a clear concept concerning the actual state of the microstructure and hardness in this severe aging condition.

To date, only a few works have been done on the performance of the Al-7Si-0.3Mg alloy on the effect of aging time and temperature. Since the cast alloy Al-7Si-0.3Mg has demand for preparation of cylinder head, and wheel rim, the alloy becomes over-aged when it is used on a long-term basis. Consequently, the microstructure and hardness behavior of these alloys in over-aged conditions is very critical.

2. EXPERIMENTAL

In this study, changes in the microstructure and the response to the hardness of the cast Al-7Si-0.3Mg alloy (A356) under-aged and over-aged conditions were investigated. The work demands casting, preparation of samples for microstructure analysis, and hardness measurement. The aluminum ingot was brought from the local grade and was silvery gray in color. The A356 ingot was unmodified and of commercial grade. The master alloy had the composition of 7% Si, 0.3% Mg alloy with 0.2% Fe (max) and 0.10% Zn (max), and the rest being Al.

The alloy was weighed and kept in a crucible which was placed in a furnace. A furnace was fired to melt the alloy at an elevated temperature of 800°C. Upon reaching the temperature to 800°C, degasser was weighed (0.2% by weight), and 6.86gm of degasser (d'gasser 20) wrapped in aluminum foil immersed in the crucible. The melt was stirred and drossing was done. Then the melt was cooled down to 750°C before pouring. So, the pouring temperature was 750°C. The melt was poured into the sand mold at a steady flow rate and care was taken to avoid turbulence. Overflow of the melt through the cavity marked the completion of casting.

20 mm diameter and 13 mm length cylindrical test samples were cut and machined from the 22 mm diameter and 200 mm length cylindrical sand-cast bars. An air circulation furnace (Nabertherm LH 15/12) is used to solution treated the samples and it is heated at 540 ± 2°C temperature for 4 hours. Then, the samples are quenched in water at 30 ± 5°C. They were then kept at -18°C in a refrigerator until they were aged effectively at 170°C for 1, 2, 5, 10, 100, 1000, 10000, and 100000 hours. With the help of the Arrhenius model, the long aging durations were minimized to a couple of hours by using a higher aging temperature [8], which means that for each 10°C temperature increase, the effective aging time decreases by half. Table 1 shows the aging scheme used during the work using the same furnace.

Table 1: Aging scheme used in the work

Aging time (170°C)	Effective aging time for Arrhenius model (170°C)	Applied aging schedule	
		Time	Temp.
1 hr	1 hr	1 hr	170°C
2 hr	2 hr	2 hr	170°C
5 hr	5 hr	5 hr	170°C
10 hr	10 hr	1.25 hr	200°C
100 hr	98 hr	3.125 (3) hr	220°C
1000 hr	1024 hr	1.95 (2) hr	260°C
10000 hr	10240 hr	2.44 (2.5) hr	290°C
100000 hr	98304 hr	3.052 (3) hr	320°C

The structural morphology of the as-cast and heat-treated samples were observed with the help of an optical microscope (Optica B-380). Standardized techniques were employed to prepare the samples.

The hardness of the cast, as well as heat-treated samples, was measured with the help of a Brinell hardness tester (Wilson BH3000).

3. RESULT AND DISCUSSION

3.1 Aging Response to Microstructure

The microstructure of as-cast A356 alloy (Fig. 1 a) consists of an α- Aluminium matrix with a blackened Al-Si eutectic and. As the as-cast alloy is unmodified (Sr or Na is absent), some coarse acicular silicon particles are present in the microstructure. Adjacent to these silicon particles, Mg_2Si are formed during solidification [9]. Apart from these entities, a long, thin plate of light gray color is detected in the microstructure. These particles are normally formed by Aluminium, silicon, and iron and can be identified as Al_5FeSi.

Dissolution of the Mg_2Si occurs when solution treatment at 540°C for 4 hours (Fig. 1 b) is performed as it is a very fast process [9]. On the other hand, Al_5FeSi is still undissolved after solution treatment. A new phase π-

FeAlMgSi in the form of network or dendrites is seen along with the long Al_5FeSi [10]. The most obvious scenario in the solution-treated microstructure is the fragmentation of the long acicular primary silicon particle.

After aging for 1 hour at 170°C (Fig. 1 c), the primary silicon phase becomes more fragmented and irregular-shaped. The rod-shaped β'-Mg_2Al is observed [11]. The Al_5FeSi is still undissolved and visible as a grayish thin plate. The network acted as the nucleation site for the precipitation of β- Mg_2Si, therefore the network is decreasing.

After aging for 2 hours at 170°C (Fig. 1 d), the microstructure is almost the same as that of aging at 170°C for 1 hour. The silicon particles are more fragmented and dispersed throughout the structure. The precipitated phase grows by Ostwald ripening process and assumed needle-shaped structures [11]. A small number of dendrites and rod-shaped particles still exist.

After aging for 5 hours at 170°C (Fig. 1 e), the microstructure has a lesser amount of π-FeAlMgSi dendrites than the previous structures. The fragmented silicon starts to spherodize and β-Mg_2Si precipitates even more from the transformation of β'- β.

After aging for 10, 100, 1000, 10000, and 100000 hours at 170°C (Fig. 1 f-j), the silicon particle starts to coarsen. Vibrant growth of Mg_2Si is observed with increasing aging time along with decreasing Mg_2Al and a slight decrease in eutectic Al-Si. During severe aging conditions, extreme grain growth of Si is observed and assumed to be a block shape. Mg_2Si particles have coarsened. Mg_2Al is almost absent along with π-FeAlMgSi.

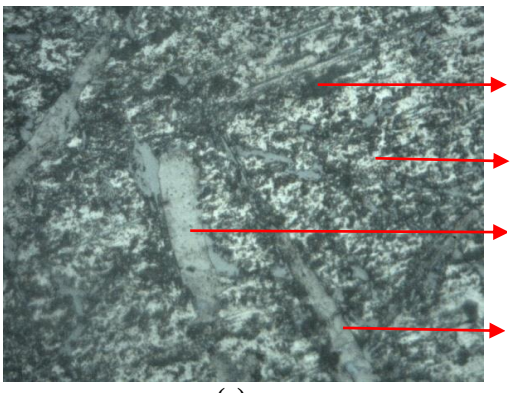

(a)

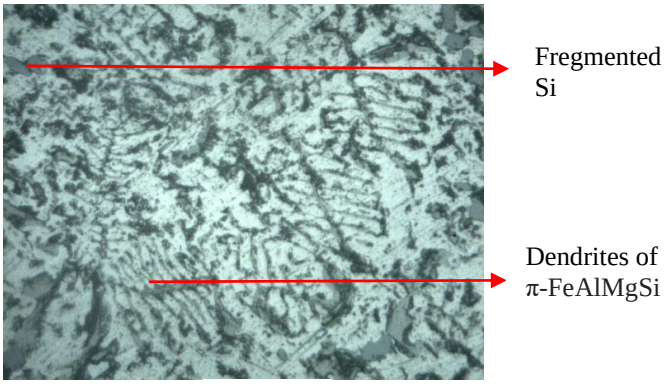

(b)

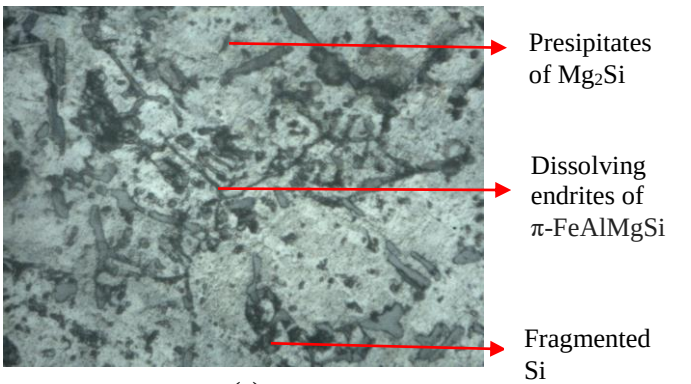

(c)

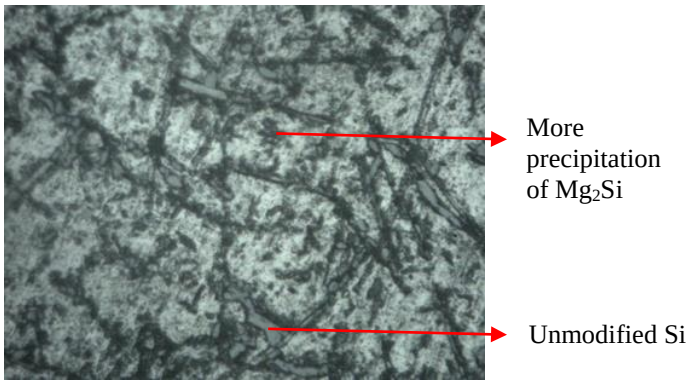

(d)

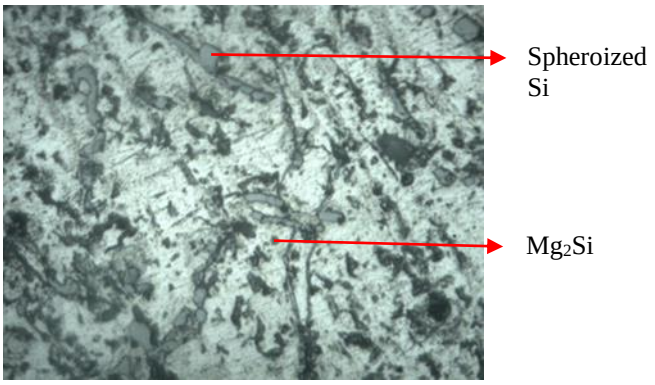

(e)

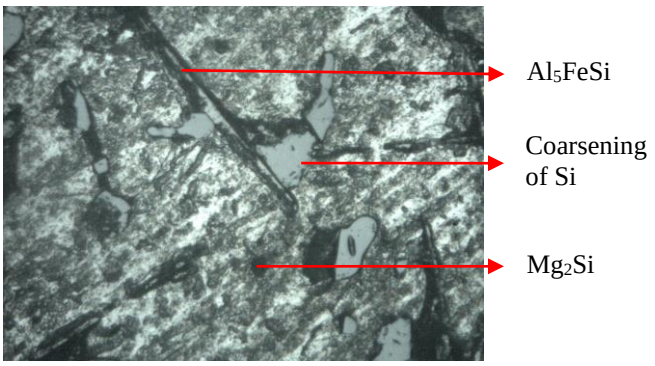

(f)

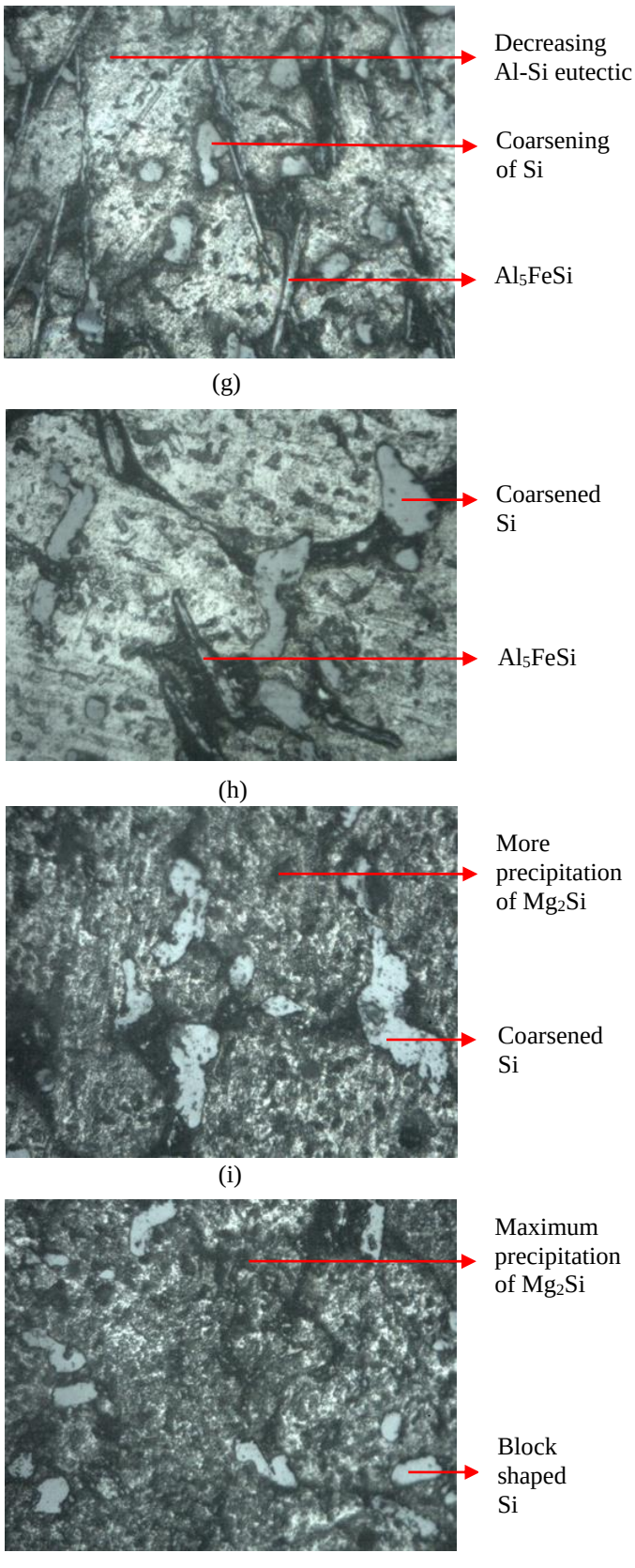

Fig. 1: Microstrcture of Al-7Si-0.3Mg alloys at different conditions observed in optical microscope (a) As-cast, (b) Solution-treated, (c) Aged at 170°C for 1 hour, (d) Aged at 170°C for 2 hours, (e) Aged at 170°C for 5 hours, (f) Aged at 170°C for 10 hours, (g) Aged at 170°C for 100 hours, (h) Aged at 170°C for 1000 hours, (i) Aged at 170°C for 10000 hours, and (j) Aged at 170°C for 100000 hours (x500).

3.2 Aging Response to Hardness

The hardness value of the as-cast sample is the lowest. And it gradually increases from the solution treatment and reaches a maximum at the aging at 170°C for 1 hour. Afterward, it gradually decreases until it is aged at 10 and 100 hours. Upon aging further, the hardness value almost maintains a plateau/flat region. There is no change in hardness after aging beyond 100 hours. It is also observed that the hardness value does not fall below the hardness of the as-cast sample. So, it can be concluded that there is no significant drop in hardness value over a longer time over aging and it stays at a steady value above the as-cast hardness.

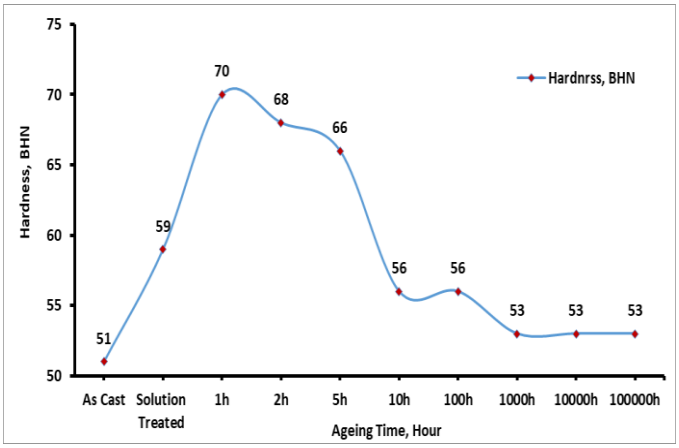

Fig. 2: Dependence of Hardness of A356 on aging time.

Due to the smaller portion and acicular structure of Si in the matrix, the indenter surface tends to land on the soft α-Al matrix. As a result, The Hardness value is low. The silicon particle appeared fibrous and undissolved Al_5FeSi, dendritic structure dispersed throughout the structure upon solution treatment, thus contributing to the high hardness value. After Aging at 170°C for 1 hour, the slightly rounded Si particle is distributed throughout the structure, and thus peak hardness is observed. During the aging of the sample at 170°C for 2 and 5 hours, the hardness slightly decreases (from 70 BHN to 66 BHN) and varied less. As the Si particle gets rounded and coarsened, the hardness value drops further at aging at 10 and 100 hours. The area of Si particle available to distribute the forces exerted by the indenter becomes less due to the wide dispersion of the Si particle and so more force land on the soft Al phase,

resulting in lower hardness. Further aging to 1000, 10000, and 100000 hours, it is seen that a steady value of hardness is maintained. As the grain grows extensively, Si particles transform from a round to a blocky shape. Moreover, there is no scope for further fragmentation of Si particles, the hardness value becomes independent of aging time and it is almost a constant value.

4. CONCLUSION

Over-aging influences the microstructural changes in the A356 alloy, that also affects the mechanical properties like hardness.

- Exposure to elevated temperature during solution treatment homogenizes the microstructure and spheroidizes the acicular Si particles. Fragmentation and spheroidization of Si particles occur (aged and over-aged) from acicular Si (as cast). Precipitates of Mg_2Si formed and started to grow with increasing aging time.
- Hardness increased after solution treatment and it is maximum at aging for 1h at 170°C. After peak hardening, incoherent precipitates are observed with respect to the matrix.
- At over-aging, the hardness value became independent of aging time and it was a constant value, but higher than the as-cast condition. The over-aged samples have better hardness than as-cast samples due to the uniform dispersion of Mg_2Si particles.
- The result is a timely reminder that materials of engine parts should be selected considering the over-aging effect on the microstructure and hardness of the alloy.

Finding the effect of pouring temperatures, solidification rates, and molding processes on the mechanical properties of the same alloy, such as fatigue, creep, and so on, could be a future goal of this research. Finding the influence of modifiers, as well as the effect of alloy fiber reinforcement, may have promising implications.

ACKNOWLEDGMENT

We recognize the financial and technical assistance of the Department of Metallurgical Materials and Engineering, Bangladesh University of Engineering and Technology (BUET).

REFERENCE

[1] G. Atxaga, A. Pelayo, and A. M. Irisarri, “Effect of microstructure on fatigue behaviour of cast Al–7Si–Mg alloy,” *Materials Science and Technology*, vol. 17, no. 4, pp. 446–450, Apr. 2001, doi: 10.1179/026708301101510023.

[2] A. Mazahery, M. Alizadeh, and M. O. Shabani, “Study of Tribological and Mechanical Properties of A356–Nano SiC Composites,” *Trans Indian Inst Met*, vol. 65, no. 4, pp. 393–398, Aug. 2012, doi: 10.1007/s12666-012-0143-8.

[3] A. M. A. Mohamed, F. H. Samuel, A. M. Samuel, and H. W. Doty, “Influence of additives on the impact toughness of Al–10.8% Si near-eutectic cast alloys,” *Materials & Design*, vol. 30, no. 10, pp. 4218–4229, Dec. 2009, doi: 10.1016/j.matdes.2009.04.041.

[4] S. G. Shabestari and H. Moemeni, “Effect of copper and solidification conditions on the microstructure and mechanical properties of Al–Si–Mg alloys,” *Journal of Materials Processing Technology*, vol. 153–154, pp. 193–198, Nov. 2004, doi: 10.1016/j.jmatprotec.2004.04.302.

[5] S. P. Ringer and K. Hono, “Microstructural Evolution and Age Hardening in Aluminium Alloys,” *Materials Characterization*, vol. 44, no. 1–2, pp. 101–131, Jan. 2000, doi: 10.1016/S1044-5803(99)00051-0.

[6] C. Lin *et al.*, “Long-Life Rechargeable Zn Air Battery Based on Binary Metal Carbide Armored by Nitrogen-Doped Carbon,” *ACS Appl. Energy Mater.*, vol. 2, no. 3, pp. 1747–1755, Mar. 2019, doi: 10.1021/acsaem.8b01865.

[7] M. N. Islam and J. Podder, “The role of Al and Co co-doping on the band gap tuning of TiO2 thin films for applications in photovoltaic and optoelectronic devices,” *Materials Science in Semiconductor Processing*, vol. 121, p. 105419, Jan. 2021, doi: 10.1016/j.mssp.2020.105419.

[8] S. Singh and D. B. Goel, “Influence of thermomechanical Aging on tensile properties of 2014 aluminium alloy,” *J Mater Sci*, vol. 25, no. 9, pp. 3894–3900, Sep. 1990, doi: 10.1007/BF00582456.

[9] E. Sjölander and S. Seifeddine, “The heat treatment of Al–Si–Cu–Mg casting alloys,” *Journal of Materials Processing Technology*, vol. 210, no. 10, pp. 1249–1259, Jul. 2010, doi: 10.1016/j.jmatprotec.2010.03.020.

[10] Q. G. Wang and C. J. Davidson, “[No title found],” *Journal of Materials Science*, vol. 36, no. 3, pp. 739–750, 2001, doi: 10.1023/A:1004801327556.

[11] F. Ernst, “EMSE-290 Materials Laboratory III,” *PRECIPITATION HARDENING*, p. 30.

Paper ID: 6336

International Conference on Mechanical, Manufacturing and Process Engineering
(ICMMPE – 2022)

Organizer: Faculty of Mechanical Engineering, Dhaka University of Engineering & Technology (DUET), Gazipur, Bangladesh Website: https://icmmpeduet.com/

Determination of Polycyclic Aromatic Hydrocarbons in smoked meat products from Sylhet region of Bangladesh by Gas Chromatography-Mass Spectrometry (GC-MS)

Nazmul Islam, Emon Das, Md. Shakir Moazzem, Iftekhar Ahmad and Wahidu Zzaman*

Department of Food Engineering and Tea Technology, Shahjalal University of Science and Technology, Sylhet-3114, Bangladesh
***** Corresponding author Email: wahid-ttc@sust.edu

ABSTRACT

Polycyclic aromatic hydrocarbons (PAHs) are carcinogenic chemicals generated during the high-temperature cooking of foods. The purpose of this study was to determine the level of contamination of PAH compounds (Naphthalene, Fluorine, Anthracene, Phenanthrene, Pyrene, Chrysene, Acenaphthalene, Benzo[a]pyrene and Benzo[a]anthracene) in smoked meat products using Gas Chromatography-Mass Spectrometry (GC-MS). The PAH content was measured in five highly consumed smoked meat samples in Bangladesh, including Grilled chicken, Chicken barbecue, Beef boti kabab, Beef shik kabab, and Beef Chap. Concentration of PAH marker Benzo[a]pyrene exceeded the EU (European Union)-mandated limit value, averaging 34.76 g/kg while many of the others are BDL (Below Detection Level). Daily exposure levels to individual PAH chemicals in samples ranges from 1.576 to 2695.176 ng/kg. As defined by the USEPA (United Nation Environment Protection Agency), it is observed that Chrysene's carcinogenic risk is negligible, and the Benzo[a]anthracene and Benzo[a]pyrene's carcinogenic risk is within acceptable range while no significant risk or exposure were found for other PAHs from smoked meat samples.

Keywords: Smoked meat products; Polycyclic aromatic hydrocarbon; carcinogenic risk; GC-MS.

1. INTRODUCTION

Polycyclic Aromatic Hydrocarbons (PAHs) are a group of organic compounds which contain two or more fused aromatic rings derived from incomplete combustion of organic materials like oil, coal, gas, waste, wood or other organic matters. PAHs have been canonized on the list of priority pollutants due to the carcinogenic and mutagenic properties they possess (Lee et al. 2016). The wide presence and persistency of PAHs, especially of the higher molecular weight PAHs, in the environment is due to the hydrophobicity and molecular stability of the PAHs (Lawal 2017). Though it is stated that there are around 200 different groups of PAHs are available in the environment (Sahin et al. 2020), 16 of these are considered as priority by the European Food Safety Authority (EFSA), the Committee of Food Additives Experts (JECFA) and the Food Scientific Committee (SCF). These 16 compounds are listed as follows; Acenaphthene, Naphthalene, Phenanthrene, Fluorene, Acenaphthylene, Anthracene, Fluoranthene, Chrysene, Pyrene, Benzo[b]fluoranthene, Benzo[k]fluoranthene, Benzo[a]pyrene, Indeno[1,2,3-cd]pyrene, Benzo[a]anthracene, Dibenzo[a,h]anthracene and Benzo[ghi]perylene (Sahin et al. 2020). Most of the time, Benzo[a]pyrene is considered as a PAH marker in food items (Es et al. 2015).

The Science Committee on Food (SCF) has done a health risk assessment of the consumers associated with PAHs exposure from foods and reported that the intake of smoked meat products can contribute notably to the intake of PAH compounds if these foods are taken as a portion of the regular diet (Jira 2004). Smoked meat is the type of meat that is flavored, cooked or preserved by the exposure to the smoke produced from burning fuels. An example of some of the world-famous smoked meat products are bacon, ham, sausage, jerky, grilled meat, kabab etc. However, the most common smoked meats in Bangladesh are grilled meat, barbecued meat, kabab, and so on. Many researchers have already established that the genesis of PAHs may occur due to the incomplete combustion of organic fuels, pyrolysis of proteins, fats, and carbohydrates at a temperature above 200°C. According to (Plant et al. 1983), PAH levels are substantially influenced by the cooking techniques and the type of heat sources utilized. Using the flame of a long fire is to grill meat result in the production of a higher amount of PAHs in the meat product. Regarding the problem that the consumption of PAH compounds at a significant level can be detrimental to humans, it is quite important to develop an accurate technique to determine the PAH content in smoked meat products for the purpose of evaluating the exposure level to PAH compounds from the intake of these products. In the last few decades, several research works have been done to

develop extraction and purification methods for PAH determination. The total process of PAH determination includes sample pretreatment, PAH separation and determination. Sample pretreatment is required to purify the PAHs as meat products contain fat, carbohydrates, inorganic salts, vitamins and cholesterol. Approaches such as solid phase extraction, liquid-liquid extraction (LLE), QuEchERS (Quick, Easy, Cheap, Effective, Rugged and Safe) extraction can be applied for extracting PAHs from the meat sample (Al-thaiban, Al-tamimi, and Helaleh 2018). And for the detection of HCAs various chromatographic techniques have been reported by research groups, such as: gas chromatography coupled to mass spectrometry (GC/MS) or with flame ionization detection (GC/FID), high performance liquid chromatography with ultraviolet (HPLC/UV) or fluorescence (HPLC/FL) detection or coupled to mass spectrometry (HPLC/MS) (Manda et al. 2012). According to (Manda et al. 2012), (GC/MS) and (HPLC/FL) methods appear to have superior selectivity and sensitivity among all these aforementioned methods. The European Food Safety Authority (EFSA, 2007) stated that (GC/MS) and (HPLC/FL) methods are used respectively for around 43% and 28% of the concerning analysis (Manda et al. 2012).

For the last few decades, the analysis of PAH content in various types of food has been a frequent concern for several research groups all around the world, especially in western countries. However, the amount of research done to evaluate the amounts of PAHs in local Bangladeshi smoked meats is very limited and insufficient to reveal the actual scenario, despite the fact that a large number of consumers consume these smoked meat products. In view of scarce information on the PAH compounds in local smoked meat products, this study targets to determine the common PAHs in several types of Bangladeshi local smoked meat products, including grilled chicken, chicken barbecue, beef boti kabab, beef shik kabab, and beef chap. Additionally, it tries to gauge the potential carcinogenic as well as non-carcinogenic risks to human health based on dietary consumption of the targeted PAHs via selected smoked meat products.

2. MATERIALS AND METHODS

2.1 Location of the experiment

The study was performed in the laboratories of the department of Food Engineering and Tea Technology (FET) of Shahjalal University of Science and Technology, Sylhet-3114 and Bangladesh Council of Science and Industrial Research (BCSIR), Dhaka-1205. The PAH compounds were extracted from the selected samples in the laboratory of the FET department, and the GCMS analysis was performed in the laboratory of the BCSIR.

2.2 Reagents

The following chemicals were employed in the analysis: methanol, potassium hydroxide, cyclohexane, anhydrous sodium sulfate, and dichloromethane. All of the solvents were of HPLC grade. The GC-MS analysis of the smoked meat samples also included the use of PAH standards such as Napthalene, Fluorene, Anthracene, Phenanthrene, Acenaphthalene, Chrysene as well as Benzo[a]pyrene and Benzo[a]anthracene.

2.3 Sample Collection

Five types of local smoked meat products viz. Grilled chicken, Chicken barbecue, Beef boti kabab, Beef shik kabab, and Beef chap were selected as sample in this investigation. All of the samples were obtained from a local restaurant in Ambarkhana, Sylhet, Bangladesh. Each of the five samples was cut into pieces of 1 cm^3 size. Then they were dried in an oven dryer at 60°C for around 48 hours. Following drying, the samples were ground into powder with a mortar and pestle. Then the powder of each sample was stored at -4°C temperature until we proceeded to the next step.

2.2 Sample preparation

2.3.1 Alkaline hydrolysis

Five grams of each sample was weighted and transferred into different round bottom flasks that were pre-cleaned. Then 100 mL of 2M methanolic potassium hydroxide solution was used to hydrolyze each sample. The mixtures were vigorously agitated in a shaking incubator at 200 rpm for 30 min. The mixtures were then refluxed in a 60°C water bath for around 2 hours. When the saponification was completed, to chill the mixture, 50 mL of distilled water was added. Fat from the samples was removed by the conduction of this alkaline hydrolysis.

2.3.2 Extraction of PAHs

To extract the PAHs from the previously treated alkaline hydrolysis cooled sample, 40 mL of cyclohexane was mixed to the flask solution and thoroughly agitated for 30 minutes in the shacking incubator. The flask was then carefully sealed and left in the dark overnight. The resulting solution was centrifuged at 3000 rpm for 10 minutes, and the limpid top cyclohexane layer was separated into a pre-cleaned conical flask. With the remaining lower two sections; 10 mL of cyclohexane was added and centrifuged for another 10 minutes at the previous speed. The cyclohexane layer was then put into the previously obtained extract solution in a conical flask. The residual water in the

extract was removed by treating it with anhydrous sodium sulfate. PAHs from all of the five samples were extracted following the same procedure.

The extracted sample solution's color was removed by running it through a cleanup column made up of cotton (one inch), silica gel (seven inch), sodium sulfate (two inch), and cotton layers (one inch) stacked from bottom to top. In order to wash and saturate the cotton, silica gel, sodium sulfate, and cotton layers, approximately 5 mL of dichloromethane (DCM) was run through the column many times. By passing nitrogen gas through a sample solution, the extracts were reduced to a volume of 1–2 mL concentrated solution after they had been decreased in color to a satisfactory level. In the following step, the pre-concentrated solution was passed through a cartridge filter containing C18 that contained solid phase extraction (SPE), which was washed with 5 ml DCM. Again, the solution was pre-concentrated to a 1–2 mL solution using nitrogen gas, which was then used for the GC-MS analysis, and it was stocked at 4°C for further investigation.

2.3 Preparation of standard solution

In order to create the stock standard PAHs solution, a known quantity of standards was dissolved in a determined amount of solvent (dichloromethane) and kept at 4°C. Then dichloromethane was used as the solvent to make calibration standard solutions at concentrations of 4, 2, 1, and 0.5 mg/kg.

2.4 GC-MS analysis

A GC-MS method was adopted using a GC (Varian CP 3800, USA) and MS (Varian Saturn 2200) with a VF-5 fused silica capillary column (30m×0.25 id., film thickness of 25 mm), for the examination of PAHs like Naphthalene, Phenanthrene, Fluorene, Anthracene, Benzo[a]anthracene, Pyrene, Benzo[a]pyrene and Chrysene in selected smoked meat samples. Helium was employed as the carrier gas at a constant flow rate of 1 mL/min. For GC-MS detection, a selected ion storage (SIS) with an ionization energy of 70 eV was used. The temperatures of the injector, transfer line, manifold, and split ratio were set at 275°C, 280°C, 40°C, and 30%, respectively. All of the above-mentioned analytical instruments and settings were identical, but the oven temperature, selected ion storage (SIS) mode, and total run duration for the measurement of the aforementioned PAHs were different. Except for benzo[a]pyrene, the GC oven temperature was designed to rise from 50°C (1-minute hold) to 320°C at a rate of 10°C/min and held for 4 minutes, whereas for benzo[a]pyrene, the temperature of the GC oven was configured to range from 100°C to 320°C in 10°C/min increments and kept for 8 minutes. Between the two techniques, the total run time for benzo[a]pyrene was chosen to be 19 minutes and 32 minutes for the other compounds. PAHs were studied using a specific ion storage mechanism. For each standard and sample solution, diluted 1 mL solutions were manually injected in split less mode. The intra and inter day precision and accuracy of replicates were used to assess the procedures' system suitability. The accuracy was determined by combining known amounts of the standard solution with the sample at the start of the extraction method. The target chemicals in the pre-concentrated samples were identified using different retention times in the chromatogram, followed by computerized matching (GC-MS NIST Library) of mass spectra with standards. To calibrate the apparatus, blank reagent measurements were taken.

2.6 Health risk assessment

Risk assessment is described as the ways of estimating the risk of any given probable amount of detrimental health consequences occurring over a certain time period (Bempah and Ewusi 2016). To quantify the risks to human health posed by PAH exposure through the intake of smoked meat products, the carcinogenic and non-carcinogenic risk values were calculated.

2.6.1 Carcinogenic risk calculation

USEPA defines carcinogenic risk as “the incremental possibility of an individual developing cancer over the course of their lifetime as a result of exposure to a probable carcinogen” (USEPA, 1991). According to the equation (1) employed by (Begum et al. 2020), (Hu et al. 2007), and many other researchers, the carcinogenic risk value was determined.

$$\text{Lifetime cancer risk (CR)} = \{(CSF \times CF \times ED \times EF \times E_D)/(AT \times BW)\} \quad (1)$$

Where, CSF is the cancer slope factor of PAHs from oral intake (mg/kg/day) according to USEPA (1991), CF is the factor of conversion (10^{-6} g/ng), ED is the exposure duration (70 years for adults), EF is the exposure frequency of individual (365 days/year), AT is the average time (70×365 days), BW is the average body weight (60 kg) and E_D is the daily exposure level (ng/day) which, in this context, refers to the level of individual PAH exposure to which an individual is subjected over the course of a day. It is calculated using the equation used by (Xia et al. 2010).

$$E_D = IR \times BEC \quad (2)$$

Where, IR is the ingestion rate of meat products (g/day), the ingestion rate for chicken samples is 12.6 g/day

and 17.4 g/day for beef samples (Shaheen, Ahmed, and Islam 2016) and BEC is the Benzo[a]pyrene equivalent concentration of PAHs in smoked meat sample (ng/g). It was quantified by equation (3) used by (Xia et al. 2010).

$$BEC = \sum C_i \times TEF_i \quad (3)$$

And in this equation, TEF means toxic equivalents of Benzo[a]pyrene (µg/kg) (Lagoy 1992) and C_i is the individual PAH concentrations in smoked meat samples.

2.6.2 Non-carcinogenic risk calculation

In addition, the non-carcinogenic risk assessment was determined based on the Hazard Index (HI). The HI was determined using the following equation (4) for the risk of the selected PAHs from smoked meat consumption. (Li et al. 2016).

$$HI = \{(C_i \times IR \times CF \times ED \times EF)/(BW \times AT \times RfDo)\} \quad (4)$$

Where, RfDo is the oral ingestion reference dose of PAHs (mg/kg/day) according to USEPA, 2012.

3. RESULTS AND DISCUSSION

3.1 Validation of methods

For evaluating the validation of the adopted GC-MS analysis method, the linearity, limit of detection (LOD), and recovery were determined. From the concentrations of 4, 2, 1 and 0.5g/kg of their standard solutions, nine calibration curves for the nine PAHs were created, and the linearity of the PAHs was assessed as the coefficient of determination values (R^2). The coefficients of determination of the standard PAH solution ranges from 0.9916 to 0.9986. The spike recovery for the aforementioned compounds was found to range between 78% and 95.5%. The coefficient of determination values (R^2) suggests that the calibration curve's linearity was excellent. The LOD results were less than the LOD 0.3 µg/kg specified in the European standard (EC, 2007). Another study (Wretling et al. 2010) revealed recovery values of 84% to 113% for 15 carcinogenic PAHs, with the LOD rounded to 0.2 µg/kg. Thus, the R^2, LOD, and recovery values found in this analysis illustrate the methodology's complete dependability and accuracy.

The validated and established approach was used to quantify the nine PAHs in all samples of smoked meat, including grilled chicken, chicken barbecue, beef boti kabab, beef shik kabab, and beef chap. The previously prepared and stored meat sample solutions were injected sequentially into a GC-MS instrument to identify and quantify the aforementioned PAHs by comparing their retention times to those of the corresponding compound in a standard solution tested under the same conditions.

3.2 Concentration of PAHs found in the tested sample

According to this analysis, grilled chicken and chicken barbecue were found to be significantly higher in PAH contamination than other types of smoked meat samples, whereas beef boti kabab, beef shik kabab, and beef chap were found to be relatively lower in PAH contamination. The results of the analysis indicate that Benzo[a]pyrene and Naphthalene were found in varying concentrations in each smoked meat sample, while Anenaphthalene levels were found to be BDL in all of the samples tested. The greatest concentration of Napthalene was reported in chicken barbecue, at 74.56 µg/kg. Anthracene was found to be the most prevalent PAH in each of the smoked meat products tested in terms of the concentration, with 698 µg/kg found in grilled chicken and 592 µg/kg found in chicken barbecue, respectively. Notably, Anthracene was found to be BDL in all of the beef samples. With the exception of Acenaphthalene, all of the PAHs were detected in some quantity in grilled chicken and chicken barbecue, with some exceeding the permissible limit, while the majority of PAHs were detected below the BDL in beef meat samples, despite the fact that some were above the EU-mandated limit value. According to the relevant regulation, the maximum allowable level of Benzo[a]pyrene in meat products is 5 µg/kg (European Union Directive, 2011; TFC, 2011). In our study, the concentration of Benzo[a]pyrene surpassed the maximum limit value in all samples, with an average concentration of 34.76 µg/kg. This study made the assumption that grilled chicken and chicken barbecue are more carcinogenic than other types of smoked meat, which was confirmed by the study's findings. This could be a result of the cooking technique used. Generally, in the case of grilled chicken and chicken barbecue, meat is smoked at a very high temperature for a prolonged amount of time (Hamidi et al. 2016). This could be one of the reasons, along with other factors such as direct or indirect exposure of meat to the smoke.

Another study (Begum et al. 2020) found an average level of Benzo[a]pyrene at 27.19 µg/kg in Bangladeshi smoked meat samples, far exceeding the allowable limit. In addition, the content of other PAHs was notably greater in grilled chicken than in beef shik kabab. Benzo[a]pyrene was found in chicken breast grilled on charcoal at a concentration of 0.57 µg/kg by (Janoszka 2015). According to a different study (Farhadian et al. 2010), PAHs were found in fish and grilled meat at varying concentrations ranging from 0 to 130 µg/kg while concentrations of Benzo[a]pyrene were ranging between 0.2 and 50 µg/kg. There was a 15 µg/kg concentration of Benzo[a]pyrene in

smoked chicken in Estonia (Taylor et al., n.d.). So, based on the information presented above, it is clear that smoked meat products, particularly in Bangladesh, have extremely high PAH levels, which should be cause for concern because of the potential carcinogenic risk they pose to consumers.

Table I: Concentration of nine PAHs in five tested samples (grilled chicken, chicken barbecue, beef boti kabab, beef shik kabab, beef chap).

Compounds	Concentration of PAHs (µg/kg)				
	Grilled chicken	Chicken barbecue	Beef boti kabab	Beef shik kabab	Beef chap
Naphthalene	68.34	74.56	14.34	19.18	9.52
Fluorene	26	32	28	1	BDL
Phenanthrene	304	401	35.6	28	BDL
Anthracene	698	592	BDL	BDL	BDL
Pyrene	82	56	BDL	BDL	BDL
Chrysene	652	465	BDL	BDL	BDL
Acenaphthalene	BDL	BDL	BDL	BDL	BDL
Benzo[a]anthracene	346	283	BDL	BDL	BDL
Benzo[a]pyrene	56.86	48.41	12.66	7.51	4.36
∑PAH	2233.2	1951.97	90.5	71.69	57.88

3.2 Health risk assessment

Estimated daily exposure level, carcinogenic and non-carcinogenic risk to humans from consuming smoked meat samples are listed in table II. Individual PAH compounds in the sample had daily exposure levels ranging from 1.576 to 2695.176 ng/day. The highest daily exposure level is for Benzo[a]pyrene, while the lowest daily exposure level is for fluorine. In their assessment (Begum et al. 2020) reported that the daily exposure level of Bangladeshi people varied from 0.284 to 471.38 ng/day. In a research done by (Alomirah et al. 2011), smoked meat products have been found to contain an average daily exposure level of Benzo[a]pyrene of 95.7 ng/day. According to the researchers, the daily exposure level of PAHs is related to the consumers' dietary habits as well as the level of PAH contamination in smoked meat products. As consumption increases, customers will be exposed to increased levels of PAHs. As defined by the USEPA, CR values lower than 10^{-6} are considered trifling and negligible, while values greater than 10^{-4} are regarded unacceptable, and values ranging from 10^{-6} to 10^{-4} are deemed to be acceptable. So, it is seen that in the present study, CR values of Chrysene was found to be within the negligible range whereas Benzo[a]pyrene and Benzo[a]anthracene was in acceptable range.

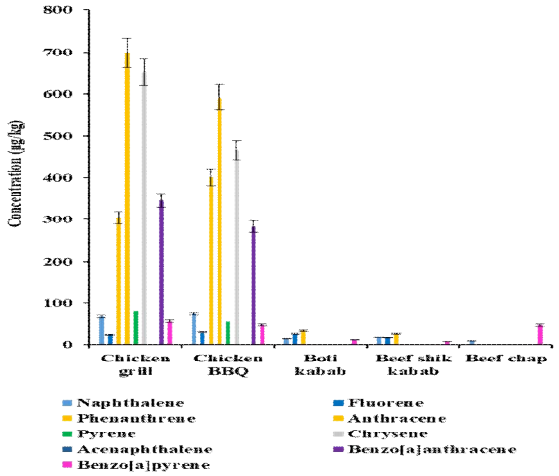

Fig. 1: Concentration of selected nine PAHs in five tested samples.

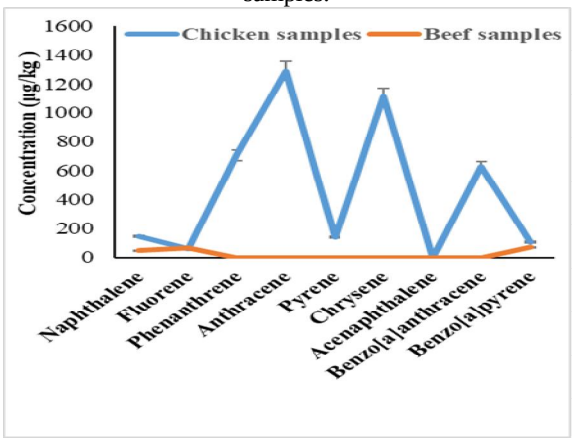

Fig. 2: Comparison between PAH concentrations in chicken and beef samples.

The Health Index was used to estimate the non-carcinogenic risk of dietary exposure to PAHs. Most programs assume that if the health index value is less than 1, the subjected group is unlikely to have evident non-carcinogenic impacts and if the health risk value is more than 1, there may be a health risk (Li et al. 2016). The findings of this experiment indicate that the non-carcinogenic risk of the considered compounds was substantially below the risk threshold value (1), implying that hardly any evident non-carcinogenic consequences would occur.

Table II: Mean concentrations, carcinogenic and non-carcinogenic risks of selected PAHs determined in tested samples.

Compounds	Mean concentration (µg/kg)	Daily exposure level, E_D (ng/day)	Carcinogenic risk (CR)	Non-carcinogenic risk (HI)
Naphthalene	37.188	3.028	-	1.262×10^{-3}
Fluorene	20.6	1.576	-	6.567×10^{-4}
Phenanthrene	153.72	13.068	-	7.260×10^{-3}
Anthracene	258	224.46	-	1.245×10^{-3}
Pyrene	27.6	2.40	-	1.334×10^{-3}
Chrysene	223.4	194.358	2.365×10^{-8}	-
Acenaphthalene	-	-	-	-
Benzo[a]anthracene	125.8	1094.46	1.331×10^{-5}	-
Benzo[a]pyrene	34.76	2695.176	3.279×10^{-4}	

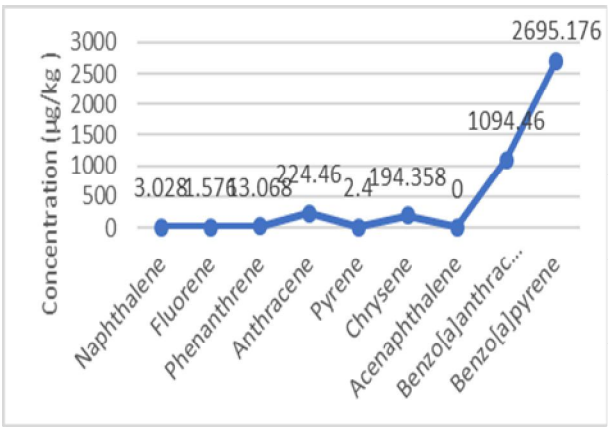

Fig. 3: Daily exposure level of selected nine PAHs in five tested samples.

4. CONCLUSION

In conclusion, the technique used to determine selected PAHs in smoked meat products was successful. All of our tested samples contained two or more PAHs. Benzo[a]pyrene and Naphthalene were detected at varied concentrations in each sample of smoked meat; however Acenaphthalene levels were determined to be below the BDL in all samples tested. Except for Acenaphthalene, all PAHs were detected in significant amounts in grilled chicken and chicken barbecue, with some surpassing the legal limit, while the most were detected below the BDL in beef meat samples. The PAH analysis results were utilized to determine the dietary exposure, carcinogenic and non-carcinogenic risk associated with the PAH compounds found in the smoked meat samples. Thus, the findings of this study suggest that awareness should be raised among those who consume smoked meat on a daily basis and that appropriate efforts should be taken to decrease exposure to these PAHs and the risk to human health. Furthermore, this study advises that the technique, temperature, and time of smoking meat be investigated further in order to determine the ideal combination for lessening the amounts of PAHs in Bangladeshi smoked meat products.

ACKNOWLEDGMENT

The authors are thankful for the financial support provided by the Advanced Research in Education (GARE), Ministry of Education, Bangladesh.

REFERENCES

Al-thaiban, Hussain, Nada Al-tamimi, and Murad Helaleh. 2018. "Development of QuEChERS Method for the Determination of Polycyclic Aromatic Hydrocarbons in Smoked Meat Products Using GC-MS from Qatar" 2018.

Alomirah, Husam, Sameer Al-zenki, Suad Al-hooti, Sahar Zaghloul, Wajih Sawaya, and Nisar Ahmed. 2011. "Concentrations and Dietary Exposure to Polycyclic Aromatic Hydrocarbons (PAHs) from Grilled and Smoked Foods." *Food Control* 22 (12): 2028–35. https://doi.org/10.1016/j.foodcont.2011.05.024.

Begum, R, A K M Atique Ullah, S Afrin, M S Hossen, A S Hashi, and Shamshad B Quraishi. 2020. "Gas Chromatography – Mass Spectrometric (GC-MS) Determination of Polycyclic Aromatic Hydrocarbons in Smoked Meat and Fish Ingested by Bangladeshi People and Human Health Risk Assessment Gas Chromatography – Mass Spectrometric (GC-MS) Determination of Polycyclic Aromatic Hydrocarbons in Smoked Meat and Fish Ingested by Bangladeshi People and Human." *Polycyclic Aromatic Compounds* 0 (0): 1–11. https://doi.org/10.1080/10406638.2020.1790017.

Es, Mohamad, Reza Ahmadkhaniha, Mojtaba Moazzen, and Masud Yunesian. 2015. "SC." *Food Control*. https://doi.org/10.1016/j.foodcont.2015.07.022.

Farhadian, Afsaneh, S Jinap, Faridah Abas, and Zaidul Islam Sakar. 2010. "Determination of Polycyclic Aromatic Hydrocarbons in Grilled Meat." *Food Control* 21 (5): 606–10. https://doi.org/10.1016/j.foodcont.2009.09.002.

Hamidi, Elliyana Nadia, Parvaneh Hajeb, Jinap Selamat, and Ahmad Faizal Abdull. 2016. "Polycyclic Aromatic Hydrocarbons (PAHs) and Their Bioaccessibility in Meat : A Tool for Assessing Human Cancer Risk" 17.

Janoszka, Beata. 2015. "Organic Compounds Formed in Thermally Treated High-Protein Food . Part I : Polycyclic Aromatic Hydrocarbons, organic compounds formed in thermally treated high-protein food part i : polycyclic aromatic hydrocarbons," no. January 2004.

Jira, Wolfgang. 2004. "A GC / MS Method for the Determination of Carcinogenic Polycyclic Aromatic Hydrocarbons (PAH) in Smoked Meat Products and Liquid Smokes," 208–12.

https://doi.org/10.1007/s00217-003-0827-8.

Lawal, Abdulazeez T. 2017. "Polycyclic Aromatic HydrocarbonsA Review," 1–89.

Lee, Joon-goo, Su-yeon Kim, Jung-sik Moon, Sheen-hee Kim, Dong-hyun Kang, and Hae-jung Yoon. 2016. "Effects of Grilling Procedures on Levels of Polycyclic Aromatic Hydrocarbons in Grilled Meats." *Food Chemistry* 199: 632–38. https://doi.org/10.1016/j.foodchem.2015.12.017.

Manda, Pierre, Djédjé Sébastien Dano, Ehouan Stephane-joel Ehile, Mathias Koffi, Ngeussan Amani, Yolande Aké Assi, Laboratoire De Toxicologie, and Sciences Pharmaceutiques. 2012. "Evaluation of Polycyclic Aromatic Hydrocarbons (PAHs) Content in Foods Sold in Abobo Market , Abidjan , Côte d ' Ivoire" 4 (June): 99–105. https://doi.org/10.5897/JTEHS11.085.

Plant, D S Physiol, Bonny K Larsson, Greger P Sahlberg, Anders T Eriksson, and A Busk. 1983. "Polycyclic Aromatic Hydrocarbons in Grilled Food," no. 1973: 867–73.

Sahin, Seyda, Halil Ibrahim Ulusoy, Suleyman Alemdar, and Selim Erdogan. 2020. "The Presence of Polycyclic Aromatic Hydrocarbons (PAHs) in Grilled Beef , Chicken and Fish by Considering Dietary Exposure and Risk Assessment" 40 (5): 675–88.

Taylor, Publisher, M Reinik, T Tamme, M Roasto, K Juhkam, T Tenno, and A Kiis. n.d. "Food Additives & Contaminants Polycyclic Aromatic Hydrocarbons (PAHs) in Meat Products and Estimated PAH Intake by Children and the General Population in Estonia," no. January 2015: 37–41. https://doi.org/10.1080/02652030601182862.

Wretling, S, A Eriksson, G A Eskhult, and B Larsson. 2010. "Journal of Food Composition and Analysis Polycyclic Aromatic Hydrocarbons (PAHs) in Swedish Smoked Meat and Fish." *Journal of Food Composition and Analysis* 23 (3): 264–72. https://doi.org/10.1016/j.jfca.2009.10.003.

Paper ID: 6533
International Conference on Mechanical, Manufacturing and Process Engineering (ICMMPE – 2022)
Organizer: Faculty of Mechanical Engineering, Dhaka University of Engineering & Technology (DUET), Gazipur, Bangladesh
Website: https://icmmpeduet.com/

Experiment on the influence of particle size & carrier gas on exhaust characteristics during the combustion of pulverized bituminous coal.

S.M. Faysal Ahmed[1], Shyamal Nath[2], Md. Tanvir Siraj[3], Md. Saiful Islam[4], Asif Kabir[5]

[1,4,5]Department of Mechanical Engineering, BUET, Dhaka-1000, Bangladesh
[2]Department of Mechanical Engineering, RUET, Rajshahi-6204, Bangladesh
[3]Department of Industrial and Production Engineering, BUET, Dhaka-1000, Bangladesh

E-mail: smfaysalahmed@gmail.com[1]

ABSTRACT

In this paper, the effects of the size of particles and carrier gas on pulverizing 'Barapukuria' bituminous coal combustion parameters were examined numerically and experimentally. The temperature and fluid flow processes in a furnace are analyzed using computational fluid dynamics (CFD) in this work. To minimize NO_x in the exhaust gas, the experiment employs High-Temperature Air Combustion (HTAC). The research focuses on the volatile matter produced by coal particles and their reactivity during combustion and their effects on NOx, CO_2, and CO generation and emission. The tests were conducted in a 1400 mm long vertical furnace with a 344 X 344mm^2 interior cross-section. CO_2 was used as a carrier gas to inject high-grade bituminous coal with particle sizes ranging from 0.001 to 0.005mm, 0.005 to 0.01mm, 0.01 to 0.015mm, and 0.015 to 0.02mm into the furnace. In all cases, there is a significant recirculation of flue gas around the furnace center. For the tiniest particles, de-volatilization happens before and after the recirculation vortex, and for the bigger particles, it occurs after the recirculation vortex. Recirculated exhaust gas was used to heat secondary air and reduce heat losses. On measures NO_x formation/destruction by combining physical and chemical properties, or by linking both combustion characteristics to particle sizes. Because the amount of NO_x produced in the case of smaller particles is reduced, the measured NO_x emission of larger particles is more than that of smaller particles. This investigation aims to the improvement of combustion efficiency, power output, and reduction of pollutant emissions.

Keywords: Exhaust characteristics; Coal; Energy; CFD analysis; Bituminous coal

1. INTRODUCTION

Our modern worldview is based on energy. In our view, material and energy are the world's foundations, with energy appearing first. All activities, such as civilization growth and human demands and activities, are based on energy consumption. [1]. Fossil fuel is the most extensively used energy source that is produced naturally, such as through the decomposition process of buried dead organic matter, and contains energy derived from ancient photosynthesis. Coal, Petroleum, and natural gases are examples of fossil fuels with high carbon content [2]. The cheapest and most abundant fossil fuel is coal. It's a biofuel. The organic stuff in coal gets pyrolyzed during heating and subsequently becomes volatile. Coal combustion releases carbon and volatiles. The procedure of burning volatiles and coal may occur concurrently, sequentially, or with overlap depending on the particular combustion parameters[3]. The following is a general chemical process that occurs during coal combustion.

$$C_xH_yO_zN_lS_n + (x/2 + y/2 - z/2 + n)O_2 = xCO + (y/2)H_2O + (l/2)N_2 + nSO_2 \quad (1) \quad [4]$$

Combustion of coal produces different types of gases like NO_x, SO_x, etc. as can see from the reaction. It has been observed that different parameters have different effects on the combustion of coal. There are different types of combustion processes of coal such as coal gasification, combustion of pulverized coal, and conventional combustion. This project is on the combustion of pulverized coal.

In the instance of fossil fuel burning, Intense Low-oxygen Dilution (MILD) combustion has been recognized as an innovative technology that provides ultra-low pollutant emissions, excellent thermal efficiency, improved combustion stability, and thermal sector uniformity, and broad fuel flexibility [5]. Kiga et al [6] reported the first impactful MILD combustion of high volatile pulverized coal with 74μm particle size using a drop tube furnace, declaring that this technology is important for increasing combustion efficiency while reducing NOx emissions significantly when compared to the conventional combustion. Sudaet al. published an experimental investigation [7] to explore the influence of air preheating on the MILD combustion characteristics of anthracite and bituminous coal, where it was discovered that increasing

the combustion air temperature considerably reduced the coal particles' ignition delay.

Many articles on the simulation-based numerical study of fossil fuel combustion are available. As a consequence, a numerical analysis of the research indicated that NO is largely formed from char-nitrogen in high-rank coal (anthracite), whose production/destruction process is yet unknown [8]. Mei et al. released a work in 2013 that numerically studied the effects of reactant injection velocity on coal MILD combustion [9] and discovered that increasing primary air velocity had a major influence in lowering combustion temperature and reducing total NOx emission. Tu et al. used simplified combustion models[10] to explore the MILD combustion characteristics of pulverized bituminous coal under O_2/N_2 and O_2/CO_2 atmospheres and found that oxy-MILD combustion has a high potential for lowering NOx production.

The International Flame Research Foundation (IFRF) completed a series of experimental studies in a 0.58 MW furnace and found a considerable NOx reduction potential of the MILD combustion of high volatile bituminous coal in another article by Weber et al. [11]. However, these experiments did not show the underlying pathways of NOx generation and destruction. Tamura et al [12] conducted an experimental examination on the MILD combustion of bituminous coal in a cylindrical bench-scale furnace and discovered that extending the residence period of the coal particles lowered total NOx emissions. Mancini et al. used CFD to evaluate the application of HTAC technology to pulverized coal boilers. The use of HTAC mode early in the startup phase reduces NOx emissions for a longer period of operation [13]. A lengthy residence period has been discovered to be necessary for the effective burning of coal particles in a recuperative furnace under MILD combustion conditions [14].

Temperature plays a significant role in the successful modeling of coal combustion and gasification processes. $HTAC$ (high-temperature air combustion) technology, which is featured in highly preheated combustion air, has drawn several investigations in the last 15 years due to its merits in energy saving, flame stability enhancement, and NOx emission reduction [15]. Katsuki and Hasegawa [16] analyzed the HTAC technology's development history and associated research efforts, whereas Weber et al. [17] reviewed the development of 11 different HTAC processes. This project included a swirl burner. As a result, knowing how to use a burner is essential. The burner has been utilized in a number of commercial boilers in China, mostly as a flame stabilizer for low volatile coals. To ensure the sufficient heat up of the fuel-air mixture stream and to improve the ignition performance, in practice, the primary air is separated into two streams and only the stream with a higher mass ratio of fuel particles to the air (C/A ratio) is sent into the preheating chamber [18]. For this purpose, a newly designed furnace is to be constructed to make possible this type of combustion and the effects of some parameters on the exhaust characteristics have to be observed. There are different Parameters such as the velocity of injected pulverized fuel, fuel injection angle, coal feed rate, particle size, carrier gas, etc. In this project, only the effect of particle size and carrier gas will be observed. Different types of carrier gas will be used to carry the pulverized coal to the furnace. The high-grade bituminous coal of the Barapukuria Coal mine was used in the experiment.

Coal is the principal source of electricity generation in several countries throughout the world. Coal provided 38 percent of the world's electricity in 2017, the same percentage as 30 years before [19]. Coal is widely used to generate electricity in both developing and developed countries. However, coal combustion has a significant negative impact on the natural environment, particularly the atmosphere. 'Clean Coal' is a broad term that refers to several technologies that reduce pollution emissions by treating or processing coal, modifying how it is burned, or sequestering pollutants. Improving energy efficiency and reducing pollutant emissions have recently been highlighted in the energy research sector as ways to control large-scale energy use and environmental disasters caused by the greenhouse effect. To improve combustion efficiency, the particle size of coal is made smaller than usual, and air staging and air preheating are also included in this project.

To improve coal combustion technology, numerical simulations using various types of software have become feasible and attractive. As a consequence, one of the most essential aspects of this research is the CFD simulation of pulverized coal combustion. Recirculation of the flue gas is also used to reduce pollutant emissions from burning. So, developing coal combustion technology is crucial. However, no research has been done on the impact of particle size and carrier gas on exhaust characteristics and NOx reduction during pulverized bituminous coal combustion using flue gas recirculation. This demonstrates the novelty of this ongoing project.

The specific objectives of this research are given below:

(a) To investigate the characteristics of pulverized coal combustion.

(b) To observe the effect of particle size on the formation of CO, CO_2, and temperature generation.

(c) To study the effect of particle size and carrier gas on the reduction of NOx emission.

The remaining sections of the work are organized as follows: Section 2 describes the experimental setup and methodology, Section 3 discusses the obtained results, and Section 4 concludes the research by briefly explaining the acquired result and the future study scope.

2. EXPERIMENTAL SETUP & METHODOLOGY

2.1. Set-up details

A unique experimental setup is required to observe the influence of particle size and carrier gas on pulverized bituminous coal exhaust characteristics. The most crucial aspect of every experiment is the experimental setup. The nature of the outcome is determined by the precision of the

experimental setup. The experimental details are briefly described here. The schematic representation of a pulverized coal combustion furnace is shown in Figure 1. To decrease asymmetry resulting from natural convection and ashes deposition, the furnace is rectangular with a vertical axis. The height of the furnace chamber is 1400 mm. The furnace's combustion chamber has a square cross-section of 344 mm^2 and a length of 585 mm. The body of the furnace is separated into three sections. The furnace has a 10 mm thickness. Outside the furnace, 75 mm thick fiberglass is utilized as insulation, allowing only around 10 % of total heat to escape through the walls. The swirl burner was utilized, which produced a steady and attached neutral flame with an equivalent ratio of 0.55 to stoichiometric ignition. The oxidant was ambient temperature air and the fuel for the burner was natural gas.

The pulverized coal and career gas are injected into the furnace via a well-insulated central jet with a 10 mm internal diameter. When the temperature is reached above the self-ignition temperature (1100K) of pulverized bituminous coal, the coal grains were injected into the furnace via the central jet using carbon dioxide (CO_2) as a carrier gas. For all situations, stable ignition was obtained, and thermal equilibrium was demonstrated.

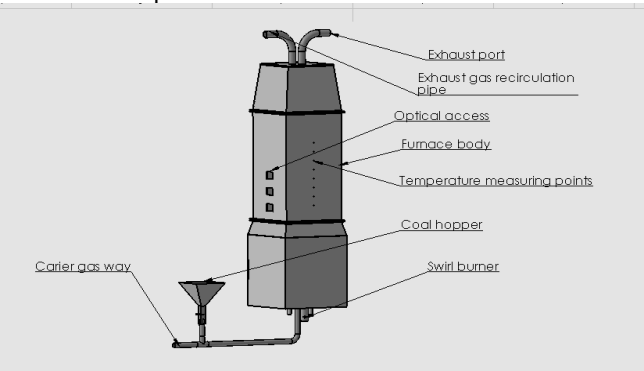

Fig. 1: Design model of coal combustion furnace.

Using CO_2 as a carrier gas, four distinct particle sizes were fed into the furnace at a steady flow rate of 1.48 kg/hr through the insulating central jet. The two-gate valve between the coal hopper and the piping system controls the coal feed rate. In both circumstances, a massive recirculation vortex forms around the furnace center. An infrared thermometer was used to observe temperatures in the furnace midsection.

2.2. Different parts of the Set-up

1. Furnace 2. Coal hopper 3. Swirl burner 4. Piping system 5. Air compressor

2.2.1. Furnace

The furnace that is used in the experiment is a forced draft furnace to combust high-grade bituminous coal. Here the carrier gas was used to carry the pulverized coal from the coal hopper to the furnace which was used to burn in the furnace with the help of air. Atmospheric air is used as the combustion air. Carbon dioxide (CO_2) is used as the carrier gas. The height of our designed furnace is 1400 mm and it is made of mild steel. The furnace body is divided into three parts furnace top, middle furnace, and bottom furnace. Combustion of pulverized coal took place at the middle part of the furnace which has an inner cross-section of 344 X 344 mm^2 and a height of 545 mm.

2.2.2. Coal hopper

The coal hopper is the primary source of pulverized coal for the furnace. It's just next to the furnace. In a coal hopper, a special arrangement is employed to keep the coal feeding rate constant. The coal hopper is constructed 80 mm long and 60 mm wide and manufactured of mild steel.

2.2.3. Burner

A burner is a device that converts fuel into a controlled flame. It is a component of the opening that produces heat. Swirling action is created in the burner to ensure adequate air and fuel mixing. The swirl burner has a diameter of 38 mm, and a length of 60 mm. Air may flow through with around 3 mm clearance, while the supply line of natural gas is 7.5 mm in diameter.

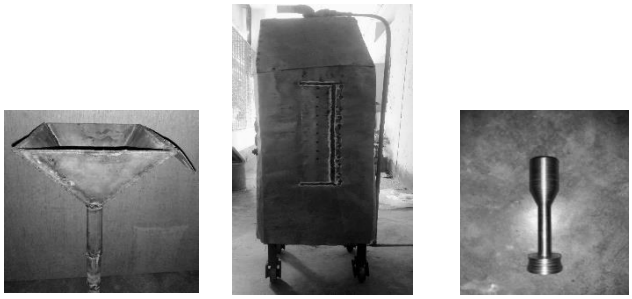

(a) (b) (c)

Fig. 2: Different parts of the setup: (a) Coal hopper (b) Furnace (c) Burner

2.2.4. Piping system

The piping system is utilized to transport the coal into the burner & carry out the exhaust burning products. During recirculation, it also transports flue gas. The piping system uses MS (mild steel) pipe with a total length of around 2600 mm. It is insulated with insulating material, preventing heat transmission from the pipe.

2.2.5. Air compressor

The setup also includes the usage of an air compressor. An air compressor is used to supply combustion air at a certain velocity. As a result, inside the furnace, a local diluted state will be formed, coupled with extensive internal recirculation. The peak temperature can also be reduced by increasing air velocity.

2.3. Accessories

1. Infrared thermometer 2. Flowmeter 3. Insulating material 4. Natural gas cylinder 5. Carbon dioxide (CO_2) gas cylinder.

2.4. Operating Conditions

In the experiment, fast coal de-volatilization is a requirement for combustion, and on the other hand, it is the oxidation within a diluted atmosphere. This might include a significant recirculation of flue gases, which could be used to heat the coal, combustion air, or both, and dilute before interactions with the de-volatilization products occur.

Recirculation is induced by high-momentum combustion air jets. The delivered velocity must not exceed 10 meters per second. The exhaust gas is used to pre-heat the combustion air, which aids in coal de-volatilization by providing extra heat for fuel heat-up. The coal carrier gas distinguishes two combustion scenarios. The first arrangement, designated as OX_{CO2}, uses CO_2 as a fuel carrier. The second design, known as OX_{Air}, employed air as the carrier gas, which is common in utility boilers. When the air was employed as the carrier gas, the combustion air flow rate was regulated to maintain the total air ratio. Four different particle sizes ranging from 0.001 to 0.005 mm, 0.005 to 0.01 mm, 0.01 to 0.015 mm, and 0.015 to 0.02 mm of 1.48 kg/h were injected into the furnace.

2.5. Methodology

Natural gas was used to initiate the combustion process. To heat the furnace up to the self-ignition temperature of coal, a swirl burner was initially employed to ignite a combination of natural gas and air. The coal was fed to the furnace by flowing carbon dioxide gas after the internal temperature reached the self-ignition temperature of the coal. So, carbon dioxide gas worked as a career gas. Then the coal Combusted and continued the combustion process. There are 9 ports in the middle part of the furnace to make it possible to measure the temperature of different sections. Each of the ports is 63.5mm away from the other.

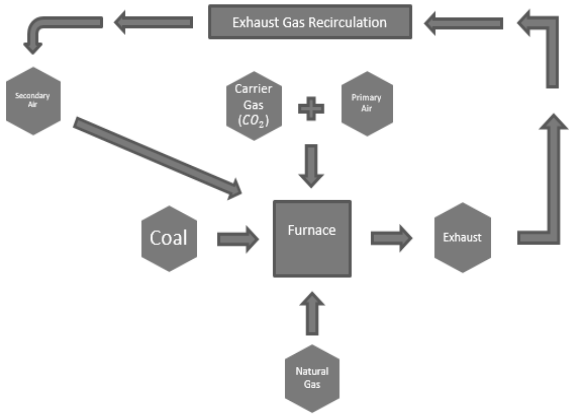

Fig. 3: Methodology

A DIGITECH QM7221 model infrared thermometer is used to measure the temperature. Coal was crushed in four different sizes of particles. The methodology can be seen in Figure 3. The ranges of particle size were 0.001 to 0.005 mm, 0.005 to 0.01 mm, 0.01 to 0.015 mm, 0.015 to 0.02 mm. All sizes of Particles were used with a constant feed rate of 1.48 kg/hr A portion of the exhaust gas was re-circulated to heat the coal.

2.6. CFD Analysis

The 3D modeling of the furnace body was done by designing software “Solidworks-2016” and the analysis was done by simulating in the ANSYS FLUENT VR15.0 code. Different steps and parameters setting were very important to find out the proper result. Important steps of the simulation were inputting the geometry, meshing, setting up parameters, running calculations, and observing results.

3. RESULTS AND DISCUSSION

Two experimental and numerical studies are performed utilizing a medium-scale laboratory furnace to evaluate the influence of particle size on the burning properties of pulverized Bituminous high-quality coal using CO_2 as a carrier gas. In addition to the pulverized coal mass flow rate (1.48 kg/h), the secondary air temperature and CO_2 content were kept constant. Four characteristics were observed for four-particle sizes. Temperature, mass fraction of carbon-di-oxide, mass fraction of carbon monoxide, and mass fraction of nitric oxide in exhaust emission were observed.

3.1. Model validation

To validate the modeling, the current simulation's output is compared to experimental data. The only temperature distribution is validated. The model was numerically analyzed using bituminous coal properties. This study used particle sizes 0.001 to 0.005, 0.005 to 0.01 , 0.01 to 0.15 , 0.015 to 0.02 mm. At a consistent rate of 1.48 kg/h, all particle sizes were employed. The plot shows that the maximum temperature difference between the numerical and experimental maximum values is only 30.9 k for particle sizes ranging from 0.001 to 0.005 mm and 26.7 for particle sizes ranging from 0.005 to 0.01 mm. The dimensionless ratio (Y/D_j) is used to indicate the vertical placements. D_j is the jet diameter, and Y is the vertical distance from the jet exit plane.

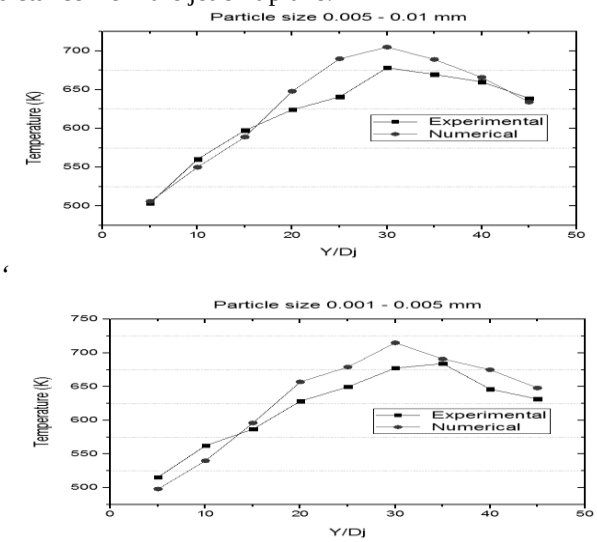

Fig. 4: Experimental and numerical profile of temperature in the furnace

3.2. Temperature contour

Figure 5 shows the observed furnace temperature profile. This figure depicts the temperature dispersion inside the furnace. Profiles for four-particle sizes are seen. The temperature difference implies a uniform temperature distribution. A comparison of the temperature profiles in examples 1, 2, 3, and 4 is made. Figure 5 demonstrates that smaller particle sizes result in greater furnace temperatures than larger particle sizes. This, of course, refers to the place

and manner in which volatile is released and responded to in the case of smaller particles. Devolatilization occurs early in the case of smaller particles and is accomplished by the end of the recirculation vortex, whereas devolatilization occurs later in the case of larger particles. The only temperature difference that is expected is at the furnace's fuel jet outflow, where a substantially lower temperature is expected. The temperature profile deviates from the centerline. It also depicts the temperature fluctuation at various points.

Table 1: Observed experimental temperature (Kelvin) data for different particle sizes in the middle part of the furnace

Particles' size ranges from 0.001 to 0.005 mm	Particles' size ranges from 0.005 to 0.01 mm	Particles' size ranges from 0.01 to 0.015 mm	Particles' size ranges from 0.015 to 0.02 mm
515.7	503.6	500.1	594.3
562.3	560.3	557.4	552.3
586.9	597.5	601.2	598.7
628.4	624.1	619.5	615.1
649.6	640.8	636.9	640.5
677.5	678.3	674.6	652.4
684.1	669.7	654.3	659.5
646.3	660.1	627.8	627.8
631.6	638.9	597.9	588.8

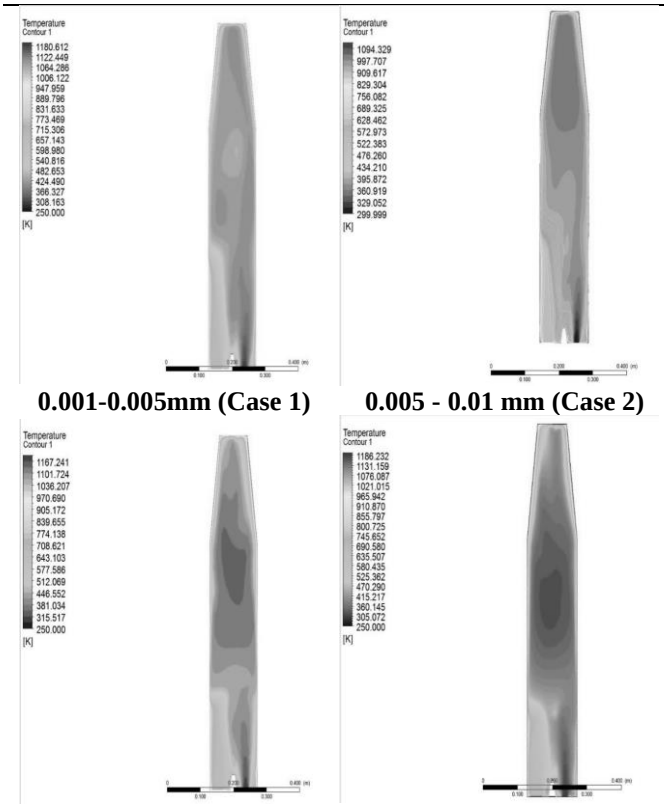

0.001-0.005mm (Case 1) **0.005 - 0.01 mm (Case 2)**

0.01 - 0.015 mm (Case 3) **0.015 - 0.02 mm (Case 4)**

Figure 5: Temperature profile

3.3. CO contours

Figure 6 shows the observed CO concentration within the furnace. In general, smaller particle sizes had lower in-furnace CO formation trends than bigger particle sizes. The lower CO generation for tiny particles was consistent with the results that the rate of volatiles release and reactions of smaller particles at upstream locations is significantly higher than that of larger particles, but due to complete combustion produces CO_2 in greater amounts than the larger particle's size. Furthermore, the CO concentration peak for smaller particle sizes is highest at the center of the furnace, whereas the highest CO concentration peak for large particles is found at the top of the furnace. This is due to bigger particles penetrating deeper into the furnace This variation might be due to a variety of factors. CO is released as a volatile substance during the coal devolatilization process. CO is also produced when volatile substances and char are oxidized. Furthermore, the water-gas reaction ($CO + H_2O \rightleftharpoons CO_2 + H_2$) affects CO concentration. CO concentration varies from the centerline and has varied values at various positions.

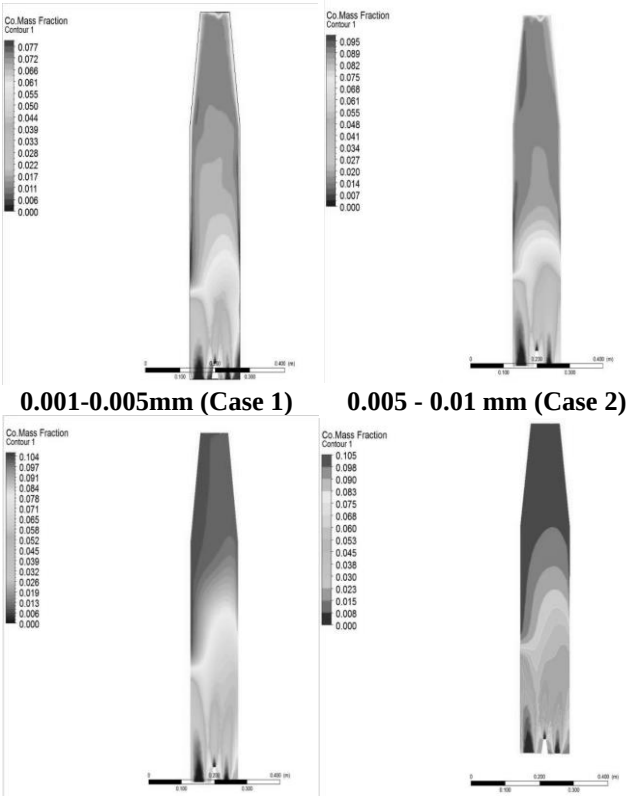

0.001-0.005mm (Case 1) **0.005 - 0.01 mm (Case 2)**

0.01 - 0.015 mm (Case 3) **0.015 - 0.02 mm (Case 4)**

Figure 6: Concentration of CO

Table 2: Observed numerical CO mass fraction data for different particle sizes in the middle part of the furnace

Particles' size 0.001 to 0.005 mm	Particles' size 0.005 to 0.01 mm	Particles' size 0.01 to 0.015 mm	Particles' size 0.015 to 0.02 mm
0.044	0.041	0.048	0.045
0.049	0.048	0.052	0.060
0.056	0.055	0.060	0.068
0.061	0.068	0.071	0.074
0.066	0.075	0.078	0.080
0.072	0.082	0.86	0.083
0.070	0.089	0.93	0.091

0.069	0.085	0.99	0.098
0.067	0.089	0.104	0.105

3.4. NO contours

Figure 7 depicts the concentration profile of NO within the furnace. The NO emission is measured for both smaller and larger particles, and the Figure shows that for the same experimental conditions, the larger particle NO concentration is higher. However, due to NO re-burning processes, the global NO emission rate from coal combustion is much larger than the measured local NO emission rate for both particle instances. The maxima of smaller particles are established near the jet exit, whereas the maxima of larger particles are observed towards the top of the furnace. It is observable that a rising trend of NO concentration is found if the particle size is increased.

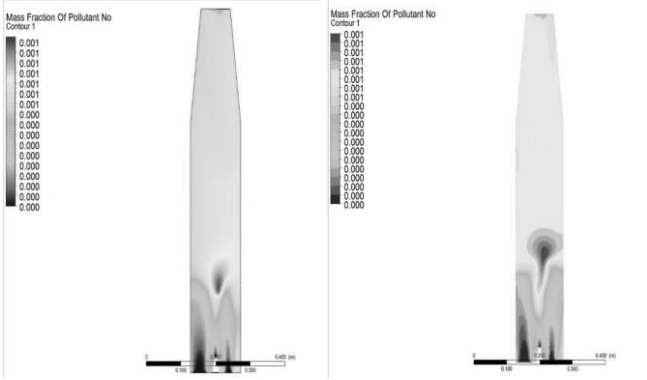

0.001-0.005mm (Case 1) **0.005 - 0.01 mm (Case 2)**

0.01 - 0.015 mm (Case 3) **0.015 - 0.02 mm (Case 4)**

Figure 7: Concentration of NO

Table 3: Observed numerical NO mass fraction data for different particle sizes in the middle part of the furnace

Particles' size ranges from 0.001 to 0.005 mm	Particles' size ranges from 0.005 to 0.01 mm	Particles' size ranges from 0.01 to 0.015 mm	Particles' size ranges from 0.015 to 0.02 mm
0.001	0.001	0.000	0.001
0.001	0.001	0.000	0.001
0.001	0.001	0.001	0.001
0.000	0.001	0.001	0.001
0.000	0.001	0.001	0.001
0.000	0.000	0.001	0.001
0.000	0.000	0.001	0.001
0.000	0.000	0.001	0.001
0.000	0.000	0.001	0.001

3.5. CO_2 (Carbon dioxide) contours

CO_2 is one of the most frequent and significant species in coal combustion exhaust emissions. Figure 8 shows that the concentration of CO_2 within the furnace is greater when the size of the particles is smaller than the size of the particles is larger. This occurs because more carbon is burned during the combustion of smaller particles than bigger particles. For the larger particle size, the lower carbon consumption rate is related to the insufficient residence time of combustion. Because bigger particles are heavier than tiny particles, they take more residence time to burn significantly as compared to smaller particles. The zenith occurs at the closest jet exit plane site. For all situations along with the height of the furnace, a decreasing trend in CO_2 concentration is found. The results show that devolatilization of coal particles occurred at the jet exit plane, however volatile matter reactions are initiated at a particular height in the furnace, and volatile matters/gases are efficiently diluted with incoming CO_2.

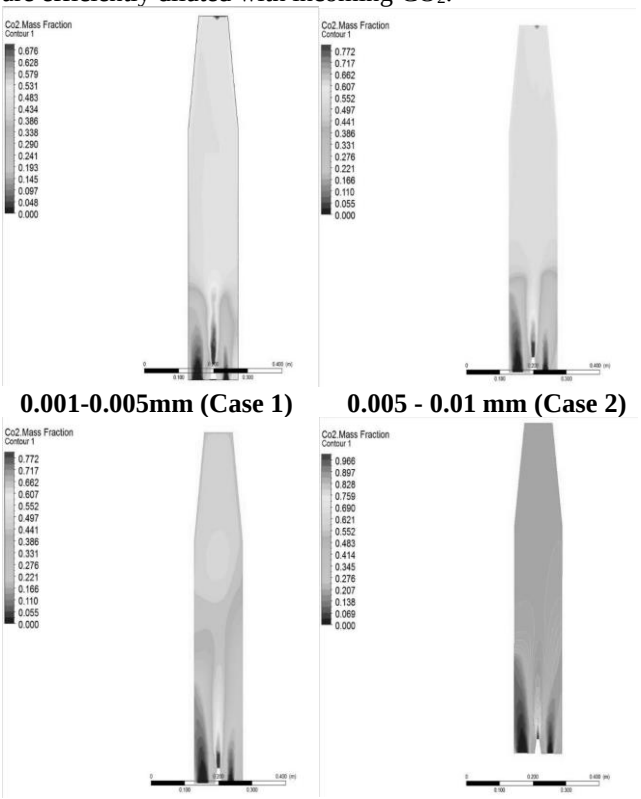

0.001-0.005mm (Case 1) **0.005 - 0.01 mm (Case 2)**

0.01 - 0.015 mm (Case 3) **0.015 - 0.02 mm (Case 4)**

Figure 8: Concentration of CO_2

Table 3: Observed numerical CO_2 mass fraction data for different particle sizes in the middle part of the furnace

Particles' size ranges from 0.001 to 0.005 mm	Particles' size ranges from 0.005 to 0.01 mm	Particles' size ranges from 0.01 to 0.015 mm	Particles' size ranges from 0.015 to 0.02 mm
0.608	0.597	0.590	0.584
0.598	0.591	0.555	0.552
0.000	0.000	0.001	0.001

0.579	0.580	0.537	0.524
0.570	0.568	0.503	0.513
0.566	0.557	0.485	0.479
0.541	0.544	0.461	0.461
0.538	0.529	0.446	0.442
0.519	0.511	0.432	0.409
0.505	0.497	0.414	0.386

3.6. Carrier Gas

In this experiment, CO_2 is used as carrier gas because of its easier availability and less expensive than other inert gas. It requires approximately 1500 degrees Celsius to turn CO_2 into C and O. So, the possibility of the formation of CO from C & O is much lower. As a result, CO_2 behaves as an inert gas, lowering overall pollutant emissions. Instead of utilizing air, it is employed as a carrier gas.

4. CONCLUSION

The effect of particle size and carrier gas on pulverized bituminous coal combustion characteristics is investigated. This research focuses on temperature rise and concentration of CO, CO_2, and NO_x from four distinct particle sizes. This experiment also shows the impact of carrier gas. These research main results are:

The furnace's maximum temperature for smaller particles (0.001-0.005 mm) is 1148 K, and for larger particles (0.015-0.02 mm) is 1040 K. The small particle scenario creates a greater furnace temperature than the larger particle. The more intense volatile combustion of smaller particles influences high-temperature production. The concentration of CO inside the furnace is higher for smaller particles. This illustrates that the rate of volatile release for large particles is substantially lower than that for small particles.

The concentration of NOx is higher for particle sizes ranging from 0.001 to 0.005 mm than for particle sizes ranging from 0.015 to 0.02 mm, according to the simulation results. The NOx generation trend is much higher for tiny particles than for larger particles. Volatiles were released earlier by the tiny particles, and combustion occurred quickly. As a result, the subsequent NO production is very high. Large particles, on the other hand, require longer to dissolve for volatile development, and volatile combustion commences after a long residence period. The global NO_x emission rate from coal combustion is much higher than the experiment's method of combustion for all particle sizes due to NO re-burning processes. Particle sizes ranging from 0.001 to 0.005 mm have a greater maximum CO_2 concentration than particle sizes ranging from 0.015 to 0.02 mm. The larger particle scenario produces less CO_2 than the smaller particle case. As a consequence, particle size must be kept small, and the furnace combustion temperature must not exceed 1700K, because NOx formation is substantially lower below this temperature.

Because CO_2 is relatively stable, there is no simple technique to convert it into Carbon & Oxygen. As a result, the potential of CO production from C and O is comparatively lesser. For that reason, carrying gas act like an inert gas in this project. Overall exhaust emission is also reduced due to the use of CO_2 as a carrier gas instead of using air. For obtaining better results, Argon & Helium can be used but they are more expensive than CO_2. The result of this research can be helpful to develop a strategy for minimizing pollutant emissions. Determining the influence of fuel injection angle & the impact of using different types of burners in the combustion process can be potential research in the future.

REFERENCES

[1] R. Liu, E. An, K. Wu, Z. Liu, Numerical simulation of oxy-coal MILD combustion with high-velocity oxygen jets, 1-2, 2015.

[2] Z. Mei, P. Li, J. Mi, F. Wang, J. Zhang, Diffusion MILD combustion of firing pulverized coal at a pilot furnace, 804-806, 2015.

[3] https://www.eolss.net/Sample-Chapters/C08/E3-04-03-01

[4] M. Saha, B. B. Dally, P. R. Medwell, A.Chinnici, Effect of particle size on the MILD combustion characteristics of pulverized brown coal, 4-5, 2015.

[5] M.de Joannon, A.M., P. Sabia, A. Cavaliere, Mild combustion in homogeneous charge diffusion ignition regime, 3409-3410, 2007.

[6] T. Kiga, K.Y., M. Sakai, S. Mochida, Characteristics of pulverized coal combustion in high temperature preheated air, 601-602, 2000.

[7] T. Suda, M.T., T. Hirata, M. Yoshino, J. Sato, A study of combustion behavior of pulverized coal in high-temperature air, 503-505, 2002.

[8] R. He, T.S., M. Takafuji, T. Hirata, J. Sato, Analysis of low No emission in high-temperature air combustion for pulverized coal, 1137-1138, 2004.

[9] Z. Mei, P.L., F. Wang, J. Zhang, J. Mi., Influences of reactant injection velocities on moderate or intense low oxygen dilution coal combustion, 380-383, 2013.

[10] Y. Tu, H.L., K. Su, S.Chen,Z. Liu, C. Zheng, W. Li., Numerical study of *H2O* addition effects on pulverized coal oxy-MILD combustion, 253-260, 2015.

[11] R. Weber, Y.P., A.M. Beckmann, S. Brinker, Combustion of biomass in jet flames, 2749-2758, 2015.

[12] M. Tamura, S.W., K. Komaba, K. Okazaki Combustion behavior of pulverized coal in high-temperature air condition for utility boilers, 446-449, 2015.

[13] Prog. Comput. Fluid Dynamics, 2015.

[14] M. Saha, B.B.D., P.R. Medwell, E.M. Cleary, Moderate or intense low oxygen Dilution (MILD) combustion characteristics of pulverized coal in a self-recuperative furnace, 6054-6060, 2014.

[15] Weinberg, F.J., Combust. Sci. Technol. 1996.

[16] M. Katsuki, T.H., Proc. Combust. Inst. 27. 1998.

[17] R. Weber, S.O., N. Laliemant, A. Verlaan,, Proc, Combust. Inst. 28. 2000.

[18] Hai Zhang a, Guangxi Yue a, Junfu Lu a, Zhen Jia a, Jiangxiong Mao a, ToshiroFujimori b, Toshiyuki Suko b, Takashi Kiga b, Development of high-temperature air combustion technology in pulverized fossil fuel-fired boilers, 2779-2789, 2007.

[19] "The most depressing energy chart of the year". Vox. 15 June 2018.

Paper ID: 6607
International Conference on Mechanical, Manufacturing and Process Engineering (ICMMPE – 2022)
Organizer: Faculty of Mechanical Engineering, Dhaka University of Engineering & Technology (DUET), Gazipur, Bangladesh
Website: https://icmmpeduet.com/

Supplier Selection and Evaluation using Genetic Algorithm : A Case Study in an Apparel Manufacturing Organization

Shibbir Ahmad[1] and Mohammad Kamruzzaman[2]

[1]Mechanical Engineering Department, Dhaka University of Engineering and Technology (DUET).
[2] Mechanical Engineering Department, Dhaka University of Engineering and Technology (DUET).

E-mail: ahmadjerin@gmail.com

ABSTRACT

Supplier selection and evaluation is a major powerful indicator for smooth business in the clothing manufacturing industry. Because the garment manufacturer is fully dependent on the supplier. That's why , supplier should be selected carefully to ensure on-time materials management. The core focus of this research is to minimize losses for apparel manufacturing by selecting the right supplier to receive materials in a timely manner. Additionally, the negative effects of delays in delivering materials into factories have been shown. Meanwhile, it has been demonstrated that the consequences of the delayed delivery of the materials, due to erroneous supplier selection ,based on the traditional supplier evaluation and selection process. This paper has also shown that the conventional supplier selection process has its drawbacks in operational aspects. In this research, a proposed supplier selection process has been portrayed and implemented in a selected apparel manufacturing organization. Moreover, the genetic algorithm (GA) method has been employed to select the best supplier for a designated garment manufacturing unit as a progressive implementation steps of the proposed supplier selection process . Overall, It can save up to 15% of the total cost.

Keywords: Supplier selection ; Supplier evaluation ; Genetic Algorthm ; Apparel supply chain ; Supplier selection criteria.

1. INTRODUCTION

Supplier selection is one of the important responsibilities for the supply chain manager in the apparel industry to survive in this competitive arena. Since then, the level of competition has grown dramatically in the garment manufacturing organizations in the last decade. Hence, the on-time shipment has to be done with good quality product to the retailer. In this context, there is no alternative way to accomplish the supplier's selection and evaluation process before placing orders with them. A supplier is the crucial partner of any well-established business. Some researchers [1] have discussed the structural methodology for supplier selection and evaluation in the supply chain. They have implemented SWOT (Strengths, Weakness, Opportunities, and Threats), DEA (Data Envelopment Analysis) and MADA (multi-attribute-decision making) tools as supplier selection and evaluation methods . The research resulted in the establishment of a collaborative relationship with the management of the potential suppliers to assist in increasing product development capability and quality, lowering product life cycle cost and time, and increasing product demand in the market .

An integrated framework has been developed for sustainable supplier selection and evaluation in the supply chain, focusing on sustainable suppliers' selection using AHP (Analytical Hierarchical Process) in the Indian automobile industry. The study has emphasised the green supply chain while selecting suppliers. There are 22 sustainable supplier selection criteria, and 3 dimensional criteria have been identified to conduct the whole analysis. The outcomes of the study were the environmental cost reduction, the improvement of the quality of the product, and the enhancement of occupational health and safety for the workforce. The research showed the way to the best supplier selection, concentrating on AHP. It helps supply chain managers to select the right supplier by analysing suppliers' selection criteria [2].

A study [3] has been conducted on supplier selection and evaluation, they principally focused on operation and strategic criteria while selecting supplier ,which emphasized on purchasing and it had an effect on purchasing performance directly through supplier selection. Furthermore, this [4] study showed that supplier selection and evaluation by implemeting the fuzzy ranking method mainly focused on the quality of the products. Additionally,the optimization problem devolved and solved to identify the best suppliers. Another researcher [5] exposed the DEA type composite indicators (CI) tools was used to study the conventional supplier selection method with environmental factors where the weight system has been considered as the selection criteria.

Suppliers' selection and evaluation have been performed, focusing on quality function deployment (QFD). They proposed an algorithm model to evaluate selected ISPs (Internet Service Providers) from a customer, performance, and competition perspective. Furthermore, a fuzzy set theory has been implemented into the implement step for the supplier's selection [6].A multi-attribute selection (MSM) model has been employed to conduct the supplier selection and evaluation method in order to ensure good quality product manufacturing by the suppliers with on-time delivery [7]. Since we are concerned about the Just-in-Time manufacturing system where there is no policy for keeping inventory, Hence, it is important to supply materials in a timely manner. A neural network-based supplier selection and evaluation tool has been executed to select the suppliers. This model is not limited to only JIT manufacturers. Through performance evaluation [8], it can help producers select the most suitable and best suppliers. In this study, AHP (Analytical Hierarchical Process) was implemented to accomplish the supplier's selection and evaluation in the apparel manufacturing organization. It has shown the way of the traditional supplier's selection method and the proposed supplier's selection and evaluation methodology, which have been applied by a leading apparel manufacturer to validate the proposed model. The outcome of the research was to select the right suppliers using the AHP method and place orders with those suppliers to maintain a smooth supply chain. The limitation of the research is the mathematical analysis of the AHP method, which is not user friendly tool for supply chain manager [9]. To overcome this difficulty, we have implemented a Genetic Algorithm (GA), which entails very basic mathematical analysis.

The remaining paper is organized as follows: Section 2 describes the problems related to traditional supplierselection. Section 3 discusses the genetic algorithm method and its implementation step in the apparel industry. Section 4 confers details on the implementation phase of the proposed supplier selection method.

2. IREGULARITIES RELATED TO TRADITIONAL SUPPLIER SELECTION

In this paper, we have selected a well-reputed apparel manufacturing organization to collect data for the analysis and validate the proposed supplier selection method. It is a challenging activity for this manufacturing unit to supply fabrics on-time to avoid line gaps. Suppliers have taken orders, but they cannot provide on-time delivery. Consequently, the company has to do air shipment or discount, which deteriorates the profitability, and thus the customer's confidence is lost, and finally, the company suffers. Initially, the merchandiser searches for suppliers both locally and overseas, conducts an opening meeting with the supplier, and negotiates the price. The supply chain team focuses on the lowest price. Once the expected price is met, they select this supplier, which is a totally non-productive approach. Meanwhile, the merchandiser takes advantage of the supplier and places orders without performing proper evaluation and selection. Subsequently, the supplier manufactured the items and supplied average-quality products to the manufacturer, thereby delaying delivery. Accordingly, buyers claim a bad quality product. On the other hand, the shipment is delayed due to the interruption in sending materials. The traditional supplier selection strategy is explained in figure 1.

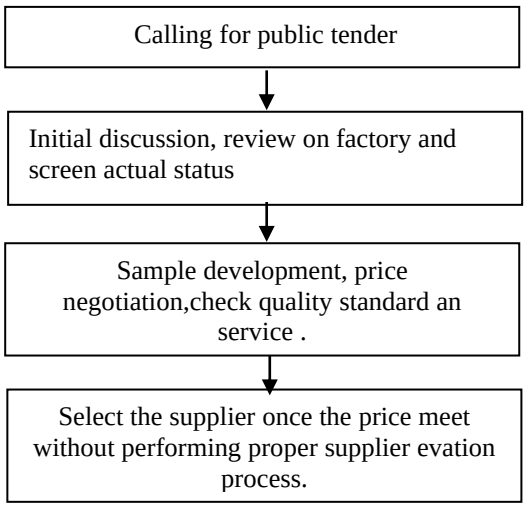

Fig 1 : Traditional supplier selection process

The proposed supplier selection selection is discussed in figure 1.

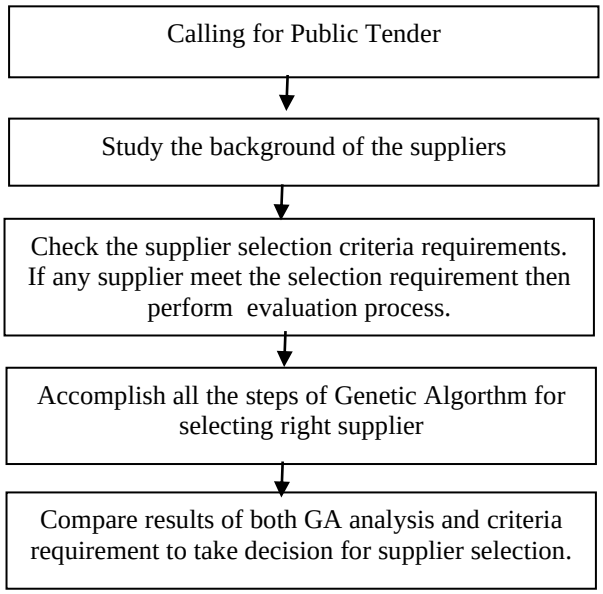

Fig 2 : Proposed supplier selection process

It is started with calling for public tender, initial investigation of the supplier's strength, checking the business requirements with the supplier, and if any supplier meets the requirements, then performing the evaluation procedure while implementing genetic algorithm. Finally, the supplier will be selected who meet the business requirements as well as gets the highest score by applying a genetic algorithm (GA).

Since the supplier is selected by the traditional approach, it negatively affects the shipment mode which shown in table 1. Customers, in general, prefer to ship by sea; however, because of the manufacturer's production delay, the actual shipment date cannot be met.

Table 1: delay delivery affect on shipment mode

PO	Delays	Effects on shipment mode	Destination
201	41	Air	Denmark
202	42	Air	Germany
203	38	Sea-air	USA
205	43	Sea-air	Canada
206	43	Sea-air	Canada
207	23	Sea-air	USA
213	15	Sea-air	Poland
214	18	Sea-air	Poland
215	17	Sea-air	Poland

Though sometimes buyers give one week's extention, if the delay is more than a week, the buyer will definitely impose a discount or ship by air, which is more costly. An analysis conducted in a leading apparel manufacturing organization is shown in table 1. It is indicated that PO Nos. 201 and 202 have been imposed on shippers by air from the buyer's end due to a delay in delivery. It happened because of the delay in receiving materials from the supplier. In this case, the supplier does not want to take full responsibility. Hence, the manufacturer has to sufffer and lose money through air shipment.

Air costs are more than manufacturing costs in some countries like the USA, Canada, and Denmark, which is shown in table 2. While shipping goods by air or sea-air mode by manufacturer's cost due to wrong supplier selection, the company will have to pay an additional penalty.

Table 2: Consequnces for air shipment

PO	Air cost per pieces ($)	Total ship quantity (pieces)	Total additional cost($)
201	0.25	7890	1973
202	0.22	9000	1980
203	0.35	8500	2975
205	0.4	10000	4000
206	0.4	15000	6000
207	0.35	20000	7000
213	0.22	7000	1540
214	0.22	8000	1760
215	0.22	5000	1100

Finding the right supplier is an important and unavoidable task for the apparel industry.

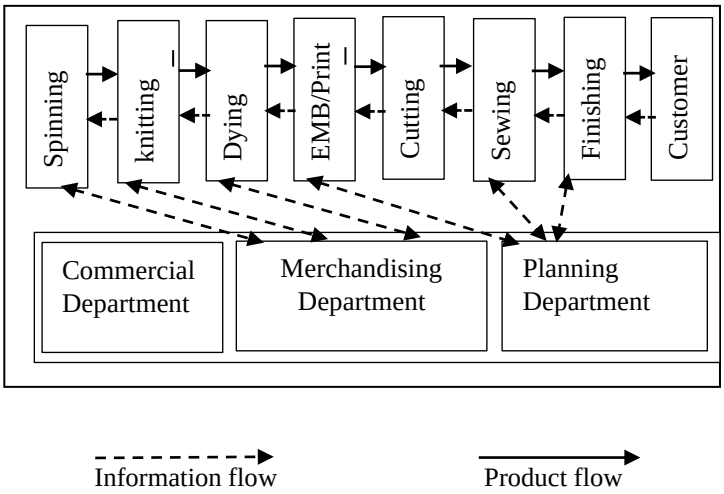

Fig 3 : Schematic view of apparel supply chain

The apparel supply chain starts with raw material suppliers and ends with the end customer. Production flow is directed from upstream to the downstream stream, and information flow is conducted from downstream to the upstream stream. In this paper, we have selected a working area for this manufacturing unit, which is shown with a bold mark. That means that we focused from knitting to printing as the manufacturer is facing a delay in receiving materials from knitting-dying-dying finishing. In some cases, the printing supplier is delayed in sending material to the manufacturer, which leads to a production gap. It generates non-productive time, which costs the apparel manufacturer, and this delay leads to the air shipment. The apparel manufacturing industry in Bangladesh started with traditional supplier selection. Nowadays, the manufacturer

has evolved a proper supplier selection and evaluation system to sustain in the competitive market since labor costs have been increased dramatically in the last decade.

3. METHODOLOGY OF THE STUDY

The research methodology has been concisely demonstrated in Figure 4. Initially, we developed a flow chart for the conventional supplier selection strategy and studied the results of the traditional supplier selection. Sencondly, they collected raw data from a leading apparel manufacturing organization and analyzed it using Microsoft Excel, showing the results in tabular form. Thirdly, we have implemented a genetic algorithm (GA) method to select the supplier in the leading apparel manufacturing organization. Finally, we have proposed a supplier selection method and implemented it to validate the outcome.

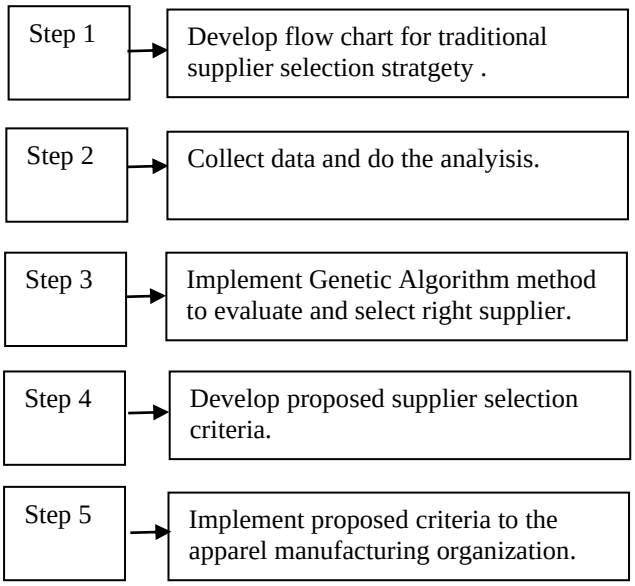

Fig 4 : Proposed supplier selection process

3.1 Decision model analysis for supplier seletion

Genetic Algorim and its associated implementation stpes are discussed as follows .

3.1.1 Genetic Algorithm

Equations for genetic algorithm has depicted below :

$$F(x)=x^2 \quad (1)$$

Where *value of x is 0-31* , n is the population size, and $x<x^2$,there are 5 steps to follow to solve the genetic algorithm which describes beneath :

Step 1: choose an encoding technique

0 = 00000

31 = 11111

Step 2: choose the population size

n= 4

step 3: Randomly choose initial population

13,24,8,29

Step 4: Select parental chromosomes Following through Roulette wheel selection method

Step 5 : crossover and mutation

4. IMPLEMENTATION STEPS OF PROPOSED SUPPLIER SELECTION METHOD

In this section, we will discuss elaborately the proposed supplier selection method. It gives the guideline for selection appropriate supplier selection .

Phase 1 : Calling for public tender

In this step, the manufacturer will arrange a public tender where suppliers will get an invitation to attend for the specific materials brought by them. In this paper, we chose a manufacturing organization that focuses on fabric and printing-related operations, so knitters, dyers, and priters, as well as embroidery suppliers, are welcome to participate in the tender.In this case, the company can publicly offer in the mass media to disseminate the information to all for an unbaised selection. It is mandatory for the company to mention their business terms and conditions and customer standards. As a result, if the suppliers see that he is favored in all business requirements, they will participate.There will be no partiality or biasness while selecting the best suppliers to operate the supply chain smoothly.

Phase 2 : It is important to study the background of the suppliers before selecting them, as the business has to be done continually and consistently with the suppliers who will be selected for their better quality, productivity, and delivery. At this stage, the main focus will be given to the financial stability of the suppliers.

Phase 3: In this phase, rate the supplier selection criteria. The highest score will be considered the right supplier selection. Lead time, quality, capacity, communications, delivery, service, legal, environment, diversity, and price have been taken into consideration as supplier criteria. We have analysed the supplier selection criteria and found that supplier 3 got the highest average score, which is depicted in table 3.

Phase 4 : There are five steps that need to be clarified to complete the implementation of the genetic algorithm. In step 1, we need to choose an encoding technique where 0 = 00000 to 31 = 11111. In step 2, we have elected a population size of n = 4. In step 3, we chose the initial population at random as 13,24,8,29, which will be converted to a binary number when calculating the

expected count f(x).In step 4, selected parental chromosomes are followed through the Roulette wheel selection method. Finally, in step 5, perform the cross over and mutation to obtain the new binary number, which will then be onverted to an integer number to calculate the final value of f(x) to select the best supplier.The highest value of f (x) will be measured as the appropriate supplier.

In stage 1, we used quantion 1 to calculate the expected count f(x) for selecting the appropriate supplier.Once we get the value of f (x), we can then find out the probability count for each value of x. f(x)/ f(x) is the probability calculation.For example, for string number 1, 169/1170 = 0.14. Similairly, the values for string numbers 2, 3, and 4 were found to be 0.49, 0.05, and 0.31, respectively. We determined that the average value of f (x) is 293.

String no	Initial population (Binary value of x)	X Value	f(x) Value	Probability count (f(x) / ∑ f(x))	Expected count (f(x))	Actual count
1	"01101	13	169	0.14	0.58	1
2	11000	24	576	0.49	1.97	2
3	01000	8	64	0.05	0.22	0
4	10011	19	361	0.31	1.23	1

Stage 1 : Calculating expected count of F(x)

String 2	11000	Parental Combination 1
String 1	01101	

String 2	11000	Parental Combination 2
String 4	10011	

Stage 2 : Segregation of parental combination

To calculate the expected count ((f(x)/Average value of f(x)) for string number 1, multiply 169/293 by 0.58.expected counts for strings 2, 3, and 4 are 1.97, 0.22, and 1.23 cronologically. To get the actual count, convert the value of the expected count into a round number. In stage 2, we have separated parnetal combination 1 and 2.

Crossover:

String 2	1100 0	11001
String 1	0110 1	01100
String 2	11000	11011
String 4	10011	10000

In stage 3, we have performed crossover functaion to get the new binary number.

Stege 3 : Performig crossover function

String no	Initial population (binary value)	X Value (integer value)	f(x) Value	Supplier selection (String no count as supplier)
1	01100	12	144	
2	11001	25	625	
3	11011	27	729	3
4	10000	10	256	

Stage 4 : Right supplier selection through genetic algorithm(GA)

Table 3: analysis of supplier selection criteria

	Supplier			
Supplier selection criteria	**1**	**2**	**3**	**4**
Lead Time	0.95	0.9	0.95	0.9
Capacity	0.98	0.88	0.95	0.97
Communication	0.98	0.9	0.98	0.98
Quality	0.98	0.89	0.98	0.89
Delivery	0.95	0.9	0.95	0.9
Service	0.95	0.9	0.95	0.9
Product Diversity	0.8	0.7	0.8	0.7
Legal	0.95	0.9	0.95	0.9
Environment	0.95	0.88	0.95	0.88
Price	0.95	0.93	0.95	0.93
Average	0.90	0.88	0.94	0.87

In stage 4, we have calculated the value of f (x) using the equation again to get the right supplier. We can see the uppermost value of f(x) for string 3, which is considered the supplier number, from stage 4.

4. DISCUSSION

We have compared the supplier selection criteria with the results of the genetic algorithm. From table 3, we see supplier 3 got the highest score while applying the same supplier selection criteria and, at the same time, by applying the genetic algorithm, supplier 3 got the top score. Hence, undoubtedly, we should select Supplier 3 as the best supplier. It was the toughest job to select the right supplier

from their criteria analysis since everyone had a very close number. However, we had to select one, so we must select Supplier 3 as the business partner of the leading apparel manufacturing organization. So, the proposed supplier selection model using genetic algorthm is a valid model. The company has placed an order with supplier number 3 and will keep these efforts continuing while selecting the supplier. Though the manufacturing capacity and communication level of suppliers 1 and 4 are good, considering the best quality materials, the company wishes to continue business with supplier number 3.

In this paper, as we have proposed a supplier selection and evaluation process comparing with the traditional supplier selection process to eliminate overprocessing , and some malpractice to save time and cost in the apparel supply chain. In addition to this , we have applied genetic algorithm method to evelauate and select the best supplier in apparel manufacturing. Though , there are many similar methods have been implemented to serve the same purpose including ANN ,AHP and so on. [10] They have implemented ANN and GA with multi-criteria decision making tools which is a mathemcatical programming techqniues to select the right supplier. Another study [9] showed that the best suppliers have been selected using AHP with multi-criteria decision making tools. It requires users to know strong mathematical knowledge to understand the supplier evaluation and selection process.

As, this reserch has been made focusing on apparel manufacturing organization, and the purpose of this paper is to select the right supplier for an apparel manufacturing industry and this process will implement by merchandiser .That's why, Genetic Algorithm(GA) method have been selected along with proposed supplier selection process (figure 4) to implement as a user friendly tool to evaluate and select the right supplier .

5. CONCLUSION

Since the clothing market has become competitive day by day, labour costs have drastically increased in the last decade. For 10 years, Bangladesh was the cheapest labor market in the apparel arena. However, this scenario has changed in the last 10 years. Therefore, the profit margin has been reduced for the manufacturer. To boost profitability by cutting costs, there is no alternative option to implementing supplier selection and evaluation techniques before selecting any supplier to continue the business.

We present a supplier selection model in this research that uses a multi-criteria decision-making process that comprises identifying key indicators, sub-indicators, andadetailed step-by-step analysis. For multi-attribute features of supplier selection problems, we employ the GA approach. In an apparel manufacturing company, the proposed supplier selection approach was put into practice. The corporation had a total of 2000 personnel, including 30 engineers, 200 officers and executives, and the balance 1770 operators, technicians, and helpers.

The major activities, like supplier selection and evaluation of suppliers' performance, and the right selection amongst many alternatives, are performed by the supply chain department. They assess the suppliers who are participating in the tender according to the proposed suppliers' selection and evauluation method described in this paper, and finally they are able to select the best one who will be their next business partner. Developing a software to implement GA would be the future recommended work, as if merchandizing manager could just enter data and take the decision which supplier will be the best one for the factory.

REFERENCES

[1] Chen, Y.J., 2011. Structured methodology for supplier selection and evaluation in a supply chain. Information Sciences, 181(9), pp.1651-1670.

[2] Luthra, S., Govindan, K., Kannan, D., Mangla, S.K. and Garg, C.P., 2017. An integrated framework for sustainable supplier selection and evaluation in supply chains. Journal of Cleaner Production, 140, pp.1686-1698.

[3] Pearson, J.N. and Ellram, L.M., 1995. Supplier selection and evaluation in small versus large electronics firms. Journal of Small Business Management, 33(4), p.53.

[4] Shu, M.H. and Wu, H.C., 2009. Quality-based supplier selection and evaluation using fuzzy data. Computers & Industrial Engineering, 57(3), pp.1072-1079.

[5] Dobos, I. and Vörösmarty, G., 2014. Green supplier selection and evaluation using DEA-type composite indicators. International Journal of Production Economics, 157, pp.273-278.

[6] Amin, S.H. and Razmi, J., 2009. An integrated fuzzy model for supplier management: A case study of ISP selection and evaluation. Expert systems with applications, 36(4), pp.8639-8648.

[7] Barla, S.B., 2003. A case study of supplier selection for lean supply by using a mathematical model. Logistics Information Management.

[8] Aksoy, A. and Öztürk, N., 2011. Supplier selection and performance evaluation in just-in-time production environments.

[9] Marufuzzaman, M., Ahsan, K.B. and Xing, K., 2009. Supplier selection and evaluation method using Analytical Hierarchy Process (AHP): a case study on an apparel manufacturing organization. International journal of value chain manufacturing organisation. International journal of va *Journal of Indian Culture and Business Management*, *11*(4), pp.457-472.

[10] Ashtana,N and Gupta,M,2015 . Supplier selection using artificial neural network and genetic algorithm. International journal of Indian Cultural and Business Management,11(4),pp.457-472.

Paper ID:6636

International Conference on Mechanical, Manufacturing and Process Engineering (ICMMPE – 2022)

Organizer: Faculty of Mechanical Engineering, Dhaka University of Engineering & Technology (DUET), Gazipur, Bangladesh

Website: https://icmmpeduet.com/

Colorometric Analysis and Fastness Properties of Mulberry Filament Silk Fabric Dyed with Azadirachta Indica Extraction

Nusrat Jahan[1,2], Sharfun Nahar Arju[3]

[1] M.Sc. Student, Department of Wet Process Engineering, Bangladesh University of Textiles, Tejgaon, Dhaka-1208, Bangladesh

[2] Lecturer, Department of Textile Engineering, Northern University Bangladesh, Dhaka-1230, Bangladesh

[3] Professor and Head, Department of Wet Process Engineering, Bangladesh University of Textiles, Tejgaon, Dhaka-1208, Bangladesh

E-mail: nusratjahanshifa@gmail.com, sharfun71@yahoo.com

ABSTRACT

This research work intended on evaluating dyeing performance and fastness properties on mulberry filament silk fabric dyed with the extraction of Azadirachta indica leaves. The absorbance of extracted dye solution was examined by UV/VIS spectrophotometer. In this research work, the samples were dyed by exhaust method and shades were developed by the simultaneous mordanting process using synthetic and natural mordants at 80 ºC temperature maintaining 1:60 liquor ratio. Colorimetric analysis of dyed samples was done using CMC color difference and tolerance system under three illuminates ie. D65, TL83, and F11. Different colorfastness tests i.e. colorfastness to wash, water, perspiration, light, and rubbing were done for evaluating color change and color staining of dyed samples. The colorometric test results revealed that in most cases, samples dyed using synthetic mordants individually intensified the color of unmordanted samples and exhibited quite altered hue against unmordanted sample and also exhibited better color strength and improved color yield compared to natural mordanted samples. The fastness results were better for natural mordant in few cases.

Keywords: Filament silk; Azadirachta indica; Extraction; Simultaneous mordanting; Spectrophotometer.

1. INTRODUCTION

The sericulture industries for silk fiber production hold out a great deal for the prosperity of our nation. Silk is a sustainable luxury animal-sourced continuous filament fiber used in making a variety of fashion clothing as well as medicinal products [1]. Today, with the increasing awareness of the importance of sustainability, the demand for naturally sourced fibers and dyestuffs in the textile sector has been garbing great attention due to having biodegradability and health protection [2],[3]. The coloration of textile materials develops the look, appeal, and value of the product. Natural dyes have organic value and eco-friendly application which has grown awareness among people towards the use of natural products over synthetic dyes. Mordant is a chemical that improves the affinity and fastness properties of natural dyes as it forms a chemical bond with the natural fiber that helps in fixation [4]. Silk fiber can easily be treated with natural dyes with the help of mordant. Azadirachta indica is a plant well known for its nontoxicity, harmless application for human beings. In recent years, dyeing of textile materials with natural dyestuffs is getting popular as synthetic dyes have carcinogenic nature. Many researchers have been studied the coloromertic properties and fastness of dyed samples using Azadirachta indica extraction, especially on cotton and cotton blended fabric. Few studies have considered silk fabric whereas only studied dyeing parameters, did not considered mordanting process [5],[6]. This research work focused on the dyeing performance of mulberry filament silk fabric with the extraction of Azadirachta indica leaves using different synthetic and natural mordants. Natural dyeing with Azadirachta indica extraction increases the value of textile products and meets the customers demands for green textile. The specific objective of this study was to evaluate the effects of dye extracts yields from Azadirachta indica leaves to explore the possibilities of natural dyeing with mordanting in terms of color value and fastness ratings.

2. EXPERIMENTAL

2.1 Materials

2.1.1 Substrate

A well degummed pure mulberry filament silk fabric was used in the experiment. It was sourced from Shopura Silk Mill Ltd. Rajshahi, Bangladesh. Table 1 represented the specification of fabric.

Table 1: The specification of fabric

Fabric	EPI	PPI	GSM	pH
Silk	110	85	37	7.6

2.1.2 Dye

Azadirachta indica leaves were used as a natural dye source that was collected from Ashkona, Dhaka, Bangladesh.

2.1.3 Mordants

Alum, Ferrous sulphate, potassium dichromate, and copper sulphate were used as synthetic mordants. Mango bark, Tomato juice, Green tea waste, Tea waste, Coffee, Paprika, and lemon juice were used as natural mordants.

2.2 Methods

2.2.1 Extraction

The aqueous extraction method was employed for extracting coloring matters from the leaves of the Azadirachta indica plant. At first, leaves were collected, washed, cleaned, and dried by sunlight for 24 hours for removing moisture from leaves, then measured weight. The extracted dye solution was prepared with 1:6 extraction ratio with 50 grams of dried materials. An electric burner was used to facilitate extraction where maintained 100 ^{o}C temperature and heated for 80 minutes by covering lid, and then simmer for overnight and filtered. The pH of extracted dye solution was measured by a digital pH meter. Fig.1 showed the extracted dye solution.

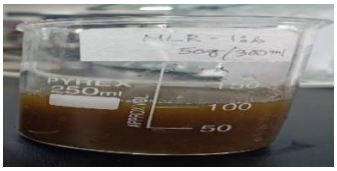

Fig.1: Extracted dye solution

Natural mordant, mango bark was prepared by aqueous extraction method maintaining 1:30 extraction ratio with 40 gram of powdered material at 100 ^{o}C temperature for 80 minutes and simmer for 8 hours and filtered whereas tomato juice and lemon juice were extracted by squeezing the tomato and lemon and collected the juices. All Synthetic mordants and natural mordant of coffee and paprika were in solid powdered state and bought from local market and green tea and tea waste were collected after using the tea bags.

2.2.2 Dyeing

Exhaust lab dyeing technique was employed for dyeing. The simultaneous mordanting method was applied for the dyeing of silk fabric with extracted dye solution considering different mordants. Samples were dyed with the extracted solution of 25g/l dye bath and 5% mordant on the weight of fabric individually maintaining 1:60 liquor ratio for 60 minutes at 80 ^{o}C temperature. The pH of extracted dye solution was 5.22 but after adding mordant, the pH of the dye liquor was changed a little bit. At first, dye baths were prepared for individual mordant and loaded into dyeing machine at 37 ^{o}C and setting time and temperature with 2 ^{o}C/min gradient. After dyeing, samples were rinsed with cold water and squeezed extra water by a hydro extractor. Then, samples were dried for 1 minute at 100 ^{o}C temperature and ironed. Table 2 represented the recipe of dyeing to develop shade. In case of natural dyeing and mordanting process, development of exact shade is quite difficult due to the variation of it's origin during the collection of dye and mordant sources. Fig. 2 displayed the dyeing curve of silk fabric.

Table 2: Recipe of dyeing

Attribute	No mordanting	Simultenous mordanting
Dye	25g/l	25g/l
Mordant	-	5% Owf
pH	5.22	4.8-6
Temperature	80^{o} C	80^{o} C
Time	60 mins	60 mins
M:L	1:60	1:60

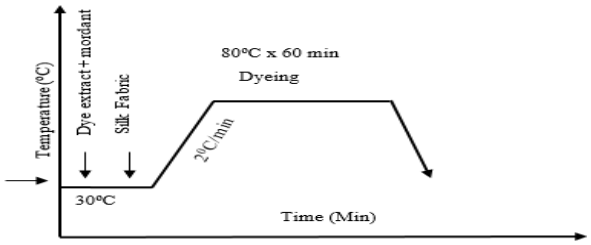

Fig. 2: Dyeing curve of silk fabric with the extraction and mordant

2.2.3 Sample labeling

Dyed samples were labeled using numbering sysem like S1, S2, S3, S4, S5, S6, S7, S8, S9, S10, S11, and S12 whereas S denoted silk fabric and S1 denoted dyed silk fabic with Azadirachta indica extraction. S2, S3, S4, and S5 denoted dyed silk fabric with synthetic mordant of alum, ferrous sulphate, potassium dichromate, and copper sulphate respectively. S6, S7, S8, S9, S10, S11, and S12 denoted dyed silk fabric with natural mordant of mango bark, tomato juice, green tea waste, tea waste, coffee, paprika, and lemon juice respectively.

2.3 Characterization

2.3.1 Extracted dye solution

The extracted dye solution was characterized by assessing absorbance through Lambda 365 UV/VIS spectrophotometer (Perkin Elmer, Germany, instrument

serial no: 365K7062102 and software version: UV Express-Version 4.1.1) that works on Beer-lambert law (qualitative analysis) [7] where absorbance was measured against wavelength of 200-700nm which determined maximum absorbance at a particular wavelength of extracted solution.

2.3.2 Dyed fabric

Color measurement

A Datacolor 850 spectrophotometer and DCI 2:1:1 was used for analyzing color coordinate values of dyed samples by CMC color difference and tolerancing system. The CMC calculation defines an ellipsoid around the standard color while the volume of the ellipsoid represents acceptable color variation. The CMC color difference Eqn.1 is based on the colorimetric principles of the CIE 1976 system [8].

$$\Delta E_{CMC} = \sqrt{\frac{\Delta L^{*2}}{lS_L} + \frac{\Delta C^{*2}}{CS_C} + \frac{\Delta H^{*2}}{S_H}} \quad (1)$$

Where S_L, S_C, and S_H are CMC weighting functions that adjust the CIE differences (ΔL*, ΔC*, ΔH*) depending upon the location of the standard in CIE 1976 color space. A user of the CMC formula usually sets values for the l and c numeric parameters according to practice in the industry.

Color Strength

K/S value was assessed to determine color strength of dyed samples, which works on kubelka- Munk Eqn. (2) [9]

$$\frac{K}{S} = \frac{(1-R)^2}{2R} \quad (2)$$

Where R is the reflectance value of dyed fiber.

Colorfastness to wash

The ISO 105 C06 B2S method was applied to measure colorfastness to wash of the dyed sample. Tested samples were assessed for color change (ISO 105 A02) and color staining (ISO 105 A03) by matching with standard grey scales against lightbox.

Colorfastness to water

The ISO 105 E01 test method was employed to measure the colorfastness to water of the dyed sample.

Colorfastness to perspiration

Colorfastness to perspiration was evaluated by the standard of ISO 105 E04 method against in acid and alkali medium.

Colorfastness to light

The ISO EN 105 B02 standard was intended to determine the resistance of the color of textiles to fade when exposed to artificial light (xenon arc) which is representative of natural daylight. The duration of light exposure was 24 hours.

Colorfastness to rubbing

The ISO 105 X 12 standard was followed to evaluate colorfastness to dry and wet rubbing.

3. RESULTS AND DISCUSSIONS

3.1 Analysis of extracted dye solution

Fig.3 showed the experimental data of extracted dye solution in terms of absorbance against wavelength of the 200nm to 700nm determined maximum absorbance at a particular wavelength. The absorbance spectrum detected three peaks of λmax: the first peak at λmax = 300nm of absorbance 5.58; the second peak at λmax = 450nm of absorbance 6.96; the third peak at λmax = 520nm of absorbance 5.91. It illustrated that dye solution will give color ranges in 300 to 520 nm of spectrum.The abosbtion pick might be changed little bit as the source of Azadirachta indica leaves would not be same and that's why maintaining the consistency of dye and mordant extract is quite difficult for natural scources.

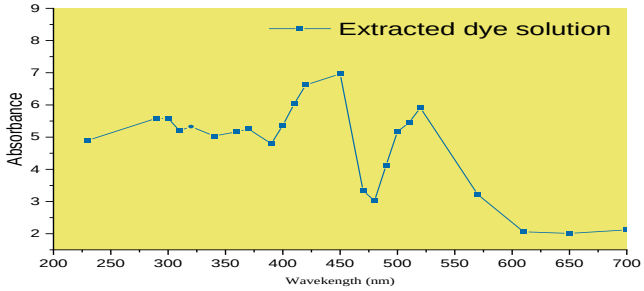

Fig. 3: Absorbance Vs wavelength curve of extracted dye solution

3.2 Visual assessment

Different shades were developed on silk fabric with the extraction using different synthetic and natural mordants. All shades are displayed in fig.4. for visual assessment of dyeing performance. Due to the electrical scanning of samples, shades were shown a little bit differently from the actual shade.

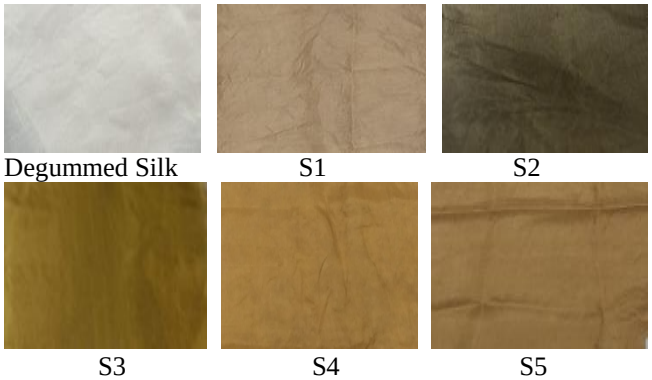

Fig. 4: Shade of different samples dyed with Azadirachta indica and different mordants

Swatches yield in the color of light green to pale brown whereas S1 gave a similar pantone shade of 16-1315 TCX named cornstalk. According to sample labeling, mordanted samples individually gave similar pantone hue of 19-0516 TCX (Dark Olive), 17-0840 TCX (Amber Green), 17-1129 TCX (Wood Thrush), 18-0939 TCX (Cumin), 17-1319 TCX (Amphora), 17-1022 TCX (Kelp), 17-2320 TCX (Tannin), 17-1038 TCX (Tiaer's Eve), 17-1115 TCX (Petrified Oak), 15-1115 TCX (Fields of Rye), and 15-1216 TCX (Pale khaki) sequentially . So, swatches dyed with mordants yield in pale yellowish to light brownish in tone as the dye solution had the maximum abosbances at 300nm to 520nm of the spectrum.

3.3 Color co-ordinate value

All of the dyed samples were assessed under three illuminates, i.e. D65 (artificial daylight), TL83, and F11 (retail and supermarkets light). Fig. 5 showed the comparison of the color co-ordinate values of mordanted dyed samples against the standard sample , S1. It is shown in fig. 5 (a) that dyed sample mordanted with alum, S2 gave averagely 816 percent darker in shade against illuminates compared to S1 in the color space. Samples mordanted with ferrous sulphate (S3) and lemon juice (S12) exhibited lighter in shade and the rest of all samples exhibited darker in shade. On the other hand, S7 gave 485 percent lighter in shade against D65 light source was highest lighter color yield. Fig. 5 (b) and Fig. 5 (c) revealed the redness or greenness and yellowness or blueness in hue. Spectrophotometry test results revealed that S2, S3, and S5 gave more reddish and yellowish in tone whereas the S2 sample gave the highest redness and S3 gave the highest yellowness in tone. Again, the natural mordanted samples gave redder and yellower in shade accept S6 and S9 that showed redder and bluer in shade. The minimum color saturation values (fig. 5 (d)) were found in S6, S7, S8, S9, S10, and S12 whereas maximum color saturation occurred in S3, S4, and S5. In addition, fig. 5 (e) displayed a difference of hue angle that all synthetic mordanted samples were closer to yellow-brownish shade whereas natural mordanted samples were nearly far from yellowish tone. Fig. 6 (f) illustrated the CMC color difference test results. The most striking results were found in the case of synthetic mordanted samples of S2, S3, S4, and S5 and that was averagely 8.5, 11.5, 11.6, and 7.9 respectively under illuminates. Natural mordanted samples gave moderate color difference except the S11, mordanted with tomato juice. On the other hand, all samples have shown metamerism (fig. 6 (g)) in the presence of different light sources.

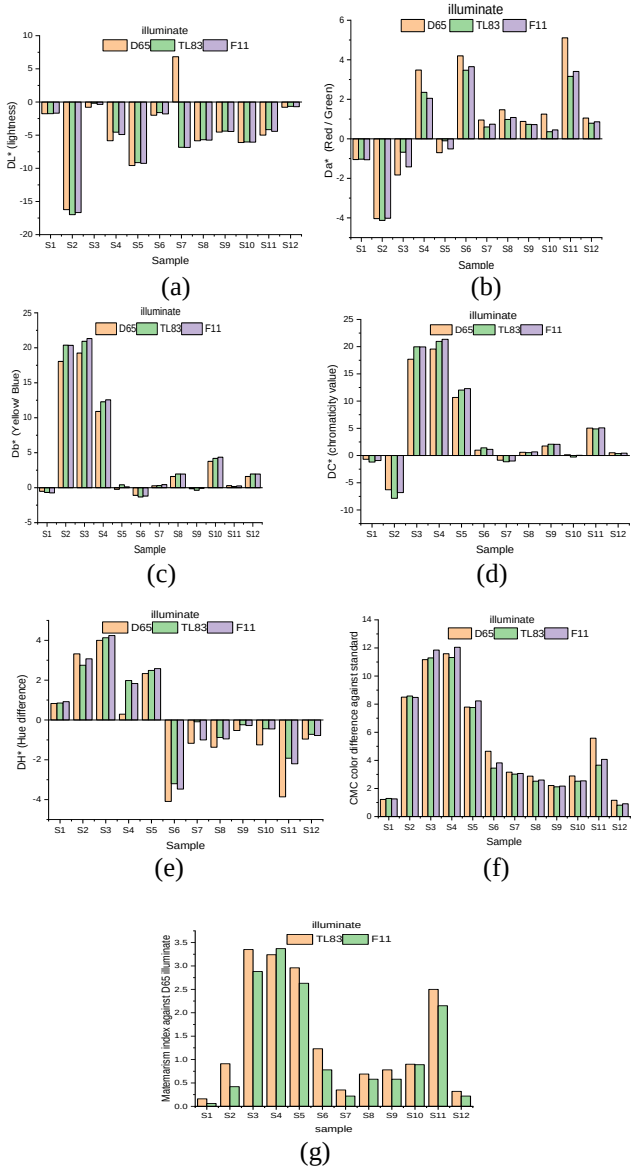

Fig. 5: Comparison of the color coordinate value of mordanted dyed samples with the unmordanted dyed sample; (a) DL*, (b) Da*, (c) Db*, (d) DC*, (e) DH*, (f) CMC DE and (g) Matemaric index

3.4 Evaluation of color strength

Fig. 6 (a) illustrated the k/s values of dyed samples whereas figure 7 (b) expressed the color yield percentage of mordanted samples against standard, S1. Color strength of S1 was found to be 12.21. Through a simultaneous mordanting process, some mordants yield to improve and intensify the color of the dyed sample S1, whereas some mordants decreased the color yield. Alum significantly increased 16.38% of color yield of dyed silk. The *K*/*S* value of S2 was found to be 14.28 using alum mordant that showed the relative surface color strength value of 116.38% considering the S1 sample as control. Besides, samples dyed with potassium dichromate,ferrous sulphate, and copper sulphate mordant individually showed color strength of 13.68, 13.83, and 12.02 respectively. Synthetic mordants alum, ferrous sulphate, and potassium dichromate improved color yield of 16.38, 12,04, and 11.63 percent respectively of dyed samples of S2, S3, and S4 whereas copper sulphate mordant diminished the color yield of 1.56 percent of dyed sample S5. Samples dyed with a natural mordant of mango bark, tomato juice, green tea waste, tea waste, coffee, paprika, and lemon juice individually showed color strength of 10.16, 11.67, 10.74, 9.65, 10.23, 8.72, and 7.36 respectively. The simultaneous natural mordanting process diminish the color yield of 16.79, 4.42, 12.04, 20.97, 16.22, 28.59, and 39.72 percentage individually of dyed samples of S6, S7, S8, S9, S10, S11, and S12 respectively. Among all of the natural mordanted samples, only S7 gave comparatively better color strength and color yield. After analysis data, it can be said that the improvement of color strength and color yield due to mordanting revealed that the dye molecules formed a metal complex with the positively charged metals. In the case of silk fibers, dye anions and metal cations are capable to attack strong attraction towards positively charged amino and negatively charged carboxyl groups, respectively, and hence, they entered the fiber and form an ionic bond between dye and fiber or metal and fiber or dye and metal ions [10]. In case of natural mordanted samples, there might be weak crosslinking with dye and fabric that's why natural mordanted sample showed lower color strength compared to synthetic mordented sample and unmordanted dyed sample.

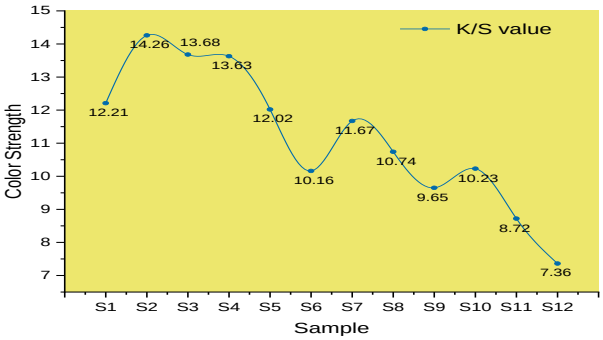

(a)

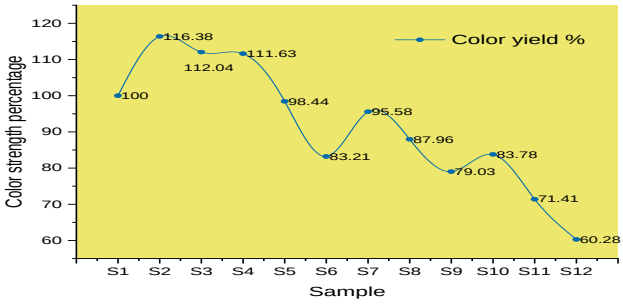

(b)

Fig. 6: Color strength and color strength percentage results of dyed samples; (a) K/S value, and (b) color yield percentage

3.5 Analysis of Colorfastness to wash test

Fig.7 showed colorfastness to wash test results. All dyed samples gave better wash fastness in terms of color change and color staining with multifiber. The greyscale rating for color change was the same for all dyed samples that was 4 out of 5. Again the color staining of all dyed samples was 4. So, it can be said that overall ratings of color change and staining were better because the color fastness due to wash is influenced by the diffusion rate of dye molecules and the state of dye molecules into the fiber structure.

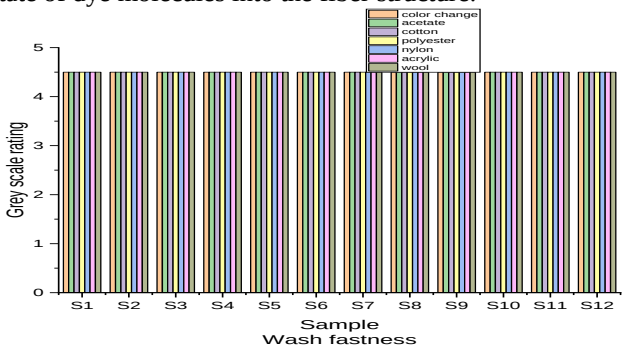

Fig. 7: Colorfastness to wash test results of all dyed samples in terms of color change and color staining

It can be explained that dye particles tend to aggregate and turn into larger particle sizes that's why dyed samples without mordant exhibited better wash fastness. In the case of mordanted samples, a metal complexing bond would have occurred with fiber that caused the insolubilizing of dye molecules to create better colorfastness.

3.6 Analysis of Colorfastness to water test

The test results of colorfastness to water was displayed in fig. 8. All the dyed samples gave a better greyscale rating of 4 except S1 and S11 which gave nearly excellent rating of 4/5 in terms of color change. Color staining with nylon was 4/5 whereas staining of other fiber of multifiber fabric was 4. S2 sample mordanted with alum gave nearly excellent wash fastness with acetate and acrylic fiber where S3 sample

mordanted with ferrous sulphate exhibited 4/5 rating with polyester, nylon, and wool fiber and S4 sample mordanted with potassium dichromate showed 4/5 rating against acetate and nylon fiber. S5, S7, and S8 exhibited 3/4 rating in terms of color staining which was the lowest rating compared to other samples. S9, S10, and S12 4/5 rating with nylon; polyester, acrylic, and wool; and nylon, acrylic, and wool fiber respectively. In summary, it can be said, during the test some dye molecules may be detached from the surface of the fabric which causes color change and color staining.

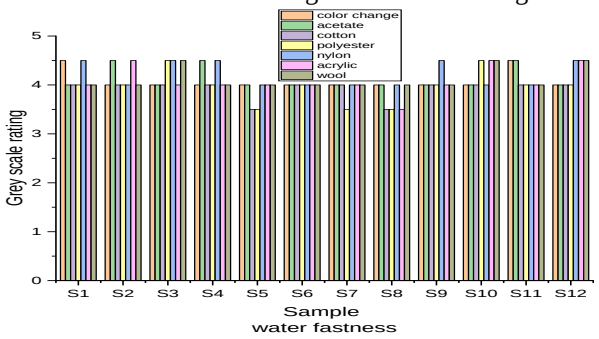

Fig. 8: Colorfastness to water test results of all dyed samples in terms of color change and color staining.

3.7 Analysis of Colorfastness to perspiration test

The results of the colorfastness to perspiration test were shown in fig. 9. In most of the cases, the color change ratings found for acid perspiration were higher than the corresponding ratings for alkaline perspiration but S1 showed equal result (rating 4) of acid perspiration and alkali perspiration. S2, S5, S12 exhibited 4/5 rating for acid perspiration whereas only S4 gave 4/5 rating for alkali perspiration in terms of color change. S8, S9 gave average rating 3/4 against both perspiration but S10 showed 4 rating against perspiration and 3/4 rating against alkali perspiration. In the case of color staining with multifiber fabric, acid perspiration of all dyed samples was better against alkali perspiration. The colorfastness to perspiration for S1 was 4 against all fibers in the multifiber fabric where color staining with acrylic fiber gave 3 rating for alkali perspiration only. S2, S4, S12 showed better color fastness but S8 and S9 showed average fastness compared to other samples.

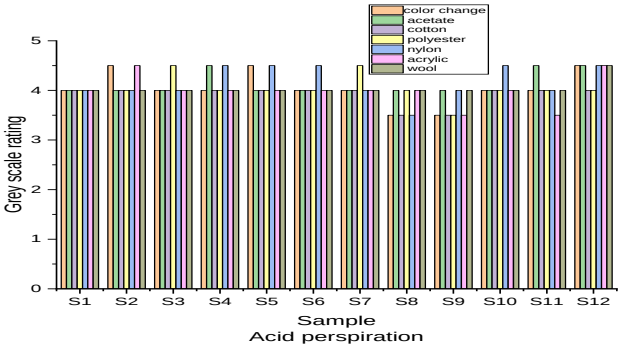

(a)

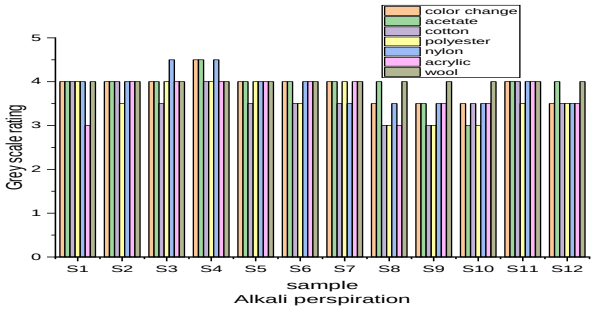

(b)

Fig. 9: Colorfastness to perspiration test results of all dyed samples in terms of color change and color staining; (a) Acid perspiration, (b) Alkali perspiration

In a conclusion, color change and color staining results were found to be satisfactory. colorfastness to perspiration test results indicated that there were changes occurred in the dyed samples due to treating with acid and alkali perspiration solutions and this scenario may have happened for several factors like ionization of some dye molecules during testing or dye molecules may detach from the fabric surface or the dye-fiber bonding zone.

3.8 Analysis of Colorfastness to light test

Fig. 10 displayed colorfastness to light test results. Test report revealed that samples dyed with mango bark, tomato juice, green tea waste, coffee, paprika, and lemon juice individually exhibited the same result of S1 and blue wool scale rating was 4 out of 8 which is considered as moderate result. It indicated that all samples mordanted with natural mordants had good light fastness except the S10 mordanted with tea waste. Again all samples dyed with synthetic mordants individually had a fair blue scale rating of 3 out of 8. It has been clearly shown that the colorfastness to light test result of all dyed samples is not satisfactory. This may be happened due to the formation of weak bond complex with transition metal which causes photolytic degradation of chromophore due to the xenon light exposure.

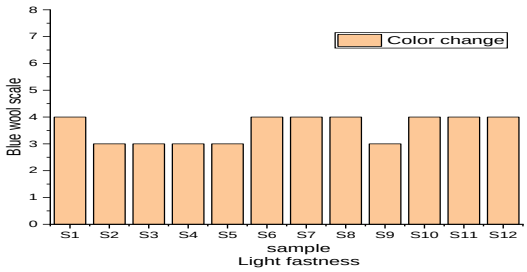

Fig. 10: Colorfastness to light test results of all dyed sample

3.9 Analysis of Colorfastness to rubbing test

From the comparison carried out between the test results of color staining due to the rubbing of dry and wet rubbing

cloth, it was noticed that dry rubbing fastness was found better than wet rubbing fastness shown in fig. 11. All the dyed sample showed better dry rubbing fastness (rating 4) except S4, S8, S9, and S10. The wet rubbing fastness was 3/4 where S4 gave poor rating of 2 and S8 gave 2/3 rating.

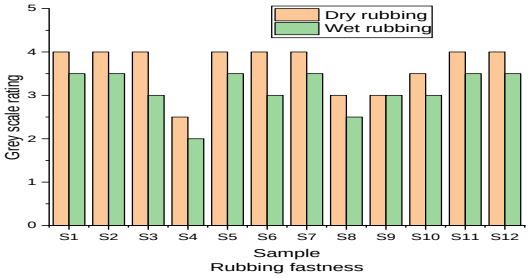

Fig. 11: Colorfastness to rubbing test result of all dyed samples

4. CONCLUSION

This empirical study demonstrated that Azadirachta indica leaves extract could be used as a potential source of dyes for dyeing of silk fabric. The experimental results revealed that the unmordanted sample exhibited good color strength with better fastness properties. Test results also illustrated that all synthetic mordants intensify the color against unmordanted sample whereas alum, ferrous sulphate, and potassium dichromate mordant gave a very interesting hue with the darker shade and highest color strength and color yield properties. The order of color yield found was Alum > Ferrous sulphate > Potassium dichromate > Copper sulphate. In terms of all colorfastness, ferrous sulphate and potassium dichromate mordant showed better colorfastness properties except lightfastness. The color strength of natural mordanted samples had average results compared to unmordanted sample and synthetic mordanted samples but had minimum metamerism. The order of color yield found was Tomato juice > Green tea waste > Coffee> Mango bark > Tea waste > Paprika > Lemon juice. On the other hand, green tea waste and tea waste mordant gave the worst perspiration and rubbing fastness results compared to other mordanted samples. Limitation of the research was that there did not show characterization of different mordant samples to estabilish recipe for reproducing shade according to standard. Unmordanted samples and natural mordanted sample showed good fastness but during laundry wash the color will fade gradually due to lack of color fixer and weak cross link. Further study of this research, would be the efficacy of the shade developed during mordanting process and fastness properties after several wash cycles. Coloromatric and fastness properties of dyed sample with Azadirachta indica leaves extract gave better results in most cases but in this research there made a attempt to compare dyed samples using mordants for the experimental development of different shades, whereas synthetic mordants provided better shade and fastness compared to natural mordants. In a conclusion, it could be said that this study will create the chance to produce different fashion hues on silk fabric with Azadirachta indica leaves extract using different synthetic and natural mordants that can be a substitute for acid dye.

ACKNOWLEDGEMENT

Heartfelt thanks to the CHT Laboratory of RH Corporation of Aziz group, Bangladesh and Hohenstein Laboratories Bangladesh Ltd. for providing lab facilities. It's a part of a M.Sc. research work, so special gratitute to my supervisor, Prof. Dr. Sharfun Nahar Arju (author 2) for her guidances & supports for the execution of the research.

REFERENCES

[1] E. Crowfoot, F. Pritchard, and K. Staniland, *Textiles and Clothing, c. 1150-c. 1450*. Boydell press, 2006.

[2] R. Saraswathi, P. Krishnan, and C. Dilip, "Antimicrobial activity of cotton and silk fabric with herbal extract by micro encapsulation," *Asian Pacific Journal of Tropical Medicine*, vol. 3, no. 2, pp. 128-132, 2010.

[3] T. Teklemedhin and L. Gopalakrishnan, "Environmental friendly dyeing of silk fabric with natural dye extracted from Cassia singueana plant," *Journal of Textile Science & Engineering*, vol. 3, no. 1, pp. 1-6, 2018.

[4] S. Saxena and A. Raja, "Natural dyes: sources, chemistry, application and sustainability issues," in *Roadmap to sustainable textiles and clothing*: Springer, 2014, pp. 37-80.

[5] N. Abdel-Zaher, A. El-Ebissy, and E. Al-Amoudy, "Application of novel eco-friendly natural dye extracted from leaves of neem on silk fabric," *Asian J. Phys. Chem. Sci*, vol. 5, no. 4, pp. 1-16, 2018.

[6] S. Adeel, K. M. Zia, M. Abdullah, F.-u.-. Rehman, M. Salman, and M. Zuber, "Ultrasonic assisted improved extraction and dyeing of mordanted silk fabric using neem bark as source of natural colourant," *Natural product research*, vol. 33, no. 14, pp. 2060-2072, 2019.

[7] H.-H. Perkampus, *UV-VIS Spectroscopy and its Applications*. Springer Science & Business Media, 2013.

[8] M. Melgosa, "Testing CIELAB-based color-difference formulas," *Color Research & Application: Endorsed by Inter-Society Color Council, The Colour Group (Great Britain), Canadian Society for Color, Color Science Association of Japan, Dutch Society for the Study of Color, The Swedish Colour Centre Foundation, Colour Society of Australia, Centre Français de la Couleur*, vol. 25, no. 1, pp. 49-55, 2000.

[9] L. Yang and B. Kruse, "Revised Kubelka–Munk theory. I. Theory and application," *JOSA A*, vol. 21, no. 10, pp. 1933-1941, 2004.

[10] Ö. E. İşmal and L. Yıldırım, "Metal mordants and biomordants," in *The impact and prospects of green chemistry for textile technology*: Elsevier, 2019, pp. 57-82.

Paper ID: 6643
International Conference on Mechanical, Manufacturing and Process Engineering (ICMMPE – 2022)
Organizer: Faculty of Mechanical Engineering, Dhaka University of Engineering & Technology (DUET), Gazipur, Bangladesh
Website: https://icmmpeduet.com/

Enhancing the Efficiency of Photovoltaic Panels by Cleaning and Cooling Techniques

Md. Sohag Hossain[1], Nibir Mondol[2]

[1,2]Department of Energy Science and Engineering,
Khulna University of Engineering & Technology
Khulna-9203.

E-mail: hossain1713029@stud.kuet.ac.bd, nibir@ese.kuet.ac.bd

ABSTRACT

Due to reduce the availability of fossil fuel, nowadays renewable energy is the crucial sector in electricity generation. Efficiency of solar panel mainly depends on sunlight, solar panel materials, radiation intensity. For getting maximum power output, minimize the losses as much as possible is concerned. Solar panel efficiency is impacted by rising the surface temperature. When the surface temperature exceeded 25 degree Celsius, the power output is also reduced. Cooling and cleaning technique is a significant process for gaining the best solar power efficiency. Solar panel temperature is controlled by giving water to the surface of solar panel at the time of temperature rising. Dust is also affected the solar panel output. Cleaning dust process is performed by servomotor which is controlled by Arduino. If cooling and cleaning methods are used at a time, the cost of the system will minimum. This research the authors aspect that maximum solar power efficiency is raised by approximately 17 percent when both strategies are used.

Keywords: renewable; efficiency; temperature; Arduino.

1. INTRODUCTION

The sun transmits energy at an amazingly enormous rate thus there is bountiful accessibility of sun based energy in the nature. On the off chance that all sun powered energy could be changed over into usable structures, it would be all the more enough to supply the world's energy interest. In any case, this is unimaginable due to conditions in the environment like impact of mists, residue and temperature. The proficiency of sun oriented board is restricted due regular conditions so it is a lot of vital for deal with boundaries like residue, mugginess and temperature.

Generally cleaning framework was done physically. The manual cleaning has burdens like danger of staff mishaps and harm of the boards, development troubles, helpless upkeep and so forth The programmed dust cleaning arrangement of sunlight based boards has taken to defeat the challenges emerge in the conventional cleaning and furthermore delivers a successful, non-rough cleaning and stays away from the abnormalities in the profitability because of the testimony of residue.

The performance of PV board is predominantly assessed under the standard test conditions (STC: 1000 W/m^2 Irradiation, 25°C module temperature, and AM 1.5 global spectrum). The module temperature range between 0 °C and 75 °C.

Temperature effects are a result of an unnatural property of glass, such as silicon cell-based modules. In general, they will generate more voltage as the temperature decreases and lose voltage as the temperature rises. Each °C increase in module temperature reduces the efficiency of a glass-like silicon PV module by around 0.5 percent.

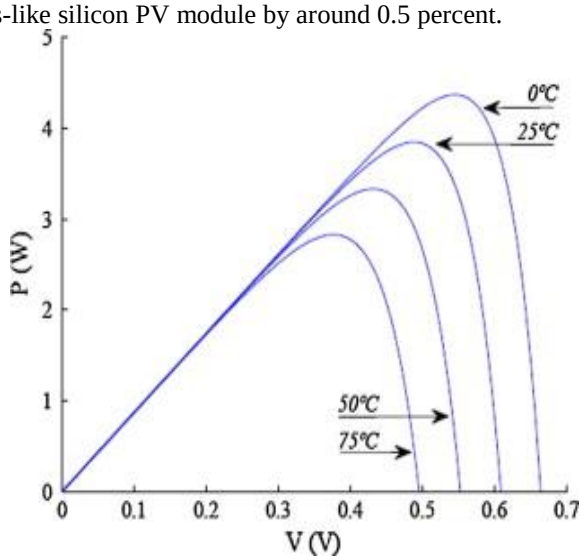

Fig. 1: *P–V* characteristics as a function of the module temperature T_m. [1]

When the temperature changes, Figure 1 displays the P-V properties at constant illumination.Temperature effects are a byproduct of crystalline silicon cell-based modules'

inherent characteristics. When the temperature drops, they produce more voltage, and when the temperature rises, they lose voltage. This temperature effect must be factored into any solar panel.

Facing the activity of photovoltaic boards which one type of fundamental impediments is overheating because of unnecessary sunlight based radiation and high encompassing temperatures. Overheating lessens the effectiveness of the boards significantly.

The V_{OC} reduces dramatically when the solar panel temperature rises over 25°C, while short-circuit current, Isc, increases just little. The temperature coefficient is used to describe the influence of temperature on solar PV performance. As a result, as the temperature rises, the power output decreases. The percentage of temperature coefficient reflects a change in production when temperature rises or decreases above or below 25°C.[2]

Internal and external elements such as structural features, aging, radiation, shade, temperature, wind, pollution, and cleanliness have a significant impact on PV system performance. Changes in solar radiation and ambient temperature are caused by any type of climatic change, resulting in changes in solar PV output performance.

The objective of this paper is to increase the PV panel efficiency by controlling the surface temperature and cleaning the dust automatically which is cost effective.

Maz on-Hern andez investigated forced convection cooling, which involved employing fans to cool the underside of ceiling PV modules .Overall efficiency increased by 2%, while the highest cell temperature dropped by 15 degrees Celsius.

Water spray on both sides of the PV panel performance was scientifically studied by Nizetic et al.The findings revealed that front-side cooling produces better outcomes than back-side cooling.The increase in electrical power was around 14.6 percent.

Anderson M et al [3] solar panel cleaning robot. Its design incorporates two automated streetcars at the board's borders for uniform movement and a vertical cleaning head operated by a belt and pulley structure. A scrubber and rotating barrel-shaped brushes wash the PV board, while a scrubber removes the earth arrangement.

S. Nizetic et al.[4] develop cooling techniqueby spraying water, which is implemented simultaneously on the front and back sides of a PV panel..Due to an evaporation and self-cleaning effect, the proposed water spray cooling technology has the ability to improve PV panel performance, which is also a significant benefit in terms of long-term feasibility.

Solar energy is the energy emitted by the sun. Solar cells turn sunlight into direct current electricity and use this energy. Solar cells are made up of a variety of semi-conductors. Semiconductors are materials that, when exposed to light or heat, become electrically conductive, but are insulators at low temperatures.[5]

Temperature increases have a negative impact on solar panel efficiency, which may appear counterintuitive. Photovoltaic modules are tested at a temperature of 25 degrees Celsius (STC) – about 77 degrees Fahrenheit – and heat can lower output efficiency by 10% to 25% depending on where they are installed. The output current of the solar panel increases exponentially as the temperature of the panel rises, whereas the voltage output decreases linearly. In fact, the voltage drop is so consistent that it may be used to precisely monitor temperature.[6]

Extra equipment like pumps, fans are ued for regulating the temperature of surface of solar PV panel.[7]

Manually solar panel cleaning, cleaning by electrostatic precipitator, and more methods are available. The efficiency of the panel may be increased by 15–20 percent by using this cleaning process. However, each strategy comes with its own set of drawbacks. Manual cleaning needs more work, and there is a risk of harm to the Photovoltaic Panel if water or fluid is used indefinitely. Scratches on the solar panel are caused by the vacuum mechanism of cleaning. So, to clean the panel, K. Jaiganesh et al[8] use Automatic Wiper Cleaning with Arduino.

2. METHODOLOGY

Firstly, it was needed to collect all components and sensors. Then set up those components. Digital waterproof temperature sensor was attached with solar PV panel and it was used to sense the temperature. Then it was signaled to the microcontroller when the temperature of the solar panel rose above 30℃. Readings (voltage, current) were taken without cleaning and cooling effect in a day. Voltage and current values were also taken after cleaning solar PV panel. Then, it was compared voltage, current and power output for this case.

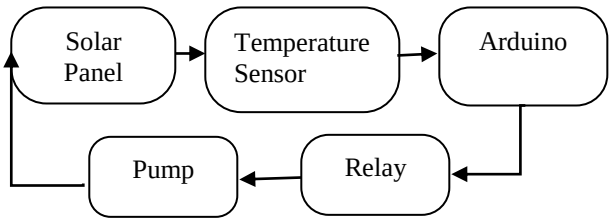

Fig. 2: Block Diagram of Cooling System.

For cleaning system, Arduino Uno, Servo motor, Solar panel, wiper, temperature sensors are required. In the early hours of the day, the microcontroller was programmed to operate the sprinklers and wipers to clean the solar panel of dust. This process continues for 2 minutes and then the sprinklers and wipers are automatically switched off.

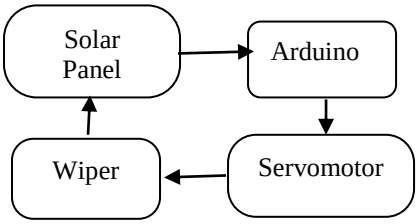

Fig. 3: Block Diagram of Cleaning System.

2.1 Component List

Table 1: Components required for implementing automatic water cooling and cleaning system.

Serial No	Name of the Component	Ratings	Quantity
01	Solar PV Panel	5W	01
02	Temperature and Humidity Sensor	DHT11	01
03	Waterproof Digital Temperature Sensor	DS18B20	01
04	Tower Pro Copper Servo Gear	MG995	01
05	Arduino Uno with R3 Cable		01
06	Red Color Relay Module	5V 1 Channel	01
07	Raspberry Pi power Supply	DC-5V 3A	01
08	LCD I2C Module Top way	16*2	01
09	Submersible Pump	12 V, 8 W	01
10	Multimeter	80 V	01

2.1.1 Digital Waterproof Temperature Sensor

The DS18B20 sensor is pre-wired and waterproofed in this version. When you need to measure anything from afar or in wet weather, this is the tool to use. The sensor can withstand temperatures up to 125°C, however the cable is PVC-coated to keep it below 100°C. Signal deterioration does not occur over vast distances because they are digital. The internal digital-to-analog converter can provide up to 12-bit precision from these 1-wire digital temperature sensors, which are precise (0.5°C throughout much of the range). They operate with any microcontroller that has a single digital pin, and you may connect numerous of them to the same pin because each one has a unique 64-bit ID burned in at the manufacture. Compatible with systems ranging from 3.0 to 5.0 volts.

Fig 04: Digital Waterproof Temperature sensor .[9]

2.1.2 Arduino Uno

Arduino is an open-source platform for building and programming electrical circuits. It can receive and transfer data to most devices, as well as deliver commands to particular electrical gadgets through the internet. It's a high-performance device featuring a low-power AVR 8-bit Microcontroller and 32K bytes of in-system memory, as well as sophisticated reduced instruction set computing.

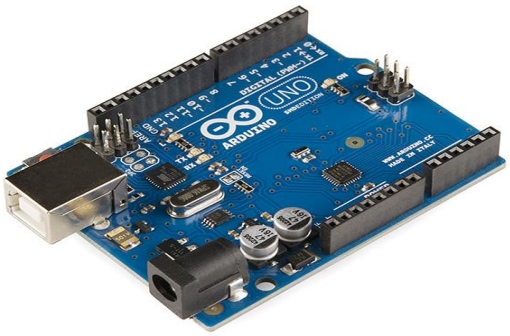

Fig 05: Arduino uno. [10]

2.1.3 Servomotor

A servo motor is a rotary actuator with high precision control capabilities. It consists of a controller, an electric motor, and a feedback device. They are more capable than any other form of motor of accommodating complicated motion patterns and profiles. When you want to spin an object at a specific angle or distance, you use a servo motor. It is made up of nothing more than a basic motor and a servo mechanism.

Fig 06: Servo motor[11]

2.4 Experimental Setup

During the experiment, 5 W solar panel was used for cleaning and cooling purposes. The specifications are given below for solar panel,

Table 2: Specification of solar panel.

Maximum Power output,Pm	5 W
Open Circuit Voltage, Isc	21.16 V
Short Circuit Current,Voc	0.35 A
Dimension	185*290*17 mm
Operating Temperature	-40℃ to +85℃

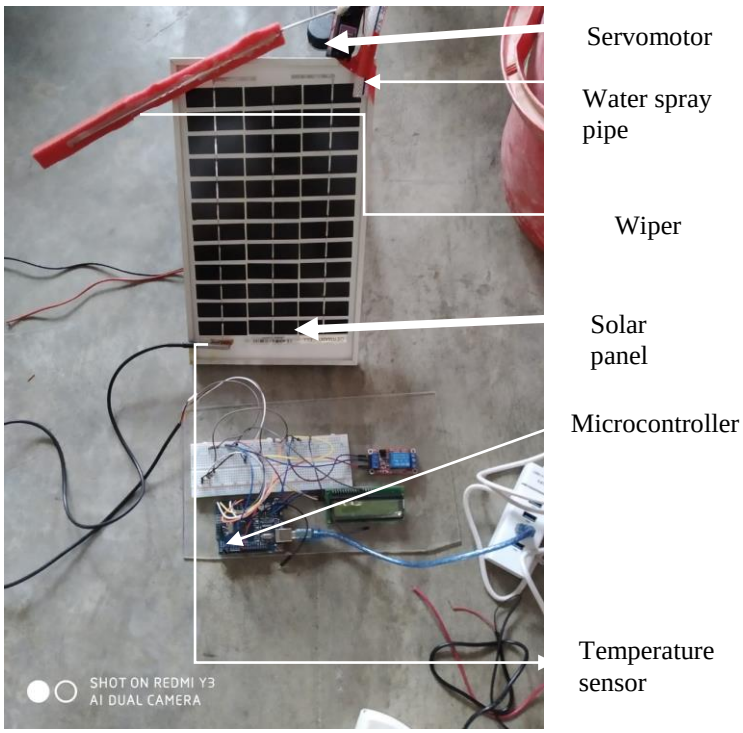

Fig. 7: Practical implementation figure.

For making a programmed water-cooling framework digital waterproof The DS18B20 sensor was used for sensing the temperature. Arduino Uno, relay Module and DC pump was used to make the system automated. Here, temperature sensor associated with the solar panel and was given the temperature of the solar panel as a yield to the microcontroller. The microcontroller was compared the yield value to the previously set value. From that point forward, the microcontroller sent the signal to relay module. The relay module was worked as a switch. Finally, when the submersible pump was turned on. At that point the water began to stream over the solar panel which

assisted with diminishing the sun oriented board temperature.

- Sense the temperature
- Above 30°C, Digital Water proof sensor send signal to Arduino Uno.
- Relay on.
- Pump on.
- Spray water.
- After getting set value, servo motor on.
- Cleaning the solar panel by wiper.

3. RESULT & DISCUSSION

The data was taken for several days. But following data table was shown for best data. Following data were recorded for two cases. One was taken without cleaning and cooling effect. Other was taken with cleaning and cooling effect. These data was recorded on 18 March,2022.

Table 3: Output from solar PV panel.

Time	Without Cleaning and Cooling		With Cleaning and Cooling	
	Open Circuit Voltage(Voc)	Short Circuit Current(Isc)	Voltage(Voc)	Current(Isc) A
10:15 AM	17	0.2	17.2	0.22
10:45 AM	17.9	0.21	18.5	0.23
11:15 AM	18.4	0.21	19.2	0.24
11:45 AM	19.5	0.22	20.1	0.24
12:15 PM	20.0	0.22	20.5	0.25
12:45 PM	19.6	0.21	20.0	0.23
1:15 PM	19.2	0.2	19.8	0.22
1:45 PM	18.6	0.21	18.9	0.22
2:15 PM	18.1	0.19	18.5	0.22
2:45 PM	17.6	0.18	18.0	0.2
3:15 PM	17.1	0.16	17.4	0.18

Fig 09 shows the temperature for two cases without and with cleaning & cooling. After regulate the temperature of solar panel and cleaning dust ,efficiency is increased.

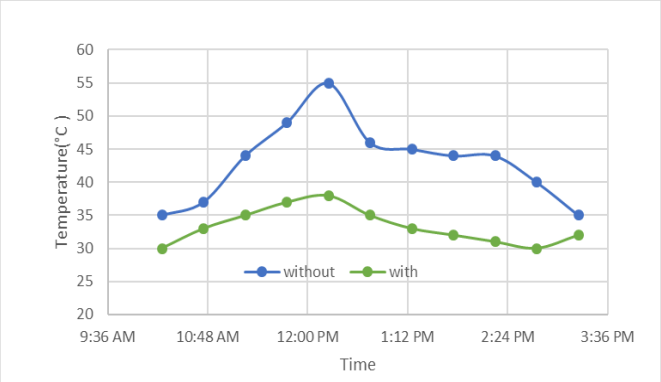

Fig 8: Variation of temperature with respect to time.

Fig 10 shows variation of current with respect to time. From the figure, it is seen the current values are increasing after cleaning and cooling of solar panel.

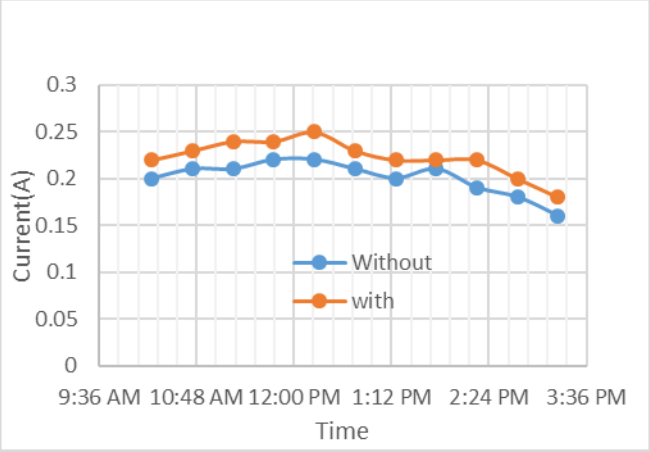

Fig 9: Variation of current with respect to time.

Fig 11 shows variation of voltage with respect to time.. The amount of increased voltage is greater than the increased current value.

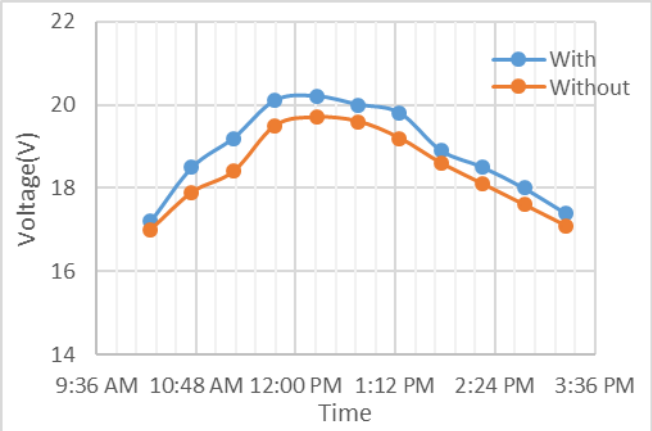

Fig 10: Variation of voltage with respect to time.

Figure 12 shows variation of power with respect to time.. Since the voltage and current values are increasing, power output also increased.

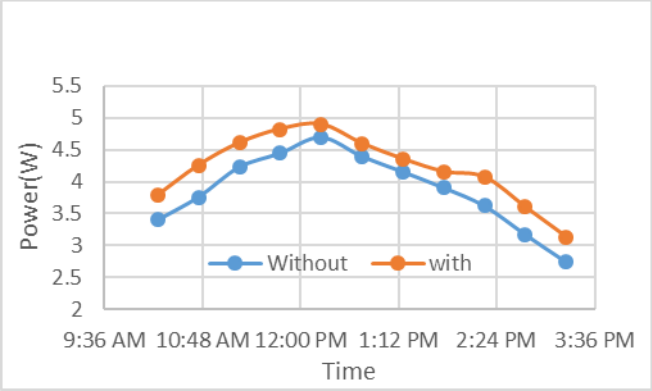

Fig 11: Variation of power with respect to time.

4. CONCLUSION

A cooling system which was non pressurized based on periodically spraying the PV panels with water has been developed. It has improved performance and system efficiency as a result of regular cleaning with proper intervals. The materials utilized in this project were low-cost and readily available. When compared to other systems, the total cost of the system is quite low. This system is simple which can be handled easily. This experiment finally has observed the output is increased around 17 % with the help of spraying water and cleaning dust.

REFERENCES

[1] K.A. Moharram, M.S. Abd-Elhady, H.A. Kandil , H. El-Sherif, "Enhancing the performance of photovoltaic panels by water cooling," Ain Shams Engineering Journal, vol. 4, pp. 869-877, 2013.

[2] Pushpendu Dwivedi, K. Sudhakar, Archana Soni, E Solomin, Kirpichnikova , "Advanced cooling techniques of P.V. modules: A state of art," Case Studies in Thermal Engineering, Volume 21, October 2020, 100674.

[3] Anderson M, Grandy A, Hastie J, Sweezey A, Ranky R,Mavroidis C, Markopoulos YP, "Robotic device for cleaning photovoltaic panel arrays," 12th International Conference on Climbing and Walking Robots and the Support Technologies for Mobile Machines; 2009; Istanbul

[4] S. Nizˇetic´, D. Cˇoko , A. Yadav , F. Grubišic´ -Cˇ abo, "Water spray cooling technique applied on a photovoltaic panel: The performance response," Energy Conversion and Management, vol. 108 , p. 287–296., 2016.

[5] Nasim Reza, Nibir Mondol, "Design and Implementation of an Automatic Single Axis Tracking with Water-Cooling System to Improve the Performance of Solar Photo voltaic Panel", 2021 International Conference on Automation,Control and Mechatronics for Industry 4.0 (ACMI), 2021.

[6] Billah, M.M., M.M. Rahman, M.A. Razzak, R.Saidur, and S. Mekhilef. "Unsteady buoyancy-driven heat transfer enhancement ofnanofluids in an inclined triangular enclosure", International Communications in Heat and Mass Transfer,2013.

[7] Akbar Maleki, Arman Haghighi, Mamdouh El Haj Assad, Ibrahim Mahariq,Mohammad Alhuyi Nazari, "A review on the approaches employed for cooling PV cells," Solar Energy, vol.209, pp. 170-185, June 2020

[8] K. Jaiganesh, K. Bharath Simha Reddy, B.K.D. Shobhitha, B. Dhanush Goud, "Enhancing the efficiency of rooftop solar photovoltaic panel with simple cleaning mechanism ," Materials Today: Proceedings May 2021,

[9] Anand Nayyar, "Smart Farming: IoT Based Smart Sensors Agriculture Stick for Live Temprature and Moisture Monitoring using Arduino, Cloud Computing& Solar Technology, "The International Conference on Communication and Computing Systems (ICCCS-2016),vol 10, p, 10-15, November 2016.

[10] Aslinda Hassan, Siah Bing Sheng, Wahidah Md Shah and Nazrulazhar Bahaman, "An Automated Irrigation System Using Arduino Microcontroller," Internet of Things: Usage and Application (pp.3-13), November 2018.

[11] Wahyu Gunawan, Aditya P. P.Prasetyo, Siti Nurmaini, Rendyansyah, Sri Desy Siswanti, "GACOBOT Navigation System for Distribution Solid Waste to Temporary Dumpsite", Sriwijaya International Conference on Information Technology and Its Applications (SICONIAN 2019), vol 172, pp. 282-288, January 2020.

Paper ID: 6901
International Conference on Mechanical, Manufacturing and Process Engineering (ICMMPE – 2022)
Organizer: Faculty of Mechanical Engineering, Dhaka University of Engineering & Technology (DUET), Gazipur, Bangladesh
Website: https://icmmpeduet.com/

Ergonomic Assessment of Helmet for Young Adults in Bangladesh

Shaikh Ishtiaque Ahmed[1], Shinthia Binte Eskender[2]

[1]Department of Industrial Engineering and Management,
Khulna University of Engineering & Technology,
Khulna 9203, Bangladesh.
[2]Department of Materials Science and Engineering,
Khulna University of Engineering & Technology,
Khulna 9203, Bangladesh.

E-mail: Ishtiaqueraj016@gmail.com

ABSTRACT

The use of an anthropometric method for product design and assessment is one of the most basic uses of ergonomics. The aim of this study is to develop an anthropometric database for head measurement and to design an ergonomic helmet using anthropometric methods. In this study, participants are consisted of 250 males and 250 females whose age range are 18 to 35. An anthropometric database of nineteen anthropometric measurements have been developed for both male and female in this study. Then make a comparison between those anthropometric data. Seven anthropometric measurements have been selected for helmet design. Then an ergonomic helmet is designed for both male and female young adults of Bangladesh. Anthropometric data are presented in this paper, and helmet size for proposed design is discussed.

Keywords: Ergonomics; Bangladesh; Head anthropometry; Helmet design.

1. INTRODUCTION

In Bangladesh, the motorcycle is the most cost-effective and commonly used means of transportation. For a variety of reasons, this is the most popular transportation. Low cost, higher fuel efficiency, smaller size for simpler parking in congested places, and high mobility transportation are just a few of the benefits.

Unfortunately, A large number of motorcycle accidents have occurred as a result of the widespread use of motorcycles [1]. According to the World Health Organization, Motorcycle riders account for more than 60% of traffic deaths, especially in low- and middle-income countries [2]. In 2020, From January through October, at least 1,026 individuals died in 1,011 motorbike accidents across Bangladesh. According to the World Health Organization (WHO), Every year, 2.17 million motorcyclists die in road accidents, with another 20 to 50 million injured [3]. Meanwhile, 353 incidents (34.91%) occurred as a result of 165 unique accidents (15.43 percent) resulted from head-on crashes, with additional vehicles hitting or running over them from behind [4].

Young adults are the victims of the majority of motorcycle accidents in Bangladesh. Young adults are those who are eighteen to thirty-five years old [5]. A motorcycle collision can result in minor, moderate, or serious injuries. A high proportion of accidents are likely to be caused by a lack of helmet use. In this situation, attempts have been made to limit the number of people killed in motorcycle accidents, including the requirement that anyone riding a motorcycle wear a helmet. Motorcycle helmets can help to decrease the number and severity of head injuries caused by collisions [6], In light of the possibility of mortality from a head injury [7]. Researchers discovered that helmeted riders had a 66 percent lower risk of intracranial damage than non-helmeted riders during the course of an 18-month motorcyclists who presented to a metropolitan trauma center in Sydney, Australia were studied [1]. Helmet stability is critical for helmet performance because it ensures that the helmet provides adequate head coverage and stays in place during regular riding and in the case of a crash. Helmet roll-off has been linked to careless helmet retention strap modifications and poor fitment following crashes. Helmets aren't the best type of protection, although in a motorbike accident, they can avoid roughly 32% of head injuries [8]. This condition is typically tied to helmet size. Helmet manufacturers choose the current helmet size without consulting an anthropometric study, resulting in a wide range of helmet sizes depending

upon head circumference. Given that head anthropometry isn't merely related to head diameter, it's unsurprising that the helmet size isn't suitable for most people. Bangladeshis do not yet have a standard size for helmets. Helmets must be made or altered for Bangladesh's young adults' comfort and stress reduction. The study's purpose is to assess anthropometry and use the results to enhance helmet sizes because young adults are more likely to be involved in motorcycle accidents and suffer head injuries. The better a helmet fits motorcycle users, the more likely they will use it, minimizing the risk of brain injury. The current study is carried out to develop an anthropometric database for head measurement and to design an ergonomic helmet by using anthropometric data.

2. METHODOLOGY

2.1 Sample Design

The participants were young adults from Bangladesh. The age of young adults ranges from 18 to 35 years. Equation (1) was used to calculate the sample size [9]. The number of individuals picked at random, "n," is required to verify that a database's 5th and 95th percentiles accurately forecast the entire population's 5th and 95th percentiles with 95% confidence, and to calculate a percentage of relative accuracy using the formula:

$$n \geq (3.006 * CV/a)^2 \quad (1)$$

Where,
n= the estimated sample size
CV = coefficient of variation
a= the percentage of relative accuracy desired

$$CV=100*SD/\overline{x} \quad (2)$$

Where,
CV = coefficient of variation;
SD = Standard Deviation
$\overline{x}$= mean of a population
The minimal sample size "n" was calculated to be 468 using the maximum coefficient of variation value from similar research [10] (CV = 7.19, as SD = 3.93, and Mean = 54.63, among the populations studied in this research), and the relative accuracy of 1%. As a consequence, the authors selected total 500 male and female volunteers to participate in the study.

2.2 Instrumental Selection

The required instruments for anthropometric measurements are:

1. Martin anthropometer
2. Spreading caliper

The anthropometric dimensions were taken using these instruments. Most of the measurements were obtained while standing and sitting with their feet flat on the floor. Before any measurements were taken, all of the equipment was calibrated against accepted standards. The measurements were taken several times to avoid any kind of error. The measurements were obtained in inches and then converted to centimeters.

2.3 Statistical Analysis

The descriptive statistics were summarized using the software SPSS version 25 in terms of standard deviation, mean, and different percentile values (5th, 50th, and 95th). To find the differences between measurements, "t" values, "p" values were calculated. Moreover, a head measurement comparison between Bangladeshi male and female young adults has been developed.

2.4 Anthropometric Measurements

Nineteen dimensions of head anthropometry were measured including (1) Head circumference, (2) Bitragion coronal arc, (3) Bitragion frontal arc, (4) Bitragion subnasale arc, (5) Bitragion chin arc, (6) Bitragion submandibular arc, (7) Head breadth, (8) Head length, (9) Bigonial breadth, (10) Menton to top of the head, (11) Head thickness, (12) Tragion top of head, (13) Bitragion breadth, (14) Bizygomatic breadth, (15) Diametric menton to back of the head, (16) Nose to top of the head, (17) Pronasale to eye, (18) Face breadth, (19) Eye to back of the head as can be seen in Figure 1.

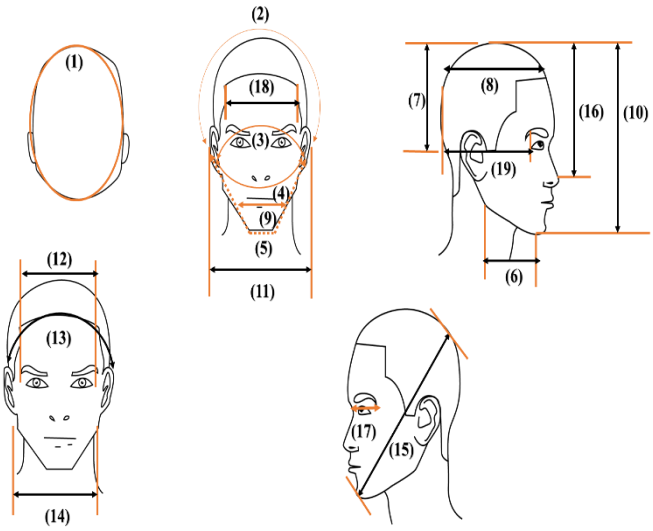

Fig. 1: Anthropometric dimensions of human head

2.5 Anthropometric Measurements for Helmet Design

Seven measurements have been selected among nineteen measurements for helmet design. These are: Head breadth, Menton to top of the head, Diametric menton back of the head, Nose to top of the head, Pronasale to eye, Face breadth, and Eye to back of the head.

3. RESULTS

Table 1: Anthropometric measurements of male population

Anthropometric measurements (cm)	Mean	Standard Deviation	Max	Min	5th Percentile	50th Percentile	95th Percentile
Head circumference	56.59	3.19	65.95	49.13	51.03	56.63	61.51
Bitragion coronal arc	35.93	2.12	42.21	30.46	32.42	36.02	39.49
Bitragion frontal arc	30.25	1.81	36.27	25.56	27.18	30.37	33.29
Bitragion subnasale arc	29.43	1.68	33.90	25.06	26.54	29.42	32.07
Bitragion chin arc	32.80	1.93	38.25	28.00	29.44	32.92	35.84
Bitragion submandibular arc	30.06	1.96	35.61	25.15	26.74	30.05	33.29
Head breadth	17.22	1.33	20.68	14.25	15.09	17.16	19.58
Head length	18.64	1.35	22.85	15.23	16.47	18.61	20.91
Bigonial breadth	11.87	0.99	14.79	9.33	10.35	11.80	13.61
Menton to top of the head	22.63	1.35	26.36	19.16	20.48	22.58	24.82
Head thickness	19.54	1.29	23.74	16.49	17.39	19.55	21.45
Tragion top of head	14.13	1.17	17.36	11.44	12.41	14.06	16.10
Bitragion breadth	13.83	1.26	16.91	11.05	11.88	13.76	15.84
Bizygomatic breadth	14.10	1.11	17.36	11.54	12.40	14.02	15.85
Diametric menton to back of the head	26.19	1.93	31.02	21.21	23.11	26.25	29.32
Nose to top of the head	15.93	1.18	19.29	13.04	13.90	16.00	17.76
Pronasale to eye	20.60	1.69	26.11	16.58	17.96	20.48	23.26
Face breadth	17.21	1.40	21.21	13.76	15.04	17.10	19.52
Eye to back of the head	18.46	1.24	22.19	15.42	16.42	18.35	20.47

Table 2: Anthropometric measurements of female population

Anthropometric measurements (cm)	Mean	Standard Deviation	Max	Min	5th percentile	50th percentile	95th percentile
Head circumference	55.26	3.88	64.90	45.42	48.63	55.28	61.51
Bitragion coronal arc	35.42	2.69	42.83	28.80	31.36	35.55	40.10
Bitragion frontal arc	26.39	2.41	33.66	20.73	22.84	26.04	30.34
Bitragion subnasale arc	24.83	1.80	29.46	20.43	21.86	24.84	27.74
Bitragion chin arc	29.28	2.19	35.19	22.71	25.38	29.37	32.60
Bitragion submandibular arc	28.39	2.30	35.63	23.28	24.40	28.42	32.43
Head breadth	17.13	1.40	21.36	13.17	14.70	17.18	19.39
Head length	16.63	1.58	20.94	12.72	14.12	16.64	19.17
Bigonial breadth	10.52	1.12	13.16	8.01	8.89	10.41	12.44
Menton to top of the head	22.76	1.87	28.48	17.94	19.65	22.77	25.88
Head thickness	19.35	2.28	24.59	14.28	15.85	19.30	23.15
Tragion top of head	14.39	1.10	17.48	11.35	12.65	14.44	16.23
Bitragion breadth	13.23	1.25	16.15	9.99	11.18	13.16	15.33
Bizygomatic breadth	13.48	1.09	16.24	10.45	11.80	13.44	15.23
Diametric menton to back of the head	25.66	2.20	31.07	19.98	22.16	25.66	29.34
Nose to top of the head	15.98	1.57	19.98	12.38	13.49	15.86	18.65
Pronasale to eye	20.09	1.71	24.51	16.13	17.11	20.16	23.14
Face breadth	16.06	1.37	19.48	12.72	13.93	16.01	18.39
Eye to back of the head	17.97	1.63	22.71	13.84	15.20	17.95	20.56

Table 3: Comparison of anthropometric data between Bangladeshi male and female

Male				Female			(t-value & p-value)	
Variables	N	Mean (cm)	SD	N	Mean (cm)	SD	t -value	p -value
Head breadth	250	17.22	1.33	250	17.13	1.4	0.804	0.422
Menton top of the head	250	22.63	1.35	250	22.76	1.87	0.933	0.351
Diametric menton to back of the head	250	26.19	1.93	250	25.66	2.2	2.852	0.005
Nose to top of the head	250	15.93	1.18	250	15.98	1.57	0.361	0.718
Pronasale to eye	250	20.6	1.69	250	20.09	1.71	3.406	0.001*
Face breadth	250	17.21	1.4	250	16.06	1.37	9.286	0*
Eye to back of the head	250	18.46	1.24	250	17.97	1.63	3.79	0*

*Statistically significant at $\alpha = 0.05$, ($p < 0.05$); N = Number of participants

Table 4: Associated helmet dimensions with anthropometric measurements

Helmet Dimensions	Anthropometric Measurements	Measurements(cm)					
		Male			Female		
		5th percentile	50th percentile	95th percentile	5th percentile	50th percentile	95th percentile
Helmet width	Head breadth	15.09	17.16	19.58	14.70	17.18	19.39
Helmet height	Menton to top of the head	20.48	22.58	24.82	19.65	22.77	25.88
Helmet diameter	Diametric menton to back of the head	23.11	26.25	29.32	22.16	25.66	29.34
Glass helmet height	Nose to top of the head	13.90	16.00	17.76	13.49	15.86	18.65
Helmet glass length	Pronasale to eye	17.96	20.48	23.26	17.11	20.16	23.14
The width of the front of the helmet	Face breadth	15.04	17.10	19.52	13.93	16.01	18.39
Helmet length	Eye to back of the head	16.42	18.35	20.47	15.20	17.95	20.56

Tables 1 and 2 indicate the anthropometric database of head dimensions for young adults, respectively, for men and women. Mean value, Standard deviation value, Maximum value, Minimum value and Percentile values (5^{th}, 50^{th}, 95^{th}) is included in these tables.

In Table 3, Seven types of measurements are selected among nineteen anthropometric measurements for designing the helmet. Nineteen measurements have been taken for creating the database. Among those seven types of measurements are required for designing a helmet. That's why, seven measurements have been taken for designing the helmet. A comparison had been done by t-test using p-values to identify the difference of anthropometric measurements for male and female to decide the variation of design for both genders. There had been found significant differences among three measurements ($p < 0.05$). These were Pronasale to eye, Face breadth, Eye to back of the head.

That's why two different types of helmets should be designed for two gender because of having significant differences among three anthropometric measurements. Associated helmet dimensions with anthropometric measurements is shown in Table 4.

There are various techniques for calculating a product's standard size, the most common of which is based on percentiles [11]. Percentile statistics are a type of order statistics that can be used to estimate the percentage of data that should fall above and below a certain value [12]. To determine the standard size of helmet, percentile method has been used where 5th ,50th and 95th percentile indicates reference size S, M and L respectively. So, in this study, 5^{th} percentile value, 50^{th} percentile value and 95^{th} percentile values are used for reference size S, M and L respectively for helmet design.

Tables 5 and 6 describe the helmet size in relation to the helmet dimensions while building a helmet. The existing helmet size for male and female population is also shown in those tables. Tables 5 and 6 represent the male and female populations, respectively. Those tables indicate the differences in values between proposed and existing helmet designs.

Table 5: Proposed helmet size and existing helmet size for male

Helmet Dimensions	Proposed Helmet Size (cm)			Existing Helmet Size (cm)		
	S	M	L	S	M	L
Helmet width	15.09	17.16	19.58	12.85	15.63	18.15
Helmet height	20.48	22.58	24.82	21.92	23.21	26.30
Helmet diameter	23.11	26.25	29.32	22.36	24.95	27.78
Glass helmet height	13.90	16.00	17.76	12.45	14.65	17.52
Helmet glass length	17.96	20.48	23.26	18.62	21.80	24.40
The width of the front of the helmet	15.04	17.10	19.52	13.77	15.89	18.01
Helmet length	16.42	18.35	20.47	17.22	20.53	23.36

Table 6: Proposed helmet size and existing helmet size for female

Helmet Dimensions	Proposed Helmet Size (cm)			Existing Helmet Size (cm)		
	S	M	L	S	M	L
Helmet width	14.70	17.18	19.39	13.58	15.80	18.91
Helmet height	19.65	22.77	25.88	21.04	24.27	27.65
Helmet diameter	22.16	25.66	29.34	20.47	23.39	27.07
Glass helmet height	13.49	15.86	18.65	12.16	14.94	17.32
Helmet glass length	17.11	20.16	23.14	19.03	22.78	25.33
The width of the front of the helmet	13.93	16.01	18.39	12.75	14.35	17.20
Helmet length	15.20	17.95	20.56	16.41	18.82	22.60

Figure 2 shows the proposed helmet design for both male and female young adults of Bangladesh. The helmet was designed by SOLIDWORKS 2016 software.

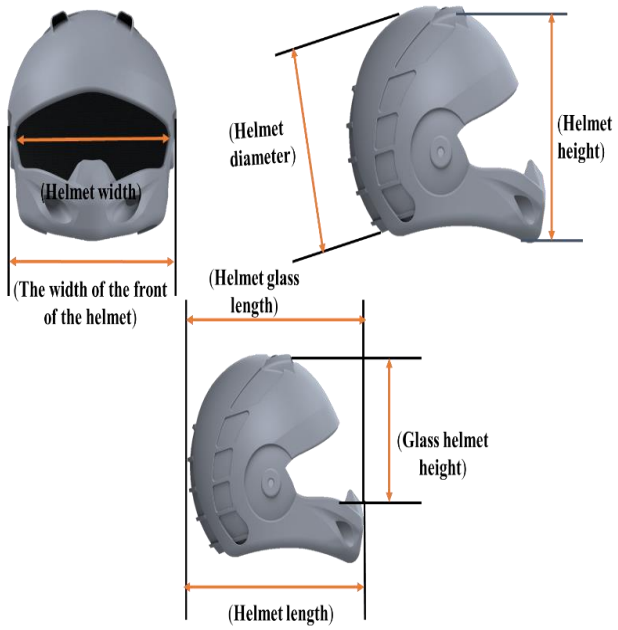

Fig. 2: Helmet design for male and female

4. CONCLUSION

The number of motor bike is increasing in a large scale around the world. The matter of safety is also an essential topic for the driver. Helmet is the vital thing to use during driving. As it is necessary for the biker, so it should be fit and comfortable to use. The main focus of the study is to make a fit and comfortable helmet for the young adults of Bangladesh. That's why an agronomical helmet has been designed for the Bangladeshi young adults who use bike to ride.

Nineteen anthropometric data for both male and female young adults of Bangladesh have been taken. The age of young adults ranges from 18 to 35 years. The measurements were collected to design the helmet. Seven anthropometric measurements have been selected among nineteen measurements to design the helmet. The measurements are Head breadth, Diametric menton to back of the head, Menton to top of the head, Nose to top of the head, Face breadth, Pronasale to eye, Eye to back of the head. An anthropometric database has been developed for young adults of both male and female. The database contains average value, maximum value, minimum value, standard deviation and 5^{th} percentile, 50^{th} percentile, 95^{th} percentile value. There have been significant differences between male and female population in three anthropometric measurements. That's why the helmet has been designed for both male and female. The helmet has been designed using percentile method. 5^{th} ,50^{th} and 95^{th} percentile indicates reference size S, M and L of

helmet size respectively. Each dimension's data is shown, and size of the helmet is suggested.

REFERENCES

[1] A. S. McIntosh, A. Lai, and E. Schilter, "Bicycle Helmets: Head Impact Dynamics in Helmeted and Unhelmeted Oblique Impact Tests," *Traffic Inj. Prev.*, vol. 14, no. 5, pp. 501–508, Jul. 2013, doi: 10.1080/15389588.2012.727217.

[2] N. Sabahiah, A. Sukor, A. K. M. Tarigan, and S. Fujii, "Analysis of correlations between psychological factors and self-reported behavior of motorcyclists in Malaysia, depending on self-reported usage of different types of motorcycle facility," *Transp. Res. Part F Psychol. Behav.*, 2016, doi: 10.1016/j.trf.2016.09.032.

[3] J. Xu, J. Yang, and J. Hu, "Injury Analysis and Prevention in Vehicle Safety," *Appl. Bionics Biomech.*, vol. 2018, 2018, doi: 10.1155/2018/9532598.

[4] "1,026 lives lost in motorcycle accidents in 10 months | Dhaka Tribune." https://www.dhakatribune.com/bangladesh/2020/11/12/1-026-lives-lost-in-motorcycle-accidents-in-10-months (accessed Feb. 14, 2021).

[5] N. M. Petry, "A Comparison of Young, Middle-Aged, and Older Adult Treatment-Seeking Pathological Gamblers," vol. 42, no. 1, pp. 92–99, 2002.

[6] K. Kanitpong, N. Boontob, and Y. Tanaboriboon, "Helmet Use and Effectiveness in Reducing the Severity of Head Injuries in Thailand," *Transp. Res. Rec.*, vol. 2048, pp. 66–76, Dec. 2008, doi: 10.3141/2048-09.

[7] T. Sass and P. Zimmerman, "Motorcycle Helmet Laws and Motorcyclist Fatalities," *J. Regul. Econ.*, vol. 18, pp. 195–215, Feb. 2000, doi: 10.1023/A:1008124703161.

[8] S. Wadhwaniya, S. Gupta, S. Mitra, S. Tetali, and L. K. Josyula, "A comparison of observed and self-reported helmet use and associated factors among motorcyclists in Hyderabad city, India *," *Public Health*, vol. 144, pp. S62–S69, 2016, doi: 10.1016/j.puhe.2016.11.025.

[9] H. Hu *et al.*, "Anthropometric measurement of the Chinese elderly living in the Beijing area," *Int. J. Ind. Ergon.*, vol. 37, no. 4, pp. 303–311, Apr. 2007, doi: 10.1016/j.ergon.2006.11.006.

[10] A. Alrashdan, A. Alkaff, and S. Khamis, "Head and face anthropometric measurements for Saudi Arabian Females," p. 5.

[11] "Anthropometric Data - an overview | ScienceDirect Topics." https://www.sciencedirect.com/topics/engineering/anthropometric-data (accessed Apr. 07, 2022).

[12] "7.2.6.2. Percentiles." https://www.itl.nist.gov/div898/handbook/prc/section2/prc262.htm (accessed Feb. 17, 2021).

Paper ID: 7145

International Conference on Mechanical, Manufacturing and Process Engineering (ICMMPE – 2022)

Organizer: Faculty of Mechanical Engineering, Dhaka University of Engineering & Technology (DUET), Gazipur, Bangladesh

Website: https://icmmpeduet.com/

Analysis of Mechanical Properties of Biocompatible Materials Magnesium Alloy for Male Femoral Bone Fracture

Mehedhi Hasan[1], H. M. Mobarak[2]

[1]Department of Mechanical Engineering, Sonargaon University, Green Road, Panthapath 1205, Dhaka, Bangladesh
[2]School of Engineering, Design and Built Environment, Western Sydney University, Penrith 2747, NSW, Australia

E-mail: mobarak.hossain@westernsydney.edu.au

ABSTRACT

Bone fracture is a common medical problem with a long history as the history of human living. The best definition for a bone fracture will be the loss of bone continuity due to the sudden impact, falling, accident, sports injuries, and many other reasons. Metal plates are highly recommended for the healing process and include some biocompatibility and stress shielding problems. However, metal plates susceptibility to corrosion and the effect of corrosion on the tissue are critical factors of biocompatibility. Therefore, biocompatibility is frequently taken into account when selecting materials for medical use. This research has been analyzed magnesium alloy mechanical properties to find the best suitable biocompatible materials for bone fracture. Magnesium alloy has been chosen considering biocompatibility and mechanical integrity. A three-dimensional male femur bone finite element model was simulated to analyze strain, stress, and deformation. The femur bone supports most of the human body's weight and has a more high impact area that is likely to fracture. The male femur bone properties and structural steel has been used to compare the results. Results showed that magnesium alloy is better than structural steel and similar to bone materials. The stress of the two materials are similar, but strain and deformation are different. The results of the magnesium alloy have been found deformation of 9.773 mm, the stress of 145.51 MPa, and the strain of 0.0036356 mm/mm. The structural steel results have been found deformation of 2.1979 mm, the stress of 140.9 MPa, and strain of 0.00079089 mm/mm. Therefore, magnesium alloy will allow the bone to be exposed to the appropriate amount of stress. So, the magnesium alloy would be the best alternative and most incredible option owing to biocompatibility and mechanical integrity.

Keywords: Biocompatibility; Bone fracture; Femoral Bone, Magnesium alloy.

1. INTRODUCTION

Bone is the strongest part of the human body. It supports vital organs and keeps them safe. The femur bone is the strongest due to high bone density—however, it fractures due to extreme stress or a disease that weakens the bones. Bone fracture is a vital issue, and the healing process might be challenging at times. Bone is responsible for providing the body with strength, structure, and health. Bone consistently adapts its structure around the biological environment accordingly to chemical stimuli [1]. Usually, bone is two compact (cortical) and spongy (trabecular) structures. They can be found in various locations throughout the body, but they all serve distinct purposes. The compact (cortical) bone is exceedingly dense, forming the outer shell that gives the bone its strength and structure. The spongy (trabecular) kind of bone has a porous, light look responsible for energy absorption and load dispersion. Bone fracture repair is a complicated procedure since it must consider the afflicted bone's characteristics and location. Proper structural and functional reconstruction of bone repair, regeneration, non-union repairs, and bone defects must be investigated [2]. Bone grafting, casting (self-healing process), metal rods, crews, plates, electrical stimulation, and physiotherapy have all been used in the past to restore bones. As previously stated, autografts, allografts, xenografts, and synthetic bone materials are all utilized to treat bone fractures [3]. Recent research has demonstrated that autografting improve patient therapy and recovery, even though accessible bone donors are restricted. Autografting's adverse effects are problematic since it slows down the rehabilitation process and requires more time in the hospital [4].

Magnesium alloy and titanium alloy are biocompatible materials that have been used for bone replacement and fractures in the medical field. Magnesium is an excellent choice because of its lightweight, low density, and inexpensive. Because of their mechanical strength and fracture toughness are regarded as the lightest material for load-bearing applications [5]. Faulty surgical implants have spawned a competition to identify the best bone grafting option. The ideal bone graft or scaffold for bone tissue engineering should meet all of the following criteria: biocompatibility, osteoconductive, osteoinductive, osteogenic, degradable, and have the same mechanical characteristics as the local bone for structural integrity [6].

Most of these materials have different properties based on the performed type of surgery. Bioinert materials are the best option for plates because bioactive materials would connect with the bone. Structural steel and cobalt alloys are appropriate and utilized for past and present patients. Bioceramics, titanium alloys, pure titanium, composite materials, and suitable polymers are all examples of acceptable materials [7].

The mathematical Modelling was used to test and manage which biomaterials may be used for bone fracture repair. As a result, investigating and understanding the properties of a particular biomaterial for bone healing is essential. Mechanical parameters and biocompatibility need to be assessed to continue research to widen the range of feasible bone fracture healing alternatives.

Metal plates are commonly used for the healing process as a foreign material. However, susceptibility to corrosion and its effect on the tissue is critical. Biocompatibility is frequently taken into account for medical use. This research has analyzed magnesium alloy mechanical properties to find the best suitable biocompatible materials for bone fracture. In this research, a three-dimensional male femur bone finite element model was simulated using ANSYS to investigate the mechanical parameters of biocompatible materials, magnesium alloy. Magnesium alloy was used because of its biocompatibility and mechanical properties. Its low young's modulus is guarding against the stress shielding effect.

2. MATERIALS AND METHODS

The male femur bone is selected for analysis in this research because it is a cortical bone. It has a dense outer shell, including the trabecular (soft) bone. The femur bone is located above the knee where the Quadriceps are attached. It is exposed to a lot of stress and strain because both legs support the majority of the human body's weight. The femur bone is a high impact area likely to fracture. Different parts of the male femur bone are shown in Fig. 1.

There are various methods for determining the best materials in terms of physiologically and mechanically for bone fracture healing. For example, in the medical field, in vivo and in vitro testing are used to understand better how an experiment would perform in a "real world" context. There is also simulation Modelling to replicate an experiment's outcome correctly. ANSYS was used to simulating the 3D Femur model as shown in Fig. 2. The model was subjected to von mises stress, deformation, and equivalent elastic strain.

The load was applied to the Knee joint along the bone length. The fixed support was considered at the ball joint end of the femur bone because the hip of the human anatomy comes to a stop at the lower ball joint, as shown in Fig. 3.

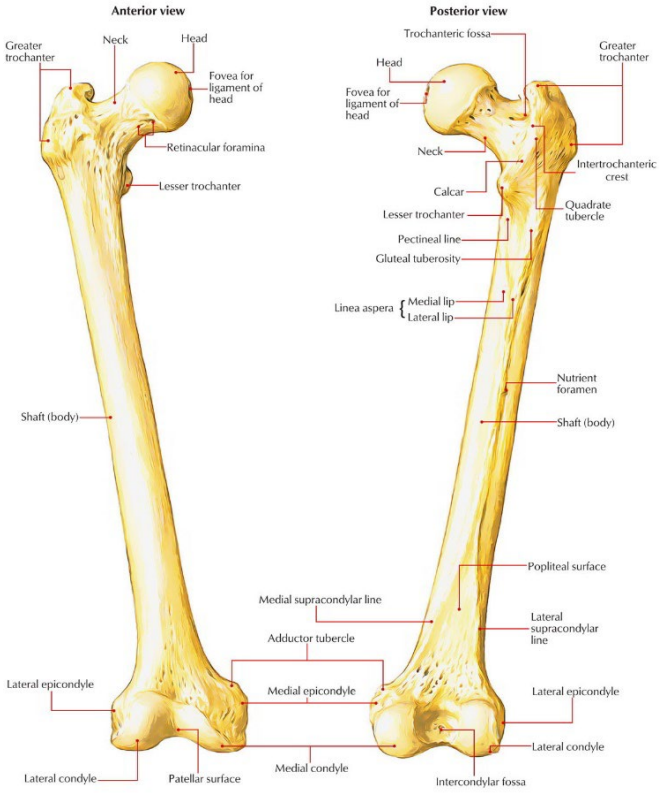

Fig. 1: Different parts of the male femur bone [3]

Fig. 2: 3D male femur bone model

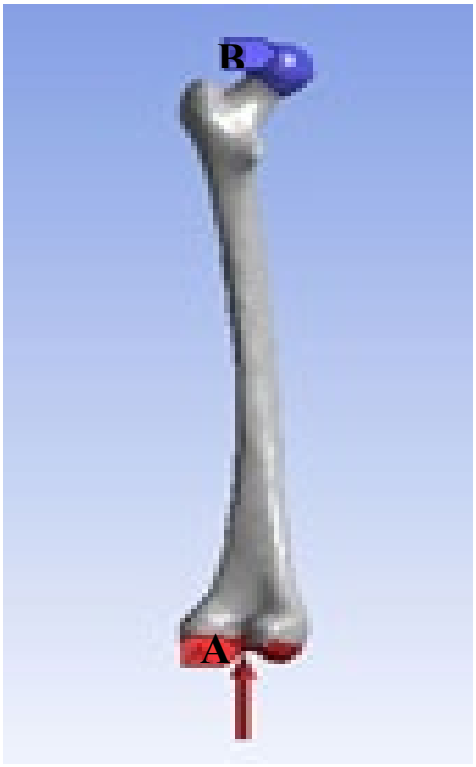

Fig. 3: Load applied on the Knee joint at point A and fixed support considered on the ball joint at point B.

Meshing is an essential aspect of simulation modelling since it cuts down on getting correct results. The mesh sensitivities analysis was performed to maximize the accuracy of the results. Mesh of roughly 5mm-10mm was employed to provide a precise simulation reading to show the bone's unambiguous stress and strain results. As shown in Fig. 4, the curvature and round surfaces of the femur bone were taken into account for fine mesh.

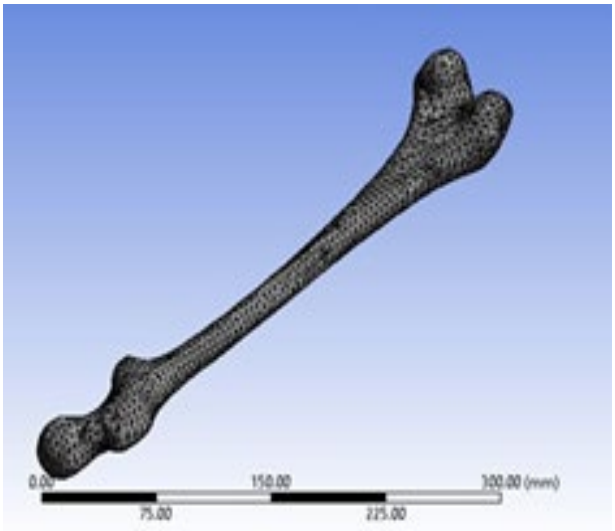

Fig. 4: Mesh analysis for the femur model

Structurural steel has been chosen to compare the biocompatible material results. Bone, Struuctural steel and Magnesium AZ31B alloy mechanical properties are given in Table 1 and Magnesium alloy chemical composition are given in Table 2.

Table 1: Properties of the male femur bone, magnesium alloy and steel used in the analysis [5].

Properties	Male Femur Bone	Magnesium Alloy	Structural Steel
Young's Modulus (MPa)	213	450	200
Density (kg/m³)	2000	1800	7850
Poisson ratio	0.3	0.35	0.3

Table 2: The chemical composition of Magnesium alloy.

Element	Content (%)
Magnesium, Mg	97
Aluminum, Al	2.50 - 3.50
Zinc, Zn	0.60 - 1.40
Manganese, Mn	0.20
Silicon, Si	0.10
Copper, Cu	0.050
Calcium, Ca	0.040
Iron, Fe	0.0050
Nickel, Ni	0.0050

3. RESULTS AND DISCUSSION

The femur is one of the longest bones in the human body. Moreover, fissures and fractures are more likely to form in the femur bone. The finite element analysis has been done using the male femur bone properties, as shown in Fig. 5. It was done to find the weakest point of the bone according to the given environmental load constraints. The average adult (male) weight has been considered about 85Kg, about pressure 1.29 MPa. One femur bone would be 0.645 MPa of pressure exerting upwards towards the hip joint. Therefore, the ultimate compressive stress of a femur bone is around 133MPa. Therefore, a significant ramped pressure of 500MPa at the knee joint, the bottom of the femur bone, has been considered.

Results indicate that the weight and pressure from a jump or fall will travel along the hip bone and cause strain to the femoral neck. The max strain is located in the femoral neck region, as shown in Fig. 5c, where the hip is conjoined to the bone. The maximum deflection of the femur bone has been found at 2.063 mm at the applied load point, as shown in Fig. 5a. The maximum stress of the bone is 140.9MPa around the centre of the bone, as shown in Fig. 5b, which is very close to the stated ultimate compressive stress of a femur bone.

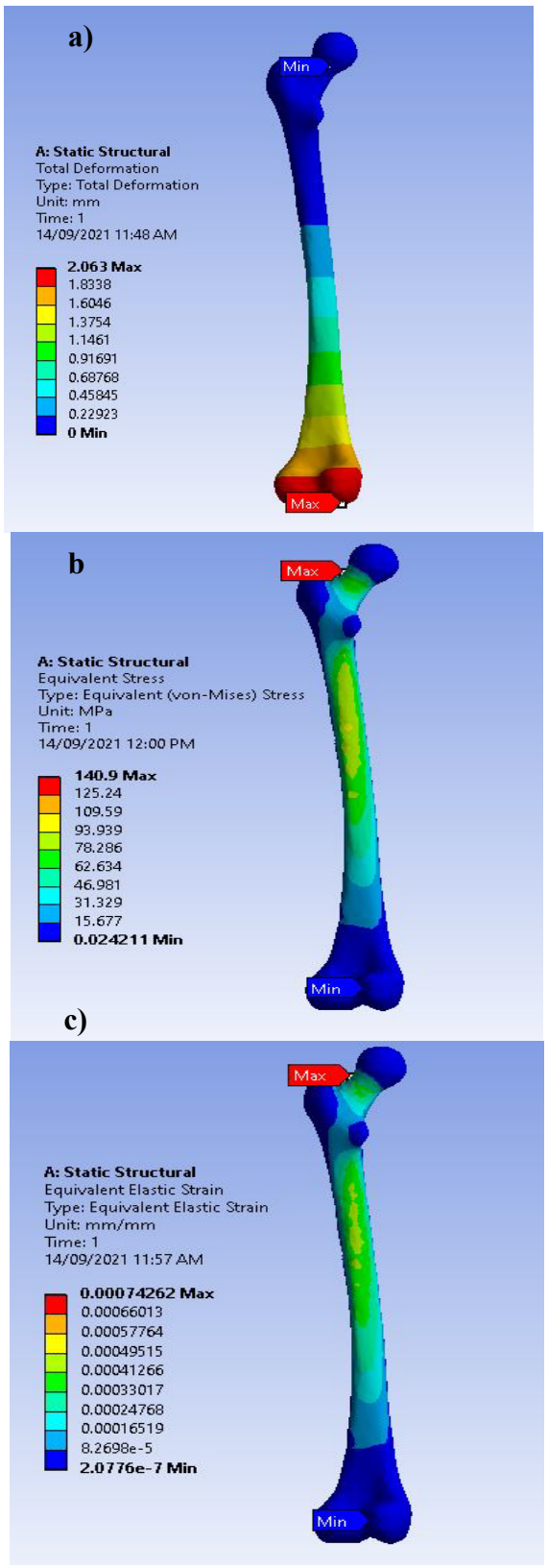

Fig. 5: The results of femur bone using male bone properties: a) deformation, b) stress, and c) strain.

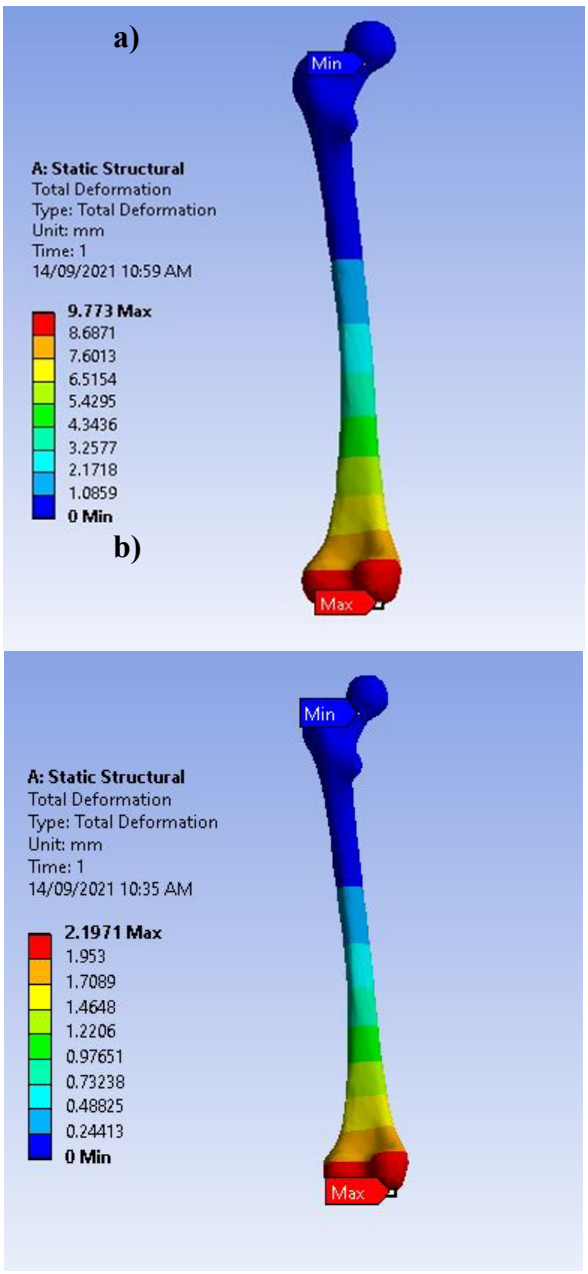

Fig. 6: Deformation analysis of male femur bone using a) magnesium alloy, and b) structural steel.

The finite element analysis results for biocompatible material, magnesium alloy, and structural steel, are shown in Figs. 6 to 8. Results show that the stress of the two materials is similar, but strain and deformation are different. The results of the magnesium alloy are on the femur bone have been found deformation of 9.773 mm, the stress of 145.51 MPa, and the strain of 0.0036356 mm/mm, as shown in Figs. 6a, 7a, and 8a. The structural steel results are as follows: deformation of 2.1979 mm, the stress of 140.9 MPa, and strain of 0.00079089 mm/mm, as shown in Figs. 6b, 7b, and 8b.

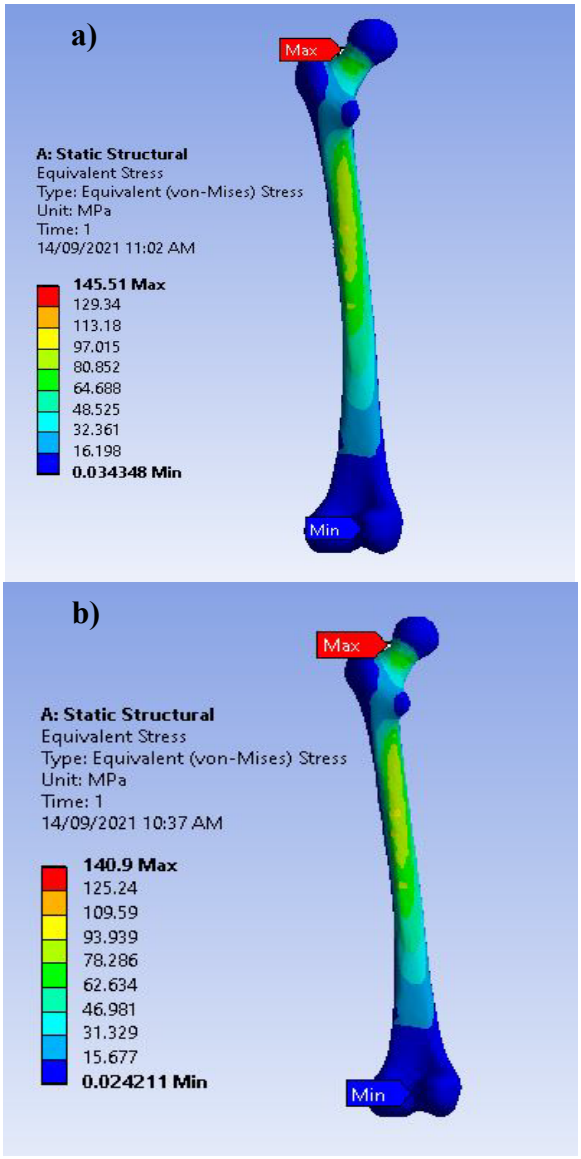

Fig. 7: Stress analysis of male femur bone using a) magnesium alloy, and b) structural steel.

Table 3: Comparison of stress, strain, and deformation of Structural Steel and Magnesium alloy

Parameter	Structural Steel	Magnesium Alloy
Maximum Deformation (mm)	2.19	9.77
Maximum Von Mises Stress (MPa)	140.90	145.51
Maximum Von Mises Strain (mm/mm)	0.00079089	0.0036356

The ramped analysis shows how the femur bone is prone to fracture at the cross-section in the middle, as shown in Figs. 5 to 8 and Table 3. In comparison to the firm bone tissue at the end joints, this section of the bone is fragile. The deformation over time is located at the knee joint, which is frequent among people with common knee difficulties. The red showing the most excellent stress site is the weakest femur bone, producing fractures. Because of the low-stress feature, the bone will be maintained to help self-healing, preventing bone stress shielding.

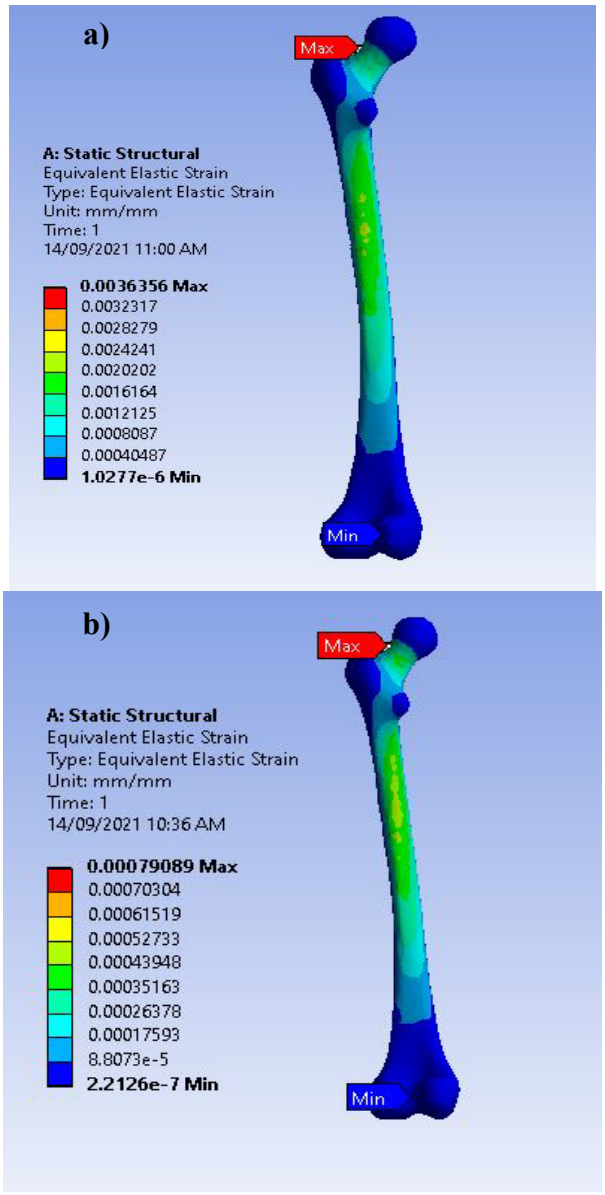

Fig. 8: Strain analysis of male femur bone using a) magnesium alloy, and b) structural steel.

4. CONCLUSIONS

Mechanical and biocompatibility properties of materials for bone fracture treatments must be investigated for human health progress. Biocompatibility is necessary for physical health improvement and mechanical strength for lifespan and solutions to bone fracture. In this research, the mechanical properties of biocompatible material, magnesium alloy, have been analyzed. A three-dimensional femur finite element model has been simulated to find suitable biocompatible materials for bone fracture. Results indicated that Magnesium alloy is suitable mechanically under stress. The minimal stress generated by the magnesium will prevent stress shielding from occurring in the femur bone-will allow the bone to encourage self-healing through the production of callus bone. Magnesium also found a more significant strain and deformation value. Overall, results show that it would be an alternative and incredible option owing to biocompatibility and mechanical integrity.

ACKNOWLEDGMENT

The authors would like to show gratitude to Western Sydney University for helping to develop and analyze the model.

REFERENCES

[1] Sabet. F 2016, Modelling of bone fracture and strength length scales: a review, University of Illinois, Urbana.

[2] Zhang, J 2021, the fate of patients after staged non-union procedure for known infection. J Orthop Trauma, vol 35, no 4

[3] Wang. Q 2016, Nanomaterials promise better bone repair. Materials Today, vol 19, no. 8.

[4] Kohli, N 2017, Bone remodeling in vitro: where are we headed?- A review on the current understanding of physiological bone remodeling and inflammation and the strategies for testing biomaterials in vitro. RAFT Institute, Northwood.

[5] Hoffmann, I 2014, Magnesium-Titanium alloys for biomedical applications, University of Kentucky, Kentucky.

[6] EI-Rashidi. 2017. Regenerating bone with bioactive glass scaffolds: A review of in vivo studies in bone defect models, Cairo University, Cairo.

[7] Ganesh, VK 2005, Biomechanics of bone-fracture fixation by stiffness-graded plates in comparison with stainless-steel plates, Nanyang Technology University, Nanyang.

Paper ID: 7156
International Conference on Mechanical, Manufacturing and Process Engineering (ICMMPE – 2022)
Organizer: Faculty of Mechanical Engineering, Dhaka University of Engineering & Technology (DUET), Gazipur, Bangladesh
Website: https://icmmpeduet.com/

Effect of Shapes and Cooling Media on the Temperature of Flexible Photovoltaic Panels under the Climatic Conditions of Khulna, Bangladesh

M I Islam*, Zahir U. Ahmed and M T Hassan

Department of Mechanical Engineering, Khulna University of Engineering & Technology, Khulna-9203, Bangladesh

*Corresponding Author: ittehadulislam53@gmail.com

ABSTRACT

Photovoltaic (PV) panels are in use for over a century to generate electricity using sunlight as a source of energy. One of the latest adaptations of PV panels is the thin-film flexible photovoltaic panel which is becoming popular due to its lightweight, low cost and convenience of being installed on various surfaces where conventional panels are not feasible. The unique feature of this panel is its flexibility and the ability to be bent in various shapes. This study aims to numerically investigate whether the change of shape has any effect on the cooling of flexible Photovoltaic (FPV) panels under the climatic condition of Khulna, Bangladesh. In this regard, finite volume based commercial software package is used to solve the mass, momentum and energy equations. The panel is bent in a curved shape and is compared with the regular (flat) panel. A cooling channel is introduced below the panel. Air and water are used as the cooling medium. Mean temperature of the PV panel, heat transfer coefficient and Wall shear stress are examined. It is found from the results that the shape of the FPV has considerable effect when air cooling is performed. For the same Reynolds number, FPV temperature for the curved plate is 1-3K lower than the flat one during air flow. However, natural air flow through the cooling channel can not keep the FPV temperature low and therefore water cooling is necessary especially in the months October-May when the PV panel temperature is excessive. For air, FPV temeperature can reach upto 434K whereas water keeps the temperature around 300K even at low Reynolds number and regular shape. For water, shape does not offer any significant additional cooling.

Keywords: Flexible PV; Cooling; Heat transfer coefficient; Nusselt number.

1. INTRODUCTION

In the last decade, energy consumption has increased tremendously, and the trend is ever increasing. Electricity is the most widely used form of energy due to its properties of easier transportation, conversion and cleanliness. The production of electricity mainly depends on the burning of coal. In 2015, 9553.5 TWh of the world's electricity had been produced by coal-burning [1]. The burning of coal produces a large amount of CO_2 causing environmemtal pollutions and global warming. To reduce such emissions, finding alternative sources of energy has become a necessity. Concentrated solar power has been considered the cleanest alternative source to satisfy the energy demand. Photovoltaics, the production of electricity by converting solar energy, has been found to be attractive and gained increasing interest by the research community. In 2020 electricity generation using solar PV has reached 821 TWh, an increase of 156 TWh (23%) from the previous year. [2]. FPVs (Flexible Photovoltaics) serve as a convenient source of energy for both outdoor and indoor applications. Lightweight, flexibility and easier integration on the various shaped surfaces have increased the installation of FPVs. According to research on Global Flexible Solar Cell Market, the market value of flexible PV was approximately 340 million USD in 2019 and it is expected to grow at a compound annual growth rate of 7.1% over the next five years reaching a market value of approximately 510 million USD in 2024 [3].

From only 3% after the war of independence in 1971, energy access in Bangladesh has reached up to 79% in 2018 [4]. More than 90% of this electricity generation is dependent on the gas reserve and imported fossil fuels whereas renewable energy accounts for only 3% of it [4]. However, increased usage of renewable energy has become a new trend. Due to its geological advantage, Bangladesh receives an average daily solar radiation in the range of 4-5 kWh/m [6]. According to the IRENA Renewable Energy Statistics 2021, the installed solar PV capacity in Bangladesh was around 301 MW in 2020, up from 255 MW in 2019 [7].

Still a good number of people around the country don't have access to electricity, and this is not an uncommon scenario in Khulna. According to a survey of 5 dimensions of poverty, namely economic, social, infrastructure, political, and spatial

in the Khulna region, 42-83% of the slum dwellers are multidimensionally poor [8]. These people barely have homes and if so, they are mostly straw made or light shaded. Placing a PV panel on the roof is both infeasible and unaffordable for these people. With their lightweight and cheaper price, FPVs can be a potential solution in this regard. Another common scenario in the streets of Khulna is the manually dirven food carts. These carts require only a fan and a light, the power of which can be easily supplied by a PV panel. The weight of a PV panel is, nevertheless too heavy for such carts. Flexible PV panels can be used here for their less weights and the ability to adjust with the curvy roof of the carts.

A good number of researches have been carried out on the development of FPVs. Still, continuous works are being performed worldwide to increase efficiency, optimize performance and develop newer kinds. U.S Department of Energy's National Renewable Energy Laboratory developed a thin-film solar cell employing CIGS technology which reached an efficiency of 19.9%, a world record in 2008, closing the efficiency gap with Multicrystalline silicon-based solar cells which has the efficiency as high as 20.3%[9]. Adrian Chirilă et al. [10] proposed a method of post-deposition treatment (PDT) employing NaF and KF in order to improve the power conversion efficiency of the CIGS layer. This resulted in a record efficiency of 20.4% in 2013. Flexible Perovskite Solar Cells (PSC) are another addition in the world of FPVs. These types of cells usually contain perovskite-structured compound, hybrid inorganic-organic lead or tin halide-based materials in general as light-harvesting layers. Starting with the PCE of 2.62% in 2013, PSC quickly reached the PCE of 18.4% [11].

Even though PV panels absorb around 80% of the incident solar radiation, only a small portion of it is converted into electrical energy. The remaining fraction is then changed into heat, causing the overheating of the PV panel [12]. In practice, only about 15% of incident solar radiation is transformed into useful energy [13]. Escalated temperature is one of the major concerns regarding the efficiency of PV panels. It has been observed that, for every 1° C rise in temperature, PV panel efficiency drops about 0.45-0.5 % [14]. Materials used in FPVs are more vulnerable to overheating than the ones used in regular PV panels. A regular rigid solar panel has an average lifespan of 25 to 30 years whereas its flexible counterpart lasts for about 10 years [15]. Although there are a lot of factors at play here, overheating is one of the significant ones.

Numerous researches have been performed to keep the temperature of the regular PV panel under control. Peyvand et al. [16] used a wind-powered turbine ventilator equipped with a dynamo to pass air beneath the solar panel beside normal ventilation, resulting in PV cell output rising up to 46.54%. Tonui et al. [17] proposed a configuration with fins at the back wall of an air duct to improve the overall performance of the PV/T system. Forced convection of air with a flow rate of $60 m^3 h^{-1}$ and channel depth of 15 cm had been adopted and the resulting efficiency was 30%. Teo et al. [13] found that when the active cooling method had been adopted, a significant temperature drop had occurred resulting in the increase in efficiency from 8-9% to 12-14%. The majority of the cooling techniques used water as the coolant. Alami [18] investigated a passive evaporative cooling technique using water as a coolant and found the outcome satisfactory- a maximum 19.1% increase in output power and 19.4% increase in output voltage. Bahaidarah et al. [19] numerically studied the performance of a PV water-cooled system using EES (Engineering Equation Solver) and achieved a 9% increase in efficiency and about 20° decrease in temperature with active water cooling. Shuang et al. [20] developed a numerical model of a water-cooled PV-T system with a cooling channel above the PV panel and analyzed the influence of various factors. He obtained an exergy efficiency of 13.8% at the optimal mass flow rate of 0.003 kg/s and an optimal channel height of 5 mm.

The objective of this paper is to investigate the cooling of two different shaped flexible PV panels in the climatic condition of Khulna all throughout the year and check how different shapes and cooling media affect the heat transfer. This study also determines whether FPVs are feasible in our environmental condition or not. While a good number of researches have been conducted in the past on the cooling of other solar-powered machines, such as rigid solar panels, PV/T collectors and parabolic trough collectors, and most of the research regarding FPVs concern their efficiency, research on the cooling of FPV is still very limited in the literature. It is apparent that although the flexible solar panel is of great importance, overheating of it may be considered to be a major problem that has to be overcome. Since experiments are typically expensive, particularly when a number of physical tests and variations are involved, numerical simulation would be an ideal candidate for such preliminary investigations.

2. DESCRIPTION OF COMPUTATIONAL MODEL

The simulation has been done numerically using ANSYS Fluent 17. The methodology for geometry, mesh along with necessary boundary conditions and validation of results have been discussed in the following section.

2.1 Geometry

The investigation is based on the thermal performance of the flexible PV panel of different shapes. In this regard, two different shapes have been designed: Flat and Curved, keeping the basic parameters the same. A flexible PV panel has the protection of Polyethylene Terephthalate (PET) and Ethylene-Vinyl Acetate (EVA) on both the top and bottom. For cooling, we introduced an additional cooling channel of height 1mm under the PV panel. For our investigation, we

ignored the bottom PET and EVA covers as they have less or no significance in heat transfer. So, we designed our PV panel with four rectangular parts on top of each other: Cooling channel, PV Panel, EVA and PET (Figs 1 and 2). The detailed parameters of each of the parts and thermophysical properties of their corresponding materials are shown in table 1 and 2 respectively.

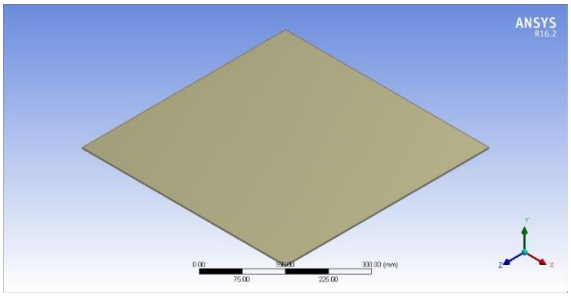

Fig. 1: Geometry of the flat PV panel

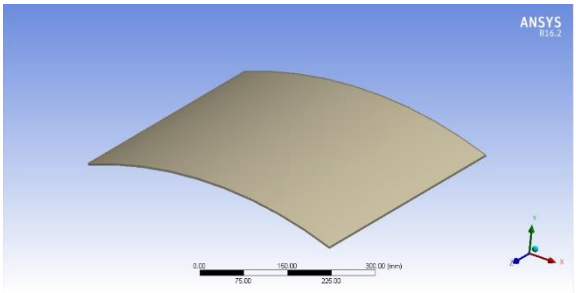

Fig. 2: Geometry of the curved PV panel

Table 1: Physical parameters of the PV

Parameter	Value
Length	500 mm
Width	500mm
Height of PET cover	0.8 mm
Height of EVA cover	0.8 mm
Height of PV panel	0.8 mm
Height of Cooling Channel	1 mm

Table 2: Thermophysical properties of FPV materials [21-23]

Material	Density, ρ (kg/m^3)	Thermal Conductivity, k (j/kg-K)	Specific Heat, C_p (w/m-K)
Monocrystalline	2329	148	0.7
Ethelyn Venyl Acetate	930	0.34	1400
Polyethylene Terephthalate	1400	0.4	1100

2.2 Mesh Generation And Grid Independence

To discretize the domain, hexahedral mesh was created with maximum face size of 4mm, minimum edge length of 0.8 mm and growth rate of 1.2. For proper visualization of fluid flow pattern in inlet and outlet, edge sizing was done with 10 divisions and a bias factor of 2 to ensure smaller mesh near the wall (Figs 3 and 4). The grid independence test has been done to ensure maximum accuracy with minimum computational power. Multiple simulations were run changing the number of elements of Flat PV under the environmental conditions of March and with air flow through the cooling channel. The results are shown in table 3.

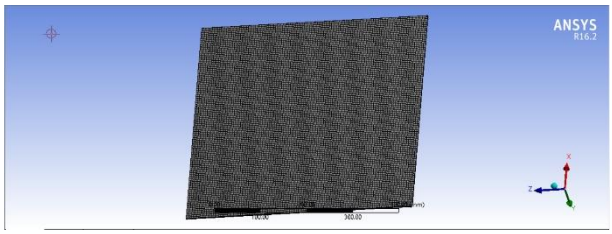

Fig. 3: Mesh of the flat PV panel

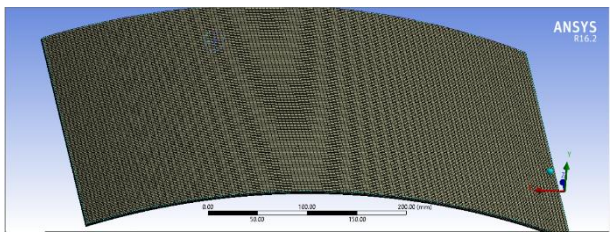

Fig. 4: Mesh of the curved PV panel

Table 3: Grid independence test

Number of elements	Outlet temperature	% Change in temperature
150000	383.80	-
184815	386.7	0.7%
234375	387.63	0.2%
306735	387.7	.01%

2.3 Validation

In order to validate the study, simulation results obtained from Fluent are compared to the theoretically obtained values. For comparison, the observation for air flowing through the flat PV panel in the month of June has been considered. For steady state heat conduction through a composite wall the equation gives,

$$Aq_0 = \frac{T_1 - T_2}{\frac{L_1}{Ak_1}} = \frac{T_2 - T_3}{\frac{L_2}{Ak_2}} = \frac{T_3 - T_\infty}{\frac{1}{Ah}} \quad (1)$$

where , A is the surface area, L_1 and L_2 are the length of PET and EVA cover (table 1), q_0 is the heat flux on the top of PET surface (table 4), k_1, k_2,k_3 are the thermal conductivities of PET, EVA and PV panels respectively (table 2), h is the heat transfer coefficient provided by Ansys and finally T_1, T_2,T_3, T_4 and T_∞ are the PET top, EVA top, PV top, PV bottom and the environmental temperatures respectively. Using the equation, the corresponding temperatures of the FPV parts have been calculated and compared with their numerically obtained counterparts. The result is shown in Fig 5.

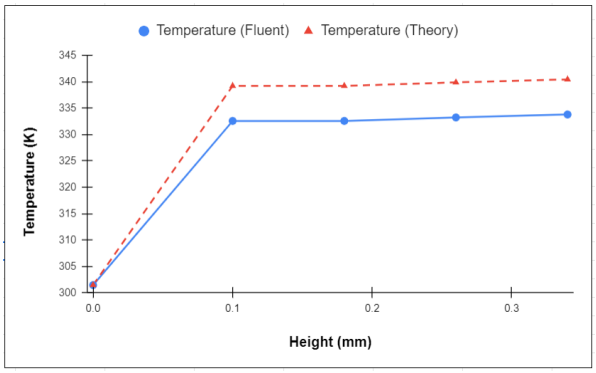

Fig. 5. Temperature VS flat FPV panel height graph for air flowing through the panel in the month of June

From the graph it is apparent that both the simulation result and theoretical one show a qualitatively similar behavior, with disagreement less than 2% . Therefore, the numerical settings are considered sufficient to resolve the thermal characteristics.

3. BOUNDARY CONDITIONS

The main purpose of the study was to investigate the temperature difference of the flexible PV panel with respect to climate and change to its shape. For that purpose, we collected the weather data from the publicly available source of NASA [24]. The daily data has been averaged to get the monthly mean of each of the variables. The parameter values are shown in table-4. The Reynolds number, *Re* corresponds to the mean wind speed varies from 304 to 674, which refers to the laminar range of flow through the channel. For comparison, we estimated the water flow for the same Reynolds number.

From the table, we can see the mean insulations vary from 2 82 W/m² to 450W/m² . The PET plate was exposed to this heat flux. The walls are considered adiabatic to avoid heat loss to the surroundings. The fluid wall is stationary and no-slip boundary condition has been assigned to it. The plates are coupled to enable heat transfer through them and also with the fluid. The inlet and outlet sections are taken as velocity inlet and pressure outlet. The temperature of the inlet fluid was also taken from the NASA weather data. Pressure based solver has been used to solve the problem.

Table 4: Climate data for Khulna region [24]

Months	Temperature (K)	Insolation (W/m^2)	Windspeed (m/s)
January	291.37	365.54	1.32
February	294.92	419.91	1.38
March	298.63	450.52	1.34
April	301.89	429.85	1.67
May	301.57	394.90	2.24
June	301.44	282.06	2.42
July	301.46	285.82	2.39
August	301.38	288.52	2.47
September	301.29	321.38	1.64
October	300.54	344.79	1.11
November	295.55	380.51	1.28
December	291.02	353.73	1.25

4. SOLUTION METHOD AND GOVERNING EQUATIONS

The flow is considered laminar, steady and incompressible. The governing equations used for solving the three dimensional numerical analysis are: continuity equation, momentum equation and energy equation. The convergence criteria for all the equations are taken as 10^{-6}. Least square

cell based SIMPLE algorithm has been used to solve the equations. The governing equations are as follows:

Continuity Equation:

$$\nabla(\rho V) = 0 \quad (2)$$

Momentum Equations:

$$\nabla(\rho uV) = -\frac{\delta \rho}{\delta x} + \mu\nabla(\nabla.u) + \rho g_x \quad (3)$$

$$\nabla(\rho vV) = -\frac{\delta \rho}{\delta x} + \mu\nabla(\nabla.v) + \rho g_y \quad (4)$$

$$\nabla(\rho wV) = -\frac{\delta \rho}{\delta x} + \mu\nabla(\nabla.w) + \rho g_z \quad (5)$$

Energy Equation:

$$\rho C_p(\nabla(TV)) = \nabla(\nabla.kT) \quad (6)$$

5. RESULT AND DISCUSSION

In this section, the results obtained from the study has been discussed.

Fig 6. shows the PV panel temperature in different months. It has been seen that, the PV panel temperature is the highest in March and the lowest in December. However, the temperature differences between the PVs with air cooling and the PVs with water cooling are significantly larger. At first glance, the question may arise that why the graphs for air cooling and water cooling show different trend. But, it has to be kept in mind that, here the months represent three different variables at once: temperature, insolation and velocity. Also, water having high specific heat is keeping the PV panel temperature almost the same as the environmental temperature even in lower velocity i.e Reynolds number. For example, temperature in April is almost 3 K higher than in March. However, as the wind velocity also increases in April, so does the heat transfer and as a result PV temperature in April for air flow is lower than in March. On the other hand, water with lower Re already does the job of keeping the PV temperature near the environmental one. And so, increase in Re does not have much significance. For the same reason, due to the higher velocity of around 2.4 m/s during June-August, FPV temperature is much lower for air cooling even though the environmental temperature is considerably higher (around 301K). But for water cooling, where velocity or Re has no significant effect, environmental temperature became the dominant factor for determining the FPV temperature.

Another thing to notice is that, for curved panel in air cooling, heat transfer is a bit higher, resulting in 1-3 K lower temperature than its flat counterpart. For water, nevertheless, shape has negligible effect in cooling, as we can see both the graphs for flat at curved plat overlapped with each other completely.

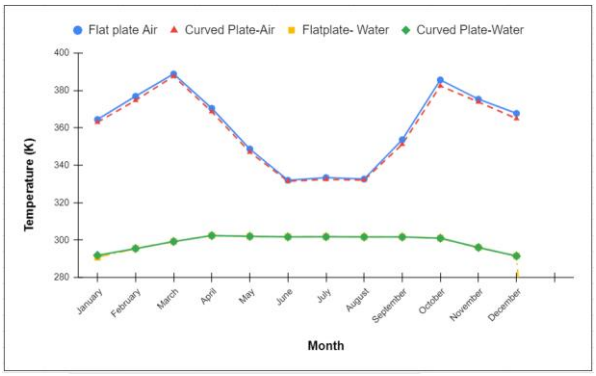

Fig.6: FPV temperature in different months for different shapes and cooling medium

From Fig. 7., the difference in heat transfer coefficient for air and water is clearly observed. For air, heat transfer coefficient varies from 4.81 to 8.19 whereas for water it ranges between 20.82 and 107.1 indicating much higher heat transfer rate.

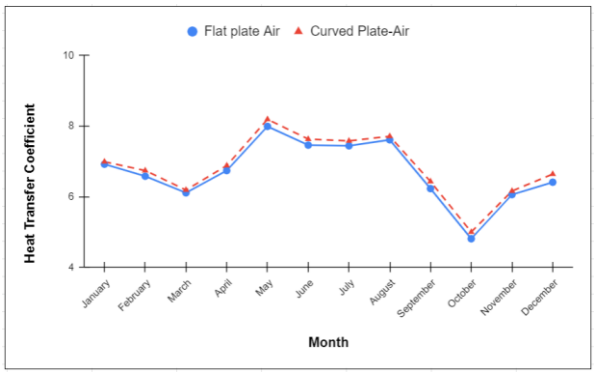

(a)

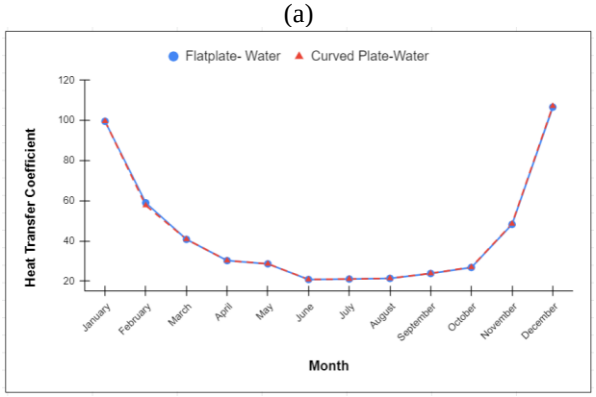

(b)

Fig. 7. Heat transfer coefficient in different months for (a) air (b) water

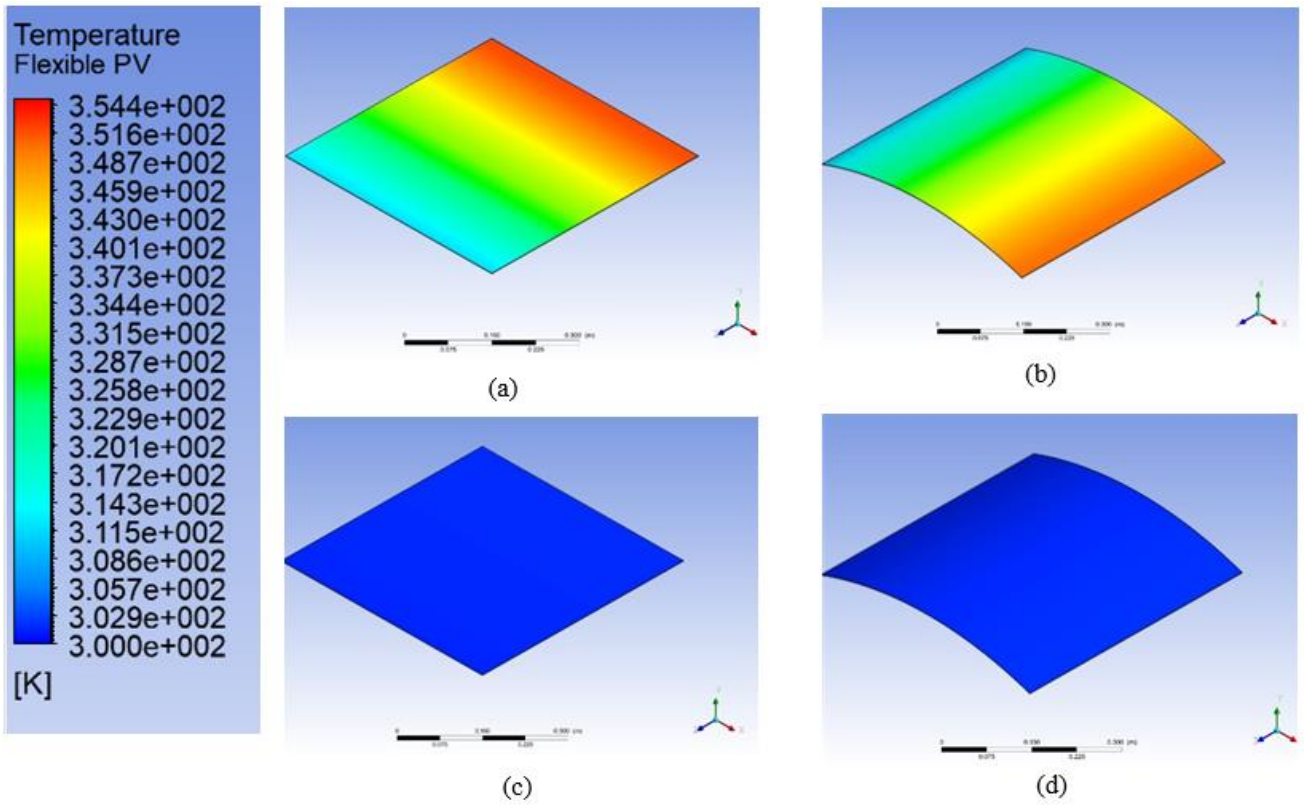

Fig.8: Contour of PV panel temperature for the month of July (a) Flat plate with air flow through the cooling channel (b) Curved PV with air flow through the cooling channel (c) Flat PV with water flow through the cooling channel (d) Curved PV with water flow through the cooling channel

Looking at the effect of shape, compared to flat panel, curved panel induce better heat transfer for air. This is due to the fact that, in the bend of the curved plate, the centrifugal forces act outward from the center of the curvature on the fluid particles as a result of which slower moving fluid particles travel along paths with smaller radii of curvatures than those of the faster ones resulting in the introduction of the secondary flow. This secondary flow field, superimposed upon the axial velocity flow field, causes the enhancement of heat transfer. For air cooling in flat FPV the heat transfer coefficient ranges between 4.81-7.99 whereas for curved panel it is 5-8.19. For water, however, shape again has barely any impact as they already have a higher heat transfer rate.

The effects can be visualized from Fig 8. as well. For air cooling, the temperature of the FPVs varies significantly, from around 308K to the inlet to around 354K to the outlet. The temperature fluctuation of FPV with water cooling is between 2K which under the same scale is insignificant as observed.

Fig 9. shows the similar trend as in the Fig 7. Wall shear stress represents the exerted force per unit area by the wall on the fluid. For water, this is again quite higher than air. Also, as the shape gets curved, stress on the fluid is increased. For flat plate with water, the minimum wall shear stress found was 0.43 Pa and the maximum was 0.95 Pa.For curved plate the range is 0.53-1.04 Pa. For air flow the values are between 0.11-0.25 Pa and 0.12-0.27 Pa respectively.

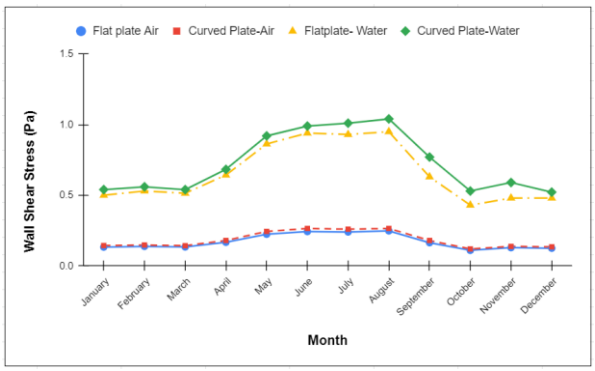

Fig.9: Wall shear stress of FPV in different months for different shapes and cooling medium

6. CONCLUSION

This study compared the cooling of two different shaped flexible PV panels using air and water as coolant under the climatic condition of Khulna. The feasibility of a flexible PV panel is greatly sensitive to temperature due to

its plastic composition. High temperature affects both its performance and longevity greatly when compared to regular PV panels. From this study, it is evident that introducing a cooling channel is not sufficient to cool the FPV as the natural flow of air through the channel does not markedly reduce its temperature. Even though curved structures increase heat transfer via better convection and reduce temperature as a result, they still are not sufficient to keep the FPV temperature in check. Water cooling, on the other hand, showed tremendous results in this regard even with plane structure. Wall shear stress for water cooling is also at a moderate level, between 0.43 to 1.04. For water, shape or Reynolds number does not have any significant effect as it already can manage to check the temperature at low Re and in regular shape. So, optimal choice for cooling an FPV should be with water.

7. ACKNOWLEDGEMENTS

The authors would like to thank University Grants Commission for funding provided via Khulna University of Engineering & Technology (KUET) for this research project (Grant no. 19, FY 2020-2021).

REFERENCES

[1] "IEA Electricity Information 2019." [Online]. Available: https://www.iea.org/subscribe-to-data-services/electricity-statistics

[2] IEA (2021), Solar PV, IEA, Paris https://www.iea.org/reports/solar-pv

[3] [Online]. Available: https://www.industryresearch.biz/

[4]"G. Plan, Power Division, Ministry of Power, Energy and Mineral Resources, Government of the people's republic of Bangladesh, in, 2018."

[5]M. N. Uddin, M. A. Rahman, M. Mofijur, J. Taweekun, K. Techato, and M. G. Rasul, "Renewable energy in Bangladesh: Status and prospects," Energy Procedia, vol. 160, pp. 655–661, Feb. 2019, doi: 10.1016/j.egypro.2019.02.218.

[6] B. K. Sovacool and I. M. Drupady, Energy access, poverty, and development: the governance of small-scale renewable energy in developing Asia. 2016. Accessed: Sep. 18, 2021. [Online]. Available: https://www.taylorfrancis.com/books/e/9781315579535

[7] "Renewable Energy Statistics 2021" https://irena.org/publications/2021/Aug/Renewable-energy-statistics-2021

[8] S. Sydunnaher, K. S. Islam, and Md. M. Morshed, "Spatiality of a multidimensional poverty index: a case study of Khulna City, Bangladesh," GeoJournal, vol. 84, no. 6, pp. 1403–1416, Dec. 2019, doi: 10.1007/s10708-018-9941-9.

[9] "Record Makes Thin-Film Solar Cell Competitive with Silicon Efficiency," Mar. 24, 2008. [Online]. Available: https://www.nrel.gov/news/press/2008/574.html

[10] A. Chirilă *et al.*, "Potassium-induced surface modification of Cu(In,Ga)Se2 thin films for high-efficiency solar cells," *Nature Mater*, vol. 12, no. 12, pp. 1107–1111, Dec. 2013, doi: 10.1038/nmat3789.

[11] C. Wang *et al.*, "Water Vapor Treatment of Low-Temperature Deposited SnO_2 Electron Selective Layers for Efficient Flexible Perovskite Solar Cells," *ACS Energy Lett.*, vol. 2, no. 9, pp. 2118–2124, Sep. 2017, doi: 10.1021/acsenergylett.7b00644.

[12] A. Luque and S. Hegedus, Eds., Handbook of photovoltaic science and engineering. Hoboken, NJ: Wiley, 2003.

[13] H. G. Teo, P. S. Lee, and M. N. A. Hawlader, "An active cooling system for photovoltaic modules," Applied Energy, vol. 90, no. 1, pp. 309–315, Feb. 2012, doi: 10.1016/j.apenergy.2011.01.017.

[14] Z. Ye, A. Nobre, T. Reindl, J. Luther, and C. Reise, "On PV module temperatures in tropical regions," Solar Energy, vol. 88, pp. 80–87, Feb. 2013, doi: 10.1016/j.solener.2012.11.001.

[15] [Online]. Available: https://www.flexible-solar-panel.com/

[16] P. Valeh-e-Sheyda, M. Rahimi, A. Parsamoghadam, and M. M. Masahi, "Using a wind-driven ventilator to enhance a photovoltaic cell power generation," Energy and Buildings, vol. 73, pp. 115–119, Apr. 2014, doi: 10.1016/j.enbuild.2013.12.052.

[17] J. K. Tonui and Y. Tripanagnostopoulos, "Improved PV/T solar collectors with heat extraction by forced or natural air circulation," Renewable Energy, vol. 32, no. 4, pp. 623–637, Apr. 2007, doi: 10.1016/j.renene.2006.03.006.

[18] A. H. Alami, "Effects of evaporative cooling on efficiency of photovoltaic modules," Energy Conversion and Management, vol. 77, pp. 668–679, Jan. 2014, doi: 10.1016/j.enconman.2013.10.019.

[19] H. Bahaidarah, A. Subhan, P. Gandhidasan, and S. Rehman, "Performance evaluation of a PV (photovoltaic) module by back surface water cooling for hot climatic conditions," Energy, vol. 59, pp. 445–453, Sep. 2013, doi: 10.1016/j.energy.2013.07.050.

[20] S.-Y. Wu, C. Chen, and L. Xiao, "Heat transfer characteristics and performance evaluation of water-cooled PV/T system with cooling channel above PV panel," Renewable Energy, vol. 125, pp. 936–946, Sep. 2018, doi: 10.1016/j.renene.2018.03.023.

[21] Silicon Single Crystal | AMERICAN ELEMENTS ® https://www.americanelements.com/silicon-single-crystal-7440-21-3

[22] Plastic & Elastomers- The Universal Selection Source https://omnexus.specialchem.com/selection-guide/ethylene-vinyl-acetate/properties-of-eva

[23] Polyethylene Terephthalate Polyester (PET, PETP) - Properties and Applications (azom.com) https://www.azom.com/article.aspx?ArticleID=2047#

[24] NASA POWER | Data Access Viewer https://power.larc.nasa.gov/data-access-viewer.

Paper ID: 7161
International Conference on Mechanical, Manufacturing and Process Engineering (ICMMPE – 2022)
Organizer: Faculty of Mechanical Engineering, Dhaka University of Engineering & Technology (DUET), Gazipur, Bangladesh
Website: https://icmmpeduet.com/

PERFORMANCE EVALUATION OF COMPOSITE POLYMER ELECTROLYTES BASED ON Li+ CONCENTRATION IN LITHIUM METAL ELECTRODE

Ashikur Rahman & Prof. Dr. Md. Arefin Kowser
Department of Mechanical Engineering
Dhaka University of Engineering & Technology, Gazipur, Bangladesh

ABSTRACT

This modern era, lithium ion is the most commonly used battery such as mobile, laptop, car, & other portable devices. Its high charge storage capacity and portability are beneficial to users. Lithium ion batteries mainly consist of anode, cathode, electrolyte and separator. This battery performs as charging and discharging.

In time of charging the lithium ions are transferred from the cathode to the anode via the electrolyte and during discharging, the opposite happens. Its performance depends on anode, cathode & electrolyte materials used. In this research, there is enhancement on electrolyte materials where some materials are taken to analyze the best performing electrolyte.

Here it is focused on mathematical modeling of ionic concentration, capacity, life cycle and potential. The development of the concentration profiles has been calculated using the standard MATLAB pdepe solver and applying discretization steps. Using MATLAB, we plotted concentration, potential density, flux distribution, potential vs capacity throughout the electrolytic phase during charging and discharging to visualize different electrolyte materials characteristics.

Lastly, the electrolyte performances are shown in the discussion section where it is chosen the better electrolyte.

Keywords: lithium polymer electrolyte, Lithium ion battery, Lithium ion battery charging and discharging simulation, mathematical modeling of lithium ion battery electrolyte

Email: ashik240521@gmail.com, arefin@duet.ac.bd

Introduction

A graphite anode (LiC_6), a lithium metal oxide cathode($LiCoO_2$), and a lithium salt electrolyte are the three primary components of a Lithium-ion battery. A nonconductive porous separator is also employed to keep the cathode and anode separate [1]. The Lithium-ion battery is charged by connecting it to a suitable external power source. The external power source drives electrons from the cathode to the anode during charging. The lithium ions are also transferred from the cathode to the anode via the electrolyte [2]. This is the primary method of transferring energy from an external power source to a rechargeable battery in chemical energy shown in Figure 1-1 [3]. When we connect the Lithium-ion battery to a load during discharging, the opposite happens. The load receives energy from the flow of electrons from the anode to the cathode. This time, the lithium ions travel to the cathode via the electrolyte. As a

result, the battery's ability to load is reduced [4]. When the battery is reconnected to the external power source, it begins to charge again in preparation for use shown in Figure 1-1. Their components determine Lithium-ion batteries' electrochemical performance. As a result, electrode design and materials, electrolyte conductivity, and separator properties are critical for a high-quality Lithium-ion battery [5].

The main electrochemical storage reactions

$$LiCoO_2 \underset{\text{Discharge}}{\overset{\text{Charge}}{\rightleftharpoons}} Li_{1-x}CoO_2 + xLi^+ + xe^-, (0 \le x \le 0.5)$$

at the LiCoO2 electrode can be represented by [6]

(1.1)

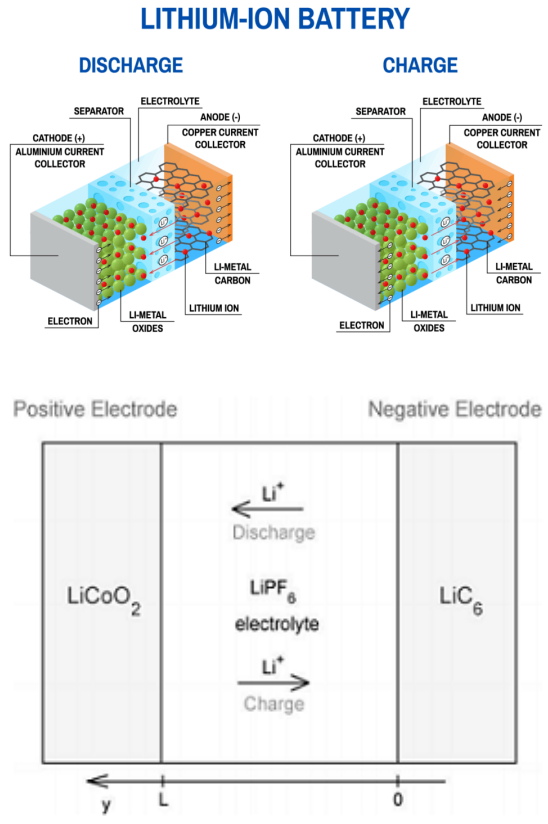

Figure 1: Basic working principle of lithium-ion (Li-ion) battery [3].

describing the extraction of Li-ions from the positive electrode during charging and the insertion of Li+ ions during discharging. The corresponding reactions at the negative, graphite, electrode can be described by [8]

$$C_6 + zLi^+ + ze^- \underset{\text{discharge}}{\overset{\text{charge}}{\rightleftharpoons}} Li_zC_6. \quad (0 \le z \le 1)$$

As a result of these electrochemical charge transfer reactions, Li-ions must cross the electrolyte under current flowing conditions shown in Figure 1-1. The electrolyte in Li-ion batteries is based on a dissociated Li-salt, e.g. $LiPF_6$ or $LiClO_4$, which cannot be considered as a well ionic-conductive medium. The ions in the electrolyte are transported both by diffusion and migration, this latter process being induced by the electric field between the electrodes across the electrolyte [7].

Methodology

Electronic devices have become an integral part of modern human existence. The use of different types of these devices, for instance, smartphones, laptops, tablets, PCs, and cameras, are rising with the change of time. An essential part of these devices is a portable power source. As a result, the demand for the portable power sources is increasing day by day. As a portable power source, rechargeable batteries are preferable due to their higher energy density, extended life, and lower cost. There are many advantages to using a Li-ion battery. The high energy density is one of the main advantages of lithium ion battery technology. In addition to this, there are many power applications from power tools to electric vehicles. Lithium ion cells are that their rate of self-discharge is much lower than that of other rechargeable cells such as Ni-Cad and NiMH forms. One major lithium ion battery advantage is that they do not require maintenance to ensure their

performance. The voltage produced by each lithium ion cell is about 3.6 volts. This has many advantages. For smartphones a single cell is all that is needed and this simplifies the power management. One advantage of lithium ion batteries is that there is no requirement for this they are supplied operational and ready to go. Thus, it is a very popular subject of research in the battery field and we have conducted a study on characteristics of lithium-ion batteries for further improvement of its performance.

Mathematical Modeling

Model set-up

In $LiCoO_2$ electrode, electrochemical reactions are mainly [9]

$$LiCoO_2 \underset{\text{Discharge}}{\overset{\text{Charge}}{\rightleftharpoons}} Li_{1-x}CoO_2 + xLi^+ + xe^-,\ (0 \le x \le 0.5)$$

(4.1)

Li-ions extraction & insertion from the electrode in time of charging & discharging are described the equation bellow[9]

$$C_6 + zLi^+ + ze^- \underset{\text{discharge}}{\overset{\text{charge}}{\rightleftharpoons}} Li_zC_6.\quad (0 \le z \le 1)$$

(4.2)

Li-ions will cross the electrolyte under current flow condition for electrochemical charge transfer reaction. Concentration of the Li+ in the electrolyte which is c_{Li+} (y, t) as well as the concentration of PF_6^- can be expressed as c_{PF6-} (y, t). The negative electrode/electrolyte and electrolyte/positive interface simultaneously y = 0; y = L. The Nernst–Planck equation can be mentioned flux for both charged species in the electrolyte, according to [9]

$$Jj = -Dj\frac{\partial cj}{\partial y} - \frac{zjF}{RT}Djcj\frac{\partial \phi}{\partial y},$$

(4.3)

where Jj(y,t) is the flux of species j ($molm^{-2}$ s^{-1}) at position y at any moment of time t, Dj is the diffusion coefficient of j (m^2 s^{-1}), ∂cj/∂y= concentration gradient ($molm^{-4}$), ∂ϕ/∂y= potential gradient (Vm^{-1}) and zj is the valence state of j with j=Li^+ or PF_6^- in the case of a dissociated $LiPF_6$ salt. Herewith it is assumed that no convection takes place in the electrolyte. Since, by definition, the electric field E(y,t) =−∂ϕ(y,t)/∂y, −E(y,t) instead of ∂ϕ/∂y will be further used in this chapter. [9]

$$\frac{\partial c_{Li^+}}{\partial t} = \frac{\partial J_{Li^+}}{\partial y},$$

(4.4)

$$c_{Li^+}(y,0) = c_0,$$

(4.5)

$$J_{Li^+}(0,t) = -\frac{I_{LiC_6}(t)}{z_{Li^+}FA},$$

(4.6)

$$J_{Li^+}(L,t) = \frac{I_{LiCoO_2}(t)}{z_{Li^+}FA},$$

(4.7)

$$\frac{\partial c_{PF_6^-}}{\partial t} = -\frac{\partial J_{PF_6^-}}{\partial y},$$

(4.8)

$$c_{PF_6^-}(y,0) = c_0,$$

(4.9)

$$J_{PF_6^-}(0,t) = 0,$$

(4.10)

$$J_{PF_6^-}(L,t) = 0,$$

(4.11)

where Eqs. (4.4) and (4.8) represent the mass balances, Eqs. (4.5) and (4.9) reflect the fact that initially at t = 0 no concentration profiles have been developed yet and hence that the concentrations across the electrolyte can be considered constant (c_0). I_{LiC6} (t) and I_{LiCoO2} (t) are currents flowing through the surfaces of the negative and positive electrodes, respectively. Eqs. (4.5), (4.6), and Eqs. (4.10), (4.11) represent the flux conditions of, respectively, at both electrode/electrolyte interfaces[9]

$$\frac{\partial c_{Li^+}}{\partial t} = D_{Li^+}\frac{\partial^2 c_{Li^+}}{\partial y^2} - D_{Li^+}\frac{F}{RT}\frac{\partial\left(c_{Li^+}E\right)}{\partial y},$$

(4.12)

$$D_{Li^+}\frac{\partial c_{Li^+}(0,t)}{\partial y} - D_{Li^+}\frac{F}{RT}c_{Li^+}(0,t)\,E(0,t) = \frac{I(t)}{FA},$$

(4.13)

$$D_{Li^+}\frac{\partial c_{Li^+}(L,t)}{\partial y} - D_{Li^+}\frac{F}{RT}c_{Li^+}(L,t)\,E(L,t) = \frac{I(t)}{FA},$$

(4.14)

$$\frac{\partial c_{PF_6^-}}{\partial t} = D_{PF_6^-}\frac{\partial^2 c_{PF_6^-}}{\partial y^2} + D_{PF_6^-}\frac{F}{RT}\frac{\partial(c_{PF_6^-}E)}{\partial y},$$

(4.15)

$$c_{PF_6^-}(y,0) = c_0,$$

(4.16)

$$D_{PF_6^-}\frac{\partial c_{PF_6^-}(0,t)}{\partial y} + D_{PF_6^-}\frac{F}{RT}c_{PF_6^-}(0,t)\,E(0,t) = 0,$$

(4.17)

$$D_{PF_6^-}\frac{\partial c_{PF_6^-}(L,t)}{\partial y} + D_{PF_6^-}\frac{F}{RT}c_{PF_6^-}(L,t)\,E(L,t) = 0,$$

(4.18)

Electro-neutrality condition

Eqs. (4.12) to (4.18) describe the development of the ionic concentrations c_{Li+} (y, t) and c_{PF6-}(y, t) but require E(y,t) to be known. In general, it is necessary to consider the Maxwell equations to determine E(y,t) and all currents (fluxes)[10]

$$c(y,t) = c_{Li^+}(y,t) = c_{PF_6^-}(y,t),$$

(4.19)

which states that the concentration of Li^+ and PF_6^- ions to be equal in each point in space and at each moment of time. Eqs. (4.12) to (4.18) can be rewritten.

$$\frac{\partial c}{\partial t} = D_{Li^+}\frac{\partial^2 c}{\partial y^2} - D_{Li^+}\frac{F}{RT}\frac{\partial(cE)}{\partial y},$$

(4.20)

$$c(y,0) = c_0,$$

(4.21)

$$D_{Li^+}\frac{\partial c(0,t)}{\partial y} - D_{Li^+}\frac{F}{RT}c(0,t)\,E(0,t) = \frac{I(t)}{FA},$$

(4.22)

$$\frac{\partial c(L,t)}{\partial y} + D_{PF_6^-}\frac{F}{RT}c(L,t)\,E(L,t) = 0,$$

(4.23)

$$\frac{\partial c}{\partial t} = \frac{2D_{Li^+}DPF_6^-}{D_{Li^+} + D_{PF_6^-}}\frac{\partial^2 c}{\partial y^2},$$

(4.24)

$$2D_{Li^+}\frac{\partial c(0,t)}{\partial y} = \frac{I(t)}{FA},$$

(4.25)

$$\frac{\partial c}{\partial t} = D\frac{\partial^2 c}{\partial y^2}, \quad (4.26)$$

$$c(y, 0) = c_0, \quad (4.27)$$

$$\frac{\partial c(0, t)}{\partial y} = \frac{I(t)}{2FAD_{Li^+}}, \quad (4.28)$$

$$\frac{\partial c(L, t)}{\partial y} = \frac{I(t)}{2FAD_{Li^+}}, \quad (4.29)$$

Results & Discussion

Lithium-ion Concentration Throughout the Electrolytic Phase During Charging and Discharging Period for Different Electrolytes:

The development of the concentration profiles has been calculated using the standard MATLAB pdepe solver and applying discretization steps. The model parameters used in this chapter are given in Table 4.1 and the Li-ion battery has a storage capacity of 720 mAh. Unless indicated, the battery charge current applied in all simulations corresponds to 1 C-rate. Constant current charging is applied during 30 min after which the current is switched off. The temperature effect is ignored to reduce complexity.

Figs. 5-1(c) to 5-18(c) show the development of the concentration profile of Li^+-ions as a function of location and time during charging and discharging. At the very first moment of time the concentration profile is completely flat, the initial concentration value is equal to 1500 mol m^{-3}. As soon as time proceeds, a concentration profile of significant magnitude starts to develop. The battery is charged for the first 30 minutes and discharged for the next 30 minutes. The concentration of Li^+ ion remains at initial value in the middle of the electrolyte from the anode and cathode throughout charging and discharging. During charging, the concentration of Li^+ ion increases as nearer to a graphite anode (LiC_6). During discharging, the concentration of Li^+ ion increases as nearer to a lithium metal oxide cathode ($LiCoO_2$). These two concentration profiles are symmetrical to each other. The concentration profiles of figs. 5-8(a), 5-10(a), 5-12(a), 5-13(a), and 5-17(a) are equal to initial concentration throughout most of the electrolyte but suddenly very high concentration near the negative electrode as time passes during charging. However, the concentrations of Li^+ of figs. 5-1(a) to 5-7(a), 5-9(a), 5-11(a), 5-14(a) to 5-16(a), and 5-18(a) increase gradually from the middle of electrolyte to the negative electrode as time passes during charging. These concentration profiles are good for the battery. Again, the concentrations of Li^+ of figs. 5-5(a), 5-6(a), 5-8(a), 5-10(a) to 5-15(a), and 5-17(a) increase gradually at the interface of electrolyte and negative electrode from initial time to the end of charging. However, the concentrations of Li^+ of figs. 5-1(a) to 5-4(a), 5-7(a), 5-9(a), 5-16(a), and 5-18(a) increase at a very high rate during few initial minutes and then gradually till the end of charging at the interface of electrolyte and negative electrode. The summary of the concentration profile is given in table 5.1.

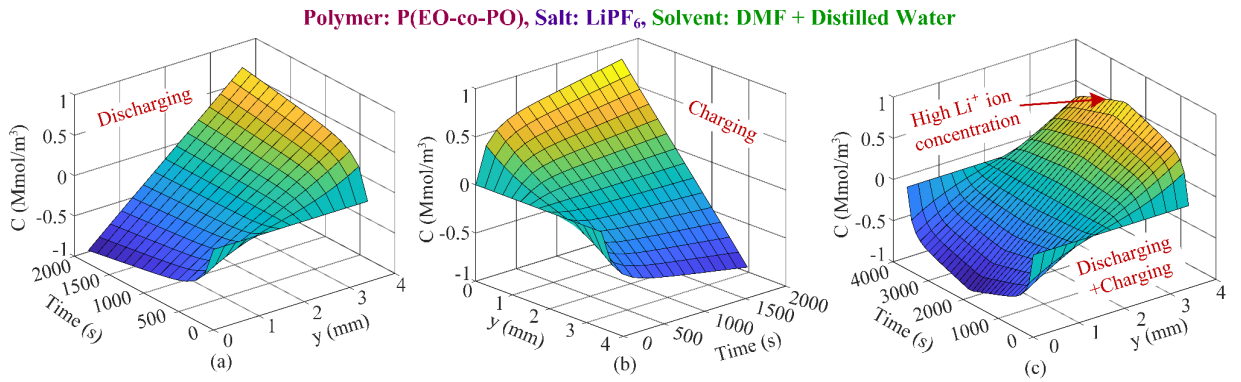

Figure 2: Lithium-ion Concentration Throughout the Electrolytic Phase During (a) Charging, (b) Discharging, and (c) Charging + Discharging Period for P(EO-co-PO) Gel Electrolyte

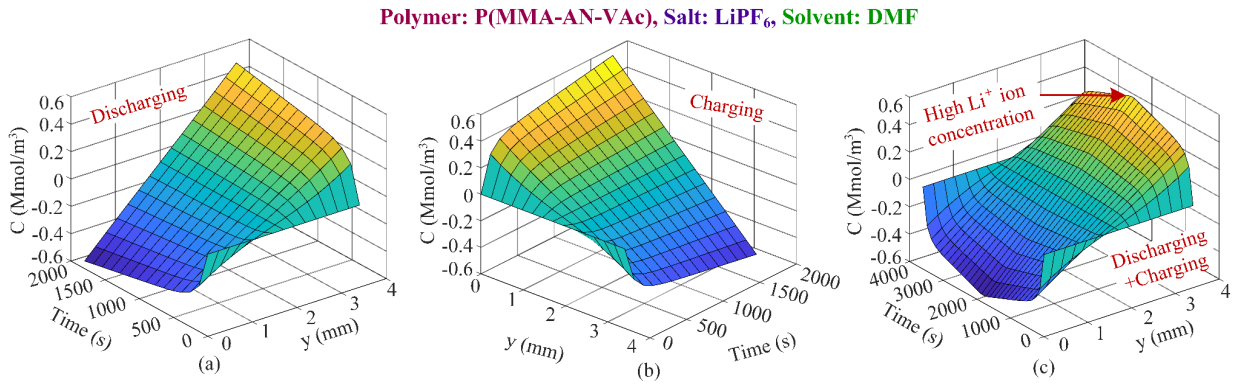

Figure 3: Lithium-ion Concentration Throughout the Electrolytic Phase During (a) Charging, (b) Discharging, and (c) Charging + Discharging Period for P(MMA-AN-VAc) Gel Electrolyte

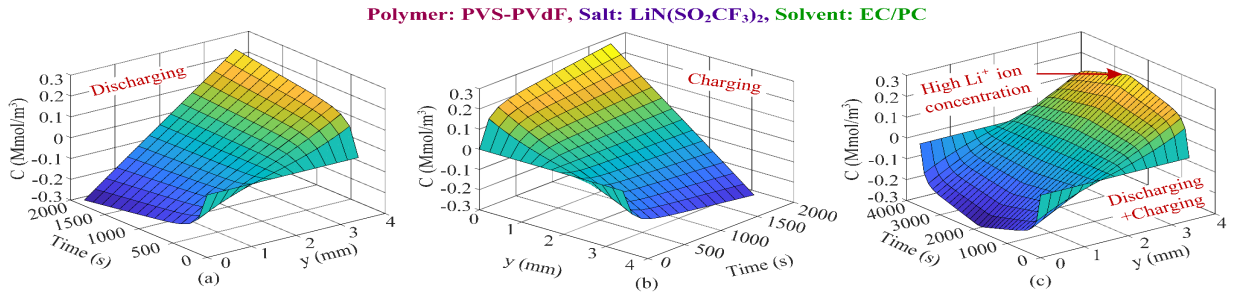

Figure 4: Lithium-ion Concentration Throughout the Electrolytic Phase During (a) Charging, (b) Discharging, and (c) Charging + Discharging Period for PVS-PVdF Gel Electrolyte

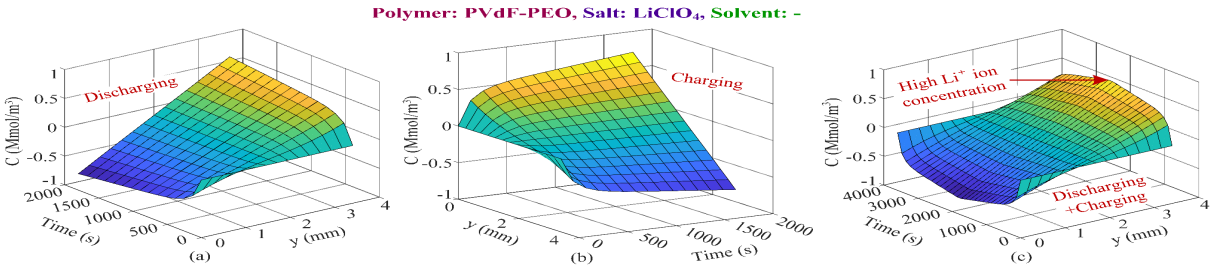

Figure 5: Lithium-ion Concentration Throughout the Electrolytic Phase During (a) Charging, (b) Discharging, and (c) Charging + Discharging Period for PVdF-PEO Gel Electrolyte

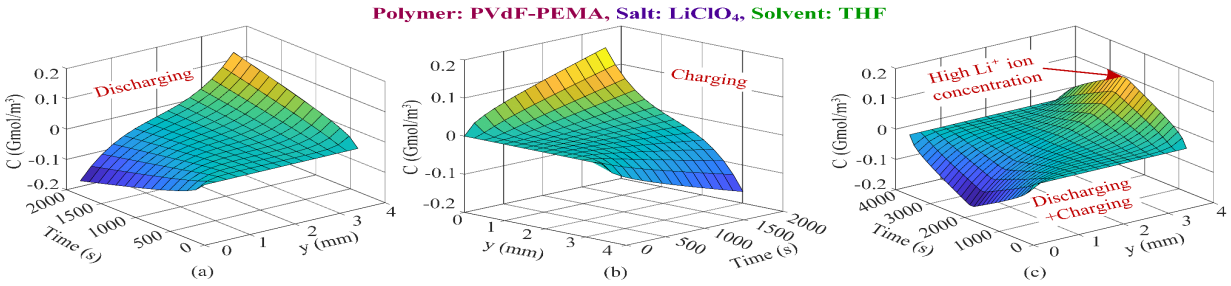

Figure 6: Lithium-ion Concentration Throughout the Electrolytic Phase During (a) Charging, (b) Discharging, and (c) Charging + Discharging Period for PVdF-PEMA Gel Electrolyte

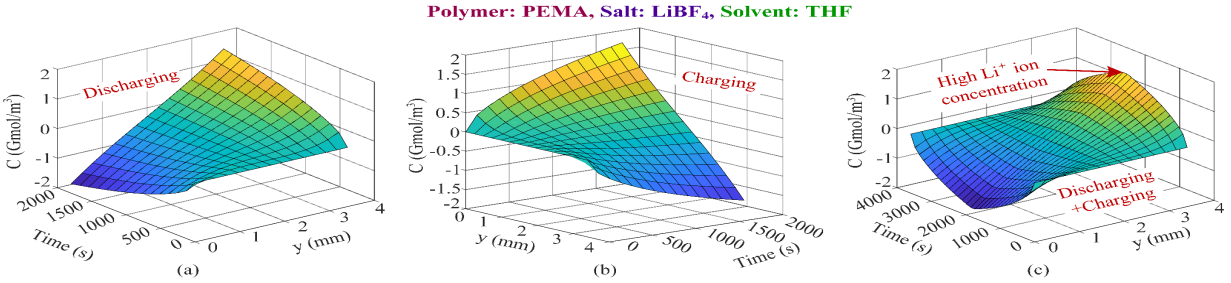

Figure 7: Lithium-ion Concentration Throughout the Electrolytic Phase During (a) Charging, (b) Discharging, and (c) Charging + Discharging Period for PEMA Gel Electrolyte

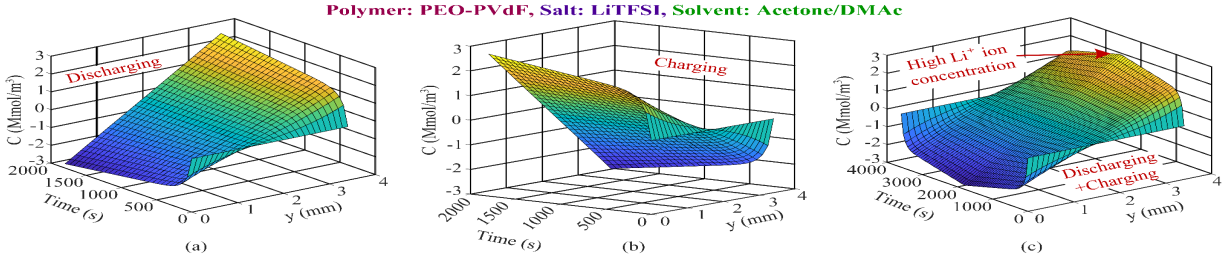

Figure 8: Lithium-ion Concentration Throughout the Electrolytic Phase During (a) Charging, (b) Discharging, and (c) Charging + Discharging Period for PEO-PVdF Liquid Electrolyte

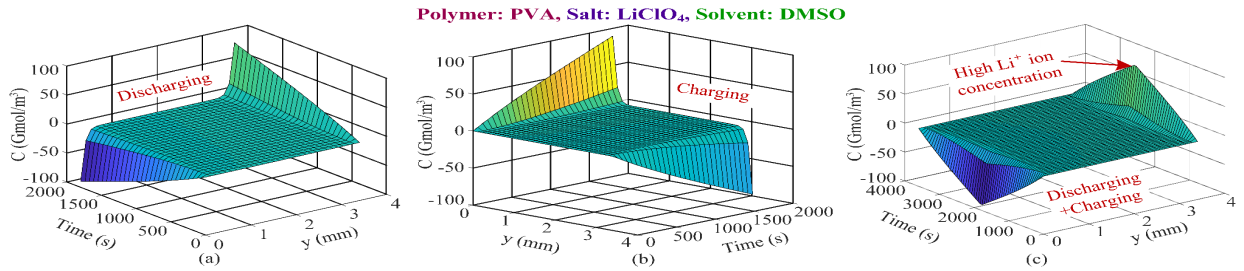

Figure 9: Lithium-ion Concentration Throughout the Electrolytic Phase During (a) Charging, (b) Discharging, and (c) Charging + Discharging Period for PVA Liquid Electrolyte

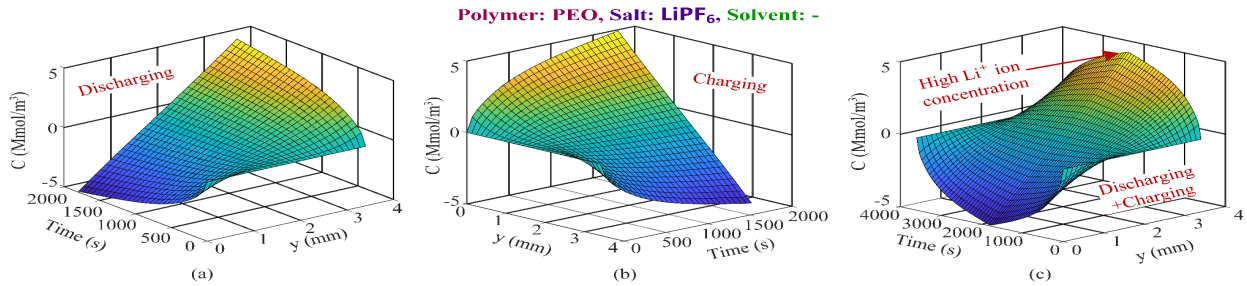

Figure 10: Lithium-ion Concentration Throughout the Electrolytic Phase During (a) Charging, (b) Discharging, and (c) Charging + Discharging Period for PEO Liquid Electrolyte

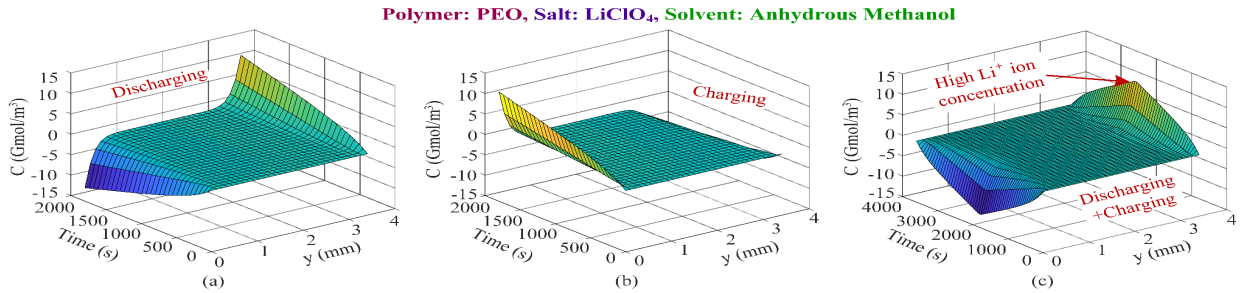

Figure 11: Lithium-ion Concentration Throughout the Electrolytic Phase During (a) Charging, (b) Discharging, and (c) Charging + Discharging Period for PEO Liquid Electrolyte

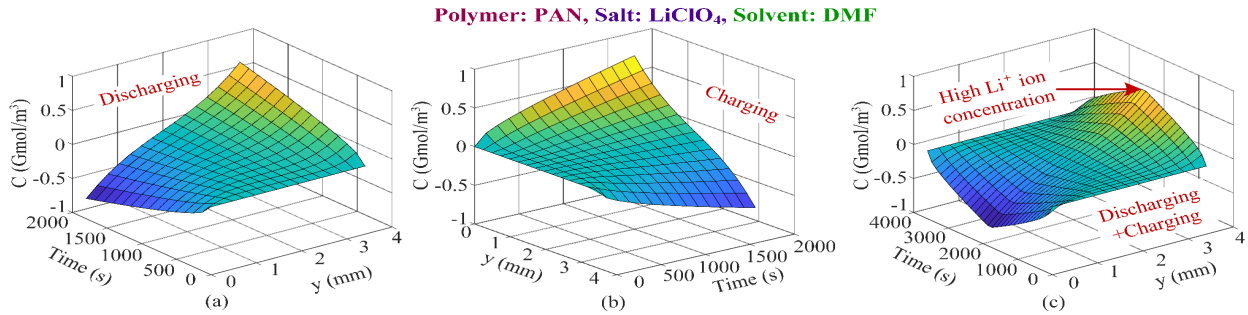

Figure 12: Lithium-ion Concentration Throughout the Electrolytic Phase During (a) Charging, (b) Discharging, and (c) Charging + Discharging Period for PAN Solid Electrolyte

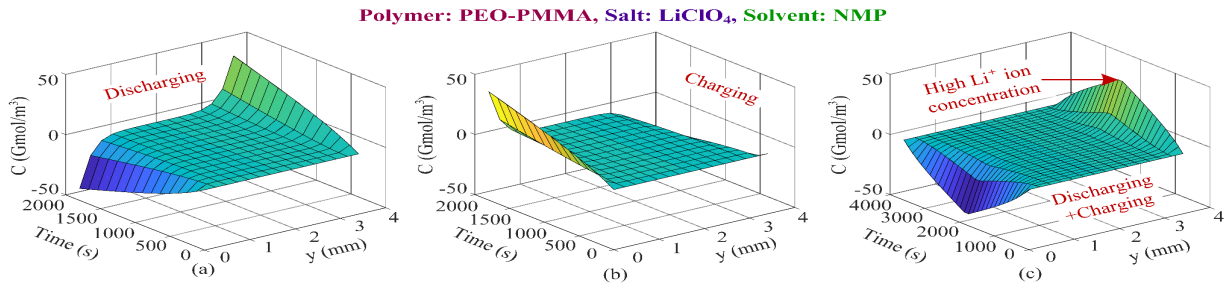

Figure 13: Lithium-ion Concentration Throughout the Electrolytic Phase During (a) Charging, (b) Discharging, and (c) Charging + Discharging Period for PEO-PMMA Solid Electrolyte

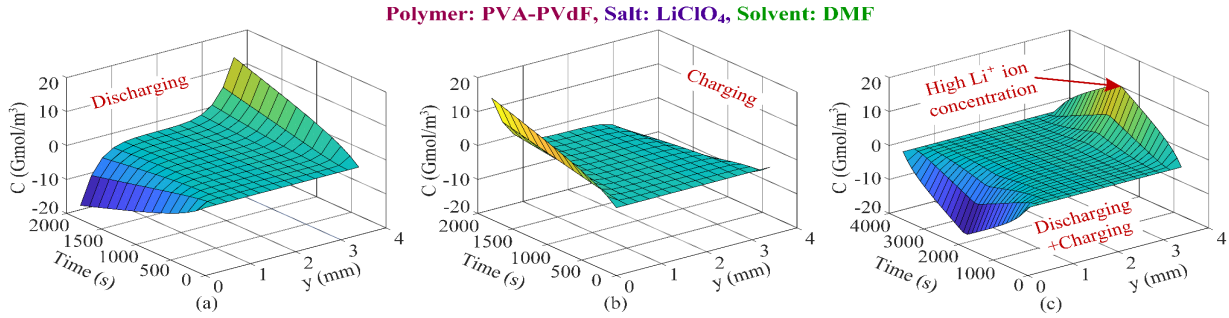

Figure 14: Lithium-ion Concentration Throughout the Electrolytic Phase During (a) Charging, (b) Discharging, and (c) Charging + Discharging Period for PVA-PVdF Solid Electrolyte

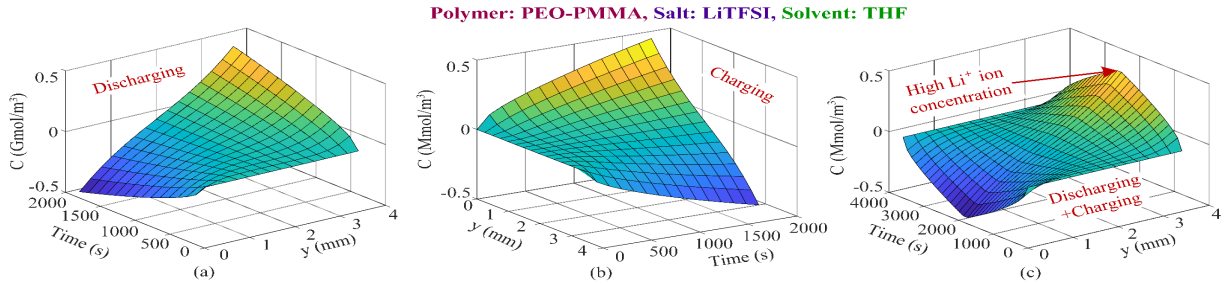

Figure 15: Lithium-ion Concentration Throughout the Electrolytic Phase During (a) Charging, (b) Discharging, and (c) Charging + Discharging Period for PEO-PMMA Solid Electrolyte

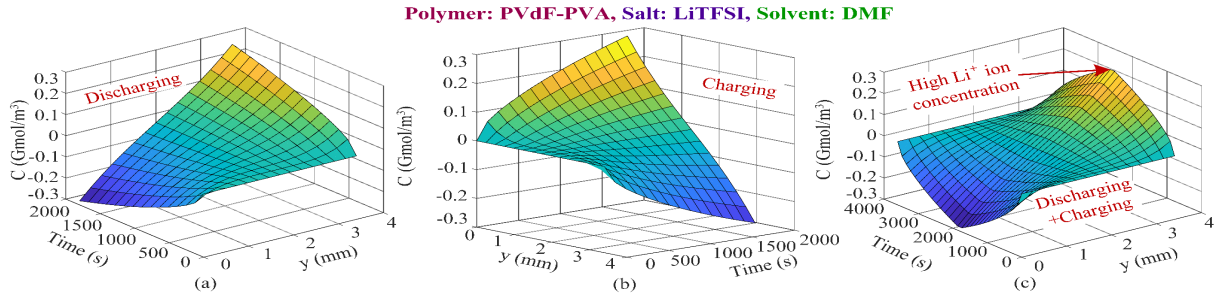

Figure 16: Lithium-ion Concentration Throughout the Electrolytic Phase During (a) Charging, (b) Discharging, and (c) Charging + Discharging Period for PVdF-PVA Solid Electrolyte

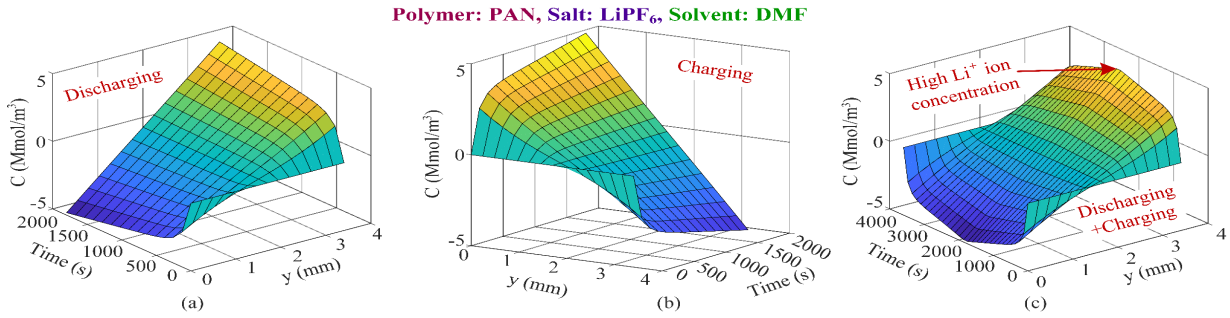

Figure 17: Lithium-ion Concentration Throughout the Electrolytic Phase During (a) Charging, (b) Discharging, and (c) Charging + Discharging Period for PAN Solid Electrolyte

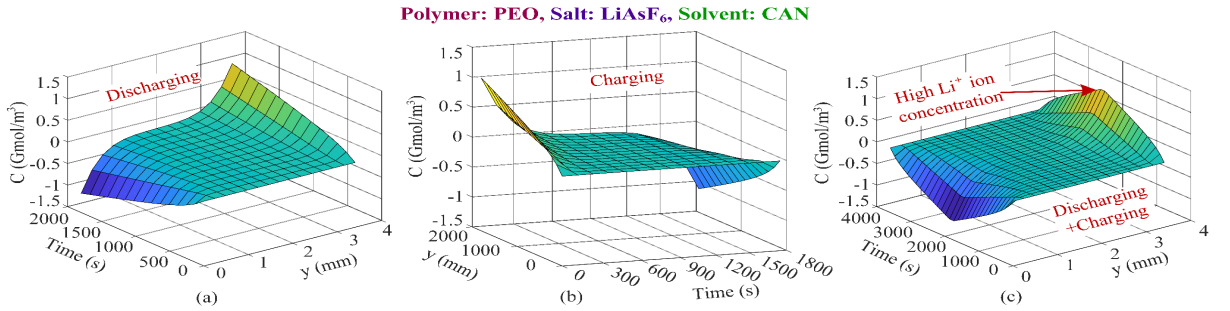

Figure 18: Lithium-ion Concentration Throughout the Electrolytic Phase During (a) Charging, (b) Discharging, and (c) Charging + Discharging Period for PEO Solid Electrolyte

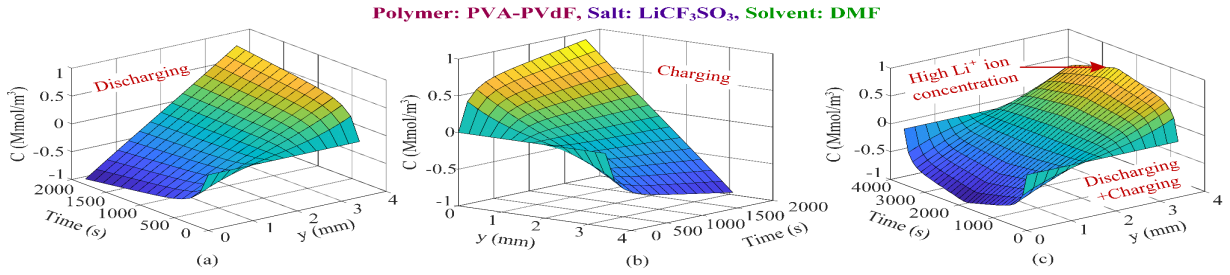

Figure 19: Lithium-ion Concentration Throughout the Electrolytic Phase During (a) Charging, (b) Discharging, and (c) Charging + Discharging Period for PVA-PVdF Solid Electrolyte

Discussion

We have shown gel, liquid and solid type electrolyte to compare Li^+ Concentration & potential density.

Table 1: Performance Summary of Different Electrolyte

No.	Phase	Polymer	Salt	Solvent	Li^+ Concentration & potential density

1	Gel	P(EO-co-PO)	$LiPF_6$	DMF + Distilled Water	Good
2		P(MMA-AN-VAc)	$LiPF_6$	DMF	Good
3		PES-PVdF	$LiN(SO_2CF_3)_2$	EC/PC	Good
4		PVdF-PEO	$LiClO_4$	-	Good
5		PVdF-PEMA	$LiClO_4$	THF	Very good
6		PEMA	$LiBF_4$	THF	Very good
7	Liquid	PVO-PVdF	LiTFSI	Acetone/DMAc	Good
8		PVA	$LiClO_4$	DMSO	Average
9		PEO	$LiPF_6$	-	Very good
10		PEO	$LiClO_4$	Anhydrous Methanol	Average
11	Solid	PAN	$LiClO_4$	DMF	Very good
12		PEO-PMMA	$LiClO_4$	NMP	Average
13		PVA-PVdF	$LiClO_4$	DMF	Average
14		PEO-PMMA	LiTFSI	THF	Very good
15		PVdF-PVA	LiTFSI	DMF	Very good
16		PAN	$LiPF_6$	DMF	Good
17		PEO	$LiAsF_6$	CAN	Average
18		PVA-PVdF	$LiCF_3SO_3$	DMF	Good

Conclusion

The performances of different electrolytes have been studied in this paper. Modeling the ionic conductivity of the electrolytic phase of the Li-ion battery, accessing some parameters of some existing Li-ion battery electrolytes, acquiring the

ionic concentration distribution performance during the charging and discharging period. From the result section it can be realized that 5, 6, 11, 14, 15 no. electrolytes show very good Li^+ Concentration & potential density according to table 1. However, 1, 2, 3, 4, 16 and 18 no. electrolytes show good results. Moreover, 8, 10, 12, 13, and 17 no. electrolytes show average results.

Future work: New materials for cathode and anode will be studied and their mathematical modelings will be synchronized with existing models described in this paper. However, the temperature effect will be added in the model.

References

[1] D. Lin, Y. Liu, Y. Cui, Nat. Nanotechnol. 2017, 12, 194.

[2] J.-H. Jiang, A.-B. Wang, W.-K. Wang, Z.-Q. Jin, L.-Z. Fan, J. Energy Chem. 2020, 46, 114.

[3] J. Liu, Z. N. Bao, Y. Cui, E. J. Dufek, J. B. Goodenough, P. Khalifah, Q. Y. Li, B. Y. Liaw, P. Liu, A. Manthiram, Y. S. Meng, V. R. Subramanian, M. F. Toney, V. V. Viswanathan, M. S. Whittingham, J. Xiao, W. Xu, J. H. Yang, X. Q. Yang, J. G. Zhang, Nat. Energy 2019, 4, 180.

[4] W. Xu, J. L. Wang, F. Ding, X. L. Chen, E. Nasybutin, Y. H. Zhang, J. G. Zhang, Energy Environ. Sci. 2014, 7, 513.

[5] P. G. Bruce, S. A. Freunberger, L. J. Hardwick, J. M. Tarascon, Nat. Mater. 2012, 11, 19.

[6] L. Chen, W. Li, L.-Z. Fan, C.-W. Nan, Q. Zhang, Adv. Funct. Mater. 2019, 29, 1901047.

[7] L. Fan, S. Wei, S. Li, Q. Li, Y. Lu, Adv. Energy Mater. 2018, 8, 1702657.

[8] L. Chen, W. Li, L.-Z. Fan, C.-W. Nan, Q. Zhang, Adv. Funct. Mater. 2019, 29, 1901047.

[9] D.A. Jones, Principles and Prevention of Corrosion, 2nd ed., Prentice Hall, 1997.

[10] V.S. Sastri, Corrosion Inhibitors, Wiley, 1998.

Paper ID:7195
International Conference on Mechanical, Manufacturing and Process Engineering (ICMMPE – 2022)
Organizer: Faculty of Mechanical Engineering, Dhaka University of Engineering & Technology (DUET), Gazipur, Bangladesh
Website: https://icmmpeduet.com/

Title: Key Factors for Automation in the Tanning Industry in Bangladesh

Sarajit Kumar Mondal[1] , S C Banik [2] , M S Rabbi [3]

[1] PhD Student, Department of Mechanical Engineering, Chittagong University of Engineering & Technology, Chattogram, Bangladesh
[2] Department of Mechanical Engineering, Chittagong University of Engineering & Technology, Chattogram, Bangladesh, baniksajal@cuet.ac.bd
[3] Department of Mechanical Engineering, Chittagong University of Engineering & Technology, Chattogram, Bangladesh, rabbi@cuet.ac.bd

E-mail: sarajitkm@gmail.com

ABSTRACT

Efficiently and effectively detecting the key factors are of great importance to the Tanning Industry that uses skins and hides as a main raw material to impose automation. This paper aims to analyse the impact, challenges and increased opportunities for leading export issues which extensively influence automation in the tanning industry in the context of Bangladesh by using a phenomenology design. Through this explorative study, experts from various categories of tanning industries are given opportunities to provide their valuable perceptions, feelings and experiences as the paramount target to the realization of automation technology revolution and to develop a coherent economic strategy in Bangladesh. A semi- structured interview method by physically and over the mobile phone/e-mail is used for data collection purpose. All the accumulated information is transformed into written text and analyzed with the use of inductive content analysis of qualitative methodology for identifying the key factors and ideas for adaption automation in tanning industries. The result clearly shows the existence of major challenges in tanneries such as: lack of top management commitment and owners' willingness, lack of monetary resources, lack of expensive installation of technology and poor infrastructure, lack of modern technical knowledge, health hazards and availability of cheaper labour. The judgment of this study will support to design an extensive fruitful measurement and world class environmental impacts of tanning industries in Bangladesh for adapting new technology.

Keywords: Tanning Industry; Automation; Phenomenology; Semi-structured interview; Inductive; Thematic.

1. INTRODUCTION

The word 'Automation' is derived from Greek words "Auto" (self) and "Matos" (moving). Automation therefore is the mechanism for systems that "move by itself". However, apart from this original sense of the word, automated systems also achieve significantly superior performance than what is possible with manual systems, in terms of power, precision and speed of operation- Prof. S Mukhopadhyay defined in his course lesson [1].

Automation is a set of technologies that results in operation of machines and systems without significant human intervention and achieves performance superior to manual operation [1].

In other words, Slava Gerovitch defined the term in his paper as: Automation is the conversion of a work process, a procedure, or equipment to automatic rather than human operation or control. Automation does not simply transfer human functions to machines, but involves a deep reorganization of the work process, during which both the human and the machine functions are redefined.

Dr. Khushal et al in [2] stated that after mechanization, automation is the second step in the future industry. Tanneries yet go after traditional old systems to handle the total industry particularly raw materials and chemicals. Today, Industrial Automation is transitioning to its 4th revolution mostly known as Industry 4.0 and is therefore major part of the megatrends of Internet of Things (IoT) and industrial internet of things (IIoT) [3].

The engineering techniques through automation could be established good working atmosphere and minimized the various losses and time consumption of tanning industries. The writer Rames et al [4] shown in his paper that improved quality control and healthy work environment in the tannery/factory could be gained through the use of Computer Aided Dosing System (CADS).

The Wikipedia defines the term Tanning as "Tanning is the process of treating skins and hides of animals to produce leather". Many manufacturing and processing industries such as apparel, steel rerolling mills and pharmaceutical industries are trying to enter into the new digital technologies and smart world. A small number of large

tanning industries are already renovated their factories with some automated and semi-automated machineries. Moreover, the availability of raw materials and the output as finished products with its exporting facilities, Bangladesh Government approved the Tanning industries as a priority sector and stepwise the leather sector stands as the second largest export sector of Bangladesh. In this respect it is necessary to find out the barriers of tanning industries in Bangladesh and look forward for a strategy to overcome the hurdles in the way of automation and semi-automation process in priority basis.

Day by day, various attractive leather goods are produced from this processed leather by applying new technology. Skins and hides having their self properties due to various biologic characteristics hold water, proteins, fat, and mineral, coloring reagents out of which proteins and fats get shifted to many products in operation. For making finished leather, raw materials are passed through a series of chemical and mechanical operations before it comes to final form. In traditional way, water and chemicals are added manually in the processing drum in most of the factory and also balance pH of the float and leather in the drum manually. But addition of appropriate quantity of treated water and chemical ingredients are essential for excellent processing of hides and skins. There are about 45 chemicals and physical operations are sequentially involved in long durations for processing raw hides and skins [4].

Jakov et al in [5] worried about traditional manner, the activities of all areas such as tannery location, cleaning management and technology, energy management and expenditure, quality assurance and development strategies, occupational safety and health at work, periodic maintenance, effluent treatment, solid waste, air emissions, financial determinative, human resources and staff welfare, corporate social responsibility (CSR) have been running. Jing Hu et al focused their circular economy (CE) model in [6] as a new way of management of materials and energy as well as how to reduce, reuse, recycle and recover of the tannery effluents with measured treatment technologies and approaches.

Irraivan et al in [7] wanted to show, automated technology is enlarging to solve barriers faced by tanning industries for raw hides and skins processing. Development of output, optimization of motion, automation and integration, and limit of solutions are the main thinking of industry now. For minimizing the manufacturing environment for challenges, networking system and software can play an important role.

A focus of attention for automation system in the tanning industries is maximizing raw material utilization and developing process approaches and production quality. The objective of this work is to identify the key factors for elaborating the way of automation technology at Tanning Industries in Bangladesh and increase potentiality. Implementing the improved automation control measurements, it would be minimizing the serious community health hazards and safety influences, losses and time consumption during the processes and operation of tanning. To achieve this goal and designing an aforementioned phenomenology, a pre-established Questionnaire is selected for sharing knowledge, feelings and experience and to collect data from the academicians/industry related scholars for analysis. Then the collected data/answers are converted into interview transcripts for analysis and finally the key factors which are the main hurdles of new technology are identified by the interviewees.

The flow chart of methodology to find the Key Factors for Automation in the Tanning Industry in Bangladesh is schematically shown in Fig 1.

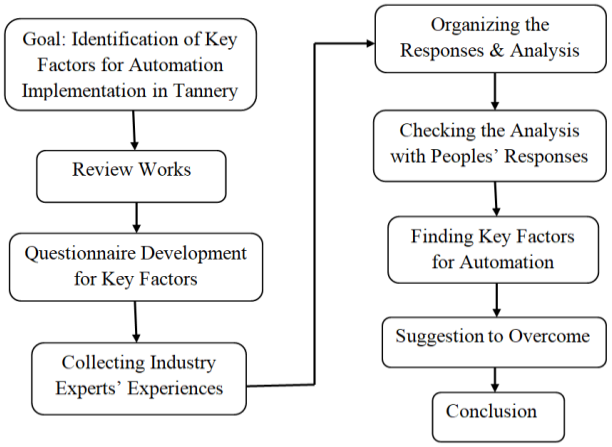

Figure 1: Flow Chart of Research Work

The remaining part of the paper has been arranged in systematic way as follows: Section "Historical Background of Tannery in Bangladesh" presents the initial movement and escalating of the tanning industry. Section "Present Status" includes a literature review of the study. Section "Export Destination" shows export position and its ubiquitous expansion. Section "Automated Equipment" indicates the modern equipment and machineries for various processes of raw hides and skins. Section "Technology" shows the envelopment of technology. Section "Government Commitment" presents the thinking about Tannery and its up-gradation. The proposed thematic methodology has been detailed in Section "Methodology". Section "Results" presents outcome of the research and judgment about the challenges. Section "Analysis and Implications" presents the exploration and action of automation transition process. Finally, Section "Conclusions and Acknowledgment" discusses the obtained results and future research suggestions.

2. HISTORICAL BACKGROUND OF TANNERY IN BANGLADESH

Earlier, the chemical and mechanical processes of raw hides and skins were completed by hand using some particular indigenous procedures. Famous businessman R. P. Saha established first a tannery at Narayanganj at times in the

1940s [8]. When the business expanded with time it was need to shift the industry at Hazaribag beside the bank of river Burigonga in Dhaka for better management. Before liberation, in 1965 the tanning sector was accumulated by 30 tanneries and after independence of Bangladesh, government transferred the 30 factories into its main revenue stream. Successful improvement of production was shown in 1970s. In 1982, the government again shifted the sector to private entrepreneurs in pursuance of its general policy of disinvestment. With the increasing of number of factory and decreasing the wastes management capacity, the initiative was taken by the government for national interest to relocate the tanneries from Hazaribagh to savar Leather Industrial Park on 200 acres of land.

3. PRESENT STATUS

United Nations Industrial Development Organization expressed that leather products are one of the most useful and necessary natural material for human and that is why leather is widely traded commodities in the world. The production of leather raw materials is increasing day by day in developing countries. In this situation, more than half of total supply of raw hides and skins are provided from the developing countries [9]. Akhi Akter et al (December 17, 2018) identified that, as a second largest export-earning industry, the leather sector of Bangladesh fulfills about 10% of the world's total demand [10].

H. L. Paul et al in [11] summarized that now a days, quality bovine and ovine, caprine (buffalo and cow; sheep and goat) leathers which have a unique reputation are exporting in outer world from Bangladesh for fine textured skins.

According to the record of 2021, there are about 220 tannery units in Bangladesh. Among them 114 units are large and medium registered and the rest of the units are mostly small and cottage type unregistered. By the judgment of potentially, about 35 tanneries have set-up modern machineries and these tanneries have the capabilities to process 60% of raw hides and skins into finished form of world class quality. Bangladesh Tanners Association conducted a survey work and identified, about 60000 workers are employed in the tanning industry. Out of 60000 workers only 200 skill educated manpower are working various factory. Overall investment in the tanning industry sector is estimated at Tk. 2.5 billion, of which government/ bank finance about Tk.1.2 billion [12]. Another mathematical record expressed approximately 200-220 million sq feet of raw hides and skins produced and about 85% of which exported.

When Md. Sadat S et al in [13] studied about troubles in tanneries; it was shown that there were some unconscious and old traditional processing caused dangerous pollution. The central effluent treatment plant (CETP) volume of 30,000 m^3 capacity is not running at full strength. That is why, sludge is now gathered in an open yard and untreated harmful water is regularly delivered into the neighboring Dhaleshwari River.

Recently, in August 2021, the Parliamentary Standing Committee on 'Ministry of Environment, Forests and Climate Change' visited the Savar Leather Industrial Park and expressed their negative feelings to bdnews24.com about non-treated liquid effluents and solid tannery wastes management activities. Respective ministry informed the committee that everyday about 40,000 m^3 wastes are produced but CETP capacity is not enough. The committee also expressed that there were no management system to treat sludges/solid wastes with highly concentrated heavy metal like chromium.

The overall picture of the most tanning industries is not satisfactory. Generally, the owners are not enough conscious about their factory residue and its proper removal like trimmed leather, pieces of flash from cow and buffalo hides, hair, liquid and solid wastes generated at different stages of production.

Figure-2: Open dumping of toxic sludge at the Tannery Industrial Estate in Savar, Bangladesh, 2020. Source: [13].

Sadat also observed there is huge number of small and medium-size factories in this sector and lack of investment issue is a common and key obligation. A common platform arranged by the Asia Foundation for conversation to discuss about tannery sectors' difficulties and how to neutralize them.

The obtained results in paper [14] identified, 'lack of technological infrastructure' is the big challenge that may obstacles the implication of Industry 4.0 whereas 'environmental side-effects' is the less among the challenges that may interrupt the application of Industry 4.0 in the Bangladeshi leather industry.

Dr Tegtmeyer (July, 2018) highlighted in his paper [15] that advance technologies exhibited by the company where tanners' would be able to generate their own self retanning chemicals premises/on-site from waste shavings. Dr Tegtmeyer also covered industry 4.0 ideas and highlighted the immediate outcomes from its ReeL project with German tannery Heller-Leder in his presentation titled; "Tannery 4.0 – an opportunity for the leather industry."

After the relocation of the tannery in Hemayetpur [16], the river Dhaleshwari seriously contaminated by discharging non-treated effluents, tannery wastes are being dumped open places, the local people and workers have to face

health related problems, the lack of proper facility of personal protective equipment for the workers. Although the tannery industry is deteriorating the very sound condition of environment and threatening the health of people, it is, fortunately, widening the employment opportunities with introducing a suitable environmental management plan.

4. EXPORT DESTINATIONS

The leading part of export earnings in Bangladesh is getting from the leather sector by sending treated raw hides & skins to China. Near about 85% of raw hides and leather products are transported in various countries in the shape of powdered/crushed form, blue wet form, finished and leather garments form. The principal portion of raw hides and finished leather are exported to the Europe, the United States, Australia, Japan, Singapore, South Korea etc. [10]. Side by side, leather sector of the country plays an important role in the national and global economy by earning mentionable foreign currency [17]. Al Mamun et al, provided in their paper that as the China is trying to change its concentration off from the footwear manufacturing sector, a new opportunity is knocking the door to regenerate and reshuffle the tradition and go for new technology [18]. Md Mizanur Rahman, treasurer of Bangladesh Tanners Association (BTA), expressed his opinion with the Dhaka Tribune (July 12th, 2020) that the US-China trade war had created a direct export opportunity for Bangladeshi leather and leather goods in the US market, but American customers did not accept source products from any non-compliant factory.

Prof. Sarwar and Md. Saifullah Khaled, expressed his educated studied [19] that Bangladesh would get better prices in the international market provided environment friendly production facilities are ensured. Due to huge cultivation/production of cows and goats in Bangladesh, hides and skins would always be available all over the year for continuous running the factory. Textile Today (August 24, 2019) analysis in [20], national economy of Bangladesh is constantly rising in last couple of years with an average 7% growth accelerating on the country's lather export sector, whereas readymade garments (RMG) export is providing about 11% to Gross Domestic Products (GDP).

So due to aforementioned trading opportunities in world market, the researcher would like to study about tanneries' challenges for transformation in digital operation.

5. AUTOMATED EQUIPMENTS

At present time, various types of integrated and sophisticated unit-wise equipment and machineries are using in modern tanning industries for fully or semi-automation and measuring systems. Such as, automatic hide measurement machine, fully or semi-automated advanced drum control system, laboratory drums controlling system, prep-tank operation system [21]. Furthermore, wireless transfer of drum measurements and controls, central pH measuring station, computer aided weighing station, precise gravimetric chemical dosing equipment, very faster and fully automated perfect volumetric liquid chemical dosing machine, economic chemical dosing machine, precise water mixing device for automatic dosing of water, PC based software for mastering data and planning, central networking system for collecting real data, visualization device for visualizing the tannery at a glance, etc. are the advanced technology to progress the technology for processing raw hides and skins to produce finished leather in a tanning industries.

6. TECHNOLOGY

Leather is unparalleled merchandise which makes relationship among grassroots countryside, modern communities and conventional exercises with flourishing new processing. Many developing countries in the world, the tanners form necessary reputable body for trading and managing foreign income. The leather sector of Bangladesh is a potential industrial zone for raw hides, skins, footwear exports. Through installing the above mentioned automated or semi-automated equipments in the tannery, the following mechanical operations and chemical processes can be done safely, efficiently and healthfully and ultimately the Tanners overcome negatively impact profitability. The processes are hair-save liming, carbon dioxide de-liming, ex-lime splitting, high exhaustion chrome tanning with full chrome preparation activities, vegetable extracts and syntans retanning, optimum exhaustion of dyes and fat liquors, beam house for segregation, chrome bearing and general streams, biodegradable surfactants and allowable biocides, most effective mechanical dewatering and drying system, principally water based finishing [5].

7. GOVERNMENT COMMITMENTS

The Finance Minister of Bangladesh Government stated in his budget speech that the leather and leather goods sector provides employment directly to 6 lakh people and indirectly to another 3 lakh people, and that the sector is one of the principal sources of export earnings. To gain productive capacity of the sector and enhance its exports, a 'guideline for development of leather and leather goods products 2019' has been framed. Further, an export guideline for the leather sector is in the process of formulation. Again, steps are being taken to facilitate the greater value chain integration of Bangladesh into the regional and global markets in the leather goods and footwear sector.

Ministry of industries and Bangladesh small and cottage industries corporation (BSCIC) are trying to solve problems and constant monitoring for smooth running the CETP. The body already has taken action to activate fully the effluent

treatment plant, with a special concentration on the chrome recuperation cell [14].

Saving workers' lives and then monetary benefit should be the slogan of every industry. For solving and developing the chronic situation, the Government is determined to introduce advance technology in tanneries which gives the absolute advantage to implement sustainable practice in a world standard suitable environment. So, the tannery owners' willingness and the commitment of top management are unavoidable for initiating new technology to exceed the poisonous effects level below the admissible threshold.

8. METHODOLOGY

This analysis of tanning industries in Bangladesh has been focused on through the phenomenology formation and automation is considered here as a phenomenon. As an explorative study, a questionnaire is designed for data/answer collection from decision makers, academics and lather industrialists. The questionnaire is developed based on the criteria/challenges that are the main hurdles for automation. The convenience feelings/answer accumulation system is conducted in the related tanning industry region. Experts and specialists from different tanning industries were invited to provide their valuable views to the realization of automation of tanning Industry. A semi-structured interview method by physically and over the mobile phone/e-mail is used for data collection purpose. Then qualitative research followed the accurate method to analyze the collected non-numeric data. Through the questionnaire, the research endeavored to focus on the various interesting aspects of the data set which has been created on the basis of themes such as strengths, weaknesses, opportunities, and threats of tanning industries. Analysis has been carried out on the basis of transcripts from all the participants and the main factors/ themes have been determined from the identifications of the interviews for adopting automation. The collected data from 60 academics and industrialists have been transformed in text and analyzed by using inductive content analysis for identifying research goal. All the responders agreed about the analysis and shown positive response towards the degree of automation escalating in tanning industries for minimizing severe health hazard, establishing top management commitment as well as increasing the profitability.

9. RESULTS

The experts' opinions accelerated the opportunity to use of advanced processing, production and operation techniques with smart digital technologies which embedded within organizations and the exportable tanning industries in Bangladesh. But it is very clear that the existence of automation and its level of implementation depend on development of infrastructure to meet the requirements for transition to smart tanning factory in Bangladesh. So, this research has tried to obtain insights regarding practical barriers to go automation or semi-automation for Tanning Industry in Bangladesh. The experts' judgments/identification and from aforementioned review papers, it is rigorously accumulated the following challenges for transition to Automation of Tanning Industries.

The common effluent treatment plant (CETP) at Savar is partly ready for use and contaminating the neighboring river as well as lands. The workers of the factories are not outside from this unhealthy environment.

The study includes key factors as major barriers of tanning industries such as: lack of monetary resources, lack of expensive installation of technology and poor infrastructure, health hazards, availability of cheaper labour, shortfall of la technical knowing, and lack of top management commitment and owners' willingness. Specially, small and medium-category factories are suffering with these obstacles. Academicians feel, proper monitoring should be planned and completed by accredited surveyors with the help of international guidelines, technical and investment assurance can change the traditional business policy.

The local and dependent obstacles for barriers are river water and land pollution, raw hides and skins procurement management problem, expensive imported chemicals, workers personal safety and privacy, transporting, harmful chemical handling, poor treatment facilities, job loss thinking etc.

According to the relative importance, the experts' given linguistic emphasis on key factors are converted into crisp numeric weights and these weightage have been shared some valuable themes. The key factors for automation of tanning industries on the basis of inductive content analysis are as shown in Figure 3.

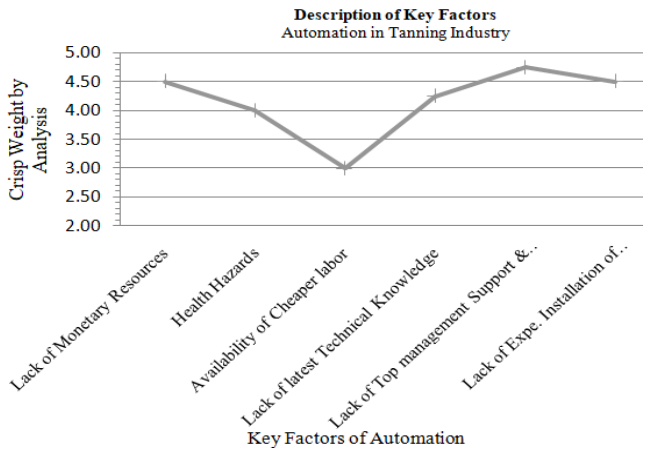

Figure 3: Prioritization Chart of Key Factors/Challenges for Automation in Tanning Industry.

The interviewee experts pointed their sincere opinions about 'lack of latest technical knowledge'. According to one factory manager, *"Lack of sufficient knowledge to*

implement automation revolution is also an important factor. Adoption of automation we need to have basic knowledge and skilled manpower, which we are lacking. Initially if we go for automation we need to bring skilled manpower and experts from other developed countries." It is also supported by two executive level Engineers and added that *"It is needed more awareness of our industrialists."* Another Engineer agreed these views and added in his comment *"No time to wait for implementation of automation. RMG is the biggest sector, try first in this sector, then we go for leather, steel, hospital etc."* Maximum academics and factory experts are assured about the factor 'Lack of Government Support & Owners' Willingness'. They believed, "*Top management, owners' and Tannery experts are the main body to make decision whether the tannery go for new technology at present or hereafter."*

Poor infrastructure has been focused from experts. One production manager quoted that *"Poor infrastructure is also an obstacle for the implementation of automation. Huge investment is required to change this traditional infrastructure. Bangladesh does not have that capacity to change this instantly."* Some experts also boosted that comment. But other participant opined *"No, most of our factory are well constructed and compliance."*

About availability of cheaper labour, one design engineer wanted to say *"No, automation is an upgraded method where people should trained accordingly."* One of the Factory Managers noted his perceptions "*Cheap labor is also an important negative factor for automation, especially in the wake of imposing of minimum wages 2018. Now it is very difficult for the employer to achieve the target. Our productivity is very poor in compare to other neighboring countries like Thailand, Srilanka, Vietnam etc. Therefore, we need to improve our productivity to compete in this global market."*

One of the participants, Ex GM of a factory, mentioned that *"Certainly the automation will decrease the employment opportunity in tanning sector. We may go for this automation step by step thinking alternative employment opportunity for the retrenched employees."*

The participants provided opinions from their expertise about the installation of technologies to gain opportunity for automation, which is very expensive. They also given same judgments in the case of production environment i.e. health hazards, availability of cheaper labour and lack of raw hides & skins procurement management.

10. ANALYSIS AND IMPLICATIONS

The informants participated in the inductive content analysis are consented to establish modern technology in Bangladesh tanning/leather sector without any delay by overcoming the prescribed challenges. Nowadays, the large and medium companies are going to equipped automated machineries for specific work with information and communication technology(ICT) and network communication, energy saving and reduced water consumption. However, it would not be difficult for the country to invite interested investors by providing them with necessary expenditures; the industry must achieve a future trend of foreign currency collector after Readymade Garments [18]. There are various lagging factor to go for automation in Tanning Industry in Bangladesh. It shows that the sector is not maintaining the process control, good quality of products and remarkable growth. At that situation, the researcher likes to advise the top management to aggregate thinking of automation facilities to accelerate its present economic revolution, to overcome the health hazard work environment and meet with international standards.

11. CONCLUSIONS

Because of raw hides and various costly chemicals are the input materials of tanning industries, this type of factory is called big funds and input intensive factory. In future, there is no alternative new materials which will challenge the natural material leather and whereas sufficient amount quality raw materials (hides and skins) are available all over the year in Bangladesh. There is a big opportunity for Tanners to achieve these facilities by developing the factories with modern technology to rise up the country economy.

Fig. 3 shows, the study has analyzed and highlighted six recoverable (variable) key development challenges due to automation such as '*lack of top management commitment & owners' willingness', is the most lacking factor for barriers.* The second critical barriers are '*lack of financial support', and* '*lack of expensive installation of technology and poor infrastructure', The third remarkable key factor is 'lack of latest technical knowledge' , and gradually the others 'health hazard' and 'availability of cheaper labour'.* The main risk factors are the most meaningful challenged for the implementation of automation in Tanneries. The removal of these main barriers by adapting automation would give good result to minimize the obstacles of local risk factors and workers' welfare related problems. 'Lack of financial support' is a huge financial involvement in automation process, raw materials, manpower and for establishing updated and improved infrastructure and modern machineries. Top management support can also help to reduce financial problem. Technical knowledge of tannery manpower would be improved through technical workshops, training programs and conferences. In addition, honorariums would give good result for this.

Moreover, it's a time factor for the nation to get the huge advantages from automation when the Government is trying to boost this industry to reach its full potential and environmental friendly. The study points out that the establishment of mechanical, chemical and management settings with the elements of Tannery Automation reduces unit production cost and health hazards. The management

of new technology also provides alternative forms of employment and environmental friendly.

Further, pollution free standard production is not always depend on tannery owners' willingness and constant government's intervention but significantly it will assure by the adaption of automated or semi-automated equipments.

ACKNOWLEDGMENT

Bangladeshi economy would be benefited from automated tanning industries if the studies must be conducted in order to identify which factories/tanneries have the most potential. These factories should be given more priority, when shifting to Automation or Semi-automation. Accordingly the transformative and deployment costs of Automation can be mitigated early on. This proposal is also a good way of determining which activities are more suitable for automation, and which tanneries those are not now.

In addition, if the government, stakeholders', political leaders, banks, industry experts from home & abroad, academics, researchers, environmental specialists, lawyers, other related institutes are agreed to design a comprehensive assessment and committed to meet up production environment challenges, then a possibility can be raised for creating awareness about tanning automation. And its continuation, it is easier to select two or three tanning industries (priority basis) for shifting/new-building automation as Model Factory. Continuous learning/instruction and iterating through model factory will uncover the knowledge of new technology to the workforces and the Savar lather industrial park will bring Bangladesh gradually to a new dimension in international market for quality leather and leather products.

REFERENCES

[1] Prof. S. Mukhopadhyay, Prof. S. Sen "Introduction to Industrial Automation and Control" Module 1 Introduction Version 2 EE IIT, Kharagpur; [Online].
Available: https://nptel.ac.in/courses/108105063/pdf/L-01(SM)(IA&C)%20((EE)NPTEL).pdf

[2] Dr. Khushal M Kapadiya, Jyoti Gohel (January 2016), "Some Basic Theory and Practical Application of Unit Operation", Publisher: Lambert Academic Publishing, ISBN: 978-3-659-86615-9

[3] "Sensors for Industrial Automation" [Online].
Available: https://www.elastisense.com/displacement-sensor-applications/industrial-automation/

[4] Rames C Panda and P G Rao; "Chemical Engineering Applications on Unit Operations of Tanning Industry–Case Studies." International Journal of Chemical Engineering and Applications, Vol. 2, No. 2, April 2011

[5] United Nations, Industrial Development Organization, *"Benchmarking in the Tanning Industry"* Jakov BULJAN, Ivan KRÁL 2012,

[6] Jing Hu et al, (January-February 2011*), " Ecological utilization of leather tannery waste with circular economy model"*, Journal of Cleaning Production, Volume 19, Issues 2-3, January-February 2011, Pages 221-228

[7] Irraivan Elamvazuthi et al, "Automation of Nesting and Cutting Processes of Leather Furniture Production: A Case Study" International Journal of Mechanical & Mechatronics Engineering IJMME-IJENS Vol: 09 No:10

[8] From Wikipedia, 'Leather industry in Bangladesh', [Online]. Available: https://en.wikipedia.org/wiki/ Leather industry in Bangladesh #cite note-11

[9] United Nations Industrial Development Organization, Vienna, 2012 "Future Trends in the World Leather and Leather Products Industry and Trade;"

[10] Akhi Akter & Mir Abdullah Al Mahfuz (December 17, 2018), "An overview of Bangladesh leather industry." https://www.textiletoday.com.bd/overview, Bangladesh leather industry/December 17, 2018

[11] H. L. Paul, A. P. M. Antunes, A. D. Covington, P. Evans and P. S. Phillips "Bangladeshi Leather Industry: An Overview of Recent Sustainable Developments", January 2013, Researchgate, Journal- Society of Leather Technologists and Chemists 97(1):25-32

[12] **"**Banglapedia - the National Encyclopaedia of Bangladesh, an intellectual output.", Jun 18, 2021, [Online].
Available: http://en.banglapedia.org/index.php? title Main Page

[13] Md. Sadat S. Shibli and Md. Taherul Islam (May 27, 2020) "In Bangladesh, Tanneries in Trouble.", The Asia Foundation. [Online]. Available: https://asiafoundation.org/

[14] Md. Abdul Moktadir et al (April 2018), "Assessing challenges for implementing Industry 4.0: Implications for process safety and environmental protection", Process Safety and Environmental Protection; Volume 117, July 2018, Pages 730-741

[15] International Leather Maker (ILM), "Tannery 4.0 – an opportunity for the leather industry" China, Published: 17 July, 2018; [Online].
Available:https://internationalleathermaker.com/news/fullstory.php/aid/5728/Tannery_4.0__96_an_opportunity_for_the_leather_industry_.html

[16] Meghna, A.J. et al., (21 May, 2020), "Qualitative Assessment of Environmental and Health Aspects of Relocated Tannery Industries at Hemayetpur, Bangladesh", Bangladesh Journal of Environmental Research, 11, 1-11.

[17] United Nations Industrial Development Organisation, Vienna, (2010) "Future trends in the world leather and leather products industry & trade."

[18] Al Mamun et al, (August, 2016), "Leather Industry of Bangladesh: A new hope for export diversification." Research Department:

[19] Prof. Sarwar Md. Saifullah Khaled, Professor of Economics, "Problems and prospects of Bangladesh leather industry" 24 October, 2015 12:00 AM, https:www.daily-sun.com/home/printnews/85599

[20] Textile Today Analysis; (August 24, 2019), "Leather industry: Let the golden goose lay for economic development."; https://www.textiletoday.com.bd/government-must-step-forward-to-protect-leather-industry/

[21] "Solutions for the Leather Industry," [Online].
Available: *https://www.incotec.world/tanware/*

Conflicts of Interest: The author declares no Conflicts of Interest.

Paper ID: 7228

International Conference on Mechanical, Manufacturing and Process Engineering (ICMMPE – 2022)

Organizer: Faculty of Mechanical Engineering, Dhaka University of Engineering & Technology (DUET), Gazipur, Bangladesh

Website: https://icmmpeduet.com/

Performance Comparison Between Flat Fin Mini Channel Heat Exchanger and Wire on Tube Heat Exchanger

Mohammad Harun-Or-Rashid

Department of Mechanical and Production Engineering, Ahsanullah University of Science and Technology, Dhaka 1208, Bangladesh

E-mail: *harun_edu@yahoo.com, harun.mpe@aust.edu*

ABSTRACT

Numerical simulation of wire on tube heat exchanger and flat tube plain fin micro channel heat exchangers are discussed in this paper. In the present study, mass of the working fluid as well as the volume of the plain fin micro channel heat exchanger were estimated. These data were compared with the data of the wire on tube heat exchanger. It was found that, at same thermal performance, micro channel heat exchanger occupies less space and requires less working fluid than conventional wire on tube heat exchanger. Therefore, it was recommended to use micro channel heat exchanger for the thermal management of the refrigerator, cold storage and power plant.

Keywords: Micro channel, Plain fin, Wire on tube, Heat exchanger design optimization.

1. INTRODUCTION

Condenser is used to transfer thermal energy.It plays an important role in cold storage and power plant refrigeration system and many other thermal management processes. Flow through the micro-channel is considered as microscale, because hydraulic diameter of each channel is less than 1mm. Selection process of the serpentine micro channel condenser is discussed in this paper. Only few experimental works have been done on micro channel heat exchanger (MCHEX). Hrnjak et al. [1] presented experimental result of charge minimization of air-cooled micro channel condenser. Liang et al. [2] used R 290 refrigerant during examining of serpentine micro channel condenser and proposed port by port method for numerical simulation. Bandhauer [3] suggested a correlation for forecasting heat transfer coefficient (HTC) in micro channel ($0.000506 < D_h < 0.001524$). In this research, it was found that, there is lack of work on comparative study of plain finned micro channel heat exchanger and wire on tube heat exchanger (WTHEX). Hence, the main objective of this research was to prepare numerical programs for the wire on tube and plain fin MCHEX; validate program and compare performance of two different types of heat exchanger.

Here, two different plain fin MCHEXs are suggested since volume is reduced. For simulation, R-134a is considered as working fluid because it is used in WTHEX.

2. CODE DEVELOPMENT PROCESS

During numerical code development of heat exchanger, a segment by segment approach was used where each tube was divided into several segments. Energy equations were resolved for every segment independently. Heat transfer and refrigerant property estimation process is shown in Fig. 1. Thermodynamic properties of refrigerant and air at the entrance and geometry of the heat exchanger (HEX) are the input parameters. Assumptions of this research are: tube wall fouling is negligible, air flow is uniform, pressure drop in bends are negligible.

In steady state situation, heat transfer from the working fluid to the walls is identical to the heat transfer from the working fluid to the atmosphere. For wire on tube HEX, Gnielinski [4] correlation was used to calculate HTC of haze and liquid section. HTC of two phase section was estimated by Cavallili and Zecchin correlation because it correlates data of working fluid quite well. For single phase vapor section of plain fin MCHEX Gnielinski correlation was applied. Since, flow of refrigerant in sub-cooled liquid region was laminar, therefore, constant Nusselt number, 2.49 (channel type: triangular) was chosen for this region. Conversely, Dobson correlation [5] was used to find out the HTC of two phase flow.

In this study, pressure drop because of friction and momentum change were considered. Refrigerant side pressure drop was estimated by Eq. (1).

$$\Delta P_{wf} = \Delta P_f + \Delta P_m \quad (1)$$

Here, ΔP_m and ΔP_f are momentum and frictional pressure drop respectively. In single phase vapor and liquid section Churchill [6] single phase friction factor model was applied. Friedel [7] correlation was used for both cases of

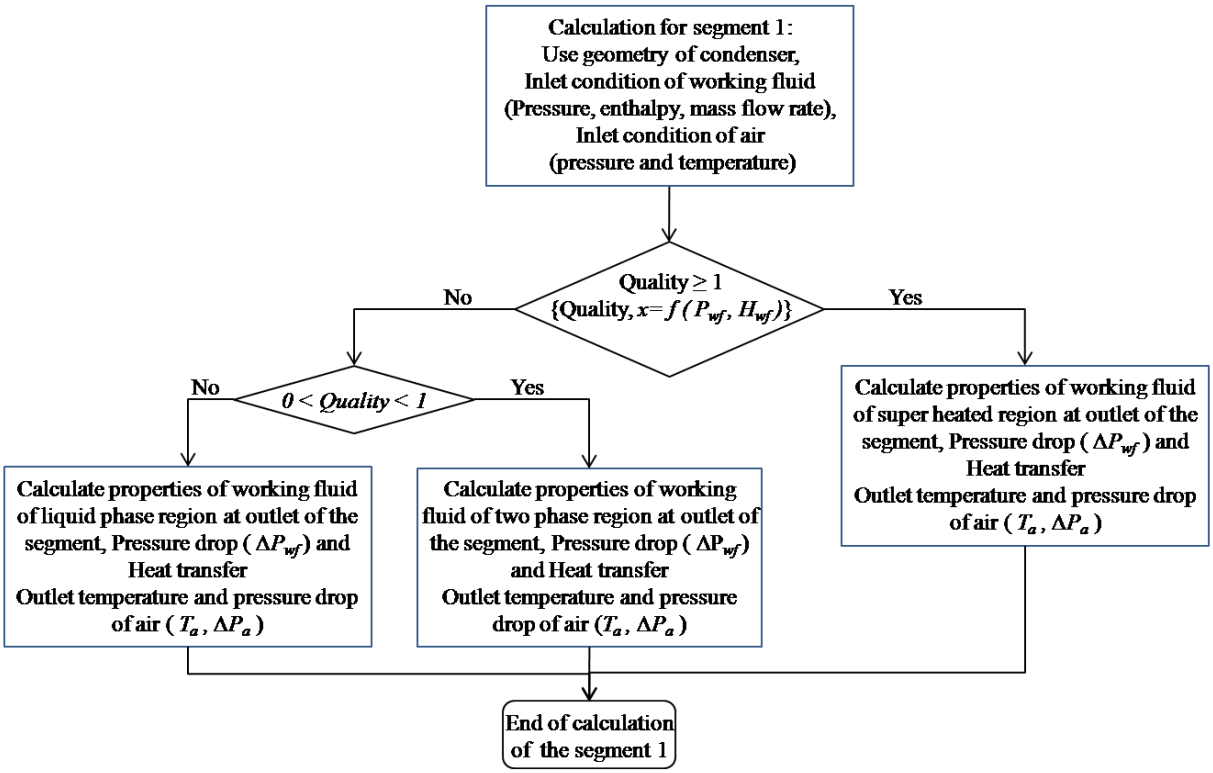

Fig. 1: Flow chart for estimating refrigerant properties at outlet of a segment

WTHEX and MCHEX.

To estimate air side heat transfer coefficient of plain fin flat tube micro channel HEX, rectangular channel methodology was used. In this case, it was assumed that air passes through rectangular channels. For plain fin MCHEX, *f*-factor was calculated by the correlation of Kays and London (1984). Considering air flow through heat exchanger, WTHEX can be classified as tube cross, all cross and wire cross. In case of tube cross, air passes through the tubes and along the wires. In all cross case, air passes through both the tubes and the wires. In case of wire cross, air passes through the wires and along the tubes. In this study, all cross case is considered as it is most commonly used. Air side HTC and *f*-factor of wire on tube HEX was calculated by the correlation of Lee et al. [8] and Kim et al. [9] respectively.

Table 1: experimental setup of WTHEX

Parameter (unit-mm)	coil 1	coil 2
Inner diameter	3.28	3.28
Outer diameter	4.9	4.9
Tube spacing	55.4	40.9
Wire diameter	1.5	1.5
Wire spacing	6.5	7.5
Number of wire	100	114
Number of tube	13	22
Tube length	487	531
Tube material	Stainless steel	

Table 2: Inlet parameters of WTHEX

Heat Exchanger Type	Pressure (Kpa)	Temperature (^{0}C)	Working fluid flow rate (kg/s)	Air Temperature (^{0}C)	Air flow rate (kg/s)
WTHEX	950	55	0.000972	25	0.02

3. VALIDATION OF THE CODE

Estimated data of simulation of WTHEX was compared with the experimental data of Ameen et al [10]. Inlet pressure and temperature of working fluid were 1300 kpa and 60 ^{0}C respectively. Geometrical data of wire on tube HEX is given in Table 1. Estimated data of four different conditions are contrasted with experimental data of four tests and presented in Figure 2. Prediction of sub-cooled temperature of working fluid shows good agreement against the experimental data.

In the present study, it was found that, simulation data of wire on tube heat exchanger shows good agreement with the experimental data. Therefore, we used same methodology for the numerical simulation of micro channel heat exchanger. In this case, wire fin and tube of wire on tube HEX were replaced by plain fin and micro channel, respectively.

Total working fluid charge in WTHEX and

MCHEX was also estimated in this research. In two phase section void fraction model of Ali et al [11] was applied and in single phase section, density of working fluid was multiplied with segment volume to compute charge.

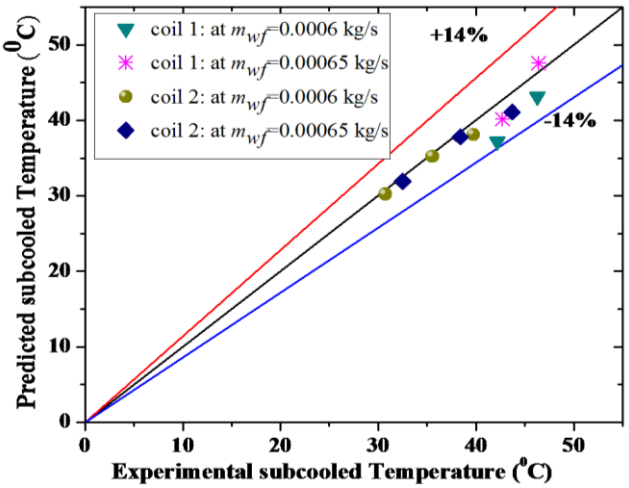

Fig. 2: Comparison of sub cooled temperature

Table 3: Design parameters for optimization study (case 1)

Parameter	Description	Value
Fixed	Diameter (m)	0.0007
	Length (m)	0.15
	Tube row	1
Change	Tube column	$8 \leq N_{column} \leq 12$
	Fin per inch	$11 \leq P_f \leq 15$
	Tube pitch (m)	$0.0268 \leq P_t \leq 0.0171$
	Number of channel	$18 \leq N_{channel} \leq 22$
Objective functions	Front area ratio	R_1=1
	Volume ratio	$R_2 \leq 1$
Constrains	Working fluid side pressure drop	$\Delta P_{wf} \leq$12.32 kPa
	Air side pressure drop	$\Delta P_a \leq 8$ Pa
	Heat transfer	Q $\geq$ 185.2 W

4. WIRE ON TUBE HEX (Reference model)

Figure 3 shows a wire on tube HEX which is currently using in refrigeration systems. This heat exchanger has nine columns, twelve rows. Tube inner and outer diameters are 0.0032m and 0.00475m respectively. Horizontal and vertical spacing of tube are 0.0140m and 0.0235m respectively. On the other hand, wire diameter, wire spacing and volume of HEX are 0.0015m, 0.006m and 0.00457 m^3 respectively. Inlet parameters of the WTHEX

Fig. 3: The reference wire on tube HEX

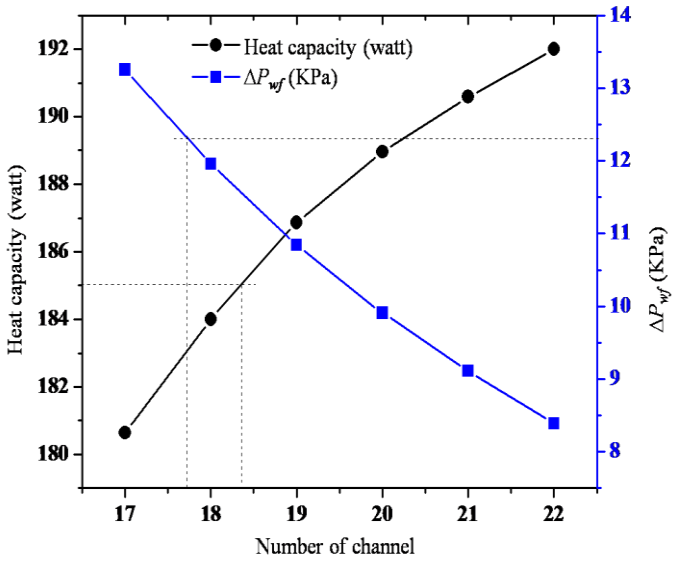

Fig. 4: Influence of number of channel on heat capacity and pressure drop

are given in Table 2. Simulation results: heat capacity, charge of working fluid (R-134a), pressure drop in air side and working fluid side of this heat exchanger is 185.2 Watt, 0.0676 Kg, 8.0 Pa and 12.322 kPa respectively.

5. PLAIN FIN MICRO CHANNEL HEX OPTIMIZATION

In the present study, best possible values of the design parameters of plain fin MCHEX are estimated. Inlet condition of WTHEX was considered for optimization

study. Two cases were taken into account. Case study 1: anterior area of both heat exchangers (WTHEX, MCHEX) was same; Case study 2: anterior area of the plain fin MCHEX was varied.

6. CASE STUDY 1

Among different geometrical parameters, fin pitch is one of the most dominant factors of the MCHEX. It has influence on heat transfer rate. Hence, fin pitch was changed. In case 1, it was guessed that tube length of MCHEX and WTHEX is same. Tube pitch was changed to maintain same frontal area. Objective functions and constrains of optimization are presented in Table 3.

Fig. 4 shows the influence of channel on heat capacity. Here, doted lines indicate constrain values. If number of channel increases then heat capacity increases and pressure drop of working fluid side decreases. Fig. 5 shows the influence of FPI on heat capacity and air side pressure drop. From figure it is clear that, FPI should be 18 or more to accomplish objective functions and assure constrains.

Fig. 6 shows that if number of tube column increases then heat capacity as well as pressure drop in working fluid side both increase. If number of tube column increases then air side pressure drop also increases. In case of 8 columns, gratify three constrains.

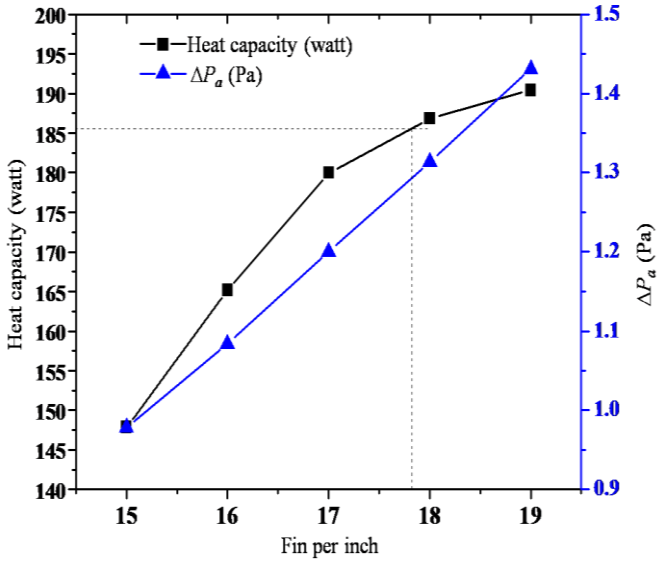

Fig. 5: Influence of FPI

Here, three main parameters (FPI, column, channel) were changed (5 steps). By using Taguchi method 25 arrangements were selected from 125. Finally, simulation was performed in 25 ways. The contour map of volume of micro channel HEX is presented in Fig. 7. The values which are gratify three constrains are presented in this figure. This figure illustrates the influence of FPI and

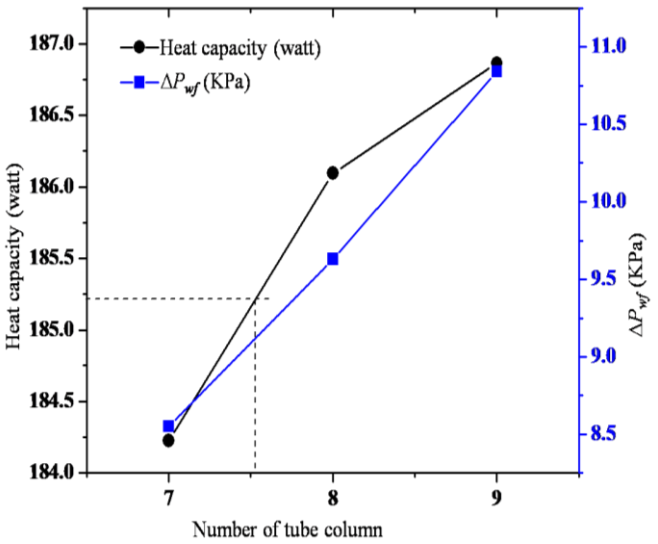

Fig. 6: Influence of number of tube column on pressure drop and heat capacity

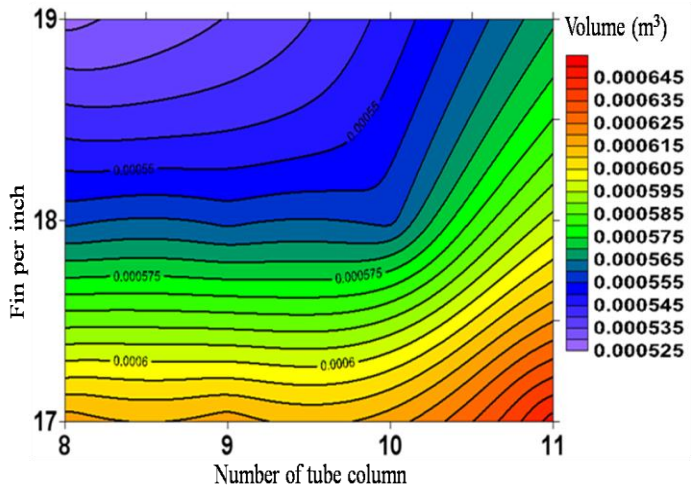

Fig. 7: Contour map of micro channel HEX (case 1)

tube column on the volume of heat exchanger. From the figure, minimum volume which fulfills objective functions is selected. Here, for 8 columns and 19 fins per inch, volume of plain finned micro channel heat exchanger becomes minimum.

Finally, for fin per inches 19, channel 18 and column 8 volume of the plain fin MCHEX becomes 0.000529 m^3. On the other hand, volume of the reference WTHEX is 0.00457 m^3. Hence, , these are the optimum values and in this case heat transfer, pressure fall in working fluid and air side is 187.73 W, 9.78 kPa and 1.32 Pa respectively.

7. CASE STUDY 2

By using MCHEX with less frontal area than

Table 4: Design parameters for optimization study (Case 2)

Parameters	Description	Value
Fixed	Channel hydraulic diameter(m)	0.0007
	Fin per inch	22
	Tube columns	9
	Tube Row	1
Change	Tube pitch(m)	$0.014 \leq P_t \leq 0.0235$
	Each tube length (m)	$0.090 \leq L_t \leq 0.15$
	Number of channels	$18 \leq N_{channel} \leq 22$
Objective functions	Front area ratio	$R_1 < 1$
	Volume ratio	$R_2 < 1$

WTHEX, it is possible to reduce the volume. Therefore, in case study 2, purposes were to reduce the frontal area and the volume of the HEX. In this case, number of fin per inch increases so that more heat is released to the atmosphere. During numerical simulation, two design variables (tube pitch and length) were varied by 12% to change the frontal area. Number of channel was also varied. Constrains were same as case 1. The design variables are shown in Table 4.

In this study, it was found that, for number of channel 20, frontal area 0.0205 m^2 (tube length 0.132 m, HEX height 0.1556m), pitch 0.0182 m; volume of HEX turns into 0.000406 m^3 and fulfill objective functions as well as constrains (Fig. 8). Hence, these are the optimum values of the proposed plain finned micro channel HEX. In this case, heat capacity, working fluid as well as air side pressure fall becomes 186.7 watt, 8.88 Kpa and 3.66 Pa correspondingly.

8. RESULTS AND DISCUSSION

Figure 9 shows that, working fluid charge in WTHEX is more than the plain fin micro channel heat exchanger. Since, the internal volume of the MCHEX is less than that of WTHEX; therefore, charge is less. Air flow length of plain fin MCHEX was 0.0178 m. Fig. 10 shows that volume of wire on tube heat exchanger is more than micro channel heat exchanger.

Comparison of frontal area of different heat exchanger is presented in Fig. 11. Fontal area of the plain fin MCHEX is less than the frontal area of the WTHEX.

From numerical simulation it was found that, in case 2, volume of plain finned micro channel heat exchanger is 0.000406 m^3. Therefore, volume decreases by 91.1%. On the other hand, charge of working in plain finned micro channel HEX is only 0.0061 kg which is lower than the charge of WTHEX.

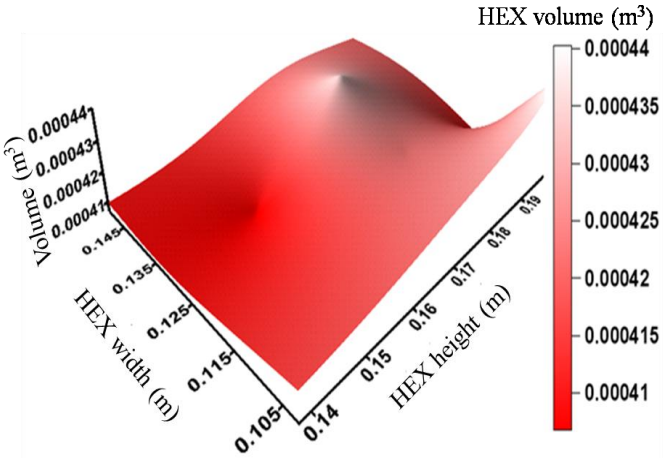

Fig. 8: 3D surface map of width, height and volume of micro channel HEX (case 2)

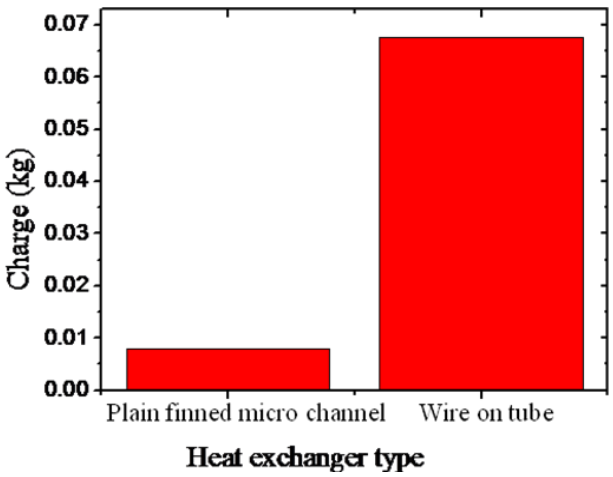

Fig. 9: Working fluid charge in different heat exchangers (case 1)

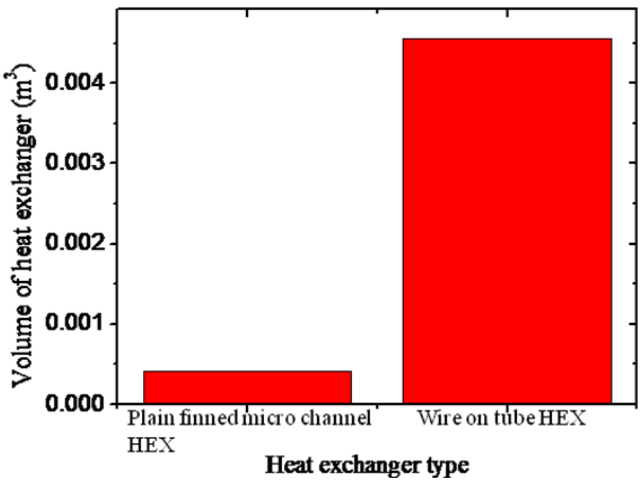

Fig. 10: Volume of different heat exchanger (case 1)

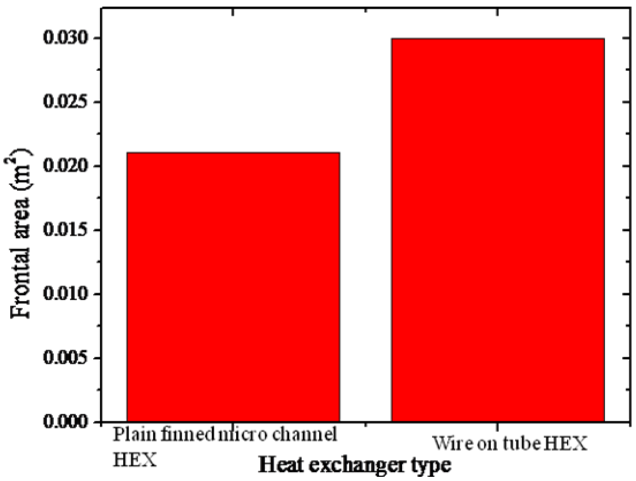

Fig. 11: Frontal area of different heat exchangers (Case 2)

9. CONCLUSION

This paper explains the numerical simulation of the wire on tube heat exchanger and the plain fin micro channel heat exchanger; validation of the predicted data of wire on tube heat exchanger against experimental data. Finally, two plain fin micro channel heat exchangers were proposed. Volume as well as working fluid charge of plain fin MCHEX were less than the volume and charge of WTHEX, respectively. Hence, it is suggested to use plain fin micro channel heat exchanger for thermal management of power plant and cold storage as well.

ACKNOWLEDGMENT

Thanks Ahsanullah University of Science and Technology (AUST), Tejgaon insdustrial area, Dhaka 1208, Bangladesh.

REFERENCES

[1] P.S. Hrnjak, Andy D. Litch (2008) Micro channel heat exchangers for charge minimization in air cooled ammonia condensers and chillers. Int. J. Refrigeration, 31: 658-668.

[2] Liang-Liang shao, Liang Yang, Chun-Lu Zhang, Bo Gu (2009) Numerical modeling of serpentine micro channel condensers. Int. J. Refrig. 32: 1162-1172.

[3] Todd M. Bandhauer, Akhil Agarwal, Srinivas Garimella (2006) Measurement and Modeling of Condensation Heat Transfer Coefficients in Circular Micro channels. J. Heat Transfer 128: 1050.

[4] Sadik Kakac, Hongtan Liu (1997) Heat exchangers selection, rating and thermal design. CRC press, New York.

[5] Reinhard Radermacher, Yunho Hwang (2005) Vapor Compression Heat Pumps with Refrigerant Mixtures. CRC Press, Boca Raton.

[6] T.S. Zhao, Q.C. Bi (2001) Pressure drop characteristics of gas-liquid two phase flow in vertical miniature triangular channels. Int. J. Heat Mass Transfer, 44: 2523-2534.

[7] John R. Thome (2010) Engineering Data Book III. Wolverine Tube, Inc.

[8] Tae-Hee Lee, Jeom-Yun, Jang-Seok Lee, Jong-Jin Park, Kwan-Soo Lee (2001) Determination of airside heat transfer coefficient on wire on tube type heat exchanger. Int. J. Heat Mass Transfer. 44: 1767-1776.

[9] P.Verma, C.W. Bullard and P.S. Hrnjak (2002) Design tool for display case heat exchanger frosting and defrosting, ACRC Technical Report 201, University of Illinois, Urbana.

[10] Ahmadul Ameen, S.A. Mollik, Khizir Mahmud, G.A. Quadir, K.N. Seetharamu (2006) Numerical analysis and experimental investigation into the performance of a wire on tube condenser of a retrofitted refrigerator. Int. J. Refrigeration, 29: 495-504.

[11] Robert Andrew Schwentker (2005) Advances to a computer model used in the simulation and optimization of heat exchangers. M.Sc. thesis, University of Maryland, College park.

[12] R.K Shah, Dusan P. Sekulic (2003) Fundamentals of Heat Exchanger Design. John Wiley & Sons, Inc., Hoboken, New Jersey.

[13] Shigeru Koyama, Ken Kuwahara, Kouichi Nakashita, Ken Yamamoto (2003) An experimental study on condensation of refrigerant R-134a in a multi-port extruded tube. Int. J. Refrig. 24: 425-432.

[14] S. Lee, I. Muddawar (2016) Thermal and thermodynamic performance, and pressure oscillations of refrigeration loop employing large micro-channel evaporators. Int. J. Heat and Mass Transfer 103: 1313-1326.

[15] Dong-Keun Yang, Kwan-Soo Lee, Simon Song (2006) Fin spacing optimization of a fin- tube heat exchanger under frosting conditions. Int. J. Heat Mass Transfer, 49: 2619-2625.

[16] Incropera, De Witt, Bergman, Lavine (2007) Introduction to heat transfer. 5th ed., John Wiley & Sons (Asia).

[17] NIST, Thermodynamic and Transport properties of refrigerants and refrigerant mixtures, REFPROP V 7.0.

[18] Man-Hoe Kim, Clark W. Bullard (2002) Air side thermal hydraulic performances of multi- louvered fin aluminum heat exchangers. Int. J. Refrig. 25: 390-400.

[19] K. M. Traeger and P.S. Hrnjak (2005) Charge minimization of Micro channel heat exchangers, ACRC Technical Report 251, University of Illinois, Urbana.

Paper ID: 7278

International Conference on Mechanical, Manufacturing and Process Engineering (ICMMPE – 2022)

Organizer: Faculty of Mechanical Engineering, Dhaka University of Engineering & Technology (DUET), Gazipur, Bangladesh

Website: https://icmmpeduet.com/

Fatigue Failure Analysis of Elevator Rope Under Vibration

Md Faiaz Al Islam[1], Sheikh Navid Shadab Jamil[2], Rafsan Ahmed[3], Md. Tanvir Siraj[4], Asif Kabir[5], and Md. Akibul Islam[6]

[1,2,3,5]Department of Mechanical Engineering, BUET, Dhaka-1000, Bangladesh
[4]Department of Industrial and Production Engineering, BUET, Dhaka-1000, Bangladesh
[6]Department of Mechanical Engineering, DUET, Gazipur, Bangladesh

E-mail: faiazalislam@gmail.com[1]

ABSTRACT

Fatigue failure analysis investigates material and/or component failure to determine the root cause using cyclic load performance under real-world conditions. There are seven steps to performing a successful fatigue analysis: Determine the load type when creating the study, define fatigue data, add events, fatigue research features, and result options, execute the analysis, and then post-process the results. This study depicts the fatigue life of an elevator rope i.e., some bends to failure have been calculated for a specific tensile load and number of ropes. A theoretical evaluation of the natural frequency of elevator ropes due to tension has been conducted. Considering the stretched length of the ropes under loading the natural frequency has been calculated. The natural frequency has also been computed for several ropes and several modes of vibration. The stress that develops in the rope due to its bending on the sheave and the stress that develops while bending due to different modes of vibration has been figured out as well.

Keywords: Natural frequency; tension; tensile stress; rope; elevator; mode of vibration

1. INTRODUCTION

Fatigue failure occurs when cracks form and propagate as a result of repetitive or cyclic loading, even if the cyclic load is much lower than the load that would cause the material to yield. This study is focused on the fatigue failure of a passenger elevator rope that is generally under cyclic loading under variable loads. The bending of the rope on a sheave pulley results in an indefinite lifetime of the elevator rope depending on the amount of load, the diameter of the sheave, and rope specifications. In this study natural frequencies of the elevator rope under tension have been calculated.

The variables are the length of the rope at different floors, 1 to 20 modes of vibration, and 1 to 8 number of hoisting ropes. The elevator rope under tension is assumed to be a flexible string.

The rope develops tensile stress in the stretched areas under bending. This bending also occurs due to its different modes of vibrations. For a maximum lateral deflection of 10% of its length due to bending of the rope in different modes of vibration, the developed tensile stress has been calculated. Here the variables are the length of the rope on different floors and 1 to 20 modes of vibrations.

Loading on the elevator rope consists of an elevator car, counterweight, self-weight of the rope, and passengers in the elevator cabin all their weight combined. Extra weight is added to them when accelerating against gravity.

In this study, the passenger elevator system (elevator cabin and counterweight) weighs 480 kg and elevates a load of 1050 kg (maximum 14 persons weighing 75kg each) from the ground floor to the fifth floor of elevation of 24 m, and the car hanging at lengths of elevator rope 4m, 8m, 12m, 16m, 20m, and 24m at fifth, fourth, third, second, first and ground floor respectively.

The highest acceleration of the elevator is 1.5 m/s^2. The elevator is supported by 6x19 IPS ropes of 13 mm diameter and 540 mm sheave diameter.

The ratio of allowable fatigue tension to tension in the rope for an indefinite life is assumed to be $\frac{F_f}{F_{td}}$ =1.3.

Fig. 1: Sheave and rope of the elevator

Elevator wire rope emerged from the ropes used by the forestry industry to transport trees straight to a staging area in the nineteenth century. (Most wire rope producers were located near the rivers that were used to transport the chopped timber, which was advantageous for loggers.) The most widely used ropes were 6x19 ropes, which were made up of six strands and 19 wires. This type of rope was abrasion-resistant but not extremely flexible.

Later, as the trees were being pulled through the woods, pulleys and sheaves were utilized to change the direction of the ropes. Because of the increased bending underweight, the 6x19 rope failed more quickly than when it was used to move logs in a straight line. The 6x19 design was enhanced by adding smaller wires to fill in the gaps between the larger diameter wires. These "filler wires" brought the total number of wires to 25. The abrasion resistance of these 6x25 ropes was more than compensated for by their fatigue resistance.

The specific objectives of this study are to calculate the natural frequencies of an elevator rope under different conditions to calculate the stress that develops in a rope due to bending. To calculate for a different number of ropes how fatigue life i.e., the number of bends to failure is affected.

2. LITERATURE REVIEW

Coleman et al. [1] analyzed the number of bending cycles to failure with a varying diameter of the sheave pulley. He compared theoretical and experimental results of elongation of rope under variable loading and variable sheave diameters. He found that the bending stress in a wire rope is much smaller than had originally been assumed. The proper size of a sheave for a fixed size of a rope is to be calculated more for wear than for bending stress.

Sung Ho Kim et al. [2] evaluated the rope's fracture strength and fracture characteristics by applying repeated bending fatigue to wire rope with diameters of 8 mm and 10 mm using 8×S (19) +SS, class Z material (as is typically used in elevators). When bending fatigue accumulates, the remaining wire receives the full load at the same time. Therefore, the fracture strength rapidly decreases.

Blodgett et al. [3] address the problem of elevator compensation rope vibration in tall buildings. An analysis is made of the vibrations of a hanging rope, whose weight per unit length is not negligible, excited by an oscillation at the upper end and having a weight suspended from the lower end.

Watanabe et al. [4] explain that the estimation of the rope lateral vibration is one of the key issues to produce a compact size of the elevator shaft. In this paper, the transient behavior of the elevator rope vibration is estimated, while the elevator car moves and the rope length changes gradually.

Kaczmarczyk et al. [5] study that the inertial and elastic characteristics of hoist ropes depend on the rope construction. Despite recent improvements in material design and the introduction of new technologies, traditional hoist steel wire ropes as well as hoist ropes constructed of aramid fibers suffer from excessive vibration.

Kimura et al. [6] researched that elevator rope for high-rise buildings is excited forcibly by the displacements of the building induced by wind forces. The exact solution of forced vibration of a rope with time-varying length is presented, on the assumption that the rope tension and the moving velocity are constant, and the damping coefficient of the rope is zero.

An elevator rope for a high-rise building is excited forcibly by the displacement of the building caused by wind forces and earthquakes. In this paper, experiments on free vibration and forced vibration of rope are presented by Kimura et al. [7] for obtaining the natural frequency and the damping coefficient of rope. And experiments of forced vibration of rope whose length varies with time due to the up-and-down movement of the cage are presented.

Phil Andrew et al. [8] recognized transient vibrations at certain locations within an elevator hoistway. He analyzed lateral and longitudinal natural frequencies for variable rope lengths at different floor positions of the elevator car. Also, the coincidence between rope natural frequency and sheave pulley vibration that may lead to resonance was discussed in his work.

In recent years, the lifting distance of elevators to be installed in a building got longer due to high-rise buildings, thus elevator rope is longer. Therefore, the natural period of the elevator rope increases and gets closer to the natural period of buildings. This present study studied by Shimura et al. [9] aimed at the construction of the elevator ropes analysis model, which can be applied to any elevator. In this report, we investigate the behavior of elevator ropes with each tension and linear density.

Dawid Bruski [10] researched the bending properties of 3 × 7 19-mm wire rope used in road safety equipment. His most important discoveries and findings are the responses of non-pre stretched and pre-stretched wire ropes are similar and one moment-curvature relation is assumed for both pre-stretched and non-pre stretched ropes, in the analyzed range of curvatures, the wire rope worked in the elastic range.

Jacket structures composed of welded tubular space frames supported by a lateral bracing system were studied by Mia et al. [11]. Structural steel is used to make tubular members. Their principal function in an offshore structure is to withstand yield and buckling loads. They can also withstand lateral loads. The XT tubular model was examined under various load conditions, and the associated stress, strain, and deformation results were tabulated. The findings revealed that when the joint thickness grows, the maximum stress, strain, and deformation values decrease.

A method to suppress the transverse vibration of elevator rope using vertical vibration of counterweight is proposed by Hirose et al. [12]. Experiments involving forced vibration of a rope whose length is constant are performed. In the experiments, a guide bar is used to suppress the rotation motion of the rope. The optimal natural frequency of vertical vibration of counterweight is about 2 times the natural frequency of the rope lateral vibration.

3. MATHEMATICAL MODELLING

In this study, the passenger elevator system supported by 6x19 IPS ropes was considered. To find the natural frequency following steps needed to be followed.

Here, Hoisting rope cross section diameter, d = 13 mm, and Sheave diameter, D = 540 mm.

From Shigley's Mechanical Engineering Design [13] Table 17–27, rope weight/length $= 0.03618d^2$

$$\text{Rope mass/length, } \mu = \frac{0.03618d^2}{9.81} = 0.6233 \text{ kg/m}$$

For n number of hoisting ropes, Total mass,

$$m_t = m_{(\text{elevator \& counterweight})} + m_{\text{load}} + m_{\text{rope}}$$
$$= 480 + (14 \times 75) + (24 \times \mu \times n)$$

$\therefore$ Total mass, $m_t = 480 + 1050 + 24\mu n$

The highest acceleration of the elevator, a = 1.5 m/s^2

$$\text{Dynamic tension per rope, } F_{td} = \frac{m_t(a+g)}{n} \quad (1)$$

For elevator, L_0(ground) = 24m, L_0(first) = 20m, L_0(second) = 16m, L_0(third) = 12m, L_0(fourth) = 8m, and L_0(fifth) = 4m.

$$\text{Loaded string length [14], } L = L_0 + l = L_0 + \frac{F_{td}\, L_0}{E_r A} \quad (2)$$

Where A = Circular cross-sectional area for hoisting rope diameter (d) $= 1.32 \times 10^{-4}$ m^2 and Young's modulus for the wire rope, E_r = 83GPa. [13]

$$\text{Natural frequency, } f_n = \frac{N}{2L}\sqrt{\frac{F_{td}}{\mu}} \quad (3)$$

Where N is the mode of vibration,

After finding the natural frequency, life cycle and tensile stress developed in the outer wires of the rope due to bending on the sheave need to be calculated.

From Shigley's Mechanical Engineering Design [13],

$$\therefore F_f = \frac{P}{S_u} S_u\, (0.5)Dd$$

$$\Rightarrow \frac{1000P}{S_u} = \frac{2000F_f}{S_u\, Dd} \quad (4)$$

At first, the value of the right side of the above equation needs to be calculated. Then using the graph from figure 2, the life cycle will be found.

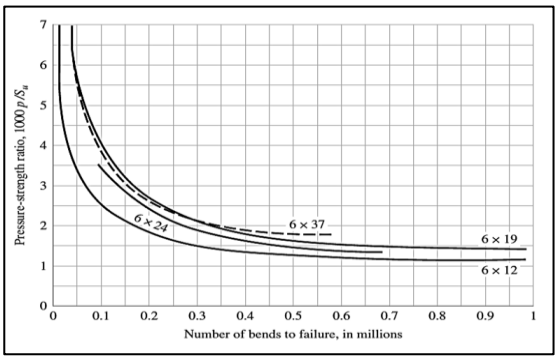

Fig. 2: Experimentally determined relation between the fatigue life of wire rope & the sheave pressure [13]

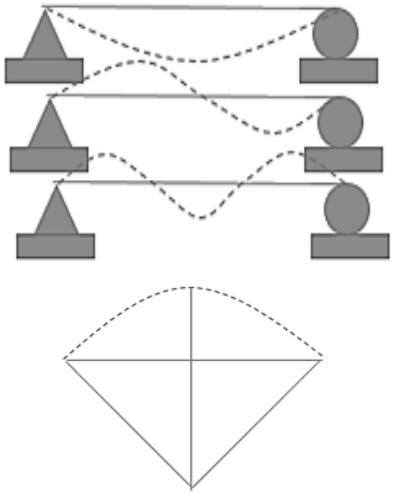

Fig. 3: Radius of curvature in a different mode of vibration

In equation 4, Allowable fatigue tension per rope, $F_f = 1.3F_{td}$ for indefinite life and the ultimate strength for improved plow steel, S_u = 1655 MPa. [13]

From Shigley's Mechanical Engineering Design [13], tensile stress developed in the outer wires of the rope due to bending on the sheave is

$$\sigma_{\text{sheave}} = \frac{0.067E_r d}{D} = 133.876 \text{ MPa}$$

$$\text{From Figure 3, } \rho^2 = \left(\frac{L'}{2}\right)^2 + (\rho - y)^2 \quad (5)$$

Here ρ is called the radius of curvature.

For, maximum deflection y = 0.1L′ and Nth mode of vibration, $L' = \frac{L}{N}$

$$\text{So, from equation no 5, } \rho = \frac{1.3L}{N}$$

From Strength of materials [15],

$$\sigma_{\text{rope}} = \frac{E_r\, c}{\rho} = \frac{E_r\left(\frac{d}{2}\right)}{\left(\frac{1.3L}{N}\right)} = \frac{415N}{L} \text{ MPa} \quad (6)$$

4. RESULT AND DISCUSSION

The results obtained in this study are theoretical values. Here, the graphs are plotted using Excel software and the papers mentioned in the literature review section are the references for validation of these graphical results.

The bending of the rope on a sheave pulley results in an indefinite lifetime of the elevator rope depending on the amount of load, the diameter of the sheave, and rope specifications. Since a fixed sheave and a fixed rope were assumed the number of bends to failure varied with varying loads. With the increase in the number of ropes, the load of the elevator system is divided among itself. A decrease in load per rope eventually resulted in a greater number of bends to failure i.e. the fatigue life. Minimum 4 hoisting ropes were required for them to last for about a million cycles.

Table 1: Number of bends to failure to the pressure-strength ratio for different numbers of ropes

n	m_t	F_{td}	F_f	$\frac{1000P}{S_u}$	Life cycle
1	1544.959	17473.488	22715.535	3.91037005	0.11M
2	1559.918	8821.338	11467.740	1.97411627	0.33M
3	1574.877	5937.288	7718.475	1.32869834	0.9M
4	1589.836	4495.263	5843.842	1.00598938	>1M
5	1604.796	3630.048	4719.063	0.812364	>1M
6	1619.755	3053.238	3969.210	0.68328042	>1M
7	1634.714	2641.231	3433.600	0.59107786	>1M
8	1649.673	2332.226	3031.893	0.52192594	>1M

Here the theoretical values for the length of stretched ropes on different floors are given in table 2. Also, 1 to 8 ropes are considered in this calculation.

In this study of natural frequencies of the elevator rope under tension, the variables are lengths of the rope on different floors, 1 to 20 modes of vibration, and 1 to 8 number of hoisting ropes. Figure 4 provides deeper insight into the behavior of natural frequency with these changing parameters. The six graphs in this figure represent the data for 24m, 20m, 16m, 12m, 8m, and 4m lengths of the rope when the elevator car is on the ground, first, second, third, fourth, and fifth floors respectively. This free length of the rope is measured from the sheave to the elevator car. The elevator hoisting rope under tension is assumed to be a flexible string.

In all of the six graphs in figure 4, it is seen that the lines get steeper when the number of hoisting ropes decreases. For example, in all graphs, the steepest lines are the ones where there is only one hoisting rope. This is because of the proportional relationship of natural frequency and the dynamic tension acting on the rope. A decrease in the number of hoisting ropes will increase the dynamic tension on the ropes and thus natural frequency will be increased. The relationship between natural frequency and mode of vibration is quite similar. With the increase in the number of modes of vibration, the natural frequency increases because of their proportional relationship.

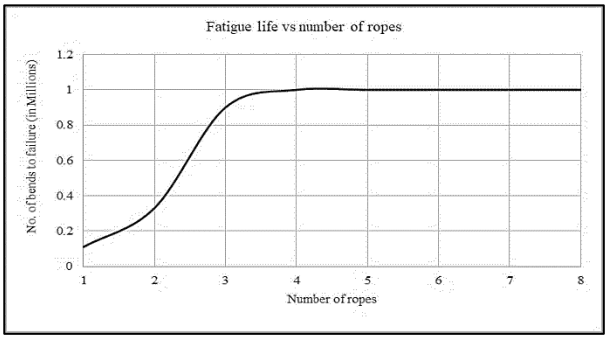

Fig. 3: Fatigue life vs number of ropes

Table 2: Stretched lengths for 1-8 ropes for the elevator on different floors

n	L(m)					
	L_0=24m	L_0=20m	L_0=16m	L_0=12m	L_0= 8m	L_0= 4m
1	24.0381	20.0317	16.0254	12.019	8.01269	4.00634
2	24.0192	20.016	16.0128	12.0096	8.00641	4.0032
3	24.0129	20.0108	16.0086	12.0065	8.00431	4.00216
4	24.0098	20.0082	16.0065	12.0049	8.00326	4.00163
5	24.0079	20.0066	16.0053	12.004	8.00264	4.00132
6	24.0066	20.0055	16.0044	12.0033	8.00222	4.00111
7	24.0058	20.0048	16.0038	12.0029	8.00192	4.00096
8	24.0051	20.0042	16.0034	12.0025	8.0017	4.00085

There is a gradual augmentation in the natural frequencies in the graphs in figure 4. When the elevator is on the ground floor, for a single hoisting rope and 20th mode of vibration, the natural frequency is 71.9587 Hz. When the elevator is on the first floor, for a single hoisting rope and 20th mode of vibration, the natural frequency is 86.3506 Hz. When the elevator is on the second floor, for a single hoisting rope and 20th mode of vibration, the natural frequency is 107.9381 Hz. When the elevator is on the third floor, for a single hoisting rope and 20th mode of vibration, the natural frequency is 143.918 Hz. When the elevator is on the fourth floor, for a single hoisting rope and 20th mode of vibration, the natural frequency is 215.8764 Hz. When the elevator is on the fifth floor, for a single hoisting rope and 20th mode of vibration, the natural frequency is 431.7532 Hz.

After analyzing figure 4, it can be said that for the same tension increasing the number of ropes will reduce its natural frequency, a decrease in the number of modes of vibration will reduce its natural frequency, and an increase in the length of rope will reduce its natural frequency.

In figure 5, for an elevator car on the fifth floor and a single hoisting rope, the natural frequencies will be 21.58766 Hz, 43.17532 Hz, 64.76298 Hz, 86.35064 Hz, 107.9383 Hz, 129.52596 Hz, 151.11362 Hz, 172.70128 Hz, 194.28894 Hz, 215.8766 Hz, 237.46426 Hz, 259.05192 Hz, 280.63958 Hz, 302.22724 Hz, 323.8149 Hz, 345.40256 Hz, 366.99022 Hz, 388.57788 Hz, 410.16554 Hz, 431.7532 Hz for 1 to 20 modes of vibrations respectively.

In figure 6, for a single hoisting rope and 20th mode of vibration, the natural frequencies will be 71.9587 Hz, 86.3506 Hz, 107.9381 Hz, 143.918 Hz, 215.8764 Hz, 431.7532 Hz for an elevator car at ground, first, second, third, fourth, and fifth floor respectively.

Again, in figure 7, for the elevator car on the fifth floor and 20th mode of vibration, the natural frequencies will be 431.7532 Hz, 307.0108 Hz, 251.9378 Hz, 219.2474 Hz, 197.03644 Hz, 180.71472 Hz, 168.08644 Hz, and 157.95256 Hz for 1, 2, 3, 4, 5, 6, 7, 8 ropes respectively.

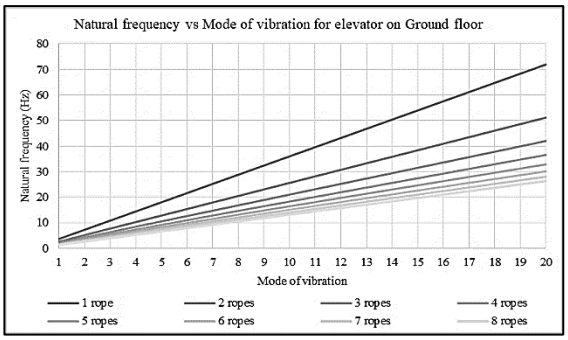

(a) On the ground floor

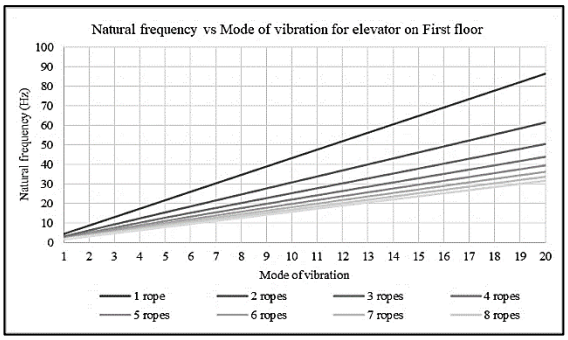

(b) On the 1st floor

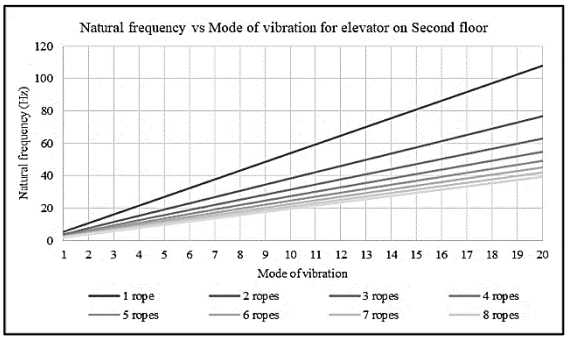

(c) On the 2nd floor

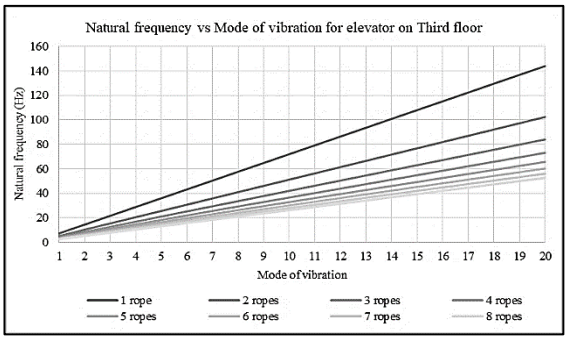

(d) On the 3rd floor

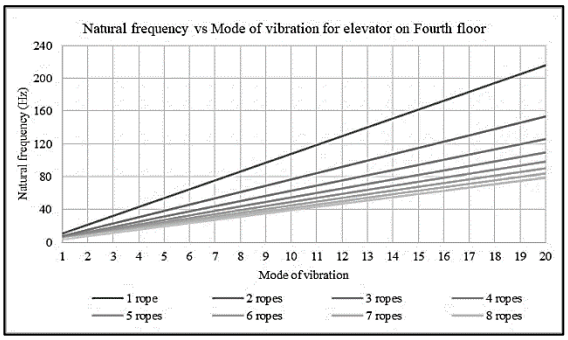

(e) On the 4th floor

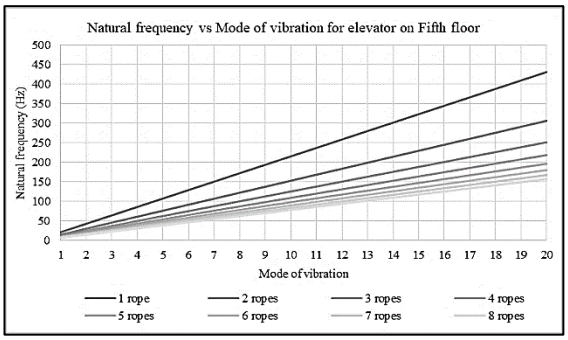

(f) On the 5th floor

Fig. 4: Natural frequency (f_n) vs mode of vibration (N)

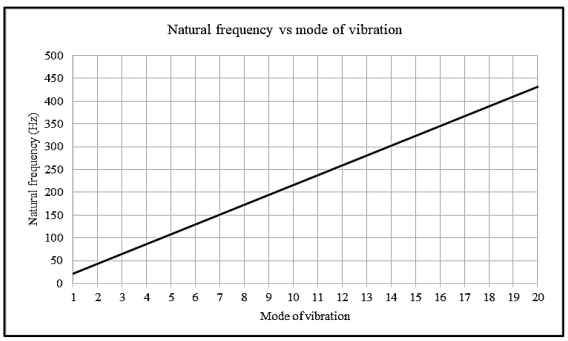

Fig. 5: f_n vs N for 1 rope on the top floor

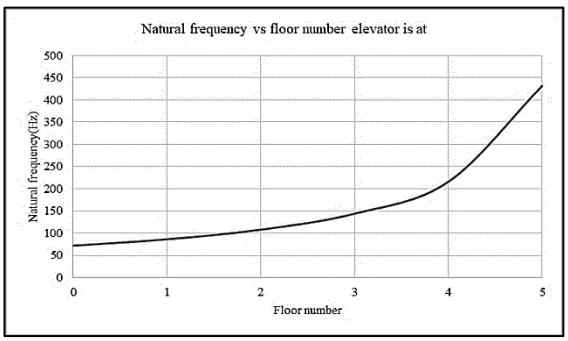

Fig. 6: Natural frequency vs floor number

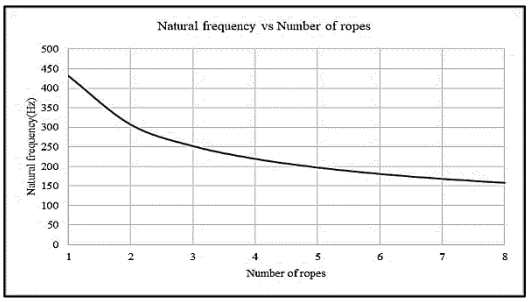

Fig. 7: Natural frequency vs number of ropes

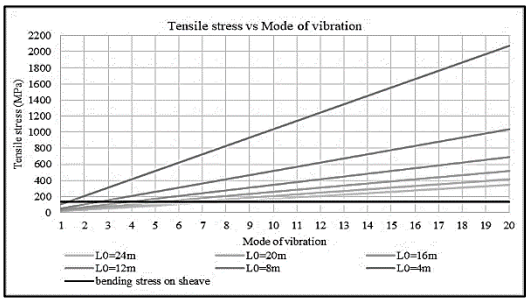

Fig. 8: Tensile stress vs mode of vibration

The rope develops tensile stress in the stretched areas under bending. The tensile stress on the outer portions of the rope varies with the radius of curvature and the radius of curvature varies with the mode of vibration or the length of the rope that was bending.

In figure 8, the tensile stress data for different modes of vibration and different lengths of the rope is seen. The lengths of the rope are 24m, 20m, 16m, 12m, 8m, and 4m for the elevator to be from the ground floor to the top floor. The graphs are steeper for shorter lengths of the rope. The tensile stress increases with an increasing number of modes of vibration, this is due to the decrease in radius of curvature. The maximum tensile stress in this study is 2075 MPa which is found for the shortest length of the rope 4m and the biggest mode of vibration 20. However, the tensile stress developed in the outer wires of the rope due to bending on the sheave is 133.876 MPa, this value is comparable to the tensile stresses developed due to bending of the rope in different modes of vibration. After the 8th mode of vibration in this study, all the tensile stresses developed due to vibration are greater than the stress developed in the rope due to bending on the sheave.

5. CONCLUSIONS

The findings of this study on elevator ropes are:

- An increase in the number of hoisting ropes will reduce the chances of fatigue failure. This study will assist in determining the number of hoisting ropes required for a maximum amount of loading and a maximum amount of acceleration.
- An increase in the natural frequency of hoisting ropes will increase the chances of fatigue failure. This study has determined that an increase in the number of hoisting ropes, an increase in rope length, and a decrease in modes of vibrations have greater chances of reducing the natural frequency.
- This study will assist in determining these variables to avoid occurrences like resonance, vibration discomfort, etc. This study will also assist in the application of dampers.
- Tensile stress that develops in the outer wires of a rope due to bending will indicate the places on the rope that are most vulnerable to fatigue failure. This will assist in checking the places of a rope that is weak and determining if the rope needs replacement.

REFERENCES

[1] Coleman, W. F., & Rugg, D. M. (1910). Stresses in wire ropes bent over sheaves.

[2] Kim, S. H., Bae, R. H., & Kwon, J. D. (2012). Bending fatigue characteristics of wire rope. Journal of mechanical science and technology, 26(7), 2107-2110.

[3] Blodgett, R. E., & Majumdar, A. K. (1983). An analysis of elevator rope vibration in tall buildings.

[4] Watanabe, S. (2002). Nonlinear vibration analysis of elevator rope. In Transportation and Logistics Conference of the Japan Society of Mechanical Engineers, 2002-12.

[5] Kaczmarczyk, S., & Andrew, P. (2005). Vibration analysis of elevator ropes. Elevator World, 6, 126-129.

[6] Kimura, H., Ito, H., & Nakagawa, T. (2007). Vibration analysis of elevator rope (forced vibration of rope with time-varying length). Journal of environment and engineering, 2(1), 87-96.

[7] Kimura, H., Iijima, T., Matsuo, S., & Fujita, Y. (2009). Vibration analysis of elevator rope (Comparison between experimental results and calculated results). Journal of system design and dynamics, 3(3), 420-428.

[8] Andrew, P., & Kaczmarczyk, S. (2011). Natural frequencies at different lengths of rope. Rope dynamics. Elevator World, 263, 45-56.

[9] Shimura, Y., Fujita, S., Tada, K., & Ogawa, Y. (2016, January). 104 Research on vibration behavior evaluation system for elevator ropes (Session 2 "Rope runout analysis"). Recent Technology and Advances Technology Lecture Lecture Proceedings 2016 (pp. 13-18). General Incorporated Association Japan Mechanical Society.

[10] Bruski, D. (2020). Determination of the bending properties of wire rope used in cable barrier systems. Materials, 13(17), 3842.

[11] Mia, M., Islam, M., Kabir, A., & Islam, M. (2022). Numerical Analysis of tubular XT Joint of jacket type offshore structures under static loading. (January 1, 2022). Bangladesh Maritime Journal (BMJ) Volume, 6, 2520-1840.

[12] Hirose, I., Kimura, H., & Ogawa, K. (2015). Suppression of lateral vibration of elevators and ropes using vertical vibration of balanced weights. Proceedings of the Japan Society of Mechanical Engineers, 81 (827), 15-00102.

[13] Shigley, J. E. Shigley's mechanical engineering design. Tata McGraw-Hill Education, 2011.

[14] Beer, F. P., Johnston Jr, E. R., Mazurek, D. F., Cornwell, P. J., Eisenberg, E. R., & Sanghi, S. Vector Mechanics for Engineers (Vol. 1). Tata McGraw-Hill Education, 2015.

[15] Singer, F. L., & Pytel, A. Strength of Materials, Harper & Row, Publishers. Inc., New York, 31, 2009.

Paper ID: 7522

International Conference on Mechanical, Manufacturing and Process Engineering (ICMMPE – 2022)

Organizer: Faculty of Mechanical Engineering, Dhaka University of Engineering & Technology (DUET), Gazipur, Bangladesh

Website: https://icmmpeduet.com/

Effect of Rice Husk Ash (RHA) on the Mechanical Properties of Aluminum-Cu Alloy based Metal Matrix Composites

Sagor Chandra Mozumder[1], Sobahan Mia[2], Pranto Karua[3]

[1]Student, Department of Mechanical Engineering, Khulna University of Engineering & Technology, Khulna-9203.
[2]Professor, Department of Mechanical Engineering, Khulna University of Engineering & Technology, Khulna-9203.
[3]Asst Professor, Department of Mechanical Engineering, Khulna University of Engineering & Technology, Khulna-9203.

E-mail: mozumder1605097@stud.kuet.ac.bd[1], smia@me.kuet.ac.bd[2]

ABSTRACT

Metal matrix composite is a great replacement for traditional materials in various technical and industrial applications. This article focuses on the potential attempt of making aluminum alloy 1350-rice husk ash (RHA) composite where RHA is the agricultural waste with high silica content. 5 % copper is added to the composite to boost its strength and hardness following the liquid metallurgy fabrication method. The prepared composites were characterized for density, hardness, tensile, and compression tests. The pattern of reinforcing particles (2-8 % wt. of RHA) throughout the matrix is also investigated. From the test findings, the incorporation of the copper results in increasing the mechanical properties of the base metal and the composite prepared with 8% rice husk ash (RHA) and aluminum matrix showed better results in terms of hardness, tensile and compressive strength. The maximum tensile strength and tensile modulus were found 72.6 MPa and 38 GPa respectively, whereas the compressive strength increased from 55.33 MPa to 147.29 MPa with the inclusion of 8% RHA. However, significant change in surface of the composites varying RHA percentages had been observed in microstructural analysis.

Keywords: Aluminium Alloy 1350; Rice Husk Ash; Tensile Strength; Compressive Strength; Metal Matrix Composite.

1. INTRODUCTION

One of the key developments in the world of materials over the last several decades has been the creation of metal matrix composites reinforced with sustainable elements. The ability to use specific qualities of these eco-friendly materials is the primary motivation for the creation of composites. The performance of the composite depends on the nature of reinforcements, the weight percentage of reinforcing materials, wettability between the reinforcements and the matrix, the methodology chosen, and the metallurgical characteristics of the matrix material [1].

In recent years, there has been a lot of interest in the development of aluminum matrix composites reinforced with agricultural waste which offers considerable cost savings in fabrication, and acceptable mechanical properties. AMCs (Aluminium metal composites) are being used in the design of vehicles, aviation, maritime buildings and facilities, defense assembly, and sports equipment. Because of its light weight, aluminum is frequently utilized as a structural material, particularly in the aircraft sector. Even aluminium's use in automotive applications has increased significantly in recent years [2]. As a result, enormous effort is being invested to improve the mechanical characteristics of aluminum. Now, the majority of research is being done to build composites utilizing diverse recycled agricultural as reinforcement material. Among these, Rice Husk Ash (RHA) is a plentiful agricultural byproduct. About 78 percent of the weight of paddy milled is obtained as rice. The remaining 22% of the weight of rice is obtained as husk. This husk comprises around 75% volatile materials and the remainder is inorganic. During the firing process, 25% of the weight of this husk is transformed into ash, which is known as rice husk ash (RHA) [3]. This RHA poses a significant environmental risk, causing harm to the ground and the surrounding region where it is disposed. According to current research findings, RHA includes between 85 and 90 percent amorphous silica [4]. So it is necessary to utilize this waste for protecting the environment.

According to Sahoo et al. [5], aluminum matrix composites are possibly appropriate for tribological applications. Palanikumar et al. [6] reported that graphite has also been employed as hybrid reinforcement with alumina and silicon carbide in AMCs, with significant improvements in wear parameters noted. Alaneme et al. [7] discovered that the percent Elongation for all composites created was between 10-13 percent and that the values were independent of RHA and graphite content. Hossain et al. [8] found that the use of rice husk ash in the production of cost-effective aluminum composites might have increased hardness and strength. Yadav et al. [9] also found that RHA particles increase composite wear resistance. They lowered the plastic deformation of the worn surface as well as the size of the wear debris produced. But Mouleeswaran et al.

[10] discovered that when more than 12% wt of RHA particles were present, the tensile strength decreased. Ahamed et al. [11] found that the mechanical properties are improved after adding the RHA in the aluminum.

Previously, several types of research on aluminum composite with RHA reinforcement were done. But there is no significant work on 1350 Aluminium grade adding 5% Cu. So the objective of this paper is to investigate the mechanical characteristics of Al-5% Cu alloy composites with RHA metal matrix composites. The fundamental concept is to use the enormous rice husk ash potentials in the region as reinforcement, hence lowering the negative environmental effect on society. In this paper, the mechanical properties of the prepared composites under different compsitions of RHA and microstructure of those composites have been presented.

2. MATERIALS AND METHODOLOGY

2.1 Materials

Aluminum alloy 1350 with 5% copper was used as the matrix material and Rice Husk Ash was the reinforcing agent in the composites.

2.1.1 Matrix Material

Aluminum alloy 1350 was extracted from the ACSR wire which was collected from the local market. According to the manufacturer catalog, the chemical composition of the Aluminum 1350 is shown in Table 1. Aluminum alloy 1350 is commonly used in situations requiring high electrical conductivity having an aluminum purity of 99.5 percent or above [11]. The thermal conductivity of aluminum is almost three times of steel, making it a valuable material for heat transfer applications [12]. Although pure aluminum is soft, most applications require higher strength and characteristics than pure aluminum can give. This is overcome by introducing different types of alloying elements. In this work, 5% copper is added with aluminum to increase the strength of the matrix.

Table 1: Chemical Composition of Al 1350 [13]

Element	**Wt. %**
Silicon (Si)	0.10
Chromium (Cr)	0.01
Manganese (Mn)	0.05
Copper (Cu)	0.05
Zinc (Zn)	0.05
Iron (Fe)	0.40
Aluminum (Al)	99.5 % or above

2.1.2 Reinforcement Material

Rice husk was sourced locally in Narayanganj, Bangladesh. The rice husks were properly cleaned with water to eliminate dust before drying for 24 hours at room temperature. The moisture and organic contents were subsequently removed. Because of the oxidization of the organic components, the color of the husk changed from yellowish to black. Following that, the husks were heated in a heat treatment furnace to remove the carbonaceous elements, leaving the grayish silica-rich ash to be utilized as the reinforcement of the composites. The chemical composition of RHA is given in Table 2.

Table 2: Chemical Composition of RHA [14]

Element	Wt. %
Silica (SiO_2)	91.56
Carbon	4.80
Calcium oxide, CaO	1.58
Magnesium oxide, MgO	0.53
Potassium oxide, K_2O	0.39
Hematite, Fe_2O_3	0.21
Others	0.93

2.2 Methodology

The metal matrix composites were prepared using the liquid metallurgy method [8]. The general characteristics of different Aluminum Copper alloys were investigated by J.R.Davis in 2001. In that study it was stated that the maximum strength of Aluminum and Copper alloy is gained when the percentage of Copper is restricted within 4 to 6% [15]. The compositions of the prepared composites formed by RHA and Aluminum 1350 with 5% Copper are presented in Fig 1.

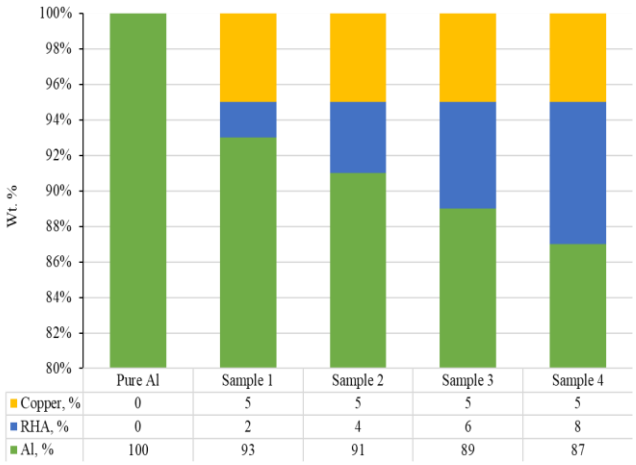

Fig. 1: Specimens having different percentages of RHA with Al 1350-5% Cu.

2.2.1 Sample Preparation

The matrix and 5% copper were placed in a crucible at 1100°C until the appropriate melting in the Foundry Shop of the Department of Mechanical Engineering, KUET. When the matrix melted, preheated reinforcement was added. While the preheated RHA was being added continuously based on the measurements, the mixture was stirred for 5-10 minutes to maintain the uniform distribution of RHA in the molten Aluminum. Then the molten composite was cast into the preheated sand mold and the composite was formed the cylindrical shape for the tensile, compression, and hardness test as shown in Fig 2 (c). Several machining processes such as turning, taper turning, face milling were performed on the cast samples using the CNC machine for making them appropriate for mechanical testing. Fig 2 (d) shows the specimens prepared for tensile test. Two specimens for each sample were prepared for conducting tensile, compression, and hardness test.

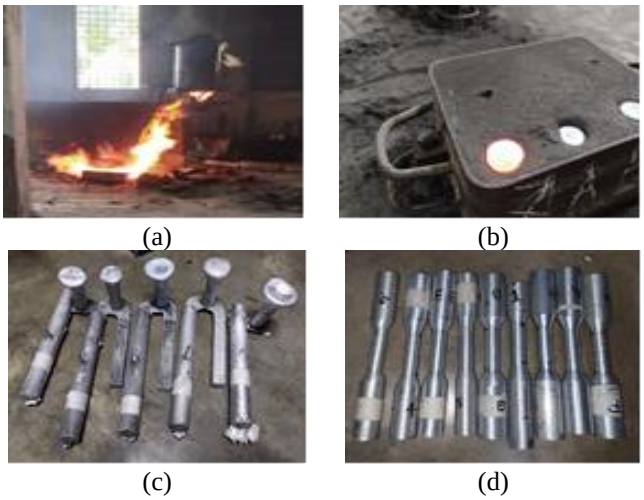

Fig. 2: Fabrication of composite (a) Furnace setup (b) Poured composite in the sand molds (c) Cast composite (d) Prepared specimens.

2.3 Test Methods

The prepared metal matrix composites with the different weight percentages of RHA were subjected to tensile, compression, and hardness tests.

2.3.1 Tensile Test

The tensile test of the casted composites was performed on the Univeral Testing Machine (Shimadzu AGX-300KN). ASTM E8 standard was followed for the tensile test. From the tensile test, ultimate tensile strength and the tensile modulus of elasticity were calculated.

2.3.2 Compression Test:

The compression test casted composites was performed on the Univeral Testing Machine (Shimadzu AGX-300KN). For the compression test, Samples were prepared according to the ASTM E9 standard. From the compression test, ultimate compressive strength and the compressive modulus were calculated.

2.3.3 Hardness Test

The hardness test was performed using the Rockwell hardness testing machine (HR-150A). The diameter of the ball was 0.0625 inches. The main load was 52 kg, while the minor load weighed 10.5 kg. The specimen was put below the ball and subjected to major and minor loads. The load was controlled via the dial gauge attached to the machine.

2.3.4 Microstructure Analysis

The microstructure analysis was conducted by the Optical Microscope (Euromex) with the help of image processing. The samples were polished thoroughly using a flat file and emery paper (240, 320, 400) to obtain a fine surface. After preparing the samples, microstructure analysis was carried out.

3. RESULT AND DISCUSSION

The variation of the experimental and theoretical densities of the prepared metal matrix composites is presented in Fig 3. The theoretical density has been measured following the rule of mixture in terms of weight fraction of the RHA and Al-5% Cu alloy and the experimental density was measured from mass and volume measurement. With the addition of the 5% Cu in the Aluminum, density increases. But the density decreases for increasing the percentage of RHA keeping the copper quantity constant. The calculated porosity is also shown in Fig 3. The percentage of porosity is also increased with the increase of RHA percentage because of air entrapment during solidification.

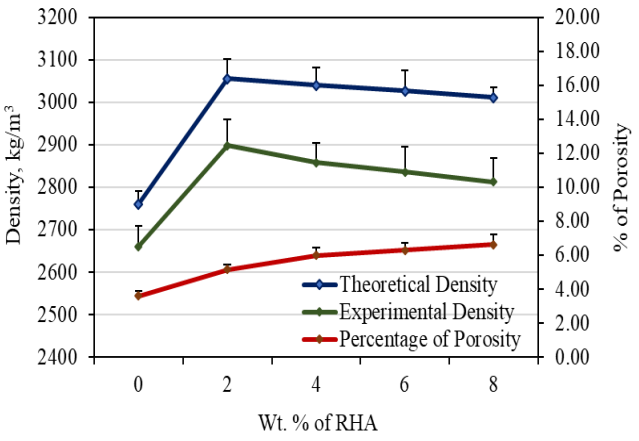

Fig. 3: Density of Al-5% Cu composites under different percentages of RHA.

The ultimate tensile strength and tensile modulus of all specimens obtained during the tensile test were presented in

Fig 4. It is seen that there is an effect on the tensile properties of the material with the increasing percentage of RHA. The presence of RHA as reinforcement increases tensile strength primarily by transferring load from the matrix to the reinforcement, besides there is an effect of introducing copper in the Aluminum matrix.

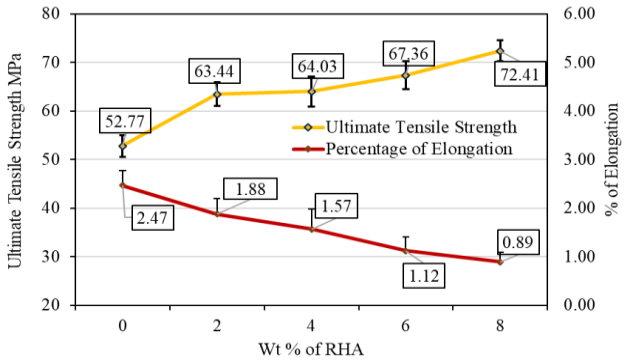

(a)

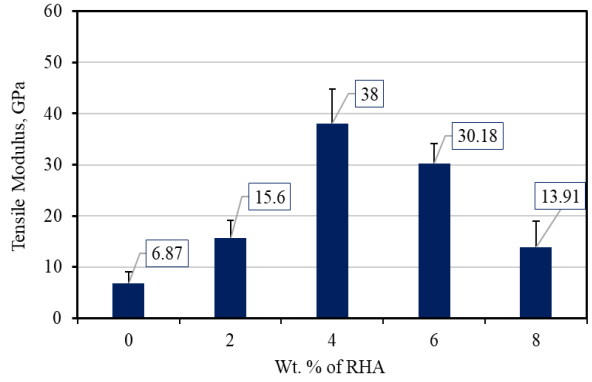

(b)

Fig. 4: (a) Ultimate tensile strength and (b) tensile modulus of Al-5% Cu composites under different percentages of RHA.

Though tensile strength increases with increasing RHA, tensile modulus starts to decrease reaching a percentage of RHA 4 % in the Aluminum matrix. The maximum ultimate tensile strength and tensile modulus are found to be 72.41 MPa and 38 GPa respectively.

Fig. 5 illustrates the ultimate compressive strength and compressive modulus with the increasing percentage of RHA (0-8 %). As observed in tensile test, compressive strength also increases as the weight % of RHA increases in the Aluminum matrix. This improvement occurred as the rice husk ash particles hardened the base alloy. Ultimate compressive strength increases almost 166.20 % as compared to the composite having zero ash content and found to be highest in the composite prepared with 8% RHA. Compressive modulus increases with the inclusion of 2 % RHA, but further increase in RHA shows an anomaly. The range of compressive modulus was 3.88-10.52 GPa.

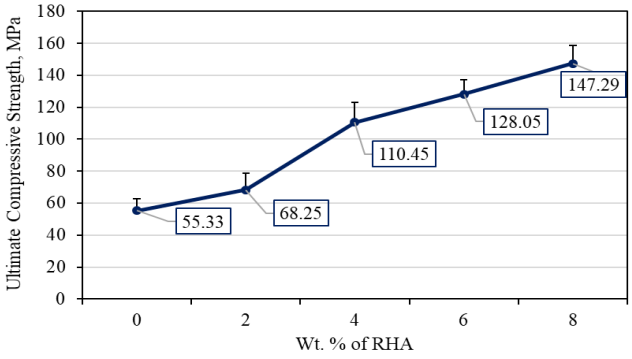

(a)

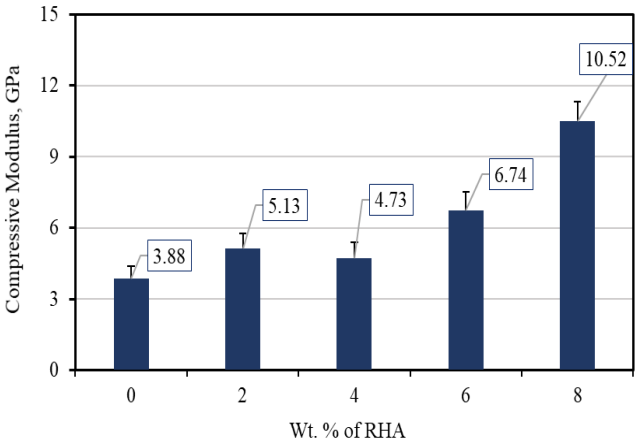

Fig. 5: (a) Ultimate compressive strength and (b) compressive modulus of Al-5% Cu composites under different percentages of RHA.

The variation of Rockwell hardness number of the prepared Al-5% Cu composites is shown in Fig. 6. The hardness increases with the increasing percentage of RHA from 0-8 % by weight. The rise in hardness is seen to be gradual as the degree of reinforcement increases. As the reinforcing particles are stiffer than the matrix, they resisted plastic deformation, which may contribute to the improvement of the hardness of the composites. The Rockwell hardness number was found maximum (75 HRB) in case of sapecimen prepared with 8 % RHA.

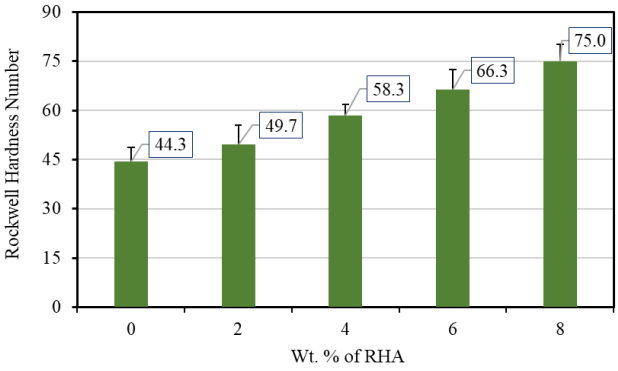

Fig. 6: Rockwell hardness number for Al-5% Cu composites under different percentages of RHA.

The microstructural view of the Al-5% Cu composites for different percentages of RHA are shown in Fig 7. Fig 7 (a) shows the base Al-5% Cu alloy without reinforcement, whereas Fig. 7 (b)-(e) shows the composites prepared with 0-8 % RHA. With the RHA reinforcement, several dark spots are seen to be visible in the surface in the optical microscopy. Though ultimate tensile strength and compressive strength increases significantly with the increasing percentage of RHA, the presence of dark spots also increases following an uniform pattern and in cluster form.

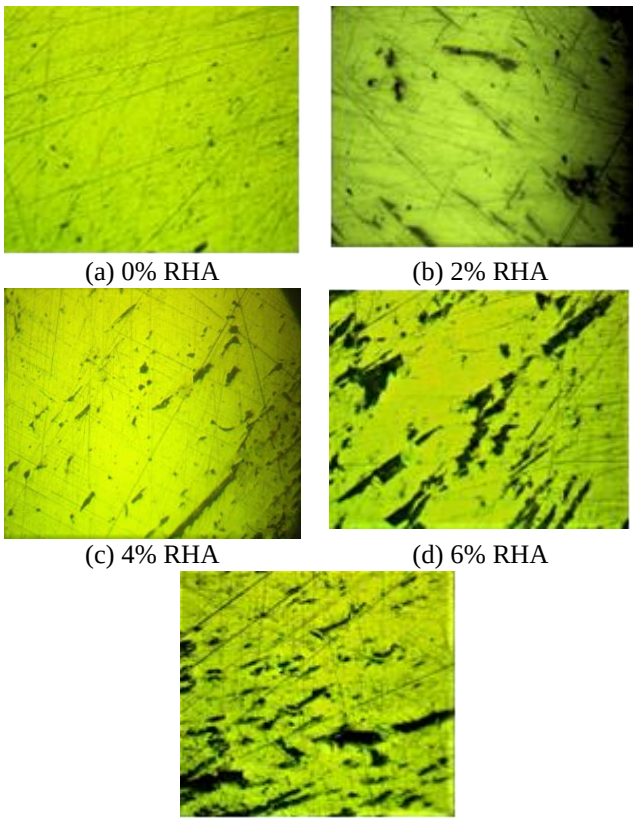

(a) 0% RHA (b) 2% RHA

(c) 4% RHA (d) 6% RHA

(e) 8% RHA

Fig. 7: Microstructural view of the composites for different percentages of RHA in the Aluminum-Cu matrix .

4. CONCLUSION

In this study, RHA particles were successfully integrated into Al 1350 with 5% Cu by using the Liquid metallurgy method. The utilization of rice husk ash (RHA) in the production of Aluminium metal matrix composites has the potential ability to convert agricultural waste into assets. A set of tests were carried out to investigate the mechanical characteristics of aluminum alloy-rice husk ash. RHA was added up to 8 % within the aluminum to fabricate the composites. The addition of Copper increases the strength and hardness of the base metal significantly. The highest ultimate tensile strength and tensile modulus were found 72.6 MPa and 38 GPa respectively. The compressive strength increased from 55.33 MPa to 147.29 MPa with the inclusion of 8% RHA. In addition to this, the Rockwell hardness number increases with increasing the RHA percentage and the highest hardness was found 75 HRB. According to the results obtained, the composite prepared with 4% RHA will perform better where stiffness becomes the significant concern, whereas the composite prepared with 8% RHA is capable of withstanding the maximum compressive load. The microstructural analysis of the composites also demonstrates the change in surface of the composites with the increasing RHA contents.

REFERENCES

[1] K.K. Alaneme, T.M. Adewale, P.A. Olubambi, Corrosion and wear behaviour of AleMgeSi alloy matrix hybrid composites reinforced with rice husk ash and silicon carbide, J. Mater. Res. Technol. 3 (1) (2014).

[2] W.S. Miller, L, Zhuang, J. Bottema, AJ. Wittebrood, P. De smet, A.Haszler, A. Vieregge " Recent development in aluminium alloys for the automotive industry"

[3] Torralba, J. M., Da Costa, C. E., and Velasco, F. (2003), "P/M aluminum matrix composites: an overview," Journal of Materials Processing Technology, 133(1), pp. 203–206

[4] Gupta, V. K., Gupta, M., and Sharma, S. (2001), "Process development for the removal of lead and chromium from aqueous solutions using red mud—an aluminium industry waste," Water Research, 35(5), pp. 1125–1134

[5] Sahoo, P. & Ghosh, S. (2011) " Tribologicalbehavior of aluminium metal matrix composites– A review" . Journal of Tribology Research, 2(1), 1-14.

[6] K. Palanikumar, A. Muniaraj, Experimental investigation and analysis of thrust force in drilling cast hybrid metal matrix (Ale15%SiCe4%graphite) composites, Measurement 53 (2014) 240e250.

[7] Alaneme, Kenneth & Sanusi, Kazeem. Microstructural characteristics, mechanical and wear behavior of aluminium matrix hybrid composites reinforced with alumina, rice husk ash and graphite. Engineering Science and Technology, an International Journal. 28. 10.1016/j.jestch.2015.02.003.

[8] Hossain, Md & Ali, Md & Al Amin, Md & Kibria, Md & Ferdous, Md. Shafiul. (2017). Fabrication and Performance Test of Aluminium Alloy-Rice Husk Ash Hybrid Metal Matrix Composite as Industrial and Construction Material..

[9] Yadav, Ajay & Pandey, Krishna & Dey, Abhijit. (2018). Aluminium Metal Matrix Composite with Rice Husk as Reinforcement: A Review. Materials Today: Proceedings. 5. 20130-20137. 10.1016/j.matpr.2018.06.381..

[10] Mouleeswaran, Senthilkumar & S.D.Saravanan,. (2013). Effect of mechanical properties on rice husk ash reinforced Al alloy (AlSi10Mg) matrix composites. Procedia Engineering. 64. pp.1505-1513. 10.1016/j.proeng.2013.09.232.

[11] Ahamed, A.A., Ahmed, R., Hossain, M.B., & Billah, M.(2016). Fabrication and Characterization of Aluminium-Rice Husk Ash Composite Prepared by Stir Casting Mehod. Rajshahi University Journal of Science and Engineering, 44. 9-18.

[12] https://www.azom.com/amp/article.aspx?ArticleID=2863 (Accessed Date 24th March 2022)

[13] https://unitedaluminium.com/1350-aluminium-alloy (Accessed Date 24th March 2022)

[14] Olaniran O, Uwaifo O, Bamidele E, et al. An investigation of the mechanical properties of organic silica, bamboo leaf ash and rice husk reinforced aluminium hybrid composite. Material Sci & Eng. 2019;3(4):129-134.

[15] J.R, Davis " Aluminum and Aluminuum alloys" DOI: 10.1361/autb2001p351.

Paper ID: 7536
International Conference on Mechanical, Manufacturing and Process Engineering (ICMMPE – 2022)
Organizer: Faculty of Mechanical Engineering, Dhaka University of Engineering & Technology (DUET), Gazipur, Bangladesh
Website: https://icmmpeduet.com/

Study of Nanoscale Plasticity in Al - Ti Alloy Nanocube by Molecular Dynamics Simulation

Md. Jahangir Alam[1*], Md. Shariful Alam Emon[1], Biplov Kumar Roy[1]

[1] Department of Mechanical Engineering, Dhaka University of Engineering & Technology, Gazipur.

*E-mail: jahangir@duet.ac.bd

ABSTRACT

Al-Ti alloys are particularly well suited for high-performance automobile engines and aircraft applications due to their structural durability at high temperatures and their low weight. This paper investigates the nanoscale plasticity of an Al-Ti alloy nanocube with varied percentages of alloying element (Ti) and distinct crystal orientations of aluminum under compression loading using Molecular Dynamics. Here, the alloying proportion of Ti is adjusting upto 0%, 5% and 10% in the directions of crystal loading i.e. <100> and <111> of Al. The present findings reveal that the alloy nanocube has the highest yield strength, 8.712 GPa, along the <111> direction for 10% percent Ti weightage and the highest strain along the <111> direction for 0 % Ti weightage. In addition, the alloy nanocube has the maximum elastic modulus of 100.32 GPa along <111> direction for 10% Ti weightage and the highest poisson's ratio of 0.392 along <100> direction for 10% Ti weightage. The dislocation density, length, and different types of dislocations, as well as their interactions, are investigated to interpret the compressive stress-strain behavior of the nanocube-sized alloy.

Keywords: Al-Ti alloy, Nanocube, Molecular Dynamics, Compression, Dislocation.

1. INTRODUCTION

There is a lot of interest in developing γ-TiAl alloys, or Ti - Al alloys, because of its potential application in aircraft components and automobile parts [1]. Because of its tolerance to extreme temperatures, this material can be used in today's airplane jet engines [2]. High-performance car engines also utilize it [3]. In terms of oxidation resistance and structural stability, this alloy material is outstanding [4, 5]. Additionally, the low weight of TiAl alloys improves acceleration and fuel economy, which reduces CO2 gas emissions in automobiles [6, 7].

Metal and alloy nanostructures such as, nanoribbon, nanowire, nanopillar, and nanocube are gaining tremendous attention due to their numerous applications in MEMS/NEMS [8]. A large number of applications involve compressive loading of nanostructures [9,10]. Nanostructure materials are better suited for compressive loads than their than bulk materials because of their superior mechanical properties. One of the most promising materials for nanostructured applications is aluminum alloyed with titanium [11].

The suitability of a material's application depends critically on its nanoscale material properties. The mechanical properties of nanopillars and nanocubes can be extracted in the lab by indenting or compressing them using various nanotools [12, 13]. A pure aluminum nanopillar has previously been experimentally constructed and its mechanical characteristics were examined to determine their performance [14]. Molecular dynamics (MD) is a technique that is commonly used to evaluate the mechanical characteristics of nanomaterials using computer simulation. The mechanical characteristics of single crystals of Al [15] and Ti [16] were previously predicted under tension test using the molecular dynamics approach.

The crystal orientation under loading has a major influence on the mechanical properties. This occurs owing to the orientation of the slip plane in FCC metal. In the past, crystal orientation effects have been studied for nanopillars made of titanium [17], aluminum[18], and iron[19]. The enhanced mechanical characteristics of nanoscale alloys make them an ideal substitute for pure metals. Solid solution strengthening has a substantial impact on mechanical characteristics when alloying in a different crystal orientation to choose the best crystal slip plane. Solid solution strengthening is the major technique that makes alloys stronger than the basic material [20]. When an alloying metal atom is inserted into the crystalline lattice of a base metal, a solid solution is obtained. Compared to the base metal, the alloying element atom provides a greater tension or compression field. This localized strain field interacts with the dislocation and affects its mobility. The solute-dislocation interaction was studied in an Al alloy comprising Mg, Si, Cu, and Cr alloying elements [21] and evaluated the energy barrier generated by the different solute atoms.

Compression after yielding results in the nanocube's plasticity. Initiation, Propagation, interaction and nucleation of different type of dislocations govern the plastic deformation of the nanocube [22]. Alloy dislocation activity and plasticity may be greatly affected by the alloying element and its proportion. As the proportion increase, the plastic behavior of the alloy gets more

complicated, requiring a greater understanding of the alloying element's proportion.

The amount of alloying elements in the nanocube and the orientation of the crystals in the loading direction are the major essential aspects that influence the plasticity of the nanocube in significant ways. The purpose of this work is to investigate the effects of compressive stress on Al-Ti alloying nanocube, which is a typical practice in nanostructure design.

2. METHODOLOGY

The simulations of uniaxial compression are carried out on an Al-Ti alloy nanocube with dimensions of 12.14nm×12.14nm ×12.14nm. Al and Ti interaction is characterized by the Modified embedding atomic potential (MEAM) alloy potential [23] which has been utilized earlier [24,25], The Modified embedding atomic potential (MEAM) of TiAl defines the basic material characteristics of Ti–Al alloys in excellent agreement with experimental or first-principles data [23]. The nanocubes are compressed along the two crystallographic direction (i.e. <100> and <111>). First, pure Al in various orientations is created for alloy modeling, and afterwards Al atoms are substituted randomly by Ti atoms for two distinct weight percentages (i.e. 5% and 10%). All of the simulations are performed using the LAMMPS software package [25] and with post-processing carried out using OVITO [26]. The NPT dynamics relaxes the alloy's initial geometry for 20 ps. Later, compression is applied along the positive X direction (see Fig. 1) at a temperature 300K altering the percentage of the Ti and the crystallographic orientation of the simulation box for strain rate of 10^{10} s^{-1}. All simulations use a 1fs timestep. When the nanocube of the simulation box is subjected to uniaxial deformation, atomic stresses are computed in order to attain the stress-strain behavior. To determine atomic stresses, virial stress [27] is defined as follows:

$$\sigma_{virial}(r) = \frac{1}{\Omega}\sum_{i}\left[\left(-m_i\dot{u}_i \otimes \dot{u}_i + \frac{1}{2}\sum_{j\neq i} r_{ij} \otimes f_{ij}\right)\right] \quad \ldots (1)$$

where the summation is over all the atoms occupying the total volume, Ω is the total volume of the domain, m_i is the mass of atom i, $\dot{u}_i$ is the time derivative which indicates the displacement of atom with respect to a reference position, r_{ij} is the position vector of atom, $\otimes$ is the cross product, and f_{ij} is the interatomic force applied on atom i by atom j.

3. Results and discussion

The stress-strain behavior of the alloy is represented in Fig. 2 that firstly, it rises linearly upto a certain point named yielding point, then collapses and has become stretched at up to 0.2 strain. The dramatic collapse is a result of the introduction of dislocations and their interactions. It will be illustrated in detail in a subsequent section using activity graphs of dislocations. The certain yield point is revealed in each case. The crystallographic directions have a considerable impact on the strength of the material. The strength is greater in the direction of <111> than in the

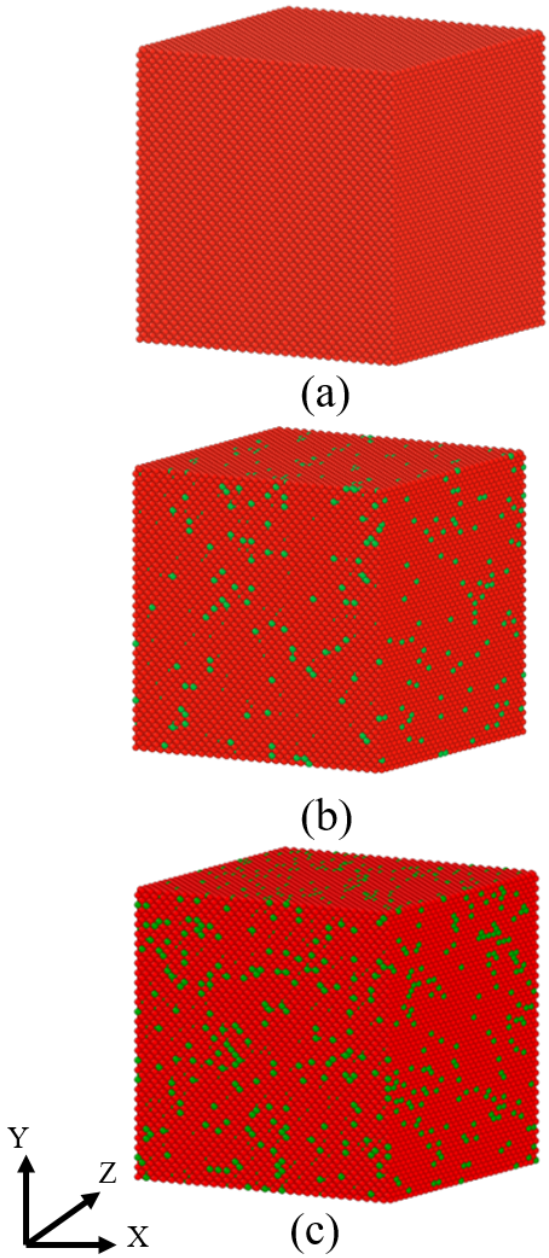

Fig. 1: (a) Crystalline Al nanocube, (b) Al-Ti alloy nanocube with 10% Cu. The Al and Ti atoms are represented by red and green color, respectively.

direction of <100>. A considerable impact on the alloying percentage is also observed in both directions.

In the <111> direction, as the alloying fraction of Ti increases, the peak of the curve climbs upward, 5.75 GPa, 7.1 GPa, and 8.7 GPa for 0%, 5%, and 10% of Ti, respectively. As the amount of alloying element rises, the yield strength improves due to the solid solution strengthening effect. Alloying element generates a

compression field inside the lattice, which aids in energizing the lattice and preventing dislocation from moving or slipping due to a greater energy barrier, resulting in a higher yield strength. The peak stress then drops to 3.5 GPa, 2.5 GPa, and 2.8 GPa correspondingly. Thereafter, it rises again somewhat as a result of several dislocation interactions. Each curve may withstand up to 0.2 strain value.

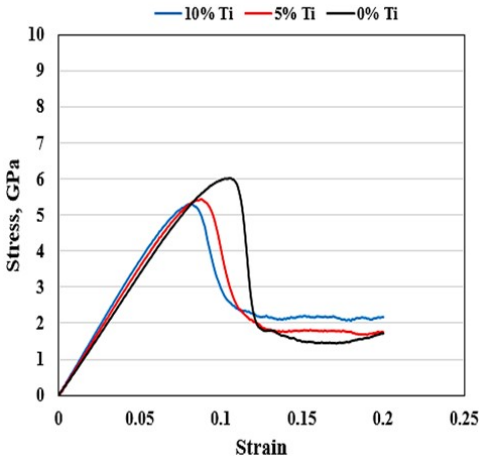

(a)

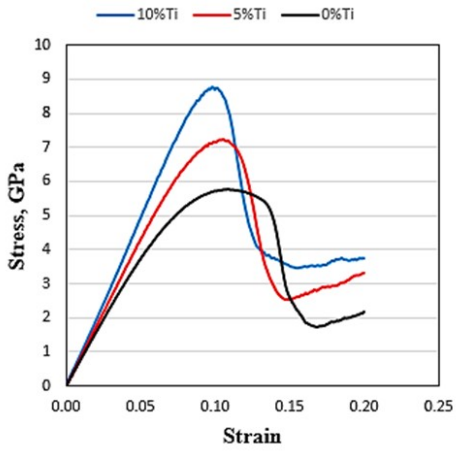

(b)

Fig. 2: Compressive stress-strain Curve for Al-Ti alloy nanocube for loading in (a) <100>, (b) <111> direction for different Ti percentage.

In the <111> direction, as the alloying fraction of Ti increases, the peak of the curve climbs upward, 5.75 GPa, 7.1 GPa, and 8.7 GPa for 0%, 5%, and 10% of Ti, respectively. As the amount of alloying element rises, the yield strength improves due to the solid solution strengthening effect. Alloying element generates a compression field inside the lattice, which aids in energizing the lattice and preventing dislocation from moving or slipping due to a greater energy barrier, resulting in a higher yield strength. The peak stress then drops to 3.5 GPa, 2.5 GPa, and 2.8 GPa correspondingly. Thereafter, it rises again somewhat as a result of several dislocation interactions. Each curve may withstand up to 0.2 strain value.

However, in the direction of <100>, the strength decreases rather than increases because the dislocations acquire more slip planes than in the direction of <111> and are able to readily move through slip, which nullifies the effect of the solid solution strengthening.

When alloying elements are added, we have seen an opposing occurrence between two crystallographic orientations. There is greater strength in the <111> direction than <100> direction.

The influence of alloying % on elastic and yielding characteristics is seen in Fig. 3. For all alloying percentages, the <111> direction has a larger elastic modulus than the <100> direction. The yielding stress is greater in the <111> direction than <100> direction and tends to rise with increasing Ti %. In the <111> direction, the yield stress of a 10 percent Ti alloy is 8.712 GPa, which is more than the yield stresses in the other directions. In the< 100> direction, the yield stress is smaller and Ti addition has minimal effect. The yield strain is lower in the <100> direction and decreases significantly more gradually as the percentage of Ti increases. The alloying element appears to have a negligible influence on the yielding strain of the material. Poisson ratio increases as the alloying percentage of Ti increases in the direction <111>, while it decreases in the direction <100> as the alloying percentage of Ti is raised.

Fig. 4 demonstrates that the dislocation density and length are excessively greater in the direction <100> than in the direction <111>.In the 100> direction, pure Al (0 % Ti) has the highest dislocation density, resulting in a much longer and sharper stress curve collapse than the other two proportions. Increasing the Ti percentage of the alloy causes early dislocation formation and a decrease in yield strength. It can be seen in Fig. 4(c) that initially, enormous partial dislocations of the shockley type form, which are then followed by dislocations moving along advantageous slip

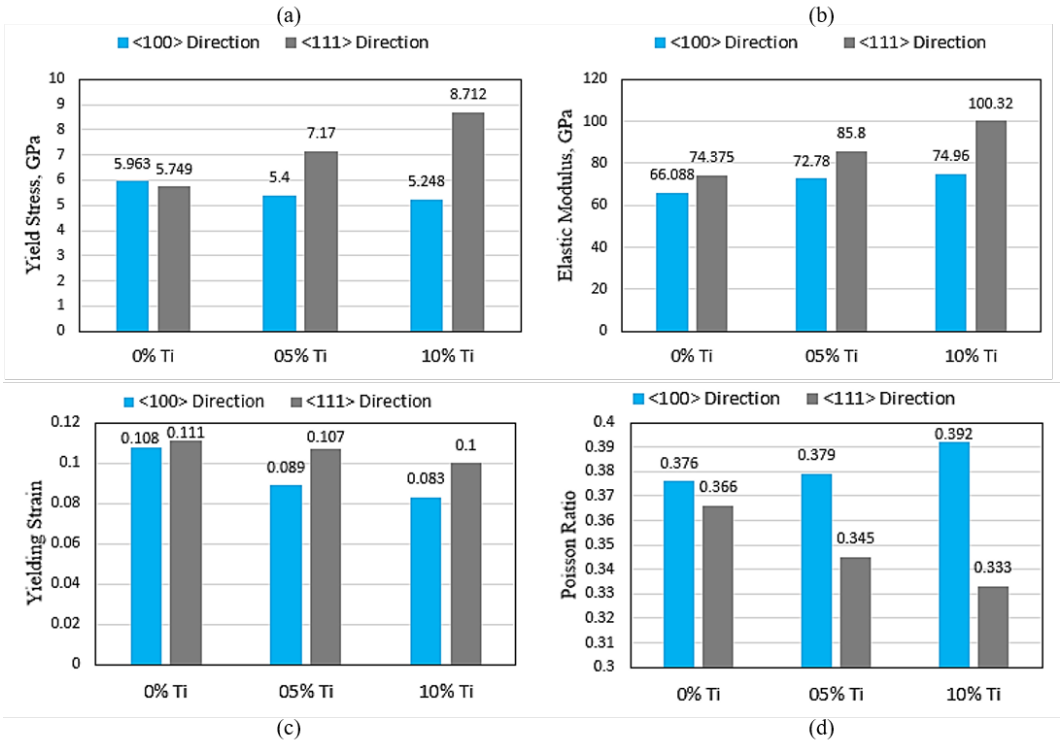

Fig.3: Variation of (a) yielding stress, (b) elastic modulus, (c) yielding strain (d) poison ratio with different *Ti* percentage of *Al-Ti* alloy.

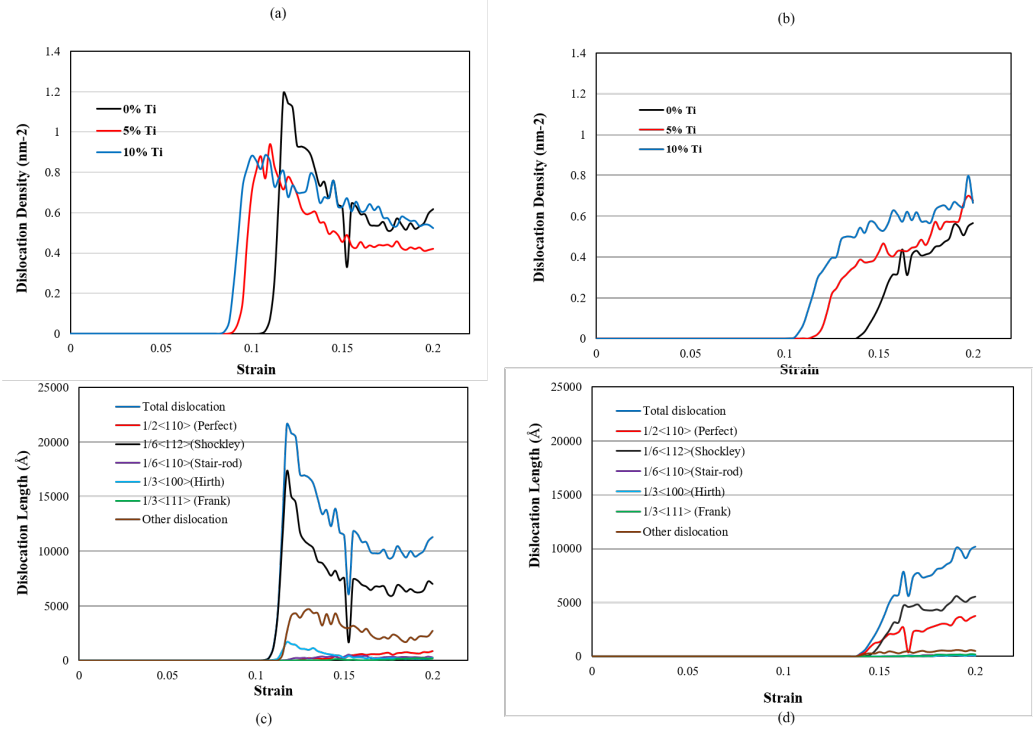

Fig. 4: Variation in dislocation density for loading in (a) <100>, (and (b) <111> direction for different Ti percentage. Variation of different dislocations length for 0% Ti in (c) <100>, and (d) <111> direction.

planes when dislocations are annihilated. The annihilation causes a drop in dislocation density, and the annihilation causes an increase in straining, which improves the ductility of the material. At 0.15 strain, the dislocation density in pure Al (0 % Ti) declines dramatically, and dislocation loops may occur when dislocations nucleate and the material approaches failure.

In the <100> direction, as the proportion of Ti increases, the strength of the alloy decreases, and the peak moves to the left, with the curve falling less than the others after the peak.

In the <111> direction, as the amount of alloying element Ti increases, the peak point moves to the left, indicating that it occurs at lower strain owing to earlier dislocation formation. More addition of alloying element, Ti itself causes more misfit in the lattice and also creates a greater compression field inside the lattice, which aids early dislocation production, as seen in Figure 4. (b). As a result, the peak of the stress-strain curve moves to the left. As the dislocations move along advantageous slip planes, the dislocation density rises continually, as seen in Figures 4(b) and (d). At about strain 0.15, the density decreases due to the nucleation of some dislocations, and then it rises again till rupture. Movement of shockley partial dislocations and complete dislocations are more prevalent than other types of dislocations in this <111> direction.

4. CONCLUSION

The results mentioned can lead to the following conclusions:

- Elastic modulus and yielding stress are lower for <100> direction for all Ti percentage. Elastic modulus is higher for <111> direction. The pattern with Ti percentage is increasing in case of <111> but opposite for <100>.
- Yielding strain has no significant effect on alloying percentage for <111> direction and slighter decreasing trend with increasing the alloying percentage of Ti, along the direction <100>.
- Poisson ratio is increased with the increasing the alloying percentage of Ti along the direction <111> but it is decreased along the direction <100>.
- The rapid drop in stress-strain curves is caused by the formation of various dislocation formations and the interactions between them. In the case of <111>, soild slotion strengthening increases the yield strength, but in the case of <100>, the effect of solid solution strengthening is mitigated by the greater availability of dislocation slip movements

A variety of other Ti percentages, as well as another crystal orientation, can be examined. Furthermore, the mechanism of transition from elastic to plastic deformation can be investigated to acquire a better knowledge of mechanical behavior.

REFERENCES

[1] H. Clemens and H. Kestler, “Processing and applications of intermetallic γ-TiAl-based alloys,” *Adv. Eng. Mater.*, vol. 2, no. 9, pp. 551–570, 2000, doi: 10.1002/1527-2648(200009)2:9<551::AID-ADEM551>3.0.CO;2-U.

[2] B. P. Bewlay, S. Nag, A. Suzuki, and M. J. Weimer, “TiAl alloys in commercial aircraft engines,” *Mater. High Temp.*, vol. 33, no. 4–5, pp. 549–559, 2016, doi: 10.1080/09603409.2016.1183068.

[3] M. Burtscher *et al.*, “An advanced tial alloy for high-performance racing applications,” *Materials (Basel).*, vol. 13, no. 21, pp. 1–14, 2020, doi: 10.3390/ma13214720.

[4] R. Pflumm, A. Donchev, S. Mayer, H. Clemens, and M. Schütze, “High-temperature oxidation behavior of multi-phase Mo-containing γ-TiAl-based alloys,” *Intermetallics*, vol. 53, pp. 45–55, 2014, doi: 10.1016/j.intermet.2014.04.010.

[5] E. Schwaighofer *et al.*, “Microstructural design and mechanical properties of a cast and heat-treated intermetallic multi-phase γ-TiAl based alloy,” *Intermetallics*, vol. 44, pp. 128–140, 2014, doi: 10.1016/j.intermet.2013.09.010.

[6] K. Gebauer, “Performance, tolerance and cost of TiAl passenger car valves,” *Intermetallics*, vol. 14, no. 4, pp. 355–360, 2006, doi: 10.1016/j.intermet.2005.08.009.

[7] D. Eylon, M. M. Keller, and P. E. Jones, “Development of permanent-mold cast TiAl automotive valves,” *Intermetallics*, vol. 6, no. 7–8, pp. 703–708, 1998, doi: 10.1016/s0966-9795(98)00036-3.

[8] T. Yasui, S. Rahong, N. Kaji, and Y. Baba, “Nanopillar, Nanowall, and Nanowire Devices for Fast Separation of Biomolecules,” *Isr. J. Chem.*, vol. 54, no. 11–12, pp. 1556–1563, 2014, doi: 10.1002/ijch.201400102.

[9] G. Sainath and B. K. Choudhary, “Deformation behaviour of body centered cubic iron nanopillars containing coherent twin boundaries,” *Philos. Mag.*, vol. 96, no. 32–34, pp. 3502–3523, 2016, doi: 10.1080/14786435.2016.1240377.

[10] L. A. Zepeda-Ruiz, B. Sadigh, J. Biener, A. M. Hodge, and A. V. Hamza, “Mechanical response of freestanding Au nanopillars under compression,” *Appl. Phys. Lett.*, vol. 91, no. 10, pp. 8–11, 2007, doi: 10.1063/1.2778761.

[11] T. Fujii, Y. Aoki, K. Fushimi, T. Makino, S. Ono, and H. Habazaki, “Controlled morphology of aluminum alloy nanopillar films: From nanohorns to nanoplates,” *Nanotechnology*, vol. 21, no. 39, 2010, doi: 10.1088/0957-4484/21/39/395302.

[12] R. J. Milne, A. J. Lockwood, and B. J. Inkson, “In-situ TEM deformation of aluminium nanopillars,” *J. Phys. Conf. Ser.*, vol. 241, pp. 1–5, 2010, doi: 10.1088/1742-6596/241/1/012059.

[13] D. Jang, X. Li, H. Gao, and J. R. Greer, “Deformation mechanisms in nanotwinned metal nanopillars,” *Nat. Nanotechnol.*, vol. 7, no. 9, pp. 594–601, 2012, doi: 10.1038/nnano.2012.116.

[14] A. Kunz, S. Pathak, and J. R. Greer, “Size effects in Al nanopillars: Single crystalline vs. bicrystalline,” *Acta Mater.*, vol. 59, no. 11, pp. 4416–4424, 2011, doi: 10.1016/j.actamat.2011.03.065.

[15] V. Yamakov, D. Wolf, S. R. Phillpot, A. K. Mukherjee, and H. Gleiter, “Dislocation processes in the deformation of nanocrystalline aluminium by molecular-dynamics simulation,” *Nat. Mater.*, vol. 1, no. 1, pp. 45–48, 2002, doi: 10.1038/nmat700.

[16] B. Zhang, L. Zhou, Y. Sun, W. He, and Y. Chen, "Molecular dynamics simulation of crack growth in pure titanium under uniaxial tension," *Mol. Simul.*, vol. 44, no. 15, pp. 1252–1260, 2018, doi: 10.1080/08927022.2018.1485150.

[17] J. Ren, Q. Sun, L. Xiao, X. Ding, and J. Sun, "Phase transformation behavior in titanium single-crystal nanopillars under [0 0 0 1] orientation tension: A molecular dynamics simulation," *Comput. Mater. Sci.*, vol. 92, pp. 8–12, 2014, doi: 10.1016/j.commatsci.2014.05.018.

[18] S. Xu, Y. F. Guo, and A. H. W. Ngan, "A molecular dynamics study on the orientation, size, and dislocation confinement effects on the plastic deformation of Al nanopillars," *Int. J. Plast.*, vol. 43, pp. 116–127, 2013, doi: 10.1016/j.ijplas.2012.11.002.

[19] C. J. Healy and G. J. Ackland, "Molecular dynamics simulations of compression-tension asymmetry in plasticity of Fe nanopillars," *Acta Mater.*, vol. 70, pp. 105–112, 2014, doi: 10.1016/j.actamat.2014.02.021.

[20] D. Ma, M. Friák, J. Von Pezold, J. Neugebauer, and D. Raabe, "Ab initio study of compositional trends in solid solution strengthening in metals with low Peierls stresses," *Acta Mater.*, vol. 98, pp. 367–376, 2015, doi: 10.1016/j.actamat.2015.07.054.

[21] G. P. M. Leyson, W. A. Curtin, L. G. Hector, and C. F. Woodward, "Quantitative prediction of solute strengthening in aluminium alloys," *Nat. Mater.*, vol. 9, no. 9, pp. 750–755, 2010, doi: 10.1038/nmat2813.

[22] X. Li, Y. Wei, W. Yang, and H. Gao, "Competing grain-boundary- and dislocation-mediated mechanisms in plastic strain recovery in nanocrystalline aluminum," *Proc. Natl. Acad. Sci. U. S. A.*, vol. 106, no. 38, pp. 16108–16113, 2009, doi: 10.1073/pnas.0901765106.

[23] Y. K. Kim, H. K. Kim, W. S. Jung, and B. J. Lee, "Atomistic modeling of the Ti-Al binary system," *Comput. Mater. Sci.*, vol. 119, pp. 1–8, 2016, doi: 10.1016/j.commatsci.2016.03.038.

[24] Q. X. Pei, M. H. Jhon, S. S. Quek, and Z. Wu, "A systematic study of interatomic potentials for mechanical behaviours of Ti-Al alloys," *Comput. Mater. Sci.*, vol. 188, no. August 2020, p. 110239, 2021, doi: 10.1016/j.commatsci.2020.110239.

[25] F. Zhao, J. Zhang, C. He, Y. Zhang, X. Gao, and L. Xie, "Molecular dynamics simulation on creep behavior of nanocrystalline tial alloy," Nanomaterials, vol. 10, no. 9, pp. 1–13, 2020, doi: 10.3390/nano10091693.

[26] S. Plimpton, "Computational limits of classical molecular dynamics simulations," *Comput. Mater. Sci.*, vol. 4, no. 4, pp. 361–364, 1995, doi: 10.1016/0927-0256(95)00037-1.

[27] A. Stukowski, "Visualization and analysis of atomistic simulation data with OVITO-the Open Visualization Tool," *Model. Simul. Mater. Sci. Eng.*, vol. 18, no. 1, 2010, doi: 10.1088/0965-0393/18/1/015012.

[28] S. Mojumder, A. Al Amin, and M. M. Islam, "Mechanical properties of stanene under uniaxial and biaxial loading: A molecular dynamics study," *J. Appl. Phys.*, vol. 118, no. 12, 2015, doi: 10.1063/1.4931572.

Paper ID: 8009

International Conference on Mechanical, Manufacturing and Process Engineering (ICMMPE – 2022)

Organizer: Faculty of Mechanical Engineering, Dhaka University of Engineering & Technology (DUET), Gazipur, Bangladesh

Website: https://icmmpeduet.com/

Selection of Air Compressor for Pharmaceuticals: An Approach with TOPSIS

Md. Tanvir Siraj[1], Noor A Masqur Islam[2], Rafsan Ahmed[3], Md Faiaz Al Islam[4], Md Saiful Islam[5], Asif Kabir[6], Md. Shariful Alam Emon[7]

[1]Department of Industrial and Production Engineering, BUET, Dhaka-1000, Bangladesh
[2]Department of Electrical and Electronic Engineering, AIUB, Dhaka-1229, Bangladesh
[3,4,5,6]Department of Mechanical Engineering, BUET, Dhaka-1000, Bangladesh
[7]Department of Mechanical Engineering, DUET, Gazipur-1707, Bangladesh

E-mail: tanvir25392@gmail.com[1]

ABSTRACT

Air compressor is one of the most essential utility machines for the pharmaceutical industry. Ensuring the engineering parameters of the industrial compressor as well as maintaining the hygiene standard of the air at the same time is a complex task. This often creates a decision-making challenge while selecting an air compressor for a pharmaceutical factory. Therefore, this study discusses the most important selection criteria of an air compressor to be used in the pharmaceutical industry. Among all the criteria, 7 measurable criteria have been sorted out to be utilized in a Multi-Criteria Decision Making (MCDM) technique, the Technique for Order Performance by Similarity to Ideal Solution (TOPSIS) method. In this study, electricity consumption, free air delivery, maximum working pressure, noise level, installation surface area, oil content in the air, and solid particulate filter have been taken as criteria in the case study of selecting the best compressor. Among the 5 alternatives, compressor A4 has obtained the most performance score by the TOPSIS method, thereby finally selected in this study. The discussion about the selection criteria of air compressors for pharmaceuticals and the selection framework presented by utilizing the TOPSIS method is expected to help the industrial managers of pharmaceuticals to overcome their decision-making challenges of compressor selection.

Keywords: Pharmaceutical; Air Compressor; Technique for Order Performance by Similarity to Ideal Solution

1. INTRODUCTION

Production processes in the pharmaceutical industry are highly dependent on the compressed air system. There are a series of operations with a pneumatic system where compressed air is required as instrumentation air. Air is required in manufacturing tablets, capsules, ointments, gels, creams, and syrups. Some other processes like bottling, canning, conveying, or packaging use compressed air as well. For various fermentation processes in pharmaceuticals, sterile air is applied to aerate a fermenter. Air quality for all the processes mentioned here is highly regulated with various strict quality parameters as those processes are directly related to public health issues [1], [2]. Moreover, a compressed air system is the most energy-consuming system in a factory which is directly related to the production cost [3]. Therefore, the selection of air compressors for a pharmaceutical factory is a critical decision for industrial managers.

Several studies in the literature discussed various characteristics and aspects of industrial air compressors. For instance, comparative analysis of energy consumption characteristics of compressors and other utility systems of the industry have been reviewed and discussed [3]; how a variable speed drive (VSD) is more energy efficient over a fixed speed drive (FSD) in case of an air compressor has been analyzed [4]; selection of the optimal location for installing a compressor to achieve the minimum air loss and the maximum effectivity has been depicted [5]; an innovative way of removing moisture from the compressed air has been presented [6]; the importance of multi-stages and intercooler system in an air compressor has been discussed by proposing a modified design [7]; oil-free air compressor is modeled by using water as the lubricant fluid [8], and so on. Some other works in literature depicted air compressor selection procedures to meet specific purposes. For example, four important criteria- air volume, air quality, downtime, and physical characteristics are described to select an air compressor [9]; MCDM techniques have been applied to select an air compressor for a textile and a marine vessel [10], [11]. However, no study has been conducted yet to assist the industrial managers of the pharmaceuticals to select air compressors to fulfill their specific requirements. Therefore, this study is going to discuss various requirements or criteria for a pharmaceutical factory before selecting a compressor. Later, by analyzing some measurable or objective criteria, a case study of compressor selection by utilizing the TOPSIS method is going to be presented.

TOPSIS is a well-known MCDM technique proposed by Yoon and Hwang in 1981 [12]. The concept of this method in short is, the selected alternative should exist at the shortest Euclidean distance from the positive ideal solution (PIS) and the farthest Euclidean distance from the negative ideal solution (NIS). TOPSIS has been used in different selection-related problems in recent studies like, prominent student selection [13], industrial hazard prioritization [14], supplier

selection [15], laptop selection [16], material selection [17], and so on. However, no study has utilized the TOPSIS method to propose a compressor selection framework for the pharmaceuticals industry. Therefore, this study aims to contribute to the literature by addressing the following specific objectives:

a) To discuss the most important technical criteria to select air compressors for pharmaceuticals.
b) To sort out some critical objective criteria to be utilized in the TOPSIS method.
c) To present a case study of compressor selection for pharmaceuticals by the TOPSIS method.

The rest of the paper is organized as: Section 2 is for discussing different criteria of compressor selection for pharmaceuticals, Section 3 is for describing the TOPSIS method, Section 4 is for presenting a numerical case study, Section 5 is for results and discussions, and Section 6 is for a conclusion of the paper.

2. AIR COMPRESSORS SELECTION CRITERIA FOR PHARMACEUTICALS

For this study, some of the basic information about the already existing air compressors in 10 renowned pharmaceutical factories of Bangladesh have been collected. Those can be found in Table 1.

Hygiene standards are very stringent in the overall product processing of pharmaceuticals [1], [2]. Therefore, it is a prior requirement to ensure the manufacturing and processing environment free of particles, and germs as well as contaminating oils. A compressor is an essential machine for the pharmaceuticals industry. The compressed air often comes into direct contact with the product in a manufacturing process. Therefore, it is also subjected to strict regulations such as being oil-free and sterile [18]. Besides this, there are some fundamental criteria for selecting industrial air compressors in any industry that can be applicable for pharmaceuticals as well [9], [10], [11], [19]. Some of the most essential criteria for selecting an air compressor are going to be discussed in this section.

Energy consumption by compressed air systems can be identified as the most important criterion for compressor selection. More than 75% of the life-cycle cost for a compressor is consumed as operating power, whereas the initial price or the maintenance cost is comparatively very little concerning for the management before selecting an air compressor [3]. For energy-saving purposes, VSD is always suggested over the FSD [4]. The machinery of a manufacturing plant is not operated with the same load during all the production hours, thus varying air consumption from time to time. A VSD system can save energy in such situations.

Outlet pressure as well as the maximum volumetric airflow rate (free air delivery) of a compressor play a vital role in selection [10], [11]. These criteria are important to maintain the required air volume by the system with proper sustainability [9]. Reciprocating and rotary-screw, are two main types of compressors to be used in industries. Among these two, screw compressors are preferred over reciprocating compressors for continuous operation for a long period [9].

Compression ratio is an important criterion to decide about the compression stages of a compressor. The higher the compression ratio is, the more the operating stages are required [19]. At the same time intercooler within the stages will be needed to get more efficient performance from a compressor [7].

The installation location of a compressor is another critical decision to be taken for achieving maximum efficiency [5]. Therefore, the accumulated surface area of a compressor can be considered as an important criterion before selection. The compactness of the packaging is always desirable.

The lubrication system of a compressor is another important feature, especially when it needs to decide for a pharmaceutical factory. Oil-free compressors are always preferred over oil-injected compressors in pharmaceuticals [8], [19]. Besides oil contamination, moisture and other particles in the compressed air should also be considered before compressor selection [6]. An installed dryer with the compressor can be an effective solution for moisture removal from the compressed air.

Table 1: Gathered information about compressors from 10 renowned pharmaceuticals factories of Bangladesh

	Electricity consumption per compressor (KW)	Maximum working pressure (Bar)	Number of Compressors	Type	Lubrication	Cooling system
Factory 1	258	10	5	Rotary screw	Oil-free	Water-cooled
Factory 2	258	13	4	Rotary screw	Oil-free	Air-cooled
Factory 3	258	10	5	Rotary screw	Oil-free	Air-cooled
Factory 4	160	13	2	Rotary screw	Oil-free	Air-cooled
Factory 5	250	10	4	Rotary screw	Oil-free	Air-cooled
Factory 6	250	13	4	Rotary screw	Oil-free	Water-cooled
	258	10	3	Rotary screw	Oil-free	Air-cooled
	160	13	2	Rotary screw	Oil-free	Air-cooled
Factory 7	250	13	5	Rotary screw	Oil-free	Air-cooled
Factory 8	258	13	4	Rotary screw	Oil-free	Water-cooled
Factory 9	250	13	1	Rotary screw	Oil-free	Air-cooled
Factory 10	55	10	1	Rotary screw	Oil-injected	Air-cooled
	75	3	3	Rotary screw	Oil-injected	Air-cooled

Physical and operational characteristics like the noise level of the running machine and the cooling system should also be taken into account for selecting an air compressor [9]. If the noise level is very high, then it will create an auditory hazard for the operators. Choosing the cooling system depends on the surroundings of the machine. The air-cooled compressor can be selected if the installation place is not very congested, whereas the water-cooling system requires a water treatment facility [19].

Another important criterion is the downtime of the selected compressor that can be considered [9]. Preventive maintenance, scheduled maintenance, service availability, spare parts availability, reliability of the machine, etc. are related to describing this criterion [10], [11]. These are often dependent on the subjective judgment of the decision-maker.

This study is going to consider some measurable or objective criteria to be analyzed mathematically by the TOPSIS method to present a case study of compressor selection for a pharmaceutical factory. The predetermined features of the compressor are rotary-screw type, oil-free, air-cooled, and VSD operated. In this regard, a summary of the nominated criteria with their unit of measurement (UOM) for depicting a simplified selection framework by the TOPSIS method can be found in Table 2. For the selection of the compressor, some criteria are desired to be with higher performance values, those are known as beneficial criteria. Some criteria are desired to be with lower performance values, those are known as non-beneficial criteria.

Table 2: Air compressor selection criteria for the pharmaceutical industry

Criteria	UOM	Type
Electricity consumption (C1)	KW	Non-beneficial
Free air delivery (C2)	m^3/h	Beneficial
Maximum working pressure (C3)	Bar	Beneficial
Noise level (C4)	dB	Non-beneficial
Installation surface area (C5)	m^2	Non-beneficial
Oil content in the air (C6)	mg/m^3	Non-beneficial
Solid particulate filter (C7)	µm	Non-beneficial

3. TOPSIS METHOD

TOPSIS method can be used to select the best alternative among multiple alternatives by evaluating with some selected criteria. The details method [12] are shown below:

Step 1. Form the initial decision matrix as shown in Equation (1).

$$D = \begin{array}{c|cccc} & C1 & C2 & \dots & Cj \\ A1 & X_{11} & X_{12} & \dots & X_{1j} \\ A2 & X_{21} & X_{22} & \dots & X_{2j} \\ \dots & \dots & \dots & \dots & \dots \\ \dots & \dots & \dots & \dots & \dots \\ Ai & X_{i1} & X_{i2} & \dots & X_{ij} \end{array}_{m \times n} \quad (1)$$

Here, Ai denotes the alternatives and Cj denotes the evaluating criteria. There are *m* alternatives and *n* criteria.

Step 2. Normalize the decision matrix by the formula of vector normalization shown in Equation (2).

$$\bar{X}_{ij} = \frac{x_{ij}}{\sqrt{\sum_{j=1}^{m} x_{ij}^2}} \quad (2)$$

Step 3. Determine the PIS by Equation (3) and NIS by Equation (4) for the beneficial criteria.

$$V_j^+ = \max(X_{1j}, X_{2j}, \dots, X_{ij}) \quad (3)$$

$$V_j^- = \min(X_{1j}, X_{2j}, \dots, X_{ij}) \quad (4)$$

For the non-beneficial criteria, PIS will be determined by Equation (5) and NIS will be determined by Equation (6).

$$V_j^+ = \min(X_{1j}, X_{2j}, \dots, X_{ij}) \quad (5)$$

$$V_j^- = \max(X_{1j}, X_{2j}, \dots, X_{ij}) \quad (6)$$

Step 4. Determine the Euclidean distance of the normalized values from the PIS with Equation (7) and NIS with Equation (8).

$$S_i^+ = \sqrt{\sum_{j=1}^{n} (\bar{X}_{ij} - V_j^+)^2} \quad (7)$$

$$S_i^- = \sqrt{\sum_{j=1}^{n} (\bar{X}_{ij} - V_j^-)^2} \quad (8)$$

Step 5. Compute the performance scores of the alternatives with Equation (9)

$$P_i = \frac{S_i^-}{S_i^+ + S_i^-} \quad (9)$$

Step 6. Select the best alternative by generating a ranking with descending order of the performance scores.

4. A NUMERICAL EXAMPLE

A pharmaceutical company is going to install a new compressor for their manufacturing plant. There are 5 alternatives from which one compressor will be selected. The offered features by the compressor brands according to the required criteria by the factory management can be found in Table 3. This will also stand for the initial decision matrix.

Table 3: Initial decision matrix formed by the offered features of the alternatives

	C1	C2	C3	C4	C5	C6	C7
A1	355	63.1	7.5	73	12.18	0.005	0.10
A2	400	66.6	8.5	74	12.65	0.009	0.05
A3	450	68.8	10	75	12.85	0.007	0.03
A4	400	70.6	7.5	74	12.72	0.004	0.04
A5	500	64.2	13	76	13.40	0.004	0.10

Here, alternatives are denoted by A1 to A5 and selection criteria are denoted by C1 to C7.

The calculated normalized matrix from the initial decision matrix is shown in Table 4. The initial decision matrix is formed by the parameters of different criteria. The measuring units of those parameters are also different. Therefore, normalization is necessary to achieve unitless and comparable values for all the different criteria with different parameters.

Table 4: Normalized matrix

	C1	C2	C3	C4	C5	C6	C7
A1	0.375	0.423	0.352	0.439	0.427	0.366	0.632
A2	0.422	0.446	0.399	0.445	0.443	0.658	0.316
A3	0.475	0.461	0.469	0.451	0.450	0.512	0.190
A4	0.422	0.473	0.352	0.445	0.446	0.293	0.253
A5	0.527	0.430	0.610	0.457	0.469	0.293	0.632

Here, the values under C2 and C3 criteria are beneficial, and the values under C1, C4, C5, C6, and C7 are non-beneficial criteria (see Table 2). The PIS and the NIS values obtained from the normalized matrix are shown in Table 5.

Table 5: Obtained PIS and NIS

PIS	0.375	0.473	0.610	0.439	0.427	0.293	0.190
NIS	0.527	0.423	0.352	0.457	0.469	0.658	0.632

Computed Euclidean distance from the PIS and the NIS for the 5 alternatives can be found in Table 5.

Table 5: Euclidian distance from PIS and NIS

	S_i^+	S_i^-
A1	0.520	0.333
A2	0.445	0.339
A3	0.281	0.486
A4	0.271	0.540
A5	0.473	0.448

Calculated performance scores and the obtained ranking of the alternatives from the descending order of the performance scores are shown in Table 6. Later, Fig. 1 is presenting a comparison chart of the alternatives based on the distances from PIS and NIS and also with the obtained performance scores.

Table 6: Ranking of the alternatives

	Scores	Ranking
A1	0.391	5
A2	0.432	4
A3	0.634	2
A4	0.666	1
A5	0.486	3

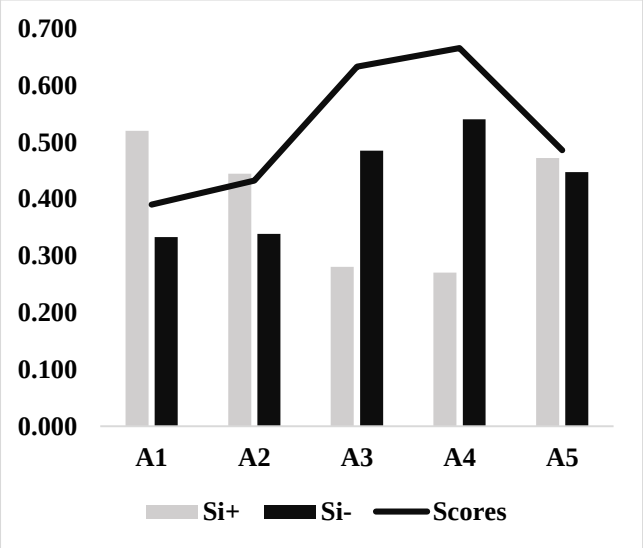

Fig. 1: Comparison of the alternatives

5. RESULTS AND DISCUSSIONS

The obtained performance scores by the 5 alternative compressors in this study as A4 (0.666)> A3(0.634)> A5(0.486)> A2(0.432)> A1(0.391). Compressor A4 has achieved the optimum scores in all the criteria, thus existing at the minimum distance from the PIS and the maximum distance from the NIS (see Fig. 1).

For having a clear overview of this result, the best (A4) and the worst (A1) alternatives can be compared. From Table 2, compressor A4's electricity consumption is 400 KW, free air delivery rate is 70.6 m^3/h, maximum working pressure is 7.5 Bar, produced noise level is 74 dB, required installation surface area is 12.72 m^2, oil content in the outlet air is 0.004 mg/m^3, and the mesh size of the solid particulate filter is 0.04 µm. Whereas compressor A1's electricity consumption is 355 KW, free air delivery rate is 63.1 m^3/h, maximum working pressure is 7.5 Bar, produced noise level is 73 dB, required installation surface area is 12.18 m^2, oil content in the outlet air is 0.005 mg/m^3, and the mesh size of the solid particulate filter is 0.10 µm.

Here it is seen that compressor A1 is comparatively better in 3 criteria than compressor A4 (electricity consumption, noise level, and installation surface area), equal in 1 criterion (maximum working pressure), and worse in 3 criteria (free air delivery, oil content in the air, and solid particulate filtering). The importance of achieving an optimum score in each criterion to get a better performance score by the TOPSIS method can be understood from this example.

This study has not considered different weights of the criteria. For this, all the criteria have achieved similar importance while calculating. If different criteria weights were assigned, the obtained result could be different. Weight assigning for the criteria needs subjective judgment of the decision-makers, and some other weights calculating MCDM techniques need to be utilized with the TOPSIS in a combined approach.

6. CONCLUSION

This study has discussed different selection criteria of the industrial air compressors to be used in the pharmaceuticals industry. An MCDM approach utilizing the TOPSIS method has also been presented to achieve a selection framework. The pharmaceuticals industry is highly sensitive to the hygiene issue. Therefore, it is required to maintain standard air quality as well as the engineering parameters of the selected compressors. In this situation, this study has considered some engineering parameters of the compressor, at the same time taken some air quality parameters as the selection criteria of the compressor. Industrial managers of the pharmaceutical factories can be benefitted from the presented framework of compressor selection, thus overcoming their challenge of balancing between the engineering parameters and the air quality

There are some in the conducted study. The selection framework has only utilized the TOPSIS method for selecting the best alternative. However, the criteria were not weighted as per their prioritization. Whenever there are several criteria for making a decision, all the criteria do not carry the same weight to the decision-makers. They impose various weights on the criteria to make their decision more accurate and object-oriented. For achieving the weights of the criteria, there are several techniques in the MCDM approach. Some approaches are based on the subjective judgment of the decision-makers, whereas weights in some techniques are obtained from the objective values of the alternatives in different criteria. The Analytic Hierarchy Process (AHP), the Best Worst Method (BWM), the Stepwise Weight Assessment Ratio Analysis (SWARA), etc. are some of the popular MCDM techniques to find the criteria weights by the subjective judgment of the decision-makers. The Entropy method, the Mean Weight method, the Standard Deviation method, the Criteria Importance Through Inter criteria Correlation (CRITIC) method, etc. are some of the popular MCDM techniques to find the criteria weights by the objective values of the alternatives. This study did not involve any decision-makers to prioritize the weights of the criteria, or any objective weighting techniques. The hybridization of any of the criteria weighting methods with the TOPSIS method can make the decision-making framework more accurate.

In future studies, criteria weights can be determined. Some other criteria that have been discussed but not utilized in the TOPSIS framework can also be utilized in the future work of compressor selection. This study only utilized the measurable criteria. However, non-measurable criteria like brand reliability, performance, service providing, were not included in the decision-making framework. In the future, these criteria can also be included to be evaluated by the subjective judgment of the decision-makers.

REFERENCES

[1] World Health Organization. Quality assurance of pharmaceuticals: a compendium of guidelines and related materials; vol. 1. World Health Organization, 1997.

[2] World Health Organization. Quality assurance of pharmaceuticals: a compendium of guidelines and related materials. Good manufacturing practices and inspection. Vol. 2. World Health Organization, 2007.

[3] Saidur, R., Rahim, N.A. and Hasanuzzaman, M., A review on compressed-air energy use and energy savings. Renewable and sustainable energy reviews, 14(4), pp.1135-1153, 2010.

[4] Mousavi, S., Kara, S. and Kornfeld, B., Energy efficiency of compressed air systems. Procedia Cirp, 15, pp.313-318, 2014.

[5] Zahlan, J. and Asfour, S., A multi-objective approach for determining optimal air compressor location in a manufacturing facility. Journal of Manufacturing Systems, 35, pp.176-190, 2015.

[6] Goodarzia, G., Dehghani, S., Akbarzadeh, A. and Date, A., Energy saving opportunities in air drying process in high-pressure compressors. Energy Procedia, 110,pp.428-433, 2017.

[7] Gurnule, S. and Banpurkar, R., Design Modification & Analysis of Industrial Air Compressor (Type: VT4). Int. J. Mech. Eng, 5(5), pp.12-18, 2018.

[8] Wang, C., Xing, Z., Chen, W., Yang, Q. and He, Z., Development of an oil free water-lubricated twin-screw air compressor. Applied Thermal Engineering, 143, pp.396-402, 2018.

[9] Greenough, G., Selecting a compressed air system. Metal Finishing, 98(6), pp.398-400, 2000.

[10] Kundakcı, N. and Işık, A., Integration of MACBETH and COPRAS methods to select air compressor for a textile company. Decision Science Letters, 5(3), pp.381-394, 2016.

[11] Kaya, A., Başhan, V. and Ust, Y., Selection of marine type air compressor by using fuzzy VIKOR methodology. Proceedings of the Institution of Mechanical Engineers, Part M: Journal of Engineering for the Maritime Environment, 236(1), pp.103-112, 2022.

[12] Hwang, C.L. and Yoon, K., Methods for multiple attribute decision making. In Multiple attribute decision making (pp. 58-191). Springer, Berlin, Heidelberg, 1981.

[13] Siregar, V.M.M., Sonang, S., Purba, A.T., Sugara, H. and Siagian, N.F., February. Implementation of TOPSIS Algorithm for Selection of Prominent Student Class. In Journal of Physics: Conference Series (Vol. 1783, No. 1, p. 012038). IOP Publishing, 2021.

[14] Bari, A. M., Siraj, M. T., Paul, S. K., & Khan, S. A., A hybrid multi-criteria decision-making approach for analyzing operational hazards in Heavy Fuel Oil-based power plants. Decision Analytics Journal, 100069, 2022.

[15] Cakar, T. and Çavuş, B., Supplier selection process in dairy industry using fuzzy TOPSIS method. Operational Research in Engineering Sciences: Theory and Applications, 4(1), pp.82-98, 2021.

[16] Goswami, S.S. and Behera, D.K., Best laptop model selection by applying integrated AHP-TOPSIS methodology. International Journal of Project Management and Productivity Assessment (IJPMPA), 9(2), pp.29-47, 2021.

[17] Yang, W.C., Chon, S.H., Choe, C.M. and Yang, J.Y., Materials selection method using TOPSIS with some popular normalization methods. Engineering Research Express, 3(1), p.015020, 2021.

[18] ISO 8573–1:2010. Compressed air — Part 1: Contaminants and purity classes, 2010.

[19] Ron, C., 6 Things to Evaluate Before Selecting an Industrial Compressor. Pumps and Systems Magazine. https://www.pumpsandsystems.com/6-things-evaluate-selecting-industrial-compressor, April 24, 2020.

Paper ID: 8137

International Conference on Mechanical, Manufacturing and Process Engineering (ICMMPE – 2022)

Organizer: Faculty of Mechanical Engineering, Dhaka University of Engineering & Technology (DUET), Gazipur, Bangladesh

Website: https://icmmpeduet.com/

Analytical Solution of Vibration of Simply Supported Beam under Eccentric Axial Compressive Loading

Rafsan Ahmed[1], Md Faiaz Al Islam[2], Sheikh Navid Shadab Jamil[3], Md. Saiful Islam[4], Asif Kabir[5] and Md. Jahangir Alam[6]

[1, 2, 3, 4,5]Department of Mechanical Engineering, BUET, Dhaka-1000, Bangladesh
[6]Department of Mechanical Engineering, DUET, Gazipur, Bangladesh

E-mail: ahmedniloyrafsun85@gmail.com[1]

ABSTRACT

A Pushrod is acting as a slender beam under axial loading and has a variety of applications, like in the automobile industry. For study purposes, a pushrod has been considered which is made of a super elastic shape memory alloy of a circular cross-section. The behavior of the pushrod is scrutinized during the applied force of vibration acting uniformly and eccentrically upon it. These dynamic loadings render a significant impact on its elastic behavior and a constructive formula for the deflection of the beam from its neutral axis is introduced. With this equation, the elastic curve deviations from its initial position are analyzed and its response to the increase in the number of modes is evaluated. The deflection of the beam is highest when the mode number is 1 and with the raise of modal shapes, the deflection tends to get decreased. A comparison with the static beam under affiliated force depicts that the deflection escalates in the beam under dynamic loading. With the change of force functions, different deflection curves have been calculated and from their comparison, the characteristics of this slender pushrod have divulged its other features too. For engineering structure study and design, vibration analysis has been marked as a must-to-do list.

Keywords: Pushrod; Super Elastic Shape Memory Alloy; Dynamic Loadings; Elastic Behavior.

1. INTRODUCTION

Both a beam and a column are continuous structures and are incorporating multi-degree freedom systems. These can be treated using discrete mass and stiffness parameters but such a model is insufficiently precise for most purposes because an infinite number of numerical values have to be needed. Additionally, creating a wall of separation between mass and elasticity cannot be always possible using pragmatic models. As a result, mass and elasticity must be deemed as dispersed characteristics. Generally, when analyzing structures with dispersed mass and elasticity, it is imperative to presume a homogeneous, isotropic material where Hooke's law is applied so that wave propagation on the structure body has to be considered from its neutral axis. Usually, free vibration is equal to the sum of the main modes. Only one of the principal modes has to be awakened if the elastic curve of the body in which motion is excited coincides exactly with one of the principal modes. The general formula of continuous systems, including the lateral vibration of beam is stemmed from considering the free-body diagram of an infinitesimally small element of the particular system and applying Newton's second law of motion. The resulting governing formula has to be generated in a form of the partial differential equation. The free vibration solution of the system can be generated by positing harmonic motion and applying the pertinent boundary conditions.

The response of the beam when computing its natural frequencies under no axial load can be calculated by applying boundary conditions to analytical formulas. If the axial load is tensile, it inclines to increase the natural frequency; if the force is compressive, it tends to decrease it. It can be estimated using established formulas to their relevant slenderness ratios. However, when the beam is under particular moments at both ends due to eccentric axial force, only applying boundary conditions doesn't reckon us the solution of the natural frequencies. So other methods of solving natural frequencies have to be introduced to provide a relation between the deflection of the beam and the vibration-induced. A reasonable illustration of vibration will be gotten analysis from this relation.

Lateral vibrations of the simply supported beam under axial compressive load and other different force functions have created substantial practical interests. Widespread usage of them in the mechanical, civil, and aircraft industries is influenced by their broad-ranging applications. For example, it is frequently crucial to recognize the inherent frequencies and mode forms of beam-type elements that are exposed to pre-stress in the design of some spacecraft structural components (such as wings). Another instance is

the influence of compressive pressures such as fluid pressure on nuclear fuel reactor rod pins. Pushrods in autos, on the other hand, act like simply supported beams when subjected to axial loads. Outside loading is also applied to tie rods in the steering system, which can have a significant impact on its structural body.

The research aims to deal with determining the deflection of the simply supported beam which is subjected to under eccentric axial compressive load on both its ends so that the propagation of elastic curves of the structure can be exhibited. That's why an extensive and methodical illustration of vibration analysis is necessary.

This research was initiated by generating a governing equation of the beam according to the trait of the loads acting upon it by using the Bernoulli-Euler equation. A general formula was constructed by using the partial differential equation. The model has to be ready by then to develop the expression of the deflection equation of the beam where the constant coefficients are determined from given initial boundary conditions. The formula is assumed to be amenable for the evaluation of any mode numbers. The illustration of the displacement of the structure from its natural axis is presented along with a different number of mode shapes. The comparison between the resultant deflections due to dynamic vibration with the corresponding static deflection is exhibited along with a comprehensive study and analysis.

2. LITERATURE REVIEW

An analytical solution of vibration of pushrod has been expected to establish. Numerous amounts of research are trying to deal with the deflection of this kind of beam structure as engineering structural prospects are largely dependent on vibration analysis.

The effect of end circumstances on the transverse frequencies of uniform straight simply supported beam under axial loading was explored by Amba Rao et al. [1]. Based on Amba-Rao's research, Galef et al. developed a correlation between the natural frequency of compressed and uncompressed beams [2]. It constructed a linear relationship between ω^2 and axial loadings applied to the beam. This relationship was further contemplated and used subsequently by Pilkington et al. to find the approximate solution of vibration of beams under terminal and axially distributed loading [3] Jacket structures composed of welded tubular space frames supported by a lateral bracing system were studied by Mia et al. [4]. However, in Galef's study, numerical results were computed using non-dimensional applications, which could make engineering circumstances more challenging.

After then, Bokaian et al. came up with a solution to these major restrictions. He looked examined how continual compressive stresses affected the natural frequencies and mode shapes of a uniform beam under a range of end conditions [5]. When the axial load is not larger than the buckling load, the accuracy of Galef's equation is generally acceptable but in the case of slender columns getting shortened, the accuracy will decrease [6]. Bokaian et al. then brought about modified Galef's formula which is dependent on the variations of end conditions so that the application of his coefficient gets priority in solving the analytical problems related to the vibration of structures [7]. Meanwhile, this study is inspired most by Bokaian et al. method of analogy to solve the deflection due to the induced vibration on the beam. He used the partial differential equation to develop a general formula corresponding to the natural frequency of the beam and used boundary conditions to get the exact equation of deflection.

By using the classical Euler-Bernoulli beam theory, the vibrational behavior of a pushrod has been explored. Because the effects of transverse shear distortion and rotatory inertia have been overlooked, it is unable to adequately explain vibration characteristics at higher modes. As the length of this designed simply supported beam under axial loading is almost 28 times higher than its diameter, the effect of shear deformation can safely be neglected and the rotary inertia on it. Timoshenko et al. explained the short beams which are under the effect of bending, shear deformations, and rotary inertia [8].

Although Euler-Bernoulli beam theory is only applicable for a selected number of continuous systems, in the case of full range axial loadings, its explicit equation gives accuracy to frequency estimation with simpler formulas. In recent times, Bing, Tao et al. developed a microscale Bernoulli–Euler beam model based on the modified gradient elasticity [9]. Binici et al. and Aydin et al. studied the analysis of vibration of the simply supported beam under axial loading under multiple numbers of cracks [10] [11].

The actual motivation has been started after studying Rahman, Hasan, and Nabil et al. where they established a relation of buckling of pushrods made of super-elastic shaped memory alloy [12]. These parameters for design have come from this study. From Rahman et al. [13], the characteristics that the designed simply supported beam under axial loading has occupied became known to us.

3. METHODOLOGY

Axial compressive load P is acting on the simply supported beam eccentrically with the distance of e from its centerline. The steady-state vibration of this beam needs to be determined.

Moment due to axial force P at point A is,

$$M_A = P\,(y+e) \tag{1}$$

According to the Bernoulli-Euler equation for beam, the governing formula of the uniform beam subjected to the axial compressive force acting eccentrically and under no transverse force is stated in Eq. 2 [14]. The method of separation of variables is used to find the solution to the below equation.

$$EI\frac{d^4y}{dx^4} + P\frac{d^2y}{dx^2} + m\frac{d^2y}{dt^2} = 0 \tag{2}$$

The roots of these equations are given by

$$S_1^2, S_2^2 = -\frac{P}{2EI} \pm \sqrt{\frac{P^2}{4E^2I^2} + \frac{m\omega^2}{EI}} \quad (3)$$

The general equation

$$Y(x) = C_1\cosh(S_1x) + C_2\sinh(S_1x) + C_3\cos(S_2x) + C_4\sin(S_2x) \quad (4)$$

From Singer et al. [15], conventional directions along with the signs of moments of a beam get to be known. A bending moment is positive if it produces bending of the beam concave upward. For all negative number of mode shapes in the elastic curves of the simply supported beam, the moment Pe acted on the extreme right section of the beam is always positive. As for all positive number of modes, the moment Pe acted on the extreme right section of the beam is always negative.

These analogies have already been considered for solving the deflection Eq.4. Applying the boundary conditions for the negative number of modes in deflection Eq. 4,

$$C_1 = \frac{Pe}{S_1^2 + S_2^2} \qquad C_3 = -\frac{Pe}{S_1^2 + S_2^2}$$

$$C_2 = \frac{Pe}{S_1^2 + S_2^2}\frac{1-\cosh(S_1l)}{\sinh(S_1l)} \quad C_4 = \frac{Pe}{S_1^2 + S_2^2}\frac{\cos(S_2l)-1}{\sinh(S_2l)} \quad (5)$$

The deflection of a simply supported beam under eccentrically axial compressive load which is showing a negative number of modes.

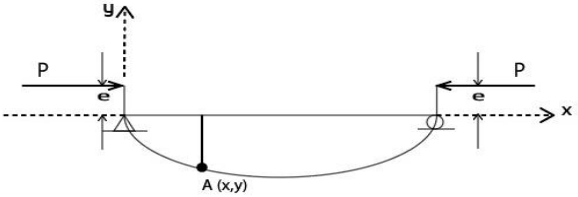

Fig. 1: Free Body Diagram of the simply supported beam under eccentric axial loading

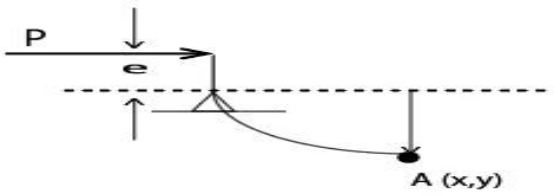

Fig. 2: Free Body Diagram of the section of the simply supported beam

Fig. 3: Boundary conditions due to n =1

$$Y(x) = \frac{Pe}{S_1^2 + S_2^2}\left[\cosh(S_1x) + \frac{1-\cosh(S_1l)}{\sinh(S_1l)}\sinh(S_1x) - \cos(S_2x) + \frac{\cos(S_2l)-1}{\sinh(S_2l)}\sin(S_2x)\right] \quad (6)$$

Applying the boundary conditions for the positive number of modes in deflection Eq. 6,

$$C_1 = \frac{Pe}{S_1^2 + S_2^2} \qquad C_3 = -\frac{Pe}{S_1^2 + S_2^2}$$

$$C_2 = \frac{-Pe}{S_1^2 + S_2^2}\frac{1+\cosh(S_1l)}{\sinh(S_1l)} \quad C_4 = \frac{Pe}{S_1^2 + S_2^2}\frac{\cos(S_2l)+1}{\sinh(S_2l)} \quad (7)$$

The deflection of a simply supported beam under eccentrically axial compressive load which is showing a positive number of modes.

$$Y(x) = \frac{Pe}{S_1^2 + S_2^2}\left[\cosh(S_1x) - \frac{1+\cosh(S_1l)}{\sinh(S_1l)}\sinh(S_1x) - \cos(S_2x) + \frac{\cos(S_2l)+1}{\sinh(S_2l)}\sin(S_2x)\right] \quad (8)$$

For determining the deflection formulas of Eq. 6 and Eq. 8, the values of S_1 and S_2 have to be founded from Eqn. 3, but during the numerical analysis, S_2 has to be derived as a complex function, so the hyperbolic formula of changing a complex function have to be introduced in Eq. 6 and Eq. 8.

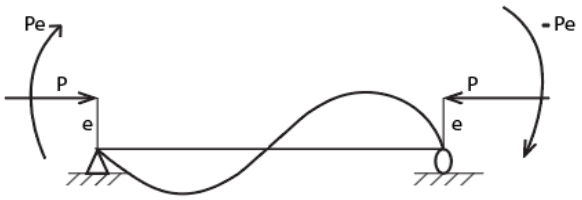

Fig. 4: Boundary conditions due to n =2

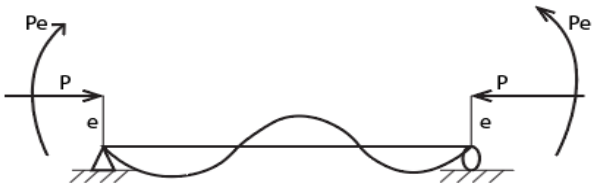

Fig. 5: Boundary conditions due to n =3

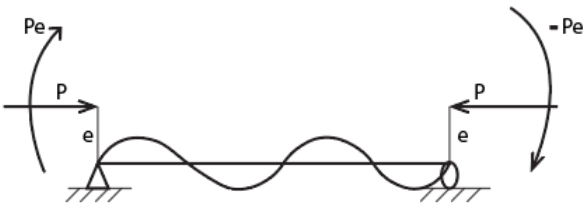

Fig. 6: Boundary conditions due to n =4

$$S_2 = iZ \text{ or, } S_2^2 = -Z^2 \quad (9)$$

$$\cos(ix) = \cosh(x) \text{ and } \sin(ix) = i\sinh(x) \quad (10)$$

Applying these formulas in Eq. 6 and Eq. 8, Deflection formula of negative number of modes,

$$Y(x) = \frac{Pe}{S_1^2 + S_2^2}\left[\cosh(S_1x) + \frac{1-\cosh(S_1l)}{\sinh(S_1l)}\sinh(S_1x) - \cosh(Zx) + \frac{\cosh(Zl)-1}{\sinh(Zl)}\sinh(Zx)\right] \quad (11)$$

Deflection formula of positive number of modes,

$$Y(x) = \frac{Pe}{S_1^2 + S_2^2}\left[\cosh(S_1x) - \frac{1+\cosh(S_1l)}{\sinh(S_1l)}\sinh(S_1x) - \cosh(Zx) + \frac{\cosh(Zl)+1}{\sinh(Zl)}\sinh(Zx)\right] \quad (12)$$

As for the beam under eccentric axial compressive loading, static methodology for determining the deflection has been considered according to the "Mechanical Engineering Design" book [16].

$$Y(x) = e\left[\tan\left(\frac{l}{2}\sqrt{\frac{P}{EI}}\right)\sin\left(x\sqrt{\frac{P}{EI}}\right) + \cos\left(x\sqrt{\frac{P}{EI}}\right) - 1\right] \quad (13)$$

Another numerical analysis has been done between Eq. 11 and Eq. 13 respectively for the dynamic and static deflections of the designed beam.

Super-elastic shape memory alloy has been selected as beam material, and considerable length and weight measurements have been taken along with the density of the beam.

Table 1: Dimensions of Beam parameters

Parameters	Symbol	Dimensions
Length	L	0.254 m
Diameter	D	0.009 m
Area	A	6.36173×10^{-5} m^2
Density	ρ	6533 kg/m^3
Mass per unit length	m_s	0.4156115 kg/m
Eccentricity	e	0.002 m
Modulus of Elasticity	E	65 GPa
Moment of Inertia	I	3.2206×10^{-10} m^4

$$\text{Critical Force, } P_{cr} = \frac{\pi^2 EI}{L^2} = 3202.474 \text{ N} \quad (14)$$

Applied Force on beam, $P = 0.8\times P_{cr} = 2561.979$ N.

4. RESULTS AND DISCUSSIONS

The goal of this research is to find a quantifiable relationship between the deformation of a beam under axial compressive force and its lateral length. Because the deformation equations in Eq. 11 for the negative number of modes and Eq. 12 for the positive number of modes have already been learned, this has to aid in viewing the beam deflection curve when it deviates from its neutral axis.

One important problem arises concerning to generation of the curves as the natural frequency (ω_n) of this simply supported beam under axial compressive load was unknown, so for this designed structure, the natural frequency of a beam under no eccentric loading (where Axial forces acting on the centroid of the transverse plane so eccentricity, e = 0) has been considered. The resultant curve has to get deviated from the actual one.

Due to the trivial substitution of axial loading from its major axis to the eccentric axis, the value of natural frequency(ω_n) for the designed beam wouldn't change that much from the standard beam (e=0). Numerical solution for the differential factors S_1^2 & S_2^2 from Eq. 3 had been generated from the value of applied axial force (P), the natural frequency (ω_n), some modes (n), and other parameters. The obtained equation in Eq. 11 and Eq. 12 would finally give the values of deformation of the beam along with lateral length. Finally, a curve deflection of the designed structure had been found to exhibit.

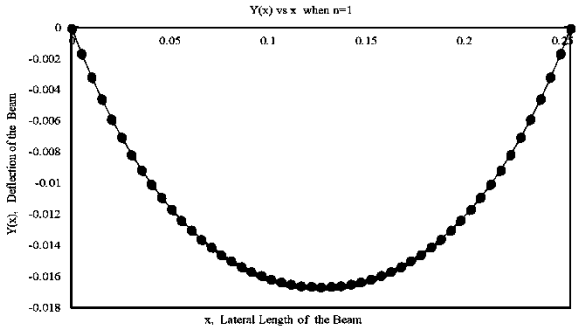

Fig. 7: Deflection of the simply supported beam under eccentric axial compressive force when n = 1

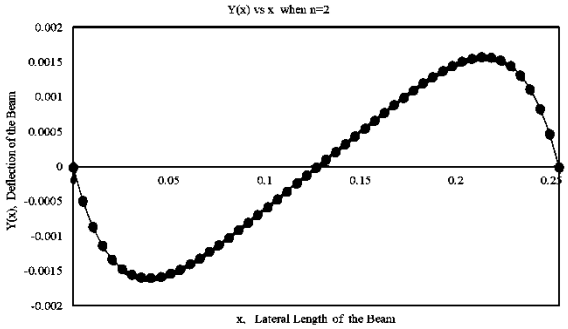

Fig. 8: Deflection of the simply supported beam under eccentric axial compressive force when n = 2

From the deflection curves, when the mode number (n) =1, With the increase of lateral length, the bending moment increases, and the maximum deflection is found at the mid-span of a beam of Fig. 7 which is 16.62mm. The ends used to be under more moments than the midspan. The deflection is quite large due to the applied axial force which is close to the value of the critical loading.

When the mode number (n)=2, the end moments generated by acting forces on the eccentric axis, act on the lateral length beam opposite to each other's direction. This causes 2 modal shapes to appear on the deflection shape of the beam Fig. 8. As for their reversible effects, the deflection of the beam is also affected. The deflection tends to decrease and, in this case, the maximum one is found at 1.588 mm. The mode shapes are identical to each other.

For the applied number of modes (n) = 3, though incidental moments act on both ends, opposite moments generated inside these two moments lead to the beam curved into 3 modal shapes in Fig. 9. The deflection gets decreased as it is largely dependent on in this case of modal analysis, the maximum deflection is 0.7177mm.

In the case of several modes (n) = 4, 4 modal shapes are seemingly apparent in Fig. 10 and the maximum deflection, in this case, is 0.3948 mm.

If the deflection curves of the different number of modes are contemplated and are likely to exhibit a comparison among them, an interesting result has to be provided. The beam (Fig. 1) designed is simply supported at both ends and the line of action of axial compressive force acting upon it is separated by the centroid axis by the eccentricity, e. This causes the beam to be fallen under bending moments at both ends which is creating effects on the beam's deflection and natural frequency.

Terminal bending moments tend to make more deflections in the beam and as this designed beam is also a compression member, buckling phenomena can also have some impressions on beam deflection.

The numerical analysis has been done on the deflection of the beam to its natural frequency (ω_n) under different mode shapes which are shown in Fig. 11.

From the comparison analysis, with the increase of the acting number of mode shapes on the beam, natural frequencies (ω_n) have to change and with them, the particular characteristic shapes of the beam have to be more prominent. Natural frequency (ω_n) has an adverse effect on deflections. Frequency encourages the rise and growth of mode shapes so deflection recedes with the growth of natural frequency and mode shapes on the elastic curve of the simply supported beam.

The direction of bending moments at the ends plays a significant role here. As these start acting reversely to each other, this creates the impacts on deflection shape of the elastic curve and although deflections getting declined, the resonance generated seen on the curve tends to diminish the buckling limit.

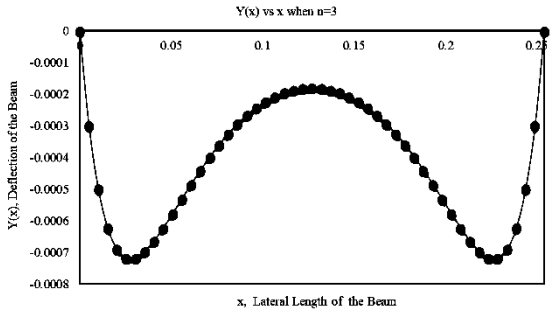

Fig. 9: Deflection of the simply supported beam under eccentric axial compressive force when n = 3

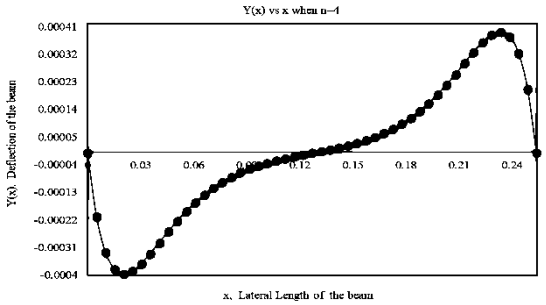

Fig. 10: Deflection of the simply supported beam under eccentric axial compressive force when n = 4

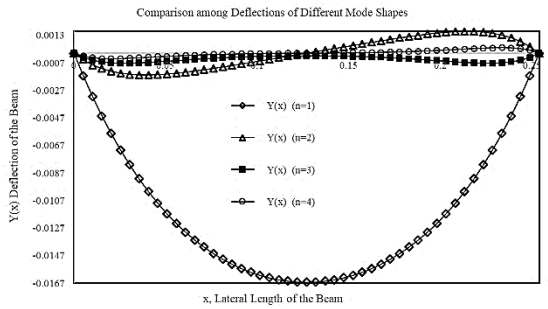

Fig. 11: Comparison among the deflections of the simply supported beam under eccentric axial compressive load

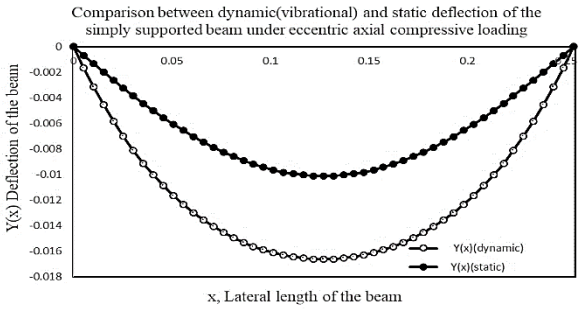

Fig. 12: Comparison between dynamic and static deflection of the simply supported beam under eccentric compressive loading.

From Fig. 12 the maximum deflection in the beam under static loading is 10 mm in mid-span while the beam is 16 mm in mid-span. A force with frequencies creates the inertia which leads to these larger dynamic deflections. Besides, in every lateral point, the beam showed greater deflection than the static simply supported beam under axial loading, this indicates that compared to the natural frequency (ω_n) of the static beam, the natural frequency (ω_n) of this designed (dynamic) beam is relatively smaller as the natural frequency (ω_n) is always adversely proportional to beam deflection. So, the dynamic outside vibrational forces shorten the natural frequency (ω_n) of the beam.

5. CONCLUSIONS AND RECOMMENDATIONS

The analytical solution of the vibration of the simply supported beam under eccentric axial loading has been derived and deflection curves commensurate to several degrees of mode number have been depicted in this course of study. So the findings of this study are:

- Although the natural frequency (ω_n), and modulus of elasticity have been deemed as constant, the result of the deflection almost accurately exhibits the mode shapes implied from the equations developed.
- When the number of modes is 1, the elastic curve of the beam has taken the concave upward shape to its neutral axis.
- With the assimilation of the increased number of modes, the beam has divulged different shapes due to the increase in vibrational loading. When mode number is 2, both concave upward and downward shapes are evident, both incorporate half of the length of the beam and subject both half to equal but reverse bending. In mode number3, a concave downward shape has taken place between two equally distributed concave upward curves. An interesting feature becomes apparent when the number of modes is 4 when concave upward then the downward pattern has repeated two times and terminal upward and downward covers a lot of lengths than their neighboring shape shifting curves.
- The noticeable trait has been found that the deflection decreases with the increasing number of modes from Fig.11.
- Fig 12 vividly describes the differences between static and dynamic deflection and dynamic vibrational loading has more impact on the deflection of the elastic curve than the static one. The maximum static deflection is 0.01012mm while the maximum dynamic deflection is 0.01662mm.

Based on this work, the following deliberations have to be taken for the future.

- Stability analysis will have to be directed to find out the life cycle of the engineering structure.
- As super-elastic shape alloys exhibit non-linear stress-strain characteristics, their exertion on the designed beam will give a more definite result.
- In this study, both modulus of elasticity and buckling are considered constant for super-elastic shape memory alloy. In the future, changes in these parameters can be incorporated into our study.

REFERENCES

[1] Amba-Rao, C. L. (1967). Effect of end conditions on the lateral frequencies of uniform straight columns. The Journal of the Acoustical Society of America, 42(4), 900-901.

[2] Galef, A. E. (1968). Bending Frequencies of The Compressed Beams. Journal of the Acoustical Society of America, 44(8), 643.

[3] Pilkington, D. F., & Carr, J. B. (1970). Vibration of beams subjected to end and axially distributed loading. Journal of Mechanical Engineering Science, 12(1), 70-72.

[4] Mia, Md. J., Islam, Md. A., Kabir, A., & Islam, M. (2022). Numerical Analysis of Tubular XT Joint of Jacket Type Offshore Structures under Static Loading. Bangladesh Maritime Journal (BMJ), 6(1), 299-318,

[5] Bokaian, A. (1988). Natural frequencies of beams under compressive axial loads. Journal of sound and vibration, 126(1), 49-65.

[6] Wei, X., Chen, Q., Xu, S., Peng, L., & Zuo, J. (2009). Beam to string transition of vibrating carbon nanotubes under axial tension. Advanced Functional Materials, 19(11), 1753-1758.

[7] Bokaian, A. (1990). Natural frequencies of beams under tensile axial loads. Journal of sound and vibration, 142(3), 481-498.

[8] Timoshenko, S. P. (1922). X. On the transverse vibrations of bars of uniform cross-section. The London, Edinburgh, and Dublin Philosophical Magazine and Journal of Science, 43(253), 125-131.

[9] Zhao, B., Liu, T., Chen, J., Peng, X., & Song, Z. (2019). A new Bernoulli–Euler beam model based on modified gradient elasticity. Archive of Applied Mechanics, 89(2), 277-289.

[10] Binici, B. (2005). Vibration of beams with multiple open cracks subjected to axial force. Journal of Sound and Vibration, 287(1-2), 277-295.

[11] Aydin, K. (2008). Vibratory characteristics of Euler-Bernoulli beams with an arbitrary number of cracks subjected to axial load. Journal of Vibration and Control, 14(4), 485-510.

[12] Rahman, M. A., Hasan, A., & Nabil, A. I. (2021). Buckling of pushrods made of superelastic shape memory alloy. In AIP Conference Proceedings (Vol. 2324, No. 1, p. 030008). AIP Publishing LLC.

[13] Rahman, M. A., Qiu, J., Tani, J. (2006). Buckling and post-buckling behavior of solid superelastic shape memory alloy shafts. Structural Engineering & Mechanics. 23(4), 339-352.

[14] Thomson, W. T. (1998). Theory of vibration with applications. CrC Press.

[15] Singer, F. L., & Pytel, A. (1962). Strength of Materials, Harper & Row, Publishers. Inc., New York, 31.

[16] Shigley, J. E. (1972). Mechanical engineering design. McGraw-Hill Companies.

Paper ID: 8238
International Conference on Mechanical, Manufacturing and Process Engineering (ICMMPE – 2022)
Organizer: Faculty of Mechanical Engineering, Dhaka University of Engineering & Technology (DUET), Gazipur, Bangladesh
Website: https://icmmpeduet.com/

Trigonella Foenum-Graecum Seeds Extract as a Natural Inhibitor for Mild Steel in HCl Solution

Nayem Hossain[1], Mohammad Asaduzzaman Chowdhury[2], Dewan Muhammad Nuruzzaman[1], A Z A Saifullah[1], Md. Sabbir Ahmed Tulon[1] and Md. Nafijur Rahman[1]

[1]Department of Mechanical Engineering, International University of Business Agriculture and Technology (IUBAT)
Uttara Model Town, Dhaka 1230, Bangladesh
[2]Department of Mechanical Engineering, Dhaka University of Engineering and Technology (DUET)
Gazipur 1700, Bangladesh

E-mail: nuruzzaman.me@iubat.edu

ABSTRACT

Our machines and structures face great threat because of corrosion. Billions of dollars are wasted every year for corrosion damage. Synthetic inhibitors are used to get rid of this fatal damage but these inhibitors are harmful for our environment. Finding a natural solution is a need of time. This research paper intends to find a suitable green inhibitor and that is why Trigonella foenum-graecum has been used in this research to find its suitability as green inhibitor in acidic medium for mild steel. Mild steel samples have been tested to observe the corrosion effect in different media. After 3 days of immersion in inhibited corrosion media, maximum 69.2% corrosion efficiency is observed. For further analysis, scanning electron microscopy (SEM) and fourier transform infrared spectroscopy (FTIR) tests are performed to identify the presence of bands and to observe surface morphology of corroded samples.

Keywords: Trigonella foenum-graecum; Natural inhibitor; Mild steel; HCL.

1. INTRODUCTION

Different elements present in the environment deteriorate the properties of metals by their interactions and make corrosion [1]. Metal corrosion is a bid challenge for world economy as it has already cost USD $2.5 trillion approximately [2]. A report reveals that the indirect cost due to corrosion in USA alone for year 2016 is over $ 1.1 trillion [3]. In order to save the world economy from this devastating effect, several strategies have been adopted including materials selection, coatings and corrosion inhibitor. Corrosion inhibitors are the chemicals that decrease rate of corrosion in aggressive environments and is the most effective among these strategies [4]. Inorganic inhibitors are considered as effective inhibitors for their inhibitive strength but these inhibitors are harmful for human being and natural environment [5]. That is why the search for green inhibitor is on high demand as these inhibitors are not harmful for the environment.

Green inhibitors are derived from the environment and mostly from plants and these inhibitors are abundant in nature and renewable. Green inhibitors usually include drugs, roots, chitosan, yeast, herbs, natural honey, flour, oil, leaves and so on [6]. Report suggest that some green inhibitors are highly effective in different environments as corrosion inhibitor [7]. Oxygen, and nitrogen present in the polar compound and heterocyclic rings, aromatic rings, aliphatic chains and functional moieties present in the non-polar compounds are abundant in plants extracts [8]. The metal surface effectively absorbs these compounds and protect themselves from corrosion without harming environment [9].

The objective of present research is to assess the suitability of Trigonella foenum-graecum seeds extract as green inhibitor for mild steel in hydrochloric acid (HCl) (50 ml) aggressive solution. 7.5g seeds extract powder was mixed with 150 ml HCl and kept in 3 containers. Each container contained 50ml mixture of HCl and Trigonella foenum-graecum seeds powder. Immersing in inhibited corrosion media 69.2% corrosion efficiency was noted. Fourier-transform infrared spectroscopy test and scanning electron test were done to identify any presence of bands and to observe the morphology of the corroded samples.

2. MATERIALS AND METHODS

2.1 Preparation of Sample

Mild steel was collected from local market to perform the experiments and were cut into pieces to make suitable for the experiments. The height of the samples was kept around 18 mm, width around 15 mm and thickness around 2.3 mm (Figure-1). The weight of the samples were measured carefully before doing the corrosion test with the help of a precision electronic balance meter to get accurate weight of each sample.

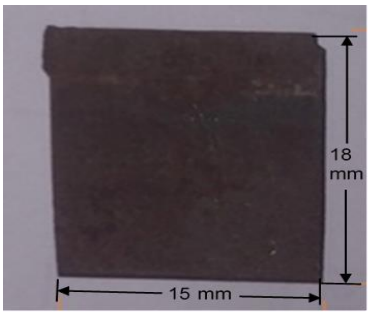

Fig. 1: Mild steel specimen for corrosion test

2.2 Green Solution Preparation

Fresh Trigonella foenum-graecum seeds were collected form the local market so that the green inhibitor can be prepared. At first, the seeds were cleaned firmly using distilled water and then dried. Then, it was blended using a blender mixing with distilled water and fresh juice of Trigonella foenum-graecum seeds is obtained. The juice is then dried and finally the powders are obtained. 0.1 M HCl which has been collected from the chemistry lab has been used as acidic medium. 50ml HCl is kept in 3 containers. Besides, 7.5g Trigonella foenum-graecum seeds powder is mixed with 150ml HCl and kept in other 3 containers where each container contains 50ml mixture of HCl and Trigonella foenum-graecum seeds powder (Figure-2).

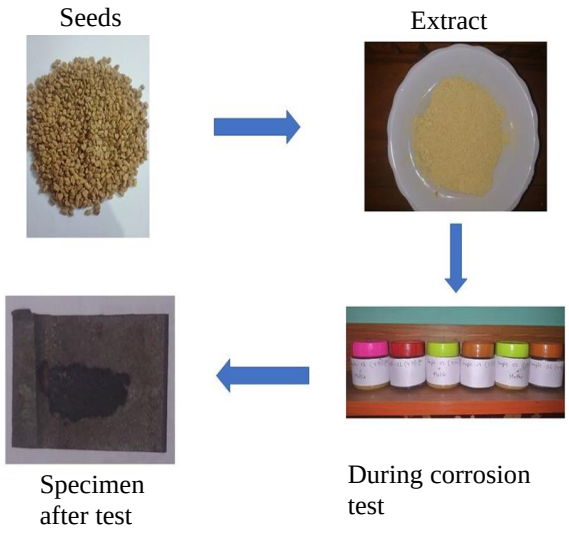

Fig. 2: Working procedure of corrosion test.

2.3 Weight Loss Measurement

After cutting into pieces, each sample weight is measured and noted. The weight of the samples is weighted again after the 3, 5 and 7 days of immersion in both inhibited and uninhibited solution. The rate of corrosion is obtained when the obtained weight after corrosion test is subtracted from the obtained weight before corrosion test. Table 1 represents weight loss data after corrosion test in both uninhibited as well as inhibited solution. To compute corrosion efficiency ($\eta_w\%$), following equation is used [10-11]:

$$\eta w\% = \frac{Wcorr - \mathrm{Wcorr(inh)}}{Wcorr} \times 100 \quad \text{.....(i)}$$

*W*corr is represented as weight loss in uninhibited solution and *W*corr(inh) is represented as weight loss in inhibited solution of the tested mild steel specimen. From this research, maximum 69.2% corrosion efficiency is obtained after 3 days of immersion.

Table-1: Weight loss data of the sample

For three days				
Solution	Weight before corrosion test (g)	Weight after corrosion test (g)	Weight change (g)	Efficiency
Uninhibited solution	4.34	4.21	0.13	69.2%
Inhibited solution	4.19	4.14	0.04	
For five days				
Uninhibited solution	4.21	4.03	0.16	62.5%
Inhibited solution	4.36	4.28	0.06	
For seven days				
Uninhibited solution	4.30	4.12	0.18	55.55%
Inhibited solution	4.35	4.27	0.08	

2.4 Characterization

The morphology of the corroded samples is characterized by FTIR and SEM analysis. FTIR spectrometer made by Perkin Elmer is employed to perform FTIR test in the range from 500 to 4000 cm^{-1}. The microstructure of the corroded surface is analyzed by SEM analysis.

3. RESULTS AND DISCUSSION

3.1 Weight Loss Measurement

Figure 3 and 4 show the comparison of weight loss and weight reduction. Data reveals that uninhibited solution

causes more corrosion compared to inhibited solution. Anodic inhibitor adsorbs the Cl^- produced from HCl and raises the anodic polarization. Films made by protective layer are formed by the polarization that keeps it repaired which in result reduce corrosion rate.

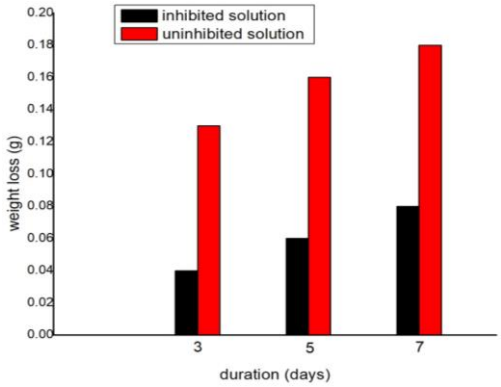

Fig. 3: Weight loss comparison in both inhibited and uninhibited solution.

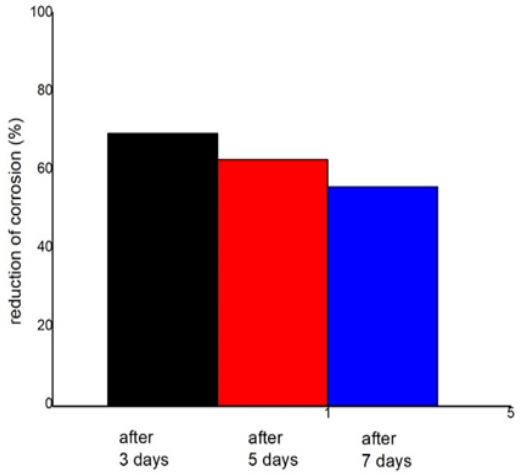

Fig. 4: Corrosion reduction using inhibited solution.

The addition of Trigonella foenum-graecum leaves extract reduces the corrosion rate as this green inhibitor resist the reaction of the media used for material. Following reasons are responsible for decreasing the corrosion rate by the chemical components present in the juice of leaf (i) ions or molecules are adsorbed from the surface of mild steel, (ii) higher cathodic or anodic reaction, (iii) diffusion rate of the reactants reduced on the surface of the mild steel, (iv) electrical resistance of the surface decreased. Different modes of chemical reaction happen with mild steel and HCl with the chemical ingredients of Trigonella foenum-graecum leaf. An obstacle is formed by the extracts of plants to form an obstacle by adsorbing the phytochemical elements and active anions and alloys are segregated in the solution. As a result, cession resistance on mild steel surface increases and corrosion process decreases. The developed insoluble complexes are responsible for the reaction is the reason for corrosion reduction between iron cations, and green inhibitors [12]. The protein present in the plants helps to reduce corrosion by the hydrolysis [13]. The efficiency of natural inhibitors are influenced by different parameters such as time of immersion, potentiality of electrodes, concentration of liquid, pH value of liquid and temperature of the environment observed by Eddy et al. [14]. Adsorption mechanism has connection with free energy as well as activation energy. Effective biocides are available on the surface of plant extract materials that resist bio-corrosion by forming a bio-film [15]. The mechanism of corrosion reduction and the effectiveness of plant extract are also discussed in previous literature [16-20].

3.2 Electrochemical Impedance Spectroscopy

The corrosion behavior of the specimens is evaluated in both uninhibited and inhibited solution at 303 K temperature. Figure 5 represents the Nyquist plots for mild steel. Only one capacitive loop is represented by the obtained impedance diagram. Same trend is obtained from the both solution. The impedance diagram contains a depressed semicircle that has a center below the real axis. The inhomogeneities and roughness of the solid surfaces also show this type of characteristics [21-22].

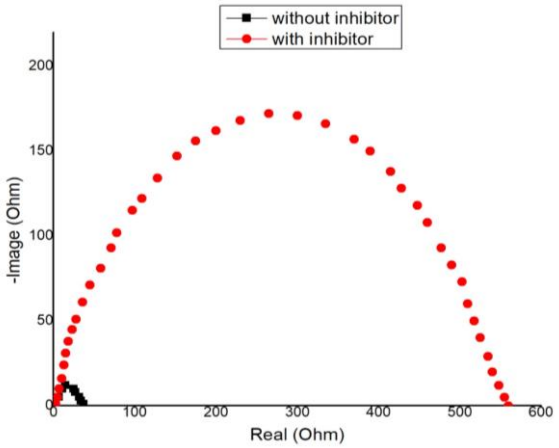

Fig. 5: Nyquist plots (EIS) of the specimens in both uninhibited and inhibited solution

3.3 FTIR Analysis

Figure 6 shows the FTIR spectra of the mild steel samples in both uninhibited and inhibited solution. The observed data shows similar peaks for both of the samples but intensities. Increased intensities are observed with the sample in inhibited solution. Sharp peak with the presence of C-O band attributed from 1200 to 1300 cm^{-1} and C=O attributed from 1700 to 1800 cm^{-1}. The increment in intensities made the band stronger contributing to the reduction in corrosion rate in inhibited solution [23].

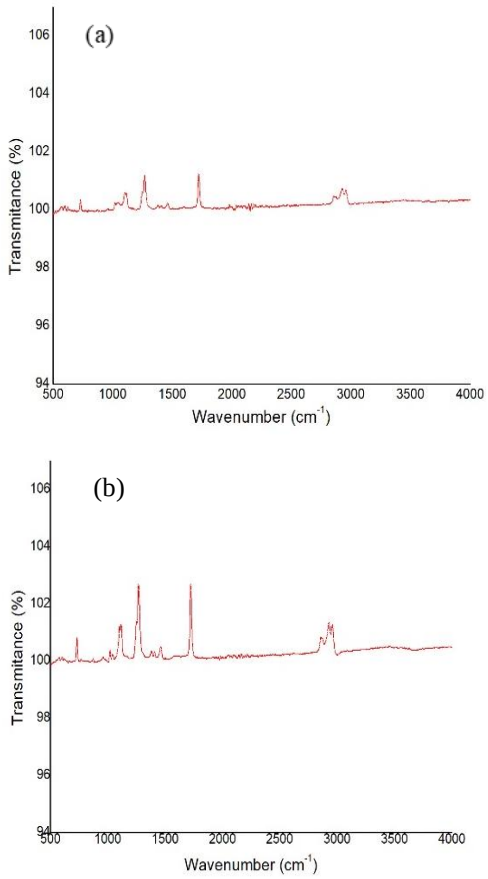

Fig. 6: FTIR spectroscopy analysis of the sample immersed in (a) uninhibited and (b) inhibited solution.

3.4 SEM Analysis

The surface SEM analysis of the corroded sample is shown by the Figure 7 in both the solutions after immersing 3 days. From the figures it is observed that sample immerged in uninhibited solution (Figure 7(a)) is breached with several cracks and micro cavities with irregular surface. However, sample immerged in inhibited solution is less irregular and smooth with fewer number of cracks and micro cavities shown in Figure 7(b).

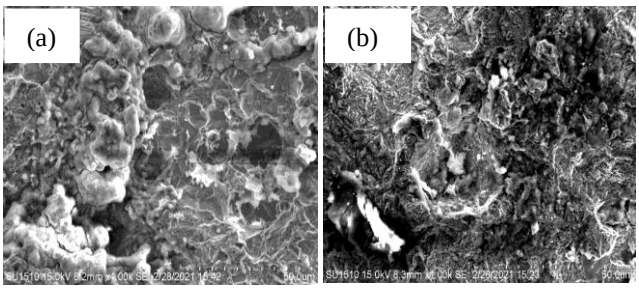

Fig. 7: SEM analysis of specimens after immersion of 3 days in (a) uninhibited and (b) inhibited solution.

3.5 Mechanism of Inhibition

The inhibition effect of Trigonella foenum-graecum can be explained from the theoretical and experimental results obtained in HCl solution as follows:

$$T.\ graecum + xH^{+} \leftrightarrow [T.\ graecum\ Hx]^{x+} \quad \ldots\ldots\ldots\ldots (ii)$$

Trigonella foenum-graecum exists either in the form of cations (protonated Trigonella foenum-graecum) or as neutral molecules in the acquis acidic solution. Two modes of adsorption can be considered in general. Via the chemisorptions mechanism the neutral Trigonella foenum-graecum may be adsorbed on the metal surface that involved the sharing of electrons between iron and oxygen atoms and the water molecules displacement from the metal surface. The adsorbent of Trigonella foenum-graecum may also happen based on the donor-acceptor interactions between vacant d-orbitals of iron and π-electrons of the heterocycle on the metal surface. However, the absorbent of the protonated Trigonella foenum-graecummay also happen through the electrostatic interactions between already adsorbed sulfate ions and the positive molecules. Therefore, the formation of metal complexes of Trigonella foenum-graecum or protonated Trigonella foenum-graecum and Fe^{2+} may be as follows:

$$T.\ graecum + Fe^{2+} \leftrightarrow [T.\ graecum - Fe]^{2+} \ldots\ldots\ldots\ldots (iii)$$
$$[T.\ graecum\ Hx]^{x+}\ Fe^{2+} \leftrightarrow [T.\ graecum_{x}- Fe]^{(2+x)+} \ldots (iv)$$

In this study, the adsorbent of these complexes might happen on the surfaces of mild steel by vander Waals force to keep the surface of mild steel free from corrosion forming a protective film [24]. Similar mechanism is also documented in the previous literature [25-26].

4. CONCLUSION

The concluding words of this research work could be that, Trigonella foenum-graecum seeds extract shows maximum 69.2% corrosion efficiency after the immersion of three days in the inhibited solution. The corrosion rate may be reduced the C=O and C-O bands present in the inhibited solution. The reduction of corrosion is proved by the SEM analysis performed on the sample immerged in both uninhibited and inhibited solution. In future research works, more natural inhibitors can be tested as natural inhibitor at different conditions to obtain more efficient, cost effective and environment friendly inhibitor. In addition, green synthesized nanoparticles can also be tested as green corrosion inhibitors in future study.

REFERENCES

[1] M. A. Omran, M. Fawzy, A. E. D. Mahmoud and O. A. Abdullatef,"Optimization of mild steel corrosion inhibition by water hyacinth and common reed extracts in acid media using

factorial experimental design," Green Chemistry Letters and Reviews, Vol. 15, pp. 214-230, 2022.

[2] B. Hou, X. Li, X. Ma, C. Du, D. Zhang, M. Zheng, W. Xu, D. Luand F. Ma, npj Mater. Degrad, 1 (4), 2017.

[3] G. H. Koch, M. P. H. Brongers, N. G. Thompson, Y. P. Virmani and J. H. Payer, "Corrosion costs and preventive strategies in the United States," NACE International Publication No. FHWA-RD-01-156, 2002.

[4] S.A. Umoren and M.M. Solomon, Open Mater. Sci. J., Vol. 8, 39, 2014.

[5] O. Gharbi, S. Thomas, C. Smithand N. Birbilis, Mater. Degradat., Vol 2, 12, 2018.

[6] O. S. Shehata, L. A. Korshed and A. Attia,"Green corrosion inhibitors, past, present, andfuture, corrosion inhibitors, principles and recent applications," London: IntechOpen, 2017.

[7] M.Chigondo andF. Chigondo, "Recent natural corrosion inhibitors for mild steel: an overview,: J Chem., pp.1–7, 2016.

[8] N. Hossain , M. A. Chowdhury and M. Kchaou,"An overview of green corrosion inhibitors for sustainable and environment friendly industrialdevelopment, Journal of Adhesion Science and Technology," 2020.

[9] S.Issaadi, T.Douadi andA.Zouaoui,"Novel thiophene symmetrical Schiff base compounds as corrosion inhibitor for mild steel in acidic media," Corros Sci., Vol. 53, pp. 1484-1488, 2011.

[10] L. M. Vracar and D. M. Dra ˇ zi, "Adsorption and corrosion ˇ inhibitive properties of some organic molecules on iron electrode in sulfuric acid," Corrosion Science, Vol. 44, pp. 1669–1680, 2002.

[11] H. A. Sorkhabi, S. Mirzaee, T. Rostamikia and R. Bagheri, "Pomegranate (Punica granatum) Peel Extract as a Green Corrosion Inhibitor for Mild Steel in Hydrochloric Acid Solution," International Journal of Corrosion, 2015.

[12] A. Y. El-Etre, "Khillah extract as inhibitor for acid corrosion of SX 316 steel," Applied Surface Science, Vol. 252, pp. 8521–8525, 2006.

[13] F. Zucchi and I. H. Omar, "Plant extracts as corrosion inhibitors of mild steel in HCl solutions," Surface Technology, Vol. 24, pp. 391-399, 1985.

[14] N. O. Eddy, S. A. Odoemelam and A. O. Odiongenyi, "Ethanol extract of musa species peels as a green corrosion inhibitor for mild steel: Kinetics, adsorption and thermodynamic considerations," Electronic Journal of Environmental, Agricultural and Food Chemistry, Vol. 8, pp. 243–255, 2009.

[15] P. D. Rani and S. Selvaraj, "Inhibitive and adsorption properties of punica granatum extract on brass in acid media," Journal of Phytology, Vol. 2, pp. 58–64, 2010.

[16] S. Rajendran, V. Ganga Sri, J. Arockiaselvi and A. J. Amalraj, "Corrosion inhibition by plant extracts—an overview," Bulletin of Electrochemistry, Vol. 21, pp. 367–377, 2005.

[17] K. Srivastava and P. Srivastava, "Studies on plant materials as corrosion inhibitors," British Corrosion Journal, Vol. 16, pp. 221–223, 1981.

[18] R. M. Saleh, A. A. Ismail and A. A. El Hosary, "corrosion inhibition by naturally occurring substances. vii. the effect of aqueous extracts of some leaves and fruit peels on the corrosion of steel, Al, Zn and Cu in acids," British Corrosion Journal, Vol. 17, pp. 131–135, 1982.

[19] P. B. Raja and M. G. Sethuraman, "Natural products as corrosion inhibitor for metals in corrosive media—a review," Materials Letters, Vol. 62, pp. 113-116, 2008.

[20] N. Hossain, M. A. Chowdhury, M. Rana, M. Hassan and S. Islam, "Terminalia arjuna leaves extract as green corrosion inhibitor for mild steel in HCl solution," Results in Engineering 14, 2022.

[21] L.R. Chauhan and G. Gunasekaran, "Corrosion inhibition of mild steel by plant extractin dilute HCl medium," Corrosion Science, Vol. 49,pp. 1143-1161, 2007.

[22] N. Hossain, M. A. Chowdhury, A.K. M. P. Iqbal, A.K. M. F. Ahmed, M. S. Islam, "Corrosion behavior of aluminum alloy in NaOH and *Syzygium Samarangense* solution for environmental sustainability," Current Research in Green and Sustainable Chemistry, Vol 5, 2022.

[23] M. T. Majd, M. Ramezanzadeh, G. Bahlakeh and B. Ramezanzadeh, "Steel corrosion lowering in front of the saline solution by a nitrogen-richsource of green inhibitors: Detailed surface, electrochemical and computational studies," Construction and Building Materials,Vol 254, 2020.

[24] P. Muthukrishnan, B. Jeyaprabha and P. Prakash, "Mild steel corrosion inhibition by aqueous extract of *HyptisSuaveolens* leaves," International Journal of Industrial Chemistry, Vol 5, 2014.

[25] N.M. Guan, L.Xueming andL.Fei, "Synergistic inhibition between o-phenanthroline and chloride ion on cold rolled steel corrosion in phosphoric acid," Mater Chem Phys,Vol 86, pp. 59–68, 2004.

[26] F.Bentiss, M.Traisnel andM.Lagrenee," "The inhibition action of 3, 6-bis(2-methoxyphenyl)-1,2-dihydro 1,2,4,5-tetrazine on the corrosion of mild steel in acidic media,"Corrosion Science,Vol. 42 pp. 703-719, 2000.

Paper ID: 8304
International Conference on Mechanical, Manufacturing and Process Engineering (ICMMPE – 2022)
Organizer: Faculty of Mechanical Engineering, Dhaka University of Engineering & Technology (DUET), Gazipur, Bangladesh
Website: https://icmmpeduet.com/

Microstructural Investigation of Seven-layered Aluminium-Aluminium Oxide Graded Composite Material Prepared Through Pressureless Sintering

Maziyana Marzuki [1], Noor Mazni Ismail [1], Dewan Muhammad Nuruzzaman[2] AKM Asif Iqbal[3] and Mohammad Asaduzzaman Chowdhury[4]

[1]Faculty of Manufacturing and Mechatronic Engineering Technology, University Malaysia Pahang (UMP)
26600 Pekan, Pahang Darul Makmur, Malaysia
[2]Department of Mechanical Engineering, International University of Business Agriculture and Technology (IUBAT)
Uttara Model Town, Dhaka 1230, Bangladesh
[3]Department of Mechanical, Materials and Manufacturing Engineering, University of Nottingham
Ningbo, China
[4]Department of Mechanical Engineering, Dhaka University of Engineering and Technology (DUET)
Gazipur 1700, Bangladesh

E-mail: nuruzzaman.me@iubat.edu

ABSTRACT

In the present study, different percentages of Aluminium (Al) and Aluminium Oxide (Al_2O_3) were integrated layer by layer for the preparation of seven-layered graded composite material. Due to large difference in properties, crack or defect is the main problem for metal-ceramic combination. The prepared graded structure was investigated layer by layer for any defect or crack that might appear in the layer or at the interface. By using a steel die set combination, different layers of different percentages of metal-ceramic were integrated in preparation of the graded composite. After that a pressureless two-step sintering method was used. During the sintering process, a maximum temperature of 630°C was applied for 3 hours sintering duration. Each layer of graded specimen and interfaces of different layers were characterized using Field Emission Scanning Electron Microscopy (FESEM). Vickers microhardness testing was carried out for different layers of composite. The obtained results showed that there is a good distribution of ceramic (Al_2O_3) particles into metallic (Al) matrix when ceramic content up to the 20% (fifth layer). On the other hand, it was also observed that when ceramic content more than 20%, agglomeration occurred for the sixth and seventh layer. Microstructural observations showed that layers boundary and all interfaces are almost parallel. Moreover, it was obvious that no crack was found in the layer or at the interface which confirmed the good preparation process of graded structure.

Keywords: Seven-layered; Aluminium; Aluminium oxide; Sintering; Microstructure.

1. INTRODUCTION

The new generation graded composite materials are gaining popularity for solving practical problems in various industrial sectors for a range of applications namely automotive, armor, aerospace, biomedical and optoelectronics components. In preparation of graded composite materials, metal and ceramic are incorporated together with varied proportions and applying different methods namely laser sintering, powder metallurgy, centrifugal casting, chemical vapor deposition, physical vapor deposition and thermal spraying. These new graded composite materials are suitable for multiple functions and able to solve practical problems with high performance [1-5]. Functionally graded composite structures are two types, continuous structure and stepwise structure. In continuous structure, microstructure and composition vary in a continuous way with the distance. On the other hand, in stepwise structure, microstructure and composition vary in stepwise way with clear identification of the interface between layers. For the stepwise structure, powder metallurgy is the most suitable method for achieving gradient structure with desired properties while centrifugal force is the suitable method to achieve the continuous structure with required properties [6]. In powder metallurgy method, compaction of powders and sintering, the two most important steps. Because of residual stress and thermal expansion, crack or camber is prevalent in the sintered specimen. To avoid the crack or camber, the parameters need to be controlled during sintering process [7]. The compaction of powder involves the influencing parameters powder density, particle shape and size. Moreover, properties and qualities of powder particles are important factors in controlling compressibility performance of powder. In addition, work hardening of particle is an important factor which influences hardness of green

compact. Density of green compact significantly influences porosity and strength of structure [8].

In recent times, aluminium based composites in high demand and these composites showed potential for successful application in industrial sectors for excellent mechanical and tribological properties, good corrosion and oxidation resistance, high stiffness and strength, moderate coefficient of thermal expansion etc. [9]. Aluminium oxide ceramic possesses good strength, high stiffness, good wear resistance, high chemical inertness and high hardness [10]. Multi-layered composites were prepared and obtained results showed that good bonding was formed between two materials of substrate and deposition [11]. Aluminium based composite structure was analysed and obtained results showed that hardness of middle or inner part of composite was lower as compared to that of outer part [12]. The strength of inner part was also lower than that of outer part. Experimental and theoretical investigations of thermo-mechanical deformation of aluminium based composite panels were carried out [13]. Thermo-mechanical response of composite panel was analysed for various loading conditions and the reported results clarified the agreement between theoretical and experimental results.

The objective of research was to prepare seven-layered aluminium-aluminium oxide (Al-Al_2O_3) graded composite specimen through two-step pressureless sintering process considering 0% to 30% aluminium oxide concentration (with 5% increment). Microstructural investigations were carried out from first layer to seventh layer and at each interface between two adjacent layers. Microvickers hardness of individual layer was also examined in this research study.

2. EXPERIMENTAL PROCEDURE

2.1 Sample Preparation

In preparation for the seven-layered aluminium-aluminium oxide graded composite, Al powders and Al_2O_3 powders were used. According to molecular weight, amount of each powder composition was calculated for individual layer. The powder constituents were sieved and then mixed in order to form each layer. The mixture for each layer was blended for achieving homogeneous mixture. In this research, the percentage compositions of the seven-layered Al-Al_2O_3 graded composite varied as 100:0, 95:5, 90:10, 85:15, 80:20, 75:25 and 70:30 from first layer to seventh layer which is presented in Figure 1. Mixed powders of varied compositions were stacked very carefully from first layer to seventh layer in cylindrical die of 30 mm diameter. Using a hydraulic press (TOYO: Model TL30, capacity 30 ton), uniaxial pressure was applied very slowly at room temperature and the pressure was increased step by step. After each step of powder compaction process, sufficient time was allowed to settle the powder compact at stable condition and the compaction process was continued until it reached to 30 Ton. After that using the hydraulic press, the seven-layered green compact sample was ejected carefully from the die so that no wear and tear occurred around any surface of specimen.

70 % Al + 30 % Al_2O_3
75 % Al + 25 % Al_2O_3
80 % Al + 20 % Al_2O_3
85 % Al + 15 % Al_2O_3
90 % Al + 10 % Al_2O_3
95 % Al + 5 % Al_2O_3
100 % Al + 0 % Al_2O_3

Fig. 1: Percentage compositions for each layer of seven-layered Al-Al_2O_3 graded composite

2.2 Sintering of Green Compact

Using a pressureless sintering furnace (Nabertherm; made in Germany), sintering of seven-layered green compact was carried out following two-step sintering cycle [15-17]. The sintering cycle was applied for this research is shown in Figure 2. In first step of sintering cycle, heating rate 2˚C/min was applied and specimen temperature started to increase from room temperature 30˚C until temperature reached to 150˚C. One hour holding time was maintained at this 150˚C temperature. In sintering cycle for second step, specimen was allowed to heat with identical heating rate up to sintering temperature 630˚C. At this temperature 630˚C, sintering time was kept for three hours. Finally, specimen was cooled to room temperature.

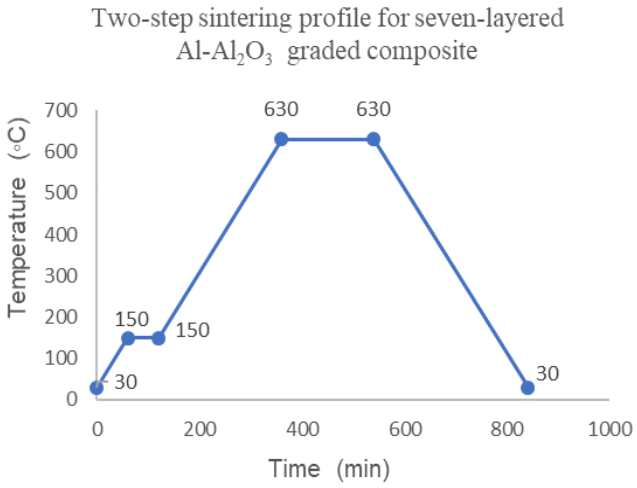

Fig. 2: Two-step sintering at sintering temperature 630˚C and 3 hours sintering duration

2.3 Characterisation of Specimen

Due to sintering process, the radial shrinkage of specimen was occurred and using a vernier caliper shrinkage was calculated by measuring specimen diameter before and after sintering process [18]. Moreover, weight of the specimen was measured before and after sintering process. In calculating specimen shrinkage and weight, ten measurements were taken and average values were considered. For examining seven-layered Al-Al_2O_3 graded composite structure, at first, specimen was cut along the layers cross section. The cross-sectional surface of the sample was prepared by grinding and polishing operations. In grinding operation, different fine grits of abrasives were used. Polishing operation was continued until fine and smooth surface was obtained for microstructural observations. After that specimen was mounted for cross-sectional surface images of seven-layered composite structure. In order to examine the surface morphology and crack / defect / imperfection (along cross section of composite specimen), field emission scanning electron microscopy (FESEM) was utilized using electron back-scattered mode. All observations were conducted for individual layer and interface between adjacent layers.

2.4 Vickers Microhardness Testing

Vickers microhardness tests were carried out on polished surface of each layer of seven-layered test specimen. Hardness was measured along the cross-sectional surface (longitudinal direction) of specimen and test procedure was followed according to ASTM E-384. In the experimentation, test was performed at every 1 mm interval for individual layer and total 10 test data were recorded for each layer. The average hardness result was considered for every individual layer of seven-layered graded composite structure [19], [20].

3. RESULTS AND DISCUSSION

3.1 Effect of Sintering

The radial shrinkage of seven-layered graded composite specimen can be clarified as diameter reduction of green specimen because of sintering process. It was noticed that because of shrinkage during sintering, diameter of green compact decreased. For this seven-layered Al-Al_2O_3 green specimen, the diameter was considered as average diameter which was measured 30 mm and equal to die diameter. After sintering process, specimen diameter decreased to 29 mm resulted in radial shrinkage 1 mm. It is believed that total porosity of specimen was influenced by sintering temperature and sintering time [20]. Moreover, test results showed that specimen lost weight after sintering. The weight loss occurred due to vaporization of alumina where oxygen diffused out at high temperature. The average weight of seven-layered green specimen was measured 22.67g and the average weight of sintered specimen was measured 20.40g, so that weight loss calculated as 2.27g or 10%. The obtained results suggest that during three hours holding time, decrease in porosities occurred which results in reduction in surface area and contributes to densification of compact and hence weight loss of specimen occurred as reported in previous work [21].

3.2 Microstructural Observation of Seven-layered Graded Structure

Microstructural studies were carried out for surface images of seven-layered Al-Al_2O_3 graded composite. Using electron back-scattered mode, FESEM images were captured for each layer and interface between two adjacent layers. Microstructural images of seven-layered composite structure are shown in Figures 3(a) to 3(g).

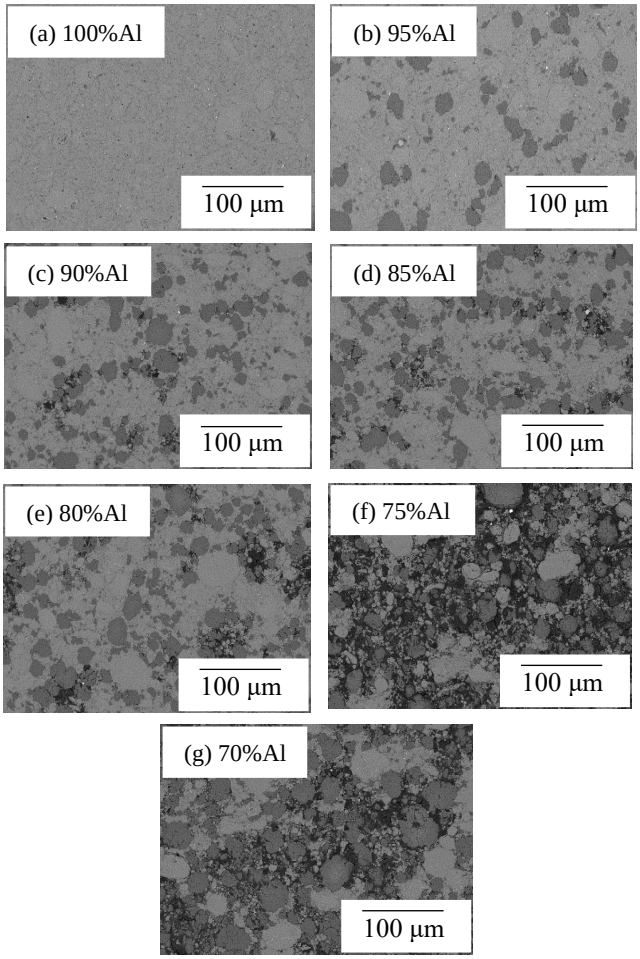

Fig. 3: Microstructures (a) First layer: 100% Al (b) Second layer: 95%Al+5%Al_2O_3 (c) Third layer: 90%Al+10%Al_2O_3 (d) Fourth layer: 85%Al+15%Al_2O_3 (e) Fifth layer: 80%Al+20%Al_2O_3 (f) Sixth layer: 75%Al+25%Al_2O_3 (g) Seventh layer: 70%Al+30%Al_2O_3

The ceramic element aluminium oxide was recognized as dark area whereas metallic phase aluminium was recognized as light grey area. Moreover, pores were observed as black spots from third layer to seventh layer which are apparently recognized in Figure 3(c) to Figure 3(g). Microstructural observations revealed that pores exist clearly in the third layer containing 10% alumina and these pores increased significantly with the increase in ceramic content up to 30% (seventh layer). The obtained results suggest that with addition of increased ceramic content, air entrapment in the layer increased which in turn contributed to increased porosity significantly in sixth and seventh layers [22]. The microstructure of graded structure also revealed that good distribution of alumina ceramic within aluminium matrix which was observed from second layer to seventh layer. The obtained results showed the existence of ceramic particles which is almost uniformly distributed in second layer (Figure 3(b)) and a gradual ceramic increment within matrix proves the stepwise gradation layer by layer up to seventh layer (Figure 3(g)) which confirms that preparation of seven-layered composite specimen is well executed.

In Figure 4, FESEM images of each interface between two adjacent layers of the seven-layered Al-Al_2O_3 graded composite specimen are presented. From these observations, it is understood that first-second, second-third, third-fourth, fourth-fifth, fifth-sixth and sixth-seventh layers are separated by the interface marked by dotted line PP', QQ', RR', SS', TT' and UU' in Figures 4(a) to 4(f) respectively. In processing of seven-layered graded structure, compaction was carried out in a careful way in order to achieve stepwise gradation and to ensure continuity of structure. On closer viewing of layer by layer, the microstructures revealed that there is no macrocrack or microcrack identified in any layer or at any interface. The findings suggest that there is a good interfacial bonding between metal and ceramic from second layer to seventh layer. The evidence also suggests that gradation of seven-layered composite took place step by step up to the seventh layer. A close inspection of microstructures revealed that each interface was nearly straight and parallel to two adjacent layers which proved that powder stacking and compaction processes of seven-layered graded composite were properly implemented [20]. Moreover, there was no sign of split off or delamination of layers at any position from first layer to seventh layer or fracture across any layer confirmed that interfacial bonding was good enough for seven-layered graded composite structure at sintering temperature 630°C and isothermal holding time of 180 min. Microstructural observations also revealed that porosities in sixth and seventh layers were increased remarkably due to addition of 25% and 30% of ceramic content respectively. The increased porosities in sixth layer and seventh layer might be reduced sufficiently by implementing higher sintering temperature or longer sintering time [23], [24].

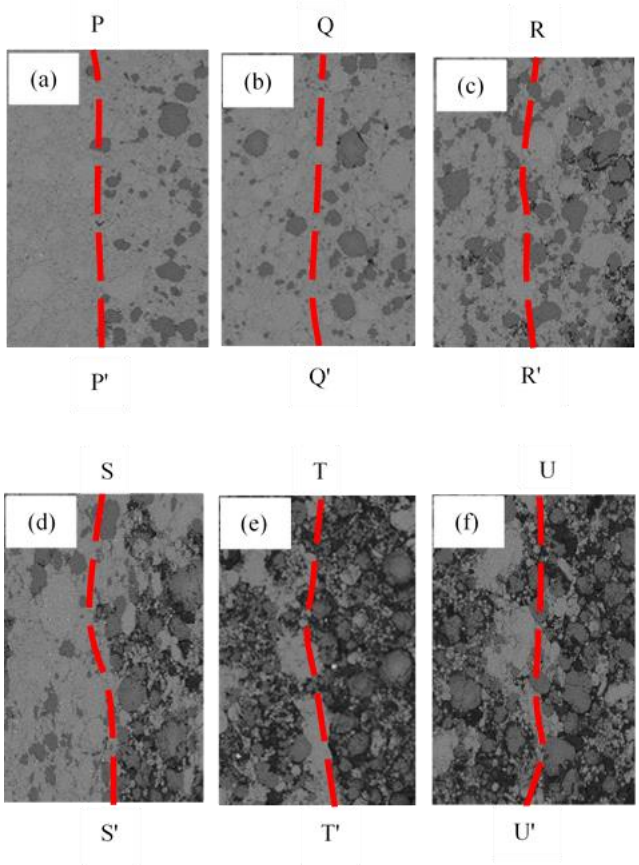

Fig. 4: Seven-layered Al-Al_2O_3 graded composite: Interface between adjacent layers: (a) Interface PP' between first-second layers (b) Interface QQ' between second-third layers (c) Interface RR' between third-fourth layers (d) Interface SS' between fourth-fifth layers (e) Interface TT' between fifth-sixth layers (f) Interface UU' between sixth-seventh layers

3.3 Vickers Microhardness

Figure 5 shows the test results of Vickers microhardness along the cross-sectional surface of each layer of seven-layered Al-Al_2O_3 graded composite. These results were considered as the average hardness result of ten test data 1 mm apart along the cross-sectional surface for every individual layer. The obtained results show that average hardness at first layer that contains 100%Al is 29.86 HV and average hardness of second layer (5%Al_2O_3) increased to 32.32 HV. Test results reveal that average hardness of third layer increased to 34.18 HV and hardness of fourth layer (15%Al_2O_3) further increased to 37.88 HV. The obtained results show that average hardness of fifth, sixth and seventh layer is 41.63 HV, 43.1 HV and 45.35 HV respectively. It is noticed that due to gradual increase in ceramic content (Al_2O_3) for next layer, hardness of graded composite specimen increases layer by layer. It is believed that addition of high hardness ceramic material into soft

ductile material contributed to increase in hardness of seven-layered graded composite progressively [15].

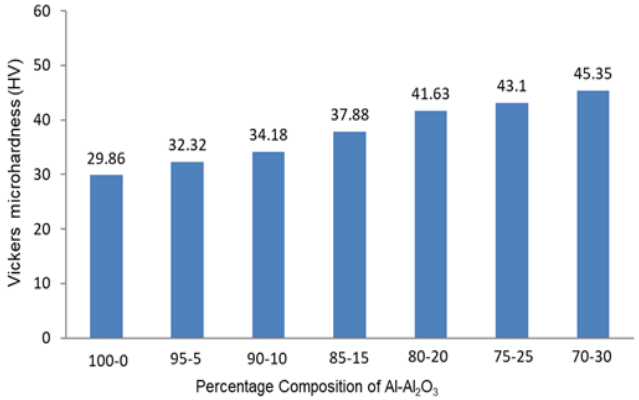

Fig. 5: Distribution of hardness in each layer of seven-layered Al-Al_2O_3 graded composite

4. CONCLUSION

Seven-layered Al-Al_2O_3 graded composite structure was prepared layer by layer using powder metallurgy and two-step pressureless sintering. During sintering process, a maximum temperature of 630ºC was applied for 3 hours duration. The microstructure of graded structure showed that there is good distribution of alumina ceramic within aluminium matrix and gradual ceramic increment reveals stepwise gradation layer by layer up to seventh layer. The microstructures also confirmed that there is no macrocrack or microcrack identified in any layer or at any interface. Microstructural observations revealed that each interface was nearly straight and parallel to two adjacent layers which confirmed that all processes during preparation of seven-layered graded composite were properly implemented. There was no sign of delamination of layers at any position from first layer to seventh layer or fracture across any layer proved that interfacial bonding was good enough for composite structure. In addition, tests data showed that hardness of graded composite increases progressively with gradual increase in alumina ceramic up to seventh layer.

REFERENCES

[1] Y. Watanabe, Y. Hattori and H. Sato, "Distribution of Microstructure and Cooling Rate in Al-Al_2Cu Functionally Graded Materials Fabricated by a Centrifugal Method," Journal of Materials Processing Technology (JMPT), Vol. 221, pp. 197-204, 2015.

[2] M. Naebe and K. Shirvanimoghaddam, "Functionally Graded Materials: A Review of Fabrication and Properties," Applied Materials Today, Vol. 5, 223-245, 2016.

[3] S. N. S. Jamaludin, S. Basri, A. Hussain, D. S. Alothmany, F. Mustapha and D. M. Nuruzzaman, "Three-Dimensional Finite Element Modeling of Thermomechanical Problems in Functionally Graded Hydroxyapatite/Titanium Plate," Mathematical Problems in Engineering, Vol. 2014, pp. 1-20, 2014.

[4] K. Wu, S. Scheler, H S. Park and M. W. Porada, "Pressureless Sintering of ZrO_2-$ZrSiO_4$/NiCr Functionally Graded Materials with a Shrinkage Matching Process," Journal of the European Ceramic Society (JECS), Vol. 33, pp. 1111–1121, 2013.

[5] N. S. Radhi, "A Review for Functionally Gradient Materials Processes and Useful Application," Journal of University of Babylon for Engineering Sciences, Vol. 26, pp. 42-46, 2018.

[6] G. Udupa, S. S. Rao and K. V. Gangadharan, "Functionally Graded Composite Materials: An Overview," Procedia Materials Science, Vol. 5, pp. 1291-1299, 2014.

[7] L. Sun, A. Sneller and P. Kwon, "Fabrication of Alumina/Zirconia Functionally Graded Material: From Optimization of Processing Parameters to Phenomenological Constitutive Models," Materials Science and Engineering: A, Vol. 488, pp. 31-38, 2008.

[8] H. A. Al-Qureshi, M. R. F. Soares, D. Hotza, M. C. Alves and A. N. Klein, "Analyses of the Fundamental Parameters of Cold Die Compaction of Powder Metallurgy," Journal of Materials Processing Technology (JMPT), Vol. 199, pp. 417-424, 2008.

[9] F. Erdemir, A. Canakci and T. Varol, "Microstructural Characterization and Mechanical Properties of Functionally Graded Al2024/SiC Composites Prepared by Powder Metallurgy Techniques," Transactions of Nonferrous Metals Society of China, Vol. 25, pp. 3569-3577, 2015.

[10] J. Zhang, S. Yang, Z. Chen, M. Wyszomirska, J. Zhao and Z. Jiang, "Microstructure and Tribological Behaviour of Alumina Composites Reinforced with SiCgraphene Core-shell Nanoparticles," Tribology International, Vol. 131, pp. 94- 101, 2019.

[11] C. H. Zhang, H. Zhang, C. L. Wu, S. Zhang, Z. L. Sun and S. Y. Dong, "Multi-layer Functional Graded Stainless Steel Fabricated by Laser Melting Deposition," Vacuum, Vol. 141, pp. 181-187, 2017.

[12] N. Radhika and R. Raghu, "Development of Functionally Graded Aluminium Composites using Centrifugal Casting and Influence of Reinforcements on Mechanical and Wear Properties," Transactions of Nonferrous Metals Society of China (TNMSC), Vol. 26, pp. 905-916, 2016.

[13] Q. Lin, F. Chen and H. Yin, "Experimental and Theoretical Investigation of the Thermo-mechanical Deformation of a Functionally Graded Panel," Engineering Structures, Vol. 138, pp. 17–26, 2017.

[14] M. Chen, L. Jing and X. Li, "The Surface Integrity in Machining Hardened Steel SKD11 for Die and Mold," Machining Science and Technology, Vol. 11, pp. 99-116, 2007.

[15] D. M. Nuruzzaman, A. K. M. A. Iqbal, M. Marzuki, M. A. Chowdhury, N. M. Ismail, M. I. A. Latiff, M. Rahman and M. A. Gebremariam, "Investigation on Microstructure and Hardness of Aluminium-Aluminium Oxide Functionally Graded Material," Lecture Notes in Mechanical Engineering (LNME), pp. 478–483, 2020.

[16] A. Yusefi and N. Parvin, "Fabrication of Three Layered W-Cu Functionally Graded Composite via Spark Plasma Sintering," Fusion Engineering and Design, Vol. 114, pp.196–202, 2017.

[17] S. N. S. Jamaludin, M. I. A. Latiff, D. M. Nuruzzaman, N. M. Ismail and S. Basri, "Investigation on Microstructure and Hardness of Nickel-Alumina Functionally Graded Material," Materials Today: Proceedings, Vol. 29, pp. 127-132, 2019.

[18] A. Shahrjerdi, F. Mustapha, M. Bayat, S. M. Sapuan and D. L. A. Majid, "Fabrication of Functionally Graded Hydroxyapatite-Titanium by Applying Optimal Sintering Procedure and Powder Metallurgy," International Journal of the Physical Sciences, Vol. 6, pp. 2258–2267, 2011.

[19] O, Carvalho, M. Buciumeanu, S. Madeira, D. Soares, F. S. Silva and G. Miranda, "Optimization of AlSi–CNTs Functionally Graded Material Composites for Engine Piston Rings, Materials and Design, Vol. 80, pp. 163–173, 2015.

[20] F. F. Kamaruzaman, D. M. Nuruzzaman, M. A. Chowdhury, S. N. S. Jamaludin, S. Basri and N. M. Ismail, "Characterisation of Four-layered Al-Al_2O_3 Functionally Graded Material Prepared through Powder Metallurgy and Pressureless Sintering," International Journal of Materials and Product Technology (IJMPT), Vol 59, pp. 48-62, 2019.

[21] Z. Xu, M. A. Hodgson, K. Chang, G. Chen, X. Yuan and P. Cao, "Effect of Sintering Time on the Densification, Microstructure, Weight Loss and Tensile Properties of a Powder Metallurgical Fe-Mn-Si Alloy," Metals, Vol. 7, pp. 1-17, 2017.

[22] M. Bhattacharyya, A. N. Kumar and S. Kapuria, "Synthesis and Characterization of Al/SiC and Ni/Al2O3 Functionally Graded Materials, Materials Science and Engineering: A, Vol. 487, pp. 524-535, 2008.

[23] M. A. Almomani, A. M. Shatnawi and M. K. Alrashdan, "Effect of Sintering Time on the Density, Porosity Content and Microstructure of Copper - 1 wt. % Silicon Carbide Composites, Advanced Materials Research (AMR), Vol. 1064, pp. 32-37, 2015.

[24] X. Yuan, X. Qu, H. Yin, Z. Feng, M. Tang, Z. Yan and Z. Tan, "Effects of Sintering Temperature on Densification, Microstructure and Mechanical Properties of Al-Based Alloy by High-Velocity Compaction," Metals, Vol. 11, pp. 1-11, 2021.

Paper ID: 8372

International Conference on Mechanical, Manufacturing and Process Engineering (ICMMPE – 2022)

Organizer: Faculty of Mechanical Engineering, Dhaka University of Engineering & Technology (DUET), Gazipur, Bangladesh

Website: https://icmmpeduet.com/

A Study on Design of Micro-Hydropower Power Plant for Run-off Water Sources in Bangladesh

Md Rakibuzzaman[1], Aminul Islam[2], Ahmad Abdullah Kauser[3] and A. K. M. Parvez Iqbal[4]

[1, 3, 4]International University of Business Agriculture and Technology, Dhaka 1230, Bangladesh
[2]SIMEC Institute of Technology, Dhaka 1230, Bangladesh

E-mail: rakibuzzaman@iubat.edu

ABSTRACT

Hydropower has been one of the most used energy sources in the world since historic times. Electricity production from hydropower has been there for decades, particularly in isolated regions. Studies conducted show that 232 rivers in Bangladesh can be used for micro-hydropower generating and energy security for isolated communities with a reasonable flow rate. The run-off water from these rivers can be used as a clean energy source for running micro-hydro powerplant. The objective of this study is to investigate and justify the potentiality of micro-hydro power in Bangladesh and design a cross-flow turbine that can be used for harnessing power from these rivers. In this study, a turbine was developed on which numerical analysis was conducted using computer simulation. Results indicated that a site with 100-150 liter/s of flow rate and a head of 5-6 meters can easily produce around 3-5 kW of power supply considering all kinds of losses. The current study is expected to provide important information for improving hydropower-based electricity generation in Bangladesh. Also based on the study, future studies should be carried out on micro-hydro by applying a more effective turbine-like Tesla turbine which can be most effective for the micro-hydro project.

Keywords: Renewable Energy; Micro-hydropower; Turbine; Sustainable power; Computational fluid dynamics

1. INTRODUCTION

Bangladesh is a developing middle-income country. The country has the fastest growing economy compared to the rest of the world; however, development is an essential part of any country's continued growth and the primary driver of that development is Energy. Energy has become one of the most essential components in improving Bangladesh's economic advancement and people's lives. After decades of reliance on the nation's primary energy resources such as natural gas, it was found that the country lacks sufficient energy supplies, forcing it to rely on imported fuels. Furthermore, there are concerns about the usage of fossil fuels rising greenhouse gases (like CO_2, CH_4, N_2O) emissions, that accelerate the greenhouse effect and pursue climate change, as well as putting Bangladesh itself at risk of natural disasters [1], [2]. According to various reports from the Hydrocarbon Unit of the MPEMR Bangladesh, the main energy resources of Bangladesh are domestic natural gas, coal, imported oil, Liquid Petroleum Gas, hydropower, and imported Liquid Natural Gas, imported electricity [2]. Biomass makes for around twenty-seven percent of primary energy, with commercial energy accounting for the remaining seventy-three percent. The report suggests that about sixty-two percent of the energy used by the commercial sector is from Natural Gas of which about twelve percent is imported and a large part of the remaining share is imported crude oil. The country has imported around 8.5 million metric tons of crude and refined petroleum products for the year 2020-2021. Renewable energy is being used instead of gas, coal, and oil all over the world, and it is critical for long-term growth and environmental protection by reducing carbon emissions. Many nations throughout the world, including Europe, America, and Asian counties are now relying heavily on renewable energy to meet their energy needs. Bangladesh uses renewable energy as well, but the percentage is very less than what is truly needed [2]. The solar power generation capacity of Bangladesh is 542.44 megawatts (MW). Bio-gas facilities produce around 0.69 MW of power. The Bio-Mass Gasification Method provides 0.4 MW of electricity in the country. According to the National Database of the Renewable Energy of Sustainable and Renewable Energy Development Authority (SREDA), for the feasible year 2020-2021, Bangladesh's total renewable energy capacity is estimated to be at 765.62 Megawatts with solar accounting for 70% of the renewable energy and hydropower accounting for about 29.4%. This represents just around 3.04 percent of the county's overall capacity of 25,235 Megawatt. The total amount of energy consumed by the country is estimated to be around 56.24 Metric tons. The average yearly increase in energy use is about 6%.

With 99.5 percent of the population having access to electricity, Bangladesh has a per capita energy consumption of 331 kgoe (Kilogram Oil Equivalent) and a per capita electricity output of 560 kWh, which is lower than neighboring nations [3], [4]. Dependency on domestic non-renewable resources and imports is a serious concern for the country's energy security. Concerning energy security, the government has taken many initiatives. Numerous feasibility studies on micro-hydropower plants have been conducted at different times. The Water Development Board (WDB) and the Ministry of Power (MOP) jointly conducted research on the country's Small/Mini-Hydropower Potential in the year 1981. The group looked over nineteen potential locations for modest hydropower plant installation. Six Chinese specialists visited Bangladesh later that month, in April 1984. They also identified 12 prospective locations for the construction of a mini-hydropower facility [5], [6]. In 2004, in another study by sustainable Rural Energy (SRE), the Local government Engineering Department (LGED) has investigated some effective micro-hydro sites in Chittagong, which is illustrated in Table 1 [6]. Moreover, the Institute of Fuel Research Development (IFRD) of the Bangladesh Council of Scientific and Industrial Research (BCSIR) has carried out a feasibility study on the research and development of renewable energy such as solar energy, wind energy, micro-mini-hydro power in Bangladesh. Then the collected data was explored in various prospects at RET laboratory of IFRD. Table 2 shows part of the data [6]. A large and growing body of literature has investigated the potential of hydropower in Bangladesh. Miskat *et al.* (2020) studied different types and technologies used for hydropower generation and they observed that small-scale hydropower was the most practical way for Bangladesh to produce sustainable electricity according to an economic and environmental assessment [7]. The study suggested 232 rivers in Bangladesh that can be used for small-scale hydropower generation and energy security for isolated communities with an acceptable flow rate.

Table 1: Potential micro-hydro sites in Chittagong identified by SRE in a study in 2004 [6]

Description Site	**Expected power generation (KW)**
Khagrachari Nunchari, Tholipara	3
Bandarban	30
Bangchari	25
Liragoan	20
Kamalchar in Rangamati	20
ThangKhrue in Rangamati	30
Monjaipara	7.5

Table 2: Potential sites identified by IFRD of BCSIR [6]

Waterfall Name	**Avg. Discharge (ltr/s)**	**Approx. Flow duration /month**	**Approx. fall for hydropower /m**	**Electric Power generated (KW)**	**Annual Energy Produced (kWh)**
Sailopropat in Banderban	100	12	6	5	43800
Madhobkundu in Moulvibazar	150	12	10	15	131400

Since, Bangladesh has limited land space, constructing large-scale hydropower plants would have negative consequences such as the destruction of the ecology in the chosen region, the displacement of living creatures, the generation of methane, and so on. Furthermore, constructing huge hydro plants of this scale necessitates a steady high flow of water as well as a significant construction cost, which is not possible for a country like Bangladesh. In developing nations like Bangladesh, small-scale hydropower plants are the best options available. As oil prices continue to rise, the position of small hydro-power plants and other renewable energy sources is planned to improve in the future. However, the dominance of one energy source over another will be determined by technological advancements that are impossible to anticipate without research being done on it. Most researchers have based their studies on small-scale hydro-powerplant technologies. One of which was done by Ali *et al.* (2021), who explored the feasibility from a technological standpoint of mini-hydropower potentiality from sewage water in four districts of Dhaka city [8]. The study has analyzed technical, economic, and environmental criteria, while taking into account the waterfall's head and the sewage system's flow rate. The system used in this study may generate 100 kW to 500 kW of power, with an annual economic gain of BDT 3.9 million to 28 million and CO_2 emissions reductions of 500 to 3000 tons. This study also shows the potential of small-scale hydro-powerplant and how it can be suitable in conditions like drain water systems. Doost *et al.* (2020), studied the potential and design procedures of Archimedes Screws Turbines (ASTs), which may create up to 355 kW of power with low water heads (less than around 5 m) and a wide variety of flow rates, with realistic efficiencies of 60% to 80% [9]. Rakibuzzaman *et al.* (2021), has shown a small-scale hydropower turbine to use the wastewater from fish farms on seas. In the study, a small-scale hydropower plant was developed with propeller-type tubular turbines with a permanent magnet synchronous generator. The guide vane shape showed decreasing flow reduction and increased the overall efficiency by about five and a half percent [10]. Park *et al.* (2021) studied the unsteady fluid flow and its

effect on the performance of rotating machines such as turbines. Experiments were conducted to analyze the flow characteristics and FFT analysis was done to observe the stability of operational conditions [11]. This study is significant since it will help us to know better design conditions for our turbine for performance improvement. Therefore, based on the feasibility study stated previously and the previous research done, it is significant to design and develop a micro-hydro power plant in Bangladesh.

This study focused on the applicability of a micro-hydropower plant in Bangladesh. We provided basic data and the process of installation of a micro-hydropower plant in run-off water sources in Bangladesh.

2. METHODOLOGY

2.1 Major parts of a micro-hydropower plant

To design a micro-hydropower plant in Bangladesh some major components should be considered. The major parts of the micro-hydropower plant are discussed in detail here.

2.1.1 Power conduit:

This is a canal that has been excavated and is made of concrete, stone, or wood metal sheet. Water can flow through most power conduits because they have adequate slopes. It is the connection between the intake and the forebay [12].

2.1.2 Forebay:

This is a basin near the entrance of the penstock. A simple dug space, pond, or reinforced concrete structure might be used. It may or may not exist, and it serves as a settling basin for sand and silt that can cause turbine blade damage. It can also be used for storage.

2.1.3 Spillway:

This is intended to drain surplus water from the forebay. The spillway water must be carefully channeled to prevent excessive erosion of the forebay [12].

2.1.4 Penstock:

This is a pipe that transports high-pressure water to the turbine. To sift unsettled sand, a decent-strength wire mesh should be placed in front of the penstock. It can be put above or below ground with severe joint temperature expansion. At the penstock's end, gates and valves can be installed.

2.1.5 Powerhouse:

This is used as the engine room. It safeguards the turbine, generator, and other electrical and mechanical equipment. It might also include a workshop/office/sanitary facility, among other things.

2.1.6 Tailrace:

This is a small, open canal that connects the power channel to the stream.

2.1.7 Dam or weir:

A weir is a particular construction that is meant to deflect the needed flow into the intake rot to store water. Dams are utilized to enhance available heads and build a reservoir to store water during high flows to compensate for power shortages during low flows. Many micro-hydro generating plants are "run of water," which implies that no huge dams or reservoirs are erected, and no land is inundated. Only a small portion of the available streamflow at any given moment is used to create power, resulting in a negligible environmental effect. The quantity of energy that may be caught is determined by the amount of water that flows per second (the flow rate) and the height from which the waterfalls fall (the head). The term "run-of-water" refers to a method of operation in which the hydro plant uses just the water available in the natural flow of a fountain's river. The term "run-of-water" means that there is no water storage and that electricity fluctuates with the flow of the stream [12].

2.2 Design consideration

The design of a micro-hydro-powerplant requires a lot of design consideration to be taken into account like site study & selection, measuring rate of water flow and head, civil work components (dam, trash rack, and penstock), turbine type, size, and power generation are all considered.

2.2.1 Flow rate measurement:

There are various ways for measuring the water flow rate (discharge). The velocity-area technique, which measures the flow's cross-sectional area and mean velocity, is a common method for small to large flows. It is a practical method for measuring discharge with the least amount of effort.

2.2.2 Weir: A Weir may be possible to build in rivers with minimal discharge (less than four cubic meters per second). It's a low wall or dam built over a stream with a notch through which all of the water may flow.

2.2.3 Trash rack design:

To prevent unwanted waste from entering the entrance flume, parallel bars looking racks are installed at a specific spacing (at an angle of 60 to 80 degrees with horizontal). Turbine makers usually specify the maximum allowable spacing between the bars. To prevent floating debris from entering both pressure pipes and intakes, a screen or grill is always near the entry. A head loss is also caused by the passage of water through the rack. The trash rack coefficient (K_{tr}) varies depending on the form of the bar and can range from (0.8) to (2.4).

2.2.4 Penstock design:

Water is transported from the intake to the powerhouse by penstocks (pipes). Considering the criteria like the nature of the ground, the penstock materials, the ambient temperature, and the surrounding requirements, they can be erected above or below ground. The flowrate, pipe length, and gross head may all be used to calculate the internal penstock diameter (D_p).

2.2.5 Head measurement:

The gross head (Hg) of a reaction turbine (such as a Francis or Kaplan turbine) or an impulse turbine (such as a Pelton, Turgo, or Cross-flow turbine) is the distance measured in-

between the surface of the water level at the input and tailrace and the outlet level. Modern electronic digital levels provide an automatic display of height and distance in around four seconds, with a measurement precision of 0.001 inches (0.4 mm). Surveying with a Global Locating System (GPS) is already ubiquitous, and a portable GPS receiver is ideal for field positioning and basic mapping. After the gross-head is calculated, we need to subtract the losses encountered along the route, like open channel loss, garbage rack loss, intake or inlet to penstock loss, gate or valve loss, and penstock friction loss, to obtain the net head.

2.2.6 Hydraulic power:

Waterfalls are required for all hydroelectric production. A hydropower plant's fuel is streamflow, and in its absence, production stops needless the flow of water through the open channel or penstock. The hydraulic power generation (lost from water potential energy) is given as [13]:

$$P_h = \rho \times g \times Q \times H_n \text{ (Watts)} \quad (1)$$

where, P_h = Power in watt generated by hydraulic force, Q = Pater flow rate (m^3/s), g = Gravity acceleration constant (9.81 m/s^2), H_n = Net head (m) respectively. Once the hydraulic power has been got, the turbine power can calculate be with the following formula [13]:

$$P_t = P_h \times \eta \quad (2)$$

where, P_t = Power in watts generated in the turbine shaft, η = Efficiency of a turbine. It should be remembered that the head of an impulse turbine is measured at the point of jet impact, which is always above the downstream water level. This results in a head decrease. When comparing the performance of impulse turbines with reaction turbines that employ the whole available head, the difference is not inconsequential for low head designs. The turbine efficiency must be multiplied by the efficiencies of the speed increase (if any) and the alternator to get the total efficiency of the micro-hydro-power plant.

2.2.7 Turbine speed:

A specific amount of rotating component inertia is necessary to regulate the turbine speed by managing the water flow rate. A flywheel mounted on the turbine or generator shaft can offer additional inertia. When the load is disconnected, the extra power accelerates the flywheel; when the load is restored, the added inertia decelerates, providing additional power that helps to reduce speed variance [14].

2.2.8 Turbine type:

The turbine type, key measurement, and height or elevation above the tailrace water surface where the turbine should be positioned to prevent cavitation may all be established if the turbine power, specific speed, and net head are known. In the case of Kaplan or Francis turbines, the head loss due to cavitation, the net head, and the turbine power must all be recalculated. Pelton turbines, in general, span the high-pressure domain for micro hydro down to (50 meters). The Francis models of turbines cover the broadest range of heads below the Pelton turbine region, with some over-lapping and down to (10 meters) heads for micro-hydro. Kaplan-type turbines with fixed or moveable blades cover the lowest region of the head below 10 m. The cross-flow impulse turbine may also be utilized for low heads and up to (50 m). The essential dimensions of the turbine may be approximated once the turbine type is understood. For our theoretical calculation, we have selected a cross-flow turbine as for theory our head is 6 meters and the flow rate is 0.1 m^3/s.

The selection of turbine depends on various parameters such as water head, discharge, demand capacity, etc. Based on that, for theoretical analysis and model development, we have chosen a site from Table 2 of the potential sites identified by the IFRD of BCSIR. From Table 2 the flow rate was found to be 100 liter/sec or 0.1 m^3/s and the net head 6 meters. Before selecting the turbine let's have a look at the Cross-flow turbine. Cross-flow turbines are a subcategory of impulse turbines. The main reason for this classification is that these turbines do not submerge like reaction turbines and function in the air. Atmospheric pressure is used to operate the set. They can be used with a variety of heads and powers. Working with heads ranging from 1.75 to 200 meters and powers ranging from 5 to 100 kW, these turbines have left a versatile machine in mind. At larger sizes, up to 3 MW, these turbines have left a flexible machine in mind. These turbines, on the other hand, are typically employed in heads under 40 meters and for lower power. These turbines run at a flow rate of 40 to 5000 liters per second on average. These turbines have several advantages, including the ability to be employed in smaller hydroelectric projects and the fact that they require less complex maintenance to keep them running. As a result, they are better suited for use in remote areas [15]. Although these turbines are helpful for a wide range of hydraulic heads and power outputs, they are most efficient when the heads and power outputs are low. So, for 0.1 m^3/s flow rate and 6 meters of the head, we have selected the cross-flow turbine based on 3 reasons: Firstly, the cross-flow turbine is a low head turbine. Secondly, this is a very simple and low-cost turbine in this low head region. Finally, for the comparison purpose as there is already a micro hydropower plant installed in Bamerchara Lake. In which cross-flow turbine is being used.

2.2.9 Crossflow Turbine Working:

The working principle of the cross-flow turbine is very simple. A drum-shaped rotor with fixed disks at both ends connects the two disks of the Cross-flow turbine. The water is delivered to the rotor from the inflow guide. For the first time, the inflow guide directs pressured water to the rotor, transferring the impulse force inside the drum. After this, the water travels through the rotor and exits the turbine at atmospheric pressure. The water pressure is then changed by the cross-flow turbine, which converts it into mechanical energy. This effect minimizes the pressure drop across the buckets of the turbine by a little amount, increasing

efficiency. The upper buckets extract the majority of the energy (about 75%), while the bottom buckets extract the remaining 25%. The kinetic energy of the water flowing through the turbine rotor buckets is converted into torque on the output shaft, which is used to operate the generator in a small hydroelectric system. The coil of the generator attached to the electrical load is subsequently turned by the cross-flow water turbine. Figure 1 shows the schematic diagram of a Cross-flow turbine.

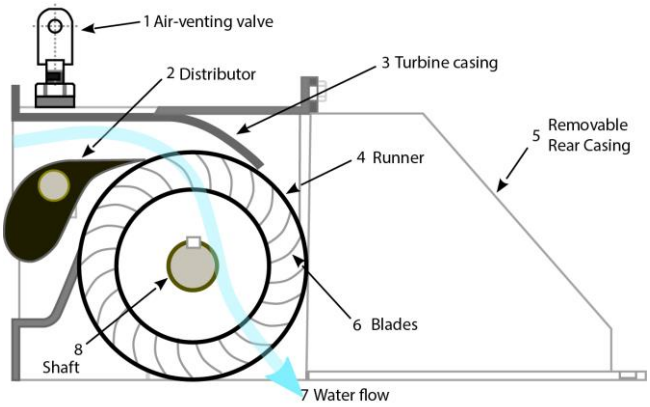

Fig. 1: Schematic diagram of cross-flow turbine [17].

2.3 Theoretical analysis:
The designing technique includes determining the many parameters related to the turbine.

2.3.1 Net head (H_n):
The difference between the gross head and the head coequal of loss is the net head. The losses account for leaks in pipelines, channels, waste rakes, penstocks, and so on.

$$H_n = H_g - H_t \quad (3)$$

H_t is the head equivalent for various losses that occur in pipelines, channels, and so on. This loss amounts to around 6 percent of the gross head. H_g is the gross head at the turbine's intake. So, the turbine's net head is

$$Hn = 6 - 0.36 = 5.64 \text{ m.}$$

2.3.2 Water flowrate (Q):
This is the measurement of the velocity of the water around the cross-section area of the turbine's outlet.
Here,

$$Q = A \times V \quad (4)$$

The flowrate taken for the turbine was Q = 0.1 m^3/s.
Turbine efficiency (η): The maximum turbine efficiency may be estimated using the formula [16], [17]:

$$H = 0.5 \times C^2 \times (1+\psi) \times (\cos\alpha)^2 \quad (5)$$

It can be seen from the following equation that a low angle of attack (α) is advantageous. Without a problem, a sixteen-degree attack angle may be manufactured. Here, Ψ = Blade roughness coefficient (0.98 for low carbon steel), C = Nozzle roughness coefficient (0.98 for low carbon steel), η = 88%.

2.3.3 Hydraulic power (P_h):
The term refers to the output power created by the turbine. In other words, potential energy from water may be expressed as [16]:

$$P_h = \rho \times g \times Q \times H_n \quad (6)$$

So, P_h =1000×9.81 × 0.1 × 5.64 = 5532.84 Watts = 5.53 kW

2.3.4 Turbine power (P_t):
The product of hydraulic power and turbine efficiency is turbine power. It can be given as:

$$P_t = P_h \times \eta = 5.53 \times 88\% = 4.87 \text{ kW} \quad (7)$$

2.3.5 Turbine speed (N):
The spinning speed at which the turbine's runner spins is called the turbine speed. The formula used to determine the turbine speed is [16]:

$$N = 513.25 \times (H_n\ 0.745\ /\sqrt{}\ P) = 513.25 \times (5.64\ 0.745\ /\sqrt{}\ 4.87)$$

$$N = 843.85 \approx 850 \text{ rpm} \quad (8)$$

2.3.6 Runner outer diameter (D_o):
The runner's outer diameter is the diameter between the center of the shaft and the runner's outermost point. The flow conditions determine its selection. A wider diameter turbine is used for a higher flow rate, whereas a smaller diameter turbine is used for the lower flow.

$$D_o = 40 \times \sqrt{H} / N = 40 \times \sqrt{5.64} / 850 \text{ (mm)}$$
$$D_o = 112 \text{ mm}$$

2.3.7 Blade spacing (t_b): The tangent blade distance can be given as

$$t_b = 0.174 \times D_o = 0.174 \times 112 \text{ (mm)}$$
$$t_b = 19.48 \text{ mm}$$

2.3.8 Radial rim width (a):
The distance between the outer and inner radius of the turbine's runner may be characterized as radial rim width.
It can be given as:

$$a = 0.174 \times D_o = 0.174 \times 112 \text{ (mm)}$$
$$a = 19.48 \text{ mm}$$

2.3.9 No. of blades in the runner (n):
An optimal no. of blades for the turbine should be used since an excessive no. of blades would generate pulsing power and lower turbine efficiency, while a low number will result in incomplete water use. The no. of runner blades can be determined as

$$n = \pi \times D_o / t_b = \pi \times 112 / 19.48$$

Then the number of blades, n = 19,

2.3.10 Runner length (L): It represents the runner's length on the turbine's axis. The calculation of (L) is:

$$L = (Q \times N) / (H \times 50) = (0.1 \times 850) / (5.64 \times 50)$$
$$L = 301 \text{ mm}$$

2.3.11 Runner inner diameter (Di): The runner's Inner diameter can be calculated as

$$D_i = D_o - 2 \times \text{radial rim width (a)} = 112 - 2 \times 19.48$$

So, Inner diameter of the runner (D_i) = 73 mm.

2.3.12 Blade radius curvature (r_b): It is the radius of the curvature of the turbine's curved blades.

It can be calculated as

$$r_b = 0.163 \times D_o = 0.163 \times 112$$
$$r_b = 18.256 \text{ mm} \approx 18 \text{ mm}$$

2.3.13 Diameter of shaft (D_s): The shaft's diameter should be large enough to bear the turbine's load. For a better flow of water through the turbine, the size should be optimal. The equation to calculate it is:

$$D_s = 0.22 \times D_o$$
$$D_s = 24.64 \text{ mm} \approx 24 \text{ mm}$$

Table 3: Design specifications of the cross-flow turbine

Descriptions	Dimension
Gross head, H_g	6 m
Net head, H_n	5.64 m
Discharge, Q	0.1 m^3/s
Turbine efficiency, η	88%
Turbine power, P_t	4.87 kW
Turbine speed, N	850 rpm
Runner outer diameter, Do	112 mm
Blade spacing, t_b	19.48 mm
Radial rim width, a	19.48 mm
Number of runner blades, n	19
Runner length, L	301 mm
Runner inner diameter, D_i	73 mm
Blade radius curvature, r_b	18 mm
Diameter of shaft, Ds	24 mm

2.4 Model development

The main part of a hydropower plant is the turbine. For the project calculation, we have used a cross-flow turbine. The model of the cross-flow turbine was designed according to the calculated value using the 64-bit SolidWorks 2016 Software. The whole model is developed into different parts; Side disk, Runner blade, Shaft, Casing, and Nozzle. Figure 2 shows the runner side disk, runner blades, runner and shaft. The final runner assembly is shown in Fig. 3. The Cross-flow turbine assembly is represented in Fig. 4. The major design specifications of the cross-flow turbine are presented in Table 3.

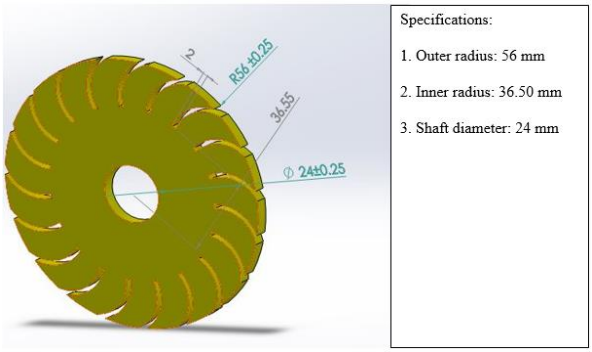

(a) Runner side disk

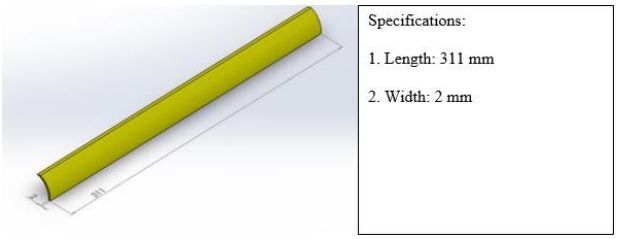

(b) Runner blade

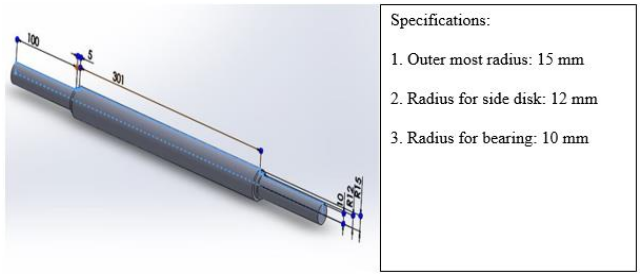

(c) Shaft

(d) Runner assembly

Fig. 2: (a) Runner side disk, (b) Runner blade, (c) Shaft.

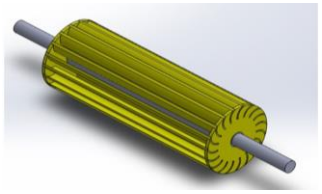

Fig. 3: Final runner assembly

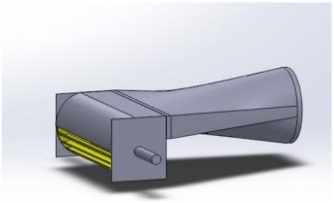

Fig. 4: Crossflow turbine assembly

2.5 Numerical Analysis

To study and conduct the numerical analysis of flow characteristics on the cross-flow turbine we used a three-dimensional geometry of horizontal propeller type turbine. Figure 5 shows the geometry of the turbine and the dimensions as well. Then, the model was meshed by using ANSYS ICEM-CFX (15.7) software [18]. The hydraulic turbine's flexible design made it possible to use the unstructured tetrahedral grid system to create the grid. There were 368686 nodes and 1886134 elements in total for

the meshing grids. Figure 6 displays the tetra meshing grids for the unstructured processes. Figure 7 shows the turbine domain prototype for analysis data. The turbulence model was set as Shear Stress Transport (SST) with boundary conditions; mass flow rate for inlet and pressure in the outlet. The outlet pressure was set as 0 Pa or atmospheric pressure. The boundary conditions were taken as smooth wall surface with rotation speed of 850 rpm.

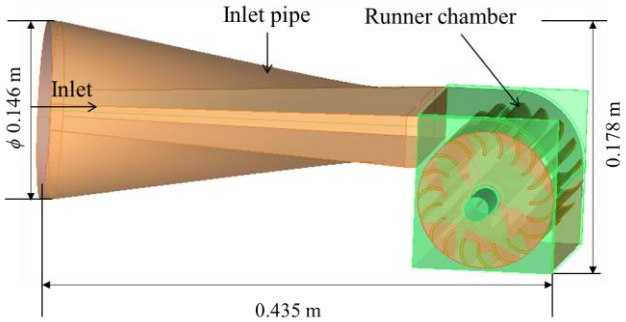

Fig. 5: Three-dimensional geometry of the turbine.

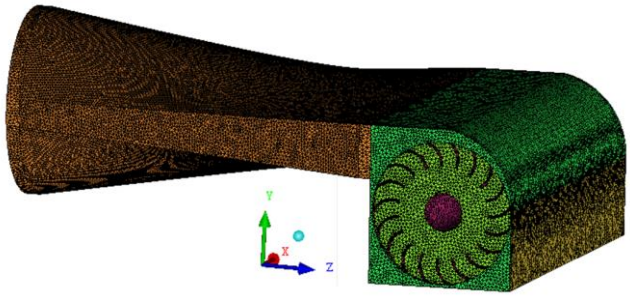

Fig. 6: Unstructured tetrahedral meshing grids.

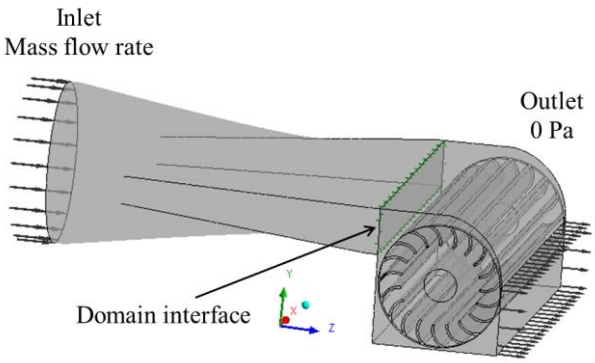

Fig. 7: Turbine domain for data analysis.

3. RESULT AND DISCUSSION

3.1 Analytical result

As it is said earlier, there is already a micro-hydropower plant at Bamerchara Lake, Banshkhali, and Chittagong. Therefore, Table 4 illustrates a comparison between the existing micro-hydro power plant and theoretical results. So here, from Table 4, we can see that theoretical design results are similar to the existing turbine.

Table 4: Design specification comparison of existing hydro and theoretical designed

Description	Bamerchara hydro unit	Theoretically designed unit
Type of turbine	Crossflow	Crossflow
Net Head	6 m–10 m	5.64 m
Flow rate	150 liter/sec	100 liter/sec
Turbine Power	4 kW- 6 kW	4.87 kW

3.2 Performance characteristics of cross-flow turbine

In our analysis, it was found that the turbine was able to produce a power of 4.83 kW with 87.65% efficiency at 0.1 m^3/s flow rate as shown in Figure 8. The efficiency drops both with increase and decrease of flow rate. The effects of pressure and velocity are shown in Figure 9 and Figure 10. From Figure 9, the pressure contour shows that the pressure is maximum around the inlet and in the shaft. In Figure 10, the velocity contour again shows higher velocity around the inlet and on the pressure side of the blades and around the outlet side. Figure 11 shows the velocity vector where we notice that around the down right side a velocity circulation is created which results in loss of energy.

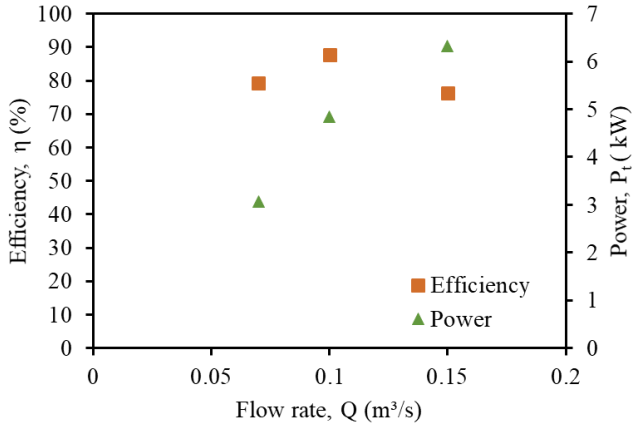

Fig. 8: Efficiency curve of the turbine model.

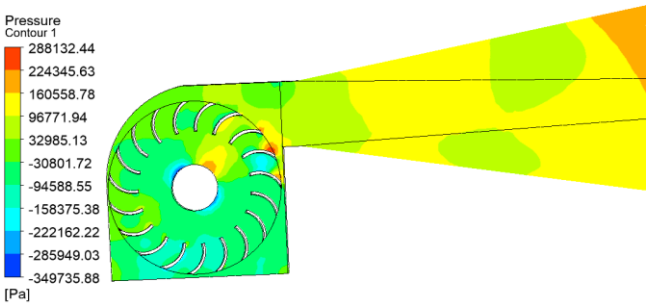

Fig. 9: Pressure contour of cross-flow turbine.

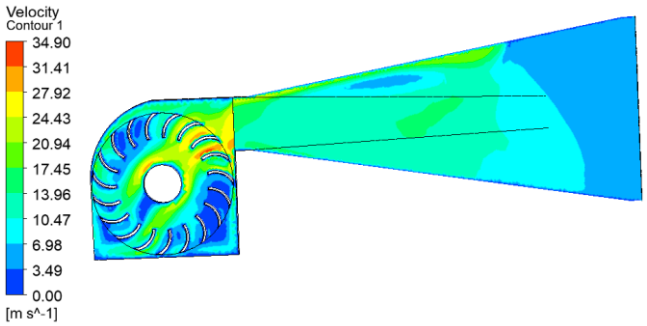

Fig. 10: Velocity contour of cross-flow turbine.

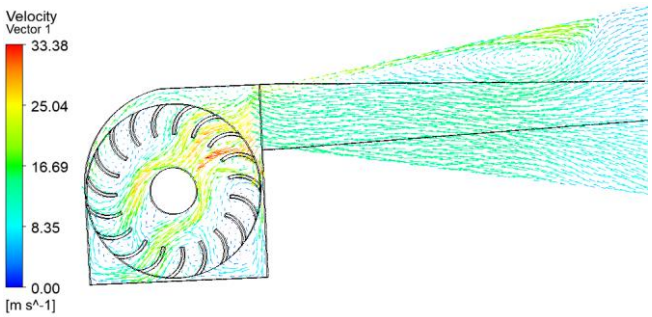

Fig. 11: Velocity vectour of cross-flow turbine.

4. CONCLUSION

The micro-hydro power plant plays a very significant part in the world's total electricity supply. Particularly in rural areas, it provides a dependable and cost-effective source of power. It has a decent potential within the northeastern hilly regions of Bangladesh. Because of the sufficient waterfalls, rivers, and canals, Bangladesh incorporates a good run-off water micro-hydro potential. Nevertheless, it has yet to be investigated. Parameters to line up a new micro-hydro plant have been considered. As the hydro powerhouse does not use non-renewable energy, it can assist to preserve a lot of other energy resources. In this study, it has been shown that the theoretical result of the targeted site was 4.87 kW which was approximately similar to the real estimated value from that site. Although there were some considerations in the theoretical part like the roughness of the material, the efficiency of the turbine, penstock length, etc., the study showed that this kind of project could be possible by the authority of the proposed area, which already has been discovered. In general, it can be said that based on the study, a site with 100-150 liter/s of flow rate and a head of 5-6 meters could easily produce around 3-5 kW of power supply considering all kinds of loss. Finally, correct parameter consideration to examine possible places may motivate interested individuals and provide an incentive to decide on micro-hydro plants for local usage.

REFERENCES

[1] (SREDA), Sustainable and Renewable Energy Development Authority. "*Energy Efficiency and Conservation Master Plan up to 2030*". May, 2016.

[2] Hydrocarbon Unit, Energy and Mineral Resources Division, Ministry of Power, Energy and Mineral Resources. "*Energy Scenario of Bangladesh*". Dhaka: s.n., 2020-2021.

[3] "Sustainable and Renewable Energy Development Authority (SREDA)"Power Division, Ministry of Power, Energy & Mineral Resources. http://sreda.gov.bd/site/page/55ef773a-18fa-4bde-94bb-9502275051b2 (accessed Mar. 28, 2022).

[4] "RE Generation Mix | National Database of Renewable Energy," http://www.renewableenergy.gov.bd/ (accessed Mar. 28, 2022).

[5] Bangladesh Renewable Energy Report by Asian and Pacific Centre for Transfer of Technology of the United Nations—Economic and Social Commission for Asia and the Pacific (ESCAP).

[6] M. A. Wazed and S. Ahmed, "Micro hydro energy resources in Bangladesh: a review," Australian Journal of Basic and Applied Sciences, vol. 2, no. 4, pp. 1209–1222, 2008.

[7] An overview of the hydropower production potential in Bangladesh to meet the energy requirements, Environmental Engineering Research. 2021; 26(6): 200514:200514-0.

[8] M. N. Ali, A. J. Nahian, A. H. Siddique, M. Hasan, N. Chowdhury and C. A. Hossain, "Prospect of Mini-Hydel Power Generation in Drainage Systems of Bangladesh," 2021 2nd International Conference on Robotics, Electrical and Signal Processing Techniques (ICREST), 2021, pp. 278-281.

[9] Yoosef Doost A, Lubitz WD. "Archimedes Screw Turbines: A Sustainable Development Solution for Green and Renewable Energy Generation—A Review of Potential and Design Procedures. Sustainability". 2020; 12(18):7352.

[10] Rakibuzzaman, M.; Suh, S.-H.; Kim, H.-H.; Ryu, Y.; Kim, K.Y. "Development of a Hydropower Turbine Using Seawater from a Fish Farm". Processes 2021, 9, 266.

[11] Nohyun Park, Md Rakibuzzaman, Sang-Ho Suh (2019) "Flow Analysis of 30 kW Gate Turbine Using Permanent Magnetic Generator, Heat Transfer Engineering", 40:17-18, 1511-1522.

[12] "3.2.2 Description of the Components of a Micro-Hydro PowerScheme."https://learning.uonbi.ac.ke/courses/SMR408/scormPackages/path_2/lecture_3.html (accessed Mar. 30, 2022).

[13] Bilal Abdullah Nasir, "Suitable Selection of Components for the Micro-Hydro-Electric Power Plant," Advances in Energy and Power, Vol. 2, No. 1, pp. 7 - 12, 2014.

[14] Nazari-Heris, M., & Mohammadi-Ivatloo, B. (2017). Design of Small Hydro Generation Systems. In Distributed Generation Systems (pp. 301–332).

[15] G. Boyle, Renewable Energy: Power for a Sustainable Future (3rd ed.), Oxford University Press and Open University.

[16] Mockmore, C. A., "The Banki water turbine. Engineering Experimental Station", Oregon State College, (1949).

[17] Celso Penche, Laymans Guidebook on how to develop a small hydro site, 2nd ed. ESHA, 1998. pp. 158.

[18] Ansys Inc. (2015) ANSYS-CFX (CFX Introduction, CFX Reference guide, CFX Tutorials, CFX-Pre User's Guide, CFX-Solver Manager User's Guide, Theory Guide), release 16, USA.

Paper ID: 8462

International Conference on Mechanical, Manufacturing and Process Engineering (ICMMPE – 2022)

Organizer: Faculty of Mechanical Engineering, Dhaka University of Engineering & Technology (DUET), Gazipur, Bangladesh

Website: https://icmmpeduet.com/

Evaluation of Mechanical Properties of SG295 Steel at Elevated Temperatures in LPG Cylinder with Heat Treatment

Md. Ruhul Amin[1], Md. Arefin Kowser[2] and Mohammad Asaduzzaman Chowdhury[3]

[1] *Senior Engineer (Mechanical), Nuclear Safety, Security & Safeguard Division, Bangladesh Atomic Energy Regulatory Authority, Dhaka, Bangladesh*
[2] Professor Dr. Md. Arefin Kowser, *Department of Mechanical Engineering, Dhaka University of Engineering and Technology (DUET), Gazipur-1707, Bangladesh*
[3] Professor Dr. Mohammad Asaduzzaman Chowdhury, *Department of Mechanical Engineering, Dhaka University of Engineering and Technology (DUET), Gazipur-1707, Bangladesh*

E-mail: ruhul_rm@yahoo.com

ABSTRACT

Steel has promising applications in the production of LPG cylinders. SG295 steel is used to manufacture LPG cylinders in most industries. Internal stress is a common limitation of the manufacture of LPG cylinders. The annealing heat treatment process is applied to regenerate overheated steel structures and remove internal stresses. In this article, the mechanical properties of SG295 steel in the production of LPG cylinders were characterized. For this purpose, samples were heat treated by annealing. The experiment was performed to determine the effect of annealing temperature on the mechanical properties of steel LPG cylinders and the goal is to achieve better mechanical properties in terms of experimentally particular ductility and elongation. Furthermore, it is aimed at experimentally achieving better mechanical properties and reducing production costs at particular ductility and elongation with lower annealing temperatures. Several samples were produced according to DOT-4BA-240, heat-treated with different annealing temperatures (800 °C, 850 °C, and 900 °C). Tensile test, elongation test, and bust test were conducted to determine the annealing effect on the steel cylinder. Obtained results showed that there was a higher percentage of elongation 34.18% El was achieved at an annealing temperature of 900 °C and which also can reduce production costs without degrading the quality of the LPG cylinder.

Keywords: Steel Cylinders; Steel SG 295; Internal Stress; Annealing; Mechanical Properties

1. INTRODUCTION

Liquid petroleum gas or liquefied petroleum gas (LPG or LP gas) may be a combustible blend of hydrocarbon gasses utilized as a fuel in warming hardware, cooking, and vehicles. There are different types of LPG buying and selling mixes that contain mostly propane (C_3H_8), butane (C_4H_{10}), and, in general, both propane and butane. In the Northern Hemisphere, in the winter, the mixtures contain more propane, but in the summer, they contain more butane [1]. The boiling point of LPG is below room temperature. LPG evaporates rapidly at normal temperature and pressure. This gas is usually supplied by pressurized steel vessels. There is 80-85% filled-in cylinder capacity due to the thermal expansion of the liquid in it. Different types of cylinders are used for the storage and distribution of LP gas. Cylinders have been made from conventional metals like steel in the world for the last many years. Steel cylinders are commonly used for its high mechanical properties and longevity. LPG cylinder production consists of several cold and hot working processes such as sheet metal shearing, forming, surface treatment and testing process. A few mechanical working frameworks with cold working courses like wire drawing, sheet metal arrangement and cold rolling result in diminished ductility as the cold working forms increment [2]. Micro structurally, this increase in internal energy is associated with the density of displacement as well as the density of point defects such as vacuums and interstices. At a more macrostructural level, the grains tend to enlarge exponentially towards work and heavier deformation. These dislocations in the grain structure allow for an overall change in the metallic shape. Increased hardness and internal stress due to cold work and welding operations are considered a threat to the LPG cylinders. Annealing is an effective mechanism for relieving internal stress, similarly, the annealing heat treatment process is especially important

for achieving the required mechanical properties in the finished cylinder. This usually means holding the cold-worked metal at a temperature of about 1/3 of the absolute melting point for a while. Through recrystallization, the deformed grains are supplanted by new grains that nucleate and develop until the initial grains have been devoured.

The average hardness values of 0.124% carbon metals were shown to be the highest values compared to metals of carbon 0.129, 0.135 and 0.119 after reduced internal stress of metal of LPG cylinders [3]. Several samples were made concurring to ISO 6892, and after that heat-treated with different annealing temperatures (850 ºC, 900 ºC and 950 ºC). The projection of the grain becomes larger with increasing the annealing temperature. As the annealing temperature increases the microhardness decreases but at 940 C it expands back, the maximum extreme decrease was 31.6% which was achieved at 900 ºC [4]. From a review of the literature, it has been observed that various studies were available for the variation in temperature and holding time has moreover been broadly dealt with by a few over time. No study was found based on the variation in the annealing temperature of the steel SG295 in the LPG cylinder manufacturing phenomenon.

2. MATERIALS AND METHODS

2.1 Material

The Steel SG 295 was used to carry out this study which is widely used for manufacturing LPG cylinders.
The mentioned steel is used for making domestic LPG cylinders due to their mechanical and chemical properties, which match the criteria of the LPG cylinder production agreeing to DOT4BA240 guidelines. The chemical composition and mechanical properties of the 2.5 mm thick hot-rolled steel sheet used for welded gas cylinders as described in standards JIS G 3116 SG295 are shown in Table 1 and Table 2.

Table 1: Chemical composition of Steel SG295

Chemical composition (%)							
Fe	C	Si	Mn	P	S	Cr	Mo
98.91	0.13	0.014	0.8	0.012	0.003	0.01	0.01

Table 2: Mechanical properties of steel SG295

Thickness (mm)	Yield point or proof stress (MPa)	Tensile Strength (MPa)	Elongation (%)
2.5	295	440	26

2.2 Methodology

2.2.1 Chemical Composition Analysis

To perform this study, we used three samples of SG 295 steel and samples were collected from hot roll coils. The chemical composition test of the sample was accomplished by spectrometry instrument.

2.3.2 Annealing process

Annealing is a heat treatment process that changes the physical and sometimes chemical properties of a material to extend its ductility and decrease its hardness, making it more workable. The iron-carbon binary phase diagrams (Figure 1) can be utilized to way better understand the annealing processes. The carbon percentage of the samples was 0.1326 and the peak temperatures were set at 800 ° C, 850 C and 900 C, respectively and heated in Gas Furnace. To achieve this study, we used three sets of LPG cylinders that were annealed at different temperatures, same holding time and in the same cooling method. The annealing conditions are shown in Table 3.

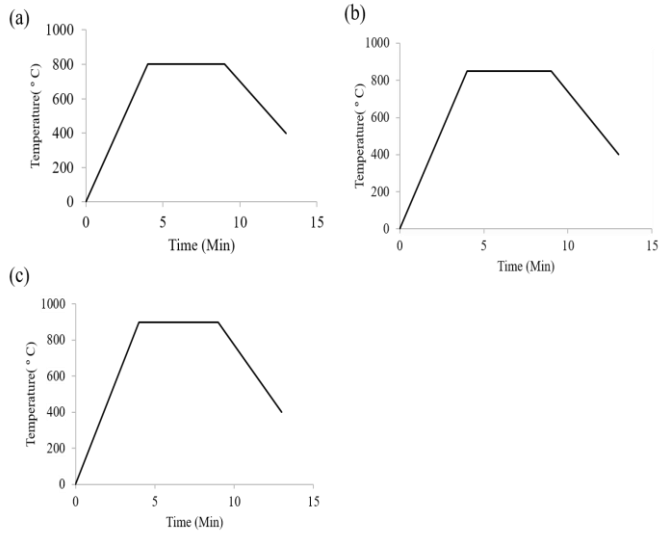

Fig.1: Annealing regimes of steel grade SG 295.

Table 3: Design process of annealing heat treatment formulation of steel SG295

Specimens	Peak Temperature (^{0}C)	Holding Time (min)	Cooling Mode
Sample 1	800	5	Air Cooling
Sample 2	850	5	Air Cooling
Sample 3	900	5	Air Cooling

2.2.3 X-ray test

X-ray testing is used to create a detailed image of the internal structure of an object. X-ray is a suitable method for weld inspections because technicians do not have to change or destroy the product to analyze it in detail. In this study, an X-ray test was used to analyze any defect in the welding joint of the LPG cylinder after annealing. Welding defects can affect the results of the cylinders bust test and elongation test.

2.2.4 Tensile Test:

The investigated LPG cylinders were fabricated by utilizing a deep drawing process from steel SG295 according to the standard DOT4BA240, which were along these lines welded together in the peripheral direction. Those cylinders were carried out for annealing heat treatment at the temperature mentioned in Table 3. The sample was cut from the welded area of the annealed cylinder. The tensile tests were performed utilizing the CMT-10 Computer Control Electronic Universal Testing Machine. All mechanical testing of the sample was conditional on agreeing to the standard strategy of DIN EN 10002-1. The test narrow section Width was 13mm, length 57mm, thickness 3.3 mm and gage length 25mm. There are three specimens were tested for each sample.

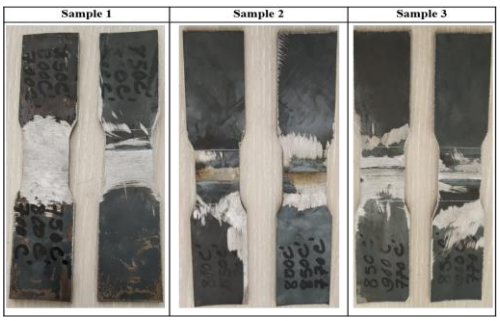

Fig. 2: Tensile test samples (weld metal).

2.2.5 Burst test

Generally, cylinders tested for volumetric extension tests can be utilized for this reason. In this test, the cylinders are subjected to nonstop hydrostatic internal pressure until they explode the inside pressure of the cylinder at which it bursts is famous and recorded as burst pressure. Nominal hoop stresses are calculated based on this burst pressure utilizing the equation below

$F_b=(P_b \times D_i) / 2t$

Where,
F_b-nominal hoop stress
P_b-Internal hydrostatic pressure (MPa)
D_i -Nominal original internal diameter of the cylinder (mm)
t - Minimum agreed finished thickness of the cylinder (mm)

The burst test was performed utilizing the computer control Burst Testing Machine, ROK Teknik, Turkey.

2.3 Results & discussion

2.3.1 Tensile Test

Fig and the table show the maximum tensile strength and the elongation of the three samples. Observing the results of the tensile test, it is seen that the mechanical strength of sample-3 is higher. Sample-1 showed the lowest mechanical strength. Tensile strength varies due to internal stress. High internal stress was removed from sample-3 at 900 ^oC temperature. Also, height elongation was found in Sample-3. The reason for the greater elongation is the better ductility of the sample which is found in sample-3.
The tensile strength of the untreated welding sample was 662MPa and elongation 8%, tensile strength after heat treatment, decreased and increased elongation for all samples (Table 5).

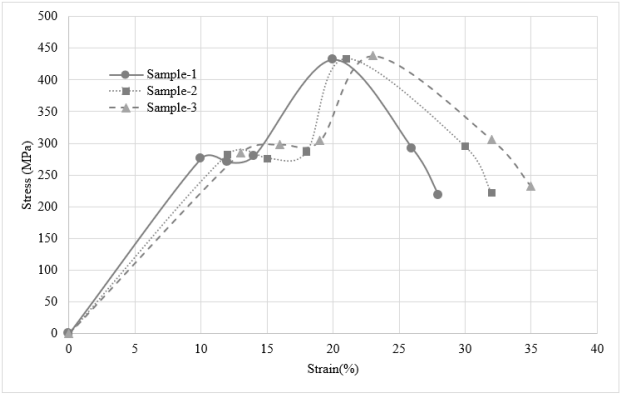

Fig. 3: Stress vs. strain curve for three sample

Table 4: Mechanical properties of three sample

Sample	Maximum Tensile Strength (MPa)	Elongation (%)
Sample-1	432	28
Sample-2	433	32
Sample-3	438	35

Table 5: Comparison of tensile strength with untreated welded sample

Sample	Max^n Tensile Strength (untreate	Max^n Tensile Strength (treated)	Elongation (untreated Samples) (%)	Elongation (treated Samples) (%)

	d) (MPa)	(MPa)		
Sample-1	662	432	8	28
Sample-2	662	433	8	32
Sample-3	662	438	8	35

2.3.2 Burst Test

The cylinder burst test was performed for three types of samples after heat treatment. Table 6 shows the results of the burst test. Sample-3 provides high burst pressure which is 94.87 bar and minimum sample-1 is 94.23 bar. Sample-2 shows better elongation during the burst test. The blast test pressure depends on the internal stress and the grain reformation of the cylinder. The test results show that sample-3 has better grain reformation and maximum internal stress has been eliminated during heat treatment.

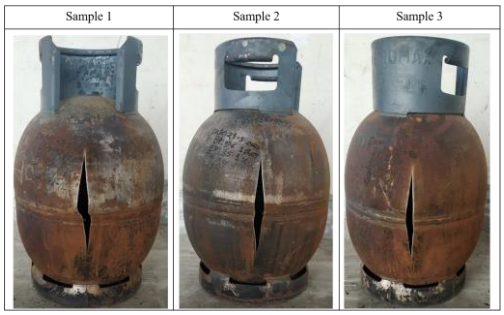

Fig. 4: Burst tested Cylinders.

Table 6: Burst properties of three sample

Specimens	Bust Test Pressure (Bar)	Elongation (%)
Sample 1	94.23	26.92
Sample 2	94.35	32.43
Sample 3	94.87	31.23

2.3.1 X-ray Test

The welding joint is a major component of LPG cylinders. Defects in welding joints can reduce tensile strength and blasting pressure. X-ray film shows that there is no defect in the welding joint. Three sample welding joints were taken. There is no discontinuity in the welding joint. Thus, the effect of the welding joint on the mechanical properties of the cylinder is negligible.

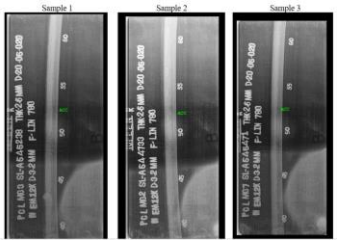

Fig. 5 X-ray tested films

4. CONCLUSION

The most usable steel grade SG295 for the LPG steel cylinder manufacturing company was used for experimental investigation after forming and welding. Three samples were prepared for annealing at different holding temperatures (800 ºC, 850 ºC, and 900 ºC). Better tensile strength, as well as elongation, was found in sample-3 which was annealing at 900 ºC temperature. The maximum tensile strength is 438 MPa and the elongation is 35% found in sample-3. The same result is found in the blast test where the sample-3 burst test pressure is 94.87 bar. The quality of the LPG steel cylinder is improved by an annealing temperature of 900 ºC and a holding time of 5 minutes.

ACKNOWLEDGMENT

All technical and financial support for this experimental investigation was provided by Petromax Cylinders Limited, Mirzapur, Tangail, Bangladesh. We also acknowledge to Department of Mechanical Engineering, Dhaka University of Engineering and Technology (DUET), Gazipur, Bangladesh for theoretical and experimental guidelines.

REFERENCES

[1] Ahmed, Y. M., Lafta, H. D., & Abdulrahman, A. A. , “Study the durability of welding and performance of base metal of L. P. G. home cylindrical manufactured in Kurdistan region,” Journal of Energy, Mechanical, Material, and Manufacturing Engineering), 4(2), 91-100, 2019.

[2] Cao, R., X. Yu, Z. Feng, M. Ojima, J. Inoue, and T. Koseki. "Effect of annealing temperature and time on microstructure and mechanical properties of multilayered steel composite sheets," Metallurgical and Materials Transactions A 47, no. 12, 6042-6055, 2016.

[3] Fayomi, O. S. I., T. O. Joshua, F. H. Olatuja, and O. Agboola. "Effect of annealing on the mechanical characteristics of steel welded joint." Procedia Manufacturing 35,1387-1394, 2019.

[4] Al-Qawabah, S.M.A., Nabeel Alshabatat, U.F. and Al-Qawabeha, G. “Effect of Annealing Temperature on the Microstructure, Microhardness, Mechanical Behavior and Impact Toughness of Low Carbon Steel Grade 45,” International Journal of Engineering Research and Applications (IJERA), 2, 1550-1553, 2012.

Paper ID:8472

International Conference on Mechanical, Manufacturing and Process Engineering (ICMMPE – 2022)

Organizer: Faculty of Mechanical Engineering, Dhaka University of Engineering & Technology (DUET), Gazipur, Bangladesh

Website: https://icmmpeduet.com/

Enhanced Mechanical Properties and Stimulation of hMSC Responses to HAp Particles Layered Porous Collagen Composite Scaffolds under 2-Phase Condition for Bone Regeneration

Md. Shariful Islam[1*], Syed Sarwar Jahan[1], Mirza Humaun Kabir Rubel[2], G. M. Shafiur Rahman[2], and Mitsugu Todo[3]

[1]Department of Veterinary and Animal Sciences, University of Rajshahi, Rajshahi-6205, Bangladesh
[2]Department of Materials Science and Engineering, University of Rajshahi, Rajshahi-6205, Bangladesh
[3]Research Institute for Applied Mechanics, Kyushu University, Kasuga, Fukuoka 816-8580, Japan

*E-mail: msips06@ru.ac.bd

ABSTRACT

The purpose of this work was to see how biocompatible porous scaffolds made from hydroxyapatite (HAp) bioceramics utilizing the sponge template method of polyurethane (PU) affected mechanical and biological qualities. The prepared HAp scaffolds were fabricated in 2-phase condition with collagen (COL) or collagen/HAp particles (COL/HAp, 9:1 ratio). The FE-SEM and Shimadzu Compact Tabletop Testing Machine (EZ Test) were used to analyze the mechanical properties as well as porous microstructure of the fabricated biomaterials. The microporous architectures of prepared and produced composite scaffolds were visible in FE-SEM micrographs. The porosities of the fabricated biomaterials were significantly reduced and the mechanical properties were enhanced by the integration of COL or COL/HAp materials into pure HAp scaffolds in 2-phase environments. The significant cell adhesion, as well as proliferation of in vitro Human Mesenchymal Stem Cell (hMSC) over the developed COL and COL/HAp, incorporated scaffolds exhibited biocompatibility. Additionally, the fabricated composite scaffolds displayed enhanced mechanical properties with the mechanical test of hMSCs seeded composite scaffolds. Thus, these findings demonstrated that the mechanical properties of manufactured porous composite scaffolds for bone tissue engineering applications were responsive to hMSCs and had progressive effects on the mechanical properties of pure HAp with COL and COL/HAp materials.

Keywords: Scaffolds; Tissue engineering; Grafting; Hydroxyapatite; Human Mesenchymal Stem Cell; Stimulation.

1. INTRODUCTION

Recently, tissue engineering approach is being used for bone implantation. Tissue engineering and regenerative medicine is a field of science in which scientists, engineers, and physicians use tools from a variety of fields to create biological substitutes that can mimic tissues for diagnostic and research purposes, as well as replace (or help regenerate) diseased and injured tissues [1]. In porous scaffolds, mesenchymal stem cells (MSCs) are seeded for bone regeneration and bone grafting. These MSCs seeded scaffolds are then implanted into the scratched region [2]. Diseases and traumatism commonly cause bone defects and osteochondral damage, posing a significant difficulty in orthopedics. The hybrid scaffold has shown promise as a possible therapeutic method for such problems [3].

Generally, the promotion of cell adhesion, proliferation, and maintenance of differentiation is assisted by scaffolds acting as substrates. These scaffold templates assist in organizing and directing the proliferation of cells. It also aids in the formation of the extracellular matrix (ECM) [4]. When put into the faulty locations in bone tissue engineering, a biodegradable scaffold acts as a temporary skeleton. It degrades over time to support and inspire bone tissue regeneration at faulty places or where the bone has been destroyed and is eventually replaced by fresh bone tissue. [5-7]. However, the scaffold might brutally distort or break, and tissue renewal will not ensue if the scaffold has considerable inferior mechanical properties in comparison to the neighboring tissue. Therefore, it is very imperative to develop and fabricate scaffolds with governable mechanical properties as well as with appropriate porous constructions to guarantee mechanical constancy with adequate tissue development during the renewal process [8].

When constructing scaffolds for the engineering of bone tissue, the selection of materials is crucial since the qualities of each material can be quite useful in the scaffold. [9]. The porous scaffold can be made-up by employing together bioactive ceramics as well as polymers. It is noted that these bioactive ceramics possess a chemical configuration similar to that of ordinary bone, permit osteogenesis, and can deliver a bony connection or ties with the host bone [10, 11]. Ceramics are used in medical

technologies and applications to restructure and replace injured body parts as well as for skeletal restoration for the last forty years. These ceramics are recognized as bioceramics [12-15]. Bioactive ceramics bond directly with living tissues when implanted. As a result, they've received a lot of attention as biomaterials. Specialized glasses and glass ceramics, as well as sintered hydroxyapatite, were the first synthetic bioactive materials [16].

Bioceramics such as hydroxyapatite (HAp) and -tricalcium phosphate (ß-TCP) have been used in bone tissue engineering because of their remarkable biocompatibility, bioactivity, and osteoconductivity. [17, 18]. HAp has been employed in bone regeneration for the creation of scaffolds due to its unique qualities such as good biocompatibility, osteoconductivity, bioactivity, and non-toxicity [18-21].

However, the extensive applications of HAp in hard tissue implants have been limited due to its low strength and brittleness [22]. Collagen (COL) is a structural protein that is said to be one of the most appropriate materials for building artificial substitutes for unhealthy or injured tissues and organs [23]. It is also a prime constituent of bone. Therefore, in 3D scaffolds design, it becomes a perfect applicant [24]. It is naturally biodegradable as well as biocompatible and stimulates the growth and distinction of stem cells as an extracellular matrix. Despite having these properties, the mechanical properties of COL are very poor [25, 26].

Composite scaffolds have been designed to achieve a substrate with various capabilities such as surface reactivity, mechanical strength, bioactivity, and drug or proliferation factor delivery competence. Generally, several composite scaffolds have been invented using different types of the matrix with dispersed phases such as ceramic/metals, polymer/ceramics, as well as polymer/metals [27, 28]. Bearing in mind these realities, a composite scaffold of high porosities with improved mechanical strength and the biological property based on a natural polymer has yet to be fabricated. Under coating circumstances, including COL or COL/HAp materials into pure HAp scaffolds considerably reduced porosity and improved mechanical characteristics [29]. A composite approach of the two components, COL and HAp, possesses the potential to be engineered biomaterials. Conventionally, the HAp-polymer composites have been formed by scattering HAp powders in the polymer solution. The mechanical strength and properties of biomaterials are critical for bone renewal to the success of the implant and it depends on the implanted tissues [30]. The mechanical necessities of the scaffolds are being calculated to restore load-bearing bone blemishes. Therefore, a strategy and approach considering the mechanical properties standards of bone as well as scaffold are required [31]. The porosities, pore sizes as well as architectures in the fabricated scaffolds are other essential considerations [32].

Because it speeds up the interchange of nutrients, metabolic waste, and other components during cell growth, porosity is an important quality to consider for a porous biomaterial. All cells seeded within the fabricated scaffold must have a uniform or alike access requirement. Interestingly, this property is normally attained by providing a construction with a higher level of permeability of an appropriate dimension [33]. It is thought that Mesenchymal stem cells (MSCs) have multipotent cells potency that can reproduce as indistinguishable cells. Therefore, it can differentiate into extractions of mesenchymal tissues, including cartilage, fat, tendon, muscle, bone, and marrow stroma. Finally, MSCs received extensive consideration owing to their potential usefulness in tissue manufacturing applications [34, 35].

As a result, in this study, pure HAp scaffolds were created using a polyurethane (PU) sponge template approach. The prepared scaffolds' porosity was adjusted by varying the compressive pressure (95, 75, and 50%) and then sintered at 1100 °C for 3 hours to harden the HAp porous scaffolds. The prepared pure HAp porous scaffolds were further fabricated by a biopolymer such as collagen (COL) and collagen-HAp powder mixer solution (COL/HAp) was employed to reinforce the HAp porous materials by 2-phase (special freeze-drying) condition. The biocompatibility of manufactured composite scaffolds for tissue engineering application was evaluated using an *in vitro* Human Mesenchymal Stem Cell (hMSC) culture as a model. This is the first report of enriched mechanical as well as biological responsive properties of the fabricated biomaterials in bone tissue regeneration developed by 2-phase conditions to the best of our knowledge.

2. MATERIALS AND METHODS

2.1 HAp porous Scaffolds Synthesis

According to Islam et al., [29] the HAp porous scaffolds were made using the polyurethane (PU) sponge template method. The commercial micro-HAp powder was used to prepare HAp slurry. HAp powders were mixed with polyvinyl alcohol (PVA) in a 5wt% solution. The mixing ratio between HAp and PVA was 1:1 (1g:1ml, respectively). The mixture was centrifuged by kneading and degassing (removing gas bubbles) for 10 min and 8 min, respectively, in a mixing machine. The sponge templates (HR-30, Bridgestone) were cut to 1x1x1 cm in size and inserted into the HAp slurry. The pore-blocking of the sponge templates was avoided by removing the excess slurry at 95, 75, and 50% compression. The produced cubes were then dried for 24 hours at 25°C to allow the HAp to settle on the sponge template. These cubes were calcinated at 400 °C maintaining a 10 °C/min heating rate for 6 h. Finally, the cubes were sintered at 1100 °C for 3 hours to firm the HAp porous scaffolds. These samples were named “pure HAp scaffolds”. Fig. 1(a) indicates the schematic illustration of the sintering process of fabricated composite scaffolds. In our previous study, sintering was done at 1000 °C, 1100 °C, and 1200 °C for 3 hours to solidify the HAp porous scaffolds. The composite scaffolds fabricated from pure HAp scaffolds sintered at 1100 °C and with COL or

COL/HAp coatings demonstrated better performances [29]. Therefore, 1100 °C sintering temperature of fabricated composite scaffolds in 2-phase condition was chosen.

2.2 Incorporation of COL and HAp particles for Fabrication of HAp porous Scaffolds

The synthesized pure Hap scaffolds were further fabricated in 2 ways, using Collagen-1 solution (a), and a mixture of HAp powders in Collagen-1 solution (b). To begin (for type a), pure HAp scaffolds were soaked in the COL-1 solution and vacuumed for 30 minutes to remove any air. The excess collagen solution was eliminated by pipette manually. Then these samples were dried out at 25°C at least for 48 hours. In contrast, for type (b), first, HAp powders were carefully mixed in COL-1 solution (1:9) and stirred magnetically at 30 °C.

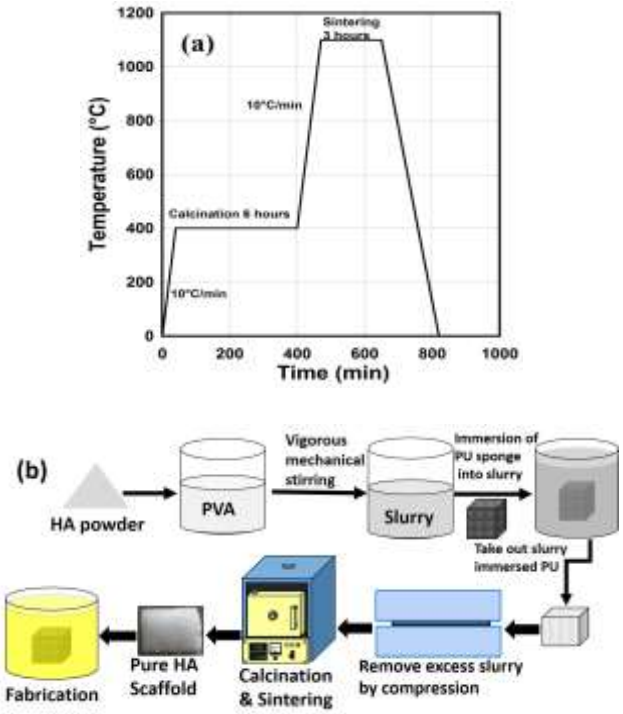

Fig. 1 shows a schematic illustration of the sintering procedure used (a) and from preparation to fabrication of HAp microporous composite scaffolds (b).

Concerning the ratio of collagen/HAp particle, the effects of the various proportion of collagen/HA particle such as 12:1, 10:1, 9:1, and 8:1 was tested. It was noticed that the 9:1 proportion of collagen/HA particles were more effective than others. It was very important to preserve the liquidity of the collagen/HA particles mixture for immersing the as-prepared pure HA scaffolds into it. Furthermore, a previous study reported that collagen solution and β-TCP powder were mixed by the fixed weight ratio of 90:10 to prepare composite scaffolds for tissue engineering [36]. So, the above-mentioned ratio was chosen. However, the pure HAp porous scaffolds were then fabricated using the procedure described in type (a). Such fabricated specimens were named 'HAp-COL or HAp-COL/HAp particles coated scaffolds'. After that, these coated porous composite scaffolds were frozen for a day at -20 °C. Again, these composite scaffolds were dried out at -50 °C (freeze) for another day by an Eyela-FDU machine where auto-mode starts vacuum pump operation after trap temperature is cooled. These samples were named 'HAp-COL or HAp-COL/HAp particles 2-phase scaffolds'. The construction of pure HAp scaffolds with COL or COL/HAp particles is depicted schematically in Fig. 1(b).

3. CHARACTERIZATION AND ANALYSIS

3.1 Compression testing

Compression, as well as mechanical tests, were accomplished by using EZ-S Series (Shimadzu, Japan) fortified with a 1mm/min crosshead speed of a load cell of 500N. In this study, mechanical strengths were determined as compressive modulus, strain energy density, and fracture stress. Samples attained after the fabrication procedure were exposed to the study of mechanical properties. The dimensions of targeted samples were estimated before the commencement of the test because shrinkage may occur after sintering. The length (L, mm), width (W, mm), and height (H, mm) were all used to calculate the dimension of the prepared biomaterials. For the calculation of stress σ (MPa) (Eqn. 1) as well as strain ϵ (Eqn. 2), first, force and displacement (F (N), ΔH (mm), respectively) were estimated. Elastic modulus (E) was attained from the preliminary slope of the curve of stress-strain prior to the sample's failure. The mean values were recorded after testing 6 samples for every condition.

$$\text{Stress } \sigma = F/(L \times W) \quad (1)$$

$$\text{Strain } \epsilon = \Delta H/H \quad (2)$$

The specimen`s porosity was measured assumed from the compactness of HAp porous material and volume. Specimen`s density was estimated based on the weight and volume of HAp porous scaffolds and the density of HAp is being considered 3.16g/cm3 [21, 22].

$$\text{Porosity } [\%] = \left(1 - \frac{\text{Weight of HA}}{\text{Volume of HA} \times \text{Density of HA}}\right) \times 100$$

3.2 Microstructural characterization

The FE-SEM (Hitachi, S-4100) was performed to characterize the porous microstructures of prepared biomaterials according to Islam et al. [26]. Samples were kept on the sample holder accustomed to employing carbon tape as well as the addition of electro-conductive dotite D-550 (Fujikura Kasei Co, Ltd.) at the lowermost of the specimens to make them conductive for analysis by FE-SEM. A tinny layer of platinum/ palladium (Pt/Pd) alloy was used to coat the specimens by a vacuum sputter (Hitachi E1030 Ion Sputter) and finally, the analysis was executed.

3.3 Cell culture and seeding

hMSCs were purchased from Riken Bioresource Center and were cultured in α-MEM (5ml), supplemented with FBS (10%) (Gibco) and penicillin-streptomycin (1%,

Pen-Strep). Incubation of the hMSCs was done at 37 °C in a condition of 5% CO_2 as well as 70% humidity. The culture medium was altered twice a week. After the cells' sub-confluence reached 80-90 percent, the Accutase enzyme (Millipore Corporation, Catal. No. SCR005) was used to collect the cultured hMSCs, which were then sub-cultured again. All the experimentations were performed under the alike condition. Stem cells were cultured over the fabricated scaffolds by COL or COL/HAp in 2-phase conditions. hMSCs were seeded on the composite scaffolds taking cells from passage 4. Fabricated composite scaffolds were sterilized under UV for 1hour by placed in 24-well plates. These scaffolds were drenched in α-MEM and the air was removed by vacuuming for 1hour. Before cell seeding, incubation of these soaked composite scaffolds was performed at 37°C at least for 30 minutes. After that, 1×10^4 No. cells were seeded on each scaffold diluted in medium (100 µl) and vacuumed for 1minute. Again, incubation of these hMSCs seeded scaffolds was performed for additional an hour to permit cell attachment. After that 1ml of the α-MEM medium was added and incubation was continued for up to 28 days under the standard environment of cell culture.

3.4 Cell adhesion and proliferation

A spectrophotometric plate reader (2030 ARVOTM X2, Perkin Elmer Co., Yokohama, Japan) was used to assess hMSC adherence and proliferative activity (cell number). The cell numbers were estimated by the Dojindo Laboratories cell-counting kit (Kumamoto, Japan). Cell number was determined at 7, 14, 21, and 28 days of culture after the beginning of cell culture. The medium was taken out and the scaffolds seeded with hMSCs were washed at least three times with PSB. Then cell counting kit (100µL) was added to each well of cells containing scaffolds with 1000 µL of PBS. These scaffolds were also incubated for 2 hours at 37 °C with a 5% CO_2 concentration. Afterward, we extracted reaction solution (1100 µL) from every sample of cells containing scaffolds. This collected reaction solution was split into 10 specimens (110 µL in each) and was filled in a well (96-well plate). the optical concentrations were finally assessed using a plate reader of Perkin Elmer at 450 nm wavelength and 37 °C. Lastly, the obtained average values of absorbance were transformed into cell numbers following the protocol described by Dojindo Laboratories (Kumamoto, Japan).

4. STATISTICAL ANALYSIS

Data were calculated in a way of means ± SD (standard deviation). These data were resulting from 3-6 individual specimens. For the ANOVA analysis, the Kaleida Graph (Synergy Software, Reading, PA, USA) was utilized, and any significant level was regarded the *p*-value ≤0.05

5. RESULTS AND DISCUSSION

5.1 Microscopic structure and fracture mechanism

Typical FE-SEM microscopic images of prepared pure HAp and fabricated scaffolds were meticulously observed. Fig. 2 showed FE-SEM microscopic images of pure HAp, as well as constructed composite scaffolds of COL or COL/HAp particles coated in 2-phase conditions compressed at various ratios and sintering at 1100 °C. It was discovered that all of the prepared and fabricated HAp scaffolds possessed distinguished porous morphology. Microstructure images of FE-SEM analysis undoubtedly revealed that porosities of the as-prepared pure scaffold were partly blocked or reduced by integration of COL or COL/HAp particles in 2-phase condition sintering at 1100 °C. Because of the enhanced densification of the materials, it was assumed that increasing the compressive pressure of pure HAp scaffolds reduced the porosities of the produced scaffolds. It was described that "at the lower temperature sintering was uncompleted and the strut was highly porous and at 1200 °C the sintered structure showed a much higher degree of densification" [4].

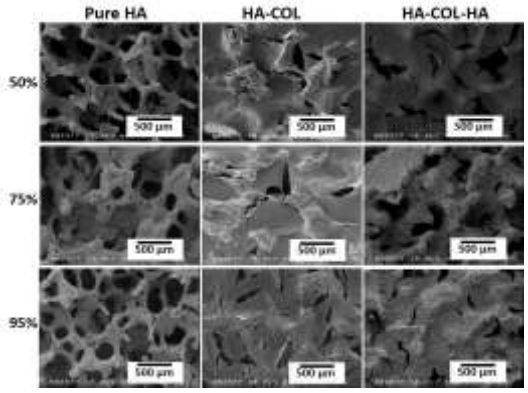

Fig. 2. FE-SEM microstructures of porous pure and composite manufactured scaffolds sintering at 1100°C at various compressive rates.

The porosities of the manufactured pure HAp scaffolds were remarkably reduced after being fabricated by the integration of COL or COL/HAp particles, as a result of this discovery. On the other hand, compressive rates affect the porosities of the fabricated composite scaffolds progressively. In the present study, fabricated composite scaffolds revealed porosity ranging from approximately 80% to 91%. It has been previously studied that "the porosity of a variety of materials ranging from 40% to 90% encourages osteointegration with the implant surface and encourages adhesion of the implant" [28].

It was noteworthy that maximum porosities were obtained at higher compressive rates of scaffolds and definitely, the lowest porosities were found at a 50% compressive ratio among that 95%, 75%, and 50% [32]. Further, the fracture mechanism of microstructures of fabricated composite scaffolds after compression tests was performed by FE-SEM. The fracture mechanism of microscopic HAp composite scaffolds fabricated by COL or COL/HAp at 50% (a, b), 75% (c. d), and 95% (e, f) compressive rate sintering at 1100 °C are denoted by Fig. 3.

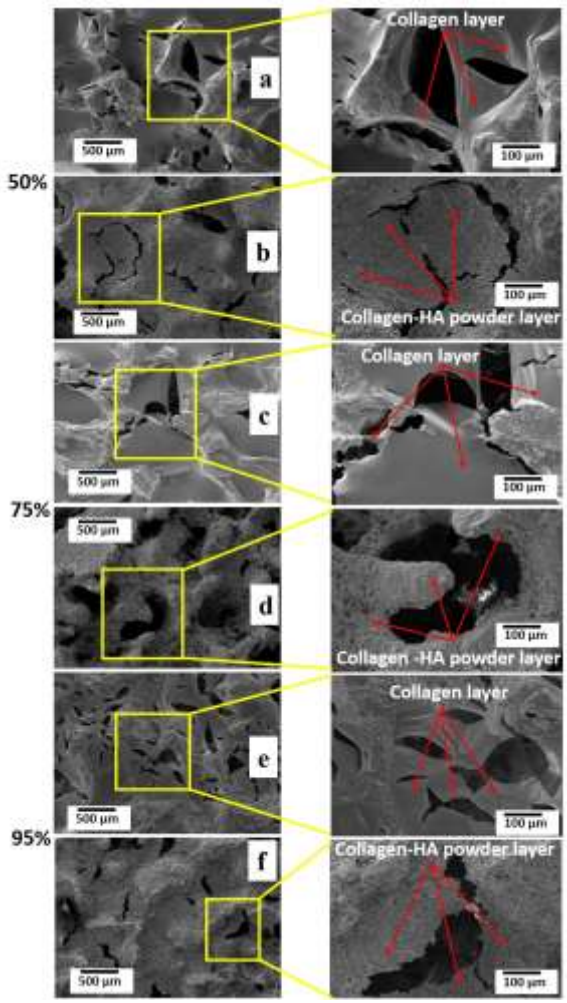

Fig. 3: Mechanism of porosity reduction and improved mechanical characteristics of COL or COL/HAp 2-phase composite scaffolds manufactured by compressive ratio at 50 percent (a, b), 75 percent (c, d), and 95 percent (e, f) sintering at 1100 °C

It was discovered from Fig. 3 that by incorporating COL or COL/HAp tributary phase, the column of HAp is strongly connected and after loading the compressive pressure this connection (red arrows) protects the fabricated composite scaffolds from breaking. It was understood that the linkage between the HAp and COL or COL/HAp of the fabricated composite scaffolds reduced the concentration of the loading stress, delayed crack commencement, and prevented the crack extension.

5.2 Evaluation of cell growth

Initially, each of the newly developed composite scaffold samples was planted with 1×10^4 cells. On the 7th and 28th days of culture, cell propagation was detected. The number of cells in the constructed composite scaffold increased until 14 days of culture for all scaffold categories, however, cell growth slowed as the culturing period progressed (Fig. 4). In our previous study, "it exhibited prevailing cell growth performance over their counterpart of pure HAp scaffolds fabricated with COL (HAp-COL scaffolds) at all sintering temperatures" [29]. It was predicted that after 7 days of culture the cell growth was decreased for all types of fabricated scaffolds due to scaffolds degradation at an early stage. In an early study, according to reports, "the proliferation of rMSCs became slow after reaching confluence at 14 days because the cell proliferation inside the collagen scaffold was thought to be suppressed because of shrinkage and ductile deformation of the porous structure" [28]. The mechanical properties of the constructed scaffolds produced in this study were close enough to those of hard tissue, suggesting that these composite scaffolds could be used for bone or hard tissue engineering. In conclusion, hMSCs growth and proliferation response to the fabricated scaffolds was outstanding and confirmatory.

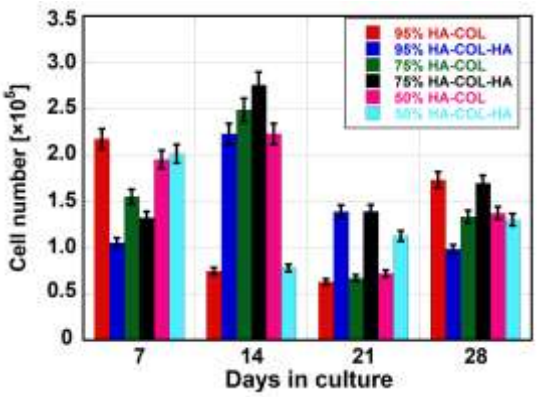

Fig. 4 showed the growth responses of hMSCs over constructed COL and COL/HAp scaffolds with 50%, 75%, and 95% compressive ratio sintering at 1100 °C over the first 28 days of the culture period. Each data point reflected the mean SD, with n = 6 and *p 0.05.

5.3 Enhanced mechanical properties of hMSC seeded Scaffolds

The scaffold fabricated and developed from COL, and COL/HAp (50, 75, and 95 % compressive rate) in 2-phase condition were used as a bed for hMSCs culture. In our previous study, "An evaluation of the mechanical properties of fabricated composite scaffolds revealed that fabricated biomaterials displayed outstanding performance at a 50% compressive ratio in almost all sintering temperatures" [29]. As a result, pure Hap scaffolds were constructed with COL or COL/HAp particles at varied compressive ratios and sintered at 1100 °C in the current work. These fabricated composite scaffolds were used in the hMSCs proliferation experiment.

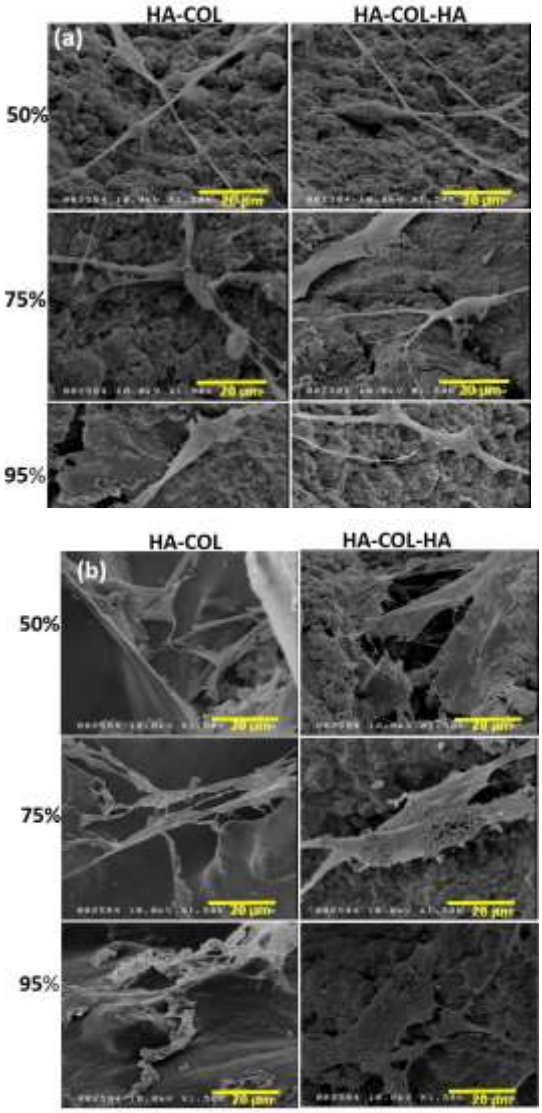

Fig. 5. FE-SEM pictures of hMSC response in manufactured composite scaffolds after 14 days of culture at various compressive rates sintered at 1100 °C. Here, (a) indicate hMSCs response before the mechanical test and (b) after the mechanical test.

Fig. 5. validated the growth performance of hMSCs 0ver fabricated COL and COL/HAp scaffolds at different compressive ratios up to a culture period of 14 days. Before the mechanical test, FE-SEM images of hMSC responses over the manufactured composite scaffolds revealed a strong cell seeding and growth tendency (Fig. 5a). Further, after the mechanical test FE-SEM images of hMSCs responses scaffolds indicated that seeded hMSCs over the fabricated composite scaffolds developed a strong network that strengthens the mechanical properties of fabricated biomaterials (Fig. 5b).

A compression test was performed on specimens from fabricated composite scaffolds at various compressive ratios sintering at 1100 °C. A considerable variation was observed in the mechanical properties of hMSCs cultured distinct scaffolds measured from every group of fabricated scaffolds. Fig. 6 showed the influences of compressive rate on the mechanical strength of hMSCs cultured over fabricated composite scaffolds. Effects of compressive ratios on the mechanical strength and properties i.e., compressive modulus for pure HAp (control), COL (50, 75, and 95 %), and COL/HAp ((50, 75, and 95 %),) scaffolds after hMSCs cultured are represented in Fig. 6. The greatest modulus was found with COL/HAp particles scaffolds sintered at 1100 °C in a 7-day culturing period with a 95% compressive rate. On the other hand, COL/HAp particles composite scaffolds with a 50% compressive ratio showed a progressive increment of modulus from 7 to 28 days of the hMSCs culture period.

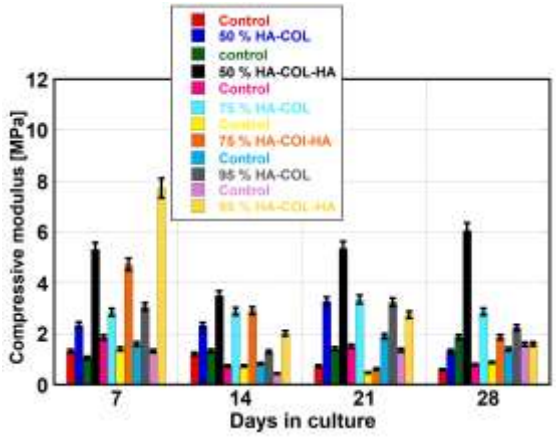

Fig. 6. Enhanced mechanical properties of hMSCs responsive fabricated scaffolds in various compressive ratios culturing up to 28 days. Each data represented mean ± SD, n = 3, *p < 0.05.

6. CONCLUSION

The current research focused on the synthesis and development of porous COL or COL/HAp composite scaffolds at different compressive speeds, sintering at 1100 °C in 2-phase circumstances. The effects of different compressive pressure on the mechanical as well as biological properties of the fabricated composite biomaterials were assessed. The results undoubtedly confirmed that the porosities of the fabricated composite scaffold were diminished by increasing compressive pressure (rate). The integration of COL or COL/HAp at a 50% compressive rate resulted in significant cell adhesion and proliferation across the produced composite scaffolds in an in vitro evaluation of hMSC. It was noticed that an increased cell culturing period triggered modulus increment in almost every sample, but the maximum modulus was detected in COL/HAp particles scaffolds with a 95% compressive rate sintered at 1100 °C in a 7-day culturing period. On the other hand, COL/HAp particles composite

scaffolds with a 50% compressive ratio showed a progressive increment of modulus from 7 to 28 days of the hMSCs culture period. It was assumed as well as evidence that at a 50% compressive rate, porosity was efficiently reduced at the maximum level to lead to the improvement of measured mechanical properties of the fabricated biomaterials. Therefore, it may conclude that fabricated biomaterials were hMSCs responsive, biocompatible, mechanically strengthen, and might be pertinent in bone tissue engineering applications.

ACKNOWLEDGMENT

This research work was financially supported by Grant-in-Aid for Scientific Research (No24•02380) and Grant-in-Aid for JSPS Fellows (No. P14362) from the Japan Society for the Promotion of Science (JSPS).

REFERENCES

[1] F. Berthiaume, T. J. Maguire, M. L. Yarmush. "Tissue Engineering and Regenerative Medicine: History, Progress, and Challenges". Annual Review of Chemical and Biomolecular Engineering, Vol. 2, No.1, pp. 403-430, 2011.

[2] H. Wang, Y. Li, Y. Zuo et al. "Biocompatibility and osteogenesis of biomimetic nano-hydroxyapatite/polyamide composite scaffolds for bone tissue engineering", Biomaterials, Vol. 28, pp.3338-3348, 2007.

[3] Li Chen, et al. "Biomimetic porous collagen/hydroxyapatite scaffold for bone tissue engineering". Journal of Applied Polymer Science, Vol. 134, pp. 45271, 2017.

[4] I. Sabree, J. E. Gough, B. Derby, "Mechanical properties of porous ceramic scaffolds: Influence of internal dimensions", Ceramic International, Vol. 41, pp.8425-8432, 2015.

[5] M. Jarcho, "Calcium phosphate ceramics as hard tissue prosthetics", Clinical Orthopaedics and Related Research, Vol. 157, pp.259-278, 1981.

[6] L. L. Hench and J. Wilson, "Surface-active biomaterials", Science, Vol. 226 pp.630-706, 1984.

[7] Z. Li, R. H. Ramay, Kip. D Hauch, D. Xiao and M. Zhang, "Chitosan-alginate hybrid scaffolds for bone tissue engineering", Biomaterials, Vol. 26, pp.3919-3928, 2005.

[8] L. L. Hench, "Bioceramics: From concept to clinic", Journal of the American Ceramic Society, Vol. 74, pp. 487-1510, 1991.

[9] T. L. T. Kitsugi, T. Yamamuro, T. Nakamura and M. Oka, "Transmission electron microscopy observations at the interface of bone and four types of calcium phosphate ceramics with different calcium/phosphorus molar ratios", Biomaterials, Vol.16, pp.1101-1107, 1995.

[10] A. S. Posner and F. Betts, "Synthetic amorphous calcium phosphate and its relation to bone mineral structure", Accounts of Chemical Research, Vol. 8, pp.273-281, 1975.

[11] R. Z. Legeros, "Apatites in biological systems", Progress in Crystal Growth and Characterization of Materials, Vol. 4, pp.1-45, 1981.

[12] S. F. Hulbert, F. A. Young, R. S. Mathews, J. J. Klawitter, C. D. Talbert and F. H. Stelling, "Potential of ceramic materials as permanently implantable skeletal prostheses", Journal of Biomedical Materials Research Part A, Vol. 4, 433-456, 1970.

[13] I. Mobasherpour, M. S. Hashjin, S. S. R. Toosi, R. D. Kamachali, "Effect of the addition ZrO2-Al2O3 on nanocrystalline hydroxyapatite bending strength and fracture toughness", Ceramic International, Vol. 35, pp.1569-1574, 2009.

[14] A. Chiba, S. Kimura, K. Raghukandan, and Y. Morizono, "Effect of alumina addition on hydroxyapatite biocomposites fabricated by underwater-shock compaction", Materials Science and Engineering A, Vol. 350, pp.179-183, 2003.

[15] Z. Xihua, L. Changxia, L. Musen, B. Yunqiang, and S. Junlong, "Fabrication of hydroxyapatite/diopside/alumina composites by hot-press sintering process", Ceramic International, Vol. 35, pp.1969-1973, 2008.

[16] A. J. Salinasab and María Vallet-Regí. "Bioactive ceramics: from bone grafts to tissue engineering". RSC Advances, Vol. 3, pp. 11116-11131, 2013.

[17] D. J. Curran, T. J. Fleming, M. R. Towler, and S. Hampshire, "Mechanical parameters of strontium doped hydroxyapatite sintered using micro-wave and conventional methods", Journal of the Mechanical Behavior of Biomedical Materials, Vol. 4, pp.2063-2073, 2011.

[18] W. Que, K. A. Khor, J. L. Xu, and L. G. Yu, "Hydroxyapatite/titanianocomposites derived by combining high-energy ball milling with spark plasma sintering processes", Journal of the European Ceramic Society, Vol. 28, pp.3083-3090, 2008.

[19] A. A. Chaudhry, et al. "High-strength nanograined and translucent hydroxyapatite monoliths via continuous hydrothermal synthesis and optimized spark plasma sintering", Acta Biomaterialia, Vol. 7, pp.791-199, 2011.

[20] F. J. O'Brien, "Biomaterials & scaffolds for tissue engineering (Review)", Materials Today, Vol. 4, pp.88-95, 2011.

[21] S. S. Kim, et al. "Poly(lactide-co-glycolide)/hydroxyapatite composite scaffolds for bone tissue engineering", Biomaterials, Vol. 27, pp.1399-1409, 2006.

[22] W. Friess and M. Schlap, "Sterilization of gentamicin containing collagen/PLGA microparticle composites", European Journal of Pharmaceutics and Biopharmaceutics, Vol. 63, pp.176-187, 2006.

[23] R. Z. Legeros, S. Lin, R. Rohanizadeh, D. Mijares, J. P. Legeros, "Biphasic calcium phosphate bioceramics: preparation, properties and applications", Journal of Materials Science: Materials, Vol. 14, pp.201-209, 2003.

[24] E. Landi, A.Tampieri, G. Celotti and S. Sprio, "Densification behaviour and mechanisms of synthetic hydroxyapatites", Journal of the European Ceramic Society, Vol. 20, pp. 2377-2387, 2000.

[25] M. L. Munar, K. I. Udoh, K. Ishikawa, S. Matsuya and M. Nakagawa, "Effects of sintering temperature over 1300 °C on the physical and compositional properties of porous hydroxyapatite foam", Dental Materials Journal, Vol. 25, pp.51-58, 2006.

[26] M. S. Islam, Y. Kusumoto and M. Abdulla-Al-Mamun, "Novel rose-type magnetic (Fe3O4, γ-Fe2O3 and α-Fe2O3) nanoplates synthesized by simple hydrothermal decomposition", Materials Letter, Vol. 66, pp. 165-167, 2011.

[27] M. F. Pittenger, A. M. Mackay, S. C. Beck, R. K. Jaiswal et al., "Multilineage potential of adult human mesenchymal stem cells", Science, Vol. 284, pp. 143-147, 1999.

[28] M. S. Islam and M. Todo, "Effects of sintering temperature on the compressive mechanical properties of

collagen/hydroxyapatite composite scaffolds for bone tissue engineering", Materials Letter, Vol. 173, pp.231-234, 2016.

[29] M. S. Islam, A. M. Z. Rahman, M. H. Sharif, A. Khan, Md. Abdulla-Al-Mamun, M. Todo, "Effects of compressive ratio and sintering temperature on mechanical properties of biocompatible collagen/hydroxyapatite composite scaffolds fabricated for bone tissue engineering", Journal of Asian Ceramic Societies, Vol. 7, No. 2, pp.183-198, 2019.

[30] V. Karageorgiou and D. Kaplan, "Porosity of 3D biomaterial scaffolds and osteogenesis", Biomaterials, Vol. 26, pp.5474-5491, 2005.

[31] S. M. Lien, L. Y. Ko, T. J. Huang, "Effect of pore size on ECM secretion and cell growth in gelatin scaffold for articular cartilage tissue engineering", Acta Biomaterilia, Vol. 5, pp.670-679, 2009.

[32] Q. L. Loh and C. Choong, "Three-dimensional scaffolds for tissue engineering applications: role of porosity and pore size", Tissue Engineering B, Vol. 19, pp.485-502, 2013.

[33] N. Sultana and M. Wang, "Fabrication of HA/PHBV composite scaffolds through the emulsion freezing/freeze-drying process and characterization of the scaffolds", Journal of Materials Science: Materials in Medicine, Vol. 19, pp.2555-2561, 2008.

[34] Y. Phanny and M. Todo, "Development and Characterization of Poly (ε-caprolactone) Reinforced Porous Hydroxyapatite for Bone Tissue Engineering", Key Engineering Materials, Vol. 529-530, pp. 447-452, 2013.

[35] A. Zamaniana et al., "The effect of sintering temperature on the microstructural and mechanical characteristics of hydroxyapatite macroporous scaffolds prepared via freeze-casting", Key Engineering Materials, Vol.529-530, pp.133-137, 2013.

[36] T. Arahira and M. Todo. "Effects of proliferation and differentiation of mesenchymal stem cells on compressive mechanical behavior of collagen/β-TCP composite scaffold". Journal of the Mechanical Behavior of Biomedical Materials, Vol. 39, pp. 218-230, 2014.

Paper ID: 8506

International Conference on Mechanical, Manufacturing and Process Engineering (ICMMPE – 2022)

Organizer: Faculty of Mechanical Engineering, Dhaka University of Engineering & Technology (DUET), Gazipur, Bangladesh

Website: https://icmmpeduet.com/

Development and Control of a Hydraulic Actuator System for Industrial Applications

Mohammad Harun-Or-Rashid[1], Tabassum Khan[2], Arnab Hasan[2], Md. Abul Hasan Bhuiyan[2] and Mohammad Rejaul Haque[3]

[1,2,3]*Department of Mechanical and Production Engineering, Ahsanullah University of Science and Technology*

E-mail: harun_edu@yahoo.com, harun.mpe@aust.edu

ABSTRACT

Control mechanism of two hydraulic actuators is developed in the present study for industrial automation. The main objective of this research was to control two actuators and push different types of objects according to necessity. Two double acting hydraulic actuators are used to do the job. A microcontroller is used to control actuators. On the other hand, a pump is used to circulate the oil and a solenoid valve is used to control the flow of oil. Finally a low cost system was developed which was capable to produce thrust of 0.4 KN- 0.6 KN. It is possible to control the speed of the actuators through the code which is uploaded in the microcontroller board. One of the main advantages of the electro-hydraulic system is that it can be moved easily from one place to another. In industries if high density force needs to be applied at different stages of a manufacturing process, this system can be implemented.

Keywords: Hydraulic actuator system, Industrial automation, Microcontroller board, Solenoid valve.

1. INTRODUCTION

Fluid is accepted and recognized as a source of power over the years. Hydraulic power has been used as the primary source to propel boats and turn water wheels for many years. Nevertheless, hydraulic has found greater applications in recent years more than its initial use as it has gained more acceptability in different fields. The use of hydraulic power spread across land moving vessels, in the aviation industry, process automation, robotics, and many other engineering branches. It is known as force transmission through pressurized fluids. Frenchman named Pascal made a publication on hydrostatics, which included his law (Principle of transmission of fluid pressure): pressure change at any point of the fluid in a confined volume distributes itself equally throughout the volume [1]. G J Zhang and M Luoj [2] describe the construction of the hydraulic cylinder. The main working mechanism of the hydraulic cylinder consists of a piston rod which is provide with a reciprocating motion by inducing fluid pressure inside the structure. R Henke et al. [3] suggested step-by-step process for hydraulic circuit design. These steps are understanding the load, choose an actuator or motor size, establish flow and pressure profiles, check basic horse power to satisfy the hydraulic profile, design circuit and the lastly redesign if compromise of any kind is needed. S. Marques et al. [4] proposed an optimal sequential method and hydraulic circuit development procedure. Mikell P. Groover [5] describes the automation and control technologies of industrial systems. A. Tony Thomas et al. [6] explains the steps for modelling of hydraulic press using MATLAB and suggested fractional order controller. T. G. Ling et al. [7] presented Electro-Hydraulic Actuator system's model by using system identification technique of MATLAB Simulink. They also designed proportional integral derivative controller to track the position of the system. In order to track the force of a hydraulic cylinder, the PID controller was implemented by Weerapong Chanbua et al. [8]. In addition, this study was focused specially on the compensation of the irregularities due to friction inside the cylinder. In the paper of Munaf F. Bader [9] the position tracking system of the hydraulic cylinder was developed. To control the flow to the cylinder chamber, DCV (Directional Control Valve) solenoid valves were used. Mohga Alrhman et al. [10] in his paper discusses about the PID controller implementation to control a hydraulic system. Tuning the traditional PID controller to control the hydraulic systems is inefficient. They aim at designing a robust PID controller which has the ability to mitigate nonlinearities and uncertainties associated with it.

In the present study, convertion of fluid pressure to mechanical engery and it's industrial application are discussed. In this work, an oil pump generates pressure energy and sends the pressurized fluid to the inlet or exhaust ports of the cylinder. The actuator than convert's fluid power to mechanical power. The solenoid DCVs control the motion of the actuator. Then operation of each solenoid valves depend upon the switching of relays situated in the 4-channel relay module. There is interface with the Arduino board. A code is uploaded in the Arduino

Uno to control the system. Therefore, Arduino Uno is responsible for the whole system operation.

There are several types of actuators and hydraulic actuator is one of them. In this study two double acting hydraulic actuators are selected because of more precise control and more suitable for repetitive works than single acting hydraulic actuator.

Over the years there have been many studies and improvements on how to control the hydraulic cylinder electrically. In the field of automation, the motion control of hydraulic actuator is done via PLC (Programable Logic Controller) or automatic mechanical switching system. Another cost-effective way to control the motion of a hydraulic actuator is to use microcontroller board. In this research, the DCVs are controlled by the Arduino Uno controller board which in turn controls the extension and retraction motion of the developed electro-hydraulic actuator system.

The main goals of this work are to design, fabricate and control the operation of the compact and portable electro-hydraulic actuator system. It can be used in industries for automation and reduce the cost of production. Total fabrication cost of the system is 38,000 Taka. Function of the developed electro- hydraulic actuaor system is presented in Fig. 1. On the other hand, Fig. 2 shows the flow chart of the work.

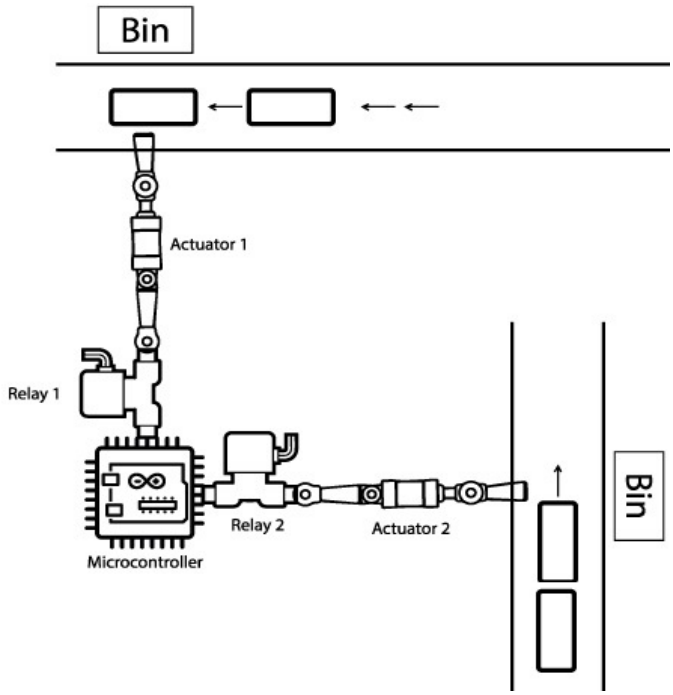

Fig. 1: Industrial application of electro-hydraulicactuator system

2. CIRCUIT DIAGRAM

Fig. 3 shows the hydraulic circuit diagam. On the other hand, relay circuit is presented in Fig. 4. A tandem type directional control valve was employed which helped to reduce the number of hose pipes by providing a bypass channel for fluid when one of the valves is turned off. The pressure in the pump line has been limited by a relief valve. Because the experiment was conducted for short time, the use of an accumulator was deemed unnecessary. Furtheremore, in order to reduce overall costs it was not added. It should be remembered that the adding of an accumulator is required for long-term usage. The motor and pump were chosen to run the cylinders adequately. A non-returnable valve was added to the design, as well as a pressure gauge to detect the pump's output pressure.

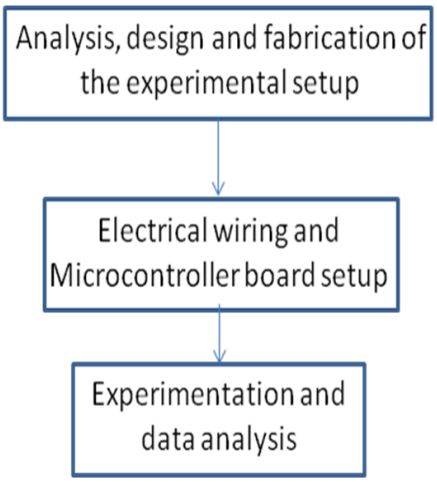

Fig. 2: Flow chart of this research

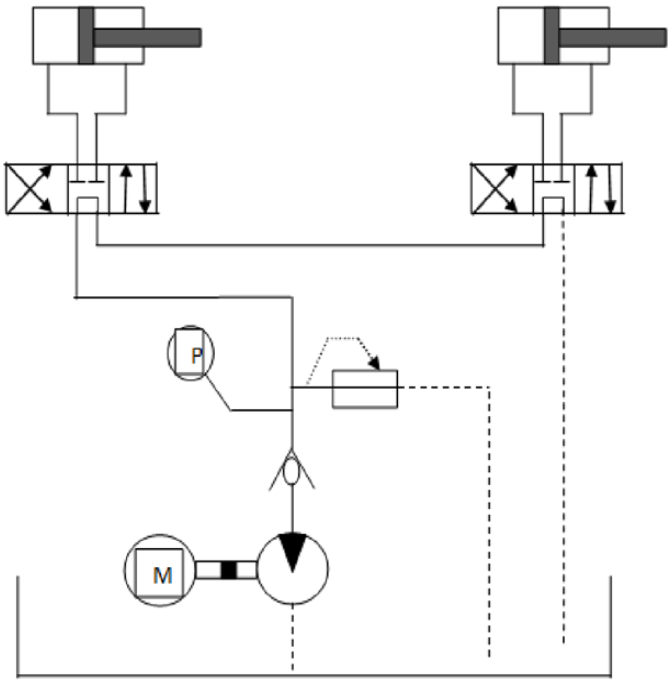

Fig. 3: Diagram of the hydraulic circuit

3. DESIGN ANALYSIS

At the beginning, the hydraulic and electric circuit of the electro-hydraulic actuator system were designed. After that some analysis like costing of the components available in the local market were studied. A tandem type directional control valve has been used which helped us reducing the number of hose pipes as fluid has a bypass pathway when any one of the valves is switched off. A relief valve has been used to limit the pressure in the pump line. Accumulator was not used because the experiment was conducted for a short period of time and to minimize total expense.

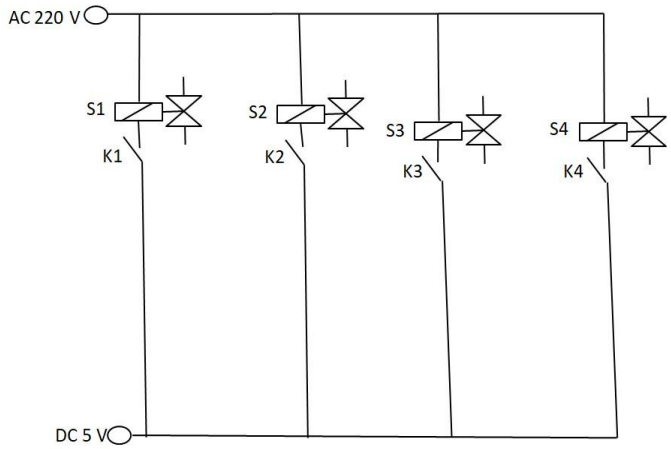

Fig. 4: Relay Circuit

The motor and pump were selected to operate the cylinders properly. The non-return valve was added to the design and a pressure gauge was placed to determine the pressure provided by the pump. The reservoir size was adopted according to the amount of oil needed which was 10 litters. The microcontroller setup was done according to the cylinder operation.

4. MAJOR COMPONENTS

4.1 Hydraulic actuator

Actuators are devices that convert one form of energy to another to operate some machines. The hydraulic actuator converts fluid pressure to lineal actuated motion. In the present study two double-acting hydraulic actuators are used. Two double-acting actuators are presented in Fig. 5. This type of actuator can move in two directions by sliding it back and forth along because fluid can in and out both sides of the piston.

4.2 Oil pump

External geared oil pump (Fig. 6) is used for supplying oil. Parts of the external gear pump are: housing, mounting flange, drive shaft, two side plates, bearing bush, two gears and a disc. The fluid fills the pumping chambers before being transported from the suction side to the pressure side via rotating gear. A 220V, 12.4A single-phase induction motor (Fig. 7) is used to operate the oil pump. The RPM of the motor is 1480.

4.3 Hydraulic oil

Fire-resistant fluids can be utilized in systems that operate at high temperatures, while petroleum-based fluids can be used in systems that operate at moderate temperatures.

Fig. 5: Double-acting hydraulic actuator

Fig. 6: Oil Pump

Fig. 7: single-phase induction motor

Fig. 8: Pressure relief valves

Hydraulic oil VG 68 is used in this research because it is suitable for havey duty. Furthermore, it has good thermal and oxidation stability under high temperature.

4.4 Reservoir

A hydraulic system must have a reservoir that contains the necessary amount of hydraulic oil to provide oil to the pumps, actuators, pipes, and other components of the system. In addition to providing storage for the reserve oil, the reservoir acts as a radiator for dissipating heat from the oil. Length, width and height of the reservoir are 21 inches, 7 inches and 4 inches respectively.

4.5 Relief valve

High-pressure and low-pressure oil return lines are connected to pressure relief valves (Fig. 8). Pressure relief valve is connected to the high-pressure lines to prevent the fluid pressure from reaching the maximum operating pressure limit. The main construction of a pressure relief valve consists of a poppet that is loaded by a spring. The maximum pressure of the relief valve is estimated to be above 10 bar.

Fig. 9: Non-returnable valve

Fig. 10: Arduino Uno

4.6 Non-returnable valve

A non-returnable valve (Fig. 9) allows the fluid to flow in only one direction. The non-return valve ensures the fluid flow in right direction, where pressure conditions may cause change in the direction. While flowing through a non-return valve there is noticeable pressure drop. There are different types of non-return valves, such as spring-loaded, swing type, and clapper type. In this study a spring-loaded non-return valve is situated just above the pump pressure line to make sure that the oil does not flow backwards.

4.7 Arduino Uno

The Arduino Uno (Fig. 10) is an open-source microcontroller board created by Arduino.cc that is based on the Microchip ATmega328P microprocessor. The board has digital and analog input/output (I/O) pins that can be used to connect to expansion boards (shields) and other circuits. In the present study an Arduino Uno is used to control two hydraulic actuators.

4.8 Solenoid valve

Solenoid valves are called directional control valves which as the name suggests, provides pathway for fluid flow. The flow path depends on the activation of the

Fig. 11: Solenoid valves

Fig. 12: Relay switch

solenoid coil that is attached to the valve. In this research 4/3-double coil solenoid valve has been used. This particular valve has 4 ports and 3 ways in which fluid can flow. Solenoid valves are an essential part of any hydraulic system. The chosen DCVs are tandem center valves which helped to reduce number of hose pipes in the design which was necessary in cost management.

4.9 Relay switch

The relay module (Fig. 12) is an electric powered switch that can be turned on or off, allowing or disallowing current flow. The output pins of an Arduino can only provide a maximum voltage of 5v but to operate the hydraulic cylinder requires 220v to be supplied to the solenoids of the DCVs. To compensate for this inconvenience relay switch is used. To control the switching of the solenoid coils of the DCVs according to the operational sequence, a 4-channel 5V relay module has been used. The module can be controlled directly by Arduino Uno microcontroller board. The relay module has a maximum switching voltage of 250V AC.

5. FABRICATION OF THE EXPERIMENTAL SETUP

The complete experimental setup is present in Fig. 13. At first a reservoir of the dimension 21 x 7 inches was built. An external gear pinion pump and a single-phase induction motor was bolted to a base plate on the reservoir and tightened properly. Proper dimension of the pump coupling and the motor coupling was selected by taking

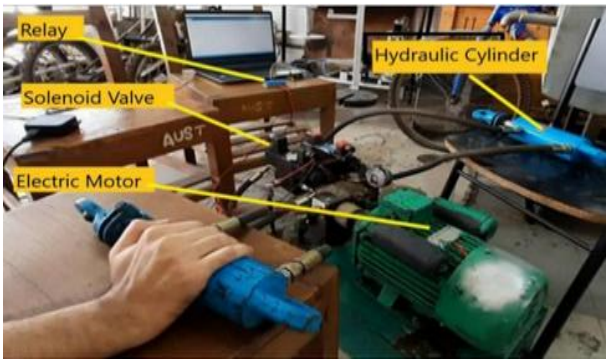

Fig. 13: Experimental setup

measurement of the shaft diameter of both the pump and the motor. Then the pump coupling and motor coupling was attached to pump and motor shaft with spider. The height of both the machines were measure to avoid misalignment which would cause excess vibration. The pump draws oil from the reservoir through elbow joint pipe. Elbow joint pipes are used to connect the hydraulic solenoid valves to the pump output line. A pressure gauge and a non-returnable valve is connected with elbow joints in-between the pump exit and one the solenoid valves. The other one has an elbow joint pipe connection to the reservoir which creates a pathway for the oil to return to the tank when all the solenoid coils are switched off. Two 4/3 direct operated double coil solenoid valves are bolted to a base plate above the reservoir. Two hydraulic hose pipes of 36 inches in length was used to connect the inlet and exhaust port of the hydraulic cylinder to the hydraulic solenoid valves enter and exhaust port.

6. RESULTS AND DISCUSSION

In the present study experiment was conducted. Fig. 14 shows the extension speed at different consecutive observations. Here observation (from 1 to 6) means, after run the system six consecutive extension speed data is taken and presented in the Fig. 14. It shows that the slope is decreasing and the system becoming stable. The push and pull side force of the hydraulic cylinder are 0.567KN and 0.49 KN respectively.

Retraction speed is presented in Fig. 15. The downward trend of the cylinder speed can be explained by the loss of fluid flow. The loss of fluid flow can be due to internal leakage in the pipes and valves, friction loss, uneven pressure drops, presence of unwanted blocking particles in the oil. Even though there was a substantial difference in the initial observations, the uncertainties in the following observations were insignificant.

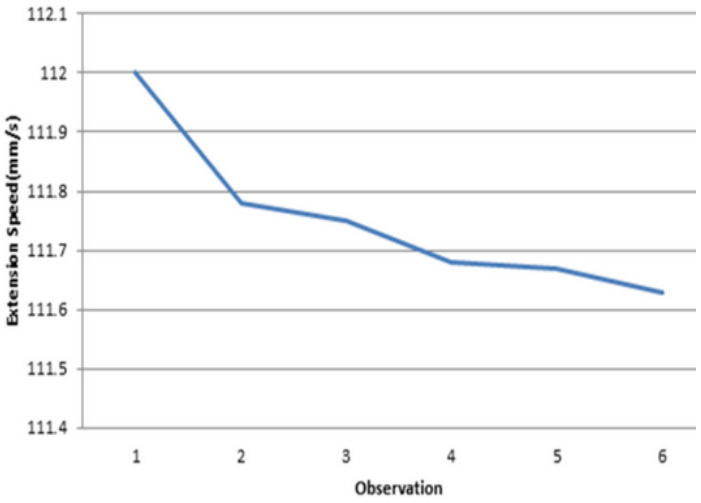

Fig. 14: Extension speed versus observation

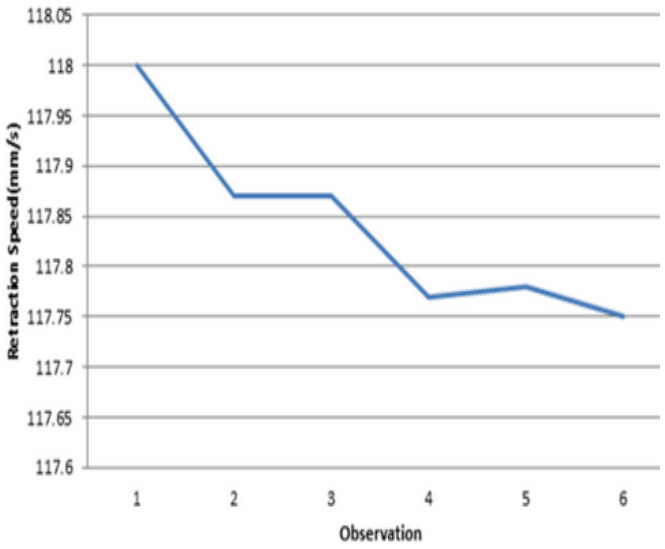

Fig. 15: Retraction speed versus Number of observations

The average extension and retraction speed of the cylinder piston are 111.75 mm/s and 117.84 mm/s respectively. The extension and retraction speed of the hydraulic cylinder was observed after each run. Although noticeable difference could be seen in the first observations, the uncertainties were negligible in the later ones. Retraction speed is greater than the extension speed because of the difference of volumetric consumption of oil in each side.

7. CONCLUSION

In this research, fabrication of an Electro-Hydraulic actuator was done. The actuator system was successfully controlled with an Arduino Uno microcontroller board proving a simple code in the Arduino Uno's IDE. The average extension and retraction speed of the cylinder piston are 111.75 mm/s and 117.84 mm/s respectively. On the other hand, push and pull side force of the hydraulic cylinder are 0.567KN and 0.49 KN respectively. T This work emphasized on the portability and compactness of the system. In industrial sector this work could be of great use because of its portability. To move heavy objects presented electro- hydraulic system can be used.

ACKNOWLEDGMENT

Thanks Ahsanullah University of Science and Technology (AUST), Tejgaon insdustrial area, Dhaka 1208, Bangladesh.

REFERENCES

[1] J. I. M. Pytel, Hydraulics and Electrical Control of Hydraulic Systems, Open Oregon Educational Resources, 2020.

[2] G. J. Zhang and M. Luoj, Design and Realization of Hydraulic actuator, vol. 8, no. 1,.pp. 195–200, 2005.

[3] A. R Henke, Fluid Power Systems and Circuits, Hydraulics and Pneumatics,1983.

[4] S. Marques et al. Optimized sequential method assisting design and implementation of electro pneumatic/hydraulic circuit, 10.21203/rs.3.rs-41484/v1, 2020.

[5] Mikell P. Groover, Automation, Production Systems, and Computer-Integrated Manufacturing, Fourth Edition, 2015.

[6] A. Tony Thomas, R. Parameshwaran, R. Deepak Kumar, S. Mohanraja, and M. Harishwaran, An investigation on modelling and controller design of a hydraulic press, IFAC Proceedings, Volume 47, Issue 1, 2014, Pages 719-725.

[7] T. G. Ling, M. F. Rahmat, and A. R. Husain, System identification and Control of an Electro-Hydraulic Actuator System, Conference: Signal Processing and Its Applications (CSPA), IEEE 8th Int. Colloq. 2012.

[8] W. Chanbua and U. Pinsopon, PID electro-hydraulic cylinder force tracking system with friction compensation, ICEAST, vol. 02019, no. 192, pp. 2–5, 2018.

[9] T. M. F. Bader, Position Control System of Hydraulic Cylinder Based on Microcontroller, J. Eng. Dev., vol. 12, no. 3, pp. 25–39, 2008.

[10] M. A. A. M. M. Ahmed, Design of a Tuned PID Controller for a Hydraulic System, Int. J. Sci. Res., vol. 5, no. 8, pp. 1218–1220, 2016.

[11] S. Salleh, M. F. Rahmat, S. M. Othman, and K. A. Danapalasingam, Review on modeling and controller design of hydraulic actuator systems, Int. J. Smart Sens. Intell. Syst., vol. 8, no. 1, pp. 338–367, 2015, doi: 10.21307/ijssis-2017-762.

[12] M. B. Rannow and P. Li, On / Off Valve Based Position Control of a Hydraulic Cylinder IMECE2007-42590, 2017, doi: 10.1115/IMECE2007-42590.

Paper ID: 9131

International Conference on Mechanical, Manufacturing and Process Engineering (ICMMPE – 2022)

Organizer: Faculty of Mechanical Engineering, Dhaka University of Engineering & Technology (DUET), Gazipur, Bangladesh

Website: https://icmmpeduet.com/

Energy Consumption Behavior Analysis and Investigation of Submersible Pumping System Efficiency in Different Bore well at Barind tract of Bangladesh

Md. Sanowar Hossain[1], Mohammad Rofiqul Islam[2], Tamal Krishna Roy[3], Noor Imani Mallik[4], Md. Sabit Hasan[5] and Md. Hasibul Hasan Himel[6].

[1,2,3,4,5,6] Department of Mechanical Engineering, Rajshahi University of Engineering & Technology, Rajshahi-6204, Bangladesh

E-mail: sanowar122086@gmail.com

ABSTRACT

The groundwater level is declining day by day and remains under 30 ft. in most of the places in the Barind tract of Bangladesh throughout the year, therefore it is mandatory to use submersible pumps in that location In this work, the energy consumption behavior and life cycle cost elements of submersible pumping system have been studied in different areas of Rajshahi division. It is found that the efficiency of the running pumps is reduced by 20-40% more than that of lab test results of the new pumps. Moreover, it has been found that the energy consumption cost of the submersible pump is almost 64% of the total life cycle cost. In the present work, the performance of a 15 HP submersible pumping system has also been studied at the laboratory scale by varying bore well diameter. It has been found that the submersible pump shows a maximum effic8-inch in 8-inch bore well (51 %) than that of 10-inch (49%) and 12-inch bore well (48%). It has been observed that the drawdown increases and efficiency decrease significantly with increasing bore well diameter.

Keywords: Submersible pump; Energy consumption behavior; Life cycle cost element analysis; Performance evaluation.

1. INTRODUCTION

The submersible pump is a multistage pump that is popular in the agricultural, residential, and industrial sectors due to its great lifting capacity and lack of cavitation [1]. Furthermore, the necessity for a submersible pumping system is increasing in other industries as well. It has been discovered that the worldwide employed pumping system consumes 20% of the world's produced electrical energy [2]. Besides, the motorized pumping system employed in the agricultural sector of India consumed 30-40% of electrical energy produced in India [3]. Drought is a regular occurrence in Bangladesh's Barind tract, and water shortage is a common occurrence during irrigation season, water falls below the necessary level due to natural and human causes and interferences.

Even though rainfall fluctuates significantly, it is the major source of groundwater recharge [4]. Furthermore, the amount of groundwater varies between 7 to 30 meters throughout the year, necessitating the use of a submersible pumping system in this area during the peak irrigation season [5]. The Barind Multipurpose Development Authority (BMDA) and Rajshahi WASA are the major water supplying authorities in the Northern Part of Bangladesh by using 15,805 and 103 nos. of submersible pumps, respectively. Besides, there are more than 10,0000 oil wells across the United States, Europe, and Asia in the petroleum industry [6]. According to a recent study, the submersible pumping system in this area operated shows 25-40% efficiency throughout the year, which is much lower than the standard laboratory efficiency. There are various reasons for the lower efficiency of submersible pumps than lab test results, such as fluctuation of groundwater level in different seasons throughout the year, pump drawdown which imposed extra pumping force, mismatch of actual discharge and head with the best condition of operation (lab report), placement of the pump at a position lower than that of the practical head that causes an extra pumping force.

The drawdown characteristics of submersible pumps impose additional pumping heads, lowering pump performance. Drawdown is inversely linked to filter length and well diameter, according to Haque et al. [4]. Groundwater level variations are a natural phenomenon that is not taken into account in this investigation.

Fig. 1. shows the monthly fluctuation of groundwater level at Shantoshpur, Paba (Rajshahi region), which is located near the river Padma. It is seen from the figure that the depth of groundwater level is high in January-June and low in July-December and it also fluctuates in a different years. From Fig.1, it is found that the maximum depth of groundwater level is almost 12 m due to the dryness of the river Padma. But it changes with the change of the month and goes to a minimum value of 5m during October/November. The static water level is declining year by year. Therefore, the necessity of submersible pumps in

that location is increasing day by day [7]. There are various brands are available in the marketplace, but some of them are cheap and have a shorter life span having high maintenance and energy consumption costs. On the other

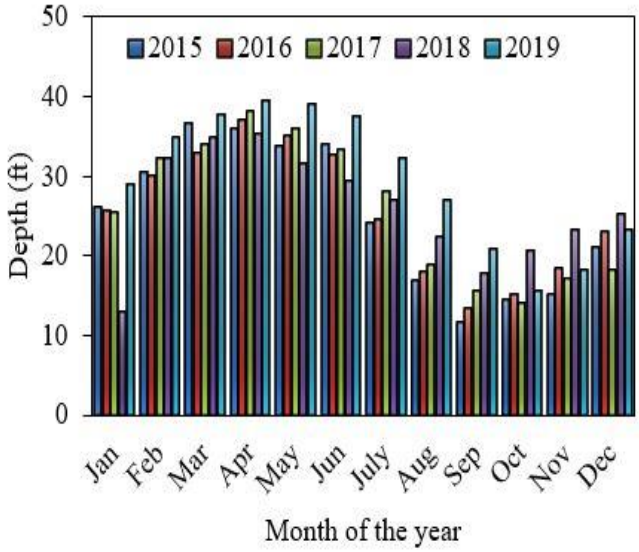

Fig. 1: Year-wise static water level fluctuation of Shantoshpur site pump, Paba, Rajshahi

hand, some brands of pumps have high prices with a longer life span with low energy and maintenance costs. Most people are attracted to the cheapest brands of pumps. Therefore, it is crucial to study the life cycle cost (LCC) and performance of submersible pumps in the Barind tract of Bangladesh.

The current study examines the energy consumption behavior and life cycle cost elements of the submersible pumping system in the Rajshahi division of Bangladesh. Besides, the performance of a 15 HP submersible pump on a laboratory scale in different bore wells was also investigated.

2. ENERGY CONSUMPTION BEHAVIOR AND LIFE CYCLE COST ELEMENTS OF SUBMERSIBLE PUMPING SYSTEM

The energy consumption cost of the submersible pump was analyzed at three different pumping sites of BMDA. These are the Amtoli-1 site, Godagari, Horipur-1 site, Paba, and Santoshpur site, Paba. The energy consumption behavior of the pumping site includes total operating head, discharge, input power, and efficiency. The necessary data of these parameters were collected from the respective BMDA office and compared to each other. The life cycle cost (LCC) of a submersible pumping system includes initial cost, installation cost, energy consumption cost, operational cost, maintenance cost, and other costs (environmental, decommissioning, and disposal cost) [7][8]. Therefore, the LCC of the submersible pumping system can be written mathematically by Eqn. (1)

$$LCC = C_{ic} + C_{in} + C_e + C_o + C_m + C_{oc} \quad (1)$$

Where, C_{ic} = initial cost of the pump, C_{ic} = installation cost of the pump, C_e = Energy consumption cost of the pump, C_o = Operational cost of the pump, C_m = maintenance, and repair cost of the pump, and C_{oc} = other costs including environmental, decommissioning, disposal and downtime cost.

3. METHODOLOGY

The experiment was conducted on a pump testing bed that has been installed in the Fluid Mechanics Lab at Rajshahi University of Engineering & Technology, Bangladesh. The test bed has a measuring tank to determine the discharge rate of the pump manually with the help of a stopwatch and a reservoir to hold the water illustrated in Fig. 2. The performance of a Pedrollo 15 HP three-phase submersible pump (model 6SR44/8-PD) was evaluated. In the experiment, three different bore well diameters were employed (8 inches, 10 inches, and 12 inches). The discharge was regulated by a gate valve. A bourdon tube pressure gauge attached to the delivery line was used to measure the head of water generated by the pump. A power analyzer was used to calculate the amount of electricity used by the pump (Lutron Power Analyzer DW-6092).

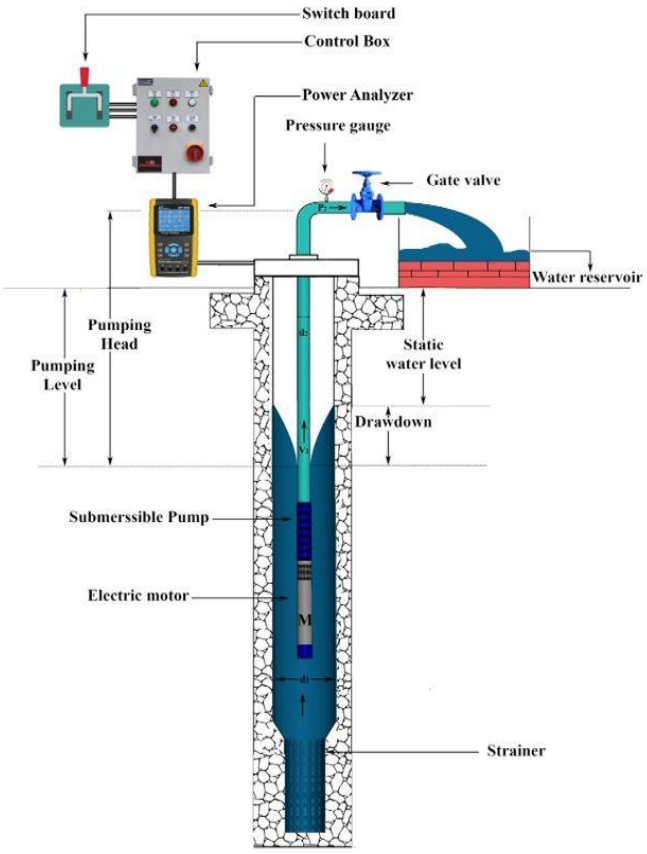

Fig. 2: Experimental setup of Submersible Pumping system

The static water level and pumping level were determined using the traditional wetted tape method during the pump's operation. Total head and efficiency were calculated by using Eq. (2) and (3), formulated by Emdad et al. 2019 [8] [4]. Then the experiment was repeated for 0.2032m and 0.3048 m bore diameter respectively. The explanation of the symbol is shown in the nomenclature table.

$$H_p = H_2 + K\frac{V_2^2}{2g} + \frac{P_2}{\rho g} \quad (2)$$

Where

$$K = \left\{1 - \left(\frac{d_2}{d_1}\right)^4 + f_b + f_m\frac{L}{d_2} + n \times f_{lf} + f_{lo}\right\}$$

and $\eta_c = \frac{\rho g Q H_p}{P}$ (3)

4. Results and discussions

4.1 Submersible Pump Performance Using in the Rajshahi Division of Bangladesh

The energy consumption behavior of submersible pumps used in the Rajshahi division of Bangladesh has been studied here. In this section, the energy consumption behavior of three pumping sites of BMDA (major water supply agencies of Barind tract) is calculated which are presented in Fig. 3 to Fig. 6. The total operating head of the Amtoli-1 site, Godagari, BMDA is higher than any other site which is presented in Fig. 3. It is clear from Fig. 6, that the overall performance of the submersible pump operated by BMDA is far away from lab test results. The average month-wise efficiency of a submersible pump is higher in May because of the lower static water level in this month.

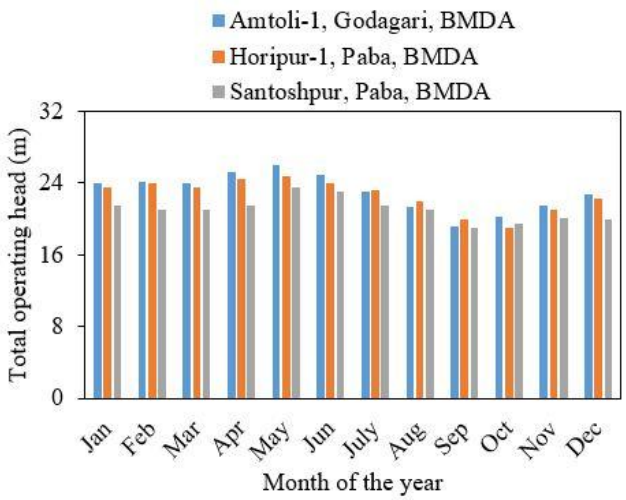

Fig. 3: Total operating head of submersible pumping system in different locations of Rajshahi division.

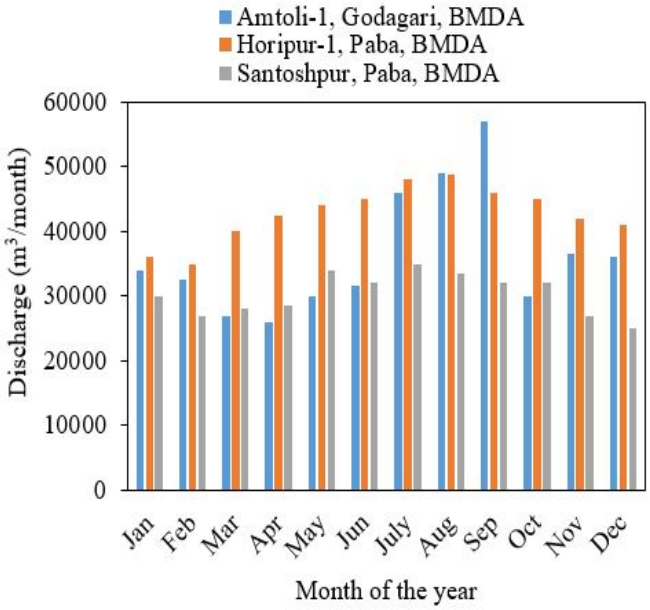

Fig. 4: Discharge of submersible pumping system in different locations of Rajshahi division.

There are various reasons for the lower efficiency of submersible pumps than lab test results, such as fluctuation of groundwater level in different seasons throughout the year, pump drawdown which imposed extra pumping force, mismatch of actual discharge and head with the best condition of operation (lab report), placement of the pump at a position lower than that of the practical head that causes an extra pumping force.

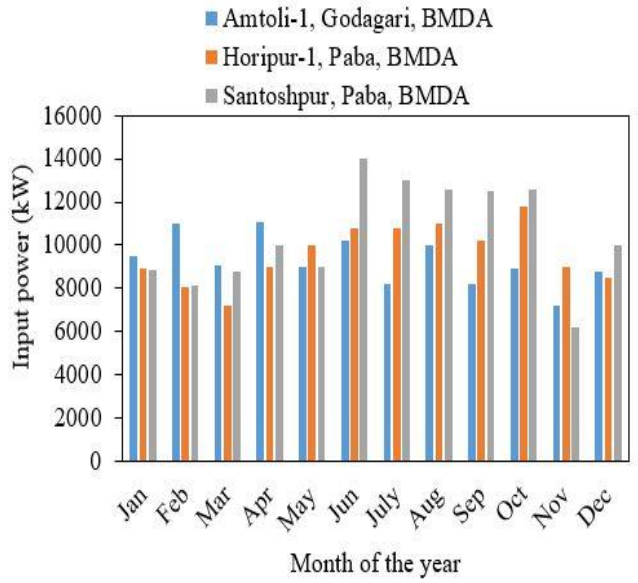

Fig. 5: Power consumption of submersible pumping system in different locations of the Rajshahi division.

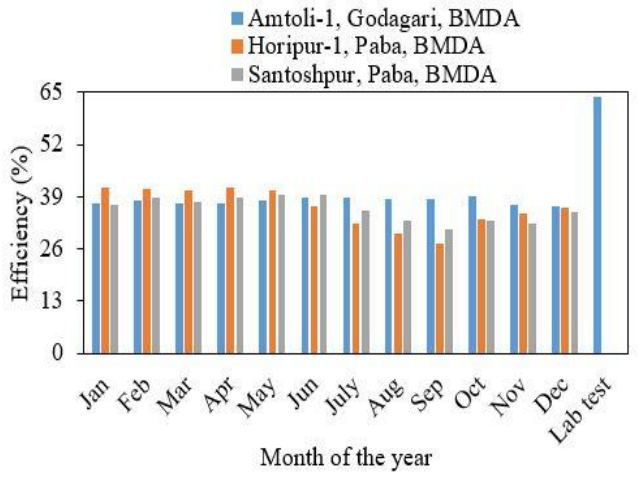

Fig. 6: Performance of submersible pumping system in different locations of Rajshahi division.

4.2 Life Cycle Cost Assessment of Submersible Pump

The Barind Multipurpose Development Authority (BMDA) and Rajshahi water supply and sewerage authority (RWASA) are the major water supply agency in the Barind tract of Bangladesh. Survey work has been completed for the assessment of the life cycle cost of the submersible pumping system which is used by BMDA and RWASA. The life span of the pump was considered 12-15 years for calculating the life cycle elements of the submersible pumping system. The various parameter values are obtained from field data and the experiences of the technicians, engineers, and operators engaged in the fieldwork. The life cycle cost of a 1 cusec submersible pumping system is presented in Fig. 7.

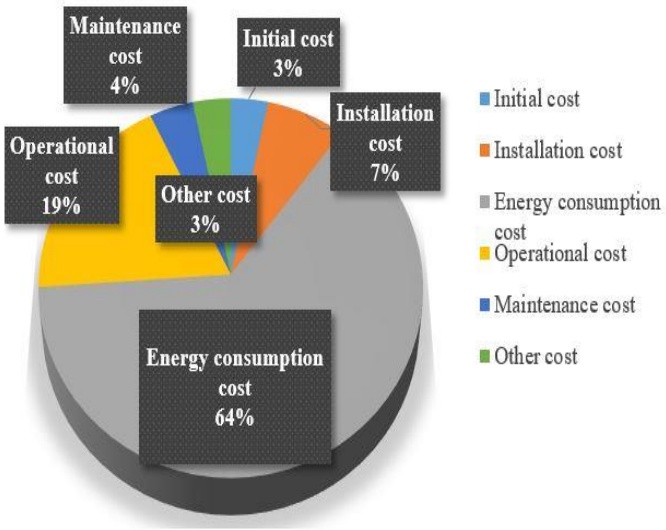

Fig. 7: Life cycle cost elements assessment of submersible pumping system

Table 1: Life cycle cost elements analysis of submersible pump

Life cycle cost elements	
Initial cost (TK)	89,160/pump
Installation cost (TK)	2,08,040/pump
Annual Operational cost (TK)	5,64,680/pump
Annual energy consumption (kWh)	1,90,208/pump
Energy rate (TK/kWh)	10
Annual Energy consumption cost (TK)	19,02,080/pump
Annual maintenance cost (TK)	1,18,880/pump
Others cost (yearly) (TK)	89,160/pump
Total cost (TK)	29,72,000/pump

From the figure, it is clear that the energy consumption cost of the submersible pumping system is the major cost and it is 64% of the total life cycle cost. The energy consumption cost of the submersible pumping system is higher than that of the laboratory test result. Table 1 represents the actual life cycle cost elements of the submersible pumping system, where the value of energy consumption cost is 19,02,080 TK of a 1 cusec submersible pump in one year which dominates the other cost elements.

4.3 Performance Investigation of Submersible Pumping System in Different Bore Well

The performance of the submersible pumping system was investigated in three different bores well (8 inches, 10 inches, and 12 inches). The performance of the submersible pumping system in different bore well is presented in Fig. 8. In every bore well three experiments were performed and then make an average to compare to each other. It has been found that the maximum efficiency of the submersible pumping system obtained in 8 inches bore well is 51%. The 12-inch bore well provides the lowest efficiency (48%) than that of 8 inches and 10-inch bore well (49%). The reason is that in 12 inches bore well the availability of the water inside the bore is much more than in 8 inches and 10-inch bore well. Thus, the pump tries to lift more water, and also the electricity consumption is more. Therefore, the efficiency of the submersible pump decrease as the bore well diameter increases.

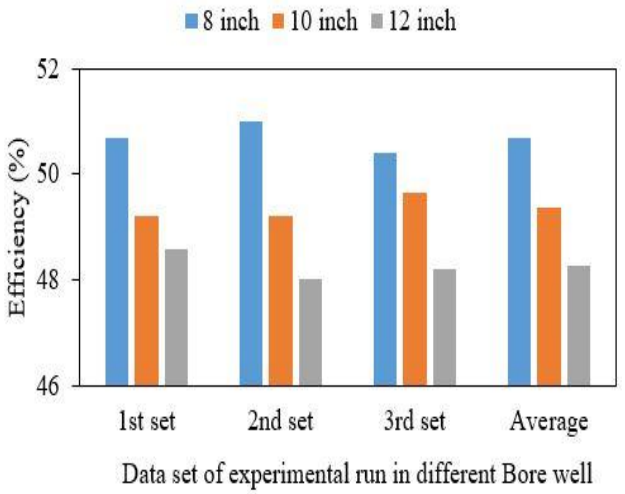

Fig. 8: Performance evaluation of submersible pumping system in different bore wells.

5. CONCLUSIONS

The groundwater level of the submersible pump is declining day by day and remains under 30 ft. throughout the year, therefore it is mandatory to use submersible pumps in most of the areas of the Rajshahi division (Barind tract). In this study, the energy consumption cost of the submersible pumping system has been analyzed as it is the major cost element in the life cycle cost analysis. It is found that the efficiency of the running pumps is reduced by 20-40 % more than that of the lab test results. Moreover, the energy consumption cost of the submersible pump is almost 64% of the total life cycle cost. There is the various reason for the lower efficiency of the pump such as fluctuation of groundwater level in different seasons throughout the year, pump drawdown which imposed extra pumping force, mismatch of actual discharge and head with the best condition of operation (lab report), placement of the pump at a position lower than that of the practical head that causes an extra pumping force. Therefore, these limitations should be reduced to increase submersible pump efficiency.

ACKNOWLEDGEMENTS

The work has been carried out under the project (dre/7/ruet/528 (39)/pro/2021-22/25), financed by the Research & Extension section, Rajshahi University of Engineering & Technology, Bangladesh. The authors would like to express their sincere gratitude and thanks to the Barind Multipurpose Development Authority (BMDA) and Rajshahi WASA (RWASA) for providing necessary information and the opportunity to study their different water pumping sites.

REFERENCES

[1] S. Shahid, O. M. Kassem, S. S. Dol, M. S. Gadala, and A. Q. Hasan, "A Review on Electrical Submersible Pump Head Losses and Methods to Analyze Two-Phase Performance Curve," vol. 16, pp. 14–31, 2021, doi: 10.37394/232013.2021.16.3.

[2] C. Gopal, M. Mohanraj, P. Chandramohan, and P. Chandrasekar, "Renewable energy source water pumping systems—A literature review," *Renew. Sustain. Energy Rev.*, vol. 25, pp. 351–370, 2013.

[3] M. B. Prasad, M. Sudha, and K. College, "Automation of submersible pumps and design using the theory of innovation and problem solving (TRIZ) technology," 2016.

[4] M. E. Haque, M. S. Islam, M. R. Islam, H. Haniu, and M. S. Akhter, "Energy efficiency improvement of submersible pumps using in Barind area of Bangladesh," *Energy Procedia*, vol. 160, pp. 123–130, 2019.

[5] S. Shahid and M. K. Hazarika, "Groundwater drought in the northwestern districts of Bangladesh," *Water Resour. Manag.*, vol. 24, no. 10, pp. 1989–2006, 2010, doi: 10.1007/s11269-009-9534-y.

[6] E. M. Ofuchi *et al.*, "Numerical investigation of the effect of viscosity in a multistage electric submersible pump," *Eng. Appl. Comput. Fluid Mech.*, vol. 11, no. 1, pp. 258–272, 2017, doi: 10.1080/19942060.2017.1279079.

[7] M. E. Haque, M. R. Islam, M. S. Islam, H. Haniu, and M. S. Akhter, "Life cycle cost and energy consumption behavior of submersible pumps using in the Barind area of Bangladesh," *Energy Procedia*, vol. 110, pp. 479–485, 2017.

[8] M. E. Haque, "Development of an Energy Saving Submersible Pumping System for Barind Tract of Bangladesh," Ph.D. Thesis, Department of Mechanical Engineering, Rajshahi University of Engineering & Technology, RUET, 2020.

Paper ID: 9230

International Conference on Mechanical, Manufacturing and Process Engineering (ICMMPE – 2022)

Organizer: Faculty of Mechanical Engineering, Dhaka University of Engineering & Technology (DUET), Gazipur, Bangladesh

Website: https://icmmpeduet.com/

Experimental Study of Granular Materials Mixing in A Slowly Rotating Drum by Image Analysis

Md. Saiful Islam[1], Asif Kabir[2], Md. Tanvir Siraj[3], Md. Monir Hossain[4], M. Mahbubur Rahman[5], and S.M. Faysal Ahmed[6]

[1,2,6]Department of Mechanical Engineering, BUET, Dhaka-1000, Bangladesh
[3]Department of Industrial and Production Engineering, BUET, Dhaka-1000, Bangladesh
[4,5]Department of Mechanical Engineering, DUET, Gazipur-1707, Bangladesh

E-mail: saifulmebuet@gmail.com

ABSTRACT

The mixing efficiency of a binary mixture in a rotating drum was evaluated using image analysis and a mixing index. Two different varieties of food were tested in this experiment to observe how they would flow and mix a rotating drum. The physical properties of granular materials were measured in a horizontal rotating drum during the slumping motion angles of repose of dynamic. The angles of dynamic are investigated as a function of rotation speed, degree of filling, and drum diameter. Mixing quality is a physical property that may be used to evaluate a mixing procedure. To compute the mixing index, image analysis is required to establish the mixing time and efficiency. After a certain amount of mixing time, the mixing efficiency is measured by a sufficient number of picture analyses. The granular materials in this experiment have different particle shapes, sizes, volumes, densities, and colors to investigate whether there is a difference in the image analysis program. The RGB color of the cutting picture was analyzed using the image processing tools given by TinEye color extraction software, which is based on MATLAB code. This application calculates the binary mixing color percentages. To further investigate the process, a mixing index is utilized to measure the evolution of mixing. The development of mixing efficiency throughout the mixing process is quantified using a mixing index. A genuine mixture's mixing index M ranges from 0 (completely separated) to 1 (Totally randomized).

Keywords: Binary Mixture; Rotating Drum; Angle of repose; Image Analysis; Mixing Index; Mixing Efficiency.

1. INTRODUCTION

A basic understanding of granular material mixing and blending can be useful in a variety of sectors, including pharmaceuticals, metallurgy, ceramics, composites, polymers, food processing, and agriculture, to mention a few. Rice, lentils, mung bean, chickpea, snow, almonds, coal, sand, coffee, corn flakes, fertilizer, and bearing balls are examples of granular materials. The mixing process of the component ingredients determines the quality of these products. It also depends on the materials' mixing volume, mass, density, shape, and size. It is critical to establish consistent mixing to get the necessary mechanical qualities in the goods. The types of mixers used, as well as the flow-ability of the granular ingredients, all, contribute to the homogeneity of the mixture. Finally, to verify adequate mixing, the image percentage was evaluated, and the mixing index was determined. A real mixture's mixing index M ranges from 0 (completely separated) to 1 (totally randomized). The mixing strength ranges from 0 to 1.

Physical parameters such as bulk density, angle of repose, dynamic angle of repose, particle size and shape, and so on influence the flow-ability and consequently mixing quality of granular materials. As a result, these characteristics may be estimated to determine the quality of mixing. Depending on the application, these parameters may have different definitions and assessment methodologies. The most relevant meanings of these words for this work are listed below.

It is an important factor of granular materials or powders that are used to assess inter particles friction. It's used to figure out how granular materials and powders move. A lesser angle of repose suggests free-flowing powders or granular materials, though a bigger point shows firm or slow-streaming granular ingredients. The angle of repose is said to be substantially influenced by material qualities such as size, shape, density, rotational speed, particle cohesiveness, dryness, and others.

It's more difficult to explain flow on a drum than it is on a heap. The free surface of granular materials seems to create an angle with the horizontal when a horizontal cylindrical drum half-filled with granular materials is rotated around its axis at a slow rotational speed. As the cylinder rotates, the angle rises. The free surface finally becomes steep enough to generate a granular debris avalanche. The inclination of the surface at this point is referred to as the higher dynamic angle

of repose. After the avalanche, the flow of granular materials stops, and the angle decreases to a lower value, the lower dynamic angle of repose. In granular material mixing, analyzing mixing performance is an important issue. It is critical to characterize such systems to the end outcome is homogeneous. The degree of homogeneity of a granular material combination will be determined using two mixing indices in this thesis. Mixing efficiency and mixing time are the two factors. The word "mixing efficiency" will be used to describe the degree of homogeneity of the granular material combination, whilst "mixing time" will be used to describe the time required to create the homogenous mixture. The mixing index is generated by calculating the mixing effectiveness of ten pictures.

Picture analysis is the process of extracting data and information from digital photographs. Image-based approaches have been frequently employed in the experiment of the rotating drum of the granular mixture. Typically, the outcome is based on a particle picture captured based on the particle. The picture was captured from a granular bed's exposed surface. Picture processing is the process of transferring an image to digital form and then conducting operations on it to improve the picture or extract relevant data. To get insight into your picture and video data, design algorithms, and investigate implementation tradeoffs, you used MATLAB. Create vision solutions using a complete range of industry-standard image processing, computer vision, and deep learning techniques.

The mixing index is based on the standard deviation that would be seen with a perfectly random, fully blended mixture, rather than zero mixing circumstances. The mixing index, as well as the concentrations of the reference component in each cell, may be specified and determined using the statistical approach. The number of cells has an impact on the mixing index.

2. LITERATURE REVIEW

Khakhar et al. [1] A prototype method for mixing the flow of granular materials in a spinning cylinder was investigated. The goal of this research is to better understand and emphasize the importance of flow in process dynamics. Granular flow in rotating drums shows a variety of intricate phenomena that are exacerbated further by the presence of liquids. Liu et al. [2] summarize our latest discrete element method (DEM) simulations of wet particle flow in rotating drums. By comparing simulation results to experimental data, the DEM model was found to be valid. The flow of particles in quasi-static and dynamic states was studied. Ding et al. [3] Hypothetical strategies for ascertaining bed turnover time in both drooping and moving modes, as well as the drooping to moving progress in free-streaming glass dabs in pivoting drums, were given. The change from drooping to rolling is expected to happen when the two turnover times are equivalent. By combining the rheological hypothesis with the convection-dissemination transport condition, Zheng et al. [4] give a consistent model for displaying the blending of monodispersed particles. The model is fleeting spatial and equipped for managing both nonstop streams and transient torrential slides, because of an administrator split approach. Hlosta et al. [5] examine the homogeneity of particulate substances in a rotating drum in terms of particle form, size, and density. Furthermore, the impact of operating factors such as drum filling capacity, rotating speed, and drum filling pattern is examined.

The mixing or segregation behavior of granular particles in a rotating drum was also analyzed experimentally and numerically by Brandao et al. [6]. Many binary mixture combinations with varying densities and sizes were looked at. The effect of filling degree and drum rotational speed on the mixing index of each binary mixture was also assessed. McCarthy et al. [7] establish a granular mixing model and show how to adapt it to solve industrially relevant challenges based on complicated geometries applicable to 3D mixers, and account for changes in particle characteristics.

Santomaso et al. [8] conducted experimental research on mixing mechanisms in drums, and the development of binary mixes of granular materials was qualitatively and quantitatively evaluated. Jiang et al. [9] examined the baffles of various forms to improve particle mixing in a revolving drum mixer. Using the discrete element approach, micro-dynamics research of mixing and segregation of a bi-disperse system of two-particle sizes in the spinning drum with these three types of baffles is carried out.

Daumann et al. [10] as of late concentrated on various molecule sizes and tones to see a distinction between them in the picture investigation program. DEM was utilized by Xiao et al. [11] to recreate the blending of equivalent estimated ABS dabs in a turning drum. Various tests, including the high bounce, backtest, grating, and wear test, L-box, and stacking point test, were utilized to acquire contact model boundaries like the coefficient of compensation, static grinding, and moving to rub.

Chou et al. [12] led tests to decide the powerful qualities of granular materials in a slurry turning drum. The objective of this examination was to decide how molecule thickness and liquid drag force connect in a granular framework. The unique attributes were estimated utilizing molecule following velocimetry. The effects of boundary conditions on the dynamic angle of repose in granular material flow in a half-filled rotating drum are investigated by Dury et al. [13] with the help of experiments and computer simulations. The effects of end caps on the angle of repose are studied using particles of various material properties.

Yamane et al. [14] used DEM simulations to study the influence of boundary surfaces on granular flows in a half-filled horizontal rotating cylinder and compared the results to MRI data. Liu et al. [15] researched the lower and upper points of the rest of the glass beads in turning drums at the slumping movement. The impact of the revolution speed, the filling degree, and the drum breadth on the lower and upper points was tentatively researched.

3. METHODOLOGY

In this investigation, the blending of granular materials with locally accessible granular materials will be analyzed. In a semi 2D pivoting drum, the blending elements of granular materials were examined tentatively. The drum's diameter is 312 mm, its axial gap width is 150 mm, and its repose angle is shown by. The front of the drum is covered with a glass plate and is composed of steel. A horizontal axis spinning drum with a transparent end cover that allows optical access. For visual examination, a glass plate with excellent transparency is ideal. After that, two types of granular materials will be placed into a section of the drum. This drum will be rotated at a very low speed immediately after the granular material charge is finished, as required by various forms of granular flow. Two layers of color particles, one on the bottom and one on the top, will be a combination for three distinct volumes (25%, 50%, and 75%) to drum.

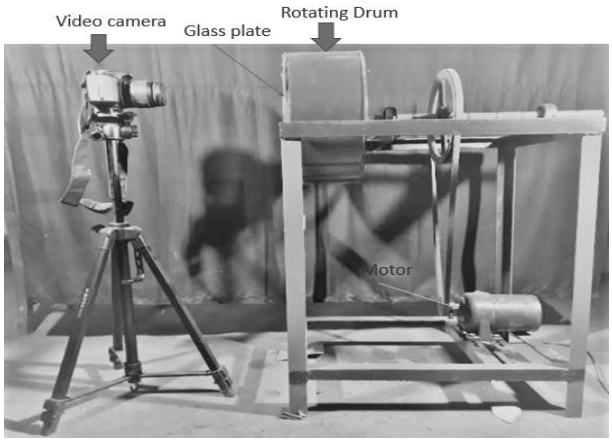

Fig. 1: Experimental setup.

The filling degree is defined as the proportion of the whole drum capacity filled by granular materials. In the experiments, particle motion is limited to rolling and cascading modes with the continuous surface flow. A portion of the drum will be filled with two types of granular materials in layers, and the drum will then be spun at a low speed of 1 rpm to mix the binary mixture. To reduce the optical noise impact in the digital photographs, the black paper was attached to the rear surface of the rotating drum Rice and Lentils were among the granular materials employed in this investigation. The material drum bed had a volume fraction of 50 percent -50 percent each fill level.

The granular material flows with the rotating drum as it rotates, increasing the slope of the free surface in the horizontal direction. The inclination angle obtains a maximum value when the granular material of the surface layer rapidly slides down and makes a lower angle with the horizontal direction to take a new stable orientation. The higher unique point of rest is the place where the powder material at the drum bed starts to torrential slide or slide down, while the lower dynamic point of rest is the place where the powder material rests when the torrential slide stops.

Before the drum was pivoted, the molecule bed's free surface was on a level plane situated. The drum was set to 1rpm to limit bed motion to the rolling pattern, which is when the surface flow is in the rolling regime. A black background was set behind the drum to achieve strong color contrast between particles and to prevent light disturbances, and two 100 watt halogen floodlights were utilized for illustration to get the best picture quality.

The transverse mixing method was used. A video camera (Model-DSLR-EOS-90D-Canon, produced by Japan with 18-135 USM Lens having High picture quality with 16 Megapixel CMOS (APS-C) sensor) set perpendicularly to the front glass plate with the tripod at a frame rate of 30 fps, ISO 1000, and a resolution of 720*1280 pixels was used. To guarantee that the subtleties of particle-to-particle interactions are recorded, each particle in the picture has a reasonably high resolution. 1 rpm drum speed and 1-minute video stored A cable connection was used to transmit the video clip to a laptop.

Using DVD Video Soft Free Studio, the video of transverse mixing was afterward framed as an image (jpg) sequence.

10 photographs were collected for the mixing index from a converted one-minute film to jpg 1800. Each image's grid was generated in Adobe Illustrator. The picture was then gridded to estimate the dynamic angle of the upper and lower angle of repose using image j software. The static images that matched the dynamic angles of repose were discovered by systematically looking through the JPEG files. Then, using the image j software, still, photos corresponding to both the upper and lower dynamic angles of repose were imported, and a tangent line was formed on the free surface of the granular ingredients, and the angle it made with the horizontal plane was determined.

Dynamic angle was determined to be the lower and upper angle of repose. The picture-only materials part was cut with Adobe Illustrator. The RGB color of the cutting picture was analyzed using the image processing tools offered by TinEye color extraction software, which is based on MATLAB code. This application calculates the binary mixing color percentages. Finally, determine mixing efficiency by calculating the mixing index using the percentages of two components' colors.

4. RESULT AND DISCUSSION

This is the first experiment with a rice and lentils mixture. This type of mixture has differing densities, colors, sizes, and shapes. The mixing experiments were done at various fill levels: 25%, 50%, and 75% of the drum by volume. Mix 50 percent of materials with top and bottom for each fill level. When it appears to fill levels, it's been observed that a fill level of 25% reduces the required mixing time and improves mixing efficiency. Mixing efficiency of 50% is lower than 25%. The mixing time is long at 75% fill because the mixing

efficiency is low. This is due to a lack of space for granular materials to move and the development of a stale center along with the drum's hub.

The speed of revolution of the drum is an essential working component. At first, the degree of mixing increases with rotating speed reaches a high peak, and then rapidly falls. In this test, the video framing speed was 30 frames per second. As a result, in the instance of a drum rotational speed of 1 rpm, which is equivalent to 6-degree rotation per sec, the angular displacement between two consecutive frames at 30 fps speed is 0.2 degrees.

From experiment Single Rice of mass, volume, density is 0.018gm, 11.7mm^3, 0.0015gm/ mm^3. Similarly, Single lentils of mass, volume, density is 0.041gm, 29.22mm^3, 0.0014gm/ mm^3.

Table 1: Summary of the binary mixture's upper and lower dynamic angles of repose

Binary Mixing of Granular Materials	1 RPM (Average 5 data)		
	25%	50%	75%
Rice+ Lentils (upper)	32.417	35.262	32.451
Rice+ Lentils (lower)	25.464	27.392	25.484

Table 2: Summary of the standard deviation of mixing for the binary mixture

Binary Mixing of Granular Materials	1 RPM (Average 5 data)		
	25%	50%	75%
Rice+ Lentils	3.329	2.600	3.178

4.1 Experiment Data for 25% Rice + Lentils

Total video Time for mixing: is 1 min. For 30FPS: 30*60 = 1800 frame. The picture is collected every 6 sec which has shown in Table 3 below.

Consider two particulate components R, pure Rice (color) & L, pure Lentils (color) placed in a mixer where R=0.50 and L=0.50

Let r and l be the proportions of each component in color fractions, respectively. A sample would consist of either pure R or pure L in the beginning when the components are separated.Ten samples of rice color percentage (r) are taken which are 0.415, 0.421, 0.421, 0.411, 0.449, 0.474, 0.463, 0.405, 0.419, and 0.441. So the variance of the real mixture is,

$$\text{Variance, } \mathbf{S^2} = \frac{\mathbf{1}}{\mathbf{n}} \sum_{\mathbf{i=1}}^{\mathbf{i=n}} (\mathbf{r} - \mathbf{R})^2 = \frac{0.051341}{10}$$
$$= 0.0051341$$

The change of the unmixed framework would be

$$\mathbf{S_0^2 = L(1 - L) = RL}$$
$$\mathbf{S_0^2 = 0.50 \times 0.50 = 0.25}$$

Expect that the blend has been randomized and that ideal blending has been accomplished. The result obtained by evaluating a sample deviates from the true composition in the case of a fully randomized mixture, and the deviation is proportional to the number of elements in the sample.

Here,
Total weight of particles (Rice) =2kg=2000gm
Weight of single particle (Rice) = 0.019gm
Total number of particles (Rice)=2000/0.019=105263
Total weight of particles (Lentils) =2kg=2000gm
Weight of single particle (Lentils) =0.035gm
Total number of particles (Lentils)=2000/0.035 = 57143
Total number of particles (Rice+ Lentils) =162406
Samples obtained from a fully randomized mixture have a variance that is

$$\mathbf{S_R^2} = \frac{\mathbf{RL}}{\mathbf{N}} = \frac{0.5 \times 0.5}{105263 + 57143} = \frac{0.25}{162406} = 1.53 \times 10^{-6}$$

Here, The quantity of particles in the examples is meant by N

$$\textbf{Mixing Index } \mathbf{M} = \frac{\mathbf{S_o^2 - S^2}}{\mathbf{S_o^2 - S_R^2}} = \mathbf{1} - \frac{\mathbf{S^2}}{\mathbf{S_o^2}} = 0.9794$$

As the sample size grows, the variance approaches zero. An actual mixture's mixing quality would be somewhere between that of a completely unmixed (segregated) combination and that of a perfectly mixed (random) mixture. A real mixture's mixing index M ranges from 0 (completely separated) to 1 (totally randomized).

Table 3: Summary of the angle of repose and percentage of lentils and rice of 25% binary mixture for different frame rate

Serial	1	2	3	4	5	6	7	8	9	10
Time (sec)	6	12	18	24	30	36	42	48	54	60
Frame No	180	360	540	720	900	1080	1260	1440	1620	1800
Angle (Degree)	32.51	27.43	25.02	32.39	27.55	25.14	32.47	27.53	25.13	32.46
% of Lentils	58.4	57.9	57.9	58.9	55.1	52.6	53.7	59.5	58.1	55.9
% of Rice	41.5	42.1	42.1	41.1	44.9	47.4	46.3	40.5	41.9	44.1

4.2 Experiment Data for 50% Rice + Lentils

Total video Time for mixing: is 1 min. For 30FPS: 30*60 = 1800 frame. The picture is collected every 6 sec which has shown in Table 4 below. Ten samples of rice color percentage (r) are taken which are 0.384, 0.371, 0.397, 0.47, 0.459, 0.441, 0.409, 0.435, 0.425, and 0.408. So the variance of the real mixture is,

$$\text{Variance, } \mathbf{S^2} = \frac{\mathbf{1}}{\mathbf{n}} \sum_{\mathbf{i=1}}^{\mathbf{i=n}} (\mathbf{r} - \mathbf{R})^2 = \frac{0.073363}{10} = 0.0073363$$

The change of the unmixed framework would be

$$\mathbf{S_0^2 = L(1 - L) = RL = 0.50 * 0.50 = \ 0.25}$$

Samples obtained from a fully randomized mixture have a variance

$$\mathbf{S_R^2} = \frac{\mathbf{RL}}{\mathbf{N}} = \frac{0.5 \times 0.5}{105263 + \ 57143} = \frac{0.25}{162406} = 1.53 \times 10^{-6}$$

Here, The quantity of particles in the examples is meant by N

$$\textbf{Mixing Index M} = \frac{\mathbf{S_o^2 - S^2}}{\mathbf{S_o^2 - S_R^2}} = \mathbf{1} - \frac{\mathbf{S^2}}{\mathbf{S_o^2}} = 1 - \frac{0.0073363}{0.25} = 0.970654$$

As the sample size grows, the variance approaches zero. An actual mixture's mixing quality would be somewhere between that of a completely unmixed (segregated) combination and that of a perfectly mixed (random) mixture. A real mixture's mixing index M ranges from 0 (completely separated) to 1 (totally randomized).

4.3 Experiment Data for 75% Rice + Lentils

Total video Time for mixing: is 1 min. For 30FPS: 30*60 = 1800 frame. The picture is collected every 6 sec which has shown in table 5 below.

Ten samples of rice color percentage (r) are taken which are 0.384, 0.371, 0.397, 0.47, 0.459, 0.441, 0.409, 0.435, 0.425, and 0.408. So variance of the real mixture are,

$$\text{Variance, } \mathbf{S^2} = \frac{\mathbf{1}}{\mathbf{n}} \sum_{\mathbf{i=1}}^{\mathbf{i=n}} (\mathbf{r} - \mathbf{R})^2 = \frac{0.115362}{10} = 0.0115362$$

The change of the unmixed framework would be

$$\mathbf{S_0^2 = L(1 - L) = RL = 0.50 * 0.50 = \ 0.25}$$

The variance of samples taken from a perfectly randomized mixture is

$$\mathbf{S_R^2} = \frac{\mathbf{RL}}{\mathbf{N}} = \frac{0.5 \times 0.5}{105263 + \ 57143} = \frac{0.25}{162406} = 1.53 \times 10^{-6}$$

Here, The quantity of particles in the examples is meant by N

$$\textbf{Mixing Index M} = \frac{\mathbf{S_o^2 - S^2}}{\mathbf{S_o^2 - S_R^2}} = \mathbf{1} - \frac{\mathbf{S^2}}{\mathbf{S_o^2}} = 1 - \frac{0.0115362}{0.25} = 0.9538$$

As the sample size grows, the variance approaches zero. An actual mixture's mixing quality would be somewhere between that of a completely unmixed (segregated) combination and that of a perfectly mixed (random) mixture. A real mixture's mixing index M ranges from 0 (completely separated) to 1 (totally randomized).

Table 4: Summary of the angle of repose and percentage of lentils and rice of 50% binary mixture for different frame rate

Serial	1	2	3	4	5	6	7	8	9	10
Time (sec)	6	12	18	24	30	36	42	48	54	60
Frame No	180	360	540	720	900	1080	1260	1440	1620	1800
Angle (Degree)	35.28	30.71	27.69	35.28	30.02	27.95	35.43	30.24	27.83	35.11
% of Lentils	61.6	62.9	60.3	53	54.1	55.9	59.1	56.5	57.5	59.2
% of Rice	38.4	37.1	39.7	47	45.9	44.1	40.9	43.5	42.5	40.8

Table 5: Summary of the angle of repose and percentage of lentils and rice of 75% binary mixture for different frame rate

Serial	1	2	3	4	5	6	7	8	9	10
Time (sec)	6	12	18	24	30	36	42	48	54	60
Frame No	180	360	540	720	900	1080	1260	1440	1620	1800
Angle (Degree)	32.68	27.93	25.13	32.75	27.84	25.59	32.14	27.71	25.48	32.21
% of Lentils	58.9	67.2	60.1	67	61.4	60.5	57.8	56.3	54.3	56.2
% of Rice	41.1	32.8	39.9	33	38.6	39.5	42.2	43.7	45.7	43.8

5. CONCLUSION AND RECOMMENDATION

The objective of this proposition is to portray the discoveries of a trial utilizing picture examination to investigate double blends of granular materials in a rotating drum. In this paper, we constructed a model of granular material mixing in basic tumblers that may be applied to more complex and industrially relevant situations. In a horizontal rotating drum, binary mixes were used to study the link between granular materials' physical attributes and mixing efficiency. The spinning drum equipment may create the principal mixing motion of granular ingredients in many sorts of tumble-type industrial mixes.

The effect of the drum's two easily changeable operating settings, the fill level, and drum flow. Variation of these two parameters in the drum is noticed, as well as near uniform mixing of the granular components. The drum's operational settings have an impact on the flow of granular ingredients in the drum. Changes in rotating drum speed and fill level have an impact on both the angle of repose and mixing efficiency.

The shape and size of the particles affected the regime. For binary mixing of lentils and rice, all fill vessel and rotational drum speed regimes are rolling. Picture investigation was utilized to portray the blending effectiveness at the outer layer of the blending volume. Particle mixing in rotating drums is regularly monitored using imaging methods. However, only an exposed bed surface may be utilized to watch the mixing process with this approach (surface mixing). As a result, it's critical to look at the complete mixing process, specifically how surface mixing is used. An image analysis approach was used to characterize the mixing efficiency.

To evaluate their performance, the mixing time and mixing efficiency of binary mixing of granular materials in the rotating drum was examined. It was revealed that the bulk density, drum fill level, drum speed, and angle of repose of the granular materials mixing all effect mixing time and efficiency. The mixing quality has also improved in this situation, and the mixing index value is near one, suggesting increased mixing efficiency. A genuine mixture's mixing index M ranges from 0 (completely separated) to 1 (Totally randomized).

The current study looks at four binary granular material mixing situations, each with three different fill levels and two different rpm variations. To help the research of mixing, certain enhancements can be recommended. The scopes of further improvement are mentioned below:

- Mixing can be improved by using a high rpm. In less time, this means better mixing efficiency.
- The mixing index may be used to calculate the mixing efficiency of a poly mixture.
- Make a rotating drum out of the glass plate so that video from both sides can be captured. The mixing efficiency may be accurately assessed.

REFERENCES

[1] Khakhar, D.V., McCarthy, J.J., Shinbrot, T. and Ottino, J.M., 1997. Transverse flow and mixing of granular materials in a rotating cylinder. Physics of Fluids, 9(1), pp.31-43.

[2] Liu, P.Y., Yang, R.Y. and Yu, A.B., 2013, June. Particle scale investigation of flow and mixing of wet particles in rotating drums. In AIP conference proceedings (Vol. 1542, No. 1, pp. 963-966). American Institute of Physics.

[3] Ding, Y.L., Forster, R., Seville, J.P.K. and Parker, D.J., 2002. Granular motion in rotating drums: bed turnover time and slumping–rolling transition. Powder Technology, 124(1-2), pp.18-27.

[4] Zheng, Q., Bai, L., Yang, L. and Yu, A., 2019. 110th anniversary: continuum modeling of granular mixing in a rotating drum. Industrial & Engineering Chemistry Research, 58(41), pp.19251-19262.

[5] Hlosta, J., Jezerská, L., Rozbroj, J., Žurovec, D., Nečas, J. and Zegzulka, J., 2020. DEM Investigation of the influence of particulate properties and operating conditions on the mixing process in rotary drums: Part 2—Process Validation and Experimental Study. Processes, 8(2), p.184.

[6] Brandao, R.J., Lima, R.M., Santos, R.L., Duarte, C.R. and Barrozo, M.A., 2020. Experimental study and DEM analysis of granular segregation in a rotating drum. Powder Technology, 364, pp.1-12.

[7] McCarthy, J.J., Shinbrot, T., Metcalfe, G., Wolf, J.E. and Ottino, J.M., 1996. Mixing of granular materials in slowly rotated containers. AIChE Journal, 42(12), pp.3351-3363.

[8] Santomaso, A., Olivi, M. and Canu, P., 2004. Mechanisms of mixing of granular materials in drum mixers under rolling regime. Chemical Engineering Science, 59(16), pp.3269-3280.

[9] Jiang, M., Zhao, Y., Liu, G. and Zheng, J., 2011. Enhancing mixing of particles by baffles in a rotating drum mixer. Particuology, 9(3), pp.270-278.

[10] Daumann, B., Fath, A., Anlauf, H. and Nirschl, H., 2009. Determination of the mixing time in a discontinuous powder mixer by using image analysis. Chemical Engineering Science, 64(10), pp.2320-2331.

[11] Xiao, X., Tan, Y., Zhang, H., Deng, R. and Jiang, S., 2017. Experimental and DEM studies on the particle mixing performance in rotating drums: Effect of area ratio. Powder Technology, 314, pp.182-194.

[12] Chou, H.T., Chou, S.H. and Hsiau, S.S., 2014. The effects of particle density and interstitial fluid viscosity on the dynamic properties of granular slurries in a rotating drum. Powder Technology, 252, pp.42-50.

[13] Dury, C.M., Ristow, G.H., Moss, J.L. and Nakagawa, M., 1998. Boundary effects on the angle of repose in rotating cylinders. Physical Review E, 57(4), p.4491.

[14] Yamane, K., Nakagawa, M., Altobelli, S.A., Tanaka, T. and Tsuji, Y., 1998. Steady particulate flows in a horizontal rotating cylinder. Physics of Fluids, 10(6), pp.1419-1427.

[15] Liu, X.Y., Specht, E. and Mellmann, J., 2005. Experimental study of the lower and upper angles of repose of granular materials in rotating drums. Powder Technology, 154(2-3), pp.125-131.

Paper ID: 9253
International Conference on Mechanical, Manufacturing and Process Engineering (ICMMPE – 2022)
Organizer: Faculty of Mechanical Engineering, Dhaka University of Engineering & Technology (DUET), Gazipur, Bangladesh
Website: https://icmmpeduet.com/

Modeling and Numerical Analysis of Spiral Tube Ground Heat Exchanger to Enhance the Performance

Nahid Hasan[1], Md. Hasan Ali[1], Nahyan Ahnaf Pratik[1] and Nafisa Lubaba[1]

[1]Department of Energy Science and Engineering, Khulna University of Engineering & Technology, Khulna-9203, Bangladesh

E-mail: hasan@ese.kuet.ac.bd

ABSTRACT

This paper presents numerical investigation on thermal performance of vertically mounted spiral tube Ground Heat Exchangers (GHEs). All of these GHEs were installed in a borehole that was 20 meters in depth. Tube material of GHEs was polyethylene. The borehole was backfilled with sand silica and soil material around the borehole was clay. Aiming to improve thermal performance of uniform pitched spiral GHE, several modifications were made where total number of turns and spiral tube materials of GHEs were same. In some modifications, loops were densified in the down part of the spiral GHEs. The position of the exit straight pipe was changed in some modifications. The spiral's diameter, total number of turns, and borehole's depth were set at 0.1398 m, 100, and 20 m, respectively. The effect of the ambient atmosphere on upper soil surfaces was neglected. The simulations were carried out with the ANSYS FLUENT software package. Water was used as the working fluid, with a flow rate of 2 liters/min and an inlet water temperature of 300.15 K. The initial temperature of the soil was 290.85 K. After 72 hours of continuous operation, the water in the uniform pitched spiral tube GHE cooled to 297.2 K. In some modifications, the average heat transfer rate improved and provided a maximum 7.67% greater performance than uniform pitched spiral tube GHE.

Keywords: Ground source heat pump, Spiral tube ground heat exchanger, Numerical simulation, Thermal performance.

1. INTRODUCTION

As energy demand is increasing rapidly, production of energy from alternative sources should be increased [1]. Energy production from renewable resources such as solar, wind, biomass, hydro, and geothermal that emit little or no CO2 is a good way to reduce CO2 and other greenhouse gases that contribute to global warming [2]. Geothermal energy is one of the most popular renewable energy sources since it is both inexhaustible and environmentally benign [3,4]. One of the most significant advantages of geothermal energy is that the temperature range of the ground becomes steady at depths of tens to hundreds of meters [5].

Geothermal energy, particularly when combined with a ground source heat pump system (GSHP), can be a desirable technology for space heating and cooling, and it is gaining popularity in countries and regions such as Europe, Australia, Korea, Japan and China [6-11]. An energy pile foundation was recently developed and implemented as a multi-purpose vertical GSHP system. Buildings can use it for both structural and GHE purposes [6]. In Europe, significant growth rates have been seen, and the total number of GSHP systems installed now exceeds 1 million, with an estimated 1.25 million used primarily for domestic space heating in 2011 [7]. The most popular use of these systems has been for energy-efficient space heating and cooling in both residential and commercial buildings [8]. Though the GSHP system has a higher initial cost, it is very efficient in space heating and cooling since it uses 25% to 50% less electricity than other traditional heating and cooling systems [2]. In a GSHP system, thermal energy is extracted from or returned to the ground via a closed-loop ground heat exchanger (GHE) buried in horizontal trenches or vertical boreholes. If there is no major limitation on land, horizontal GHE is the common choice of GHE. Recently, the vertical GHE, also called borehole ground heat exchanger, has been widely used in GSHP systems because it requires a small land area of installation and has higher energy performance compared to horizontal GHE systems [12].

Jalaluddin and Miyara [13] numerically evaluated the thermal performance of a spiral tube GHE with uniformly distributed various pitches and flow rates. This result was also compared to U-tube GHE. Reduced pitched spiral tubes GHE were found to have greater heat transfer rate. A larger flow rate was also observed to result in a greater heat transfer rate. The spiral tube GHE performed better than the U-tube GHE. Jalaluddin et al. [14] experimentally evaluated the thermal performance of U-tube, double-tube and multi-tube GHEs. In the short-time period of operation, multi-tube GHE performed better than the other two types.

Hasan and Miyara [15] evaluated the thermal performance of Slinky Horizontal GHE both computationally and empirically. To increase GHE's performance, several measures were taken. Horizontal slinky

GHEs with variable loop pitch intervals were installed to maximize the utilization of soil heat energy around GHEs. From leading to trailing loops, loop pitch intervals gradually decreased. The average heat transfer rate improved in the majority of their modifications. The average heat transfer rate decreased in two cases when loop pitch intervals were too large in leading loops and too dense in trailing loops.

The present study was carried out to investigate the effect of loop pitch and operational time on the performance improvement of spiral tube GHE's. Therefore, attempts were made to modify uniform pitched GHE by increasing the number of turns in the lower part of GHE and by changing the position of the exit straight pipe. This repositioning of the exit straight pipe and redistribution of loops may improve the thermal performance of the vertically mounted spiral GHEs.

2. DESCRIPTION OF PHYSICAL MODEL

Fig. 1 shows a schematic of the geometric parameters of a spiral tube GHE for a description of the model. The diameter of the spiral D, total number of turns N, and height of the spiral H are 0.1398m, 100, and 20m, respectively, in this study.

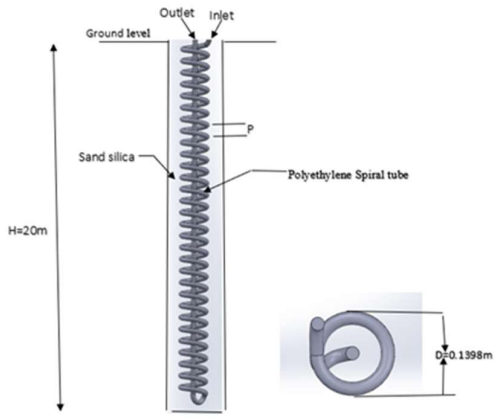

Fig. 1: Schematic diagram and geometric parameters of the Spiral tube GHE.

For a comparison study, different measures were taken, such as:

Case 1: All GHE loops are spread evenly. Exit pipe was positioned at inside of the spiral coil.

Case 2: Spiral GHE is divided into two sections, each of which is 10 meters long. There are 60 and 40 turns in the lower and upper sections, respectively. Exit pipe was positioned at inside of the spiral coil.

Case 3: The spiral is divided into four sections, each of which is 5 meters long. There are 45 turns in the lowest section. From bottom to top, the other sections have 27,17, and 11 turns, respectively. Exit pipe was positioned at inside of the spiral coil.

Case 4: All GHE loops are spread evenly. Exit pipe was positioned at outside of the spiral coil.

Case 5: The spiral is divided into four sections, each of which is 5 meters long. There are 45 turns in the lowest section. From bottom to top, the other sections have 27,17, and 11 turns, respectively. Exit pipe was positioned at outside of the spiral coil.

Fig. 2 demonstrates geometric perspectives of physical models in all cases. All of the spiral tube GHEs have a spiral diameter of 0.1398 m and 100 turns. All of these GHEs were installed in a borehole that was 20 meters in depth. Borehole was backfilled with sand silica. For each model analysis, the ground domain around the borehole was 5 meters in diameter and 25 meters in depth.

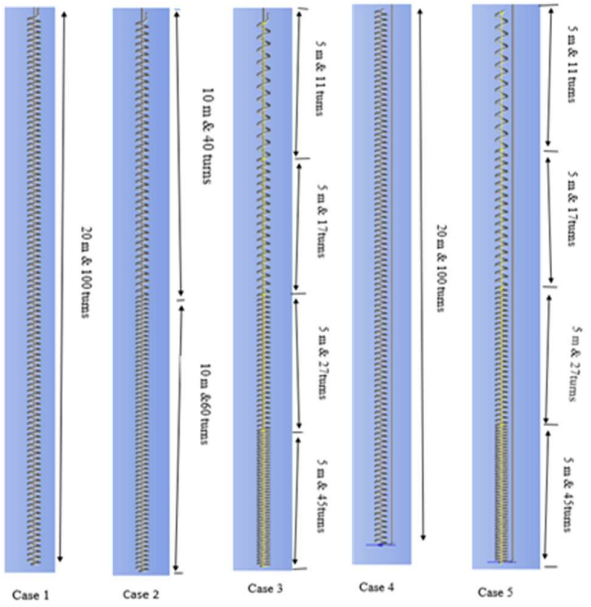

Fig. 2: Different arrangement of spiral GHEs.

Clay was used as the ground material. The GHE tubing was made of polyethylene. The GHE used spiral tube as the inlet tube and straight tube as the exit pipe. For each case, the outer and inner diameter of the tube are 0.033m and 0.026m, respectively. Table 1 lists the material's thermophysical properties. Fig. 3 shows the mesh pattern for case 1 as an example.

The mashes contain GHE tube, working fluid and soil material. The mesh around and inside the GHE tube was densified, and the mesh size far away from the GHE tube was gradually increased, in order to reduce the total number of elements and improve accuracy. Similar technique was applied to all cases.

Table 1: Thermophysical properties of the materials

Material	Density (kg/m^3)	Specific Heat (j/kg-k)	Thermal conductivity (w/m-k)
Polyethylene	920	2300	0.35
Sand-silica	2210	750	1.4
Clay	1700	1800	1.2
Water	998.2	4182	0.6

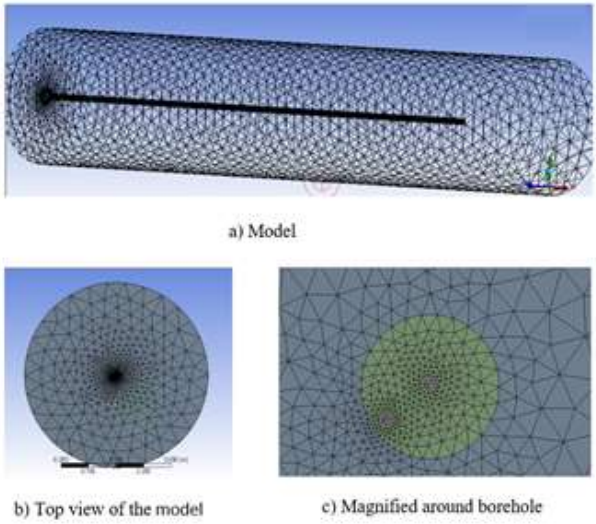

Fig. 3: Mesh generation of spiral GHE, borehole and ground.

2.1 Initial and Boundary Conditions

All of the simulations were performed in cooling mode. Inlet water temperature was kept constant at 300.15 K. Initial temperature of the ground was assumed to be 290.85 K and effect of ambient atmosphere on upper soil surfaces was neglected. Circulated water flow rate was set to 2 liter/min (Re =1900) and hence flow is laminar.

2.2 Numerical Simulation Setup

These numerical simulations were carried out by using a computational fluid dynamic software ANSYS FLUENT. The simulation solution in this software is achieved by solving the conservation equations for energy, continuity, and momentum. Simulations were done in cooling mode for 72 hours of continuous operation for all of the cases. In the simulation set up, pressure-based transient option was applied for all cases. Inlet and outlet were considered as mass flow inlet and pressure outlet, respectively. For velocity pressure coupling, the SIMPLE algorithm was used in the solution technique. For the initialization of the solution, hybrid initialization was employed.

3. Mesh Elements Independency Test

In order to perform a mesh independency test, four different sets of grids such as 4746630, 9187513, 11470933, and 14328492 elements were considered. Case 1 was simulated with an inlet water temperature of 300.15 k and a flow rate of 2 liters/minute. Average heat transfer rates after 72 hours of continuous operation were 480.30 W, 470.74 W, 468.84 W, and 467.98W, respectively for 4746630, 9187513, 11470933, and 11328432 number of elements. Figure 4 shows the average heat transfer rate vs. the number of elements.

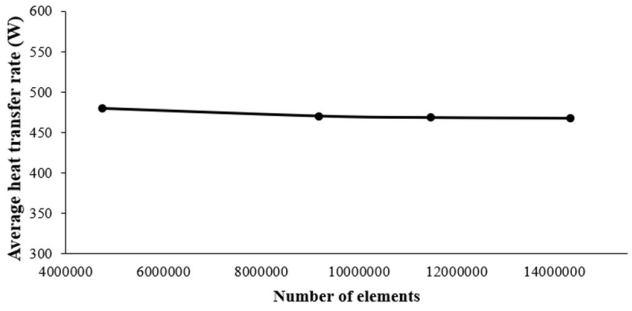

Figure 4: Average heat transfer rate vs element number

Average heat transfer rate changes little with increasing number of elements. Thus, in this study 9187513 grid system was used.

4. MODEL VALIDATION

The results of these numerical simulations must be compared to earlier work in order to be validated. The results of Case 1 were compared to previous work by Jalaluddin and Miyara [13]. All of the parameters were taken from Jalaluddin's work. We know the ground temperature is affected by atmospheric temperature up to 5 m depth, the main attention of the present paper is the modifications of spiral GHE geometry, hence the modified designs are giving better result or not. Therefore, the effect of the ambient environment on temperature variation in the top soil was overlooked. Consequently, the initial ground temperature was kept constant at 290.85K, which is similar to the previous work of Jalaluddin and Miyara [13]. After that, validation and all other simulations were performed considering this constant ground temperature of 290.85K.

The present results are nearly identical with the previous work. After validating case 1, other simulations were conducted using the same technique. Fig. 5 shows a graph of outlet temperature vs. time.

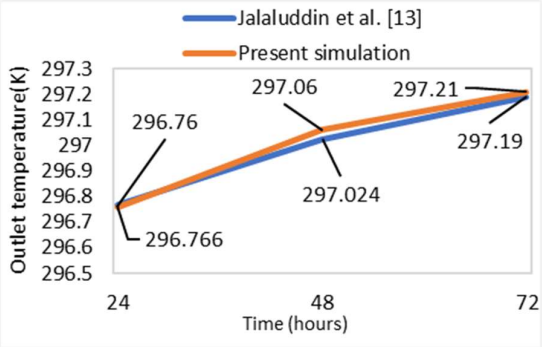

Fig. 5: Variation of outlet temperature with time .

5. RESULT AND DISCUSSION

Performance analysis of spiral tube GHEs were performed for all cases. The results of all models are presented on the basis of outlet water temperature (OWT) and average heat transfer rate. The performance of GHEs were evaluated for 72 hours of continuous operation with inlet water temperature (IWT) 300.15K.

5.1 Comparisons of Outlet Water Temperature

To improve performance, the temperature difference between IWT and OWT should be as large as possible. Fig. 6 depicts the OWT for all cases. Table 2 shows the OWT for all cases after 24, 48, and 72 hours.

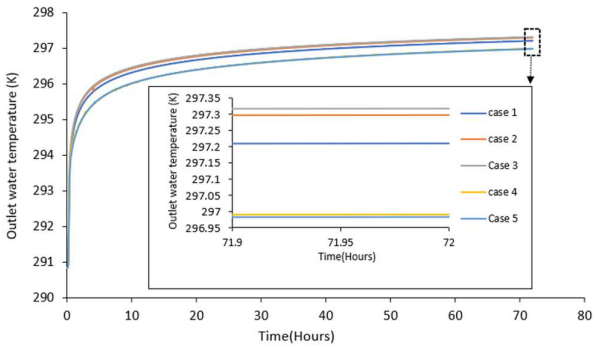

Fig. 6: Outlet water temperature with operational time.

Table 2: Outlet water temperature for all of the cases after 24, 48 and 72 hours

Cases	Outlet water temperature (K)		
	After 24hrs	After 48hrs	After 72hrs
Case 1	296.76	297.06	297.21
Case 2	296.86	297.15	297.30
Case 3	296.88	297.17	297.32
Case 4	296.49	296.82	296.99
Case 5	296.45	296.81	296.98

As a result, in the cooling mode, water inside GHE transfers more heat to the ground soil, and OWT is low. The OWT gradually increases as the operational time increases. This occurs when the operational period of the GHE increases, the water inside the GHE releases heat into the ground soil, and the temperature difference between the water and the ground soil decreases. As a result, OWT increases in all of the cases. The impact of GHE thermal response is represented by OWT. Lower value of OWR in cooling mode operation indicates that heat is well transferred to soil and there is a higher difference between IWT and OWT.

5.2 Thermal Performance Analysis

Heat transfer rate of GHEs was evaluated by following equation.

$$Q = m \times c_p \times \Delta T \quad (1)$$

Where m is the flow rate of water, c_p is the specific heat of water and ΔT is the temperature difference between inlet and outlet of circulating water. Fig. 7 shows the average heat transfer rate from case 1 to case 5 after 72 hours of continuous operation.

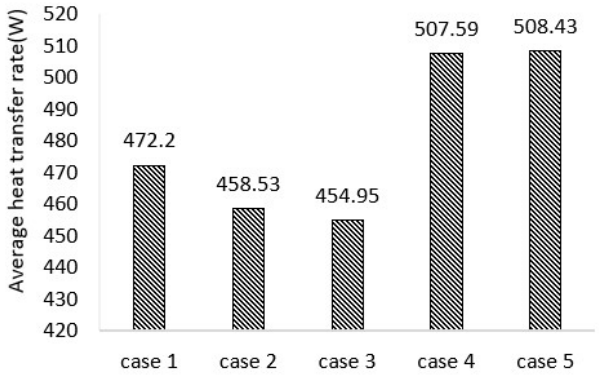

Fig. 7: Average heat transfer rate for all cases.

Heat transfer rate is high in leading loops and decreases gradually in tailing loops. To homogeneously use the heat energy of soil around GHEs, loop pitch intervals were enlarged in the leading loops and loops were densified in the tailing loops in cases 2,3 and 5. When compared to a uniform distribution of loops, the heat transfer rate for cases 2 and 3 decreases. Hasan et al. [15] used the same kind of modification for slinky type horizontal GHE and got better thermal performance in most scenarios. The loop diameter in their work was 1 m. However, the loop or spiral diameter in the present study is 0.1398 m, which is too small. As a result, the ground soil around GHEs became saturated almost equally in the present study using uniform spiral tube GHE, and therefore, these modifications did not improve thermal performance. Thermal interference from the inlet pipe has a

significant impact on the exit pipe. In cases 4 and 5, the exit straight pipe was placed outside of the spiral to reduce this impact.

As a result of these measures, thermal performance has improved significantly. The only difference between cases 1 and 4 is the position of the exit straight pipe. For cases 4 and 5 heat transfer rate increased by 7.5% and 7.67 % respectively, compared to case 1. However, in case 5, gradually decreasing the pitch in the trailing loops did not result in a significant improvement. However, the heat transfer rate in case 5 did not reduce as much as it did in cases 2 and 3. Heat transfer rate after 72 hours of continuous operation through the inlet and exit pipes is shown in fig. 8. The rate of heat transfer through spiral inlet pipe is higher than through straight exit pipe.

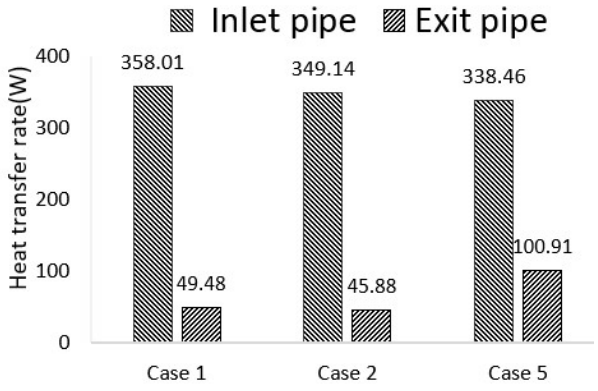

Fig. 8: Heat transfer rate of inlet and exit pipe after 72 hours of continuous operation.

5.3 Comparative Study Between Case 1, 2 and 4

Fig. 9 shows the temperature distribution of soil for cases 1,2 and 4 in the YZ plane.

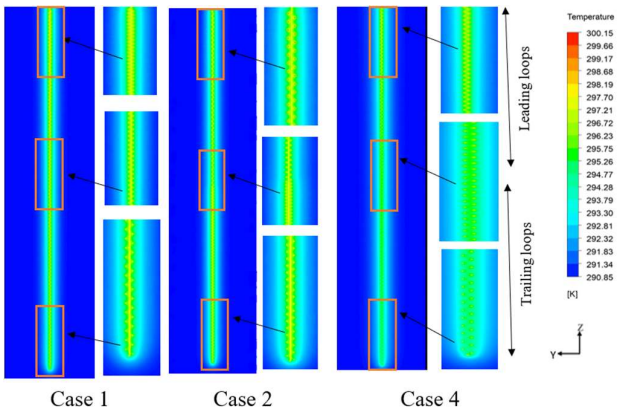

Fig. 9: Temperature distribution at YZ plane after 72 hours of continuous operation for case 1,2 and 4.

The impact of temperature degradation for case 1 and 4 decreases gradually from leading loop to trailing loop due to uniform distribution of spiral coils. But in case 2 temperature degradation is higher in trailing loops because of more dense loops arrangement. Definitely heat load is higher in leading loops during water to soil heat transfer. For case 2,3 and 5 adequate loop to loop intervals in leading loops permits easy to heat flow in soil.

6. CONCLUSION

Aiming to improve the thermal performance heat transfer rate of spiral tube GHEs, various arrangements were numerically evaluated. At the beginning, the simulation result was validated with an existing previous work. Several modifications were made where the total number of turns and spiral tube material of GHEs were the same. When the exit tube of GHE was outside of the spiral coil, the heat transfer rate increased by 7.5% and 7.67%, respectively, for a flow rate of 2 liters/min and inlet temperature of 300.15 K as compared to uniform pitched spiral GHE. This happens because the thermal interference effect from its inlet tube to exit tube is lower than traditional spiral tube GHEs. This kind of modification can be promising for performance improvement. For other modifications, there is no improvement because of the very low spiral diameter and soil around GHEs got saturated equally. Increasing the spiral diameter may improve thermal performance in this case.

REFERENCES

[1] U. Durmaz and O. Yalcinkaya, “Experimental investigation on the ground heat exchanger with air fluid,” International Journal of Environmental Science and Technology, 2019, vol. 16(9), pp. 5213–5218.

[2] M. H. Ali, K. Kariya, and A. Miyara, “Performance analysis of slinky horizontal ground heat exchangers for a ground source heat pump system,” J. Resources, 2017, vol. 6(4), pp. 1–18.

[3] C. Lee, H. Gil, H. Choi and S. H. Kang, “Numerical characterization of heat transfer in closed-loop vertical ground heat exchanger,” J. Science China Technological Sciences, 2010, vol. 53(1)

[4] P. Cui, H. Yang and Z. Fang, Z, “Heat transfer analysis of ground heat exchangers with inclined boreholes,” Applied Thermal Engineering, 2006, vol. 26(11–12), pp. 1169–1175.

[5] Jalaluddin, A. Miyara, K. Tsubaki, S. Inoue and K. Yoshida, “Experimental study of several types of ground heat exchanger using a steel pile foundation,” J. Renewable Energy, 2011, vol. 36(2), pp. 764–771.

[6] S. Yoon, S. R. Lee, G. H. Go and S. Park, “An experimental and numerical approach to derive ground thermal conductivity in spiral coil type ground heat exchanger,” J. Energy Institute, 2015, vol. 88(3), pp. 229–240.

[7] P. Bayer, D. Saner, S. Bolay, L. Rybach, and P. Blum, “Greenhouse gas emission savings of ground source heat pump systems in Europe: a review,” Renew. Sustain. Energy Rev., 2012, vol. 16, pp. 1256–1267.

[8] M. D. Moel, P. M. Bach, A. Bouazza, R. M. Singh and J. L. O. Sun, “Technological advances and applications of geothermal

energy pile foundations and their feasibility in Australia," Renew. Sustain. Energy Rev., 2010, vol. 14, pp. 2683–2696.

[9] J. Y. Lee, "Current status of ground source heat pumps in Korea, Renew. Sustain. Energy Rev., 2009, vol. 13, pp. 1560–1568.

[10] Y. P. Yuan, X. L. Cao, L. L. Sun, B. Lei and N. Y. Yu, "Ground source heat pump system: a review of simulation in China," Renew. Sustain. Energy Rev., 2012, vol. 16, pp. 6814–6822.

[11] Y. Yuan, X. Cao, J. Wang and L. Sun, "Thermal interaction of multiple ground heat exchangers under different intermittent ratio and separation distance," Applied Thermal Engineering, 2016, vol. 108, pp. 277–286.

[12] M.H. Ali, A. Miyara, and K. Kariya, "Numerical optimization of double tube GHE for ground source heat pump," International Journal of Sustainable and Green Energy, 2017, vol. 6(5), pp. 64-75.

[13] Jalaluddin, and A. Miyara, "Thermal performance and pressure drop of spiral tube ground heat exchangers for ground-source heat pump," Applied Thermal Engineering, 2015, vol. 90, pp. 630–637.

[14] A. Miyara, K. Tsubaki and K. Yoshida, "Thermal performances of three types of ground heat exchangers in short-time period of operation," Refrigeration and Air Conditioning, 2010, pp. 1–8.

[15] M. H. Ali, and A. Miyara, "Analysis of optimum slinky loop arrangement for horizontal ground heat exchanger," Transactions of the Japan Society of Refrigerating and Air Conditioning Engineers, 2017, vol. 34(4), pp. 473-483.

Paper ID: 9363

International Conference on Mechanical, Manufacturing and Process Engineering (ICMMPE – 2022)

Organizer: Faculty of Mechanical Engineering, Dhaka University of Engineering & Technology (DUET), Gazipur, Bangladesh

Website: https://icmmpeduet.com/

A Universal Battery Charging System for Ultra-Low Power Energy Harvester Applications in IoT Devices

Arnob Barua[1] and M. Salauddin Rasel[2*]

[1]Department of Electrical and Electronic Engineering, University of Science and Technology Chittagong, Bangladesh
[21]Department of Electrical and Electronic Engineering, East Delta University, Bangladesh

[*]E-mail: salauddin.rasel@gmail.com

ABSTRACT

We report a Battery Management Circuit (BMC) in this paper that significantly enhances the battery longevity of components that are triggered by events, primarily without being in standby mode and having enormous power switches on or off-chip. The main role of the proposed BMC is to monitor and regulate the battery operation, such as charging or discharging processes, to maintain the battery's health, and to reduce the chance of battery damage by ensuring that the battery delivers the optimal amount of energy to operate the load. Battery management systems are crucial for lowering battery power usage and extending the system's lifespan. The proposed method uses a novel battery management system which is ideal for wireless sensor systems that require a high intensive burst of power to complete a task and consume low average power. If the duty cycle of these bursts is low, that means the entire energy required for a burst can be gathered within bursts, then the output can be maintained totally by the harvester itself. Therefore, spare power consumption is significantly decreased, making the proposed system suitable for IoT sensors and event-driven devices in general. This work aims to implement a complete energy harvesting system with a proper battery management circuit. The commitment of the proposed circuit is to generate a steady output power over a broad range of input. Experiments with the proposed battery management circuit demonstrate that the voltage stored in the capacitor was largely stable at 5V at varied inputs from 2V to 4.5V at an input frequency of 10Hz.

Keywords: battery management circuit, standby mode, IoT sensors, event-driven devices, steady output power

1. INTRODUCTION

The Internet of Things (IoT) is rapidly evolving, laying the framework for billions of items, wireless sensor nodes, and devices to be connected wirelessly over the internet [1]. IoT applications and services can be used in any kind of industry where embedded devices can accomplish activities that humans cannot. Agriculture, home automation, smart cities, industrial automation, etc. are all potential applications for the Wireless Sensor Network (WSN) [2]. The implementation of WSN is limited by various factors, the most important of which is energy. A traditional WSN relies on batteries to provide a decent amount of energy for sophisticated computations and interactions, but its lifespan is confined. The WSN is rendered inactive after the battery is drained. In most real operation scenarios, supplanting batteries is cumbersome, even impossible, and thus limits the sustainability of WSN [3]. As a result, battery charging systems must be constructed utilizing established and efficient methods to enhance battery life and increase charging intervals [4]. EH-WSN may capture environmental energy like light, radio frequency (RF), wind, etc., and convert it to electrical energy, which can then be preserved for WSN junction. The vast majority of WSN energy is preserved in capacitors or rechargeable batteries [5]. Several sensors necessitate that a system is in sleeping state, waiting for an action to wake it up, and performing operations like initiating a contact to transmit the acquired sensory information. Portable devices like watches, smartphones, and distant IoT systems are occurrence-based gadgets that spend the majority of their lives in inactive mode. In such applications, lowering standby power usage is a challenge [6]. Batteries in portable gadgets are typically recharged via a wall adaptor. Lithium-ion batteries are the most often used batteries in portable devices because of their huge density of energy, low pace of self-discharge, and unavailability of memory influence [7]. Pulse-based chargers may charge at a quicker rate while retaining a higher charge efficiency. Since the time between pulses, battery electrolyte ions are uniformly dispersed, resulting in improved battery charge efficiency [8]. A voltage pulse-charge technique with a varying duty cycle was proposed in prior research on pulse chargers to identify and constantly track the best duty cycle of the pulse charger to maximize battery charge efficiency and reduce charge time [9], [10]. A phase-locked battery charger that uses the intrinsic features of a phase-locked loop (PLL) to charge a battery has also been proposed [11]. However, these solutions lack a pre-charge stage for the battery's preconditioning, i.e., heavily drained cells, or a charging option while a micro energy harvesting device is

available. Some pulse chargers [12], [13] have a pre-charge stage, but they are unable to manage the low output power of micro energy harvesting systems (EHS) for charging battery and where under-voltage protection has not been investigated adequately.

The aim of this paper is to tackle these aforecited issues. Therefore, a novel cost-effective shunt battery charging system is suggested in this paper which is different from other literature because of its versatility. It enhances Li-Ion battery charging efficiency while reducing the duration of the charge. It can also handle a broad extent of input voltages, ranging from 2 to 4.5 volts meanwhile keeping the output voltage constant at 5V. The proposed battery charging system can also effectively charge the Li-Ion battery through EHS with a high output voltage. It also contains safety features like an inbuilt preventive shunt controller to drain out any excessive input power, an under-voltage lockout circuit to safeguard both the battery and the user when charging, and a weak battery decouple technique that secures the battery from greatly discharging.

The following is a summary of the contents of this paper. Section 2 presents the modeling of the proposed system. Results and discussions are discussed in Section 3. The conclusion is described in Section 4.

2. MODELING OF THE PROPOSED SYSTEM

Fig. 1 presents a conceptual block diagram of an independent and ubiquitous energy harvesting mechanism with battery management, which includes several energy harvesters, a battery management circuit, and some loads. Since an IoT system is made up of a large number of nodes, it is required to manipulate the availability of alternative resources. IoT nodes are commonly powered by batteries. Thus, the power consumption of individual devices and the entire system from the network to the hardware (i.e., actuators, sensors, and microcontrollers) must be minimized throughout the architecture of an IoT set-up.

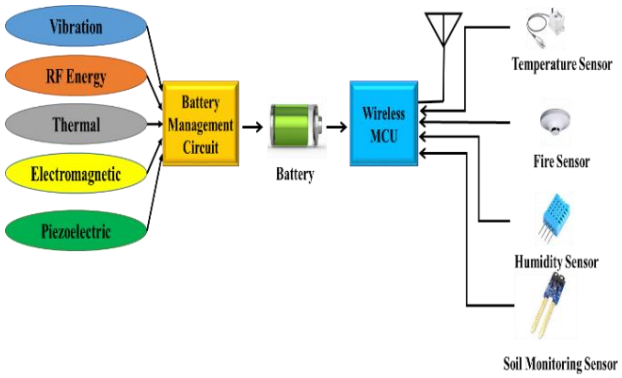

Fig. 1: Conceptual diagram of a ubiquitous energy harvesting mechanism with battery management.

2.1 Modeling of the Rectifier Circuit

The output from the energy harvester's is a varying current, which must be rectified prior it can be applied to power the load of the sensor node. The rectifying bridge circuit of our suggested system is made up of four compact Schottky diodes. The rectifier input and output voltages are shown in Fig. 2 Origin 2016 software has been used to analyze the output voltage waveform. In this case, the input voltage is 2V, and the output voltage is 1.7V (Vpk). Because the peak output voltage of energy harvesters is generally lower than 1 Vpk, conventional silicon diode-bridge rectifiers are impractical as an AC-to-DC resolution. This is the case because a full-wave bridge rectifier must surpass two forward-bias voltage drops. A Schottky diode, however, can utilize fewer voltages than a typical diode because its junctions only use 0.30~0.40V. Another advantage of Schottky diodes is that they have a faster recovery time, which helps make them ideal for elevated switching operations. It is very well-suited for low-voltage operations since it requires lower power. These diodes were preferred particularly for rectification since they have a low forward voltage drop and leakage current. Buck-Boost converters can perform in either continuous or discontinuous conduction mode. The discontinuous conduction mode (DCM) can handle a greater variety of duty ratio applications while reducing device voltage stress and providing equal current across boost inductors. Since in the DCM mode, the reverse recovery loss of the diode is minimum and it has a softer MOSFET turn-on, it is more efficient than CCM. That's why the rectifier output has been shown in the DCM mode.

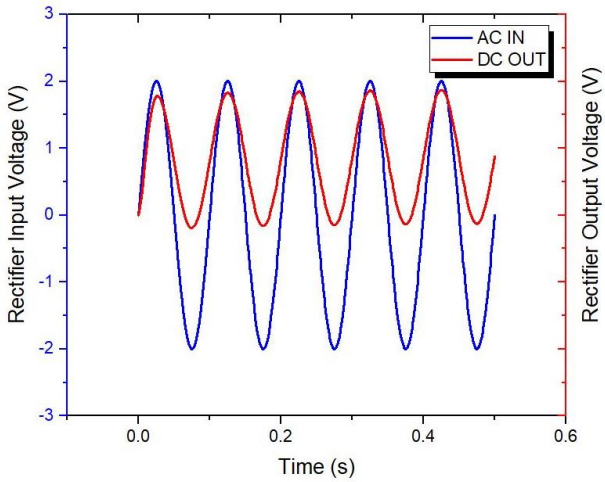

Fig. 2: Input and output voltage waveforms of the rectifier.

2.2 Modeling of the Battery Management Circuit

Because a network of wireless sensors necessitates far more high electricity than an energy extractor can supply, the inadequate generated energy should be stored in the energy storing platform for a longer period to appropriately operate the load. In this recommended battery charging method, a capacitor C7 of 1500uF is utilized as a storing component. The load's capacitor should be unplugged throughout the energy accumulation phase to block energy discharge from the load, and it should only be reconnected if the obtained energy is adequate to drive it. In our suggested circuit

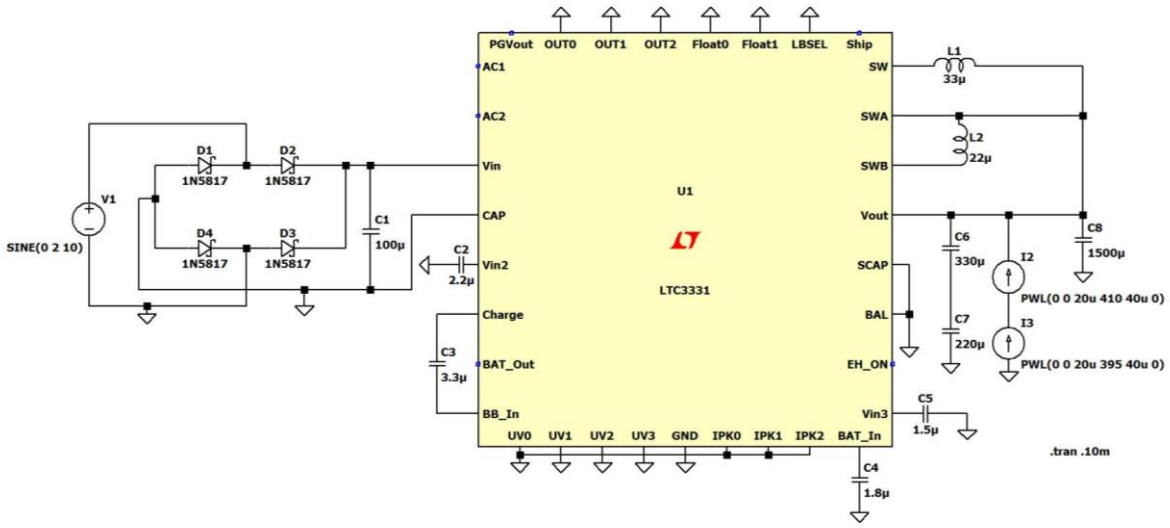

Fig. 3: A universal energy harvester with a battery management circuit.

architecture, we have utilized an LTC3331 Nano power Buck-Boost DC/DC with Energy Harvesting Battery Charger IC that was capable of keeping the output voltage steady at 5V for different input voltages ranging from 2V to 4.5V. The LTC3331 is a low-quiescent-current shunt battery charger that can be used to charge a battery using green energy. A low-battery cutoff capability protects the battery from over-discharge by detaching the battery from the buck-boost input at a predefined value. This feature safeguards Li-Ion batteries from long-term damage caused by deep discharge. The load, and the LTC3331 quiescent current, are prevented from additional draining the battery when the battery is disconnected. The complete battery management circuit is shown in Fig. 3 which includes an energy source, a full-wave bridge rectifier circuit, and a battery management circuit. The LTspice XVII software has been used to develop and simulate the entire circuit.

3. RESULTS AND DISCUSSIONS

Fig. 4 illustrates the BMC's output voltage. The energy harvesting input is an oscillatory voltage with a magnitude of 2V, a DC offset voltage of 0V, and a frequency of 10Hz. Three capacitors (1200uF, 1500uF, and 2000uF) are utilized at the BMC's output to achieve the best-regulated voltage. The highest stable output voltage is 5V when a 1500uF capacitor is utilized, as shown in the figure. Whenever the 1200uF and 2000uF capacitors are employed, however, the output voltage keeps fluctuating. Since the 1500uF capacitor can create a consistent voltage of 5V, this particular capacitor has been taken into account.

Fig. 5 depicts the capacitor discharging time at 50-ohm load. A greater capacitance value paired with the same resistance value in the suggested circuit would be able to store more charge. As a result, charging up to the supply voltage while charging and discharging all of its energy will take longer. In the preceding circuit, if a bigger resistance was employed with the same value of capacitance, a lesser current would flow, causing the capacitor to charge and discharge to take longer.

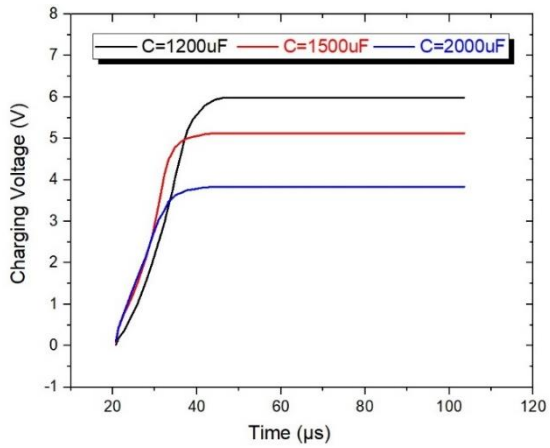

Fig. 4: Capacitor charging voltage waveforms at different capacitance.

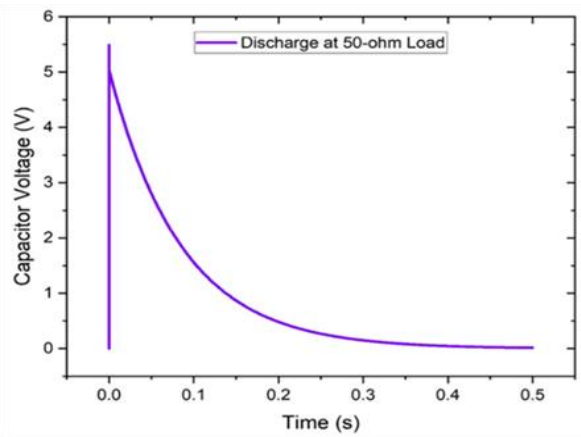

Fig. 5: Capacitor discharging time at 50-ohm load resistance.

A curve of output power as a function of the duty cycle is shown in Fig. 6. The optimum power can be provided from the energy extractor to a battery during a variety of duty cycles, as shown in this diagram. Furthermore, the voltage that comes through the battery management circuit from the energy harvester is dependent on the current. This suggests that the duty cycle's optimized value isn't constant for this type of energy harvester. To deliver flexibility and maximum output power, the ubiquitous energy transformation and monitoring circuit should handle the power output to perform consistently at the best duty cycles.

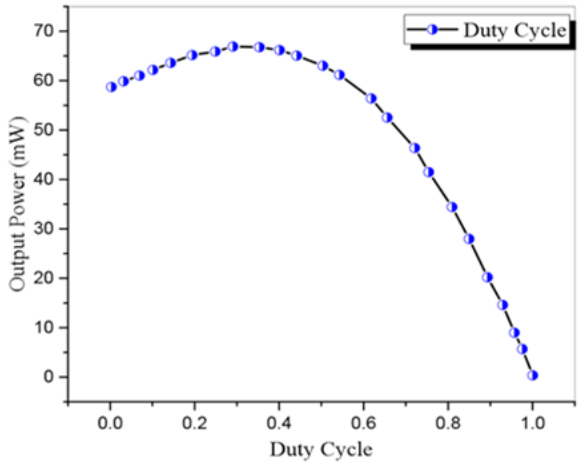

Fig. 6: Output power as a function of the duty cycle.

To the best of the author's understanding, this suggested battery management circuit produces one of the finest outcomes compared to the published circuit works. A comparison of the suggested battery management circuit's performance to that of other generator circuits is presented in Table 1.

Table 1: Evaluation of results among different battery management systems

Reference	Technique	Output Voltage	Power Density
[14]	Triboelectric	3.44V	6.78mW/m^3
[15]	Electromagnetic	2.68V	0.244mW/3
[16]	Piezoelectric	3.34V	0.0023mW/3
[17]	Hybrid	1.26V	1.68mW/ m^3
[18]	Thermoelectric	0.5V	0.10mW/ m^3
This Work	Universal	5V	33mW

Table 2 illustrates the expense of various system equipment gathered from diverse electronic device distributors. More than half of the entire component expenses are accounted for by the LTC3331. The LTC3331 can harvest energy from a myriad of substitute energy sources to run a wireless sensor system and can manage the charging of a battery.

Table 2: Expense calculation of the presented battery management system

Parts	Distributor	Items	Cost/ Items	Subtotal
LTC3331	Analog Devices Ltd.	1	$4.75	$4.75
Schottky Diode	Cheng Industrial Ltd.	4	$0.05	$0.20
Resistor	Cheng Industrial Ltd.	1	$0.04	$0.04
Capacitor	Cheng Industrial Ltd.	7	$0.08	$0.56
Inductor	Cheng Industrial Ltd.	2	$0.30	$0.60
			Total	$6.15

4. CONCLUSION

This research presented a novel and cost-effective battery management system that could be customized for intermittent operations. Battery management systems are essential for limiting battery power usage and increasing the life of the system. The proposed technique employs a novel battery management method that is well-suited to wireless sensor systems that necessitate a high-intensity burst of power to fulfill a task with low average power consumption. This paper discusses the factors that impact the power management of IoT systems, as well as the limitations of currently used batteries and power sources in IoT. The approach included a versatile shunt battery charger that can effectively charge a Li-Ion battery through EHS with a high output voltage, a built-in protective shunt controller to cut off any excessive input power, an under-voltage lockout circuit to secure both the user and the battery when charging, and a low battery cut-off mechanism that prevents the battery from deep discharging. The proposed circuit can also regulate a broad extent of input voltages, ranging from 2 to 4.5 volts while keeping the output voltage constant at 5V. The battery charging system may charge spontaneously from a micro-energy collecting source based on the input sources' accessibility. The recommended shunt charging method was used to charge three different capacitors at different voltage ranges. Experiments demonstrate that charging these capacitors at the frequency with the lowest impedance yields the most efficient charge. For battery-powered applications that stay in standby mode for the bulk of their lifespan and are activated by an event that might potentially operate at half of the battery's voltage, therefore the suggested approach is expected to be incredibly efficient. Some energy harvesters can’t produce the desired level of input voltage (2V) that has been used in the proposed work. Our future work will be to make the input voltage as much lower as we can so that the proposed circuit can operate from an ultra-low input voltage.

ACKNOWLEDGMENT

I decided to devote this paper to my parents for their immense support within the research.

REFERENCES

[1] P. Kamalinejad, C. Mahapatra, Z. Sheng, S. Mirabbasi, V. C. M. Leung, and Y. L. Guan, "Wireless energy harvesting for the Internet of Things," *IEEE Commun. Mag.*, vol. 53, no. 6, pp. 102–108, Jun. 2015, doi: 10.1109/MCOM.2015.7120024.

[2] M. Shirvanimoghaddam *et al.*, "Towards a Green and Self-Powered Internet of Things Using Piezoelectric Energy Harvesting," *IEEE Access*, vol. 7, pp. 94533–94556, 2019, doi: 10.1109/ACCESS.2019.2928523.

[3] T. Qiu, A. Zhao, R. Ma, V. Chang, F. Liu, and Z. Fu, "A task-efficient sink node based on embedded multi-core SoC for Internet of Things," *Futur. Gener. Comput. Syst.*, vol. 82, pp. 656–666, May 2018, doi: 10.1016/j.future.2016.12.024.

[4] J. M. Amanor-Boadu, M. A. Abouzied, and E. Sanchez-Sinencio, "An Efficient and Fast Li-Ion Battery Charging System Using Energy Harvesting or Conventional Sources," *IEEE Trans. Ind. Electron.*, vol. 65, no. 9, pp. 7383–7394, Sep. 2018, doi: 10.1109/TIE.2018.2793243.

[5] Z. Chen, A. Liu, Z. Li, Y.-J. Choi, H. Sekiya, and J. Li, "Energy-Efficient Broadcasting Scheme for Smart Industrial Wireless Sensor Networks," *Mob. Inf. Syst.*, vol. 2017, pp. 1–17, 2017, doi: 10.1155/2017/7538190.

[6] R. Piyare, A. L. Murphy, C. Kiraly, P. Tosato, and D. Brunelli, "Ultra Low Power Wake-Up Radios: A Hardware and Networking Survey," *IEEE Commun. Surv. Tutorials*, vol. 19, no. 4, pp. 2117–2157, 2017, doi: 10.1109/COMST.2017.2728092.

[7] X. Pu, W. Hu, and Z. L. Wang, "Toward Wearable Self-Charging Power Systems: The Integration of Energy-Harvesting and Storage Devices," *Small*, vol. 14, no. 1, p. 1702817, Jan. 2018, doi: 10.1002/smll.201702817.

[8] S. Li *et al.*, "Effects of pulse charging on the performances of lithium-ion batteries," *Nano Energy*, vol. 56, pp. 555–562, Feb. 2019, doi: 10.1016/j.nanoen.2018.11.070.

[9] Q. Lin, J. Wang, R. Xiong, W. Shen, and H. He, "Towards a smarter battery management system: A critical review on optimal charging methods of lithium ion batteries," *Energy*, vol. 183, pp. 220–234, Sep. 2019, doi: 10.1016/j.energy.2019.06.128.

[10] J. Amanor-Boadu, A. Guiseppi-Elie, and E. Sánchez-Sinencio, "The Impact of Pulse Charging Parameters on the Life Cycle of Lithium-Ion Polymer Batteries," *Energies*, vol. 11, no. 8, p. 2162, Aug. 2018, doi: 10.3390/en11082162.

[11] J. M. Amanor-Boadu and A. Guiseppi-Elie, "Improved Performance of Li-ion Polymer Batteries Through Improved Pulse Charging Algorithm," *Appl. Sci.*, vol. 10, no. 3, p. 895, Jan. 2020, doi: 10.3390/app10030895.

[12] Y. Gao, X. Zhang, Q. Cheng, B. Guo, and J. Yang, "Classification and Review of the Charging Strategies for Commercial Lithium-Ion Batteries," *IEEE Access*, vol. 7, pp. 43511–43524, 2019, doi: 10.1109/ACCESS.2019.2906117.

[13] H. Fang, C. Depcik, and V. Lvovich, "Optimal pulse-modulated Lithium-ion battery charging: Algorithms and simulation," *J. Energy Storage*, vol. 15, pp. 359–367, Feb. 2018, doi: 10.1016/j.est.2017.11.007.

[14] B. Huang, P. Wang, L. Wang, S. Yang, and D. Wu, "Ecent advances in ocean wave energy harvesting by triboelectric nanogenerator: An overview," *Nanotechnol. Rev.*, vol. 9, no. 1, pp. 716–735, Jan. 2020, doi: 10.1515/NTREV-2020-0055/ASSET/GRAPHIC/J_NTREV-2020-0055_FIG_011.JPG.

[15] M. Li and X. Jing, "A bistable X-structured electromagnetic wave energy converter with a novel mechanical-motion-rectifier: Design, analysis, and experimental tests," *Energy Convers. Manag.*, vol. 244, p. 114466, Sep. 2021, doi: 10.1016/j.enconman.2021.114466.

[16] K. Uchino, "Piezoelectric Energy Harvesting Systems—Essentials to Successful Developments," *Energy Technol.*, vol. 6, no. 5, pp. 829–848, May 2018, doi: 10.1002/ENTE.201700785.

[17] X. Wang *et al.*, "Fully Packaged Blue Energy Harvester by Hybridizing a Rolling Triboelectric Nanogenerator and an Electromagnetic Generator," *ACS Nano*, vol. 10, no. 12, pp. 11369–11376, Dec. 2016, doi: 10.1021/acsnano.6b06622.

[18] H. Lv *et al.*, "A flexible spring-shaped architecture with optimized thermal design for wearable thermoelectric energy harvesting," *Nano Energy*, vol. 88, p. 106260, Oct. 2021, doi: 10.1016/j.nanoen.2021.106260.

Paper ID: 9411

International Conference on Mechanical, Manufacturing and Process Engineering (ICMMPE – 2022)

Organizer: Faculty of Mechanical Engineering, Dhaka University of Engineering & Technology (DUET), Gazipur, Bangladesh

Website: https://icmmpeduet.com/

Energy, Exergy and Performance Analysis of High Temperature Heat Pump Cycle Using Low GWP Refrigerants

Mostafizur Rahaman[1], Monjur Morshed[1] and Mohammad Ariful Islam[2]

[1]Department of Energy Science and Engineering, Khulna University of Engineering & Technology, Khulna 9203, Bangladesh

[2]Department of Mechanical Engineering, Khulna University of Engineering & Technology, Khulna 9203, Bangladesh

E-mail: ariful@me.kuet.ac.bd

ABSTRACT

Heat pump gained significant interest in industry for high-temperature applications due to its usage in heat recovery system. Vapor compression high temperature heat pump cycle (high temperature production at condenser side between 80°C to 100°C) is analyzed in this study. Low global warming potential (GWP) refrigerants i.e., R1234ze(Z), R1234ze(E), R1243zf are considered as working fluid for the cycle. The analysis is based on computer simulation of theoretical vapor compression heat pump cycle using Python. For this analysis compressor work rate, condenser heat transfer rate, exergy destruction rate and COP are considered as performance parameters. The performance of these refrigerants are analyzed for the same evaporator load by varying evaporation and condensation temperature. According to the findings the COP of R1234ze(Z) is higher than that of R1234ze(E) and R1243zf. So, for the same evaporator heat transfer rate, the power required for an R1234ze(Z) based vapor compression high temperature heat pump system is somewhat less than that of R1234ze(E) and R1243zf. For the variation of evaporation temperature from 20°C to 40°C, maximum energetic COP and exergetic COP is obtained by value 3.485 and 0.384 respectively for R1234ze(Z) at 40°C. Again, for the variation of condensation temperature from 80°C to 100°C, maximum energetic and exergetic COP is obtained by value 4.258 and 0.248 respectively for R1234ze(Z) at 80°C. Also, a thermodynamic comparison of these refrigerants is also offered, with exergy destruction as a performance assessment measure. These findings suggest that among these refrigerants, R1234ze(Z) is more attractive than R1234ze(E) and R1243zf for high temperature heat pump due to provide better performance also having lowest GWP.

Keywords: Heat Pump; Energy Analysis; Exergy Analysis; Performance Analysis; Low GWP Refrigerant.

1. INTRODUCTION

Industrial sector consumes more than 37% of the total energy production to run various industrial processes and the required temperature level for various industrial processes are above 100°C [1]. A significant amount of waste heat is generated by various industrial processes that are often released into the environment. Forman et al. [2] showed that waste heat has a comparatively high-grade energy at a temperature level of 30-85°C. This could be improved and put to use for some useful purposes There is a limitation of applicable technologies to capture and utilize it, lead to energy waste and environmental thermal pollution.

Any mechanical system that recovers thermal energy from industrial waste streams that are above ambient temperatures is referred to as waste heat recovery (WHR) equipment. Different types of waste heat recovery technology used in industries to recover heat from heat pump, heat exchanger, heat pipe, boiler, refrigeration and power cycle. The recovered heat is utilized to create heat, generate electricity, and in certain situations, for cooling. Where, Industrial waste heat is defined as heat that is created but not fully used in industrial operations and escapes from the boundaries of a facility or building into the environment. Waste heat is commonly in the form of waste stream of air, exhausts, greenhouse gases and fluids such as water or other liquids. Heat pumps for high-temperature applications and industrial usage are one of the possible systems for heat recovery, and they have recently generated significant interest in industry due to their diverse technological applications. The phrase "high temperature heat pump" (HTHP) is widely used to refer to industrial heat pumps, which are primarily utilized as waste heat recovery for process heat supply [3]. In the literature, however, the phrasing for an HTHP's temperature level is inconsistent. Arpagaus Cordin [4] defines heat pump as sink temperature level below 80°C, high temperature heat pump as sink temperature level between 80-100°C and very high temperature heat pump as sink temperature level above 100°C.

Mota-Babiloni et al. [5] showed that, in a High Stage cycle, pentane and R1336mzz(Z) provide the best system performance. The COP of R1233zd(E) and R1224yd is

somewhat higher than that of third-generation refrigerants (R245fa/R134a). Kondou and Koyama [6] compared the performance of the refrigerants R365mfc, R717, R1234ze(Z), R1234ze(E) to raise the temperature of heat media to 160°C with a waste heat of 80°C and a cascade cycle utilizing In four different cycle configurations, COP of R1234ze(Z) and R365mfc was relatively high and advantages in practice. Deng et al. [7] studied the performance of the novel refrigerant NBY-1 in a high temperature heat pump and achieved a COP of 2.74 using the NBY-1 prototype refrigerant at a heat sink temperature of 130°C and a temperature raise of 50°C. Fukuda et al. [8] investigated that the operational performance of the HTHP system using R1234ze(E) and R1234ze(Z) was compared by, and the results showed that R1234ze(Z) was suitable for high-temperature applications instead of traditional air conditioners.

The refrigerants with high GWP used in HTHPs, such as R245fa, R245ca, R365mfc, and R134a may be phased out or phase down in the near future due to environmental restriction. In recent years, selecting eco-friendly refrigerants having low GWP for high temperature heat pumps have been a hot issue of research. High Temperature Heat Pumps (HTHPs) are a rapidly developing technology with significant promise for waste heat use and CO2 reduction. HTHPs work on the premise of extracting heat from low-temperature sources of energy and pumping it to higher temperatures [9]. In this work, energy, exergy and performance analysis of HTHP have been carried out for three low GWP refrigerants such as R1234ze(Z), R1234ze(E) and R1243zf using Python.

2. METHODOLOGY

Three HFO refrigerants are selected for this investigation as shown in Table 1. The criteria for the selection is zero ODP and low GWP.

Table 1: Low GWP Refrigerants for analysis.

Type	Working Fluid	T_c [°C]	P_c [Mpa]	ODP [-]	GWP [-]
HFO	R1234ze(E)	109.40	3.635	0	<1
	R1234ze(Z)	150.10	3.531	0	<1
	R1243zf	103.78	3.518	0	1

The basic vapor compression heat pump system is shown in Fig. 1. At low temperatures, the working fluid absorbs heat from the heat source by evaporation. The compressor compresses the working fluid to high pressure and it condenses to delivers heat to the sink at a high temperature. Then, the working fluid expands to evaporation pressure after condensation to complete the cycle.

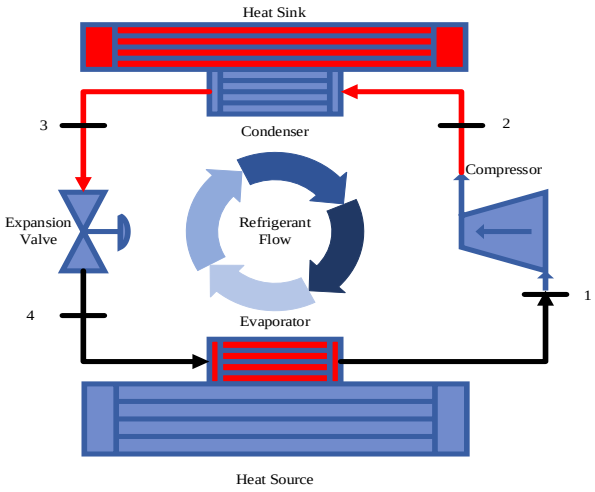

Fig. 1: Vapor compression high temperature heat pump system.

The T-s diagram of the basic vapour compression heat pump cycle is shown in Fig. 2. There are four basic balancing principles such as mass balance, energy balance, entropy balance and exergy balance are applied on a system to find out the system performance parameter. The mass balance for the compressor, condenser, expansion valve, and evaporator can be given as follows:

$$\dot{m}_1 = \dot{m}_2 = \dot{m}_3 = \dot{m}_4 = \dot{m}_{ref} \quad (1)$$

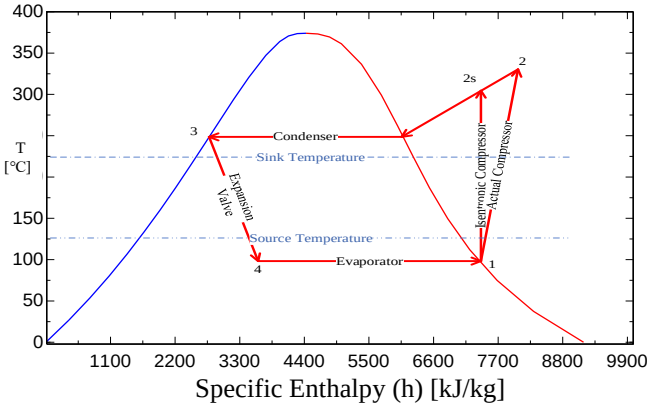

Fig.2: T-s diagram of the basic vapor compression heat pump cycle.

For steady-state operation, steady-flow with negligible potential and kinetic energy changes, energy balances for each of the operations of the heat pump cycle in can be represented as follows:

Compressor: $\dot{W}_{act-comp} = \dot{m}_{ref}(h_2 - h_1)$ (1)

Condenser: $\dot{Q}_{cond} = \dot{m}_{ref}(h_2 - h_3)$ (2)

Evaporator: $\dot{Q}_{exp} = \dot{m}_{ref}(h_4 - h_3)$ (4)

Expansion Valve: $\dot{Q}_{evap} = \dot{m}_{ref}(h_1 - h_4)$ (5)

Here, isentropic efficiency of the compressor is defined as

$$\eta_{isen-comp} = \frac{h_{2s} - h_1}{h_2 - h_1} \quad (6)$$

An energy rate balance for the entire system gives

$$\dot{W}_{act-comp} = \dot{Q}_{cond} - \dot{Q}_{evap} \quad (7)$$

For the components of the system in Fig. 1, entropy balances may be stated as

Compressor: $\dot{S}_{gen-comp} = \dot{m}_{ref}(s_2 - s_1)$ (8)

Condenser: $\dot{S}_{gen-cond} = \dot{m}_{ref}(s_3 - s_2) + \frac{\dot{Q}_{cond}}{T_{sink_avg}}$ (9)

Expansion Valve: $\dot{S}_{gen-exp} = \dot{m}_{ref}(s_2 - s_1)$ (10)

Evaporator: $\dot{S}_{gen-evap} = \dot{m}_{ref}(s_2 - s_1) - \frac{\dot{Q}_{evap}}{T_{source_avg}}$ (11)

The determination of exergy destruction rates and available energy (exergy) efficiencies for the whole system and each one of its components are two key goals. The components with the highest exergy degradation rates also have the most improvement potential. An exergy rate balance for a component can be used to calculate the component's exergy destruction rate. For the components of the system in Fig.1, exergy rate balances may be stated as

Compressor: $\dot{X}_{des-comp} = T_0 \dot{S}_{gen-comp}$ (12)

Condenser: $\dot{X}_{des-cond} = T_0 \dot{S}_{gen-cond}$ (13)

Expansion Valve: $\dot{X}_{des-exp} = T_0 \dot{S}_{gen-exp}$ (14)

Evaporator: $\dot{X}_{des-evap} = T_0 \dot{S}_{gen-evap}$ (15)

The difference between both the exergy input rate (power input) and the exergy output rate (the exergy rate of heat transported to the high-temperature medium) may be stated as the overall exergy destruction rate of the cycle:

$$\dot{X}_{des-total} = \dot{W}_{act-comp} - \dot{Q}_{cond}\left(1 - \frac{T_0}{T_{sink\ avg}}\right) \quad (16)$$

The mechanical power input is equal to the product of the needed heating load $\dot{Q}_{cond}$ (in the heating mode) as well as the temperature-related factor in parentheses in the preceding equation when the overall exergy destruction rate is zero. That is to say,

$$\dot{W}_{min} = \dot{Q}_{cond}\left(1 - \frac{T_0}{T_{sink\ avg}}\right) \quad (17)$$

The performance of a refrigerator and a heat pump is expressed in terms of coefficient of performance named COP, defined as.

$$COP = \frac{desired\ \ output}{work\ \ input} \quad (18)$$

$$COP_{refrigerator} = \frac{\dot{Q}_{evap}}{\dot{W}_{act-comp}} \quad (19)$$

$$COP_{heat-pump} = \frac{\dot{Q}_{cond}}{\dot{W}_{act-comp}} \quad (20)$$

$$COP_{heat-pump} = COP_{refrigerator} + 1 \quad (21)$$

The highest COP of a Carnot heat pump cycle running within the temperature limitations of $T_{source\ avg}$ and $T_{sink\ avg}$ may be stated as

$$COP_{carnot} = \frac{T_{sink_avg}}{T_{sink_avg} - T_{source_avg}} \quad (22)$$

Energetic COP, also called first law efficiency, The heat pump cycle's energy COP in heating mode at the condenser side is defined as

$$COP_{energy} = \frac{\dot{Q}_{cond}}{\dot{W}_{act-comp}} \quad (23)$$

The exergetic COP, also called second law efficiency, which again is specified as the cycle's exergy efficiency in heating mode, is expressed as

$$COP_{exergy} = \frac{\dot{W}_{min}}{\dot{W}_{act-comp}} = \frac{COP_{carnot}}{COP_{energy}} \quad (24)$$

Based on the first and second laws of thermodynamics, an energy and exergy analysis was performed to find out the performance of the vapor-compression heat pump system. Some of the study's assumptions are stated here for ease of reference

- Steady state operation is carried by all the components.
- Negligible kinetic and potential energy and exergy changes
- Isobaric evaporation and condensation processes.
- The expansion valve's throttling operation is isenthalpic.
- There is no heat transfer to the environment from the heat exchanger, including the evaporator and condenser.
- System frictions are negligible.

Table 2: List of parameters for the investigation

Parameters (Unit)	For the variation of evaporator temperature	For the variation of condenser temperature
$T_{evaporating}$ (°C)	20-40	30
$T_{condensing}$ (°C)	100	80-100
$\eta_{comp-isen}$ (-)	0.7	0.7
Q_{evap} (W)	5000	5000
$T_{source-avg}$ (°C)	50	50
$T_{sink-avg}$ (°C)	90	70
T_o (°C)	50	50

The simulation procedure is given in Fig. 3. For this investigation Python 3.7.3 is used for running the simulation. Different libraries were used for doing the simulation using Python. Libraries that are used for doing the simulation are:

- Coolprop 6.3.0: Coolprop is used to find the property of the different refrigerants.
- NumPy 1.19.5: NumPy is a Python library that is generally used to perform a range of mathematical operations on arrays.
- Pandas 1.1.3: Pandas is a data-analytical Python module. DataFrames are Pandas' fundamental data structures, making analytical operations.

The step 3 usages a function to calculate the heat pump performance parameter; this functional diagram is shown in Fig. 4. The function is created to calculate the performance properties of the HTHP. By taking seven input parameters (Refrigerant Name, Evaporation heat transfer rate, Evaporation Temperature, Condensation Temperature, Heat Source Temperature, Heat Sink Temperature and Dead State Temperature), it finds the various state properties of the refrigerant using ProsSI function to calculate Compressor Work Rate, Condenser Heat Transfer Rate, Total Exergy Destruction, Energetic COP and Exergetic COP.

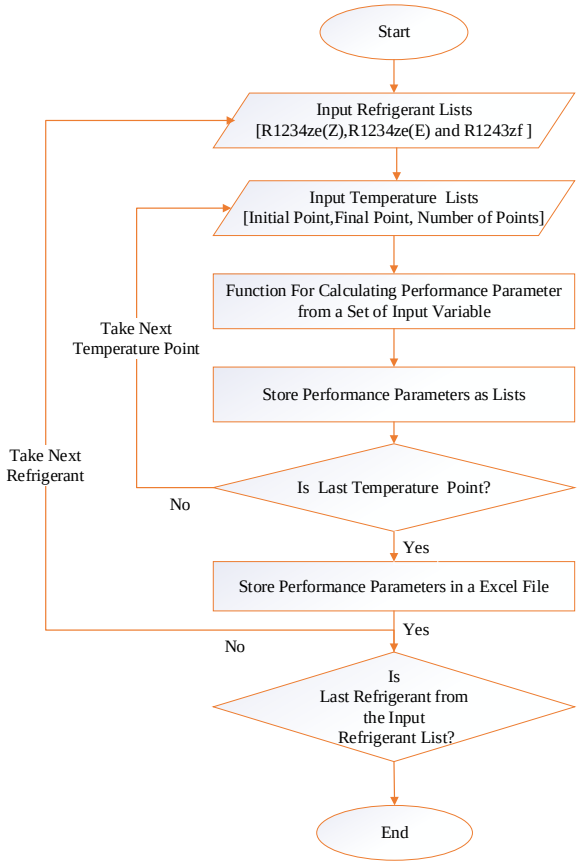

Fig. 3: Simulation Procedure of heat pump for different evaporator temperature.

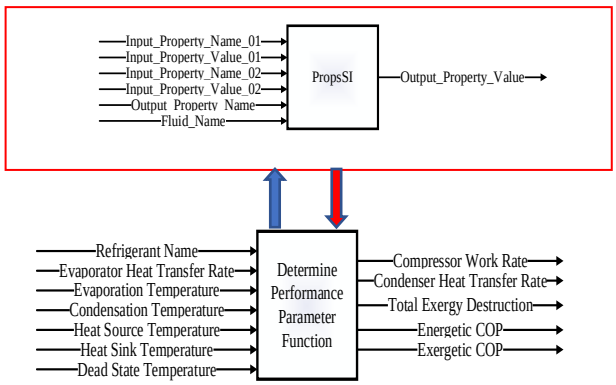

Fig. 4: Functional block diagram for the calculation of performance parameter.

3. RESULTS AND DISCUSSION

The present simulation results are compared with the sumlation results of Chen et al. [10] for validation. The simulations are performed at the same conditions of Chen et al. [10]. Fig. 5-7 showed the variation of COP, compressor work rate and total exergy destruction with respect to evaporation temperature. The present simulation results showed identical behavior that of Chen et al. [10] with slight deviation in lower evaporator temperature. For both simulation energetic COP decreases with the decreasing evaporation temperature. Compressor work and exergy destruction are increase with the decreasing evaporation temperature.

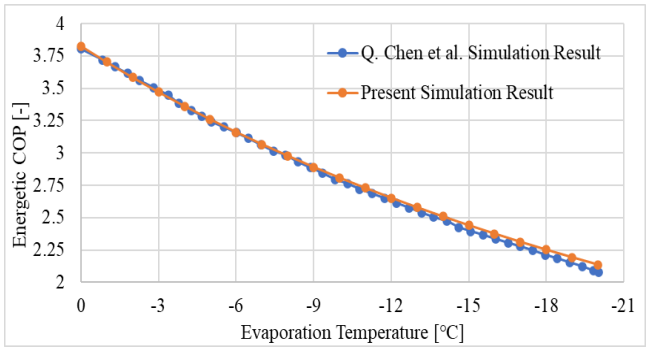

Fig. 5: Variations of energetic COP with evaporation temperature.

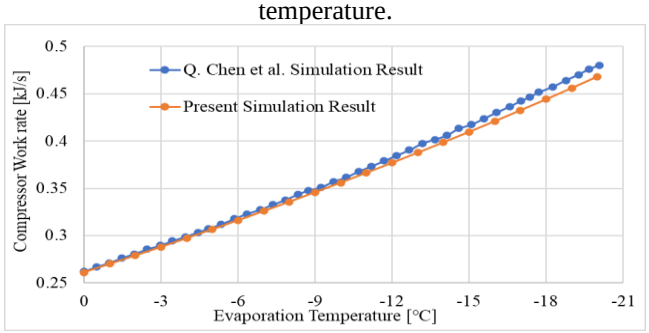

Fig. 6: Comp. work for different evaporative temperature.

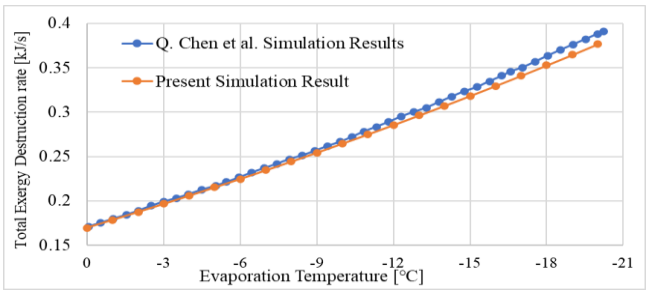

Fig. 7: Total exergy destruction for different evap. Temp.

Fig. 8 shows the variation of compressor work for different evaporation temperature. The compressor work reduces with the increases of evaporation temperature since higher evaporation temperature means higher compressor inlet temperature that's reduces the compressor work which is desirable. Among the chosen refrigerant, R1243zf refrigerant required highest compressor work followed by R1234ze(E) and R1234ze(Z). In this case, R1234ze(Z) is preferred from other refrigerants due to lower compressor work, enhance COP of the HP system.

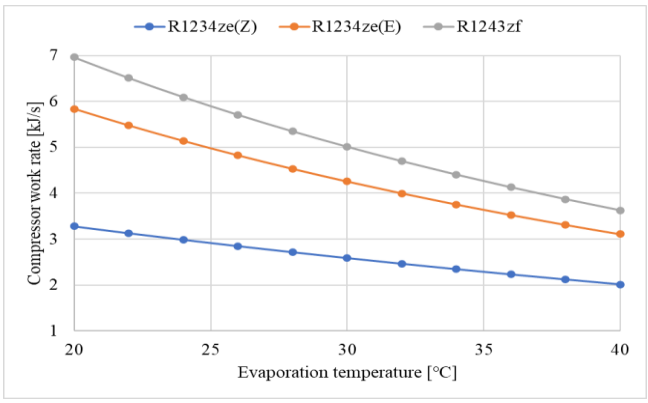

Fig. 8: Compressor work for different evaporation temp.

Fig. 9 shows the variation of condenser heat transfer for different evaporation temperature. With the increase of evaporation temperature condenser heat transfer reduce due to lower mass flow rate of refrigerant at higher evaporation temperature. R1243zf gives higher condenser heat transfer followed by R1234ze(E) and R1234ze(Z). where R1234ze(Z) gives lowest condenser heat transfer but compressor work is also lowest and dominated. For the fixed heat sink temperature Higher condenser heat transfer rate is not desirable that's why R1234ze(Z) is good refrigerant to perform effectively.

Fig. 10 represents the variation of total exergy destruction for different evaporation temperature. For increasing evaporation temperature total exergy destruction decrease. The total exergy destruction of the system is primarily due to the compressor and expansion device, since in both cases refrigerant goes to lower to higher or higher to lower temperature zone respectively. Lower exergy destruction increases COP of the heat pump, which is desirable. R1243zf gives higher exergy destruction rate followed by R1234ze(E) and R1234ze(Z). So, R1234ze(Z) will give best performance for the heat pump system.

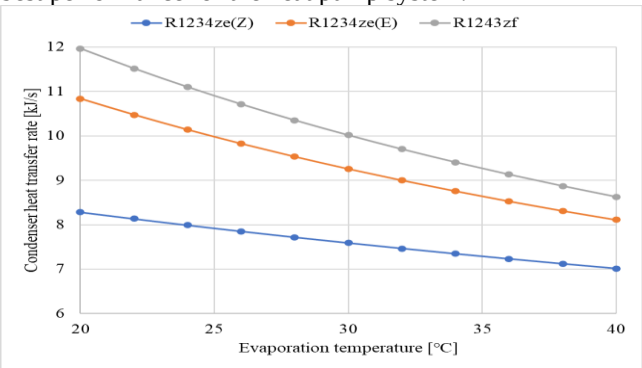

Fig. 9: Condenser heat transfer rate for evap. temperature.

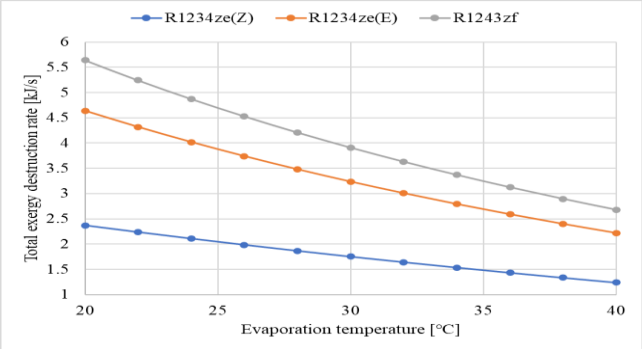

Fig. 10: Total exergy destruction rate for different evaporation temperature.

Figure 11 represents the variation of energetic COP for different evaporation temperature. An increase in evaporation temperature increases energetic COP of the system; since higher evaporation temperature reduce compressor input work which increase the system energetic COP. At 20°C evaporation temperature, energetic COP of R1234ze(Z), R1234ze(E) and R1243zf, is 2.52, 1.857 and 1.718 respectively; And the COP is increased to 3.485, 2.607 and 2.378 respectively at 40°C evaporation temperature. So, R1234ze(Z) is the suitable fluid which will give optimized output for the heat pump.

Fig. 12 represents the variation of exergetic COP for different evaporation temperature. An increase in evaporation temperature increases exergetic COP of the system; since higher evaporation temperature reduce compressor input work as well as exergy destruction. The heat pump system must be run at higher evaporation temperature as possible. At 20°C evaporation temperature, Exergetic COP of R1234ze(Z), R1234ze(E) and R1243zf, is 0.286, 0.204 and 0.189 respectively; And the exergetic

COP is increased to 0.384, 0.287 and 0.262 respectively at 40°C evaporation temperature. So, R1234ze(Z) is the suitable fluid which will give optimized output for the heat pump.

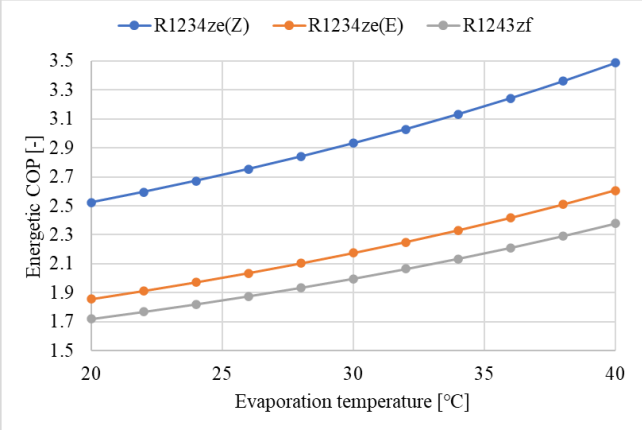

Fig. 11: Energetic COP for different evaporation temp.

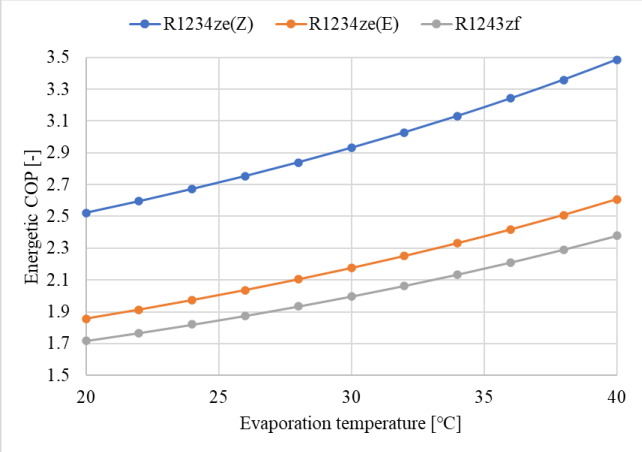

Fig. 12: Exergetic COP for different evaporation temp.

Fig. 13 shows the variation of compressor work for different condensation temperature. With the increases of condensation temperature compressor work increase, since higher condensation temperature required higher compressor outlet temperature which increase compressor work. And greater compressor work reduces the overall system efficiency. R1243zf taken high compressor wok and R1234ze(Z) taken low compressor work for higher condensation temperature, in this case R1234ze(Z) will give higher COP for the system; which is desirable.

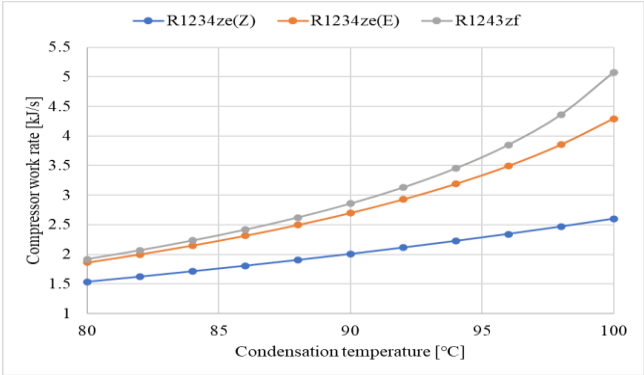

Fig. 13: Compressor work for different condensation temp.

Fig. 14 shows the variation of condenser heat transfer for different condensation temperature. With the increase of condensation temperature condenser heat transfer increase due to higher mass flow rate of refrigerant at higher evaporation temperature. R1243zf gives higher condenser heat transfer followed by R1234ze(E) and R1234ze(Z). Where R1234ze(Z) gives lowest condenser heat transfer but compressor work is also lowest and dominated. For the fixed heat sink temperature higher condenser heat transfer rate is not desirable that's why R1234ze(Z) is good refrigerant to perform effectively.

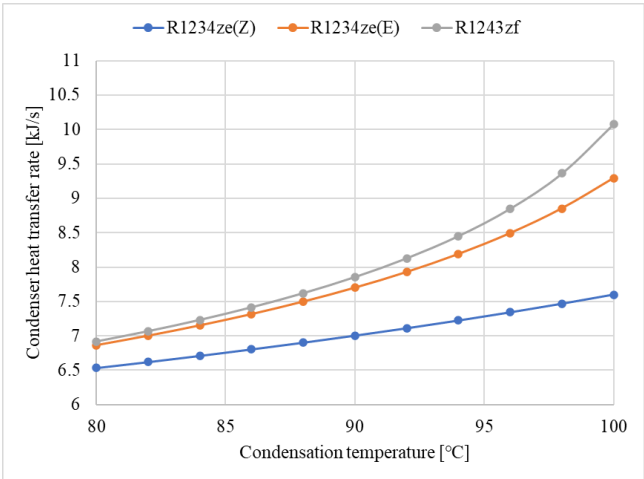

Fig. 14: Condenser heat transfer rate for different condensation temperature.

Fig. 15 represents the variation of total exergy destruction for different condensation temperature. For increasing condensation temperature total exergy destruction increase. The total exergy destruction of the system is primarily due to the compressor and expansion device, since in both cases refrigerant goes to lower to higher or higher to lower temperature zone respectively. Higher exergy destruction decreases COP of the heat pump, which is undesirable. R1243zf gives higher exergy destruction rate followed by R1234ze(E) and R1234ze(Z). R1243zf gives highest exergy destruction and R1234ze(Z)

gives lowest exergy destruction. So, R1234ze(Z) is preferrable in this case for the optimized operation of the heat pump.

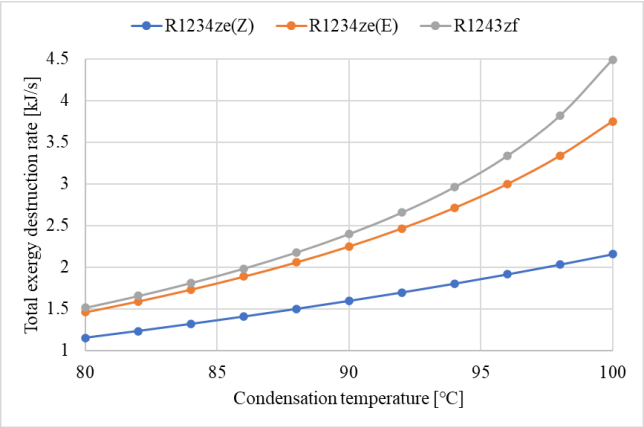

Fig. 15: Total exergy destruction for different condensation temperature.

Fig. 16 represents the variation of energetic COP for different condensation temperature. An increase in condensation temperature decreases energetic COP of the system; since higher condensation temperature increase compressor input work which decrease the system energetic COP. The heat pump system must be run at lower condensation temperature as much as possible.

At 80°C condensation temperature, energetic COP of R1234ze(Z), R1234ze(E) and R1243zf is 4.258, 3.685 and 3.605 respectively. And the COP is decreased to 2.923, 2.165, and 1.985 respectively at 100°C condensation temperature. So, R1234ze(Z) is the suitable fluid which will give optimized output for the heat pump.

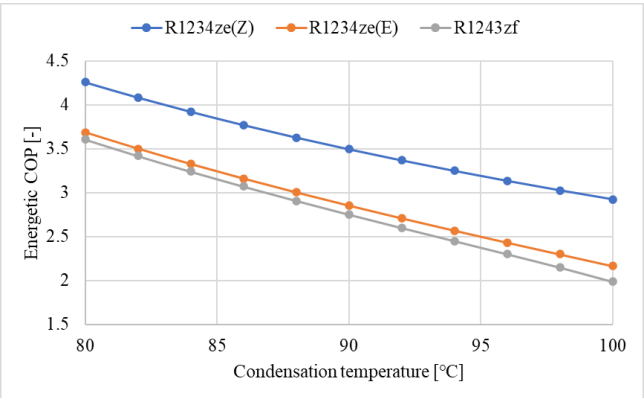

Fig. 16: Energetic COP for different condensation temperature.

Fig. 17 represents the variation of exergetic COP for different condensation temperature. An increase in condensation temperature decreases exergetic COP of the system; since higher condensation temperature increase compressor input work as well as exergy destruction, which decrease exergetic COP of the system. The heat pump system must be run at lower condensation temperature as much as possible, while maintaining the sink temperature above 80°C for HTHP application.

At 80°C condensation temperature, energetic COP of R1234ze(Z), R1234ze(E) and R1243zf is 0.248, 0.215 and 0.210 respectively; which is decreased to 0.17, 0.126, and 0.115 respectively at 100°C condensation temperature. So, R1234ze(Z) is the suitable fluid which will give optimized output for the heat pump.

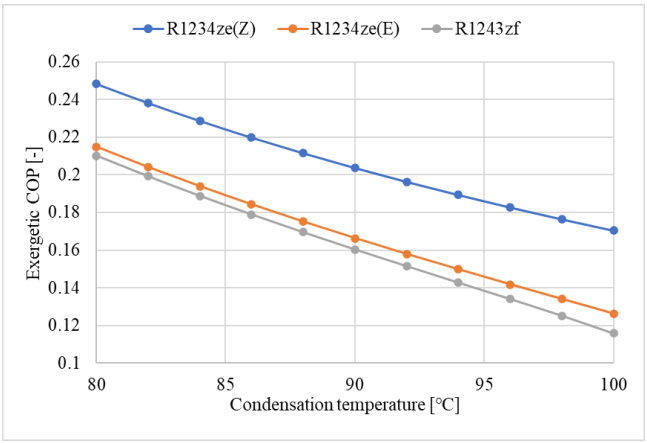

Fig. 17: Exergetic COP for different condensation temperature.

Table 3 and Table 4 show a comparison of energetic COP and exergetic COP for various low GWP refrigerants. Higher the COP value is more effective the refrigerant as high temperature heat pump.

Table 3: Maximum Obtainable COP for $T_evaporation$ = 20°C to 40°C is at 40°C

Refrigerant Name	Energetic COP		Exergetic COP	
	COP_i	Higher than R1234zf $= \frac{COP_i - COP_{reference}}{COP_{reference}} * 100\%$	COP_i	Higher than R1234zf $= \frac{COP_i - COP_{reference}}{COP_{reference}} * 100\%$
R1234ze(Z)	3.485	46.60%	0.384	46.5%
R1234ze(E)	2.607	9.63%	0.287	9.5%
R1243zf	2.378	Reference	0.262	Reference

Table 4: Maximum Obtainable COP for $T_condensation$ = 80°C to 100°C is at 80°C

Refrigerant Name	Energetic COP		Exergetic COP	
	COP_i	Higher than R1234zf $= \frac{COP_i - COP_{reference}}{COP_{reference}} * 100\%$	COP_i	Higher than R1234zf $= \frac{COP_i - COP_{reference}}{COP_{reference}} * 100\%$
R1234ze(Z)	3.485	46.60%	0.384	46.5%
R1234ze(E)	2.607	9.63%	0.287	9.5%
R1243zf	2.378	Reference	0.262	Reference

4. CONCLUSIONS

Energy, exergy and performance analysis of HTHP is done by varying evaporation and condensation temperature of low GWP refrigerants i.e., R1234ze(Z), R1234ze(E) and R1243zf. Analysis is done based on the parameters like compressor work rate, condenser heat transfer rate, total exergy destruction rate, energetic COP and exergetic COP.

For the variation of evaporation temperature from 20℃ to 40℃, maximum energetic COP and exergetic COP is obtained by value 3.485 and 0.384 respectively for R1234ze(Z) at 40℃. Energetic COP of R1234ze(Z) and R1234ze(E) is 46.6% and 9.63% higher that of R1243zf. Exergetic COP of R1234ze(Z) and R1234ze(E) is 46.5% and 9.5% higher that of R1243zf.

Again, for the variation of condensation temperature from 80℃ to 100℃, maximum energetic and exergetic COP is obtained by value 4.258 and 0.248 respectively for R1234ze(Z) at 80℃. Energetic COP of R1234ze(Z), and R1234ze(E) is 18.1% and 2.2% higher compared with the value of R1243zf. Exergetic COP of R1234ze(Z) and R1234ze(E) is 18.09% and 2.38% higher than that of R1243zf.

REFERENCES

[1] C. Arpagaus, Frédéric Bless, Michael Uhlmann, Jürg Schiffmann Stefan, S. Bertsch, “High temperature heat pumps: Market overview, state of the art, research status, refrigerants, and application potentials,” Energy, 2018, doi: 10.1016/j.energy.2018.03.166.

[2] C. Forman, I. K. Muritala, R. Pardemann, and B. Meyer, “Estimating the global waste heat potential,” Renew. Sustain. Energy Rev., vol. 57, pp. 1568–1579, 2016, doi: 10.1016/j.rser.2015.12.192.

[3] R. Rieberer, “IEA Heat Pump Programme Annex 35: Anwendungsmöglichkeiten für industrielle Wärmepumpen,” Nachhalt. Berichte aus Energie- und Umweltforsch. 17/2015, pp. 1–265, 2015, [Online]. Available: www.nachhaltigwirtschaften.at

[4] Dr. Arpagaus Cordin, “Literaturstudie_Hochtemperatur_Waermepumpen,” Förderverein Inst. für Energiesysteme, pp. 1–115, 2017, [Online]. Available: http://www.fv-ies.ch/fileadmin/NTB_Institute/IES/FV-IES/Literaturstudie_Hochtemperatur_Waermepumpen.pdf

[5] A. Mota-Babiloni, C. Mateu-Royo, J. Navarro-Esbrí, F. Molés, M. Amat-Albuixech, and Á. Barragán-Cervera, “Optimisation of high-temperature heat pump cascades with internal heat exchangers using refrigerants with low global warming potential,” Energy, vol. 165, pp. 1248–1258, 2018, doi: 10.1016/j.energy.2018.09.188.

[6] C. Kondou and S. Koyama, “Thermodynamic assessment of high-temperature heat pumps using low-GWP HFO refrigerants for heat recovery,” Int. J. Refrig., vol. 53, pp. 126–141, 2015, doi: 10.1016/j.ijrefrig.2014.09.018.

[7] N. Deng et al., “Molecular simulation and experimental investigation for thermodynamic properties of new refrigerant NBY-1 for high temperature heat pump,” Energy Convers. Manag., vol. 179, no. October 2018, pp. 339–348, 2019, doi: 10.1016/j.enconman.2018.10.076.

[8] S. Fukuda, C. Kondou, N. Takata, and S. Koyama, “Low GWP refrigerants R1234ze(E) and R1234ze(Z) for high temperature heat pumps,” Int. J. Refrig., vol. 40, pp. 161–173, 2014, doi: 10.1016/j.ijrefrig.2013.10.014.

[9] D. Mikielewicz and J. Wajs, “Performance of the very high-temperature heat pump with low GWP working fluids,” Energy, vol. 182, pp. 460–470, 2019, doi: 10.1016/j.energy.2019.05.203.

[10] Q. Chen and R. C. Prasad, “Simulation of a vapour-compression refrigeration cycles using HFC134A and CFC12,” Int.

Paper ID: 9435
International Conference on Mechanical, Manufacturing and Process Engineering (ICMMPE – 2022)
Organizer: Faculty of Mechanical Engineering, Dhaka University of Engineering & Technology (DUET), Gazipur, Bangladesh
Website: https://icmmpeduet.com/

Effective Removal of Lead from Wastewater Using Functionalized Magnesium/Aluminium-Layered Double Hydroxide

Md. Tofazzal Hossain[1,2], Shahjalal Khandaker[1], M Mahbubul Bashar[3], Minhaz Ahmed[4] and Palash Kumar Saha[1,2]

[1]Department of Textile Engineering, Dhaka University of Engineering & Technology, Gazipur, 1707, Bangladesh.
[2]Department of Textile Engineering, Northern University Bangladesh.
[3]Department of Textile Engineering, Mawlana Bhashani Science and Technology University, Santosh, Tangail, 1902, Bangladesh.
[4]Department of Agroforestry and Environment, Bangabandhu Sheikh Mujibur Rahman Agricultural University, Gazipur 1706, Bangladesh.

E-mail: tofazzal.te@gmail.com

ABSTRACT

The adsorption method was used to remove Pb^{2+} from simulated wastewater using Magnesium/Aluminium-Layered Double Hydroxides (Mg/Al LDH-SHMP). To determine the functional characteristics of the adsorbent, the produced Mg/Al LDH-SHMP composite adsorbent was characterized using FESEM, XRD, and Point of zero charges (pHpzc). Pb^{2+} adsorption capacity was examined using Mg/Al LDH-SHMP from wastewater in batch adsorption experiments. Additionally, the influence of several factors such as solution pH, contact duration, adsorbent dosage, and initial solution concentration was examined, which reveals that the aforementioned parameters have a substantial impact on Pb^{2+} absorption. 100% for waste samples, the highest adsorption capacity of Mg/Al LDH-SHMP was determined to be 45.66 mg/g, and 100% Pb^{2+} can be removed quickly. Therefore, it may be concluded that the developed adsorbent is highly effective in removing lead ions (Pb^{2+}) from wastewater.

Keywords: Layered Double Hydroxide; Lead ions; Intercalation; Adsorption parameters.

1. INTRODUCTION

Water contamination is a significant environmental and health issue as a result of the release of poisonous and harmful heavy metal ions from numerous actions [1]. Waste stream discharges from mining, electroplating, and battery manufacturing industries often contain heavy metals, which can potentially enter the human body and pose a severe warning to human health and aquatic organisms [2]. Among the heavy metal ions, lead (Pb^{2+}) is the most common contaminant from numerous notable industrial applications [3]. Because of the multiple harmful effects on aquatic life, animals, plants, humans, and the environment, considerable prominence has been dedicated to the harmfull of these heavy metal ions. For example, lead is highly toxic and has severe effects such as kidney disease, nervous system damage, liver damage, renal dysfunction, inflammation of the lungs, chest pain, and decreased sense of smell after breathing [4]. Therefore, it is essential to eliminate heavy metal ions from wastewater before discharging from the industry. Researchers are searching for an easy, simple, and effective technique to eliminate heavy metal ions from wastewater.

Over the few decades, several treatments have been investigated to remove heavy metals from wastewater, such as ion exchange, chemical precipitation, flocculation, neutralization, membrane separation, and adsorption [5], [6]. The adsorption technology is highly appreciable among the physicochemical treatment options due to its simplicity, cost-effectiveness, efficiency, and minimum generation of secondary by-products [7]. Numerous adsorbents such as active carbon, clay material, silica, natural adsorbents, zeolites, rice husk biochar, etc., were well-studied to remove heavy metals [8]. However, the traditional adsorbents have poor selectivity, designability, and adsorption efficiency. Therefore, efficient and cost-effective adsorbents are highly in demand and a vital quest for researchers.

Layered double hydroxides (LDHs) are two-dimensional nanostructured substances with positive ions at outside layers and charge-balancing anions and water in the interlayer regions. The chemical composition of LDHs are normally $M^{2+}_{1-X}\ M^{3+}_{X}\ (OH)_2\ (A^{n-})_{X/n}\ X\ mH_2O$, where M^{2+} and M^{3+} are cation in the LDHs. A is an exchangable anion, n^- is the charge of the interlayer ion, and x and m are fractional constants. The layered double hydroxides have established increasing attention for heavy metals adsorption owing to their hydrophilic property, large surface area, and good thermal stability. Moreover, LDHs have been extensively studied owing to its lower cost, higher

efficiency, and preparation process is easy [9]. However, for lacking functional groups in immaculate LDHs, its adsorption capacity is limited. Functionalized LDHs have better absorption capacity due to their favorable structure and multiple reactive sites. The recent studies show that the efficiency of LDHs in the adsorption process can be enhanced by incorporating the different chelating agents such as ethylenediaminetetraacetic acid [10], diethylenetriaminepentaacetic acid [11], nitrilotriacetate [12], and sodium alginate [13].

Sodium hexametaphosphate (SHMP) is one of the competent chelating agents as it possesses favorable hydrophilicity and several ion-exchange groups. The chemical structure of SHMP is presented in Fig. 1.

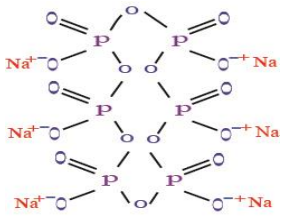

Fig. 1: Chemical structure of sodium hexametaphosphate (SHMP).

The intercalation of SHMP with LDH may significantly enhance the functional properties of LDHs and improve the removal capacity of heavy metals from aqueous solution. However, to the best of our knowledge, SHMP has not been used with LDH to remove lead till date. In this study, Mg/Al-LDH-SHMP composite adsorbent was prepared by the co-precipitation method. The physical and chemical characteristics of the composite adsorbents were investaged by XRD, FESEM. The effect of different adsorption parameters on lead removal is also examined.

2. MATERIALS AND METHODS

2.1 Materials and reagents

All reagents including aluminium chloride hexahydrate ($AlCl_3.6H_2O$), Sodium hexametaphosphate ($(NaPO_3)_6$), Magnesium chloride hexahydrate ($MgCl_2.6H_2O$), Hydrochloride acid (HCl), Sodium chloride (NaCl), and Sodium hydroxide (NaOH) were obtained from Merck (Germany).

2.2 Synthesize of the Mg/Al LDH-SHMP

Mg/Al LDHs-SHMP was developed by a co-precipitation method [14]. Briefly, $MgCl_2.6H_2O$ and $AlCl_3.6H_2O$ with a Mg^{2+}/Al^{3+} molar ratio of 2:1 dissolved in 250 mL distilled water, which was considered as solution A. Solution B contained 1.50 M of NaOH into 200 mL distilled water. Solution A was added dropwise by a burette to a beaker containing 3.21 g of SHMP in 250 mL distilled water at room temperature under N_2 atmosphere to avoid carbonate contamination and vigorously stirred. Simultaneously, solution B was added from another burette into the same solution to control the pH at 10.5-10.7. After completing the addition of solution A, the addition of solution B was stopped, and then the resulting white precipitate was aged for 30 min with starring under N_2 atmosphere. The obtained precipitate was washed until the pH to neutral and was filtrated using a vacuum filter. The adsorbent was dried at 80 ^{0}C in an air dryer overnight. Finally, the synthesized Mg/Al LDH-SHMP absorbent was crushed by hand mortar and sieved with 75µm size for further experimental use.

2.3 Characterization of composite adsorbent

The surface characteristics of the developed adsorbent was detected by using a Field-Emission Scanning Electron Microscopy (FESEM) (ZEISS Sigma 300, Germany). The physical properties of the composite was investigated by X-ray diffraction (XRD, Japan). The point of zero charge pH (pHpzc) of the adsorbents was measured using a method described in elsewhere [15] that indicates the surface charge.

2.4 Adsorption experiments

A stock solution of Pb^{2+} (1000 mg/L) was made through the dissolution of lead nitrate in DI water. Furthermore, by diluting the Pb^{2+} solution, the required experimental concentrations were prepared. All adsorption experiments were performed at 180 rpm (fixed) at room temperature in the batch method. Experiments were performed in 100 mL conical flasks by adding 0.1 g of adsorbent into 20 mL of the aqueous solution containing Pb^{2+} ions. After adsorption, the solution was filtered through a nylon membrane filter (0.45 µm) to separate the solids from the liquid. Before and after the test, the concentration of Pb^{2+} was measured by an Atomic Adsorption Spectrophotometer (AAS) (PinAAcle 900H, The USA). Average values were obtained from at least three tests.

The amount of Pb^{2+} ion absorbed by the absorbent was calculated by the following Eqn. (1).

$$q_e = (C_o - C_e)\frac{V}{m} \qquad \text{(i)}$$

Where, C_0 (mg/L) is amount of Pb^{2+} ion before adsorption and C_e (mg/L) is amount of Pb^{2+} ion after adsorption, V (mL) of Pb^{2+} ion in solution and m(g) is the mass of Mg/Al LDH-SHMP used in the experiments.

The effect of pH was measured by changing the pH ranges from 1.0 to 8.0 and the pH was adjusted using NaOH and HCl. The effect of the adsorbent dose was observed consuming different amounts of adsorbent (0.02 g

to 2.0 g) into a fixed (20 mL) Pb^{2+} solution. The effect of the contact time was investigated at predetermined time intervals from 0-180 min. The effect of initial concentration was performed with varying the initial concentrations (25-800 mg/L).

3. RESULTS AND DISCUSSION

3.1 Characterization of the composite

The Fig. 2 (a) and (b) shows the FESEM images of Mg/Al LDH, Mg/Al LDH-SHMP composite adsorbent, respectively. The immaculate Mg/Al LDH revealed agglomerated and compact structure with a small pore size [16]. Moreover, the prepared Mg/Al LDH-SHMP adsorbent showed amorphous regions with porous structures resulting in increased surface areas. Therefore, it is estimated that the porous structure of the developed composite adsorbent may enhance the physical adsorption of Pb^{2+} ions.

The XRD analysis was performed to understand the intercalation of SHMP into LDHs as shown in Fig. 2 (c). The characteristic peak of Mg/Al LDH at 2θ angle was observed in the range of 11.5°, 23.26° and 34.96° indicating the plane 003, 006 and 009, respectively. The high intensity and very sharp reflection of the crystal planes indicated the layered phase with interlayer molecular structure confirming the crystallinity of the LDH [17]. The board peak at 39.50 (015) and 47.12 (018) exposed the formation of a hexagonal LDH lattice [18]. On the contrary, the characteristic peak of Mg/Al LDH-SHMP for the planes 003 and 006 are shifted to a small angle and weaker compared to pure Mg/Al LDH. The displacing value of plane 003 was calculated 0.76 nm by using Bragg's Law suggesting the Cl^- anion type Mg/Al LDH [19]. Meanwhile, the basal spacing of Mg/Al LDH SHMP was 0.81nm for the interaction of SHMP into Mg/Al LDH. The enhanced interlayered space advocated hexametaphosphate's existence as interlayer anion inside the Mg/Al LDH-SHMP.

The pHpzc shows the potential outward charge of the functional group of the composite adsorbents which mainly directed by the solution pH. The Fig. 2(d) shows the effect of pH on the point of zero charge of Mg/Al LDH-SHMP.

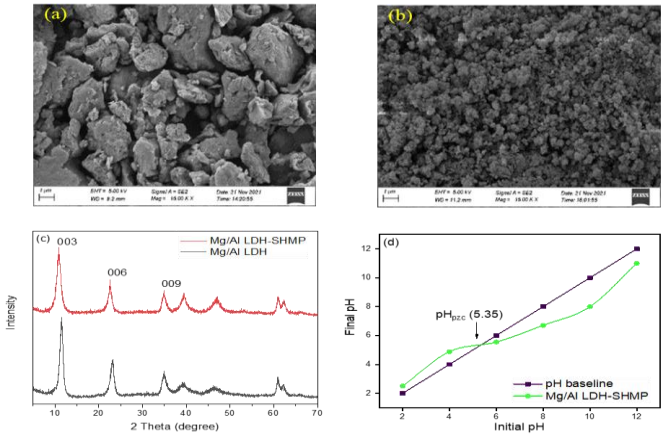

Fig. 2: (a) FESEM images of Mg/Al LDH; (b) Mg/Al LDH-SHMP; (c) XRD pattern of Mg/Al LDH and Mg/Al LDH-SHMP composite; (d) pHpzc of the Mg/Al LDH-SHMP composite.

3.2 Adsorption of Pb^{2+}

The influence of different experimental parameters on Pb^{2+} adsorption is described in below:

3.2.1 Effect of solution pH

pH is very crucial in the whole experimental procedure, which significantly affects the adsorbent's surface charge density and the types of the adsorbate [20]. The effect of pH on of Pb^{2+} with varying solution pH from 1.0 to 8.0 is shown in Fig. 3(a).

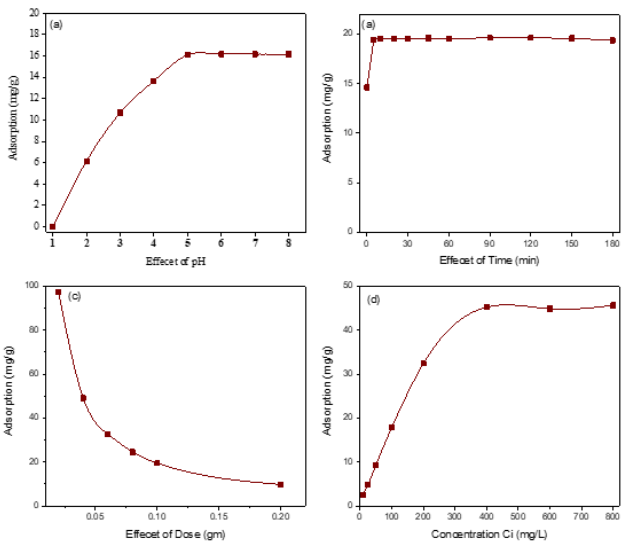

Fig. 3: (a) Effect of pH; (b) Effect of contact time; (c) Effect of adsorbent dosage; (d) Effect of initial concentration.

It was observed that the adsorption is increased due to the rise of the pH from 1.0 to 5.0 rapidly. The Pb^{2+} capture was stable at pH 5.0 and above.

As shown in Fig. 3 (d), the pHpzc of Mg/Al LDH-SHMP was found as 5.35, suggesting that the adsorbents are negatively charged at pH below 5.35 and positively at above 5.35. Due to the repulsive force between protons and metallic cations, a positively charged surface always prevents the attraction of metallic cations from absorbing solutions [21]. As showed that the adsorption of Pb^{2+} achevied rapidly with pH ranging from 1.0–3.0, indicating that the electrostatic interaction was occurred to uptake of Pb^{2+} ions by Mg/Al LDH-SHMP. Therefore, the following adsorption experiments were carried out at a pH 5.0.

3.2.2 Effect of contact time

The influence of contact time on heavy metal absorption by Mg/Al-LDH-SHMP is significant. The Fig. 3 (b) represents the effect of contact time on absorption. It can be observed; the initial 20 min was sufficient to reach the equilibrium adsorption by Mg/Al LDH-SHMP. The adsorption was fast in the initial stages might be the reason for porous properties, activation of surface functional groups, and vacant binding sites at the initial stages so that the interaction occurred quickly. The quick (20 min) equilibrium time will be benefited for large-scale treatment for Pb^{2+} removal from practical wastewater. Moreover, this shorter period benefits in the reduction of investment cost as well as operation cost in adsorption.

3.2.3 Effect of Mg/Al LDH-SHMP dose

Adsorbent's dose determines the interact regions between the adsorbate and the Pb^{2+} ion. The effect of adsorbent dose was observed using different adsorbent dosages on adsorption is shown in Fig. 3 (c). It can be seen that the adsorption capacity was decreased with the increase of the adsorbent dose. It can be explained that when the dose of adsorbent increase, the available active sites also increase. Therefore, the lack of accessible Pb^{2+} in the reaction bath to adsorbate by the adsorbent [22].

3.2.4 Effect of initial concentrations

The initial metal ion concentration has a significant effect on the absorption process as shown in Fig. 3(d). At a lower concentration of Pb^{2+} ion, the concentration ratio of the initial Pb^{2+} ions in the solution is less than the number of available adsorption site in the adsorbents. As the initial metal amout in the solution increases, the driving energy of the metal increases towards the function sites of the adsorbents [23]. Therefore, the absorption at the equilibrium level will increase with the increase of the initial metal concentration in the solution then it will be the saturation point due to the absorption sites occupied by the adsorbate. The investigational results exhibited that the optimum Pb^{2+} adsorption was obtained to be 45.66 mg/g.

3.2.5 Pb^{2+} removal efficiency

Based on the effect of initial concentration on Pb^{2+} adsorption, the Pb^{2+} removal efficiency is exposed in Fig. 3. It can be understood that 100% of Pb^{2+} can be removed up to 100 mg/L concentrated solution whereas above the concentration, the Pb^{2+} removal performance gradually decreased.

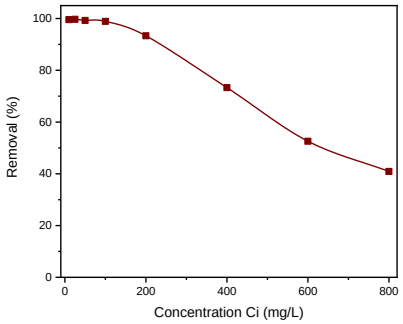

Fig. 4: Pb^{2+} removal efficiency

4. CONCLUSIONS

This study synthesized the Mg/Al LDH-SHMP composite by the co-precipitation method to remove Pb^{2+} ion from simulated wastewater. The different physical and chemical properties of the synthesized adsorbent were investigated using XRD, FESEM, and pHpzc, indicating the successful preparation of Mg/Al LDH interacted with sodium hexametaphosphate. The adsorption of Pb^{2+} ion depends on several factors such as solution pH, adsorption time, adsorption dosage, and initial metal concentration. The experimental results show that pH 5.5 was suitable for Pb^{2+} adsorption. The maximum adsorption occurred within 30 minutes. A suitable adsorbent dose for Pb^{2+} adsorption was obtained 1: 1000 (adsorbent: adsorbate), indicating that the synthesized adsorbent is highly effective. At lower concentration (up to 100 mg/L), 100% Pb^{2+} can be removed from wastewater. Therefore, the main findings of this study indicate that Mg/Al LDH-SHMP adsorbent can be successfully used for Pb^{2+} removal from wastewater. However, future studies regarding adsorption kinetic, isotherm, and thermodynamic are crucially essential to know the adsorption mechanism as well as for the large-scale application.

ACKNOWLEDGEMENT

The authors are thankful to the Bangabandhu Sheikh Mujibur Rahman Agricultural University, Gazipur and Jashore University of Science and Technology, Jashore, Bangladesh, for providing to use their laboratory during the experimental study.

REFERENCES

[1] M. A. Hashem, M. S. Nur-A-Tomal, N. R. Mondal, and M. A. Rahman, “Hair burning and liming in tanneries is a source of pollution by arsenic, lead, zinc, manganese and iron,” Environmental Chemistry Letters, Vol. 15, No. 3, pp. 501–506, 2017.

[2] H. Sun, B. Shi, F. Yang, and D. Wang, “Effects of sulfate on heavy metal release from iron corrosion scales in drinking water distribution system,” Water Research, Vol. 114, pp.

69–77, 2017.

[3] M. Cabral, A. Toure, G. Garçon, C. Diop, S. Bouhsina, D. Dewaele, F. Cazier, D. Courcot, A. Tall-Dia, P. Shirali, A. Diouf, M. Fall, and A. Verdin, "Effects of environmental cadmium and lead exposure on adults neighboring a discharge: Evidences of adverse health effects," Environmental Pollution, Vol. 206, pp. 247–255, 2015.

[4] W. Pan, C. Pan, Y. Bae, and D. Giammar, "Role of Manganese in Accelerating the Oxidation of Pb(II) Carbonate Solids to Pb(IV) Oxide at Drinking Water Conditions," Environmental Science and Technology, Vol. 53, No. 12, pp. 6699–6707, 2019.

[5] W. Zou, M. Filatov, D. Atwood, and D. Cremer, "Removal of mercury from the environment: A quantum-chemical study with the normalized elimination of the small component method," Inorganic Chemistry, Vol. 52, No. 5, pp. 2497–2504, 2013.

[6] L. Y. Blue, M. A. Van Aelstyn, M. Matlock, and D. A. Atwood, "Low-level mercury removal from groundwater using a synthetic chelating ligand," Water Research, Vol. 42, No. 8–9, pp. 2025–2028, 2008.

[7] R. Dai, Y. Zhang, Z. Q. Shi, F. Yang, and C. S. Zhao, "A facile approach towards amino-coated ferroferric oxide nanoparticles for environmental pollutant removal," Journal of Colloid and Interface Science, Vol. 513, pp. 647–657, 2018.

[8] D. Eeshwarasinghe, P. Loganathan, and S. Vigneswaran, "Simultaneous removal of polycyclic aromatic hydrocarbons and heavy metals from water using granular activated carbon," Chemosphere, Vol. 223, pp. 616–627, 2019.

[9] D. Zhao, G. Sheng, J. Hu, C. Chen, and X. Wang, "The adsorption of Pb(II) on Mg2Al layered double hydroxide," Chemical Engineering Journal, Vol. 171, No. 1, pp. 167–174, 2011.

[10] D. Huang, C. Liu, C. Zhang, R. Deng, R. Wang, W. Xue, H. Luo, G. Zeng, Q. Zhang, and X. Guo, "Cr(VI) removal from aqueous solution using biochar modified with Mg/Al-layered double hydroxide intercalated with ethylenediaminetetraacetic acid," Bioresource Technology, Vol. 276, pp. 127–132, 2019.

[11] X. Liang, W. Hou, Y. Xu, G. Sun, L. Wang, Y. Sun, and X. Qin, "Sorption of lead ion by layered double hydroxide intercalated with diethylenetriaminepentaacetic acid," Colloids and Surfaces A: Physicochemical and Engineering Aspects, Vol. 366, No. 1–3, pp. 50–57, 2010.

[12] Y. Zhang, L. Wang, G. Wu, A. Chang, and D. G. Evans, "Hydrothermal synthesis of Mg/Al layered double hydroxides intercalated with a [Zn(NTA)]− complex," Journal of Physics and Chemistry of Solids, Vol. 69, No. 5–6, pp. 1095–1097, 2008.

[13] X. Zhang, R. Shan, X. Li, L. Yan, Z. Ma, R. Jia, and S. Sun, "Effective removal of Cu(II), Pb(II) and Cd(II) by sodium alginate intercalated MgAl-layered double hydroxide: adsorption properties and mechanistic studies," Water Science and Technology, Vol. 83, No. 4, pp. 975–984, 2021.

[14] S. Khandaker, M. T. Hossain, P. K. Saha, U. Rayhan, A. Islam, T. R. Choudhury, and M. R. Awual, "Functionalized layered double hydroxides composite bio-adsorbent for efficient copper(II) ion encapsulation from wastewater," Journal of Environmental Management, Vol. 300, p. 113782, 2021.

[15] S. Khandaker, T. Kuba, S. Kamida, and Y. Uchikawa, "Adsorption of cesium from aqueous solution by raw and concentrated nitric acid-modified bamboo charcoal," Journal of Environmental Chemical Engineering, Vol. 5, No. 2, pp. 1456–1464, 2017.

[16] M. A. Teixeira, A. B. Mageste, A. Dias, L. S. Virtuoso, and K. P. F. Siqueira, "Layered double hydroxides for remediation of industrial wastewater containing manganese and fluoride," Journal of Cleaner Production, Vol. 171, pp. 275–284, 2018.

[17] X. Yang, T. Kameda, Y. Saito, S. Kumagai, and T. Yoshioka, "Investigation of the mechanism of Cu(II) removal using Mg-Al layered double hydroxide intercalated with carbonate: Equilibrium and pH studies and solid-state analyses," Inorganic Chemistry Communications, Vol. 132, p. 108839, 2021.

[18] D. G. Evans and R. C. T. Slade, "Structural Aspects of Layered Double Hydroxides," Structure and Bonding, Vol. 119, pp. 1–87, 2005.

[19] S. Ma, Q. Chen, H. Li, P. Wang, S. M. Islam, Q. Gu, X. Yang, and M. G. Kanatzidis, "Highly selective and efficient heavy metal capture with polysulfide intercalated layered double hydroxides," Journal of Materials Chemistry A, Vol. 2, No. 26, pp. 10280–10289, 2014.

[20] B. Jiang, Y. Lin, and J. C. Mbog, "Biochar derived from swine manure digestate and applied on the removals of heavy metals and antibiotics," Bioresource Technology, Vol. 270, pp. 603–611, 2018.

[21] H. Hao, Y. Wang, and B. Shi, "NaLa(CO3)2 hybridized with Fe3O4 for efficient phosphate removal: Synthesis and adsorption mechanistic study," Water Research, Vol. 155, pp. 1–11, 2019.

[22] A. Heidari, H. Younesi, and Z. Mehraban, "Removal of Ni(II), Cd(II), and Pb(II) from a ternary aqueous solution by amino functionalized mesoporous and nano mesoporous silica," Chemical Engineering Journal, Vol. 153, No. 1–3, pp. 70–79, 2009.

[23] A. A. Taha, M. A. Shreadah, A. M. Ahmed, and H. F. Heiba, "Multi-component adsorption of Pb(II), Cd(II), and Ni(II) onto Egyptian Na-activated bentonite; Equilibrium, kinetics, thermodynamics, and application for seawater desalination," Journal of Environmental Chemical Engineering, Vol. 4, No. 1, pp. 1166–1180, 2016.

Paper ID: 9447

International Conference on Mechanical, Manufacturing and Process Engineering (ICMMPE – 2022)

Organizer: Faculty of Mechanical Engineering, Dhaka University of Engineering & Technology (DUET), Gazipur, Bangladesh

Website: https://icmmpeduet.com/

MCDM framework of stock market using AHP, GRA, and ANP incorporated with TOPSIS followed by a SWOT analysis

K.M. Mohammad Ullah[1], Rakibul Islam[1], Maisha Mehrin[1] and Prof. Dr. M. T. Islam[2]

[1]Dept. of Mech. & Prod. Eng., Ahsanullah University of Science and Technology (AUST), Bangladesh.
[2]Dept. of Mech. Eng., Chittagong University of Engineering and Technology (CUET), Bangladesh.

kmmohammad060@gmail.com

ABSTRACT

Decision-making is a challenging issue in stock markets since the success or failure of the shareholder depends a lot on the appropriate decision-making. That's why in recent years, appropriate decision-making has become a key strategic consideration. However, these decisions usually involve multiple objectives or criteria which are characterized by complexity, elusiveness, and uncertainty in nature; and it is often necessary to trade-off among conflicting factors. Thus, the Multi-Criteria Decision Making (MCDM) framework has become a useful approach to solving this kind of problem. This research paper proposes a novel evaluation framework of three decision making approaches in three types of situations occurs in stock market: Whether the investor should invest or not? if investors want to buy a share, then which company's share they should buy and if an investor wants to sell a company share then which company's share, he/she should sell. This research study designs and implements a framework for MCDM through ANP incorporated with TOPSIS, GRA and AHP. Through a SWOT analysis of Dhaka Stock Market (DSE) considering strengths, weaknesses, opportunities and threats as criteria and sub criteria, the whole research study resembles the real selection situations, where all the data have been collected for A, B, C, and D company from local share market experts of DSE. Based on expert's different opinion for different situations, we found at that time it is not suitable for a new investor to invest in the share market of DSE because throughout the SWOT analysis on experts opinion the final value of ANP-TOPSIS framework found C_{No}^{*}= 0.55 has the higher priority value in terms of alternatives (Yes/No). Although if the investor wants to buy shares from A, B and C companies (Alternatives) on the basis of Earning per share, Brand value in market and Price-earnings ratio (P/E ratio) as criteria for the framework then 'A' company share will be best for him/her because by the grey relational grade found, γ_1 (0.8779) > γ_3 (0.8407) > γ_2 (0.8613) so, A > C > B, 'A' company having the highest value among the alternatives for GRA framework. And if the shareholders want to sell shares from A, B, C and D companies (Alternatives) based on four essential criteria like Dividend, Earnings per share, Brand value in the market, and Price-earnings ratio (P/E ratio) using AHP framework, 'A' company shares will be the best choice to sell out from those alternatives because, in terms of negative aspects it has the lowest score/priority value 0.042. The proposed evaluation framework is simple and reasonable, and it is effective to determine the optimal company share even with the interactive and interdependent criteria. This research study also illustrates a MCDM framework in the stock market and shares a guideline with all the shareholders who would like to make decisions in a more realistic, sophisticated, logical, and mathematical way.

Keywords: SWOT; Stock Market; Share; Investor; MCDM.

1. INTRODUCTION

The aim of this research study is to propose a combined MCDM framework to deal with the glamor stock selection problem, which has caused increased interest in both academic and practical fields [1]. The stock selection problem was stemmed from the efficient market hypothesis (EMH) [2]. From the assumption of EMH, investors cannot use available information to formulate a strategy that consistently outperforms the market [3]. To examine the EMH some previous studies tended to apply various investing styles to test the hypothesis. Value investing and growth stock (also termed glamor stock in financial literature) investing are two of the commonly examined strategies [4]. These two investing strategies use simple valuation criteria separately to form different investment portfolios, the value stock portfolio was found to outperform the diversified portfolio or market index in the long term [2]. Which has been gathered attention from both practical and academic fields. But the emerging recognition of growth stock investing strategy also caught investors' interest in practice from the definition of the previous study [5]. Although the discussion of growth stock investing in academic research has formed a foundation for investment practice [4] while making real investment decisions investors still have to make selections among the growth stock

portfolios because of limited capital constraints. Thus, this research study focuses on finding out the criteria for the MCDM frameworks and provides a guideline about the implementation of the frameworks.

Multi-Criteria Decision Making (MCDM) is a sub-discipline of operation research where decisions are made considering multiple criteria. MCDM tools have become the most utilized analytic approaches since the nature of selection has become rather complex and multi-faced. Basically, the multiple criteria decision issue focuses mainly on distinguishing the evaluation criteria and on the determination of the preference structure. Since the results of evaluating and comparing alternatives are based on decision makers' preferences, the determination of preference structures is very important during the decision-making process [6]. People have found that using traditional methods is not always proper because of the dependence and feedback among the criteria to somewhat different degrees in the real-world [7]. MCDM is one of the active fields where ANP, TOPSIS & GRA provide a useful basis for a variety of solution approaches [8]. It is a modelling and methodological tool for dealing with complex engineering problems.

Decision-making is a common scenario in the stock market business. There are like millions of investors who are directly and indirectly involved in the stock market. And ups and downs in company share price happen on a regular basis. And that's why perfect timing in decision-making makes a huge difference between profit and loss, people make a profit when they can buy/sell company shares at an appropriate time, and on the contrary, other people make losses. There is the usage of MCDM tools; those help people taking decisions considering various situations, criteria, and the number of decision-makers.

Over the past two decades, many MCDM frameworks have been developed to aid decision-makers such as Analytic Hierarchy Process (AHP), Analytic Network Process (ANP), TOPSIS, Fuzzy Set Theory (FST), Simple Multi-Attribute Rating Technique (SMART), Genetic Algorithm (GA), Goal Programming (GP), Data Envelopment Analysis (DEA), Grey Relational Analysis (GRA), Value Analysis (VA), Weighted Product Model (WPM), Distribution Service Technologies (DST), Particles Swarm Optimization (PSO), Decision Expert (DEX), etc. [9]. Out of many MCDM tools, we are focusing on the application AHP, ANP, TOPSIS, GRA, and SWOT analysis. TOPSIS is used when few alternatives are present, and attributes are high. GRA is a special decision-making tool where the opinions of multiple decision-makers can be considered along with multiple criteria and alternatives. SWOT analysis is a strategic tool to determine the strength, weaknesses, opportunities, and threats of a prospective decision.

AHP and ANP are the two most significant and popular MCDM methods aiding the decision-makers to select the best choice under situations characterized by having more than one criterion [10]. AHP, introduced by Saaty 1980 [11], is a useful approach to solving complex decision problems. ANP was proposed by Saaty 1990 [12] for extending the AHP to address restrictions of the hierarchical structure where criteria are independent of each other. Many decision problems cannot be built as hierarchical because of dependencies (inner/outer) and influences between and within clusters (criteria/alternatives). ANP is very useful to solve this kind of problem [13]. ANP provides a general framework to deal with decisions without making assumptions about the independence of higher-level elements from lower-level elements and about the independence of the elements within a level. In fact, ANP uses a network without the need to specify levels as in a hierarchy [12].

In a study [14], after the AHP method, the most used method of MCDM is TOPSIS with a 63.14% selection rate, which does not require pairwise comparison. Furthermore, it is shown that TOPSIS has good performance for large numbers of alternatives [15] compared to AHP which requires a huge amount of pairwise comparison. In this research, TOPSIS has been incorporated with ANP for better results.

In this research study, we make three types of decisions related to stock markets using ANP-TOPSIS, GRA and AHP followed by a SWOT analysis. First of all, a new investor needs to decide if investing in a stock market is appropriate or not. To decide on such a situation, we have shown an integrated procedure of ANP and TOPSIS followed by a SWOT analysis of the stock market. If investors decide to invest in the share market, then another question arises which company's share should they buy. Hence, we illustrate a procedure for choosing a company's share to buy. Since there are multiple decision-makers; we follow the GRA method for making the choice. Finally, we decide on the selling of an existing share following the AHP method.

The main objective of this research study is to illustrate a guideline with methodological examples for the investors so that they can easily understand the methods and input their own evaluation values for making decisions in different situations of stock market business.

2. METHOD OF ANALYSIS

SWOT analysis: It's a strategic planning technique used to help a person or organization identify strengths, weaknesses, opportunities, and threats which are mainly

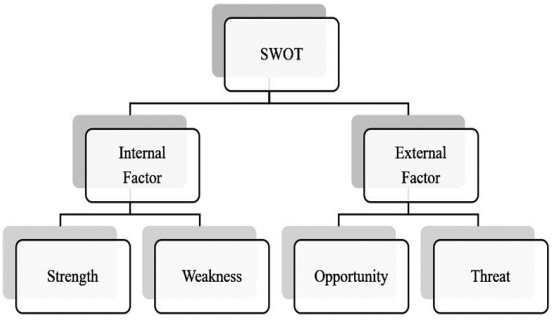

Fig. 1: The process flow chart of SWOT analysis.

related to business competition or project planning. It is very helpful to generate meaningful information for both internal factors (Strengths and Weaknesses) and external factors (Opportunities and Threats).

Main purpose of using SWOT analysis is to specify the objectives and identify the internal and external factors that are helpful and unhelpful to achieving those objectives. The sequential steps of a SWOT analysis are shown in Fig. 1.

Analytic Hierarchy Process (AHP): An effective complex decision-making tool was invented by great Iranian Professor Thomas L. Satty in 1980 [11]. which may help the decision-maker to set priorities and make the best decision and capture both subjective and objective aspects.it is a very useful technique for checking the consistency of the decision maker's evaluations.

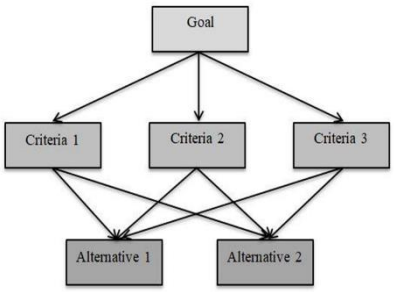

Fig. 2: The process flow chart of AHP method.

The AHP is a very flexible and powerful tool because the scores, and therefore the final ranking, is obtained based on the pairwise relative evaluations of both the criteria and the options provided by the user. The computations made by the AHP are always guided by the decision maker's experience, and the AHP can thus be considered a tool that is able to translate the evaluations (both qualitative and quantitative) made by the decision-maker into a multi-criterion ranking. In addition, the AHP is simple because there is no need of building a complex expert system with the decision maker's knowledge embedded in it.

The AHP can be implemented in three simple consecutive steps, a) Computing the vector of criteria weights, b) Computing the matrix of option scores and c) Ranking the options.

AHP is designed to structure a decision process in a scenario affected by multiple independent factors. Based on this methodology, a complex problem is divided into sub-problems organized according to hierarchical levels, with each level denoting a set of criteria. The top level of the hierarchy denotes the main goal, the bottom level contains the alternative when achieving the goal, and the intermediate levels denote the factors that influence the upper levels (Fig. 2). In this context, the AHP methodology makes it possible to compare different factors, where each factor's importance influences the final solution and the rank of the alternative that is to be used for reaching this solution

Analytic Network Process (ANP): Another multiple-criteria decision analysis methodology developed by Thomas L. Saaty in 1996 [16] based on evaluating, prioritizing, and selecting services. AHP framework describe uni-directional hierarchical affiliation, in ANP replaces the hierarchies with network where the affiliations of decision levels are not easy to describe as higher or lower, Dominated or being dominated, directly or indirectly [23]. ANP was developed because the structures of decision-making problems are not organised hierarchy because they have interdependency in criteria or factors. A network system is considered in that kind of interdependent functional structure along with clusters to solve complex decision-making problems. The structural outline of ANP is shown in Fig. 3. It used a variety of decision-making fields such as government, business, industry, healthcare, and education.

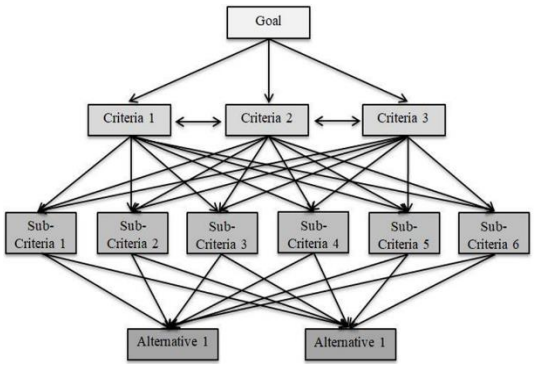

Fig. 3: The process flow chart of ANP method.

ANP can be determined by four major steps [22]; 1) Model construction and problem structuring, 2) Pairwise comparison metrices and priority vectors, 3) Super-matrix formation & 4) Selection of best alternatives.

The methodology of the AHP method and ANP are closely similar, but ANP is more of clustering than a weighing technique. When the decision-making problem may be simple or less complex type then it better to use AHP but if it is a very complex type then ANP is preferable because it may need well structure and less time-consuming technique with the help of using software (Super Decision).

Technique for Order of Preference by Similarity to Ideal Solution (TOPSIS): This is a multi-criteria decision-making approach created by Ching-Lai Hwang and Kwangsun Yoon in 1981 [17]. The process flow chart of TOPSIS is demonstrated in Fig. 4.

TOPSIS is a compensatory aggregation method based on the concept that the best alternative should have the shortest geometric distance to a positive ideal solution (PIS) and the geometric farthest distance from a negative ideal solution (NIS). This provides a more realistic form of modelling than non-compensatory methods, which include or exclude alternative solutions based on hard cut-offs. The main advantages of this method are the following [18] a) simple, rational, comprehensible concept, b) Intuitive and

clear logic that represents the rationale of human choice, c) Ease of computation and good computational efficiency, d) A scalar value that accounts for both the best and worst alternative's ability to measure the relative performance for each alternative in a simple mathematical form and e) Possibility for visualization.

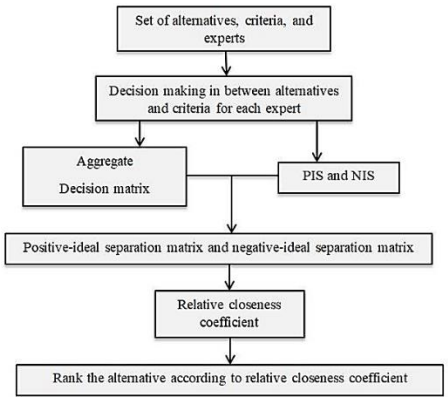

Fig. 4: Process flow chart of TOPSIS method.

Grey Relational Analysis (GRA): This technique is basically an important part of grey system theory which was developed by Professor Julong Deng, 1989 [19].

It's an impact evaluation methodology that uses the relationship to determine the degree of similarity or difference between two sequences. the basic principle of GRA is: if a similarity sequence converted from one of the alternatives which has the highest grey relational grade in between the known sequences and itself, then the alternative will be the best selection [21]. The operational steps of GRA framework are shown in Fig. 5.

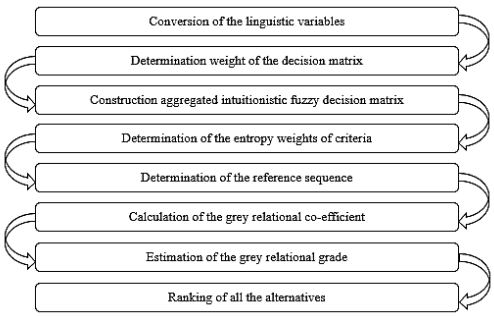

Fig 5: Process flow chart of GRA method.

GRA actually a methodology based on information. This means that systems have a lack of information in which a part of the information is known, and part of the information is unknown. This means somewhere in the middle, somewhere between the extremes, somewhere in the grey (incompletes) area uncertainty always may exist, GRA then gives the solution to the system with comes to a clear set of statements.

3. GOVERNING EQUATIONS AND FRAMEWORK MODELLING

Case-1: ANP-TOPSIS jointly used to find the decision for a new investor investing in share market or not with respect to SWOT analysis of DSE.

Analytic network Process (ANP) is a technique to solve MCDM problems in which the criteria have a nonlinear connection. It also allows the measurement of dependency among criteria. ANP is a generalization of the AHP that represents a framework with a unidirectional hierarchical AHP relationship, the ANP allows for complex interrelationships among decision levels and attributes.

Table 1: SWOT matrix of DSE

Strength (S)	**Weakness (W)**
- Ability to provide high return (S1) - Invest money in robust shares (S2) - DSE has a solid trading infrastructure (S3)	- Volatility (W1) - Political influence (W2) - Decision making inability of management committee (W3)
Opportunities (O)	**Threats (T)**
- Money lender & seeker can make money (O1) - To own & contribute to a company (O2) - Economic growth (O3)	- Change in economic condition (T1) - Change in government rules (T2) - The incompatibility between the supply and demand of shares (T3)

In this research study, ANP model constructed based on SOWT analysis of Dhaka Stock Exchange (Table 1) to make the decision of investing stock market incorporated with Technique for Order of Preference by Similarity to Ideal Solution (TOPSIS) method for an investor.

The ANP-TOPSIS framework is done through a few steps-

Step 1: Model construction and problem structuring: At first the problem is stated clearly and is decomposed into a rational system. It can be obtained through decision-makers brainstorming. To make the decision of investing on share market by ANP incorporated with TOPSIS with SOWT analysis network structure is shown in Fig. 6.

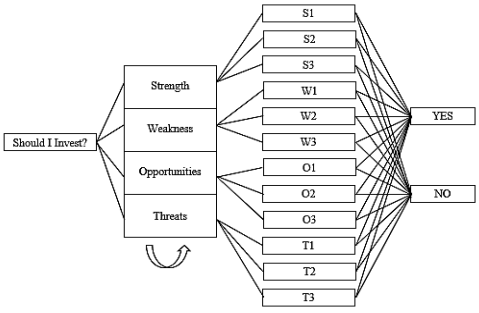

Fig. 6: ANP model of the problem with SWOT analysis.

Step 2: Pairwise comparison of criteria and determination of priority factors (W1) on basis of Table 1 assuming there is no dependence among those criteria. Priority factors can be drive by pairwise comparison of criteria (Table 3) by the relative importance of criteria estimations using Saaty's 1-9 scale [20] (Table 2).

Table 2: Scores for the importance of variables

Importance Scale	Definition of Importance Scale
1	Equally Important Preferred
3	Moderately Important Preferred
5	Strongly Important Preferred
7	Very Strongly Important Preferred
9	Extremely Important Preferred
2,4,6,8	Values for inverse comparison

Table 3: Pairwise comparison of criteria

	S	W	O	T	Weight factor, d_{ij}	Weight factor of importance, r_{ij} or W1
S	b_{11k}	b_{12k}	b_{13k}	b_{14k}		m
W	b_{21k}	b_{22k}	b_{23k}	b_{24k}		n
O	b_{31k}	b_{32k}	b_{33k}	b_{34k}		o
T	b_{41k}	b_{42k}	b_{43k}	b_{44k}		p

Weight factor, (d_{ij})

$$d_{ij} = \sqrt[k]{\prod_{k=1}^{k} b_{ijk}} \tag{1}$$

Weight factor of importance, (r_{ij} or W1)

$$r_{ij} = \frac{d_{ij}}{\sqrt{\sum_{i=1}^{n} d_{ij}^2}} \tag{2}$$

*** All the Priority vector calculations follow the same normalization method. ***

$$W1 = \begin{bmatrix} m \\ n \\ o \\ p \end{bmatrix} \tag{3}$$

Step 3: Pairwise comparison of criteria and determination of priority factors (W2) with respect to a single criterion.

$$W2 = \begin{bmatrix} 1 & b_1 & c_1 & d_1 \\ a_1 & 1 & c_2 & d_2 \\ a_2 & b_2 & 1 & d_3 \\ a_3 & b_3 & c_3 & 1 \end{bmatrix} \tag{4}$$

Step 4: Determination of the interdependent priority of criteria or overall priority of criteria ($W_{criteria}$ or W3)

$$W3 = W2 \times W1 = \begin{bmatrix} A1 \\ A2 \\ A3 \\ A4 \end{bmatrix} \tag{5}$$

Step 5: Pairwise comparison of sub-criteria with respect to the respective criterion, ($W_{sub\text{-}criteria}$ or W4)

a) Pairwise comparison of sub-criteria with respect to 'Strength', to get Weight factors of sub-criteria, (W_S)

$$(W_S) = \begin{bmatrix} s_1 \\ s_2 \\ s_3 \end{bmatrix} \tag{6}$$

b) Pairwise comparison of sub-criteria with respect to 'Weakness', to get Weight factors of sub-criteria, (W_W)

$$(W_W) = \begin{bmatrix} w_1 \\ w_2 \\ w_3 \end{bmatrix} \tag{7}$$

c) Pairwise comparison of sub-criteria with respect to 'Opportunities', to get Weight factors of sub-criteria, (W_O)

$$(W_O) = \begin{bmatrix} o_1 \\ o_2 \\ o_3 \end{bmatrix} \tag{8}$$

d) Pairwise comparison of sub-criteria with respect to 'Threats', to get Weight factors of sub-criteria, (W_T)

$$(W_T) = \begin{bmatrix} t_1 \\ t_2 \\ t_3 \end{bmatrix} \tag{9}$$

Step 6: Overall priorities of the sub criteria, (Wg)

$$W_g = W3 \times W4 = \begin{matrix} a \\ b \\ c \\ d \\ e \\ f \\ g \\ h \\ i \\ j \\ k \\ l \end{matrix} \tag{10}$$

Table 4: Overall presentation of weight factors

Criteria	Weight factors of criteria, (W_3)	Sub-criteria	Weight factors of sub-criteria, (W_4)	Overall priority factor of sub-criteria, (W_g)
Strength	A1	S1	s_1	a
		S2	s_2	b
		S3	s_3	c
Weakness	A2	W1	w_1	d
		W2	w_2	e
		W3	w_3	f
Opportunities	A3	O1	o_1	g
		O2	o_2	h
		O3	o_3	i
Threats	A4	T1	t_1	j
		T2	t_2	k
		T3	t_3	l

It has been seen from Table 4 the overall weight factor can be obtained from the multiplication of weight factors of criteria and weight factors of sub criteria. After that the pairwise comparison of alternatives, which is 'Yes' and 'NO' for this framework with respect sub criteria S1 by using Saaty's 1-9 scale (Table 2) shown in Table 5.

Step 7: Pairwise comparison of alternatives with respect to sub-criteria

Table 5: Pairwise comparison of Yes and No with respect to sub-criteria

	Yes	No	Local weight, s_{ij}	Weight factor, A_{ij}or S_a
Yes	s_{11k}	s_{12k}		S_{a1}
No	s_{21k}	s_{22k}		S_{a2}

Step 8: Determination of the decision matrix, R_{ij}

$$R_{ij} = \begin{bmatrix} s_{a1}\ s_{b1}\ s_{c1}\ w_{a1}\ w_{b1}\ w_{c1}\ o_{a1}\ o_{b1}\ o_{c1}\ t_{a1}\ t_{b1}\ t_{c1} \\ s_{a2}\ s_{b2}\ s_{c2}\ w_{a2}\ w_{b2}\ w_{c2}\ o_{a2}\ o_{b2}\ o_{c2}\ t_{a2}\ t_{b2}\ t_{c2} \end{bmatrix} \quad (11)$$

Step 9: Determination of the weighted decision matrix, V_{ij}

$$V = V_{ij} = W_{ij} \times R_{ij} \quad (12)$$

Where 'W_{ij}' is the weight factors of the criteria determined from ANP method. Here,

$$W_{ij} = W_g$$

Step 10: Identifying the positive and negative ideal solution.

V^+ = Best possible solutions of each column

V^- = Worst possible solutions of each column

Step 11: Computation of separation distance of each competitive alternative from the idea solution.

$$S^+ = \sqrt{\sum_{j=1}^{n}\left(V^+{}_j - V_{ij}\right)^2}\ ,\ i = 1 \dots\dots m \quad (13)$$

$$S^- = \sqrt{\sum_{i=1}^{m}\left(V^-{}_j - V_{ij}\right)^2}\ ,\ j = 1 \dots\dots n \quad (14)$$

Step 12: Measurement of relative closeness to the idea solution.

$$C_i{}^* = \frac{s_i{}^-}{s_i{}^+ + s_i{}^-} \quad (15)$$

Step 13: Ranking of the preference order.

According to the value of $C_i{}^*$the higher the value of the relative closeness, the higher the ranking order and hence the better the performance of the alternative.

Case-2: Grey Relational Analysis (GRA) is used to find which company's share the investors should buy from many companies.

Alternatives, M = {1, 2…….m}

Criteria, N = {1, 2……. n}

Decision makers, T = {1, 2…….t}

Table 6: Conversion between linguistic variables and IFNs [21]

Linguistic variables	IFNs
Extreme poor (EP)	0.05, 0.95, 0.00
Very poor (VP)	0.15, 0.80, 0.05
Poor (P)	0.25, 0.65, 0.10
Medium poor (MP)	0.35, 0.55, 0.10
Fair (F)	0.50, 0.40, 0.10
Medium good (MG)	0.65, 0.25, 0.10
Good (G)	0.75, 0.15, 0.10
Very good (VG)	0.85, 0.10, 0.05
Extreme good (EG)	0.95, 0.05, 0.00

Step 1: The rating of alternatives by decision makers needs to express linguistic variables with respect to criteria

Step 2: Construct the intuitionistic fuzzy decision matrices for each decision makers by conversion of the linguistic variables are given in Table 6.

$$R^{(k)} = \left(r_{ij}^{(k)}\right)_{m\times n} = \begin{bmatrix} r_{11}^{(k)} & r_{12}^{(k)} & r_{1n}^{(k)} \\ r_{21}^{(k)} & r_{22}^{(k)} & r_{2n}^{(k)} \\ r_{m1}^{(k)} & r_{m2}^{(k)} & r_{mn}^{(k)} \end{bmatrix}, k \in T \quad (16)$$

Where, $r_{ij}^{(k)} = \left(\mu_{ij}^{(k)}, v_{ij}^{(k)}, \pi_{ij}^{(k)}\right)$

Step 3: Determination of the weights of the decision maker (λ_k) by conversion of the linguistic variables are given in Table-7. Let, $T_k = (\mu_k, v_k, \pi_k)$ be a IFNs for ratting the *K*th decision maker.

Table 7: Linguistic variables for the importance of decision makers [21]

Linguistic variables	IFNs
Very importance	0.90, 0.05, 0.05
Importance	0.75, 0.20, 0.05
Medium	0.50, 0.40, 0.10
Unimportance	0.25, 0.60, 0.15
Very unimportance	0.10, 0.80, 0.10

$$\lambda_k = \frac{\left(\mu_k + \pi_k \frac{\mu_k}{\mu_k + v_k}\right)}{\sum_{k=1}^{t}\left(\mu_k + \pi_k \frac{\mu_k}{\mu_k + v_k}\right)} \quad (17)$$

Where, $\sum_{k=1}^{t} \lambda_k = 1$

Step 4: Construction of the aggregated intuitionistic fuzzy decision matrix based on the opinions of decision maker. Let $R^{(k)} = \left(r_{ij}^{(k)}\right)_{m\times n}$ be an intuitionistic fuzzy decision matrix of the *k*th decision maker.$\lambda = \{\lambda_1, \lambda_2, \dots, \lambda_t\}$ Be the weight of all decision makers and $\sum_{k=1}^{t} = 1, \lambda_k \in [0,1]$. [21]

$$r_{ij} = \left(1 - \prod_{k=1}^{t}(1-\mu_{ij}^{(k)})^{\gamma_k}, \prod_{k=1}^{t}((v_{ij}^{(k)})^{\gamma_k}\right), \prod_{k=1}^{t}(1 - \mu_{ij}^{(k)})^{\gamma_k} - \prod_{k=1}^{t}((v_{ij}^{(k)})^{\gamma_k})) \quad (18)$$

The intuitionistic fuzzy decision matrix can be defined as follows:

$$R^{(k)} = \begin{bmatrix} (r_{\mu 11}, r_{v11}, r_{\pi 11}) & (r_{\mu 12}, r_{v12}, r_{\pi 12}) & (r_{\mu 13}, r_{v13}, r_{\pi 13}) \\ (r_{\mu 21}, r_{v21}, r_{\pi 21}) & (r_{\mu 22}, r_{v22}, r_{\pi 22}) & (r_{\mu 23}, r_{v23}, r_{\pi 23}) \\ (r_{\mu 31}, r_{v31}, r_{\pi 31}) & (r_{\mu 32}, r_{v32}, r_{\pi 32}) & (r_{\mu 33}, r_{v33}, r_{\pi 33}) \end{bmatrix} \quad (19)$$

Where,

$$r_{ij} = (\mu_{ij}, v_{ij}, \pi_{ij}), \mu_{ij} = 1 - \prod_{k=1}^{t}(1-\mu_{ij}{}^{(k)})^{\gamma_k},$$

$$v_{ij} = \prod_{k=1}^{t}((v_{ij}^{(k)})^{\gamma_k}),$$

$$\pi_{ij} = \prod_{k=1}^{t}(1-\mu_{ij}{}^{(k)})^{\gamma_k} - \prod_{k=1}^{t}((v_{ij}^{(k)})^{\gamma_k}), i \in M \in N.$$

Step 5: Determination of the entropy weights of the criteria, ω_j

$$H_j = -\frac{1}{n\, ln\,(2)} \sum_{i=1}^{m} [\mu_{ij} \ln \mu_{ij} + v_{ij} ln\, v_{ij} - (1-\pi_{ij}) ln\,(1-\pi_{ij}) - \pi_{ij} \ln 2] \quad (20)$$

Here, if $\mu_{ij} = 0, v_{ij} = 0, \pi_{ij} = 1$, then,

$\mu_{ij} l\, n\, \mu_{ij} = 0, v_{ij} ln\, v_{ij} = 0,$

$(1-\pi_{ij})\, ln\,(1-\pi_{ij}) = 0$, finally, the entropy weight of jth criterion is

$$\omega_j = \frac{1-H_{ij}}{n-\sum_{j=1}^{n} H_j} \quad (21)$$

Step 6: Determination of the reference sequence, r_o

$$r_o = (r_{0j})_{1\times n} = \{\alpha^+ \alpha^+ \dots\dots\dots \alpha^+\} \quad (22)$$

Where, the maximum value $\alpha^+ = (1, 0, 0)$ can be used as the reference in the intuitionistic fuzzy decision matrix.

Step 7: Calculation of the grey relational co-efficient, ξ_{ij}

$$\xi_{ij} = \frac{\delta_{min} + \rho\delta_{max}}{\delta_{ij} + \rho\delta_{max}}, i \in M, j \in N \quad (23)$$

Where, ξ_{ij} is the grey relational co-efficient between r_{ij} and r_{0j}.

$$\delta_{min} = Min\{\delta_{ij}, i \in M; j \in N\}$$
$$\delta_{max} = Max\{\delta_{ij}, i \in M; j \in N\}$$

ρ is the distinguishing co-efficient, generally the value of ρ applied is equal to 0.05 [21]

Step 8: Estimation of the grey relational grade

$$\gamma_i = \sum_{j=1}^{n} \omega_j \xi_{ij}, i \in M \quad (24)$$

Step 9: Ranking of all the alternatives.

The alternative, having the highest value will be selected.

Case-3: Analytical Hierarchy Process (AHP) is used to find which company's share the investors should sell from many companies.

Step 1: Identify the problem

Which company share should investor sell out from these A, B, C, D companies?

Step 2: Develop a hierarchical framework (shown in Fig. 7)

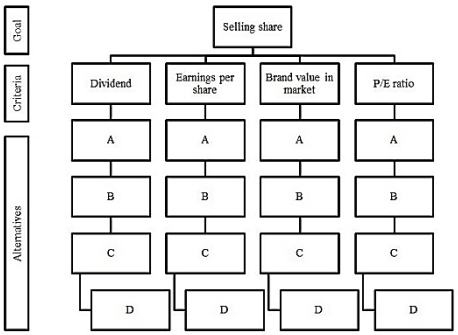

Fig. 7: A hierarchical framework for AHP method.

Step 3: Pairwise comparison of criteria

Priority factors can be drive by pairwise comparison of criteria (Table 8) by the relative importance of criteria estimations using Saaty's 1-9 scale [20] (Table 2).

Table 8: Pairwise comparison of criteria

	Dividend	Earnings per share	Brand value in market	P/E ratio	Priority, d_{ij}	Priority vector, r_{ij} or W1
Dividend	b_{11k}	b_{12k}	b_{13k}	b_{1nk}		m
Earnings per share	b_{21k}	b_{22k}	b_{23k}	⋮		n
Product value in market	b_{31k}	b_{32k}	b_{33k}	⋮		o
Net income	b_{n1k}	...	...	b_{mnk}		p

Weight factor, d_{ij} calculate by Eq. (1)

Weight factor of importance, r_{ij} or W1 calculate by Eq. (2) and Eq. (3)

Step 4: Pairwise comparison of Alternatives respect of criteria

a) Pairwise comparison of Alternatives with respect to Dividend (C_1).

$$W_{C_1} = \begin{bmatrix} m_a \\ n_a \\ o_a \\ p_a \end{bmatrix} \quad (25)$$

b) Pairwise comparison of alternatives with respect to Earnings per share (C_2).

$$W_{C_2} = \begin{bmatrix} m_b \\ n_b \\ o_b \\ p_b \end{bmatrix} \quad (26)$$

c) Pairwise comparison of alternatives with respect to Brand value in market (C_3).

$$W_{C_3} = \begin{bmatrix} m_c \\ n_c \\ o_c \\ p_c \end{bmatrix} \quad (27)$$

d) Pairwise comparison of alternatives with respect to P/E ratio (C_4).

$$W_{C_4} = \begin{bmatrix} m_d \\ n_d \\ o_d \\ p_d \end{bmatrix} \quad (28)$$

Step 5: Develop overall priority ranking

Table 9: Priority rating and final score

Criteria / Alternatives	Dividend	Earnings per share	Brand value in market	P/E ratio	score
	m	n	o	p	1
A	m_a	m_b	m_c	m_d	x_1
B	n_a	n_b	n_c	n_d	x_2
C	o_a	o_b	o_c	o_d	x_3
D	p_a	p_b	p_c	p_d	x_4

The overall weight factor can be obtained from the multiplication of weight factors of criteria and weight factors of alternatives. The pairwise comparison of alternatives, which is A, B, C and D for this framework with respect criteria C_1, C_2, C_3 and C_4 is shown in Table 9 to get final score.

Step 6: Selecting best Alternative by score.

4. FRAMEWORK MODEL IMPLEMENTATION

All the data used in the study have been collected from stock market experts. To make this study more realistic we have gone through capital research department of a broker house named LankaBangla Securities. We have consulted with a few high personnel as well. They helped us determining the criteria and required data for model evaluations.

Case-1: Goal is to find the solution for an investor to decide he/she should invest or not.

1. Pairwise comparison of SWOT criteria assuming there is no dependence among them

$$W_1 = \begin{bmatrix} 0.129 \\ 0.359 \\ 0.069 \\ 0.443 \end{bmatrix}$$

2. Priority factors (W2) with respect to a single criterion of SWOT

$$W_2 = \begin{bmatrix} 1.000 & 0.222 & 0.314 & 0.222 \\ 0.669 & 1.000 & 0.372 & 0.651 \\ 0.088 & 0.127 & 1.000 & 0.127 \\ 0.127 & 0.651 & 0.314 & 1.000 \end{bmatrix}$$

3. Overall priority ranking criteria

$$W_{criteria} = W_2 \times W_1 = \begin{bmatrix} 0.328 \\ 0.759 \\ 0.182 \\ 0.729 \end{bmatrix}$$

4. Weight factors of sub criteria

$$(W_S) = \begin{bmatrix} 0.221 \\ 0.460 \\ 0.319 \end{bmatrix} \qquad (W_W) = \begin{bmatrix} 0.186 \\ 0.658 \\ 0.156 \end{bmatrix}$$

$$(W_O) = \begin{bmatrix} 0.221 \\ 0.319 \\ 0.460 \end{bmatrix} \qquad (W_T) = \begin{bmatrix} 0.080 \\ 0.234 \\ 0.685 \end{bmatrix}$$

5. Overall priorities of the sub criteria

$$W_g = (W_{criteria} \times W_{sub-criteria}) = \begin{bmatrix} 0.072 \\ 0.151 \\ 0.105 \\ 0.141 \\ 0.499 \\ 0.118 \\ 0.040 \\ 0.058 \\ 0.084 \\ 0.058 \\ 0.171 \\ 0.499 \end{bmatrix}$$

6. Decision matrix by pairwise comparison of alternatives with respect to others sub-criteria

$$R = \begin{bmatrix} 0.833 & 0.125 & 0.750 & 0.875 & 0.100 & 0.250 \\ 0.167 & 0.875 & 0.250 & 0.125 & 0.900 & 0.750 \\ 0.875 & 0.100 & 0.875 & 0.250 & 0.167 & 0.833 \\ 0.125 & 0.900 & 0.125 & 0.750 & 0.833 & 0.167 \end{bmatrix}$$

7. Weighted decision matrix

$$V = \begin{bmatrix} 0.059 & 0.018 & 0.079 & 0.123 & 0.049 & 0.029 \\ 0.012 & 0.132 & 0.026 & 0.018 & 0.449 & 0.089 \\ 0.035 & 0.006 & 0.074 & 0.015 & 0.029 & 0.416 \\ 0.005 & 0.052 & 0.011 & 0.044 & 0.142 & 0.083 \end{bmatrix}$$

8. Ideal solutions

Positive ideal solution

$V^+ = 0.059,0.132,0.079,0.123,0.449,0.089,$
$0.035,0.052,0.074,0.044,0.142,0.416$

Negative ideal solution

$V^- = 0.012,0.018,0.026,0.018,0.049,0.029,$
$0.005,0.006,0.011,0.015,0.029,0.083$

9. Separation distance computation

$$S^+_{Yes} = 0.44 \qquad S^-_{Yes} = 0.36$$

$$S^+_{No} = 0.36 \qquad S^-_{No} = 0.44$$

10. Ranking the decisions

$$C^*_{Yes} = 0.45$$
$$C^*_{No} = 0.55$$

Since 'No" has the higher priority value, that's why the investor chooses 'No' as the decision.

Case-2: Goal is to achieve highest score to grey relational grade to buy a company share.

Alternatives, M = A, B & C

Criteria, N = C1, C2 & C3

Decision makers, T = T1, T2 & T3

1. Conversion of the opinion of decision maker between linguistic variables and IFNs [21]

Table 10: Linguistic assessment of alternatives by decision makers.

Decision makers	Alternatives	Criteria		
		Earnings per share (C_1)	Brand value in market (C_2)	P/E ratio (C_3)
T_1	A	MP	VG	G
	B	VG	G	MG
	C	G	MG	VG
T_2	A	EP	MP	VG
	B	F	P	EG
	C	VG	EG	P
T_3	A	G	MP	VG
	B	VP	VG	P
	C	VG	MG	EG

Table 10 elaborate the conversion of linguistic variables on decision makers opinion about criteria with respect to alternative using Table 6.

2. Conversion of the linguistic variables.

$$R^1 = \begin{bmatrix} 0.35,0.55,0.10 & 0.85,0.10,0.05 & 0.75,0.15,0.10 \\ 0.85,0.10,0.05 & 0.75,0.15,0.10 & 0.65,0.25,0.10 \\ 0.65,0.25,0.10 & 0.65,0.25,0.10 & 0.65,0.25,0.10 \end{bmatrix}$$

$$R^2 = \begin{bmatrix} 0.05,0.95,0.00 & 0.65,0.25,0.10 & 0.65,0.25,0.10 \\ 0.50,0.40,0.10 & 0.25,0.65,0.10 & 0.95,0.05,0.00 \\ 0.65,0.25,0.10 & 0.65,0.25,0.10 & 0.65,0.25,0.10 \end{bmatrix}$$

$$R^3 = \begin{bmatrix} 0.65,0.25,0.10 & 0.65,0.25,0.10 & 0.65,0.25,0.10 \\ 0.65,0.25,0.10 & 0.15,0.80,0.05 & 0.65,0.25,0.10 \\ 0.65,0.25,0.10 & 0.65,0.25,0.10 & 0.65,0.25,0.10 \end{bmatrix}$$

3. Determine the weights of the decision makers.

The importance of decision makers; T1 is important; T2 is very important & T3 is medium.

These linguistic variables used can be converted into IFNs by utilizing Table 7 to obtain the weights $\lambda_{K=1,2,3}$ of the decision makers; Eq. (17) is used:

$\lambda_1 = 0.3488; \lambda_2 = 0.4186; \lambda_3 = 0.2326$

4. The aggregated intuitionistic fuzzy decision matrix based on the opinions of decision makers by utilizing Eq. (18) and (19)

$r_{\mu 11} = 0.34; r_{v11} = 0.57; r_{\pi 11} = 1 - r_{\mu 11} - r_{v11} = 0.09$

$$R = \begin{bmatrix} (0.34,0.57,0.09) & (0.73,0.18,0.09) & (0.68,0.20,0.12) \\ (0.62,0.28,0.10) & (0.57,0.31,0.12) & (0.84,0.12,0.40) \\ (0.65,0.25,0.10) & (0.65,0.25,0.10) & (0.65,0.25,0.10) \end{bmatrix}$$

5. The entropy weights of the criteria found from Eq. (20) and (21).

$H_1 = 0.91$ $\omega_1 = 0.17$

$H_2 = 0.85$ $\omega_2 = 0.29$

$H_3 = 0.73$ $\omega_3 = 0.53$

6. The reference sequence

$$R_o = \{(1,0,0),(1,0,0),(1,0,0)\}$$

7. Calculation of the grey relational coefficient by utilizing Eq. (23)

Table 11: Decision matrices

	C_1	C_2	C_3	Min δ_{ij}	Max δ_{ij}
δ_{1j}	0.62	0.27	0.32	0.27	0.62
δ_{2j}	0.38	0.43	0.34	0.34	0.43
δ_{3j}	0.35	0.35	0.35	0.35	0.35
δ_{min}				0.27	
δ_{max}					0.62

The distance δ_{ij} between r_{ij} and r_{0j}, here; i= 1, 2, 3 and j= 1, 2, 3 compering them the highest value of δ_{max} and lowest value of δ_{max} are shown in Table 11 to obtain grey relational co-efficient matrix

$$\xi = \begin{bmatrix} 0.59 & 1.00 & 0.92 \\ 0.84 & 0.78 & 0.89 \\ 0.87 & 0.87 & 0.87 \end{bmatrix}$$

8. Estimation of the grey relational grade by utilizing Eq. (24)

$$\gamma_1 = 0.8779,\ \gamma_2 = 0.8407, \gamma_3 = 0.8613$$

Here, $\gamma_1 > \gamma_3 > \gamma_2$ So, $A > C > B$

A is selected.

Case-3: Goal is to achieve lowest score on pairwise evaluation of criteria with the alternative provided by the decision maker to select a company for selling share.

Here,

Alternatives are A, B, C & D companies

Criteria are Dividend (C1), Earnings per share (C2), Brand value in market (C3) & P/E ratio (C4)

1. Pairwise comparison of criteria in terms of importance scale (Table 2) by the decision maker shown in Table 12.

Table 12: Pairwise comparison of criteria

Criteria	C_1	C_2	C_3	C_4
C_1	1	3	5	7
C_2	1/3	1	7	1/9
C_3	1/5	1/7	1	5
C_4	1/7	9	1/5	1

$$W1 = \begin{bmatrix} 0.611 \\ 0.135 \\ 0.118 \\ 0.136 \end{bmatrix}$$

2. Pairwise comparison of alternatives respect of criteria using Saaty's 1-9 scale [20] (Table 2) is shown in Table 13.

Table 13: Pairwise comparison of alternatives respect of criteria

C_1	A	B	C	D
A	1	1/9	1/3	1/7
B	9	1	7	5
C	3	1/7	1	1/3
D	7	1/5	3	1

C_2	A	B	C	D
A	1	1/7	1/7	1/3
B	7	1	3	5
C	7	1/3	1	3
D	3	1/5	1/3	1

C_3	A	B	C	D
A	1	1/5	1/3	1/9
B	5	1	1/3	1/9
C	3	3	1	1/9
D	9	9	9	1

C_4	A	B	C	D
A	1	1/9	1/3	1/5
B	9	1	9	7
C	3	1/9	1	1/3
D	5	1/7	3	1

$$W_{C_1} = \begin{bmatrix} 0.041 \\ 0.645 \\ 0.095 \\ 0.219 \end{bmatrix}, W_{C_2} = \begin{bmatrix} 0.049 \\ 0.553 \\ 0.281 \\ 0.117 \end{bmatrix}$$

$$W_{C_3} = \begin{bmatrix} 0.042 \\ 0.092 \\ 0.139 \\ 0.727 \end{bmatrix}, W_{C_4} = \begin{bmatrix} 0.042 \\ 0.701 \\ 0.083 \\ 0.172 \end{bmatrix}$$

3. Overall priority ranking

Table 14: Priority rating and result

	C_1	C_2	C_3	C_4	Score
	0.611	**0.135**	**0.118**	**0.136**	**1.000**
A	0.041	0.049	0.042	0.042	**0.042**
B	0.645	0.553	0.092	0.701	**0.575**
C	0.095	0.281	0.139	0.083	**0.124**
D	0.219	0.117	0.727	0.174	**0.259**

The overall weight factor can be obtained from the multiplication of weight factors of criteria and weight factors of alternatives. The pairwise comparison of alternatives, which is A, B, C and D for this framework with respect criteria C1, C2, C3 and C4 is shown in Table 14 to get final score.

Since, 'A' has got the lowest score. So, the investors will sell 'A' company share.

5. RESULT AND DISCUSSION

This research illustrates a decision-making framework and guides the decision makers on how to use MCDM tools in different situations of stock businesses and to select criteria while using the tool. In this study, investors make decisions in three different situations.

Three decisions have been made using four MCDM methods. The decision-making problems are- investing in the Dhaka stock market, selling any company's share, and buying a company's share; used MCDM methods are ANP incorporated with TOPSIS, AHP, and GRA. Firstly, SWOT analysis of the Dhaka Stock Exchange (DSE) is done. Considering strengths, weaknesses, opportunities, and threats of DSE (as criteria and sub-criteria), this paper applies ANP and TOPSIS jointly to decide on investing in the stock market for a new investor (Case-1). After deciding to join the stock market, investors need to decide on, out of thousands of companies which company's share to buy (Case-2). This paper solves such a decision-problem using GRA that effectively considers opinions of multiple decision-makers. Finally, a decision has been made on selling a share out of several alternatives applying AHP (Case-3). All the data used in this study have been collected from stock market experts. The obtained results of this study depicted that- 1) A new investor should not invest in local share market because raking of decisions in term of alternatives final value is $C_{Yes}^* = 0.45$ and $C_{No}^* = 0.55$, "No" has found higher priority value (Case-1), 2) Existing investors should buy the share of 'A' company based on GRA ranking $\gamma_1 = 0.8779$, $\gamma_2 = 0.8407$, $\gamma_3 = 0.8613$, in that case, $\gamma_1 > \gamma_3 > \gamma_2$ so, A > C > B, having the highest value "A" is selected out of three companies considered in (Case-2), 3) investor should sell "A" company share because of the final score of company ''A" is the lowest (A-0.042, B-0.575, C-0.124 & D-0.259) out of four companies in (Case-3).

Experienced professionals can use the proposed models to evaluate a stock market and a company's share. With the implementation of these models, an individual can easily take decision about the investment and analytically select a company's share to buy or sell. In other words, considering these models, people can reduce the risk of losses and can expect a tentative profit. Thus, people will be more interested in stock market businesses. Furthermore, broker houses can use the proposed approaches to make better deals. The proposed techniques are robust and can be customized according to the user's need. Obtained decisions through these techniques will be more reliable if users consider long-term data and intuitions based on long-term experience.

6. CONCLUSION

In this research study from the above result & discussion decision-making with the experts opinion of DSE using MCDM framework three decisions have been made-

1. It was not suitable for a new investor to invest in the DSE share market since the final value of the ANP-TOPSIS

methodology through SWOT analysis of DSE determined NO has the higher priority value in terms of alternatives (Yes/No) based on expert's different opinions for various situations at that time.

2. If an investor or shareholder wants to buy shares from different companies like, A, B, and C companies based on Earnings per share, Brand value in the market, and Price-earnings ratio (P/E ratio), 'A' company shares will be the best choice for buying shares because, according to the GRA ranking, $\gamma_1 > \gamma_3 > \gamma_2$ so, A > C > B, with 'A' company having the highest value. It is possible for him/her to get an optimal and mathematical decision by using GRA.

3. If the shareholders want to sell shares from different companies like, A, B, C and D companies based on important criteria using AHP, 'A' company shares will be the best choice because, it has the lowest score/priority value 0.042 in terms of negative aspects for selling shares in stock market.

7. LIMITATIONS

It is to be mentioned, the prescribed model of using ANP incorporated with TOPSIS is very lengthy; hence, the implementation of the model might be time consuming. Nevertheless, if mutual interdependencies of sub-criteria are ignored, then using AHP instead of ANP could fasten the decision-making process.

8. RECOMMENDATIONS

For further study, the models can be shortening down for making these users friendly. Reduction of questions, criteria can be a way to make the models shorter. In addition, the presented methodology can be applied in other business fields (supplier, vendor and manufacturer selection as well as daily life decision making situations). Other MCDM methods such as ELECTRE, PROMETHEE, SMART, GA, GP, DEA etc. can be used for decision making and the new results can be compared with the results of this study. Moreover, some other criteria (paid up capital, authorized capital, net operating cash flow per share, dividend yield etc.) except the ones used in this study can be considered for the decision-making problem.

REFERENCES

[1] Mohanram, P. S. (2005). Separating Winners from Losers among Low Book-to-Market Stocks using Financial Statement Analysis, (2000), 133–170.

[2] Fama, E. F., & French, K. R. (2006). Profitability , investment and average returns $, 82, 491–518. https://doi.org/ 10.1016/j.jfineco. 2005.09.009.

[3] R. Bird, X.Z. He, S. Thosar, P. Woolley, The case for market inefficiency: investment style and market pricing, Journal of Asset Management 5 (6) (2005) 365–388.

[4] K.C. Chan, J. Lakonishok, Value and growth investing: review and update, Financial Analyst Journal 60 (1) (2004) 71–86.

[5] J. Lakonishok, A. Shleifer, R.W. Vishny, Contrarian investment, extrapolation, and risk, Journal of Finance 49 (5) (1994) 1541–1578.

[6] Yang, J. L., & Tzeng, G. H. (2011). An integrated MCDM technique combined with DEMATEL for a novel cluster weighted with ANP method. Expert Systems with Applications, 38(3), 1417–1424.

[7] Leung, L. C., Hui, Y. V, & Zheng, M. (2003). Analysis of compatibility between interdependent matrices in ANP, 758

[8] Stewart, T. J. (1996). Robustness of Additive value Function Methods in MCDM, 5(June 1995), 301–309.

[9] Ho, W. (2010). Review on Supplier Selection.

[10] Hashemi, S. H., Karimi, A., & Tavana, M. (2015). An integrated green supplier selection approach with analytic network process and improved Grey relational analysis. International Journal of Production Economics, 159, 178–191.

[11] Saaty, T. (1980). The analytic hierarchy processes. New York: Mc Grae-Hill.

[12] Saaty, T. L. (1990). How to make a decision : The Analytic Hierarchy Process, 48.

[13] Gencer, C., & Gürpinar, D. (2007). Analytic network process in supplier selection: A case study in an electronic firm. Applied Mathematical Modelling (Vol. 31).

[14] Chai, J., Liu, J. N. K., & Ngai, E. W. T. (2013). Application of decision-making techniques in supplier selection: A systematic review of literature. Expert Systems with Applications, 40(10), 3872–3885.

[15] Rodrigues, F., Junior, L., Osiro, L., Cesar, L., & Carpinetti, R. (2014). A comparison between Fuzzy AHP and Fuzzy TOPSIS methods to supplier selection. Applied Soft Computing Journal, 1–16.

[16] Saaty, T. L. (1996). Decision making with dependence and feedback: The analytic network process. Pittsburgh: RWS Publications Publishers.

[17] C. L. Hwang and K. Yoon, Multiple Attributes Decision Making Methods and Applications, Springer, Berlin Heidelberg, 1981.

[18] Chen, C. T., Hung, W. Z., Lin, K. H., & Cheng, H. L. (2009). An evaluation model of service quality by applying linguistic TOPSIS method. 2009 IEEE/INFORMS International Conference on Service Operations, Logistics and Informatics, SOLI 2009, (1), 335–340.

[19] Deng, J. L. (1989). Introduction to grey system theory. The Journal of Grey System, 1(1), 1–24.

[20] Saaty, T. L. (2008). Decision making with the analytic hierarchy process. International Journal of Services Sciences (Vol. 1).

[21] Zhang, S. F., & Liu, S. Y. (2011). A GRA-based intuitionistic fuzzy multi-criteria group decision making method for personnel selection. Expert Systems with Applications, 38(9), 11401–11405.

[22] Yüksel, I., & Dağdeviren, M. (2007). Using the analytic network process (ANP) in a SWOT analysis - A case study for a textile firm. Information Sciences, 177(16), 3364–3382.

[23] Meade, L. M.; Sarkis, J. (1999). Analyzing organizational project alternatives for agile manufacturing processes: An analytical network approach. International Journal of Production Research, 37(2), 241–261.

Paper ID: 9771

International Conference on Mechanical, Manufacturing and Process Engineering (ICMMPE – 2022)

Organizer: Faculty of Mechanical Engineering, Dhaka University of Engineering & Technology (DUET), Gazipur, Bangladesh

Website: https://icmmpeduet.com/

The Use of Portable Electricity Generators in Edo State Nigeria

Mustapha Adeboye Zubair[1]*, Nicholas Akhaze Musa[1], Olawale James Okegbile[1] and Massin Muhammadu[1]

[1]Department of Mechanical Engineering, Federal University of Technology, Minna, Niger State, Nigeria.

*E-mail: mustaphazubair5@gmail.com

ABSTRACT

The use of backup power supplies such as generators fueled by petrol or diesel, as well as solar powered generators, has resulted from the constant power failure or epileptic power supply from the electrical distribution company. The goal of this study was to determine the amount of usage of the aforementioned backup power supplies in Edo State, Nigeria. The state has eighteen local government units that are divided into three senatorial districts: Edo North, Edo Central, and Edo South. For the investigation, a two-stage sampling approach was used. Each of the state's three senatorial districts had one Local Government Area (LGA) picked at random. Their headquarters were chosen at random from the studied LGAs, with Benin city coming from Oredo, Ekpoma from Esan-west, and Auchi from Etsako-west. Out of target populations of 1200, 800, and 1000 households, 1000 households were randomly picked from Benin city, 750 households from Ekpoma, and 840 households from Auchi. In the study area, 2590 questionnaires were distributed as part of the instrument. Only 2579 copies of the questionnaire were completed and utilized for descriptive statistical analysis (%) of the respondents' use of portable generators or other power sources. According to the findings of the study, everyone uses a generator, with 70.7 percent using it solely for domestic purposes, 25% using it for both domestic and business purposes, and 4.3 percent using it solely for business purposes, with 91.8 percent serviceable and 8.2 percent non-serviceable generators. The majority of people (80.2%) use petrol generators with rated power between 2500 and 3000W.

Keywords: Generator; Gasoline; Questionnaires; People; Power; Edo state.

1. INTRODUCTION

In order to keep pace with the rise in social economic activities and demand for uninterrupted power supply, in developing economies, many people have resulted in the use of fossil fuel (gasoline and diesel) generators. Electric generators, as in [1], are in high demand in Nigeria today. Generator sales are gradually increasing in Nigeria since they are considered essential commodities. This increase in demand for power generators is a result of continuous power outages in some places and lack of power in other areas of Nigeria, as well as population growth. Nigeria's power generation capacity is now around 4,000MW, significantly less than the expected national demand of over 40 000MW. Fossil fuel fired generators are mostly used as backup power sources in most nations when the national grid is underutilized or unavailable, or to provide power in remote locations that are not linked to the national grid [2]. A gasoline generator is a type of engine-generator that combines an electrical generator and an engine into a single self-contained unit. The majority of the engines used are piston engines. However, a gas turbine can be utilized for small-scale power or electricity production, fueled with gasoline or petrol. Engine generators have the advantage of being able to supply electricity on their own, making them ideal for backup power [3].

However, determining the viability of using a generator fueled with gasoline as well as one fueled with diesel based on fuel consumption, energy or power quality, and efficiency is critical, so as in [4], comparison of generators fueled with gasoline, liquefied petroleum gas, and biogas were individually carried out . This was done in order to determine the quality of power used in electricity generation. According to the researchers observations, there was no discernible variation in power quality between the aforementioned fuels. Investigation of the variation in energy and exergetic efficiency for gasoline, diesel, and natural gas generators was carried out as in [5]. According to the researchers findings, energy/exergetic efficiencies ranged from 0.19 percent to 16.20 percent, with average energy/exergetic efficiencies of 9.59 percent, 4.43 percent, and 0.27 percent for diesel, gasoline, and natural gas generators, respectively. As in [6], investigation of the effects of ethanol, butanol, and methanol mixes with gasoline in various quantities on engine performance was carried out. The engine's performance was assessed using the power generated by the electrical generator. It was stated that when the engine was operated with a 1:10 ethanol gasoline blend, the engine performance rose by 6%, and when ran with regular gasoline, the engine performance increased by 6%.

Performance of a single cylinder four-stroke spark-ignition engine with a compression ratio of 10:1 on the one hand and 11:1 on the other, using unleaded fuel and a blend of unleaded gasoline and ethanol, respectively was studied as in [7]. The emissions from the engine's exhaust were also investigated. The usage of a blend of unleaded gasoline and ethanol resulted in an improvement in torque, power, and fuel consumption of the engine, as well as a reduction in CO, NOx, and HC emissions. According to the author, using a mixture of ethanol and gasoline increases compression ratio and eliminates knocking. In the researchers' work, as in [8], used methanol with a high compression ratio (CR) to improve the performance and lower emissions of a single-cylinder engine. The engine with a CR of 6/1 was first tested using gasoline and methanol at full load and at various speeds. The CR was gradually increased from 6/1 to 8/1 to 10/1 after that. The researchers reported that knock was not noticed at the CRs of 8/1 and 10/1 when using methanol, but it was noticed at the CR of 8/1 when using gasoline. The researchers used cylinder pressure time curves to determine the knock. The researchers also stated that when they used methanol with a CR of 6/1, the results demonstrated some reductions in CO, CO2, and NOx emissions without any notable power loss.

Due to the extremely low supply from the national grid in Nigeria, generators have become the principal source of energy for most businesses and households. These generators are either gasoline or diesel or solar powered type with different power ratings. The generator is chosen depending on the fuel or source of energy for operation, the designed power requirements of the lighting, appliances, and other equipment. In developing nations such as Nigeria, however, most people buy generators without considering the designed power requirements of whatever function they are used for but with some consideration for the sort of fuel or energy used for operation. In the literature, the motivations for this action are unknown. The goal of this study is to identify the most popular or demanded generator type based on the fuel or source of energy utilized for operation, its power rating and the reasons for this. This is done with a view to providing would be marketers information about the most sought and engineers who would like to improve on the performance of the generators that is widely used by all and sundry.

2. METHODOLOGY

2.1 Research Area

The research area is Nigeria's Edo State, which is divided into eighteen local government areas. Edo state is located between 40 45' and 70 40' north latitude and 50 00' and 60 45' east longitude of the Greenwich Meridian [9]. The state is divided into three senatorial districts, notably Edo North, Edo Central, and Edo South Senatorial Districts ([9], [10]). Edo State has a population of 3,233,366 persons according to the 2006 national census[10]. Benin city has a population of 1,719,258 people [11], whereas Ekpoma and Auchi have 77,483 and 108,346 people respectively[10].

2.2 Design of Experiments

The study used a multistage sampling strategy similar to that used as in [9]. The first stage entailed taking a basic random sample of one LGA from each of the state's three senatorial districts. Oredo in Edo-south, Esan-west in Edo-central, and Etsako-west in Edo-north were the LGAs. In the second stage, a purposive sample of an LGA headquarters was used as a proxy for urban centers, with Benin City representing Oredo, Ekpoma representing Esan-west, and Auchi representing Etsako-west.

2.3 Techniques for Taking Samples and Sampling

Out of a target population of 1200, 800, and 1000 houses, 1000 households were randomly picked from Benin city, 750 households from Ekpoma, and 840 households from Auchi, using the method described as in [9], but multiplying the number of households by a factor of ten.

2.4 The Research Instrument

A structured questionnaire was used to collect data in this study because the respondents were limited to certain response alternatives, the utilization of portable electrical generators" was the title. The instrument was divided into two portions, Section A and Section B. The respondents' demographic information was collected in Section A. The respondents' level of use of a portable generator was measured in Section B, which included ten questions.

2.5 The Instrument's Administration

In the study area, 2590 questionnaires were distributed as part of the instrument. To achieve a 100% return rate, the surveys were collected on the same day they were given out. Only 2579 copies of the questionnaire were completely filled out, while 11 copies were incomplete and were not included in the study. This represents 99.6% of the surveys delivered across the same research area.

The respondents' level of use of a portable generator was analyzed using descriptive statistics such as percentage.

3. RESULTS AND DISCUSSION

The demographic data of the respondents is shown in Table 1

Table 1: Demographic data of Respondents

Age		Sex		Educational Status	
18-35	1121(43.5%)	Male	1767(68.5%)	Illiterate	725(28.1%)
36 and above	1458 (56.5%)	Female	812(31.5%)	Literate	1854(71.9%)
Total	2579		2579		2579

As seen in Table 1, the biggest percentage of respondents to the survey were those aged 36 and up (56.5%). This is due to the fact that the majority of homeowners are in this age group. Only 28.1 percent of the respondents were illiterate, whereas 71.9 percent were literate, as seen in Table 1. Literacy is defined as the capacity to read and write, whereas illiteracy is the opposite. Table 1 shows that male respondents outnumber female respondents by 37%. Table 2 shows the replies of the evaluated respondents regarding the level of use of a portable energy generator.

Table 2: The evaluated respondents responses to the level of use of portable electricity generators

S/N	Level of use of portable electricity generators		
	Items	YES	NO
1	What type of house do you live? (A) single room apartment (B). Two bedroom apartment (C), three bedroom apartment (D) Four bedroom apartment and (E) a bungalow.	 256(9.9%) 458(17.8%) 982(38.1%) 231(8.9%) 652(25.3%)	 2323(90.1%) 2121(82.2%) 1597(61.9%) 2348(91.1%) 1927(74.7%)
2	Do you use electricity generator?	2579(100%)	0(0%)
3	Is your generator serviceable?	2367(91.8%)	212(8.2%)
4	What do you use generator for? A. domestic purposes B. business only C. both domestic and business	1824(70.7%) 110(4.3%) 645(25%)	755(29.3%) 2469(95.7%) 1934(75%)
5	Do you use the same generator for both domestic and business purpose?	120(18.6%)	525(81.4%)
6	What type of generator do you use? A. petrol generator (B) diesel generator (c) solar	 2069(80.2%) 442(17.2%) 68(2.6%)	 510(19.8%) 2137(82.8%) 2511(97.4%)
7	If it is A or B or C above which of the range of power rating does it fall. (A) less than or equal to1200W, (B) 1800-2400W, (C) 2500-3000W (D) 3500-5000W and (E) Above 5000W	 238(9.2%) 466(18.1%) 1201(46.6%) 538(20.9%) 136(5.2%)	 2341(90.8%) 2113(81.9%) 1378(53.4%) 2041(79.1%) 2443(94.8%)
8	Why the choice of the power rating? (A) it is because of affordability although it is not meeting with your lightings and appliances power requirement. (B) it is because of affordability and its meeting with your appliances power requirement.	 1743(67.6%) 836(32.4%)	 836(32.4%) 1743(67.6%)
9	If it is yes in in 6A above, what do you do to make up the power requirement? (A). Nothing. (B). Switching off some lightings and appliances. (C) Using solar for make up.	 765(43.9%) 932(53.5%) 46(2.6%)	 978(56.1%) 811(46.5%) 1697(97.4%)
10	Will you welcome development of alternative power supply to boost the power requirement of your home or business.	2559(99.2%)	20(0.8%)

Table 2 shows that single, two, three, four, and five bedroom flats, as well as a bungalow, are occupied by 9.9%, 17.8%, 38.1 percent, 8.9%, and 25.3 percent of the population, respectively. More specifically, generators are used in every household in Edo state's metropolitan regions, with 91.8 percent serviceable and 8.2 percent non-serviceable generators, respectively. The epileptic power supply from the electrical distribution corporation or national grid is causing this widespread use of generators. As shown in Table 2, 1,824 individuals (70.7 percent) use generators for residential purposes, 110 people (4.3 percent) for business, 645 people (25 percent) for both domestic and business purposes, and 18.6 percent use the same or one generator for both domestic and business purposes.

Around 80.2 percent, 17.2 percent, and 2.6 percent of people utilize gasoline generators, diesel generators, and solar energy, respectively. The power ratings of the generators of 9.2 percent, 18.1 percent, 46.6 percent, 20.9 percent, and 5.2 percent users, respectively, are less than or equal to 1200W, 1800-2400W, 2500-3000W, 3500-5000W, and over 5000W, as indicated in Table 2. According to 67.6% of generator users, the choice of generator power rating is based on affordability, even though it does not meet the power requirements of lighting and appliances, while the remaining 32.4 percent indicated that it is because of affordability and meeting the power requirements of their appliances, as shown in Table 2.

Around 43.9 percent of users do nothing to compensate for the power shortage, while 56.1 percent do something to compensate, namely 53.5 percent load share by not using certain appliances at the same time, for example, not using a pressing iron and a refrigerator at the same time, and 2.6 percent use solar energy to compensate, as shown in Table 2. 99.2 percent of people support the development of alternative power sources to meet the growing demand for electricity in households and businesses.

4. CONCLUSION

Many Nigerians have turned to backup power sources such as petrol generators, diesel generators, and solar-powered generators due to fluctuations in power supply and, in certain cases, a lack of power from the electrical distribution company or the national grid. According to the findings of this study, generators are used in every household in Edo state's urban zones, with 91.8 percent of serviceable generators and 8.2 percent of non-serviceable generators, respectively. Gasoline generators are the most regularly used or requested backup power source, with generators having a rated output of 2500-3000W being the most typical. To fulfill the increased demand for electricity in homes and businesses, almost everyone in Edo state supports the development of alternative energy sources.

REFERENCES

[1] P. Okafor. (2018). Source Power Generators Intro: Diesel & Petrol Generator.[Online]. Available:https://www.naijatechguide.com/2007/09/as-we-wait-for-constant-power- supply.html

[2] F. Asu. (2017). Heavy use of generators puts Nigeria's climate plans in jeopardy. [Online]. Available: http://punchng.com/heavy-use-of-generators-puts-nigerias-climate-plans-in-jeopardy/

[3] L. Mark. (2018). Hurricane preparedness: Protection provided by power generators. [Online]. Available: https://www.wpowerproducts.com/news/hurricane-preparedness-protection-provided-by-power-generators/

[4] S. D. Panjaitan, Y. Sukandar, and B. Sitorus, Comparative study of electricity generation fueled by gasoline, liquefied petroleum gas and biogas from Municipal Solid Waste. International Journal of Electrical and Computer Engineering, Vol.3, No. 6, pp.762-769, 2013.

[5] H. U. Ugwu, B. N. Nwankwojike, E. A. Ogbonnaya, and E. J. Ekoid, Energy and economic losses due to constant power outages in Nigeria, Nigerian Journal of Technology, Vol. 33, No. 2, pp.181-188, 2012.

[6] M. Norhisam, R. Suhairi, V. Aravind, F. M. Nashiren, T. Hanamoto, H. Yamada and Y. Shirai, Performance improvement of a portable electric generator using an optimized bio-fuel ratio in a single cylinder two-stroke engine, Energies, Vol. 4, pp.1937-1949, 2011.

[7] M. Koc, Y. Sekmen, T. Topgu and H. S. Yucesu, The effects of ethanol unleaded gasoline blends on engine performance and exhaust emissions in a spark ignition engine, Review Energy, Vol. 34, pp.2101-2106, 2009.

[8] C. M. Bahattin, B. Ozdalyan and F. Alkan, The use of pure methanol as fuel at high compression ratio in a single cylinder gasoline engine, Fuel, Vol. 90, pp.1591-1598, 2011.

[9] O. Ojogho and O. S. Imade, Households Food Consumption Pattern in Edo State, Nigeria: Application Of Alternative Demand Model, Journal of Research in Forestry, Wildlife & Environment, Vol. 12, No. 3, pp162-171, 2020.

[10] O. M. Ojeifo and O. E. Joseph, Categorization of Urban Centres in Edo State, Nigeria IOSR Journal of Business and Management, Vol. 3, No. 6, pp.19-25, 2012.

[11] K. Dimuna, and A. Olotuah, Assessing Residents Satisfaction with Planning and Neighbourhood Facilities of Some Public Housing Estates in Benin City, Nigeria, Journal of Educational and Social Research, Vol. 9, No. 1, pp. 21-28, 2019.

Paper ID: 9812

International Conference on Mechanical, Manufacturing and Process Engineering (ICMMPE – 2022)

Organizer: Faculty of Mechanical Engineering, Dhaka University of Engineering & Technology (DUET), Gazipur, Bangladesh

Website: https://icmmpeduet.com/

Title: An Environment Friendly Combined Method of Axial Hydro Floating and Kinetic River Turbine Based on Water Depth

Md. Najibullah[1], Md. Mominur Rahman[2], Mizanur Rahman[3], Md. Moine Mu Shabbir[4] , Md. Arif Sarkar[5] and Kazi Firoz Ahmed[6]

[1,2,3,4,5,6]Department of Electrical & Electronic Engineering, Faculty of Engineering, American International University-Bangladesh, Dhaka 1229, Bangladesh

E-mail: [1]najib.ullah.169@gmail.com, [2]mominur18aiub@gmail.com, [3]mizanur.aiub23@gmail.com, [4]shabbir.aiub163@gmail.com, [5]arifsarkar5838@gmail.com, [6]k.firoz@aiub.edu

ABSTRACT

Abstract: Converting from conventional energy production methods to renewable and other green energy worldwide is now holding a strong position in power generation. Escalation of burning fossil fuels has already augmented the greenhouse gasses, mutilated the ozone layer, and deteriorated our descendants' existence on our very own planet [1]. The use of renewable natural resources such as solar energy, wind energy, and hydro energy on full scale instead of fossil fuels, coal, and atomic energy will be commendable. Approximately 20% of the total energy consumption worldwide is now from renewable energy [2]. Many of the riverine countries are blessed with spontaneous water flow along with strong streams from rivers throughout the year. The continuous flow of water generates a stream, which can be used for rotating turbines, and will help to produce green energy [3]. Several hydro turbine methods has been implemented so far. Here two types of hydro turbines is going to be implemented together for higher energy production. One of the turbines is a floating axial hydro turbine, which will be implemented on the shallow water surface and, another turbine is a kinetic river turbine, which will be situated on the river bed. The system will use two separate energy, kinetic and potential energy, from the stream as well as the turbine blade, will make this operation viable. Depth of water will play a prominent role for implementation. Maximum electric power production from the system can be obtained by following proper block diagram.

Keywords: hydrokinetics, axial hydro turbine, water flow, turbine blade, working principle, Pico hydro turbine, structural affiliation, energy production.

1. INTRODUCTION

In quotidian life water is indispensable. People utilize water for different purposes, such as drinking, household work, production in industry, cooling machinery, and so on. Besides Sun, the existence of life without water can't be imagined. Water is obtained from different founts. The ocean is the largest source of freshwater among these. On the mainland Rivers, ponds, canals, and lakes are the main sources of freshwater. All these sources contain stagnant water except the river. Many of these rivers are generating huge currents because of continuous water flow in a unidirectional way. Considering water flow as a fount can be a very green source of energy to rotate the turbine of an electricity generator. The worldwide spread of enhancing renewable and green energy concepts suggests the water flow of rivers is undoubtedly a green source to produce energy. The utilization of water flow for producing electricity will minimize the mining and consuming underground fuel, coal, natural gas, and other conventional sources. As well as it may reduce the emission of greenhouse gas and carbon dioxide [4]. It will help to mitigate the upcoming catastrophic damage by reducing global warming.

The purpose of using the stream of water flow to rotate the turbine blade of hydro turbine [5]. Two types of turbine, Axial Hydro Floating, and Kinetic River Turbine will be used. To ensure the maximum production of electric energy the project will rely on two eminent criteria. The first one is the location and the second one is water depth. Based on variation of water flow the installation process of the two turbines will be varied. The combined system will be useful for remotest areas that are not connected with the main grid power supply. As most of the islands apart from the mainland and surrounded by river water, are sometimes deprived of electricity, because of the high cost of transportation and other challenges. Hydroelectric turbine installation will enlighten those remotes area as well as the mainland.

2. METHODOLOGY AND MODELING

The block diagram of Fig.1 will be followed as the basic concept of energy production. Water flow is mandatory because the speed of water will rotate the turbine blade, and

the rotating turbine blade will deliver force to move the belt pulley of a generator.

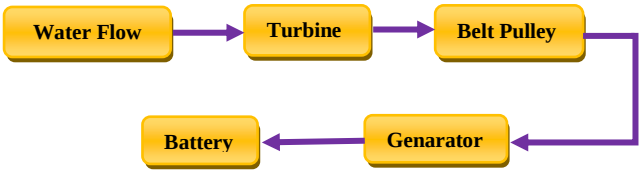

Fig. 1: Block Diagram of Combinational Hydro Turbine

Through this process, electricity will be generated. The produced electricity from the generator will be stored in a battery. Two different types of turbines have identical operational differences but follow the same modus operandi to generate electricity. A further case study is going to take place throughout the paper.

3. AXIAL HYDRO FLOATING TURBINE

The utilization of hydro floating turbine lies in its floating characteristic, and mobility in terms of implementation. Consumption of the energy from river water flow might be viable by selecting an axial hydro turbine.

3.1 Working Principle

The axial hydro turbine is one of the typical types of turbine floating on the river water with the support of floating materials. A wooden structure or plastic will be suitable for floating above the water and protect the full structure from submerging. The turbine blade is made of thin material. Moreover, a wooden turbine or steel turbine could be applicable for the turbine blades. More the lighter in weight more the rotation will be gained. Which will ensure the maximum rotation of the turbine. The whole structure represents a cylindrical shape. When the structure is placed in water the turbine blade will partially sink in water. The stream of river water flow will hit the turbine blade and give a primary rotational force [6]. This force will rotate the turbine blade as well as the shaft. The empty spaces between the blades uplift some quantity of water during the continuous rotation. This remaining water inside the hollow space of each pair of two blades will rotate the turbine with the help of containing water's potential energy. So there is gotten the additional speed, first one stream kinetic energy, the second one is the potential energy of remaining water between blades.

$$P_{maximum} = P_{kintetic} + P_{potenial} \quad (1)$$

The main calculation of maximum power will be obtained from equation (1). Here the resultant power is the summation of power absorbing from kinetic and potential energy respectively from two kinds of turbines..

3.2 Structural Affiliation

The simple structure of the axial hydro turbine makes it easy to transport. It can perform well on flowing freshwater sources such as rivers. Besides the flowing water of the water drain at a constant speed can be suitable location. The structure gives flexibility for any kind of wastage material, dust floating with the water will easily pass through under the turbine blade easily.

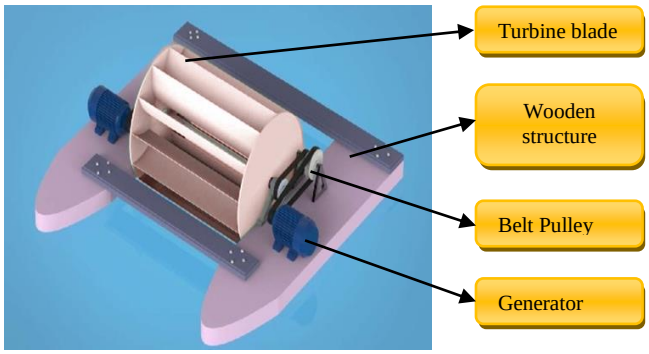

Fig. 2: 3-Dynamic design of hydro turbine solely

On this facile machine has curvature blades in angular position, giving the mobility of passing any kind of obstacle on its way [7]. Because the turbine established between the two legs creates a space for objects on its way. From Fig.2, a clear visualization is being developed of the mechanism. The space between the two adjacent blades is designed such as it can uplift some quantity of water during rotation equations consecutively.

3.3 Implementation Observation

- Remains floating above the water surface always.
- Efficient enough in generating rotational speed with the kinetic of water flow and potential energy of uplifting water between two adjacent blades.
- The ohmic losses perturb because of using wire quality from generator to battery storage.
- Friction losses happened for unsteady water stream. The direction of stream skewed with times.

Surrounding factors are notable such as wind flow cause variation in rotational speed of turbine blade.

4. AXIAL HYDRO FLOATING TURBINE

Hydro kinetic river turbine concept is developed based on the concept of variable water speed on a river. Because depth is an issue for variation of speed. The fluctuation of water flow, temperature, and disturbance in surface tension might hamper performing the floating turbine.

4.1 Working Principle

The kinetic turbines utilize the underwater kinetic energy. Because the structure will be situated on the deep riverbed. The existing model of kinetic hydro turbine [8] is simple as a pipe valve connected with the main structure. As the continuous water flow passes through the pipe valve towards the turbine blade. The flow of water between the blades keeps rotating the turbine at a constant speed. Besides the harness of deep-water is much lesser than the surface water. It gives a solid advantage of using this turbine.

When the term kinetic turbines come it is needed to describe the reason behind it. Basically, the kinetic energy from water flow in the depth of river water is obtained at a large scale. And from the earlier discussion, the whole structure of the turbine is placed on the riverbed. For this, the kinetic energy of flowing water inside the pipe valve supplies the rotational speed of the turbine blade. The energy can be calculated by applying the equation described bellow

$$Kinetic\ Energy = ½\ mv^2 \quad (2)$$

Using the above equation (2) kinetic energy of water stream will be calculated, as well as the rotational speed and power generation from the turbine are interrelated.

4.2 Advantages and Key Features

The wasted water flowing through the drain from our home, industry, and sky rain by the drain. This drain water is capable enough to deliver the rotational speed for a floating Hydro Turbine. The produced electricity by following this method can be produced definitely coming from a green natural source. On the other hand, the coldest area in the world might freeze the surface water during the winter season of a river but under the ice coat, there is always an available water flow at a certain depth. In those harsh weather and location, the Kinetic River turbine will be most suitable. The amount of produced electricity can enlighten a house even a small workshop. The generated electricity can be used for future use by storing it in a cell battery. Furthermore, the proposed turbine model implementation cost is relatively half of the water dam construction-based production.

The structural implementation and operation of kinetic River Turbine will follow the following block diagram

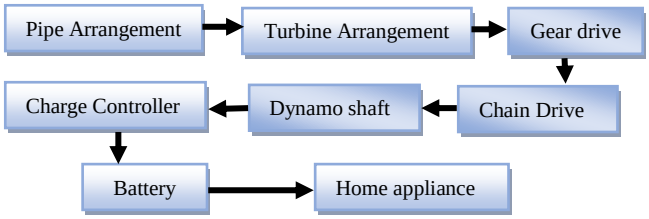

Fig. 3: Block diagram of Hydro Kinetic River turbine

The structure is on the riverbed and makes balance with the stream and holds the structure stability a frame is made of steel. In the time of making structure depth of water should be considered. Because the structure will survive against the pressure of water as well as the stream speed. A prototype is shown below figure4

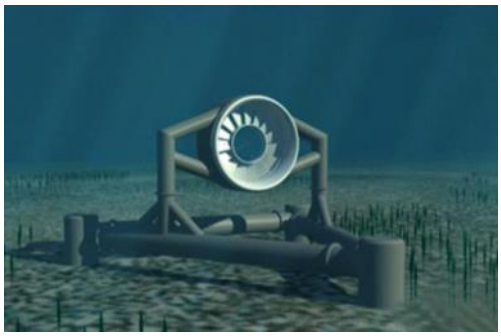

Fig. 4: 3D prototype of a pico-hydro kinetic turbine

Among other types of kinetic river turbine, Pico hydro kinetic turbine needs the small space with respect to the large scale hydropower plant, which uses the potential energy of deep water, and turns the turbine. As the RPM will increase the rotation of the turbine blade will increase. Through this process, the goal of the proposed system will be feasible. Besides, the stream speed at the nadir point of the river is approximately remains constant always, because the water deep down remains quietude.

5. SPEED VARIATION METHODOLOGY OF WATER DEPTH

The speed of water is basically the speed of the wave. It's varied from shallow water to deep underground water [9]. The wavelength of ripple on the upper surface is much larger in scale than the underground wave. The speed can be calculated from below equation

$$v^2 = g\lambda/2\pi + 2\pi\gamma/\lambda\rho \quad (3)$$

Here, 'v' is the speed of water. Which directly depends on wave length 'λ'. And 'g' is the gravitational field strength.

The equation has basically two parts. From the equation (3), the first part for deep water

$$v^2 = g\lambda/2\pi \quad (4)$$

And remaining part of the equation for the shallow water,

$$v^2 = 2\pi\gamma/\lambda\rho \quad (5)$$

By considering some characteristics of water, finally the wave speed equation be like

$$v_{shallow} \approx \sqrt{(gh)} \quad (6)$$

Besides, the final equation (5) suggests that dipper the river will increase of speed. Here 'h' is the height or depth of the water. The whole process can be represented through the figure.5.

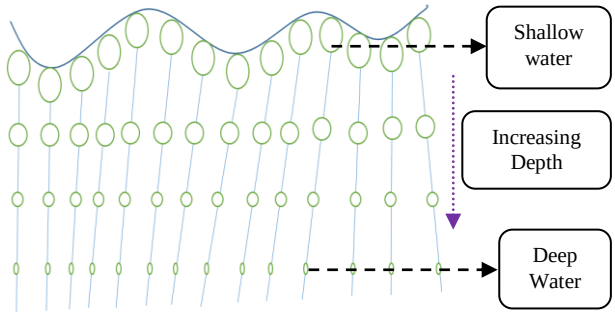

Fig. 5: Speed variation in terms of depth

Without considering the density of water, it is clearly explained that the upper surface of water flows at comparatively lower speed than the deep down river.

6. SPEED VARIATION METHODOLOGY OF WATER DEPTH

As it early mentioned that the water depth is a prominent factor to implement the combined hydro floating and kinetic hydro turbine. From figure.5 the idea of speed ascending with increasing depth is developed. By using this method one can implement the proposed combined system to gain the apex usage of green electric energy from the river water.

The Floating Axial hydro turbine is being selected based on its characteristics and operational efficiency achievement, which will be situated on the shallow upper surface of the water. And the Kinetic Hydro Turbine is implemented on the riverbed for getting maximum efficiency from the combined system.

Implementation of the Kinetic Hydro turbine is plausible in any depth with strong support instead, it is implemented only on the riverbed because the water speed, as well as kinetic energy of water flow, is highest at the nadir of the river. As a result, it will help to gain maximum electricity production. The terms will be conspicuous after scrutinizing the graphs below.

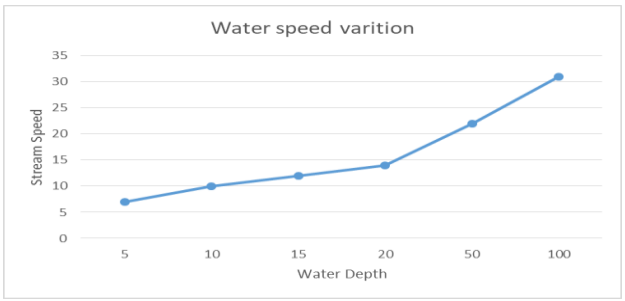

Fig. 6: Speed variation of combinational hydro turbine with the augment of depth

From the above graph Fig.6, it is clear that water speed is increasing gradually when the depth is increasing. So the wise decision for consuming maximum power generation, the setup of the kinetic hydro turbine will be placed at the nadir point of the riverbed.

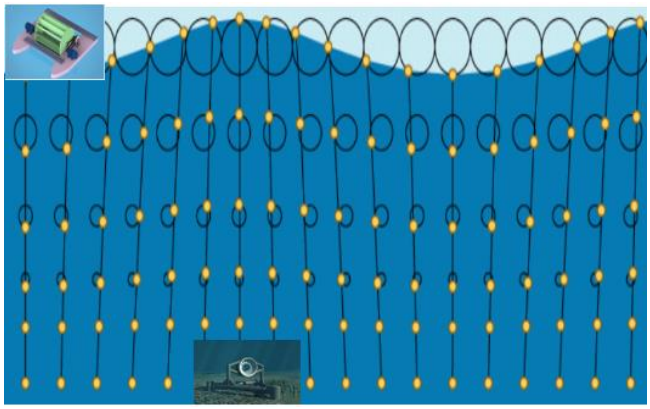

Fig. 7: Prototype Implementation of Combinational Hydro Turbines both in surface and river bed respectively

The prototype visualization of the two different types of hydro turbines can be implemented in river water as shown in the above figure.7.

7. DATA AND RESULTS ANALYSIS

The goal of this combinational hydro turbine is to gain maximum electricity output. Implementation of the floating axial hydro turbine delivers a chart of power production like the bellow figure

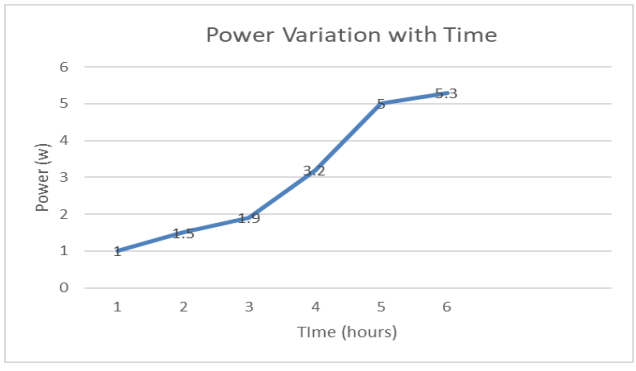

Fig. 8: Variation of combinational hydro turbine's power with consecutive 6 hours

The above figure suggests that power production is increasing with time. A coastal river generates fluctuation in the height of water depending on High tide and Low tide time variation. As a result, when high tides begin to form, the speed is increasing with time, as well as the RPM of the turbine waxes, for the 6 hours, then it is decreasing, for the

next 6 hours. This process is recurring after 6 hours throughout the day.

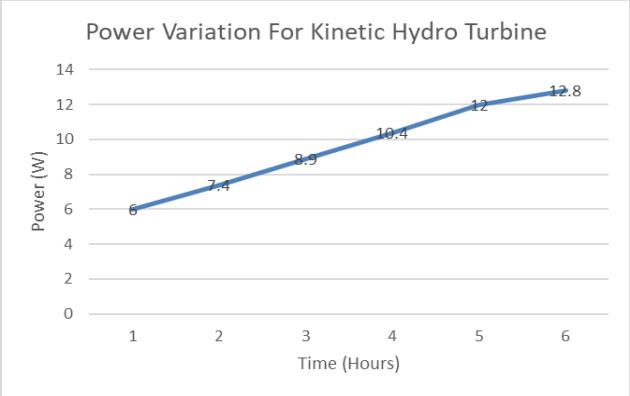

Fig. 9: Variation of kinetic hydro turbine solely in consecutive six hours

The implemented Kinetic hydro turbine is also in operating mode at the same time at the same location under the surface water located at the riverbed. That means the structure of the kinetic hydro turbine is placed in the same location just under the floating hydro turbine at the nadir depth. The cross-flow of water through the tube of the turbine connected with machinery will help to rotate the turbine at maximum R.P.M. So the required power generation could be produced. The output of power is going to be achieved by following the above figure.9 as well.

Then combined system could be sum up the respective obtained power of two identical turbines. It delivers the extended power output from both hydro turbines. In figure.10 the graph is presented with the data table as well.

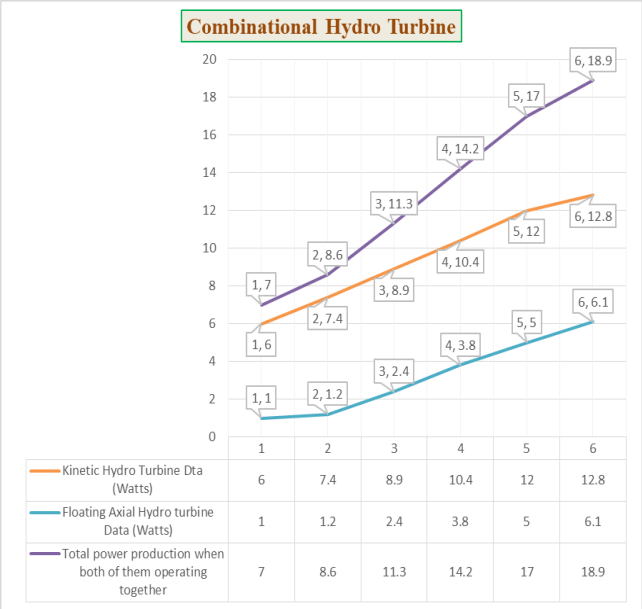

	1	2	3	4	5	6
Kinetic Hydro Turbine Dta (Watts)	6	7.4	8.9	10.4	12	12.8
Floating Axial Hydro turbine Data (Watts)	1	1.2	2.4	3.8	5	6.1
Total power production when both of them operating together	7	8.6	11.3	14.2	17	18.9

Fig. 10: Overview of obtained power from the combined hydro turbine

Analyzing the above Fig.10, the obtained energy from the combined system is impressive. The line remains always upper than the two different types of hydro turbines. The lowest power was **7 watts**, highest power was **18.9 watts**. If one used either one of the turbines then the output will be lesser than the combined system. So it is more effective when it's acting as a combined system.

8. DISCUSSION AND KEY FINDINGS

The value was measured with a time variation. All the graphical representation regarding result analysis was performed in MS Excel, are indicating the clear observation of the required goal. For the prototype design Illustrator was used for providing real-life visualizations of the proposed model. The equation for water depth was collected from an authentic source. Which was helpful to reach one of the major goals of the proposed system.

By analyzing the power variation curves it is clear that the combined system is producing much energy in scale, which fulfills another major goal. All the concepts was stood still on an environment-friendly green energy basis. The block diagram will be helpful for the implementation of the combined hydro turbine system. The water depth discussion is notable, an essential knowledge to know the cause and effect of the relation between depth and turbine positioning, in terms of maximum gain.

9. COMPARISON WITH TRADITIONAL MODELS

Hydropower generation is a well-known electricity generation method. A lot of projects have been undertaken in this sector. Most of the existing methods and models are very costly and consume massive space in implementation scale. Sometimes, very time-consuming, such as making a dam through the heart of the river, existing complex designing of kinetic turbines as well.

The proposed combined hydro turbine system implementation is an extended idea of using green energy, without conflicting with any natural balance. No dam is needed to be implemented on a river's natural flow, making no obstacle, no submerging any new area [10]. But the main issue to choose the proposed system for its power generation efficiency rate is much more satisfying in a small scale generation. This prototype is related to the Pico hydropower generation system.

10. LIMITATION AND FUTURE SCOPE

The Combined Axial Hydro Turbine and Kinetic Hydro Turbine is the idea developed from the Pico-hydro turbine arena. Though it is a concept for utilizing the maximum green resource of water available on earth. The water flow is a must for the successful gain from this concept. But most of the rivers around the world are losing depth for various human-made disasters, it will face a challenging situation to implement the system in every river. The

coastal river's water depth variation over time in a single day will cause hampering the smooth production of power. The implementation of the kinetic hydro turbine needs a strong base to hold it still against the scary stream and pressure underwater as well. A synchronizer is needed to add before making the produced electricity suitable for consumer usage. The variation of power production in the two different types of hydro turbine needs to be synchronized, for this purpose further development is required.

The consciousness about natural resource use for energy production and cost reduction, lead the concept in a huge scale implementation from home to home, in remote areas, hilly areas, where grid connection of electricity was unavailable.

11. CONCLUSION

The vast industrialization consumes a greater percentage of total power production throughout the world [11]. Inhabitants should be aware of the planet first over industrialization. Because industrialization by impairs natural harmony, cannot bring any real development. So to keep world civilization in a harmonious state with nature, people should have to convert from the typical power generation methods to environment-friendly renewable energy concept. If the combined Floating Axial Hydro Turbine and Kinetic Hydro Turbine concept can develop there will be a maximum 18.9 watts/hour can be produced. It will be very useful for any household in remote areas where hardly access of electricity grid connection have. Considering implementation reliability and other environmental issues the Combined Method of Hydro Floating and Kinetic River Turbine is very suitable. Besides, the usage of fossil fuels, natural gas will reduce as well as the emission of greenhouse gas will decrease. That will protect our planet from natural catastrophe for future generation as well.

REFERENCES

[1] Perera FP. Multiple Threats to Child Health from Fossil Fuel Combustion: Impacts of Air Pollution and Climate Change. Environ Health Perspect. 2017 Feb; 25(2):141-148. doi: 10.1289/EHP299. Epub 2016 Jun 21. PMID: 27323709; PMCID: PMC5289912.

[2] M. Piekut, "The Consumption of Renewable Energy Sources (RES) by the European Union Households between 2004 and 2019," Energies, vol. 14, no. 17, p. 5560, Sep. 2021, doi: 10.3390/en14175560.

[3] Ž. Kos, B. Đurin, D. Dogančić, and N. Kranjčić, "Hydro-Energy Suitability of Rivers Regarding Their Hydrological and Hydrogeological Characteristics," Water, vol. 13, no. 13, p. 1777, Jun. 2021, doi: 10.3390/w13131777.

[4] Garba Danjumma Sani, Abubakar Ibrahim, Suleiman Sahabi, Bashar Badamasi Lailaba, 2019, "Renewable Energy: Environmental Impacts and Economic Benefits for Sustainable Development", International Journal of Engineering Research & Technology (IJERT) Volume 08, Issue 08 (August 2019).

[5] A. H. Elbatran, Mohamed Walid Abdel-Hamed, O. B. Yaakob, Yasser M. Ahmed, 2015, "Hydro Power and Turbine Systems Reviews", Vol. 74 No. 5: Special Issue on Ship and Offshore Engineering .

[6] Štefan Tkáč, "Hydro power plants, an overview of the current types and technology," in Selected Scientific Papers - Journal of Civil Engineering, Volume 13: Issue s1, 30 Mar 2018, doi: 10.1515/sspjce-2018-0011

[7] Mominur Rahman, Abu Shufian, Md. Najibullah, Md. Momin Miah Hridoy, "Design and implementation of axial hydro turbine", in NSysS '19: Proceedings of the 6th International Conference on Networking, Systems and Security, pages 79–87, December 2019. doi:10.1145/3362966.3362973

[8] A Ruopp, A Ruprecht, S Riedelbauch, G Arnaud, I Hamad, "Development of a hydro kinetic river turbine with simulation and operational measurement results in comparison", in 27th IAHR Symposium on Hydraulic Machinery and Systems (IAHR 2014), Volume 22, 2014. doi:10.1088/1755-1315/22/6/062002

[9] Miles, J. (1966). Bores, Breakers, Waves and Wakes. By R. A. R. TRICKER. Mills and Boon, 1964. 250 pp. 35s. Journal of Fluid Mechanics, 24(3), 620-622. doi:10.1017/S0022112066210867

[10] D. Li, D. Lu, E. Moran, and R. da Silva, "Examining Water Area Changes Accompanying Dam Construction in the Madeira River in the Brazilian Amazon," Water, vol. 12, no. 7, p. 1921, Jul. 2020, doi: 10.3390/w12071921.

[11]T.Berglund, L.Modén, "Optimization of the Power Production System Taking into Consideration Security in Supply, Load and Different Types of Production", Electrical Load-Curve Coverage, Elsevier, 17 November 2013